europhysics
conference
abstracts

1992 International Conference on Plasma Physics

Joint Conference of the

9th Kiev International Conference on PLasma Theory
and the
9th International Conference on Waves and Instabilities in Plasmas
combined with the
19th EPS Conference on Controlled Fusion and Plasma Physics

Innsbruck, 29 June - 3 July 1992
Editors: W. Freysinger, K. Lackner, R. Schrittwieser, W. Lindinger

Contributed Papers, Part III

ned by: The European Physical Society
Editor: Prof. K. Bethge, Frankfurt/M
ging Editor: G. Thomas, Geneva

VOLUME 16C Part III

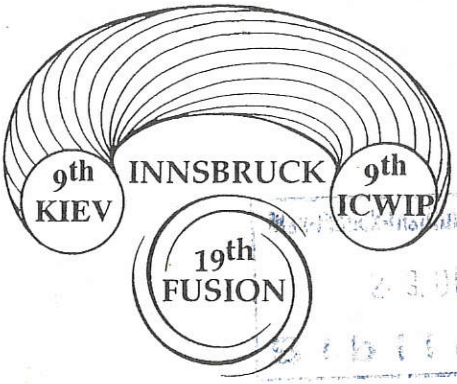

Bibliothek

Topics 9-13

1992 International Conference on Plasma Physics

Joint Conference of the

9th Kiev Interational Conference on Plasma Theory

and the

9th International Conference on Waves and Instabilities in Plasmas

combined with the

19th EPS Conference on Controlled Fusion and Plasma Physics

Innsbruck, 29 June - 3 July 1992
Editors: W. Freysinger, K. Lackner, R. Schrittwieser, W. Lindinger

Contributed Papers, Part III

07795-92

EUROPHYSICS CONFERENCE ABSTRACTS is published by the European Physical Society, © 1992

Reproduction rights reserved.

This volume is published under copyright of the European Physical Society. We wish to inform the authors that the transfer of the copyright to the EPS should not prevent an author from publishing an article in a journal quoting the original first publication or to use the same abstract for another conference. This copyright is just to protect EPS against using the same material in similar publications.

The Proceedings may be purchased from the Institute for Ion Physics, University of Innsbruck, Technikerstr. 25, A-6020 Innsbruck, Austria

PREFACE

The 1992 International Conference on Plasma Physics is held as a joint conference of the 9th Kiev International Conference on Plasma Theory and the 9th International Congress on Waves and Instabilities in Plasmas with the 19th EPS Conference on Controlled Fusion and Plasma Physics in Innsbruck, Austria, from 29 June to 3 July 1992. The conference is organized by the Institute of Ion Physics of the University of Innsbruck.

The programme, format and schedule of the Conference were determined by the International Programme Committee, which also selected the plenary and topical invited lectures based on suggestions from the International Advisory Committee of the ICPP and from other members of the scientific community. Some topical invited lectures were selected from among the contributed papers. The programme included 12 plenary, 35 topical invited lectures presented orally, and 532 poster contributions.

Innsbruck, May 1992 — The Editors

Acknowledgement:

The conference organizers acknowledge the financial support of the following agencies and institutions:

The Austrian Federal Ministry of Science and Research
The State Government ofyrol
The City of Innsbruck
The International Union of Pure and Applied Physics (IUPAP)
The Kongresshaus Innsbruck

INTERNATIONAL ADVISORY COMMITTEE

K. Appert . . . . . Switzerland
D.E. Baldwin . . . . . USA
H.A.B. Bodin . . . . . UK
T.J.M. Boyd . . . . . UK
F.F. Cap . . . . . Austria
F.F. Chen . . . . . USA
B. Chirikov . . . . . Russia
A. Dalgarno . . . . . USA
J.M. Dawson . . . . . USA
F. De Marco . . . . . Italy
S. Denus . . . . . Poland
F. Engelmann . . . . . Germany
E. Fabre . . . . . France
B.D. Fried . . . . . USA
A. Gibson . . . . . UK
D. Grésillon . . . . . France
M. Haines . . . . . UK
S. Hamberger . . . . . Australia
A. Hasegawa . . . . . USA
M.A. Hellberg . . . . . South Africa
Y.H. Ichikawa . . . . . Japan
R. Janev . . . . . Yugoslavia
A.N. Kaufman . . . . . USA
P.K. Kaw . . . . . India
T. Kawabe . . . . . Japan
L.M. Kovrizhnykh . . . . . Russia
H.J. Kunze . . . . . Germany
S. Lee . . . . . Malaysia
Zhengwu Li . . . . . China
W. Lindinger (Chairman) . . . . . Austria
J. Lingertat . . . . . Germany
P. Michelsen . . . . . Denmark
G. Murtaza . . . . . Pakistan
K. Nishikawa . . . . . Japan
T.M. O'Neil . . . . . USA
A.P. Rodrigo . . . . . Argentinia
P.H. Rutherford . . . . . USA
D.D. Ryutov . . . . . Russia
P.H. Sakanaka . . . . . Brasil
K. Sauer . . . . . Germany
F.C. Schüller . . . . . Netherlands
A.G. Sitenko . . . . . Ukrainia
H.M. Skarsgard . . . . . Canada
F.W. Sluijter . . . . . Netherlands
M.P. Srivastava . . . . . India
P. Šunka . . . . . CSFR
S. Tanaka . . . . . Japan
J.B. Taylor . . . . . UK
F. Troyon . . . . . Switzerland
P. Vandenplas . . . . . Belgium
R.R. Weynants . . . . . Belgium
H.P. Winter . . . . . Austria

PROGRAMME COMMITTEE

K. Lackner (Chairman) . . . . . Germany
W. Lindinger (Vice-chairman) . . . . Austria
F. Engelmann . . . . . Germany
V.E. Golant . . . . . Russia
G. Haerendel . . . . . Germany
M.G. Haines . . . . . UK
R. Janev . . . . . Yugoslavia
G. Laval . . . . . France
T.D. Märk . . . . . Austria
D. Robinson . . . . . UK
D.D. Ryutov . . . . . Russia
K. Sauer . . . . . Germany
F.W. Sluijter . . . . . Netherlands
R.R. Weynants . . . . . Belgium

LOCAL ORGANIZING COMMITTEE

F.F. Cap (Honorary Chairman), Institute for Theoretical Physics, University of Innsbruck;
W. Lindinger (Chairman), W. Freysinger (Scientific Secretary), M. Heigl, T.D. Märk, and R. Schrittwieser, Institute for Ion Physics, University of Innsbruck;
S. Kuhn (Minutes Secretary), Institute for Theoretical Physics, University of Innsbruck.

CONTENTS

PART I	Topic 1:	Tokamaks	I-1
	Topic 2:	Stellarators	I-487
	Topic 3:	Alternative Magnetic Confinement Schemes	I-593
PART II	Topic 4:	Plasma Edge Physics	II-721
	Topic 5:	Heating and Current Drive	II-879
	Topic 6:	Diagnostics	II-1029
	Topic 7:	Inertial Confinement Fusion	II-1223
	Topic 8:	General Plasma Theory	II-1269
PART III	Topic 9:	Space and Astrophysical Plasmas	III-1565
	Topic 10:	Basic Collisionless Plasmas	III-1675
	Topic 11:	Partially Ionized Plasmas	III-1955
	Topic 12:	Elementary Processes in Plasmas	III-2053
	Topic 13:	Plasma Applications	III-2107

LIST OF TITLES

PART I

Topic 1: Tokamaks

Poster-No. Volume/Page
Title,
Author(s)

1-1 I-3
High current, high power H-modes in JET,
Jones T.T.C., Balet B., Brusati M., Bures M., Hugon M., Lawson K.D., Lomas P.J., Morgan P.D., Morsi H., Nielsen P., Sadler G., Sartori R., Start D.F.H., Summers D.D.R., Tanga A., Taroni A., Thomsen K., Ward D.J.

1-2 I-7
Influence of divertor geometry and boronization on the ELM-free H-mode confinement in ASDEX,
Ryter F., Kardaun O.J.W.F., Kus A., Vollmer O., Stroth U., Wagner F., ASDEX-, NI-Teams

1-3 I-11
VH-mode discharges in the DIII-D tokamak,
Greenfield C.M., Jackson G.L., Burrell K.H., DeBoo J.C., Lao L.L., Osborne T.H., Rettig C., Schissel D.P., Taylor T.S., Winter J.

1-4 I-15
Current scaling of plasma confinement,
Christiansen J.P., Challis C., Cordey J.G., Gormezzano C., Gowers C., Kramer G.J., O'Rourke J., Taroni A., Tibone F., Tubbing B., Stubberfield P.M.

1-5 I-19
Dependence of confinement on plasma ion species in JET,
Tibone F., Balet B., Bures M., Cordey J.G., Jones T.C.C., Lomas P.J., Lawson K., Morsi H.W., Nielsen P., Start D.F., Tanga A., Taroni A., Thomsen K., Ward D.J.

1-6 I-23
Energy confinement of FTU ohmic plasma,
Alladio F., Berton F., Bracco G., Buratti P., Tudisco O., FTU Team, Bruschi A., De Luca F., Jacchia A., Mantica P.

1-7 I-27
Global energy confinement in TORE SUPRA,
Hoang G.T., Bizarro J.P., De Gentile B., Hutter Th., Laurent L., Litaudon X., Moreau D., Peysson Y., Tonon G., Van Houtte D.

1-8 I-31
Energy confinement in the tight aspect ratio tokamak, START,
Appel L.C., Duck R., Fielding S.J., Gibson K.J., Hugill J., Li J., Manhood S.J., Morris A.W., Robinson D.C., Sykes A., Turner M.F., Valovic M., Walsh M.J.

1-9 I-35
Confinement scaling for the ASDEX L-mode in different divertor configurations,
Stroth U., Kardaun O.J.W.F., Kus A., the ASDEX-, the NI-Teams

1-11 I-39
Recycling perturbations of supershot plasmas,
Scott S.D., McCune D.C., Bell M.G., Bell R., Budny R.V., Fredrickson E., Grek B., Hill K.W., Jassby D., Jobes F., Johnson D.W., Johnson L.C., Mansfield D.K., Park H.K., Ramsey A.T., Snipes J.A., Stratton B.E., Synakowski E.J., Taylor G., Towner H.H., Zarnstorff M.C.

1-12 I-43
Simulations of beam-fueled supershot-like plasmas near ignition,
Budny R.V., Grisham L., Jassby D.L., Manickam J., McCune D., McGuire K.M., Sabbagh S.A., Scott S.D., Stotler D., Wieland R., Zarnstorff M.C., Zweben S.J.

Poster-No. Title, *Author(s)*	Volume/Page
1-13 The investigation of properties of ohmic, ion-cyclotron plasma heating in the condition of boronized tokamak first wall, *Azizov E.A., Buzhinskij O.I., Chernobaj A.P., Dmitriev V.I., Jakovenko V.P., Kanaev A.I., Kovan I.A., Krasilnikov A.V., Mirnov S.V., Monakhov I.A., Petrov A.A., Petrov V.G., Portnov D.V., Romannikov A.N., Semenov I.B., Sharapov V.M., Sotnikov S.M., Tugarinov S.N., Sharapov V.M., Zakharov A.P.*	I-47
1-15 Confinement scaling for kinetic energy in tokamak L-mode plasmas, *Takizuka T.*	I-51
1-16 The effect of current profile changes on confinement in the DIII-D tokamak, *Ferron J.R., Lao L.L., Taylor T.S.*	I-55
1-17 Heat transport with strong on/off axis heating, *Balet B., Boucher D., Cordey J.G., Muir D., Neudatchin S.V., Schmidt G.*	I-59
1-18 Energy confinement in high performance JET D-T plasmas, *Stubberfield P.M., Balet B., Cordey J.G., O'Brien D.P., Thomsen K., Von Hellermann M.*	I-63
1-19 Determination of the ion thermal diffusivity from neutron emission profiles in decay, *Sasao M., Adams J.M., Conroy S., Jarvis O.N., Marcus F.B., Sadler G., Van Belle P.*	I-67
1-21 Local power balance analysis in ohmic, ECR heated plasmas in RTP, *Konings J.A., Hogeweij G.M.D., Lopes Cardozo N.J., Oomens A.A.M., Schüller F.C., RTP Team*	I-71
1-22 Perturbative transport analysis in RTP, *Hogeweij G.M.D., Lopes Cardozo N.J., Peters M., RTP Team, De Luca F., Gorini G., Jacchia A., Mantica P.*	I-75
1-23 Experiments on heat pulse propagation generated by localized electron cyclotron heating on the WT-3 tokamak, *Tanaka S., Hanada K., Minami T., Maehara T., Makino K., Kisigami Y., Kishino T., Nakamura M., Maekawa T., Terumichi Y.*	I-79
1-24 Characteristics of heat pulse propagation at JT-60U, *De Haas J.C.M., Nagashima K., Shirai H.*	I-83
1-25 Gas puff modulation experiment on JT-60U, *Nagashima K., Sakasai A., De Haas J.C.M., Fukuda T.*	I-87
1-27 Modeling simultaneous sawtooth measurements of the thermal and energetic electron diffusivities from the TEXT tokamak, *Catto Peter J., Myra J.R., Bengtson Roger D., Wootton A.J.*	I-91
1-28 Asymmetry of radial heat pulse propagation at TEXTOR, *Krämer-Flecken A., Tokar M.Z., Waidmann G., Wolf G.H.*	I-95
1-29 Transport studies in TJ-1 tokamak from steady and perturbative methods, *Pardo C., Rodriguez-Yunta A., Vega J., Branas B., Estrada T., Ochando M.A., Tabares F.L., Zurro B.*	I-99
1-30 Magnetic turbulence measurement from pellet striations: first comparison with energy transport, *Dubois M.A., Pégourié B., Sabot R., Hoang G.T.*	I-103

Poster-No. Volume/Page
Title,
Author(s)

1-31 I-107
Transport and turbulence in TORE SUPRA ohmic discharges,
Garbet X., Payan J., Laviron C., Devynck P., Saha S.K., Capes H., Chen X.P., Coulon J.P., Gil C., Harris G., Hutter T., Pecquet A.L., Truc A., Hennequin P., Gervais F., Quéméneur A.

1-32 I-111
Study of the plasma turbulence by means of reflectometry methods in the TUMAN-3, FT-2 tokamaks,
Aleksandrov V.O., Bulanin V.V., Korneev D.O.,Sergeyev A.A.

1-33 I-115
Particle flux in a tokamak: fundamental experimental constraints on the form and relation to fluctuations,
Gentle K.W., Richards B., Austin M.E., Bravanec R.V., Brower D.L., Gandy R., Li W.L., Phillips P.E., Ross D.W., Rowan W.L., Schoch P.M., Sing D.C., Valanju P.M., Wootton A.J.

1-34 I-119
Diffusion of fast electrons after a monster sawtooth crash,
Hugon M., Bartlett D., Brusati M., Froissard P., Gormezano C., Morgan P., Porte L., Rimini F., Stamp M.

1-35 I-123
Electron temperature and density gradients across magnetic m=2 structures in RTP,
Van Milligen B.Ph., Van Lammeren A.C.A.P., Lopes-Cardozo N.J., Schüller F.C., Verreck M.

1-37 I-127
Profile consistency on FTU,
Buratti P., Zerbini M., Bracco G., Segre S.E., Zanza V.

1-38 I-131
Theory-based transport simulation of tokamaks: density scaling,
Ghanem E.-S., Kinsey J., Singer C.

1-40 I-135
Role of Alfvén-Wave filaments in tokamak transport,
Morales G.J., Ramachandran H.

1-41 I-139
Energy and current transport: symmetry breaking and degradation,
Coppi B., Pegoraro F.

1-42 I-143
On relaxation of tokamak discharges with toroidal plasma rotation,
Throumoulopoulos G.N., Pantis G.

1-45 I-147
Perturbative measurement of suprathermal electron diffusion in JET,
Gonhhalekar A., Bartlett D., Lomas P., Martin-Solis R., O'Brien M.

1-46 I-151
Measurements of MeV energy ICRF driven minority ions in JET,
Khudoleev A.V., Afanasyev V.I., Corti S., Gondhalekar A., Maas A.C., Petrov M.P.

1-47 I-155
Observation of relativistic runaway electrons by synchrotron radiation in TEXTOR,
Jaspers R., Finken K.H., Mank G., Rusbüldt D., Lopes-Cardozo N.J., Schüller F.C., Boedo J., Hoenen F.

1-48 I-159
Combined repetitive pellet injection and lower hybrid current drive experiments in TORE SUPRA,
Géraud A., Foster C.A., Pégourié B., Peysson Y., Bibet P., Chatelier M., Drawin H.W., Moreau D.

1-49 I-163
Observations of suprathermal electrons in the edge region on JET H-mode plasmas,
Bartlett D.V., Porte L., Costley A.E., Jones S.E., Smith R., Zolfaghari A.

Poster-No. Volume/Page
Title,
Author(s)

1-50 I-167
Effects of enhanced toroidal field ripple on JET plasmas,
Sadler G., Barabaschi P., Bertolini E., Conroy S., Deksnis E., Dietz J., De Esch B., Green B., Huguet M., Huart M., Jacquinot J., Jarvis O.N., Khudoleev A., Loughlin M.J., König R., Last J., Maas A., Petrov M., Putvinskii S., Sborchia C., Stork D., Tubbing B., Van Belle P.

1-51 I-171
Two-dimensional measurement of heat load on the first wall due to fast ion ripple loss in JT-60U with near-perpendicular NBI,
Tobita K., Tani K., Neyatani Y., Takeuchi H., Miura S., Nishitani T., Matsuoka M.

1-52 I-175
Profile measurements of localized fast electrons and ions in TORE SUPRA,
Basiuk V., Roubin J.-P., Becoulet A., Carrasco J., Martin G., Moreau D., Saoutic B.

1-53 I-179
Investigation of microturbulence drive and damping mechanism in DIII-D,
Rettig C.L., Peebles W.A., Burrell K.H., Doyle E.J., Groebner R.J., La Haye R.J., Luhmann Jr. N.C., Philipona R., Rhodes T.L.

1-54 I-183
Edge ion dynamics in H-mode discharges in DIII-D,
Groebner R.J., Burrell K.H., Gohil P., Kim J., Seraydarian R.P.

1-55 I-187
Investigation of the effect of large core changes in toroidal plasma rotation and radial electric field on confinement in H-mode discharges in the DIII-D tokamak,
La Haye R.J., Groebner R.J., Hyatt A.W., Scoville J.T.

1-56 I-191
Characteristic features of density fluctuations associated with the L-H-transition in the ASDEX tokamak,
Dodel G., Holzhauer E.and the ASDEX-Team

1-57 I-195
H-mode power threshold in ASDEX,
Ryter F., Stroth U., Wagner F., ASDEX-Group, NI-Group

1-58 I-199
Measurement of the toroidal motion of fine-scale density structures in JET plasmas,
Costley A.E., Cripwell P., Fukuda T.

1-60 I-203
Plasma flows and fluctuations during H-modes in TFTR,
Bush C.E., Stratton B.C., Synakowski E., Bretz N., Budny R., Darrow D.S., Durst R., Fonck R., Fredrickson E.D., Mazzucato E., McGuire K.M., Medley S.S., Nazikian R., Paul S., Ramsey A.T., Schivell J., Scott S.D., Taylor G., Wieland R.M., Zweben S.

1-61 I-207
Autooscillating L-H transitions under ECCD in T-10,
Voitsekhovich I.A., Kislov D.A., Parail V.V., Razumova K.A.

1-62 I-211
Rotation in ohmically heated tokamaks: a detailed comparison of experiment with theory,
Rowan W., Calvin M., Hazeltine R., Meigs A., Solano E., Valanju P.

1-63 I-215
Divertor plate biasing and current injection on TdeV,
Lachambre J.-L., Couture P., Boileau A., Boucher C., Decoste R., Gregory B., Janicki C., Lafrance D., Le Clair G., Liu-Hinz C., MacLatchy C., Martin F., Michaud D., Ross G.G., Stansfield B., St.-Onge M., Terreault B., Wang Z.

1-64 I-219
Edge fluctuations at regimes with improved confinement on CASTOR tokamak,
Stöckel J., Kryska L., Zacek F., Badalec J., Jakubka K., Mlynar J., Magula P., Kletecka P.

Poster-No. Title, *Author(s)*	Volume/Page
1-66 H mode induced by the biased electrode and transition of low density to high density with optimized gas puffing in HL-1, *Ran L.B., Yang H.R., Yang S.K., Zhang S.X., Zheng Y.Z., Wang E.Y., Wang Z.H., Yao L.H., Sun S.Q., Qin Y.W., Dong J.F., Deng Z.C., Deng H.C., Guo G.C., Jiang Y.X., Li H.Z., Li K.H., Zuo H.N., Yang J.W., Yang Q.W., Huang K.Q., Yuan C.J., HL-1 Team*	I-223
1-67 ELM precursors in JET, *Ali-Arshad S., Campbell D., Colton A., Cripwell P., De Kock L., Kramer G.J., Nave M.F.F., Neill G.F.*	I-227
1-68 Reflectometry measurements of the m=1 satellite mode in L-, H-mode plasmas in ASDEX, *Serra F., Manso M.E., Silva A., Matias J., Wagner F., Zohm H., Kallenbach A., Varela P.*	I-231
1-69 A quantitative analysis of the effect of ELMS on H-mode thermal energy confinement in DIII-D, *Schissel D.P., Osborne T.H., Carlstrom T.N., Zohm H.*	I-235
1-70 Steady state H-modes in JET, *Thomas P.R., Campbell D.J., Gondhalekar A., Lowry C.J.*	I-239
1-71 ELM studies on DIII-D and a comparision to ASDEX results, *Zohm H., Osborne T.O., Burrell K.H., Chu M.S., Doyle E.J., Gohil P., Hill D.N., Lao L.L., Taylor T.S., Turnbull A.D.*	I-243
1-72 MHD stability models of edge localized modes in JET discharges, *Huysmans G.T.A., De Blank H.J., Kerner W., Goedbloed J.P., Nave M.F.F.*	I-247
1-73 Neutron profile measurements during the tritium experiments in JET, *Marcus F.B., Adams J.M., Bond D.S., Conroy S. Howarth P.J.A., Jarvis O.N., Loughlin M.J., Sadler G., Smeulders P., Van Belle P., Watkins N.*	I-251
1-74 Fuelling of JET limiter, x-point plasma by deuterium pellet injection, *Schmidt G.L., Bartlett D., Baylor L., Bures M., Edwards A., Gadeberg M., Gottardi N., Jones T., Kupschus P., Lomas P., Morgan P., Morsi H., Nielsen P., O'Rourke J., Sadler G., Start D.F.H., Stubberfield P., Tanga A., Ward D.*	I-255
1-75 Measurements of the electron source distribution and implications for particle transport, *O'Rourke J., Kramer G.J., Simonini R., Sips A.C.C.*	I-259
1-76 Particle transport during the tritium experiments in JET, *Balet B., Cordey J.G., Jones T.T.C., König R., Marcus F., Sadler G., Stubberfield P.M., Von Hellermann M.*	I-263
1-79 First results of pellet injection in ECR and ohmic heated discharges in RTP, *Oomens A.A.M., da Cruz Jr. D.F., Van Dijk G., Van Gelder J.F.M., Lok J., Rommers J.H., Tielemans A.J.H., RTP-Team*	I-267
1-80 On the bootstrap current calculations based on values of the radial electron transport, *Petrzilka V.*	I-271
1-81 Helium transport studies on DIII-D, *Finkenthal D., Hillis D.L., Wade M.R., West W.P., Hogan J.T., Burrell K.H., Seraydarian R., Groebner R.J., Gohil P., Klepper C.C., Mioduszewski P.K.*	I-275

Poster-No. Title, *Author(s)*	Volume/Page
1-83 Poloidal asymmetry of impurity in co-, counter-injection experiment at JET, *Giannella R., Christensen M., De Angelis R., Gottardi N., Lauro-Taroni L., Mattioli M., Pasini D.*	I-279
1-84 Scaling of impurity transport in JET, *Pasini D., Giannella R., Lauro-Taroni L., Magyar G., Mattioli M.*	I-283
1-85 Particle and impurity transport in JET versus neoclassical theory, *Lauro-Taroni L., Giannella R.*	I-287
1-86 Components of P_{rad} and Z_{eff} derived from X-ray spectroscopy of the main inpurities in JET, *Barnsley R., Brzozowski J., Coffey I.H., Lawson K.D., Melnick I.M., Patel A., Patel T.K., Peacock N.J.*	I-291
1-87 Effective ion charge and impurity behavior in the Frascati tokamak upgrade, *McNeill D.H., Zanza V., Mazzitelli G., Bracco G., Condrea I., De Angelis R., Orsitto F., Panaccione L., Segre S.*	I-295
1-88 Studies of impurity confinement injected by laser blow-off in the TJ-1 tokamak, *Zurro B., Vega J., Aragon F., Burgos C., Pacios L., Pardo C.*	I-299
1-89 Toroidal diffusion of injected impurities in the MT-1M tokamak, *Zoletnik S., Veres G., Bakos J.S., Bürger G., Ignacz P.N., Kardon B., Kalvin S., Kocsis G., Szigeti J.*	I-303
1-94 Long pulse operation in JET, *Brusati M., Bures M., Clements S., Ehrenberg J., Horton L., Jones T.T.C., Lawson K., Lomas P., Morgan P., Nielsen P., Sartori R., Schmidt G., Stamp M., Summers D.*	I-307
1-95 Evolution of the current profile in JET high bootstrap current plasmas, *O'Rourke J., Challis C.D., Jacquinot J., O'Brien D., Stamp M.F., Stork D., Stubberfield P., Tibone F., Tubbing B.J., Zwingmann W.*	I-311
1-96 Bootstrap current driven by alpha particles in a fusion reacting tokamak, *Chang C.S.*	I-315
1-97 Fast wave spectral properties in ITER tokamak, *Elfimov A.G., Medvedev S.Yu., Pestryakova G.A.*	I-319
1-99 Expansion of the ablated pellet substance along the magnetic field lines, *Spathis P.N. , Lengyel L.L.*	I-323
1-100 Identification of ion cyclotron emission from fusion alpha particles during JET deuterium-tritium experiments, *Cottrell G.A., Bhatnagar V.P., da Costa O., Dendy R.O., Edwards A., Jacquinot J., Nave M.F.F., Schmid M., Sibley A., Smeulders P., Start D.F.H.*	I-327
1-102 MHD limiting phenomena in high performance JET plasmas, *Alper B., Edwards A.W., Gill R.D., Pasini D., Smeulders P.*	I-331
1-103 High-β_p MHD activity in JET, *Hender T.C., Alper B., Ali-Arshad S., DeBlank H.J., Challis D.C., Gimblett C., Han J., Jacquinot J., Kramer G.J., Kerner W., Nave M.F., O'Brien D.P., O'Rourke J., Smeulders P., Stamp M., Summers D., Tibone F., Tubbing B., Zolfaghari A., Zwingmann P.W.*	I-335

Poster-No. Volume/Page
Title,
Author(s)

1-104 I-339
High β studies in the H-mode and hot ion H-mode in JET,
Stork D., Alper B., Ali-Arshad S., De Blank H.J., De Esch H.P.L., Edwards A., Hender T.C., König R., Kramer G., Marcus F.B., Nave M.F., O'Brien D.P., O'Rourke J., Smeulders P., Stamp M., Tibone F., Tubbing B.J.D., Zolfaghari A., Zwingmann P.W.

1-105 I-343
Ideal-MHD operational limits for highly elongated tokamaks,
Eriksson G., Bondeson A., Ward D.J., Hofmann F., Villard L.

1-107 I-347
Fine structure in tokamak operating region,
Li L.H., Deng C.B., Li G.X., Guo D.Q., Xie J.K., Huang R.

1-108 I-351
The high density and high β_{pol} disruption mechanism on TFTR,
Fredrickson E., Manickam J., McGuire K.M., Monticello D., Nagayama Y., Park W., Taylor G., Drake J.F., Kleva R.G.

1-109 I-355
Generation and loss mechanisms of runaway electrons following disruptions in JET,
Gill R.D., Edwards A.W.

1-110 I-359
Density turbulence and disruptive phenomena in TEXTOR,
Waidmann G., Jadoul M., Kuang G.

1-111 I-363
Electron density profile and microturbulence modification by MHD instabilities,
Brower D.L., Yu C.X., Jiang Y., Chen J.Y., Lin H., Luhmann Jr. N.C., Peebles W.A., Yang X.Z., Zhao S.J.

1-112 I-367
Investigation of tearing modes with toroidal coupling in a tokamak with arbitrary cross-section and aspect ratio,
Atanasiu C.V., Zakharov L.E., Subbotin A.A., Chudin N.V.

1-115 I-371
Internal MHD perturbations in T-10 tokamak,
Savrukhin P., Kislov D., Lyadina E., Razumova K., Bagdasarov A., Volkov V.

1-117 I-375
The sawtooth collapse in rotating JET plasmas,
Büchse R., Campbell D.J., Edwards A.W., Gill R.D.

1-118 I-379
A comparison of JET sawtooth behaviour in plasmas with co- and counter-neutral beam injection,
Edwards A.W., Bickley A., Büchse R., Challis C.D., König R., Marcus F.B., O'Rourke J., Stork D.

1-119 I-383
Investigation of the sawtooth precursor oscillations of electron density and electron temperature in ohmic tokamak discharges on TEXTOR,
Koslowski H.R., Krämer-Flecken A.

1-120 I-387
The influence of mode locking by resonant helical fields on fluctuations induced particle transport in Tokoloshe Tokamak,
Van Vurren G.W., Roberts D.E., Fletcher J.D., Hellberg M.A. , De Villiers J.A.M.

1-122 I-391
Sawtooth oscillations with q_o, the safety factor on axis, below unity,
Anderson D., Kolesnichenko Ya.I., Lisak M., Wising F., Yakovenko Y.V.

1-123 I-395
Sawtooth activity and photoneutron production,
Guo G.C., Zhong Y.Z., Dong J.F., Fu B.Z., Yang J.W., Zhang G.Y., Liang W.X., Gong D.F., Shi M.L.

Poster-No. Title, *Author(s)*	Volume/Page
1-124 MHD properties of low-aspect-ratio tokamak plasmas, *Gryaznevich M., Bondeson A., Duck R., Hender T., Robinson D.C., Sykes A.*	I-399
1-125 Excitation of fast density oscillations by pellet injection and its relation with sawtooth activity in TEXTOR plasmas, *Sato K.N., Akiyama H., Kogoshi S., Noda N., Sakamoto M., Dippel K.H., Finken K.H., Fuchs G., Koslovski H.R., Soltwisch H., KFA TEXTOR Team*	I-403
1-126 First measurements of fast MHD fluctuations in JET by ECE correlation radiometry, *Zolfaghari A., Bartlett D.V., Costley A.E., Cripwell P., Jones S.E., Kesner J., Luckhardt S.C., Porte L., Ramos J.J., Smith R.J., Woskov P.P.*	I-407
1-128 Fluid rotation and resonant magnetic perturbations in COMPASS-C, *Carolan P.G., Fitzpatrick R., Hender T.C., Morris A.W.*	I-411
1-129 A study of the difference in confinement properties between large rotating and large locked modes on Tokoloshe tokamak, *Fletcher J.D., Roberts D.E., Nothnagel G., Van Vuuren G.W., De Villiers J.A.M.*	I-415
1-130 Activation/inibition of plasma instabilities caused by resonant magnetic fields, *Araujo M.S.T., Vannucci A., Caldas I.L.*	I-419
1-131 Feedback stabilisation of resistive tearing modes in tokamaks, *Morris A.W., Fitzpatrick R., Hender T.C., O'Brien M.R.*	I-423
1-132 Nonlinear mechanism for the suppression of error field magnetic islands by plasma flow, *Parker R.D.*	I-427
1-133 Observations of beam ion losses in TFTR during TAE modes and other MHD activity, *Darrow D.S., Fredrickson E.D., Mynick H.E., Nazikian R., White R.B., Wong K.-L., Zweben S.J., Tuszewski M.*	I-431
1-135 Global Alfvén Eigenmodes in DIII-D, *Turnbull A.D., Chu M.S., Strait E.J., Heidbrink W.W., Duong H., Lao L.L., Greene J.M., Chance M.S., Taylor T.S.*	I-435
1-136 Energetic particle driven instabilities at JET, *Nave M.F.F., Borba D., Cripwell P., Von Hellermann M., Kerner W., Porcelli F., Sadler G., Smeulders P.*	I-439
1-137 Plasma characteristics during soft disruptions, *Lazzaro E., Simonetto A., Tanga A.*	I-443
1-138 Disruption behavior of plasma and vacuum vessel in JT-60U, *Neyatani Y., Ushigusa K., Matsukawa M., Ninomiya H.*	I-447
1-140 Discharge scenarios for the first operational phase of ASDEX-Upgrade, *Seidel U., Gruber O., McCarthy P., Cha S.S., Köppendörfer W., Krause A., Mertens V., Woyke W. and ASDEX-Upgrade Team*	I-451
1-141 Performance of the equilibrium control system for ASDEX upgrade, *Woyke W., Gernhardt J., Gruber O., Jülich A., Lackner K., McCarthy P.J., Seidel U., ASDEX-Upgrade Team*	I-455

Poster-No. Volume/Page
Title,
Author(s)

1-142 I-459
MHD equilibrium identification on ASDEX-upgrade,
Mc Carthy P.J., Schneider W., Lackner K., Zehrfeld H.P., Büchl K., Gernhardt J., Gruber O., Kallenbach A., Lieder G., Wunderlich R., ASDEX-Upgrade Team

1-143 I-463
Volt-second consumption and current ramp experiments on FTU,
Apruzzese G., Crisanti F., Frigione D., Kroegler H., Lovisetto L., Mazzitelli G., Podda S., Buratti P., Zerbini M., Romanelli F., Tudisco O.

1-144 I-467
Stabilization of axisymmetric modes and the effects of plasma deformability in elongated tokamak plasmas using active feedback coils inside and outside the vacuum vessel,
Ward D.J., Hofmann F.

1-145 I-471
Plasma performance, equilibrium and stability in spherical tokamak GLOBUS,
Belyakov V.A., Bender S.E., KavinA.A., Kostsov Yu.A., Minyaev O.A., Vasiliev V.I., Golant V.E., Levitsky A.N., Sakharov N.V., Fedorov O.V., Shakhovets K.G.

1-146 I-475
Rapid controlled shutdown of a burning plasma,
Pacher G.W., Pacher H.D.

1-147 I-479
Neutral beam heating in Alvand IIC tokamak,
Ghorannevisse M., Moradshahi M., Avakian M.

1-149 I-483
Operational start-up and vessel conditioning of the Novillo tokamak,
Melendez-Lugo L., Lopez-Callejas R., Valencia-Alvarado R., Chavez-Alarcon E., Colunga-Sanchez S., Jimenez-Dominguez H., Gaytan-Gallardo E.

Topic 2: Stellarators

Poster-No. Volume/Page
Title,
Author(s)

2-1 I-489
Confinement studies in recent NBI experiments of Heliotron E,
Sano F., Kondo K., Zushi ., Sudo S., Sato M., Mizuuchi T., Matsuura H., Hanatani K., Nakasuga M., OKada H., Besshou S., Nakamura Y., Nagasaki K., Ijiri Y., Iima M., Senju T., Yaguchi K., Baba T., Kobayashi S., Toshi K., Sakamoto K., Wakatani M., Obiki T.

2-2 I-493
Electron heat transport in the LMFP-regime for the stellarators W7-A, W7-AS and L2,
Dyabilin K.S., Gasparino U., Maaßberg H., Renner H., Ringler H., W7-AS Team, ECRH Group

2-3 I-497
Diffusive and convective transport modelling from analysis of ECRH-stimulated electron heat wave propagation,
Erckmann V., Gasparino U., Giannone L., Hartfuß H.J., Maaßberg H., Tutter M., W7-AS Team, IPF-ECRH Group, KFK-Gyrotron Group

2-4 I-501
Towards higher β in the stellarator Wendelstein W7-AS,
Renner H., Ringler H., Kißlinger J., Kühner G.and the W 7AS-Team, NBI-Group

2-5 I-505
The optimum ion confinement mode in W7-A stellarator induced by fast orbit losses of the nearly perpendicular NBI,
Gasparino U., Kick M., Maaßberg H., Renner H., Ringler H., Sardei F., W7-AS Team

Poster-No.
Title,
Author(s)
Volume/Page

2-6
Local neutral particle density in the W7-AS stellarator,
Junker J., Kick M., Maaßberg H., Sardei F., Stroth U., Zöpfel S., WVII AS-Team, NBI-Team
I-509

2-7
ECH power deposition control in CHS,
Kubo S., Idei H., Hosokawa M., Takita Y., Iguchi H., Yamada I., Arimoto H., Ueda M., Ida K., Matsuoka K., Morita S., Nishimura K., Okamura S., Takahashi C., Yamada H., Fujiwara M., Noda N., Sagara A., Sanuki H., Todoroki J., Toi K.
I-513

2-8
Density profile and particle transport of NBI-heated plasmas in the low-aspect-ratio Heliotron/torsatron CHS,
Iguchi H., Ida K., Morita S., Yamada H., Okamura S., Matsuoka *K., Akiyama R., Arimoto H., Hosokawa M., Idei H., Kaneko O., Kohmoto T., Kubo S., Nishimura K., Noda N., Ozaki T., Sagara A., Sakakibara S., Sanuki H., Takeiri Y., Takita Y., Takahashi C., Ueda M., Yamada I., Uchino K., Takenaga H., Muraoka K., Maeda M.*
I-517

2-9
Transport studies using modulation of dimensionless parameters in the advanced toroidal facility,
Murakami M., Bigelow T.S., Carreras B.A., Dory R.A., Wilgen J.B., Baylor L.R., Dyer G.R., England A.C., Hutchinson D.P., Isler R.C., Jernigan T.C., Ji H., Ma C.H., Morimoto S., Motojima O., Rasmussen D.A., Sato M., Wing W.R., Yamada H., the ATF Group
I-521

2-10
Fluctuation studies of ECH plasmas in the ATF torsatron,
Harris J.H., Hanson G.R., Wilgen J.B., Bell J.D., Murakami M., Carreras B.A., Baylor L.R., Aceto S., Bigelow T.S., Colchin R.J., Dunlap J.L., Dominguez N., Dyer G.R., England A.C., Isler R.C., Jernigan T.C., Leboeuf J.N., Lee D.K., Lyon J.F., Ma C.H., Quallis A.L., Rasmussen D.A., Thomas C.E., Uckan T., Zielinski J., Shats M.G., Likin K.M., Sarksyan K.A., Kovrizhnykh L.M.
I-525

2-11
Results of the heavy ion beam probe measurements on the advanced toroidal facility,
Aceto S.C., Schwelberger J.G., Connor K.A., Zielinski J.J., Glowienka J.C., Isler R.C., Murakami M., Bell J.D., Uckan T.
I-529

2-13
A general solution of the ripple-averaged kinetic equation (GSRAKE),
Beidler C.D., W.D. D'haeseleer
I-533

2-14
Influence of electric fields on the heating efficiency in the W7-AS stellarator,
Teubel A., Penningsfeld F.-P.
I-537

2-15
Change of adiabatic invariant in trap-detraping processes in stellarator,
Bulanov S.V., Shasharina S.G.
I-541

2-16
-particle behaviour outside the last closed magnetic surface in divertor stellarators,
Alladio F., Batistoni P., Mancuso A.
I-545

2-17
Mode activity at high plasma pressure in the stellarator Wendelstein W7-AS,
Weller A., Jaenicke R., Kißlinger J., Lazaros A., Maaßberg H., Sardei F., Schwab C., W7-AS Team, ECRH Group, NI Group
I-549

2-18
Finite ion gyro radius stabilization of ideal MHD ballooning modes in optimized stellarators,
Nührenberg J., Zheng L.-J.
I-553

2-19
Linear MHD stability computations in 3D plasmas,
Cooper W.A., Nakamura Y., Wakatani M., Gruber R., Merazzi S., Anderson D.V., Schwenn U.
I-557

2-20
Interchange modes in torsatrons, heliacs,
Jimenez J.A., Varias A., Dominguez N.
I-561

Poster-No. Title, *Author(s)*	Volume/Page
2-21 Ideal MHD studies of the TJ-IU Torsatron, *Alejaldre C., Ascasibar E., Garcia L., Lopez-Fraguas A., Varias A., Carreras B., Dominguez N.*	I-565
2-22 Progress in the studies of URAGAN-2M stability and transport properties, *Besedin N.T., Grekov D.L., Pavlichenko O.S., Shishkin A.A., Zolotukhin A.V., Beidler C.D., Kißlinger J., Maaßberg H., Rau F., Wobig H., Carreras B.A., Dominguez N., Lynch V.E.*	I-569
2-23 Destruction of Alfvén modes on a torus due to large nonaxisymmetry, *Salat A.*	I-573
2-24 Study of magnetic surfaces with islands using the PIES code, *Lopez-Fraguas A., Salas A., Reiman A.H., Monticello D.A., Johnson J.L.*	I-577
2-25 Modifies vacuum fields and compensation of islands in the stellarator W7-AS, *Beidler C., Harmeyer E., Gasparino U., Kißlinger J., Kühner G., Maaßberg H., Rau F., Ringler H., Wobig H., W 7-AS Team, ECRH-Group, W7-X Team*	I-581
2-26 Optimization of coils and a sweep coil system for W7-X, *Merkel P., Kißlinger J.*	I-585
2-27 Anisotropic pressure numerical 3D MHD equilibria, *Hirshman S.P., Cooper W.A., Merazzi S., Gruber R.*	I-589

Topic 3: Alternative Magnetic Confinement Schemes

Poster-No. Title, *Author(s)*	Volume/Page
3-1 Confinement studies of a high current density RFP in the extrap T1 upgrade device, *Drake J.R., Brzozowski, Brunsell P., Hellblom G., Karlsson P., Mazur S., Nordlund P., Welander A., Zastrow K.-D.*	I-595
3-2 Reversed field pinch equilibria and profile dynamics in a high aspect ratio geometry, *Nordlund P., Mazur S., Drake J.R.*	I-599
3-3 Stability of kink modes in a noncircular z pinch surrounded by a resistive and a conducting wall, *Jiang Z.X., Wahlberg C.*	I-603
3-4 Studies of edge plasma and impurities in extrap T1 using surface probes, *Bergsåker H., Gudowska I., Emmoth B., Tennfors E.*	I-607
3-5 Plasma spectroscopy at the extrap T1 RFP experiment, *Zastrow K.-D., Hörling P., Brzozowski J., Källne E.*	I-611
3-6 RFP set-up and confinement in SWIP-RFP device, *Zhang P., Fang S., Li J., Luo C., Li Q., Zhang S., Yi P., Xu Y.*	I-615

Poster-No. Title, *Author(s)*	Volume/Page
3-7 Ion temperature measurements in the reversed field pinch plasmas, *Schiavi A., Buffa A., Costa S.*	I-619
3-8 Generation of fast electrons by magnetic reconnection processes in RFP plasmas, *Erba M., Martin P., Ortolani S., Rossi A.*	I-623
3-9 Relaxed states for a driven reverse field pinch, *Paccagnella R.*	I-627
3-10 Electron diffusion and energy loss in a reversed field pinch plasma, *Antoni V., Bagatin M., Martines E.*	I-631
3-11 Self-similar solutions for trapping and diffusion of magnetic flux during formation of field-reversed configuration, *Bud'ko A., Karlson E.T., Liberman M.A.*	I-635
3-12 Study of current drive and particle flux in the SPEX spheromak, *Browning P.K., Cunningham G., Gee S.J., Al-Karkhy A., Martin R., Roe G., Rusbridge M.G.*	I-639
3-13 Toroidal current enhancement with strong poloidal plasma current drive in FBX-II spherical torus, *Irie M.*	I-643
3-14 Parametric investigation of the rotamak discharge in a 10-litre spherical vessel, *Donaldson N., Hahnheuser R., Jones I.R., Staines G.W., Xu S.*	I-647
3-17 An alternative configuration of axially pinched spherical torus, *Sinman S., Sinman A.*	I-651
3-18 Centrally peaked temperature profiles due to the Ettinghausen effect, *Haines M.G., Chittenden J.P.*	I-655
3-19 Viscous effects on equilibrium states of isolated z-pinches, *Miyamoto T.*	I-659
3-21 FIGARO: A large larmor radius stability code, *Coppins M., Scheffel J.*	I-663
3-22 The interrupted z-pinch dynamics modeling, *Kubes P., Kravarik J., Hakr J., Kulhanek P., Pichal J.*	I-667
3-23 Stabilization of the long wavelength sausage and kink modes of a Z-pinch by nonlinear radial oscillations, *Bud'ko A., Karlson E., Liberman M.A.*	I-671
3-25 Ideal and resistive MHD analysis of rotational instabilities in FRC, *Sakanaka P.H., Machida M., Honda R.Y., Aramaki E.A., Berni L.A., Santiago M.A.A., Tsui K.-H., Tavares-Azevedo M.*	I-675
3-26 Discrete Alfvén waves in reversed field pinches, *Sakanaka P.H., Shigueoka H., Azevedo C.A., Assis A.S.*	I-679

Poster-No. Title, *Author(s)*	Volume/Page
3-27 Hot spot X-ray and microwave emission of the DPF-78 plasma focus, *Antsiferov P., Franz D., Pfau R., Rupasov A., Schmidt H., Schulz D.*	I-683
3-28 The relative role of the macroscopic and microscopic phenomena in the plasma focus performance, *Zambreanu V., Zoita V.*	I-687
3-29 Investigation of charged-particle and X-ray pulses emitted from PF-type discharges, *Sadowski M., Szydlowski A., Zebrowski J., Al-Mashhadany E.M.*	I-691
3-30 Fusion reaction yield in focused discharges with variable energy and plasma fine structure, *Bortolotti A., Brzosko J.S., DeChiara P., Kilic H., Mezzetti F., Nardi V., Powell C., Wang J.*	I-695
3-35 Parametric study of mirror plasma based neutron source FEF-II, *Mizuno N., Yamaguchi H., Kawabe T., Hirayama S.*	I-699
3-37 Direct conversion of a fusion energy into an electric one in the DRACON-trap, *Glagolev V.M., Kuvshinov B.N., Proshin M.A., Timofeev A.V.*	I-703
3-39 Electrodynamics of plasma-molecular systems with drift motion of charged and neutral particles, *Moiseev S.S., Suyazov N.V., Yakimenko I.P.*	I-707
3-41 D-^{3}He fusion reactor based on a dipole magnetic field, *Hasegawa A., Fowler T.K., Mauel M.E.*	I-711
3-42 Proposed experiment with injection of a small angular spread beam in the oscillated REB regime, *Piffl V., Sunka P., Clupek M., Raus J.*	I-713
3-43 Confinement of laser-produced plasma by a strong external magnetic field, *Miklaszewski R., Farynski A., Fiedorowicz H., Mroczkowski M., Parys P., Pisarczyk T., Szczurek M.*	I-717

PART II

Topic 4: Plasma Edge Physics

Poster-No. Title, *Author(s)*	Volume/Page
4-1 Edge measurements in the divertor region in high density discharges at JET, *Clement S., Erents S.K., Gottardi N., Harbour P.J., Jaeckel H., Janeschitz G. De Kock L., Loarte A., Lowry C., Saibene G., Summers D., Tagle J.A., Vlases G.*	II-723
4-2 High power operation with a radiative divertor in JET, *Janeschitz G., Clement S., Gottardi N., Lesourd M., Lingertat J., Lowry C., Radford G., Saibene G., Stamp M., Summers D., Taroni A., Thomas P.R., Vlases G.*	II-727
4-3 Energy exhaust through neutrals in a tokamak divertor, *Watkins M.L., Rebut P.-H.*	II-731

Poster-No. Title, *Author(s)*	Volume/Page
4-4 Modelling of the density limit in JET beryllated limiter discharges, *Borrass K., Campbell D., Clement S., Vlases G.*	II-735
4-5 Modelling of neutral and charged helium transport in scoop of a pump limiter, *Tokar M.Z., Reiter D.*	II-739
4-6 Marfe detection by radiation monitoring and control of density limit disruptions, *Steuer K.-H., Junker W., Röhr H., Büchl K., Engelhardt W., Gruber O., Kaufmann M., Mertens V., Neuhauser J., Stäbler A., Zohm H., ASDEX-, ASDEX-Upgrade Teams*	II-743
4-7 Modelling of the ASDEX-Upgrade scrape-off layer plasma, *Bosch H.-S., Neuhauser J., Bachmann P., Schneider R., Kaufmann M., Reiter D., Baelmans T., Braams B.*	II-747
4-8 Modeling the DIII-D plasma boundary with the LEDGE code, Porter G.D., Rensink M.E., Rognlien T.D., Jong R.A., Hill D.N.	II-751
4-9 2-D edge modelling: convergence and results for next step devices in the high recycling regime, *Pacher H.D., D'haeseleer W.D., Pacher G.W.*	II-755
4-10 Modelling of TEXTOR edge plasma in discharges with auxiliary heating, neon puffing, *Tokar M.Z., Samm U.*	II-759
4-12 A study of the SOL density profile behaviour in ASDEX, *McCormick K., Schweinzer J., Pietrzyk Z.A.*	II-763
4-13 Power flux widths in the ASDEX divertor, *Kyriakakis G., Kakoulidis E., Tsois N., McCormick K., Neuhauser J.*	II-767
4-14 Spatial distribution of carbon ions and ion temperature measurements in the plasma edge of TEXTOR using emission spectroscopy, *Telesca G., Claaßen H.A., Graffmann E., Van Oost G.*	II-771
4-15 Poloidal rotation in the limb of the TEXTOR plasma measured by the Doppler shift of a BII-line, *Conrads H., Euringer H., Rusbüldt D.*	II-775
4-16 The effect of radial electric field on fast ion losses in divertor tokamaks, *Chankin A.V., Summers D.D.R., McCracken G.M.*	II-779
4-17 Density, potential and temperature fluctuations in Wendelstein 7-AS, ASDEX, *Balbin R., Carlson A., Endler M., Giannone L., Hidalgo C., Niedermeyer H., Rudyj A., Theimer G., W7-AS Team, ASDEX Team*	II-783
4-18 Attempt to model the edge turbulence of a tokamak as a random superposition of eddies, *Endler M., Theimer G., Weinlich M., Carlson A., Giannone L., Niedermeyer H., Rudyj A., the ASDEX-Team*	II-787
4-19 Mechanisms inducing changes on the edge turbulence in the TJ-I tokamak, *Pedrosa M.A., Garcia-Cortes I., Balbin R., Hidalgo C., Ochando M.A., Liniers M.*	II-791
4-20 m=1 activity prior to the onset of sawtoothing on Tokoloshe tokamak, *Nothnagel G., Sherwell D., Roberts D.E., Fletcher J.D., De Villiers J.A.M., Walters P.E.*	II-795

Poster-No. Title, *Author(s)*	Volume/Page
4-21 Role of edge plasma in a high ß very low q tokamak regime, *Kiyama H., Kiyama S.*	II-799
4-22 Fluctuations and transport in a tokamak with high MHD activity, *Heller M.V.A.P., Castro R.M., Caldas I.L., da Silva R.P., Brasilio Z.A., TBR-1 Team*	II-803
4-23 Kinetic instabilities in a plasma in E x B fields, *Shoucri M., Bertrand P., Ghizzo A., Knorr G.*	II-807
4-24 Coherent vortical structures in two-dimensional plasma turbulence, *Lynov J.P., Nielsen A.H., Pécseli H.L., Rasmussen J.J.*	II-811
4-25 Guided Alfvén beams in the Tortus tokamak, *Cross R.C., Miljak D.G.*	II-815
4-26 Measurement of sputtering yields at the JET beryllium and carbon x-point tiles, *Stamp M.F., Thomas P.R.*	II-819
4-27 Radial carbon flux profiles in the upper divertor in JET at high target load, *Jäckel H.J., Clement S., Lesourd M., Lingertat J., Maggi C.F., Matthews G.F., Summers D.D.R., Summers H.P.*	II-823
4-28 Chemical impurity production under boronized wall conditions in TEXTOR, *Philipps V., Vietzke E., Erdweg M.*	II-827
4-29 Divertor retention for recycling impurities, *Krieger K., Roth J., Fussmann G.*	II-831
4-30 Particle influx and impurity behaviour in the ASDEX-Upgrade tokamak, *Kallenbach A., Fuchs C., Fussmann G., Jenichen F., Mast K.F., H.-M.Mayer, Schumacher U., the ASDEX-Upgrade Team*	II-835
4-31 Reduction in SOL Φ_p increases and impurity generation caused by RF near ω_{ci} by the use of insulating Faraday shield limiters in the Phaedrus-T tokamak, by elimination of Faraday shields, *Hershkowitz N., Majeski R., Diebold D., Tanaka T., Sørensen J., Breun R., Brouchous D., Fonck R., Intrator T., McKee G., Probert P.*	II-839
4-32 Plasma induced material transport on limiter probes in the boundary plasma of fusion experiments, *Naujoks D., Behrisch R.*	II-843
4-33 Production and control of an edge radiating layer with the ergodic divertor on TORE SUPRA, *Poutchy L., Vallet J.C., DeMichelis C., Grosman A., Hess W., Mattioli M., Monier-Garbet P.*	II-847
4-34 Edge transport induced by the interaction of a stochastic layer with the wall, *Nguyen F., Ghendrih Ph., Samain A., Grosman A.*	II-851
4-35 Control of the MHD activity with the ergodic divertor on TORE SUPRA, *Vallet J.C., Edery D., Van Houtte D., Mohamed-Benkadda M.S., Joffrin E., Lecoustey P., Pecquet A.L., Samain A., Talvard M.*	II-855

Poster-No. Title, *Author(s)*	Volume/Page
4-36 Plasma edge structure of a tokamak with ergodic magnetic limiter, *Takamura S., Oda Y., Sakurai S.*	II-859
4-37 Stochastic broadening in the scrape-off layer of a single-null divertor tokamak, *Punjabi A., Verma A., Boozer A.*	II-863
4-38 On stationary flow in the boundary region of toroidal systems, *Wobig H.*	II-867
4-39 Sheath potential at a target with almost parallel magnetic field, *Chodura R.*	II-871
4-41 Boundary conditions for the momentum and energy flux of ions at the plasma-sheath interface, *Günther K.*	II-875

Topic 5: Heating and Current Drive

Poster-No. Title, *Author(s)*	Volume/Page
5-1 Enhanced performance of neutral beam heated hot-ion H-modes on JET by central ICRF heating, *Bures M., Balet B., Campbell D., Cottrell G.A., Elevant T., Eriksson L-G., Jacquinot J., Jarvis N., Jones T., König R., Lomas P., Marcus F., Righi E., Sadler G., Start D.F.H., Tanga A., Van Belle P., Von Hellerman*	II-881
5-2 RF heating and current drive experiments in TORE SUPRA, *Hoang G.T., Agarici G., Beaumont B., Becoulet A., Berger G.By, Bibet P., Bizarro J.P., Capitain J.J., Carrasco J., Goniche M., Joffrin E., Kupfer K., Kuus H., Litaudon X., Moreau D., Parlange F., Peysson Y., Rey G., Saoutic B., Tonon G., Van Houtte D.*	II-885
5-3 ICRF power limitation relation to density limit in ASDEX, *Ryter F., ICRH-Group, ASDEX-Group*	II-889
5-4 Fast wave current drive experiments on the DIII-D tokamak, *Petty C.C., Pinsker R.I., Porkolab M., Baity F.W., Chiu S.C., Goulding R.H., DeGrassie J.S., Harvey R.W., Hoffman D.J., James R.A., Kawashima H., Lohr John, Luce T.C., Mayberry M.J., Prater R.*	II-893
5-5 Observation of fast wave ion current drive effects on sawteeth in JET, *Start D., Bhatnagar V., Bosia G., Brusati M., Bures M., Campbell D., Cottrell G., Cox M., DeEsch H., Edwards A., Eriksson L-G., Gormezano C., Jacquinot J., Lomas P., Marcus F., O'Brien M.R., Porcelli F., Rimini F., Stork D., Tanga A., Tubbing B., Warrick C.D., Wesson J.*	II-897
5-6 Resistive internal kinks and ICRF phasing current drive, *Porcelli F., Bhatnagar V.P., Bosia P., Cherubini A., Jacquinot J., Start D., Taroni A.*	II-901
5-7 Kinetic effects in fast wave current drive, *Becoulet A., Giruzzi G., Kupfer K., Moreau D., Saoutic B.*	II-905
5-8 Theoretical studies of fast wave plasma heating and current drive in tokamaks, *Moroz P.E., Hershkowitz N., Tataronis J.A.*	II-909

Poster-No. Volume/Page
Title,
Author(s)

5-9 II-913
Influence of various physics phenomena on fast-wave current drive in advanced tokamaks,
Batchelor D.B., Jaeger E.F., Carter M.D., Goldfinger R.C., Stallings D.C.

5-11 II-917
Current density profile control in reversed field pinch plasma by RF current drive,
Shiina S., Saito K., Kondoh Y., Ishii H., Shimada T., Hirano Y.

5-15 II-921
A method of increasing the ion Bernstein wave excitation efficiency in plasmas,
Longinov A.V., Lukinov V.A., Pavlov S.S.

5-16 II-925
The local power dissipation of ion Bernstein waves in a weakly inhomogeneous plasma,
Werthmann H., Brambilla M.

5-17 II-929
The slot-in-recess antenna system for ion Bernstein wave excitation in plasmas,
Gribok V.A., Longinov A.V., Lukinov V.A.

5-18 II-933
RF system for plasma production, heating in TJ-IU torsatron,
Ascasibar E., Castejon F., Rodriguez L., Navarro A.P., Dyakov V.E., Longinov A.V., Pavlichenko O.S., Pavlov S.S., Stepanov K.N.

5-20 II-937
The separation of ion Bernstein waves and incoherent ion gyroresonant ballistic waves in a dispersive, spatially varying medium,
Flå T., Cook D., Tracy E., Kaufmann A.N.

5-21 II-941
Plasma heating and generation current drive study in the torsatron U-2M using ion Bernstein wave,
Dyakov V.E., Longinov A.V.

5-22 II-945
Resistive flux saving, current profile control during lower hybrid waves assisted current rise in TORE SUPRA,
Van Houtte D., Hoang G.T., Joffrin E., Lecoustey P., Moreau D., Parlange F., Tonon G., Vallet J.C.

5-23 II-949
Initial lower hybrid current drive results and first two-dimensional images of hard X-ray emission in PBX-M,
Von Goeler S., Asakura N., Bell R., Bernabei S., Chance M., Chu T.K., Dunlap J., England A., Fishman H., Gettelfinger G., Greenough N., Harris J., Hatcher R., Herrmann H., Ignat D., IslerR., Jardin S., Jones S., Kaita R., Kaye S., Kesner J., Kugel H., LeBlanc B., Luckhardt S., Levinton F., Manickam J., Okabayashi M., Ono M., Paul S., Preische S., Roney P., Sauthoff N., Seki S., Sesnic S., Stevens J., Takahashi H., Valeo E., Voss K.

5-24 II-953
Performance of the LHCD in high current regime in JT-60U,
Imai T., Ushigusa K., Ikeda Y., Ide S., Naito O., Seki M., Kondoh T., Nemoto M., Wolfe S., Sato M., Takeuchi H.

5-25 II-957
Change of internal inductance and anisotropy during lower hybrid current drive in ASDEX,
Leuterer F., Söldner F.X., Bartiromo R., Bernabei S.

5-26 II-961
Electron and ion heat transport with LH, NBI heating in ASDEX,
Söldner F.X., Pereverzev G.V., Bartiromo R., Fahrbach H.U., Leuterer F., Murmann H.D., Steuer K.-H., LH-Team, NBI-Team, ASDEX-Team

5-27 II-965
Experimental studies of high energy X-ray emission and bootstrap current generation in high β_p lower hybrid driven plasmas,
Squire J.P., Porkolab M., Bonoli P.T., Colborn J.A., Villasenor J.

Poster-No. Volume/Page
Title,
Author(s)

5-28 II-969
Investigation of high energy electrons produced by lower hybrid waves with measurement of the hard X-ray in JT-60U,
Kondoh T., Ide S., Imai T., Ushigusa K., Ikeda Y., Seki M., Takeuchi H.

5-29 II-973
Characterization of LH induced current carrying fast electrons in JET,
Ramponi G., Airoldi A., Bartlett D., Brusati M., Froissard P., Gormezano C., Rimini F., da Silva R.P., Tanzi C.

5-30 II-977
A phenomenological description of fast electrons induced by LH waves in tokamaks,
Conceicao P., Brusati M., Froissard P., Varandas C.A.F.

5-31 II-981
Impurity transport during RF current drive in WT-3 tokamak,
Nakamura M., Sawada K., Kawachi T., Suemitu H., Maekawa T., Terumichi Y., Tanaka S.

5-32 II-985
The distant coupling of LHCD launcher in the JT-60U,
Seki M., Ikeda Y., Imai T., Ushigusa K., Naitou O., Ide S., Kondoh T., Nemoto M., Takeuchi H., Suganuma K., Sawahata M., Takasa A., Takahashi S., Yamamoto T.

5-33 II-989
Coupling analysis and experiment of the multijunctional grill near the lower hybrid frequency,
Ohkubo K., Matsumoto K.

5-36 II-993
Modulational instability development and current drive,
Popel S.I., Vladimirov S.V., Tsytovich V.N.

5-39 II-997
Fast ion generation during RF discharge on the FT-2 tokamak and parametric decay instabilities,
Budnikov V.N., Dyachenko V.V., Esipov L.A., Its E.R., Lashkul S.I., Novik K.M., Stepanov A.Yu., Shcherbinin O.N., Alexandrov V.O., Sakharov I.E., Shatalin S.V.

5-43 II-1001
Measurements of electron cyclotron emission during high power ECRH in the W7-AS stellarator,
Gasparino U., Hartfuß H.J., Tribaldos V., Tutter M., W7-AS Team, ECRH Group

5-44 II-1005
Simulations of fast electron generation by stimulated Raman forward scattering in a magnetized plasma,
Bertrand P., Ghizzo A., Karttunen S.J., Pättikangas T.J.H., Salomaa R.R.E., Shoucri M.

5-45 II-1009
Effects of fluctuations on magnetohydrodynamic wave heating and current drive,
Tataronis J.A., Antani S.N.

5-46 II-1013
Radial diffusion of toroidally trapped particles induced by lower hybrid and fast waves,
Krlin L.

5-47 II-1017
ICRF Minority plasma heating in realistic geometries,
Friedland L., Cohen D.

5-48 II-1021
Simulation of runaway electrons in a toroidal geometry,
Sipilö S.K., Heikkinen J.A., Pättikangas T.J.H.

5-49 II-1025
Modelling of the FMS wave propagation and transformation in the ion-cyclotron frequency domain for the TUMAN-3 tokamak plasma,
Irzak M.A., Pavlov I.P., Shcherbinin O.N.

Topic 6: Diagnostics

Poster-No. Title, *Author(s)*	Volume/Page
6-2 Neutral particle analysis in the MeV range in JET, *Petrov M.P., Afanasyev V.I., Corti S., Gondhalekar A., Khudoleev A.V., Korotkov A.A., Maas A.C.*	II-1031
6-3 Investigation of alpha particle slowing-down features in helium neutral beam fuelling experiments at JET, *Von Hellermann M., Core W.G.F., Frieling J., Horton L.D., König R., Mandl W., Summers H.P., Wolle B.*	II-1035
6-5 Prospects for investigation of alpha particles velocity distribution by charge exchange spectroscopy in ITER, *Korotkov A.A., Belik V.P., Shmaenok L.A., Platonov Yu.Ya., Salashchenko N.N.*	II-1039
6-6 Helium stopping cross-section in fusion plasma taking into account the multistep collision processes, *Korotkov A.A.*	II-1043
6-7 Neutron spectrometry concepts for diagnosing DT plasmas of Q ~ 1, *Källne J., Gorini G., Condé H., Renberg P.U.*	II-1047
6-8 Effects of neutron on the JET soft X-ray detectors, *Gill R.D., Alper B., Edwards A.*	II-1051
6-9 The application of x-mode reflectometry to the study of large scale density fluctuations in TFTR, *Mazzucato E., Nazikian R., the TFTR-Group*	II-1055
6-11 A multi-channel reflectometer for the RTP tokamak, *Heijnen S.H., Hugenholtz C.A.J., Van de Pol M.J.*	II-1059
6-12 A microwave reflectometric system for tokamak ASDEX upgrade, *Silva A., Manso M.E., Serra F., Söldner F.X., Cupido L., Pereira J., Neves J., Nunes F., Varela P., Moreira A., Fernandes C., Loureiro C., Correia C., Santos J., Zilker F.*	II-1063
6-13 Simulation of correlation reflectometry, *Michelsen P., Pécseli H.L.*	II-1067
6-14 Microwave reflectometry as a density fluctuation diagnostic: a comparison between a controlled laboratory experiment and a one dimensional numerical model, *Rhodes T.L., Baang S., Chou A.E., Domier C.W., Luhmann Jr. N.C., Peebles W.A.*	II-1071
6-15 Amplitude modelation reflectometry for large fusion devices, *Sanchez J., Zhuravlev V., De la Luna E., Estrada T., Branas B.*	II-1075
6-17 Fluctuations spectra in TORE SUPRA from scattering experiment, *Gervais F., Grésillon D., Hennequin P., Quéméneur A., Truc A., Devynck P., Garbet X., Payan J., Laviron C., Saha S.K.*	II-1079
6-18 From incoherent to collective scattering, *Maafa N., Grésillon D., Cabrit B.*	II-1083

Poster-No. Title, *Author(s)*	Volume/Page
6-19 Effects of the ohmic plasma current on collective scattering spectra, *Tartari U., Castiglioni S., Lontano M.*	II-1087
6-20 Ion temperature measurements by Rutherford scattering at TEXTOR, *Tammen H.F., Van Blokland A.A.E., Oyevaar Th., Schüller F.C., Donné A.J.H.*	II-1091
6-21 CO_2-scattering and RF probe measurements of lower-hybrid wave spectra in the presence of low-frequency fluctuations, *Fischer B., Krämer M.*	II-1095
6-22 Measurement of coherent temperature fluctuations on the stellarator Wendelstein 7-AS, *Hartfuß H.J., Sattler S., W7-AS Team, NBI-Team, ECRH-Group*	II-1099
6-23 Electron cyclotron non thermal spectra during ohmic and RF assisted discharges on TORE SUPRA, *Talvard M., Giruzzi G., Liu W.D.*	II-1103
6-24 First electron cyclotron emission and electron temperature profile measurements on ASDEX-upgrade, *Salmon N.A.,Eberhagen A.*	II-1107
6-26 The heavy ion beam diagnostic for the tokamak ISTTOK, *Cabral J.A.C., Malaquias A., Praxedes A., Van Toledo W., Varandas C.A.F., Dias J.M.*	II-1111
6-27 Development of Boxcar imaging system for visualizing magnetic field structure in tokamak plasma, *Sakurai S., Ohno N., Takamura S.*	II-1115
6-29 Statistical analysis of luminescence signals observed during pellet injection, *Baldzuhn J., W7-AS Team*	II-1119
6-31 Dispersion interferometer for controlled fusion devices, *Drachev V.P., Krasnikov Yu.I., Bagryansky P.A.*	II-1123
6-32 Visible spectroscopic measurements on FTU, *Condrea I., Bartiromo R., Mazzitelli G., McNeill D.H.*	II-1127
6-33 Determination of O^{8+} to electron density ratio by the intensity ratio of the charge exchange recombination and the Doppler-shifted H_α emissions of the injected neutral beam, *Kondo K., Sano F., Sudo S., Zushi H., Mizuuchi T., Okada H., Besshou S., Nagasaki K., Higashijima S., Hanatani K., Nakasuga M., Wakatani M., Obiki T.*	II-1131
6-34 Spatial structure of nonthermal fluctuating electric fields in the TJ-I tokamak, *Zurro B., Castejon F., Burgos C.*	II-1135
6-37 Fast analysis of spectral data using neural networks, *Roach C.M.*	II-1139
6-38 Tomography algorithms for visible light tomography on RTP, *Pickalov V.V., Ingesson L.C., Donne A.J.H., Schram D.C.*	II-1143
6-39 Investigation of the sensitivity of visible continuum $Z_{eff}(0)$ to edge radiation, *Telesca G., Van Oost G., Ongena J., Leys C., Schoon N.*	II-1147

Poster-No. Volume/Page
Title,
Author(s)

6-40 II-1151
Spatially resolved diagnostics of inhomogeneous low temperature plasmas: new techniques,
Neger T., Jäger H.

6-41 II-1155
Localized impurity flux measurements on Wendelstein 7-AS,
Hofmann J.V., W7-AS Team, ECRH Group, NI Group

6-42 II-1159
Diagnostic for hydrogen behaviour at edge regions of high temperature plasmas,
Muraoka K., Maeda M., Honda C., Okada T., Uchino K., Kajiwara T., Takenaga H.

6-43 II-1163
Determination of plasma edge parameters with fast lithium beams,
Schweinzer J., McCormick K., Fiedler S., Aumayr F., Pöckl M., Winter H.

6-44 II-1167
Sniffer probe measurements in W7-AS,
Wolff H., Grigull P., Poschenrieder W., Roth J., Pech P., the W7-AS Team

6-47 II-1171
Electric current collection by Langmuir probe in strong magnetic fields,
Stanojevic M., Cercek M., Jelic N., Gyergyek T.

6-48 II-1175
A double probe for electron flux measurements in inhomogeneous and time-varying plasmas,
Axnäs I., Torvén S.

6-49 II-1179
A processing method of the probe characteristic in a two electron temperature plasma,
Ruscanu D., Popa G., Stamate E.

6-50 II-1183
Comparison of the wavenumber sensitivity and spatial resolution between Langmuir probes and reflectometry in a longitudinally magnetized RF plasma waveguide,
Anabitarte E., Senties J.M., Bustamante E.G., Calderon M.A.G., San Jose M.A.G., Monterde P., Vila J.

6-51 II-1187
RF pulse interaction with low density plasma diagnosed by gated Langmuir probe,
Cicconi G., Paris P.J., Rosatelli C., Tarditi A.

6-57 II-1191
Development of a diagnostic system for high power microwave (FEL) electric fields in the microwave tokamak experiment,
Oda T., Odajima K., Takiyama K., Foote J.H., Mizuno K., Ogawa T., Sato K., Ohasa K., Hoshino K., Maeda H., Nilson D.G.

6-59 II-1195
Laser shadowgraphic study of plasma sheath in dense plasma focus in the presence of external axial magnetic field,
Rawat R.S., Srivastava M.P., Mohanty S.R.

6-61 II-1199
Measurement of plasma drifts in space and laboratory plasmas by the resonance cone technique,
Rohde V., Piel A.

6-62 II-1203
The time-delay of a microwave signal, backscattered at the hybrid resonance and new possibilities for the diagnostics of small-scale plasma fluctuations,
Arhipenko V.I., Simonchik L.V., Budnikov V.N., Gusakov E.Z., Piliya A.D., Selenin V.L.

6-65 II-1207
Excimer laser driven soft X-ray plasma source: preliminary results,
Palladino L., Reale A., Taglieri G., Batani D., Bollanti S., Di Lazzaro P., Flora F., Letardi T., Schina G., Belli M., Scafati A.

Poster-No. Title, *Author(s)*	Volume/Page
6-67 Measurements of intense plasma streams with Faraday-type collectors, *Baranowski J., Sadowski M., Skladnik-Sadowska E.*	II-1211
6-68 New Cerenkov detectors for studies of fast electron beams from plasma discharges, *Jakubowski L., Sadowski M., Zebrowski J.*	II-1215
6-70 Application of laser induced ionisation to atomic hydrogen density measurements in high temperature plasma, Gladuschak V.I., Gusev V.K., Kantor M.Yu., Petrov Yu.V., Razdobarin G.T., Semenov V.V., Tolstyakov S.Yu.	II-1219

Topic 7: Inertial Confinement Fusion

Poster-No. Title, *Author(s)*	Volume/Page
7-1 Absorption of KrF laser pulses in laser produced plasmas, *Matsushima I., Koyama K., Tomie T., Matsumoto Y., Owadano Y.*	II-1225
7-3 Nonstationary stimulated Brillouin scattering in laser plasma, *Rubenchik A.M., Ochirov B.D., Kozochkin S.M., Maluyta D.D., Strel'tsov A.P., Shirokikh A.V.*	II-1229
7-4 Absorption process by ion acoustic turbulence, *Torres-Silva H., Sakanaka P.H.*	II-1233
7-5 Absorbed power into the plasma by laser radiation and determination of reflection coefficient in the implosion of deuterium-tritium pellets corresponding to the inertial confinement fusion, *Blazquez J.F.M.*	II-1237
7-7 Effect of electron velocity distribution on the heating of core by corona in spherical pellet, *Singh D.P., Giammanco F., Salvetti A., Vaselli M.*	II-1241
7-8 Influence of partial charge exchange on effective charge of swift heavy ions flowing through dense hydrogen plasmas, *Maynard G., Katsonis K., Deutsch C.*	II-1245
7-9 Numerical simulations of X-ray diagnostics in ICF, *Humbert P.*	II-1249
7-11 Plasma driven liners, *Kilic H., Linhart J.G., Bortolotti A., Bilbao L., Nardi V.*	II-1253
7-13 Axial magnetic field generation in a nonuniform laser produced plasma, *Srivastava M.K., Lawande S.V., Khan M., Das C., Chakraborty B.*	II-1257
7-14 Stabilization of the Rayleigh-Taylor instability by convection and thermal conduction in smooth density gradient: WKB analysis, *Bud'ko A., Liberman M.A., Bondarenko E.A.*	II-1261

Poster-No. Title, *Author(s)*	Volume/Page
7-17 Fusion-fission triggers for advanced fuels, *Linhart J.G.*	II-1265

Topic 8: General Plasma Theory

Poster-No. Title, *Author(s)*	Volume/Page
8-1 Wave collapse of strong lower-hybrid turbulence, *Bingham R., Su J.J., Dawson J.M., Shapiro V.D., Shevchenko V., Tsytovich V.N.*	II-1271
8-2 Empirical spectral codes for tokamak turbulence, *Smith G.R., Cohen R.H., Boerner E.D., Dimits A.M.*	II-1275
8-5 Frequency and heater power dependency of RF generated Langmuir turbulence, *Hanssen A., Mjølhus E.*	II-1279
8-7 Nonlinear modulational instability of whistler waves, *Karpman V.I., Lynov J.-P., Michelsen P., Rasmussen J.J.*	II-1283
8-8 Low-frequency kinetic structures in plasma quasiparticle concept, *Sitenko A.G., Sosenko P.P.*	II-1287
8-15 A novel approach to the interaction between the plasma wake field and the driving relativistic electron beam, *Fedele R., Shukla P.K.*	II-1293
8-18 Simultaneous emissions at harmonics and half harmonics of the electron gyrofrequency, *Krafft C., Matthieussent G., Belmont G.*	II-1297
8-20 Intense laser pulse propagation in a plasma, *Kaw P.K., Sen A., Katsouleas T.*	II-1301
8-21 Nonlinear depletion of short, relativistically strong laser pulses in an underdense plasma, *Bulanov S.V., Inovenkov N., Kirsanov V.I., Naumova N.M., Sakharov A.S.*	II-1305
8-25 Nonlinear modulated waves near marginal state of instability, *Flå T., Wyller J.*	II-1309
8-27 Plasma oscillations wave breaking in inhomogeneous collisional plasmas, *De Nicola S., Nappi C.*	II-1313
8-30 Nonlinear absorption on the front of relativistically strong electromagnetic pulse in an underdense plasma, *Bulanov S.V., Inovenkov I.N., Kirsanov V.I., Naumova N.M., Sakharov A.S., Shah H.A.*	II-1317'
8-31 "Plasma maser" effect in turbulent plasma with regular and random magnetic fields, *Pryadko J.M., Tsytovich V.N.*	II-1321

Poster-No. Title, *Author(s)*	Volume/Page
8-32 Nonlinear evolution of the modulational instability and chaos by using ID-Zakharov equations, *Sharma R.P., Verga A.D.*	II-1325
8-33 Energy of linear quasi-neutral electrostatic drift waves, *Pfirsch D., Correa-Restrepo D.*	II-1329
8-34 General theory of modulational interactions of two modes, *Vladimirov S.V., Tsytovich V.N.*	II-1333
8-35 Nonlinear evolution of solitons with oscillations under the influence of resonant ions, *Honzawa T., Arakawa M., Singh S.*	II-1337
8-36 3D non-linear kinetic equation for the calculation of neoclassical effects in tokamak plasmas, *Zaitsev F.S., O'Brien M.R., Cox M.*	II-1341
8-37 Nonlinear Langmuir pulses in the active plasma, *Bachin I.V., Prudsky V.V.*	II-1345
8-39 Soliton formation in quasiparallel MHD waves, *Hamilton R.L., Kennel C.F., Mjølhus E.*	II-1349
8-41 Nonlinear wave behaviour determined by high-frequency plasma response, *Georgieva M., Khristova D., Shivarova A.*	II-1353
8-42 Evolution of electron two-stream instability and generation of nonlinear structure, *Tanaka M.*	II-1357
8-44 Gyroinvariant second order drifts in electric fields of the same order of the magnetic field, *Martin P.*	II-1361
8-45 Charge shielding by trapped ion orbits in a dusty plasmas, *Goree J.*	II-1365
8-48 Vlasov solution describing nonabdiabatic plasma heating by magnetic compression, *Persson H., Ågren O.*	II-1369
8-50 The Pade approximate method for solving problems in plasma kinetic theory, *Jasperse J.R., Basu B.*	II-1373
8-51 Correlation theory of particle distribution near the plasma boundary in the presence of strong electric field, *Korchinsky G.M., Yakimenko I.P., Zagorodny A.G.*	II-1377
8-54 Possible changes of temperature and density power law exponents in expressions for plasma transport quantities under many particle interaction conditions, *Larenz R.W.*	II-1381
8-56 Dynamical screening in the Coulomb relaxation of anisotropic plasmas, *Wolf U., Schamel H.*	II-1385

Poster-No. Title, *Author(s)*	Volume/Page
8-57 Wiedemann-Franz-Law for magnetized plasmas, *Hensler E.*	II-1389
8-58 The influence of toroidicity, pressure and local profile changes on tearing mode stability, *Connor J.W., Cowley S.C., Hastie R.J., Martin T.J.*	II-1393
8-60 Linear and non-linear modelling of island control in tokamaks, *Hansen B.M.S., Hellberg M.A., Sherwell D., Roberts D.E., McLoud W.S.*	II-1397
8-61 Resistive wall instabilities for axisymmetric systems, *Berge G., Freidberg J.P.*	II-1401
8-62 Stability of force-free axisymmetric spherical plasma with flow, *Sugimoto H., Ashida H., Kurasawa T.*	II-1405
8-64 Internal disruption = catastrophic ergodisation, *Dubois M.A., Hennequin P., Nakach R., Sabot R.*	II-1409
8-65 Stability of ideal ballooning modes near a magnetic island, *Hegna C.C., Callen J.D.*	II-1413
8-66 Sheared flow effects on resistive pressure-gradient-driven turbulence, *Garcia L., Carreras B.A., Lynch V.E., Diamond P.H.*	II-1417
8-67 Mechanism of MHD modes stabilization by the ergodic divertor, *Edery D., Samain A., Vallet J.C., Morera J.P., Joffrin E., Lecoustey P., Pecquet A.L., Talvard M.*	II-1421
8-68 Nonlinear island dynamics, *Schep T.J., Pegoraro F., Rem J.*	II-1425
8-69 Magnetic reconnection in electron-magnetohydrodynamics, *Bulanov S.V., Pegoraro F., Sakharov A.S.*	II-1429
8-70 Radial propagation of microturbulence in tokamaks, *Garbet X., Laurent L., Roubin J.P., Samain A.*	II-1433
8-71 On the threshold of the ion temperature gradient driven mode, *Guo S.C., Romanelli F., Rewoldt G., Tang W.M.*	II-1437
8-72 Stability and transport due to ITG modes in a toroidal plasma with impurities, trapped electrons and vortex formation effects, *Jarmen A., Fröjdh M., Pavlenko V., Weiland J.*	II-1441
8-74 Dissipative-drift wave instability in the presence of impurity radiation, *Bharuthram R., Shukla P.K.*	II-1445
8-75 Nonadiabaticity and toroidal mode coupling in collisional drift waves, *Schlüter M., Scott B.D.*	II-1449

Poster-No. Volume/Page
Title,
Author(s)

8-76 II-1453
On the "captured" energy in freely decaying two-dimensional hydrodynamic and drift-wave plasma turbulence,
Bazdenkov S.V., Kukharkin N.N.

8-77 II-1457
Effect of parallel heat flows on electron heat conduction losses due to electrostatic turbulence,
Becker G.

8-79 II-1461
An energy balance approach to L-H transition at the edge,
Martinell J.J., Ramos G.

8-80 II-1465
Pedestal sustenance, heat transport at the edge in the H-transition,
Minardi E.

8-81 II-1469
Non-standard high energy ion orbits,
Eriksson L.-G., Berk H., Porcelli F., Stankiewicz R.

8-83 II-1473
Plasma transport as a dissipative structure,
Uehara K.

8-84 II-1477
Ambipolar transport in a magnetically perturbed tokamak edge-region,
Wittenberg R.W., Hellberg M.A., Feneberg W.

8-85 II-1481
Neoclassical transport with surface variation of the macroscopic quantities,
Feneberg W.

8-87 II-1485
Time-dependent neutron rate interpretation for deuterium injection into deuterium plasmas,
Wolle B., Eriksson L.-G., Hübner K., Morgan P.D., Sadler G., Tsintsadze L.N., Von Hellermann M.G.

8-88 II-1489
Multidimensional WKB solution of a wave equation,
Pereverzev G.V.

8-89 II-1493
Electron cyclotron emission and absorption in two dimensional momentum distribution,
Bornatici M.

8-90 II-1497
Oblique propagation of electron-cyclotron-waves in non-maxwellian, weakly relativistic Vlasov-plasmas,
Moser F.

8-92 II-1501
Partially transient plasma response near an attainable harmonic state,
Lim C.S., Suchy K.

8-94 II-1505
Mode coupling of the ordinary and extraordinary waves in a cylindrical plasma,
Ramsay D., Laing E.W.

8-97 II-1509
High frequency electrostatic plasma instabilities and turbulence in the lower ionosphere,
Basu B., Jasperse J.R., Retterer J.M., Decker D.T., Chang T.

8-99 II-1513
Numerical calculation based on multipole expansions was used to study the linear instability in a DP-Machine,
Cereceda C., Ruiz J., Puerta J.

Poster-No. Title, *Author(s)*	Volume/Page
8-100 Dispersion characteristics of electromagnetic waves in dipolar (m=+/-1) modes travelling along a magnetized plasma column, *Benova E., Ghanashev I., Zhelyazkov I.*	II-1517
8-102 Cyclotron autoresonance current drive in tokamaks, *Kuyanov A.Yu., Skovoroda A.A., Timofeev A.V., Zvonkov A.V.*	II-1521
8-103 Application of a reconstructive MHD code based on the formalism of the toroidal multipoles to the ITER tokamak, *Alladio F., Lalousis P., Micozzi P.*	II-1525
8-105 MHD theory with induced surface current effects, *Lehnert B.*	II-1529
8-107 Exact surface waves on spheres, cylinders, *Yu M.Y., Stenflo L.*	II-1533
8-109 1st and 2nd elliptic solutions to the extended Grad-Shafranov-Schlüter equation for asymmetric tokamak plasma with stationary flows, *Zelazny R., Stankiewicz R., Galkowski A., Potempski S.*	II-1537
8-110 A new fast 2-d MHD-equilibrium solver, *Hübner G.*	II-1541
8-111 A civil engineering approach to ideal MHD, *Jensen V.O.*	II-1545
8-112 A general formulation of the nonlinear plasma theories, *Kuhn S., Assis A.S.*	II-1549
8-113 Uniqueness of solution to a stationary boundary kinetic problem, *Zhykharsky A.*	II-1553
8-114 Solution to the boundary kinetic problem presenting the interaction of plasma flows with a solid, *Zhykharsky A., Shmykov V.*	II-1557
8-115 A theoretical model for transient cataphoretic segregation, *Dumitrascu N., Berbece D., Popa Gh.*	II-1561

PART III

Topic 9: Space and Astrophysical Plasmas

Poster-No. Title, *Author(s)*	Volume/Page
9-1 Modulational instability of lower hybrid wave in a cylindrical plasma, *Sharma S.K., Sudarshan A.*	III-1567

Poster-No. Title, *Author(s)*	Volume/Page
9-5 Interaction of a magnetized plasma stream with an immobile ion cloud, *Baumgärtel K., Sauer K.*	III-1571
9-7 Rayleigh-Taylor instability favoured drift turbulence in a spread F simulation experiment, *Prasad G., Bora D., Saxena Y.C.*	III-1575
9-9 Simulation of electron beam-driven instabilities by a 3-D electromagnetic particle code, *Nishikawa K.-I., Buneman O., Neubert T.*	III-1579
9-13 Night time equatorial spread F simulation in a laboratory plasma, *Prasad G., Bora D., Saxena Y.C.*	III-1583
9-14 Stimulated attachment instability of electromagnetic waves in the ionosphere, *Shukla P.K., Stenflo L., Borisov N.D.*	III-1587
9-17 Radar collective backscattering and the high latitude plasma turbulence, *Grésillon D., Cabrit B., Hanuise C., Villain J.P., Greenwald R.A., Baker K.B.*	III-1591
9-19 Stimulated scattering of EM wave by ICW in a two electron temperature plasma, *Sudarshan A., Sharma S.K.*	III-1595
9-20 Binding energy and triplet-splitting of the hydrogen molecule in ultrahigh magnetic fields, *Korolev A., Liberman M.A.*	III-1599
9-21 Behaviour of two-dimensional ion-acoustic soliton in relativistic plasmas of radiation belts, *Singh S., Honzawa T.*	III-1603
9-23 The Rayleigh-Taylor instability in a super-dense igniting plasma, *Garcia D., Serichol N., Bravo E., Diaz-Pinto A.*	III-1607
9-26 New electrostatic instabilities in nonuniform partially ionized magnetoplasmas, *Shukla P.K., Dwivedi C.B., Das A.C.*	III-1611
9-27 Spontaneous formation of intermediate shocks, *Chao J.K., Chiu C.Y., Chiueh T.H.*	III-1615
9-33 Spectrum of MHD waves in cometary tails, *Matsuura O.T., Azevedo C.A., Assis A.S., Shigueoka H., Sakanaka P.H.*	III-1619
9-34 Low-frequency resonant ion-beam turbulence in cometary plasmas, *Verheest F., Lakhina G.S.*	III-1623
9-35 Lower hybrid resonance acceleration of electrons and ions in the aurora and solar flares, *Bingham R., Bryant D.A., Hall D.S., Su J.J., Dawson J.M.*	III-1627
9-38 Solar flare mechanism based on MHD relaxation model, *Kusano K., Kubo H., Tamano T., Sato T.*	III-1631

Poster-No. Title, *Author(s)*	Volume/Page
9-39 Nonlinear MHD surface waves on plasma interfaces and their evolution equation in solar and magnetospheric conditions, *Nenovski P., Zhelyazkov I., Murawski K.*	III-1635
9-42 Generation of large amplitude plasma waves in space phenomena, *Dudnikova G.I., Vshivkov V.A.*	III-1639
9-43 Parametric instabilities of Langmuir waves in dusty plasmas, *Shukla P.K., Feix G., Rao N.N.*	III-1643
9-44 Magnetic reconnection in the plasma within clusters of galaxies, *Jafelice L.C., Friaca A.C.S.*	III-1647
9-46 Quantitative analysis of cosmic noise coming from plasma jets of quasar, *Tanizuka N., Kawaguchi N., Mikoshiba H., Inoue M.*	III-1651
9-47 A theory on the evolution process of the fine structure in space, *Nejoh Y.*	III-1655
9-48 The effects of slightly oblique propagation on nonlinear Alfvén waves, *Spangler S.R., Plapp B.B.*	III-1659
9-50 Mathematicl theories of resonant absorption of Alfvén waves in space plasmas: time dependent solution, *Uberoi C.*	III-1663
9-51 Runaway electrons in the presence of kinetic Alfvén waves, *Assis A.S., Leubner C.*	III-1667
9-52 Polarization changes through stimulated Raman scattering, Krishan V., Gangadhara R.T.	III-1671

Topic 10: Basic Collisionless Plasma Physics

Poster-No. Title, *Author(s)*	Volume/Page
10-1 Transition to chaos in periodically driven thermionic diodes at low pressure, *Klinger T., Timm R., Piel A.*	III-1677
10-3 Equilibrium double layers in extended Pierce diodes, *Ciubotariu-Jassy C.I.*	III-1681
10-4 New results on weakly nonlinear driven oscillations in the Pierce diode, *Hörhager M., Kuhn S.*	III-1685
10-7 Laboratory study of collisionless interaction processes between supernova-like ejectas and magnetized background under conditions of a laser-produced-plasma experiments, *Zakharov Yu.P., Orishich A.M., Ponomarenko A.G., Snytnikov V.N.*	III-1689

Poster-No. Title, *Author(s)*	Volume/Page
10-8 Total energy conservation, Manley-Rowe relations for plasma-maser interaction, *Nambu M.*	III-1693
10-9 Phase-space topology in the dynamics of cyclotron-masers, *Pakter R., Schneider R.S., Rizzato F.B.*	III-1697
10-10 RF production of long, dense plasma columns, *Chen F.F., Chevlaier G.*	III-1701
10-11 Plasma potential formation in the presence of localized radio-frequency electric fields, *Sato N.Y., Hatakeyama R., Sato N.*	III-1705
10-12 Inward and outward plasma motion induced by axisymmetric electromagnetic fields around the ion cyclotron frequency, *Hatakeyama R., Miyakuni S., Sato N.Y., Sato N.*	III-1709
10-13 The exact and drift Hamiltonian, *Yao Q., Boozer A.H.*	III-1713
10-14 Collisionsless driftwaves in anisotropic cylindrical plasmas, *Korn J., Schamel H.*	III-1717
10-15 Instabilities of gyro-kinetic plasmas with a guiding center density gradient, finite Larmor radius and polarization drift, *Knorr G., Shoucri M.*	III-1721
10-16 The launching and propagation of drift waves in a steady-state plasma, *Sandeman J., Elliott J.A., Sutcliffe M., Rusbridge M.G.*	III-1725
10-17 Studies of non-linear interactions of drift waves in the UMIST quadrupole "GOLUX", *Duncan P.J., Chekroud D., Rusbridge M.G.*	III-1729
10-18 Excitation of electron cyclotron waves and related physics experiments, *Tanaka M., Tamaoki M., Shoyama H., Nagao K., Komori A., Kawai Y.*	III-1733
10-19 An Eulerian Vlasov plasma simulation code for ion phase space phenonema, *Cherkhani R., Bonhomme G., Ghizzo A., Bertrand P.*	III-1737
10-20 An Eulerian code for the study of the gyro-averaged kinetic Vlasov equation, *Ghizzo A., Bertrand P., Shoucri M., Fijalkow E., Feix M.*	III-1741
10-21 Relativistic Vlasov-Maxwell equilibria of anisotropic charge-separation-free plasmas, *Kamp L.P.J., Van Bruggen-Kerkhof M.J., Sluijter F.W.*	III-1745
10-22 A new action principle for the Vlasov-Maxwell system, *Larsson J.*	III-1749
10-23 Negative-energy waves in an inhomogeneous force-free Vlasov plasma with sheared magnetic field, *Correa-Restrepo D., Pfirsch D.*	III-1753

Poster-No. Title, *Author(s)*	Volume/Page
10-24 Electrons passing through a negatively biased grid due to collective trapping, *Popa G., Schrittwieser R.*	III-1757
10-26 Experimental analysis of a low frequency instability in a magnetized discharge plasma, *Gyergyek T., Cercek M., Jelic N., Stanojevic M.*	III-1761
10-27 Ion cyclotron oscillations induced by an emissive electrode floating in a magnetized collisionless plasma column, *Sato N., Hatakeyama R., Aoyama K., Ding W.X.*	III-1765
10-28 On the double layer phenomenology, *Sanduloviciu M., Lozneanu E.*	III-1769
10-29 A probe sheath instability in a double plasma device, *Dempers C.A., Krumm P., Schrittwieser R.*	III-1773
10-30 Progress in the kinetic modeling of collisionless two-dimensional bounded plasma systems, *Pedit H., Kuhn S.*	III-1777
10-31 Anisotropic conductivity of the collisionsless magnetized plasma, its application to the cylindrical plasma column, *Kiyama S.*	III-1781
10-32 Analytic solution to longitudinal eigenmodes in a collisionless bounded plasma, *Kuhn S., Schupfer N., Assis A.S., Santiago M.A.M.*	III-1785
10-36 A collisionless ExB instability with large ion orbits, *Chen F.F.*	III-1789
10-37 Influence of the thermoionic emission on the current-driven ion-acoustic instability, *Donoso G., Martin P.*	III-1795
10-38 Modulational instability of relativistic ion acoustic waves in a plasma with trapped electrons, *Nejoh Y.*	III-1799
10-39 Cross-field ion acoustic instability and turbulence in a weakly magnetized plasma, *Barrett P.J., Popov G.H.*	III-1803
10-40 Numerical study of potential formation and negative resistance in a current-carrying ion sheath, *Ohno N., Komori A., Takamura S., Kawai Y.*	III-1807
10-41 Asymmetric ExB equilibria and diocotron adiabatic invariants, *Chu R., Wurtele J.S., Notte J., Fajans J.*	III-1811
10-43 Compression of multiple ion acoustic solitons at the plasma sheath edge, *Nagasawa T., Nishida Y.*	III-1815
10-44 The effects of finite electron mass on ion-acoustic solitons, *Rice W.K.M., Hellberg M.A., Mace R.L., Baboolal S.*	III-1819

Poster-No. Title, *Author(s)*	Volume/Page
10-45 Effect of second ion species on ion-acoustic rarefactive soliton in two-electron temperature plasma, *Sayal V.K., Yadav L.L., Sharma S.R.*	III-1823
10-46 Transport of time-varying currents by whistler waves, *Urrutia J.M., Stenzel R.L., Rousculp C.*	III-1827
10-47 Excitation of low-frequency whistlers by magnetic loops, *Stenzel R.L., Urrutia J.M., Rousculp C., Golubyatnikov G.Yu.*	III-1831
10-49 Non-stationary propagation of nonlinear ion acoustic waves in a plasma with negative ions, *Uehara M., Maciel H.S.*	III-1835
10-52 Relaxation and self-organization of a nonneutral plasma, *Ramachandran H., Morales G.J., Decyk V.K.*	III-1839
10-53 Low-dimensional attractors arising from the interaction of drift waves with low frequency instabilities, *Klinger T., Piel A.*	III-1843
10-54 Ion-holes associated with rarefactive ion acoustic pulse, *Singh A.K., Saxena Y.C.*	III-1847
10-55 Cascading bifurcations to chaos in a current carrying ion sheath, *Kono M., Komori A.*	III-1851
10-56 Experimental measurements of cascading bifurcations to chaos in an ion sheath, *Komori A., Kono M., Norimine T., Tanaka M., Kawai Y.*	III-1855
10-57 Nonlinear evolution and localized structure of unstable waves in an electron-beam plasma, *Yamagiwa K., Mieno T., Tanaka M.*	III-1859
10-58 Observation of two wave induced chaos in a magnetized plasma, *Fasoli A., Paris P.J., Tran M.Q., Skiff F.*	III-1863
10-59 Observations of intermittent structures in association with low frequency turbulence in toroidal magnetized plasma, *Singh A.K., Saxena Y.C.*	III-1867
10-60 Lower hybrid turbulence excited by electron diamagnetic drifts, *Stenzel R.L.*	III-1871
10-61 Experimental studies of anomalous potential drops due to ion density inhomogeneities, *Axnäs I., Bohm M., Torvén S.*	III-1875
10-62 Ion resonance cones and intrinsic diffraction, *Pierre T., Bonhomme G.*	III-1879
10-63 Reflection of a divergent resonance cone near the plasma layer in a magnetized inhomogeneous plasma, *Boucher I., Pierre T., Leclert G.*	III-1883

Poster-No. Title, *Author(s)*	Volume/Page
10-64 Production of a high density plasma by helicon waves, *Komori A., Sugimoto M., Kono M., Tanaka M., Kawai Y.*	III-1887
10-65 Development of spiral structures on a rotating plasma column with large ion-gyroradius, *Ikehata T., Mase H.*	III-1891
10-66 Waves driven by strong transverse potential structures, *Koepke M.E., Alport M.J., Sheridan T.E., Amatucci W.E., Carroll III J.J.*	III-1895
10-67 Experimental dynamics of 2-D vorticity rings, *Peurrung A.J., Fajans J.*	III-1899
10-68 Dynamics of non-stationary dipole vortices in the Hasegawa-Mima equation, *Hesthaven J.S., Lynov J.-P., Nycander J.*	III-1903
10-69 Localized vortices in η_i-modes, *Nycander J., Lynov J.-P., Rasmussen J.J.*	III-1907
10-72 Breaking of waves into wave packets observed in a beam-plasma system, *Honzawa T., Singh S.*	III-1911
10-74 Experimental measurement of the deflection of an electron beam due to the ponderomotive force of a HF wave in a waveguide, Hadjoudj Y., Heuraux S., Pierre T., Leclert G.	III-1915
10-76 Generation of ion cyclotron wave in an ion beam by a periodic magnetic field, *Mieno T., Hatakeyama R., Sato N.*	III-1919
10-77 Non-linear ion acceleration in electrostatic wave fields, *Alava M.J., Heikkinen J.A.*	III-1923
10-78 Electron acceleration by $\mathbf{v}_p \mathrm{x} \mathbf{B}$ mechanism in vacuum, *Yugami N., Nishida Y.*	III-1927
10-79 Plasma wave wake field excited by short pulse microwave, *Nishida Y., Kusaka S., Yugami N.*	III-1931
10-82 Direct measurements of velocity space transport in a fully ionized plasma, *Rynn N., Bowles J., McWilliams R.*	III-1935
10-83 Phase conjugation via Brillouin enhanced four-wave mixing in a plasma, *Domier D.W., Luhmann Jr. N.C., Peebles W.A.*	III-1939
10-84 High frequency modes of a plasma column loaded in a sheath helix, *Ganguli A., Appala N.P., Umesh G.*	III-1943
10-85 Estimation of electron temperature and density by deconvolving the absorption part of the plasma dispersion function, *Jimenez-Dominguez H., Cabral-Prieto A., Melendez-Lugo L., Lopez-Callejas R., Colunga-Sanchez S., Valencia-Alvarado R., Cruz-Jimenez S., Gaytan-Gallardo E., Chavez-Alarcon E.*	III-1947

Poster-No. Title, *Author(s)*	Volume/Page
10-86 Kinetic description of modulated electromagnetic wave in relativistic plasma, *Ekiel-Jezewska M., Flå T., Kaufman A.N.*	III-1951

Topic 11: Partially Ionized Plasmas

Poster-No. Title, *Author(s)*	Volume/Page
11-2 Experimental evidence of self-organization and chaos in some plasma devices, *Sanduloviciu M., Alexandroaei D., Talasman S.J. and Ianopol B.*	III-1957
11-5 Tomographic time-resolved reconstruction of the three dimensional electron velocity distribution in a partially ionized RF plasma, *Matsumoto K., Iwama N., Ishii S.*	III-1961
11-6 Large amplitude striations in an RF discharge, *Sato T., Shoji T., Sakawa Y., Hori M.*	III-1965
11-9 Ionization front structure in the lateral spreading of a DC discharge along cylindrical coaxial electrodes, *Gavrilescu C., Popa G.*	III-1969
11-10 Plasma heating in low pressure RF discharges, *Skorik M.A., Braithwaite N.St.J., Allen J.E.*	III-1973
11-11 Ion energy distribution in an RF Argon plasma, *Annaratone B.M., Skorik M.A., Goruppa A.A., Allen J.E.*	III-1977
11-12 Observation of coherent drift structures in the turbulence of a DC discharge, *Kauschke U., Schlüter H.*	III-1981
11-13 Effects of magnetic field on a magnetron discharge, *Mase H., Tanabe T., Ikehata T., Sato N.Y.*	III-1985
11-17 The Langmuir probe study of the electron energy distribution function in the flowing afterglow plasma, *Glosik J., Cermak I., Sicha M., Tichy M., Zakouril P.*	III-1989
11-18 Computer simulation of RF discharges and comparison with laboratory results, *Vahedi V., Surendra M., DiPeso G., Mirrashidi P., Birdsall C.K.*	III-1993
11-19 On modelling of steady states in toroidal machines for basic plasma physics, *Øien A.H.*	III-1997
11-23 A one-dimensional q-machine model taking into account charge-exchange collisions, *Maier H., Kuhn S.*	III-2001
11-24 Determination of composition and physical properties of partially ionized plasmas in the function of temperature, *Zaporowski B.*	III-2005

Poster-No. Title, *Author(s)*	Volume/Page
11-25 Thermodynamic functions for partially ionized plasmas in the mean spherical approximation, *Kahlbaum T., Schneidenbach H.*	III-2009
11-26 Dielectric constant of weakly-ionized magnetized plasmas, *Kiss'ovski Zh., Pironkova A., Shivarova A.*	III-2013
11-28 Ion Bernstein waves in a toroidal steady-state device, *Batani D., Fontanesi M., Galassi A., Riccardi C., Sindoni E.*	III-2017
11-33 Study of low frequency flute type oscillations, their nonlinear interaction in toroidal plasma, *Prasad G., Bora D., Saxena Y.C., Sethia G.C.*	III-2021
11-39 Behaviour of charged particle motion along an inhomogeneous magnetic field and a retarding electric field - evidence for the existence of discrete energy states, *Varma R.K., Punithavelu A.M.*	III-2025
11-40 Unstable behaviour of globular anode structures, *Biborosch L., Toma M., Sanduloviciu M.*	III-2029
11-41 On the electrodynamic explanation of the retrograde motion of the electric arc, *Hong J.S., Allen J.E.*	III-2033
11-42 Nonequilibrium transport phenomena of a plasma in a nonuniform electric field, *Cicconi G., Molinari V., Sumini M.*	III-2037
11-43 Experimental study of the axial structure of an argon plasma column sustained by an electromagnetic wave in the presence of an external magnetic field, *Staikov P., Grozev D., Zhelyazkov I., Benova E.*	III-2041
11-46 Electromagnetic surface waves for large-area RF plasma productions between large-area planar electrodes, *Nonaka S.*	III-2045
11-49 CO_2-TE laser-produced cadmium plasma in vacuum experiment, kinetics, *Apostol I., Bahrim B., Bahrim C., Vasilescu C.*	III-2049

Topic 12: Elementary Processes in Plasmas

Poster-No. Title, *Author(s)*	Volume/Page
12-1 Measured and calculated charge density in Ce, Cu vapor produced by an electron gun, *Blumenfeld L., Gonella C., Morin M.*	III-2055
12-5 Stokes parameters for Compton scattering in a strong magnetic field, *Chou C.K., Chen H.H.*	III-2059

Poster-No. Title, *Author(s)*	Volume/Page
12-6 CTMC study of collisions of Carbon ions with H and He, relevant to magnetically confined fusion plasmas, *Katsonis K., Maynard G.*	III-2063
12-8 Investigation on the metastable fragmentation of mixed argon-oxygen, argon-krypton cluster ions: the observation of two new fragmentation decay channels - evidence for the existence of metastable excited dimer ions ArO^{+*}, $ArKr^{+*}$, *Foltin M., Lukac P., Märk T.D.*	III-2067
12-12 Ion attachment to van der Waals clusters: reactions of NO^+ with Ar_m, *Lezius M., Scheier P., Märk T.D.*	III-2071
12-13 On the interation of low energy electrons with vdW-Clusters: electron attachment reactions, auto-scavenging, *Rauth T., Lezius M., Foltin M., Grill V., Märk T.D.*	III-2075
12-16 Particle exchange reactions at low kinetic energies, *Praxmarer C., Freysinger W., Hansel A., Lindinger W.*	III-2079
12-17 Collisional induced dissociation of Kr_2^+, $(CO)_2^+$, N_4^+, N_2Ar^+, *Praxmarer C., Glosik J., Smith D., Freysinger W., Lindinger W.*	III-2083
12-18 Theoretical studies of the vibrational relaxation of $N_2^+(v=1)$ in collisions with He using the semiclassical method, *Zenevich V.A., Freysinger W., Lindinger W.*	III-2087
12-20 Ionization, recombination processes in dense nonideal plasmas, *Bornath Th., Schlanges M., Kremp D., Bonitz M.*	III-2091
12-23 Experimental, theoretical determination of electron impact ionization cross sections of atoms and molecules, *Grill V., Margreiter D., Walder G., Scheier P., Winkler C., Kurdel M., Poll H.U., Deutsch H., Stephan K., Märk T.D.*	III-2095
12-26 Microwave determination of the coefficient of dissociative recombination of molecular ions of argon, *Okada T., Sugawara M.*	III-2099
12-27 On the laser cooling of ions in oscillating traps, *Reyna L.G., Sobehart J.*	III-2103

Topic 13: Plasma Applications

Poster-No. Title, *Author(s)*	Volume/Page
13-2 One-dimensional modeling for magneto-microwave plasma using the Monte Carlo method, *Ikegawa M., Kakehi Y., Kobayashi J.*	III-2109
13-3 ECR plasma source in ICR separation device, *Meis C., Compant La Fontaine A., Louvet P., Meyer R.L.*	III-2113

Poster-No. Title, *Author(s)*	Volume/Page
13-6 Current and geometry dependence of mass and energy fluxes in capillary, ablative critical flows, *Cuperman S., Zoler D., Ashkenazy J., Caner M., Kaplan Z.*	III-2117
13-7 New method of ion extraction from plasma by using radio-frequency electric field, *Matsui T., Tuchida K., Nishio R., Suzuki K., Shoji T.*	III-2121
13-8 Density and temperature measurements by laser absorption diagnostic on a magnetized plasma, *Compant La Fontaine A., Le Gourrierec P., Louvet P.*	III-2125
13-9 The plasmachemical reactions in negative corona discharges, *Skalny J.D., Lukac P., Gabris R.*	III-2129
13-12 Plasma parameter profiles and fluctuation properties of an ECR process plasma source for Si etching at LN_2 temperatures, *Kim S.K., Park C.W., Cho S., Choi E.H., Kwak J.K., Park J.K., Rhee C.*	III-2133
13-14 Magnet plasma dynamic accelerator with ultra high frequency resonator, *Kubarev Y.V., Tashaev Y.N., Safronov V.P., Kholin N.N.*	III-2137
13-16 Ion irradition studies from dense plasma focus for change of phase for thin film of CdS, *Sagar R., Srivastava M.P., Rawat R.S.*	III-2141
13-17 Influence of metastable atoms on the characteristics of surface wave produced plasmas, *Kortshagen U., Schlüter H.*	III-2145
13-19 Use of cold plasmas in film deposition and structuring, *Edlinger J., Pulker H.K., Rille E., Vogl G.*	III-2149
13-22 Experimental study of plasma effect on oxidation of solid surface, *Kitajima M., Kuroki H., Shinno H., Kawabe T.*	III-2155

Topic 8: General Plasma Theory
(Contribution added in print)

8-116 Langevin-equation for charged particles in microturbulent plasma, *Meister C.-V.*	III-2159

Topic 9:

Space and Astrophysical Plasmas

MODULATIONAL INSTABILITY OF LOWER HYBRID WAVE IN A CYLINDRICAL PLASMA

S.K. SHARMA and A. SUDARSHAN
Department of Physics
I.I.T. Delhi , New Delhi - 110016, INDIA

I. Introduction: A number of workers/1-5/ have studied the Modulational instablity (M.I) because of its relevnce to plasma heating, laser plasma interaction and ionosphere experiments. Recently Konar et al/6/ have investigated M.I. of lower hybrid wave (LHW) in a plasma slab taking into account non - local effects. For the purpose of direct experimental verification, however, it is more useful to study M.I. of LHW in a realistic geometry. In this paper, we develop a non local theory of modulational instability in a cylindrical plasma.

To calculate the electron density fluctuation, it is most convenient to use the ponderomotive force. The non-linear currents produced by the coupling of the pump to the density perturbation generates mixed electromagnetic-electrostatic modes at $\omega \pm \omega_o$ and $k \pm k_o$. These side bands in turn, beat with the pump field to generate a slowly varying envelope of the electric field which gives rise to a ponderomotive bunching force that amplifies the original perturtbation.

In Section II, we derive the mode structure equation of the LHW pump and the side-bands and obtain their solution. In Section III, we derive the non linear dispersion relation for modulational instability and then us it to obtain an analytic expression for its growth rate. The explicit expression for γ is used to study its variation with ω and ω_o for a typical cylindrical plasma.

II. Mode Structure for LHW pump and side bands

We consider a cylindrical plasma which is infinite in the z-direction and confined within a radius 'a'. The plasma is immersed in a static magnetic field $B = B_o z$. Following Liu and Tripathi/5/, the mode structure equation for the LHW is given by the equation

$$\nabla_\perp^2 \phi_o + K_o^2 \phi_o = 0 \qquad (1)$$

where

$$K_o = k_{oz} \left[\frac{\left(\omega_{pe}^2 + \omega_{pi}^2\right)/\omega_o^2 - 1}{1 + \omega_{pe}^2/\omega_{ce}^2 - \omega_{pi}^2/\left(\omega_o^2 - \Omega_c^2\right)} \right]^{1/2} \qquad (2)$$

and ω_{pi} , ω_{pe} and ω_{ce} are the ion plasma, elctron plasma and electron cyclotron frequencies respectively. In a cylindrical plasma, ϕ_o (z,r) may be written as

$$\phi_o = \phi_o(r)\, e^{(-i\omega_o t + ik_{oz} z)}$$

Substituting the above expression for ϕ_o in Eq(1) and introducing a new variable $R = K_o r$, we

obtain:-

$$R^2 d^2\phi_o/dR^2 + R d\phi_o/dR + R^2\phi_o = 0 \quad (3)$$

Eq(3) is a standard equation whose solution is $J_o(R)$ - a zeroth order Bessel function of the first kind and may be written as

$$\phi_o = \phi_m = A_m J_o(R) = A_m J_o(rK_o) \quad (4)$$

where $K_o = j_{o,m}/a$ and $j_{o,m}$ represents the mth zero of the zeroth order/7/ Bessel function of the first kind. Similarly, the mode structure equation for the lower and upper side bands can be written as

$$R^2 d^2\phi_j/dR^2 + R d\phi_j/dR + R^2\phi_j = 0 \quad (5)$$

The solution to Eq(5) is given by

$$\phi_j = \phi_{nj} = A_n J_o(rK_j) \quad (6)$$

Equation for K_j may be obtained from K_o i.e. eqn (1) by substituting ω_j for ω_o

III. Nonlinear coupling and Dispersion Relation

The linear response of the electron to the high frequency modes i.e. ω_o, ω_1 and ω_2 is given by the EXB drift and may be written as

$$\vec{v}_j = e\vec{\nabla}\phi_j \times \vec{\omega}_{ce} / m_e\omega_{ce}^2 ; \quad v_{oz} = - ek_{jz}\phi_o / m_e\omega_{ce} \quad (7)$$

(Where subscript j = 0, 1, 2.)

Using Eq (7), one can write the expression for the ponderomotive potential ϕ_p as

$$\phi_p = - \left[ek_{oz}^2/2m\omega_o^2\right]\left(\phi_o^*\phi_2 + \phi_o\phi_1\right) \quad (8)$$

The non-linear response of the electrons is given by

$$n_\omega = \left[\omega_{pe}^2/4\pi e\omega^2\right]\nabla^2\left(\phi + \phi_p\right) \quad (9)$$

Obtaining the side band density perturbation from equations of continuty and substituting them in the poisson equation we obtain the following mode structure equations for the two side bands:

$$\nabla_\perp^2\phi_1 + K_1^2\phi_1 = - \left[e^2 k_{oz}^4 k^2/4m_e^2\omega_o^4 eP\right]\chi_e(1+\chi_i)\phi_o^*(\phi_o^*\phi_2 + \phi_o\phi_1) \quad (10a)$$

and $$\nabla^2_\perp \phi_2 + K_2^2 \phi_2 = -\left[e^2 k_{oz}^4 k^2 / 4m_e^2 \omega_o^4 \epsilon P\right] \chi_e(1+\chi_i)\, \phi_o(\phi_o^* \phi_2 + \phi_o \phi_1) \qquad (10b)$$

where $\epsilon = 1 + \chi_e + \chi_i$ and $P = 1 + \omega_{pe}^2 / \omega_{ce}^2 - \omega_{pi}^2 / \left(\omega_o^2 - \Omega_c^2\right)$

To find the solution to Eq. (10a) and Eq. (10b), we expand ϕ_1 and ϕ_2 in terms of a complete set of orthonormal functions in terms of ϕ_{1n} and ϕ_{2m} respectively as

$$\phi_1 = \sum_n A_n^{(1)} \phi_{1n}(K_1 r) \quad \text{and} \quad \phi_2 = \sum_m A_m^{(2)} \phi_{2m}(K_2 r) \qquad (11)$$

As indicated in Eq. (4) and (6), these orthonormal functions are zeroth order Bessel functions of the first kind. Subtracting Eq. (10a) from corresponding linear mode structure equation and multiplying the resulting equation by $r\phi_1$ and integrating over r we obtain:

$$\left(K_1^2 - K_{in}^2 - \eta \int r \phi_o \phi_o^* \phi_{1n} \phi_{1n}^* \, dr\right) A_n^{(1)} = \eta \sum_m A_m^{(2)} \int r \phi_o^* \phi_o^* \phi_{2m} \phi_{1n}^* dr \qquad (12)$$

where $$\eta = -\left[e^2 k_{oz}^4 k^2 / 4m_e^2 \omega_o^4 \epsilon P\right] \chi_e (1 + \chi_i) \qquad (13)$$

Similarly for ϕ_2, we have

$$\left(K_2^2 - K_{2m}^2 - \eta \int r \phi_o \phi_o^* \phi_{2m} \phi_{2m}^* \, dr\right) A_m^{(2)} = \eta \sum_n A_n^{(1)} \int r \phi_o^* \phi_o^* \phi_{1n} \phi_{2m}^* \, dr \qquad (14)$$

Multiplying Eq. (12) and Eq. (14), and taking the mode numbers for the upper and lower sidebands to be equal (m=n), we obtain the following dispersion relation

$$\left[K_1^2 - K_{1n}^2 - \Delta_1\right]\left[K_2^2 - K_{2n}^2 - \Delta_2\right] = \mu \qquad (15)$$

where $$\Delta_1 = \eta \int \phi_o \phi_o^* \phi_{2n} \phi_{2n}^* \, dr \; ; \quad \Delta_2 = \eta \int \phi_o \phi_o^* \phi_{1n} \phi_{1n}^* \, dr \qquad (16)$$

and $$\mu = \eta^2 \int \phi_o^* \phi_o^* \phi_{2n} \phi_{1n}^* \, dr \int \phi_o^* \phi_o^* \phi_{1n} \phi_{2n}^* \, dr \qquad (17)$$

Using Taylor's expension for K_1^2 and K_2^2 and assuming ω to be complex we obtain from equtions (15) to (17) the following expression for ω_r and growth rate γ :

$$\omega_r = \left[k_z \omega_o^2 / k_{oz} A\right]\left[A/\omega_o^2 - 1\right] \qquad (18)$$

$$\gamma = 1/D \left\{\mu - \Delta_1\Delta_2 + (\Delta_1 + \Delta_2)\left[2\omega_r A k_{oz}^2 / \omega_o^3 + 3\omega_r^2 A k_{oz}^2 / \omega_o^4 + k_z^2 (A/\omega_o^2 - 1)\right]\right\}$$

$$+2k_z k_{oz}(A/\omega_o^2 - 1)(\Delta_1 - \Delta_2) - 8\omega_r^4 A^2 k_{oz}^4 / \omega_o^8 + 4\omega_r^2 A^2 k_{oz}^4 / \omega_o^6 - \left(A/\omega_o^2 - 1\right)^2 \left[k_z^4 - 4k_z^2 k_{oz}^2\right]$$

$$\left\{-(A/\omega_o^2 - 1)\left[6\omega_r^2 A k_{oz}^2 k_z^2 / \omega_o^4 + 8\omega_r A k_z k_{oz}^9 / \omega_o^9\right]\right\}^{1/2} \qquad (19)$$

where $D = \left\{4A^2 k_{oz}^4/\omega_o^6 - 36\omega_r^2 A^2 k_{oz}^4/\omega_o^8\right\}^{1/2}$ and $A = \omega_{pe}^2 + \omega_{pi}^2$

In evaluating the integrals occuring in Δ_1 and Δ_2 we have taken n=7. We have also assumed in our calculations that $\mu \cong \Delta_1\Delta_2$.

IV. RESULTS AND DISCUSSION

Equation (19) gives the expression for growth rate of modulation instability of a lower hybrid pump in a cylindrical plasma. To obtain numerical appreciation of the growth rate of M>I. of lower hybrid wave, we assume the following values for a typical cylindrical plasma

$\omega_{ce} = 1\times10^{12}\ s^{-1}$, $k_z = 0.025\ cm^{-1}$, $k_{oz} = 50k_z$, $\delta = 8\times10^4$,
$\omega_{pe} = 2.5\times\omega_o$; radius of cylinder "a" = 3 cm.

Fig (1) and Fig (2) shows the variation of γ of M.I. in a cylindrical plasma as a function of perturbation frequency ω_r and the pump wave of frequency ω_o respectively. It is seen from Fig.1 and Fig.2 that γ increases monotonically with increasing values of ω_r and ω_o.

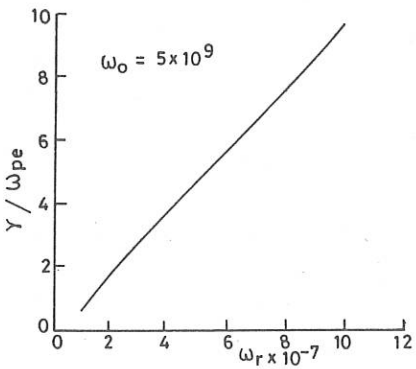

Fig.1 Variation of γ/ω_{pe} with ω_r

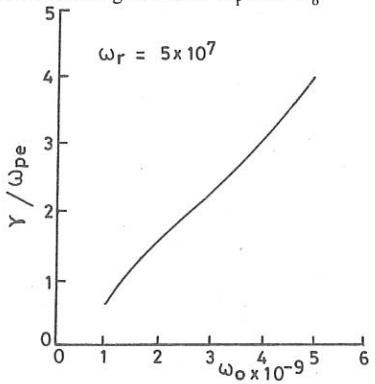

Fig.2 Variation of γ/ω_{pe} with ω_o

References

/1/ R. BINGHAM and C.N. lASHMORE - DAVIES, J. Plasma Physics, 21, 51 (1979).
/2/ B.N. BREIZMAN and V.M. MALKIN, Soviet JETP, 52, 435(1980).
/3/ M.K.SAXENA, A.K. ARORA and S.R. SHARMA, Plasma Physics, 23, 491(1981).
/4/ G.MURTAZA and M. SALAHUDDIN, Plasma Physics, 24, 451(1982).
/5/ C.S.LIU and V.K. TRIPATHI, Physics Rep., 130, No.3, 143-216 (1986).
/6/ S.KONAR AND V.K. JAIN, V.K. TRIPATHI, J. Appl. Physics, 65, 10 (1989).
/7/ Handbook of Mathematical Functions. Ed. M Abramowitz and I.A. Stegun, Dover Pub., New York, p.307 (1972).

III-1571

INTERACTION OF A MAGNETIZED PLASMA STREAM WITH AN IMMOBILE ION CLOUD

K. Baumgärtel ,K. Sauer
Max-Planck-Institut für extraterrestrische Physik
Aussenstelle Berlin, O-1199 Berlin, Germany

The interaction between a magnetized plasma and a localized ensemble of 'heavy' ions in relative motion arises in a variety of situations in space plasmas (Critical ionization velocity experiments /1/; neutral gas releases in the solar wind: experiment AMPTE /2/; interaction of the solar wind with a charged cloud of dust particles /3/; encounter of the solar wind with the ionosphere of an unmagnetized body or its interaction with the atmosphere of a comet). Common features of these situations are (1) an unspecified orientation of the magnetic field to the flow direction; (2) both electron cyclotron radius and Debyelength are small compared to interesting scale lengths, while the ion gyroradius is in general not; (3) the relative kinetic energy of flow ions in the cloud frame is large compared to their thermal energy; (4) the cloud ion mass is large compared to the mass of the ions in the plasma stream; and (5) collisions between ions are largely neglegible. Conventional MHD theory does not apply here, but a different treatment of electrons and ions and the inclusion of a second ion species is required. Several simulations in this context (mainly to model the AMPTE experiment) have been carried out, most of them based on hybrid code simulations /4-7/. We use a lower level of description, and our interest is primarily in basic phenomena of the collisionless coupling that survive even when the plasma model is rigorously simplified /8/.

Characteristic features of the plasma model are (1) 1-D geometry, i.e., the ion cloud degenerates to a plane-layered slab (Fig. 1); (2) Cloud ions are assumed immobile, i.e., mass loading, cloud expansion and ion production are ignored; (3) electrons are treated as masseless, strongly magnetized, isothermal flow; (4) ions are considered as weakly magnetized cold fluid, (5) quasineutrality is assumed throughout. Thus, Debyelength and lower hybrid frequency are excluded, but the model produces ion dominated low frequency phenomena (ion acoustic waves, compressive and shear Alfvén waves). The basic

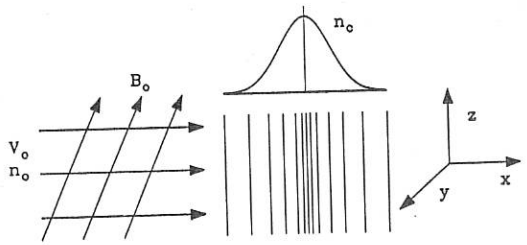

Fig. 1

equations are

$$\frac{\partial n_i}{\partial t} + \frac{\partial}{\partial x}(n_i v_{ix}) = 0$$

$$\frac{\partial \boldsymbol{v}_i}{\partial t} + v_{ix}\frac{\partial}{\partial x}\boldsymbol{v}_i = \frac{e}{m_i}(\boldsymbol{E} + \boldsymbol{v}_i \times \boldsymbol{B})$$

$$\boldsymbol{E} = \boldsymbol{E}_\parallel + \boldsymbol{E}_\perp = -\frac{k_B T_e}{e n_e}\frac{\partial n_e}{\partial x}(\boldsymbol{x}\cdot\boldsymbol{b})\,\boldsymbol{b} - (\boldsymbol{v}_e \times \boldsymbol{B})$$

$$\frac{\partial \boldsymbol{E}}{\partial t} = -\frac{e}{\varepsilon_o}(n_i \boldsymbol{v}_i - n_e \boldsymbol{v}_e) + c^2 \frac{\partial}{\partial x}(0, -B_z, B_y)$$

$$\frac{\partial \boldsymbol{B}}{\partial t} = -\frac{\partial}{\partial x}(0, -E_z, E_y)$$

$$n_e = n_i + n_c$$

Subscripts e, i, c denote electrons, flow ions and cloud ions, respectively. Our general strategy is to look for the steady-state response of the plasma flow to the ion layer. To this end we solve the ordinary differential equations which result from the basic system by cancelling time derivatives .

(a) *Magnetic field aligned to the flow*: Fig. 2 illustrates the response of the plasma stream to an ion layer with Gaussian shape and a peak density $n_{c,max}=0.2n_o$ for two ion acoustic Mach numbers. A fairly supersonic flow penetrates the layer with almost no effects on the ions (layer charge balanced by electrons, weak electric field). In a fairly subsonic flow, however, charge neutrality at the layer is maintained by an ion density depletion and a much stronger electric DC field with opposite sign is established. Electrons are too 'stiff' to react and are almost unaffected. In gasdynamic terms, the model obstacle acts on the plasma flow like a nozzle. If the peak layer density exceeds a (Mach number-dependent) critical value,

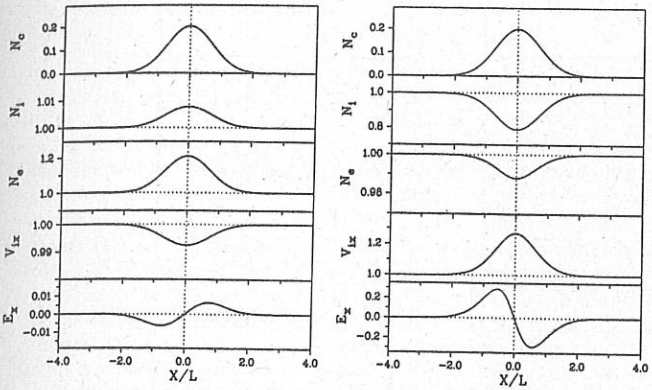

Fig. 2 (a) M_s=5 (b) M_s=0,2
Distance, densities, velocity and electric field normalized, respectively, by the ion skin depth L, n_o, v_o and $m_i v_o^2 eL$

the plasma stream cannot longer penetrate the layer. In a three-dimensional situation, the ion cloud would then act like a 'rigid' obstacle to the flow. The critical density tends to zero when the flow becomes sonic.

(b) *Magnetic field perpendicular to the flow*: In this case, the electron temperature does not enter the analysis and the Alfven Mach number is the relevant quantity. Unlike the former case, however, the layer size comes into play. One can distinguish between a 'small' and a 'large' column density case. In the first one typical features of the magnetic field-free interaction are reproduced. In the latter case, the flow distortion is no longer confined to the area covered by the obstacle but a super-Alfvenic (sub-Alfvenic) flow undergoes a pronounced compression (expansion) when passing the ion layer. In both cases the flow is significantly deflected in y-direction. Consequently, even a low-density ion ensemble may become impenetrable in case of a large enough size. These results are largely consistent with hybrid code simulations /7/.

(c) *Magnetic field inclined to the flow*: The most interesting feature in this case is the excitation of stationary waves (waves with ω=0 in the layer rest frame, i.e., phase velocity in the plasma frame equal but opposite to the flow velocity). They are absent for $\mathbf{B}_0 \| \mathbf{v}_0$, $\mathbf{B}_0 \perp \mathbf{v}_0$ because of the acoustic-like dispersion of the relevant modes. Stationary waves develop either downstream or upstream of the layer according to whether

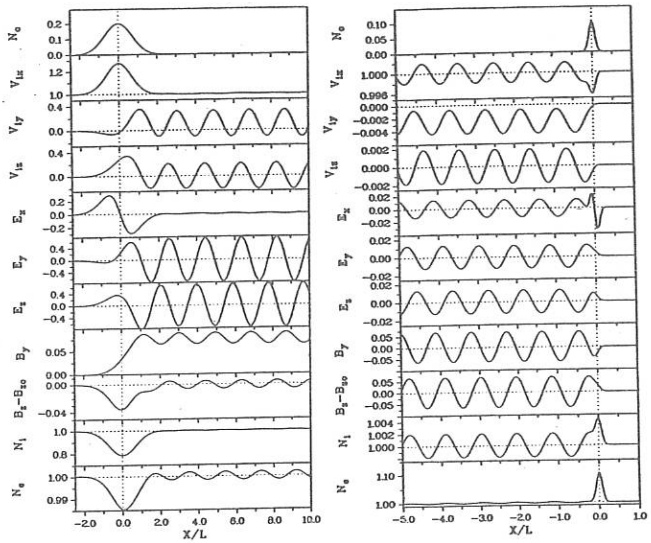

Fig. 3 (a) $M_S=M_A=0.2$ (b) $M_S=M_A=5$
Magnetic field 45° inclined to the flow direction

the component of the associated group velocity in flow direction is smaller or greater than v_o (Fig. 3). While the downstream wave is basically electrostatic in nature, the upstream waves is a fast Alfven mode. The layer does not admit a steady-state penetration of the plasma stream for flow velocities ranging between the smallest and greatest group velocity of the three low-frequency modes.

/1/ P.T.Newell, *Rev. Geophys.*, **23**, 93, 1985
/2/ D.Bryant, S.M.Krimigis, G.Hearendel, *IEEE Transact. on Geoscience and Remote Sensing*, **GE-23**, 177, 1985
/3/ C.K.Goertz, *Rev. Geophys.*, **27**, 271, 1989
/4/ R.Bingham, R.Bollens, F.Kazeminejad, J.M. Dawson, Geophysical Monograph Vol. 61, 73, 1991
/5/ S.H.Brecht, V.A.Thomas, *J.G.R.*, **92**, 2289, 1987
/6/ S.C.Chapman, S.J.Schwartz, *J.G.R.*,**92**, 11059, 1987
/7/ U.Motschmann, K.Sauer, Th.Roatsch, *G.R.L.* **19**, 225, 1992
/8/ K.Baumgärtel, K. Sauer, Workshop on Plasma experiments in the Laboratory and in Space, Alpbach/Austria, July 1991, to be published Ann.Geophys.

Rayleigh–Taylor Instability favoured Drift Turbulence in a Spread F Simulation Experiment

G. Prasad, D. Bora and Y. C. Saxena
Institute for Plasma Research, India

In bottom side of F–region of the ionosphere, the density gradient (∇n) and electric field are antiparallel to gravity (g), the ∇n is perpendicular to magnetic field (B), ions and electrons are magnetised ($\nu_{in}/\Omega_i \ll 1, \nu_{en}/\Omega_e \ll 1$) and the crossfield term (E_o/B_o) is less effective than gravity i.e., $E_o/B_o < g/\nu_{in}$. In this region the long wavelength modes ($k\rho_i \ll 0.1$) are found to have power spectral form of $S(k) \propto k^n$ with n = – 2 to – 2.5. Rayleigh – Taylor instability mechanism has been invoked to explain the k^{-2} spectrum (Chaturvedi and Kaw, 1976; Sudan and Keskinen, 1984; Zargham et al., 1987). In the short wavelength regimes ($0.1 < k\rho_i < 1$) the experimental observations exhibit a spectral index n = – 4 to – 5 in density fluctuations and electric field fluctuations have n = –2 to –3 (Singh and Szuszczewicz (1984), LaBelle et al., 1986). Drift waves, with spectral index in range of –4.5 to –5.0, are favoured as good candidate for the generation of short wavelength fluctuations (Hasegawa and Mima, 1978; Fyfe and Montgomery,1979; Hasegawa et al., 1979; Tchen et al.,1980; Pécseli et al., 1980; LaBelle et al., 1986). The theory of Chaturvedi and Kaw (1977) predicts R – T instability as the primary source of irregularity which is effective at wavelengths of the order of vertical density gradient scale lengths, and the growth of R–T instability is followed by generation of short scale length drift waves.

We have recently reported, for the first time, experiments on low frequency instabilities in laboratory plasma simulating conditions obtained in the equatorial spread–F (Prasad et al. 1992 a,b). The experiments satisfy the conditions on the dimensionless parameters $\nu_{in}/\Omega_i \ll \nu_{en}/\Omega_e \ll 1$ for the F–region. The equilibrium plasma density and potential profiles satisfy $E_o \parallel \nabla n \perp B_o$ and gravity is simulated by the curvature of the magnetic field. In this paper we report a study of spectral characteristics of density and potential fluctuations of plasma as a function of ν_{in}/Ω_i keeping $\nu_{en}/\Omega_e \ll 1$ in all cases. The k-spectra obtained indicate dominance of R–T instability in long wavelength regime and existence of R–T favoured Drift turbulence in shorter wavelength regime. The results are compared with theoretical predictions, numerical simulations, experimental observations of F region and laboratory studies.

The experiment is conducted in a toroidal device BETA, having toroidal magnetic field, a major radius (R) of 45 cm and minor radius of 15 cm. A radially movable cylindrical Langmuir probe with exposed tip of 2.5 mm in length and 0.75 mm in diameter insulated with glass is used to measure equilibrium profiles of plasma density, floating potential and electron temperature. A pair of probes placed at radial location of 6 cm with angle of separation 5^o is used to get wave number and frequency spectra using the technique outlined by Beall et al. (1985) when the fluctuations are turbulent. The data is acquired on dual channel Lecroy oscilloscope with a sampling time of $20\mu sec.$ of 8 bit resolution with 32 kbyte of samples per channel.

The plasma has peak density $\sim 10^{11}/cm^3$, with electron temperature in the region where experiment is performed is $\sim 4eV$ with $T_i = 0.23 \pm 0.06eV$. The effect of gravity is simulated by curved magnetic field, $g = C_s^2/R \simeq 2 \times 10^9$ cm/sec^2 for Argon plasma. Typical density and floating potential profiles measured are shown in figure 1. The fluctuations have $\tilde{n}/n_o \sim e\tilde{\phi}/T_e$. The density gradient scale length $L_n = n/\nabla n \sim 18cm$. During the experiment we varied the neutral Argon gas pressure from 10^{-4} Torr to 4×10^{-4} Torr. Under these operating conditions $\nu_{en}/\Omega_e \ll 1$ is satisfied and hence electrons

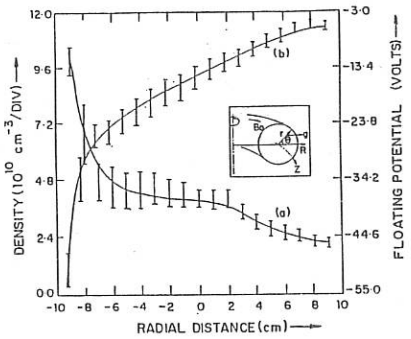

Figure 1: Radial profiles for (a) density and (b) floating potential.

are magnetised. The k – spectra in density and potential fluctuations are obtained at different magnetic fields and at different pressure. Under most of these conditions the power spectrum indicates turbulence. The density fluctuation spectrum (figure 2) has a shallower slope of $n = -2.2 \pm 0.2$ for $k\rho_i < 0.5$ and has steeper slope of $n = -4.2 \pm 0.5$ for $0.5 < k\rho_i < 2$ whereas potential spectrum (figure 3) has only one slope n = – 4.5 for the variation of ν_{in}/Ω_i from 0.04 to 0.1. The variation of k – spectral indices in density and potential as a function of ν_{in}/Ω_i is shown in figure 4 and indicates that the density spectrum has dual slope where as the potential spectrum has only one slope for the variation of ν_{in}/Ω_i from 0.04 to 0.1. It is also clear from figure 4 that the difference between the shallower slope of density spectrum and potential spectrum is$\sim$ 2 and steeper slope of density spectrum and potential spectrum are nearly similar. One of the important tool used in identifying the nature of the instability is the spectral relation between density and electric field (or potential) in different scale length regimes. The relation between density and potential for R – T instability is given (Kelley, 1989) by

$$\tilde{E}(k) = - \left(\frac{gB}{\nu_{in}}\right)\frac{\tilde{n}}{n} \tag{1}$$

The spectral index for electric field fluctuations should, for this case,be similar to that of density fluctuation implying that the density and potential spectral indices should differ by $\sim$ 2. The relation between density and potential spectral indices for drift waves for which Boltzmann relation is valid and is given by

$$\tilde{E}(k) = - ik \left(\frac{K_B T_e}{e}\right)\frac{\tilde{n}}{n} \tag{2}$$

where K_B is the Boltzman constant. Electric field and density fluctuation spectra should have spectral indices differing by $\sim$ 2 or the potential and density fluctuation spectra should have a similar form. In our experiment, the observed spectral indices, of $n = -2.4 \pm 0.2$, and $n = -4.2 \pm 0.3$, for density and potential fluctuations respectively for the case of $k\rho_i < 0.5$ is in agreement with equation (1), and the measurements of LaBelle et al. (1986) in night time F – region. The theory of Chaturvedi and Kaw (1976) predicts

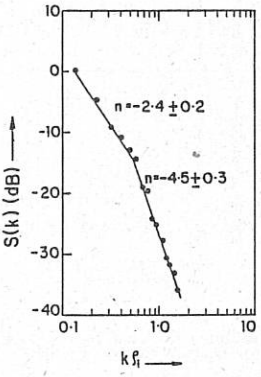

Figure 2: k-Spectrum of density fluctuations. The power law least square fits are shown by solid lines and experimental data points are shown by dots.

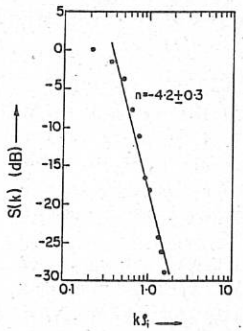

Figure 3: k-Spectrum of potential fluctuations. The symbols are same as in figure 2.

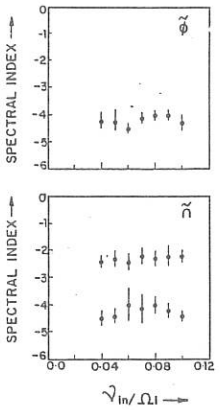

Figure 4: Variation of spectral index with ν_{in}/Ω_i for density and potential fluctuations.

similar spectral form. Sudan and Keskinen (1984) predict a spectral index of n = – 5/3 for one dimensional case; however many numerical simulation studies and experimental observations differ with this theoretical value . This theory is applicable when inertial ranges are well developed and turbulence is strong, and is not applicable in present case. The observed spectral indices of n = - 4.5 ±0.3 and n = -4.2±0.3 for density and potential fluctuations respectively, in the range $0.5 < k\rho_i < 1$, are in close agreement with equation (2), the drift wave spectral index measured in laboratory (Pécseli et al.,1980) and F – region (LaBelle et al., 1986) experiments.

In conclusion we have observed density and potential fluctuations at low frequency in a toroidal magnetised plasma, simulating conditions of equatorial spread-F conditions. The observed spectra are turbulent and indicate Rayleigh -Taylor instability as dominant mechanism for production of long wave length fluctuations while R-T induced Drift waves appear to be responsible for the shorter wavelength turbulence.

References

Beall, J.M., Y.C. Kim, & E.J. Powers, *J.Appl.Phys.*, **53** , 3933, 1982.
Chaturvedi, P.K. & P.K. Kaw, *J. Geophys. Res.*, **81**, 3257, 1976.
Fyfe, D., & D. Montegomery, *Phys. Fluids*, **22**, 246, 1979.
Hasegawa A., & K. Mima, *Phys. Fluids.*, **21**, 87, 1978.
Hasegawa A., C. G. Maclennan & Y. Kodama, *Phys. Fluids.*, **22**, 2122, 1979.
Kelley M.C., The Earth's Ionosphere plasma physics and electrodynamics, Academic Press, California, 1989.
LaBelle, J., M.C. Kelley, & C.E Seyler, *J. Geophys. Res.*, **91**, 5513, 1986.
Pécseli, H.L., T. Mikkelsen & S.E. Larsen, *Plasma.Phys.*, **25**, 1173, 1983.
Prasad, G., D. Bora & Y.C. Saxena,*Geophys.Res.Lett.*, **19**, 241 1992a.
Prasad, G., D. Bora & Y.C. Saxena,*Geophys.Res.Lett.*, **19**, 245 1992b.
Singh, M. & E. P. Szuszczewicz, *J.Geophys.Res*, **89**, 2313,1884.
Sudan, R.N. & M.J. Keskinen, *J.Geophys.Res*, **89**, 9840, 1984.
Tchen C . M., Pécseli, H.L., S.E. Larsen, *Plasma.Phys.*, **22**, 817, 1980.

SIMULATION OF ELECTRON BEAM-DRIVEN INSTABILITIES BY A 3-D ELECTROMAGNETIC PARTICLE CODE

K. – I. Nishikawa
Department of Physics and Astronomy, The University of Iowa,
Iowa City, IA 52242, U.S.A.

O. Buneman
Space Telecommunication and Radioscience Laboratory, Stanford University,
Stanford, CA 94305, U.S.A.

T. Neubert
Space Physics Research Laboratory, The University of Michigan,
Ann Abor, MI 48109, U.S.A.

Abstract

We have developed a 3-D electromagnetic and relativistic particle code in which the fields are directly updated through current deposition of the particles, eliminating Poisson's equation and its time-consuming solution /1/, /2/. We have used this code to investigate waves excited by a localized electron beam along the magnetic field (in the z-direction). Periodic boundary conditions are applied along this direction, while in the y- and z- directions we apply boundary conditions which allow radiation to escape freely out of the simulation domain without reflection /3/. Particles which hit the radiating boundaries are arrested there and redistributed more uniformly by having the boundaries slightly conducting: this allows electrons to recombine with ions and provides a realistic way of eliminating escaping particles from the simulation system. The simulation results using a mesh of dimension $85 \times 85 \times 160$ with a few million particles show whistler emissions and beam modes like those evidenced by wave data from the Spacelab 2 mission. The modulation of the parallel current density, due to bunching of the beam electrons, is responsible for the generation of whistler waves. The waves are saturated due to the slowdown and heating of the beam electrons. The hodogram of the magnetic field in the $x - y$ plane shows a right-hand polarization, consistent with whistler mode propagation. In the initialisation of the beam-plasma system, "quiet start" conditions were approached by including the poloidal magnetic field of the beam: thermal noise was the only cause of the excitation of the growing modes.

Introduction

During the Spacelab 2 flight, which was launched on July 29, 1985, a spacecraft called the Plasma Diagnostics Package (PDP) performed a fly-around of the shuttle at distance of up to 300 meters while an electron beam was being ejected from the shuttle in a steady (d.c.) mode. *Gurnett et al.* /4/ have investigated the plasma waves observed during a magnetic conjunction between the PDP and the shuttle while the electron gun was being operated. A spectrogram of the plasma wave electric field intensities during a 30-minute period around the magnetic conjunction is shown in Figure 2 of the work by *Gurnett et al.* /4/. At higher frequencies a very well-defined funnel-shaped feature can be seen extending up to about the electron cyclotron frequency, $f_c \approx 1$ MHz, spreading out at higher frequencies. At even higher frequencies, the intense narrowband emission at about 3.1 MHz is believed to be either the electron plasma frequency, f_p or the upper

hybrid resonance frequency, $f_{UHR} = (f_c^2 + f_p^2)^{1/2}$, where $f_p \approx 3.1$ MHz /4/.

In this work we use a newly developed 3-d relativistic electromagnetic particle code /1/. The mixed boundary conditions are developed in order to investigate the localized electron beam. The periodic condition is used along the magnetic field (z-direction). The radiating boundary conditions are used for x- and y-directions. A larger system than the previous work /5/ is used with all components of the magnetic fields and the relativistic effects.

Simulation model and results

The simulations are performed on the Cray-2 at National Center for Supercomputing Applications (NCSA), The University of Illinois at Urbana-Champaign. The localized electron beam is located in the middle of the simulation domain. The system size used for simulations is $L_x = L_y = 85\Delta, L_z = 160\Delta$, where L_x, L_y, and L_z are the lengths of the system in three directions and $\Delta(= 1)$ is the grid size. The magnetic field is in the z-direction. Along the z-direction, the fields and particles are periodic. On the other hand, "radiating" boundaries, which allow radiation to escape freely out of the simulation domain without reflection, are used for the boundaries perpendicular to the magnetic field.

We consider the column of electron beam in the middle of the system along the z-direction, whose radius, r_{eb} is 4.47Δ (its center is located at $x_{cnt} = y_{cnt} = 43$). The beam electrons are randomly chosen in the column. The beam density in the column is about the half (0.502) of the total electron density. The total number of beam electrons in the column, N_{eb} is 4899. The drift velocity of beam electrons, V_d is $3.5v_{et}$, where v_{et} is the electron thermal velocity. The temperature of the beam electrons, T_{eb} is $0.09T_e$, where T_e is the temperature of the background electrons. In this study the ion drift velocity, V_i is zero.

Based on the observed data, we chose a set of parameters. The parameters used for the simulations are the following: $m_i/m_e = 64$, $T_e/T_i = 1$, $\Omega_e/\omega_{pe} = 0.4$, $c/v_{et} = 10.67$, $\omega_{pe}\Delta t = 0.10$, $\beta = 0.111$, where m_i, m_e, T_i, Ω_e, ω_{pe}, c, are the ion and electron mass, the temperatures of the background ions, the electron cyclotron and plasma frequencies, and the speed of light, respectively. The Debye length, λ_{De} is 0.469Δ. The simulation plasma is quasi-neutral all over the system. Other parameters used for the simulation are the electron and ion gyro-radii, $\rho_e = 1.17$, and $\rho_i = 9.38$, skin depth, $c/\omega_{pe} = 5.00$.

Several simulations have been performed with different parameters. The most important development in this study is including the initial poloidal magnetic field (IPMF) generated by the beam electrons which corresponds to a quiet start. In this way the transient stage due to the instant onset of the parallel current was greatly reduced. For the detailed simulation results see /6/. The hodogram shown in Fig. 1 is one of the new unique results obtained by this 3-D electromagnetic code.

In order to examine the excited electromagnetic waves, the local magnetic fields were sampled at the two different distance (a) at $x = 16$, (b) $x = 43$ from the electron beam (at $y = 43$, $z = 55$). Figure 1 shows hodograms of the magnetic fields ($B_x - B_y$) in the $x-y$ plane. The value is plotted for every 5 time steps ($\omega_{pe}\Delta t = 0.5$). Figure 1a show the hodogram at $x = 16$ for the time period $10 \leq \omega_{pe}t \leq 30$. The ambient magnetic field is coming out of the surface. Due to the larger distance from the electron beam the signal is mixed with thermal noise, however, the direction of the rotation is clearly seen and the same direction as electron cyclotron motion, therefore the field is right-hand polarized.

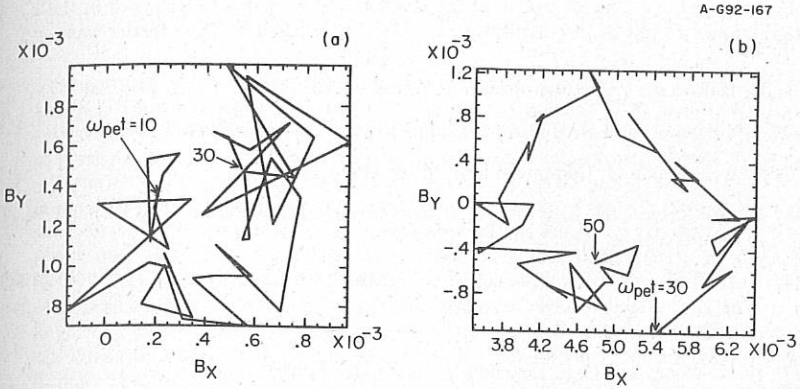

Fig 1: Hodograms of the magnetic field amplitude (relative) $B_x - B_y$ at $y = 43$, $z = 55$.
(a) at $x = 16$
(b) at $x = 43$ (at the center of the beam)

At the middle of the electron beam (Fig. 1b) the hodogram ($30 < \omega_{pe}t < 50$) shows a clear rotation with larger amplitudes. This confirms that the whistler waves are emitted from the electron beam and propagate obliquely.

Conclusion

We have investigated whistler and electrostatic waves driven by the electron beam ejected from the shuttle. The simulations have been performed by using a newly developed 3-D electromagnetic and relativistic particle code.

The simulation results show a whistler emission and beam mode as shown by wave data obtained from the Spacelab 2 mission. The wave analysis of the local electric and magnetic fields show the growing whistler waves whose frequencies are less than the electron cyclotron frequency. The simulation results show that the frequencies of whistler waves are depend on the distance from the electron beam. The more distant from the beam, the frequencies become closer to the electron cyclotron frequency which is consistent with the characteristics of the funnel shaped spectrum observed the PDP /7/. Besides whistler waves electron plasma waves and/or upper hybrid waves are also excited. As we expect, these simulation results are very similar to the previous results /8/, /9/, /5/, /10/, /11/.

The detail analysis of the generation mechanism of the whistler wave conclude the previous results by *Pritchett et al.* /11/. The perturbed parallel current density due to the bunching of beam electrons is responsible to the generation mechanism of the whistler waves /12/, /13/, /14/. The electrostatic waves are saturated due to the slowdown and heating of the beam electrons around $\omega_{pe}t = 25$. It should be noted that even at the stage (after $\omega_{pe}t = 25$) where the electrostatic waves are decaying, the whistler waves are still being excited. At this stage the bunching of beam electrons disappears in the phase space $z - v_z$. The 3-dimensional spiral bunching structure of the beam electrons which is not

well shown in the 2-dimensional display may be responsible for this prolonged excitation of whistler waves. The hodogram of the magnetic field amplitude (relative) in the $x - y$ plane shows a right-hand polarized wave which is consistent with a whistler wave.

/1/ O. Buneman, *Proceeding of ISSS-4*, Kyoto, Japan, (1991)

/2/ J. Villasenor, and O. Buneman, Comp. Phys. Comm., submitted, (1991)

/3/ E. L. Lindman, J. Comput. Phys. **18**, 66 (1975)

/4/ D. A. Gurnett, W. S. Kurth, J. J. Steinberg, P. M. Banks, R. I. Bush, and W. T. Raitt, Geophys. Res. Lett. **13**, 225 (1986)

/5/ K.-I. Nishikawa, L. A. Frank, and C. Y. Huang, J. Geophys. Res. **94**, 6855 (1989)
/6/ K.-I. Nishikawa, O. Buneman, T. Neubert, to submitted to J. Geophys. Res. (1992)

/7/ H. K. Wong, and C. S. Lin, Radio Sci. **25**, 277 (1990)

/8/ Y. Omura, and H. Matsumoto, Geophys. Res. Lett. **15**, 319 (1988)

/9/ Y. Omura, and H. Matsumoto, in *Numerical Simulation of Space Plasma* edited by B. Lembège and J. W. Eastwood, p. 133, North-Holland, Amsterdam, (1988)

/10/ P. L. Pritchett, H. Karimabadi, and N. Omidi, Geophys. Res. Lett. **16**, 883 (1989)

/11/ R. M. Winglee, and P. J. Kellogg, J. Geophys. Res. **95**, 6167 (1990)

/12/ W. M. Farrell, D. A. Gurnett, P. M. Banks, R. I. Bush, and W. J. Raitt, J. Geophys. Res. **93**, 153 (1988)

/13/ W. M. Farrell, D. A. Gurnett, and C. K. Goertz, J. Geophys. Res. **94**, 443 (1989)

/14/ T. Neubert, and P. Banks, Planet. Space Sci. **40**, 153 (1992)

Night Time Equatorial Spread F Simulation in a Laboratory Plasma

G. Prasad, D. Bora and Y. C. Saxena
Institue for Plasma Research, Gandhinagar 382 424, INDIA

The night time equatorial F-region plasma has two distinct regions: The region I is well known as bottom side of F region in which the density gradient (∇n) is antiparallel to gravity (g). In region II (above the F-region peak density) the density gradient parallel to gravity. The numerical simulation and theoretical predictions suggest that Rayleigh – Taylor (R – T) instability plays crucial role in the generation of irregularities of the order of density gradient scale length in the region I where cross field (E_o/B) and velocity shear forces are less dominant. The in-situ observations exhibit power spectrum, S(k) $\propto$ k ^{n} with index n = –2.0 for $k\rho_i \ll 1$(Singh and Szuszczewicz 1984). In-situ and rocket observations (Kelley et al., 1982) in the region II exhibit similar features to that of the region I. The theoretical prictions cannot explain this because gravity is ineffective in good curvature region. The numerical simulations of R-T instability by Scannapieco and Ossakow (1976) clearly exhibit the occurence of similar fluctuations in either sides. In order to clarify some of these features of F-region plasma we performed a laboratory experiment in which the plasma has both regions similar to F-region (region I and region II) with $\nu_{in}/\Omega_i \ll 1, \nu_{cn}/\Omega_c \ll 1$ at low operating pressures ($1 \sim 5\ 10^{-4}$ torr).

The experiment is performed in device BETA (Bora 1984), which is toroidal in shape having a major radius (R) of 45 cms and a minor radius of 15 cms. A variable toroidal field upto 1 kG can be applied. A tungsten filament 2 mm in diameter and 21 cm in length, is placed vertically at major radius of 45 cm. The plasma is produced by striking a discharge between the cathode (incadescent tungsten filament) and the anode (vessel wall). Gravity is simulated by the curvature of the toroidal magnetic field ($g = C_s^2/R$ where C_s is ion accoustic speed and R is major radius of the system). The density is measured by ion saturation currents drawn by a low-impedance probe together with current to voltage converter. The floating potential is measured by a high impedance probe terminated with a voltage follower. The plasma produced has peak density $\sim 10^{11} cm^{-3}$. The electron temperature at the radial locations where these instability measurements are made (± 5 to ± 8) varies from 5eV to 3eV, ion-temperature $T_i \simeq 0.2eV$. The typical density and potential profiles are shown in figure 1 which exhibits two regions i.e. between radial locations 9 cm to 1 cm, the g is antiparallel to ∇n and between – 1 cm to – 9 cm, g is parallel to ∇n. The value of local $E_o \simeq 1.0$ V/cm in the region $\pm$ 4 to $\pm$ 8 suggests that effects of gravity is relatively strong.

The fluctuations in density and floating potential are picked up by Langmuir probes at different radial and azimuthal locations. Low pass filter with upper band limit of 25 kHz is used to avoid aliasing. The data is acquired on a PC based dual channel Lecroy oscilloscope with a sampling time of 20 μsec . The signals are picked up by a pair of probes whose distance of separation is $\simeq$ 0.5 cm. The local wave number and frequency spectrum $S(k,\omega)$ are computed using probe pair technique (Beall et al., 1984). A pair of probes which are separated by 0.5 cm at radial locations $\pm$ 6 in the azimuthal direction is used to obtain $S(k,\omega)$ spectrum both in region I and region II.

In the region I the gravity effects are relatively strong at $\nu_{in}/\Omega_i \ll 1$. The k-spectrum of density and potential shown in figure 2 is obtained at $\nu_{in}/\Omega_i \simeq 0.04$. The density spectrum has clearly two breaks with a spectral index n $\simeq$ – 2 for $k\rho_i \leq 0.6$ and n = – 4.2 for $k\rho_i \geq 0.6$. The potential spectrum has only on spectral index with n = -4.2.

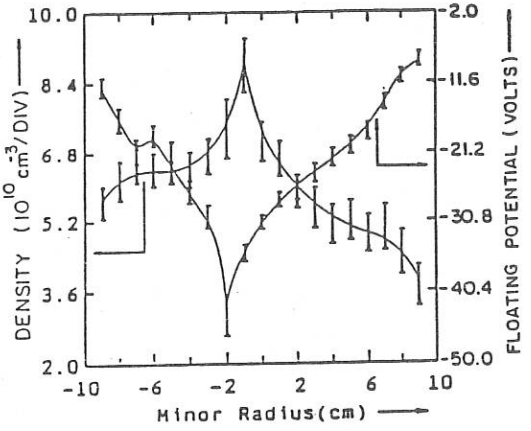

Figure 1: Density and Potential profiles of the plasma simulating Region I and Region II of night time F-region of equatorial Ionosphere.

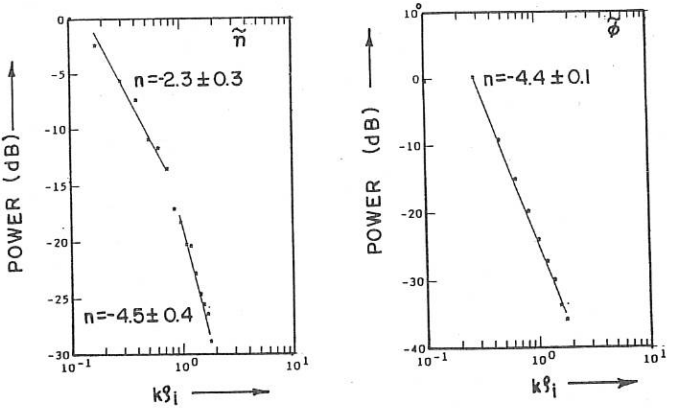

Figure 2: k-Spectra of density and potential in region I.

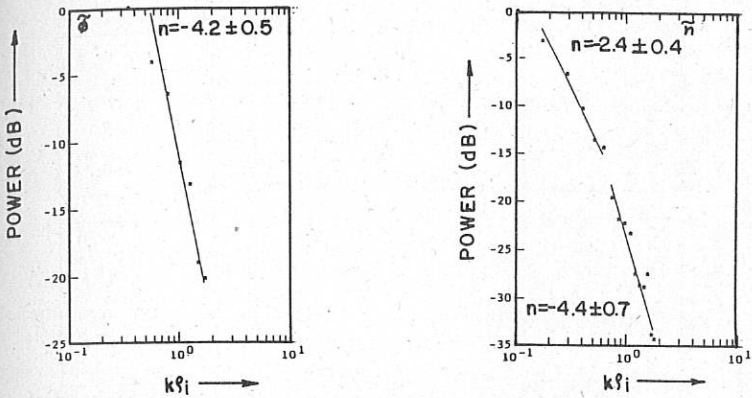

Figure 3: k-Spectra of density and potential in region II.

We also observe that the difference between density and potential spectral index ~ 2 for $k\rho_i \leq 0.6$ have similar spectral nature for $k\rho_i \geq 0.6$. The k – spectrum of density and potential fluctuations obtained in region II are shown in figure 3 indicates that the spectral nature is similar to that of the region I . The spectral index of density and electric field fluctuations in both region I and region II for $k\rho_i \leq 0.6$ is ~ 2, which is consistent with spectral relation for R – T instability (Kelley 1989). However the good curvature region, in principle, is not conducive for excitation of R – T instability. As we have already mentioned, the numerical simulation studies of R – T instability (Scannapieco and Ossakow, 1976) showed that the irregularities first excitied, in the region of the plasma where g is antiparallel to ∇n, by R – T instability then bubble to the top side of the F region density peak by $E \times B$ polarization motion. The in-situ obseration (Kelley et al 1982) have confirmed the observation of similar spectra in density fluctuation above the F region peak density. We observed similar spectra in region I and II. However we observe the fluctuations simultaneously in both regions. The observation of lag in the onset of these fluctuations in region II as in the case of numerical simulation or in - situ experiments is not possible in our case due to large growth rate and $E_o \times B$ motion of the instabilities and geometrical constraint of the system. The polarisation drift in our experiment is dominated by $E_o \times B$ drift. The steeper part of the k- sectrum (n = –4.5) in density and potential k - spectrum satisfy conditions of drift wave (Kelley 1989) similar to other laboratory experiments on drift wave turbulence (e.g. Pecseli et al. 1983).

Parametric studies have been conducted in the region I and II. The ratio ν_{in}/Ω_i is varied in both regions. This is achieved by varying either the neutral ressure or the ambient toroidal magnetic field. Thus we have varied the value ν_{in}/Ω_i from 0.04 to 0.1 which is still much smaller than unity. Therefore we have confined ourselves to the regime when the effectie gravity term is dominant over the cross-field term in the bad curvature region. The variation of spectral index in both region I and II with respect to ν_{in}/Ω_i is shown in figure 4. It is clear from figure 4 that the spectral index in density in both region I and II have dual slope of n $\simeq$ – 2 and n $\simeq$ – 4.5 where as the potential fluctuation

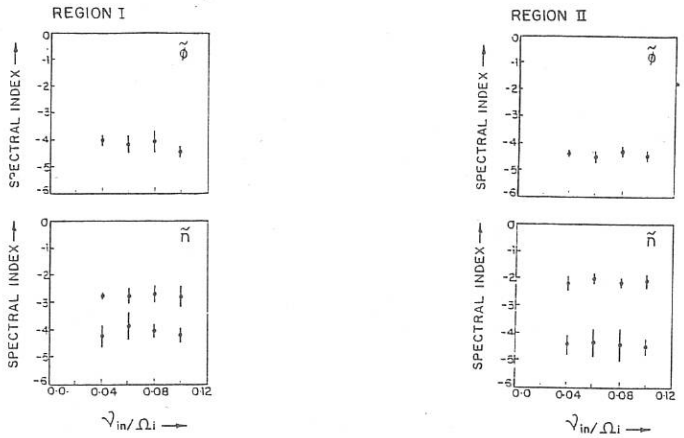

Figure 4: Variation of Spectral index with ν_{in}/Ω_i for density and potential in region I and II.

has only one spectral index of n = – 4.5.

Thus in conclusion in a laboratory plasma, simulating the characterstics of night time equatorial F region, electrostatic fluctuations are observed. The characteristics of the fluctuations in density and potential are as follows:

i). the k - spectra of $\tilde{n}$ exhibit two slopes with values of n$\simeq$ – 2 and –4.5, both in region I and in region II;

ii). the potential fluctuation exhibits only one slope with index n$\simeq$ – 4.5 in these regions.

The observed fluctuations satisfy the power spectral relation between $\tilde{n}$ and $\tilde{\phi}$ for R - T and drift wave instabilities in different scale length regimes. The observations of similar power spectral characteristics in the region of plasma where g is parallel to∇n is attributed to the fact that the fluctuations excited by R - T instability in the region of plasma where g is antiparallel to ∇n is carried by $E_o \times B$ drift which is consistent with direction of propagation of these waves. The results are in good agreement with in - situ experiments and nuemrical simulation studies.

References:

Beall, J.M., Y.C. Kim, & E.J. Powers, *J. Appl. Phys.*, 53, 3933, 1982.

Bora D., *Phys. Lett.*, 139A, 308, 1984.

Kelley M.C., *The Earth's Ionosphere Plasma Physics and Electrodynamics*, Academic Press, California, 1989.

Pécseli H.L., T. Mikkelsen & S.E. Larsen, *Plasma Phys.*, 25, 1173, 1983.

Kelley M.C., R.C. Livingston, C.L. Rino, & R.T. Tsunoda, *J. Geophys. Res.*, 87, 5217, 1982.

Scannapieco A.J., and S.L. Ossakow, *Geophys. Res. Lett.*,3, 451, 1976.

Singh M., & E.P. Szuszczewicz, *J. Geophys. Res.*, 89, 9840, 1984.

STIMULATED ATTACHMENT INSTABILITY OF ELECTROMAGNETIC WAVES IN THE IONOSPHERE

P. K. Shukla
Institut für Theoretische Physik IV, Ruhr-Universität Bochum
D-4630 Bochum 1, Germany

L. Stenflo and N. D. Borisov
Department of Plasma Physics, Umeå University
S-90187 Umeå, Sweden

Powerful radio waves can be used for artificial modification of the Earth's ionosphere [e.g. 1,2]. It is then well-known that the nonlinear interaction of an intense electromagnetic wave with the background plasma can give rise to parametric instabilities involving resonant three- wave decay interactions, as well as modulational and filamentation instabilities. In the three-wave interaction processes, the radio wave pump decays in most cases into a high-frequency daugther wave and a low-frequency electrostatic wave, whereas the modulational and filamentational instabilites involve both the upper- and lower-radio sidebands as well as non-resonant static (or finite frequency) density fluctuations. In a fully ionized collisional plasma, the latter are basically reinforced by the radiation pressure and the differential Joule heating of the electrons.

The plasma in the lower part of the Earth's ionosphere (viz. in the mesosphere or in the E-region) is partially ionized and highly collisional. Here, the number density of the neutrals is so high that it becomes essential to account for the collisions of the charged particles with the neutral atoms, and to pay particular attention to electron impact ionization and recombination processes that depend on the radio wave energy, as well as to accommodate the electron energy dependence of the frequency of the attachment of the charged particles on the oxygen molecules. Some of these effects have been included in a recent study [3] which, however, did not treat the differential heating nonlinearity in the Earth's ionosphere in a correct manner. Here we present an improved investigation of the stimulated attachment instability of radio waves in the ionosphere.

Let us consider the propagation of a high-frequency radio wave $(\omega_o, \mathbf{k}_o)$ in the lower part (heights below 130 km) of the Earth's ionosphere whose constituents electrons, ions, and neutrals form a partially ionized plasma. The nonlinear interaction between this pump wave and the ionospheric electron number density perturbation n_1 gives rise to radio wave sidebands which are governed by the equation

$$2i\omega_o(\partial_t + \mathbf{v}_g \cdot \nabla)\mathbf{E} + c^2\nabla^2\mathbf{E} = \frac{\omega_{pe}^2}{n_o} n_1 \mathbf{E}\,, \tag{1}$$

where $\mathbf{E}$ is the high-frequency electric field amplitude, $\mathbf{v}_g = \mathbf{k}_o c^2/\omega_o$ is the group velocity of the pump, c is the speed of light, n_o is the equilibrium density, and ω_{pe} is the electron plasma frequency. For simplicity, we have assumed that $\omega_o \approx (k_o^2 c^2 + \omega_{pe}^2)^{1/2}$ is much larger than the electron gyrofrequency ω_{ce}. The right-hand side of (1) represents the

usual nonlinear electron current density arising from the coupling of the rapidly varying electron quiver velocity of the pump electric field with the electron density perturbations associated with the plasma slow motion.

We shall now derive the expressions for n_1 in the presence of a strong radio wave in a partially ionized collisional magnetoplasma. Combining the electron continuity, momentum and energy equations [e.g. 2], assuming that $\mid \partial_t \mid << (v_{te}^2/\nu_{en}) \mid \partial_z \mid^2 << 1/\tau_e$, (where v_{te} is the electron thermal velocity, ν_{en} is the electron-neutral collision frequency which is much larger than the electron- ion collision frequency, the $z-$ axis is defined by the direction of the geomagnetic field $B_0\hat{\mathbf{z}}$, and τ_e is the electron energy relaxation time) and noting that the ponderomotive force as well as heat diffusion can be neglected because $\tau_e\nu_{en} >> 1$, we obtain the approximate relation

$$\frac{e\phi}{m_e} - v_{te}^2\frac{n_1}{n_o} - \frac{4}{3}\frac{e^2\tau_e\nu_{en}}{m_e^2\omega_o^2} \mid \mathbf{E} \mid^2 \approx 0\,, \tag{2}$$

where ϕ is the electrostatic potential, $-e/m_e$ is the electron charge to mass ratio, and $n_0(x) + n_1$ is the electron number density.

Next, combining the ion continuity and momentum equations, assuming that $\mid \partial_t \mid << \omega_{ci}$ and ν_a, where ω_{ci} is the ion gyrofrequency which is assumed to be much larger than the ion-neutral collision frequency ν_{in}, and where ν_a is the attachment frequency which is a function of the radio wave intensity $\mid \mathbf{E} \mid^2$ [1], and assuming quasi-neutrality, we obtain

$$\frac{\nu_{in}}{\omega_{ci}}\nabla_\perp^2\phi + \frac{\omega_{ci}}{\nu_{in}}\partial_z^2\phi \approx \frac{B_o}{c}[\nu_a\frac{n_1}{n_o} + (\partial\nu_a/\partial \mid E_o \mid^2) \mid \mathbf{E} \mid^2]\,, \tag{3}$$

where $\mid E_o \mid^2$ is the mean value of $\mid \mathbf{E} \mid^2$. As we consider heights lower than 130 km, it has here been possible to neglect ionization and recombination proesses [3]. Eliminating ϕ from (2) and (3), we have

$$(D_\perp\nabla_\perp^2 + D_z\partial_z^2 - \nu_a)\frac{n_1}{n_o} = [\frac{\partial\nu_a}{\partial \mid E_o \mid^2} - \frac{4e^2\tau_e\nu_{en}}{3v_{te}^2m_e^2\omega_o^2}(D_\perp\nabla_\perp^2 + D_z\partial_z^2)] \mid \mathbf{E} \mid^2\,, \tag{4}$$

where $D_\perp = \nu_{in}c_s^2/\omega_{ci}^2$ and $D_z = c_s^2/\nu_{in}$, and where $c_s = (T_{eo}/m_i)^{1/2}$ is the ion sound velocity.

We note that (4) is significantly different from the corresponding result in Ref. [3] beause $\tau_e\nu_{en}$ generally is much larger than unity. In order to estimate the importance of the $\partial\nu_a/\partial \mid E_o \mid^2$ term in (4), we now insert some numerical values in order to compare the magnitudes of the two terms on the right-hand side of (4). Thus, choosing $E_o \approx 1V/m, \tau_e\nu_{en} \approx 10^3, m_e/m_i \approx 3\times10^{-5}, \omega_o = 2\times10^7 s^{-1}, \nu_{in} \approx 700 s^{-1}$ and $\mid \partial/\partial z \mid \approx 10^{-6} cm^{-1}$, we find that the attachment nonlinearity dominates the Joule heating nonlinearity as $(\partial\nu_a/\partial \mid E_o \mid^2) \mid E_o \mid^2 > 5\times10^{-5} s^{-1}$ at the height 110 km [3]. Clearly, (1) and (4) are basic for studies of the filamentation and self-focusing of intense radio waves in the ionosphere.

Acknowledgments.- This work was supported by the Deutsche Forschungsgemeinschaft through the Sonderforschungsbereich 191.

REFERENCES

[1] A. V. Gurevich, *Nonlinear Phenomena in the Ionosphere*, (Springer, Berlin, 1978).

[2] L. Stenflo, Phys. Scripta, **T30**, 166, (1990).

[3] A. A. Arykov, N. D. Borisov, and V. F. Larin, Geomag. Aeronomy, **30**, 847, (1990).

RADAR COLLECTIVE BACKSCATTERING AND THE HIGH LATITUDE PLASMA TURBULENCE

D. Grésillon, B. Cabrit, C. Hanuise[1], J.P. Villain[2], R.A. Greenwald[3], and K.B. Baker[3]
Laboratoire de Physique des Milieux Ionisés (UPR 287 du CNRS)
Ecole Polytechnique, F 91128, Palaiseau, France.

Long wavelength radar collective scattering is a continuous observation means of the terrestrial plasma environment, especially in the northern auroral zone. The radar pulsed emission, combined with programmed delayed echo reception, provides several key informations: The (small scale) delay time defines the echoing plasma distance. The signal mean square amplitude is proportional to the plasma non-uniformity at that distance. While the long time scale signal fluctuations provide a measurement of the plasma motion.

Interpreting these fluctuations in term of plasma motion is far from obvious. The most commonly accepted view is that of Doppler frequencies. Indeed, a plasma collective scattering device is known[1] to define a virtual network of interference planes, characterized by a "scattering wavevector" $\mathbf{k}$, through which the spatial electron density distribution is analyzed. This k-vector depends on the electromagnetic waves "incident" ($\mathbf{k}_i$), and "scattered" ($\mathbf{k}_s$), wavevectors, as

$$\mathbf{k} = \mathbf{k}_s - \mathbf{k}_i \qquad (1)$$

Any density irregularity moving at a velocity $\mathbf{v}$ through this analysing network, provokes a scattered signal fluctuation at the Doppler frequency

$$\omega = \mathbf{k} \cdot \mathbf{v}$$

Here we like to point out, that in the case of convection motion, the resulting frequency spectrum is not the velocity probability distribution, but a more elaborate, and more informative, statistical transform of the plasma turbulent motion.

This point will be brought forwards by a brief theoretical analysis, and an examination of significant auroral plasma scattered signal time correlations.

1/ Collective scattering out of a non-uniform, unsteady fluid.

The collectively scattered signal collected at time t, is a spatial Fourier transform, at the scattering wavenumber k, of the plasma density distribution $n(\mathbf{r}, t)$.)

The signal time correlation is

---

[1] LSEET / CNRS, Université de Toulon et du Var, BP 132, F 83957, La Garde Cedex, France.

[2] LPCE / CNRS, 3A, Avenue de la Recherche Scientifique, F 45045, Orléans, France.

[3] Applied Physics Laboratory, Johns Hopkins Rd., Laurel, MD 20707, USA.

$$< s(t)\, s^*(t+\tau) > = \frac{1}{n_e^2} \int_V \int_V \left\langle e^{-i\bar{k}\cdot(\bar{r_1}-\bar{r_2})} [n(\bar{r_1}, t)\, d r_1^3][n(\bar{r_2}, t+\tau)\, d r_2^3] \right\rangle \quad (2)$$

Since plasma motion is particle conserving, the integration over position r_2 at time $(t + \tau)$ can be changed into an integration over the position (r'_2) the same volume element occupied at time t. In the transformation, this given volume element is moved by a vector $\Delta(r'_2, \tau)$,

$$\bar{\Delta}(\bar{r'_2}, \tau) = \bar{r_2} - \bar{r'_2} \quad (3)$$

while its number of particules is kept constant.

Furthermore, in case of "frozzen-in" turbulence, the plasma motion $\Delta(r'_2, \tau)$ is statistically independant of the local density $n(r'_2, t)$. This hypothesis is especially justified for incompressible fluid turbulent flows, including the two dimentionnal MHD plasma motion.

In those cases, the averaging operator can be factorized, providing two different statistical moments[2],

$$< s(t)\, s^*(t+\tau) > = \Sigma(k) \left\langle e^{i\bar{k}\cdot\bar{\Delta}(\bar{r'_2}, \tau)} \right\rangle \quad (4)$$

Where $\Sigma(k)$ is the "Form factor", a mean square of the electron density space Fourier transform at wavenumber k. For statistically stationnary fluctuations, the form factor is independant of time,

Let be $P(\Delta, \tau)$ the probability distribution of the plasma displacement Δ during time τ. The averaged term in Eq.(4) is the statistical "characteristics"of this probability distribution. That is, the Fourier transform (of argument the scattering wave vector k) of this probability distribution.

The scattered signal intensity is thus proportionnal to the form factor, while

"The collectively scattered signal time correlation is the statistical characteristics of the fluctuating fluid motion probability distribution at the same time." The characteristics function argument is the scattering, analyzing wave vector.

A non trivial relation thus exists between plasma motion probability and signal time correlation. Its analysis requires some extent [3]. Its result can be sketched in Figure 1. It depends on the plasma motion correlation length L_c compared to the scattering wavelength:

-For long correlation length, $k L_c >> 1$, the plasma motion through the scattering network is seen along almost straight lines. The plasma displacement $\Delta(\tau)$ is proportionnal to the fluid velocity v, and its probability distribution is a straightforward transform of the fluid velocity probability distribution. The "characteristics" is (most likely, although not necessarily) a gaussian function of time (Fig. 1 trace "a", where $k L_c = 2$). Whatever is this characteristics, the frequency spectrum is readily shown to be exactly the familiar "Doppler spectrum" of the fluid velocity probability distribution.

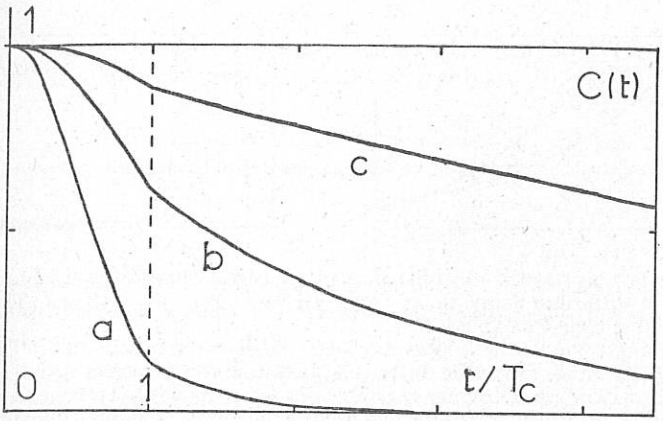

-For short correlation length instead ($k L_c << 1$), the plasma motion is seen as a random, brownian wandering through the scattering grid. The plasma motion is of a (turbulent) diffusive type, its "characteristics" is a damped exponential function of time (Fig. 1 trace "c", where $k L_c = 0.5$). Its time Fourier transform, the signal frequency spectrum, then becomes a lorentzian.

-For intermediate scales, when $k L_c \approx 1$, the correlation time argument is to be compared to the plasma motion correlation time T_c. At short times, the plasma motion is almost straight, the correlation function is nearly gaussian. At long times, the plasma motion is random, the correlation is exponential (Fig. 1 trace "b", with $k L_c = 1$).

2/ Auroral plasma scattered signals.

The "SHERPA" HF radar is observing the high latitude ionosphere on the North-eastern Canada. Backscattered echoes are obtained from regions where the scattering wavevector (along the line-of-sight) is strictly perpendicular to the earth magnetic field: the plasma densities irregularities are "field aligned". The scattered signal time correlations have been systematicaly monitored over long period of time, and recently analyzed[3] in order to find their dominant shape, whether gaussian, or damped exponential.

A majority of these correlations were found of the exponential type, corresponding to lorentzian frequency spectra, and a significant minority, of the gaussian type. Some of them shows an interresting transition between these two canonical shapes. An exemple of these transition type of correlations, is shown in Figure 2.

Figure 2 is an analysis of the backscattered signal coming from the ionospheric E-region, on May 22, 1991 at 06:07:53 UT. The probed plasma distance was 600 Km, and its depth 30 Km. The radar frequency was 9.4 MHz, corresponding to a scattering wavelength of 16 meters.

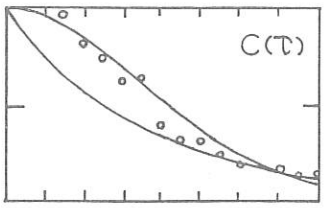

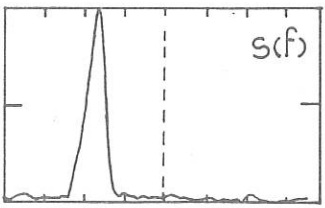

The left part is the modulus of the time correlation function, obtained on thirteen different delay times (open circles), from 0 to 48 ms. The data integration time was 12 seconds.

The right part is the frequency spectrum, shown between -400 to +400 Hz. It is calculated from the full (complex) correlation by a time Fourier transform. The peak frequency is -167 Hz (corresponding to a mean plasma velocity of 2673 m/s, directed away from radar), and its standart deviation 20 Hz.

The two full lines shown in the correlation figure, are the best gaussian and exponential fits. The gaussian is seen to fit the early times, while the exponential fits the later times. This is a common experimental feature, in agreement with our analysis and Fig. 1. From this observation, we are able to obtain two significant parameters of the plasma fluctuations in the plasma mean frame:

-the transition time, between "Gauss" and "exponential", is the correlation time T_c ,

-the correlation amplitude at transition is $\exp[-(k L_c)^2 / 2]$, thus a measurement of the correlation length L_c ,

From the data of Fig. 2 we find successively T_c = 22.5 ms, and L_c = 3 metres. To our knowledge, these are the first experimental direct measurements. To get some understanding or the auroral plasma fluctuations, these parameters can then be compared to other characteristics, like the ion gyroperiod and radius, or the ion-neutral collision time and length, respectively.

References:

1/ HOLZHAUER E., and J.H. MASSIG, An analysis of optical mixing in plasma scattering experiments, Plasma Physics 20, 867-877 , 1978.

SLUSHER R.E., and C.M. SURKO, Study of density fluctuations in plasmas by small-angle CO_2 laser scattering, Phys. Fluids 23, 472-490 , 1980.

GRESILLON D., C. STERN, A. HEMON, A. TRUC, T. LEHNER, J. OLIVAIN, A. QUEMENEUR, F. GERVAIS, and Y. LAPIERRE, Density fluctuation measurement by far infrared light scattering, Physica Scripta T2:2, 459-466, 1982.

2/ D. GRESILLON and B. CABRIT, "Collective Scattering and Fluid Velocity Fluctuations" , in "A Variety of Plasmas"(Proceed. of the Internat. Conf. on Plasma Physics, New-Delhi, 1989), A.Sen and P.K.Kaw, Editors (Pramana, Bengalore,India, 1991), p. 173.

3/ C. HANUISE, J.P. VILLAIN, D. GRESILLON, B. CABRIT, R.A. GREENWALD,and K.B. BAKER, Interpretation of HF radar ionospheric Doppler spectra by collective wave scattering theory (submitted for publication, May 1992).

STIMULATED SCATTERING OF EM WAVE BY ICW IN A TWO ELECTRON TEMPERATURE PLASMA

A. Sudarshan and S.K. Sharma
Department of Physics, I.I.T. New Delhi, INDIA

I. INTRODUCTION

Recently Guha and Asthana/1/ and Sharma and Sudarshan/2/ have studied stimulated scattering of electromagnetic waves by hydrid waves in a two electron temperature plasma. In this paper, we extend our previous work (Sharma and Sudarshan/2/) to derive the dispersion relation of the electromagnetic wave scattered by the low frequency ion cyclotron wave perturbation using the hydrodynamic equations for a plasma having three species - hot electrons, cold electrons and ions. The dispersion relation is used to obtain an explicit expression for growth rate using standard procedures and study the numerical variation of the growth rate with n_{oh}/n_{oc}.

II. DISPERSION RELATION

We assume that the ion-cyclotron wave propagates in plasma in a direction making a very small angle with the x-direction (so that $k_z << k_x$) in a plasma in which magnetic field is present in the z-direction. We consider a plasma having three species - hot electrons, cold electrons and ions. We assume that both electrons and ions are magnetized. The equation which described the behaviour of the plasma are:

$$m_j \frac{\delta \vec{v}_j}{\delta t} = -e\vec{E} - e(\vec{v} \times \vec{B}) + e\vec{\nabla}\phi_{pe} - m_j c_j^2 \vec{\nabla}(n_j / n_{oj}) \quad (1)$$

$$m_i \frac{\delta \vec{v}_i}{\delta t} = e(\vec{E} + v_i \times \vec{B}_o) - e\vec{\nabla}\phi_{pi} - m_i c_i^2 \vec{\nabla}(n_i / n_o)_i \quad (2)$$

$$\frac{\delta n_j}{\delta t} + \vec{\nabla}.(n_{oj}\, \vec{v}_j) = 0 \quad (3)$$

$$\frac{\delta n_i}{\delta t} + \vec{\nabla}.(n_o\, \vec{v}_i) = 0 \quad (4)$$

$$\nabla^2 \phi = 4\pi e\,(n_c + n_h - n_i) \quad (5)$$

Where the subscript j = h,c stands for hot and cold electrons respectively, ϕ_{pe} and ϕ_{pi} are the ponderomotive potentials for electrons and ions respectively and c_j is the velocity of the electrons.

Linearizing eqns. (1) to (5) one can easily obtain the x and z components of drift velocities of electrons. Substituting these expressions in eqn (1) we get:

$$n_c = -\left(e n_{oc} / \Delta_c m_c\right) \left(k_x^2 / \Delta + k_z^2 / \omega^2\right) \left(\phi + \phi_{pe}\right) \tag{6}$$

where $\Delta = \left(\omega^2 - \omega_{ce}^2\right)$; $\Delta_c = 1 - c_c^2 k_x^2 / \left(\omega^2 - \omega_{ce}^2\right) - c_c^2 k_z^2 / \omega^2$ (7)

The corresponding expression for the hot electrons is obtained by replacing the subscript 'c' by 'h'. The expression for n_i may be obtained by proceeding exactly in the same manner as for cold electrons.

Thus one obtains the following expression for n_i :

$$n_i = \left(e n_{oi} / m \Delta_i\right) \left(k_x^2 / \Delta + k_z^2 / \omega^2\right) \left(\phi + \phi_{pi}\right) \tag{8}$$

where $\Delta_i = 1 - k_x^2 c_i^2 / \Delta' - k_z^2 c_i^2 / \omega^2$; $\Delta' = \omega^2 - \Omega_c^2$ and Ω_c is the ion-cyclotron frequency.

Using Eq.(6) and Eq.(8) in the linearized expressionfor Poisson's equation, we get:

$$\phi + \phi_{pe} = \frac{k^2 - (1+\delta)\,\omega_{pi}^2 / \Delta_i \left(k_x^2 / \Delta + k_z^2 / \omega^2\right)}{k^2 - \left(\omega_{pc}^2 / \Delta_c + \omega_{ph}^2 / \Delta_h\right) \left(k_x^2 / \Delta + k_z^2 / \omega^2\right) - \omega_{pi}^2 / \Delta_i \left(k_x^2 / \Delta' + k_z^2 / \omega^2\right)} \phi_{pe} \tag{9}$$

and $\phi + \phi_{pi} = \phi - \delta \phi_{pe}$

$$= \frac{\left(\omega_{pc}^2 / \Delta_c + \omega_{ph}^2 / \Delta_h\right) \left(k_x^2 / \Delta + k_z^2 / \omega^2\right) (1+\delta) - k^2 \delta}{k^2 - \left(\omega_{pc}^2 / \Delta_c + \omega_{ph}^2 / \Delta_h\right) \left(k_x^2 / \Delta + k_z^2 / \omega^2\right) - \omega_{pi}^2 / \Delta_i \left(k_x^2 / \Delta' + k_z^2 / \omega^2\right)} \phi_{pe} \tag{10}$$

Now we can express the number densities of cold electrons, hot electrons and ions in terms of the ponderomotive potentials as

$$n_j = -\left[\omega_{pj}^2 / (4\pi e \Delta_j)\right] \left[k_x^2 / \Delta + k_z^2 / \omega^2\right] [A / G] \phi_{pe} \tag{11}$$

$$n_i = \left[\omega_{pi}^2 / (4\pi e \Delta_i)\right] \left[k_x^2 / \Delta' + k_z^2 / \omega^2\right] [B / G] \phi_{pe} \tag{12}$$

where $A = k^2 - \omega_{pi}^2 / \Delta_i [1+\delta] \left[k_x^2 / \Delta' + k_z^2 / \omega^2\right]$ (13a)

$$B = \left(\omega_{pc}^2 / \Delta_c + \omega_{ph}^2 / \Delta_h\right) \left(k_x^2 / \Delta + k_z^2 / \omega^2\right) (1+\delta) - k^2 \delta \tag{13b}$$

and $$G = k^2 - \left(\omega_{pc}^2 / \Delta_c + \omega_{ph}^2 / \Delta_h\right) \left(k_x^2 / \Delta + k_z^2 / \omega^2\right) - \omega_{pi}^2 / \Delta_i \left(k_x^2 / \Delta' + k_z^2 / \omega^2\right) \tag{13c}$$

The electron and ion velocities varying as the pump wave (of frequency ω_o) are given by

$$v_{oj} = \frac{ie\omega_o E_o}{m_e\left(\omega_o^2 - \omega_{ce}^2\right)} \quad (14); \qquad v_{oi} = \frac{-ie\omega_o E_o}{m_i\left(\omega_o^2 - \Omega_c^2\right)} \quad (15)$$

Maxwell's equation give the following relation between nonlinear current density and the electric vector of the waves:

$$\left(\omega_1^2 - k_1^2 c^2\right)\vec{E}_1 = 4\pi i\omega_1 \vec{J}_1 \quad (16)$$

where $\vec{J}_1$ is the nonlinear current density and is given by

$$\vec{J}_1 = -en_{oc}\vec{v}_{1c} - en_c\vec{v}_{oc} - en_{oh}\vec{v}_{1h} - en_h\vec{v}_{oh} + en_o\vec{v}_i + en_i\vec{v}_{oi} \quad (17)$$

Substituting for v_{oj} , v_{oi} etc. from Eqs. (14) and (15) into Eq. (16) we get the following dispersion relation

$$\omega_1^2 - k_1^2c^2 - \frac{\omega_{pe}^2\omega_1^2}{\left(\omega_1^2 - \omega_{ce}^2\right)} - \frac{\omega_{pi}^2\omega_1^2}{\left(\omega_1^2 - \Omega_c^2\right)} = \frac{-e^2E_o^2A}{4m_e^2\left(\omega_o^2 - \omega_{ce}^2\right)G} \times$$

$$\left[\left(\omega_{pc}^2/\Delta_c + \omega_{ph}^2/\Delta_h\right)\left(k_x^2/\Delta + k_z^2/\omega^2\right)\right] + \frac{e^2E_c^2\omega_{pi}^2B}{4m_im_i\left(\omega_o^2 - \Omega_c^2\right)\Delta_iG}\left[k_x^2/\Delta' + k_z^2/\omega^2\right] \quad (18)$$

The growth rate " γ " of the coupled modes can now be obtained from Eq. (18) by substituting $\omega = \omega_r + i\gamma$ and solving the resulting equation for γ . Thus we get the following expression for normalized growth rate γ/γ_o :

$$\gamma^2/\gamma_o^2 = \left[\frac{n_{oh}\left(\omega_r^2 - c_c^2k_z^2\right)}{n_{oc}\left(c_h^2k_z^2 - \omega_r^2\right)} - 1\right] \quad (19)$$

where $\gamma_o^2 = \dfrac{4e^2E_o^2k^2\left(\omega_r^2 - c_c^2k_z^2\right)}{4m^2\omega_o^2\left(\omega_o - \omega_r\right)\omega_r}$

III DISCUSSION

Equation (19) gives the dimensionless growth rate γ/γ_o of the coupled waves i.e. side-band and the ion-cyclotron wave as a consequence of the three wave interaction in a plasma having two distinct species of electrons i.e. hot electrons and cold electrons. To have a numerical

appreciation of our analytical results, we consider a typical Q-machine plasma having the following parameters

$\omega_r = 10^7\ s^{-1}$, $c_c^2 = 1.75\times10^{15}\ cm^2 s^{-2}$, $c_h^2 = 1.75\times10^{17}\ cm^2 s^{-2}$, $k = 10\ cm^{-1}$

$k_z = 0.1\ cm^{-1}$, $T_{ec} = 1\ eV$, $T_{eh} = 100\ eV$, $\omega_{pe}^2 = 10^{20}\ s^{-2}$, $\omega_o = 2\times10^{11}\ s^{-1}$, $k_o = 6\ cm^{-1}$

Using the above given parameters in Eq(19), we have calculated the dimensionless growth rate γ/γ_o of the coupled waves as a function of n_{oh}/n_{oc}. Fig.(1) shows the variation of dimensionless growth rate γ/γ_o with n_{oh}/n_{oc}. It is seen from Fig.(1) that the growth rate increases with increasing population of hot electrons which is qualitatively similar to that of the growth rate of lower and upper hybrid waves investigated by the authors in a recent paper/2/.

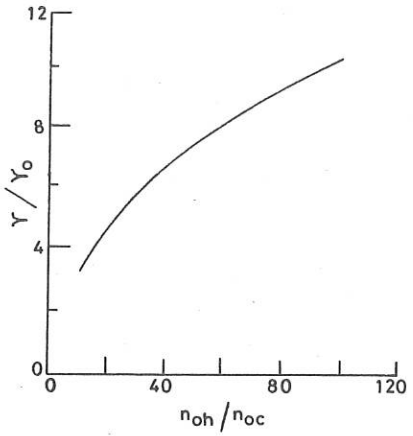

Fig. 1 Variation of γ/γ_o with n_{oh}/n_{oc}.

REFERENCES

/1/ S. GUHA and M. ASTHANA, J. Plasma Physics, 42, (II), 241 (1989).

/2/ S.K. SHARMA and A. SUDARSHAN, J. Plasma. Phys., 46 part 1, 99 (1991).

/3/ K. ESTABROOK and W.L. KRUER, Phys. Rev. Lett. 40, 42 (1978).

/4/ B. BEZZERIDES, D.W. FORSLUND and E.L. LINDMAN, Phys. Fluids, 21, 2179 (1978).

/5/ F.S. MOZER, et. al., J. Geophys. Res., 84, 5875 (1979).

Binding Energy and Triplet-Singlet Splitting for the Hydrogen Molecule in Ultrahigh Magnetic Fields

A.V.Korolev and M.A.Liberman

Department of Technology, Uppsala University,
Box 534, S-75121, Uppsala Sweden

The properties of the simplest hydrogen systems or hydrogen-like systems (exitons) are changed dramatically in the strong magnetic field which exceeds the atomic magnitude: $H >> H_c = m^2e^3c/\hbar^3$ for hydrogen atom, and $H >> H_{ex} = m_{eff}^2e^3c/\hbar^3\varepsilon^2$ for exitons. We perform analytical solution for the interaction of the hydrogen atoms in a strong magnetic field $H >> H_C$, and calculate the energy difference of the singlet and triplet states, the binding energy and wave functions for the hydrogen molecule.

The Schrödinger equation for the electrons is (all quantities are expressed in atomic units $\hbar=m=c=e=1$)

$$(H(1,2) + \frac{1}{2}\hat{\sigma}_1\cdot H + \frac{1}{2}\hat{\sigma}_2\cdot H)\,\Psi = E\,\Psi, \qquad (1)$$

where

$$(H(1,2) + \frac{1}{2}\hat{\sigma}_1\cdot H + \frac{1}{2}\hat{\sigma}_2\cdot H)\,\Psi = E\,\Psi,$$

$\rho_1^2 = y_1^2 + (b + z_1)^2$, $\rho_2^2 = y_2^2 + (b - z_2)^2$ are the coordinates of motion for the electrons 1 and 2 in the plane perpendicular to H; the vector potential is $\mathbf{A} = \frac{1}{2}\mathbf{H}\times\mathbf{r}$,

$\hat{\sigma}_1$ and $\hat{\sigma}_2$ are Pauli matrices, $\lambda = \sqrt{1/H}$.

We will consider two energy levels, which are the singlet term and the triplet term. Let Ψ_s be the exact solution of the two-electron coordinate wave equation that is symmetrical in the coordinates of the two electrons. The singlet wave function is thus a product of Ψ_s and an appropriate spin function for the sum of electron spins S = 0. Thus, for the singlet wave function Ψ_s, the Schrödinger equation is

$$H(1,2)\,\Psi_s = E_s\,\Psi_s. \qquad (2)$$

The triplet wave function is the product of the exact solution of the two-electron wave function that is antisymmetrical in the coordinates of the two electrons and an appropriate spin function for the sum of the electron spins S = 1. The lowest energy level corresponds to spin projection -1. Thus, the Schrödinger equation for the triplet term is

$$(H(1,2) - \frac{1}{2\lambda^2} - \frac{1}{2\lambda^2})\,\Psi_a = E_a\,\Psi_a. \qquad (3)$$

Using the new variable $E_{s1} = E_s - \frac{1}{\lambda^2}$, one can reduce Eq.(2) to the form

$$\left(H\,(1,2) - \frac{1}{2\lambda^2} - \frac{1}{2\lambda^2} \right) \Psi_{s,a} = E_{s1\,a}\, \Psi_{s,a} \qquad (4)$$

Let us consider the functions $\Psi_1 = (\Psi_s + \Psi_a)/2$, and $\Psi_2 = (\Psi_s - \Psi_a)/2$ which are large only when electron 1 is localized near proton a and electron 2 is near proton b. If the phases of Ψ_1 and Ψ_2 are properly chosen, the function $\Psi_1\,(r_1,r_2)$ for $r_1 \Rightarrow -R/2$, and $r_2 \Rightarrow R/2$ and $\Psi_2\,(r_1,r_2)$ for $r_1 \Rightarrow R/2$ and $r_2 \Rightarrow -R/2$ are the product of the two hydrogen single-atom wave functions in an ultrahigh magnetic field.

We seek the wave function Ψ_1 as the product of the two hydrogen-atom wave functions /1,2/, for the first electron being near the first proton and the second electron near the second proton.

$$\Psi_1 = B^2\, \chi_1 \exp\left(-\frac{\rho_1^2 + \rho_2^2}{4\lambda^2} \right) W_{\alpha,1/2}\left\{ \frac{2}{\alpha}\,(a + x_1 + \lambda) \right\} W_{\alpha,1/2}\left\{ \frac{2}{\alpha}\,(a - x_2 + \lambda) \right\} \qquad (5)$$

where $B^2 = (1/\alpha)\,(1/2\pi\lambda^2)$, and χ_1 is a slowly varying function compared with the exponential decay. Substituting expression (5) in Eq.(3) we obtain equation for χ_1:

$$\left(\frac{1}{\alpha}\frac{\partial}{\partial x_1} - \frac{1}{\alpha}\frac{\partial}{\partial x_2} - \frac{2}{R_{12}} + \frac{1}{r_{12}} + \frac{1}{R} \right) \chi_1 = 0. \qquad (6)$$

The singlet-triplet energy splitting due to the exchange coupling of the spins for the hydrogen molecule can be represented with the exponential accuracy in the following form /3,4,5/:

$$E_{s1} - E_a = 2 \oint_S \left(\Psi_2 \nabla_1 \Psi_1 - \Psi_1 \nabla_1 \Psi_2 \right) \cdot d\mathbf{S}, \qquad (7)$$

where S is the hyperplane ($x_1 = x_2$) in the six-dimensional space $\{r_1, r_2\}$.
Substituting the expression Ψ_1 and Ψ_2 and using the condition $0 < \alpha << 1$, we obtain for the part of the energy difference ΔE between the singlet and triplet states due to the excange coupling of the spins of two atoms

$$\Delta E = (E_s - H) - E_a = -\frac{2\,R\,\ln^2(H)}{\cos^2(\theta)} \left(2\ln(H)\cos(\theta) + \frac{1}{2} R\,H \sin^2(\theta) \right) \times \exp\left\{ -R\left(2\ln(H)\cos(\theta) + \frac{1}{4} R\,H \sin^2(\theta) \right) \right\}, \qquad (8)$$

For large distances R between the two hydrogen atoms in an ultrahigh magnetic field, the atoms interact like two quadrupoles. Since the electron density distribution is $\psi^2(x)$, and the

quadrupole moment for the atoms is $Q = 2\,\overline{x^2} = \alpha^2/2$, thus the energy of interaction of the two quadrupoles at distance R is $U_{qq} = (9/8\,(\ln^4 H)\,R^5)\,P_4(\cos(\theta))$,
where $P_4(\cos(\theta)) = (1/8)\,(35\,\cos^4(\theta) - 30\cos^2(\theta) + 3)$ is the Legendre polynomial.

Taking into account the quadrupole interaction as well as the exchange coupling of spins as the singlet-triplet splitting, we can write the final expression for the energy levels of the hydrogen molecule with the condition $R >> -\alpha$. For the triplet term:

$$U_S = E_S - E_0 = -\frac{1}{2}\Delta E + H + U_{qq}\,, \tag{9}$$

and for triplet term:

$$U_A = E_A - E_0 = +\frac{1}{2}\Delta E + U_{qq}\,, \tag{10}$$

where E_0 is the ground-state energy of the two isolated hydrogen atoms.

Since the energy of the quadrupole interaction has a deep negative minimum for $\theta \approx 49^\circ$, binding states are possible for both singlet and triplet states. However, for the condition $H >> 1$, the triplet energy level lies much deeper than the singlet level, which means that the triplet is the ground state for the hydrogen molecule in an ultrahigh magnetic field.

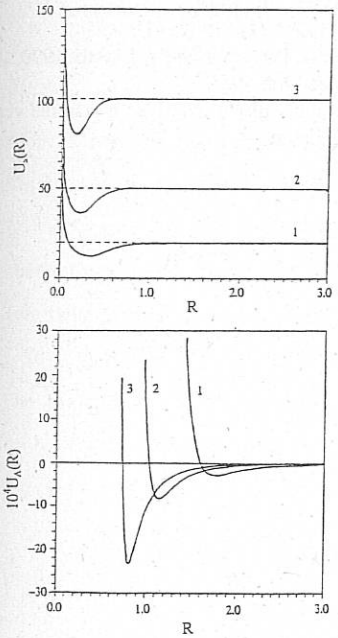

The results of the numerical calculation /6/ according to Eqs. (9) and (10) are shown in Fig. The curves in the figure correspond to the singlet level (top) and the triplet level (bottom), respectively; the numbering 1, 2, 3, on the curves corresponds to the values of the magnetic field, 20, 50, 100, respectively. At a very small distance $R \leq \alpha$ the quadrupole interaction is replaced by the Coulomb repulsion. For the distance $\alpha << R \cong 1$the interaction energy has a deep minimum for both singlet and triplet terms, which may be the ground or exited states of the hydrogen molecule. The depths of the potential wells for the two terms are increasing with increasing magnetic fields. With increasing values of the magnetic field the molecular size decreases. As long as the molecular size remains comparable to or larger than the atomic size in an ultrahigh magnetic field, the solutions obtained above are asymptotically exact. This result is correct up to a value for magnetic field of about 1000, where the atomic size become

approximately equal to the molecular size.

Thus, a substantial change in the physical properties of matter occurs in the presence of an ultrahigh magnetic field. The interaction of the two hydrogen or hydrogen - like atoms means that a hydrogen molecule or biexiton can form with a ground state that is a triplet state but not a singlet state, as it is for a H_2 molecule in the absence of a magnetic field. If the pair interaction occurs according to the triplet state than the transition into the superfluid state of the hydrogen gas in the strong magnetic field is possible due to the very shallow potential well in this state which means a weak pair interaction /7/. From the other hand the depth of the potential well in the singlet state is extremly large. It is of order of a few hundred eV for the hydrogen atoms. It means that the creation of spin-oriented molecules, long polymeric chain or structures of the liquid crystal type in the metastable state would be possible.

Magnetic fields of the scale of order $10^{10} - 10^{12}$G exist on the surface of neutron stars and pulsars and are significant interest for astrophysics. The characteristic value of the "atomic" magnetic field for a hydrogen-like systems (exitons) is available in laboratories. For example, the value of a few kOe is an "ultrahigh" field for InSb.

1. L.P.Gor'kov and L.P.Pitaevskii, Sov. Phys. Dokl. **8**, 788 (1964).
2. C.Herring and M.Flicker, Phys. Rev. **A 134**, 362 (1964).
3. R.J.Elliot and R.Loudon, J. Phys. Chem. Solids **15**, 19 (1960).
4. H.Hasegava and R.E.Howard, J. Phys. Chem. Solids **21**, 179 (1961).
5. L.D.Landau and E.M.Lifshits, Quantum Mechanics, Pergamon Press, Oxford, 1976.
6. A.B. Korolev, M.A. Liberman, Phys. Rev. **A 68**, 1762 (1992)
7. A.B. Korolev, M.A. Liberman, On the Superfluidity of the hydrogen gas in the very strong magnetic field, Phys. Letters A, will be published.

BEHAVIOUR OF TWO-DIMENSIONAL ION ACOUSTIC SOLITON IN RELATIVISTIC PLASMAS OF RADIATION BELTS

Sanjay Singh[a] and Tadao Honzawa

Department of Electric and Electronic Engineering,

Utsunomiya University, Utsunomiya 321, Japan

1. INTRODUCTION

In this paper we have made attempts to study the effects of ion temperature, plasma density and streaming velocity of the ions on the propagation of a two-dimensional ion acoustic soliton in a collisionless relativistic plasma. For this purpose we consider a two-dimensional magnetic field-free, collisionless and inhomogeneous plasma. It is assumed that the velocity of ions is relativistic in only the x direction, and that the spatial and temporal variations of the physical quantities associated with the nonlinear evolution of the ion acoustic soliton are larger in x direction than in y direction. Since the results of this theory are applied to the radiation belt plasma, we choose in it a region where electron temperature kT_e = 120 keV. The effect of terrestrial field ($B \simeq 10^{-7}$ T) on the plasma particles is assumed to be negligible. The two-dimensional Korteweg-de Vries (KdV) equation is obtained and a few limiting cases are presented.

2. THE KdV EQUATION AND ITS SOLUTION

The two-dimensional normalized fluid equations can be written as[1-3]

$$n_t + nu_x + nv_y + un_x + vn_y = 0, \tag{1}$$

$$(\gamma u)_t + u(\gamma u)_x + v(\gamma u)_y + \phi_x + p_x/n = 0, \tag{2}$$

$$v_t + uv_x + vv_y + \phi_y + p_y/n = 0, \tag{3}$$

$$p_t + up_x + vp_y + 3pu_x + 3pv_y = 0, \tag{4}$$

$$(\phi_{xx} + \phi_{yy}) - n_e + n = 0, \tag{5}$$

where; $n_e = \exp(\phi)$; $\gamma = (1 + u^2/2c^2)$.

In the above equations n and n_e are respectively the ion and electron density. u and v are respectively the streaming velocities in x and y directions. c is the speed of light. ϕ and p are respectively the electrostatic potential and ionic pressure. Now we expand the physical quantities about equilibrium as[2,3]

$$\psi = \sum_j \varepsilon^j \psi_j \ , \ j = 0,1,2,\cdots \ ; \ v = \sum_k \varepsilon^{k+1/2} v_{k+1} \ , \ k = 0,1,2,\cdots \tag{6}$$

where $\psi \equiv (n,u,\phi,p)$. The stretched co-ordinates can be written as under[1,3]

$$\xi = \varepsilon^{1/2}[\int dx'/\lambda_0(x') - t \,]; \ X = \varepsilon^{3/2} x \ ; \ \tau = \varepsilon y \ , \tag{7}$$

where λ_0 is the phase velocity and ε is a small ($0 < \varepsilon << 1$) expansion parameter. The use of eqs. (6) and (7) in eqs. (1)-(5) gives the following first order equations in ε

$$- n_{1\xi} + (u_0/\lambda_0) n_{1\xi} + (n_0/\lambda_0) u_{1\xi} + n_0 v_{1\tau} + (n_0 u_0)_X = 0, \tag{8}$$

$$\begin{aligned} &- n_0 u_{1\xi} + n_0 u_0 u_{0X} + (n_0 u_0/\lambda_0) u_{1\xi} + p_{0X} + (1/\lambda_0) p_{1\xi} + n_0 \phi_{0X} \\ &+ (n_0/\lambda_0)\phi_{1\xi} - (3n_0 u_0^2/2c^2) u_{1\xi} + (3n_0 u_0^3/2\lambda_0 c^2) u_{1\xi} + (3n_0 u_0^3/2c^2) u_{0X} = 0, \end{aligned} \tag{9}$$

$$- p_{1\xi} + (u_0/\lambda_0) p_{1\xi} + (3p_0/\lambda_0) u_{1\xi} + u_0 p_{0X} + 3p_0 u_{0X} + 3p_0 v_{1\tau} = 0, \tag{10}$$

$$- n_0 \phi_1 + n_1 = 0. \tag{11}$$

Integration of eqs. (8)-(11) with appropriate boundary conditions ($n_0 = 1$, $u_0 = 0$, $\phi_0 = 0$, $p_0 = 1$ as $\xi \to \pm \infty$) yields the following relation for soliton phase velocity:

$$\lambda_0 = u_0 + \mu_0/\gamma_1, \tag{12}$$

$$\text{where;} \quad \mu_0 = (1 + 2p_0/n_0)^{1/2}; \quad \gamma_1 = (1 + 3u_0^2/2c^2)^{1/2}. \tag{13}$$

Now we write the second-order equations in ε as under:

$$\begin{aligned} &- n_{2\xi} + (1/\lambda_0)(n_0 u_2 + n_1 u_1 + u_0 n_2)_\xi + (n_0 u_1 + n_1 u_0)_X \\ &+ n_0 v_{2\tau} + n_1 v_{1\tau} + v_1 n_{1\tau} = 0, \end{aligned} \tag{14}$$

$$\begin{aligned} &- n_0 u_{2\xi} - n_1 u_{1\xi} + (n_0 u_0/\lambda_0) u_{2\xi} + n_0 u_0 u_{1X} + [(n_0 u_1 + n_1 u_0)/\lambda_0] u_{1\xi} \\ &+ (n_0 u_1 + n_1 u_0) u_{0X} + (1/\lambda_0)(n_0 \phi_{2\xi} + n_1 \phi_{1\xi}) + (n_0 \phi_{1X} + n_1 \phi_{0X}) \end{aligned}$$

$$+ (1/\lambda_0)p_{2\xi} + p_{1X} - (3n_0u_0^2/2c^2)u_{2\xi} + (3n_0u_0^3/2\lambda_0c^2)u_{2\xi} - (3u_0^2/2c^2)n_1u_{1\xi}$$
$$-(3n_0u_0/c^2)u_1u_{1\xi} + (3u_0^3/2\lambda_0c^2)n_1u_{1\xi} + (9n_0u_0^2/2\lambda_0c^2)u_{1\xi} + (3n_0u_0^3/2c^2)u_{1X}$$
$$+(3u_0^3/2c^2)n_1u_{0X} + (9n_0u_0^2/2c^2)u_1u_{0X} + n_0v_1u_{1\tau} + (3n_0u_0^2/2c^2)v_1u_{1\tau} = 0, \quad (15)$$

$$- p_{2\xi} + (1/\lambda_0)(u_0p_{2\xi} + u_1p_{1\xi}) + u_0p_{1X} + u_1p_{0X} + (3/\lambda_0)(p_0u_{2\xi} + p_1u_{1\xi})$$
$$+ 3(p_0u_{1X} + p_1u_{0X}) + v_1p_{1\tau} + 3(p_0v_{2\tau} + p_1v_{1\tau}) = 0, \quad (16)$$

$$(1/\lambda_0^2)\phi_{1\xi\xi} - n_0\phi_2 - (n_0/2)\phi_1^2 + n_2 = 0. \quad (17)$$

Using eqs. (12), (13) and eqs. (8)-(11) in the second-order equations, one can obtain the following two-dimensional KdV equation:

$$W_X + (1/n_0^{1/2}\lambda_0)[(2\mu_0^2 - 1)/\mu_0^2\lambda_0^2 + \mu_0(1 - \gamma_1^2)/\mu_0\lambda_0^2\gamma_1^3]WW_\xi$$
$$+ (1/2n_0\mu_0\gamma_1\lambda_0^4)W_{\xi\xi\xi} + \mu_0\Delta_1W_\tau = 0, \quad (18)$$

where $W = n_0^{1/2}\lambda_0u_1$ and $\Delta_1 = 2\gamma_1^2\lambda_0n_0v_1$. The one-soliton solution of eq. (18) is,

$$W = W_0 \operatorname{sech}^2(\zeta/\ell), \quad (19)$$

where $\zeta = \xi + (B/A)\tau - (C/A)X$. B/A and C/A are the velocities of the stationary wave in two dimensions. The peak soliton amplitude W_0 and the soliton width ℓ are:

$$W_0 = (6\mu_0\gamma_1^2\lambda_0n_0/\alpha) \; ; \; \ell = (2\beta\delta^{-1}/\mu_0\gamma_1^2\lambda_0n_0)^{1/2}. \quad (20)$$

Here, $\delta \simeq$ constant and α and β are respectively the coefficients of nonlinearity and dispersion. Using $W = n_0^{1/2}\lambda_0u_1$ in eq. (19) we can obtain the following expressions[3].

$$n_m = (6\gamma_1^3n_0^{3/2}\delta/\alpha); \; \phi_m = (6\gamma_1^3n_0^{1/2}\delta/\alpha); \; p_m = 6\gamma_1^3(\mu_0^2 - 1)n_0^{3/2}\delta/\alpha, \quad (21)$$

where n_m, ϕ_m and p_m are respectively the peak ion density, peak potential and peak pressure of the two-dimensional soliton.

3. APPLICATION TO RADIATION BELTS AND LIMITING CASES

We choose a typical region in the radiation belt plasma with $kT_e = 120$ keV. The effect of earth's magnetic field ($B \simeq 10^{-7}$ T) is assumed to be negligible on the motion of plasma particles. Three values of plasma densi-

ty n_o = 0.1, 0.5 and 0.9 are chosen. We fix the temperature ratio $T_i/T_e = T_o$ = 0.03. For kT_e = 120 keV, kT_i = 3.6 keV. In addition to this three values for the streaming velocity of ions, i.e, u_o/c = 0.06, 0.08 and 0.10 are chosen.

It is evident from the phase velocity relation [eq. (12)] that λ_o increases continuously with u_o/c for fixed T_o. The effect of ion temperature on λ_o is, however, negligible as is evident from eq. (12). This is because the ratio of the ion thermal speed and speed of light u_{th}/c (= 0.002 for T_o = 0.03) is much smaller compared with even the minimum value u_o/c (= 0.06). The propagation of the soliton is influenced by the plasma density also. A careful observation of eqs. (20) and (21) reveals that while W_o, n_m, ϕ_m and p_m increase, soliton width ℓ decreases with increasing u_o/c for all the values of n_o. In brief we can say that propagation of two-dimensional soliton is influenced both by the plasma density and streaming velocity of ions. However, since $u_{th}/c \ll u_o/c$, the thermal effects are almost negligible.

For a one-dimensional non-relativistic plasma ($u_o/c \to 0$, T_o = finite), our KdV equation reduces to equation (44) of Singh and Dahiya[3]. And for one-dimensional non-relativistic cold plasma (u_o/c, $T_o \to 0$), our equation attains the form of the KdV equation of Kuehl[1]. Thus, we see that our two-dimensional KdV equation has few interesting limiting cases.

4. REFERENCES

a Permanent address: Indian Institute of Technology, New Delhi, India.

1. H.H.Kuehl, Phys. Fluids 26, 1577 (1983).

2. Y.Nejoh, J. Plasma Phys. 38, 439 (1987).

3. S.Singh and R.P.Dahiya, Phys. Fluids B 2, 901 (1990).

THE RAYLEIGH-TAYLOR INSTABILITY IN A SUPER-DENSE IGNITING PLASMA

Garcia, D. [1,2] , Serichol, N. [1] , Bravo, E. [1,2] and Diaz-Pinto, A. [1,2]

1) Dpt. Física i Enginyeria Nuclear U.P.C., Av. Diagonal 647, 08028 Barcelona (Spain)
2) Laboratori d'Astrofisica (Institut d'Estudis Catalans)

1. Introduction

The Rayleigh-Taylor (RT) instability arises when two fluids of different density are in contact, and the denser fluid is accelerated towards the lighter. Such a situation is present in a variety of physical scenarios and has important implications. In Inertial Confinement Fusion applications the RT instability, which appears due to inhomogeneous heating of the target pellet, leads to a deformation of the imploding shock front and to the degradation of its convergence. In stellar evolution, the RT instability plays a crucial role in the propagation of the combustion wave in Type Ia supernovae (Woosley 1986). It is therefore important to account for this effect in simulations in order to explain observations.

Combustion flames in supernovae are thought to propagate as deflagration waves especially in the early phases of combustion near the center of the star. Through the subsonic deflagration front the pressure is continuous and thus the incinerated hot material must be less dense than the cold fuel on top of it. The density inversion in the strong gravitational field of the star produces RT instability. The propagation of the combustion passes through at least two distinct phases. Near the center the instability hasn't enough time to develop and the combustion advances exclusively by conduction (conductive propagation of the burning front). After a while, the instability is capable of mixing the hot material in the front with the fuel, and thus increases the speed of the burning wave.

To date numerical simulations of supernovae explosion have relied on analytical parametrizations of the mixing or of the deflagration velocity, and results therefore depend largely on the approximation adopted (Woosley 1986, Nomoto et al 1984, Bravo et al 1992). Much effort has been devoted to the calculation of the conductive velocity of the laminar flame (Woosley 1986, Timmes and Woosley 1992, Garcia et al 1990, Khokhlov 1992). Timmes and Woosley have fitted an analytical expression to the conductive velocity in a white dwarf star composed of ^{12}C and ^{16}O :

$$v_{\rm cond} = 80.2 \left(\frac{\rho}{2\,10^9}\right)^{0.839} \left(\frac{X(^{12}C)}{0.5}\right)^{1.12} \quad \text{km/s}$$

where ρ is the density in g cm $^{-3}$ (typical values are 10^8 - 10^{10} g cm $^{-3}$), and $X(^{12}C)$ is the relative abundance of ^{12}C by number. The same authors have proposed a treatment of the propagation in the turbulent phase. The deformation of the front surface produced by RT instability is responsible for the increasing efficiency of heat transport through the burning front. In this approximation the rate of the turbulent velocity of the burning front to the conductive velocity is the same as the rate of the front surface to the non-deformed spherical surface at the position of the

front. Various authors have pointed out that the RT front has a fractal geometry and therefore can be described by only 3 parameters, the fractal dimension ν , and the two length scales λ_{min} and λ_{max} , between which the flow is self-similar (Peters and Franke 1990, and references therein). The effective velocity of the deflagration is then given by (Woosley 1990)

$$v_{eff} = v_{cond} \left(\frac{\lambda_{max}}{\lambda_{min}} \right)^{\nu-2}$$

The aim of this study is to propose a method of analysis of the unknown parameters of the structure of the burning front that determine the velocity of the deflagration wave, i.e., ν , λ_{min} and λ_{max} , for the physical conditions characteristic of supernovae arising from white dwarf stars. In this astrophysical context λ_{min} is the minimum flame deformation compatible with the conductive advance of the front, and λ_{max} is of the order of the size of the burnt zone. The fractal dimension has been found on the basis of theoretical arguments for turbulence, in the limit of large Reynolds numbers, to be $\nu = 7/3$ (Peters and Franke 1990, and references therein). The approach proposed here is to simulate RT instability with a hydrodynamical particle code, SPH, and to study the scaling properties of the frontier between ashes and fuel. In section 2 the numerical treatment of the hydrodynamic equations as well as the physics involved is described. In section 3 the processing procedure of the outputs in order to obtain the fractal parameters of the front surface is presented.

2. Method of calculation

The growth of RT instabilities in the star plasma is an inherent tridimensional phenomenon. To follow its evolution and to extract the main parameters without an excessive use of too much computer time a simple, but robust hydrocode is needed. Smooth Particle Hydrodynamics (SPH) is a Lagrangian particle method which has been specially devised for astrophysical problems when large departures from spherical geometry are expected. In this method fluid properties are concentrated in a set of imaginary *particles* with mass m which move according to the hydrodynamic equations. An accurate interpolation procedure allows the reconstruction of the continuous properties of the fluid from the calculated *particle* positions. SPH has the advantage of not requiring a grid.

As a first approximation in order to evaluate λ_{min} , λ_{max} , and ν values neither nuclear nor transport processes are included and a relatively simple equation of state is used. With this hypothesis the equations which govern the evolution are (Monaghan 1985):

$$\rho_i = \sum_{j=1}^{N} W_{ij} m_j$$

$$\frac{d\vec{v}_i}{dt} = -\sum_{j=1}^{N} m_j \left(\frac{P_i}{\rho_i^2} + \frac{P_j}{\rho_j^2} \right) \left[1 - \frac{\alpha h \sigma_{ij}}{c} + \beta \left(\frac{h\sigma_{ij}}{c} \right)^2 \right] \vec{\nabla}_i W_{ij} - \vec{g}_i$$

$$\frac{d\varepsilon_i}{dt} = \frac{P_i}{\rho_i^2} \sum_{j=1}^{N} m_j (\vec{v}_i - \vec{v}_j) \cdot \vec{\nabla}_i W_{ij}$$

where N is the number of *particles* which transport mechanical as well as thermodynamical properties, W_{ij} is a smoothing interpolant kernel, $\vec{g}_i$ is the gravitational acceleration, σ_{ij} is the artificial viscosity, and α , β are constants of order unity. The other quantities have their usual meaning.

The equation of state which is used is that of an ideal gas of ions plus radiation plus totally degenerate electrons with a first order temperature correction (Chandrasekhar, 1939).

We start the calculation by constructing an initial model in hydrostatic equilibrium with a central density according to that expected for a Type Ia supernova explosion. The equilibrium configuration is reached after letting the initial random *particle* distribution evolve with a dissipative term. Then, a selected quantity of mass is incinerated and a set of perturbations, of different size and wavelength is introduced which modifies the initial equilibrium configuration. The subsequent instability evolution will be followed with the SPH code, and the results analyzed as described in the next section.

3. Analysis of the results

The results of the hydrodynamic computation provide a distribution of *particles* of both the incinerated fluid and the fuel fluid. The following information is extracted from this distribution, fractal dimension of the front surface ν , maximum wavelength of the perturbation λ_{max} , and minimum wavelength λ_{min} . The fractal nature of the front surface implies that it is self-similar, at least over some significant length scales. A method of computation of the fractal dimension ν from Viecelli (1988) is adopted. In this method, the fractal dimension is approximated by the correlation dimension of the sample of points defining the solution (Grassberger and Procaccia 1983). First, one must choose randomly distributed points as centers for sets of spherical surfaces of decreasing radius. Then one must count the number of *particles* inside each sphere for a given radius and sum over all the centers. The correlation dimension is then obtained as

$$\nu = \lim_{N \to \infty} \lim_{r \to 0} \frac{ln\, n(r)}{ln\, r}$$

When plotted on a graph of $n(r)$ vs. r the data are distributed on a straight line, where self-similarity is present. The maximum length scale λ_{max} can be derived from this plot, as the larger scale at which self-similarity is lost.

The correlation dimension is strictly a lower bound to the fractal dimension, and one of its various possible estimators. The correlation dimension has been shown to provide a good determination of the fractal dimension, within the error limits, for some dynamical systems (Grassberger and Procaccia 1983). It is also a relatively straightforward method to use. In this case, the results of the hydrocode must be sorted in order to extract the front surface geometry. The *particle*-counting algorithm is restricted to

particles near the front surface, to avoid calculating the correlation dimension of the whole figure inside the front instead of the front itself.

By limiting the calculation to the frontier another problem is avoided that would have arisen in the interpretation of the results. The correlation dimension of a dynamical system measures the geometry of a sample of points weighting them according to the frequency at which the different parts of the figure are visited as the system evolves. It is important to note that a geometrical measure of the front is only taken into account. If this measure were carried out on the whole figure, then the weighting of the different points would have taken place as a result of the different density of the fluid, caused by a variable accumulation of *particles*. For instance, a lower density near the front surface would have produced a steeper dependence of $n(r)$ on r, and thus an artificially enhanced correlation dimension.

As to the minimum length scale of self-similarity $\lambda_{\min}$, it will be the greatest of various quantities: $r_{\min}$, d, λ_c. $r_{\min}$ is the lower length scale of self-similarity in the plot of $n(r)$ vs. r. λ_c is the minimum wavelength that grows without being absorbed by the advance of the conductive front, and is determined from the results of the hydrocode in a straightforward way.

This work is part of the project Numerical Simulation of Hydrodynamics and Nuclear Processes in Dense Plasmas, of the Universitat Politècnica de Catalunya, and the EASI-CESCA project Hydrodynamics, Radiative Transfer and Thermonuclear Burning in Astrophysics.

References

Bravo, E., Isern, J., Canal, R. and Labay, J., 1992, Astronomy and Astrophysics (in press).

Chandrasekhar, S., 1939, in An Introduction to the Study of Stellar Structure. (Univ. of Chicago Press. Reprinted 1958 by Dover Publ.)

Garcia, D., Labay, J., Canal, R. and Isern, J., 1990, in Proceedings of symposium Nuclear Astrophysics, 97. Ed: H. Oberhummer and W. Hillebrandt.

Grassberger, P., Procaccia, I., 1983, Physica 9D, 189.

Khokhlov, A.M., 1992, preprint.

Monaghan, J.J., 1985, Computer Physics Reports 3, 71.

Nomoto, K., Thielemann, F.K. and Yokoi, K., 1984, Astrophysical Journal 286, 644

Peters, N., Franke, Ch., 1990, in Dissipative Structures in Transport Processes and Combustion, ed. D.Meinköhn, Springer-Verlag, p. 40.

Timmes, F. and Woosley S., 1992, Astrophysical Journal (in press).

Viecelli, J.A., 1988, Journal of Comp.Phys 74, 456.

Woosley, S., 1986, in Nucleosynthesis and Chemical Evolution, eds. B.Hauck, A.Maeder and G.Meynet, Geneva Observatory, p. 1.

Woosley, S., 1990, in Supernovae, ed. A.Petscheck, Springer-Verlag.

NEW ELECTROSTATIC INSTABILITIES IN NONUNIFORM PARTIALLY IONIZED MAGNETOPLASMAS

P. K. Shukla
Institut für Theoretische Physik IV, Ruhr-Universität Bochum
D-4630 Bochum 1, Germany

C. B. Dwivedi and A. C. Das
Physical Research Laboratory, Ahmedabad 380009, India

The electron- temperature- gradient drift wave instability involving low-frequency long wavelength electrostatic waves in fully ionized collisional magnetoplasmas with equilibrium density and electron temperature gradients has been investigated by many authors /1-3/. Here consideration of the electron energy equation is very essential. In the long mean free path limit in which the wave motion is sufficiently slower than the electron diffusion along the external magnetic field lines, there exists a phase difference between the wave potential and the density and electron temperature perturbations. We thus have the possibility of the collisional temperature gradient drift instability.

However, most of the plasma in radio-frequency discharges, in the E-region of the Earth's ionosphere, in cometary tails, and in the ionosphere of the Venus are weakly ionized and inhomogeneous. In partially ionized plasmas, collisions between charged particles and neutrals play a dominant role and wave activities can occur provided that there exists free source of energy in the system. For example, during strong auroral activities in the E-region of the Earth's ionosphere, one /4/ encounters low-frequency electrostatic turbulence and strong η_e due to the heating of the background plasma electrons. Furthermore, recent experiments /5/ in flybys of comet Giacobini and comet Halley have observed small scale density and temperature fluctuations in the transition and sheath regions around the comets. Drift-like activities have also been seen in a partially ionized laboratory plasma /6/. Since fluctuations are seen to exist in the regions where there are equilibrium density and electron temperature gradients, it is of practical interest to enquire whether free energy stored in plasma inhomogeneities could be coupled to low-frequency fluctuations in a weakly ionized magnetoplasma which is dominated by neutrals.

In this paper, we present new instabilities of low-frequency ($\omega << \nu_{in}$) and long wavelength ($\lambda >> \rho_j$, λ_{Dj}) electrostatic modes in a weakly ionized magnetoplasma with equilibrium density and electron temperature inhomogeneities. Here, ν_{in} denotes the ion-neutral collision frequency, which is usually much smaller than ω_{ce} ; and ρ_j and λ_{Dj} are , respectively, the gyroradius and the Debye length of the particle species j (equals e for electrons and i for ions). We consider the dynamics of both the electron and ion fluids, but assume the neutral fluid to be at rest. For wave frequencies of our interest, the charged particles are magnetized and collisional.

Consider a nonuniform partially ionized magnetoplasma consisting of electrons (e), ions (i), and neutrals (n). The plasma is embedded in a uniform magnetic field $\mathbf{B}_0$ which is along the z axis, and has the equilibrium density and electron temperature gradients along the x axis: i.e., $n_{e,i} = n_0(x)$ and $T_e = T_e(x)$. In the presence of low-frequency (viz. $| \partial_t | << \nu_{jn} << \omega_{ce} = eB_0/m_e c$) electrostatic potential ϕ, the perpendicular (to $\mathbf{B}_0$) component of the electron fluid velocity is given by

$$\mathbf{v}_{e\perp} \approx \mathbf{v}_E + \mathbf{v}_D \,, \tag{1}$$

where $\mathbf{v}_E = (c/B_0)\,\hat{\mathbf{z}} \times \nabla\phi$ and $\mathbf{v}_D = -(c/eB_0 n_e)\,\hat{\mathbf{z}} \times \nabla(n_e T_e)$ are the $\mathbf{E} \times \mathbf{B}_0$ and the diamagnetic drift velocities, respectively. The parallel component of the electron fluid velocity is determined by

$$v_{ez} \approx (e/m_e\nu_e)\partial_z[\phi - (T_{e0}/en_0)n_{e1} - T_{e1}/e]\,, \tag{2}$$

where $\nu_e = \nu_{en} + \nu_{ei} \approx \nu_{en}$, $n_{e1} = n_e - n_0(x) << n_0$, and $T_{e1} = T_e - T_{e0}(x) << T_{e0}$.

For $m_e\nu_{ei}/m_i << \nu_{in}$, the perpendicular component of the ion fluid velocity is

$$\mathbf{v}_{i\perp} \approx [\omega_{ci}^2/(\omega_{ci}^2 + \nu_{in}^2)](c/B_0)[\hat{\mathbf{z}} \times \nabla\phi - (\nu_{in}/\omega_{ci})\nabla_\perp\phi]\,, \tag{3}$$

where $\omega_{ci} = eB_0/m_i c$ is the ion gyrofrequency. The parallel component of the ion fluid velocity is given by

$$v_{iz} \approx -(e/m_i\nu_{in})\partial_z\phi\,. \tag{4}$$

Letting $n_j = n_0(x) + n_{j1}$ and $T_e = T_{e0}(x) + T_{e1}$, assuming the perturbations (denoted by the subscript 1) to be small in comparison with the equilibrium quantities (denoted by the subscript 0), and inserting (1) and (2) into the continuity and the energy equations of the electron fluid, we obtain, respectively,

$$(\partial_t + \nu_R - D\partial_z^2)n_{e1} - (c/B_0)\hat{\mathbf{z}} \times \nabla n_0 \cdot \nabla\phi + (en_0 D/T_{e0})\partial_z^2(\phi - T_{e1}/e) = 0\,, \tag{5}$$

and

$$\begin{aligned}[\partial_t - (1/\tau_e) + (2/3)\gamma_{ex} - D_\parallel\partial_z^2 - D_\perp\nabla_\perp^2]T_{e1} - (c/B_0)\hat{\mathbf{z}} \times \nabla T_{e0} \cdot \nabla\phi \\ +(2cT_{e0}/3B_0)\hat{\mathbf{z}} \times \nabla ln\, n_0 \cdot \nabla\phi - (2T_{e0}/3n_0)\partial_t n_{e1} = 0\,,\end{aligned} \tag{6}$$

where $D = v_{te}^2/\nu_e, D_\parallel = 2C_x v_{te}^2/3\nu_e, D_\perp = 2C_r v_{te}^2\nu_e/3\omega_{ce}^2, \tau_e = n_0 m_n/2n_s m_e \nu_{es}$, and $v_{te} = (T_{e0}/m_e)^{1/2}$ is the electron thermal velocity. The recombination rate is denoted by ν_R.

On the other hand, substituting for $\mathbf{v}_i$ from (3) and (4) into the ion continuity equation, we obtain

$$\begin{aligned}(\partial_t + \nu_R)n_{i1} - [c\omega_{ci}^2/B_0(\omega_{ci}^2 + \nu_{in}^2)][\hat{\mathbf{z}} \times \nabla n_0 \cdot \nabla\phi + (\nu_{in}/\omega_{ci})\nabla n_0 \cdot \nabla_\perp\phi] \\ -(cn_0/B_0)[(\omega_{ci}\nu_{in}/(\omega_{ci}^2 + \nu_{in}^2))\nabla_\perp^2 + (\omega_{ci}/\nu_{in})\partial_z^2]\phi = 0\,,\end{aligned} \tag{7}$$

Thus, (5), (6), and (7) together with $n_{e1} = n_{i1}$ constitute a coupled set for studying electrostatic instabilities in nonuniform partially ionized magnetoplasmas.

We now derive a general local dispersion relation assuming that the wavelength of the electrostatic waves is much smaller than the scale lengths of the density and electron temperature gradients. Supposing that the perturbed quantities ϕ and T_{e1} are proportional to $\exp(i\mathbf{k} \cdot \mathbf{r} - i\omega t)$, where ω and $\mathbf{k}$ are the frequency and the wave vector, we can Fourier analyze (5), (6) and (7) and combine them assuming $n_{e1} = n_{i1}$. The result is

$$(A_r + iA_i)\omega^2 + (B_r + iB_i)\omega + G_r + iG_i = 0\,, \tag{8}$$

where $A_r = \omega_*[1 + f\omega_{ci}^2/(\omega_{ci}^2 + \nu_{in}^2)], \omega_* = -(cT_{e0}/eB_0 n_0)k_y d_x n_0, f = 1 + (k_x/k_y)(\nu_{in}/\omega_{ci})$, $A_i = Dk_z^2 - [1 + \nu_{in}^2 k_\perp^2/(\omega_{ci}^2 + \nu_{in}^2)k_z^2)](k_z^2 c_s^2/\nu_{in}) \equiv \omega_D - \Gamma, B_r = \omega_D(\omega_L + \nu_R) + (\omega_L + \omega_R + 2\omega_D/3)\Gamma, B_i = (\omega_L + \omega_R + 2\omega_D/3)(A_r - \omega_*) - \omega_*(\nu_R + \omega_L + \omega_D(\eta_e - 2/3)), G_r = \nu_R\omega_*[\omega_L - \omega_D(\eta_e - 2/3)] - (A_r - \omega_*)\omega_R\omega_L$, and $G_i = \omega_L(\nu_R\omega_D + \Gamma\omega_R)$. We have denoted $\omega_R = \nu_R + \omega_D$ and $\omega_L = (1/\tau_e) + 2\gamma_{ex}/3 + D_\parallel k_z^2 + D_\perp k_\perp^2$.

Some useful analytical results can be obtained in three limiting cases. Firstly, for $\mid \omega \mid >> \nu_R, \omega_L, \omega_D$, the relevant dispersion relation is solved letting $\omega = \omega_r + i\gamma$. We obtain for the real part of the frequency

$$\omega_r = -(\omega_D \omega_{ci}/\nu_{in})[(2a/3)(\kappa_n^{'} \cdot \mathbf{k})(ak_\perp^2 + k_z^2) + (\kappa_T - 2a\kappa_n^{'}/3) \cdot \mathbf{k} \times (ak_\perp^2 + bk_z^2)]/[a^2(\kappa_n^{'}.\kappa)^2 + (\omega_{ci}/\nu_{in})^2(ak_\perp^2 + bk_z^2)^2], \quad (9)$$

and an expression for the growth rate

$$\gamma = \omega_D[a(\kappa_n^{'} \cdot \mathbf{k})(\kappa_T - 2a\kappa_n^{'}/3) \cdot \mathbf{k} - (2/3)(\omega_{ci}/\nu_{in})^2(ak_\perp^2 + k_z^2) \times (ak_\perp^2 + bk_z^2)]/[a^2(\kappa_n^{'} \cdot \mathbf{k})^2 + (\omega_{ci}/\nu_{in})^2(ak_\perp^2 + bk_z^2)^2]. \quad (10)$$

where $\kappa_n^{'} = \kappa_n - (\omega_{ci}/\nu_{in})\nabla ln\, n_0, \kappa_n = \hat{\mathbf{z}} \times \nabla ln\, n_0, \kappa_T = \hat{\mathbf{z}} \times \nabla ln\, T_{e0}, a = \nu_{in}^2/(\omega_{ci}^2 + \nu_{in}^2)$, and $b = 1 + mi\nu_{in}/m_e\nu_e$.

For $\omega_{ci}/\nu_{in} << k_y/k_x$, it is seen that there is a growth when $\eta_e (= dln\, T_{e0}/dln\, n_0 \equiv L_n/L_T)$ is greater than $2a/3$. However, it is of particular interest to note that for $\omega_{ci}/\nu_{in} >> k_y/k_x$ the instability occurs when η_e is negative and $\mid \eta_e \mid > (2a/3)(\omega_{ci}/\nu_{in})(k_x/k_y)$, otherwise for $d_x ln\, T_{e0} > 0$ and $d_x ln\, n_0 > 0$ there is no instability. The resistive instability in a partially ionized plasma arises provided that

$$(\kappa_n^{'} \cdot \mathbf{k})(\kappa_T - 2a\kappa_n^{'}/3) \cdot \mathbf{k} > (2/3a)(\omega_{ci}/\nu_{in})^2(ak_\perp^2 + bk_z^2)(ak_\perp^2 + k_z^2). \quad (11)$$

Secondly, we consider the limit $\nu_R << \mid \omega \mid << \omega_D$ and assume that the magnetic field-aligned electron thermal diffusion rate dominates over cross-field diffusion rate, the electron energy relaxation rate, as well as the heat exchange loss. This case, which is of significant interest to a recent laboratory experiment /6/ puts a restriction on the parallel wavelength $\lambda_z = 2\pi/k_z$, viz. $4\pi^2 D_\parallel/\lambda_z^2 >> D_\perp k_\perp^2 + (1/\tau_e) + (2/3)\gamma_{ex}$. Here, the dispersion relation is of the form

$$\omega + i(\omega/\omega_D)\{(1 + D/D_\parallel)\omega - \omega_*[1 + (D/D_\parallel) - (3D/2D_\parallel)\eta_e]\} - [\omega_*(1 + k_x\nu_{in}/k_y\omega_{ci})/(1 + \nu_{in}^2/\omega_{ci}^2)] + i\Gamma = 0. \quad (12)$$

Letting $\omega = \omega_r + i\gamma$ in (12), and assuming $\gamma << \omega_r$, we obtain for the real part of the frequency

$$\omega_r \approx \omega_*(1 + k_x\nu_{in}/k_y\omega_{ci})/(1 + \nu_{in}^2/\omega_{ci}^2), \quad (13)$$

and an expression for the growth rate

$$\gamma \approx [\omega_*^2(1 + k_x\nu_{in}/k_y\omega_{ci})/\omega_D(1 + \nu_{in}^2/\omega_{ci}^2)][a + (D/D_\parallel)(a - 3\eta_e/2) - k_x\nu_{in}/k_y\omega_{ci}(1 + \nu_{in}^2/\omega_{ci}^2)] - \Gamma. \quad (14)$$

Thirdly, in order to illuminate the effect of recombinational damping, we consider a simple case in which $\mid \omega \mid \sim \nu_R << \omega_D, \omega_L$. Here the growth rate is found to be

$$\gamma = [\Omega(A_r - \omega_*)/(1 + \Omega^2)] - \nu_R - \Gamma/(1 + \Omega^2). \quad (15)$$

where $\Omega = (\omega_*/\omega_L)[\eta_e - (2/3) - \omega_L/\omega_D]$. The growth rate is positive provided that $\Omega > 0$ and the first term is larger than the last two terms on the right-hand side of (15). The effect of recombination is stabilizing.

As an illustration, we apply our result to the E-region of the Earth's ionosphere at heights below 130 km where during strong auroral activities a strong $\eta_e(\geq 7)$ has been observed /4/, and where the recombinational effect is negligibly small. Accordingly, we take some typical plasma parameters: $n_o = 10^5 cm^{-3}$, $B_0 = 0.5$ G, $T_{e0} = 600$ K, $m_i/m_e = 16 \times 1836$ $L_n = 36$ km, and $L_T = 5$ km. We thus have $\omega_{pe}/\omega_{ce} \approx 2, \omega_{ci} \approx 300\, s^{-1}$, $c_s = 4.72 \times 10^4$ cm/s, $v_{te} = 8 \times 10^6$ cm/s, $\nu_R = 0.001\, s^{-1}$, $\nu_{ei} = 2300\, s^{-1}$, $\nu_{en} = 9.2 \times 10^4\, s^{-1}, L_n = 36$ km, and $L_T = 5$ km. For $k_z/k_y = 0.001$, $k_x/k_y = 0.1$, and $k_y = 10^{-3}\, cm^{-1}$, we analyze (10) and (11) numerically. Our results show that the present instability, which involves modes with $k_\perp L_n$, $k_\perp L_T >> 1$, can rapidly generate the auroral E-region irregularities whose transverse scale size ($viz. \lambda_y = 2\pi/k_y$) is of the order of 63 m.

To summarize, we have presented new electrostatic instabilities that are driven by the combined effect of the equilibrium density and electron temperature inhomogeneities in partially ionized magnetoplasmas in which collisions of charged particles with neutrals play an important role. Physically, plasma nonuniformities in conjunction with charged particles-neutral atom collisions provide a proper phase difference between the electrostatic potential, the density and electron temperature perturbations, so that electrostatic perturbations grow. The growth rates of the instabilities critically depend on η_e as well as electron-neutral and ion-neutral collision frequencies. The unstable modes may cause anomalous resistivity, thereby changing the transport properties of the weakly ionized plasma.

Our results could have relevance to the understanding of the origin of nonthermal electrostatic fluctuations in space and laboratory plasmas. For example, the European Incoherent Scattering (EISCAT) observations show a strong enhancement of the electron temperature and a strong electron temperature gradient during strong auroral activities in the E-region of the Earth's ionosphere. The free energy stored in the equilibrium density and electron temperature inhomogeneities is then coupled to electrostatic fluctuations by the instability mechanism discussed here.

This research was supported by the Deutsche Forschungsanstalt für Luft and Raumfahrt (DLR) and the Indian Space Research Organization (ISRO) Exchange Program, as well as the Deutsche Forschungsgemeinshaft and the Euoropean Economic Community.

/1/ B. Coppi and E. Mazzucato, Phys. Fluids **14**, 134 (1971).
/2/ B. Coppi and C. Spight, Phys. Rev. Lett. **41**, 551 (1978).
/3/ B. Coppi, Phys. Lett. A **128**, 193 (1988).
/4/ K. Igarshi and K. Schlegel, J. Atmos. Terr. Phys. **49**, 273 (1987).
/5/ S. J. Bame, R. C. Anderson, J. T. Cosling, D. J. Mc Comas, M. F. Thomson, D. T. Young, and R. D. Zwickl, Science **232**, 356 (1986).
/6/ P. Frank, G. Himmel, and H. Schlüter, Plasma Phys. Contr. Fusion, in press, 1992.

SPONTANEOUS FORMATION OF INTERMEDIATE SHOCKS

J.K. Chao, C.Y. Chiu
Institute of Space Science, National Central University, Chung-Li, Taiwan
Tzihong Chiueh
Physics Department, National Central University, Chung-Li, Taiwan

(I) Introduction:

Evolutionary arguments given by Kantrowitz and Petschek (1967) purport that the intermediate shock is an extraneous solution of the Rankine-Hugoniot relation and hence cannot exist in nature[1]. In the pioneer work of C.C. Wu (1987), the intermediate shock was found to form under a special initial condition[2]. A large-amplitude slow wave was initially set up to let evolve. The leading edges of the wave steepen and finally a train of intermediate shocks form. As the transverse magnetic field, in Wu's calculation, has already reversed the signs in the initial slow wave, it does not strike as such a great surprise to find that the transverse magnetic field has different signs across the shock in the final configuration. (Note that the sign change of the transverse magnetic field is an important characteristic of the intermediate shock.) The suspicion raised by Kantrowitz and Petschek that the presence of an initial intermediate wave may make the intermediate shock unstable is found, in Wu's simulation, not to occur. Despite that Wu's result shows the intermediate shock appearing stable, this model can be vulnerable to a criticism that the intermediate shock results merely from a special arrangement of the initial condition. That is, as the intermediate shock has already been demonstrated to exist, at issue is not whetcher the intermediate shock can exist, but whether the intermediate shock can appear in a more natural setting and a more natural initial condition.

We confront this issue with the following line of consideration. If a slow shock propagates into a medium of increasing density, for which both the Alfven speed and sound speed decrease, the shock can be slowed down (in response to the decreasing characteristic speeds of the background plasma). However, the shock speed may not decrease as rapidly as the Alfven speed. Therefore, the longitudinal Alfven Mach number may increase as the shock evolves, to such an extent that it exceeds unity, and the slow shock can become an intermediate shock. During this process, a rotational discontinuity should appear downstream of the intermediate shock. The appearance of the rotational discontinuity is to re-reverse the downstream transverse magnetic field to attain the original sign in the region far downstream.

It is known that switch-off shocks occur only for the slow shocks[1], where a finite upstream transverse magnetic field dissappears in the downstream region. As far as the parameter space, such as the plasma β or the upstream field angle, is concerned, the switch-off shock marks the boundary between the slow shock and the intermediate shock, where the downstream transverse magnetic field just begins to change sign. We find that for those slow shocks that are near the switch-off shock in the parameter space, it is easier to convert them into intermediate shocks. In fact, there exists a second boundary in the parameter space, outside which the slow shocks can no longer be converted into intermediate shocks (c.f. Table 1).

(II) Numerical Simulation: We computed the following results with a one-dimensional resistive/viscous MHD code, which uses the two-step Lax-Wendroff scheme to advance the calculation in time. The background plasma has a density ramp within a finite region of the computation domain. At t=0, we send in a slow shock from the left boundary toward the ramp. The shock will eventually come out of the ramp, either with or without its character changed to become an intermediate shock. Figure 1 shows a time sequence of the evolution, when a slow shock runs into a density ramp. The physical quantities shown from the top are the density, the normal component of velocity, the transverse component of magnetic field and the gas pressure, respectively. The upstream parameters for the initial slow shock are: the slow-wave Mach number $M_s = 1.76$, the upstream magnetic field angle $\theta = 45$, $\beta = .42$ and the density ratio across the ramp =3. The width of the ramp can be much larger than that in Figure 1, but the outcome has no noticeable change. Although it is not so clearly shown in Figure 1, we note that the reversal of the transverse magnetic field has already occurred while the shock is still within the ramp. Upon coming out of the ramp, the intermediate shock is not steady, but can gradually settle into a steady one, whose Mach number can, at this stage, be accurately determined. The steadiness of the intermediate shock depends on the width of the ramp; the smoother the ramp is the more steady the shock is. As is obvious from Figure 1, the by-products in company with the intermediate shock are a 180 degree rotational discontinuity, where B_z changes sign but the total pressure is continuous, a fast shock which leads the intermediate shock and a rebounced fast shock of small upstream field angle, moving backwards into the high β plasma and behaving like a gas dynamic shock.

For a given longitudinal Alfven Mach number M_A, the success of the conversion depends on the plasma β, the incident angle with respect to the magnetic field θ, the amount of dissipation and the height of the density ramp. The latter two factors are in fact intercorrelated. For a shock conversion to occur, we find that the larger the resistivity is the *higher* the ramp must be; however, with a fixed resistivity, the height of the density ramp can hardly affect the final Alfven Mach number. This implies that whether the conversion can successfully occur depends *weakly* on the height of the ramp, as long as the height exceeds some value. This also suggests that some kind of dynamical conservation law prevails during the interaction, in such a way that the final Alfven Mach number remains unchanged regardless of the height and the width of the density ramp.

Another interesting finding of our results is that when measured by the range of the upstream plasma β, a slow shock with a *larger* slow-wave Mach number has a *narrower* range of β for a successful conversion to occur. This is shown in Table 1, where several slow-wave Mach numbers are examined for three different upstream field angles separately. The upper limit of β marks the initial shock's being a switch-off shock and the lower limit marks the boundary, below which no slow shock can be converted into intermediate shocks. The tendancy of the outcome clearly depends on the strength of the slow shock. The details of our results will be published elsewhere.

Reference:

1. Kantrowitz, A.R. and Petschek, H.E., in **Plasma Physics in Theory and Application**, ed. by W.B. Kunkel, McGraw-Hill, New York, (1967).
2. Wu, C.C., Geophys. Res. Lett., **14**, 668-671 (1987).

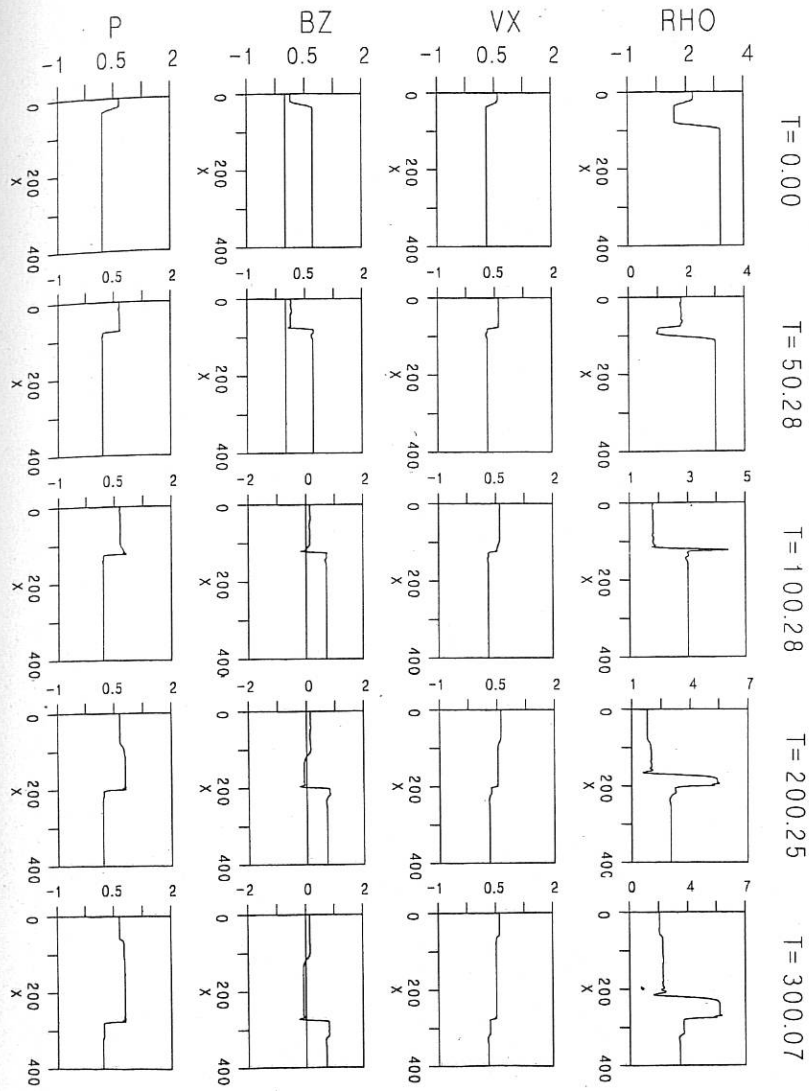

Figure 1: A time sequence of evolution for quantities such as the plasma density, the normal component of velocity, the transverse component of magnetic field and the pressure.

$\theta = 20°$

Ms	1.25	1.50	1.75	2.0	2.5
Max β	0.927	0.58	0.41	0.31	0.19
Min β	0.780	0.45	0.30	0.21	0.13

$\theta = 45°$

Ms	1.25	1.50	1.7625	2.0	2.5
Max β	1.450	0.746	0.477	0.349	0.21
Min β	1.170	0.567	0.343	0.243	0.140

$\theta = 70°$

Ms	1.25	1.50	1.75	2.0	2.5
Max β	1.97	0.91	0.55	0.38	0.22
Min β	1.61	0.72	0.43	0.29	0.17

Table 1: Limits of the plasma beta for various upstream field angles and slow-wave Mach numbers.

SPECTRUM OF MHD WAVES IN COMETARY TAILS

O. T. Matsuura, C. A. Azevedo[1], A. S. Assis[2], H. Shigueoka[3], and P. H. Sakanaka[4]

Instituto Astrônomico e Geofísico, Universidade de São Paulo, 01061 C.P. 9635, São Paulo, SP, Brazil,

Abstract. The wave structure of rays from cometary plasma tails is modeled using the MHD formulation. Since cometary rays are essentially of cylindrical shape, the model will be constructed using the simple cylindrical geometry. The observational data concerning the dynamical behaviour of rays are very scarce in certain cases there is an ambiguity between wave phenomena and the motion of matter. However, we have searched the available data in the literature, comprising ground based and satellite observations to show that the spectrum of MHD waves might explain some features of the plasma dynamics of cometary rays. Based on our theoretical results, we have also proposed cometary observations combining morphological and spectrosopic techniques attempting to disentangle wave phenomena from mass motions.

Introduction. Usually the Type I (or plasma) tail of comets exhibits time varying fine structures in the light of ions CO^+ ($\lambda = 3500 - 5500\AA$) and H_2O^+ ($\lambda = 5500 - 7500\AA$). Such fine strutures consist on rays, kinks, helical strutures and bright condensations/1/. Rays are narrow, long and straight strutures with typical thickness $\leq 2000\ km$ and length usually reaching over $10^7\ km$. What will be modeled using the MHD approach is the individual struture of one ray. The time evolution of rays can be found in references /2,3,4/. Helical features, kinks, undulations and bright knots appear affecting the rays. All these affections can exhibit apparent downstreaming velocity ranging from 20 to 300 km/s. This velocity tends to be larger far away from the nucleus, and far from the axis of the

[1]Instituto de Física, Universidade do Estado do Rio de Janeiro, 20550, Rio de Janeiro, RJ, Brazil.
[2]Instituto de Matemática, Universidade Federal Fluminense, 24024, Niterói, RJ, Brazil.
[3]Instituto de Física, Universidade Federal Fluminense, 24024, Niterói, RJ, Brazil.
[4]Instituto de Física, Universidade Estadual de Campinas, 13081, Campinas, SP, Brazil.

plasma tail /5,6/. It is still unclear weather such apparent motions correspond to motions or simply to MHD perturbations/7/. An ion number density of $10^3\ cm^{-3}$ can be assumed according to /8,9,10/, but the abundance ratio H_2O^+/CO^+ is highly variable from one comet to other, and even for one same comet at different times/11/. The ICE data /12/ from the tail of the Comet P/ Giacobini-Zinner indicated that two lateral lobes of high intensity magnetic field ($6 \times 10^{-4}G$) were confining in between a plasma sheet with a field of only $5 \times 10^{-5}G$. This last number will be assumed for the magnetic field of the rays. This means that rays are magnetic struture with high β value (≥ 4). As a consequence the MHD wave spectrum will show the usually property to be described below. In the following sections we will present the model, the results and the conclusions.

The Model. From the first order perturbation MHD equation we obtain a second order differential equation (Hain-Lüst equation) on ξ_r (r-component of the plasma displacement) derived in /13/ by taking the perturbation quantities as $f(r)exp(-i\omega t + ik_z z + im\theta)$. In /14/ a stability code has been developed to solve the Hain-Lüst equation using the shooting method and the discrete slow wave modes have been obtained in the region of stable spectrum.

The eigenfrequency ω and the corresponding eigenmode ξ_r, for a given and m, can be obtained by solving the Hain-Lüst equation with the following boundary conditions: $r\xi_r = 0$ at $r = 0$ and $r = a$/14/.

The profiles for p, B_z, and B_θ obey the equilibrium equation for the total pressure

$$\frac{d}{dr}(p + \frac{B^2}{2}) + \frac{B_\theta^2}{r} = 0$$

where $B^2 = B_z^2 + B_\theta^2$. From three, two profiles can be chosen arbitrarily. We assume that the gas pressure profile is constant. The B_θ profile is obtained by solving the Ampère's law with a given J_z profile. For the sake of simplicity, we choose profile of the equilibrium current as $J_z(r) = J_0\{1 - (r/a)^2\}^2$ and density profile $\rho(r) = \rho_0\{1 - 0.95(r/a)^2\}$. The constant J_0 is determined from the condition that the safety factor at the axis, $q(0)$ ($q = 2\pi a\ B_z/L\ B_\theta$, where L denotes the length of the tube), is greater than 1. The shooting method is used to obtain the normalized eigenvalue ω^2 which satisfies the boundary conditions

at $r = 0$ and $r = a$. We choose the normalized quantities such that, $B_{zN} = 1$, $\rho_{0N} = 1$, and $a_N = 1$. Also we choose $m = 1$, $k_z = 0.606$ and $\beta = 4$. The effect of the high β is that $C_S > V_A$, where C_S and V_A are the sonic and the Alfvén velocities, respectively.

Results. The numerical solution has been carried out varying β and the normalized current density J_{0N}. When $\beta > 1$ discrete Alfvén modes can overlap onto the continuum of slow modes. As a consequence the discrete Alfvén modes are expected to suffer a mode conversion into slow modes. Also some discrete Alfvén modes may oscillate at the same frequency of discrete slow modes.

For typical observational values: ion number density = 1000 cm^{-3}, $B = 5 \times 10^{-5} G$ and tail disturbance length scale = $10^6 km$, aperiod of the Alfvén wave is obtained of about 1.7 day.

Conclusions. This analysis on the MHD spectrum of cometary rays opens interesting possibilities for modeling and observationally testing the unusual character of the discrete Alfvén modes in high β plasmas. With regards to the observational efforts, the indication of surviving alfvenic and sonic modes in cometary rays is auspiciuos. However the future experiments should pay attention to the fact that both discrete modes have the same frequency. Therefore a way to distinguish one mode from the other is crucial for testing our results. This distinction seems to be viable in practice, since the sonic modes can show up as brightness variations, while alfvenic modes can appear as morphological variations. Based on such a knowledge the task of disentangling mass motions from wave phenomena may become easier.

Acknowledgements. This work was partially suported by CAPES - Coordenação de Aperfeiçoamento do Pessoal de Ensino Superior, CNPq - Brazilian National Research Council, and FAPESP - Fundação de Amparo a Pesquisa do Estado de São Paulo for financial support.

References.

/1/ D. A. Mendis, W.-H. Ip., Spa. Sci. Rev. **20**, 145 (1977).

/2/ K. Wurm, Astron. **66**, 362 (1961).

/3/ K. Wurm, A. Mammano, Astrophys. Spa. Sci. **18**, 273 (1972).

/4/ M. R. Voelzke, *M. Sc. Thesis*, IAG, Universidade de São Paulo, Brazil (1979)[in portuguese].

/5/ K. Jockers, Rh. Lüst, Th. Nowak, Atron. Astrophys. **21**, 199 (1972).

/6/ W. E. Celnik, Th. Schmidt-Kaler, Astron. Astrophys. **187**, 233 (1987).

/7/ L. S. Morochnik, Sov. Astron. **7**, 218 (1963).

/8/ K. Wurm, *The Moon, Meteorites and Comets*, B. M. Middlehurst, G. P. Kuiper(Eds.), University of Chicago Press, 573 (1963).

/9/ W.-H. Ip, W. I. Axford, *Comets*, L. Wilkening (Ed.), University of Arizona Press, 585 (1982).

/10/ S. Wyckoff, P. A. Wehinger, Astrophys. J. **204**, 604 (1976).

/11/ L. Kresák, IAU Commission 15 (PHysical Study of Comets, Minor Planets and Meteorites) Report, 10 (1988).

/12/ E. J. Smith, B. T. Tsurutani, J. A. Slavin, D. F. Jones, G. L. Siscoe, D. A. Mendis, Science **232**, 382 (1986).

/13/ K. Hain, R. Lüst, Z. Naturfor. **13a**, 936 (1958).

/14/ H. Shigueoka, P. H. Sakanaka, C. A. de Azevedo, A. S. de Assis, Rev. Bras. Fis. **21**, 297 (1991).

LOW-FREQUENCY RESONANT ION-BEAM TURBULENCE IN COMETARY PLASMAS

Frank Verheest
Instituut voor theoretische mechanika, Universiteit Gent, B-9000 Gent, Belgium

G.S. Lakhina
Indian Institute of Geomagnetism, Colaba, Bombay 400 005, India

A theoretical framework is established, based upon Fowler's theorem for unstable plasmas, for estimating the upper bound on magnetic field fluctuations produced in ion-beam systems, due to the excitation of low-frequency resonant modes. In the region upstream of the cometary bow shock such modes can be excited due to pickup of cometary ions, at Doppler-shifted frequencies equal to the cometary ion gyrofrequencies. The estimates of the present theory show that $\delta B/B_0$ is fairly small, in agreement with observational evidence faraway from the cometary nucleus.

INTRODUCTION AND THEORETICAL FRAMEWORK

In previous papers /1,2/ we used a version of Fowler's theorem for unstable plasmas /3/ to estimate the magnetic field turbulence levels for low-frequency nonresonant unstable modes in a multibeam plasma. Here we apply the same formalism to *resonant* modes excited due to pickup of cometary ions in the region upstream of the cometary bow shock. For such modes the Doppler-shifted frequencies equal the cometary ion gyrofrequencies.

We start with a homogeneous, charge neutral beam-plasma system immersed in a uniform magnetic field. Both beam and plasma constituents can in principle have parallel drift velocities, as perpendicular equilibrium drifts are eliminated by going to a deHoffmann-Teller frame. We assume charge and current neutrality for both beams, consisting of ions with a given set of characteristics (N_s, e_s, m_s, U_s) plus the electrons necessary to provide the return current. Then in the context of cometary environments, by resonant ion- ion modes one means that the Doppler-shifted wave frequency $\omega - kU_{ci}$ resonates with the gyrofrequency Ω_{ci} of the pickup ions of cometary origin. Let us start from equation (6) of *Lakhina and Verheest* /4/, written as

$$\Big((\omega - k\overline{U})^2 + k^2(W - V_A^2)\Big)(\omega - kU_{ci} \pm \Omega_{ci}) = \rho(\omega - kU_{ci})^3. \tag{1}$$

This dispersion law is valid for frequencies small compared with the proton gyrofrequencies ($\omega \ll \Omega_p = \Omega_{sw}$), and the line of reasoning followed is specifically for cometary environments, where the cometary ions of the water group have 16 to 17 times the proton mass /5,6/. In (1), $\overline{U}$ is the mean bulk velocity of the plasma as a whole, V_A the global Alfvén velocity,

$$W = \frac{N_{sw}m_{sw}(U_{sw} - \overline{U})^2 + N_{ci}m_{ci}(U_{ci} - \overline{U})^2}{N_{sw}m_{sw} + N_{ci}m_{ci}} = \rho(1-\rho)U_{ci}^2 \tag{2}$$

the normalized kinetic energy in the relative drift motions /1/, and $\rho = N_{ci}m_{ci}/(N_{sw}m_{sw} + N_{ci}m_{ci})$ the dimensionless mass density of the energetic cometary ion beam, viewed in the solar wind frame (where $U_{sw} = 0$). We can now put

$$\varpi = \omega - kU_{ci} \pm \Omega_{ci}, \tag{3}$$

use the abbreviations

$$A = kU'_{ci} \mp \Omega_{ci}, \qquad B = k^2(V_A^2 - W) \equiv k^2 c_A^2, \tag{4}$$

and get a compact form for the dispersion law:

$$F(\varpi) \equiv \varpi\Big((\varpi + A)^2 - B\Big) = \rho(\varpi \mp \Omega_{ci})^3. \tag{5}$$

For resonant modes $\varpi \simeq 0$ and the dominant terms in $F(\varpi)$ are either $(A^2 - B)\varpi$ or $2A\varpi^2$, and on the r.h.s. of (5), $\mp\rho\Omega_{ci}^3$. This supposes ρ small enough, so that the roots of the full dispersion law (5) are close to the roots of $F(\varpi)$ /7/. From the choices for the dominant terms one sees that unstable modes need at least $A^2 - B \simeq 0$, in other words when $W < V_A^2$. Then

$$\varpi^2 = \mp\frac{\rho\Omega_{ci}^3}{2A} \tag{6}$$

leads to unstable solutions provided $A = \pm|A|$, depending on whether we deal with the right-hand (RH) or left-hand (LH) polarized mode. Now from $A^2 \simeq B$ and (4) we find that

$$A \equiv kU'_{ci} \mp \Omega_{ci} = skc_A, \tag{7}$$

with $s = \pm 1$ but not yet related to the RH/LH polarized modes and c_A defined as the positive root $\sqrt{V_A^2 - W}$. Hence the wavenumber is given by

$$k = \pm\frac{\Omega_{ci}}{U'_{ci} - sc_A}. \tag{8}$$

In the solar wind frame the cometary ions form a sunward beam upstream of the nucleus, and it is their velocity component parallel to the interplanetary magnetic field (IMF) which is denoted by U_{ci}. Hence a positive (negative) value for U_{ci} means that the IMF has a parallel (antiparallel) component, in other words pointing towards (away from) the Sun. Keeping the sign of U_{ci} in mind, the different quantities can be expressed as follows:

$$\overline{U} = \rho U_{ci}, \qquad U'_{ci} = (1 - \rho)U_{ci}, \qquad c_A^2 = (1 - \rho)(1 - \rho M^2)V_{A,sw}^2, \tag{9}$$

where M is the Alvénic Mach number with the solar wind Alfvén velocity as the reference, $M = |U_{ci}|/V_{A,sw}$, $V_{A,sw}$ being taken as a positive quantity.

Starting from $s = +1$, (7) shows that $k = \pm|k|$, since for instability $A = \pm|A|$. In (8) this means that $U'_{ci} - c_A$ has to be positive, in other words only the choice $U'_{ci} > c_A > 0$ is possible and the IMF has a parallel component. In the opposite case where $s = -1$, (7) imposes $k = \mp|k|$ and from (8) there follows that $U'_{ci} + c_A$ should be negative. This means that $U'_{ci} < -c_A < 0$, leading to an antiparallel component for the IMF. As one can check, $|U'_{ci}| > c_A$ in both cases, implying $M > 1$. From (6) and (7) we get for the unstable waves that

$$\mathrm{Re}\,\omega = \pm\,\Omega_{ci}\frac{|\overline{U}| + c_A}{|U'_{ci}| - c_A}, \qquad \mathrm{Im}\,\omega \equiv \gamma = \Omega_{ci}\sqrt{\frac{\rho(|U'_{ci}| - c_A)}{2c_A}}. \tag{10}$$

Note that in both cases ($s = +1$ and $s = -1$) the RH mode has $\mathrm{Re}\,\omega > 0$ and k directed along the sunward direction, whereas the LH mode has $\mathrm{Re}\,\omega < 0$ and k directed in the antisunward

direction. Hence both the RH and LH modes always propagate sunward, viewed in the solar wind frame, with phase velocities $|\overline{U}| + c_A$.

In order to compute an upper estimate for the ultimate levels of magnetic turbulence in the case of unstable modes, we will make use of Fowler's equipartition ideas /3/. Performing the same approximations as when deriving the dispersion law (1), one gets

$$\left\{ V_A^2 + W + \left(\frac{\mathrm{Re}\,\omega}{k} - \overline{U}\right)^2 - \rho\left(\frac{\mathrm{Re}\,\omega}{k} - U_{ci}\right)^2 + (1-\rho)\left(\frac{\mathrm{Im}\,\omega}{k}\right)^2 \right.$$
$$\left. + \rho\frac{|\omega - kU_{ci}|^2}{k^2}\,\frac{\Omega_{ci}^4 + \Omega_{ci}^2|\omega - kU_{ci}|^2}{\left[\Omega_{ci}^2 - (\omega - kU_{ci})^2\right]\left[\Omega_{ci}^2 - (\omega^* - kU_{ci})^2\right]} \right\} \frac{\delta B^2}{B_0^2} \leq F. \tag{11}$$

Here F represents the normalized free energy associated with the unstable modes. The most unstable mode will grow fastest and use up the available free energy, so that F will be equal to γ^2/k^2, as shown more clearly in the case of nonresonant modes /1/. Using (10) we can rework (11) and get

$$\frac{\delta B^2}{B_0^2} \leq \left\{ \frac{2k^2V_A^2}{\gamma^2} + 1 - \rho + \rho\frac{\Omega_{ci}^4(2\Omega_{ci}^2 - \gamma^2)}{\gamma^4(4\Omega_{ci}^2 + \gamma^2)} \right\}^{-1}. \tag{12}$$

COMETARY APPLICATIONS

In an 8 nT field one finds that $\Omega_{ci} = 0.046/\mathrm{s} \ll \Omega_p \ll |\Omega_e|$, so that the restrictions inherent in our theory will be obeyed provided $\mathrm{Re}\,\omega$ and γ do not exceed Ω_{ci} very much. At an angle of about 45° between the solar wind flow and the IMF we have a Alfvénic Mach number of about 3.5, keeping in mind that $V_{A,sw} \simeq 80$ km/s and assuming a mean solar wind flow with $V_{sw} \simeq 400$ km/s. Table I then shows the relevant quantities computed for those parameters, namely ρ, $\mathrm{Re}\,\omega$, $\gamma = \mathrm{Im}\,\omega$, $\lambda = 2\pi/k$ and $\delta B^2/B_0^2$.

TABLE I

ρ	$\mathrm{Re}\,\omega$ (s^{-1})	$\mathrm{Im}\,\omega$ (s^{-1})	$\lambda = \frac{2\pi}{k}$ (10^3 km)	$\frac{\delta B^2}{B_0^2}$
0.1	0.018	0.005	27.7	0.020
0.2	0.017	0.008	28.1	0.046
0.4	0.015	0.013	29.1	0.128
0.6	0.012	0.019	30.5	0.302
0.8	0.006	0.044	33.7	0.866

The maximum levels of magnetic turbulence given in Table I are in good agreement with *in situ* observations near comet P/Halley /8–10/. We may point out that computer simulations of cometary-ion resonant instabilities as reported by *Gary et al.* /11,12/ predict saturation amplitudes which show good overall agreement with the estimates given in Table I. However, at strong injection of free energy, *Gary et al.* /11,12/ found that a single Fourier mode emerges from the noise to exhibit exponential growth. The peak value of the fluctuating magnetic field amplitude associated with this mode can be quite large ($\delta B \sim B_0$) but the energy decays within a few hundred proton gyroperiods to a much smaller value. Our formalism deals with the saturated amplitudes and we cannot predict what happens in the intermediate regime. Also, we consider the cometary ion density as given, whereas in the computer simulations /11,12/ cometary ions were continuously injected. These subtle differences must be kept in mind while making any comparison between our theory and the computer simulations!

CONCLUSIONS

Since the observed ULF turbulence at both comets P/Giacobini–Zinner and P/Halley is transverse and characterized by a spectral peak near 0.01 Hz and since water-group ions dominate the pickup ions, it is natural to investigate whether the water-group ions and waves are in gyroresonance and to compute the contribution of such resonant modes to the observed turbulence. However, in order to discriminate between resonant and nonresonant modes as being more important, one would need wavelength measurements, but these are not (yet) available. So the case for the resonant modes, as advanced by a majority of the researchers in the field and as investigated here, rests for the time being solely on frequency measurements, only half of the criterion.

Importantly, the linear polarization of the MHD turbulence observed closer to comets is explained naturally by nonresonant modes rather than by resonant modes which predict RH or LH polarization. However, farther away from the cometary nucleus the cometary ion density is lower and one would expect the resonant modes to dominate. It is thus clear that the last word has not been said yet on the identification of the modes responsible for MHD turbulence. Perhaps future cometary missions might shed more light on this aspect.

Acknowledgments. FV thanks the (Belgian) National Fund for Scientific Research for research and travel grants, and the Indian Institute of Geomagnetism for their kind hospitality during a stay in which the work was initiated.

REFERENCES

/1/ Verheest F. and Lakhina G.S., *J. Geophys. Res.* **96**, 7905 (1991)

/2/ Verheest F. and Lakhina G.S., in: *Proc. Solar Wind 7 Conf.*, Springer 1992, in press

/3/ Fowler T.K., in: *Advances in Plasma Physics* (Ed. A. Simon and W.B. Thompson, Wiley Interscience) **1**, 201 (1968)

/4/ Lakhina G.S. and Verheest F., *Astrophys. Space Sci.* **143**, 329 (1988)

/5/ Balsiger H., Altwegg K., Bühler F., Geiss J., Ghielmetti A.G., Goldstein B.E., Goldstein R., Huntress W.T., Ip W.-H., Lazarus A.J., Meier A., Neugebauer M., Rettenmund U., Rosenbauer H., Schwenn R., Sharp R.D., Shelley E.G., Ungstrup E. and Young D.T., *Nature* **321**, 330 (1986)

/6/ Mukai T., Miyake W., Terasawa T., Kitayama M. and Hirao K., *Nature* **321**, 299 (1986)

/7/ Lee M.A. and Ip W.-H., *J. Geophys. Res.* **92**, 11041 (1987)

/8/ Neubauer F.M., Glassmeier K.H., Pohl M., Raeder J., Acuña M.H., Burlaga L.F., Ness N.F., Mussmann G., Mariani F., Wallis M.K., Ungstrup E. and Schmidt H.U., *Nature* **321**, 352 (1986)

/9/ Riedler W., Schwingenschuh K., Yeroshenko Ye.G., Styashkin V.A. and Russell C.T., *Nature* **321**, 288 (1986)

/10/ Saito T., Yumoto K., Hirao K., Nakagawa T. and Saito K., *Nature* **321**, 303 (1986)

/11/ Gary S.P., Madland C.D., Omidi N. and Winske D., *J. Geophys. Res.* **93**, 9584 (1988)

/12/ Gary S.P., Akimoto K. and Winske D., *J. Geophys. Res.* **94**, 3513 (1989)

LOWER HYBRID RESONANCE ACCELERATION OF ELECTRONS AND IONS IN THE AURORA AND SOLAR FLARES

R Bingham, D A Bryant, D S Hall, (Rutherford Appleton Laboratory, Chilton, Didcot, Oxon, OX11 0QX, UK)
J J Su, J M Dawson, (Dept. of Physics, University of California, Los Angeles CA 90024)
K McClements (AEA Fusion, Culham Laboratory, Abingdon, Oxfordshire OX14 3DB, UK)

Abstract
Nonlinear wave processes at the lower-hybrid frequency are extremely important in transferring energy between different particle populations and fields in both astrophysical and laboratory plasmas. In this paper we describe a new acceleration model for auroral and solar flare particles based on free energy in the form of ion anisotropies or plasma inhomogeneities generating lower-hybrid turbulence which undergoes collapse producing cavitons within which particles are accelerated. We have identified a number of free energy sources in the aurora and solar flares for the generation of these wave modes, examples are anisotropic ion distribution functions such as loss cones produced by magnetic mirrors, ring distributions produced in shocks and gradients in temperature and density. Analytical studies reveal that a possible saturation mechanism for lower-hybrid wave growth is the modulational instability, which ultimately leads to wave collapse and caviton formation. Numerical simulations of ion conics and ion ring relaxation processes using a $2\frac{1}{2}$-D fully electromagnetic, relativistic particle in cell code are described. The results indicate strong collapse at the lower-hybrid resonance resulting in simultaneous acceleration of both electrons and ions, together with electromagnetic wave generation at the electron cyclotron frequency. Arrest of wave collapse is due to particle acceleration. Comparison of theory and simulations with observations of measured electron and ion distributions in the aurora and inferred from X-ray and γ-ray emission from solar flares indicate that the acceleration model is in good agreement.

Introduction

The detailed model of the solar flare shock acceleration model is well described by McClements et al.[1] This paper assumed that unstable ion ring distributions are formed due to shock formation. Reconnection[2] can also produce such ion distribution functions, making the model much more general. In this paper we will show that not only electron acceleration takes place but also simultaneously ion acceleration to MeV energies. This result dispels the view that there are two different types of flares ie. electron or proton flares, we show that the accelerated electrons and ions have a common mechanism. Particle simulations were carried out using a fully electromagnetic, relativistic particle-in-cell code. There are two space dimensions and three velocity dimensions with the possibility of the magnetic field lying in or out of the coordinate plane. The ratio of proton mass m_i to electrons mass m_e is taken to be either 100 or 400. This choice of mass ratio is sufficiently small that significant electron and ion acceleration can occur within a computationally convenient interval of simulated time. The initial ion distribution consisted of a monoenergetic perpendicular (to $\mathbf{B}_o$) ring and a Maxwellian core, the ratio of the

density of ring ions n_r to core ions n_c being 3:7. This is close to density ratios observed at the Earth's bow shock.[3] In the absence of in situ measurements, it is not possible to say with certainty that ring densities as high as this could occur in the solar case. However, our plasma parameters were chosen such that gyrating ions constituted only a small fraction ($\sim 4\%$) of the energy potentially available in the downstream magnetic field.[1] The electron gyrofrequency ω_{ce} was taken to be twice the electron plasma frequency ω_{pe}, this condition being satisfied in a flaring loop with, for example $n_e = 6 \times 10^9 cm^{-3}$ and $B_o = 300G$.

Ion ring distributions have been shown by Mikhailovskii[4] to excite waves in the lower hybrid frequency range

$$\omega = \omega_{LH}\left(1 + k^2R^2 + \frac{m_i}{m_e}\frac{k_\parallel^2}{k^2} - \frac{\omega_{pe}^2}{k^2c^2}\right) \tag{1}$$

with a growth rate

$$\gamma_o \simeq \frac{n_r}{n_c}\omega_{LH} \tag{2}$$

where ω_{LH} is the lower hybrid frequency $\omega_{LH} = \omega_{pi}/\left(1+\omega_{pe}^2/\omega_{ce}^2\right)^{\frac{1}{2}}$, $R = \left(\frac{3T_i}{\omega_{LH}^2 m_i}\right.$ $\left.+\frac{2T_e}{\omega_{ce}^2 m_e}\frac{\omega_{pe}^2}{(\omega_{pe}^2+\omega_{ce}^2)}\right)^{\frac{1}{2}}$, ω_{pi} is the ion plasma frequency and $T_{e,i}$ is electron, ion temperature. The last term in equation (1) is the electromagnetic correction to the frequency. Resonant oscillations grow for $\omega = \mathbf{k}.\mathbf{v}_r$ where $\mathbf{v}_r$ is the velocity of the ion ring.

The initial ion distribution is given by

$$f_i\left(v_\parallel, v_\perp\right) = \frac{n_c}{(2\pi)^{3/2}v_c}\exp\left(-\frac{v_\parallel^2+v_\perp^2}{2v_c^2}\right) + \frac{n_r}{2\pi v_r}\delta(v_\parallel)\delta(v_r - v_\perp) \tag{3}$$

where δ is the Dirac delta function, v_c the core ion thermal speed, v_r the ring speed. As stated $n_r/n_c \simeq 3/7$ and $v_r \simeq 20v_c$, with $m_e/m_i = 100$ this means $v_r = 2v_e$ and with $m_e/m_i = 400, v_r = v_e$ where v_e is the electron thermal speed. The ion ring speeds are easily computed from knowledge of the Alfven speed in the solar flare[1]. The core ion temperature, which is assumed equal to the initial electron temperature, was set equal to 800eV.

The results of the simulation are shown in figures 1-3. Figure 1 depicts the time evolution of the wave spectral density as a function of the parallel phase velocity, the lower-hybrid waves appear at the low phase velocity and are seen to grow then fall to a saturated value level determined by particle absorption. Figure 2a represents the time evolution of the electron distribution as a function of $v_\parallel$ with the final electron distribution is represented in figure 2b. The flux of electrons with energy above $20keV$, for a bimaxwellian plasma, is given by

$$F(> 20keV) = 2\pi \int_{v_\parallel}^{\infty} dv_\parallel \int_{o}^{\infty} v_\perp f_e(v_\parallel, v_\perp) dv_\perp$$

using a plasma density of $10^{10} cm^{-3}$ we find from our simulations

$$F(> 20keV) \sim 10^{18} \text{electrons } cm^{-2} sec^{-1}$$

ie. a typical "thick target flux". Figure 3 depicts the initial and final ion core distribution function showing significant energization in the perpendicular plane. Protons with energies in the MeV range are observed to be produced within distances of the order of 10's of meters and within a few ion-gyroperiods, both electrons and ions are observed to be accelerated in localized regions of space indicating the presence of cavitons. The acceleration of electrons and ions takes place simultaneously indicating that it is not a two stage process but is due to a similar mechanism in this case due to the waves generated at the lower-hybrid resonance frequency. This is in agreement with the simultaneous observations of x-rays and γ-rays by Forrest and Chupp[5]. Detailed studies of the electron distribution function reveal the presence of beams with $+ve$ slopes in f_e ie. $\partial f_e / \partial v > 0$. This cannot be due to a simple quasi-linear diffusion process which at best can only produce a plateau in f_e. We find that at the end of the simulations approximately 10% of the ring energy has been transferred to the background electrons and ions while less than 1% of the energy is stored in all the waves generated.

Simulations show the transfer of perpendicular ion energy to energetic electrons via the process described above. The results have shown perpendicular shocks, such as might be associated with coronal mass ejection, or reconnection processes which produce ion ring distributions that can give rise to 10^{18} electrons cm^{-2} sec^{-1} at hard x-ray emitting energies. Protons are accelerated to MeV energies in the same time scale. Therefore this mechanism for particle acceleration can account for both the nonthermal hard x-ray and γ-ray emission observed in solar flares[5]. A similar mechanism is also responsible for auroral electron acceleration[6].

References

1. K G McClements, J J Su, R Bingham, J M Dawson and D S Spicer, *Solar Phys.*, 130, 229, (1990)

2. J N Leboeuf, T Tajima and J M Dawson, *Phys. Fluids*, 25, 784, (1982)

3. G Paschmann, N Sckopke, S J Bame and J T Gosling, *Geophys. Res. Lett.*, 9, 881 (1982)

4. A B Mikhailovskii, Theory of Plasma Instabilities Vol 1, Consultants Bureau, New York, (1974)

5. D J Forrest and E L Chupp, *Nature*, 305, 291, (1983)

6. D A Bryant,A C Cook, Z S Wang and U de Angelis, *J. Geophys. Res.*, 96, 13829, (1991)

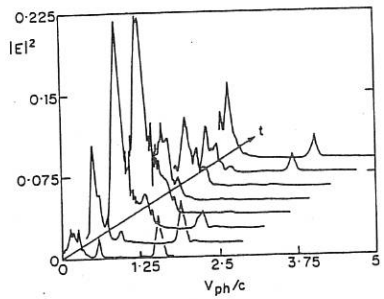

Fig.1. Time evolution of the wave spectral density as a function of the parallel phase velocity.

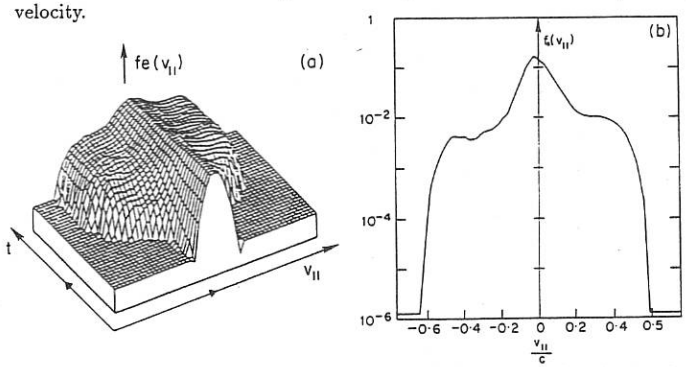

Fig.2. (a) Time evolution of the parallel component of the electron distribution function.
(b) Final electron parallel distribution showing bump on tail.

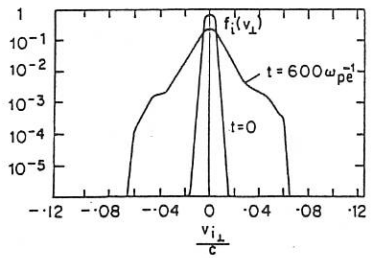

Fig.3. Initial and final perpendicular ion core distribution functions.

Solar Flare Mechanism Based on MHD Relaxation Model

Kanya Kusano, Hiroko Kubo, Teruo Tamano[1] and Tetsuya Sato[2]

Department of Materials Science, Faculty of Science, Hiroshima University, Higashi-Hiroshima 724, Japan

In order to reveal the solar flare mechanism, the dynamics of a solar coronal magnetic arcade are investigated by modeling it as an MHD relaxation process. Our work is composed of the following two parts: the equilibrium analysis and the dynamic simulations.

Equilibrium Analysis

According to Taylor's conjecture [1], the minimum energy state for the magnetized plasma is described by

$$\mathrm{rot}\boldsymbol{B} = \alpha \boldsymbol{B}. \tag{1}$$

In the two dimensional system which has a translational symmetry along z-axis, the magnetic field $\boldsymbol{B}$can be written by using the flux function ψ,

$$\boldsymbol{B} = (\partial\psi/\partial y, \partial\psi/\partial x, B_z).$$

The equation (1) is modified to

$$\nabla^2\psi = -B_z\frac{\partial B_z}{\partial \psi}, \tag{2}$$

$$B_z = \alpha\psi + c, \tag{3}$$

where the coefficients α and c are constant. By numerically solving the equation (2) and (3) in the rectangular domain of the coronal region, we obtain the minimum energy state for the magnetic arcade. The boundary condition for ψ is given as following: $\psi = \psi_0(1 - \cos 2\pi x)/2$ at $y = 0$, $\psi = 0$ at $y = L_y$ and at $x = 0$ and L_x, where the bottom boundary ($y = 0$) corresponds to the photosphere. The solution is calculated as a function of the magnetic helicity $K = \int_S \boldsymbol{A}\cdot\boldsymbol{B}dS$ and the magnetic flux across

[1] *Plasma Research Center, University of Tsukuba, Tsukuba 305, Japan*

[2] *National Institute for Fusion Science, Nagoya 464-01, Japan*

the domain $\Phi = \int_S \boldsymbol{B} \cdot d\boldsymbol{S}$. As a result, we find that the Taylor's minimum energy state for the magnetic arcade has three different types of solution, which have different topology each together; a simple arcade (type 1), an arcade plus an island above the arcade (type 2), and an arcade plus an island within the arcade (type 3), respectively. The typical solution is presented in Fig.1 for each type. What type of solution appears depends on the parameters K and Φ. In the space of the helicity K vs. the flux Φ, the solution of type 1 occupies the low helicity region. The solution of type 1 changes to the types 2 and/or 3, as the magnetic helicity K becomes larger than a critical amount. The critical helicity, above which the type 2 or 3 appears, depends on the magnetic flux across the arcade. When the helicity is sufficiently large, the solution has both features of type 2 and 3, having the islands above and also within the arcade. From the fact that the topology of the magnetic arcade is changed by the change of the helicity, the magnetic reconnection process is expected when the magnetic helicity is injected into the arcade by a certain mechanism.

Dynamic Simulation

Secondly, we directly carry out the dynamic simulations of the magnetic arcade, where the magnetic helicity is injected by the shearing motion on photosphere ($y = 0$) into the arcade. The basic equations are given by the following,

$$\rho \frac{d\boldsymbol{V}}{dt} = \boldsymbol{J} \times \boldsymbol{B}, \tag{4}$$

$$\frac{\partial \boldsymbol{B}}{\partial t} = -\mathrm{rot}\boldsymbol{E}, \tag{5}$$

$$\boldsymbol{E} + \boldsymbol{V} \times \boldsymbol{B} = \eta \boldsymbol{J}, \tag{6}$$

$$\boldsymbol{J} = \mathrm{rot}\boldsymbol{B}, \tag{7}$$

where the pressure gradient force is neglected. The simulation box is same as the domain using in the equilibrium analysis, and the translational symmetry is also assumed. The boundary conditions are given by the impermeable and the perfectly conductive condition. Only for the photospheric boundary ($y = 0$), however, the plasma velocity v_z is given by the analytic function of x to model the shearing motion. Two different

shearing motions are considered, those being given by

$$v_z = v_0 \sin 2\pi x/L_x \quad \text{for case 1,}$$
$$v_z = v_0 \sin 4\pi x/L_x \quad \text{for case 2.}$$

The characteristic difference between these cases is that the flux injection rate $\dot{\Phi} = \int_0^{L_x} v_z B_y dx$ is given by $\pi v_0 \psi_0 / 2L_x$ for case 1, but is vanished for the case 2. On the other hand, the helicity injection rate is positive for both cases. In the case 2, hence, only the magnetic helicity is injected and the magnetic flux across the domain is kept to be zero. As a result of it, the resultant orbit for the case 1 in the $K - \Phi$ space remains in the region for the type 1 of the minimum energy state considered in the equilibium analysis. However, the orbit for the case 2 progresses in the region for the type 2 and 3 of it.

Figure 2 shows the resultant magnetic field lines of force from the simulation for the case 1. By investigation about the evolution of the total magnetic energy $W = \int B^2 dS$ for this simulation, we find that the energy W from the simulation well agrees with the Taylor's minimum energy. On the other hand, the simulation result in the case 2 has a large excess energy compared to the Taylor's minimum energy. From these results, we can conclude that Taylor's minimum energy state can be obtained by 2D dynamics, if the helicity and the flux remains in the region where the minimum energy state is given by the type 1 of solution. However, if the parameters are in the region for types 2 and 3, 2D dynamics no longer generate Taylor's minimum energy state spontaneously.

The accumulation of the excess energy suggests the presence of three dimensional dynamics to release itself. Such an energy relaxation process is discussed as a possible mechanism of solar flare. We are now developing the three-dimensional simulation in order to confirm the relaxation model for solar flare. The details will be reported in the conference.

Reference

[1] J.B.Taylor, *Phys. Rev. Lett.* **33** (1974) 1139.

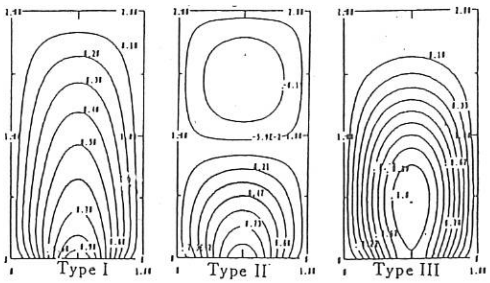

FIG. 1. The contour of the flux function of the Taylor's minimum energy state for three different types of solutions.

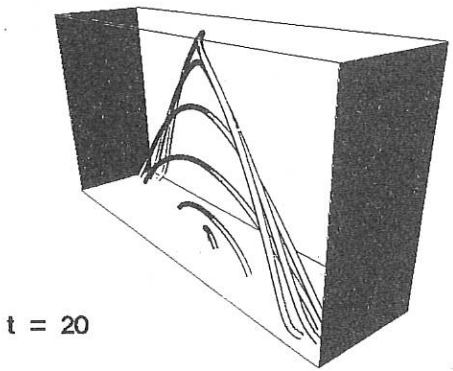

FIG. 2. The three dimensional structure of the magnetic field lines of force, which is generated by the simulation with the case 1 of shearing motion.

NONLINEAR MHD SURFACE WAVES ON PLASMA INTERFACES AND THEIR EVOLUTION EQUATION IN SOLAR AND MAGNETOSPHERIC CONDITIONS

P. Nenovski, I. Zhelyazkov* and K. Murawski†

Space Research Institute, BG-1000 Sofia, Bulgaria
* Faculty of Physics, Sofia University, BG-1126 Sofia, Bulgaria
† Department of Applied Mathematics, University of St Andrews, St Andrews KY16 9SS, Scotland, United Kingdom

Nonlinear (NL) MHD waves have been studied in connection with various plasma processes in magnetically structured solar atmosphere and solar wind. The propagation of MHD surface waves, supported by plasma-plasma, or plasma-magnetic field boundaries has been also a subject of intense study. During last decade some aspects of NL MHD surface waves have been considered. Roberts and Mangeney /1/ have proposed that the nonlinear behaviour of surface waves in a magnetic slab is governed by the Benjamin-Ono equation. The result by Roberts /2/ on dispersive MHD surface waves has been generalized by Merzlyakov and Ruderman /3/ for stratified plasmas. On the other hand, the self-modulation of NL MHD waves is examined by Hasegawa /4/, Mio et al. /5/ using perturbation method /6/ as a generalized scheme for deriving NL Schroedinger equation. It was shown that long-time behaviour of the complex amplitude of the MHD wave train is governed by modified, or derivative NL Schroedinger equation (NLSE). The problem of stability of NL MHD surface waves against a modulation was firstly examined by Merzlyakov /7/ and Sahyouni et al. /8/. It was shown that the behaviour of NL MHD surface waves in a magnetic slab depends on both parameters $\eta = \rho_e/\rho$ and $K = k_0 x_0$, where η is the ratio of plasma densities and K is the normalized with respect to the slab half-thickness x_0 wavenumber. Merzlyakov's result yields a soliton-like propagation at great enough K's. In Sahyouni et al. /8/ by using the ponderomotive forces approach a usual NLSE which governs the propagation of magnetosonic waves is derived. The analysis yields that only dark soliton solution are possible. This analysis was however performed under assumption that the folding of the slab interface is neglected. In the present study we use free boundary approach and consider modulation only along the MHD surface wave propagation.

Let us consider a magnetic slab of thickness x_0 surrounded by plasmas.

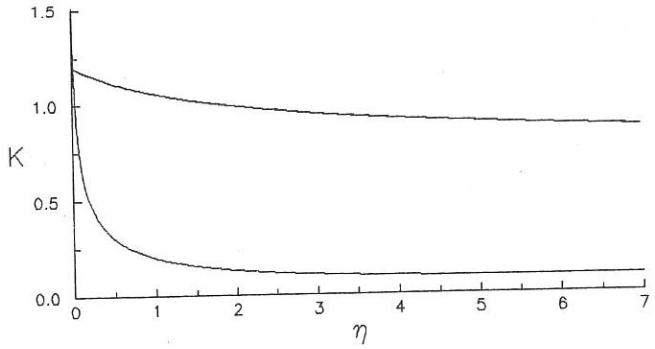

Fig. 1 Neutral curves $[\beta(K,\eta) = 0]$ for NL MHD surface waves

regions. Hence, the dark soliton solution could be dominating either when the plasma and wave parameters η, x_0, v_A, $k_0 = k_0(\omega_0)$ are such that we are away from the neutral curves, or as the soliton lengths are large enough in order the effects of the derivative NL term to be diminished.

The second neutral curve reduces the region of stability of the NL MHD surface waves. Merzlyakov's assumption for modulation in the form of a localized perturbation (with an evanescent amplitude) /7/ has a stabilizing rather than a destabilizing effect. In the usual modulation treatment (in z direction only) the region of stability is as follows:

$$0.1x_0^{-1} < k_{01}^{root} < k_0 < k_{02}^{root} < x_0^{-1}.$$

Here $k_{01,2}^{root}$ are the roots of the equation $\beta(\eta, K, v_g, v_A, k_0 V) = 0$.

Which form of the evolution equation for the NL MHD surface waves is operative depends strongly on the plasma geometry and parameters, namely x_0, ρ_e, ρ, v_A. In the limit $K \longrightarrow 0$ the MHD surface waves are dispersive and their evolution is governed by the Benjamin-Ono equation /1/. For large K's the dispersion goes to zero (Fig. 2) and when the amplitude is small (but finite) a bright soliton solution is possible. In the intermediate case $0.1 < k_{01}^{root} x_0 < K < k_{02}^{root} x_0 < 1$ the hybrid character of the MHD surface waves is most pronounced and the wave evolution is more sensitive to NL term conditions.

Finally, we mention that in our present analysis a one-dimensional

The static magnetic field in the slab is oriented along the z axis. The x coordinate is normal to the interfaces $x = \pm x_0$. Following the derivative expansion method /6/ and Merzlyakov's /7/ notation we get the following NLSE

$$i\,\partial f_{11}/\partial\tau + 0.5\,\partial^2\omega_0/\partial k_0^2\,\partial^2 f_{11}/\partial\zeta^2 + \beta|f_{11}|^2 f_{11} = 0.$$

Here f_{11} is the complex amplitude of a sausage MHD surface-wave train along the slab, τ is the slow time variable, $\omega_0 = \omega_0(k_0)$ is the linear dispersion relation, $\zeta = z_1 - Vt_1$ is the slow spatial variable (V being equal to the wave group velocity $v_g = \partial\omega_0/\partial k_0$) and β is

$$-k_0^4(1 + \eta\,\tanh K)^{-1}\Big\{0.5\eta\,\tanh K\big[1 + 9\cosh^2 K + 4.5\sinh 2K + 4\cosh^2 K\,\sinh 2K$$

$$+ 2\sinh^2 2K\big] + 2.5\eta\,\sinh^2 K(1 - \tanh K) + 8\eta\,\sinh^2 K\,\tanh K + 2\eta(1 - V_g^2)^{-1}$$

$$\times\big[\tanh K(-3 + k_0V/\omega_0 + \omega_0/k_0V) - 2\cosh 2K(1 - k_0V/\omega_0)^2\big]$$

$$(1 - k_0V/\omega_0)(1 - V_g^2)^{-1}(k_0^2v_A^2/\omega_0^2 - 1)^{-1}\Big[8\eta\,\tanh K\,\sinh^2 K(1 + k_0V/\omega_0$$

$$- 2k_0^2v_A^2/\omega_0^2) + 2(1 - k_0V/\omega_0)\big[2(k_0V/\omega_0)(1 + \eta\,\tanh K) - 2 - \eta\,\tanh K\big]\Big]\Big\}/\omega_0$$

Here $V_g \equiv v_g/v_A$ is the normalized wave group velocity, v_A being the Alfvén velocity.

This coefficient differs, of coarse, from that of Merzlyakov /7/. Examining it we obtain two roots instead of one as in Merzlyakov case. Surprisingly, one of the root coincides precisely with that of Merzlyakov's (see Fig. 1). It is seen that in the region of $K > 1$ (above Merzlyakov curve) there exist compressive (bright) solitons whose parameters (velocity, amplitude, etc.) are given by

$$f_{11} = A\,\mathrm{sech}\big[A(\beta/\alpha)^{1/2}(\zeta - W\tau)\big]\exp\Big(iA^2\beta\tau/2 + i(\zeta - W\tau/2)W/\alpha\Big),$$

where A is the soliton amplitude, W its velocity, $\alpha = \partial^2\omega_0/\partial k_0^2$ is the wave group velocity dispersion. Between the neutral curves, defined by $\beta = 0$ (Fig. 1), we observe a wide region of stable waves. In this region, where $0.1 < K < 1$ and $\eta > 1$ only dark solitons are possible which resemble the magnetosonic case in the plasma slab (see /8/). Near the neutral curves the NL term is however small and there a fourth order approximation should be adopted, i.e. a derivative NLSE should govern the wave evolution in those

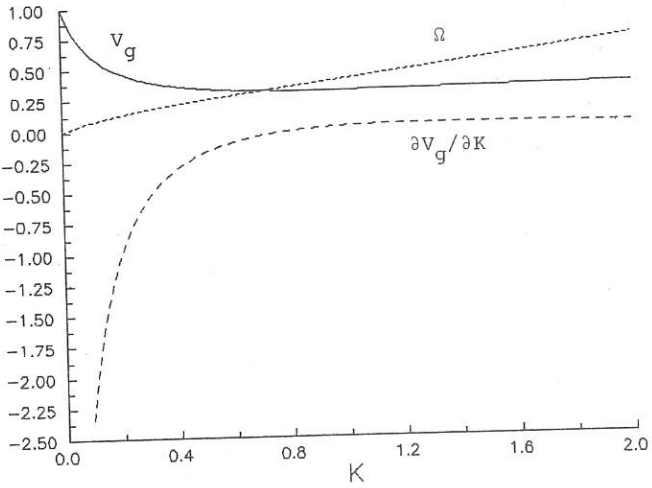

Fig. 2 Normalized wave frequency Ω ($= \omega_0/x_0 v_A$), wave group velocity $V_g = v_g/v_A$ and its derivative V_g' as functions of K at $\eta = 6.75$

modulation has been assumed. Further studies have to be performed in order to account for the two- and/or three-dimensional feature of the NL MHD surface-wave problem. The latter includes two-dimensional modulation (in arbitrary form) and a propagation at arbitrary angles to the ambient static magnetic field. Such an analysis is in progress.

Acknowledgements: This work was supported by the Ministry of Education and Science under grant F-50/91.

References

/1/ B. Roberts, A. Mangeney, Monthly Not. Roy. Astron. Soc. **198**, 7P (1982)
/2/ B. Roberts, Phys. Fluids **28**, 3280 (1985)
/3/ E.G. Merzlyakov, M.S. Ruderman, Solar Phys. **95**, 51 (1985)
/4/ A. Hasegawa, Phys. Fluids **15**, 870 (1972)
/5/ K. Mio, T. Ogino, K. Minami, S. Takeda, J. Phys. Soc. Japan **41**, 265 (1976)
/6/ T. Taniuti, N. Yagima, J. Math. Phys. **101**, 1369 (1969)
/7/ E.G. Merzlyakov, Mechanics of Fluids and Gases No 2, 164 (1985) (in Russian)
/8/ W. Sahvouni. I. Zhelvazkov. P. Nenovski. Solar Phvs. **115**. 17 (1988)

GENERATION OF LARGE AMPLITUDE PLASMA WAVES IN SPACE PHENOMENA

G.I. Dudnikova, V.A. Vshivkov
Institute of Computational Technologies, Russia Academy of Sciences, Novosibirsk 630090, Russia

Nonstationary astrophysical phenomena as Supernova burst and solar flares are accompanied by generation of waves and shocks. The problems of the generation are connected with collisionless interaction of the high- speed plasma flows. In general form this problem may be expressed as the collisionless expansion of the plasma cloud in the magnetized background. As a result of such expansion the energy of the plasma cloud is transformed into the directed heat energy of medium fast particles flows that allow the character of the formed disturbance. The energy change mechanism of the cloud-background interaction connected with the action of the curl electric field E_φ has been investigated in [1,2]. The physical model of such interaction (called magnetic laminar mechanism-MLM [1]) is based on the displacement of the magnetic field $\bar{B}_0$ by the cloud, and a moving compressed magnetic field formed on its boundary, and generating $\bar{E}_\varphi \| [\bar{B}\bar{V}_0]$. To supply the effective energy change of cloud -background system it is necessary to fulfill the requirement for magnitude of MLM-parameter $\delta = \tilde{R}^2 / R_H R_H^* \geq 1$. That is the requirement for the ions magnetization at the scale $\tilde{R} = \sqrt[3]{3N/4\pi n_*}$ of the gasdynamic deceleration of the cloud by the background. There N is number of particles on the cloud n_* is the background density R_H, R_H^* -Larmor radius of the cloud and background respectively (calculated according to the initial velocity of the cloud expansion $\bar{V}_0$).

This paper will discuss the character of background disturbance generated by the expanding cloud with large $M_A \geq 5$,

there $M_A = V_0/V_A$ is Mach-Alfven number, $V_A = B_0/\sqrt{4\pi n_* m_1}$ is Alfven velocity. Let's consider the problem of interaction of laser-produced plasma cloud with ionized magnetized background. The condition of collisionless interaction at various Alfven-Mach numbers have to take into account a finite Larmor radius of ions and magnetized electron. Hybrid fluid-particle model is based on kinetic description of the ion plasma component and the hydrodynamic approximation for electrons. The original set of the simulation equations includes Vlasov's equation for ions, motion equations and energy change equation for electrons and Maxwell's equations [3]. Let us discuss the following problem. At the initial moment of time t=0 in the center of the cylindrical chamber with the uniform magnetic field $\bar{B}=(0,0,B_0)$ filled up the background plasma with density n_* there is the spherical dense plasma cloud with the directed movement energy E_0 and total particles number N. In the case of axisymmetrical two-dimensional flow $\left\{\frac{\partial}{\partial r}\neq 0,\ \frac{\partial}{\partial z}\neq 0,\ \frac{\partial}{\partial \varphi}=0\right\}$ we studied the cloud expansion in uniform background with density n_* and non-uniform background: $n_*=n(z)$. We use the standard PIC-method for determination coordinates and average velocities of particles and finite-difference splitting up scheme for definition of temperature, electric and magnetic fields. On the scales of gasdynamic radius of deceleration $\tilde{R}=(3N/4\pi n_*)^{1/3}$ asymmetric interaction of the expanding cloud with background was observed. The perpendicular to $\bar{B}_0$ flow was decelerated by most intensity, and displacement of the field, and formation of magnetic cavity took place. The magnetic cavity is asymmetrical in the case of the plasma expansion in non-uniform background. The calculations show that formation of large amplitude waves takes place for the region of angles $\vartheta \approx 90^\circ$ (Fig.1). The amplitude of the wave at distance $R \sim \tilde{R}$ is $n/n_* \approx 4$ (M_A=10). The disturbance of density is propagated for various angles with different velocity and within a some time difference of velocity disappears at distance $R > 2\tilde{R}$ in the whole region of angles ϑ=90°-26°. As it was shown in [3]

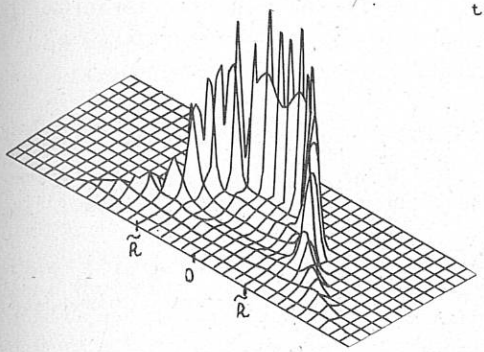

Fig 1: The plasma density in the r-z plane at t=2 μs. M_A=10.

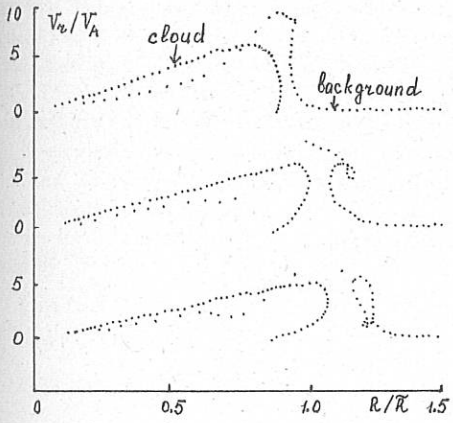

Fig 2: Ion phase space at t=2μs, 2.4μs, 3μs for parameters M_A=10, ϑ=90°.

the initial disturbances of magnetic field formed at small $M_A < 3$ are decayed into a wave packet at the distance $R \approx 2\tilde{R}$. In the calculations the disturbances structure is determined by the positive dispersion due to which the short wavelength one run forward. The oscillator disturbances on the profile of magnetic field for large $M_A > 5$ are not observed. The vector of transverse magnetic field was polarized linearly. The alteration of circular polarization of transverse magnetic field vector to the linear one with the increase of M_A means a change possibility of the wave generation conditions and it is likely may be connected with the total decreasing of Hall currents with the growth of M_A.

In Figure 2 we show the distribution of cloud ions and background ions in the phase space at three times for $M_A >> 1$.

One can see the dynamics of the plasma cloud deceleration and the generation of large amplitude wave at the distance $R \sim \tilde{R}$. This wave breaks up with the time.

/1/ Yu.P.Zakharov, A.M.Orishich, A.G.Ponomarenko, Laser-produced Plasma and Laboratory Simulation of Nonstationary Space Processes, Novosibirsk, IPAM Press, (in Russian),(1988)

/2/ V.M.Antonov, V.P.Bashurin, L.B.Gevorkyan et al., Proc. XVI Inform. Conf. of Phen. in Ioniz. Gases., Düsseldorf, v.1, 88 (1983)

/3/ G.I.Dudnikova, A.M.Orishich, A.G.Ponomarenko et al. Proc. Workshop on Plasma Astrophys., Telavi, Georgia (1990).

PARAMETRIC INSTABILITIES OF LANGMUIR WAVES IN DUSTY PLASMAS

P. K. Shukla, and G. Feix
Fakultät für Physik und Astronomie, Ruhr-Universität Bochum
D-4630 Bochum 1, F. R. Germany

N. N. Rao
Physical Research Laboratory, Ahmedabad 380009, India

Recently, there has been a growing interest in dust plasma physics. A dusty plasma may contain electrons, ions, and a large number of charged dust grains of micrometer or submicrometer size. Such a plasma is usually found in many low-temperature laboratory devices, as well as in space and astrophysical environments.

Collective effects in dusty plasmas are of great importance. The presence of charged dust grains can affect low-frequency wave motions in an electron-ion plasmas. For example, recently it has been shown [1-3] that the presence of stationary charged dust grains changes the quasi-neutrality condition, thereby modifying considerably the existing wave spectra. On the other hand, a novel dust acoustic wave [4] arises in a uniform plasma with mobile charged dust fluid and Boltzmann distributed electron and ion fluids.

In this paper, we consider parametric instabilities [3] of a large amplitude Langmuir wave with new types of low-frequency electrostatic oscillations in an unmagnetized dusty plasma. The latter consists of singly charged positive ions, electrons, and negatively charged dust grains. We assume that the dust grains all have uniform size and that they neither break up nor coalesce. When the grain size is much smaller than the inter-particle distance and the wavelength of any perturbations, then the dust grains can be treated as negatively charged point masses.

The nonlinear interaction of finite amplitude Langmuir waves with dusty plasmas is governed by

$$\partial_t n_j + \nabla \cdot (n_j \mathbf{v}_j) = 0\,, \tag{1}$$

$$(\partial_t + \mathbf{v}_j \cdot \nabla)\mathbf{v}_j = -(Z_j q_j/m_j)\nabla\phi - (\gamma_j T_j/m_j n_j)\nabla n_j\,, \tag{2}$$

and

$$\nabla^2\phi = -4\pi \sum_j Z_j q_j n_j\,, \tag{3}$$

where $n_j, \mathbf{v}_j$, and T_j are, respectively, the total particle number density, the fluid velocity, and the constant temperature of the particle species j (equals e for electrons, i for ions, and d for dust grains). Furthermore, $q_e(q_i) = -e(e), q_d = -e$, e is the magnitude of the electron charge, Z_d refers to the number of electrons that reside on a dust grain, m_j is the mass, and $Z_{e,i} = 1$. The electrostatic potential is denoted by ϕ. The ratio of specific heats γ_j takes the value 1(3) for isothermal (adiabatic) compression.

In order to investigate the nonlinear interaction of high-frequency Langmuir waves with low-frequency oscillations in dusty plasmas, we decompose all the physical quantities as: $n_j = n_{jo} + \sum_j n_{j1}^h + \sum_j n_{j1}^l$, $\mathbf{v}_j = \mathbf{v}_j^h + \mathbf{v}_j^l$, and $\phi = \phi^h + \phi^l$, where n_{jo} is the unperturbed particle number density ($n_{eo} + Z_d n_{do} = n_{i0}$), and the superscript h (l) denotes the high- (low-) frequency plasma motion. Thus, the equation for the Langmuir sidebands, which is derived from (1) to (3), reads

$$(\omega_\pm^2 - \omega_{pe}^2 - 3k_\pm^2 v_{te}^2)\mathbf{E}_\pm \approx (4\pi e^2/m_e) n_{e1}^l \mathbf{E}_{o\pm}\,, \tag{4}$$

where $\mathbf{E} = -\nabla\phi^h$ is the electric field vector, $\omega_\pm = \omega \pm \omega_o$, $\mathbf{k}_\pm = \mathbf{k} \pm \mathbf{k}_o$, and the subscript $\pm(o\pm)$ denotes the sidebands (pump). The plasma frequency and the thermal velocity of the electron fluid are denoted by $\omega_{pe} = (4\pi n_{eo} e^2/m_e)^{1/2}$ and $v_{te} = (T_e/m_e)^{1/2}$, respectively. The plasma frequency of the electron fluid is much larger than those of the ion and dust fluids. Note that sidebands are created due to the coupling of the pump $(\omega_o, \mathbf{k}_o)$ with low-frequency $(\omega, \mathbf{k})$ plasma motions.

Assuming that the phase velocity of the dusty plasma slow motion is much smaller than v_{te}, we find that the electron number density perturbation n_{e1}^l is given by

$$n_{e1}^l = (k^2/4\pi e)\chi_e(\phi^l - \phi_{pe})/T_e\,, \tag{5}$$

where $\chi_e = 1/k^2\lambda_{De}^2$ and $\phi_{pe} \approx e \mid \nabla\phi^h \mid^2 /2m_e\omega_{pe}^2$ is the low-frequency electron susceptibility and the ponderomotive potential, respectively. The electron Debye length is denoted by $\lambda_{De} = (T_e/4\pi n_{eo} e^2)^{1/2}$. The ion number density perturbation is given by

$$n_{i1}^l \approx -(k^2/4\pi e)\chi_i\phi^l\,, \tag{6}$$

where $\chi_i = -\omega_{pi}^2/(\omega^2 - \gamma_i k^2 v_{ti}^2)$ is the low-frequency ion susceptibility, $\omega_{pi} = (4\pi n_{io} e^2/m_i)^{1/2}$ and $v_{ti} = (T_i/m_i)^{1/2}$ are, respectively the plasma frequency and the thermal velocity of the warm ion fluid. On the other hand, the number density perturbation of the cold dust fluid is

$$n_{d1}^l \approx (k^2/4\pi Z_d e)\chi_d\phi^l\,, \tag{7}$$

where $\chi_d = -\omega_{pd}^2/\omega^2$ is the low-frequency dust susceptibility and $\omega_{pd} = (4\pi n_{do} Z_d^2 e^2/m_d)^{1/2}$ is the dust plasma frequency. The ponderomotive force acting on the dust fluid is negligibly small as $Z_d m_e << m_d$.

Inserting (6) and (7) into (3), we obtain

$$\phi^l = -4\pi e n_{e1}^l/k^2(1 + \chi_i + \chi_d)\,. \tag{8}$$

Eliminating ϕ^l from (5) and (8), we have

$$n_{e1}^l = -n_{eo}(1 + \chi_i + \chi_d)e\phi_{pe}/T_e\epsilon\,, \tag{9}$$

where $\epsilon = 1 + \chi_e + \chi_i + \chi_d$.

The dispersion relation for parametric instabilities in dusty plasmas is obtained by eliminating n_{e1}^l from (4) and (9). The result is

$$\epsilon = -k^2\chi_e(1 + \chi_i + \chi_d)\sum_{\pm}(\mathbf{k}_\pm \cdot \mathbf{v}_o)^2/k_\pm^2\omega_\pm^2\epsilon_\pm\,, \tag{10}$$

where $\epsilon_\pm = 1 - (\omega_{pe}^2/\omega_\pm^2)(1 + 3k_\pm^2\lambda_{De}^2)$ and $\mathbf{v}_o = e\mathbf{E}_o/m_e\omega_{pe}$.

We consider two types of plasma slow response. Firstly, we assume that the dust grains are static so that $\chi_d = 0$. For $k^2\lambda_{De}^2 << 1$, (10) takes the form

$$(\omega^2 - \omega_{ss}^2) = k^2\omega_{pi}^2 \sum_{\pm} (\mathbf{k}_\pm \cdot \mathbf{v}_o)^2/k_\pm^2 D_\pm \,, \tag{11}$$

where $\omega_{ss}^2 = k^2c_{ss}^2 \equiv k^2[\gamma_i v_{ti}^2 + (n_{io}/n_{eo})c_s^2]$, $c_s^2 = T_e/m_i$, $D_\pm \approx \pm 2\omega_{pe}(\omega - \mathbf{k}\cdot\mathbf{v}_g \mp \delta)$, $\mathbf{v}_g \approx 3\mathbf{k}_o v_{te}^2/\omega_{pe}$, and $\delta \approx 3k^2v_{te}^2/2\omega_{pe}$.

For the three- wave resonant interaction, the upper- sideband is off-resonant (viz. $D_+ \neq 0$), and the maximum growth rate found from (11) is

$$\gamma \approx \omega_{pi} k \mid \hat{\mathbf{k}}_- \cdot \mathbf{v}_o \mid /2(\omega_{pe}\omega_{ss})^{1/2} \,. \tag{12}$$

It follows that the presence of static charged dust grains reduces the growth rate because the dust acoustic frequency ω_{ss} is larger than $k(3v_{ti}^2 + c_s^2)^{1/2}$, which is the frequency of the ion sound wave when the dust grains are absent.

For the modulational instability, the upper- and lower- sidebands are resonant. For quasi-static modulations ($\omega << \omega_{ss}, \gamma_i = 1$), (11) becomes

$$(\omega - \mathbf{k}\cdot\mathbf{v}_g)^2 = \delta^2 \left\{1 - \omega_{pi}^2(\hat{\mathbf{k}}_- \cdot \mathbf{v}_o)^2/\omega_{pe}\delta c_s^2[(n_{io}/n_{eo}) + (T_i/T_e)]\right\} \,. \tag{13}$$

It emerges that the growth rate of the modulational instability is also reduced in dusty plasma.

Next, we consider the dynamics of the dust grains and concentrate in the frequency regime $\omega << kv_{tj}$. Accordingly, we have $\chi_e = 1/k^2\lambda_{De}^2$ and $\chi_i = 1/k^2\lambda_{Di}^2$, where $\lambda_{Di} = (T_i/4\pi n_{io}e^2)^{1/2}$ is the ion Debye length. Here the dispersion relation for $k^2\lambda_{Dj}^2 << 1$ is of the form

$$(\omega^2 - \omega_{rs}^2) = -[(\omega^2 - \omega_D^2)/\lambda_{De}^2] \sum_{\pm} (\mathbf{k}_\pm \cdot \mathbf{v}_o)^2/\alpha k_\pm^2 D_\pm \,, \tag{14}$$

where $\omega_D = k\lambda_{Di}\omega_{pd} \equiv kc_D, \omega_{rs} = \omega_D/\sqrt{\alpha} \equiv kc_{rs}$, and $\alpha = 1 + T_i n_{eo}/T_e n_{io} \equiv 1 + \tau$.

The growth rate of the three-wave decay interaction for this case is

$$\gamma \approx \omega_{pd} k\sqrt{\tau}\lambda_{Di} \mid \hat{\mathbf{k}}_- \cdot \mathbf{v}_o \mid /2\lambda_{De}[(1+\tau)\omega_{pe}\omega_{rs}\alpha]^{1/2} \,. \tag{15}$$

The modulational instabilities invloving extremely low-frequency dust-acoustic perturbations are likewise investigated by analyzing (14). For example, for $\omega << \omega_D$, we have

$$(\omega - \mathbf{k}\cdot\mathbf{v}_g)^2 = \delta^2[1 - (\hat{\mathbf{k}}_- \cdot \mathbf{v}_o)^2/\lambda_{De}^2\omega_{pe}\delta] \,. \tag{16}$$

Equation (16) admits an oscillatory instability.

We now present the relevant equations governing the dynamics of the modulated Langmuir wave packets. For the Langmuir wave envelope, we have

$$i(\partial_t + \mathbf{v}_g \cdot \nabla)\mathbf{E} + (3v_{te}^2/2\omega_{pe})\nabla^2\mathbf{E} - \omega_{pe}(n_{e1}^l/2n_{eo})\mathbf{E} = 0 \,. \tag{17}$$

On the other hand, low-frequency density responses are given by

$$(\partial_t^2 - c_{ss}^2\nabla^2)n_{e1}^l = (1/2)(n_{io}e^2/m_e m_i\omega_{pe}^2)\nabla^2 \mid \mathbf{E} \mid^2 \,, \tag{18}$$

for the case in which the dust grains are static, and

$$(\partial_t^2 - c_{rs}^2 \nabla^2) n_{e1} = -(1/4\pi T_e \alpha)(\partial_t^2 - c_D^2 \nabla^2) \mid \mathbf{E} \mid^2 , \tag{19}$$

for the case in which the dust grains are mobile and the electron and ion fluids have the Boltzmann distribution. Equations (17) to (19) can be used for the study of envelope soliton formation, wave collapse, etc.

To summarize, we have investigated parametric instablities of a finite amplitude Langmuir wave in a uniform unmagnetized dusty plasma. It is found that the growth rates of the three-wave decay as well as the modulational instabilities are reduced as compared with those cases without the dust grains. Also presented are the dynamical equations that govern the spatio-temporal evolution of the modulated Langmuir wave packets in dusty plasma. Our results should be useful for the understanding of the nonlinear wave phenomena in dusty plasmas, such as those in cometary comae and tails, in interstellar clouds, as well as in noctilucent clouds on the night sky of the Earth's north pole during the summer season.

Acknowledgments.- This work was supported by the Deutsche Forschungsanstalt für Luft-und Raumfahrt (DLR)-Indian Space Research Organization (ISRO) Exchange Program.

REFERENCES

[1] P. K. Shukla, Physica Scr. **44**, May 1992.

[2] P. K. Shukla and V. P. Silin, Physica Scr. **44**, May 1992.

[3] P. K. Shukla and L. Stenflo, Astrophys. Space Sci. **190**, 23 (1992).

[4] N. N. Rao, P. K. Shukla, and M. Y. Yu, Planet. Space Sci. **38**, 534 (1990).

MAGNETIC RECONNECTION IN THE PLASMA WITHIN CLUSTERS OF GALAXIES*

Luiz C. Jafelice†
Institute of Astronomy, University of Cambridge,
Madingley Road, Cambridge CB3 0HA, England

Amâncio C. S. Friaça
Instituto Astronômico e Geofísico da Universidade de São Paulo,
C.P. 9638, CEP 01065 - São Paulo, Brazil

Abstract: The process of magnetic reconnection (MR) can be responsible for the liberation of magnetic energy in the plasma of the medium within clusters of galaxies in a rate $\sim 10^{43}$ erg s^{-1} in the more central regions (i.e., $< 10^{23}$ cm) of clusters. Such a process can work as a mechanism of ionization and heating of the gas intracluster, and certain observations of filaments with optical emission lines can perhaps be explained if MR is considered as an exciting source, as suggested by some recent observational studies. In this work we use hydrodynamical time-dependent calculations: 1) To follow the evolution of cooling condensations until the phase of optical line emission; and 2) To study the effects of MR as a mechanism of excitation of filaments in cooling flows in clusters of galaxies. We treat the cases in which the magnetic field is: a) Null,; b) Present and passive (i.e., acting just as magnetic pressure); and c) Present and contributing energetically through the MR process. Our results clearly indicate that the agreement between theoretical and observational results concerning emission line intensities and line ratios is much better when the effect of MR is included. The approach proposed here has several implications related to important plasma physics processes of wide interest and which deserve further studies in those plasmas as, for example, processes of particle acceleration, generation of plasma wave modes, and transport.

1 Optical Filaments and Magnetic Reconnection (MR)

X-ray observations (in the range 1 – 10 kev) of clusters of galaxies show that in many cases the gas in the centre of the cluster presents a cooling time less than the age of the system. This leads to the formation of a pressure-driven mass flow (called "cooling flow") towards the centre of the cluster (e.g., /1/). Moreover, in some cooling flows optical filaments are observed around the central dominant galaxy associated with these flows. Such filaments are expected to be a phase of the evolution of thermal instabilities taking place within the cooling flow. The flux ratio of the emission lines allows us to divide the filaments into two classes, namely: Class I, when <[NII]/Hα>=2.0, and Class II when <[NII]/Hα>=0.9 /2/.

What are the mechanisms which ionize and heat the gas of the filament? Several models consider different kind of such mechanisms; it is beyond the scope of this work to discuss these mechanisms here. The present work belongs to a series where time dependent models are developed for these optical filaments. In previous works of the series the effects of shock

*To be presented in the 1992 International Conference on Plasma Physics, Innsbruck, Austria, 29 June-3 July.

†Supported by a grant from the Brazilian agency CNPq. Work partially done while on leave from the Faculdade de Ciências Matemáticas e Físicas da PUC-SP, São Paulo, Brazil. Presently at the Departamento de Física, Universidade Federal do Rio Grande do Norte (UFRN), 59072 Natal, RN, Brazil.

as well as those of photoionization (by soft X-rays produced within the cooling flow or by an OB stellar population formed within the filaments) have been included /3/. In the present work we consider the process of magnetic reconnection as a source of ionization and excitation of the gas of the filament.

The magnetic reconnection (MR) is a well known process of conversion of magnetic energy into other forms of energy (e.g., /4/). What characterizes the process of MR is the topological change it causes in the magnetic field. This aspect is very important in the treatment of transport processes in magnetized plasmas, particularly for collisionless plasmas as those observed in the intracluster medium of galaxies.

The possibility of MR as source of excitation for such filaments was generically suggested by Soker and Sarazin 1990 /5/. There have been some observations /6, 2/ which seem to support that suggestion. Here we treat the process of MR in those filaments in greater detail through a quantitative approach and the results are compared with observational ones.

2 Evolutive Models for the Optical Filaments

The evolution of the density perturbations which will give rise to the optical filaments is obtained by the resolution of the hydrodynamic equations of mass, momentum and energy conservation.

We assume here that: a) The perturbations are self-gravitating; b) The thermal conductivity is reduced by a factor of 10^{-4} in comparison with the classical (Spitzer) value, in order not to inhibit the growth of the thermal instabilities; c) The cooling function used is a non-equilibrium isochoric one, in order to take into account the fact that the recombination time of important ions is longer than the cooling time for temperatures below 10^6 K; d) The initial density (ρ) perturbations are of the form $\delta\rho/\rho = A \sin x/x$, where $x = 2\pi r/L$, with A standing for a characteristic amplitude and L a typical dimension (see below); e) The geometry is plane-parallel; and f) The perturbations are isobaric and non-linear ($A = 1$).

We analyse two regimes for the cooling flow, namely: **1.** For the outer regions: $r \simeq 20$ kpc; $\rho_0 = 5 \times 10^{-26}$ g cm^{-3}; and $T_0 = 2.5 \times 10^7$ K; and **2.** For the inner regions: $r \simeq 3$ kpc; $\rho_0 = 5 \times 10^{-25}$ g cm^{-3}; and $T_0 = 10^7$ K. These values were obtained from a time dependent modeling applied to the cooling flows of the clusters A496 and A1795 /7/.

We study six models, namely: **A.** For extended filaments far from the centre of the cooling flow: $L = 10$ kpc and regime 1; **B.** For inner filaments: $L = 1.5$ kpc and regime 2; **C.** Model B including magnetic pressure (i.e., including a passive participation of the magnetic field), where the initial value adopted for the plasma beta, β_{pl}, is 100, as suggested by radio and X-ray observations of the central regions in cooling flows (e.g., references in /5/); **D.** Model C with the parameter $\lambda \equiv l_{MR}/l_B = 1$. The parameters l_{MR} and l_B stand, respectively, for the length scale of the region where the MR takes place (i.e., the scale over which the magnetic field changes its direction) and the width of the region where the magnetic pressure becomes important (i.e., $\beta_{pl} \leq 1$); both length scales are usually $<< L$; **E.** Model D with $\lambda = 0.5$; **F.** Model D with $\lambda = 0.2$.

3 Discussion and Results

The properties of our models are presented in Table 1: t_{col} is the time for the collapse, i.e., the time interval between the beginning of the collapse until the moment in which the temperature reaches 10^5 K; t_{op} is the duration of the phase of emission of optical lines; and $L_{H\alpha,max}$ is the maximum luminosity in Hα. We consider t_{op} as the time interval between the

instant in which T is less than 10^5 K and that in which $L_{H\alpha}$ is reduced to $L_{H\alpha,max}/3$. The luminosities have been normalized to $\dot{M} = 100\,M_\odot\ \mathrm{yr}^{-1}$, where the rate of mass deposition through cooling, $\dot{M}$, is estimated from the ratio between the filament mass and its time of collapse (where one solar mass $M_\odot \simeq 2 \times 10^{33}$ g).

For model A, as soon as the temperature decreases below 3×10^4 K a shock is created. For $t = 10^4$ years the shock velocity is 122 km s^{-1}, and it is dissipated in $t = 9 \times 10^4$ years. A similar scenario takes place with model B, with the only difference that in this case the time scales involved are about 2.5 times longer than those in model A. This fact added to that the time for collapse in model B is much shorter than that of model A implies that model B spends a much greater fraction of its life in the phase of optical emission than model A.

As there is no ionization equilibrium for $T < 10^6$ K, the state of ionization of the gas is obtained by solving the ionization equations during each temporal step by using the program SUMA (see /8/). In model A the line of [OI], and possibly of [SII] are more intense than those observed, and $L_{H\alpha}$ is too faint (Table 2). On the other hand, model B presents values of $L_{H\alpha}$ which are adequate for Class I filaments. The line ratios, however, are still in disagreement with observations (Figure 1). Therefore, aparently the models including only shock are not consistent with observations.

It remains to be investigated if magnetic fields can offer a solution for such difficulties. We will restrict this investigation only to models from regime 2, because they are those presenting a higher optical luminosity. We consider then model C. As one can see from Table 1 and from Figure 1 the effect of the magnetic pressure is nearly negligible. The term including such an additional pressure just contributes to slow down the collapse and to reduce the intensity of the emission, although always by very small amounts. The line ratios also remain practically unchanged.

On the other hand, while the kinetic energy of the gas is lost through radiative cooling, which occurs almost completely out of the optical range, the magnetic field represents an energy reservoir which remains available for processing the optical emission. This can occur thanks to the MR.

In fact, as the gas compression evolves the magnetic energy density increases proportionally to ρ^2, while the gas is cooling radiatively. As a consequence, soon β_{pl} will become $<< 1$. In this regime there are a series of mechanisms of fast reconnection which proceed at a rate $\approx 0.1\, v_A/l_{MR}$ (/5/; where v_A is the Alfvén velocity in the considered region). As previously mentioned, here we consider that the MR takes place only in the region where $\beta_{pl} \leq 1$; such a region has its half-width given by l_B ($\sim l_{MR} << L$).

From models D to F we have an increasingly greater efficiency of the process of MR. Although these models are not much different from model B in what concerns the Hα luminosity and the time for collapse, the line ratios in these models become much nearer to observed ones. What happens is that in the case of models D, E and F the ratios [OI]/Hα and [NII]/Hα increase, in comparison with the model including only shock. This occurs because the Hα line is produced by recombination but the forbidden lines are produced by collisional excitation. When one has a heating source, it contributes more effectively to the rate of collisional excitation rather than to the ionization rate.

One of the main conclusions from this work, therefore, is that the MR can be an important mechanism of heating and ionization of optical filaments in cooling flows (see Figure 1).

The future development of this work involves to extend the parameter space studied, i.e., the regime of the cooling flow, the thickness of the perturbation, the value of β_{pl}, and the efficiency of the MR. Besides that, a further improvement of this work is concerned with the inclusion of other processes associated with the MR, as the production of suprathermal

particles and the interference in the transport processes in the plasma.

References

/1/ Fabian, A.C., Nulsen, P.E.J., and Canizares, C.R. 1991, *Astron. Astrophys. Rev.*, **2**, 191.

/2/ Heckman, T.M. et al. 1989, *Astrophys. J.*, **338**, 48.

/3/ Friaça, A.C.S. 1991, in *NATO/ASI - Clusters and Superclusters of Galaxies - Contributed Talks and Poster Papers*, edited by M.M. Colless et al. (IoA, Cambridge), p. 75.

/4/ Spicer, D.S. 1990, *Adv. Space Res.*, **10**, 943.

/5/ Soker, N. and Sarazin, C.L. 1990, *Astrophys. J.*, **348**, 73.

/6/ Johnstone, R.M. and Fabian, A.C. 1988, *MNRAS*, **233**, 581.

/7/ Friaça, A.C.S. 1992, *Astron. Astrophys.*, submitted.

/8/ Viegas-Aldrovandi, S.M. and Contini, M. 1989, *Astron. Astrophys.*, **215**, 253.

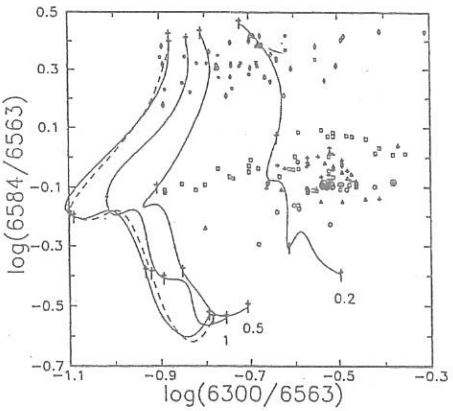

Figure 1: Evolution of [NII]/Hα versus [OI]/Hα for the models with L = 1.5 kpc. The daggers upon the curves indicate (beginning from the upper extreme) the instants of time t = 2.5, 7.5, 10, 25 and 40 × 10^4 years, respectively. The dashed curve refers to the model without magnetic pressure and the solid curves to the models with initial value of β_0 = 100. Models with magnetic reconnection are marked with the value of λ below, in the right extreme of the curves. Observational points (Heckman et al. 1989) of several filaments in cooling flows are represented as follows: A262, diamonds; Perseus, squares; PKS0745-191, plus signs; 3C218, plus signs surrounded by circles; Virgo, asterisks; A1795, triangles; A2052, crosses; A2597, circles. Notice the clear separation between Class I filaments (higher values of [NII]/Hα) and those of Class II.

Table 1: Properties of the models.

Model	t_{rad} (10^4 years)	t_{sp} (10^4 years)	$L_{Ne,max}$ (10^{37}erg/s)
A	144.5	2.06	5.4
B	1.606	4.04	15.7
C	1.607	4.04	15.3
D	1.609	4.03	15.5
E	1.609	4.03	15.9
F	1.611	4.03	16.9

Table 2: Model A: Line ratios in relation to Hα.

t (10^4 years)	L_{Ne} (10^{37}erg/s)	Hβ	[NII] 6583	[OI] 6300	[SII] 6716
0.4	0.43	0.373	5.43	<0.01	2.66
1.5	1.44	0.356	3.20	0.22	2.22
3	4.13	0.351	2.23	1.31	2.75
7	3.19	0.352	2.61	2.57	2.56
21	1.73	0.347	1.71	0.82	1.10

QUANTITATIVE ANALYSIS OF COSMIC NOISE COMMING FROM PLASMA JETS OF QUASAR

N.Tanizuka, N.Kawaguchi*, H.Mikoshiba*, M.Inoue*
Integrated Arts & Sciences, University of Osaka Prefecture
Gakuen-cho 1-1, Sakai, 593 Japan
*Nobeyama Radio Observatory, Nobeyama, Minamisaku,
Nagano, 384-13 Japan

1. INTRODUCTION

This is an article of taking cosmic plasmas of quasar by means of cosmic noise and a measure of information entropy. We take microwave noise from quasars of the band width: $0.01 \leqq f \leqq 100$ GHz (wave length: $3\text{mm} \leqq \lambda \leqq 30\text{m}$). A quasar emits strong microwave from its plasma jets by an interaction with magnetic flux. The microwave noise is a superposition of noise from multiple jets (microwave sources). Since a quasar is distributed at the edge of the universe and the farthest galaxy (and very active), we observe microwave noise from it by a parabolic antenna as if it is from a point source. Observations of microwave from a quasar by VLBI show complexity in structure of its microwave sources.

Let $x(t)$ be the intensity of microwave with t the time and $P(f)$ the power spectral density with f the frequency of microwave, respectively. In $x(t)$, information on the energy or something of the quasar's gravity or the jets, relating tc physical events is contained. The frequency f in the spectral density are very probable to have a concern with the energy, reflecting a structure of from where (or which level of the gravity) in the quasar the plasma jets spout out.

2. MEASURE OF STRUCTURE

An information entropy is defined as a measure of structure of plasma jets. It needs an object of event. Let $p(s)$ being the joint probability distribution of a time series $x(t): t=0,1,\cdots,m$ of an event, then the entropy for the time series is

$$H=-\int p(s)\log p(s)\,dv.$$

If $p(s)$ follows Gaussian distribution, the entropy rate

$h=\overline{\lim_{m\to\infty}}\frac{H}{m+1}$ is defined. Let f_k being Nyquist frequency, h is/1/

$$h=\frac{1}{4f_k}\int_{-f_k}^{+f_k}\log P(f)df+\frac{1}{2}\log 2f_k. \qquad (1)$$

Eq.(1) is a transformation of the spectral density P(f) into the entropy rate h. The author obtained h for a continuous spectral density function the n-th domain of which is $P_n\propto f^{-\alpha_n}$ with α_n being the spectral index $(f_{n-1}<f\leq f_n)$/2/. We take important terms in h for our problem and call them as Δh. It is

$$\Delta h=\sum_n(\alpha_{n+1}-\alpha_n)\log f_n. \qquad (2)$$

Eq.(2) is the entropy rate of noise event in a needed frequency band. The measure Δh is a summation of the product of the difference between adjacent indices and the logarithm of the frequency the index changes. If $\alpha_{n+1}>\alpha_n$, then the measure is positive and if $\alpha_n>\alpha_{n+1}$, the measure is negative (provided that log $f_n>0$). Usually an event is considered to create a structure for the negative entropy ($\Delta h<0$). Higher the frequency f_n and sharper an angle the adjacent lines make, the absolute value of Δh is larger. A radiospectral index reflects a physical process of event; a different index means a different physical or locational (because of gravitation energy) process. The frequency f_n corresponds to the energy of quasar (velocity and density of plasma jets, magnetic flux density). As a whole, the measure Δh intuitively fits a measure of complexity in structure of the microwave sources.

The microwave frequency f_n at a quasar is different from the observation frequency f_n' at an antenna by the red shift z of the quasar. By substituting $f_n=(1+z)f_n'$ into eq.(2), we have

$$\Delta h=1.66\sum_n\Delta\alpha\{\log_{10}f_n'+\log_{10}(1+z)\}\ \text{bit}. \qquad (3)$$
$$\Delta\alpha=\alpha_{n+1}-\alpha_n$$

We use the unit 'bit' (amount of information) for Δh the measure of structure.

3. MEASURE OF QUASAR PLASMA JETS

In many radio-observatories on the earth, they have observed microwave flux densities of quasars at their respective band widths according to the ability of antennas. Observation data were collected and dotted for the flux density and frequency, for example, shown in Fig.1. The lines in the figure were drawn by the author so as to fit on the dots, with slope index α. The dimensions of the flux density and the power spectral density are $Wm^{-2}Hz^{-1}$ and WHz^{-1}, respectively; however, it does not prevent for our discussion to apply eq.(3) to each diagram of Fig.1. We obtained the measure Δh for each plasma jets of eight quasars and two radio garaxies in the frquency band $0.01 \leqq f \leqq 100$GHz: for quasars, 3C273($z=0.16, \alpha=0.59, 0, f'=0.6$ GHz; $\Delta h=-8.7$bit), 3C48($z=0.37, \alpha=0, 0.78, f'=0.2$GHz; $\Delta h=11$bit), 3C279 ($z=0.54, \alpha=0.57, -0.16, 0.41, f'=0.6, 10$GHz; $\Delta h=-1.2$bit), 3C345 ($z=0.595, \alpha=0.40, -0.10, f'=1.3$GHz; $\Delta h=-7.7$bit), 3C216($z=0.67, \alpha=0.79$ $, 0.33, f'=3.5$GHz; $\Delta h=-7.4$bit), 3C380($z=0.692, \alpha=0.67$; $\Delta h=0$), 3C454.3 ($z=0.86, \alpha=0.77, -0.64, 0.27, f'=0.2, 0.5$GHz; $\Delta h=-6.5$bit) and 3C446 ($z=1.40, \alpha=0.63, -0.15, f'=2.5$GHz; $\Delta h=-12.7$bit); for radio garaxies, 3C274:M87($z=0.0043, \alpha=0.82$; $\Delta h=0$) and 3C84:Seyfert($z=0.017, \alpha=1.4$, $-0.37, 0, f'=0.5, 10$GHz; $\Delta h=-19.5$bit). In Fig.2 we show the measure Δh of the quasars and radio garaxies, with the abscissa being the red shift z in logarithmic scale. Their optical magnitudes are shown as well/3/. The Δh is a meaningful measure in a sense : 3C446(-12.7bit) is a very active body; 3C454.3(-6.5bit) is an active body; 3C380(0bit) is a little active body; a structure of 3C279(-1.2bit) has not yet been found; a pair of jets of 3C273(-8.7bit) have not been yet found but one jet/4/. Now we can not give Δh a systematic meaning as the measure of structure by only such few examples. It depends on our future research. The red shift z reflects each age of the galaxy and if we find a systematic distribution in the red shift z and the measure Δh, we will discover an observational cosgomony.

We are thankfull to Professor M. Morimoto for his comments and encouragement, to S.Kameno(under doctorate) and Dr.R. Kato for their advices, and to Professor H. Tabara for the data edited by him.

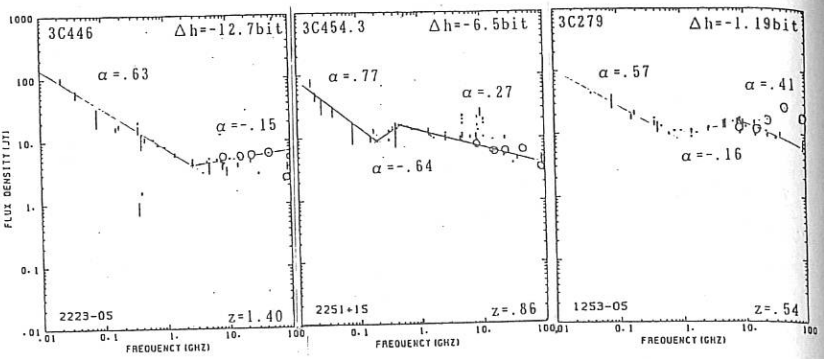

Fig.1 Collected data of flux density and frequency(by H.Tabara)

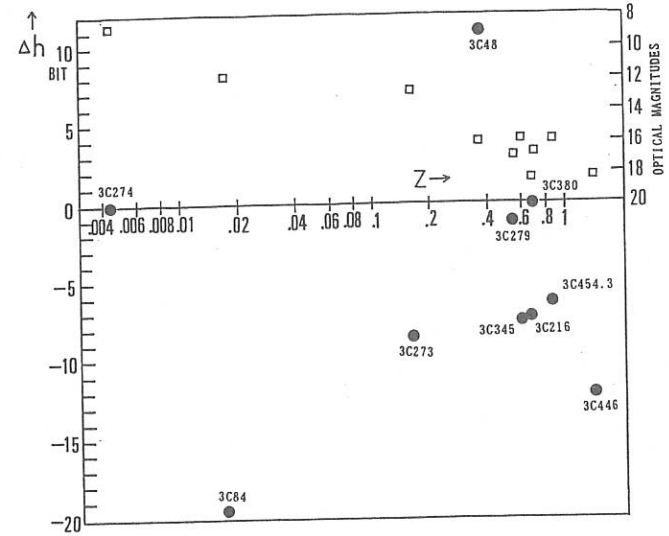

Fig.2 Distribution of the measure Δh and red shift z.

REFERENCES

/1/M.Hino, Spectral Analysis, p.83(Asakura,Tokyo,1986)

/2/N.Tanizuka, Proc.Int.Conf.on Noise in Physical Systems and 1/f Fluctuations, p.401(Ohmsha,Tokyo,1991)

/3/R.A.Preston,D.D.Morabito,J.G.Williams,J.Faulkner,D.L.Jauncey and G.D.Nicolson, Astron.J.90(9),1599(1985)

/4/T.Heckman,C.O'Dea,Nature 354,355(1991)

A Theory on the Evolution Process of the Fine Structure in Space

Yasunori Nejoh

Department of Physics, Hachinohe Institute of Technology, 88-1, Obiraki, Myo, Hachinohe, 031, Japan

I. Introduction

High speed and energetic streaming ions with the energies from 0.1MeV to 100MeV are frequently observed in solar atmosphere and interplanetary space. When we assume that the ion energy depends only on the kinetic energy, such plasma ions have to attain relativistic speeds. By considering relativistic effects where the ion velocity is about $0.1c$, we can describe the relativistic motion of such ions in the study of nonlinear interaction. In this situation, ion temperature and relativistic effects are important for energetic ion acoustic waves propagating in space. It has been suggested that relativistic double layers occur in space plasmas. However, little attention has been given to relativistic ion acoustic double layers. Interesting features such as the formation of the precursor of the ion acoustic waves and the long wavelength ion wave modes[1] are discussed as astrophysical phenomena. Although the relativistic ion acoustic solitary waves in space are described by the nonlinear evolution equation[2], the effect of the ion temperature is an indispensable factor[3]. It is recognized that, in the recent astrophysical observations, the fine structure is important[4] to understand the properties of spaceplasmas. Double layers and spiky solitary waves form the fine structure. We show a new point of view with respect to both waves. The object ofthis paper is to show the formation of relativistic double layers, spiky solitary waves and explosive modes in a plasma.

II. A mixed MK-dV equation

We consider small but finite amplitude ion acoustic waves propagating in a relativistic plasma. The plasma is quasineutral. It is assumed that the velocity distribution of each species is Maxwellian everywhere and the relativistic plasma is composed of a mixed fluid with hot and isothermal electrons and hot ion species. We assume that the ion flow velocity is relativistic. The basic equations are described by the fully relativistic ion fluid equations;

$$\frac{\partial}{\partial t}(\gamma n) + \frac{\partial}{\partial x}(\gamma n v) = 0 \quad , \tag{1.a}$$

$$\left(\frac{\partial}{\partial t} + v\frac{\partial}{\partial x} \right) \gamma v + \frac{\sigma}{n}\frac{\partial p}{\partial x} + \frac{\partial \phi}{\partial x} = 0 \quad , \tag{1.b}$$

$$\left(\frac{\partial}{\partial t} + v\frac{\partial}{\partial x} \right) p + 3\gamma^2 p \left(\frac{\partial}{\partial x} + \frac{1}{c^2} v \frac{\partial}{\partial t} \right) v = 0 \, , \tag{1.c}$$

where the Lorentz factor is $\gamma = [1-(v/c)^2]^{-1/2}$. The system of equations is closed with the help of the Poisson's equation

$$\frac{\partial^2 \phi}{\partial x^2} - n_e + n = 0 \quad , \tag{1.d}$$

with $$n_e = \exp(\phi) \quad . \tag{1.e}$$

We assume $1 > v/c$. The densities, the velocities, the pressure, the potential, the time and the distance are normalized. The parameter σ is the ratio of the positive ion temperature to the electron temperature. In order to solve eqs.(1.a)−(1.e), we expand the quantities n, v, p, ϕ and n_e as power series in terms of the small parameter ε :

$$n=1+\sum_{l=1}^{\infty} \varepsilon^l n_l, \quad v=v_0+\sum_{l=1}^{\infty} \varepsilon^l v_l, \quad p=1+\sum_{l=1}^{\infty} \varepsilon^l p_l, \quad \phi=0+\sum_{l=1}^{\infty} \varepsilon^l \phi_l, \tag{2}$$

We introduce the stretching coordinates $\xi = \varepsilon^{1/2}(x-st)$, $\tau = \varepsilon^{3/2}t$, where s refers to the phase velocity. We substitute (2), ξ and τ into (1.a)−(1.e). To the lowest order of ε, we represent n_1, v_1, p_1 by ϕ_1 and obtain the phase velocity. To the second order of ε, we have the K-dV equation. In order to take into account the higher-order nonlinearity, we use the modified coordinates $\xi = \varepsilon(x-st)$, $\tau = \varepsilon^3 t$, (3) Substitution (2) and (3) into (1.a)−(1.e) yields a mixed MK-dV equation

$$\frac{\partial \phi}{\partial \tau} + \alpha \phi \frac{\partial \phi}{\partial \xi} + \frac{1}{2} \beta \phi^2 \frac{\partial \phi}{\partial \xi} + \frac{1}{2} \frac{\partial^3 \phi}{\partial \xi^3} = 0 \, . \tag{4}$$

where α is positive and β is negative. Here $\phi = \phi_1$.

III. Stationary solutions of eq. (17)

We introduce a variable $\eta = \xi - u\tau$ in a stationary frame, where u is a constant velocity. Inserting η into (4), we obtain

$(d\phi/d\eta)^2 + \Psi = 0$ and $\Psi \equiv (\beta/6)\phi^4 + (2\alpha/3)\phi^3 - 2u\phi^2$, (5)

under the boundary conditions ϕ, $\partial^n \phi/\partial \eta^n \to 0$ at $|\eta| \to \infty$, when n=1,2.

III-A. We consider that Ψ has two double roots. In order to obtain solutions, we transform eq.(5) to $\Psi = (\beta/6)\phi^2(\phi-\phi_m)^2$, (6)

where $\phi_m = -2\alpha/\beta$, $u = -\alpha^2/3\beta$. Here, ϕ_m denotes the maximum potential. Integrating eq.(5) with eq.(6), we have a solution

$$\phi = \frac{1}{2}\phi_m \left\{ 1 - \tanh\left[\frac{1}{2} \left| \left(-\frac{\beta}{6} \right)^{1/2} \right| \phi_m (\eta - \eta_0) \right] \right\}, \tag{7}$$

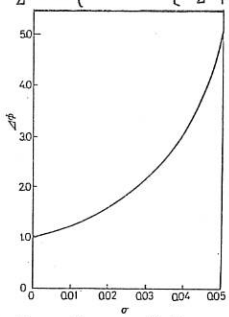

Fig.1 Dependency of the potential drop $\Delta\phi$ of the double layer on the ratio σ, for $v_0/c=0.2$.

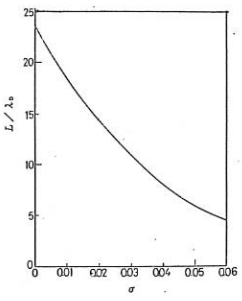

Fig.2 The double layer thickness as a function of the ratio σ, for $v_0/c=0.2$.

for $0<\phi<\phi_m$. We regard eq.(7) as a relativistic compressive double layer. The dependency of the potential drop $\Delta\phi$ on the ion temperature ratio σ is shown in Fig.1 and the double layer thickness L is shown in Fig.2. For the condition $\phi>\phi_m$ or $\phi<0$, we obtain an explosive mode.

III-B. We consider the case where Ψ has one double root. Then Ψ of eq. (5) requires $\Psi=(\beta/6)\phi^2(\phi-\phi_a)(\phi-\phi_b)$, (8) with $\phi_{a,b}=(2/\beta)\{-\alpha\pm(\alpha^2+3\beta u)^{1/2}\}$. Here when we put $u=-\alpha^2/4\beta>0$, ϕ_a and ϕ_b take a form of $\phi_a=-\alpha/\beta>0$, $\phi_b=-3\alpha/\beta>0$, provided that $\phi_a<\phi_b$. Equation (5) with eq.(8) has a solution

$$\phi(\alpha,\beta,\eta;\phi_m)=-\frac{3\alpha}{\beta}\frac{\operatorname{sech}^2\left[\mathscr{A}(\alpha,\beta;\phi_m)-\left|\alpha\left(\frac{-1}{2\beta}\right)^{1/2}\right|(\eta-\eta_0)\right]}{1+3^{1/2}\tanh\left[\mathscr{A}(\alpha,\beta;\phi_m)-\left|\alpha\left(\frac{-1}{2\beta}\right)^{1/2}\right|(\eta-\eta_0)\right]},\quad(9)$$

for $|\phi-\{\phi^2+(4\alpha/\beta)\phi+(12\alpha^2/\beta^2)\}^{1/2}|\leqq-2\cdot3^{1/2}\alpha/\beta$, and

$$\phi(\alpha,\beta,\eta;\phi_m)=\frac{3\alpha}{\beta}\frac{\operatorname{cosech}^2\left[\mathscr{B}(\alpha,\beta;\phi_m)+\left|\alpha\left(\frac{-1}{2\beta}\right)^{1/2}\right|(\eta-\eta_0)\right]}{1+3^{1/2}\coth\left[\mathscr{B}(\alpha,\beta;\phi_m)+\left|\alpha\left(\frac{-1}{2\beta}\right)^{1/2}\right|(\eta-\eta_0)\right]}.\quad(10)$$

for $|\phi-\{\phi^2+(4\alpha/\beta)\phi+(12\alpha^2/\beta^2)\}^{1/2}|>-2\cdot3^{1/2}\alpha/\beta$, where

$$\mathscr{A}(\alpha,\beta;\phi_m)=\operatorname{arctanh}\left\{\frac{\beta}{2\cdot3^{1/2}\alpha}\left[\phi_m-\left\{\phi_m^2+\frac{4\alpha}{\beta}\phi_m+\frac{12\alpha^2}{\beta^2}\right\}^{1/2}\right]\right\},$$

and

$$\mathscr{B}(\alpha,\beta;\phi_m)=\operatorname{arccoth}\left\{\frac{\beta}{2\cdot3^{1/2}\alpha}\left[\phi_m-\left\{\phi_m^2+\frac{4\alpha}{\beta}\phi_m+\frac{12\alpha^2}{\beta^2}\right\}^{1/2}\right]\right\},$$

respectively. Here ϕ_m denotes the peak amplitude of the potential. Equations (9) and (10) are a spiky solitary wave solution and an explosive solution, respectively. When $\phi_m=0.75$, we illustrate the spiky solitary wave in Fig.3. We show the dependency of the amplitude of the solitary wave on the ion temperature effect in Fig.4.

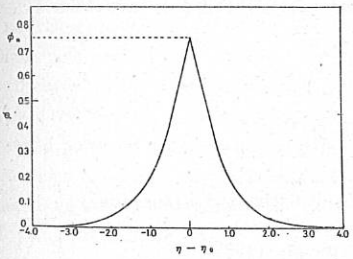

Fig.3 The profile of the relativistic spiky solitary wave, in the case where $v_0/c=0.2$ and $\sigma=0.03$.

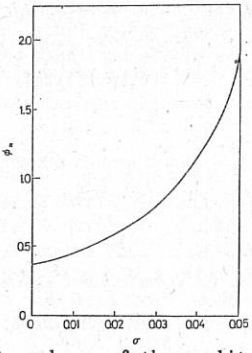

Fig.4 Dependency of the amplitude ϕ_m of the spiky solitary wave on the ratio σ, for $v_0/c=0.2$.

The dispersion relation in this system is obtained as

$$\omega = k \left\{ v_0 + \left[(\gamma_1 + 3\sigma\gamma_0)/\gamma_0\gamma_1 \right]^{1/2} - \frac{1}{2}\left[1 + v_0 \left(\frac{\gamma_0\gamma_1}{\gamma_1 + 3\sigma\gamma_0} \right)^{1/2} \right] \frac{3\sigma\gamma_0\gamma_3 + (2/3)\gamma_2}{\gamma_0\gamma_1} - \sigma\frac{\gamma_2}{\gamma_1} - \frac{1}{2}\left[\frac{\gamma_0\gamma_1(s - v_0) + (1/3)\gamma_2 + \sigma\gamma_0\gamma_2\left[1 + (v_0/c)^2\right]}{\gamma_1 - (2/3)\gamma_2 s} \right]^{-1} k^2 \right\}.$$

V. Discussion

The author has derived the mixed MK-dV equation and has shown the new nonlinear wave modes, that is, the relativistic double layer, the spiky solitary wave and the explosive solutions. We have shown the peculier feature that the amplitude of the double layer grows as the relativistic and the ion temperature effects increase, and its thickness narrows with both effects increasing. The potential drop of the double layer grows as the ion temperature increases. These are shown for the first time for the relativistic double layers. It is clarified that the amplitude of the spiky solitary wave grow as the ion temperature increases. Both the modes also exist complimentarily; if spiky solitary waves exist, explosive modes disappear and *vice versa*. This is proved by the boundary condition. As is seen in space and computer simulations, the solitary waves are not bell-shaped but spiky-shaped. The author think that the formation of the double layer is essentially associated with strong nonlinearity. Hence, the solitary waves which contribute to the generation and the disappearance between solitary waves and double layers need to be spiky-shaped and need to possess the same order of nonlinearity as the order of nonlinearity of the double layer. Recently, the existence of the streaming ion flux is worthy of notice as the condition of the formation of spiky solitary waves and double layers[4]. This is an idea associated with the thought that high speed streaming ions form solitary waves and double layers. The present investigation presents a point of view that not only spiky solitary waves and double layers but also explosive events are generated by the high speed streaming ions[5]. This investigation finds the peculiar feature concerning the evolution process of the nonlinear wave structure in which the relativistic double layer, the spiky solitary wave and the explosive modes form the fine structure in space.

References

1. Y. Nejoh, *J. Plasma Phys.* 37, 487 (1987).
2. Y. Nejoh, *J. Phys. A: Math. Gen.* 23, 1973 (1990).
3. Y. Nejoh, *IEEE Trans. Plasma Sci.* PS-20, (1992).
4. R. Boström, G. Gustafson, B. Holback, G. Holmgren and H. Koskinen, *Phys. Rev. Lett.* 61, 82 (1988).
5. Y. Nejoh, *Phys. Fluids* B: *Plasma Physics* 4, (1992).

THE EFFECTS OF SLIGHTLY OBLIQUE PROPAGATION ON NONLINEAR ALFVÉN WAVES

S.R. Spangler and B.B. Plapp
Department of Physics and Astronomy, University of Iowa
Iowa City, Iowa 52242 USA

The region of space adjacent to the Earth's bow shock, as well as other shock waves in the solar wind, is filled with large-amplitude magnetohydrodynamic (MHD) waves, here generically referred to as Alfvén waves. The theory presented in this paper is addressed toward an understanding of these waves. These waves show a number of properties which are generally supposed to be the result of nonlinear wave evolutions. These properties become more pronounced as one goes deeper into the "foreshock" (the term for the region upstream of the bow shock), corresponding to more advanced nonlinear development. The characteristics of interest are as follows. First, the initially sinusoidal waveforms become steepened. Second, there appears a shorter wavelength wavepacket near the front of the initial wavepacket. These short wavelength wavepackets are referred to as "shocklets," and presumably are generated from the initial wavepacket by nonlinear processes. Third, there is an evolution in the polarization of the Alfvén waves, from circular at shallow depths in the foreshock to elliptical/linear at greater depths, where nonlinear effects have become pronounced.

For some time we have been interested in interpreting these waves in terms of the Derivative Nonlinear Schrödinger Equation (DNLS), a nonlinear wave equation for Alfvén and Fast Magnetosonic waves /1/, /2/. For the simplest case of wave propagation parallel to the large-scale magnetic field (the case considered in the aforementioned papers), the equation may be written as follows.

$$\frac{\partial \phi}{\partial t} + \frac{1}{2}\left[\frac{1}{8\pi\rho_0 V_A(1-\beta)}\right]\frac{\partial}{\partial x}\left\{\phi(|\phi|^2 - \phi_0^2)\right\} \mp i\frac{V_A^2}{2\Omega_i}\frac{\partial^2\phi}{\partial x^2} = 0 \qquad (1)$$

Equation (1) describes one-dimensional waves propagating in the x direction. The wave field is $\phi \equiv b_y + ib_z$, where b_y and b_z are the components of the wave field in directions perpendicular to the mean field. The plasma through which the wave propagates is characterized by the plasma density ρ_0, Alfvén speed V_A, ion-cyclotron frequency Ω_i, and plasma β. In equation (2) the second term describes wave nonlinearity, and the third term describes dispersion due to right- or left-hand polarized waves.

As discussed in /1/ and /2/, equation (1) yields solutions which reproduce some of the properties of the observed upstream waves. For the case of left-hand polarized waves and $\beta < 1$, or right-hand polarized waves with $\beta > 1$, an amplitude-modulated wavepacket will steepen and produce an associated wavepacket with a much smaller wavelength. These requirements regarding β and the sense of polarization are the same as for the occurrence of a modulational instability of a plane MHD wave.

The aforementioned conditions for the occurrence of wavepacket steepening, as well as equation (1) from which they are derived, are based on fluid theory which will be a poor description of the plasma when $\beta \simeq 1$. A treatment based on kinetic theory /3/ has shown that substantial changes will occur in the structure of (1) in that the coefficient in the nonlinear term is not such a strong function of β, and that an additional term is introduced in the equation. It has been pointed out /4/ that this has serious ramifications for interpreting the nonlinear evolution of foreshock waves in terms of (1), since right-hand polarized waves will not readily undergo steepening. The observed waves are predominantly right-hand polarized.

We are presently considering the possibility that other physical processes, not included in (1) for the simple case of parallel propagation, actually cause the observed properties summarized at the beginning of the paper.

This paper is concerned with the effect of slightly oblique wave propagation. The waves are observed to be propagating at slight angles with respect to the large-scale magnetic field. Propagation angles of $5° - 15°$ are typical. A nonlinear wave equation can be simply derived in the case $|b_{y,z}| \simeq B_0 \sin\Theta \equiv B_{Y0} \ll B_0$, where B_0 is the large-scale field and Θ is the angle of propagation with respect to the field /5/. A rigorous but more complex derivation is also available in the literature /6/.

The novel features introduced by oblique propagation may be illustrated by the equation for the y component of the magnetic field /5/.

$$\frac{\partial b_y}{\partial t} + \frac{1}{2}\left[\frac{1}{8\pi\rho_0 V_A(1-\beta)}\right]\frac{\partial}{\partial x}\left\{b_y\left(b_y^2 + b_z^2\right)\right\} + \underline{\frac{B_{0y}}{4\pi\rho_0 V_A(1-\beta)}\, b_y \frac{\partial b_y}{\partial x}}$$

$$+ \underline{\frac{B_{0y}}{8\pi\rho_0 V_A(1-\beta)}\left[b_y\frac{\partial b_y}{\partial x} + b_z\frac{\partial b_z}{\partial x}\right]} + \frac{B_{0y}^2}{8\pi\rho_0 V_A(1-\beta)}\frac{\partial b_y}{\partial x} = 0 \qquad (2)$$

In equation (2) we have not written terms describing the effect of dispersion on the equation of motion for b_y. The convention employed in equation (2) is that b_y is the component of the wave field which lies in the plane determined by the large-scale magnetic field $\vec{B}_0$ and the direction of wave propagation ($\hat{x}$).

There are two important features about equation (2). First, the underlined terms represent *Korteweg-deVries like* nonlinearities which vanish in the limit of parallel propagation ($B_{Y0} \to 0$). In view of the well-known proclivity of the Korteweg-deVries equation for wave steepening, this result immediately suggests that a slight degree of oblique propagation might be important for the steepening of nonlinear MHD waves. The second important fact is that the equation for b_z (the component of the wave field perpendicular to the plane containing $\vec{B}_0$ and $\hat{x}$) differs from (2) in that it does not contain Korteweg-deVries like nonlinearities. *Since the differential equations for b_y and b_z differ in the case of oblique propagation, polarization evolution is an inevitable consequence of nonlinear evolution.*

While equation (2) appears to be much more complicated than the DNLS, it has been shown in /3/, /6/ that obliquely propagating nonlinear waves also obey the DNLS, provided that the field is redefined as

$$\phi = b_y + ib_z + B_{Y0} \tag{3}$$

in other words, the real part of the field now has a constant part. The results presented in this paper concern analytic and numerical solutions to (1), given (3) as a field variable.

We have explored stationary solutions to (1), i.e., solutions of the form $\phi(x,t) = \Phi(x - V_E t)$. Such solutions were considered at length in /7/; but our work has consisted mainly of a detailed inspection of the solutions. We solve the equation using the pseudopotential method /5/.

For extremely small angles of obliquity, simple analytic expressions for the wave field are possible. An example of our results is shown in Fig. 1. The left panel represents b_y as a function of the comoving coordinate $\xi = x - V_E t$, and the right panel b_z. The dashed line shows a circularly polarized wave (a stationary solution in the case of parallel propagation) but with a constant term added to y component. Such a wave train might be considered a zeroth-order model for an obliquely propagating Alfvén wave. The solid line displays a true stationary solution for the case of very small obliquity. A comparison of the two waveforms yields two conclusions of immediate interest. First, the noncircular polarization is obvious. The stationary waveforms in b_y and b_z differ. It will be noticed that the stationary solution for b_y is more rounded near maximum than the circularly polarized wave. The solution for b_z shows a continual decrease at the position where the circularly polarized wave is at maximum. Second, the waveform in b_z shows a more rapid increase to maximum than the circularly polarized wave, a tendency which may be considered incipient steepening of the wavepacket.

In the case of more pronounced oblique propagation, analytic solutions for the stationary waves exist, but they are not of such simple functional form as those shown in Fig. 1. However, the properties noted in Fig. 1 persist and become more pronounced /5/.

We do not expect waves in real space plasmas to be formed as stationary wave trains, so the question arises as to the relation between these stationary solutions and more arbitrary, obliquely propagating wavepackets. To explore this, we have carried out numerical solutions to the DNLS, using circularly polarized, oblique wavepackets of the sort shown in Fig. 1 as initial conditions. We expect that if the initial wave train does not differ significantly from a stationary solution wave, subsequent evolution will be relatively minor, whereas if the initial wave train differs markedly from any stationary solution, substantial evolution will occur. Criteria for assessing similarity of an initial condition to a stationary wave train are presented in /5/.

An example of a case in which substantial evolution occurred is shown in Fig. 2. The four rows show the wave intensity, components of the wave field, and spatial power spectrum at $t = 0$ (initial condition, top row) and three subsequent times. The calculation shows strong evolution of the initial wave train, as expected from the remarks above. The evolved wave train shows some of the properties of the stationary solutions, as may be seen by comparing the b_y

and b_z waveforms at $t = 40$ and 80 in Fig. 2 with those in Fig. 1. This may be interpreted as a tendency of the initial wave train to evolve towards a stationary solution wave train.

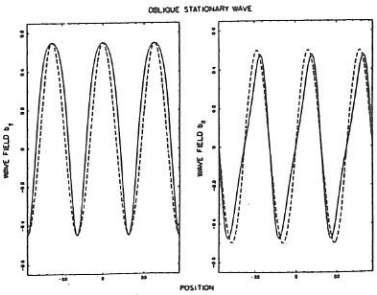

Fig. 1: Comparison of waveforms for circularly polarized wave and stationary, oblique solution to DNLS

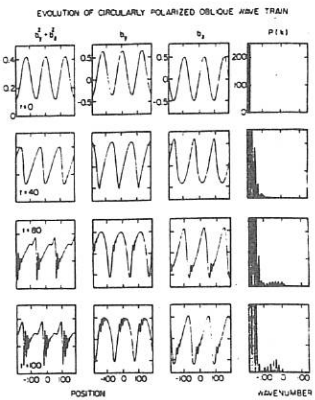

Fig. 2: Example of strong evolution of an initial wave train. Shown are the wave intensity, both field components, and the spatial power spectrum at dimensionless times of 0, 40, 80, and 100

The most striking feature of the calculation in Fig. 2 is the development of short wavelength wavepackets late in the evolution. This development is most clearly illustrated in the plots of $b_y^2 + b_z^2$ at $t = 80$ and 100. These wavepackets closely resemble the shocklets observed in spacecraft data.

We conclude that oblique propagation of nonlinear Alfvén and Fast Magnetosonic waves is an important effect which can account for several observed characteristics of MHD waves in space plasmas.

/1/ S.R. Spangler, Astrophys. J. **299**, 122 (1985)
/2/ S.R. Spangler, Phys. Fluids **29**, 2535 (1986)
/3/ E. Mjølhus, J. Wyller, J. Plasma Phys. **40**, 299 (1988)
/4/ S.R. Spangler, Phys. Fluids B **2**, 407 (1990)
/5/ S.R. Spangler, B.B. Plapp, Phys. Fluids B (submitted) (1992)
/6/ C.F. Kennel, B. Buti, T. Hada, R. Pellat, Phys. Fluids **31**, 1949 (1988)
/7/ T. Hada, C.F. Kennel, B. Buti, J. Geophys. Res. **94**, 65 (1989)

MATHEMATICAL THEORIES OF RESONANT ABSORPTION OF ALFVÉN WAVES IN SPACE PLASMAS: TIME DEPENDENT SOLUTION

C. Uberoi
Department of Mathematics, Indian Institute of Science
Bangalore - 560 012, INDIA

The Alfvén wave equation governing the dynamics of an ideal MHD system in the presence of inhomogeneous magnetic fields has been extensively studied both by normal mode analysis and as an initial value problem. The time-dependent solutions, however, have been either found asymptotically or for very specific initial conditions. Recently, Uberoi and Sedlaček /1/ have given an integro-differential formulation for this equation and constructed a time-dependent solution for very general smooth initial conditions. The aim of this note is to discuss this solution, firstly, to understand the phase mixing as current sheets crossover phenomena and secondly, with relevance to earlier studies especially those which were made to understand some of the magnetospheric phenomena.

Considering an incompressible medium with density ρ and the magnetic field $\mathbf{B}_o(x) = [o, B_{o1}(x), B_{o2}(x)]$ the linearized ideal MHD equations give the Alfvén wave equation:

$$\nabla \cdot \{\rho_o [\frac{\partial^2}{\partial t^2} - \frac{(\mathbf{B}_o \cdot \mathbf{k})^2}{4\pi\rho_o}] \nabla U_{xk} \} = 0 \qquad (1)$$

where $U_{xk}(x,\mathbf{k},t)$ is the Fourier transform in y and z of the perturbed velocity component $v_x(x,y,z,t)$. The wave number $\mathbf{k}=(o,k_y,k_z)$. The integro-differential formulation of eqn.(1) as given in /1/ is:

$$(\frac{\partial^2}{\partial x^2} - k^2) (\frac{\partial^2}{\partial t^2} + \omega_A^2(x)) e_k(x,t) = \frac{\partial \omega_A^2(x)}{\partial x} \int_{-\infty}^{x} e_k(s,t)\, ds \qquad (2)$$

/1/ C. Uberoi, Z. Sedlacek, Phys. Fluids B. Feb., (1992).

Eqn.(2) is to be solved with boundary conditions and initial conditions: $e_k(x,t) \to o$ as $|x| \to \infty$ and $e_k(x,o) = \phi(x,k)$ and $\dot{e}_k(x,o) = \psi(x,k)$ where $|\phi(x,k)|$ and $|\psi(x,k) \to o$ as $|x| \to \infty$. Here $e_k(x,t) = \partial \xi_{xk}/\partial x$ where $v_x = (\partial \xi_x/\partial t)$ and $\omega_A^2(x) = (\mathbf{B}_o(x).\mathbf{k})^2/4\pi\rho_o$.

The left side of eqn.(2) shows the coupling of surface waves to the local Alfvén oscillations arising due to the inhomogeneous Alfvén frequency $\omega_A(x)$ as seen on the right hand side of the eqn. The solution of (2) is

$$e_k(x,t) = \frac{\partial \xi_x}{\partial x} = \phi(x,k) \cos t\omega_A(x) + \psi(x,k) \frac{\sin t\, \omega_A(x)}{\omega_A(x)} + \int_o^t \frac{\sin(t-\tau)}{\omega_A(x)} K(x,\tau,k)\, d\tau, \qquad (3)$$

where $K(x,\tau,k) = Z(1+T^{-1}Z+T^{-1}ZT^{-1}Z+\ldots)\, e_{ko}(x,\tau)$. $e_{ko}(x,t)$ is the first two terms of the solution in (3). Z is an integral operator with kernel $Q(s,t)$ /1/.T is the operator $[\partial^2/\partial t^2+\omega_A^2(x)]$.

Considering $\phi(x,k) = Ae^{-kx}$ and $\psi(x,k) = Be^{-kx}$ we get dominant asymptotic terms for ξ_x by integrating (3) and taking the limit $t \to \infty$. For $\omega_A(x)$ as a linear function of x:

$$\xi_x = Ae^{-kx} \frac{\sin \omega_A(x)t}{t} + Be^{-kx} \frac{\cos \omega_A(x)t}{t} + O(\frac{1}{t^2}).$$

This value corresponds to the asymptotic solution obtained by Barston /2/. Also we note that $\xi_z \propto \partial \xi_x/\partial x$ does not show decay with time whereas ξ_x decays as 1/t. Hence, eventually for large t the wave becomes a longitudinal wave. This result was arrived at by numerical simulation of the Alfvén wave equation /3/.

/2/ E.M. Barston, Ann. Phys. 29, 282 (1964).

/3/ R.S. Steinoltson, Phys. Fluids, 27, 781 (1984).

To understand the phase-mixing we take $\mathbf{B}_o(x).\mathbf{k}=B_o(x)k_z$, calculation of the current density **J** shows that

$$4\pi J_y = \frac{(4\pi\rho_o)^{1/2}}{k_z}\,\omega_A(x)t\,\omega'_A(x)\{-\psi(x,k)\sin\omega_A(x)t + \frac{\phi(x,k)\cos\omega_A(x)t}{\omega_A(x)}\}$$

+ terms showing no increase with t. (4)

From (4) we see that J_y has terms which show that the amplitude increases linearly with time. This is the manifestation of the cross-over phenomena of current sheets. Each current sheet oscillates with its local Alfvén frequency $\omega_A(x)$ but after time $t > \tau$ the current sheets begin to cross-over and get phase mixed. The phase mixing time $\tau \equiv k/(d\omega_A/dx)$ as obtained from eqn.(4) is same as calculated by initial value problem /4/. The eqn.(4) shows that J_y increases at every point in space and not just near the neutral sheet /5/. The implication of this result on the surface wave induced magnetic reconnection is discussed by Uberoi /6/.

Now we consider an initial perturbation of the type $\phi(x,k) = Ae^{-kx}e^{i(k_x x+k_y y+k_z z)}$ with $u_o = k_x/k_y$ as an inclination of the surface 'wavelet'. For simplicity $\psi(x,k) = 0$. Taking a linear function for the magnetic field, $\omega_A(x)=(v_A k_z+v_A k_y x/a)$. Integrating (3) and taking $A = (k_x^2+k_y^2)^{1/2}$, we have

$$\xi_x = \left[\frac{1+u_o^2}{1+(u_o-v_A t/a)^2}\right]^{1/2} \exp i[k_y y+k_z(z-v_A t)+ik_y x(u_o-v_A t/a)] \qquad (5)$$

+ other terms.

/4/ L. Chen and A. Hasegawa, J. Geophys. Res. 79, 1033 (1974).

/5/ T.S. Hahm and R.M. Kulsrud, Phys. Fluids 28, 2418 (1985).

/6/ C. Uberoi, Proc. Basic Plasma Processes in the Sun, 9AU (1990) Eds. E.R. Priest and V. Krishan, Netherlands.

The first part of eqn.(5) gives the amplification of the amplitude for $t < au_o/v_A$, the other terms do not add to the amplification. This transient amplification was first noted by Lau /7/ by solving the eqn.(1) approximately and using numerical analysis technique. The application of this to understand the excitation of resonant Alfvén waves by sudden impulse in magnetoplasma was discussed by Uberoi /8/. The solution (3), however, points that such a transient amplification can be experienced by a general class of perturbations which are like a surface 'wavelet' when released on to the shear hydromagnetic flow.

In order to explain certain observations of magnetic pulsations a time-dependent solution of eqn.(1) was discussed in the presence of a wide-band source /9/. The solution given by eqn.(2) in this paper can be shown to correspond to the solution in /9/, thus suggesting that the presence of an external wide band source is not necessary for driving the local field line oscillations in the magnetosphere but as discussed in our earlier paper /10/ with the approximate solution of the Alfvén wave equation, any surface perturbation caused by K-H instability, for example, can be responsible for driving these oscillations.

/7/ Y.Y. Lau, Phys. Rev. Lett., 42, 779 (1979)

/8/ C. Uberoi, J. Geophys. Res. 93, 7595 (1988)

/9/ A. Hasegawa, H.T. King and A.S. Assis, Geophys. Res. Lett. 10, 765 (1983)

/10/ C. Uberoi, J. Geophys. Res. 93, 295 (1988).

RUNAWAY ELECTRONS IN THE PRESENCE OF KINETIC ALFVÉN WAVES

A. S. de Assis and C. Leubner*
Institute for Theoretical Physics
University of Innsbruck, A–6020 Innsbruck, Austria
**Permanent address: Instituto de Matemática, Universidade Federal Fluminense, 24020 Niterói, RJ, Brazil*

ABSTRACT

It is shown by the quasilinear Fokker – Planck approach that the shear kinetic Alfvén wave (KAW) cannot by itself produce runaway electrons, although it carries an electric field aligned with the ambient magnetic field. However, it can enhance the runaway production rate if it propagates in the presence of a background DC electric field.

1 – INTRODUCTION

It is well known that when an uniform electric field is acting on an uniform plasma, a certain fraction of the electrons will run away, that is, they will gain an energy such that the electric force acting on them exceeds the collisional drag force (Kulsrud et. al. 1973 and references therein).

In this work we consider the runway production by a DC electric field when the KWA is present. This is a relevant and open problem in space plasma physics, mainly in solar, magnetospheric and extragalactic plasmas, where there is observational evidence of energetic particles (electrons/ions) being generated when the KWA or/and a DC electric field is/are present in that plasmas (Jafelice and Opher 1990; Hasegawa 1987; Borovsky 1986; Otani and Silberstein 1991; Melrose 1980). Also, there are still questions on how the KAW affects the runaway production rate and the nonthermal emission (Hollweg 1981).

The KWA was introduced by Hasegawa and Chen 1975 in the context of plasma heating: it is the shear Alfvén wave with a finite perpendicular wavelength, and its name was chosen because of its kinetic properties. Along the direction of the background magnetic field its scale length is that of MHD waves, whereas in the direction perpendicular to the background magnetic field, its scale length is that of the ion Larmor radius. It can be excited by an MHD surface wave through linear resonant mode conversion, or by a drift wave instability (Hasegawa and Mima 1978). The kinetic nature makes it possible that the KWA can be damped via Cherenkov interaction (CHD), that is the Landau damping (LD) and Transit Time Magnetic Pumping (TTMP). Here, only Landau damping will be considered since the KWA has no TTMP due to its vanishing parallel wave magnetic field. The Landau damping of the KWA can affect the runaway production rate via the wave particle interaction (de Assis and Tsui 1991).

To determine this runaway production rate, which is the main goal here, it is necessary to use the Fokker–Planck quasilinear approach.

2 – FOKKER – PLANCK QUASILINEAR EQUATIONS

For simplicity, we consider a homogeneous, uniformly magnetized, singly ionized plasma situated in a constant uniform background DC electric field. Also, as a first approach, we restrict ourselves to the one–dimensional case. Therefore, we can write:

$$\frac{\partial F}{\partial t} = \left.\frac{\partial F}{\partial t}\right|_{KAW} + \left.\frac{\partial F}{\partial t}\right|_{col} + \left.\frac{\partial F}{\partial t}\right|_{\vec{E}-field} + S \qquad (1)$$

and,

$$\frac{\partial U_{\vec{k}}}{\partial t} = 2[\mathrm{Im}\omega_{\vec{k}}^{KAW} - \nu_{col}/2]U_{\vec{k}} + (\vec{\nabla}\cdot\vec{P})_{\vec{k}}. \tag{2}$$

The quasilinear operator can be written as (Tsui and de Assis 1989),

$$\left.\frac{\partial F}{\partial t}\right|_{KAW} = \frac{d}{dv_{\parallel}} D(v_{\parallel}) \frac{dF}{dv_{\parallel}} \tag{3}$$

with

$$D(v_{\parallel}) = \pi(e/m_e)\int |E_{\parallel\vec{k}}|^2 \delta(\omega_{\vec{k}} - k_{\parallel}v_{\parallel}) d^3k. \tag{4}$$

The collision operator is

$$\left.\frac{\partial F}{\partial t}\right|_{col} = \frac{d}{dv_{\parallel}} \nu(v_{\parallel})[v_{\parallel}F(v_{\parallel}) + v_{th}^2 \frac{dF}{dv_{\parallel}}], \tag{5}$$

where

$$\nu(v_{\parallel}) = \begin{cases} \nu_{ee} + 3\nu_{ei}/4, & v_{\parallel} << v_{th} \\ \\ \nu_0(2 + Z)/v_{\parallel}^3, & v_{\parallel} >> v_{th} \end{cases} \tag{6}$$

with $\nu_0 = \nu_{ei}v_{th}^3$. $\nu_{e\alpha}$ is the rate at which the electrons collide with particles of species α, (α = e,i): $\nu_{e\alpha} = 4\sqrt{2}\ln\lambda(ee_{\alpha})^2 n_{\alpha}/(3\sqrt{m_e}T_e^{3/2})$; $\ln\lambda$ is the Coulomb logarithm and Z is the ion charge state [Trubinikov 1965]. This collision operator is appropriate to describe collisions between particles with velocities much smaller than the electron thermal velocity (first case), and much larger than the thermal velocity (second case). This term is linear and models the situation where the dissipated energy goes into a thermal reservoir [Kulsrud et al. 1973]. It is suitable to model the relaxation of the perturbed distribution function towards a Maxwellian.

The DC electric field term is

$$\left.\frac{\partial F}{\partial t}\right|_{\vec{E}-field} = E\frac{dE}{dv_{\parallel}}. \tag{7}$$

Finally, S is the necessary particle source term, since a stationary distribution function involving a loss of particles at $+\infty$ implies an equivalent source at $v_{\parallel} = 0$, and $\vec{P}$ is the Poynting vector. Assuming the steady – state situation $\partial F/\partial t = 0$, Eq. (1) can be rewritten as

$$\frac{d}{dv_{\parallel}}\left[\nu(v_{\parallel})[v_{\parallel}F(v_{\parallel}) + v_{th}^2\frac{dF}{dv_{\parallel}}]\right] + \frac{d}{dv_{\parallel}}\left[D(v_{\parallel})\frac{dF}{dv_{\parallel}}\right] + \frac{eEdF}{m_e dv_{\parallel}} + A\delta(v_{\parallel}) = 0. \tag{8}$$

On introducing the Heaviside function in the source term of (8), all terms are total derivatives with respect to $v_{\parallel}$, and can immediately be integrated to yield,

$$\frac{dF}{dv_{\parallel}}\left[\nu(v_{\parallel})v^2_{th} + D(v_{\parallel})\right] + F(v_{\parallel})\left[\nu(v_{\parallel})v_{\parallel} + \frac{eE}{m_e}\right] = C - AH(v_{\parallel}), \tag{9}$$

where a convenient regrouping has been carried out.

In order to determine the constant of integration C, we consider the limit $v_{\parallel} \to \infty$, where $H(v_{\parallel})$ is equal to unity, and $\frac{dF}{dv_{\parallel}}$ as well as $\nu(v_{\parallel})$ are equal to zero. Hence, (9) becomes

$$F(\infty)\frac{eE}{m_e} = C - A \tag{10}$$

The first term is the flux of the runaway electrons, which in the steady–state must be equal to the source term constant A. Therefore, consistency requires that the integration constant C is taken to be equal to zero. As a consequence, the general solution of Eq. (9) is

$$F(v_{\parallel}) = F(0)\exp\left[-\int_0^{v_{\parallel}} \frac{\nu(u)\,u + eE/m_e}{\nu(u)\,v^2_{th} + D(u)}\,du\right]$$

$$-A\int_0^{v_{\parallel}} \frac{\exp\left[-\int_w^{v_{\parallel}} \frac{\nu(w)w + eE/m_e}{\nu(w)v^2_{th} + D(w)}dw\right]}{\nu(u)v_{th}^2 + D(u)}du. \tag{11}$$

Note that the result (11) remains valid if $\nu(v_{\parallel})$ and $D(v_{\parallel})$ are taken to be generalized functions,

$$\nu(v_{\parallel}) = \nu_{ei}\left[H(v_{th} - v_{\parallel}) + \frac{v_{th}^3}{v_{\parallel}^3}H(v_{\parallel} - v_{th})\right], \tag{12}$$

$$D(v_{\parallel}) = D_0\left[H(v_{\parallel} - v_{\parallel_1}) - H(v_{\parallel} - v_{\parallel_2})\right]. \tag{13}$$

In order to gain information about the runaway production rate A, we let $v_{\parallel} \to \infty$, with the result

$$A = F(0)\,\frac{\exp\left[-\int_0^{\infty} \frac{\nu(u)u + eE/m_e}{\nu(u)v^2_{th} + D(u)}du\right]}{\int_0^{\infty} \frac{\exp\left[-\int_u^{\infty} \frac{\nu(w)w + eE/m_e}{\nu(w)v^2_{th} + D(w)}\right]}{\nu(u)v_{th}^2 + D(u)}du - \frac{m}{eE}}, \tag{14}$$

where use has been made of Eq. (14) (with C = 0) in order to eliminate $F(\infty)$ in favor of A.

In Figure 1, we plot Eq. (14) for low phase velocity, taking $v_{1_{\parallel}}$ and $v_{2_{\parallel}}$. We see that the KAW cannot by itself generate runaway electrons, but can only enhance the production rate. Also, this enhancement is not so strong as in the case of lower hybrid waves (An et al. 1982), the discrepancy stemming from different velocity dependence of the diffusion coefficient of these two modes. The high phase velocity case was also investigated, but is not shown here for it does not show any new features over the low phase velocity one.

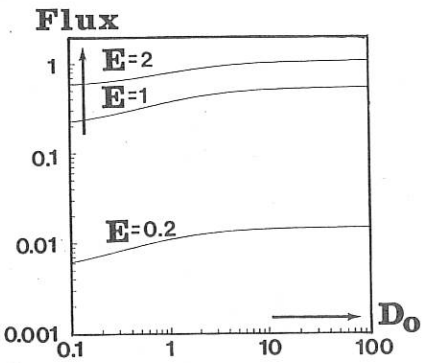

FIGURE 1: Normalized runaway flux $A/n\nu$ versus normalized diffusion coefficient $D_0 = D^{KAW}/\nu v_{the}^2$ for three different electric fields E in units of the critical field E_c.

REFERENCES

An Z. G., Liu C. S., Lee Y. C., and Boyd D. A., Phys. Fluids **25**, 997 (1982).
Borovsky J. E., Ap. J. **306**, 451 (1986).
de Assis A. S. and Tsui, K. H., Ap. J., **366**, 324 (1991).
Hasegawa A., JGR, **92/A10**, 11221 (1987).
Hasegawa A., and Chen, L., Phys. Rev. Lett. **35**, 370 (1975).
Hasegawa A., and Mima K., JGR **83/A3**, 1117 (1978).
Hollweg J. V., Solar Active Regions: A Monograph from Skylab Solar Workshop III, p. 303, Sec. 10.5.3, ed. F. Q. Orral, (Colorado Assoc. Univ. Press 1981; D. Reidel).
Jafelice L. C., and Opher R., VI Latin American Regional Meeting of the Int. Astron. Union "Kinetic Alfvén waves and the Thermal Population in Extragalactic Jets", Gramado, RS, Brazil, 16–20 October 1989.
Kulsrud R. M., Sun Yung–Chiun, Winsor N. K., and Fallon H. A., Phys. Rev. Lett. **31**, 690 (1973).
Melrose D.B., *Plasma Astrophysics*, Vol. 2, Gordon and Breach (New York 1980).
Otani N.F., and Silberstein M., AGU 1991 Fall Meeting, San Francisco CA, Paper SA42A – 4
Trubinikov B.A., *Reviews of Plasma Physics*, Vol. 1, ed. M.A. Leontovich, Consultants Bureau (New York 1965).
Tsui K.H., and de Assis A.S., Phys. Fluids B1, 823 (1989).

Acknowledgment: A.S.A. would like to thank the Brazilian agency CNPq for research support.

POLARIZATION CHANGES THROUGH STIMULATED RAMAN SCATTERING

V. Krishan and R.T. Gangadhara
Indian Institute of Astrophysics, Bangalore 560 034, India

Change of polarization of electromagnetic radiation due to its propagation in a magnetized plasma (Faraday rotation) and due to electron scattering is well known. In this paper, the change in the polarization due to the coherent scattering of the electromagnetic wave off the electron plasma wave (stimulated Raman scattering (SRS)) is investigated /1/, /2/. It is found that some of the observed polarization properties of the pulsar and quasar radio radiation, not accountable by Faraday rotation and electron scattering, can be explained by the SRS.

Consider a large amplitude elliptically polarized electromagnetic wave

$$\vec{E}_o = \varepsilon_{1o}[cos(k_o z - \omega_o t)\hat{x} + \alpha_o cos(k_o z - \omega_o t + \delta_o)\hat{y}], \tag{1}$$

where $\alpha_o = \varepsilon_{2o}/\varepsilon_{1o}$, which can be thought of as the superposition of two linearly polarized waves, $\vec{E}_1 = \varepsilon_{1o}cos(k_o z - \omega_o t)\hat{x}$ and $\vec{E}_2 = \varepsilon_{2o}cos(k_o z - \omega_o t + \delta_o)\hat{y}$, propagating in a plasma of density n_o and temperature T. Let $\vec{E}_1$ induces density perturbation $\delta n_{1e} = \delta n_1 cos(kz - \omega t)$ and $\vec{E}_2$ induces $\delta n_{2e} = \delta n_2 cos(kz - \omega t + \delta_e)$.

The scattered wave

$$\vec{E}_s = \varepsilon_{1s}[cos(k_s z - \omega_s t)\hat{x} + \alpha_s cos(k_s z - \omega_s t + \delta_s)\hat{y}], \tag{2}$$

where $\alpha_s = \varepsilon_{2s}/\varepsilon_{1s}$, satisfies the wave equation

$$\left(\frac{\partial^2}{\partial z^2} - \frac{1}{c^2}\frac{\partial^2}{\partial t^2}\right)\vec{E}_s = \frac{4\pi}{c^2}\frac{\partial \vec{J}}{\partial t}. \tag{3}$$

The current density is given by $\vec{J} = -en_e\vec{u}_e$, where $\vec{u}_e$ is the velocity of oscillation of electrons in the radiation field. We obtain $\vec{u}_e$ from the equation:

$$\frac{\partial \vec{u}_e}{\partial t} = -\frac{e}{m}[\vec{E}_o + \vec{E}_s],$$

where e and m are the charge and the mass of an electron.

From equation (3), we get

$$D_s\varepsilon_{1s} = -\frac{4\pi e^2\varepsilon_{1o}}{m}\delta n_1, \tag{4}$$

$$D_s\varepsilon_{2s} = -\frac{4\pi e^2\varepsilon_{2o}}{m}\delta n_2 \frac{cos(kz-\omega t+\delta_e)}{cos(kz-\omega t+\delta_o-\delta_s)}, \tag{5}$$

where $D_s = k_s^2c^2 - \omega_s^2 + \omega_p^2$; $\omega_s = \omega_o - \omega$, $\vec{k}_s = \vec{k}_o - \vec{k}$.

The density fluctuations δn_1 and δn_2 can be determined using the standard procedure /3/:

$$\delta n_1 = -\frac{\varepsilon_{1o}\varepsilon_{1s}}{8\pi m\omega_o^2}k^2\frac{\chi}{(1+\chi)}, \tag{6}$$

$$\delta n_2 = -\frac{\varepsilon_{2o}\varepsilon_{2s}}{8\pi m\omega_o^2}k^2\frac{\chi}{(1+\chi)}\frac{sin(kz-\omega t+\delta_o-\delta_s)}{sin(kz-\omega t+\delta_e)}, \tag{7}$$

where χ is the electron susceptibility.

We find the dispersion relation from equations (4) and (5):

$$1+\frac{1}{\chi} = \frac{1}{8}v_o^2k^2\left[\frac{1}{D_-}+\frac{1}{D_+}\right] \tag{8}$$

with $\delta_o - \delta_s = \delta_e$, $\alpha_o^2 = 1$, $p = \delta n_2/\delta n_1$, $\alpha_s = p/\alpha_o$, $v_o^2 = e^2\varepsilon_o^2/m^2\omega_o^2$ and $D_\pm = (k_o \pm k)^2c^2 - (\omega_o \pm \omega)^2 + \omega_p^2$.

Stokes Parameters: For the incident wave ($\alpha_o = \pm 1$), the Stokes parameters are/4/: $I_o = 2\varepsilon_{1o}^2$, $Q_o = 0$, $U_o = 2\varepsilon_{1o}^2 cos(\delta_o)$, $V_o = 2\varepsilon_{1o}^2 sin(\delta_o)$.

The angle β describing the sense of rotation of the electric field is given by $sin(2\beta_o) = V_o/I_o = sin(\delta_o)$ or $\beta_o = \delta_o/2$. The magnitudes of the principle axes of the ellipse are $a_o = \sqrt{I_o}\,|cos(\beta_o)|$ and $b_o = \sqrt{I_o}\,|sin(\beta_o)|$. The orientation of the axes of the ellipse relative to x and y axes, is given by $tan(2\chi_o) = U_o/Q_o$, so that $\chi_o = \pi/4$ for $0 \le \delta_o < \pi/2$.

The corresponding parameters for the scattered wave are: $I_s = \varepsilon_{1s}^2(1+p^2)$, $Q_s = \varepsilon_{1s}^2(1-p^2)$, $U_s = 2\varepsilon_{1s}^2 p\,cos(\delta_s)$, $V_s = 2\varepsilon_{1s}^2 p\,sin(\delta_s)$, $sin(2\beta_s) = V_s/I_s = 2p\,sin(\delta_s)/(1+p^2)$, $a_s = \sqrt{I_s}\,|cos(\beta_s)|$, $b_s = \sqrt{I_s}\,|sin(\beta_s)|$ and $tan(2\chi_s) = 2p\,cos(\delta_s)/(1-p^2)$.

From the condition, $\delta_o - \delta_s = \delta_e$ we find: (1) for $\delta_o - \delta_e = 0$; $\delta_s = 0$, the incident elliptically polarized wave scatters into a linearly polarized wave; (2) for $\delta_o = 0$; $\delta_s + \delta_e = 0$, the linearly polarized wave scatters into an elliptically polarized

wave; (3) for $\delta_e = 0$; $\delta_o = \delta_s$, there is no change in polarization; (4) for $\delta_o - \delta_e = \delta_s$, in general for $\delta_o \neq 0$, $\delta_s \neq 0$ and $\delta_e \neq 0$ elliptically polarized wave scatters into another elliptically polarized wave with or without change in the sense of rotation.

When $\omega \gg kv_e$, v_e is the thermal velocity of electrons, the electrostatic modes are relatively well defined since they are not heavily damped on electrons. In this limit, the expression for growth rate, obtained from (8), is given by

$$\gamma = -\frac{1}{2}(\Gamma_p + \Gamma_-) \pm \frac{1}{2}\sqrt{(\Gamma_p - \Gamma_-)^2 + \frac{1}{2}\left(\frac{v_o}{c}\right)^2 \omega_o \omega_p \cos^2(\theta)}, \qquad (9)$$

where θ is the angle between $\vec{k}_o$ and $\vec{k}$, Γ_p and Γ_- are the Landau and collisional damping rates, and ω_p is the plasma frequency. The typical plasma parameters of a quasar at a distance of 0.01 pc from the central engine are: $n_o = 10^{10}\, cm^{-3}$, $T = 10^4\, K$. The luminosity of radiation in the radio band $\Delta\nu < 10^{10}\, Hz$ is $10^{42} erg\, sec^{-1}$. For these parameters, the value of the growth rate of the SRS is $\gamma = 7.5 \times 10^5\, sec^{-1}$. Which shows that changes in the polarization can occur extremely rapidly with a characteristic time as small as a few micro seconds. Reversal in the sense of polarization over a few milli to micro seconds has been observed in some pulsars/5/. We conclude that SRS may provide a possible explanation for such a fast change in polarization.

/1/ V. Krishan, P.J. Wiita, Mon. Not. R. astr. Soc. **246**, 597 (1990)

/2/ R.T. Gangadhara, V. Krishan, Mon. Not. R. astr. Soc. (Accepted) (1991)

/3/ C.S. Liu, P.K. Kaw, Advances in Plasma Phys. **6**, 83 (1976)

/4/ G.B. Rybicki, A.P. Lightman, Radiative Processes in Astrophysics, A Wiley–Interscience Publication, (1979)

/5/ R.N. Manchester, J.H. Taylor, Pulsars, W.H. Freeman and Company, San Francisco, (1977)

Topic 10:

Basic Collisionless Plasma Physics

III-1677

TRANSITION TO CHAOS IN PERIODICALLY DRIVEN THERMIONIC DIODES AT LOW PRESSURE

T. Klinger, R. Timm, A. Piel
Institut für Experimentalphysik, Universität Kiel
D-2300 Kiel, Germany

1. Introduction. The static I(U) characteristic of thermionic diodes at mbar pressures shows a large hysteresis, which describes the transition from the 'anode-glow-mode' (AGM), with essentially negative plasma potential, to the 'temperature-limited-mode' (TLM), with positive plasma potential.[1] Many features of these modes are also found in magnetic-box discharges with filament cathodes at pressures of $10^{-2} - 10^{-1}$ Pa. Although these two pressure regimes are basically different concerning the transport properties (diffusion vs. free streaming), the elementary processes that establish the AGM in the low pressure regime are very similar to the high pressure regime. Ions are produced in that part of the anode sheath where the potential exceeds the ionisation energy. The production rate is enhanced by multiple reflections of electrons between the magnetic fields of the permanent magnet array at the anode and the repulsive potential of the cathode plasma. Although the mean free path for charge exchange or elastic collisions substantially exceeds the anode-cathode distance, some few ions are stopped and trapped within the potential well of the virtual cathode. This accumulation of ions forms a cathodic plasma, which is essentially at cathode potential. Plasma formation in the anode sheath is suppressed as long as the ion production time is larger than the ion transit time through the sheath. These model ideas are supported by 1d-Particle-in-cell simulations[2] using a modified PDP1-code.[3] The AGM is attractive for studies of nonlinear dynamics because of its feedback processes and oscillations, which occur close to the hysteresis point.

When the static point of operation is chosen in the AGM, and the system is periodically forced to attain the TLM transiently, two different routes to chaos have been observed. Cheung et al.[4] reported the appearance of intermittency for a diode with superimposed sine-modulation, when the selfspiking was suppressed by a suitable choice of the system's length. In the opposite case the same authors[5] found mode-locking, Arnol'd tongues, and a quasi-periodic way to chaos. Timm and Piel[6], by applying sine-waves, observed a truncated period-doubling sequence for the case, in which selfspiking was not excited. The system attained a 'chaotic' state, which could be characterized by short laminar sequences of periods 4, 2, and 1. Apparently the system was hopping between different stages of a period doubling sequence.

2. Period doubling. For sine-modulation it is not distinguishable, whether the modulation amplitude or an effective width of the sine-wave, for which the hysteresis threshold is exceeded, acts as control parameter. We have therefore changed the modulation to pulse-trains of independently controllable width and height (Fig. 1(a)). Our experiments are performed in a stainless steel vessel of 325mm dia. and 330mm height, which acts as anode. The cathode is a single straight tungsten filament (0.2mm dia., 160mm length, 4.0-4.5A) in the center of the vessel. The outer wall is covered by rows of permanent magnets (10x20x15, 0.12T) that form a set of line cusps of alternating polarity with a separation of 10cm. The discharge is operated in Argon at $p = 10^{-2} - 10^{-1}$ Pa. Figure 1(b) shows the typical hysteresis of the I(U) characteristic. The part A-B represents the AGM, whereas E-D is the TLM. In the interval B'-B selfspiking is observed. In comparing the voltage of the hysteresis point B with the ionisation energy $\Phi_{argon} = 15.6V$, one must take the

voltage drop along the cathode filament ($U_{fil} = 15V$) into consideration, which raises the starting potential of primary electrons.

A period doubling sequence is observed, when the discharge is periodically pulsed from a stable state in the AGM ($U = 27V$) to an unstable state ($U = 41V$), and when the pulse repetition frequency is chosen between 2.5kHz and 3kHz. An optimum choice is 2.82 kHz and the pulse width is varied from $60 - 90\mu s$. Figure 2(a) shows the time series of current pulses, Fig. 2(b) gives the corresponding bifurcation diagram of the stroboscopically sampled current pulses, taken at the end of the driving pulse. Period 1, 2, 4, and chaos are clearly distinguishable. A nearly identical bifurcation diagram is found, when the pulse frequency is varied for constant pulse width. The choice of the pulse height in the regime 40-60V has only a minor influence. It may therefore be concluded that the pulse-width, i.e., the rate of ions produced in the anode sheath is the control parameter for the dynamics, whereas the pulse height is unimportant, because the associated electron energy corresponds to the maximum of the ionisation cross-section.

The return map for the chaotic state (D) is displayed in Fig. 2(c). Evidently, the chaotic dynamics is given by a non-invertible quadratic map. The correlation dimension at this point is $D_2 = (0.68 \pm 0.2)$, which has to be compared with the dimensionality of the standard logistic mapping at the accumulation point $D_2 = 0.5$. We attribute the slightly increased dimensionality to the influence of the noise in the system. The logistic mapping with a noisy control parameter: $x_{n+1} = (\lambda + \Delta\lambda \cdot rnd(n))x_n(1 - x_n)$ yields a very similar bifurcation diagram for $\Delta\lambda = 0.03$, that only consists of periods 1, 2, 4, and chaos without windows.

3. Mode locking. Operating the discharge in the regime B'-B of the characteristic, unstable selfspiking occurs, which becomes nearly periodic close to B. The formation of a current spike is initiated by a Buneman-instability of the cathodic plasma, formation of an electron hole, and reduction of negative space charge by ions streaming to the cathode.[2] Two time scales are involved, the removal of ions from the cathodic plasma by a double layer type field, and the refilling and expansion of the cathodic plasma by trapping of new ions. Similar processes have recently been suggested for oscillations in thermionic converters and Q-machines.[7]

A small sinusoidal signal applied to the cathode is found considerably amplified on the plasma potential halfway between anode and cathode. This amplification is indicative of the inherent plasma instability. The selfspiking can be mode-locked even by weak signals (i.e. a few per-cent of the dc-voltage). Figure 3 gives a measured phase diagram for the mode-locked states. A typical pattern of Arnol'd tongues is found. The arrangement of mode-locked states gives the expected Farey sequence. Within the Arnol'd tongues, period doubling transitions to chaos are observed. Outside the mode-locked states quasi-periodic states are observed. For strong modulation various transition to chaos can be observed. Especially for the period-doubling route within the mode-lock-2 state, the reconstructed phase space attractor has a simple unimodal shape similar to Fig. 2(c). This finding hints at close relationships between the period-doubling sequence reported above and the period-doubling observed in the mode-lock-2 state. The Arnol'd tongues observed in Ref.5 are in two respects rather different from our case. They are extremely narrow for low modulation voltage, and overlap of the tongues is only observed for modulation voltages in excess of 30V. In our case the modulation index is typically an order of magnitude smaller.

For the case of suppressed selfspiking, it is justified to represent the internal oscillator by a complex frequency, whose imaginary part changes sign at point B'. In addition it

is reasonable to assume only a small change of the real part when crossing B'. Hence, we can compare the frequency of selfspiking with that value of the modulation frequency that yields the period-doubling route. This frequency is typically twice the natural spiking frequency. Therefore, the period-doubling route may be interpreted as mode-locking of a damped oscillation, which is destabilized by the modulation.

Conclusions. We have demonstrated how period doubling and mode-locking phenomena in thermionic diodes are connected with selfspiking instabilities of the cathodic plasma in the AGM. The internal control parameter of the nonlinear dynamics is the number of ions per driver period produced in the anode sheath, which can be varied by altering either the pulse-width or repetition frequency. Similar shapes of phase space attractors with a simple quadratic extremum were found at the accumulation point of the period- doubling sequence and at chaos-onset inside the period-2 Arnol'd tongue.

Acknowledgement. We gratefully acknowledge financial support from Deutsche Forschungsgemeinschaft under contract Pi185/2-1.

References.

[1] L. Malter, E.O. Johnson, W.M. Webster, RCA Rev. **12**, 415 (1951)
[2] F. Greiner, T. Klinger, A. Piel, R. Timm, 4th Symp. on Double Layers, Innsbruck (1992)
[3] W.S. Lawson, J. Comput. Phys. **80**, 253 (1989); PDP1 Reference Manual, Plasma Theory and Simulation Group, Univ. California, Berkeley (1990)
[4] P.Y. Cheung, S. Donovan, A.Y. Wong, Phys. Rev. Lett. **61**, 1360 (1988)
[5] P.Y. Cheung, S. Donovan, A.Y. Wong, 1990 ICPP, New-Delhi, India p. 793
[6] R. Timm, A. Piel, XXth ICPIG, Pisa, Italy, p. 259
[7] F. Bauer, H. Schamel, Physica **D54**, 235 (1992)

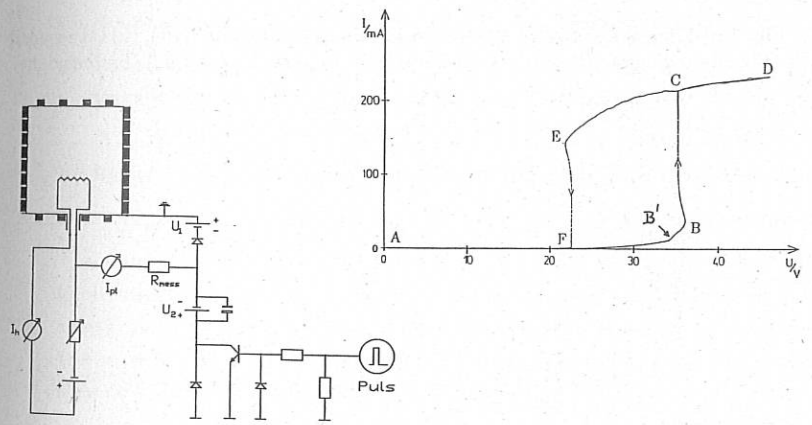

Fig.1(a) Thermionic diode with pulse modulation (left), (b) static hysteresis curve. A-B: anode-glow-mode, B'-B: selfspiking regime, E-D: temperature-limited-mode (right)

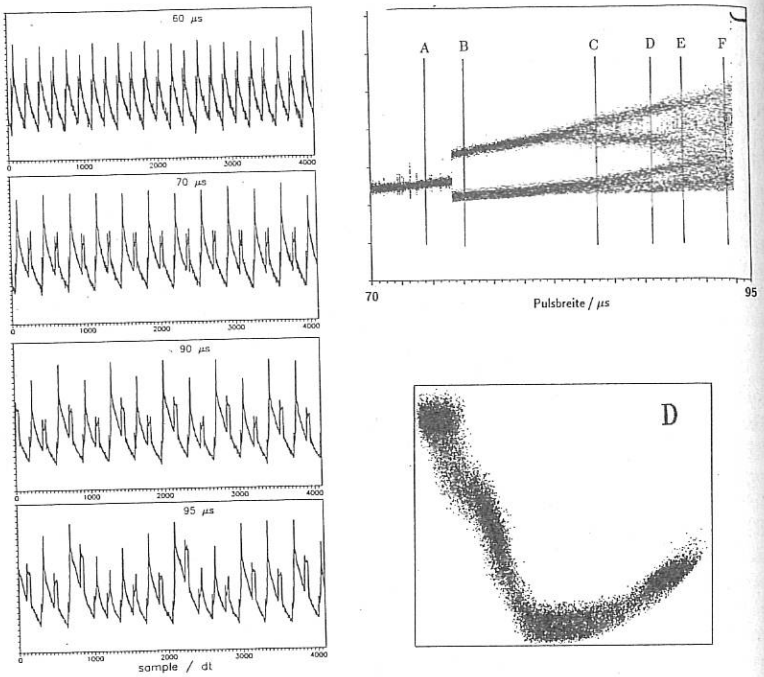

Fig. 2(a) Time series of current pulses for increasing pulse width (left), (b) Corresponding bifurcation diagram (top right), (c) Chaotic return map $I_{n+1} = f(I_n)$ (bottom right).

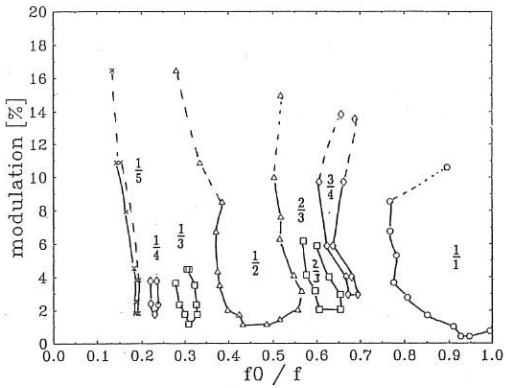

Fig. 3 Mode locking regimes in the m vs. f_0/f plane.

EQUILIBRIUM DOUBLE LAYERS IN EXTENDED PIERCE DIODES

Carmen Iuliana Ciubotariu-Jassy*
Laboratoire de Physique des Gaz et des Plasmas
Universite Paris Sud, Bat 212
91405 Orsay Cedex, France

1. Introduction

The extended Pierce diode is similar to the standard (or classical) Pierce diode, but has passive circuit elements (R, L, C) in place of the short circuit between the electrodes (Fig.1)/1//2/. This device is important as an approximation to real bounded plasma systems. It consists of two parallel plane electrodes(an emitter located at x=0 and a collector located at x=ℓ) and a collisionless cold electron beam traveling between them. The electrons are neutralized by a background of comoving massive ions. This situation is analysed in this paper and new equilibrium double layer (DL) plasma structures are obtained.

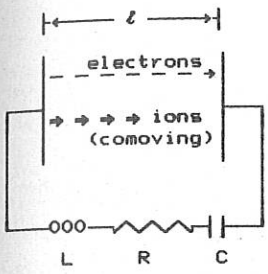

Fig.1. Extended Pierce diode model

2. Basic Equations

We introduce the adimensional quantities:

$\omega = \omega_p/\omega_t$ (Pierce prameter), $\rho' = \rho/\rho_o$, $v' = v/v_o$, $x' = x/\ell$,

$E' = q\ell E/mv_o^2$, $\Phi = q\varphi/mv_o^2$, $X = \omega x'$, $\Psi = E'/\omega$, $E'_o/\omega = \epsilon$, $r = \rho' - 1$,

where $\omega_p = (n_o e^2/\varepsilon_o m)^{1/2} \equiv (q\rho_o/\varepsilon_o m)^{1/2}$ is the electron plasma frequency of the beam, m=electron mass, $\rho_o = -en_o$, ρ=the electron charge density, n_o=both the ion background density and electron emission density, $\omega_t \equiv v_o/\ell$ = the transit frequency. The electrons leave the emitter with velocity v_o, and are absorbed when hitting either electrode.

---

*Permanent address: Phys. Dept., Str. Sfintu Lazăr 21, F4-15, 6600 Iaşi, Romania

The equilibrium equations are

$$\rho' v' = 1, \quad v'(dv'/dx') = E', \quad dE'/dx' = \omega^2(\rho' - 1) \qquad (2.1)$$

with the boundary conditions

$$\rho'(0) = 1, \quad v'(dv'/dx') = 1, \quad \int_0^1 E'(x')dx' = -\Phi_t, \qquad (2.2)$$

where Φ_t is the (transit) potential drop across the system. To solve these equations, we define t' (orbit variable /3/) such that

$$t' = \int_0^{x'} \frac{dx'}{v'(x')} \equiv \int_1^{v'(x')} \frac{dv'}{E'(v')} \equiv \int_{E'_o}^{E'(x')} \frac{dE'}{\omega^2(1-v')} . \qquad (2.3)$$

This time represents the time it took a fluid element (or particle) to arrive at position x' from its time of injection at emitter, that is, t' is a local transit time. It is not an independent variable in the usual sense, but rather a parameter of which x', v', E' and Φ depend on. From the equations (2.1)-(2.3) we find

$$X = \tau + \epsilon(1 - \cos\tau), \qquad (2.4)$$

$$v' = 1 + \epsilon \sin\tau \equiv V, \qquad (2.5)$$

$$\mathcal{E} = \epsilon \cos\tau, \qquad (2.6)$$

$$\Phi(\tau) = \epsilon \sin\tau \,(1 + 0.5\,\epsilon \sin\tau), \qquad (2.7)$$

$$r = (dE'/dx')/(\omega^2) \equiv -1 + (1/v') \equiv -1 + (1+\epsilon\sin\tau)^{-1}, \qquad (2.8)$$

where ϵ is the "extended Pierce parameter", $\tau = \omega t'$, r is the charge density, and

$$\Phi(\tau) = +\int_0^{\tau} E' \frac{dx'}{d\tau} d\tau \qquad (2.9)$$

is the local(equilibrium) potential drop. It is interesting to note that the equations (2.5)-(2.7) describe a curve in three-dimensional phase space (V,$\mathcal{E}$,Φ), and τ is some parameter along the curve. A set of neighboring curves, forming a congruence, may be obtained by the variation of the parameter ϵ. For example, in the 2D phase space (Φ,$\mathcal{E}$) we have the diagrams indicated in Fig.2.These phase space plots can be related to the presence of DLs, but we shall not be concerned with this method here (see /4/).

3. Double Layers

The equilibrium of classical and extended Pierce diodes is described by the local behavior of function V, $\mathcal{E}$, Φ, and r given by the equations (2.5)-(2.8). These quantities, as functions of X, are diagrammed in Fig.3 for $\epsilon = 0.5$. The curves enable us to conclude the following: (a) The appearance in a collisionless cold electron beam of the Pierce diode of potential drops corresponding to those of DLs can be correlated with the energy conservation law. An electron of the beam, coupled to the electric field of the plasma, has an energy $(mv^2/2)+q\varphi$ = constant, and forms an electrostatic structure which we call **"spatial plasmon"** or **"spatial quantum"**. The electrons lose and gain their kinetic energy in interaction with the essentially changing electric field, but the energy of spatial plasmon remains constant. (b) As in the case of a collisional plasma /5/, the generation of DLs can be correlated with certain quantum processes (spatial plasmon ↔ electron+photon). Although the DLs discussed in this work refer to a state of equilibrium, these remain essentially dynamical in nature. The electrons in DLs are continuously changed. The electrons passing the potential minimum form a beam accelerated by the potential difference φ_{DL} on the high potential side. Hence we have the characteristcs of "strong" DLs /6/.

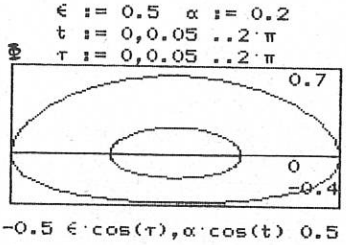

Fig.2. Quasi-Phase space plots (Φ, $\mathcal{E}$).

4. An Example: New Methods of UHF Generation

For the case of $v_o \simeq 10^{10}$ cm/sec, $\ell \simeq 0.1$cm, ω_t corresponds to cm-range which may be of interest in developing of new methods of UHF generation. If the diode works as a classical one the electrons will hit the collector with V=1, that is the device is a passive element of circuit, and $X=\omega=10^{-11}\omega_p = 2n\pi$, so that $\varphi_{collector}=0$. If the diode works as an extended Pierce diode with positive (or negative) resistance, the electrons will hit the collector with $V < 1$ (or $V > 1$).

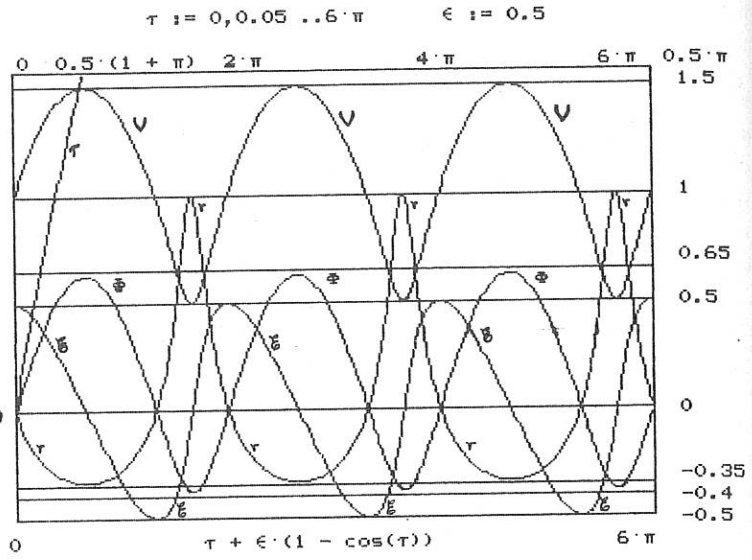

Fig.3. V, $\bar{x}$, $\bar{\Phi}$, r, and τ as functions of X for ϵ = 0.5.

An interesting, and to my knowledge unreported, result is noticeable: **A Pierce diode can work as a classical (or an extended) one even if there is(or there is not) an external circuit); the condition is to realize φ=0(or $\varphi\neq$0) at X = ω.**

Acknowledgements. I gratefully acknowledge the advice, assistance and support of Professors A.M. Pointu, M. Fitaire, M. Sanduloviciu, and G. Popa.

References

/1/ M.Horhager, S.Kuhn, Phys.Fluids B2, 2741(1990).

/2/ W.S.Lawson, Phys.Fluids B1, 1483(1989).

/3/ V.C.Boffi, V.G.Molinari, D.E.Parks, R.Scozzafava, Nuovo Cimento 36, 150(1965).

/4/ Carmen Ciubotariu,Quasi-Phase Space Topology for Plasma Diodes, preprint, 1992.

/5/ M.Sanduloviciu, E.Lozneanu, Plasma Phys.Controlled Fusion 28, 585(1986).

/6/ M.A.Raadu, Phys.Rep.178, 25(1989); H.Schamel, Phys.Rep. 140, 161(1986).

NEW RESULTS ON WEAKLY NONLINEAR DRIVEN OSCILLATIONS IN THE PIERCE DIODE

M. Hörhager and S.Kuhn

Plasma and Energy Physics Group, Institute for Theoretical Physics
University of Innsbruck, A–6020 Innsbruck, Austria

Introduction and Model. The simplest and most fundamental model of a bounded plasma system is the "classical" Pierce diode,[1-5] in which a collisionless cold electron beam is injected into the plasma region with constant density n_0 and velocity v_0 at the emitter surface ($x = 0$) and the electrons are absorbed on impact on either the emitter or the collector (located at $x = d$), the two electrodes being externally shorted. The ions form an immobile neutralizing background of uniform density n_0.

In the present paper, however, we consider an "extended" Pierce–diode model including nontrivial (RLC) external–circuit elements and an ac source in the external circuit (Fig. 1). In particular, we study small–amplitude, steady–state, driven oscillations about the uniform dc ("equilibrium") state (in which the electrons have constant density n_0 and velocity v_0, and the electric field vanishes everywhere inside the diode gap). The linear stability behavior of this system, including the influence of external–circuit elements, was discussed in Refs. 2 and 3, and weakly nonlinear steady–state oscillations of the *undriven* system were studied in Refs. 4 and 5.

An analytical theory of weakly nonlinear, steady–state *driven* oscillations was first presented by us in Ref. 6, where the basic principles and assumptions were outlined and first results were presented. The driving ac generator produces a small–amplitude periodic signal with fundamental frequency ω. This theory is applicable to situations where (i) linear theory yields no unstable eigenmodes and (ii) we are far away from "resonance", e.g. we must avoid the case $\omega \simeq \mathrm{Re}\omega_{\mathrm{lin}}$, where ω_{lin} is the dominant linear eigenfrequency. As in the undriven case[5], all perturbation quantities are expanded in time Fourier series with fundamental frequency ω; the n–th harmonic is assumed to be small of n–th order, and the time–averaged perturbation is assumed to be of second order. All quantities of higher than third order are neglected.

In Ref. 6, some dependencies of the nonlinear current amplitudes on the driving frequency in the short–circuit case were given. In *this* paper, we present new results for a different short–circuit case and for a diode with a purely inductive external circuit. These analytic results are compared with particle simulations performed with the code PDP1.[7]

Basic Equations. The basic equations governing the extended Pierce–diode model of

Fig. 1 are[6]

$$\frac{\partial n}{\partial t} + \frac{\partial}{\partial x}(nv) = 0 \qquad (1) \qquad \left(\frac{\partial}{\partial t} + v\frac{\partial}{\partial x}\right)v = -\frac{e}{m}E \qquad (2)$$

$$\frac{\partial E}{\partial x} = \frac{e}{\epsilon_0}(n_0 - n) \qquad (3) \qquad \epsilon_0\frac{\partial E}{\partial t} + j_p = J \qquad (4)$$

$$V(l,t) - V(0,t) = -\int_0^d dx\, E(x,t) = L\frac{dI}{dt} + RI + \frac{Q}{C} + U_B + \tilde{U}_g(t)\,, \qquad (5)$$

with $v(x,t)$ the electron velocity, $E(x,t)$ the electrostatic field, $n(x,t)$ the electron number density, $\tilde{U}_g(t)$ the periodic, small–amplitude driving ac voltage, $j_p(x,t) = -env$ the plasma current density, and $J(t) = I(t)/A$ the total, or external–circuit, current density. $I(t)$ is the total external–circuit current and A the electrode area; R, L and C are the external–circuit resistance, inductance and capacitance, respectively, and $Q(t)$ is the electric charge on the right–hand plate of the capacitor C. The latter is short–circuited dc–wise by the (large) inductance L_c. The external dc battery has to compensate the dc–potential drop across the resistance R, so that $U_b = -\bar{I}R$, with $\bar{I}$ the dc current. In addition, the following particle boundary conditions must be satisfied at the emitter surface:

$$n(0,t) = n_0 \qquad (6) \qquad v(0,t) = v_0\,. \qquad (7)$$

<u>Nonlinear Perturbation Theory and Fourier Analysis</u>. We now write any physical quantity involved in the form

$$u(x,t) = \bar{u} + \tilde{u}(x,t) \qquad (8)$$

with $\bar{u}$ the constant equilibrium value ($\bar{n} = n_0$, $\bar{v} = v_0$, $\bar{E} = 0$, $\bar{J} = -en_0v_0$, $\bar{Q} = 0$) and $\tilde{u}$ the (small) perturbation. Inserting (8) into the basic equations (1)–(7) and expressing $\tilde{E}$ and $\tilde{n}$ in terms of $\tilde{v}$ results in the integro–differential system

$$\frac{\partial^2\tilde{v}}{\partial t^2} + 2\bar{v}\frac{\partial^2\tilde{v}}{\partial x\partial t} + \omega_p^2\,\tilde{v} + \bar{v}^2\frac{\partial^2\tilde{v}}{\partial x^2} + \frac{\partial\tilde{v}}{\partial x}\frac{\partial\tilde{v}}{\partial t} + 2\tilde{v}\frac{\partial^2\tilde{v}}{\partial x\partial t} + \bar{v}\left[\frac{\partial\tilde{v}}{\partial x}\right]^2 + 2\bar{v}\tilde{v}\frac{\partial^2\tilde{v}}{\partial x^2} + \tilde{v}\left[\frac{\partial\tilde{v}}{\partial x}\right]^2 + \tilde{v}^2\frac{\partial^2\tilde{v}}{\partial x^2} = -\frac{e}{m\epsilon_0}\tilde{J}\,, \qquad (9)$$

$$-\int_0^d dx\,\tilde{E}(x,t) = \frac{m}{e}\left[\frac{\partial}{\partial t}\int_0^d dx\,\tilde{v}(x,t) + \bar{v}\tilde{v}(d,t) + \frac{1}{2}[\tilde{v}(d,t)]^2\right] = A\left[L\frac{d\tilde{J}}{dt} + R\tilde{J} + \frac{1}{C}\int_0^t d\tau\,\tilde{J}(\tau)\right] + \frac{\tilde{Q}(0)}{C} + \tilde{U}_g(t)\,, \qquad (10)$$

with the boundary conditions for v and n now expressed in the form

$$\tilde{v}(0,t) = 0 \qquad (11) \qquad \tilde{n}(0,t) = \frac{m\epsilon_0}{e^2}\left[\frac{\partial^2\tilde{v}}{\partial x\partial t} + \bar{v}\frac{\partial^2\tilde{v}}{\partial x^2} + \left[\frac{\partial\tilde{v}}{\partial x}\right]^2\right]_{x=0} = 0\,. \qquad (12)$$

Since we are only interested in *periodic* steady–state oscillations, we expand all per–

turbation quantities in Fourier series of the form

$$\tilde{u}(x,t) = \sum_{n=-\infty}^{\infty} \hat{u}_n(x) e^{-in\omega t} . \qquad (13)$$

Since all perturbations and the driving frequency ω are assumed to be real, each spatial profile function must satisfy the relation $\hat{u}_n(x) = [\hat{u}_{-n}(x)]^*$. Inserting (13) into (9)–(12) and collecting terms belonging to the same harmonic orders, we obtain relations between the velocity profile functions $\hat{u}_n(x)$, external–circuit current amplitudes $\hat{J}_n$, and driving– voltage amplitudes $\hat{U}_{g,n}$. These relations are given in Eqs. (35)–(38) of Ref. 5. As already mentioned above, all quantities with $|n| > 3$ are neglected here ("3–harmonic approximation").

Numerical Results. (a) Short–circuit–case: In this section we present results for the special short–circuit case characterized by the normalized length $\alpha = 2.95\pi$ (where $\alpha \equiv \omega_p d/v_0$, with ω_p the electron plasma frequency). The current history for a sinusoidal driving voltage with amplitudes $\hat{U}_{g,1} = 0.01\ v_0^2 m/e$ and $\hat{U}_{g,2} = \hat{U}_{g,3} = 0$ and a driving frequency $\omega = 2.5\ v_0/d$ is shown in Figs. 2a (theory[6]) and 2b (simulation[7]). From the Table, where the theoretical current amplitudes are quantitatively compared with those obtained from the simulations, we see that the agreement is very good. This becomes plausible because the dominant linear eigenfrequency is $\omega_{lin} d/v_0 = 1.95082 - 0.23902i$, which means that we are quite far away from resonance and are dealing with a strongly damped eigenmode, as required by the theory.

(b) Inductive case: Figures 3a (theory) and 3b (simulation) show the current history for a Pierce diode having normalized length $\alpha/\pi = 0.55$ and a purely inductive external circuit with normalized inductance $L_{nd} = \omega_p^2(\epsilon_0 A/d)L = 0.1/\pi$, for which linear theory yields a damped dominant eigenmode with $\omega_{lin} d/v_0 = 9.74478 - 0.058958i$. The driving voltage amplitudes are $\hat{U}_{g,1} = 0.1\ v_0^2 m/e$ and $\hat{U}_{g,2} = \hat{U}_{g,3} = 0$, and the driving frequency is chosen to be $\omega = 5\ v_0/d$, i.e., far away from resonance. According to the Table, the agreement between theory and simulation is good again.

In the cases shown here the resulting oscillations are clearly regular, but simulations show that for larger amplitudes and/or weaker damping the system seems to undergo subharmonic bifurcations and finally becomes chaotic. It would thus be desirable to have a predominantly analytic theory of such dynamic phenomena as well, and pertinent efforts are under way.

Acknowledgments. This work was supported by the Austrian Research Association (Project 09/0018) and the Austrian Science Foundation (Project P8405–PHY).

Table

Figure	α/π	L_{nd}	R_{nd}	C_{nd}^{-1}	$\frac{J^{\pm}_{s\,im}}{J_0}$	$\frac{J^{\pm}_{3\,h}}{J_0}$	$\frac{\lvert J^{\pm}_{3\,h}\rvert - \lvert J^{\pm}_{s\,im}\rvert}{\lvert J^{\pm}_{s\,im}\rvert}$
2a, 2b	2.95	0	0	0	±.0103	±.0105	2%
3a, 3b	0.5	$0.1/\pi$	0	0	±.38	.397 −.391	4%

[1]J.R. Pierce, J. Appl. Phys. **15**, 721 (1944).

[2]S. Kuhn, Phys. Fluids **27**, 1834 (1984).

[3]S. Kuhn and M. Hörhager, J. Appl. Phys. **60**, 1952 (1986).

[4]B.B. Godfrey, Phys. Fluids **30**, 1553 (1987).

[5]M. Hörhager and S. Kuhn, Phys. Fluids B **2**, p. 2741 (1990).

[6]M. Hörhager and S. Kuhn, *International Conference on Plasma Physics,* New Delhi, 1989, Contributed Papers, Vol. **2**, 377.

[7]V. Vahedi, M.A. Lieberman, M.V. Alves, J.P. Verboncoeur, and C.K. Birdsall, J.Appl.Phys. **69**, 2008 (1991).

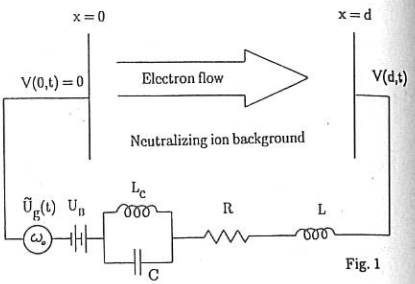

Fig. 1

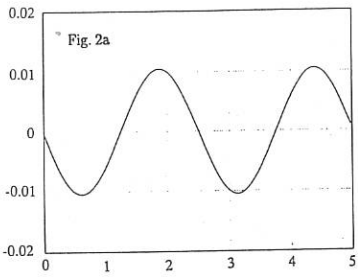

Fig. 2a

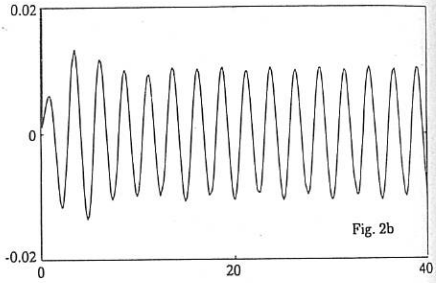

Fig. 2b

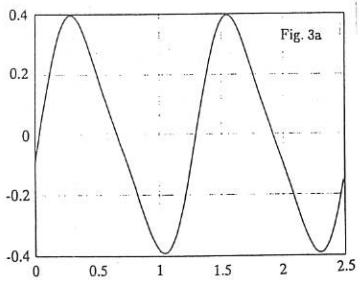

Fig. 3a

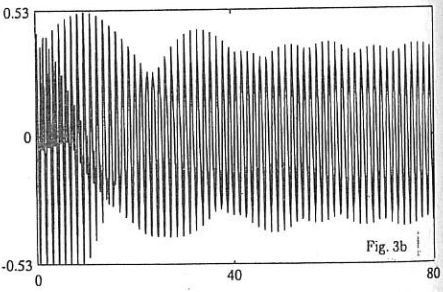

Fig. 3b

LABORATORY STUDY OF COLLISIONLESS INTERACTION PROCESSES BETWEEN SUPERNOVA-LIKE EJECTAS AND MAGNETIZED BACKGROUND UNDER CONDITIONS OF LASER-PRODUCED-PLASMA EXPERIMENTS

Yu.P. Zakharov, A.M. Orishich, A.G. Ponomarenko
V.N. Snytnikov

Institute of Laser Physics, Siberian Division of the Russian Academy of Sciences, Novosibirsk 630090, Russia

I Introduction

Recently in astrophysics and geophysics one can see a great interest in plasma collisionless effects in the interaction processes between expanded plasma cloud an ionized magnetized background. Possible processes[1, 2]deceleration of such clouds by the background plasma (with concentration n_*) or by the magnetic field B_0 are being under consideration as well as the generation [3] of shock waves at $M_A \gg 1$ and at last global effects similar to the influence[4] of SN explosions with high energy $\mathcal{E}_0$ and mass M upon the structure and evolution of diffuse galactic medium.

The same processes must play the determinable role in the dynamics of some geoeffective phenomena connected to the injection of space plasma clouds of the different scale. Such clouds expanding with large velocity $v_0 \sim 10 - 1000$ km/s in rarefied interplanetary (coronal mass ejections) or near-Earth plasma (active experiments of the AMPTE, CRPES or "Starfish" type) may not experience pronounced collisions on scale $\mathcal{D}$ of their deceleration by the background ($\mathcal{D} \sim R_* = \sqrt[3]{3M/4\pi n_* m_*}$) or field ($\mathcal{D} \sim R_B = \sqrt[3]{3\mathcal{E}_0/B_0^2}$). Under such conditions (non-adequately described by the known MHD-models) with allowance for the problems of natural measurements of such seldom-repeated explosion phenomena (as a rule, having the global and 3 D-character) the application of laboratory simulation methods allows us to obtain detailed and even unique data about the character of early-not investigated processes of the cloud-background interaction.

II "KI-1" Simulation Facility

In the table one can see the basic parameters of the "KI-1" facility (in the Institute of Laser Physics), created at the end of the 70-s and designed for the simulation of a wide range of non-stationary processes of the explosion character in space plasma [5] . The experimental opportunities of the facility supply the generation with the controlled delay of several clouds of spherical laser plasma with different energy ($\mathcal{E}_0 \sim 0{,}1 \div 300$ J) by the two-side radiation method [6] of the spherical carbon-hydrogen targets. This allows us to investigate the processes of the interaction:

- between the clouds;
- between the clouds and neutral gas in the magnetic field;
- between the clouds and surrounding magnetized background

(including inhomogeneous in density: $\nabla n_* \| \bar{B}_o$ or $\nabla n_* \perp \bar{B}_o$);
- between the clouds and magnetospherical plasma configuration, created by the background flow in a nonuniform field $\bar{B}_д$ of the magnetic dipole.

"KI-1" chamber scales		1,2m×5m
background pressure	P	10^{-7} Torr
axial magnetic field	B_o	1 kG
magnetic moment of the dipole (Ø 20 cm)	m	10^7 G·cm^3
background plasma density (H^+,.....)	n_*	10^{14} cm^{-3}
output energy of the pulsed CO_2-lasers (0.1-3 mcs duration)	Q_r	2 kJ
laser-target diameter	$Ø_t$	0,1 ÷ 6 mm
expansion velocity of the laser-produced-plasma cloud (C^+ , H^+)	V_o	$(1 \div 3)\cdot 10^7$ cm/s

The facility is supplied with different systems of plasma diagnosttics to measure space distributions of $n_e, T_e, \bar{B}$,.... with high time-resolution ($\lesssim$ 50ns), namely: double electric and 3D-magnetic probes, calorimetr and ion collectors, mass-analysers, interferometrs in a visible, infrared and microwave ranges as well as frame/streak camera and various spectral methods.

III Collisionless interaction processes.

The main advantage of the simulation experiments carried out at the "KI-1" facility consists in the fact that at different regimes of the cloud-background interaction we have managed for the first time to realize the laboratory conditions sufficiently close to space ones in such important similarity criterion as Larmor parameter ϵ . It describes the degree of ion magnetization [5] and defines as $\epsilon = R_H/\mathcal{D}$, where $R_H = v_o mc/eZB_o$ is a directed ion Larmor radius in cloud.

a) In particular, in regime of super-Alfvenic cloud expansion ($M_A = v_o\sqrt{4\pi n_* m_i}/B_o \gg 1$) it has been established[7] that its deceleration by the background at $\mathcal{D} \sim R_*$ may be effectively fulfilled owing to the Magnetic Laminar Mechanism (MLM) connected to the action on ions of the transverse electric field $\bar{E}_\varphi \| [\bar{B}_o \times \bar{v}_o]$, coused by the effect of magnetic field exclusion from the high-β cloud interior. The necessary condition for collisionless MLM-interaction is namely $\epsilon_* = R_H/R_* \lesssim 1$

b) In the opposite, "vacuum" case ($M_A \ll 1$) we have proved[8] the important role of anomalous magnetic field diffusion (with $\nu_{eff} \sim \omega_{Be}$) in the processes of cloud-field interaction and established the similarity criterion $\epsilon_B = R_H/R_B \lesssim 1$, determing them. Only at $\epsilon_B \lesssim 1$ the cloud may be effectively decelerated by field up to $v \sim v_o/2$ at radius $R \sim R_B$, but it does not stop there and

propogates futher $\perp \bar{B}_0$ in the form of separate jets(flutes), being curled in the direction of ion Larmor rotation [9].

In the transition regime ($M_A \gtrsim \sqrt{m_* z / m z_*}$) the effect of the supressing influence of the background plasma upon the development of the flute and lower-hybrid instabilityes of the cloud boundary [10] has been revealed for the first time.

c) With the interaction of the clouds of sufficiently large energy $\mathcal{E}_0$ with real inhomogeneous space medium the so-called global effects may play the crucial role, when the scales of the cloud deceleration region reaches the scales of medium inhomogeneity: $L_* \sim |n_*/\nabla n_*|$ or $L_B \sim |B/\nabla B|$. The preliminary data of experiments [10] in the uniform field $\bar{B}_0 \perp \nabla n_*$ have shown, that in this case also (at the initial stage of the asymmetrical cloud deceleration, $t \lesssim \mathcal{D}_{ma}/v_0$) one can use in the "sectorial" approximation the described above conformityes, obtained under homogeneous conditions.

IV Simulation results for some cosmophysical phenomena.

To analyse the statement and results of the "KI-1" simulation experiments we apply [5,9] the similarity criteria method, based upon π-theorem of the dimension analysis. Besides given above determinable criteria of processes (M_A and ϵ), we are carrying out the comparison with the cosmophysical conditions upon the set of such criteria as: Re_m, $Kn = \lambda_{coll}/D$, m/m_*, z/z_*, zm_e/m, V_0/c, ...and, at last, in the simplest inhomogeneous cases- $\gamma \cong D/L$. The relations between laboratory and space temporal and spatial scales one can establish according the condition of the maintenance the next dimensionless variables: $\tau = tV_0/D$ and $s = R/D$.

a) Collisionless deceleration of Supernova Remnants (SNR) was simulated for the first time [9] at the "KI-1" facility namely owing to realization the necessary $\mathcal{E}_* \lesssim 1$ condition for MIM-interaction, in contrast to experiments [11] at "HELIOS" and "PHAROS" facilityes with negative results. The comparison of our simulation deceleration low of cloud front with corresponding data of the histirical SNR allow us to speculate about initial, non-"Sedov" phase of their deceleration, characterized by $M_A \gg 1$ value

b) Evolution of the Ba-clouds in magnetosphere at $M_A \sim 1$ condition (typical for modern active experiments) was simulated in our experiments without background plasma [9,12], where it was predicted for the AMPTE or CRRES class releases (with $\mathcal{E}_B \sim 1$) the development of flute-type instability with mode-number $K \approx 8\pi/\mathcal{E}_B$. This dependence was confirmed later on in computer [13] and recent laboratory [14] experiments with symmetrical plasma clouds.

c) The development of global pertubations of the magnetosphere it is very possible while realizing the some projects of the Earths protection against collisions with asteroids by super-high energy explosions of the "Starfish" class. Indeed the modern level of energy $\mathcal{E}_0 \sim 10^{18}$ J in such kind of phenomena in geoplasma are comparable with the proper energy of geomagnetic field $\mathcal{E}_m = m_E^2/3R_p^3$. To investigate the plasma processes connected with this pertubations we begun the new class of simulation experiments [15] devoted the reseach of global dynamics of plasma clouds, injected at the distance r from the center of magnetic dipole, imbedded in vacuum or background plasma flow.

This experiments are carried out for the first time under conditions rather strong magnetization of cloud ions ($\epsilon_B < 1$) and at the different values of the similarity criterion of the problem $\varkappa = \gamma_B^3 = \mathcal{E}_0/\mathcal{E}_m \simeq 0.01 \div 10$. For example on Fig.it is shown the frame foto result of "vacuum" dipole experiment with $\mathcal{E}_0 \simeq 10$J at $r = 22$ cm and moment $t = 2{,}5$ ms after laser-produced-plasma ejections in the equatorial plane (at point denote by asterisk). One can see the filling of the "first" and "second" artificial Van Allen belts by the cloud ions, with their precipitation on both poles (top and bottom on Fig.)

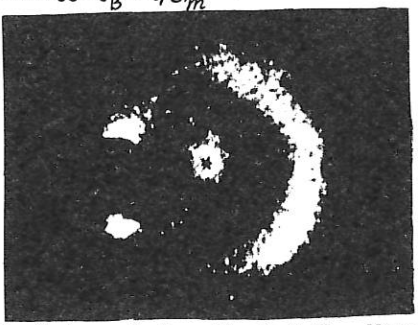

1. Spicer D.S., Clark R.W., Maran S.P., ApJ, 356, 549(1990).
2. Ferriere K.M., Mac Low M.-M., Zweibel E.G., ApJ, 375(1991).
3. Roger R.S., Milne D.K., Kesteven M.J. et al, ApJ, 332(1988).
4. Tomisaka K., ApJ(Letters), 361, L5(1990).
5. Zakharov Yu.P., Orishich A.M., Ponomarenko A.G. "Laser-Produced-Plasma and Laboratory Simulation of Non-Stationary Space Processes", Novosobirsk (1988), 220p. -In Russian.
6. Avdyeva A.A., Zakharov Yu.P., Maximov V.V., et al, J. Appl. Mech. & Techn. Phys., N6,62(1989).-In Russian.
7. Antonov V.M., Bashurin V.P., Golubev A.I,, Zhmailo V.A., Zakharov Yu.P. et al, Ibid, N6, 3(1985).
8. Zakharov Yu.P. et al, Sov. J. Plasma Phys. 12, 674(1986).
9. Zakharov Yu.P., Orishich A.M., Ponomarenko A.G. et al, Proc. Intern. Workshop on Plasma Astrophys., ESA SP-251,37(1986).
10. Antonov V.M., Zakharov Yu.P., Orishich A.M., Ponomarenko A.G., et al, Ibid, ESA SP-311, 189(1990).
11. Tan T.-H., Borovsky J.E., J.Plasma Phys., 35,239(1986).
12. Zakharov Yu.P., Orishich A.M., Ponomarenko A.G., Proc. XIX Intern. Conf. Phenom. Ioniz.Gas.,Belgrade, 2, 276(1989).
13. Winske D., J. Geophys. Res., 93A, 2539(1988).
14. Dimonte G., Wiley L.G., Phys. Rev. Lett., 67, 1755(1991).
15. Zakharov Yu.P., Orishich A.M., Ponomarenko A.G., Abstracts of III Zababakhin's Memory Lectures, Chelyabinsk-70, 133 (1991).

TOTAL ENERGY CONSERVATION AND MANLEY-ROWE RELATIONS FOR PLASMA-MASER INTERACTION

Mitsuhiro NAMBU
Department of Physics, College of General Education
Kyushu University, Ropponmatsu, Fukuoka 810, JAPAN

ABSTRACT

The total energy conservation relation between particles kinetic energy and wave energy is satisfied for the plasma-maser process. The Manley-Rowe relation among plasma waves is violated and as a result an efficient energy up-conversion from the low-frequency mode to the high-frequency mode is possible even for a normal unreversed electrons population in plasma turbulence.

Since the prediction of the plasmas-maser[1,2] which is an intersting mode-coupling process in plasma turbulence[3], it has been subjected to careful scrutiny regarding its validity and probable limitations as an energy up-conversion process in plasma turbulence. Let us first define the plasma-maser interaction. We consider the nonlinear mode-mode coupling between two kinds of plasma waves. The first type is the low-frequency waves with the frequency ω and the wavevector k. These waves satisfy the Landau resonance condition [$\omega - kv = 0$] with the resonant electrons. The second type of the plasma wave is the nonresonant mode with the frequency Ω and the wavevector K which do not obey the Landau resonance [$\Omega - Kv \neq 0$] and nor the nonlinear Landau resonance [$\Omega - \omega - (K - k)v \neq 0$]. This paper reports on the total energy conservation relation and the violation of the Manley-Rowe relation for the plasma-maser process.

According to the standard results[1-3], the nonlinear dielectric constant of the Langmuir wave in the presence of the ion-sound turbulence which causes plasma-maser is

$$\varepsilon_h(K,\Omega) = \left(\frac{e}{m}\right)^2 \frac{\omega_{pe}^2}{K} \sum_{k,\omega} |E_\ell(k,\omega)|^2 \int \frac{1}{\Omega - Kv} \frac{\partial}{\partial v} \times \frac{1}{[\Omega - \omega - (K-k)v]} \frac{\partial}{\partial v} \frac{1}{\omega - kv - i0} \frac{\partial}{\partial v} f_{oe}\, dv, \qquad (1)$$

where Ω,K and ω,k are frequency, wavenumber for the Langmuir and ion sound wave, respectively. $E_\ell(k,\omega)$, f_{0e} are the electric field of the ion sound wave, the electron distribution function, respectively, +i0 shows small imaginary part, -e and m are charge and mass for electrons. The plasma-maser contribution comes from the condition $\omega = kv$ which produces high frequency nonlinear forces for electrons [4]. It should be stressed that the plasma-maser contribution is always accompanied by the reverse absorption process due to the slow time change of medium due to the quasilinear interaction between ion-sound wave and resonant electrons.

For closed system, the both processes cancell out each other exactly and the up-conversion does not occur. Here, we consider the plasma-maser process for open system where the electron distribution function is fixed by external agent.

The growth rate of the Langmuir wave [$\gamma_h(K,\Omega)$] due to the plasma-maser for open system is

$$\gamma_h(K,\Omega) = - \frac{I_m \varepsilon_h(K,\Omega)}{\frac{\partial \varepsilon_0(K,\Omega)}{\partial \Omega}} , \qquad (2)$$

where $\varepsilon_0(K,\Omega)$ is the linear dielectric constant of the Langmuir wave, thus we get $\partial\varepsilon_0(K,\Omega)/\partial\Omega \simeq 2/\Omega$, and I_m shows the imaginary part. Inserting Eq.(1) into Eq.(2), we obtain the total energy change of the Langmuir wave energy density [$W_h(K,\Omega) \equiv |E_h(K,\Omega)|^2/4\pi$] as

$$\frac{\partial}{\partial t} \sum_K W_h = 2 \sum_K \gamma_h(K,\Omega)\, W_h = - \pi \frac{|e|^4}{m^3} \sum_{K,k} \frac{\Omega}{K} |E_\ell(k,\omega)|^2 \, |E_h(K,\Omega)|^2$$

$$\times \int \frac{1}{\Omega - Kv} \frac{\partial}{\partial v} \frac{1}{[\Omega - \omega - (K-k)v]} \frac{\partial}{\partial v} \delta(\omega - kv) \frac{\partial}{\partial v} f_{oe} \, dv . \qquad (3)$$

In deriving Eq.(3), we put $I_m[(\omega - kv - i0)]^{-1} = \pi\, \delta(\omega - kv)$.

According to the linear response theory of a turbulent plasma, the inverse of the plasma-maser effect, i.e., the nonlinear effect of resonant and nonresonant waves simultaneously on the electron distribution reduces to

$$\frac{\partial f_{0e}}{\partial t} = i \left(\frac{|e|}{m} \right)^4 \sum_{K,k} |E_\ell(k,\omega)|^2 \, |E_h(K,\Omega)|^2 \times$$

$$\frac{\partial}{\partial v} \frac{1}{\Omega - Kv} \frac{\partial}{\partial v} \frac{1}{[\Omega - \omega - (K-k)v]} \frac{\partial}{\partial v} \frac{1}{\omega - kv - i0} \frac{\partial}{\partial v} f_{oe} . \qquad (4)$$

From Eq.(4), the rate of change of total electron kinetic energy density [$\partial/\partial t\, E$] may be expressed as

$$\frac{\partial}{\partial t} E = \int \frac{mv^2}{2} \frac{\partial f_{0e}}{\partial t} \, dv . \qquad (5)$$

Inserting Eq.(4) into Eq.(5), we get

$$\frac{\partial}{\partial t} E = \pi \frac{|e|^4}{m^3} \sum_{K,k} \frac{\Omega}{K} |E_\ell(k,\omega)|^2 \, |E_h(K,\Omega)|^2 \times$$

$$\int \frac{1}{\Omega - Kv} \frac{\partial}{\partial v} \frac{1}{[\Omega - \omega - (K-k)v]} \frac{\partial}{\partial v} \delta(\omega - kv) \frac{\partial}{\partial v} f_{oe} \, dv$$

$$= - \frac{\partial}{\partial t} \sum_K W_h(K,\Omega) \quad , \tag{6}$$

which simply states that the total energy density is conserved by the plasma-maser interaction between Langmuir waves and electrons.

Next, we consider the rate of decrease of ion-sound wave energy corresponding to the plasma-maser emission of Langmuir wave. The most dominant imaginary part contribution to the ion-sound waves comes from the polarization term as

$$I_m \varepsilon_\ell(k,\omega) = - \left(\frac{e}{m}\right)^2 \omega_{pe}^4 \sum_K \frac{|E_h(K,\Omega)|^2}{\varepsilon_0(k-K,\omega-\Omega)} \times I_m[A^2] \quad , \tag{7}$$

where

$$A = \int \frac{1}{(\omega - kv + i0)(\Omega - Kv)[\omega - \Omega - (k - K)v]} \frac{\partial}{\partial v} f_{0e} \, dv$$

$$\simeq - \frac{1}{\Omega^2} \int \frac{1}{\omega - kv + i0} \frac{\partial}{\partial v} f_{oe} \, dv \quad . \tag{8}$$

The plasma-maser interaction is effective even without the electron population inversion. Here, we assume the Maxwell distribution function for f_{oe} and obtain

$$I_m \varepsilon_\ell(k,\omega) = - \left(\frac{e}{m}\right)^2 \left[\frac{\omega_{pe}}{\Omega}\right]^4 \frac{2m^2 \pi \, c_s}{k|k|T^2} \left[\frac{m}{2\pi T}\right]^{1/2} \sum_K \frac{|E_h(K,\Omega)|^2}{\varepsilon_0(k-K,\omega-\Omega)} \quad , \tag{9}$$

where $c_s = (2T/M)^{1/2}$ is the phase velocity for ion-sound wave, T and ω_{pe} is the temperature and plasma frequency for electrons, M is the mass for the ion. Accordingly, the damping rate of the ion-sound wave due to the plasma-maser is

$$\gamma_\ell(k,\omega) = - \pi \omega \frac{k}{|k|} \left(\frac{k_e}{k}\right)^2 \left(\frac{m}{M}\right)^{1/2} \sum_K \frac{|E_h(K,\Omega)|^2}{4\pi N T} \quad , \tag{10}$$

here k_e and N are electron Debye wavenumber and electron number density, respectively. In deriving Eq.(10), we put $\varepsilon_0(k-K,\omega-\Omega) \simeq - (k/k_e)^2$. Accordingly, the rate of the change of the ion sound wave energy density [$W_\ell(k,\omega) \equiv |E_\ell(k,\omega)|^2/4\pi \times (k_e/k)^2$] reduces to

$$\frac{\partial}{\partial t} \sum_k W_\ell = 2 \sum_k \gamma_\ell W_\ell = - \frac{2\pi}{NT} \left(\frac{m}{M}\right)^{1/2} \sum_{K,k} \left(\frac{k_e}{k}\right)^2 \omega \frac{k}{|k|} W_\ell W_h \quad . \tag{11}$$

The Manley-Rowe relation [5] is widely believed to hold in nonlinear plasma wave phenomena. It is true that the relation is valid to the standard mode-mode couplings, viz. the three waves resonance and the nonlinear Landau resonance. One may think that the Manley-Rowe relation or the conservation of the total plasmon number is satisfied for the

plasma-maser process. However, as is shown below, it is violated and as a result an efficient energy up-conversion from the ion-sound to Langmuir wave is possible. The plasmon number for ion-sound $[N_\ell(k,\omega)]$ and for Langmuir wave $[N_h(K,\Omega)]$ is defined as

$$N_\ell(k,\omega) = \frac{W_\ell(k,\omega)}{\omega} \quad ,$$

$$N_h(K,\Omega) = \frac{W_h(K,\Omega)}{\Omega} \quad . \tag{12}$$

From Eq.(3), for the Maxwell electron distribution function, the rate of increase of the Langmuir wave energy density for mode (K,Ω) reduces to

$$\frac{\partial}{\partial t} W_h(K,\Omega) = \frac{3\pi}{NT}\left(\frac{m}{M}\right)^{1/2} K\,\Omega\, W_h(K,\Omega) \sum_k \frac{W_\ell(k,\omega)}{|k|}\left(\frac{k}{k_e}\right)^2 . \tag{13}$$

Inserting Eqs.(11) and (13) into Eq.(12), we obtain the rate of change of the plasmon number for ion-sound wave(k_0,ω_0) and Langmuir wave(K_0,Ω_0)

$$\frac{\partial}{\partial t} N_\ell(k_0,\omega_0) = -\frac{2\pi}{NT}\left(\frac{m}{M}\right)^{1/2}\left(\frac{k_e}{k_0}\right)^2 W_\ell(k_0,\omega_0)\,\frac{k_0}{|k_0|}\sum_K W_h(K,\Omega) \quad ,$$

$$\frac{\partial}{\partial t} N_h(K_0,\Omega_0) = \frac{3\pi}{NT}\left(\frac{m}{M}\right)^{1/2} K_0\, W_h(K_0,\Omega_0) \sum_k \frac{W_\ell(k,\omega)}{|k|}\left(\frac{k}{k_e}\right)^2 . \tag{14}$$

If we put $W_h(K,\Omega) = W_h(K,\Omega)\,\delta(K-K_0)\,\delta(\Omega-\Omega_0)$, $W_\ell(k,\omega) = W_\ell(k,\omega) \times \delta(k-k_0)\,\delta(\omega-\omega_0)$ in Eq.(14), then we find for $K_0 \ll k_0 \lesssim k_e$

$$\frac{\left|\frac{\partial}{\partial t} N_\ell\right|}{\frac{\partial}{\partial t} N_h} \simeq \frac{k_e^4}{k_0^3\, K_0} \gg 1 \quad . \tag{15}$$

Accordingly, we may conclude that the Manley-Rowe relation is violated for the plasma-maser interaction and as a result an efficient energy up-conversion from the low-frequency mode to the high-frequency mode is possible even for a normal unreversed electrons population. This is markedly different from the standard nonlinear Landau resonance where the Manley-Rowe relation is satisfied and the energy up-conversion is possible only for a reversed electrons population.

REFERENCES

(1) M.Nambu, Phys.Rev.Letters 34, 387 (1975).
(2) V.N.Tsytovich, L.Stenflo, and H.Wilhelmsson, Physica Scripta 11, 251 (1975).
(3) K.Nishikawa, J.Phys.Soc.Japan 29, 449 (1970).
(4) M.Nambu, T.Hada, S.N.Sarma and S.Bujarbarua, J.Phys.Soc.Japan 60, 3004 (1991).
(5) J.M.Manley and H.E.Rowe, Proc.of IRE 44, 904 (1956).

PHASE-SPACE TOPOLOGY IN THE DYNAMICS OF CYCLOTRON-MASERS

R. PAKTER, R. S. SCHNEIDER and F. B. RIZZATO
Instituto de Física - Universidade Federal do Rio Grande do Sul
Caixa Postal 15051
91500 Porto Alegre RS Brasil

With the advent of radiation generating systems like free-electron lasers, cyclotron autoresonance masers, gyrotrons, ion-channel lasers and others, a good deal of effort has been directed toward the analysis of the nonlinear interaction of relativistic particles and large amplitude electromagnetic waves. In most of the cases, quantities of interest like energy gain or energy exchange are obtained by considering the electron dynamics in given external wave fields. This kind of approximation can be fairly justified if one considers either waves with large enough amplitudes or beams with very tenuous densities, so that particles do not appreciably react back on the electromagnetic fluctuations. On the other hand, when these conditions are not satisfied, a self-consistent analysis is necessary where particles *and* fields are to be simultaneously treated as dynamical entities [1],[2]. The purpose of the present paper is to analyze cyclotron masers systems. To do so we consider a model in which a beam of homogeneously magnetized electrons propagating along a **z** axis coexists with an electromagnetic wave polarized along the **x** axis with the fast wave-vector lying along **z**. With that model we basically intend to show that the topology of the phase space in those cases where we disregard the dynamics of the fluctuating field may be very different from the one corresponding to the self-consistent situation where fields are also treated as dynamical entities. To begin with, let us write the Hamiltonian that governs the electron dynamics. If one writes the vector potential of the electromagnetic field as

$$\frac{e}{mc^2}A_x \equiv -\frac{1}{2}\sqrt{\rho}\, e^{i\sigma}\, e^{i(z-t)} + c.c. \tag{1}$$

where ρ and σ have a slow time dependence, e is the electron charge and where time and space have been normalized to ω and $\omega/c \approx k$ with ω and k respectively as the wave frequency and wave-vector, one obtains

$$\mathcal{H} = [1 + [P_x + \sqrt{\rho}\, cos(z - t + \sigma)]^2 + (x + P_y)^2 + P_z^2]^{1/2}, \tag{2}$$

with $\mathcal{H}/mc^2 \rightarrow \mathcal{H}$ and $\mathbf{P}/mc \rightarrow \mathbf{P}$, and where we assume $eB_{z,equilibrium}/mc \approx \omega$. The simpler form

$$\mathcal{H} = -I + \Gamma + \frac{\sqrt{\rho}\sqrt{2I}}{2\Gamma} cos(\phi + \sigma) \tag{3}$$

is obtained if now one performs a power series expansion in $\sqrt{\rho}$ considering only the leading order contribution and introduces new canonical variables defined by the relationships

$$P_x = \sqrt{2I}\, cos\phi,$$
$$P_z = P_z',$$

$$x = -P_y + \sqrt{2I}\, sin\phi$$
$$\phi + z - t \rightarrow \phi,$$
$$P_z \rightarrow P_z + I,$$
$$H \rightarrow H + I$$

and

$$z = z',$$

with $I \equiv P'_x$, $\phi \equiv x'$. Besides, we have used the cyclotron approximation $d_t(\phi + z(t) - t) \approx 0$, $d_t \equiv d/dt$ and

$$\Gamma \equiv \sqrt{1 + 2I + (P_z + I)^2}.$$

Were our interest to study the dynamics of electrons in given electromagnetic fields, we could stop with the calculations at the present stage. However, as said before, we wish to understand what happens when the dynamics of the fluctuational wave field is taken into consideration. In order to do that one has to derive the equations for the fields and then to analyze the whole set of dynamical laws on the same basis. So, let us proceed to see what can be done with those fields and how to derive all the relevant dynamical equations from a generalized Hamiltonian principle. From the Maxwell equation for the laser vector potential and the usual expressions for the current densities, considering eq.(1), assuming the radiation field to be slowly modulated in time and making use of the cyclotron and macroparticle [3] approximations, one can write

$$-id_t(\sqrt{\rho}\, e^{i\sigma}) = -\frac{e^2 k^3}{4\pi^3\, m\, S\, \omega^2} N_t \frac{\sqrt{2I}}{2\Gamma}\, e^{-i(\phi + z(t) - t)}, \tag{4}$$

where N_t is the total number of electrons over the periodicity length. Splitting eq.(4) into real and imaginary parts and noticing that the factor $\phi + z(t) - t$ is to be considered as the new canonical ϕ co-ordinate, leads to

$$d_t\rho = -2\omega_p^2 \frac{\sqrt{2\,I}}{2\Gamma} \sqrt{\rho}\, sin(\phi + \sigma), \tag{5}$$

and

$$d_t\sigma = -\omega_p^2 \frac{\sqrt{2\,I}}{2\Gamma}\, \frac{1}{\sqrt{\rho}}\, cos(\phi + \sigma). \tag{6}$$

where

$$\omega_p^2 \equiv \frac{e^2 \left(\frac{N_t k^3}{S}\right)}{2\pi^3\, m\, \omega_p^2}.$$

Now, if one re-scales ρ according to

$$\rho = \lambda\rho',$$
$$\lambda \equiv 2\omega_p^2,$$

the interesting and final conclusion is that *all* the relevant dynamical equations for both particles *and* fields can be derived from one generalized Hamiltonian given by

$$\mathbf{H} = -I + \Gamma + \frac{\sqrt{\lambda\rho}\sqrt{2I}}{2\Gamma} cos(\phi - \sigma'), \tag{7}$$

where ρ is the "momentum" corresponding to the wave field and σ' $(= -\sigma)$ is the canonically conjugated co-ordinate. If one drops the primes once again, the following canonical transformation

$$\phi - \sigma \rightarrow \phi$$
$$\rho \rightarrow \rho - I,$$

reduces the degrees of freedom (ρ is now a constant of motion) and allows to write a final effective Hamiltonian as

$$\mathbf{H} = -I + \Gamma + \frac{\sqrt{\lambda(\rho - I)}\sqrt{2I}}{2\Gamma} \cos\phi, \tag{8}$$

which is the function we shall analyze next. The key point of this paper is to compare the overall characteristics of the system with and without wave dynamics included. When such a dynamics is considered, the Hamiltonian is given by eq.(8) and when it is not, what one is really doing is to assume $\rho >> I$, approximating therefore the factor $\rho - I$ of $\mathbf{H}$ simply by ρ. So, by assuming small values of ρ, I and λ as to represent usual experimental conditions, from now one let us proceed with the comparative study focusing our atention on the calculation of fixed points for the dynamics in the following physically relevant situations; $P_z = 0$ and $P_z >> 1$.

(a) $P_z = 0$

In that case the fixed point equations indicate that $sin\phi_{fp} = 0$ and that the two values of I_{fp} (one for each value of $cos\phi_{fp}$) are to be calculated approximately from the relation

$$\rho - 2\, I_{fp} = 0, \tag{9}$$

which yields $I_{fp} = \rho/2$ in both cases. One can not satisfy eq.(9) under the assumption of absence of wave dynamics (in that case one should set $I_{fp} \rightarrow 0$ in eq.(9)) from which it is possible to conclude that there is a dramatic change of phase space topology between the two cases. These topological changes can be better appreciated from figs.1 and 2, where we plot the phase space corresponding to the cases without and with wave dynamics respectively. From fig.(1), it is particularly seen that some particles that have small initial energies may be accelerated to large final values of this quantity, for the curves of constant $\mathbf{H}$ with $\phi_{initial} = \pi/2(mod\, 2\pi)$ are open upwards. This process, known as the autoresonance one, is seen to be saturated for large values of I, when the dynamics of the wave field is included.

(b) $P_z \rightarrow \infty$

In this case, the fixed point is approximately determined by

$$1 + \frac{\lambda}{2P_z} \frac{(\rho \mp 2I_{fp})S}{\sqrt{2\lambda I_{fp}(\rho - I_{fp})}} = 0, \tag{10}$$

where $S \equiv cos\phi_{fp} = \pm 1$. From this equation it is possible to notice the following variety of situations: i) $S = +1$ with wave dynamics $\Rightarrow I_{fp} \approx \rho$; ii) $S = +1$ without wave dynamics $\Rightarrow$ no possible I_{fp}; iii) $S = -1$ with wave dynamics $\Rightarrow I_{fp} \approx 0$; iv) $S = -1$ without wave dynamics $\Rightarrow I_{fp} \approx 0$. In other words, in the cases of large values of P_z, there exists a root for "large" values of I which is not present when wave dynamics is not taken into account. Once again, like in the previous cases of small values of the momentum, a dramatic change in the topology of the phase space takes place. Such a change can be observed with help of figs.3 and 4, where once again we plot the phase space without and with wave dynamics respectively.

References

[1] F. B. Rizzato, Phys. Scripta, *in press*, (1992).

[2] R. Bonifacio, F. Casagrande and A. Airoldi, Optics. Comm. **80**, 370 (1991).

[3] K. R. Chen, J. M. Dawson, A. T. Lin and T. Katsouleas, Phys. Fluids **B3**, 1270 (1991).

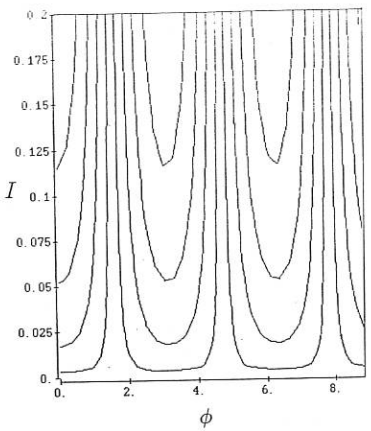

Fig.1 - Phase-space of the effective Hamiltonian for $P_z = 0.0$ without wave dynamics; $\lambda = 0.2$ and $\rho = 0.2$

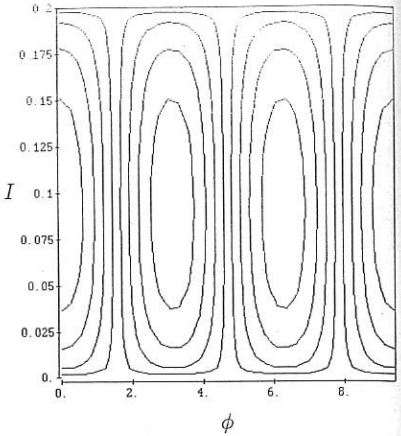

Fig.2 - The same as in fig.1 with wave dynamics included.

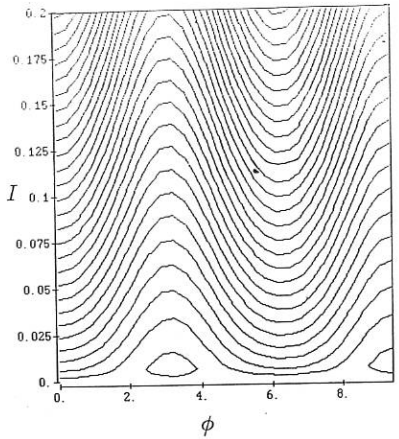

Fig.3 - Phase-space without wave dynamics for large values of P_z; $P_z = 30$. Other quantities as in the previous figures.

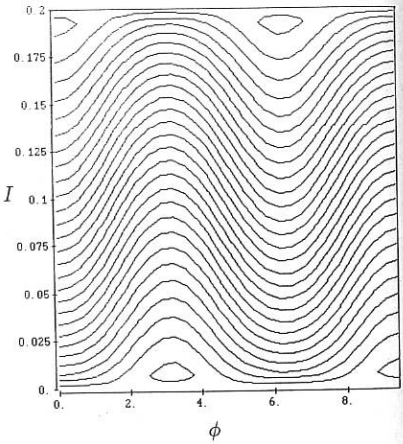

Fig.4 - The same as in fig.3 with wave dynamics included.

RF PRODUCTION OF LONG, DENSE PLASMA COLUMNS

Francis F. Chen and Gaétan Chevalier
Electrical Engineering Department and
Institute of Plasma and Fusion Research
University of California, Los Angeles, CA 90024-1594, U.S.A.

Novel accelerator concepts /1/ such as wake-field accelerators, plasma lenses, and inverse free-electron lasers, often call for uniform plasma sources of high, controllable densities of order 10^{14} cm^{-3} or above. The beat-wave concept, which needs the order of 10^{17} cm^{-3}, falls in a different category /2/. To produce 10^{14} cm^{-3} plasmas, we have been studying the use of helicon waves, which themselves are accelerators, in this case bringing primary electrons to their optimum energy by Landau damping /3/. Evidence for this absorption mechanism has been given previously /4/. Measurements on 4- and 2-cm diameter tubes /5/ showed that a right-hand helical antenna is more efficient than others, and that densities of order 10^{14} cm^{-3} can be attained at 60 mTorr of A and a field of 1.2 kG, using 2 kW of rf power at 27.12 MHz.

Creation of a plasma of 10^{14} cm^{-3} density is facilitated by experimental techniques not easily foreseen from theory. Ions are confined in a radial potential well but escape freely along the axial magnetic field B at the acoustic speed c_s. Electrons are confined by an axial potential well and are scattered out radially. To supply the ion losses, neutral gas must be injected into the discharge at a fast enough rate. We have previously found /5/ that a 4-cm diam tube housing a 2-cm diam plasma acts as a reservoir of gas which can feed radially into the plasma. The constriction of the plasma can be accomplished in three ways. An antenna wound helically in a direction to launch a right-hand polarized wave toward the midplane tends to produce a peaked density profile /5/. By reversing the endcoils and producing a cusp field at the antenna, we can produce a magnetic aperture limiter which is very effective in narrowing the column. We can also insert a carbon limiter into the tube to constrict the plasma directly. To optimize these effects, the apparatus was configured as shown in Fig. 1.

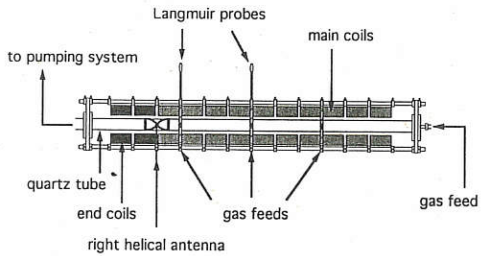

Fig. 1

Argon gas was fed in at four places along the tube. The endcoils near the antenna were controlled independently to shape the magnetic field there. To avoid overheating, both the field and the rf power were pulsed for 100-150 msec, with less than 5% duty factor. At these densities, the sputtering of tungsten probe tips would change the collection area during a run. This was remedied by using carbon tips (0.3 mm pencil lead), 1.5 mm long, centered in an alumina tube of 1.6 mm o.d. The probe was biased at −130 V with floating batteries, and it was made to follow potential fluctuations at the rf frequency by an rf choke with a resonance frequency around 30 MHz, connected within 5 cm of the probe tip. The probe was thus effectively terminated in 200

KΩ at rf frequencies, and in 50 Ω at low frequencies. Though the ion saturation current was calibrated against the density measured by microwave interferometry, the densities reported here are uncertain by ±10%, mainly due to variations in probe area.

The effect of varying the magnetic field shape is shown in Fig. 2, which gives the density on axis vs. voltage on the end coils for two antennas – a right-hand helical (R.H.) and a plane-polarized Nagoya Type III. The standard conditions were B = 600 G, p = 5.5 mTorr of argon, and P_{rf} = 1.9 kW at 27.12 MHz. A voltage of +40 gives a nearly uniform field; and −40, a strongly cusped field. The density from a plane-polarized antenna increases about a factor of 5 with a cusp field. Fig. 3 shows the density profiles with a uniform field, with the end coils off, and with the end coils reversed. At least part of the density increase is due to the peaking of the profile with cusped fields. The density increase is smaller with the R.H. antenna (Fig. 2), because this gives a peaked profile even in a uniform field.

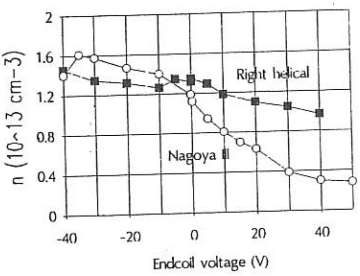

Fig. 2

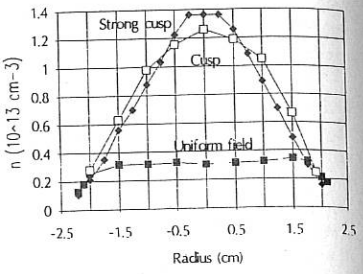

Fig. 3

We next investigated the effect of material limiters, carbon disks with holes of 1.2 and 2.0 cm. The density profiles with the 1.2-cm limiter are shown in Fig. 4 for a uniform B-field, and in Fig. 5 for a cusped B-field (end coils reversed). Other conditions were the same as above. Fig. 4 shows that the density was sensitive to the position of the limiter; a large increase in density occurred when the limiter was located just under the rear loop of the antenna, at −6 cm from the midplane of the antenna. When a cusped field was added (Fig. 5), the profile was more sharply peaked, and the density further increased, showing that a magnetic limiter is more effective. In this case, the position of the limiter was not important, except when it is located well downstream, near the probe (+22 cm). Restricting the column at that point decreased the density.

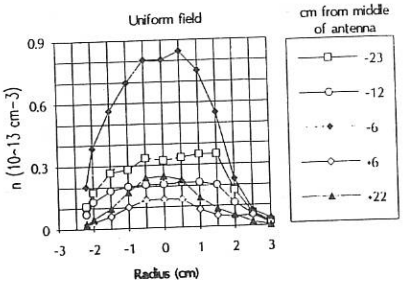

Fig. 4

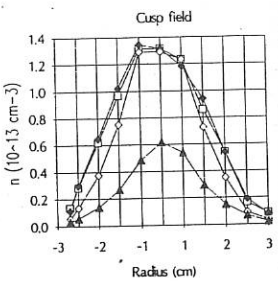

Fig. 5

The combined effect of magnetic and material limiters is shown in Fig. 6, which shows the density on axis under standard conditions for different positions of the 1.2-cm limiter as the endcoil voltage is varied. Since the limiter is effective at the rear end of the antenna (−6 cm), there is relatively little improvement with a cusp field. When the limiter is at the front end of the antenna, however, there is a great improvement with a cusped field, because the performance in a uniform field is so poor. These observations are not yet understood.

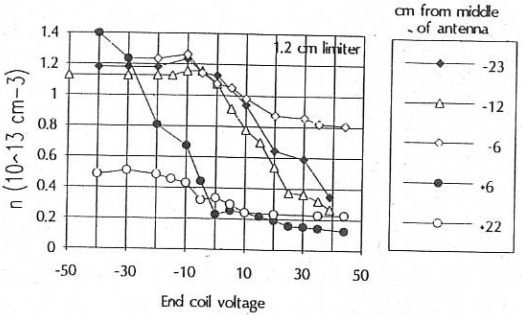

Fig. 6

Even a solid carbon block has an effect on the density, depending on its position. Fig. 7 shows density profiles with the block at the rear end of the antenna (−6 cm), far back near the pump (−22 cm), and in between (−12 cm). There is an increase in density at the −6 cm position. Possible explanations include image currents in the limiter, reflection of helicon waves by the limiter, and the recirculation of neutral atoms formed by recombination of ions on the surface. By comparison, Fig. 8 shows the performance of the limiter with a 2-cm diam hole. These data were for a uniform B-field.

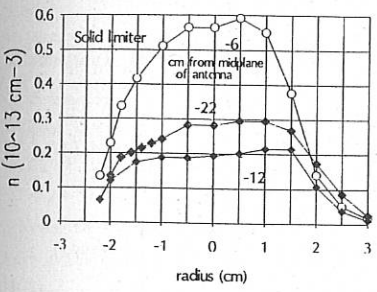

Fig. 7

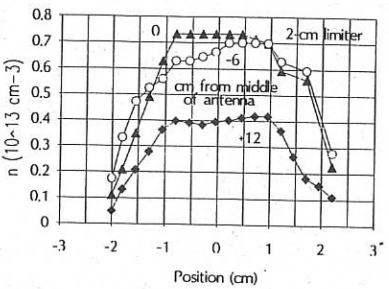

Fig. 8

To obtain the highest density with the available rf power, we operated at 1 kG with a cusped field, with no limiter, using a helical antenna and a probe located near it. The importance of gas feed is shown in the pressure scan of Fig. 9. The density pulse had a peak of about 5 msec, followed by a plateau for the remainder of the 100-msec pulse. The peak density did not vary with pressure above a few mTorr, but the plateau density fell off at low pressures, indicating a

deficiency in neutral gas. Apparently, unless the flow rate is very high, densities of order 10^{14} cm^{-3} are sustained only by the gas stored inside the tube, feeding radially into the plasma. Fig. 10 shows radial profiles at the peak and the plateau for the upstream probe, as well as for the downstream probe, which does not show a density spike at the beginning of the pulse. The field was increased to 1.2 kG. There was a large axial density gradient because of the high pressure of 20-30 mTorr. At normal operating pressure, the plasma is much more uniform along the axis.

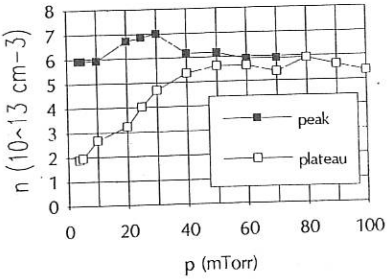

Fig. 9

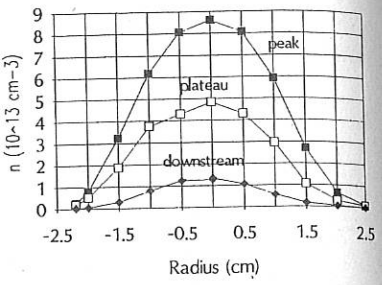

Fig. 10

Since there is no need for internal electrodes in this device, it should be possible to produce arbitrarily long plasma columns of density 10^{14} cm^{-3} by adding antennas periodically. This paper has shown the importance of magnetic field shaping near the antenna and of arranging for radial gas feed. Other investigators /6//7/ have found that, above a power threshold of 2-3 kW, the helicon discharge can burn out all the neutral atoms near the axis and constrict itself to a narrow, fully ionized column. We hope to add enough power to see this in the near future.

This work was supported by the National Science Foundation, Grant No. ECS-8901249.

/1/ F.F. Chen, "Laser Accelerators", in *Physics of Laser Plasma*, ed. by A.M. Rubenchik and S. Witkowski, Vol. 3 of *Handbook of Plasma Physics*, ed. by M.N. Rosenbluth and R.Z. Sagdeev, pp. 483-517 (Elsevier Science Publishers, B.V., Amsterdam, 1992).

/2/ F.F. Chen, "Excitation of Large Amplitude Plasma Waves", *Physica Scripta* **T30**, 14-23 (1990).

/3/ F.F. Chen, *Plasma Physics and Controlled Fusion* **33**, 339 (1991).

/4/ F.F. Chen and C.D. Decker, *Plasma Phys. and Controlled Fusion* **34**, 635 (1992).

/5/ F.F. Chen, *J. Vac. Sci. and Technol.* **10**, (Jul/Aug 1992).

/6/ P. Zhu and R.W. Boswell, *Phys. Fluids* **B3**, 869 (1991).

/7/ A. Komori, T. Shoji, K. Miyamoto, J. Kawai, and Y. Kawai, *Phys. Fluids* **B3**, 893 (1991).

PLASMA POTENTIAL FORMATION IN THE PRESENCE OF LOCALIZED RADIO-FREQUENCY ELECTRIC FIELDS

N.Y.Sato,[a] R.Hatakeyama, and N.Sato
Department of Electronic Engineering, Tohoku University
Sendai 980, Japan

Researches on plasma potential formation have recently attracted considerable attention in basic plasma, space plasma and fusion plasma physics. Electrostatic potential formations as a result of interaction between radio frequency (rf) fields and plasmas are of particular interest concerning effective plasma heating and confinement. Experiments on rf sustained electrostatic potential barrier like thermal barrier /1/ and rf plugging /2/ have been performed in open ended machines, resulting in reducing end plasma losses. In this connection it is basically significant to experimentally clarify the potential formation process in the presence of spatially localized rf fields. Here we demonstrate a clear potential formation along the magnetized plasma flow when externally-excited nonlinear electron plasma waves are generated.

A collisionless plasma, 5.0 cm in diameter, is produced in a single-ended Q machine, as shown in Fig.1. The plasma of density n_o=(5-50)$\times 10^6$ cm^{-3} (electron plasma frequency $\omega_{pe}/2\pi$=20-64 MHz) and electron temperature $T_{eo}\simeq$0.2 eV is confined radially by a uniform axial magnetic field B=2.3 kG. An electron plasma wave is excited by applying an external rf potential V_{RF} of a frequency $\omega/2\pi$ (=10-100 MHz) to a 5-cm-diam ring antenna, which is axisymmetrically set near the center of the plasma column (z=0 cm). The plasma with a speed $V_o\simeq 2.7\times 10^5$ cm/sec flows downstream almost without being disturbed by the antenna when V_{RF}=0 V.

The electron wave is observed to symmetrically propagate from the exciter toward the upstream (z<0) and downstream (z>0) sides along the plasma column, satisfying the linear dispersion relation for $V_{RF}\lesssim$50 mV ($\ll T_{eo}/e$). With an increase in V_{RF} over T_{eo}/e, well-known nonlinear phenomena such as

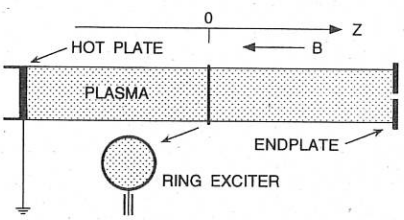

Fig.1: Schematic of experimental setup.

amplitude oscillation appear /3/, and asymmetric propagations simultaneously occur. For much larger values of V_{RF}, the wave is measured to damp even more strongly near the exciter and the wavelength at $z>0$ becomes shorter than at $z<0$, as typically shown at the top of Fig.2. When $\omega/2\pi$ and n_o are changed, this nonlinear behavior of the wave is typically observed under the condition that $P=\omega/\omega_{pe}<1$.

Measurements of the plasma potential ϕ profile for the case of $P<1$ show that ϕ at $z>0$ is varied to be deeply negative and ϕ around $z=0$ becomes a positive maximum in spite of almost no change of ϕ at $z<0$, as given in Fig.2. A large-scale potential drop, $\Delta\phi=\phi(z<0)-\phi(z>0)\simeq 20T_{eo}/e$, is formed in the result. A drastic increase of the electron temperature T_e is also observed on the downstream side [$\Delta T_e=T_e(z>0)-T_e(z<0)\simeq 30T_{eo}$]. A density drop $\Delta n\simeq 0.2n_o$ arises around $z=0$ in addition to a plasma loss over the whole column. Here, the characteristic scale length of $\Delta\phi$ observed is several ten times the Debye length, which is nearly equal to the theoretical width of classical electric double layer.

In the case of $P>1$, no particular changes of both ϕ and T_e are recognized even for $V_{RF}>>2T_{eo}/e$ on the upstream and downstream sides except a region near the exciter, where ϕ and T_e are increased to a positive and a high value, respectively, as shown in Fig.3. Instead, n at $z<0$ becomes larger than n_o and the resultant density drop is formed, indicating a clear plugging effect for the plasma flow along the B-field. It is to be noted that the electron wave can not propagate over the exciter because of the

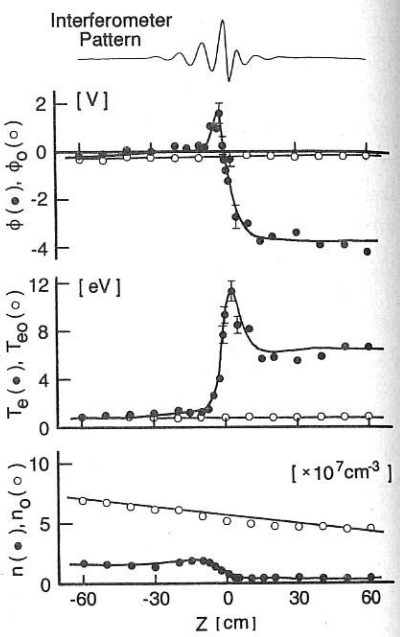

Fig.2: Spatial profiles of the electrostatic potential, electron temperature and plasma density. V_{RF}=8 V, and the subscript "o" refers to a value with V_{RF}=0 V. $n_o\simeq 5\times 10^7$ cm^{-3}. $\omega/2\pi$=45 MHz (P=0.71).

strong Landau damping for $P>1$ [seen at the top of Fig.3].

Typical temporal evolutions of the ϕ profile are presented for the case of $P<1$ in Fig.4. Applying V_{RF} ($t>0$), ϕ at both $z>0$ and $z<0$ are positively raised with the profile symmetrical up to $\simeq$60 μs (a few tens of ion plasma period), while ϕ near the exciter almost keeps constant. This potential increase over the exciter suggests that electrons are axially repelled by the strong damping of the nonlinear electron wave. However, ϕ near the exciter increases to a positive value up to $\simeq$150 μs during the whole decrease of ϕ. At the second stage (t=150-∞ μs), ϕ at $z>0$ becomes deeply negative and ϕ at $z<0$ approaches the value before applying V_{RF} with ϕ near the exciter positively constant. Not only electrons but also ions can be reflected near the exciter under such a potential structure. For $P>1$, ϕ and T_e near the exciter monotonously increase as a function of time. Independently of P, the potential profile attains to a stationary state around 700 μs, which is of the order of the plasma relaxation time (plasma-length/V_o). According to time-resolved measurements of electron energy distributions, the high-temperature Maxwellian distribution yielding ΔT_e and also Δn is formed within 100-200 μs well before the $\Delta\phi$ generation.

In our experiment, the large-amplitude localized rf electric fields are present in the magnetized collisionless plasma flowing toward the endplate. Since plasma parameter variations near the exciter are almost independent of the frequency applied (or P), near fields of the antenna are expected to predominantly determine the phenomenon in the vicinity of the exciter. The localized rf field with the axial gradient provides a ponderomotive force repelling electrons. Thus there should appear a potential increase in this region of the localized rf field. A part of the ions are reflected by this local increase in ϕ. As a result, n decreases in the downstream

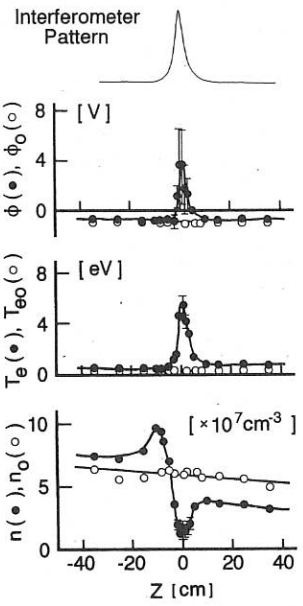

Fig.3: Spatial profiles of the plasma parameters. $\omega/2\pi$=95 MHz (P=1.49). Other parameters are same as those of Fig.2.

region. As shown in Fig.3, however, a large $\Delta\phi$ ($>>T_{eo}/e$) is not generated by only the plugging effect due to the ponderomotive force. On the other hand ($P<1$), the enhanced wave damping gives rise to a number of detrapped electrons /3/. All electrons passed through $z=0$ are largely accelerated and heated in the region of $z>0$, while the electron reflected at $z=0$ are not heated in the hot plate side because of the high electron thermal conductivity. The electron energy increase implies a decrease of the electron density in the region of $z>0$ because the electron flux is conserved. Since the ion density must decrease at $z>0$ to satisfy the charge neutrality, the potential becomes negative at $z>0$ to accelerate ions, yielding the $\Delta\phi$. The $\Delta\phi$ generation is essentially ascribed to the nonlinear electron acceleration (or heating) by waves in the downstream region.

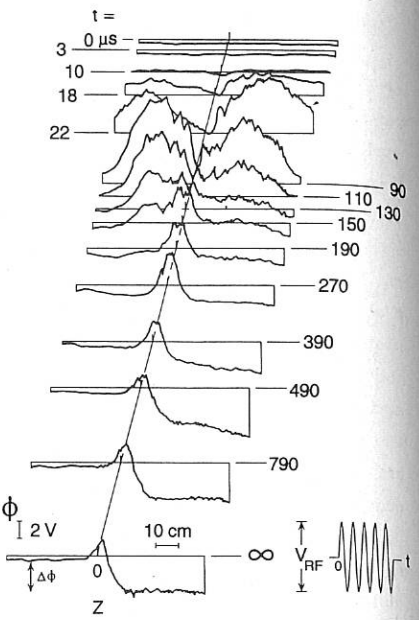

Fig.4: Temporal evolution of potential profile ϕ at $n_o \simeq 5\times 10^7$ cm^{-3}, $\omega/2\pi$=45 MHz (P=0.71), and V_{RF}=8 V.

In summary, a potential structure with local hill and large drop has been observed across a localized rf electric field in a collisionless plasma flow. The electrostatic potential formation is considered to result from the electron acceleration due to the highly nonlinear electron wave in addition to the ponderomotive force.

REFERENCES

(a) Permanent Address: Department of Electrical and Electronic Engineering, Ibaraki University, Hitachi 316, Japan.

/1/ Hershkowitz *et al.*, Phys.Rev.Lett. 49, 1489(1982).

/2/ H.Fujita *et al.*, J.Phys.Soc.Jpn. 57, 504(1987).

/3/ J.H.Malmberg and C.B.Wharton, Phys.Rev.Lett. 19, 775(1967); N.Sato *et al.*, Phys.Rev.Lett. 37, 1684(1976).

INWARD AND OUTWARD PLASMA MOTION INDUCED BY AXISYMMETRIC ELECTROMAGNETIC FIELDS AROUND THE ION CYCLOTRON FREQUENCY

R. Hatakeyama, S. Miyakuni, N. Y. Sato,* and N. Sato

Department of Electronic Engineering, Tohoku University, Sendai 980, Japan

ABSTRACT: Large-scale plasma motions across a magnetic field are observed in the vicinity of an antenna which inductively generates axisymmetric radio-frequency fields. The phenomenon is due to the ion cyclotron resonance under the antenna near-zone nonuniform electromagnetic fields.

To understand mechanisms of impurity production during rf plasma heating is a topic of considerable contemporary interest.[1] An ion-Berstein-wave heating is observed to result in a peaked density profile and plasma-confinement improvement, although the mechanism is not elucidated.[2] It is basically important to clarify rf induced plasma-transport processes in the vicinity of powered antennas. Here we present a significant finding of inward and outward plasma motion induced by axisymmetric rf fields around the ion cyclotron frequency.

Experiments are carried out in a single-ended Q machine, where a potassium plasma of $n \simeq 10^{10}$ cm^{-3} and $T_e \simeq 0.2$ eV is produced on a hot tungsten plate in a uniform magnetic field $B_0 =$ 1.5-3.5 kG. The plasma (4 cm in diameter) flows toward a negatively biased endplate at a distance of 142 cm from the hot plate. An antenna consisting of a 1.2-cm-long solenoid (6.9 cm in average diameter, 4×5 turns) is set at distance 54 cm from the hot plate. Faraday shields (4.6 cm in innerdiameter) are mounted on the antenna to allow magnetic coupling and excitation of cylindrically symmetric rf mode. The frequency ratio ω/ω_{ci} to the ion cyclotron frequency $\omega_{ci}/2\pi$ is varied by changing the B-field ($\omega/2\pi$=0.1 MHz: applied frequency). Profiles of near-zone electromagnetic fields are calculated by using the exact dyadic Green's function for the cylindrical structure[3] in case of a typical antenna rf current

$\hat{I}_A$=60 A (amplitude). The oscillating axial magnetic field just under the antenna (z=0) is almost constant ($\hat{B}\simeq$230 G) within the plasma radius ($r\lesssim$2 cm), and the azimuthal electric field simply increases from the center ($\hat{E}_\theta$=0 V/cm) toward the antenna edge (1 V/cm at r≃1.5 cm). They rapidly damps in the axial direction, almost disappearing beyond |z|=10 cm (z>0: on the downstream side toward the endplate.

Langmuir probe measurements in the vicinity of the antenna show that small density perturbations are induced for the case of ω/ω_{ci}<1 or >1 even when large-amplitude rf fields are applied to the plasma. However, a large-scale density modification is caused as ω/ω_{ci} approaches to unity. The maximum modulation on the order of 100 % is observed for $0.95<\omega/\omega_{ci}\lesssim 1.05$ and $\hat{I}_A\gtrsim$60 A. Typical density profiles at z≃0 are presented as a function of time in Fig.1 for the case of ω/ω_{ci}=1.05 and $\hat{I}_A$=60 A. The profile is periodically modified to be largely peaked and hollow in strict correspondence with the applied rf period 2π/ω (=10 μsec). An ion temperature $T_{i\perp}$ perpendicular to the B-field at z≃0 is observed to oscillate strongly with the rf period when ω/ω_{ci} approaches to unity, as shown in Fig.2(a) for $\hat{I}_A$=60 A. Here $T_{i\perp}$ is estimated from e-folding slope of the ion energy ditribution

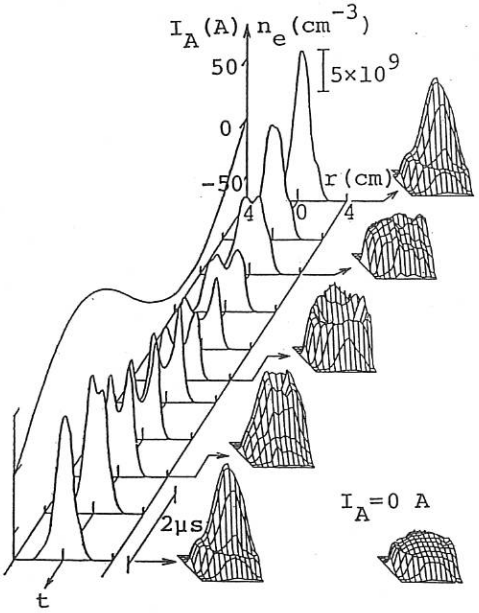

Fig.1. A temporal evolution of plasma density profile at z=2 cm. A profile without rf is also shown.

measured by a grided energy analyzer. Radial profiles of $T_{i\perp}$ for typical phases are given in Fig.2(b). High-energy ions concentrate near the center of the plasma cross section at a phase, while they come up to the antenna edge after half a period. Time-averaged $T_{i\perp}$ radially increases a little bit toward the antenna edge, while $T_{i\perp}$ for $\hat{I}_A$=0 A is almost constant (≃0.3 eV). The result implies that ions strike the antenna, leading to the impurity generation.

It is observed that the electrostatic potential becomes positive in the antenna region, the difference of which (0.5-1 V) is comparable to the ion flow energy. Since the estimated ponderomotive potential at ω/ω_{ci}≃1 is also comparable to the flow energy, the plasma potential increase may be attributed to the ion deceleration by the axial ponderomotive force.

Ion trajectories around the cyclotron resonance are computed by numerically solving the equation of motion in order to clarify a mechanism for the phenomenon observed. Figure 3 depicts the trajectory for the typical electromagnetic field profile at z=0 ($\hat{B}/B_0$=0.09) as described previously, where the ion drifts from an initial position toward the antenna edge with its Larmor radius increasing. More importantly, the ion at the typical initial position never overshoots the axisymmetry center. These ion behaviors are insensitive to initial phase of the ion velocity for larger rf fields. In our experiments most of the ions flowing along the B-field are considered to circulate several times between the column center

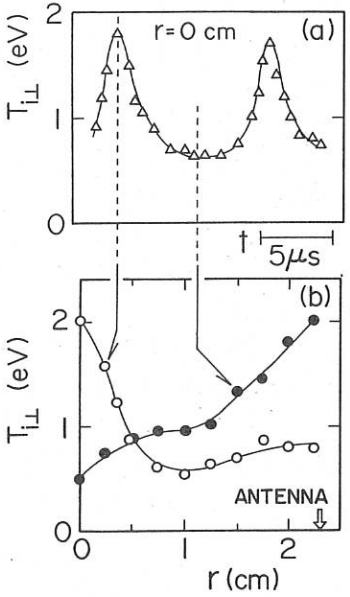

Fig. 2. A temporal change of perpendicular ion temperature at z=2 cm (a), and radial profiles for typical phases (b).

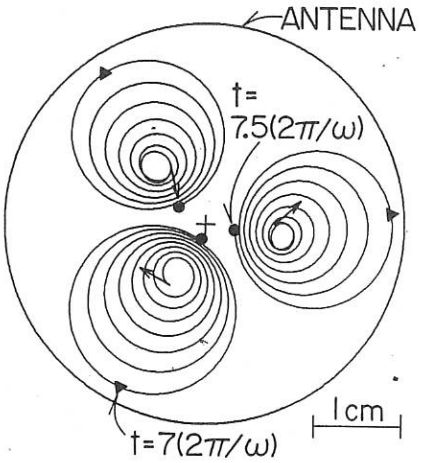

Fig.3.
Ion trajectories computed for various initial phases of a speed 1.2×10^5 cm/sec (arrows).

and edge due to the cyclotron resonance during passing through the antenna region (≃50 μsec), where the ion-flow speed is greatly reduced by the axial ponderomotive force. Since electrons can neutralize ions by crossing the B-field at the conducting end (≃4 μsec), strong radial motions arise in the plasma near the antenna, as if a collective mechanism acts.

In summary, nonuniform axisymmetric-fields around the ion cyclotron frequency induce a large-scale plasma motion across the B-field with the rf period. Our results imply an important rf-induced plasma transport, being instructive for understanding impurity generation mechanisms or peaking phenomena in ion-cyclotron heating experiments.

We acknowledge technical assistances from H. Ishida.

REFERENCES

*Present address: Department of Electrical and Electronic Engineering, Ibaraki University, Hitachi 316, Japan.

[1]A. Messian et al., Plasma Phys. Controlled Fusion 31, 921(1989); I. S. Lehrman et al., ibid. 32, 518(1990); S. Puri, Phys. Rev. Lett. 61, 959(1988); J. R. Myra et al., Nucl. Fusion 30, 845(1990).

[2]M. Ono et al., Phys. Rev. Lett. 60, 294(1988); J. D. Moody et al., ibid. 60, 298(1988).

[3]C. T. Tai, Dyadic Green's Function in Electromagnetic Theory (Intext Educational Publishers, London, 1971), p.81.

The Exact and Drift Hamiltonian

Q. Yao Department of Physics, College of William and Mary, Williamsburg, Va 23187

A. H. Boozer Department of Physics, College of William and Mary, Williamsburg, Va 23187
Max-Planck-Institut für Plasmaphysik, D-8046 Garching bei München, Germany

Abstract The Hamiltonian of the exact trajectory and first order corrections to the standard drift Hamiltonian are given in the Boozer coordinates for vacuum magnetic field with magnetic surfaces. The exact Hamiltonian depends on both the field strength and the shape of the magnetic surfaces while the standard drift Hamiltonian depends only on the field strength. The first order correction, in gyroradius to system size, to the standard drift Hamiltonian depends in a generic way on the metric tensor of the magnetic coordinates, as does the exact Hamiltonian.

The speed and efficiency with which the drift equations can be integrated has mandated their use for studying the trajectories of charged particles in complicated magnetic fields. An extreme example of such a study is the effect of toroidal asymmetries on the confinement of fusion α's. Fusion α's have a slowing down time that is of order $\left(\varepsilon^4\Omega\right)^{-1}$ with Ω the gyrofrequency and ε the ratio of their gyroradius to the system size, $\varepsilon \sim \rho/a$. Unfortunately, the standard derivation of the drift equations, which is due to Alfvén,[1] is only guaranteed to be valid for a time $(\varepsilon\Omega)^{-1}$. Despite the obvious importance, there has been little study of the accuracy with which the drift trajectories approximate the exact particle trajectories, which is the subject of this paper.

We call the Hamiltonian that most accurately describes the guiding center motion using only four canonical coordinates the guiding center Hamiltonian, H_g. The exact Hamiltonian H_e for the particle trajectories, which has six canonical coordinates, can be written as the sum of the guiding center Hamiltonian H_g and a perturbation H_e', which is chosen to be as small as possible,

$$H_e\left(\mu,\theta_g,\boldsymbol{P},\boldsymbol{Q}\right)=H_g\left(\mu,\boldsymbol{P},\boldsymbol{Q}\right)+H_e'\left(\mu,\theta_g,\boldsymbol{P},\boldsymbol{Q}\right).$$

The four canonical coordinates of the guiding center Hamiltonian are $(\boldsymbol{P},\boldsymbol{Q})$, the magnetic moment is $\mu \approx mv_\perp^2/2B$, and the canonically conjugate gyrophase is θ_g. As a field becomes

spatially uniform $\varepsilon \to 0$, the evolution of the magnetic moment goes to zero faster than ε to any power,[2,3] which implies, using $d\mu/dt = -\partial H_e'/\partial \theta_g$, that the perturbation H_e' scales as $exp(-c_0/\varepsilon)$ with c_0 a positive constant.

The standard drift Hamiltonian H_d, which is equivalent to the drift equations of Alfvén, differs from the guiding center Hamiltonian H_g by H_g',

$$H_g(\mu, \boldsymbol{P}, \boldsymbol{Q}) = H_d(\mu, \boldsymbol{P}, \boldsymbol{Q}) + H_g'(\mu, \boldsymbol{P}, \boldsymbol{Q}).$$

The perturbation H_g' has a magnitude of order εH_d.

The importance of the term H_g' is made clearer if one uses the magnetic coordinates (ψ, θ, φ) that were introduced by Boozer[4,5] to study particle drift motion. Boozer found that in these coordinates the standard drift Hamiltonian H_d depends on the complexity of the magnetic field structure only through the magnetic field strength $B(\psi, \theta, \varphi)$.[6] We find that both the exact Hamiltonian H_e and the lowest order in ε expansion of H_g' depend on the metric tensor g^{ij} of the transformation from the ordinary spatial coordinates $\boldsymbol{x}$ to the magnetic coordinates (ψ, θ, φ). The importance of this property of the drift equations is manifest for the quasi-helically symmetric stellarator in which the field strength has the form $B(\psi, \theta - N\varphi)$ with N an integer but the metric tensor g^{ij} depends in a complicated way on all three spatial coordinates.[7,8] For quasi-helical symmetry, the standard drift Hamiltonian H_d has an exact symmetry, and a conserved canonical momentum P_h, that does not exist for either the exact Hamiltonian H_e or the guiding center Hamiltonian H_g. Indeed, we find that the lowest order in ε expansion of H_g' depends on the metric tensor g^{ij} in a generic way and breaks the the invariance of P_h. Although quasi-helical symmetry is broken by terms of order ε in the Hamiltonian, the primary effect is an oscillation in value of the canonical momentum P_h rather than a total loss of this invariant.

To explain these results in more detail we assume a curl-free magnetic field that is written in the forms $\boldsymbol{B} = \nabla\psi \times \nabla\theta + \iota(\psi)\nabla\varphi \times \nabla\psi$ and $\boldsymbol{B} = \mu_0 G_0 \nabla\varphi$ given by Boozer.[4] One can show that ψ is the toroidal flux, $-\chi$ is the poloidal flux, θ is the poloidal angle, φ is the toroidal angle, and G_0 is the current, in ampere-turns, flowing in the external coils. The rotational transform is $\iota = d\chi/d\psi$. It is useful to define $\boldsymbol{e}_s = \nabla\theta - \iota\nabla\varphi$, so $\boldsymbol{B} = \nabla\psi \times \boldsymbol{e}_s$.

The metric tensor g^{ij} can be given in terms of $g^{\psi} = \nabla\psi \cdot \nabla\psi$, $g^{s} = e_s \cdot e_s$, $g^{c} = \nabla\psi \cdot e_s$, the field strength B^2, and the external current G_0. It is a general result of the canonical transformation theory that if the position x is given as a function of coordinates ξ^i, $x = x\left(\xi^1, \xi^2, \xi^3\right)$, the canonical coordinates x, p of a Hamiltonian can be canonically transformed to ξ^i, p_{ξ^i} by letting $p_{\xi^i} = p \cdot \partial x / \partial \xi^i$. The theory of coordinate transformations implies $\nabla\xi^i \cdot \partial x / \partial \xi^j = \delta^i_j$. The linear momentum mv can be written in a covariant representation

$$mv = mv_{\|}B/B + ese_s - p_s\nabla\psi,$$

with the particle charge e, and the canonical momentum $p = mv + eA$ with the vector potential $A = \psi\nabla\theta - \chi\nabla\varphi$. One can then show that the exact Hamiltonian, $H_e = mv^2/2$, has canonical coordinates (s, Θ, φ) and canonical momentua p_s, $P_\Theta = e\Psi = e(\psi + s)$, and $p_\varphi = (\mu_0 G_0/B)mv_{\|} - e\chi - es\iota$. In these canonical coordinates, the exact Hamiltonian is

$$H_e\left(p_s, s; P_\Theta, \Theta; p_\varphi, \varphi\right) = \frac{1}{2m}\left(\frac{B}{\mu_0 G_0}\right)^2\left[p_\varphi + e\chi + es\iota\right]^2 + \frac{1}{2m}\left[e^2 g^s s^2 - 2eg^c s p_s + g^{\psi} p_s^2\right].$$

If the magnetic field is uniform in space, one can easily show that Ψ and Θ are constants of the motion and are the coordinates of the center of the circle about which a particle located at (ψ, Θ) gyrates, the coordinate φ advances due to the motion along the field lines, and the canonical coordinates p_s and s oscillate at the gyrofrequency.

To obtain Hamiltonians that are in the forms that were discussed earlier, we use a generating function to effect a transformation from the (p_s, s) coordinate pair to the (μ, θ_g) pair. This canonical transformation makes changes of order ε^2 to the $\left(P_\Theta, \Theta; p_\varphi, \varphi\right)$ canonical coordinates, which become the (P, Q) coordinates. If one is retaining only the lowest order in ε expansion of H'_g, one need not make a distinction between (P, Q) and $\left(P_\Theta, \Theta; p_\varphi, \varphi\right)$. The expressions that we obtain for H_d and the lowest order expansion of H'_g are

$$H_d = \frac{1}{2m}\left(\frac{B(\Xi)}{\mu_0 G_0}\right)^2\left[p_\varphi + e\chi(\Psi)\right]^2 + \mu B(\Xi),$$

and $H_g' \approx \left[p_\varphi + e\chi(\Psi)\right]\Delta(\Xi)$ with $\Xi = (\Psi, \Theta, \varphi)$, $\Psi = P_\Theta / e$ and

$$\Delta = -\frac{\mu B(\Xi)}{2e(\mu_0 G_0)^2}\left[\frac{d\iota(\Psi)}{d\Psi} g^\Psi(\Xi) + \left(\iota\frac{\partial}{\partial\Theta} + \frac{\partial}{\partial\varphi}\right)g^c(\Xi) - \frac{g^c(\Xi)}{g^s(\Xi)}\left(\iota\frac{\partial}{\partial\Theta} + \frac{\partial}{\partial\varphi}\right)g^s(\Xi)\right].$$

One of the biggest differences between the exact Hamiltonian and the standard drift Hamiltonian is that the exact Hamiltonian depends on the metric tensor elements while the standard drift Hamiltonian does not. The first order correction is of great interest because it depends on the metric tensor elements in a generic way. The generic dependence follows from the fact that the elements of the metric tensor must be periodic functions of (Θ, φ). Whenever the symmetry of the exact Hamiltonian H_ϵ is broken by the metric, the symmetry of the guiding center Hamiltonian H_g is also broken.

Acknowledgments

Part of this work was performed while one of the authors, Q. Yao, was a visitor at the University of Wisconsin Torsatron/Stellarator Laboratory. The author had useful discussions with the colleagues at the Laboratory. The authors thank the U.S. Department of Energy for support under Grant No. DE-FGO5-84ER53176.

References

/1/ H. Alfvén, Ark. Mat. Astron. Fys. **27A**, 1 (1940)

/2/ M. Kruskal, in *Pendiconti del Terzo Congresso Internazionale sui Fenomeni D'Ionizzazione nei Gas tenuto a Venezia* (Societa Italiana di Fisica, Milan, 1957), p.56.

/3/ L. D. Landau and E. M. Lifshitz, *Mechanics*, 3rd ed. (Pergamon, New York, 1976), p. 159.

/4/ A. H. Boozer, Phys. Fluids **24**, 1999 (1981); Phys. Fluids **25**, 520 (1982)

/5/ G. Kuo-Petravic, A. H. Boozer, J. A. Rome and R. H. Fowler, J. Comp. Phys. **51**, 261 (1983)

/6/ A. H. Boozer, Phys. Fluids **27**, 2441 (1984)

/7/ J. Nührenberg and R. Zille, Phys. Lett. **A129**, 113 (1988)

/8/ D. A. Garren and A. H. Boozer, Phys. Fluids **B3**, 2822 (1991)

COLLISIONLESS DRIFTWAVES IN ANISOTROPIC CYLINDRICAL PLASMAS

J. Korn and H. Schamel
Physikalisches Institut, Universität Bayreuth
W 8580 Bayreuth, Germany F. R.

An integral formulation for the normal mode structure of electrostatic drift waves in cylindrical and slab geometry is developed. No drift ordering is assumed nor is the mode frequency ω assumed to be ordered compared with the ion gyrofrequency Ω_i. Two extensions are presented, namely anisotropic temperatures and arbitrary density and temperature profiles. A local analysis of the η_i-mode is performed yielding a dispersion relation. It is evaluated by means of a four-pole approximation of the plasma dispersion function to get growth rates. Furthermore a Nyquist technique is applied resulting in a stability criterion for $\eta_{i\|}$. As an application, the concept of maryinal stability combined with the requirement of a minimum critical threshold is used for profile determination. Finally for the isotropic case, the absolute and convective character of unstable modes is discussed.

I. General Integral Formulation for Collisionless Drift Waves

We consider the stability of an infinitely long azimuthally symmetric collisionless cylindrical plasma imbedded in an uniform axial magnetic field $\vec{B}_0$. The equilibrium distribution functions for the ions and electrons are chosen to be of the form:

$$f_{s0} = \left(\frac{M_s}{2\pi}\right)^{\frac{3}{2}} \frac{n_{s0}(R)}{T_{s\perp}(R)T_{s\|}^{\frac{1}{2}}(R)} \exp\left[-\frac{M_s}{2}\left(\frac{v_\perp^2}{T_{s\perp}(R)} + \frac{v_\|^2}{T_{s\|}(R)}\right)\right]. \tag{1}$$

They are exact solutions of the VLASOV-equation since $v_\perp$, $v_\|$ and R are constants of motion, where R represents the radial coordinate of the guiding center. It is a generalization of MARCHAND et al. /1/ due to the anisotropy and the R-dependence of the temperatures in (1).
We assume electrostatic perturbations of the form

$$\phi_1 = \tilde{\phi}(r) \exp\left[i\left(m\theta + k_z z - \omega t\right)\right] \tag{2}$$

with the azimuthal mode number m, wave number k_z and wave frequency ω. Linearizing the perturbed VLASOV-equation, we get the response f_{s1} of the system by integrating along the unperturbed helical particle trajectories. In this solution the rather complicated time-dependence of the integrand can be handled by writing (2) as a superposition of plane waves, an idea suggested by /1/. This means that any perturbed quantity g_1 is written in the form:

$$\begin{aligned} g_1 &= \tilde{g}(r,\theta) \exp\left[i\left(k_z z - \omega t\right)\right] \\ \tilde{g}(r,\theta) &= \frac{1}{2\pi}\int_0^\infty dk_\perp k_\perp \int_0^{2\pi} d\alpha \hat{G}(\vec{k}_\perp) \exp\left(i\vec{k}_\perp \cdot \vec{r}\right) \\ \hat{G}(\vec{k}_\perp) &= \hat{g}(k_\perp)\exp\left(im\alpha\right) \end{aligned} \tag{3}$$

where $\vec{r}$, $\vec{k}_\perp$ are the position and wave vectors in a plane perpendicular to the cylinder axis. α is the azimuth of $\vec{k}_\perp$. The solution reads, dropping subscripts:

$$\begin{aligned} \tilde{f} = & -\frac{qf_0}{T_\perp}\tilde{\phi} - \frac{i}{2\pi}\int_{-\infty}^{t} dt' \int_0^\infty dk'_\perp k'_\perp \int_0^{2\pi} d\alpha' \hat{\phi}(k'_\perp) \cdot \\ & \cdot \exp\left[i\left(m\alpha' + \vec{k}'_\perp \cdot \vec{R} + \vec{k}'_\perp \cdot \frac{\hat{b}\times\vec{v}(t')}{\Omega} + \left[k_z\left(z(t')-z\right) - \omega\left(t'-t\right)\right]\right)\right] \cdot \\ & \cdot \left\{\omega\frac{qf_0}{T_\perp} - k_z\frac{qf_0}{T_\perp}\left(1-\frac{T_\perp}{T_\|}\right)v_\| - \frac{1}{B_0}k'_\perp \sin\left(\alpha'-\Theta\right)\frac{\partial f_0}{\partial R}\right\} \end{aligned} \tag{4}$$

Max-Planck-Institut für Plasmaphysik
8046 Garching bei München

In (4), Θ is the azimuth of the position vector of the guiding center $\vec{R}$. Making use of (3) and integrating over the velocity, the FOURIER-transform $\hat{N}(\vec{k}_\perp)$ of the perturbed density is obtained:

$$\begin{aligned}\hat{N}(\vec{k}_\perp) &= -\int_0^\infty dRR\int_0^\infty dk_\perp' k_\perp' \hat{\phi}(k_\perp')\sum_j J_{m+j}(k_\perp R)J_{m+j}(k_\perp' R)\frac{qn_0}{T_\perp}\cdot \\ &\cdot\left\{\Gamma_j(b_1,b_2)\left[1+\zeta_0 Z(\zeta_j)+(1-\frac{T_\perp}{T_\parallel})(1-\zeta_j Z(\zeta_j))\right]-\right. \\ &\left.-\frac{T_\perp}{qn_0}\frac{m+j}{|k_z|B_0 R}\frac{T_\perp^{\frac{1}{2}}}{v_{th\perp}}\frac{\partial}{\partial R}n_0 T_\parallel^{-\frac{1}{2}} Z(\zeta_j)\Gamma_j(b_1,b_2)\right\}\exp\left[i\,(m\alpha)\right] \qquad (5)\end{aligned}$$

with
$J_n(x)$ BESSEL-function of first kind and n-th order, $I_n(x)$ modified BESSEL-function of first kind and n-th order, $\Gamma_n(x,y) := I_n(\frac{xy}{2})\exp(-\frac{x^2+y^2}{4})$, $Z(z) := 2i\exp(-z^2)\int_{-\infty}^{iz} dt\exp(-t^2)$ plasma dispersion function, $v_{th\parallel,\perp} := \sqrt{\frac{2T_{\parallel,\perp}}{M}}$ parallel and perpendicular thermal velocity, $\zeta_j := \frac{\omega - j\Omega}{|k_z v_{th\parallel}|}$, $b_1 := \frac{v_{th\perp}}{\Omega}k_\perp$, $b_2 := \frac{v_{th\perp}}{\Omega}k_\perp'$.
Inserting $\hat{N}(\vec{k}_\perp)$ into the FOURIER-transformed POISSON's equation we obtain the integral formulation of the normal mode spectrum:

$$(k_\perp^2 + k_z^2)\,\hat{\phi}(k_\perp) = \frac{1}{\epsilon_0}\sum_s q_s \hat{N}_s(\vec{k}_\perp)\exp(-im\alpha) \qquad (6)$$

with $\hat{N}_s(\vec{k}_\perp)$ given by (5).

It generalizes previous expressions by

- R dependent temperature profiles
- anisotropic temperatures.

We also note that no drift ordering is assumed and that the mode frequency ω is arbitrary and not assumed to be small against the ion gyrofrequency Ω_i. It is also possible to get the corresponding slab version /2/.

II. Local Analysis

Assuming an adiabatic electron response, quasineutrality, drift approximation and the following ordering of the frequencies

$$\begin{aligned}\frac{|\omega|}{|k_z v_{the}|} &\ll \frac{|\omega|}{|k_z v_{th\parallel i}|}\sim 1 \\ |\omega|, |k_z v_{th\parallel i}| &\ll \Omega_i \end{aligned} \qquad (7)$$

we get the local dispersion relation for the η_i-mode in slab geometry ($\zeta_* \equiv \zeta_{*e}$):

$$\begin{aligned}D(\omega,\vec{k}) &:= 1+\tau_\perp\left[1+S_0\zeta Z(\zeta)-(1-\epsilon)(1+\zeta Z(\zeta))S_0\right]- \\ &-\zeta_* S_0\left[-\eta_\perp b G(b)Z(\zeta)+\eta_\parallel\left(\zeta^2-\frac{1}{2}\right)Z(\zeta)+\zeta\eta_\parallel+Z(\zeta)\right]=0 \qquad (8)\end{aligned}$$

with
$S_0 = S_0(b) := e^{-b}I_0(b)$, $\epsilon := \frac{T_{i\perp}}{T_{i\parallel}}$, $\tau_\perp := \frac{T_e}{T_{i\perp}}$, $b := \frac{k_y^2 T_{i\perp}}{M_i\Omega_i^2}$, $\zeta \equiv \zeta_0 = \frac{\omega}{|k_z v_{th\parallel i}|}$, $\omega_{*e} := \frac{k_y T_e}{qB_0 r_n}$, $\zeta_{*e} := \frac{\omega_{*e}}{|k_z v_{th\parallel i}|}$, $G(b) := 1-\frac{I_1(b)}{I_0(b)}$, $\eta_{\parallel,\perp} := \frac{\partial \ln T_{\parallel,\perp i}}{\partial \ln n_0}$, $r_n := \frac{n_0}{\partial_r n_0}$.
For isotropic systems, $\epsilon = 1$, (8) reduces to the dispersion relation of ANTONSEN et al. /3/. Making

use of the NYQUIST technique /3/ it is possible to find a criterion for instability, namely ($\mu := \frac{\partial \ln \epsilon}{\partial \ln T_i}$, $\eta_\parallel \equiv \eta_{i\parallel}$):

$$\eta_\parallel > \frac{1}{1+2(1+\mu)\,bG} \cdot \left\{1+\sqrt{1+\frac{k_x^2 r_n^2}{b\epsilon}\left\{-\epsilon^2+\frac{4}{S_0^2}\left[\frac{1}{\tau_\perp}+(1-S_0)+\frac{1}{2}S_0\epsilon\right]^2\right\}[1+2(1+\mu)bG]}\right\} \quad (9)$$

$$\vee$$

$$\eta_\parallel < \frac{1}{1+2(1+\mu)\,bG} \cdot \left\{1-\sqrt{1+\frac{k_x^2 r_n^2}{b\epsilon}\left\{-\epsilon^2+\frac{4}{S_0^2}\left[\frac{1}{\tau_\perp}+(1-S_0)+\frac{1}{2}S_0\epsilon\right]^2\right\}[1+2(1+\mu)bG]}\right\} \quad (10)$$

A typical example of the threshold as a function of b for (9) is given in Fig. 1 for three values of the parameters $k_x r_n$. It shows that there exists a minimum critical threshold for b of order unity.
We have also solved the dispersion relation (8) numerically by using a four-pole-approximation for the Z-function /4/, suggested by HAMMETT and PERKINS. Some results are shown in Fig. 2 ($x := \frac{Re\ \omega}{|k_x v_{th\parallel i}|}$, $y := \frac{Im\ \omega}{|k_x v_{th\parallel i}|}$).

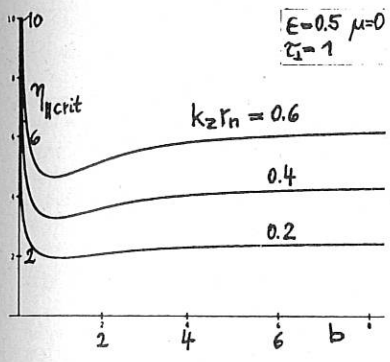

Fig.1 : The stability criterion (9)

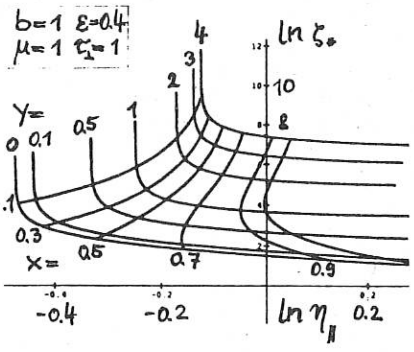

Fig. 2 : Numerical solution of the dispersion relation (8)

III. Marginal Stability Concept for Profile Determination

As an application of the local dispersion relation (8) and of the instability criterion (9) for the η_i-mode it is possible to present a unique method for profile determination. The latter requires that the plasma persists in an marginal stable state and that locally that value of b is adopted which corresponds to the above mentioned minimum threshold. With other words, the plasma has adjusted a state in which the most dangerous mode has just become marginally stable. In the case of equal isotropic

temperatures, $\tau = 1$, $T_{\|i} = T_{\perp i}$, the recipe can be formulated as follows:
For a given density profile $n(x)$ and for a given position x, (9) is used to get the values of b and $\eta_{crit.}$ corresponding to the minimum threshold. These values are then used to get the temperature profile by an x-integration:

$$T(x) = T(0) \exp\left[\int_0^x dx' \frac{\eta_{crit,min}(x')}{r_n(x')}\right] \tag{11}$$

Formula (11) follows from the definition of the η_i-parameter. The result $T(x)$ for a GAUSSian density profile (dashed line) is shown for two different values of $k_z L$, where L is the inhomogenity length, in Fig. 3.

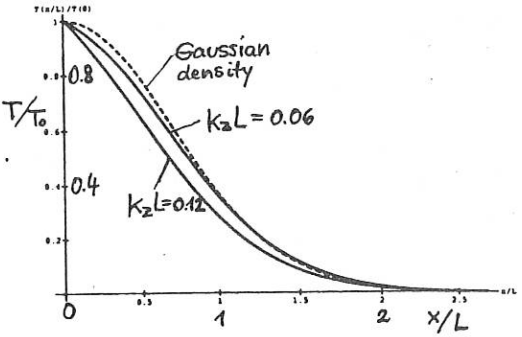

Fig. 3 : Calculated temperature profiles

As one notices, the obtained temperature profile has the qualitative feature of measured profiles without singularities or negative values. A similar concept can be developed for anisotropic plasmas with $\tau_\perp = \frac{T_e}{T_{\perp i}} \neq 1$ /2/.

IV. The Convective and Absolute Character of Unstable ITG-Modes

In the isotropic limit $T_e = T_{\|i} = T_{\perp i}$ the local dispersion relation (8) becomes:

$$D_0(\omega, \vec{k}) := \eta_i - \frac{1 + \tau(1 + S_0\zeta Z(\zeta)) - Z(\zeta)\zeta_* S_0}{\zeta_* S_0[\zeta + (\zeta^2 - \frac{1}{2})Z(\zeta) - bGZ(\zeta)]} = 0 \tag{12}$$

An inspection of the second term shows that it is independent of $\partial_x T_i$. This implies that η_i can be regarded as a free parameter which is a necessary requisite to apply the criterion of BERS-BRIGGS /5/ for absolute instability in the modified form of McCUNE and CALLEN /6/. Hence, it is expected that an upper threshold for η_i exits characterizing the transition from convective to absolute instability.

/1/ R. Marchand, C.F. Zhang, Y.C. Lee, Phys. Flüids **26**, 194 (1983)
/2/ J. Korn, Diplomarbeit, Universität Bayreuth (1992)
/3/ T. Antonsen, B. Coppi, R. Englade, Nucl. Fusion **19**, 641 (1979)
/4/ G.W. Hammett, F.W. Perkins, Phys. Rev. Lett. **64**, 3019 (1991)
/5/ A. Bers, R.J. Briggs, Bull. Am. phys. Soc. **9**, 304 (1964)
/6/ J.E. McCune, J.D. Callen, Plasma Physics **12**, 305 (1970)

Instabilities of Gyro-Kinetic Plasmas with a Guiding Center Density Gradient, Finite Larmor Radius and Polarization Drift

G. Knorr[1], M. Shoucri

Centre Canadien de Fusion Magnétique
Varennes, Québec, Canada, J3X 1S1

1 Introduction

Experimental and theoretical studies have revealed the importance of turbulence in the physics of the plasma edge in tokamaks. The theoretical research has concentrated on linking this turbulence to instabilities which involves a motion of the plasma along the field line as well as a gradient and a drift perpendicular to $\vec{B}$, such as the ion-temperature gradient instability [1,2] or possibly other drift-wave instabilities [3].

In this work we show that a two-dimensional plasma with a guiding center density gradient and no variation along the magnetic field lines is already unstable with regard to disturbances located only in the plane perpendicular to the magnetic field, if the charge separation between ions and electron due to the finite ion Larmor orbits in $\vec{E} \times \vec{B}$ drifts is taken into account, and if the polarization drift (which gives rise to an additional charge separation in a time varying electric field) is also taken into account [4].

2 The Guiding Center Model

For simplicity, we consider a straight and constant magnetic field, leaving the treatment of a plasma in a sheared magnetic field to a later publication. In the finite Larmor radius guiding center equations, the finite Larmor radius of the ions is taken into account by a filtering operation [5]. It has been shown [5] that this system possesses three "rugged" invariants", with the consequence that charges of equal sign tend to concentrate and form large vortices under certain conditons. In the present work, we extend these models by including the polarization drift, which has a different sign for ions and electrons and thus give rise to a charge separation in a time varying electric field. These equations have been recently presented [4] and are written as follows:

$$\frac{\partial n_e}{\partial t} + (V_D + V_{Pe}) \cdot \nabla n_e + n_e \nabla \cdot V_{Pe} = 0 \tag{1}$$

$$V_D = -\nabla\phi \times \vec{e}_z / B \tag{2}$$

$$\frac{\partial n_i}{\partial t} + (\bar{V}_D + \bar{V}_{pi}) \cdot \nabla n_i + n_i \nabla \cdot \bar{V}_{Pi} = 0, \tag{3}$$

$$\bar{V}_D = g \otimes V_D = -\nabla\bar{\phi} \times \vec{e}_z / B\,; \qquad \bar{V}_{Pi} = g \otimes V_{Pi} \tag{4}$$

$$\nabla^2\phi = -\frac{q}{\varepsilon_o}(\bar{n}_i - n_e) \tag{5}$$

[1]Department of Physics, University of Iowa, Iowa City, Iowa 52242, U.S.A.

$$\bar{\phi} = g \otimes \phi, \qquad \bar{n}_i = g \otimes n_i \tag{6}$$

$$V_{Pi} = \frac{1}{\Omega_i^2}\frac{q}{m_i}\frac{dE}{dt} \qquad V_{Pe} = -\frac{1}{\Omega_e^2}\frac{q}{m_e}\frac{dE}{dt} \tag{7}$$

$$\text{and} \qquad \frac{dE}{dt} = \frac{\partial E}{\partial t} + V_D.\nabla E \tag{8}$$

As described in [4,5], g is a convolution integral operator, so that we have, for instance

$$\bar{n}_i = g \otimes n_i = \int g\,(\vec{r} - \vec{r}')\; n_i\,(\vec{r}')\; dxdy \tag{9}$$

In the Fourier k-space, it becomes a filter operation, which is easily incorporated in the different Fourier modes. Each coefficient a_k of the mode $e^{i\vec{k}.\vec{r}}$ is multiplied by a factor $g = \exp(-\frac{1}{2}k^2 r_i^2)$, where k is total wave vector and r_i, is the ion Larmor radius. We emphasize that the densities are not particle but guiding center densities and this explains the absence of any pressure gradient terms in the present model.

3 Linear Stability Analysis

We will show now that as soon as there is a spatial gradient of the guiding center density in a neutral plasma, there will be an instability. It follows that a magnetized plasma with a guiding center gradient can never be in a stationary state, but rather it goes over into a turbulent state.

We consider a geometry of experimental interest, namely a plasma between two conducting plates, in the x direction d is the separation between the two plates. As boundary conditions we take $n_i(d) = n_e(d) = N = \text{const}$, $n_i(0) = n_e(0) = 0$, and for the potential $\phi(d) = \phi_0, \phi(0) = 0$. Initially we let the guiding center densities depend on x only. The system is periodic in the y direction, and is initially charge neutral, but we allow a potential difference across the plasma. Then the zeroth order potential becomes $\phi_0(x) = \frac{x}{d}\phi_0$. We linearize the equations by expanding around a steady state and assuming only small deviations from it, *i.e.* $\phi = \phi_0(x) + \delta\phi(x,y,t), n_{i,e} = n^0_{i,e}(x) + \delta n_{i,e}(x,y,t)$, etc. The result is a linear sytem:

$$\begin{aligned}
&\partial_t \delta n_e - \frac{1}{B}\partial_y \delta\phi \partial_x n_e^0 - \beta_e(\partial_t + \frac{1}{B}\partial_x\phi_0\partial_y)\partial_x\delta\phi\partial_x\delta n_e^0 + \frac{1}{B}\partial_x\phi_0\partial_y\delta n_e \\
&\qquad - n_e^0\beta_e(\partial_t + \frac{1}{B}\partial_x\phi_0\partial_y)\nabla^2\delta\phi = 0\,, \\
&\partial_t \delta n_i - \frac{1}{B}\partial_y g\delta\phi\partial_x n_i^0 - \beta_i(\partial_t + \frac{1}{B}\partial_x g\phi_0\partial_y)\partial_x g\delta\phi\partial_x n_i^0 + \frac{1}{B}\partial_x g\phi_0\partial_y\delta n_i \\
&\qquad - n_i^0\beta_i(\partial_t + \frac{1}{B}\partial_x g\phi_0\partial_y\nabla^2 g\delta\phi = 0\,. \\
&\nabla^2\delta\phi = -\frac{q}{\epsilon_0}(g\delta n_i - \delta n_e)\,,
\end{aligned} \tag{10}$$

where $\bar{n}_i = g n_i$ etc. and $q = q_i = \mid q_e \mid$.

All zero order gradients are constant; $n_e^0 = n_i^0 = \alpha x$, with $\alpha d = N$. Note further that $d_x\phi_0 = -E_0 = Bv_D^0$. As the equilibrium equations do not depend on y or t, we make the ansatz $\delta\phi(x,y,t) = \delta\phi(x)\exp(ik_y y - i\omega t)$, solve for the guiding center densities and insert them into Poisson's equation. The resulting equation for the potential is given by

$$\nabla^2\delta\phi = -\frac{q}{\epsilon_0}\left\{\frac{(1-g^2)\alpha}{1+\frac{k_y E_0}{\omega B}}\frac{k_y}{\omega B}\delta\phi + (\beta_i g^2 - \beta_e)\alpha\partial_x\delta\phi + \alpha x(\beta_i g^2 - \beta_e)\nabla^2\delta\phi\right\}. \qquad (11)$$

Note that $\mid \beta_e/\beta_i \mid = \frac{m_e}{m_i}$, which justifies to drop β_e in (11). In other words, the electron polarization drift is negligible. The coefficient of the last term in (11) can be written $\frac{q}{\epsilon_0}\alpha x\beta_i g^2 = \frac{x}{d}(\frac{\omega_{pi}}{\Omega_i})^2 g^2$, where $\omega_{pi}^2 = \frac{q^2 n_0}{\epsilon_0 m_i}$ and $\Omega_i = \frac{qB}{m_i}$. If $\omega_{pi}^2/\Omega_i^2 \ll 1$, this term can be neglected because it is small. (This is tantamount to neglecting the divergence of the polarization drift.) In the opposite case the coefficient of $\nabla^2\delta\phi$ becomes dependant on x, but remains always positive, so that our results derived with (11) are still qualitatively valid. With these approximations (11) can be written

$$\partial_x^2\delta\phi + \left(\frac{\omega_{pi}}{\Omega_i}\right)^2 g^2 d^{-1}\partial_x\delta\phi - \left[k_y^2 - \frac{\omega_{pi}^2}{\Omega_i d}\frac{k_y(1-g^2)}{\omega - k_y v_D^0}\right]\delta\phi = 0 \qquad (12)$$

The term $\left(\frac{\omega_{pi}}{\Omega_i}\right)^2 g^2 d^{-1}\partial_x\delta\phi$ originates from the polarization drift (12) is an ODE of second order with constant coefficients, which is solved by $\delta\phi \sim e^{ik_x x}$. The boundary conditions $\delta\phi(x=0) = \delta\phi(x=d) = 0$ are satisfied for

$$k_x = \pi n/d, \qquad n = 1,2,3\ldots \qquad (13)$$

From Eq. (12) follows the dispersion relation

$$\frac{\omega}{\Omega_i} = \frac{k_y}{\Omega_i}v_D^0 + \frac{\omega_{pi}^2}{\Omega_i^2}\frac{k_y d^{-1}}{k^2}\frac{1 + i\frac{\omega_{pi}^2}{\Omega_i^2}\frac{k_x d^{-1}}{k^2}}{1+\left(\frac{\omega_{pi}}{\Omega_i}\right)^4\left(\frac{d^{-1}k_x}{k^2}\right)^2}(1-g^2), \qquad (14)$$

with $g = \exp(-\frac{1}{2}k^2 r_i^2) \approx 1 - \frac{1}{2}k^2 r_i^2$

Without the finite Larmor radius correction, *i.e.* for $g = 1$, (14) describes a drift wave. The ion polarization drift is responsible for the imaginary term. Thus without the polarization drift but with finite Larmor radius correction, we would have a small correction to the drift wave only. It is the combination of both, finite Larmor radius and polarization drift which makes the plasma unstable. With $\omega = \omega_r + i\gamma$ we obtain

$$\frac{\gamma}{\Omega_i} = \left(\frac{\omega_{pi}}{\Omega_i}\right)^4\frac{k_x k_y}{k^2}\frac{r_i^2/d^2}{1+\left(\frac{\omega_{pi}}{\Omega_i}\right)^4\left(\frac{k_x d^{-1}}{k^2}\right)^2}$$

The sign of k_x and k_y are arbitrary, so that there is always an instability. The thickness of the plasma sheath, d, is a measure of the density gradient which supplies the free energy for the instability. For a numerical example we take $k_x = k_y = \pi d^{-1}, k^2 = 2\pi^2 d^{-2}$, and $r_i/d = 10^{-1}$. Then

$$\frac{\gamma}{\Omega_i} = \frac{\left(\frac{\omega_{pi}}{\Omega_i}\right)^4}{1 + \left(\frac{\omega_{pi}}{\Omega_i}\right)^4 \left(\frac{1}{2\pi}\right)^2} \frac{1}{2} \cdot 10^{-2}$$

The choice $\frac{\omega_{pi}}{\Omega_i} = \frac{1}{2}$ results in $\frac{\gamma}{\Omega_i} = 1.56 \cdot 10^{-4}$. Within 100 ion gyrations the amplitude increases by 10%. This is a weak instability. The choice $\frac{\omega_{pi}}{\Omega_i} = 1$ violates an approximation in our derivation, however we may still expect qualitative results. The amplitude grows in 100 periods by a factor of 23.

Acknowledgements

The CCFM is a joint venture of Hydro-Québec, Atomic Energy of Canada Limited and the Institut National de la Recherche Scientifique, in which MPB Technologies Inc., and Canatom Inc. also participate. It is principally funded by AECL, Hydro-Québec and INRS.

References

1 S. Migliuolo and A.K. Sen. Phys. Fluids, B2, 3047 (1990).

2 M. Shoucri, P. Bertrand, A. Ghizzo "Ion-Temperature gradient Instability in an Inhomogeneous Quasi-Neutral Plasmas" Report CCFM 354 (August 1991).

3 M. Shoucri, G. Knorr, Plasma Phys. 18, 187 (1976); M. Shoucri J. Appl. Phys. 47, 518 (1976); M. Schoucri, Plasma Phys. 19, 295 (1977).

4 G. Knorr, M. Shoucri, "Instabilities of Gyro-Kinetic Plasmas with a Guiding Center Density Gradient, Finite Larmor Radius and Polarization Drift", Centre Canadien de Fusion Magnétique Report 367 (1992).

5 F. Hansen, G. Knorr, J. Lynov, H. Pecseli, J. Rasmussen Plasma Phys. 31, 173 (1989); G. Knorr, H. Pecseli, J. Plasma Phys. 41, 157 (1989).

THE LAUNCHING AND PROPAGATION OF DRIFT WAVES IN A STEADY-STATE PLASMA

J Sandeman, J A Elliott, M Sutcliffe and M G Rusbridge
Physics Department, UMIST, Manchester M60 1QD, UK.

The UMIST linear quadrupole GOLUX is a steady-state device in which hydrogen plasma is continuously injected axially, at one end, from an external duoplasmatron source [1]. The magnetic field configuration is shown in cross-section in figure 1. The electron temperature in the drift wave region is about 1 eV, and the density about 10^{15} m^{-3}. Self-excited intrinsic drift modes are observed in the shared flux region of GOLUX, forming a broad band between 30 and 50 kHz. A typical power spectrum is shown in fig. 2.

Drift waves may also be launched into the system [2], by passing an AC current through the plasma between the two flag antennae shown in fig. 1. A typical launched wave at 60 kHz is shown superimposed on the intrinsic modes in fig. 2. These coherent launched waves present a powerful means of studying drift wave phenomena.

We obtain information about the launched wave by detecting both density and potential fluctuations, using a small cylindrical Langmuir probe and lock-in amplifier techniques. Scanning the probe in the longitudinal (z) direction yields the spatial variation of amplitude and phase with respect to the launching signal; the ratio of the wave potential, extrapolated back to the probe, to the launching current gives the launching impedance, a measure of the effectiveness of the launching process.

Waves can be launched in the frequency range 10 - 60 kHz. The upper frequency marks a sharp cut-off above which waves cannot be launched: the theory presented below shows that this is because the wavelength has become comparable with the z scale-length of the effective launching antenna, which is set by the disturbance in the plasma, not by the flag thickness. There appears to be no lower cut-off, and waves can be launched well below the frequency band of the intrinsic modes.

When waves are launched within the intrinsic band, we observe an exponential decay in z, the decay length being about 1.0 m. Below the intrinsic band, the observed wave exhibits strong interference effects, which we interpret as due to the simultaneous launching of the expected wave and also the second radial harmonic, which has a different wave-number [3]. The dispersion curves for both modes are shown in fig. 3. We have investigated the frequency dependence

of the launching impedance by measuring the wave potential amplitude as a function of distance z from the flags, with a constant amplitude of the launching current. Results for two values of z, shown in fig. (4), clearly show the existence of two windows of good propagation. The upper one corresponds to the intrinsic band of unstable drift waves, while the lower one, corresponding to a mode apparently stable under present operating conditions, may be identified with the second radial harmonic [4].

This mode can be positively identified by measuring its radial co-variance in relation to its maximum radial amplitude. Figure 5 shows such results for both the observed modes. The co-variance of the second harmonic changes sign showing the presence of a radial node, in contrast with the fundamental mode. The additional evidence from the dispersion curve (fig. 3), which matches that predicted by theory [4], confirms the identification. We have performed a theoretical analysis of the wave launching mechanism, using the formulation introduced by Ashraf and Rusbridge [5]. The plasma response is given by

$$\tilde{\phi}(k,\omega) = \frac{\tilde{\rho}_e(k,\omega)}{k^2 \epsilon(k,\omega) \epsilon_o}$$

where φ is the wave potential, ρ_e is the externally induced charge density, and ϵ the dielectric function. The charge density ρ_e is determined from the potential distribution in the plasma arising from the flow of current between the two launching electrodes. Although the two electrodes are linked by a common flux-tube, this is not capable of carrying the whole current, and the current channel therefore expands; the resulting cross-field current flow leads to a $\underline{j} \times \underline{B}$ force which drives the wave as suggested by Tessema et al [2]. The potential distribution in the current channel is given by the equation $d^3V/dz^3 = ik\,V$, with the acceptable solution

$$V = V_0 \exp\left[\left(-\frac{\sqrt{3}}{2} + \frac{1}{2}i\right)\kappa z\right] \quad \text{where } \kappa \text{ is defined by } \kappa^3 = \frac{e^2 B^2}{2 m_i m_e R L D v_D \omega}$$

where R is the mirror ratio, L is the length of a quadrant of a field line (i.e. from minimum to maximum field points), D is the probe length, v_D the plasma drift speed, and ω the launching frequency. V_0 is determined by the impedance of the current channel. From the potential distribution we obtain ρ_e using Poisson's equation; this is then Fourier transformed to determine ρ_e. For the dielectric function we use a model form suggested by that of a drift wave in the "slab model", given by

$$\epsilon = \frac{1}{k^2\lambda_D^2}\left(1 - \frac{\Omega(k)}{\omega} + i\frac{\gamma}{\omega}\right)$$

where $\Omega(k)$ is the observed dispersion relation and γ the damping rate. For light damping, leading to a narrow resonance, we may approximate the dispersion curve by its tangent at the launching frequency, giving $\Omega(k) \approx kv_g + C$ where v_g is the group velocity and C is a constant. Then, using eq.(1) and back transforming to obtain the wave potential φ in physical space, we finally obtain the launching impedance $Z_L = \varphi/I$ in the form

$$Z_L = \frac{\lambda_D^2 B^2 \kappa^2 F}{2Anm_i v_g}\left(\frac{2\kappa^2 - (1 - i\sqrt{3})k^2}{\kappa^4 - k^2\kappa^2 + k^4}\right)$$

which may be expressed as a function of ω using the dispersion curve. This expression shows that κ represents the upper limit on the wave number that can be launched effectively; Z_L has a maximum at $k = \kappa/\sqrt{2}$, and becomes constant in the limit $k \ll \kappa$. In this expression F represents the overlap integral between the potential distribution and the eigenfunction of the drift mode [3]. An approximate calculation gives $F \approx 1$ and we may ignore this factor. The dependence of Z_L on frequency (derived from $Z_L(k)$ above) is shown in fig.(6). We use the following data: B = 14 mT; $n = 1.0 \times 10^{15}$ m^{-3} ; probe dimensions 2 cm by 3 cm; $T_e = 1.4$ eV; $v_g = 1500$ m/sec. The largest uncertainty is in the density, about ± 30%. Then the predicted value of Z_L in the limit $k \ll \kappa$ is 10 Ω ± 50%. To estimate κ, we also need the mirror ratio $R \approx 7$, and the plasma drift speed $v_D \approx 1000$ m/sec, giving $\kappa = 480$ m^{-1} at 60 kHz. Note that there are no fitted parameters in these estimates.

The experimental results for $Z_L(\omega)$ are also shown in fig 6. In the intrinsic drift band, the observed value of ≈ 15 Ω is within the theoretical limits of uncertainty; however, there is no maximum in the impedance, and the high-frequency cut-off occurs at $k \approx 120$ m^{-1} , much less than the predicted value $k \approx \kappa = 400$ m . The observed rise of Z_L at low frequencies does not appear in our theory, and has not yet been explained. Nevertheless, there is qualitative, and to some extent quantitative, agreement between theory and experiment.

References:
[1] Phillips, Rusbridge and Young, Plas.Phys. 20, 653 (1978)
[2] Tessema, Elliott and Rusbridge, Plas.Phys.Cont.Fus. 31, 2177 (1989)
[3] Carter et al, Plas.Phys. 23, 819 (1981)
[4] Edwards and Rusbridge, Plas.Phys. 24, 789 (1982)
[5] Ashraf and Rusbridge, Plas.Phys.Cont.Fus. 29, (1987)

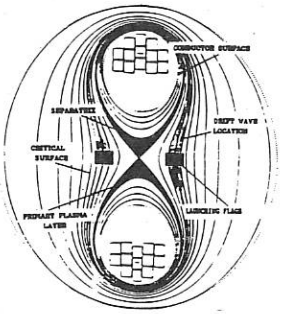

Fig 1: Magnetic field profile and launching configuration

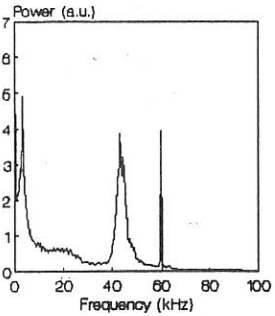

Fig 2: Typical power spectrum of GOLUX with launched wave at 60 kHz

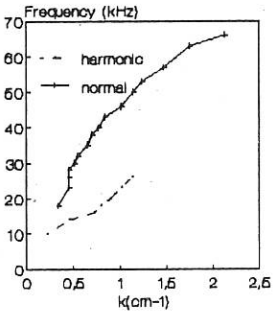

Fig 3 : Launched wave dispersion curve

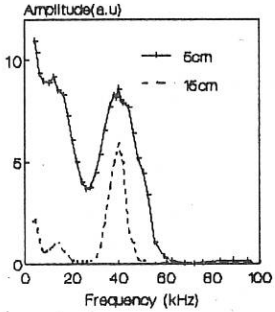

Fig 4 : Wave amplitude versus frequency

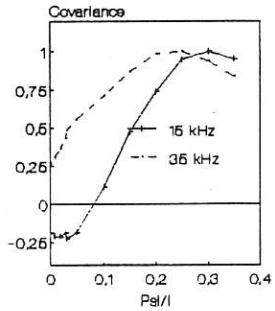

Fig 5 :Covariance of launched wave

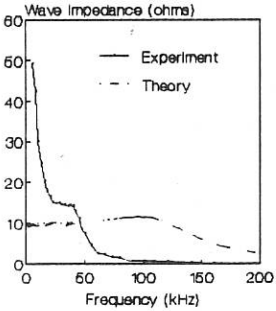

Fig 6 :Wave impedance versus frequency

STUDIES OF NON-LINEAR INTERACTIONS OF DRIFT WAVES IN THE UMIST QUADRUPOLE "GOLUX"

P.J.Duncan, D.Chekroud, and M.G.Rusbridge
Physics Department, UMIST, Manchester M60 1QD, U.K.

The UMIST linear quadrupole GOLUX is a steady-state plasma confinement system in which the plasma is injected along the null-line of the magnetic field and drifts along the vacuum vessel in the field; a detailed desciption is given in [1], and a cross-section of the magnetic field configuration is shown in [2]. Drift waves are spontaneously excited in the system, covering the frequency range 30 - 50 kHz; propagation is parallel to the symmetry axis, with wave-number about 100 m^{-1} at 40 kHz. It has been shown [3] that the dispersion curve agrees well with theory. In previous work two possible non-linear saturation mechanisms have been considered: (1) the "frequency-doubling" process in which a basic drift wave (ω,k) drives another, the "f.d." mode at $(2\omega,2k)$, on a different branch of the dispersion curve, and (2) a cascade mechanism in which energy flows through the drift wave spectrum towards smaller k, mediated by the low frequency ($\approx$ 5 kHz) flute-like mode which is also present [3]. Greb and Rusbridge [4,5] developed the theory of process (1) and showed experimentally that the energy flow in the process is insignificant, while Crossley et al [6] introduced a new approach to the analysis of experimental results, that of "amplitude correlations", and used it to confirm that process (2) is the dominant saturation mechanism.

In introducing the amplitude-correlation method, Crossley et al [6] did not give a rigorous justification, but relied on its coherence with other evidence to provide confirmation. In this paper, we extend the work of Greb and Rusbridge [4] to provide a rigorous derivation of the method for the frequency-doubling process, and show that it can give estimates of the damping rate of the driven mode and of the rate of energy flowing into it through non-linear interactions.

The basic equation is that for the slow time variation of the potential amplitude ϕ_3 of a mode (ω_3,k_3) driven by the non-linear interaction of modes 1 and 2:

$$i\frac{\partial\varepsilon}{\partial\omega}\frac{\partial\phi_3}{\partial t} + \varepsilon\phi_3 = A\phi_1\phi_2\delta(\omega_3-\omega_1-\omega_2)\delta(k_3-k_1-k_2) \qquad (1)$$

where A is the coupling constant, $\varepsilon = \varepsilon(\omega_3,k_3)$ is the dielectric response function of the driven mode, and the δ-functions enshrine the selection rules. We formally expand $\phi_3 = \phi_{30} + \phi_{31}(t)$, where ϕ_{30} is the steady state solution. Multiplying eq.(1) by ϕ_3^*, substituting ϕ_{30}^* for ϕ_3^* in the r.h.s. and dropping the subscript 1, we obtain

$$i\frac{\partial\varepsilon}{\partial\omega}\frac{\partial\phi_3}{\partial t}\phi_3^* + \varepsilon\phi_3\phi_3^* = \frac{AA^*\phi_2\phi_2^*\phi_1\phi_1^*}{\varepsilon^*} \qquad (2)$$

where the delta-functions have been absorbed into A for convenience. By taking the complex conjugate of this equation and separating out the real and imaginary parts we can obtain an equation for $W_3 = \phi_3\phi_3$ in the form

$$- \frac{\left[\left(\frac{\partial \varepsilon_r}{\partial \omega}\right)^2 + \left(\frac{\partial \varepsilon_i}{\partial \omega}\right)^2\right]}{\left(\varepsilon_r \frac{\partial \varepsilon_i}{\partial \omega} - \varepsilon_i \frac{\partial \varepsilon_r}{\partial \omega}\right)} \frac{\partial W_3}{\partial t} + 2W_3 = \frac{2AA^* W_2 W_1}{\varepsilon\varepsilon^*} \qquad (3)$$

To proceed further we need an explicit form for ε, and we use one modelled on that for drift waves in the slab model:

$$\varepsilon = \frac{1}{k^2 \lambda_D^2}\left(1 - \frac{\omega_o(k)}{\omega} + i\frac{\gamma}{\omega}\right) \qquad (4)$$

where $\omega_o(k)$ is the dispersion relation and γ the damping rate. From this it is straightforward to obtain the final equation in the form

$$\frac{\partial W_3}{\partial t} + 2\Gamma W_3 = \frac{2A^2 \Gamma W_1 W_2}{\varepsilon^2} \qquad (5)$$

where $\Gamma = \omega^2\gamma/(\omega_o^2+\gamma^2)$, or for light damping $\Gamma = \gamma(\omega/\omega_o)^2$. The steady state solution to this equation leads to the power ratio [4]; it is governed by the quantity $(A/\varepsilon)^2$, so that neither A nor ε can be determined separately from it. In the time-dependent form above, the equation describes the response to fluctuations in $W_{1,2}$; we see that the response always lags the driving terms, and from the phase shift we can determine Γ and thus obtain additional information specifically about the damping rate of the driven mode. Thus, if the product W_1W_2 oscillates at a frequency Ω, the phase lag is θ where $\tan\theta = \Omega/2\Gamma$, and $0 < \theta < \pi/2$.

The experiments are carried out by recording a series of records of the fluctuating density signal from GOLUX, using a transient recorder. Individual records are 1024 μsec in length, digitised at 2 μsec intervals. Records are Fourier-transformed using an FFT routine; the resulting power spectrum is shown in fig.(1). Frequency bands around the drift peak ($\approx$ 40 kHz) and the frequency doubled peak ($\approx$ 80 kHz) are isolated, squared, and again filtered to pass identical low-frequency (LF) bands, typically 1 - 10 kHz. The resulting signals are then correlated in the usual way. The use of 50 - 100 independent records is sufficient to give a random level of correlation of $\pm$ 0.1, as can be seen at large time delay in the result shown in fig.(2).

It can be seen that this result agrees qualitatively with the theory presented. The maximum correlation is positive, and the phase lag is less than $\pi/2$. In quantitative terms, the average frequency determined from the number of visible maxima is 6.9 kHz, consistent with the 1 - 10 kHz LF band limits: we identify this with $\Omega/2\pi$. The delay of the maximum is 21 μsec, equivalent to a phase lag of 0.93 rad and leading to $\Gamma = 1.6 \times 10^4$ sec^{-1}.

With $\omega/2\pi$ = 80 kHz we obtain Γ/ω = 0.032, consistent with weak damping of the f.d. mode; in fact, if the interaction is no more than 20% off resonance, i.e. $0.8 < \omega_o/\omega < 1.2$, then $0.020 < \gamma/\omega < 0.046$.

The maximum correlation is consistent with the level of background shown in fig.(1). We estimate the background by interpolation between the power levels above the f.d. band and below the drift band, as shown by the dashed curve; averaging over the upper frequency band, we obtain the signal-to-background ratio S/N $\approx$ 1.62. Assuming that the background is unrelated to the drift waves, we find that the maximum possible value of the correlation is S/(S+N) = 0.62 The maximum observed correlation shown in fig.(2) is almost as large as this; we interpret this as confirming that the f.d. mode is completely driven by the non-linear coupling from the drift mode [5]. The high value also effectively rules out the possibility that the apparent correlation could be due to the modulation of both drift and f.d. modes by the same signal (e.g. the low frequency flute mode which is also seen in the system).

For greater precision, we need to determine experimentally the f.d. mode dispersion curve $\omega_o(k)$. We expect to do this through an application of the wave launching technique described in refs [2,3]. With this information available, we expect to be able to determine the dielectric function and thus obtain an experimental measurement of the coupling constant for comparison with theory.

In conclusion, we have shown that the intuitively appealing approach of the amplitude correlation method can be rigorously justified for the case of a non-linear interaction of the "frequency-doubling" type, and we have shown that the theory agrees well with observations made in the GOLUX Quadrupole. The results give a direct experimental measurement of a quantity related to the damping rate of the driven mode; we now require only a determination of the driven mode dispersion curve to obtain complete information about the interaction including a measurement of the coupling constant.

References

[1] K.Phillips, M.G.Rusbridge and K.M.Young, Plas.Phys. 20, 653 (1978)3 (1978)
[2] J.Sandeman, J.A.Elliott, M.Sutcliffe and M.G.Rusbridge, this conference
[3] G.Y.Tessema, J.A.Elliott and M.G.Rusbridge, Plas.Phys. Cont.Fus. 31, 2177, (1989)
[4] U.Greb and M.G.Rusbridge, Plas.Phys.Cont.Fus. 30, 537 (1988)
[5] U.Greb and M.G.Rusbridge, Plas.Phys.Cont.Fus. 30, 551 (1988)
[6] F.J.Crossley et al, Plas.Phys.Cont.Fus. 34, 235 (1992)

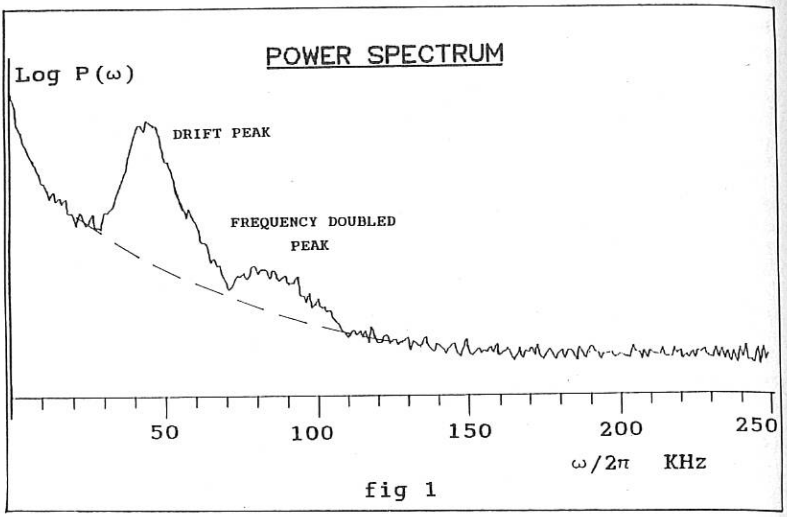
POWER SPECTRUM
Log P(ω)
DRIFT PEAK
FREQUENCY DOUBLED PEAK
50
100
150
200
250
ω/2π KHz

fig 1

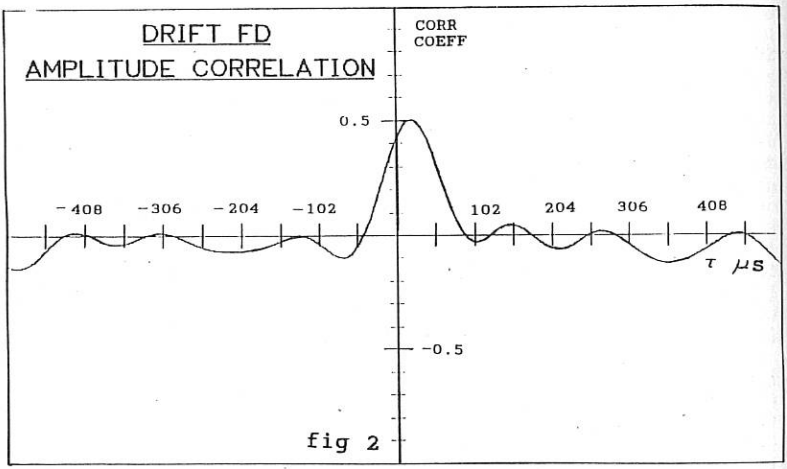
DRIFT FD
AMPLITUDE CORRELATION
CORR COEFF
0.5
-0.5
-408
-306
-204
-102
102
204
306
408
τ μs

fig 2

Excitation of Electron Cyclotron Waves and Related Physics Experiments

Masayoshi Tanaka, Makoto Tamaoki, Hiroaki Shoyama, Keisuke Nagao
Akio Komori and Yoshinobu Kawai

Department of High energy Engineering Science, Kyushu University
Kasuga, Fukuoka 816, JAPAN

Abstract Experiments on electron cyclotron wave excitation are carried out. Mode conversion of a left-hand polarized wave into an electron cyclotron wave is examined in detail. When small inhomogeneity exists in the magnetic field, the trapped electrons chaotically accelerated to a few tens of KeV range. The experimental results on the onset of chaos are presented.

1. Introduction

Excitation of electron cyclotron wave (ECW) /1/ is experimentally studied with a 2.45GHz microwave. The TE_{10} rectangular mode is converted into the TE_{11} circular mode, and launched from an open end of the field line. By controlling the microwave polarization, we excite a ECW (R-wave).

One of the most important application of ECW is to produce overdense plasmas. In the case of R-polarized microwave injection, ECW generates a plasma density 1×10^{13} cm^{-3} at 5 KW input. While, we use the L-polarized microwave, mode conversion process occurs; a L-wave is excited in the initial traveling distance and converted into a ECW as it propagates. The detailed results on the mode conversion process including the wave form and the polarization are presented.

When there is small inhomogeneity in the applied magnetic field, some of electrons (initially $\approx$ 20 eV) are accelerated up to a few tens of KeV range. To examine the mechanism of acceleration to such the high energy region, we have measured the wave propagation and the soft X-ray emission from the accelerated electrons. It is found that this phenomenon is understood as a Hamilton chaos of mirror trapped electrons interacting with ECW.

2. Experimental Apparatus

The experiments are carried out in a cylindrical chamber with 8 magnetic coils. The chamber dimension is 16 in diameter, and 150 cm in axial length. Microwave source with a frequency 2.45 GHz and 5KW output is used to excite ECW. Magnetic fields are applied to satisfy the high field side injection at the launching point, $\omega/\omega_{ce} < 1.0$, where ω_{ce} is the electron cyclotron frequency and ω the microwave frequency. The TE_{10}

rectangular mode from a magnetron oscillator is transformed into the circular TE_{11} mode, and then polarized by a dielectric-plate-type polarizer. The rotation direction of the electric field is selected by the polarizer. The circularly polarized microwave is introduced from an open end of the field line through a tapered waveguide and a quartz window. Filling gas is Argon, and the operation pressure is $1 \times 10^{-4} - 1 \times 10^{-2}$ *torr*. The electron temperature and density measured with a Langmuir probe inserted from a radial port are 4 - 20 eV and $5 \times 10^{11} - 1 \times 10^{13}$ cm^{-3}, respectively. An axially movable dipole-antenna, covered with ceramic for thermal insulation, is introduced for the wave detection. A Si(Ge) solid state detector is connected to the radial port located between the third- and the fourth coil, and the output signal is processed by a Multichannel Analyzer. Figure 1 shows the experimental setup.

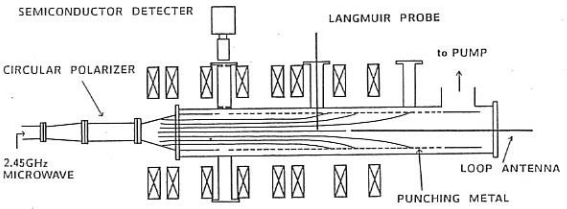

Fig.1 Schematic diagram of experimental setup.

3. Mode Conversion of L-wave into ECW

In our experimental condition, two wave modes can propagate in a plasma along the magnetic field line. Right-hand wave (ECW) is accessible to any high dense plasmas and strongly interacts with electrons through the electron cyclotron resonance, while left-hand wave is only accessible to low density cases, whose interaction is negligible.

When we use the R-polarized microwave to produce a plasma, an ECW is excited in the plasma and a density $1 \times 10^{13} cm^{-3}$ is achieved at 5 KW microwave input /2/. This is 140-times higher than the cutoff density for the ordinary wave of the same frequency. When the L-polarized microwave is injected into the evanescent plasma, mode conversion process is observed. Figure 2 shows the perpendicular component of the electric field, E_y, detected by the dipole antenna. As seen in this figure, a long-wavelength mode is excited in the initial propagation distance (broken line) and decays within the one period of oscillation. During this process, a short-wavelength mode grows from $z \approx 5$ cm, and dominates after $z \approx 15$ cm, showing the mode conversion.

Rotating the dipole antenna by 90 degrees, we have measured the E_x component to determine the polarization of the long- and the short-wavelength modes. Figure 3 shows the polar plot of the observed electric fields. It is found that the long-wavelength mode is a left-hand polarized wave (Fig.3(a)), and the short-wavelength mode a right-

hand polarized one (Fig.3(b)). These waves are identified as the L-wave and the ECW, respectively. Since the conversion into ECW is complete, the plasma density achieved in this case is almost the same as obtained with the R-polarized microwave. It is interesting that, in the growing phase, the ECW is almost linearly polarized.

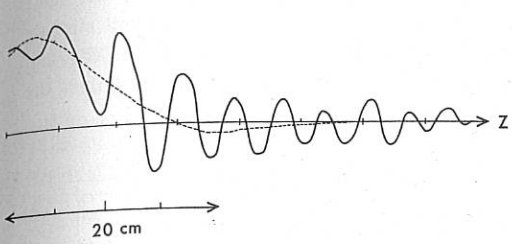

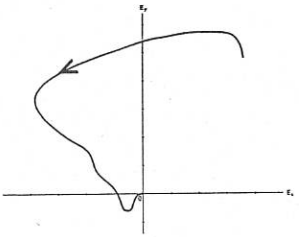

Fig.2 Interferometer trace of E_y component (upper left).

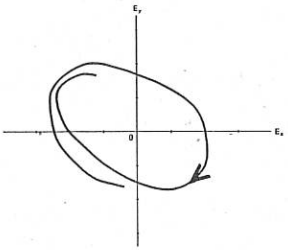

Fig.3(a) Polar plot of $E_\perp$ for long-wavelength mode indicating left-hand polarization (upper right).

Fig.3(b) Polar plot of $E_\perp$ for short-wavelength mode indicating right-hand polarization (lower right).

4. Hamilton Chaos of Electrons Interacting with ECW

It is well known that an oscillating particle kicked by a force exhibits chaos. Such the situation is realized in a plasma with trapped ions moving in the potential well of an electrostatic wave /3/. We present another example of chaos in a plasma; electrons trapped in the weak inhomogeneity of the applied magnetic field suffer chaotic acceleration by an electromagnetic wave (ECW), reaching a few tens of KeV range.

The mirror ratio is less than 1.3, and the field intensity at the bottom of the mirror is kept constant to provide the constant interaction with the ECW. The accelerated electrons radiate soft X-rays through the bremsstrahlung, which is measured with a Si(Ge) solid state detector. Changing the inhomogeneity of the magnetic field and the input microwave power, we have carefully measured the onset of X-ray emission.

The X-ray emission doesn't occur with the straight magnetic field, but, at a finite mirror ratio, it does /4,5/. The observed spectrum is shown in Fig.4. The energy covers from 2 KeV, the lower limit of the detector, to 15 KeV, and the peak at 3 KeV is the characteristic X-ray form Argon (K-shell). This means that electrons are accelerated to

the same range of energy. The count rate rises with increasing the field inhomogeneity, indicating that the mirror trapped electrons are responsible for the X-ray radiation. Figure 5 shows the X-ray total count as a function of mirror ratio. The onset of emission is so sudden that only a 3% change in mirror ratio triggers this phenomenon. The X-ray emission is also sensitive to the input microwave power. Beyond the threshold value between 1 KW and 2 KW, the total count rapidly increases. These results strongly suggest that the mirror trapped electrons are chaotically accelerated by the ECW, and that our system is equivalent to a harmonic oscillator(trapped electron) periodically kicked by an external force (ECW).

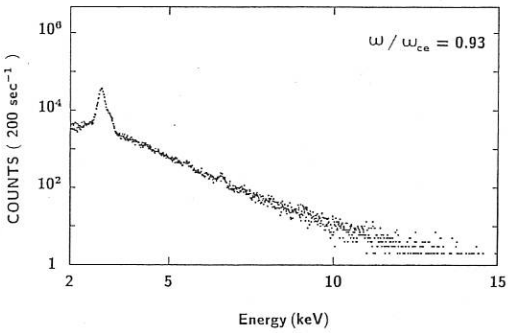

Fig.4 Soft X-ray energy spectrum. Input power: 3 KW; mirror ratio: 1.08 (upper left).

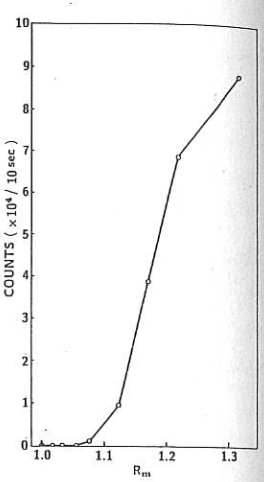

Fig.5 X-ray total count as a function of mirror ratio. Input power: 3 KW (upper right).

Reference

[1] G. Lisitano, M. Fontanesi and S. Bernabei, Phys. Rev. Lett. **26** (1971) 747.
[2] M. Tanaka *et al.*, J. Phys. Soc. Jpn. **50** (1991) 1600
[3] F. Skiff, *et al.*; Phys. Rev. Lett **58**(1987)1430
[4] R. A. Dandl, *et al.*; Nucl. Fusion 4(1964)334
[5] H. Ikegami, *et al.*; Phys. Rev. Lett. **19**(1967)778

AN EULERIAN VLASOV PLASMA SIMULATION CODE FOR ION PHASE SPACE PHENOMENA

R. Cherkhani, G. Bonhomme, A. Ghizzo, P. Bertrand
Lab P.M.I., U.R.A. 835 du CNRS, Université de Nancy I
BP 239, F-54506 Vandoeuvre Cedex, France

1 INTRODUCTION

A number of papers have been devoted during the last years to the nonlinear saturation of various instabilities. One proposed mechanism is the formation of vortices in phase-space. P.I.C. simulations have shown [2], [3] the occurence of such structures in the nonlinear saturation regime of the ion beam driven acoustic instability. The need of a a low noise level and a very good phase-space resolution to study the long time behaviour of these structures leads us to prefer an eulerian Vlasov simulation code. Thus we have modified a one-dimensional electron Vlasov code [1] to model ion beam-plasma systems.
In this paper we shall discuss the first results obtained with this code. Namely we shall report detailed comparisons between the P.I.C. and the eulerian Vlasov simulation approaches.

2 THE THEORETICAL MODEL AND SIMULATION METHODS

We consider a one-dimensional collisionless unmagnetized plasma in which ions are described by the Vlasov equation and electrons are assumed to be in a Boltzmann equilibrium. The ion distribution function $F(x,v,t)$ and the normalized self-consistent electrostatic potential $\Phi(x,t)$ are thus described by the following dimensionless Vlasov-Poisson system:

$$\begin{cases} \dfrac{\partial F}{\partial t} + v\dfrac{\partial F}{\partial x} - \dfrac{\partial \Phi}{\partial x}\dfrac{\partial F}{\partial v} = 0 \\ \dfrac{\partial^2 \Phi}{\partial x^2} = -\int F dv + \exp(\Phi / T) \end{cases}$$

Here $T = T_e / T_i$ and $x \in [0, L]$, $v \in (-\infty, +\infty)$ and t are the space, velocity and time variables respectively measured in units of ion Debye length, ion thermal velocity and inverse plasma period. Periodic boundary conditions are used.

Eulerian Vlasov simulation code: This code is based on the splitting scheme algorithm described by Cheng & Knorr (1976) [4], or Gagné & Shoucri (1977) [5]. It consists of alternately integrating the free streaming term and the acceleration term in Vlasov equation, using cubic spline interpolations.

But, contrary to the problem of electron dynamics in a background of static ions, our Poisson equation is nonlinear. To solve it, a regular grid with grid spacing ΔX and N_G grid points is introduced. Thus the Poisson equation can be written:

$\Phi_{j+1} - 2\Phi_j + \Phi_{j-1} = (\exp(\Phi_j / T) - \rho_j)\Delta X^2$, where $\rho(x) = \int F(x,v)dv$ is the ion charge density. The resulting set of equation in matrix form, i.e. $\mathbf{A\Phi = B + C(\Phi)}$, can be solved iteratively by the formula $\mathbf{A\Phi^{(n)} = B + C(\Phi^{(n-1)})}$.

The x-v phase-space is discretized as a 256×128 grid.

P.I.C. simulation code: The ion distribution function is discretized using N_P=512000 superparticles and the leap-frog scheme is chosen for the solution of the simulation particle trajectories. The self-consistent electric field is obtained from the Poisson equation solved with the same iterative method as above, with a grid of N_G=256 points. The ion charge density at a grid point is calculated according to the formula:

$$\rho_j(X_j) = \sum_{i=1}^{N_p} \frac{q_i}{\Delta X} W(x_i - X_j)$$ where $W(x)$ is the quadratic spline interpolation function.

3 RESULTS

Initial data: We consider the following initial distribution function: $F(x,v,t=0) =$

$$(2\pi)^{-1}\left[\alpha(T_{ib}/T_i)^{-1/2}\exp\left(-\frac{(v-v_b)^2}{2T_{ib}/T_i}\right)+(1-\alpha)\exp\left(-\frac{v^2}{2}\right)\right]\times\left(1+\sum_n a_n \sin(k_n x+\varphi_n)\right)$$

where a_n (resp. φ_n) is the amplitude (resp. phase) of the initial perturbation of the mode with wavevector k_n, with $k_n = n(2\pi/L)$, and v_b is the beam velocity.

The following plasma parameters are chosen: $T=30$, $T_{ib}/T_i = 0.05$, $v_b = 6$, $\alpha = 0.1$

For this data set the n=4 mode (four wavelengths in a box of length L=150) is the most linearly unstable, as predicted by the linear dispersion relation [2].

All the simulations are run with a time step $\Delta t = 0.25$.

P.I.C. simulations need no initial perturbation and thus $a_n = 0, \forall n$. On the contrary the intrinsically noiseless Vlasov code needs some $a_n \neq 0$. We will discuss the results obtained with the following data sets:

Vlasov1: $a_1 = a_2 = 10^{-5}, a_3 = 10^{-3}$

Vlasov2: all modes initially excited with amplitudes a_n distributed according to the thermal levels in a maxwellian plasma and randomly distributed φ_n.

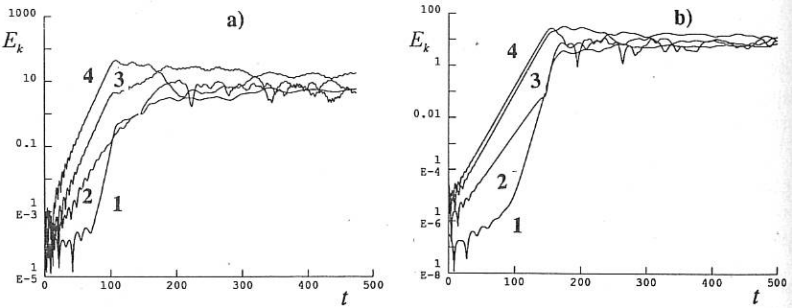

Fig. 1 Time evolution of the first Fourier modes for P.I.C. **a)** and Vlasov2 **b)** simulations

In the corresponding simulations we have observed the growth and the nonlinear saturation of the ion acoustic instability. The growth rates for the various Fourier modes supported by

the box have been obtained from their time evolution (fig. 1) and the main results are summarized in the following table:

	growth rates				
	γ_2	γ_3	γ_4	γ_5	$\gamma_{n>5}$
linear theory	0.081	0.101	0.103	0.048	≈ 0
P.I.C.	0.079	0.100	0.102	0.044	≈ 0.2
Vlasov1	0.081	0.101	0.18	0.19	≈ 0.2
Vlasov2	0.081	0.101	0.103	0.044	≈ 0.2

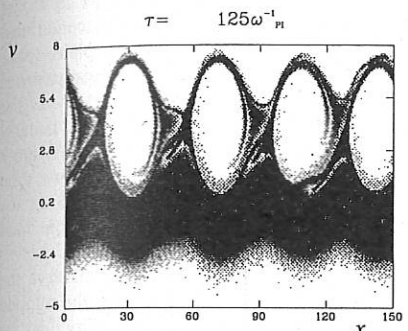

Fig. 2 Phase-space plot showing the formation of vortices (P.I.C. simulation)

It is seen that in Vlasov simulations only the growth rates of the modes initially excited are in agreement with the predictions of the linear theory. Now the number of vortices observed in the early saturated regime is fixed by the dominant mode. Thus, four vortices are observed in the P.I.C. (see fig. 2) and in the Vlasov2 simulations, instead of three in the Vlasov1 simulation.
Nonetheless the modes not present in the initial perturbation are excited by nonlinear coupling processes taking place before the saturation is reached. Thus higher growth rates are observed (see table). The great efficiency of this mode coupling process can be explained by the nearly linear ω-k dependance for the ion beam-plasma system, so that the resonance condition is satisfied for the excited modes.

Finally it appears that the actual evolution of the system depends strongly on the choice of the initial perturbation.

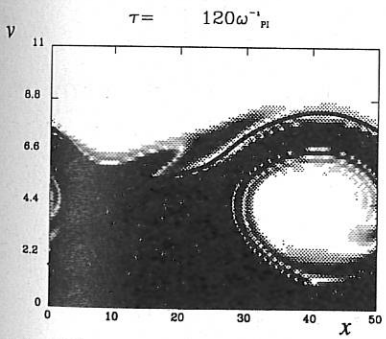

Fig. 3 Phase-space plot showing detrapped particles above the separatrix

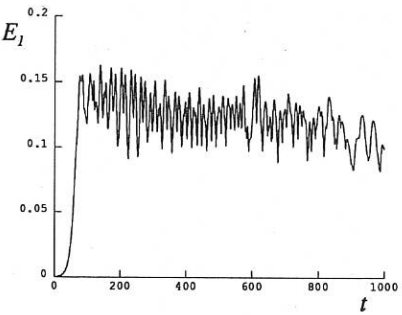

Fig. 4 Time evolution of E_1 showing large amplitude side-bands

Finally the excellent phase-space resolution of the Vlasov simulation code enables to study the long time behaviour of the trapped particles. It has been observed (fig. 3 and 4) as previously reported for the electron beam-plasma instability [6] that growing side-bands can destroy the trapped particle oscillations which follow the saturation of the ion acoustic instability. The phase velocity of the side-bands oscillations is in agreement with the velocity detrapped particles.

4 CONCLUSION

A one-dimensional eulerian Vlasov simulation code has been developped to model ion beam-plasma systems. The simulations are performed using spatial boundary conditions. The results obtained on unstable ion beam-plasma systems exhibit the ion phase-space vortices formation previously observed in P.I.C. simulations. Moreover careful comparisons of the Fourier modes in the two approaches has been done. This allows to point out the crucial importance of the choice of the initial perturbation, particularly in the case of linearly unstable systems. Indeed, in the case of P.I.C. simulations, unstable modes grow spontaneously from the numerical noise, while Vlasov simulations are noiseless and then require some initial perturbation. When this initial perturbation is distributed among the different modes according to the thermal levels in a maxwellian plasma the results obtained with Vlasov simulations are in close agreement with those of P.I.C. simulations. However the Vlasov code displays more complex phase-space correlations and permit to observe the long time behaviour of trapped particle structures. We thus have observed that the trapped particle oscillations which follow the saturation of the ion acoustic instability can be destroyed by growing side-bands.
Improvements of this code are under way and will permit to study the long time behaviour of more realistic non periodic ion beam-plasma systems.

Références:

[1] A. GHIZZO, *et al.*, Phys. of Fluids, $\mathbf{31}_1$ (1987) 72
[2] G. BONHOMME, *et al.*, Plasma Physics and Controlled Fusion, **335**, 507,(1991).
[3] H.L. PECSELI, *et al.*, Phys. Scripta **29** (1984), 241.
[4] C.J. CHENG, G. KNORR, Journal of Computational Physics, **22**, 330, (1976).
[5] R.J. GAGNE, M.M. SHOUCRI, Journal of Computational Physics, **24**, 445, (1977).
[6] M.M. SHOUCRI, Phys. of Fluids, $\mathbf{23}_{10}$ (1987) 2030

An Eulerian Code for the Study of the Gyro-Averaged Kinetic Vlasov Equation

A. Ghizzo[1], P. Bertrand[1] M. Shoucri, E. Fijalkow[2], M. Feix[2]

Centre Canadien de Fusion Magnétique
Varennes, Québec, Canada, J3X 1S1

1 Introduction

Strong magnetic fields are commonly used for plasma confinement in large devices. In many of these devices electric field $\vec{E}$ exists which results in an $\vec{E} \times \vec{B}$ drift. Any inhomogeneity in these electric fields results in a shear in the plasma flow and can lead to the appearance of low-frequency instabilities. The basic equation to describe such a system is the gyro-averaged kinetic Vlasov equation which couples the $\vec{E} \times \vec{B}$ motion across a magnetic field to the motion parallel to the magnetic field. We also note the recent interest in ion-temperature-gradient instabilities, also known as η_i modes [1], coupled with $\vec{E} \times \vec{B}$ shear. An important problem in the study of these instabilities is their small growth rate and the relatively low saturation level of their potential, which makes their simulation using particle codes difficult [1]. An obvious way to improve the understanding of these instabilities is to use an eulerian Vlasov model where, unlike particles in cell codes, we have a good description of vortex structures and phase space resolution and very low numerical noise.

2 The drift-kinetic Vlasov model

2.1 The basic equations and the numerical code

The basic equations that govern the plasma dynamics in the case of a uniform magnetic field $B = (B_x, O, B_z)$ tilted in the xz plane have been previously presented [2]. We use the guiding center drift approximation. The electron and ion velocity can be written in the following form

$$\vec{v}_{e,i} = \vec{v}_{\|e,i} + \vec{v}_1 \quad \text{with} \quad \vec{v}_1 = \frac{\vec{E} \times \vec{B}}{B^2} \tag{1}$$

The drift-kinetic Vlasov equation is written:

$$\frac{\partial f_{i,e}}{\partial t} + \vec{v}_{\|} \cdot \frac{\partial f_{i,e}}{\partial \vec{r}_{\|}} + \frac{\vec{E} \times \vec{B}}{B^2} \cdot \frac{\partial f_{i,e}}{\partial \vec{r}_1} + \frac{e}{m_{i,e}} \vec{E}_{\|} \cdot \frac{\partial f_{i,e}}{\partial v_{\|}} = 0 \tag{2}$$

The electron and ion distributions functions are reduced to a 3D phase space function $f_e\,(x, y, v_{\|e})$ and $f_i\,(x, y, v_{\|i})$ where $v_{\|}$ is the velocity variable along the magnetic field. We assume periodic boundary condition in the x-direction and finite-boundary in y-direction. Thus we perform the numerical experiment in a rectangular domain with $0 \leq x \leq L_x$ and $-L_y \leq y \leq L_y$.

[1]Physique Théorique, Université de Nancy, France
[2]PMMS/CNRS - Université d'Orléans, France

The electric field are then given by:

$$\vec{E} = -\nabla\varphi \tag{3}$$

where the electric potential φ obeys Poissons's equation:

$$\frac{\partial^2\varphi}{\partial x^2} + \frac{\partial^2\varphi}{\partial y^2} = +\frac{e}{\varepsilon_o}\ [n_e(x,y,t) - n_i(x,y,t)] \tag{4}$$

where n_e and n_i denote respectively the electron and ion density given by

$$n_{e,i}(x,y,t) = \int f_{e,i}(x,y,v_{\|e,i})\ dv_{\|e,i} \tag{5}$$

The numerical integration of Eq. 2 is performed by using a splitting scheme in which we separate the integration in both directions successively according to the sequence of operators $\frac{\hat{X}}{2}\ \frac{\hat{Y}}{2}\ \hat{V}_{\|}\ \frac{\hat{Y}}{2}\ \frac{\hat{X}}{2}$ were the operators $\hat{X}, \hat{Y}$ and $\hat{V}_{\|}$ denote the shift in x, y, and $v_{\|}$ direction for both particle species, and over a full time step Δt. (The term 1/2 denotes that the shift is effected over a half time step)[2]. The shifts are calculated using a cubic spline interpolation. This sequence allows us to compute the electron distribution function f_e (or f_i in a similar way) at each grid points at time t_{n+1} from the known values of f_e (or f_i), and this scheme is correct in the second order in Δt.

3 The ion temperature gradient instabilities

These are basically very low frequency electrostatic waves, which can become destabilized when the parameter $\eta_i = d(lnTi)/d(lnn_i)$ exceeds a critical value. The Vlasov code presents a powerful tool for the investigation of these instabilities, because of their very low noise levels. We present in this section the result of a simulation with the following initial equilibrium profiles:

$$T_i = T_{io}\ \left(0.2 + 0.8 \times e^{-\beta y^2}\right) \qquad \text{with} \qquad T_{io} = 1$$

$$n_o = \sqrt{\frac{\alpha}{\pi}}\ e^{-\alpha y^2}$$

with $\alpha = 0.025$, $\beta = 7\alpha$. This corresponds to a maximum value $\eta_i = 5.2$.

The initial ion distribution function is then given by

$$f_i\left(x,y,v_{\|},t=0\right) = \frac{n_o}{\sqrt{2\pi Ti}}\ e^{\frac{-v_{\|}^2}{2Ti}}\ (1 + \varepsilon \sin k_o x + \varepsilon \sin 2k_o x + \varepsilon \sin 3k_o x)$$

where we have introduced a perturbation term with $\varepsilon = 0.001$ to start up the instability. In this simulation the space variables x and y are normalized to $\rho_s = C_s/\omega_{pi}$ where C_s is the ion acoustic velocity, the velocity $v_{\|}$ is normalized to C_s and the time is normalized to the inverse ion plasma frequency ω_{pi}^{-1}. The electrons are taken to follow an adiabatic law [1]:

$$n_e(y) = n_o(y)\ \left(1 + \frac{e\phi}{T_e}\right)$$

We take $T_e = T_{io}$ and we assume at each time step Δt the quasi-neutrality of plasma $< n_e > = < n_i >$ by computing the value of the potential constant. We note that the ion gyroradius effects are neglected in the present drift kinetic approximation. (Work is in progress to include the gyro-averaging effect in the previous equations.) The simulation was effected with $\omega_{ci}/\omega_{pi} = 0.50$. Figure 1 shows on a logarithmic scale the growth and saturation of the potential (growth rate $\frac{\gamma}{\omega_{pi}} = 7 \times 10^{-4}$) at the center of the plasma for the mode $k_o = \frac{2\pi}{Lx}$. Contours plots of the potential at a time $t\omega_{pi} = 9100$ and $t\omega_{pi} = 9500$ at saturation are shown in Figs. 2 and 3. They show vortices traveling at what appears to be the phase velocity of the wave. Figure 4 and figure 5 show the corresponding $\vec{E} \times \vec{B}$ flow at the same time.

The present results are effected with a time step of $\Delta t\omega_{pi} = 1$ and we use a mesh of $N_x N_y N_{v_\parallel} = 64 \times 128 \times 32$ which is equivalent to 262144 particles. This simulation took about 4 hours (CPU time) on the CRAY - 2 computer for 10^4 time steps. The present results show how the solutious obtained from a Vlasov code are noiseless, and an instability with weak growth rate is described untill saturation.

Acknowledgments

The Centre Canadien de fusion magnétique is a joint venture of Hydro-Québec, Atomic Energy of Canada Limited and the Institut-national de la recherche scientifique, in which MPB Technologies Inc. and Canatom Inc. also participate. It is principally funded by AECC, Hydro-Québec and INRS.

References

1 W.W. Lee and W.M. Tang, Phys. Fluids 31, 612 (1988); W. W. Lee, J. Comp. Phys. 72, 243 (1987).

2 A. Ghizzo, P. Bertrand, M. Shoucri, E. Fijalkow, M. Feix, Centre Canadien de Fusion Magnétique CCFM Report No. 356, (1991). A. Ghizzo et al., Proc. 18th Euro. Conf. Contr. Fusion, Berlin (Ed. P. Backmann, D.C. Robinson) Vol. 15C, p. IV-153 (1991).

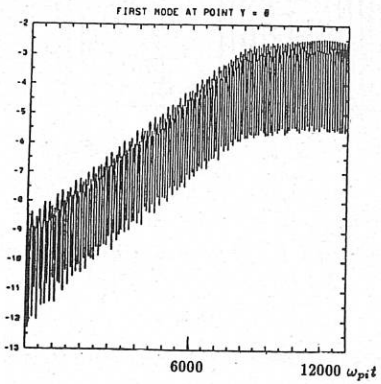

Fig. 1

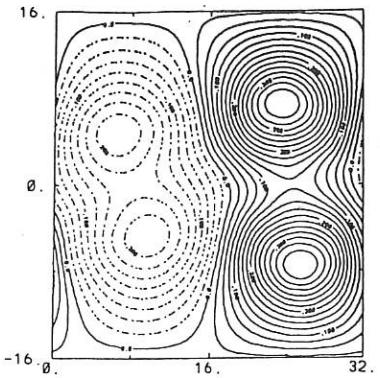

Fig. 2

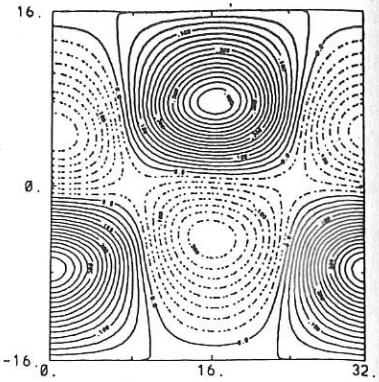

Fig. 3

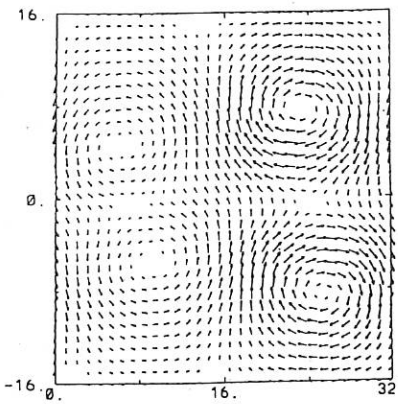

Fig. 4

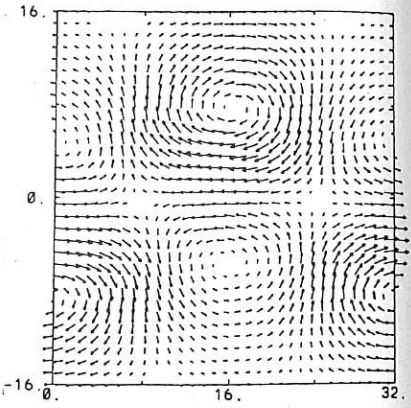

Fig. 5

RELATIVISTIC VLASOV-MAXWELL EQUILIBRIA OF ANISOTROPIC CHARGE-SEPARATION-FREE PLASMAS

Leon P.J. Kamp, M.J. van Bruggen-Kerkhof and F.W. Sluijter
Eindhoven University of Technology, Physics Department
P.O. Box 513, NL-5600 MB Eindhoven, The Netherlands

Introduction

The behavior of laboratory plasma containment devices is often modelled by so-called magnetic solutions of the Vlasov-Maxwell system (describing a collisionless plasma). For these magnetic solutions charge neutrality prevails at all times implying that electric fields are negligible or even completely absent. In the present contribution we investigate why charge neutrality prevails in a confined plasma and under which conditions the charge-separation electric field is indeed negligible. More specifically we demonstrate that with fully-relativistic anisotropic plasmas, equilibria can be realized only if the distribution functions of the electrons and ions are related to each other in a special manner provided that their dependence on the constants of motion is separable. This relation is non-local in momentum space and reduces to a local one in the non-relativistic limit. Furthermore, as an example we analyze a relativistic model for the plasma-magnetic field boundary and demonstrate how to choose distribution functions that lead to neutral steady states in which electric fields are completely absent.

Basics

Consider a one-dimensional static configuration that consists of a plasma, which is inhomogeneous in the x-direction and is permeated by a static magnetic field in the z-direction (laboratory-frame). In this case the electric and the magnetic fields can be derived from the potentials V and A respectively, in the following manner:

$$\vec{E}_0 = -\frac{dV}{dx}\vec{e}_x, \quad \vec{B}_0 = \frac{dA}{dx}\vec{e}_z. \tag{1}$$

The relativistic Vlasov-Maxwell system for this stationary situation is given by

$$\frac{c\rho_x}{\gamma}\frac{\partial f_e}{\partial x} - \frac{e}{m_e c}\left(\vec{E}_0 + \frac{c\vec{\rho}}{\gamma}\wedge\vec{B}_0\right)\cdot\nabla_\rho f_e = 0, \tag{2a}$$

$$\frac{c\rho_x}{\gamma}\frac{\partial f_i}{\partial x} + \frac{q_i}{m_i c}\left(\vec{E}_0 + \frac{c\vec{\rho}}{\gamma}\wedge\vec{B}_0\right)\cdot\nabla_\rho f_i = 0, \tag{2b}$$

$$-\frac{d^2A}{dx^2} = \mu_0(J_{e_y} + J_{i_y}), \tag{3a}$$

$$-\frac{d^2V}{dx^2} = \frac{1}{\epsilon_0}(q_i N_i - eN_e). \tag{3b}$$

Here, f_s and $\vec{J}_s$ denote the distribution function and the current density respectively, of particles of species s and

$$\vec{\rho} = \frac{\gamma}{c}\vec{v}, \quad \gamma(\rho) = \sqrt{1+\rho^2}. \tag{4}$$

The other symbols have their usual meaning. The relation between the particle density N_s and $\vec{J}_s = J_{s_y}\vec{e}_y$ on the one hand and f_s on the other hand is given by

$$N_s(x) = N_{s_0}\int d^3\rho\; f_s(x,\rho), \quad J_{sy}(x) = N_{s_0}q_s c\int d^3\rho\frac{\rho_y}{\gamma(\rho)}f_s(x,\rho), \tag{5}$$

where N_{s_0} is the density of particles of species s when there are no fields. For the equilibrium distribution functions f_s we choose the following functions of the constants of motion that resemble relativistic Maxwellians (and that coincide with them when $A \equiv 0$):

$$f_s = \overbrace{\frac{\mu_s \exp(-\mu_s)}{4\pi K_2(\mu_s)} \exp\left(-\frac{\mu_s H_s}{m_s c^2}\right)}^{\text{Jüttner-Synge distribution function /1/}} \times h_s\{\mathrm{sgn}(q_s) P_{s_y}\}, \tag{6}$$

where the Hamiltonians H_s and the canonical momenta in the y-direction P_{s_y} are given by

$$\begin{aligned} H_s &= H_s(\rho, x) = \left(\sqrt{\rho^2 + 1} - 1\right) m_s c^2 + q_s V(x), \\ P_{s_y} &= P_{s_y}(\rho, x) = \rho_y + \frac{q_s}{m_s c} A(x) \end{aligned} \tag{7}$$

and where $\mu_s = m_s c^2 / k_B T_s$. K_2 is the modified Bessel function of the second kind and of order 2. The functions h_s are meant to model the departure from global thermodynamic equilibrium (if one ignores the gyro-radiation field) due to the presence of the inhomogeneous (confining) magnetic field.

Analysis

If we introduce the kernel function

$$K_s(\rho_y) = \frac{2\pi}{K_2(\mu_s)} \left(\sqrt{1 + \rho_y^2} + \frac{1}{\mu_s}\right) \exp\left(-\mu_s \sqrt{1 + \rho_y^2}\right) \tag{8}$$

and the parameters

$$Z = \frac{q_i}{e}, \quad \alpha = \frac{T_i}{T_e}, \quad \beta = \frac{m_i}{m_e}, \tag{9}$$

then, from (5), (6) and (7) we can deduce

$$N_e(x) = N_{e_0} \exp\{\Phi_e(x)\} g_e\{\Psi(x)\}, N_i(x) = N_{i_0} \exp\left\{-\frac{Z}{\alpha}\Phi_e(x)\right\} g_i\{\Psi(x)\}, \tag{10}$$

$$J_{ey}(x) = \frac{N_{e_0} ec}{\mu_e} \exp\{\Phi_e(x)\} g_e'\{\Psi(x)\}, J_{iy}(x) = \frac{\beta N_{i_0} ec}{\mu_i} \exp\left\{-\frac{Z}{\alpha}\Phi_e(x)\right\} g_i'\{\Psi(x)\}, \tag{11}$$

where the functions g_e and g_i are defined by

$$g_e\{\Psi(x)\} = \int_{-\infty}^{\infty} d\rho_y \; K_e(\rho_y) h_e\{\Psi(x) - \rho_y\}, \tag{12a}$$

$$g_i\{\Psi(x)\} = \int_{-\infty}^{\infty} d\rho_y \; K_i(\rho_y) h_i\left\{\frac{Z}{\beta}\Psi(x) + \rho_y\right\} \tag{12b}$$

and Φ_e and Ψ are dimensionless potentials according to

$$\Phi_e(x) = \frac{eV(x)}{k_B T_e}, \quad \Psi(x) = \frac{eA(x)}{m_e c}. \tag{13}$$

The primes in equations (11) denote differentiation with respect to Ψ. Finally upon introducing

$$\Phi(x) = \frac{1}{2}\left(1 + \frac{Z}{\alpha}\right)\Phi_e(x), \quad \delta = \frac{Z - \alpha}{Z + \alpha}, \quad \bar{g} = \frac{g_e + g_i}{2}, \quad g_d = \frac{g_e - g_i}{2}, \tag{14}$$

Maxwell's equations (3) may be written as follows:

$$\frac{d^2\Phi}{d\xi^2} = \Big(1+\frac{Z}{\alpha}\Big)\mu_e \exp\{-\delta\Phi(\xi)\}[\sinh\{\Phi(\xi)\}\bar{g}\{\Psi(\xi)\} + \cosh\{\Phi(\xi)\}g_d\{\Psi(\xi)\}], \quad (15a)$$

$$\frac{d^2\Psi}{d\xi^2} = -\frac{2}{\mu_e}\sqrt{\frac{\alpha}{Z}}\exp\{-\delta\Phi(\xi)\} \times [\cosh\{\Phi(\xi)+\phi_\delta\}\bar{g}'\{\Psi(\xi)\} + \sinh\{\Phi(\xi)+\phi_\delta\}g_d'\{\Psi(\xi)\}], \quad (15b)$$

where

$$\phi_\delta = \operatorname{arctanh}(\delta), \quad \xi = \sqrt{\frac{\mu_0 N_{e_0} e^2}{m_e}}\,x. \quad (16)$$

In the electrostatic situation ($\Psi \equiv 0$) the functions h_e and h_i become identically one. The equations (15a) and (15b) then reduce to a single equation for Φ only, i.e.

$$\frac{d^2\Phi}{d\xi^2} = \Big(1+\frac{Z}{\alpha}\Big)\mu_e \exp\{-\delta\Phi(\xi)\}\sinh\{\Phi(\xi)\}. \quad (17)$$

This situation essentially reviews the solutions of the pure Vlasov-Poisson problem for the Ansatz (6) (a homogeneous magnetic field may still be present).
The coupled second-order equations (15a) and (15b) may be combined into a single differential equation of fourth order. The highest derivative of this fourth-order equation is multiplied by $1/\mu_e$. For the fusion-relevant case of a weakly-relativistic plasma, $1/\mu_e \ll 1$. This means that (15) is a candidate for boundary-layer theory. A boundary layer is a narrow region where the solution of (15) changes far more rapidly than outside of it. By definition, the thickness of such a boundary layer must approach zero as $\mu_e \to \infty$. Outside these isolated regions of rapid variations it is justified to neglect the second derivative of the potential Φ (divided by μ_e) in (15a) which is in fact tantamount to the commonly employed quasi-neutrality approximation. Thus we arrive at the conclusion that the quasi-neutrality assumption is closely related to the non-relativistic limit relevant to fusion plasmas.
In the absence of an electric potential ($\Phi \equiv 0$) the plasma must be locally neutral. In that case equation (15a) is necessarily trivial which leads to the condition that $g_d = 0$. So the functions h_e and h_i must satisfy the equation

$$\int_{-\infty}^{\infty} d\rho_y\; K_e(\rho_y)h_e\{\Psi(x)-\rho_y\} = \int_{-\infty}^{\infty} d\rho_y\; K_i(\rho_y)h_i\Big\{\frac{Z}{\beta}\Psi(x)+\rho_y\Big\}. \quad (18)$$

The integrals in this expression are of the convolution type. This fact offers the possibility to obtain the following integral relation between the functions h_e and h_i by employing the Fourier transform:

$$h_e(\Psi) = \int_{-\infty}^{\infty} dy\; K(y)h_i\Big\{\frac{Z}{\beta}(\Psi-y)\Big\}, \quad (19)$$

where

$$K(y) = \frac{\mu_i^2 \mathrm{K}_2(\mu_e)}{\mu_e^2 \mathrm{K}_2(\mu_i)}\sqrt{\frac{2}{\pi}}\int_0^{\infty} dk\;\cos(ky)\frac{\mathrm{K}_2\big(\sqrt{\beta^2 Z^2/k^2+\mu_i^2}\big)}{\mathrm{K}_2\big(\sqrt{k^2+\mu_e^2}\big)}. \quad (20)$$

In the non-relativistic limit ($c \to \infty$) $K(y)$ reduces to the Dirac delta function and relation (19) then becomes a local one in momentum space.

Application

The previous results may be employed to simulate various relativistic equilibria in which the plasma is everywhere exactly neutral ($\Phi \equiv 0$; deviations from exact neutrality due to finite gyro-radius effects are ignored). More specifically we will now use our approach to construct a fully-relativistic steady-state model for the plasma-magnetic field boundary in which the plasma is free of charge separation and becomes relativistic Maxwellian for $|x| \to \infty$ where the confining magnetic field becomes homogeneous. To that end we prescribe $\bar{g}\{\Psi(\xi)\}$ as follows:

$$\frac{d\bar{g}}{d\Psi} = \frac{1}{\cosh^2(\xi)}. \tag{21}$$

Since we assume exact neutrality everywhere in the plasma, equation (15b) reduces to

$$\frac{d^2\Psi}{d\xi^2} = -\frac{2}{\mu_e}\sqrt{\frac{\alpha}{Z}}\cosh(\phi_\delta)\frac{d\bar{g}}{d\Psi}, \tag{22}$$

from which we easily deduce

$$\Psi(\xi) = C\xi - \frac{2}{\mu_e}\sqrt{\frac{\alpha}{Z}}\cosh(\phi_\delta)\log\{\cosh(\xi)\}, \tag{23}$$

where C is an arbitrary integration constant to be determined by the boundary conditions. The function $\bar{g}$ (and herewith the particle density profile $N = N_e = N_i$) is established by using (21) and (22) and integrating. This yields

$$\bar{g}(\xi) = \int_{-\infty}^{\xi} d\eta \frac{C\mu_e - 2\sqrt{\alpha/Z}\cosh(\phi_\delta)\tanh(\eta)}{\mu_e\cosh^2(\eta)} = C\tanh(\xi) + \frac{\sqrt{\alpha/Z}\cosh(\phi_\delta)}{\mu_e\cosh^2(\xi)} + C. \tag{24}$$

The Fourier transform of this expression and of the convolution integrals (12a) and (12b) finally leads to the following result for the function h_i:

$$h_i\Big(\frac{Z}{\beta}\Psi\Big) = -\frac{4\mu_i^2}{Z\mathrm{K}_2(\mu_i)}\sqrt{\frac{2}{\pi}}\int_0^\infty \frac{dk}{k}\sin(k\Psi)\frac{\exp\{ik\sqrt{\alpha/Z}\cosh(\phi_\delta)\log(4)/\mu_e\}}{\mathrm{K}_2\big(\sqrt{\beta^2k^2/Z^2+\mu_i^2}\big)}$$
$$\times\Big(\frac{\beta^2k^2}{Z^2}+\mu_i^2\Big)\mathcal{B}\Big\{1+ik\Big(\frac{\sqrt{\alpha/Z}}{\mu_e}\cosh(\phi_\delta)+\frac{C}{2}\Big), 1+ik\Big(\frac{\sqrt{\alpha/Z}}{\mu_e}\cosh(\phi_\delta)-\frac{C}{2}\Big)\Big\}, \tag{25}$$

where $\mathcal{B}$ is the beta function. Finally we note that h_e is found with (19) after which the particle and current densities may be found with (10), (11) and (12).
Note that the steady-state model of the plasma-magnetic field boundary considered above is by no way unique. Different choices of $\bar{g}$ in (21) are possible. Moreover the problem at hand is non-unique because of the presence of trapped particles somewhere in the plasma, which could never reach the relativistic Maxwellian part of it.
For further details and references see /1/ where we treated the special case of $Z = 1 = \alpha$.

/1/ Leon P.J. kamp, M.J. Kerkhof, F.W. Sluijter, M.P.H. Weenink, Phys. Fluids B: Plasma Phys. 4, 521 (1992).

A NEW ACTION PRINCIPLE FOR THE VLASOV-MAXWELL SYSTEM

Jonas Larsson
Department of plasma physics, University of Umeå
S-901 87 Umeå, Sweden

Abstract: Everyone interested in action principles for the Vlasov-Maxwell system has probably noticed the difficulty to use the particle distribution function as a field to be independantly varied. A solution to this old problem is presented in this paper.

1. Introduction

The purpose of this paper is to present new action principles for the VP equation (i.e. the Vlasov-Poisson equation) and the VM system (i.e. the Vlasov-Maxwell system). These results will be useful for perfoming standard reduction procedures (like linearization, geometric optics, gyro-kinetics) in a manifestely Hamiltonian structure preserving way. In this short paper we will however concentrate on the relations to previous theory on the Lagrangian-Hamiltonian structure of these equations and more details will be published elsewhere.[1]

The VP equation and the VM system have the structure of a Lagrangian field theory found by Low (1958).[2] The corresponding Hamiltonian structure follows in the usual way using the Legendre transformation. We then have field theories in the material (i.e. Lagrangian) coordinaters such that the solutions monitors the motion of each particle. One would like use Eulerian coordinates instead so that all this redundant information is eliminated and thus the particle distribution function give all information about the plasma particles. The needed reduction procedures make necessary generalizations of standard Hamiltonian mecanics. It is instructive to consider the relation to standard formulations of classical mecanics. We have

(a) Lagrangian action principle: $\delta I(q) = 0,\ I(q) = \int L(q,\dot{q})\, dt$

(b) Hamilton's canonical equations: $\dot{q} = \partial H/\partial p$, $\dot{p} = -\partial H/\partial q$

(c) Poisson-bracket formulation: $dA(q,p)/dt = \{A,H\}(q,p)$

(d) Hamiltonian action priciple: $\delta I(q,p) = 0$, $I(q,p) = \int [p\cdot\dot{q} - H(q,p)]\, dt$

This reduction program have been carried out on the level (c) for the VP equation and the VM system.[3,4,5] The necessary generalization to noncanonical field variables results in new Poisson-brackets which still possess the usual algebraic properties including the Jacobi identity. The corresponding results on the other levels, i.e. (a), (b) and (d), seems to be lacking. An underlying reason for the difficulties is the singular structure of the non-canonical Poisson brackets (i.e. the existence of Casimirs).[5]

A basic novel feature underlying the new theory is that we consider the dynamics of extended systems so that the VP equation or the VM system are "embedded" in larger systems. The results are generalizations on the levels (b) and (d).

2. The Vlasov-Poisson equation

For notational brevity we now consider the VP equation. Let $f = f(t,\underline{r},\underline{v})$ denote the particle distribution function. As discussed in the Introduction there is no known action principle $I(f)$ such that $\delta I(f) = 0$ produces the VP equation. A startingpoint for finding the new action principle presented below was the idea that it might be possible to find an phase-space action principle of the form $I(f,S)$ where the function $S = S(t,\underline{r},\underline{v})$ is a canonically conjugate field to f. This approach was further modified by the introduction of a continous parameter ε, $0 \leq \varepsilon \leq 1$, such that $\varepsilon = 0$ corresponds to a reference state of the particles and $\varepsilon = 1$ to the true physical state. We then consider functions $\tilde{f} = f(\varepsilon,t,\underline{r},\underline{v})$ and $\tilde{S} = \tilde{S}(\varepsilon,t,\underline{r},\underline{v})$ and an action principle $I(\tilde{f},\tilde{S})$. The function $\tilde{S}$ is the Hamiltonian for the ε motion of the particles from

their reference position in $(\underline{r},\underline{v})$ space to their physical position in this space. The new action principle is

$$I(\tilde{f},\tilde{S}) = \int [\int \tilde{f}\, \partial_t \tilde{S}\, d\varepsilon\, d^3r\, d^3v - H(\tilde{f},\tilde{S})]\, dt \qquad (1)$$

where

$$H(\tilde{f},\tilde{S}) = -\int \frac{1}{2}\, \underline{v}^2\, \{\tilde{f},\tilde{S}\}_{rv}\, d\varepsilon\, d^3r\, d^3v + \frac{1}{2} \int [\partial_\tau \phi(\tilde{f},\tilde{S})]^2\, d^3r \qquad (2)$$

with $\{\ ,\ \}_{rv}$ as the Poisson-bracket for the plasma particle motion in $(\underline{r},\underline{v})$-coordinates and with $\phi(\tilde{f},\tilde{S})$ defined from

$$\partial_\tau^2 \phi(\tilde{f},\tilde{S}) = -\int \tilde{f}(\varepsilon=1)\, d^3v + \int \varepsilon\, (\partial_\varepsilon \tilde{f} + \{\tilde{F},\tilde{S}\})\, d\varepsilon\, d^3v \qquad (3)$$

The Euler-Lagrange equations from (1) are Hamilton's field equations

$$\partial_t \tilde{f} = -\delta H/\delta \tilde{S}\ , \qquad \partial_t \tilde{S} = \delta H/\delta \tilde{f} \qquad (4)$$

The following diagram displays the relation between (4) and the VP equation:

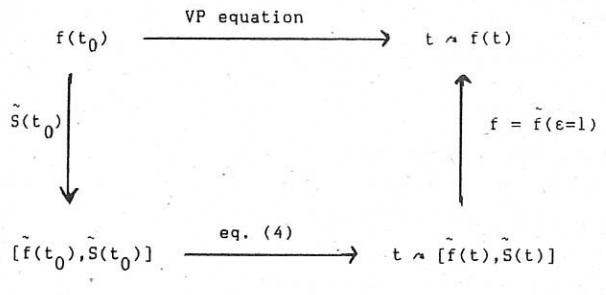

In the upper left of the diagram an initial condition for the VP equation is given. The upper arrow towards the right shows that the VP equation together with the initial condition determine a solution. The arrow pointing downwards indicate that a corresponding initial condition $[\tilde{f}(t_0),\tilde{S}(t_0)]$ for (4) may be found for an arbitrary choice of $\tilde{S}(t_0)$: $\tilde{f}(t_0)$ is determined by the requirements (a) $\tilde{f}(\varepsilon=1,t=t_0) = f(t_0)$ and (b) $\partial_\varepsilon \tilde{f}(t_0) + \{\tilde{f}(t_0),\tilde{S}(t_0)\}_{rv} = 0$. The lower arrow towards the right shows that eq. (4) have a unique solution with this initial condition. Finally by the upward arrow in the diagram we again get the solution to the VP equation

3. The Vlasov-Maxwell system

A corresponding action principle for the VM system is

$$I(\tilde{f}^c,\tilde{S}^c,\underline{E},\underline{A}) = \int [\int \tilde{f}^c \partial_t \tilde{S}^c \, d\varepsilon \, d^3p + \underline{E}\cdot\partial_t\underline{A}\,) \, d^3r - H(\tilde{f}^c,\tilde{S}^c,\underline{E},\underline{A})\,)] \, dt$$

where the superscript c indicates the use of canonical coordinates and

$$H(\tilde{f}^c,\tilde{S}^c,\underline{E},\underline{A}) =$$
$$\int [-\tilde{H}^c\{\tilde{f}^c,\tilde{S}^c\}_{rp} + \tilde{F}^c\partial_\varepsilon\tilde{H}^c] \, d\varepsilon \, d^3r \, d^3p \; - \int [\;\tfrac{1}{2}\,(\underline{E}^2 + \underline{B}^2)\;] \, d^3r$$

where $\tilde{H}^c(\varepsilon,t,\underline{r},\underline{p}) = \frac{1}{2}\,[\underline{p} - \varepsilon\underline{A}(t,\underline{r})]^2$ and $\underline{B} = \partial_r \times \underline{A}$ (but not $\underline{E} = -\partial_t\underline{A}$, since this relation is now obtained as a dynamical equation).

References

1. J. Larsson, 1992 J. Plasma Phys., in press.
2. F.E. Low, 1958 Proc. Roy. Soc., A 248, 282.
3. R. Iwinski & L.A. Turski, 1976 Lett. Appl. Eng. Sci. 4, 179.
4. P.J. Morrison, 1980 Phys. Lett. A80, 383.
5. J. Marsden & A. Weinstein, 1982 Physica 4D, 392.

III-1753

Negative-Energy Waves in an Inhomogeneous Force-Free Vlasov Plasma with Sheared Magnetic Field

Darío Correa-Restrepo and Dieter Pfirsch

Max-Planck-Institut für Plasmaphysik
EURATOM Association
D-8046 Garching bei München, Federal Republic of Germany

I. Introduction

Considering arbitrary perturbations of general Vlasov-Maxwell equilibria, Morrison and Pfirsch [1, 2] derived expressions for the second variation of the free energy and concluded that negative-energy perturbations (which are potentially dangerous because they may become nonlinearly unstable and cause anomalous transport [4, 3]) exist in any Vlasov-Maxwell equilibrium whenever the unperturbed distribution function $f_\nu^{(0)}$ of any particle species ν deviates from monotonicity and/or isotropy in the vicinity of a single point, i.e. whenever the condition $(\mathbf{v}\cdot\mathbf{k})\left(\mathbf{k}\cdot\frac{\partial f_\nu^{(0)}}{\partial \mathbf{v}}\right) > 0$ holds for any particle species ν for some position vector $\mathbf{x}$ and velocity $\mathbf{v}$ and for some vector $\mathbf{k}$. The proof of this result is based on infinitely strongly localized perturbations. This raises the question of the degree of localization actually required for negative-energy modes to exist in a certain equilibrium. Studying a homogeneous Vlasov-Maxwell plasma with constant magnetic field, Correa-Restrepo and Pfirsch [5] showed that negative-energy waves exist for any deviation of the equilibrium distribution function of any of the species from monotonicity and/or isotropy, *without having to impose any restricting conditions on the perpendicular wave number* $k_\perp$, i.e. without requiring large $k_\perp$. These investigations are extended in the present paper to the more interesting case of an inhomogeneous, force-free equilibrium with a sheared, y-dependent magnetic field. The method of investigation consists in evaluating the general expression for the second-order wave energy derived by Morrison and Pfirsch [1, 2] in the form given by Correa-Restrepo and Pfirsch [5]. Although the calculations are considerably more involved than in the case of the homogeneous magnetic field, substantial simplification of the problem is achieved by the introduction of appropriate coordinates in $\mathbf{v} - y$ space and by a convenient representation of the perturbations. It is concluded that negative-energy modes exist in the inhomogeneous configuration as well whenever any of the equilibrium distribution functions deviates from monotonicity and/or isotropy (in fact, owing to the inhomogeneity, the equilibrium distribution function for at least one particle species must be anisotropic!), and that large perpendicular wave numbers are not required in this case either. If there is only anisotropy, the presence of shear merely requires that the perturbations have a characteristic variation

length in the direction perpendicular to the equilibrium magnetic field $\mathbf{B}^{(0)}$ smaller than (or of the order of) the shear length a^{-1}, which is *not* an important restriction, i.e. negative-energy modes persist without any major modification in the presence of shear, a feature which enhances their importance.

II. Equilibrium Electromagnetic Field and Distribution Functions

It is assumed that there is no equilibrium electric field, and that the equilibrium magnetic field has constant magnitude and straight field lines which twist as one proceeds in a given direction. In Cartesian coordinates x, y, z with unit basis $\mathbf{e}_x, \mathbf{e}_y, \mathbf{e}_z$, the equilibrium magnetic field is given by $\mathbf{B}^{(0)} = B^{(0)}\mathbf{e}_B = B^{(0)}(\sin ay\, \mathbf{e}_x + \cos ay\, \mathbf{e}_z)$. In this case, there is an electric current parallel to the magnetic field, and the charged particles of any species belong (according to the values of their constants of the motion) to either one of two essentially different groups, either to the group of gyrating particles (the overwhelming majority in all cases of interest), which move around the field lines, their motion being confined to a certain y-region around $y = \mathcal{Y}_\nu$, where $\mathcal{Y}_\nu$ is a constant of the motion, or to the group of swinging particles, which move freely in the y-direction. The two groups of particles must be investigated separately. Owing to the presence of the electric current associated with nonvanishing a, the equilibrium distribution function of at least one particle species ν *must* be anisotropic, unlike in the homogeneous case. For the inhomogeneous, force-free equilibrium, the distribution functions for particles of charge e_ν and mass m_ν are of the form $f_\nu^{(0)} = f_\nu^{(0)}\left(\mathcal{H}_\nu = \frac{m_\nu}{2}(\dot{x}^2 + \dot{y}^2 + \dot{z}^2), \mathcal{U}_\nu = \frac{a}{2\omega_\nu}\dot{y}^2 + \dot{x}\sin ay + \dot{z}\cos ay\right)$, where $\omega_\nu \equiv \frac{e_\nu B^{(0)}}{m_\nu c}$. The energy $\mathcal{H}_\nu$ and the velocity $\mathcal{U}_\nu$ are constants of the motion.

III. Second-Order Wave Energy

Within the framework of Maxwell-Vlasov theory, Morrison and Pfirsch [1, 2] derived expressions for the free energy $\delta^2 H$ available upon arbitrary perturbations of an arbitrary equilibrium. For electrostatic perturbations with $\delta\mathbf{B} = 0$, and in the absence of an equilibrium electric field, $\delta^2 H$ can be expressed as [5]

$$\delta^2 H = \sum_\nu \int \frac{d^3x\, d^3v}{2m_\nu}\left[\frac{\partial f_\nu^{(0)}}{\partial \mathbf{v}}\cdot\left\{-\left(\mathbf{v}\cdot\frac{\partial G_\nu}{\partial \mathbf{x}}\right)\frac{\partial G_\nu}{\partial \mathbf{x}} - \left(\mathbf{a}_\nu^{(0)}\cdot\frac{\partial G_\nu}{\partial \mathbf{v}}\right)\right.\right.$$
$$\left.\left(\frac{e_\nu}{m_\nu c}\mathbf{B}^{(0)}\times\frac{\partial G_\nu}{\partial \mathbf{v}} + 2\frac{\partial G_\nu}{\partial \mathbf{x}}\right) + \frac{e_\nu}{m_\nu c}G_\nu\,\mathbf{v}\times\frac{\partial}{\partial \mathbf{v}}\left(\mathbf{B}^{(0)}\cdot\frac{\partial G_\nu}{\partial \mathbf{x}}\right)\right\}$$
$$\left. + \frac{\partial f_\nu^{(0)}}{\partial \mathbf{x}}\cdot\left\{-\left(\frac{\partial G_\nu}{\partial \mathbf{x}}\cdot\frac{\partial G_\nu}{\partial \mathbf{v}}\right)\mathbf{v} + (d_\nu G_\nu)\frac{\partial G_\nu}{\partial \mathbf{v}}\right\}\right] + \frac{1}{8\pi}\int d^3x(\delta E^2)\,, \qquad (1)$$

where $G_\nu(\mathbf{x}, \mathbf{v})$ is a generating function for the perturbation of the particle position and velocity, and $\delta E^2/8\pi$ is the perturbation in the electric energy density. The operator d_ν is the equilibrium Vlasov operator, i.e. $d_\nu = \mathbf{v}\cdot\frac{\partial}{\partial \mathbf{x}} + \mathbf{a}_\nu^{(0)}\cdot\frac{\partial}{\partial \mathbf{v}}$, $\mathbf{a}_\nu^{(0)} = \frac{e_\nu}{m_\nu c}\mathbf{v}\times\mathbf{B}^{(0)}$

(in the absence of an equilibrium electric field). Since the equilibrium is independent of x and z, an appropriate ansatz for the generating function $G_\nu(\mathbf{x},\mathbf{v})$ is $G_\nu(\mathbf{x},\mathbf{v}) = \frac{1}{2}\left[g_\nu(y,\mathbf{v})e^{i\mathbf{k}_{xz}\cdot\mathbf{x}} + g_\nu^*(y,\mathbf{v})e^{-i\mathbf{k}_{xz}\cdot\mathbf{x}}\right]$, with $\mathbf{k}_{xz} = k_x\mathbf{e}_x + k_z\mathbf{e}_z$. Setting $g_\nu(y,\mathbf{v}) = \Psi_\nu(y,\mathbf{v})e^{i\Gamma_\nu(y,\mathbf{v})}$, where Ψ_ν and Γ_ν are *real* functions, $d_\nu = \hat{d}_\nu + \dot{x}\frac{\partial}{\partial x} + \dot{z}\frac{\partial}{\partial z}$, $\mathcal{D}f_\nu^{(0)} = m_\nu\frac{\partial f_\nu^{(0)}}{\partial \mathcal{H}_\nu} + \frac{a}{\omega_\nu}\frac{\partial f_\nu^{(0)}}{\partial \mathcal{U}_\nu} = 2\frac{\partial f_\nu^{(0)}}{\partial \dot{y}^2}$, $\mathbf{w} = \mathbf{v} - \dot{y}\mathbf{e}_y$, $s = 4\pi^2/k_xk_z$, the second-order wave energy can be expressed as

$$\delta^2 H = \sum_\nu \frac{s}{4m_\nu}\int d^3v\, dy\Big\{-\left[\mathcal{D}f_\nu^{(0)}\right]\left[\left(\hat{d}_\nu\Psi_\nu\right)^2 + \Psi_\nu{}^2\left[\hat{d}_\nu\Gamma_\nu + (\mathbf{v}\cdot\mathbf{k}_{xz})\right]^2\right]$$

$$+\Psi_\nu{}^2\frac{\partial f_\nu^{(0)}}{\partial \mathcal{U}_\nu}\left[\frac{a}{\omega_\nu}\mathbf{w} - \mathbf{e}_B\right]\cdot\mathbf{k}_{xz}\left[\hat{d}_\nu\Gamma_\nu + (\mathbf{v}\cdot\mathbf{k}_{xz})\right]\Big\} + \frac{1}{8\pi}\int d^3x\delta E^2\,, \qquad (2)$$

which is the general expression for the second-order energy of *electrostatic* perturbations of the equilibrium considered. Note that $\delta^2 H$ is a functional of Ψ_ν, which appears as Ψ_ν and $\hat{d}_\nu\Psi_\nu$, and of Γ_ν, *which appears only as* $\hat{d}_\nu\Gamma_\nu$. Taking Ψ_ν as a function of the constants of the motion only (which can be shown to have no influence on the results), and carrying out the minimization with respect to Γ_ν, which is straightforward, yields

$$\delta^2 H = -\sum_\nu \frac{s}{4m_\nu}\int d^3v\, dy\langle\tilde{\omega}_\nu\rangle^2\Psi_\nu^2\left[\mathcal{D}f_\nu^{(0)}\right]\left[N_\nu + a_\nu k_{\|0}\cos a\mathcal{Y}_\nu\right]\left[N_\nu + b_\nu k_{\|0}\cos a\mathcal{Y}_\nu\right] \qquad (3)$$

Here, $\tilde{\omega}_\nu \neq 0$ is a certain frequency, and the angles represent mean values along the particle orbits. $b_\nu = \left\langle\tilde{w}_\|\right\rangle / \langle\tilde{\omega}_\nu\rangle$, with $\left\langle\tilde{w}_\|\right\rangle$ a mean value of a parallel velocity $\tilde{w}_\|$, and $a_\nu = \dfrac{1}{\langle\tilde{\omega}_\nu\rangle\left[\mathcal{D}f_\nu^{(0)}\right]}\left\langle\mathbf{e}_B(\mathcal{Y}_\nu)\cdot\dfrac{\partial f_\nu^{(0)}}{\partial\mathbf{v}}\right\rangle$, with $\mathbf{e}_B(\mathcal{Y}_\nu)$ a unit vector in the direction of $\mathbf{B}^{(0)}$ at the plane $y = \mathcal{Y}_\nu$. N_ν is an arbitrary integer (positive or negative) for gyrating particles, and it is a completely arbitrary quantity for swinging particles. $k_{\|0} = k_z$ if one sets $\mathbf{k}_{xz} = k_z\mathbf{e}_z$, which can be done without restriction. The electrostatic energy term $(1/8\pi)\int d^3x\delta E^2$ has been dropped since the perturbed charge density can be made zero by appropriate choice of the signs of Ψ_ν, which do not influence (3).

If $k_{\|0} = 0$, there is wave propagation only in the y-direction, perpendicular to $\mathbf{B}^{(0)}$. Then, $\delta^2 H < 0$ if $\mathcal{D}f_\nu^{(0)} = 2\dfrac{\partial f_\nu^{(0)}}{\partial\dot{y}^2} > 0$ for some $\mathcal{H}_{\nu 0}, \mathcal{U}_{\nu 0}$. It suffices to localize Ψ_ν to the region in $\mathcal{H}_\nu, \mathcal{Y}_\nu$ where $\mathcal{D}f_\nu^{(0)} > 0$. Outside this region Ψ_ν vanishes. All other Ψ_μ are set equal to zero. The sign of $\delta^2 H$ is then determined only by the sign of the integrand in the region of localization.

If $k_{\|0} \neq 0$ and $\mathcal{D}f_\nu^{(0)} > 0$ for some $\mathcal{H}_{\nu 0}, \mathcal{U}_{\nu 0}$, one again localizes Ψ_ν around these values and sets all other Ψ_μ equal to zero. It is easy to show that N_ν can be chosen such that $\delta^2 H < 0$ without imposing any conditions on either $k_{\|0}$ or the spatial dependence of Ψ_ν perpendicular to $\mathbf{B}^{(0)}$. This is also the case if $k_{\|0} \neq 0$, $\mathcal{D}f_\nu^{(0)} < 0$ but $\left\langle\tilde{w}_\|\right\rangle\left\langle\mathbf{e}_B(\mathcal{Y}_\nu)\cdot\frac{\partial f_\nu^{(0)}}{\partial\mathbf{v}}\right\rangle > 0$.

If $k_{\|0} \neq 0$, and *both* $\mathcal{D}f_\nu^{(0)}$ *and* $\left\langle\tilde{w}_\|\right\rangle\left\langle\mathbf{e}_B(\mathcal{Y}_\nu)\cdot\frac{\partial f_\nu^{(0)}}{\partial\mathbf{v}}\right\rangle < 0$, $\delta^2 H$ can also be made negative in a way similar to that in the preceding cases, localizing Ψ_ν in $\mathbf{v}$ space and exploiting the freedom in the choice of N_ν. Here, however, the possible values of $k_{\|0}$

are limited to a certain interval (as is also the case for a homogeneous equilibrium with $a = 0$), and the spatial variation of Ψ_ν perpendicular to $\mathbf{B}^{(0)}$ is not completely arbitrary, but has a characteristic length $\lesssim a^{-1}$, which is not an important restriction.

IV. Conclusions

In the case of an inhomogeneous, force-free Vlasov-Maxwell plasma with sheared magnetic field, waves of negative energy ($\delta^2 H < 0$) exist for any local deviation from monotonicity (i.e. if $\mathcal{D}f_\nu^{(0)} := m_\nu \dfrac{\partial f_\nu^{(0)}}{\partial \mathcal{H}_\nu} + \dfrac{a}{\omega_\nu}\dfrac{\partial f_\nu^{(0)}}{\partial \mathcal{U}_\nu} = 2\dfrac{\partial f_\nu^{(0)}}{\partial \dot{y}^2} > 0$ for some $\mathcal{H}_\nu$,$\mathcal{U}_\nu$) *for any wave number* $\mathbf{k}$, irrespective of its magnitude and orientation.

If $\dfrac{\partial f_\nu^{(0)}}{\partial \dot{y}^2} < 0$, only the waves with a component $\mathbf{k}_{\|0}$ of $\mathbf{k}$ in the direction $\mathbf{B}^{(0)}(y_0)$ can possess negative energy.

If $\dfrac{\partial f_\nu^{(0)}}{\partial \dot{y}^2} < 0$, but $k_{\|0}^2 \left\langle \tilde{w}_\| \right\rangle \left\langle \mathbf{e}_B(y_0) \cdot \dfrac{\partial f_\nu^{(0)}}{\partial \mathbf{v}} \right\rangle > 0$, negative-energy waves also exist, *with no restriction imposed on either* $k_{\|0}$ (other than $k_{\|0} \neq 0$) *or the spatial variation of the perturbation perpendicular to* $\mathbf{B}^{(0)}$. This result agrees with, and closely resembles, that obtained for a homogeneous plasma by Pfirsch and Morrison [6], Eq.(144.b), within the frame of drift-kinetic theory.

If *both* $\dfrac{\partial f_\nu^{(0)}}{\partial \dot{y}^2} < 0$ *and* $k_{\|0}^2 \left\langle \tilde{w}_\| \right\rangle \left\langle \mathbf{e}_B(y_0) \cdot \dfrac{\partial f_\nu^{(0)}}{\partial \mathbf{v}} \right\rangle < 0$, negative-energy modes also exist. In this case, the characteristic length for the variation of the perturbation Ψ_ν perpendicular to $\mathbf{B}^{(0)}$ is of the order of the shear length a^{-1} (or smaller), and there is generally a restriction on the possible *parallel* wave numbers, which are limited to a certain interval, this also being so in the homogeneous case. The results of that case are of course regained by taking the limit of vanishing shear, $a \to 0$. The new results show that large perpendicular wave numbers are *not* necessary for the existence of negative-energy waves in the system under consideration, a feature which enhances the relevance of these modes.

References

[1] P. J. Morrison and D. Pfirsch, Phys. Rev. A **40**, 3898 (1989).

[2] P. J. Morrison and D. Pfirsch, Phys. Fluids B **2**, 1105 (1990).

[3] M. Kotschenreuther and P. J. Morrison, The free energy principle, negative energy modes, and stability, Technical Report ISFR No. 280, Institute for Fusion Studies, Austin (Texas), 1989.

[4] P. J. Morrison, Z. Naturforsch. **42a**, 1115 (1987).

[5] D. Correa-Restrepo and D. Pfirsch, Phys. Rev. A **45**, 2512 (1992).

[6] D. Pfirsch and P. J. Morrison, Phys. Fluids B **3**, 271 (1991).

III-1757

ELECTRONS PASSING THROUGH A NEGATIVELY BIASED GRID DUE TO COLLECTIVE TRAPPING

G.Popa* and R.Schrittwieser
Institute for Ion Physics, University of Innsbruck
A-6020 Innsbruck, Austria
*Department of Physics, "Al.I.Cuza" University
RO-6600 Iasi, Romania

Grid are widely used in plasma experiments for various purposes. For example, the various plasma waves are either excited /1/ or detected /2/ by grids. Grids of different mesh size are also used as electromagnetic screen of an electron plasma, wave exciter /3/. In electrostatic energy analyzers /4/ and ion sources grids serve also for the separation of one charge carrier species from the other. In both double /5/ and triple /6/ plasma devices the grids are used in order to cut out the electron coupling between the chambers.

Usually it is assumed that a negatively biased grid reflects all electrons if two conditions are fulfilled: (i) the mesh size is smaller than Debye length and (ii) the potential of the grid (V_G) has to be enough negative so that: $|V_G| > \mathcal{E}/e$, where $\mathcal{E}$ is the kinetic energy of the most energetic electron in the system.

In this paper, experimental results are presented which show that a considerable number of electrons is able to pass through a grid in spite of both of the above conditions being fulfilled.

The experiments were performed in both the Innsbruck /7/ and the Iasi DP-machines /8/ (Fig.1). In both cases an argon plasma was produced only in one chamber (the driver) with a density of less than 10^{9} cm^{-3} and effective electron temperature larger than about 1.5 eV_e i.e. the Debye length was

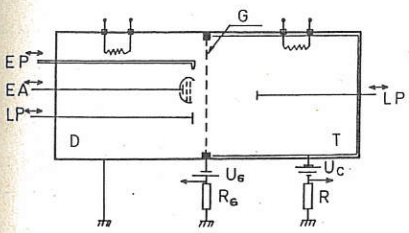

Fig.1

larger than about 0.7 mm. The most energetic electron was considered to have $\mathcal{E} = eV_d$ where V_d is the cathode potential with respect to the anode. The argon pressure was 10^{-4} mbarr. The separation grids (G) between two chambers of the DP-machines have a transparency of 81 % and a mesh width of 90 μm for Innsbruck DP-machine and a transparency of 60% and a meshwidth of 70 μm for Iasi DP-machine. The plasma parameters were measured using plane probes (LP) and electrostatic analyzers (EA) with two grids. Plasma density (n) in the driver chamber and bias of the separation grid (U_G) were used as parameters.

a) Driver chamber grounded.

In this case target chamber (T) is used as a large "collector" of an electrostatic analyzer and the grid (G) of the machine as first grid of the analyzer (fig.1). Plasma was not produced in this chamber. In fig.2.a the current voltage characteristic of the "collector" is presented . As long as the "collector" is biased (U_c) negatively with respect to plasma potential of the driver chamber (D) (where $n = 2.10^7$ cm^{-3} ; plasma potential $V_p = 1.5$ V; $V_d = -55$ V), an ion beam is passing the G into the T chamber. When the U_c is positive with respect to the driver plasma a small electron current is still present in the T chamber. A clear hysteresis of the characteristic is present when the ion beam has to be formed. Thus, the ion beam is still flowing towards the T chamber until the U_c is close but still negative with respect to driver plasma, while this beam is set-up only then when the U_c becomes a few volts negative with respect to the driver plasma potential. The hysteresis might be related with a process of space charge forming around the grid which regulate the flux of particles between the chambers. Moreover strong oscillations of both

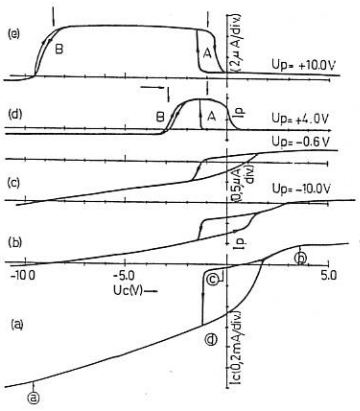

Fig.2

currents of the grid and of the "collector" and oscillations of plasma parameters into the driver are registered as long as the ions are reflected into the driver.

The presence of the electrons in the target chamber in spite of the negative bias of the grid ($U_G = \mathcal{E} - 75$ V and < 55 eV) but when ion beam is there, could be proved by saturation current of the probe. Thus when the Langmuir probe is biased negative with respect to the "collector" (-10 V curve b and -0.6 V curve c, Fig.2) the probe current (I_p) versus U_c shows a similar dependence as that of the I_c (curve a, Fig.2). The I_p is an ion current which preservse also the hysteresis as the I_c and practically does not depend on the probe potential. But, when the probe is biased positive with respect to the "collector" (4 V and 10 V for curves d and e, Fig.2) then constant and rather large electron current is measured as soon as ions penetrate into the target chamber but are reflected by the positive bias of the probe (limit A of the curves d and e of fig.2). When the probe potential becomes also negative with respect to the plasma potential of the driver chamber (limit B of the curves d and e, fig.2) then the probe collects also ions. Moreover, probe characteristics registered in the target chamber for fixed U_c value are presented in fig.3. They show that as long as the ion beam penetrates in the T chamber, then rather large number of electrons is present (curves a and d registered for U_c bias indicated in fig.2.a).

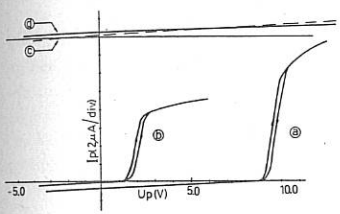

Fig.3

When ions are reflected into the D chamber, then probe characteristics registered in fig.3 (curves c and b) show that very few electrons are present in the T chamber. This result shows that in spite of the very negative bias of the grid (-75 V) comparing with the most energetic electron produced in the driver chamber ($\mathcal{E} = 55$ eV), the electrons could pass that grid mainly when ions could also penetrate in the T chamber.

b) Target chamber grounded.

In that case the T chamber is used as a "collector" of the

electrostatic analyzer (EA) with a fixed bias. The G remains also as the first grid of the EA. By anode biasing of the D chamber with respect to the ground, an ion beam could be push into the T chamber as long as the potential (V_p) of the D plasma is positive with respect to the ground.

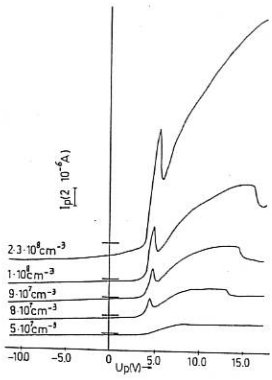

Fig.4

The probe characteristics recorded in the target chambers are presented in fig.4 for U_a =- 80 V, V_p = +5 V, V_d=60 V, p = 10^{-4} mbarr, and plasma density in the driver chambers as parameter. A large electron current is also measured by the probe as long as probe bias is positive with respect to the potential of the D chamber which gives the energy of the ion beam. The electron current increases with both the plasma density and the U_a because in both cases more electrons could penetrate the grid.

It must also be stress that PRI-like instabilities /9/ are excited when probe bias exceed a positive value so that a decreasing of the electron saturation current is registered.

1. S.Takamura, Y.Tanaka and T.Okuda, J. Phys. Soc. Japan 29, 431 (1970)
2. Y.Kawai and Ch.Hollenstein, Phys.Letters 59A, 353 (1976)
3. H.Sugai and E.Märk, Phys. Rev. Lett. 34, 127 (1975)
4. W.Lochte-Holtgreven, Plasma Diagnostics, North-Holland 1969
5. R.Y.Taylor, K.R.Mac Kenzie and H.Ikezi, Rev. Sci. Instrum. 43, 1679 (1972)
6. P.Leung, A.Y.Wong and B.H.Quon, Phys. Fluids 23, 992 (1980)
7. M.Oertl and R.Armstronsg, Tromso. Report Nr.82/1, Univ. of Tromso, Norway (1982)
8. D.Ruscanu, G.Popa, Proc. VIII-th ESCAMPIG, Greifswald 208 (1986)
9. S.Kuhn, An.St.ale Univ."Al.I.Cuza" Iasi, 34, 25 (1988)

EXPERIMENTAL ANALYSIS OF A LOW FREQUENCY INSTABILITY IN A MAGNETIZED DISCHARGE PLASMA

T. Gyergyek, M. Čerček, N. Jelić and M. Stanojević
J. Stefan Institute, University of Ljubljana,
Jamova 39, 61111 Ljubljana, Slovenia

1 Introduction

The Potential Relaxation Instability (PRI) [1], [3] appears in a laboratory plasma if an electrode is inserted into the magnetized plasma column perpendiculary to the axis and electron current is drawn to the electrode. The diameter of the electrode must be comparable to the diameter of the plasma column. The instability appears as a moving double layer that travells in the axial direction along the plasma column from the plasma source towards the electrode. Travelling double layer is followed by a potential depression on the low potential side that limits electron current to the electrode. The instability is accompanied by coherent oscillations of the electrode current. The frequency ν of the instability is proportional to $\nu \propto c_s/L$. Here L is the distance between the plasma source and the electrode. The ion sound velocity c_s is given by $c_s = \sqrt{kT_e/m_i}$, where k is Boltzmann's constant T_e is electron temperature and m_i is the ion mass. The frequency of the PRI described above is determined only by the axial motion of the positive ions so that it can be called 1-D PRI.

In this paper we report the observation of a low-frequency (30 - 100 kHz) instability in a weakly magnetized discharge plasma. The instability is excited by a disc electrode that is immersed in the magnetized plasma column perpendiculary to the axis. Coherent oscillations of the current I_a collected by the electrode appear when the electrode is bias U_a is just above the plasma potential V_s. It is found that the frequency of the observed instability is determined by the axial and radial motion of the ions. In section 2 the experimental procedure is described. In section 3 the experimental results are presented. In the final section the observed phenomenon is tentatively discussed as a 2-D PRI type of oscillations and some conclusions are given.

2 Experimental procedure

The experiments were performed in a linear magnetized plasma device 1.5 m long 18 cm inner diameter. The basic pressure in the vacuum chamber is below 10^{-4} Pa. Working pressure of argon is between 10^{-3} and 10^{-1} Pa. The plasma is produced by a discharge from hot tungsten filaments. The electron temperature in our plasma machine is $kT_e = 1 - 3$ eV and ion temperature is approximately $kT_i \approx 0.1$ eV.

The magnetic field density is $B = 0.02$ T so that the Larmor radius for ions is approximately $r_{Li} \approx 1cm$ and for electrons about $r_{Le} \approx 0.2mm$. If we compare this to the diameter of the plasma column which is about 7 cm we can conclude that electrons are strongly magnetized, while ions are weakly magnetized.

For the plasma diagnostics Langmuir and emissive probes are used. The plasma density is proportional to the ion saturation current I_{is} collected by a negatively biased cylindrical (0.15 mm diameter, 5 mm lenght) Langmuir probe. The plasma potential V_s is determined as the floating potential V_f of an emissive probe.

The instability is excited by a disc electrode. The diameters of the exciter electrodes range from $2r = 2.5$ mm to $2r = 35$ mm so that r_{Le} is always much smaller than the electrode diameter, while r_{Li} is comparable to the electrode diameter. Time resolved measurements are performed using the boxcar sampling and averaging technique. The data are analyzed by a computer.

Periodic signal from the collector is used as a trigger for the boxcar integrator (SR250 Stanford Research Systems) for the time resolved measurements. When the electrode potential U_a exceeds the plasma potential V_s the electrode current I_a starts to oscillate periodicaly. Frequency ν of these oscillations is usually between 30 and 100 kHz. The amplitude of the oscillations can achieve up to 30 % of the DC value of the anode current I_a.

3 Experimental results

Dependence of the frequency ν on various parameters was measured. The oscillations appear just after the electrode bias U_a exceeds the plasma potential V_s. If U_a is further increased, the frequency ν at first increases and when U_a exceeds V_s for roughly 2 V ν becomes constant (figure 1 a).

The frequency ν is inversely proportional to the electrode diameter (figure 1 b). It does not depend much on the plasma density and on neutral gas pressure. It is interesting that the frequency decreases with increasing magnetic field density B. In figure 2 axial (figures b

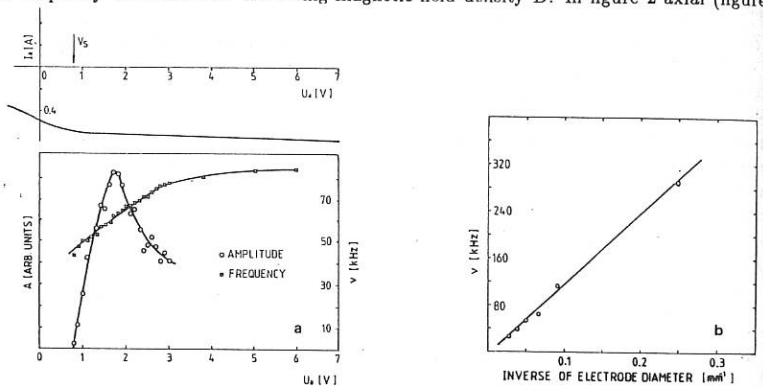

Figure 1: Dependence of the frequency ν and amplitude A of the electrode current oscillations on the electrode bias U_a (a).The very sudden onset of the oscillations at $U_a = V_s$ can be observed. In figure (b) the frequency ν versus the inverse value of the electrode diameter is shown.

and c) and radial (figures d and e) profiles of the plasma potential V_s and plasma density that is proportional to the ion saturation current I_{is} to a Langmuir probe in different phases of the electrode current oscillation are shown. Different phases are marked by numbers that are

explained in figure 2 a. It can be observed that during the phase of the current decrease (phases 6, 7, 8 and 9 in figure a) a potential hill of the height Φ_H folowed by a potential depression of the depth Φ_D travels towards the electrode in the axial direction. The travelling potential structure is followed by a plasma with higher density that penetrates into a region with lower density. During the phase of current increase (phases 2, 3 and 4 in figure a) the plasma potential increases rapidly in the whole experimental region. The phase of current increase is followed by

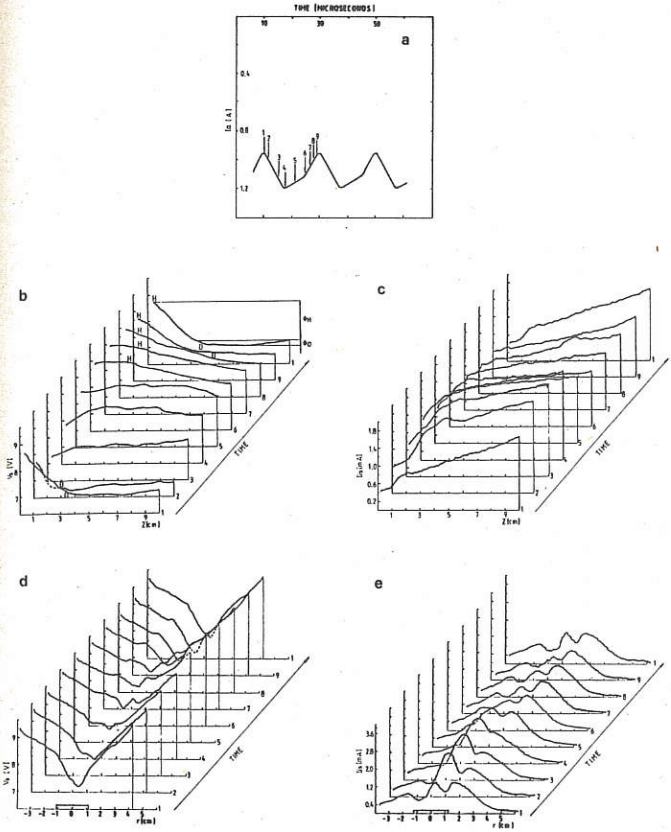

Figure 2: Axial (b and c) and radial (d and e) profiles of the plasma potential (b and d) and density (c and e) in different phases of the electrode current oscillations. Phases are marked by numbers that are explained in figure a.

a phase of almost constant electrode current. During that phase the plasma density decreases while the plasma potential still increases. Then the potential structure that limits the electrode current is formed again and the whole cycle repeats.

The plasma density was measured by a Langmuir probe and the plasma potential by an emissive probe. In both cases the probe was fixed in the center of the electrode while the electrode was moved in the axial direction away from the probe and from the source. It must be emphasized that the axial distance between the electrode and the source does not affect the frequency.

In figures 2 d and e radial profiles of the plasma potential and density are shown. The electrode was fixed at the distance 4 cm from the probe while the probe was moved in the radial direction. On the density profiles one can see that during the phases of the current increase and of the constant current the ions are pushed out of the current channel in the radial direction. In the same time the plasma potential in the current channel increases rapidly.

4 Conclusions

We observed a low frequency instability excited by a positive electrode in a magnetized discharge plasma. The oscillation of the electrode current is caused by a travelling potential hill followed by a potential dip that limits the electron current to the electrode. The double layer is formed a few cm from the electrode. We assume that the position of the potential structure formation is determined by the collection lenght L of the electrode. This distance is proportional to the diameter of the electrode and it increases with increasing magnetic field [4], [5]. A more detailed presentation of the model that explains the observed phenomenon as a 2-D PRI will be given elsewhere [6].

The plasma in front of the electrode oscillates between two quasisteady states. In the phase of maximum electrode current the plasma is in the state of high potential and low density and in the phase of minimum electrode current the plasma is in the state of low potential and high density.

The observed phenomenon can be explained as a relaxation type of oscillation similar to the PRI observed in a Q machine [1], [3] or in a double plasma machine [2]. But there are two important differences. First in our experiment the distance L that the double layer has to travel is determined by the diameter of the exciter electrode and the magnetic field and not by the position of the plasma source [1], [3] or separation grid [2]. Second the radial motion of the ions is also important for the determination of the frequency as the axial motion.

References

[1] S. Iizuka, P. Michelsen, J. J. Rasmussen, R. Schrittwieser, R. Hatakeyama, K. Saeki and N. Sato, *Phys. Rev. Lett.*, **48**, 145, (1982)

[2] H. Fuyita, S. Yagura, T. Harada and H. Matsuo, *IEEE Trans. Plasma Sci.*, **PS-15**, 445, (1987)

[3] S. Iizuka, P. Michelsen, J. J. Rasmussen, R. Schrittwieser, R. Hatakeyama, K. Saeki and N. Sato, *J. Phys. Soc. Jap.* , **54**, 2516, (1985)

[4] M. Stanojević, M. Čerček, N. Jelić and T. Gyergyek, submitted to *J. Phys. D: Appl. Phys.*

[5] P. C. Stangeby, *J. Phys. D: Appl. Phys.*, **15**, 1007, (1982)

[6] T. Gyergyek, M. Čerček, N. Jelić and M. Stanojević, to be published

10-27

ION CYCLOTRON OSCILLATIONS INDUCED BY AN EMISSIVE ELECTRODE FLOATING IN A MAGNETIZED COLLISIONLESS PLASMA COLUMN

N. Sato, R. Hatakeyama, K. Aoyama, and W. X. Ding*
Department of Electronic Engineering,
Tohoku University, Sendai 980, Japan
*Modern Physics Department, University
of Science and Technology of China,
Hefei, Anhui 230026, P. R. of China

Abstract Measurements have been performed on ion cyclotron oscillations induced by a small emissive electrode (electron gun) floating in a magnetized collisionless plasma column. The oscillations are observed only when the emission is so large that the electrode potential becomes higher than the plasma potential. This means that the oscillations are induced without dc electric current passing through the plasma column if the electrode potential is positive with respect to the plasma potential. Main features of the oscillations are the same as those of well-known electrostatic ion cyclotron oscillations induced by applying positive potentials to a small cold disc electrode immersed in a magnetized collisionless plasma column.

1. Introduction

The first clear-cut observation of electrostatic ion cyclotron oscillations in a laboratory plasma was reported by D'Angelo and Motley in 1962 /1/. In their experiment, the electrostatic ion cyclotron oscillations were driven by applying positive potentials to a small cold disc electrode immersed in a single-ended Q machine with uniform magnetic field. Under this configuration, an electric current is generated in the plasma along the magnetic field. Thus, the oscillations observed were ascribed to current-driven electrostatic ion cyclotron instability predicted by Drummond and Rosenbruth /2/. Many subsequent measurements of the electrostatic ion cyclotron oscillations and related phenomena, which were made under almost the same con-

figuration, were discussed also on the basis on this "current-driven" mechanism.

On the other hand, Hatakeyama et al./3/ made measurements on the electrostatic ion cyclotron oscillations in nonuniform magnetic fields under the same configuration as in Ref./1/ except the axial profile of the magnetic field. The oscillation frequency was observed around the ion cyclotron frequency defined by a local magnetic field near the position of the electrode biased positively to drive the oscillations. According to the observation, Sato and Hatakeyama pointed out an importance of two-dimensional potential structure near the electrode and have proposed a new mechanism for the generation of these oscillations /4/. The mechanism is based on a direct plasma response to the applied potential, which gives rise to a two-dimensional relaxation oscillation in a magnetized plasma column. Details of the related investigations on the electrostatic ion cyclotron oscillations were reviewed by Rasmussen and Schrittwieser /5/ although there was no clear conclusion for genaration mechanism.

In this report, the ion cyclotron oscillations are induced by a small emissive electrode (electron gun) floating in a magnetized plasma column. Under this configuration, there is no dc electric current passing through the plasma column. The oscillations are observed when the emission is so large that the electrode potential becomes higher than the plasma potential, being consistent with the "potential-driven" mechanism proposed by Sato and Hatakeyama.

2. Experimental Methods and Results

The experiment has been performed on a single-ended Q machine at Tohoku University, which is schematically shown in Fig. 1. A potassium plasma column of 150 cm long [density$\simeq(5\text{-}10)\times10^{8}\mathrm{cm}^{-3}$, electron temperature$\simeq$0.2 eV ($\gtrsim$ion temperature)] is produced by surface ionization at a hot tungsten plate of

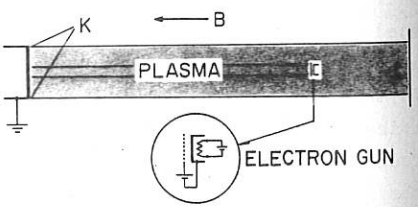

Fig. 1.

52 mm in diameter and is terminated by an endplate of 80 mm in diameter under a strong magnetic field B. A background gas pressure is about 1×10^{-6} Torr. Under our experimental condition, we can neglect particle collisions.

An electron gun of 10 mm in diameter, consisting of oxide cathode and acceleration grid (50 mesh/inch), is set at a distance of about 110 cm from the hot plate as shown in Fig. 1. The cathode can provide high electron emission, the amount of which is larger than the plasma electron flux. But, in our experiment, the gun is kept floating electrically and then there is no dc electric current between the gun and the plasma. The gun emits electrons into the plasma just to cancel out the electric current from the plasma into the gun. With an increase in the acceleration potential applied between the grid and cathode of the gun, the grid potential increases and becomes positive with respect to the plasma in order to prevent the excess electron emission into the plasma. Thus, we can make the grid potential positive with respect to the plasma without dc electric current passing through the plasma column, being in contrast with the situation where the positive dc potential is externally applied to the cold electrode in the plasma.

According to the measurements, only when the grid potential is higher than the plasma potential, there appears a coherent oscillation a little above the ion cyclotron frequency in the plasma column. The measured spectra of the oscillations are shown with the magnetic field B as a parameter in Fig.2. A dependence of the frequency on B is shown in Fig.3 which also includes the oscillation frequencies measured when the positive potentials are applied to the grid without heating of the cathode just as in case of cold disc plate, where the grid is biased at the same positive potentials as the gun (grid)

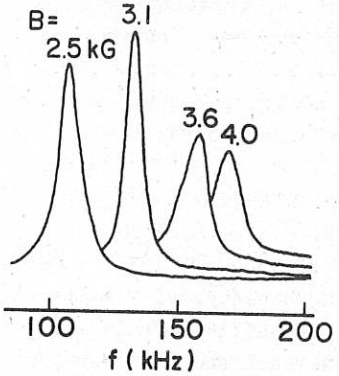

Fig. 2.

floating potentials. We can find a good agreement between the frequencies obtained under different situations. The oscillation amplitudes are smaller by an order of magnitude in case of the electron gun than in case of the cold plate. When the magnetic field is changed only in the region around the gun, the frequency is observed to follow the ion cyclotron frequency near the gun position as in case of the cold plate.

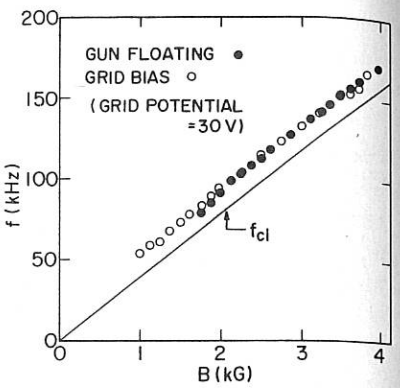

Fig. 3.

4. Summary

Measurements have been performed on ion cyclotron oscillations induced by using a small emissive electrode (electron gun) kept floating electrically in a magnetized collisionless plasma column. There appear the oscillations only when the electrode potential is positive with respect to the plasma. This means that the oscillations are generated even if there is no electric current passing through the plasma column. The result is consistent with the "potential-driven" model of Sato and Hatakeyama. Even if electron and ion velocity distributions are taken into account under our experimental situation, we can find no ion cyclotron instability based on nonequilibrium velocity distributions.

/1/ N. D'Angelo and R. W. Motley, Phys. Fluids 5, 633(1962).
/2/ W. E. Drummond and M. N. Rosenbluth, Phys. Fluids 5, 1507 (1962).
/3/ R. Hatakeyama, N. Sato, H. Sugai, and Y. Hatta, Phys. Lett. 63A, 28(1977) and Plasma Phys. 22, 25(1980).
/4/ N. Sato and R. Hatakeyama, J. Phys. Soc. Jpn. 54, 1661(1985).
/5/ J. Rasmussen and R. Schrittwieser, IEEE Trans. Plasma Sci. 19, 457(1991).

ON THE DOUBLE LAYER PHENOMENOLOGY

M.Sandulovíciu and E.Lozneanu
Plasma Physics Department, "Al.I.Cuza" University
RO-6600 Iasi, Rumania

Space charge double layer (DL) appears frequently both in collisional and in collisionless considered plasmas /1/. As a consequence, the up-today dominant theoretical explanations start with the assertion that elementary processes like excitations and ionizations are not essential for understanding of the DL phenomenology. However, many experimental physicists /2/ evidence the fact that ionizations within the DL are the dominant processes in spite of the fact that the typical ionization mean free path for electrons is much greater than the thickness of the DL.

In this paper we present experimental results that evidence the essential role played both by the excitation and the ionization processes in the DL phenomenology. To investigate the causes which determine the profile of the electron concentration and also of their energy distribution function, we have performed spectral measurements in the region where the DL is formed (figs.1 and 2)

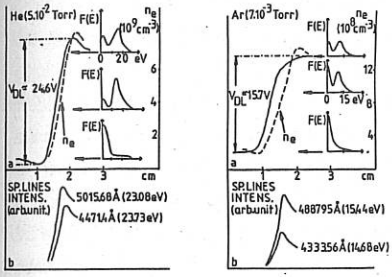

Figs. 1 and 2

Spectral lines which evidence the direct connection between the excitation processes and the alure of the electron concentration n_e and of the energy distribution function F(E) and consequently of the DL potential profile

The results presented in figs.1 and 2 prove that the DL is formed and maintained only in a region where electrons are accelerated so that they achieve kinetic energies for which the excitation cross section increases suddenly. Such a situation is present near a positive electrode immersed in a plasma /3/ or in a constricted region of a current carrying plasma column. The DL formation process is usually started near the positive electrode but in certain condition /1/, in the further evolution, the DL is shelling off from the positive electrode and fixed at a certain distance from this (electrode free DLs). In such situations the space charge layer formed of positive ions in the high potential side of the DL plays the role of a virtual anode /5 / which locally assures the electric field necessary to

maintain the electron acceleration inside the DL. Evidently in the region where the kinetic energy of the electrons, accelerated inside the DL, has values for which the neutral excitation cross section increases suddenly, the intensity of spectral lines is maximal and, as a consequence of inelastic collisions, a great number of the electrons are accumulated. Because of their Maxwellian distribution, at first are accumulated the electrons with high kinetic energies and afterwards the electrons with small energies are trapped at the negative barrier already formed. In a first phase the profile of the electron concentration which corresponds to a negative potential barrier is determined by both phenomena. The part of electrons with sufficiently high energy, able to penetrate the negative potential barrier so formed, gain by acceleration in the present electric field, a kinetic energy sufficient to produce positive ions. Taking into consideration the energy dependence of the ionization cross section, the maximum rate of the ion production occurs at a certain distance from the well localized negative space charge. Because of their high mobility, the electrons producing ionization and the resulting electrons are quickly collected by the anode so that, between the negative space charge and the anode, a plasma enriched with positive ions appears. The potential drop V_{DL} developed between the plasma enriched with electrons (placed at the low potential side of the DL) and that enriched with positive ions (placed at the high potential side of the DL) is maintained by the current by a dynamical equilibrium between the accumulation of electrons after excitation processes and different electron loosing processes as recombinations and diffusion. The final arrangement of the negative and positive space charges inside of a DL strongly depends by a self-confination mechanism determined by the electrostatic forces which act between the well localized negative space charge and the positive ions. These forces determine the formation and the maintenance of two adjacent layers with opposite electric sign , having properties similar to cell membranes. Since the electrostatic forces also determine an important increase of the local concentration of electrons and positive ions, the recombination probability is very high in this region so that the neutral concentration necessary to assure the excitation and ionization rate required for the DL maintenance is locally also present in collisionless considered plasmas. The well localized light phenomena observed for example in Tokamaks /6/ confirm that the neutral concentration in the region where a DL is formed is different from those existent in the region where usually this is measured. This assertion is confirmed by the experimental results presented in fig.3 which evidence that inside a globular DL (plasmoid) the neutral pressure is higher than in the surrounding plasma.

As it was shown /4,7/, the DL becomes unstable when the DL potential drop V_{DL} is equal with the ionization potential of the gas V_i. We have already discussed /7/ the

connection between different time sequences of an unstable DL and different elementary processes.

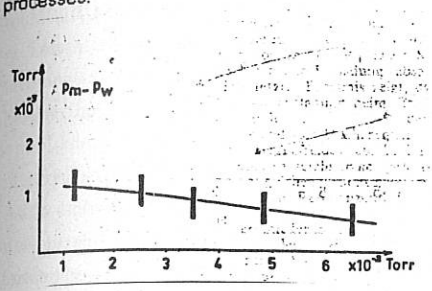

Fig.3.

The difference between the inside and outside pressures (p_m and p_w) in a plasmoid for different gas pressure.

Here we mention only the fact that a direct connection between V_i and the V_{DL} exists only under conditions for which the ionization rate at the high potential side of the DL is sufficiently high to determine an important increase of the positive ion concentration so that the DL turns into a moving one and finally disrupts. When this condition is not satisfied the V_{DL} is not related with V_i and depends only on the external imposed potential differences although the DL generation mechanism does not differ qualitatively from those above described. In this case the DL disruptions process does not appear.

The described self-organization process (sustained by the current) during of which the spatial non uniform distributions of electrons and positive ions themselves assure the necessary rates of the mentioned quantum processes (local potential drop and neutral concentration) explains the property of a DL to act as an autonomous body /11/. Such bodies initially appear in the region of a gaseous conductor where external imposed causes determine a local acceleration of thermalized electrons.

Time resolved measurements /4,7/ prove that the DL becomes movable (expands) when $V_{DL} = V_i$. This is a consequence of the increase of the positive ion concentration at the high potential side of the DL, so that this region acts as a virtual anode with increasing potential. Under such conditions the region where the electrons are accumulated after excitation processes and , consequently , also the adjacent sheath of positive ions is shifted toward the plasma enriched in electrons. This moving phase of the DL takes place as long as the production rate of the positive ions is sufficient to locally assure the conditions required for the DL maintenance. When such conditions are present along the entire plasma column, the observed phenomenon is known as soliton. When the positive ion production rate decreases during of the DL displacement after covering of a certain distance, this disrupts. In this case an internal triggering mechanism /4,5,7/ assures the periodical formation and disruption of the movable DLs. The described phenomenology explains the ability of DLs to act as stimulators for different instabilities and chaotic phenomena usually present in all plasma devices /9/.

A very interesting phenomenon is the appearance in low voltage arcs of electrode-free globular space charge structures (fireballs FB) surrounded by a spherical DL /10/. More frequently the FB behaves in a pulsatory state /4,10/ during of which the potential inside it, in respect of the surrounding plasma, reaches V_i. Pulsatory FBs were also observed in thermionic converters, so that, very probably, their maintenance can be assured , without external dc power supply , only by thermal energy /10/.

The knowledge of the phenomenology implied in the DL dynamics can contribute to solve problems related with different instabilities observed in modern applications of the plasma physics (Tokamaks, plasma focus, etc.) and also to understand the phenomena taking place in the high region of the polar Earth atmosphere and also in extraterrestrial plasmas. The described phenomenology is, in our opinion, also able to explain the appearance of ordered structures in semiconductors and electrolytes (wandering domains) and the transition from a disordered to an ordered (cellular) state of the matter, in general /9,11/. Evidently, spectral investigations are able to give essential information on the role played by quantum processes in the DL phenomenology. Because DLs appear in all plasma devices as visible images /6/, the results of such investigations are decisive answers whether a collisionless plasma theory is appropriate to describe such phenomena.

/1./ R.Schrittwieser, SASP 92 Symposium on Atomic and Surface Physics, Italy 1992 25
/2/. R.Plamandon, I.Teichmann and S.Torven, J.Phys.D Appl. Phys. (1988) 21 286
/3/. Bin Song, N. D'Angelor and R.Merlino, J.Phys.D. Appl.Phys (1991) 24 1789
/4/. M.Sanduloviciu (1987) Int. Conf.Plasma Phys. Kiev Proc. Invited Papers.
/5/. M.Sanduloviciu and G.Popa, (1988) An.St.Univ.Iasi, XXXIV 93
/6/. B.J.Zweben and S.S.Medley (1989) Phys. Fluids B1 (10) 2058
/7/. D.Alexandroaei and M.Sanduloviciu (1987) Phys. Lett. A122 173
/8/. H.Alfven (1986) DL in Astrophys. Symp. Marshall Space Flight Center. Huntsville, Alabama
/9/. M.Sanduloviciu (1991) Int.Workshop on Plasma Phys. Pichl.Austria.
/10/ .M.Sanduloviciu (1991) XX Int. Conf. Phen. Ionized Gases Pisa, Italy 265
/11/.M.Sanduloviciu (1989) The 6-th ISSOL Meeting and 9-th Int. Conf. on the Origin of Life Prague Czechoslovakia, 802.

A PROBE SHEATH INSTABILITY IN A DOUBLE PLASMA DEVICE

C.A. Dempers[1]), P. Krumm[1]), R. Schrittwieser
Institute for Ion Physics, University of Innsbruck, A–6020 Innsbruck, Austria

Introduction:

It is well known that the sheath regions of a plasma can generate electrostatic instabilities [1,2]. One such ion–beam driven instability at a disc probe has been investigated recently in a Double Plasma (DP) device [3]; it appears to be related to the formation of a double layer in front of the probe when the probe potential exceeds the beam energy. This double layer is also understood to be responsible for the appearance of a second knee in the probe characteristic: its presence increases the effective collecting area of the probe and thus leads to a further increase in electron saturation current.

Here we report on an instability that is observed, as in [3], at frequencies somewhat less than the ion plasma frequency (ω_{pi} = 660 kHz, ω_{pe} = 180 MHz) when an ion beam is directed at a positively biased disc probe. However, in our case, it is destabilized at much lower beam energies ($V_b \simeq \kappa T_e$), for certain values of grid potential. In particular we investigate how the onset of the instability depends on beam energy, probe bias and the negative potential of the separator grid of the DP.

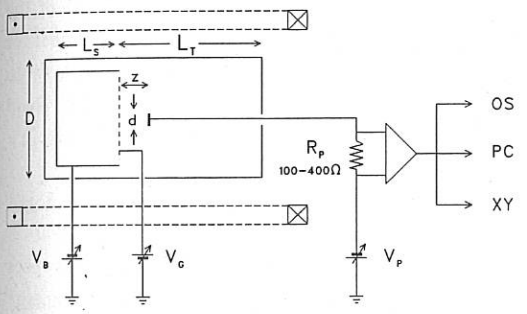

Fig. 1: *Experimental set up. Dimensions and parameters of the Innsbruck (Durban) machine:* L_s = 40 cm (30 cm), L_t = 50 cm (60 cm), D = 44 cm (60 cm), d = 1 cm (1.8 cm). *Typical range of variables:* V_b = 2 – 10 V (4.5 – 20 V), V_g = –40 – –100 V (–40 – –60 V), V_p = –10 – 30 V (–10 – 50 V).

Experimental set–up:

Experiments were performed in DP devices at the University of Innsbruck (Austria) and the University of Natal, Durban (South Africa). Fig. 1 shows the experimental set up,

---

1) Permanent address: IPPR, Physics Department, Univ. of Natal, Durban 4001, R.S.A.

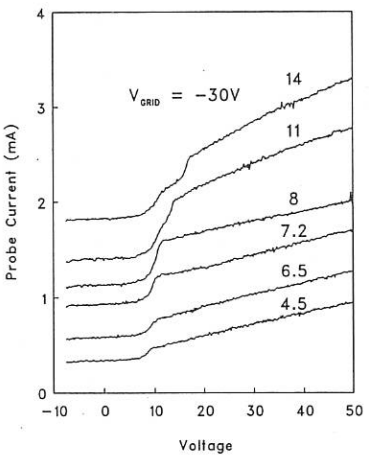

Fig.2: *Set of probe characteristics* $-10\ V \lesssim V_p \lesssim 50\ V$ *for values of* $4.5 \lesssim V_b \lesssim 14\ V$ *at* $V_g = -30\ V$.

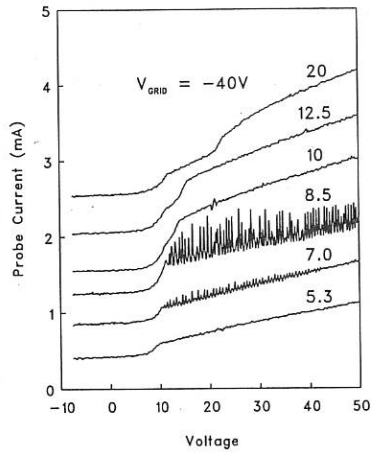

Fig. 3: *The same as* Fig.2 *but with* $5.3 \lesssim V_b \lesssim 20\ V$ *and* $V_g = -40\ V$.

which is essentially the same in both machines, the main difference being the size of the tungsten disc used ($d = 1$ cm diam. in Innsbruck, 1.8 cm diam. in Durban) and the availability of a weak magnetic field perpendicular to the ion beam in the Durban machine. In both experiments fast or arbitrarily slow Langmuir sweep traces were captured on a digital oscilloscope or displayed on an XY recorder. Thus the onset and quenching of probe current oscillations could be detected and the shape of the probe characteristics checked for changes due to the formation of a double layer in front of the disc. The disc position could be altered between $z = 0$ cm and $z = 40$ cm from the grid.

Experimental Results:

Fig. 2 shows a set of Langmuir sweeps (−10 to +50 V) for variable beam energy (source chamber bias $4.5\ V < V_b < 14\ V$) and a grid bias $V_g = -30$ V. Note that the zero of probe current has been shifted for clarity. The two curves marked 11 V and 14 V show the formation and shifting of the "second knee" discussed in [3]. However, there is no instability for a probe bias well above this knee, and the electron saturation current increases with the ion beam voltage for all curves.

Fig. 3 shows some similar traces for $V_g = -40$ V, with a certain value of V_b resulting in the occurrence of oscillations (typical $f \simeq 100$ kHz) without visible change of the (time averaged) shape of the characteristics. The subsequent quenching of the instability for higher V_b–values is also apparent. This behaviour was more noticeable when time averaged Langmuir traces were plotted on the XY recorder, in the presence of oscillations as displayed on the digital oscilloscope. For particular values of beam energy and probe bias different modes could be observed, as displayed in Fig. 4. Fig. 4 (a) shows a mode destabilized at low probe bias, while Fig. 4 (b) shows a mode that is quenched for low probe potential $V_p < V_b$. Although captured separately both modes appeared in rapid succession, i.e. the system could switch between them intermittently.

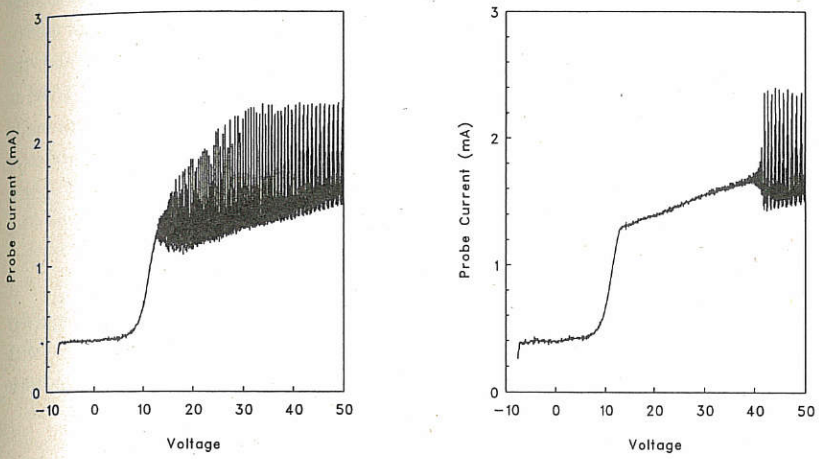

Fig. 4: *Two modes at $V_b = 7.2$V, destabilized at low and high V_p respectively. Although captured separately, the system continously switched between both modes intermittently.*

Discussion:

In both (Innsbruck and Durban) experiments, although for different grid bias and discharge parameters, the current oscillations reported here occurred long before a deformation of the disc probe characteristic became evident. Their frequency was sensitive to changes in the beam voltage (it decreased with increasing beam energy) and, to a much lesser degree, to probe bias. In both machines the onset (and quenching) of the instability depended on grid and probe bias, ion beam energy and the potential of the separator grid. This, together with the fact that a typical scale length computed from $\lambda_{De} \simeq$

$(\kappa T_e/M_i)^{\frac{1}{2}}/f$ is in the order of a few millimeters ($\lambda_{De} \simeq 0.5$ mm) makes us suspect, that we are here, as in [3], dealing with a sheath instability, related to the sheath in front of the disc (e.g. a double layer) and in the vicinity of the grid. This is in agreement with the observed quenching of the instability by an extremely weak magnetic field ($B < 0.2$ mT) perpendicular to the ion beam which affects the electron behaviour over a sheath width but should leave the ions unmagnetized.

In contrast to [3] there was no obvious frequency dependence on probe position in the Innsbruck experiment, which was confirmed in the Durban machine. However, in both machines a frequency dependence on plasma density, base pressure of the Argon plasma ($p = 10^{-4}$ mbar) and electron temperature ($\kappa T_e \simeq 1 - 2$ eV) was noticeable. The formation of a double layer at low ion beam energies and its consequent collapse at higher beam energies would explain the destabilization and quenching of different modes, the increase in electron saturation current for beam voltages $V_b < \kappa T_e$, and the deformation of the characteristics for higher beam voltages, $V_b \gg \kappa T_e$. We are thus led to extend the explanation offered in [3] to lower beam energies: a double layer, forming in front of the disc when the beam ions can no longer reach it, increases the effective collecting area of the probe and may under certain conditions drive the electron current unstable.

Conclusion and Acknowledgements:

These experiments provide further evidence for the destabilization of low frequency electron current oscillations, which we attribute to the presence of an ion beam, with energies comparable to the probe bias, affecting the sheath conditions in front of the disc and in the vicinity of the grid.

The work at the Innsbruck machine was undertaken while one of us (P.K.) was on leave from the University of Natal, Durban. He would like to express his sincere gratitude for the warm hospitality experienced and the financial assistence rendered. Part of this work was supported by the "Österreichische Forschungsgemeinschaft" under grant No. 06/1619, the "Auslandsabteilung der Universität Innsbruck", the "Jubiläumsfonds der Universität Innsbruck zur Förderung der Forschung und Lehre" and the "Fonds zur Förderung der wissenschaftlichen Forschung" (Austria) under project P8709–PHY. Finally, we wish to thank P.J. Barrett for stimulating and helpful discussions.

References:

[1] R.L. Stenzel, *Phys. Rev. Lett.* **60** (1988), 704.

[2] P.J. Barrett and R. Greaves, *Phys. Fluids* **B1** (1989), 1776.

[3] R. Armstrong and R. Schrittwieser, *Plasma Phys. Contr. Fus.* **33** (1991), 1407.

Progress in the kinetic modeling of collisionless two-dimensional bounded plasma systems

H. Pedit and S. Kuhn

Institute for Theoretical Physics, University of Innsbruck
Technikerstrasse 25, A-6020 Innsbruck, Austria

1. Introduction and summary. In Ref. 1, a two-dimensional slab model was developed for calculating self-consistent dc states of a collisionless single-ended Q-machine in which the potential distribution decreases monotonically in the axial direction (i.e., the direction of the constant applied magnetic field). This method combines trajectory integration of the Vlasov equation for each particle species (electrons and ions)[2] and a well-known Poisson solver[3] into a numerical iteration scheme yielding the two-dimensional self-consistent potential and space-charge distributions. Typical results for "short" systems (just a few Debye lengths) were presented in Refs. 1, 4 and 5.

In the present contribution, the method is used to calculate the dc states of a "long" system (i.e., several hundred Debye lengths), and typical potential and space-charge distributions are shown. In addition, related ion and electron velocity distribution functions are presented for a position near the plasma-vacuum transition region, where the largest potential and electric-field gradients occur. These results demonstrate that our method is well capable of describing the complex fine structure of the distribution functions. Finally, a comparison is made between electron trajectories obtained in the guiding-center approximation used by us and the numerically exact electron trajectories, which shows that the approximation is good even in the plasma-vacuum transition region.

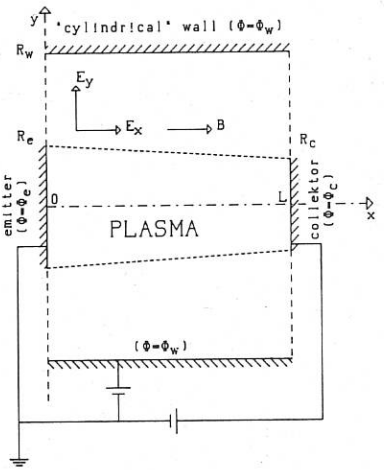

Fig. 1. A 2d-model of the single-ended Q-machine

2. Model and assumptions. Figure 1 shows our two-dimensional model of the single-ended Q-machine. Although the model is still cartesian, the y-coordinate simulates to some extent the radial coordinate of the cylindrical Q-machine geometry. Both the ions and the electrons leave the emitter with half Maxwellian distribution functions corresponding to the

hot–plate temperature T, but their emission densities may be different. All particles reaching the collector, the emitter or the surrounding wall are absorbed. A uniform magnetic field B is applied in the x–direction, and the plasma is assumed to be sufficiently rarefied ($n_p \lesssim 10^8$ cm^{-3} for typical Q–machines) to be tractable as collisionless. The physical parameters are chosen such that the potential is monotonically decreasing in the axial direction, but due to the vastly different particle Larmor radii and our fairly realistic boundary conditions the potential changes in the normal direction are still nontrivial. The system is specified by prescribing the following parameters: axial length L, emitter "radius" R_e, collector "radius" R_c, wall "radius" R_w; emitter potential $\Phi_e \equiv 0$, collector potential Φ_c, wall potential Φ_w; emitter temperature T, electron emission density n^+_{e0}, ion emission density n^+_{i0} (or, equivalently, the "neutralization parameter" $\alpha \equiv n^+_{i0}/n^+_{e0}$).

3. Potential and space–charge distributions. Solving the time–independent Vlasov equation for each particle species (a = e,i),

$$\left[\mathbf{v}\cdot\nabla + \frac{q_a}{m_a}\Big(\mathbf{E}(\mathbf{x})+\mathbf{v}\times\mathbf{B}\Big)\cdot\nabla_{\mathbf{v}}\right] f_a(\mathbf{x},\mathbf{v}) \equiv \frac{d_a}{dt} f_a(\mathbf{x},\mathbf{v}) = 0, \tag{1}$$

and Poisson's equation,

$$\nabla^2\Phi(\mathbf{x}) = -\frac{\rho(\mathbf{x})}{\epsilon_0} = \frac{e}{\epsilon_0}[n_e(\mathbf{x}) - n_i(\mathbf{x})], \tag{2}$$

together with the boundary conditions

$$\begin{aligned} &\Phi(0,0\le|y|\le R_e) = \Phi_e = 0\,,\ \Phi(0,R_e<|y|\le R_w) = \Phi_e + (\Phi_w-\Phi_e)\,(|y|-R_e)/(R_w-R_e) \\ &\Phi(L,0\le|y|\le R_c) = \Phi_c\,,\quad \Phi(L,R_c<|y|\le R_w) = \Phi_c + (\Phi_w-\Phi_c)\,(|y|-R_c)/(R_w-R_c) \\ &\frac{\partial\Phi}{\partial y}(x,0) = 0\,, \qquad\qquad \Phi(x,R_w) = \Phi_w\,, \end{aligned} \tag{3}$$

by a numerical–iterative scheme as described in Refs. 1 and 4, we find the self–consistent dc potential distribution, the density distributions for both particle species and, hence, also the space–charge distribution. In Fig. 2, the potential and space–charge distributions are shown for a system of length L = 5 cm (which is short but still easily realizable) and $R_e = R_c = 1.5$ cm, $R_w = 6.5$ cm, $\Phi_e = \Phi_w = 0$, $\Phi_c = -3$ V, T = 2000 K, $n^+_{e0} = 5.12\cdot10^{14}$ m^{-3}, and $\alpha = 0.1$. With these parameters we have a plasma density $n_p = 1.3\cdot10^{13}$ m^{-3} and the associated Debye length becomes $\lambda_{Dp} \simeq 8.8\cdot10^{-4}$ m, so that the plasma region is about sixty λ_{Dp} long. In the center of the plasma ($y \simeq 0$), the results are in good agreement with one–dimensional theory.[2] The plasma region, which is determined by $\rho(\mathbf{x}) \simeq 0$, is seen to be much more extended than both the emitter and the collector sheaths. In the normal direction, the potential and space–charge distributions are flat near the center but jump quite sharply at the plasma–

vacuum transition. This is where the largest potential gradients in the normal direction occur, and we will show that even in this region our method is able to resolve the complex structure of the electron and ion distribution functions very well.

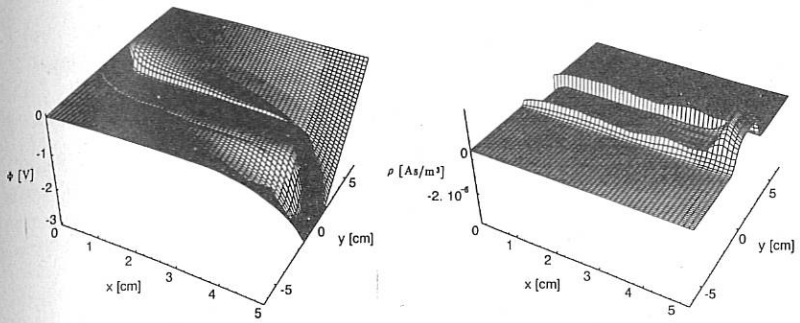

Fig. 2. Potential and space–charge distributions

4. **Velocity distribution functions.** Integrating the appropriate particle trajectory back in time until it intersects with some boundary, we are able to calculate, from Eq. (1), the ion and electron velocity distribution functions for a given phase–space point. Discretizing velocity space (i.e., the parallel velocity v_x, the normal velocity v_n, and the polar angle ϑ), we calculate the velocity distribution functions for each particle species as a function of all three velocity coordinates. Due to the nontrivial structure of the electric field and the boundary conditions, these distribution functions have a

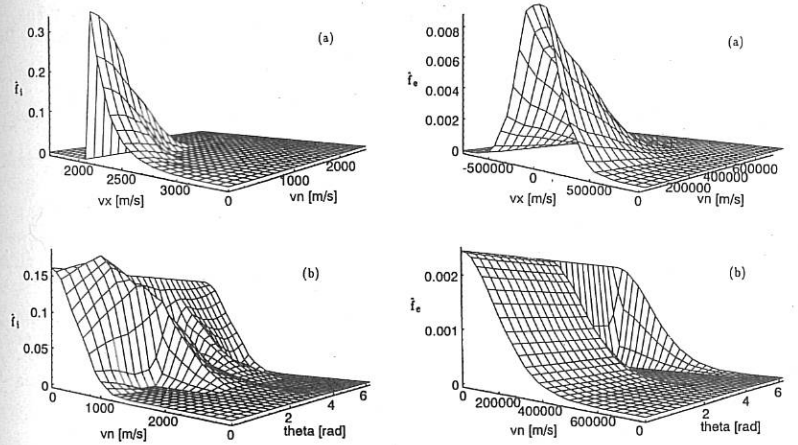

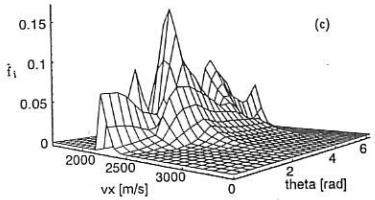

Fig. 3. Ion distribution function
for x = 2.5 cm and y = 1.4995 cm
(a)$\vartheta = 5.28$ rad
(b)$v_x = 2302$ m/s
(c)$v_n = 885$ m/s

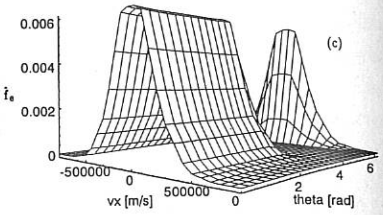

Fig. 4. Electron distribution function
for x = 2.5 cm and y = 1.4995 cm
(a)$\vartheta = 3.27$ rad
(b)$v_x = 3.02 \cdot 10^6$ m/s
(c)$v_n = 1.48 \cdot 10^5$ m/s

complex form which cannot be calculated analytically. Figures 3 and 4 show typical normalized electron and ion velocity distribution functions near the plasma–vacuum transition for the above parameters at the position (x = 2.5 cm, y = 1.4995 cm). In each of these plots one velocity variable is fixed, so that the velocity distribution functions shown depend only on two velocity variables.

5. Particle trajectories. In view of the high gyration frequency of the electrons and practical limitations on computing time, we are treating electron motion in a guiding–center approximation. To convince ourselves that this approximation is indeed good we have made a comparison with the numerically exact guiding–center motion. These calculations show that even in the plasma–vacuum transition region, where the steepest field gradients are located, our approximation is excellent (cf. Ref. 6).

Acknowledgments.

This work was supported by the Austrian Science Foundation, contract No. P8405.

References.

[1]H. Pedit, Diploma thesis, University of Innsbruck (November 1990).
[2]S. Kuhn, Plasma Phys. 23, 881 (1981).
[3]S. Koonin, Physik auf dem Computer, Oldenbourg Verlag (1987).
[4]H. Pedit and S. Kuhn, *17th EPS Conference on Controlled Fusion and Plasma Heating*, Amsterdam, 1990, edited by C. Briffod, Adri Nijsen–Vis and F.C. Schüller (European Physical Society, 1990), Contributed Papers, IV, 1786.
[5]H. Pedit and S. Kuhn, in Proceedings of the 1991 International Workshop on Plasma Physics, Pichl/Schladming, 28 February – 2 March 1991 (in press).
[6]H. Pedit and S. Kuhn, to be published.

ANISOTROPIC CONDUCTIVITY OF THE COLLISIONLESS MAGNETIZED PLASMA AND ITS APPLICATION TO THE CYLINDRICAL PLASMA COLUMN

S.Kiyama
Electrotechnical Laboratory,
1-1-4 Umezono, Tsukuba-shi, Ibaraki, Japan

1. INTRODUCTION

The effective conductivity perpendicular to the magnetic field of the collisionless plasma is shown to be very low, by the classical macroscopic equation without adding any anomalous effect and assumptions. This highly anisotropic conductivity is clearly understood also by the microscopic picture of the individual particle motions in the magnetic fields and is the common characteristic of the high temperature magnetized plasma in most of the nuclear fusion devices such as in tokamaks. The consideration based on the anisotropic conductivity may give the good explanation for the specific and common behavior of the plasma, such as the self organization, the fast relaxation and the various anomalous transport phenomena which have been considered to be the results of the various turbulences and instabilities.

2. EFFECTIVE TRANSVERSE CONDUCTIVITY

In the case where the stepped electric field perpendicular to the magnetic field is applied abruptly to the magnetized uniform plasma, the electric currents can be analytically described by the macroscopic equation derived from the Boltzmann equation. If the electron to ion collision frequency is low as compared with the electron cyclotron frequency, the electron current approaches rapidly to a steady value after a few electron cyclotron oscillations, and the ion current which is carried by the ion accelerated directly to the electric field, becomes dominant after a half period of the ion cyclotron motion. However, this ion current and the Hall current may also vanish in a few ion cyclotron periods, and the transverse electron conduction current parallel to the electric fields will remain after this phase.

The electron conduction current density $j_\perp$ perpendicular to the magnetic field and parallel to the perpendicular electric field $E_\perp$, and the effective perpendicular electrical conductivity $\sigma_{\perp eff}$ parallel to $E_\perp$ are expressed by [1],

$$j_\perp = \sigma_{\perp eff} E_\perp , \qquad \sigma_{\perp eff} = \sigma_s \cdot \frac{1}{1+(\omega_{ce}/\nu_{ei})^2} \sim \sigma_s \cdot (\frac{\nu_{ei}}{\omega_{ce}})^2 \tag{1}$$

Here σ_s, ν_{ei}, ω_{ce} are the Spitzer conductivity, the electron ion collision frequency and the electron cyclotron frequency, respectively. In the final state both ions and electrons drift in the same direction so as to eliminate the electric fields and all the transverse currents except the diamagnetic current may vanish. However, if the particle diffusion speed is same as the drift velocity, the steady density profiles might be sustained, as usual the case in most of the experiments. In any case, the transverse conduction current should be less than the value given by the equation (1). It should be noted that this relation may universally hold in the real plasma with space and time variation of the electromagnetic field and the plasma pressure.

3. CONDITIONS FOR THE HIGHLY ANISOTROPIC CONDUCTIVITY

The highly anisotropic conductivity may realize, if $(\nu_{ei}/\omega_{ce})^2$ is much less than unity. In **Fig.1**, the criteria for the condition $(\nu_{ei}=\omega_{ce})$ are shown as the function of T_e and n_e, for the characteristic magnetic field B as a parameter. In the region below each line, the anisotropy may appear more extremely as the distance from the line is longer. The typical experimental

conditions in the common devices are also shown. In the large tokamak, $(\nu_{ei}/\omega_{ce})^2$ is less than 10^{-16} and then the plasma may behave as the dielectric substance. Even in most of the small devices, $(\nu_{ei}/\omega_{ce})^2$ is less than 10^{-8} and then the perpendicular conduction current can be neglected. As for the diffusion of the magnetic fields, the ideal anisotropic conductivity approximation that the parallel conductivity is infinite and the transverse conductivity is zero, is applicable over the very wide time scale. In the large tokamaks, this approximation may be valid in the time scale from 0.1μs to 1s.

The highly anisotropic conductivity may give the relaxation dominant character of the plasma, which is caused by the frequent reconnection process of the magnetic fields. The relaxation process combined with the diamagnetic current provides the self-organized configurations in high β regime. In the next two examples with very simple configuration, the specific phenomena may be clearly explained by the consideration based on the anisotropy.

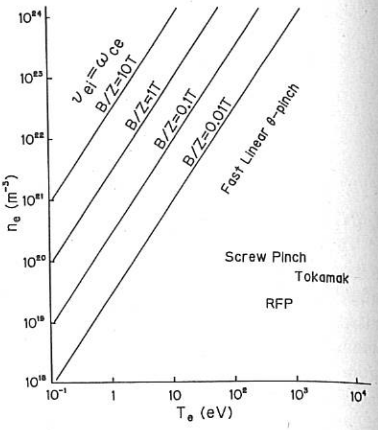

Fig.1 Criteria for the anisotropy.

4. APPLICATION TO THE CYLINDRICAL PLASMA COLUMN

The highly anisotropic characteristics are applied to the implosion phase of the θ-pinch and the force-free configuration in a cylindrical geometry, and the skin depth of the magnetic fields and the flux generation mechanism are discussed, respectively.

(I) Magnetic Skin Depth in the Implosion Phase of θ-pinch

In the cylindrical configuration of the fast θ-pinch geometry, the diffusion of the axial magnetic field into the plasma is much faster than the value derived from the classical isotropic conductivity. It has been observed that the skin depth of the axial magnetic field in the implosion phase is about c/ω_{pi} (c is the light speed and ω_{pi} is the ion plasma frequency), and consequently the many theoretical considerations and computer simulations were devoted to the subject [2]. These discussions mostly employed the anomalous transport which is caused by the microscopic instabilities or turbulences to explain the high resistance in the skin region. However, in the well preheated plasma of the fast θ-pinch devices, the condition $(\nu_{ei}/\omega_{ce})^2 \ll 1$ was already satisfied and then the transverse resistance should be estimated to be very high without any anomalous transport. In the ideal simplified process, the electrons simply behave so as to keep the quasi-charge neutrality and cannot carry any conduction current. In this situation, each ion moves as the individual particle in the induced electric fields and the self-consistent magnetic fields. The fast ions which are accelerated by the induced electric fields, carry the diamagnetic-like current. An ion particle simulation was done on this simple model. The results well explain the whole structures in detail, which were observed in the fast θ-pinch experiment [3]. In **Fig.2**, the time dependent skin depth obtained by the computer simulation **(a)** is compared with the experimental one **(b)**. Here, ω_{pi0} is the ion plasma frequency correspond to the initial ion density. In both experiment and simulation, the skin depth is approximately c/ω_{pi0} in the early stage and transits to $c/2\omega_{pi0}$ after a few ion gyration. A slight discrepancy is recognized only in very early stage (<50ns), where the electron conduction current may have some effects. The physical pictures of the magnetic

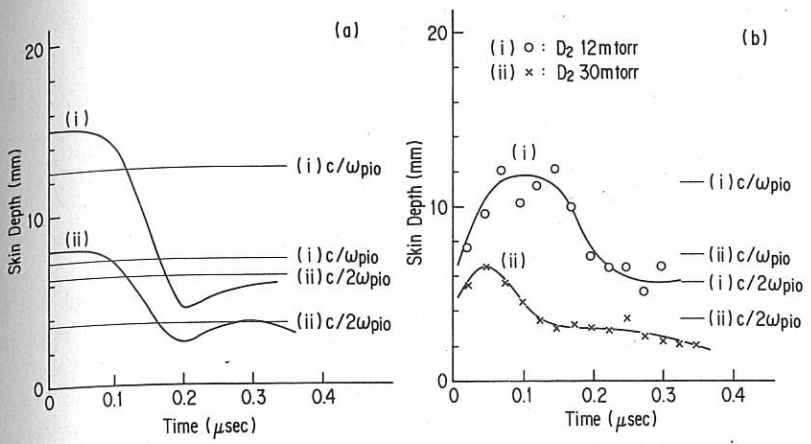

Fig.2 Time dependnt magnetic skin depth. (a) Computer simulation by the ion particle model, (b) Experimental results in the fast θ-pinch.

structure are also obtained by the analytical solution based on the reflected ion model together with the anisotropic electron conductivity model. The analysis also shows that the skin depth (c/ω_{pio}) corresponds to the ion larmor radius.

(II) Formation of Force-Free Configuration and Flux Generation in Stabilized Pinch

It is well known that the magnetic flux generation phenomena are widely observed in RFP and Z-pinch geometry. The various mechanisms for the flux generation and dissipation, including the dynamo effect and the modes coupling of the MHD instabilities, have been proposed. However, this specific phenomena can be easily understood by the analysis based on the anisotropic conductivity without any complicated mechanism.

The plasma of this specific character may be represented by the linear cylindrical plasma column of radius a and the axi-symmetric magnetic field B_z and B_θ. Here, we choose a force free equilibrium configuration with the constant pitch magnetic field, which was used for the screw pinch stability analysis [4] and given in the following form,

$$B_z(\mu r,t) = B_0(t)\frac{1}{1+\mu^2 r^2}, \qquad B_\theta(\mu r,t) = B_0(t)\frac{\mu r}{1+\mu^2 r^2} \tag{2}$$

Here, $2\pi/\mu$ is the pitch length and the pinch parameter $\theta=\mu a$. This configuration is nearly same as the bessel function model in the regime $\theta<0.3$ and therefore belongs to the energy minimum state [5]. This configuration is also similar to the low q tokamak configuration if θ is small and tends to that of the stabilized pinch if θ is large.

If the magnetic field changes keeping the similar profile as in the equation (2), it can be verified that the electric field is everywhere perpendicular to the magnetic field and the electric fields components $E_z(a)$ and $E_\theta(a)$ at the wall should be as,

$$E_z(a,t) = \frac{1}{2\mu}\ln(1+\mu^2 a^2)\frac{dB_0(t)}{dt}, \quad E_\theta(a,t) = -\frac{1}{2\mu^2 a}\ln(1+\mu^2 a^2)\frac{dB_0(t)}{dt} \tag{3}$$

In the ideal highly anisotropic conductor where the parallel conductivity is infinity while the

perpendicular conductivity is zero, the magnetic field can increase or decrease, keeping the similar configuration just as the equation (2) indicates, if the matched electric field given by equation (3) are applied at the wall. The condition for the matched electric fields may expressed as $E_z(a)/E_\theta(a)=\mu a=\theta$. There are two cases according to θ, in which the interesting experimental results might be explained by this fundamental mechanism.

(A) $\theta<1$

The constant pitch screw pinch configuration can be definitely established in the range $\theta<0.3$, if the magnetic fields are ramped up keeping the pitch at the wall constant, that is, if the matched condition is kept at the wall. This fact was found at the early phase of the screw pinch research and it has been understood by the frozen-in magnetic fields and the compression of the highly conductive plasma under the MHD approximation. However, more recent experiment shows that the constant pitch configurations are established even in the case where any compression effect cannot be observed both in the fast and slow screw pinch experiment [6]. Therefore, in any case the consideration based on the anisotropic conductivity might be appropriate for the mechanism of the formation of the constant pitch configuration.

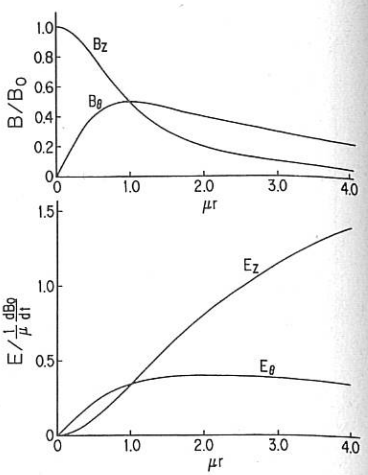

Fig.3 Electromagnetic configuration of the constant pitch force free model.

(B) $\theta\gg1$

As θ increases, the configuration tends to the stabilized z-pinch type in which the axial magnetic fields is enhanced in the center, and the ratio $E_z(a)/E_\theta(a)(=\mu a=\theta)$ become very large. This means that the axial magnetic fields can be created by the axial electric field, that is, the axial magnetic flux can be generated by increasing the axial current which is excited by the axial electric field. This phenomena may be explained by the frozen-in magnetic field and the compression of the plasma column under the MHD approximation or $\boldsymbol{E}\times\boldsymbol{B}/B^2$ drift motion as well. However, in most experiment, the compression effects or the drift motions are scarcely recognized. Therefore, in any case except in the extremely high density and low temperature plasma, the mechanism based on the highly anisotropic conductivity might be responsible for the flux generation in the configuration with high θ.

REFERENCES

[1] L.Spitzer, *Physics of Fully Ionized Gases,* Interscience, New York (1962).
[2] R.C.Davidson, N.A.Krall, *Nuclear Fusion*, **17**, 1313 (1977).
[3] S.Kiyama, K.Ogawa, *in Plasma Physics and Controlled Nuclear Fusion Research (Proc. 4th Int. Conf. Madison, 1971)*, **Vol.1** IAEA Vienna 287 (1972).
[4] W.Schuurman, C.Bobeldijk, R.f.de Vries, *Plasma Physics*, **11**, 495 (1969).
[5] J.B.Taylor, *in Plasma Physics and Controlled Nuclear Fusion Research (Proc. 5th Int. Conf. Tokyo, 1975)*, **Vol.1** IAEA Vienna 161 (1975).
[6] H.Kiyama, et. al., *in Plasma Physics and Controlled Nuclear Fusion Research (Proc. 12th Int. Conf. Nice, 1988)*, **Vol.1** IAEA Vienna 437 (1989).

ANALYTIC SOLUTION TO LONGITUDINAL EIGENMODES IN A COLLISIONLESS BOUNDED PLASMA

S. Kuhn, N. Schupfer, A.S. de Assis,* and M.A.M. Santiago*
Institute for Theoretical Physics, University of Innsbruck
A–6020 Innsbruck, Austria
*Instituto de Matemática, Universidade Federal Fluminense
24020 Niterói, RJ, Brazil

1. Introduction and summary. In Ref. 1, an integral–equation method was developed for solving the general linearized perturbation problem for a one–dimensional, uniform collisionless plasma with thin sheaths, bounded by two planar electrodes. The underlying system of equations consists of (i) the Vlasov equations for all particle species involved, (ii) Poisson's equation, (iii) the equation of total–current conservation, (iv) the particle boundary conditions at the left– and right–hand electrodes, and (v) the external–circuit equation. The method allows for very general equilibrium, boundary, and external–circuit conditions. Using Laplace transformations in both time and space, it is set up to handle the complete initial–value problem but also yields the solution to the eigenmode problem as a by–product.

In the present paper, this method is used to study, in a general and predominantly analytical manner, eigenmodes in a system modeling the *negatively biased Q–machine*. This problem was already considered in Refs. 2 and 3, though only by purely numerical means and in the "low–frequency approximation (LFA)", yielding discrepant results.

2. The collisionless plane–diode model and its linearized basic equations. We consider a one–dimensional diode as shown in Fig. 1, where the surfaces of the (ideally conducting) electrodes are located at $x = 0$ ("left–hand electrode") and $x = L$ ("right–hand electrode"), and the electrodes are connected through an external circuit with specified properties. The intervening space is filled with a collisionless plasma consisting of n_s particle species, denoted by the species index σ. Each physical quantity Q involved is decomposed in the form $Q(x,v,t) = \bar{Q}(v) + \tilde{Q}(x,v,t)$, with $\bar{Q}$ the given dc part and $\tilde{Q}$ the sought–for small–amplitude perturbation.

The basic equations, listed at the beginning of Sec. 1 and given in full in Refs. 1 and 2, determine the evolution of the perturbations $\tilde{E}(x,t)$ (electrostatic field), $\tilde{f}^{\sigma}(x,v,t)$ (velocity distribution function of species σ), $\tilde{j}_e(t)$ (external–circuit current density), and the global goal is to solve them for given initial, injection and external–circuit perturbations. To this end we follow the Laplace–transformation method formulated in Ref. 1, to which the reader is here and henceforth referred for full details.

The first step consists in transforming the basic equations into a set of $(2+2n_s)$ coupled linear integral equations for the $(2+2n_s)$ time Laplace transforms $\tilde{j}_e(\omega)$,

$\tilde{E}(x,\omega)$, $\tilde{f}_l^{\sigma}(v>0,\omega)$, and $\tilde{f}_r^{\sigma}(v<0,\omega)$, with $\tilde{f}_l^{\sigma}$ and $\tilde{f}_r^{\sigma}$ the injection distribution functions at the left– and right–hand electrodes, respectively. These "Laplace–transformed integral equations" [Eqs. (37)–(40) of Ref. 1] can be symbolically written in the form

$$\mathscr{D}(x,v,[x'],[v'],\omega)\ \tilde{u}([x'],[v'],\omega) = \tilde{k}(x,v,\omega) \ , \tag{1}$$

where $\tilde{u}(x,v,\omega) \equiv [\tilde{j}_e, \tilde{E}, \tilde{f}_l^1, \ldots, \tilde{f}_l^{n_\sigma}, \tilde{f}_r^1, \ldots, \tilde{f}_r^{n_s}]^T$ is the column vector of the unknown perturbations, $\mathscr{D}(x,v,[x'],[v'],\omega)$ is a matrix of known linear operators acting on $\tilde{u}$ (with the variables of operation indicated by brackets), and $\tilde{k}(x,v,\omega) \equiv [-\tilde{V}_{e0}, \tilde{k}_8, \tilde{k}_{10}^1, \ldots, \tilde{k}_{10}^{n_s}, \tilde{k}_{13}^1, \ldots, \tilde{k}_{13}^{n_s}]^T$ is the column vector of the known perturbations $-\tilde{V}_{e0}$ etc.[1] The specific form of the system (1) which is appropriate to the physical situation considered here (Sec. 3) will be given in Sec. 4.

Basically, the solution of our linearized perturbation problem is found by solving the system (1) for $\tilde{u}(x,v,\omega)$,

$$\tilde{u}(x,v,\omega) = \mathscr{D}^{-1}(x,v,[x'],[v'],\omega)\ \tilde{k}([x'],[v'],\omega) \ , \tag{2}$$

(with $\mathscr{D}^{-1}$ the inverse to $\mathscr{D}$), and by then Laplace inverting the latter:

$$\tilde{u}(x,v,t) \equiv \int \frac{d\omega}{2\pi} e^{-i\omega t}\, \tilde{u}(x,v,\omega) = \int \frac{d\omega}{2\pi} e^{-i\omega t}\, \mathscr{D}^{-1}(x,v,[x'],[v'],\omega)\ \tilde{k}([x'],[v'],\omega) \ , \tag{3}$$

where, as usual, the original path of integration in the complex ω–plane is a straight line with $-\infty \leq \mathscr{R}e\,\omega \leq +\infty$ and $\mathscr{I}m\,\omega$ a "sufficiently large" positive number. In the present context, we are only interested in the "natural eigenmodes" of the system, i.e., the contributions of the poles of $\mathscr{D}^{-1}$ to $\tilde{u}(x,v,t)$, cf. Sec. 4.

3. Special case: longitudinal oscillations in the negatively biased single–ended Q–machine. For Q–machines under a wide range of operating conditions, the sheath regions are usually far less extended than the plasma region,[4] so that the uniform–plasma, thin–sheath approximation is applicable. Assuming half–Maxwellian emission from the hot plate (whose temperature is T), the injection distribution functions at the left–hand plasma boundary are cut–off Maxwellians for both the electrons and the ions.[4] At the right–hand boundary plane ($x = L_-$), on the other hand, all ions are absorbed, while all electrons are specularly reflected due to the cold–plate sheath, cf. Fig. 1.

In the present, rather new approach to the linear perturbation problem, we try to simplify our model as much as possible, while still keeping the essential physics. In particular, we approximate the electron velocity distribution function by the "waterbag" $\bar{f}^e(v) = \bar{n}_p[U(v+\bar{v}_{cw}^e)–U(v–\bar{v}_{cw}^e)]/(2\bar{v}_{cw}^e)$ [with $\bar{n}_p$ the equilibrium plasma density and $\bar{v}_{cw}^e = \sqrt{(3kT/m^e)}$ the waterbag cutoff velocity], and the ion distribution by the cold beam $\bar{f}^i(v) = \bar{n}_p\delta(v–\bar{v}^i)$ [with $\bar{v}^i$ the ion average velocity]. It is assumed that the only externally imposed perturbations are initial ones.

4. **Solving the eigenmode problem by** means of the integral–equation method. With the specifications of Sec. 3, the Laplace–transformed integral equations (cf. Sec. 2) yield the explicit relations $\tilde{f}^e_1(v>0,\omega) = \tilde{f}^i_1(v>0,\omega) = \tilde{f}^i_r(v<0,\omega) = 0$ and the "reduced" system of coupled integral equations

$$\hat{Z}_e(\omega)\tilde{j}_e(\omega) + \int_{0_+}^{L_-} dx' \tilde{E}(x',\omega) = -\tilde{V}_{e0}(\omega), \qquad \text{[external–circuit equation]} \tag{4}$$

$$-k_5(x,\omega)\tilde{j}_e(\omega) + \tilde{E}(x,\omega) + \mathscr{S}_0(x,[x'],\omega)\,\tilde{E}([x'],\omega)$$
$$+ \mathscr{K}^e_{0r}(x,[v<0],\omega)\,\tilde{f}^e_r(v,\omega) = \tilde{k}_8(x,\omega)\,, \qquad \text{[Poisson's equation]} \tag{5}$$

$$\mathscr{S}^e_r(v<0,[x'],\omega)\,\tilde{E}([x'],\omega) + \tilde{f}^e_r(v,\omega) = 0\,, \qquad \begin{bmatrix}\text{right–hand electron}\\ \text{boundary condition}\end{bmatrix} \tag{6}$$

from which the remaining unknowns $\tilde{j}_e(\omega)$, $\tilde{E}(x,\omega)$ and $\tilde{f}^e_r(v,\omega)$ must be determined. Here, k_5, $\tilde{k}_8$, $\hat{Z}_e$, and $\tilde{V}_{e0}$ are known functions, $\mathscr{S}_0$ and $\mathscr{S}^e_r$ are known x–space operators, and $\mathscr{K}^e_{0r}$ is a known v–space operator.[1]

By successively eliminating $\tilde{f}^e_r$ and $\tilde{E}$ via Eqs. (6) and (5), respectively, the system (4)–(6) can now be cast into a single equation for $\tilde{j}_e(\omega)$:

$$\tilde{j}_e(\omega) = [\tilde{V}_{di}(\omega) - \tilde{V}_{e0}(\omega)]/\hat{Z}_{tot}(\omega) \tag{7}$$

where $\tilde{V}_{di}$ and $\tilde{V}_{e0}$ are expressions describing the effects of initial perturbations and

$$\hat{Z}_{tot}(\omega) \equiv \hat{Z}_d(\omega) + \hat{Z}_e(\omega) \tag{8}$$

is the "total" impedance, with $\hat{Z}_e(\omega)$ the external–circuit impedance and

$$\hat{Z}_d(\omega) \equiv \int_{0_+}^{L_-} dx'\, \mathscr{B}^{-1}(x',[x''],\omega)\, k_5([x''],\omega)\,, \tag{9}$$

the diode impedance. The operator $\mathscr{B}$ is defined by

$$\mathscr{B}(x,[x'],\omega)\,\tilde{E}([x'],\omega) = \left[1 + \mathscr{S}_0(x,[x'],\omega) - \{\mathscr{K}^e_{0r}\mathscr{S}^e_r\}(x,[x'],\omega)\right]\tilde{E}([x'],\omega)\,. \tag{10}$$

According to the remarks following Eq. (3), the n^{th} linear eigenfrequency is the n^{th} pole of the integrand of the Laplace integral, which from Eq. (8) is seen to be the n^{th} zero of $\hat{Z}_{tot}(\omega)$. Hence, we have the eigenfrequency equation

$$\hat{Z}_{tot}(\omega_n) = 0\,. \tag{11}$$

In the present paper we restrict ourselves to solving this equation. While $\hat{Z}_e(\omega)$ is usually given as a simple analytic function of ω and can hence be evaluated easily, $\hat{Z}_d(\omega)$ is defined by the integral (9), whose evaluation has hitherto been possible only by purely numerical means and only in the LFA.[2,3] By contrast, we have now obtained, without further approximations, the following analytic form of $\hat{Z}_d(\omega)$:

$$\hat{Z}_d(\omega) = I_1(\omega) - \frac{\bar{a}(\omega)}{A(\omega)+1} I_2(\omega) , \tag{12}$$

with $I_1(\omega) = \int_{0_+}^{L_-} dx' k_5(x',\omega)$, $I_2(\omega) = \int_{0_+}^{L_-} dx' k_5(x',\omega) \sin\left[\omega \frac{L-x'}{\bar{v}^e_{cw}}\right]$,

$\bar{a}(\omega) = a_0(\omega) \int_{0_+}^{L_-} dx' k_6(x',-\bar{v}^e_{cw},\omega)$, $A(\omega) = a_0(\omega) \int_{0_+}^{L_-} dx' k_6(x',-\bar{v}^e_{cw},\omega) \sin\left[\omega \frac{L-x'}{\bar{v}^e_{cw}}\right]$,

and $a_0(\omega) = -i \frac{(\omega_p^e)^2}{(\bar{v}^e_{cw})^2} \exp\left[i \frac{\omega L}{\bar{v}^e_{cw}}\right]$.

The integrals occurring here can be represented by elementary functions, so that the eigenfrequency equation (11) has now become an analytically explicit transcendental equation which is valid for all frequency ranges.

5. Results and discussion. As previously,[2,3] we consider the eigenmodes of a negatively biased single–ended Q–machine characterized by the following parameters: electron–K^+ plasma; interelectrode distance L = 30cm; hot–plate temperature T = 2200 K, electron emission density $n_{e0^+} = 10^{10}$ cm^{-3}, ion emission density $n_{i0^+} = 10^8$ cm^{-3} (hence neutralization parameter $\alpha \equiv n_{i0^+}/n_{e0^+} = 10^{-2}$), plasma density $\bar{n}_p = 2\times10^7$ cm^{-3}, plasma potential $\Phi_p = -1.3$ V, electron waterbag cutoff velocity $v_{cw}^e = 2.7\times10^5$ cm/s, electron plasma frequency $\omega_p^e = 2.5\times10^8$ s^{-1}, ion–beam velocity $v^i = 2.7\times10^5$ cm/s, ion plasma frequency $\omega_p^i = 9.4\times10^5$ s^{-1}, external short–circuit.

The eigenfrequencies corresponding to the first three eigenmodes are $\omega_1 = (1.5862 - 3.1950i) \times 10^4$ s^{-1}, $\omega_2 = (4.7975 - 3.2137i) \times 10^4$ s^{-1}, $\omega_3 = (7.9967 - 3.2044i) \times 10^4$ s^{-1}, while in the "low–frequency approximation" the first two eigenfrequencies had been found[2] to be $\omega_1^{lf} = (3.2204\times10^4 + 1.5235\times10^3 i)$ s^{-1} and $\omega_2^{lf} = (6.2512\times10^4 + 6.6399\times10^2 i)$ s^{-1}. This discrepancy, which seems to indicate that the "low–frequency approximation" is inappropriate for bounded plasmas, will need further study.

Acknowledgment. This work was supported by the Austrian Science Foundation (projects P7005 and P8405), the Austrian Academic Exchange Service, and the Conselho Nacional de Desenvolvimento Cientifico e Tecnológico (CNPq), Brazil.

[1] S. Kuhn, Phys. Fluids **27**, 1821 (1984).
[2] S. Kuhn et al., *17th EPS Conf. on Contr. Fusion and Plasma Heating*, Amsterdam, 1990, Contributed Papers **4**, 1786.
[3] N. Schupfer et al., *1991 Int'l Workshop on Plasma Physics*, Pichl/Schladming, Austria, 1991 (in press).
[4] S. Kuhn, Plasma Phys. **23**, 881 (1981).

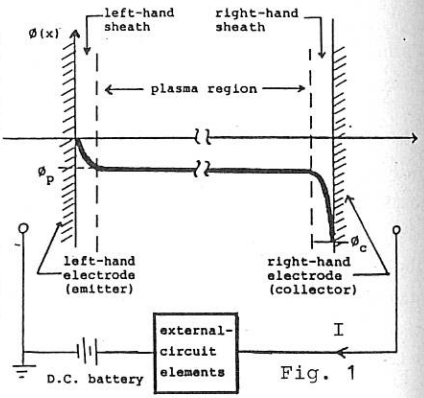

Fig. 1

A COLLISIONLESS E × B INSTABILITY WITH LARGE ION ORBITS

Francis F. Chen
Electrical Engineering Department and
Institute of Plasma and Fusion Research
University of California, Los Angeles
Los Angeles, CA 90024-1594, U.S.A.

Introduction

A flute instability of a partially ionized, magnetized plasma with a transverse electric field was shown by Simon /1/ and Hoh /2/ to be responsible for the violent instability of reflex discharges which allows electron current to cross the magnetic field. The main cause of this instability is the difference between the electron and ion $\mathbf{E} \times \mathbf{B}$ drifts due to ion-neutral drag. This effect is not present in collisionless plasmas, but the instability is still found if the ion drift is slowed by the finite Larmor radius effect /3//4/. In a recent experiment by Sakawa /5/, clear evidence of this collisionless instability was found in a plasma which was much smaller than the ions' Larmor radii. The observed frequency was much higher than the ion cyclotron, diamagnetic drift, and $\mathbf{E} \times \mathbf{B}$ frequencies, thus eliminating both the $\mathbf{E} \times \mathbf{B}$ and the drift instabilities. The ions trapped in the potential well of the E-field had nearly straight-line orbits, with only a small curvature due to the Lorentz force. The ion fluid then has an $\mathbf{E} \times \mathbf{B}$ drift much smaller than that of the electrons, even though there are no collisions.

It is easy to show that such a fluid suffers from a strong flute (not drift) instability with a phase velocity close to that of the slow ion drift, as observed. The equilibrium, however, has to be treated kinetically, since the system is much smaller than the ion orbits; and it is the equilibrium which is difficult to treat. An expansion in a small Larmor radius parameter would not be suitable; rather, the curvature of the ion orbits is the small quantity. By choosing a particular functional form for the electric field profiles, we have found a simple way to model the equilibrium in both plane and cylindrical geometries. The cylindrical case is applicable to beam-plasma experiments /5/, while the plane case can be used to devise experiments to clarify the edge physics in tokamak H-mode boundary layers which are thinner than the ion Larmor radius.

Equilibrium: plane geometry

Consider a plasma confined between infinite planes at $x = \pm L$, embedded in a uniform magnetic field $\mathbf{B} = B_0 \hat{z}$. A jet-like $\mathbf{E} \times \mathbf{B}$ velocity distribution in the y direction in the slab can be modeled by the following analytic functions:

$$\phi = \phi_0 \tanh \xi \tag{1}$$

$$\mathbf{E} = -(N/L)\,\phi' \hat{x} = -(N/L)\,\phi_0 \operatorname{sech}^2 \xi \, \hat{x} \tag{2}$$

$$\rho = (N/L)\,\varepsilon_0 E_x' = 2\varepsilon_0 (N/L)^2 \phi_0 \operatorname{sech}^2 \xi \tanh \xi \quad , \tag{3}$$

where

$$\xi \equiv Nx/L \quad , \tag{4}$$

ϕ is the potential, ρ is the charge density, and N is a parameter for adjusting the sharpness of the profile. These profiles are shown in Fig. 1 for $N = 2$. We take $\phi_0 > 0$, so that $E_x < 0$,

and ions are driven to the left. The magnetic field is so weak that the ions bounce between their birthplace and the left wall in nearly straight lines, but there is a small curvature to the orbits, giving the ions a drift in the y direction. For a tokamak edge layer, the left boundary would be the main plasma, and the right boundary would be the first wall. For a cylindrical beam-plasma experiment, the left boundary would simulate the axis, and the right boundary would be the wall.

We next construct a density profile that is consistent with this potential profile. Let $v(\xi, \xi_0)$ be the velocity of an ion, located at ξ, which was born (at rest) at ξ_0. Its kinetic energy $\frac{1}{2}Mv^2(\xi, \xi_0)$ is gained from the potential drop between ξ_0 and ξ. Thus,

$$v^2(\xi, \xi_0) = (2e\phi_0 / M)(\tanh \xi_0 - \tanh \xi) \quad . \tag{5}$$

The y component of the ion equation of motion reads

$$dv_y / dt = -(e/M) v_x B = -\Omega_c v_x \quad , \tag{6}$$

where Ω_c is the ion cyclotron frequency. The Lorentz force accelerates the ions in the y direction at the rate

$$\frac{dv_y}{dt} = \frac{dv_y}{dx}\frac{dx}{dt} = \frac{dv_y}{dx} v_x \qquad \therefore \quad \frac{dv_y}{dx} = -\Omega_c \quad . \tag{7}$$

The velocity v_y of an ion at ξ which was born at ξ_0 is thus

$$v_y(\xi, \xi_0) = -\Omega_c(x - x_0) = (L/N)\Omega_c(\xi_0 - \xi) \quad . \tag{8}$$

Note that this depends only on position; it is independent of the strength of the E-field. Combining Eqs. (7) and (10), we find for the x velocity component,

$$v_x^2(\xi, \xi_0) = v^2 - v_y^2 = (2e\phi / M)(\tanh \xi_0 - \tanh \xi) - (L\Omega_c / N)^2 (\xi_0 - \xi)^2 \quad . \tag{9}$$

Let the ions be created at a rate $S(x_0)$ m^{-3} sec^{-1}. Since the flux nv_x is conserved, the density at x due to a source $S(x_0)dx_0$ is proportional to $1/|v_x(x, x_0)|$. The constant of proportionality is 0, 1, or 2, depending on whether the ion is turned around before reaching x, is absorbed at the left boundary, or is reflected at $-L$ or turned around at a radius between $-L$ and x. For simplicity we assume a reflecting boundary. Integrating over all source positions upstream of x and changing to the variable ξ, we obtain

$$n(\xi) = \frac{2L}{N}\int_{\xi}^{\xi_{max}} \frac{S(\xi_0)d\xi_0}{|v_x(\xi, \xi_0)|} \quad . \tag{10}$$

Here, ξ_{max} is the smaller of N and that value of ξ_0 beyond which v_x^2, given by Eq. (9), becomes negative, indicating that the ion turns around before ξ. One needs only to end the integration when v_x becomes imaginary. The integrand is singular at two points: $\xi = \xi_0$, and $v^2 = v_y^2$, but these are obviously integrable singularities because the density physically has to be finite if the source S is finite. The experimental density profile can be matched by choosing a suitable function $S(\xi_0)$. Fig. 2 shows sample n_1 profiles which are consistent with Eq. (1).

To obtain the ion fluid drift v_{0y} at any position x, we need only to sum over all source positions the values of $v_y(\xi, \xi_0)$, given by Eq. (8), weighted by the source strength $S(\xi_0)$ and the residence time $1/|v_x|$, and normalize:

$$v_0(\xi) = \frac{2}{n(\xi)}\int_{\xi}^{\xi_{max}} v_y(\xi, \xi_0) \frac{S(\xi_0)\, d\xi_0}{|v_x(\xi, \xi_0)|} \quad . \tag{11}$$

The corresponding profiles of v_0 are also shown in Fig. 2.

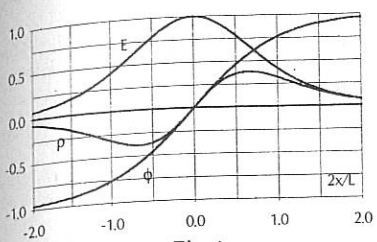

Fig. 1

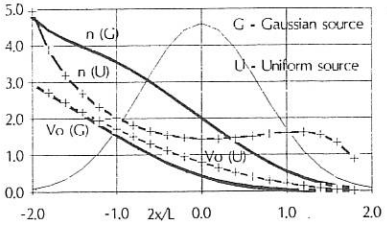

Fig. 2

Equilibrium: cylindrical geometry

In the experiment in question /5/, a beam of electrons injected along the axis depresses the potential there and gives rise to a nonuniform radial electric field. The corresponding sheared $\mathbf{E} \times \mathbf{B}$ drift is in the θ direction and falls to zero at $r = 0$ and $r = a$. This situation can be modeled by a consistent set of Bessel functions:

$$\phi = -\phi_0 [J_0(Tr) - J_0(w_1)] \tag{12}$$

$$E_r = -\frac{\partial \phi}{\partial r} = \phi_0 \frac{\partial}{\partial r} J_0(Tr) = -\phi_0 T J_1(Tr) \tag{13}$$

$$\rho = \frac{\varepsilon_0}{r} \frac{\partial}{\partial r} (r E_r) = -\varepsilon_0 \phi_0 T^2 J_0(Tr) \quad , \tag{14}$$

where w_1 is a zero of J_1; for instance, the first zero is $w_1 = 3.83$. That Eq. (16) is true can be verified by substituting for E_r from Eq. (15), taking the r-derivative of ρ in both parts of the equation, and recognizing the differential equation that defines J_1. Setting $T = w_1/a$ ensures that both ϕ and E_r vanish at $r = a$. These profiles are shown in Fig. 3.

The kinetic energy $\frac{1}{2} M v^2(r, r_0)$ of an ion at r which was born at rest r_0 has been gained from the potential drop between r_0 and r. Defining $z = Tr$, we can therefore write

$$v^2(z, z_0) = \frac{2e\phi_0}{M} [J_0(z) - J_0(z_0)] \quad . \tag{15}$$

The Lorentz force curves the ion orbits, which would otherwise be straight lines through the axis, as the ions bounce in the dc potential well. The θ component of velocity can be found from the conservation of canonical angular momentum:

$$P_\theta = M r v_\theta + \tfrac{1}{2} e B_0 r^2 = \tfrac{1}{2} e B_0 r_0^2 \quad , \tag{16}$$

where $\frac{1}{2} B_0 r$ is the vector potential A_θ in a uniform field, and we have taken (for the time being) v_θ to be zero at $r = r_0$. Solving for v_θ, we have

$$v_\theta(z, z_0) = \frac{\Omega_c}{2T} \frac{z_0^2 - z^2}{z} \quad . \tag{17}$$

Eqs. (15) and (17) give

$$v_r^2(z, z_0) = v^2 - v_\theta^2 = \frac{2e\phi_0}{M} [J_0(z) - J_0(z_0)] - \left(\frac{\Omega_c}{2T}\right)^2 \left(\frac{z_0^2 - z^2}{z}\right)^2 \quad . \tag{18}$$

To calculate the density, we again integrate over a source distribution $S(z_0)$, weighted by the residence time $1/|v_r|$ and a geometrical compression factor z_0/z due to the cylindrical geometry:

$$n(z) = 2\int_z^{z_{max}} \frac{z_0}{z}\,\frac{S(z_0)\,dz_0}{|v_r(z, z_0)|} \quad . \tag{19}$$

Here, z_{max} is the smaller of w_1 and the value of z_0 at which v_r^2, given by Eq. (18), is zero; beyond that, the ions do not reach z. Since all ions are "reflected", they contribute twice to the density at any radius. The factor 2 included for this is not important, since $S(z_0)$ is to be adjusted to fit the experiment anyway. The fluid drift v_0 in the θ direction is given by the weighted average of v_θ, as given by Eq. (17):

$$v_0(z) = \frac{2}{n(z)}\int_z^{z_{max}} v_\theta(z, z_0)\,\frac{z_0}{z}\,\frac{S(z_0)\,dz_0}{|v_r(z, z_0)|} \quad . \tag{20}$$

Examples of n and v_0 profiles are given in Fig. 4.

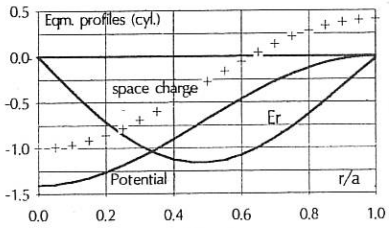

Fig. 3

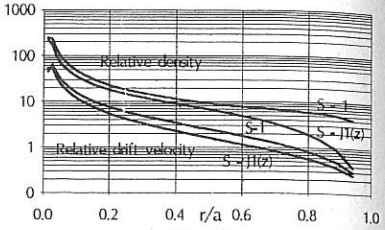

Fig. 4

Although the ions are born with very little energy, a small amount of angular momentum at large radii could greatly affect the ions' turnaround radius, and thus the density at small radii. To examine this effect, we can add a thermal velocity $v_\theta(r_0) = \pm v_t$. A term $mrv_\theta(r_0)$ is then added to Eq. (16), resulting in a term $v_\theta(r_0)$ added to Eq. (17), with corresponding changes in subsequent equations. The results, which we cannot show here, indicate that $v_\theta(r_0)$, has more effect when it is in the same direction as the Lorentz force, but that the effect is small unless $\frac{1}{2}Mv_\theta^2$ is comparable to $e\phi_0$.

The instability

Since the instability is basically a fluid effect, we use the fluid equations. We confine ourselves here to plane perturbations of the form $\exp i(ky - \omega t)$. For the ions, the linearized equations are:

$$M\left(\frac{\partial \mathbf{v}}{\partial t} + \mathbf{v}_0\cdot\nabla\mathbf{v} + \mathbf{v}\cdot\nabla\mathbf{v}_0\right) = e(\mathbf{E} + \mathbf{v}\times\mathbf{B}_0) \tag{21}$$

$$\frac{\partial n}{\partial t} + n_0\nabla\cdot\mathbf{v} + \mathbf{v}\cdot\nabla n_0 + n\nabla\cdot\mathbf{v}_0 + \mathbf{v}_0\cdot\nabla n = 0 \quad . \tag{22}$$

Here, $v_0(x)$ is the averaged velocity computed above. From the electron equations, we obtain the modified Boltzmann relation /6/ appropriate for $k_\parallel = 0$ and finite ∇n_0 and E_0:

$$\frac{n}{n_0} = \frac{e\phi}{KT_e}\,\frac{\omega_*(x)}{\omega - \omega_E(x)} \quad . \tag{23}$$

Here, ω_* is the electron diamagnetic drift frequency $-k(KT_e/eB_0)n_0'/n_0$, and ω_E is the $\mathbf{E}\times\mathbf{B}$ drift frequency $-kE_0/B_0$. Solving Eq. (21) for the first-order ion fluid velocity $\mathbf{v}$,

substituting into Eq. (22), and eliminating n with Eq. (23), we obtain a second-order differential equation for $\phi(x)$. We keep all x-derivatives ($'$) in both zero- and first-order quantities. The result can be written in the form

$$\phi'' + f(x)\phi' + g(x)\phi = 0 \quad . \tag{24}$$

Defining $\varpi(x) = \omega - kv_0(x)$ and

$$\delta(x) = n_0'(x)/n_0(x) \,, \qquad \gamma(x) = \frac{2\varpi k v_0' + \Omega_c v_0''}{\varpi^2 - \Omega_c(\Omega_c + v_0')} \quad , \tag{25}$$

we can write the coefficients as

$$f(x) = \delta(x) + \gamma(x) \tag{26}$$

$$-g(x) = k^2 \left[1 + \frac{\Omega_c}{\varpi} \frac{\delta + \gamma}{k} + \frac{\delta}{k} \frac{\varpi^2 - \Omega_c(\Omega_c + v_0')}{\Omega_c(\omega - \omega_E)} \right] \quad , \tag{27}$$

where all the quantities are x-dependent except k, Ω_c, and ω. Eq. (24) is to be integrated between $-L$ and L using the self-consistent profiles of n_0, E_0, and v_0 computed above to obtain the eigenvalues of ω. By eliminating the velocity shear terms, one can study the Kelvin-Helmholtz effect on this instability.

The basic instability can be uncovered by making the local approximation $g(x) = 0$. This yields a cubic equation for ϖ:

$$\varpi^3 + (k/\delta)\Omega_c(\varpi^2 - \omega_d\varpi) - \Omega_c^2\omega_d = 0 \quad , \tag{28}$$

where

$$\omega_d = \omega_E - kv_0 \tag{29}$$

is the difference between the electron and ion $\mathbf{E} \times \mathbf{B}$ drifts. The unstable root can be seen by taking the limit $\omega_E \gg \Omega_c$ and small v_0, so that $\varpi \approx \omega_d \approx \omega_E$. The last term in Eq. (28) can then be neglected; and, for $n_0'/n_0 < 0$, the resulting quadratic equation yields

$$\omega = kv_0 + k\Omega_c/2|\delta| + i(k\Omega_c\omega_d/|\delta|)^{1/2} \quad . \tag{30}$$

The frequency is of order kv_0, and the growth rate depends on the difference between electron and ion drifts in the equilibrium.

/1/ A. Simon, *Phys. Fluids* **6**, 382 (1963).

/2/ F.C. Hoh, *Phys. Fluids* **6**, 1184 (1963).

/3/ M.N. Rosenbluth, N.A. Krall, and N. Rostoker, *Nucl. Fusion Suppl.*, Part 1, 143 (1962).

/4/ F.F. Chen, *Phys. Fluids* **9**, 965 (1966).

/5/ Y. Sakawa, *Thesis*, UCLA (1992).

/6/ R.W. Motley, *Q Machines*, p. 49, Academic Press, New York (1975).

INFLUENCE OF THE THERMOIONIC EMISSION ON THE CURRENT-DRIVEN ION-ACOUSTIC INSTABILITY

G. Donoso and P. Martin, Dpto. de Física, Universidad Simón Bolívar, Apdo. 89000, Caracas 1080A, Venezuela.

1. INTRODUCTION.

In this paper we analyze the conditions for the onset of the instability in an electron emitter cathode and plasma system in a DP machine. Three kinds of particles are considered: plasma ions, electrons and thermoionic electrons. The distribution functions of the first two species of particles is considered to be maxwellians. The distribution function of the thermoionic electrons is determined through the following steps: The starting point is the Fermi-Dirac distribution of the electrons inside the cathode. Then the quantum reflexion of these particles is considered and a suitable transmission coefficient found. This factor is considered together with the transformed distribution function originated by the electrons escaping from the metal to the plasma.In this way we arrive to the thermoionic distribution function. Now the dispersion relation for the ion acoustic waves is analyzed using the well known Landau treatment. The marginal stability is considered and a characteristic product $x\bar{v}$ is found in terms of the critical density ratio x and drift velocity $\bar{v}$. Finally using this density ratio, the critical current for the onset of the instability is determined. The theoretical values and compared with some experiments and good agreement is found.

2. THEORY.

The dispersion relation for the ion-acoustic wave is well known [1].

$$\epsilon(k,\omega) = 1 - \sum_{\alpha} \frac{\omega_{p\alpha}^2}{k^2} \int_L \frac{\partial f\alpha/\partial v}{v - w/k} \, dv \qquad (1)$$

where k, ω are the wave number and frequency and $\omega_{p\alpha}$, $f\alpha$ are

the plasma frequency and distribution function for the species α. L means the Landau contour of integration under the pole. We consider a plasma composed of n_o ions at rest plus two kinds of electrons: $(1-x)n_o$ plasma electrons and xn_o thermoionic electrons. The temperatures are $Ti \equiv Te/\Theta$, Te, and $T_f \equiv \tau Te$, respectively. a) Distribution function for the thermoionic electrons. Inside the cathode the electrons have a Fermi-Dirac distribution, which is approximated by a maxwellian since $(E - E_F)/T_f$ is large,

$$F(E) = A\,(\mathrm{Exp}((E-E_F)/T_f) + 1)^{-1} \cong A\,\mathrm{Exp}(-(E - E_F)/T_f) \qquad (2)$$

where $E = \frac{1}{2}\, m\, (v')^2$ is the kinetic energy, E_F the Fermi energy and T_f the cathode temperature. The quantum transmission coefficient $T(E)$ of a plane wave incident on a potential barrier $E_B = E_F + \phi_w$ (ϕ_w is the work function) is given by [2].

$$T(E) = 4k\beta \,/\, (k + \beta)^2 \qquad (3)$$

where $k = (\,2mE/\,\hbar^2\,)^{1/2}$ and $\beta = (2m(E - E_B)/\,\hbar^2)^{1/2}$ are the propagation constants for the wave functions inside and outside the cathode. Using $\frac{1}{2}\, m\, v^2 = E - E_B$ and $E_B \equiv \frac{1}{2}\, m\, v_E^2$ we obtain

$$T(v) = 2v(v^2 + v_B^2\,)^{1/2}/(\,v^2 + \tfrac{1}{2}\, v_B^2 + v\,(v^2 + v_B^2\,)^{1/2}) \qquad (4)$$

Considering this transmission coefficient and the velocity change across the potential barrier we arrive at the distribution function $g(v)$ for the thermoionic electrons just outside the cathode surface,

$$g(v) = C_o\, T(v)\, \mathrm{Exp}(-(\tfrac{1}{2} m\, v^2 + \phi_w\,)/\,T_f) \qquad (5)$$

where C_o is the normalization constant.

b) Dispersion Relation

Using the distribution function Eq.(5) and the dispersion relation Eq.(1) we obtain

$$\epsilon(k,\omega) = 1-(k_e^2/\,k^2)\,((1-x)\,Z'(s\mu^{1/2}) + x/\tau\; G'(s\mu^{1/2}) + \theta Z'(s\theta^{1/2}))=0 \qquad (6)$$

Here $s = \omega/kc_s$ is the phase velocity, $c_s = (T_e/m_i)^{1/2}$ is the ion acoustic speed, $\mu \equiv m_e/m_i$, $\Theta = T_e/T_i$ and $\tau = T_f/T_e$. Z' is the derivative of the plasma dispersion function and G' is defined by:

$$G'(s) = A_o \int_o^\infty \partial/\partial u \; (T(u) \exp(-u^2)) (u - s)^{-1} \, du \qquad (7)$$

We consider the problem of spatial excitation with real ω and complex k. For marginal stability we compute the principal part of the integral plus one half the residue from the pole. The integrals are evaluated in the usual way [3]: We expand the denominator of $Z'(s)$ in powers of $s/u \ll 1$ for the plasma electrons and in powers of $u/s \ll 1$ for the plasma ions. As for $G'(s)$ we consider $s \ll \bar{u}$ where $\bar{u}$ is the mean velocity of the thermoionic electrons and expand the denominator in powers of $(u - \bar{u})/\bar{u}$. Separating the real and imaginary part of Eq.(6) we get

$$\epsilon_r (k,\omega) = 1 + (1 - x + ax/\tau) \; k_e^2/k^2 - \omega_{pi}^2/\omega^2 \qquad (8)$$

$$\epsilon_i (k,\omega) = (\pi/2)^{1/2} (k_e^2/k^2)(T_e/m_e)^{-1/2} [(1 - x)\,\omega/k -$$

$$- 4(\pi/2)^{1/2} \, x \, \bar{v} \, v_{Te}^3 / (A_1 \, v_B \, v_{Tf}^2) +$$

$$+ (m_i T_e^3/m_e T_i^3)^{1/2} \, (\omega/k) \exp(-(\omega/k)^2/(2T_i/m_i))] \qquad (9)$$

here $a = (v_{Tf}^2/\bar{v}^2)(1 - 3(\overline{v^2} - \bar{v}^2)/\bar{v}^2 - 4(\overline{v^3} - 3\overline{v^2}\,\bar{v} + 2\bar{v}^3)/\bar{v}^3)$.

From Eq.(8) we obtain the real part of the wave number

$$k_r = (\omega/\alpha c_s)(1 - \omega^2/\omega_{pi}^2)^{-1/2} \cong \omega/(\alpha c_s) \qquad (10)$$

where $\alpha \equiv (1 - x - ax/\tau)^{-1/2}$.

The threshold condition for instability, $\epsilon_i = 0$, gives the product $x\bar{v}$ of the critical density and drift velocity

$$x\bar{v}/c_s = (\alpha\tau C_1/4(\pi/2)^{1/2})(v_B/v_{Te})(m_i/m_e)^{1/2}\Theta^{3/2}\exp(-\alpha^2\Theta/2) \qquad (11)$$

The term $(1-x)\omega/k$ in Eq.(9) is small and has been neglected.

3. DISCUSSION.

Eq.(11) gives the critical value for the product $x\bar{v}$, which is a measure of the thermoionic current density from the cathode. The instability develops when the thermoionic electron current interacts with the plasma some Debye lengths from the cathode filament.

Consider the following Argon plasma $\Theta = 10$; $\tau = 0.2$; $\phi_w = 4.5$ eV; $E_f = 8.9$ eV (for a Tungsten filament) then $v_B/v_{th} = 3.6$; $C_o = 0.329$; $C_1 = 0.264$; $a = 1.43$ and we obtain $x\bar{v}/c_s = 3$. A simple model for plasma production in the DP machine has been given in Ref.[4]: The total electron current I_d of the discharge is equal to the thermoionic current from the N filaments: $I_d = e \times n_o \bar{v} N A_o$; A_o is the surface where the beam impinges in the plasma. The loss ion current I_i to the DP walls (area = A) is given by the Bohm diffusion: $I_i = 0.8\, e\, n_o\, c_s\, A$. The ions are produced by electron collisions: $I_i = N_o\, \sigma\, l\, I_d$ (where N_o = neutral density, σ = ionization cross section, l= mean free path for ionization). From these relations we obtain

$$(x\bar{v}/c_s)_{exp} = (0.8/N_o\, \sigma\, l)(A/N\, A_o) \qquad (12)$$

For typical DP parameters we obtain $(x\bar{v}/c_s)_{exp} = 8$, which is close to our value.

REFERENCES.

1. B.D. Fried, R.B.White and T.K.Samec, Phys. Fluids 14 , 2388 (1971)

2. C.Cohen - Tannoudji, B. Diu and F.Laloë. " Quantum Mechanics" John Willey and sons 1977, p. 69.

3. S. Ichimaru. " Basic Principles of Plasma Physics. A Statictical Approach ". W.A. Benjamin 1973, p.71.

4. R.J.Taylor "Steepening of Ion Acoustic Waves and Formation of collisionless Electrostatic Shock ". Ph. D. Tesis, UCLA, 1970, pp.16 - 19.

Modulational instability of relativistic ion acoustic waves in a plasma with trapped electrons

YASUNORI NEJOH

Department of Physics, Hachinohe Institute of Technology, 88-1, Obiraki, Myo, Hachinohe, 031, Japan

I. Introduction

Interplanetary space and the Earth's magnetosphere encompass a rich variety of plasma physical processes and nonlinear wave phenomena. In a high speed solar wind and the magnetosphere, the phenomena of trapped electrons are frequently observed [1]. When we consider such particles, the effect of trapped electrons has to be included in addition to the relativistic and ion temperature effects. Although the existence of the nonlinear modulation of electrostatic ion acoustic waves is suggested by space observations [2], relativistic ion acoustic waves with trapped electrons in space have not been so well investigated. The effect of ion temperature and relativistic effect of ion acoustic waves have been considered as energetic phenomena in space plasma [3]. Although the nonlinear modulation phenomenon due to trapped electrons has been considered by Dewer *et al.* [4], they have not shown the solution of the modified nonlinear Schrödinger equation. Moreover, nonlinear modulation of relativistic ion acoustic waves associated with trapped electrons have not yet been investigated. The purpose of this investigation is to show the modulational instability due to trapped electrons in a relativistic plasma.

II. Relativistic solitary waves

We consider the small but finite amplitude ion acoustic wave propagating in an unmagnetized plasma. The plasma is quasineutral. It is assumed that the relativistic plasma is composed of a mixed fluid with nonisothermal resonant electrons and hot and adiabatic ions. We assume that there exist high speed streaming ions in equilibrium state and the ions have a relativistic effect. The dynamics of the relativistic ion fluid in non-dimensional form can be written as

$$\frac{\partial n}{\partial t} + \frac{\partial}{\partial x} nv = 0 \quad , \tag{1.a}$$

$$\left(\frac{\partial}{\partial t} + v\frac{\partial}{\partial x}\right)\gamma v + \frac{\sigma}{n}\frac{\partial p}{\partial x} + \frac{\partial \phi}{\partial x} = 0 \quad , \tag{1.b}$$

$$\left(\frac{\partial}{\partial t} + v\frac{\partial}{\partial x}\right)p + 3p\frac{\partial}{\partial x}v = 0 \quad , \tag{1.c}$$

where the Lorentz factor is $\gamma = [1-(v/c)^2]^{-1/2}$. Poisson's equation is

$$\frac{\partial^2 \phi}{\partial x^2} + n - n_e = 0 \quad , \tag{1.d}$$

with the electron density in the small amplitude limit,

$$n_e = \exp(\phi) - \frac{4}{3} b \phi^{3/2} \, . \tag{1.e}$$

The effect of trapped electrons is expressed in terms of $b = \pi^{-1/2}(1-\beta)$. b introduces the deviation from the isothermality due to the contribution of nonlinear resonant electrons (both free and trapped) to the electron density. β is defined by $\beta = T_t / T_t$. T_t and T_t are the free and trapped electron temperature. We assume $\beta > 0$ and $T_t < T_t$. We expand

$$\begin{bmatrix} n \\ v \\ p \\ \phi \end{bmatrix} = \begin{bmatrix} 1 \\ v_0 \\ 1 \\ 0 \end{bmatrix} + \varepsilon \begin{bmatrix} n_1 \\ v_1 \\ p_1 \\ \phi_1 \end{bmatrix} + \varepsilon^{3/2} \begin{bmatrix} n_2 \\ v_2 \\ p_2 \\ \phi_2 \end{bmatrix} + \varepsilon^2 \begin{bmatrix} n_3 \\ v_3 \\ p_3 \\ \phi_3 \end{bmatrix} + \cdots\cdots \, . \tag{2}$$

We introduce a scaling $\xi = \varepsilon^{1/4}(x - \lambda t)$, $\tau = \varepsilon^{3/4} t$, (3)
where ε and λ refer to the smallness parameter and the velocity of the moving frame, respectively. Inserting eqs.(2) and (3) into eqs.(1.a)–(1.e)′, we easily obtain a MKdV equation

$$\frac{\partial \phi_1}{\partial \tau} + \frac{b}{[\gamma_1(1+3\sigma)]^{1/2}} \phi_1^{1/2} \frac{\partial \phi_1}{\partial \xi} + \frac{1}{2[\gamma_1(1+3\sigma)]^{1/2}} \frac{\partial^3 \phi_1}{\partial \xi^3} = 0, \tag{4}$$

with $\lambda(\sigma, \gamma_1) = v_0 + [(1+3\sigma)/\gamma_1]^{1/2}$, and $\gamma_1 = 1 + 3/2(v_0/c)^2$.

III. Relativistic ion oscillation modes and modulational instability

III. A *Envelope solitary wave type of oscillatory solution*

In order to seek the oscillatory wave solution in the small wavenumber region, we apply the following expansion. ϕ_1 is to be expanded as

$$\phi_1 = \sum_{n=0}^{\infty} \mu^n \sum_{l=-\infty}^{\infty} \phi_l^{(n)}(\eta, \zeta) \exp[il(k\xi - \omega\tau)] \, , \tag{5.a}$$

where the condition $\phi_l^{(n)} = \phi_{-l}^{(n)*}$ be satisfied. We select a scaling

$$\eta = \mu^{1/4}(\xi - \chi\tau), \quad \zeta = \mu^{1/2}\tau, \tag{5.b}$$

and apply eqs.(5.a) and (5.b) to a MKdV equation (4), where μ is the smallness parameter. Substituting (5.a) and (5.b) into eq. (4), we can obtain the corresponding sets of equations. To the third order in μ the $l=1$ term implies a modified nonlinear Schrödinger equation

$$i \frac{\partial \phi_1^{(1)}}{\partial \zeta} - \frac{3k}{2[\gamma_1(1+3\sigma)]^{1/2}} \frac{\partial^2 \phi_1^{(1)}}{\partial \eta^2} - \frac{bk}{[\gamma_1(1+3\sigma)]^{1/2}} |\phi_1^{(1)}|^{1/2} \phi_1^{(1)} = 0 \, , \tag{6}$$

by using the first and second order equations in μ. Although Dewer *et al.* derived a similar type of (6) with the different coefficients, they didn't find the solution. In order to obtain the solution of eq.(6), we simplify the problem. We rewrite eq.(6) using the transformations

$$\phi_1^{(1)} = \varphi/B^2 , \quad \eta = A^{1/2}\eta' , \quad \zeta = \zeta'/C , \tag{7}$$

where $A = 3k/2$, $B = bk$, $C = [\gamma_1(1+3\sigma)]^{-1/2}$.

Substitution of eq.(7) to eq.(6) yields

$$i\frac{\partial \varphi}{\partial \zeta'} - \frac{\partial^2 \varphi}{\partial \eta'^2} - |\varphi|^{1/2}\varphi = 0 . \tag{8}$$

In order to obtain the solution of (8), we replace φ by $\varphi = \Psi(\nu)\exp[i(K\eta' - \Omega\zeta')]$, where $\Psi(\nu)$ is a slowly varying real amplitude and $\nu = \eta' - s\zeta'$. Substituting φ into eq.(8), we obtain

$$\frac{\partial^2\Psi}{\partial\nu^2} - (K^2 + \Omega)\Psi + \Psi^{3/2} = 0 , \tag{9}$$

and $$(s+2K)\partial\Psi/\partial\nu = 0 , \tag{10}$$

for the real and the imaginary part, respectively. We have

$$\left(\frac{\partial\Psi}{\partial\nu}\right)^2 - (K^2 + \Omega)\Psi^2 + \frac{4}{5}\Psi^{5/2} = 0 . \tag{11}$$

When we set $\Phi = \Psi^{1/2}$, eq.(11) reduces to

$$\left(\frac{\partial\Phi}{\partial\nu}\right)^2 = -\frac{1}{5}\Phi^2(\Phi - \Phi_0) , \tag{12}$$

where $\Phi_0 = 5/4(\Omega + K^2)$. We note that Φ_0 has to be positive for the stable solution. Integrating eq.(12), we then get

$$\Psi(\nu) = \Phi_0^2 \operatorname{sech}^4\left[\frac{1}{2}\left(\frac{\Phi_0}{5}\right)^{1/2}(\nu - \nu_0)\right] . \tag{13}$$

where ν_0 is the integration constant. Using φ and eq.(13), and returning to the original expressions, we obtain an envelope solitary wave

$$\phi_1^{(1)}(\Psi_0, \nu) = \frac{\Psi_0}{(bk)^2}\operatorname{sech}^4\left\{\left(\frac{\Psi_0^{1/2}}{30k}\right)^{1/2}\left[\eta - s\left[\frac{3k}{2\gamma_1(1+3\sigma)}\right]^{1/2}\zeta - \nu_0\right]\right\} \times \exp\left\{i\left(\frac{2}{3k}\right)^{1/2}\left[Kx - \left[\frac{3k}{2\gamma_1(1+3\sigma)}\right]^{1/2}\Omega\zeta\right]\right\} . \tag{14}$$

Next, let us consider the velocity of this solution. Using Φ_0, eq.(12) for the imaginary part requires $s = -2[-\Omega + (4/5)\Psi_0^{1/2}]^{1/2}$. In the low frequency limit, the linear dispersion relation is obtained as

$$\omega = k\{\lambda(\sigma, \gamma_1) - \frac{k^2}{2[\gamma_1(1+3\sigma)]^{1/2}}\} . \tag{15}$$

III. B The stability of the oscillatory wave solution

In order to consider the stability of the envelope solitary wave, we define the coefficients and the potential of the modified nonlinear Schrödinger equation (8) as

$p \equiv -3k/(2[\gamma_1(1+3\sigma)]^{1/2})$, $q \equiv -(bk/[\gamma_1(1+3\sigma)]^{1/2})|\phi_1^{(1)}|^{1/2}$, and $\phi \equiv \phi_1^{(1)}$. We consider the sum of three waves, *i.e.* a carrier wave $\phi_0(\zeta) = \phi_0\exp(-i\Omega_0\zeta)$ and two small sidebands at $k \pm K$ and $\omega \pm \Omega$. Then ϕ is represented as

$$\phi=\phi_0(\zeta)\{1+\phi_+\exp[i(K\eta-\Omega\zeta)]+\phi_-^*\exp[-i(K\eta-\Omega^*\zeta)]\}, \tag{16}$$

Substituting eq.(16) into eq.(8), we find

$$\begin{pmatrix} \Omega-K\frac{\partial\omega}{\partial k}-pK^2-\frac{1}{2}|\phi_0|\frac{\partial q}{\partial|\phi_0|} & -\frac{1}{2}|\phi_0|\frac{\partial q}{\partial|\phi_0|} \\ \frac{1}{2}|\phi_0|\frac{\partial q}{\partial|\phi_0|} & \Omega-K\frac{\partial\omega}{\partial k}+pK^2+\frac{1}{2}|\phi_0|\frac{\partial q}{\partial|\phi_0|} \end{pmatrix}\begin{pmatrix}\phi_+\\ \phi_-\end{pmatrix}=0.$$

We obtain the nonlinear dispersion relation

$$\left(\Omega-K\left(\frac{\partial\omega}{\partial k}\right)\right)^2=p\left(-|\phi_0|\frac{\partial q}{\partial|\phi_0|}+pK^2\right)K^2 . \tag{17}$$

When the nonlinearity is stronger than the dispersion, that is $|\phi_0|\partial q/\partial|\phi_0| > pK^2$, $p|\phi_0|\partial q/\partial|\phi_0|$ is positive. In this case, since the right-hand side of eq.(17) is negative, then sidebands turn out to be unstable. When K and $Re(\Omega)$ satisfy the conditions $K_M=||\phi_0|(\partial q/\partial|\phi_0|)\times(1/2p)|^{1/2}$ and $\Omega_M=K_M(\partial\omega/\partial k)$, the maximum growth rate is obtained as $\Gamma_M=(1/2)|\phi_0|\partial q/(\partial|\phi_0|)$, where K_M and Ω_M are the maximum wave number and maximum frequency, respectively. The relativistic ion acoustic envelope solitary wave is therefore modulationally unstable against the nonlinear self-modulation.

IV. Concluding discussion

We have found modulational instability due to trapped electrons of relativistic ion acoustic waves. The following facts are found by the present investigation. (i)We have shown for the first time that there is a relation between a MKdV solitary wave and a modulationally unstable envelope solitary wave of a modified nonlinear Schrödinger equation in the long wavelength region. (ii)The amplitude of the solitary wave increases as a number of trapped electrons decrease. The velocity of the envelope solitary wave is proportional to the amplitude and is in inversely proportion to the relativistic and the ion temperature effects. Hence, the velocity of the solitary wave decreases as the ion temperature and the relativistic effects increase. Since these results are in quantitative agreement with several features seen in the observations [5], it appears reasonable to assume that the modulational instability of relativistic ion acoustic solitary waves can be described by the nonlinear self-interaction in the plasma. Therefore, these results are applicable to the study of nonlinear modulation phenomena of energetic ion acoustic waves associated with trapped electrons propagating in space.

References

[1] L.R.Lyons & D.J.Williams, *Quantitative Aspects of Magnetospheric Physics*, D.Reidel, Chapt.3, 1984.
[2] M.L.Goldstein, K.Papadopoulos & R.A.Smith *Wave Instabilities in Space Plasmas*, D.Reidel, pp.245-261, 1979.
[3] Y.Nejoh, *J. Plasma Phys.* 37, p.487, 1987.
[4] R.Dewer, W.L.Kluer & W.Manheimer, *Phys. Rev. Lett.* 28, p.215, 1972.
[5] Y.Nejoh, *IEEE Trans. Plasma Sci.* PS-20, 1992.

Cross-field ion acoustic instability and turbulence in a weakly magnetized plasma

P.J. Barrett and G.H. Popov

Plasma Physics Research Institute, University of Natal, Durban
South Africa

ABSTRACT

In a discharge plasma with a weak axial magnetic field the plasma conditions can be appropriate for the generation of the cross-field ion acoustic instability by azimuthally drifting electrons. This is observed either as a single mode near the lower hybrid frequency or as broadband turbulence up to the ion plasma frequency.

INTRODUCTION

In this paper we are concerned with the cross-field ion acoustic instability which occurs when (i) the relative drift between ions and electrons exceeds the ion acoustic speed c_s , and (ii) the electrons are magnetized whereas the ions are not ($\rho_e \lesssim \lambda \ll \rho_i$ and $\omega_{ce} \gg \omega \gg \omega_{ci}$) /1,2/. In the present experiment the electron drift occurs as a combination of diamagnetic and ExB (and sometimes ∇T_e xB) drift in the azimuthal direction. When the magnetic field and electron temperature lie above certain onset values, the instability appears either as a single mode or as broadband turbulence, or in both forms simultaneously. It was observed during an attempt to set up the modified two-stream instability, which likewise occurs at about the lower hybrid frequency but requires the stringent condition $k_\parallel /k \sim (m_e /m_i)^{1/2}$ /1/. The present ion acoustic instability appears to be the same as that reported recently by Stenzel /3/ who used similar plasma conditions.

EXPERIMENTAL LAY-OUT

The experiment is performed in a cylindrical discharge plasma device of length 65 cm and diameter 40 cm, shown in Fig 1. Two concentric arrays of hot filaments are located at one end of the chamber and biased at -60V to form the cathode. A nearby grounded grid A_1 and similar grid A_2 at the far end share duty as anodes and make the intervening region almost free of axial electric field while allowing the existence of a weak radial field. Large Helmholtz coils provide an axial magnetic field that is uniform to about 5 per cent. Plasma and wave properties are measured with the usual electrostatic probes (including an emissive probe EP) and energy analyzer EA. The latter receives ions either axially or azimuthally but is not strongly directional. Particle drifts are obtained from differential flux measurements with one-sided plane probes. The wave number of a given spectral component of the turbulence can be measured by correlating the signals from say P_1 and P_2 in a spectrum analyzer as P_1 is rotated.

Typical plasma conditions are as follows: $n \lesssim 5 \times 10^9$ cm^{-3} , $T_e \sim 2.5$ eV (but can range up to 8 eV), $T_i \sim 0.4$ eV, $B \lesssim 30$ G, p (argon) $\sim 1 \times 10^{-4}$ torr, with the electron gyroradius

several mm and f_{pe} /f_{ce} ranging from 3 to 30.

EXPERIMENTAL RESULTS

Steady state profiles: With two cathode filament arrays available, C_1 and C_2, the radial profiles of n, T_e , V_p (plasma potential) and electron drifts can be varied greatly. In Fig 2 two sets of profiles are presented: in (a) the inner cathode ring C_1 is dominant, while in (b) both C_1 and C_2 are at high power. In order to obtain a sufficiently large value of T_e , the argon pressure is set at 1 x 10^{-4} torr, which makes for a marked tail of fast primary electrons. (At 2 x 10^{-4} torr the instability is usually absent). The effective temperature T_f of the tail is especially large at the radial locations r_1 and r_2 of C_1 and C_2 respectively; see Fig 2(b). It appears that the tail is responsible for the observed high frequency electron turbulence (not shown) around r_1 and r_2, and that this in turn creates the peaks in the bulk electron temperature T_s. Figure 2(b) also shows a particular profile of V_p for which ∇n and E_r (= -∇V_p) have the same sign; opposite signs can, however, be arranged. Generally, the combined effect of the gradients is to produce an azimuthal electron drift v_θ of order 5 x 10^6 cm s^{-1}, which greatly exceeds the ion acoustic speed c_s (~2.5 x 10^5 cm s^{-1}). The n_1 profile in Fig 2(a) represents the relative amplitude of the single mode, labelled S, and of the low level turbulence N in the region of C_2.

Single mode properties: At the lower values of the magnetic field (< 20 G) density and potential oscillations are observed near the lower hybrid frequency, as in the similar experimental conditions of /3/. In Fig 3 we show the dependence of the frequency on the magnetic field for a mode which has maximum amplitude at r = 6.5 cm, together with the corresponding azimuthal mode number m. (There is some uncertainty about the assignment m=5). There are discontinuities in k_θ (= m/r) as the mode maintains the parameter $k_\theta \rho_e$ fairly constant, within the range 0.2 to 0.3 , i.e. somewhat lower than the theoretical value for maximum growth rate, 0.7 /4/. The frequency lies close to ω_{LH} at the higher values. Also, throughout the frequency range the azimuthal phase velocity is appreciably greater than c_s. Phase measurements show that the single mode propagates in the direction of the azimuthal electron drift and is a standing wave axially, with $\lambda_z \gtrsim$ 120 cm.

In Fig 4 the amplitude of a single mode is observed as a function of T_e and B, where T_e is controlled by varying the argon pressure (between 0.2 and 0.08 mtorr). In both cases the onset is sharp. As found in /3/, T_e needs to be sufficiently large to avoid ion Landau damping. Furthermore, it is clear from kinetic theory (see Fig 8 in /4/ for example) that the growth rate falls rapidly as $k_\theta \rho_e$ rises above the value for maximum growth rate.

Turbulence properties: The strongest noise occurs usually near the radial position of the outer filament ring but becomes more widespread radially as the single mode gives way to turbulence at the highest values of B (> 25 G). Typical outer region noise spectra are shown in Fig 5. As B is increased there is a rise in amplitude and frequency width, and in the frequency f_m of the sharp peak at the low frequency end. From the inset, f_m is close to the lower hybrid frequency. Also, as found by Stenzel et al /5/ in an experi-

ment on ExB driven turbulence, the spectrum extends from f_{LH} to about the ion plasma frequency ($\sim$ 2 MHz in this case). An initial noise correlation measurement at a very low frequency, 10 kHz, indicated an azimuthal phase velocity of $0.4c_s$.

DISCUSSION

The above single mode propagates mainly in the azimuthal direction, with $k_{\|}$ /k ranging from 0.2 to 0.02, i.e. $\gg (m_e/m_i)^{1/2}$. This suggests that it is an ion acoustic rather than a modified two-stream instability. The unduly high value of its phase velocity (several times c_s) may be due to the presence of an ion drift, but it is not clear what could create the latter. The question of electron heating by the turbulence is clouded by the presence of axial electron drift and its effects. Also, the energy analyzer shows no difference between axial and azimuthal ion energies; there appears not to be any ion heating, in agreement with /3/.

ACKNOWLEDGEMENTS

The authors are indebted to Craig Moran for experimental assistance and to the SA Foundation for Research Development for financial support.

REFERENCES

/1/ C N Lashmore-Davies and T J Martin, Nucl Fusion 13, 193 (1973)
/2/ A J Hayzen and P J Barrett, Phys Fluids 20, 1713 (1977)
/3/ R L Stenzel, Phys Rev Lett 65, 3001 (1990) & Phys Fluids B3, 2568 (1991)
/4/ R Jones and P J Barrett, Phys Fluids 23, 956 (1980)
/5/ R L Stenzel et al, Tech Rep 24357-6001-RU-00, TRW, Redondo Beach, CA (1974)

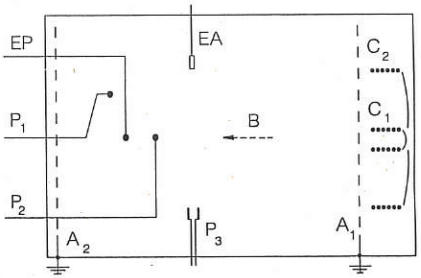

Fig 1. Experimental lay-out. C_1, C_2 cathode filaments; A_1, A_2 anodes; P electrostatic probes, EP emissive probe, EA energy analyzer; B axial magnetic field.

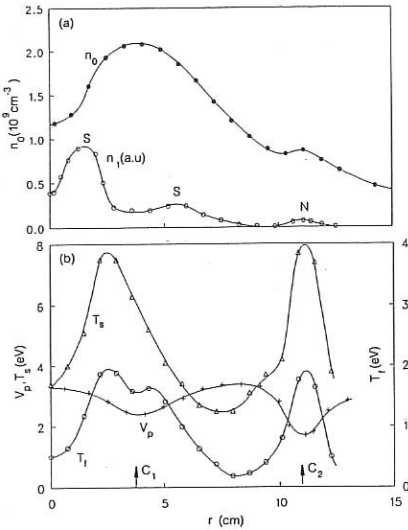

Fig 2. Radial profiles for two cathode settings: (a) plasma density n_0 and oscillation amplitude n_1; typically $n_1/n_0 \lesssim 10\%$ for single mode S and $\lesssim 50\%$ for noise N; (b) plasma potential V_p; electron temperature T_s (bulk) and T_f (tail).

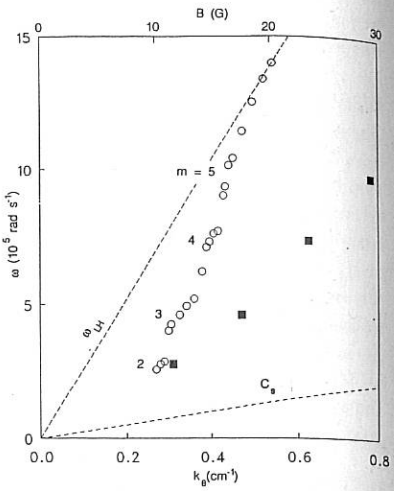

Fig 3. Frequency versus magnetic field for single mode with azimuthal mode number m, peaked at r = 6.5 cm (circles); upper line represents lower hybrid frequency $(\omega_{ce}\omega_{ci})^{1/2}$. These data give the four ω, k_θ points (squares), showing $\omega/k_\theta > c_s$. $n_0 \sim 3 \times 10^9$ cm^{-3}, $T_e \sim 3$ eV, $p = 1 \times 10^{-4}$ torr, $v_\theta \sim 5 \times 10^6$ cm s^{-1}.

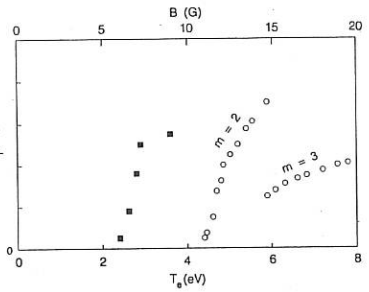

Fig 4. Amplitude of single mode as a function of electron temperature (squares) and of magnetic field (circles).

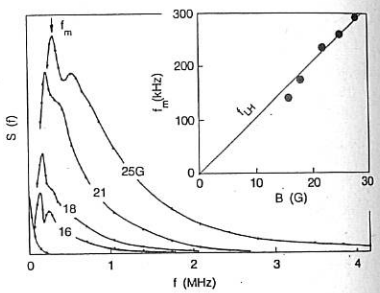

Fig 5. Noise spectrum at different values of magnetic field. The frequency f_m of the low frequency peak is plotted in the inset where the line represents $(f_{ce}f_{ci})^{1/2}$.

NUMERICAL STUDY OF POTENTIAL FORMATION AND NEGATIVE RESISTANCE IN A CURRENT - CARRYING ION SHEATH

N. Ohno*, A. Komori, S. Takamura* and Y. Kawai
Interdisciplinary Graduate School of Engineering Sciences, Kyushu University,
Kasuga, Fukuoka 816, Japan

Abstract Potential formation of a current-carrying ion sheath on a negatively charged grid is numerically studied using the one-dimensional particle code. The imbalance of ion which are injected into the sheath region from two plasmas divided by the grid, that is , the difference in plasma density produces a potential difference between the two plasmas, which reflects some ions injected from the high-density plasma. The thickness of the sheath facing low-density plasma is obtained to be thinner than at the sheath facing the high density plasma. A negative resistance is also numerically demonstrated by applying a perturbed voltage to the grid, and found to be associated with the ion inertia in the ion sheath. These numerical results are in good agreement with those obtained experimentally.

1. Introduction

In our previous paper, the coherent instability has been observed in the current-carrying ion sheath on the negatively charged grid/1/. When the instability is excited, there are the density and potential differences between two plasmas divided by the grid , and the sheath thickness on the low-density plasma side is thinner than that on the high-density plasma side. On the basis of these experimental results, we have proposed the physical model of the instability; the instability is excited when a negative rf resistance associated with the ion inertia in the ion sheath is coupled to an ion resonance caused by a positive feedback due to the reflection of ions in the sheath region. However, the experimental observations mentioned above are not clearly understood and are still open to studies of their physics.

The present paper gives a numerical study of potential formation and negative resistance in a current-carrying ion sheath by using the one-dimensional particle code.

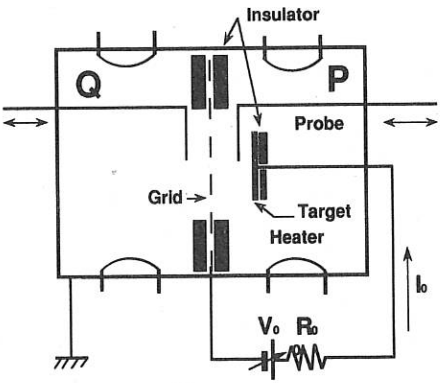

FIG. 1. Schematic of experimental apparatus. R_0=50Ω .

2. Experimental Results

The experiments are performed in a large, unmagnetized plasma device 70 cm in diameter and 120 cm in length, equipped with multidipole magnets for surface plasma confinements, as shown in Fig. 1. The argon plasma produced by the dc discharge between the filaments and the chamber wall is divided by a fine-meshed grid. Typical plasma parameters in the region designated P are $ne = 10^7$-10^8 cm^{-3}, Te~1 eV and Ti~0.1eV. The density of the plasma Q is chosen to be less than that of the plasma P by about one order of magnitude. The plasma densities are controlled by the heater currents. A dc voltage is applied between the grid and a movable 12 cm diam target located at a distance of 4-6cm from the grid. Plane Langmuir probes 6 mm in diameter are used to measure the plasma parameters and their fluctuations. The ion temperature and the plasma potential are measured with Faraday cups and emissive probes, respectively. The time averaged value I_0 and fluctuating component of the current through the plasma are obtained from the voltage drop across the resistor R_0. The gas pressure is kept at about 2×10^{-4} torr.

Figure 2(a) shows the dependence of the time-averaged current I_0 on the applied dc voltage V_0. The distance between the grid and target is kept at 5 cm. This I_0-V_0 curve is very similar to the current-voltage characteristic of the Langmuir probe. As shown in Fig. 2(b), a coherent instability appears when I_0 begins to saturate. A typical example of the frequency spectrum is illustrated in the inset. The frequency f_0 of the instability is found to decrease with an increase in V_0, and this frequency change is explained by the dependence of f_0 on the sheath thickness.

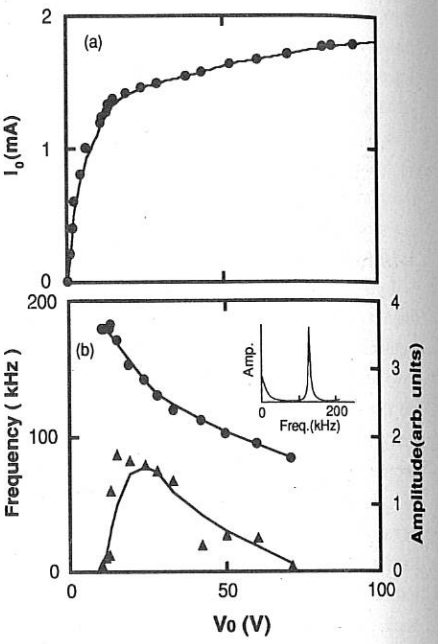

FIG. 2. Dependences of time-averaged value I_0 and fluctuating component I of the plasma current on the applied dc voltage V_0: (a) I_0 - V_0 characteristic; (b) V_0 dependence of the frequency and amplitude of I. A typical example of the frequency spectrum of I is illustrated in the inset at V_0 = -60V.

Figures 3(a) and (b) show the axial profiles of space potential ϕ and ion saturation current I_{is}, respectively. The ion saturation current I_{is} is known to be proportional to n_e if T_e is constant. It is found that ϕ of the plasma Q is higher than that of the plasma P and the sheath thickness in the plasma Q is thinner than that in the plasma P. The

ion saturation current I_{is} is also shown to have maximum at the sheath edge in the plasma Q.

3. Numerical Procedures and Results

In order to study the formation mechanism of the current-carrying ion sheath, we have used the one-dimensional particle-code (P. I. C). The ion fluxes are injected towards the grid from d=10 and -10, as shown in Fig. 3(c), where d is the coordinate normalized by the Debye length. Based on the experimental results, we make the following assumptions : (1) At d=10 and -10, electrons obey the Boltzmann relation and ions have the drifting Maxwellian distribution whose averaged ion velocity is about the ion sound velocity and satisfies the Bohm sheath criterion ; (2) The electron density at d=-10 is below one tenth of that at d=10; (3) The potential ϕ at d=10 and d=0 are kept at 0V and -30V, respectively and the ϕ at d=-10 is determined to keep charge neutrality; (4) The transmission rate of the grid is 0.71. The potential profile is obtained selfconsistantly from solving Poisson's equation. Figure 3(c) shows the typical profiles of potential ϕ, ion density n_i and electron density n_e. The potential ϕ at d=-10 is found to be larger than that at d=10, as expected. This potential difference results from the ambipolar potential due to the imbalance between the ion fluxes in opposite directions. Some ions injected from d=10 and passing through the grid are reflected by this potential difference back to d=10. The ion density has a maximum at the position where most ions are reflected. This makes the sheath thickness at the low-density plasma side thinner than that on the other side, although the plasma density in the region of $d \leq 0$ is smaller than that in the region of $d \geq 0$.

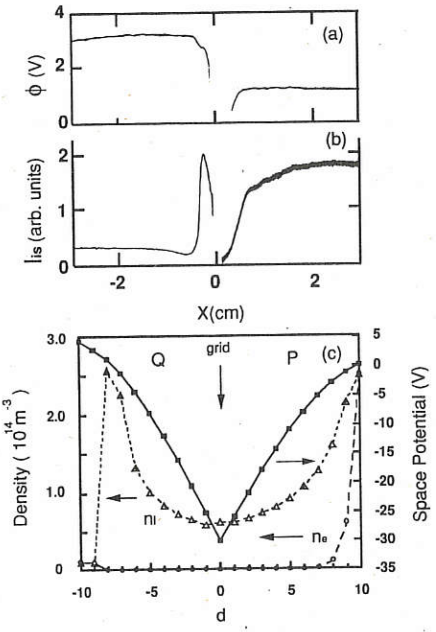

FIG. 3. Axial profiles of (a) potential and (b) ion saturation current, obtained experimentally. (c)Axial profiles of ϕ, n_i and n_e, obtained numerically.

In order to confirm the existence of the negative resistance in such a current-carrying ion sheath, the relation between the current at grid and the sheath potential is obtained by applying a perturbed potential $\phi(t)=V_0+V_1\sin\omega t$ to the grid. The phase difference between the fluctuating components of current and potential, $I(t)$ and $\phi(t)$, is obtained by using Fast Fourier Transformation. The frequency ω is normalized by the bounce frequency ω_b, which is defined to be the inverse

of time necessary for the ions to come back to d=0. Figures 4(a) and (b) show the time series of I_1 and ϕ_1 at ω=0.7. When the grid bias is minimum (~29.9V), the ion flux is found to be maximum, i.e., I_1 and ϕ_1 are out of phase. The ω dependences of the phase difference between I_1 and ϕ_1 and the differential conductance G ($=\partial I/\partial V$) are shown in Fig. 4(c). Here, G is calculated from the amplitudes of I_1 and ϕ_1. Both G and phase difference depend strongly on the frequency ω and G is negative at ω's below ω~1.0. These results indicate that such a current-carrying ion sheath can be used as element of oscillator. When this negative resistor cancels out all loss including the resistor of external electric circuit, the system oscillates spontaneously.

4. Summary

A potential profile and negative resistance in a current-carrying ion sheath, which are strongly associated with ion-sheath instabilities, are numerically analysed by using the P. I. C. code. It is shown that the density difference between two plasmas divided by a negatively charged grid produces the space potential difference which reflect ions injected from the high-density plasma. The current-carrying ion sheath is also found to work as a negative resistor for a certain frequency range.

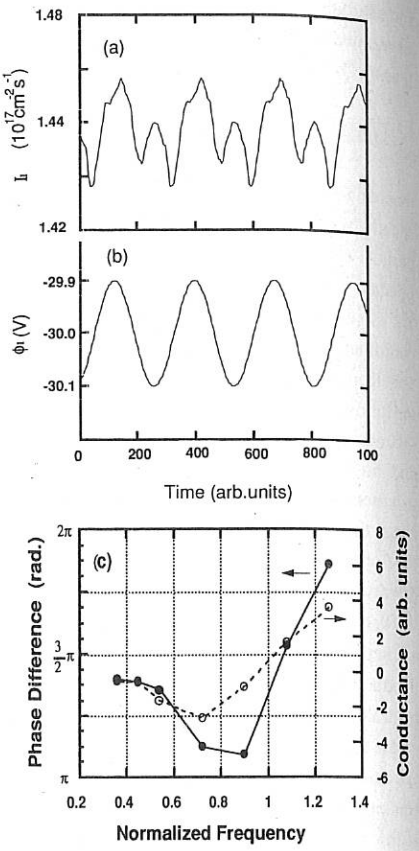

FIG. 4 Dependences of (a) I_1 and (b) ϕ_1 on time, respectively. (c) Conductance and phase difference between I_1 and ϕ_1 as a function ω.

*Permanent address: Department of Electrical Engineering, Faculty of Engineering, Nagoya University, Furo-cho, Chikusa-ku, Nagoya 464-01, Japan.

Reference

/1/ N. Ohno, A. Komori, M. Tanaka and Y. Kawai Phys. Fluids **B3** (1991) 228.

Asymmetric $\vec{E} \times \vec{B}$ Equilibria and Diocotron Adiabatic Invariants

R. Chu and J.S. Wurtele, MIT
J. Notte and J. Fajans, UCB

Recent results on theoretical and experimental studies of nonlinear collective modes and asymmetric equilibria in pure electron plasmas will be presented. The standard cylindrical shape of a pure electron plasma can be distorted by applying voltages on azimuthal sections of the confining cylindrical walls. Because of the applied perturbing electric fields, the asymmetric equilibria have guiding centers which $\vec{E} \times \vec{B}$ drift along non-circular closed paths. The resulting plasma is asymmetric, but stationary in the lab frame. Some of the equilibria are dramatically convoluted. The plasma is imaged in a single shot. The equipotential contours are found using both a vortex-in-cell simulation and an analytical model. As expected, these contours are in excellent agreement with the observed plasma shapes. By displacing the plasma off axis, a diocotron-like mode is excited. The center of charge of the plasma follows a circular path when there is no applied voltage on the azimuthal sections. Measurements indicate that the area enclosed by the center of charge is an adiabatic invariant when the external applied electric field is slowly varying. A simplified Hamiltonian model is used to study this phenomenon.

The pure electron plasma is confined inside a highly conducting cylinder. The radial confinement is provided by a strong axial magnetic field of 1-2 kG. The axial confinement is achieved by biassing the end caps with negative potentials. More extensive descriptions of this type of setup can be found elsewhere /1/.The confining cylinder has a radius of 1.9 cm and a length of 5.0 cm. A typical electron column confined has density $\geq 5 \times 10^7 \mathrm{cm}^{-3}$, temperature 3eV, and length ~3cm, while the radius can be chosen to suit the purpose of the experiments. The experiments are performed in a repeated inject/manipulate/dump cycle. During the inject phase, electrons from a hot tungsten filament are trapped inside the conducting cylinder. The plasma is then manipulated and, finally, in the analyze phase, one of the negatively biased end caps is grounded, allowing the electrons to rapidly dump out along the magnetic field lines onto a phosphor screen. The resulting image is captured by a CCD camera. There are 3 50° azimuthal sections on the wall, any of which can be biased to different potentials individually, hence changing the boundary conditions of the cylinder. The changes in boundary conditions can be used either to manipulate the equilibrium shapes of the column or to change the shapes of the diocotron-like mode orbits.

Initially a circular electron column located on axis is created in the inject phase. The asymmetric equilibria are then obtained by applying voltages to the azimuthal sectors on the wall, hence changing the boundary conditions of the confining cylinder. The unperturbed electron columns are ~1.0cm in radii. The applied voltages are turned on slowly (~1ms) compared to the l=1 diocotron period (~ 10μs), so that no diocotron oscillations are excited while the equilibrium shape of the column deforms slowly. Examples of the different shapes that can be formed are shown in Figure 1.

For the time scales studied here, which are slow compared to the gyro-frequency and fast compared to the plasma lifetime, the electrons can be described by their guiding center coordinates. Furthermore, the motion along the axial magnetic field is fast compared to any drift motions of the guiding centers. The electric field experienced by a particle can, therefore, be approximated by the bounce-averaged field. Consequently, the dynamics of the system is two-dimensional, being determined by the bounce averaged $\vec{E} \times \vec{B}$ drifts along the electrostatic potential lines. The time scale for these experiments is short enough so that collisional effects and any transport due to misalignment are negligible. In summary, the system is treated analytically as a two-dimensional system in which guiding centers drift along potential lines.

For a uniform density plasma to be in equilibrium in the laboratory frame, the electrostatic potential on its surface must be constant. In such a case, the guiding centers on the surface will drift along the surface, and the shape of the plasma column will, therefore, remain unchanged. Hence, the condition for the plasma column to be in equilibrium is:

$$\phi(r_p(\theta),\theta) = \phi_p(r_p(\theta),\theta) + \phi_a(r_p(\theta),\theta) = \text{constant}, \tag{1}$$

where $r_p(\theta)$ specifies the shape of the uniform density plasma, ϕ_a is the externally applied sector potential, and ϕ_p is the potential induced by the plasma itself, which can be found by integrating the Green function for the cylindrical geometry with zero potential on the wall. In general, the integral can only be evaluated numerically. Analytic insight can be gained by replacing the field induced by an asymmetric plasma column with that of a circular column with the same area as the asymmetric column and an appropriately calculated surface charge density. Thus,

$$r_p(\theta) = r_0 + \delta r(\theta) = r_0 + \sum_{l=1}^{\infty}[\delta r_l^c \cos(l\theta) + \delta r_l^s \sin(l\theta)], \tag{2}$$

where r_0 is the radius of the cylindrical plasma used in the approximation. The surface charge density is $\sigma(\theta) = n\delta r(\theta)$, where n is the density of the plasma. This approximation is valid when $\delta r \ll r_0$. The potential field, $\phi_p(r,\theta)$, can then be easily solved for, both inside and outside of the cylindrical column. Gauss's law relates the discontinuity of the electric field on the surface with the surface charge:

$$\phi_p(r,\theta) = 2\pi en \begin{cases} r_0^2 \ln(\frac{r}{R}) + \sum_{l=1}^{\infty} \frac{1}{l}[(\frac{r}{R})^l - (\frac{R}{r})^l](\frac{r_0}{R})^l r_0[\delta r_l^c \cos(l\theta) + \delta r_l^s \sin(l\theta)] \\ \qquad\qquad \text{for } r > r_0, \\ \frac{r^2}{2} + r_0^2[\ln(\frac{r_0}{R}) - \frac{1}{2}] + \sum_{l=1}^{\infty} \frac{1}{l}[(\frac{r_0}{R})^l - (\frac{R}{r_0})^l](\frac{r}{R})^l r_0[\delta r_l^c \cos(l\theta) + \delta r_l^s \sin(l\theta)] \\ \qquad\qquad \text{for } r < r_0, \end{cases} \tag{3}$$

where R is the radius of the confining wall (assumed to be at zero potential). The externally applied electrostatic potential inside the confining cylinder, $\phi_a(r,\theta)$, which obeys the Laplace equation, can be written as:

$$\phi_a(r,\theta) = \phi_{a0} + \sum_{l=1}^{\infty}[\phi_{al}^c \cos(l\theta) + \phi_{al}^s \sin(l\theta)](\frac{r}{R})^l, \tag{4}$$

where ϕ_{a0} and $\phi_{al}^{c,s}$ can be expressed in terms of the applied perturbation on the boundary, $\phi_a(R,\theta)$. The total field, $\phi = \phi_p + \phi_a$, is now given by the applied perturbations, $\phi_a(R,\theta)$, and by the parameters that specify the shape of the plasma column, $\delta r_l^{c,s}$. Since the potential is constant on the plasma boundary in equilibrium configurations (Eq. 1), these parameters can be calculated in terms of the externally applied perturbations. Substituting ϕ_p in Eq. 3 and ϕ_a in Eq. 4 into Eq. 1 and keeping the lowest order term in δr yields

$$\delta r_l^{c,s} = -\frac{(r_0/R)^l}{2\pi enr_0\{1 - [1 - (r_0/R)^{2l}]/l\}}\phi_{al}^{c,s}. \tag{5}$$

The shape of the asymmetric plasma column can then be plotted out. Figure 2 shows the good agreements between the analytic theory, simulations, and the experimental results shown in Figure 1(a). The simulations are performed with a two-dimensional vortex-in-cell electrostatic code in which the plasma is represented by a finite number of line charges. Typically 4096 line charges are used in the simulation. In one cycle of the simulation, the charges are weighted to a uniform polar grid, the Poisson equation is then solved, and the line charges are moved

according to the $\vec{E} \times \vec{B}$ dynamics. The external applied field is also slowly turned on in the simulations.

The preceding experiments were conducted in a manner so as not to excite bulk motion of the plasma. The well studied $l = 1$ diocotron mode /2/ is excited when a centered electron column is displaced from the center of the *grounded* conducting cylinder. (The image charge on the cylindrical wall creates a radial electric field which causes the electron column to $\vec{E} \times \vec{B}$ drift in the azimuthal direction.) In a second set of experiments, the boundary conditions on the cylinder wall are changed after a strong diocotron oscillation has been excited. Both the shape of the diocotron orbit and the shape of the column are then distorted by the changes in the boundary conditions. Measurements indicate that if the perturbations are applied slowly, the area enclosed by the orbit of the center of charge of the column is invariant, even through the shape of the orbit is substantially distorted.

For these experiments, a typical electron column has radius 0.5cm, length 3cm, density $5 \times 10^7 \text{cm}^{-3}$, and temperature 3eV. During the manipulate phase, the electron column is first displaced from the cylinder center by growing an $l = 1$ diocotron mode orbit to about 1cm off center. The period measured is $6\mu s$. Perturbations are then applied to the boundary conditions by ramping the voltage on one of the azimuthal sectors up to the value V_p over a time T_r. Finally, during the analyze phase, the shape of the orbit is ascertained. The plasma is then dumped through one end so that its location can be determined. This cycle is repeated fifty times, each time dumping the electron column at a slightly different orbital position, thereby obtaining a set of points which defines the diocotron orbit.

Figure 3 shows an undistorted orbit, and two diocotron orbits that have been distorted by perturbations. Figure 4 shows the area, A_Φ, for a wide range of perturbation voltages. A_Φ is an invariant for $V_p > 0$. For $V_p < 0$, some electrons cross the separatrix and are lost to the wall. In that case, the invariant no longer holds.

In order to understand the origin of the A_Φ adiabatic invariant, a Hamiltonian treatment of the guiding center system is necessary. The plasma can be modeled as a distribution of line charges, each with charge per length, q, and mass per length, m. For the case in which magnetic field, $\mathbf{B}$, is constant the Hamiltonian is simply the total electrostatic energy per unit length.

The dynamics described by an N particle Hamiltonian is in general quite complicated. However the analysis is greatly simplified if the shape of the plasma is assumed. In the simplest case we can model the plasma as being circularly shaped throughout its motion. This assumption is appropriate when the plasma radius is small compared to the wall radius and the diocotron orbit radius. Under these assumptions, the motion of the center of charge is governed by

$$H(P_c, \Theta_c) = -enA_p\varphi_a(r_c, \Theta_c) + (enA_p)^2 \ln(1 - \frac{r_c^2}{R^2}), \tag{6}$$

where the coordinates of the center of charge are (r_c, Θ_c), with $P_c = (\frac{BenA_p}{2c})r_c^2$ being conjugate variable to Θ_c. A_p is the area of the plasma, and n is the density of the plasma. Since the system is dynamically one-dimensional, the motion is always periodic in the phase space (P_c, Θ_c). Hence, the set of orbits is a nested set of non-intersecting loops, each with a unique orbital area and a total electrostatic energy associating with it. When the externally applied perturbation is slowly varying, the area enclosed by the phase space orbit is an adiabatic invariant /3/:

$$\oint p dq = \left(\frac{BenA_p}{c}\right) \oint \frac{r_c^2}{2} d\Theta_c$$

$$= \left(\frac{BenA_p}{c}\right)\mathbf{A}_\Phi. \qquad (7)$$

Thus, the area enclosed by the center of charge orbit is an adiabatic invariant in the circular plasma approximation. A more realistic elliptical model has also been developed, where the plasma shape is assumed to be elliptical but the aspect ratio and the orientation are allowed to change.

/1/ J. H. Malmberg, C. F. Driscoll, B. Beck, D. L. Eggleston, J. Fajans, K. Fine, X-P. Huang and A.W. Hyatt, "Experiments with Pure Electron Plasmas," in *Non-neutral Plasma Physics* (C. W. Roberson and C. F. Driscoll, editors), New York: AIP, 28 (1988).

/2/ R. C. Davidson, *Physics of Nonneutral Plasmas* (Addison-Wesley, Reading, Mass., 1990).

/3/ L. D. Landau and E. M. Lifshitz, *Mechanics* (Pergamon Press, New York, 1976), p.156.

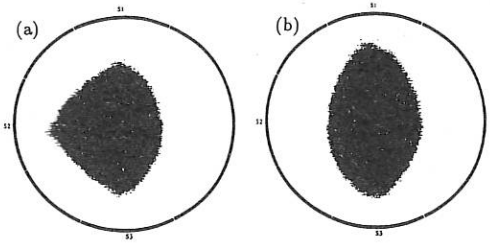

Fig. 1: (a) $V_1 = V_2 = V_3 = -30$V, (b) $V_1 = V_3 = -30$V, and $V_2 = 0$V.

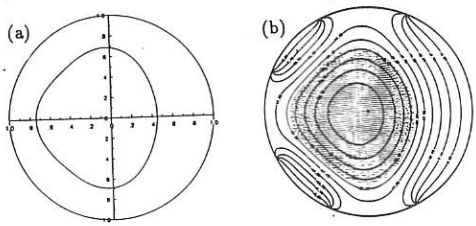

Fig. 2: (a) Analytic theory, (b) simulation.

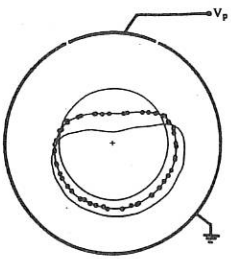

Fig. 3: Orbits for perturbations $V_p = 0, 30, 50$V.

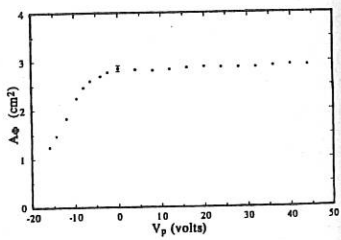

Fig. 4: A_ϕ vs. V_p, for $T_r = 2$ms.

Compression of multiple ion acoustic solitons at the plasma sheath edge

T.Nagasawa and Y.Nishida
Department of Electrical and Electronic Engineering
Utunomiya University, Utunomiya, Tochigi 321, Japan

Behavior of multiple ion acoustic solitons at the plasma sheath edge is experimentally investigated. We present experimental results which show the evidence of new mechanism for the compression phenomenon of multiple ion acoustic solitons. These characteristics are similar to the calculated results which emploied a particle model for the pulse.

1. Introduction

When the multiple ion acoustic solitons propagate obliquely towards the reflector which is biased deeply negative potential, the velocity of each soliton is changed just before the plasma sheath edge with smaller change of the first pulse, but with greater change of the second and/or third pulse. In this result, the multiple solitons are once compressed into one soliton at the sheath edge, and it breaks into the multiple solitons again such as the incident ones after going through certain sheath area. This phenomenon is similar to the recurrence phenomenon[1~3] of the plane soliton. In the present experiment recurrence seems to take place at the edge of the plasma sheath. The velocity ratio of the second pulse of the transmitted solitons, which goes through the plasma sheath edge, to that of the incident soliton becomes smaller than unity. The change of this velocity ratio could clarify the reflection and/or transmission phenomena[4~6].

2. Experimental set up and Results

The experiments are carried out in a double plasma device with multidipole magnets described elsewhere. The typical parameters in an argon plasma at a pressure of $3\sim4\times10^{-4}$ Torr are the plasma density $n_e=5\times10^{8}$ cm^{-3}, the electron temperature $T_e=2$ eV, and the ion temperature $T_i=T_e/(10\sim12)$ eV. The reflector, (350×300 mm, 6 mesh/cm), can be rotated around its axis within an angle ($0<\theta_1<60^{\circ}$), and be biased at the desired potential V_b with respect to the plasma potential (floating potential=$-25V<V_b<-500V$). The ion acoustic solitons are picked up with cylindrical probes (0.1mm diameter by 1mm length). It was biased to collect electron saturation current. The wave is excited by a double plasma action by applying a positive pulse to the driver plasma with a typical pulse width $\Delta t\simeq10\,\mu s$.

The typical wave forms are shown in Fig.1(a), where an incident (I), reflected (R_1, R_2), and transmitted (T) pulses are seen. The incident multiple solitons are compressed to be piled up near z=1.5 cm the sheath edge, and multiple solitons become a single soliton. After passing through this point, it again separates into multiple solitons (T).

Loci of the maximum amplitude of each pulse are figured in Fig.1(b). From this figure, we can obtain the velocity of each pulse. As also seen from

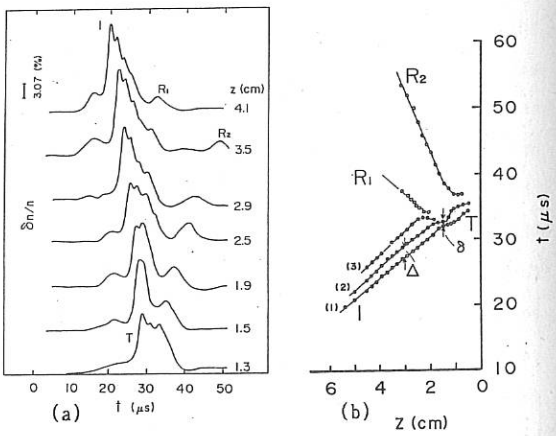

Fig.1(a) Typical wave forms of the excited ion acoustic soliton. (b) Loci of the maximum amplitude of each pulse.

this figure, the second (I_2) and/or third (I_3) pulses of the incident solitons are accelerated more than the first pulse (I_1) when the incident multiple-soliton goes to the sheath edge, and they are compressed there. The reflected soliton (R_1) is produced at this point. As the second pulse goes towards the reflector with larger velocity, the reflected second pulse (R_2) is produced near the reflector. Here, the velocity of each pulse is observed to be $v_I=(2.7\sim3.1)\times10^5$ cm/sec for the initial soliton, and $v_{R1}=(0.94\sim1.0)\times v_I$, and $v_{R2}=(0.35\sim0.41)\times v_I$ for reflected 1st and 2nd pulse, respectively. The point z=0 corresponds to the reflector position.

3. Discussions

An outline of the profile of the space potential in front of the reflector, which is biased deep in negative, is shown in Fig. 2(a), where D is a typical soliton width of the incident first soliton, ϕ is a space potential, dotted line is a static space potential $\phi_0(z)$ which is produced by the reflector and $\phi_1(z)$ is illustration of the fluctuating potential caused by the ion bunch of the first pulse going into the sheath edge. From these results the space potential could be given as follows,

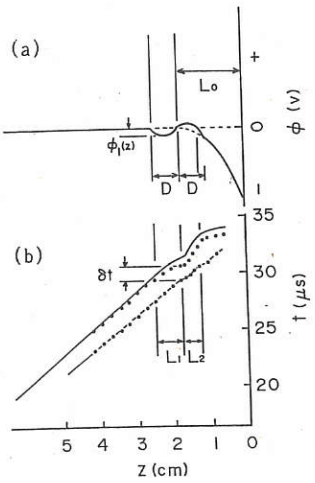

Fig.2(a) Outline of space potential (b)Loci of each pulse

$$\phi(z)=\phi_0(z)+\phi_1(z). \tag{1}$$

Now, we focus our discussions on the locus of the second pulse from the point of view of the energy conservation law. By employing a particle model for the pulse for the second pulse, we can obtain,

$$v_{i2}^2 = v^2 + 2e\phi(z)/m, \quad (2)$$

where, v_{i2}, v and $\phi_1(z)=\delta\phi$ are, respectively, the velocity of the second pulse at $z=\infty$, that in the area L_1 and the space potential. m is an ion mass. From the experimental results on the amplitude of the first pulse, we can obtain $|\delta\phi|=0.26v$ as $\delta n/n=0.13=e\delta\phi/KT_e$, with the electron temperature $KT_e=2ev$. Therefore, we may put $\delta\phi=-0.26\sin(z-1.5)\pi/D$, at L_1. The point z=1.5 corresponds to the sheath edge. From Eq.(2), the ion velocity v in the area L_1 is given as follows,

$$v/v_{i2}=\sqrt{1+0.53\sin(z-1.5)\pi/L_1}. \quad (1.5<z<2.0) \quad (3)$$

Here, we put $v_{i2}=C_s(1+0,4\times0.11)$ at $1.5<z$ with C_s the ion acoustic speed and/or $\phi_0(z)=0$. In the area L_2 we can also put,

$$v/v_{i2}=\sqrt{1-0.53\sin(z-1.1)\pi/L_2}, \quad (1.1<z<1.5) \quad (4)$$

where, $\phi_0(z)=0$, and z=1.1 is the point of $\phi(z)=0$. When we put $\phi_1(z) << |\phi_0(z)| = 50e^{-z}$ in the area $0<z<1.1$,

$$v/v_{i2}=\sqrt{1+22.6e^{-z}}, \quad (0<z<1.1) \quad (5)$$

should be satisfied. In Fig.2(b), the calculated results of Eqs.(3) through (5) for the locus of the second pulse are shown with solid lines, and solid circles show the experimental results for $\theta_i=30^\circ$ and $V_b=-50$ v.

A present work is supported in Part by the Grant-in-Aid from the Ministry of Education, Science and Culture, Japan.

References

1. N.J.Zabusky and M.D.Kruskal, Phys. Rev. Lett. 15, 34 (1965).
2. H.Ikezi, Phys. Fluids 16, 1668 (1973).
3. Y.Nishida and T.Nagasawa, Phys. Rev. Lett. 45, 1626 (1981).
4. T.Nagasawa and Y.Nishida, Phys. Rev. Lett. 56, 2688 (1986).
5. Y.Nishida, K.Yoshida and T.Nagasawa, Phys. Lett. A131, 83 (1988).
6. C.Matsuoka and N.Yajima, J, Phys. Soc. Japan 58, 3939 (1989).
7. T.Nagasawa and Y.Nishida, Phys. Lett. A162, 278 (1992).

THE EFFECTS OF ELECTRON MASS ON ION-ACOUSTIC SOLITONS

W.K.M. Rice, M.A. Hellberg, R.L. Mace, S. Baboolal*

Plasma Physics Research Institute, Department of Physics, University of Natal, Durban, South Africa

**Also at Dept of Computer Science, University of Durban-Westville, Durban, South Africa*

1 Introduction

It is usual in studies of solitons and double layers in fluid plasmas to make the assumption of Boltzmann electrons, i.e. because of their high mobility, the electron mass is neglected[1-5]. In a recent paper[6] it has, however, been suggested that electron inertia effects on ion-acoustic solitons may exceed relativistic effects.

The purpose of this study is to determine finite electron mass effects on the amplitudes and existence domains of ion-acoustic solitons. We consider a plasma consisting of cold hydrogen ions and two isothermal electron fluids at different temperatures. The electron density distributions are determined using the plasma fluid equations, thus introducing the electron mass.

Instead of using the small-amplitude KdV equation we carry out arbitrary-amplitude calculations from the fluid equations[1-5]. The existence of a soliton is deduced from the form of the Sagdeev pseudopotential[2,3].

Our main result is that particularly in the case of rarefactive solitons, the existence domain is considerably over-estimated by the Boltzmann electron model.

2 Basic Equations

The plasma is assumed to be infinite, collisionless and unmagnetised. The normalised plasma fluid equations are then given by

$$\frac{\partial n_j}{\partial t} + \frac{\partial (n_j u_j)}{\partial x} = 0, \tag{1}$$

$$\frac{\partial u_j}{\partial t} + u_j \frac{\partial u_j}{\partial x} + \frac{\gamma_j}{m_j n_j} \frac{\partial p_j}{\partial x} = \frac{Z_j e_j}{m_j} \frac{\partial \phi}{\partial x}, \tag{2}$$

$$\frac{\partial^2 \phi}{\partial x^2} = n_h + n_c - n_i, \tag{3}$$

where standard normalisations have been used except for temperature which is normalised with respect to an effective electron temperature given by $T_{eff} = T_h T_c / (n_{co} T_h + n_{ho} T_c)$. The subscript $j = i, c, h$ refers to the ions, cold and hot electrons. Equation (2) explicitly introduces the electron mass, with the isothermal electrons having $\gamma_{c,h} = 1$. The plasma is regarded as being undisturbed at $\mid x \mid \rightarrow \infty$ and the following normalised boundary conditions hold there:

$$\phi, \frac{\partial \phi}{\partial x}, u_i, u_c, u_h \rightarrow 0;\ n_i, n_c, n_h \rightarrow 1, n_{co}, n_{ho};\ p_i, p_c, p_h \rightarrow 0, n_{co} T_c, n_{ho} T_h. \tag{4}$$

3 Arbitrary-amplitude theory

We present an outline of this approach here. Further details can be found elsewhere[1-4]. We seek time-independent stable soliton solutions and transform into a frame that is stationary with respect to the soliton using $\xi = x - \mu t$, where the Mach number μ represents the normalised soliton speed. This enables us to integrate (1) immediately, yielding

$$u_j = \mu(1 - \frac{n_{oj}}{n_j}) \tag{5}$$

for the velocities of both the electrons and the ions. With the aid of the equation of state $p_j n_j^{-\gamma_j} = p_{oj} n_{oj}^{-\gamma_j}$, one finds

$$p_i = 0; \quad p_{c,h} = n_{c,h} T_{c,h}. \tag{6}$$

Using equations (5) and (6) in equation (2) and integrating, we obtain the ion density explicitly,

$$n_i = \frac{1}{(1 - \frac{2\phi}{\mu^2})^{\frac{1}{2}}}, \tag{7}$$

while the densities of the two electron species may be found by solving equations of the form

$$m_e \mu^2 \frac{n_{co,ho}^2}{n_{c,h}^2} + 2T_{c,h} \ln(\frac{n_{c,h}}{n_{co,ho}}) = 2\phi + m_e \mu^2. \tag{8}$$

Once n_i, n_c and n_h have been determined, equation (3) becomes

$$\frac{d^2\phi}{d\xi^2} = n_h + n_c - n_i = N(\phi, \mu) = -\frac{d\psi(\phi, \mu)}{d\phi} \tag{9}$$

where $\psi(\phi, \mu)$ is the Sagdeev potential, defined as

$$\psi(\phi, \mu) = -\int_o^\phi N(\xi, \mu) d\xi. \tag{10}$$

To obtain soliton solutions for fixed μ, the following conditions must hold: $\psi(0) = \partial\psi(0)/\partial\phi = 0$, $\psi(\phi_o) = 0$ for some ϕ_o and $\psi(\phi) < 0$ for $0 <| \phi |<| \phi_o |$. Equation (9) can then be integrated with initial value $\phi(0) = \phi_o$ to yield a soliton solution.

4 Results and discussion

We have studied both compressive (positive electrostatic potential) and rarefactive (negative potential) solitons. In general we find that for compressive solitons the inclusion of finite electron mass has a smaller effect on amplitude and existence criteria than is the case for rarefactive solitons.

In all the figures below, the dashed line corresponds to the case where the electrons have a Boltzmann density distribution and the solid line to that in which the electron mass is taken into account. The former are essentially the results found by Baboolal, *et al* [3]. The data presented here are for a temperature ratio $T_h/T_c = 30$, but they are typical of results for other values of the temperature ratio. In Figure 1 we show the Sagdeev potential for a typical rarefactive soliton ($\mu = 1.1; n_{co} = 0.2$). The pseudopotential well is seen to be deeper in the

case of finite electron mass than for the Boltzmann electrons, and it cuts the x-axis at a greater negative value of electrostatic potential. Thus the corresponding soliton has a slightly larger amplitude than one would deduce from a model neglecting the electron mass, as is shown in Figure 2. Our calculations for compressive solitons showed little effect on amplitude and are not presented.

A more important consideration than the effect on soliton amplitude is the effect of finite electron mass on the existence domains of the solitons. Figure 3 shows a comparison between such domains for compressive solitons. The parameter space we consider is the soliton amplitude plotted against the normalised unperturbed cold electron density. The parameter labelling the different curves is the Mach number. As can be seen, in general the curves for the Boltzmann and finite mass electron cases lie on top of one another, which indicates, as already mentioned, that the soliton amplitude is well-represented by the 'massless' model. However, we do note that solitons for a particular Mach number exist for a larger range of cold electron density values in the Boltzmann case[3] than when the electron mass is taken into account. The 'massless' electron model also admits soliton solutions for higher Mach numbers (e.g. $\mu = 1.55$), where no solitons exist for finite electron mass.

In Figure 4 we present the existence domain for rarefactive solitons. As was seen earlier for a particular value of n_{co}, the maximum negative potential (amplitude) of a soliton is generally found to be somewhat greater when the electron mass is considered than when it is neglected. On the other hand, the Boltzmann electron model overestimates considerably the range of n_{co} and ϕ_o over which solitons will occur[3]. This result obviously has considerable importance in that, guided by the 'massless' electrons model, one may seek solitons in a part of parameter space which is totally inappropriate.

Using a temperature ratio value of 15, we sought double layers which were predicted by the Boltzmann electrons model[1,3], but were unable to find them when including finite electron mass. A careful search did, however, reveal their existence for $T_h/T_c \geq 20$. Details will be presented elsewhere.

We should note that our calculations have dealt with the case of the smallest possible ion/electron mass ratio, viz. a hydrogen plasma. Clearly if one is dealing with more massive ions, the neglect of electron mass is more easily justified.

In dealing with finite electron mass in this paper, we have nevertheless assumed that because of their high mobility, both electron species are isothermal fluids. An alternative model for higher temperature ratio is one in which the more sluggish cold electrons are assumed to form an adiabatic fluid, while the hot electrons are isothermal. Results of these calculations will be presented elsewhere.

5 References

1. Baboolal, S, Bharuthram, R & Hellberg, M A *J. Plasma Phys.* **40**, 163 (1988)
2. Baboolal, S, Bharuthram, R & Hellberg, M A *J. Plasma Phys.* **41**, 341 (1989)
3. Baboolal, S, Bharuthram, R & Hellberg, M A *J. Plasma Phys.* **44**, 1 (1990)
4. Baboolal, S, Bharuthram, R & Hellberg, M A *J. Plasma Phys.* **45**, 247 (1991)
5. Mace, R L, Baboolal, S, Bharuthram, R & Hellberg, M A *J. Plasma Phys.* **45**, 323 (1991)
6. Kuehl, H H & Zhang C Y, *Phys. Fluids.* **3**, 26 (1990)

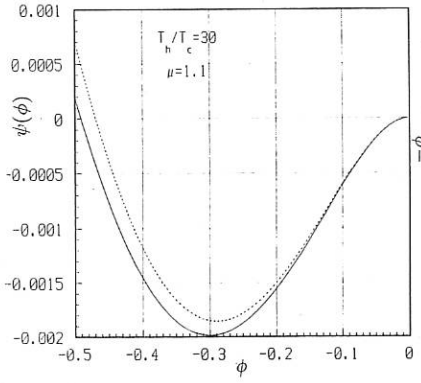

Figure 1: Typical Sagdeev potential.

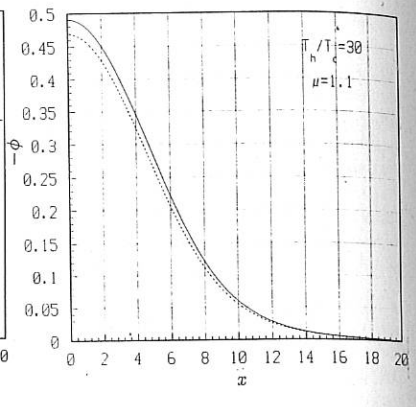

Figure 2: Typical rarefactive soliton.

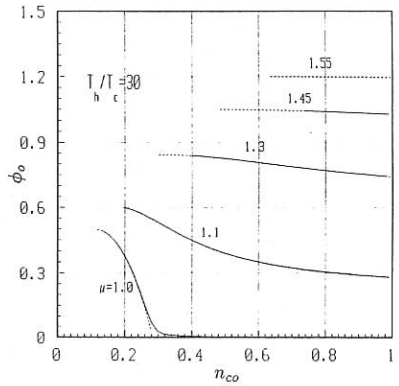

Figure 3: Existence domains for compressive solitons in $\phi_o - n_{co}$ plane.

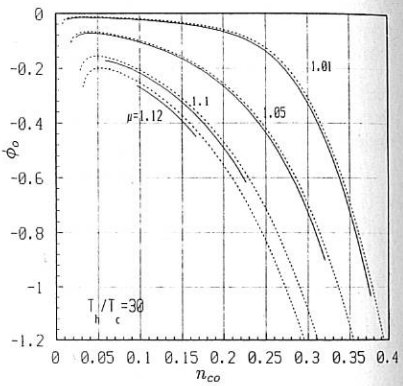

Figure 4: Existence domains for rarefactive solitons in $\phi_o - n_{co}$ plane.

EFFECT OF SECOND ION SPECIES ON ION-ACOUSTIC RAREFACTIVE SOLITON IN TWO-ELECTRON TEMPERATURE PLASMA

V.K. Sayal, L.L. Yadav and S.R. Sharma
Department of Physics, University of Rajasthan,
Jaipur - 302004 (INDIA)

The theoretical studies using the fluid model show that, in a two electron temperature plasma, the ion-acoustic rarefactive soliton (IARS) exists only for certain density and temperature ratios of the hot and cold electron species /1,2/. This is in broad agreement with experimental observations /3/. However, experimental study of the propagation characteristics of the IARS shows that there are discrepancies between the theoretical predictions and experimental observations. Recently, Sayal and Sharma /4/ have studied IARS taking kinetic effects of electrons and using fluid equations for cold ions. Their results are closer to the experimental observations /3/ but some discrepancy in the variation of width with amplitude is still unexplained. Here, we try to explain this discrepancy assuming that there might be a small fraction of impurity ions in the experiment /3/. It is found that the results are improved qualitatively as well as quantitatively.

We consider a plasma consisting of two cold ions having densities N_1, N_2, masses m_1, m_2 and ionization z_1, z_2 and two electron components having different temperatures T_c, T_h and densities n_c, n_h. We assume that electrons follow the kinetic model while the ions are governed by the fluid equations.

The density of the electrons can be given as follows /4/:

$$n_s = \alpha_s A_s \left(I(\theta_s\phi) + 1/\sqrt{|\beta_s|}\, X(\beta_s\theta_s\phi)\right) \qquad (1)$$

where $s = c$ or h corresponds to cold or hot component respectively. β_s is an arbitrary number associated with reflected electrons. ψ is amplitude of the potential φ and $-\psi \leq \varphi \leq 0$ for the rarefactive soliton. $\alpha_s = n_{os}/n_o$, $\theta_s = T_{eff}/T_s$, $\phi = \psi + \varphi$ is normalized with T_{eff}/e, $T_{eff} = T_h T_c/(\alpha_c T_h + \alpha_h T_c)$

$A_s = (1(\theta_s\psi) + 1/\sqrt{|\beta_s|}\ X(\beta_s\theta_s\psi))^{-1}$,

$X(\beta_s x) = \exp(\beta_s x)\ \mathrm{erf}(\sqrt{(\beta_s x)})$ or $\frac{2}{\sqrt{\pi}}\ W(\sqrt{(-\beta_s x)})$ for $\beta_s \geq$ or <0 respectively,

$W(x) = \exp(-x^2) \int_0^x \exp(t^2)\,dt$, $1(x) = \exp(x)\ (1 - \mathrm{erf}(\sqrt{x}))$.

Since ions are assumed to be cold, the dynamics of the ions can be determined by fluid equations

$$\frac{\partial N_i}{\partial t} + \frac{\partial}{\partial x}\ (N_i u_i) = 0 \tag{2}$$

$$\frac{\partial u_i}{\partial t} + u_i \frac{\partial u_i}{\partial x} = - \mu_i z_i \frac{\partial \varphi}{\partial x} \tag{3}$$

where $i = 1$ and 2, $\mu_1 = 1$ and $\mu_2 = m_1/m_2$. ion density N_i, velocity u_i, x and t are normlized by n_o, $\sqrt{(T_{eff}/m_1)}$, λ_{Deff}, and ω_{pl}^{-1} respectively.

For the steady state solution of (2) and (3), we use the transformation $\xi = x - Mt$ and get,

$$N_i = M\ \alpha_i/(M^2 - 2\mu_i z_i \varphi)^{1/2} \tag{4}$$

where $M = V_o/\sqrt{(T_{eff}/m_1)}$, α_i = normalized unperturbed density of ith ion species.

Ions and electrons densities are coupled with the normalized Poisson's equation

$$\frac{\partial^2 \varphi}{\partial \xi^2} = n_c + n_h - z_1 N_1 - z_2 N_2 \tag{5}$$

Using the conditions that as $|\xi| \to \infty$, φ and $\varphi' \to 0$ we get from (1), (4) and (5)

$$\frac{1}{2}\ (\frac{d\varphi}{d\xi})^2 = - V(\varphi) \tag{6}$$

where

$$V(\varphi) = M^2(\alpha_1 + \alpha_2/\mu_2) - M((M^2 - 2z_1\varphi)^{1/2} + (M^2 - 2\mu_2 z_2 \phi)^{1/2}) - \alpha_c A_c/\theta_c\ f_c(\varphi) - \alpha_h A_h/\theta_h\ f_h(\varphi) \tag{7}$$

$$f_s(\varphi) = 1(\theta_s(\psi+\varphi)) - 1(\theta_s\psi) + \frac{2}{\sqrt{\pi}}\ (1-1/\beta_s)\ \sqrt{\theta_s}\ (\sqrt{(\psi+\varphi)} - \sqrt{\psi}) + 1/\beta_s\sqrt{|\beta_s|}\ \ [X(\beta_s\theta_s(\psi+\varphi)) - X(\beta_s\theta_s\psi)]$$

In order to get rarefactive solitary solution of (6), Sagdeev potential (7) must satisfy following conditions

at $\varphi=0$, $V''(0) = (z_1^2\alpha_1 + z_2^2\ \mu_2\alpha_2)/M^2 - n_c'(0) - n_h'(0) \leq 0$ (8.a)

$$\text{at } \varphi = -\psi,\ V'(-\psi) = M(z_1\alpha_1/(M^2 + 2z_1\psi)^{1/2} + z_2\alpha_2/(M^2 + 2\mu_2 z_2\psi)^{1/2}) - \alpha_c A_c - \alpha_h A_h \leq 0 \qquad (8.b)$$

$$\text{and } V(-\psi) = 0 \qquad (8.c)$$

where $n_s'(0) = \alpha_s A_s \theta_s\ I(\theta_s\psi) \pm \sqrt{|\beta_s|}\ X(\beta_s\theta_s\psi))$ and + or - sign refer to $\beta_s > 0$ or < 0.

The nonlinear dispersion relation for IARS obtained from (7) using condition (8.c) is

$$M^2(\alpha_1 + \alpha_2\mu_2) - M((M^2 + 2z_1\psi)^{1/2} + (M^2 + 2\mu_2 z_2\psi)^{1/2}) - \alpha_c A_c/\theta_c\ f_c(-\psi) + \alpha_h A_h/\theta_h\ f_h(-\psi) = 0 \qquad (9)$$

Perturbation in bulk ion density N_1 at $\xi = 0$ i.e. at $\varphi = -\psi$ is

$$\delta N_1 = \alpha_1(M/(M^2 + 2z_1\psi)^{1/2} - 1) \qquad (10)$$

From (6) we can define the width of the soliton as follows

$$D = \int_{-\psi/2}^{-\psi} \frac{d\varphi}{\sqrt{(-2V(\varphi))}} = (2(\psi_1 - \psi)/V'(-\psi))^{1/2} + \int_{-\psi/2}^{-\psi_1} \frac{d\varphi}{\sqrt{(-2V(\varphi))}} \qquad (11)$$

where $\psi_1 = 0.99\ \psi$.

Numerical analysis is performed with (9), (10) and (11) along with the conditions (8.a&b) for different values of charge multiplicity and concentration of impurity ions, taking suitable values of $\beta_c = 1.28$ and $\beta_h = 0.1$ as in ref./4/ and keeping $T_h/T_c = 14$, $\alpha_h/\alpha_c = 12.6$ as in experiment /3/.

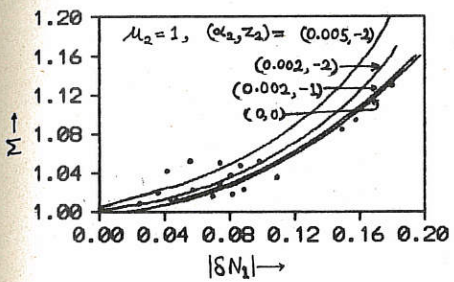

Fig 1: Variation of Mach number, M with amplitude, δN_1 of IARS. (●) experimental values /3/.

Fig.(1) shows the variation of Mach number with the amplitude (δN_1) of the IARS. We have chosen suitable values of z_1, z_2 and α_2 and compare with the experimental values as obtained by Nishida and Nagasawa /3/ and erlier theoretical results (i.e. $\alpha_2 = 0$) /4/. In fig.(2) the variation

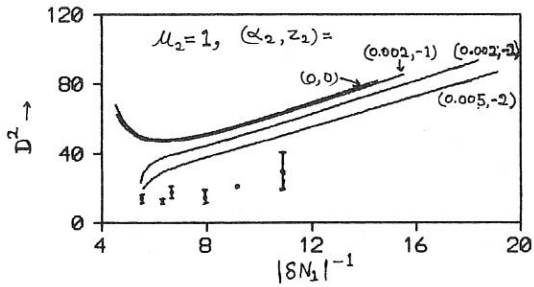

Fig 2: Variation of square of width, D^2 with inverse of amplitude, $|\delta N_1|^{-1}$ of IARS. (•) experimental values /3/.

of square of width with the inverse of the amplitude is shown for the same sets of parameters as in fig.(1). We find that the presence of a very little concentration of negative ion impurity (α_2=0.002, z_2=-2) improves the results qualitatively as well as quantitatively. In fig. (2) we see that in the absence of impurity ions (i.e. α_2=0), the width decreases as amplitude increases up to a certain value of amplitude after that the width abruptly increases while in the presence of a small fraction of negative ion impurity (α_2=0.002, z_2= -2) the width decreases as amplitude increases and the graph is more nearer to the experimental values. We also see, from fig. (1) that for α_2=0.002, z_2= -2 the curve is seen to be in good agreement with experimental observations.

One of the authors (VKS) thanks CSIR, Government of India for financial support.

/1/. B. Buti, Phys. Lett. A **76**, 251 (1980).

/2/. K. Nishihara and M. Tajiri, J. Phys. Soc. Jpn. **50**, 4047 (1981).

/3/. Y. Nishida and T. Nagasawa, Phys. Fluid **29**, 345 (1986).

/4/. V.K. Sayal and S.R. Sharma, Phys. Lett. A **151**, 72 (1990).

TRANSPORT OF TIME-VARYING CURRENTS BY WHISTLER WAVES

J.M. Urrutia, R.L. Stenzel, and C.L. Rousculp,
Dept. of Physics, University of California
Los Angeles, CA 90024-1547, USA

Time-varying currents in magnetized plasmas are of fundamental interest as electromagnetic wave phenomena and of importance in many applications such as plasma switches /1/, pulsed beams /2/, and electrodynamic tethers /3/. The present work addresses switched and pulsed plasma currents in the parameter regime of electron MHD /4/, i.e. magnetized electrons, unmagnetized ions, time scales $\omega_{ce}^{-1} \ll t \ll \omega_{ci}^{-1}$, spatial scales $r_{ce} \ll r \ll r_{ci}$. Transient currents are established between electrodes immersed into a uniform, effectively unbounded magnetoplasma. It will be shown that the currents are not only due to particle collection or emission but also induction by the insulated conductors connecting the two electrodes. The unique feature of the present experiment is the capability to map with probes the vector magnetic field in three-dimensional space and time $\underline{B}(\underline{r},t)$, from which the total current density (conduction + displacement) is calculated $[\underline{J}(\underline{r},t) = \nabla \times \underline{B}/\mu_o]$ for arbitrary (asymmetric) field topologies /5/. The major results include the observations that (i) pulsed currents are transported by whistler wave packets, (ii) the associated electromagnetic fields are essentially force-free $\underline{J} \times \underline{B} + \rho\underline{E} \approx 0$ such that large currents can be transported without pinching, kinking, etc.; (iii) that cross-field current closure is established by Hall currents associated with space-charge fields; and (iv) that moving dc current sources emit transient currents forming Cherenkov-like structures.

The experiments are performed in a device schematically shown in Fig.1. Time-varying magnetic fields associated with currents from biased electrodes are measured with a magnetic probe consisting of 3 orthogonal loops movable throughout the central uniform plasma volume. From many ($> 10^5$) highly reproducible pulses the field topology $\underline{B}(\underline{r},t)$ is assembled with the help of digital data storage and analysis.

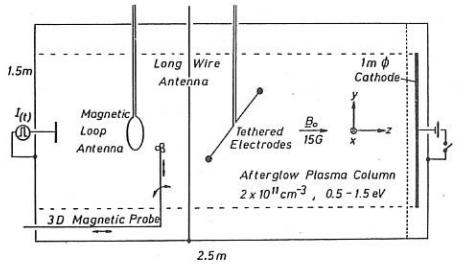

Fig.1: Experimental setup. The present paper deals with pulsed currents from biased electrodes.

/1/ B.V. Weber et al, Appl. Phys. Lett. 45, 1043 (1984).

/2/ R. Lee and R.N. Sudan, Phys. Fluids 14, 1213 (1971).

/3/ Tethers in Space Handbook, ed. by R.A. Penzo and P.W. Ammann (NASA, Washington, DC, 1989) 2nd. edn., p. 119.

Fig.2 shows contours of constant axial current densities $J_z(y,z)$ at different times after switching on a positive bias to a 5cm dia. disk electrode. The current front propagates at a speed $v_z \approx 10^8$ cm/s which exceeds the electron thermal velocity. By modulating the current ($0.5 \leq f \leq 5 MHz$) and measuring the axial wavelength, a dispersion $\omega/\omega_{ce} \approx (k_\parallel c/\omega_{pe})^2$ matching that of low frequency whistlers along $\underline{B}_o$ has been measured /6/. The propagation speed is independent of the thermal speed of the collected particles, i.e. the same when collecting slow ions or emitting a fast electron beam /7/. The dashed contours in Fig.2 ($J_z < 0$) are due to induced return currents providing a coaxial current closure to the chamber wall which is the negative electrode. In addition to the axial current component there are azimuthal and radial currents to be shown next.

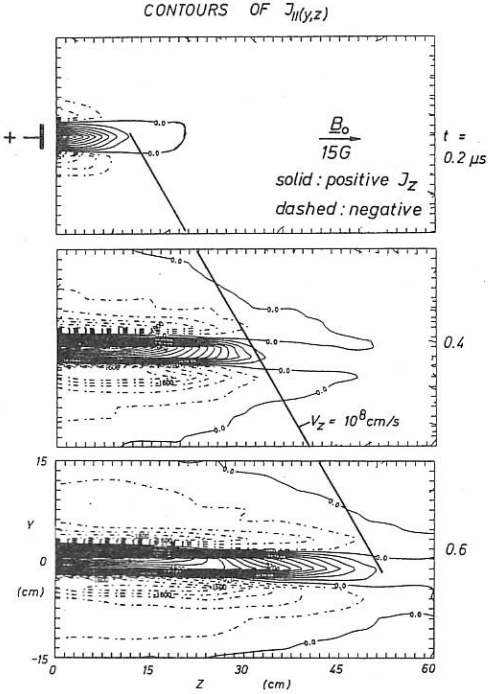

Fig.2: Current density contours $J_z(y,z)$ at different times after applying a positive bias between an electrode and the chamber wall. The current front propagates in the whistler mode. Induced return currents (dashed contours) flow coaxially back to the wall.

/4/ A.S. Kingsep, K.V. Chukbar, and V.V. Yankev, "Electron MHD", in Reviews of Plasma Physics, Vol.16, ed. by B.B. Kadomtsev (Consultants, N.Y., 1990) p. 243.

/5/ R.L. Stenzel and J. M. Urrutia, J. Geophys. Res. 95, 6209 (1990).

/6/ J.M. Urrutia and R.L. Stenzel, Phys. Rev. Lett. 62, 272 (1989).

Fig.3 displays magnetic field components $\underline{B}(\underline{r},t)$ produced by a current pulse rather than a current step (Fig.2). The duration of the pulse ($\Delta t \approx 0.2\mu s$) is shorter than the transit time through the device such that the current pulse becomes detached from all boundaries, hence all fields and currents must close within the plasma. The axial current J_z produces an azimuthal magnetic field B_θ shown as vectors (d) and field lines (c). A radial space-charge electric field produces an electron Hall current J_θ which generates an axial magnetic field component (a,b). Superimposing the solenoidal and toroidal field contributions schematically yields coaxial helices (e). Both the time-varying magnetic field $\underline{B}(\underline{r},t)$ and $\underline{J}(\underline{r},t)$ have similar topologies. A study of the electromagnetic force density $\underline{f} = \underline{J} \times \underline{B} + \rho\underline{E}$ (where $\underline{B} = \underline{B}(\underline{r},t) + \underline{B}_o$) has indicated a negligible force on the conducting fluid, i.e. the electrons /8/. Large current pulses ($I \approx 150A$) with B_{wave} approaching B_o exhibit the same field topologies as small pulses (0.05A).

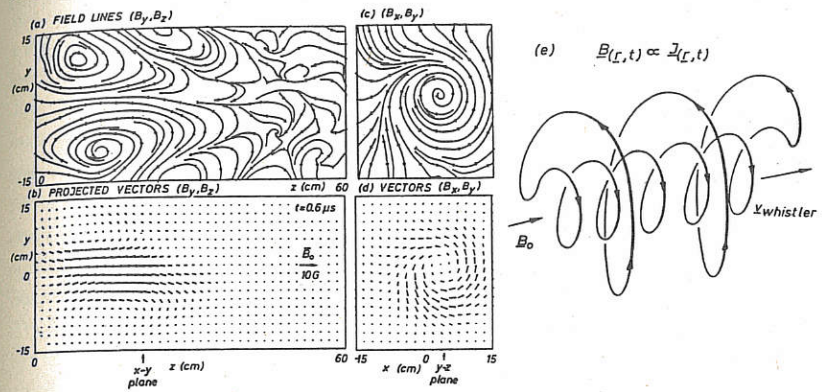

Fig.3: Field topology $\underline{B}(\underline{r},t)$ for a short current pulse detached from all boundaries. Based on field lines (a,c) or vector fields (b,d) from orthogonal planes a simplified picture of the resulting field line is displayed (e). The nearly force-free electromagnetic field propagates as a whistler wave packet along $\underline{B}_o$.

In many situations, the two electrodes which feed current into the plasma are separated across $\underline{B}_o$ such that plasma currents must also close across $\underline{B}_o$. A typical example is an electrodynamic tether /3/, a laboratory model of which is shown in Fig.4. The contour maps of the current density components $J_y = J_\theta$ and J_z indicate that two field-aligned current channels propagate away from the electrodes. Since the total current must be closed ($\nabla \circ J_{tot} = \nabla \circ (\nabla \times \underline{H}) = 0$) there must be a cross-field current J_x. This current is induced by the insulated wire connecting the two electrodes. Fig.4b shows magnetic field lines in a plane perpendicular to the tether wire. One can see two induced image currents $(\nabla \times \underline{B})_x = \mu_o J_x$ flowing across $\underline{B}_o$ and propagating in the whistler mode along $\underline{B}_o$. The total current $\iint J_x dydz$ equals the current I_x in the wire, hence the whistler wave current provides for the cross-field closure between the field-aligned current channels. The wave current is

/7/ R.L. Stenzel and J.M. Urrutia, Geophys. Res. Lett. 13, 797 (1986).
/8/ R.L. Stenzel and J.M. Urrutia, Phys. Rev. Lett. 65, 2011 (1990).
/9/ R.L. Stenzel and J.M. Urrutia, Geophys. Res. Lett. 16, 361 (1989).

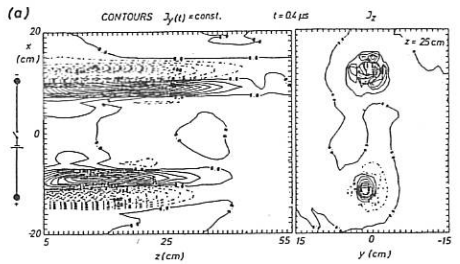

Fig.4: (a) Pulsed currents established by two tethered electrodes separated across $\underline{B}_o$. The current closure across $\underline{B}_o$ is accomplished by wave currents J_x induced by the insulated tether wire as evident from the field line map $(B_y, B_z)(y,z)$ in (b).

essentially an electron Hall current due to a space charge electric field $E_y \perp \underline{B}_o$. Polarization and displacement currents are negligible in the electron MHD regime ($\partial/\partial t << \omega_{ce}$).

When a dc current-carrying conductor such as the electrodynamic tether moves with high velocity across $\underline{B}_o$ the stationary plasma carries a time-varying current due to the finite time the conductor spends in a flux tube ($\Delta t = d/v$, where d is the conductor size and v the spacecraft velocity). By superimposing many delayed current pulses ($t_{delay} = \Delta t$) emitted at displaced electrode positions ($\Delta y = d$) one can obtain the approximate plasma current distribution behind a moving dc current source /9/. Fig.5 presents contours of J_x in the y-z plane $\perp$ to the tether which moves with v_y across $\underline{B}_o$. Similar currents (J_y, J_z) flow from each end electrode as whistler "wings" which provide for the necessary current closure.

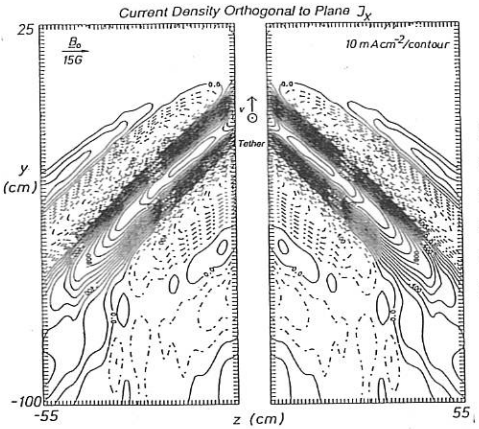

Fig.5: Cherenkov-like "eddy" currents induced by an insulated tether wire with dc current moving at whistler wave speeds across $\underline{B}_o$. A wave-supported current system will be established by an electrodynamic tether moving through space /3/.

In summary, time-varying currents are associated with electromagnetic waves which, in the electron MHD regime, are low frequency whistlers. Besides establishing the basic physics through careful experiments a practical model for an electrodynamic tether in space has been investigated.

EXCITATION OF LOW FREQUENCY WHISTLERS BY MAGNETIC LOOPS

R.L. Stenzel, J.M. Urrutia, C.L. Rousculp and G. Yu. Golubyatnikov,
Department of Physics, University of California,
Los Angeles, CA 90024-154705, USA

The physics of wave excitation from magnetic loop antennas in magnetized plasmas is of general interest in space and fusion plasmas. In the former area, large scale structures such as electrodynamic tethers and magnetic loops /1/ are useful for exciting very low frequency electromagnetic waves for communication purposes. In the fusion area antennas are used for rf heating near ion cyclotron and hybrid frequencies /2/. Fundamental questions deal with the coupling, often lumped into a single parameter, between the antenna and a plasma eigenmode, the radiation resistance /3/, and the radiation patterns /4/, nonlinear effects at high power levels /5/, sheath resonances and instabilities /6/, motional effects /7/ and noise limits for receiving antennas /8/. In the present work the excitation of low frequency whistlers ($\omega_{ci} << \omega << \omega_{ce}$) by magnetic antennas is investigated in a uniform, effectively unbounded magnetoplasma. In contrast to previous studies, the complete wave magnetic field in space and time is measured. This yields a detailed picture of the three-dimensional field topology between near-zone and far-zone, and it allows the calculation of plasma currents ($\nabla \times \underline{B} = \mu \underline{J}$) which are often ignored in wave studies. The major findings are that spatial whistler wave packets generally assume a 3-D magnetic field configuration ($B_x, B_y, B_z \neq 0$) consisting of nested toroidal and solenoidal contributions. The electric field is dominated by a radial space charge field while cross field currents are mainly Hall currents. The coupling efficiency (B_{wave}/B_{ant}) increases with density. The real part of the antenna impedance is not only due to the radiation resistance but predominantly due to transit-time electron damping. The latter also causes efficient electron heating which can modify the plasma conductivity and modulate the radiation pattern /5/. Moving an antenna across $\underline{B}_0$ causes a Cherenkov-like radiation pattern, consisting of whistler "wings" /7/.

The experiments are performed in a large (1m diam. x 2.5m length), magnetized (B_0 = 15G) afterglow plasma with parameters given in Fig.1. Time-varying magnetic fields are detected with a magnetic probe containing three orthogonal loops movable thoughout the central uniform plasma volume. From many (>10^5), highly repeatable events, the field topology $\underline{B}(r,t)$ is assembled with the help of digital data storage and processing.

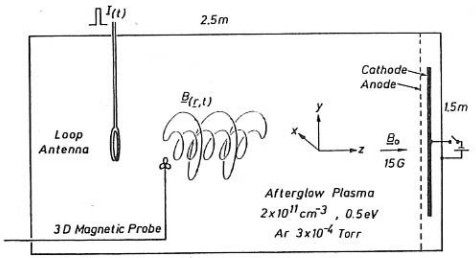

Fig.1 Experimental setup.

/1/ Tethers in Space Handbook, ed. by P.A. Penzo and P.W Ammann (NASA, Washington DC, 1989) 2nd edtn., p.119.

Fig.2 displays magnetic "field lines" (B_y, B_z) in the y-z plane at different times after applying a single current pulse to the magnetic loop antenna which is sketched in the top panel. The actual magnetic field lines pass at different angles through the y-z plane since there is also a B_x component (Fig.3). One can see both the dipolar near-zone field of the loop as well as two induced image loops propagating in ± z direction away from the antenna. The propagation speed ($v_z \approx 10^8$ cm/s) is that of low frequency whistlers, $v_g \approx 2v_{ph} \approx 2(c/\omega_{pe})(\omega \omega_{ce})^{1/2}$, although the single pulse introduces a spread in frequencies ($\langle f \rangle \approx \Delta t_{pulse}^{-1} \approx 5$ MHz), hence also in group and phase velocities. However, an advantage of the pulse excitation is the easy distinction between plasma response and imposed antenna fields, the latter vanishing after the end of the pulse (bottom two panels).

Fig.3 shows the magnetic fields and current densities in an x-y plane at a distance z = 30cm from a 5cm

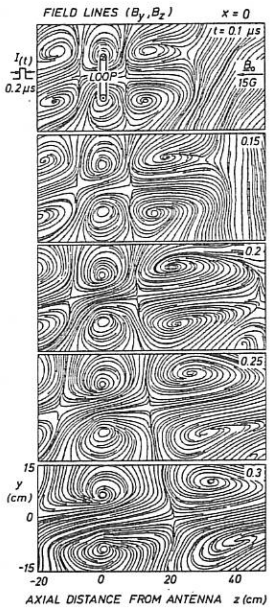

Fig.2 Field lines connecting the (B_y, B_z) components in the y-z plane at different times t after applying a current pulse to the loop antenna sketched in the top panel. Induced image current loops propagate in the whistler mode away from the antenna.

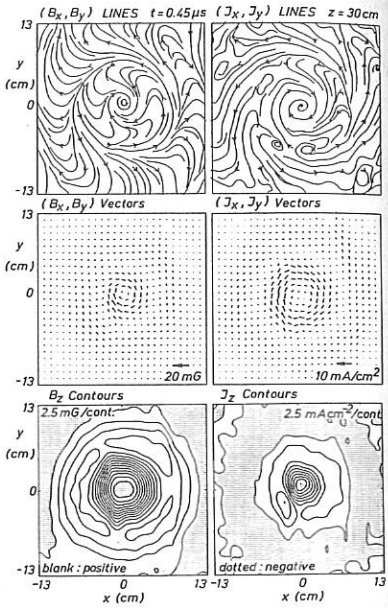

Fig.3 Comparison of magnetic field lines and current density lines for the transverse field components in the x-y plane $\perp \underline{B}_0$. Field lines and vector fields show a toroidal topology, linked with the axial B_z and J_z components (bottom panels).

/2/ E.A. Berro and G.J. Morales, IEEE Trans. Plasma Sc. 18, 142 (1990).

/3/ K.G. Balmain, Radio Sci. 7, 771 (1972).

/4/ R.L. Stenzel, Radio Sci. 11, 1045 (1976).

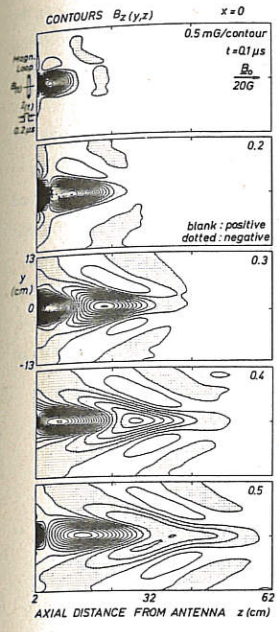

Fig.4 Contours of the axial wave magnetic field component $B_z(y,z,t)$ showing the evolution of the wave from the near-zone into the far-zone. V-shaped contours arise from the higher propagation speed along $\underline{B}_o$ than oblique to $\underline{B}_o$. Small wavelets are due to dispersion of the whistler wave pulse.

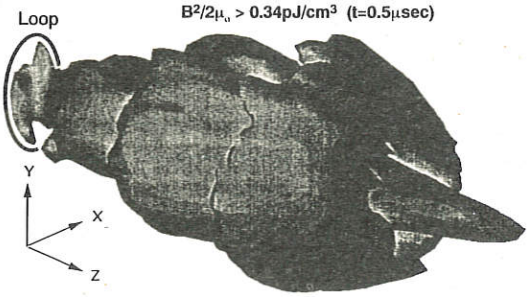

Fig.5 Three-dimensional view of the loop excited whistler wave packet. The surface indicates a constant value of the wave magnetic energy density $B^2/2\mu_o$ at one instance of time.

diam. loop antenna. From the projected field lines or the vector fields one can identify a toroidal field topology for both $\underline{B}$ and $\underline{J}$. The sense of rotation reverses with radius. Likewise the axial field and current density components which are shown as contour plots in the bottom panels also exhibit sign reversals as a result of wave packet dispersion.

The transition of the wave packet from the near zone into the far-zone is shown in Fig.4. Contours of axial wave magnetic field at different times show the formation of V-shaped phase and amplitude profiles. These arise from the higher wave propagation speed along $\underline{B}_o$ than oblique to $\underline{B}_o$. The major negative B_z distribution is the response to the antenna current rise, the subsequent positive B_z maximum is induced by the antenna current drop. Several small wavelets near the wave front are created by dispersion or, alternatively, by successive induction with sign reversals according to Lenz's law. Note that the wave energy flows predominantly along $\underline{B}_o$ while the phase normals are highly oblique to $\underline{B}_o$. A three-dimensional display of the wave magnetic energy density is given in Fig.5. The surface $B^2/2\mu_o$ = const. is azimuthally quite symmetric. Note that this field distribution develops self-consistently in a uniform plasma free of boundary effects. The wave packets are neither plane waves nor column eigenmodes such as helicons.

/5/ J.M. Urrutia and R.L. Stenzel, Phys. Rev. Lett. 67, 1867 (1991).

/6/ R.L. Stenzel, Phys. Fluids B1, 2273 (1989).

/7/ R.L. Stenzel and J.M. Urrutia, Geophys. Res. Lett. 16, 361 (1989).

Fig.6 presents a physical model which explains the observed field topology in simple terms. During the antenna current rise an inductive electric field $\underline{E}_i = -\partial\underline{A}/\partial t$ anti-parallel to the antenna current is imposed on the plasma. The response of the unmagnetized ions can be neglected compared with that of the electrons which undergo radial $\underline{E}_i \times \underline{B}_o$ (adiabatic compression). A negative space charge accumulates on axis near the antenna, while a positive charge remains off axis due to the loss of electrons. The excess space charge has two consequences: (i) A radial space charge electric field $\underline{E}_{sc} = -\nabla\phi$ drives an azimuthal Hall current $\underline{J}_\theta = -ne\underline{E}_{sc} \times \underline{B}_o/B_o^2$ which generates the axial "induced" magnetic field $B_z(t)$ (see Fig.5). (ii) Field-aligned currents $\pm J_z$ are set up to neutralize the excess space charges. These generate the observed azimuthal magnetic fields $B_{\theta(t)}$ (see Fig.4). The induced currents and fields are accelerated by $\underline{J} \times \underline{B}$ forces away from the antenna. Far from the antenna near-zone they propagate at approximately constant speed as electromagnetically force-free fields, $\underline{J}\times\underline{B}+ne\underline{E} = 0$ /9/. When the antenna current decreases in time, the sign of the induced fields, charges, and currents reverses. The space charge electric field in the whistler wave has been directly measured with an emissive dipole probe.

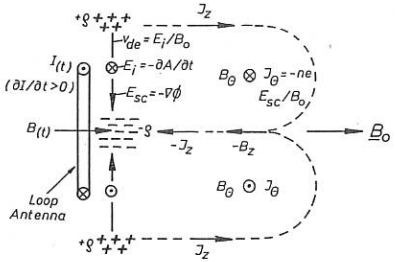

Fig.6 Physical model explaining the observed fields and currents induced by a rising current in the magnetic loop antenna.

The near-zone fields are at least one order of magnitude larger than the wave magnetic fields. When the antenna current is increased, significant electron acceleration and heating is observed. As long as the plasma is collisionless ($\nu_e << \omega << \omega_{ce}$), the field topology and wave propagation are not significantly changed up to $B_{wave} \approx B_o$. However, in an initially cold, Coulomb-collision dominated plasma the electron heating creates a channel of highly conducting plasma in which the wave propagates without damping. Such conductivity modifications produce nonlinear propagation effects similar to filamentation instabilities /5/.

In summary, a detailed study of the excitation of low frequency whistlers by magnetic antennas has been performed. The plasma anisotropy and space charge effects in the regime of electron MHD /10/ give rise to complicated fields for even symmetric antenna geometries. Nonlinear effects need further investigations.

/8/ R.L. Stenzel, Phys. Fluids B1, 1369 (1989).

/9/ R. Stenzel and J.M. Urrutia, Phys. Rev. Lett. 65, 2011 (1990).

/10/ A.S. Kingsep, K.V. Chukbar, and V.V. Yankev, "Electron Magnetohydrodynamics", in Reviews of Plasma Physics, Vol.16, ed. by B.B. Kadomtsev (Consultants Bureau, N.Y., 1990) p. 243.

NON-STATIONARY PROPAGATION OF NONLINEAR ION ACOUSTIC WAVES IN A PLASMA WITH NEGATIVE IONS

Mituo Uehara [(a),(b)] and Homero S. Maciel [(b)]

a. UNIVAP, Praça Cândido D. Castejon, 116, S.J.Campos,SP, 12245, Brasil

b. Depto. de Fisica, ITA, S.J.Campos, SP, 12225, Brasil

1. INTRODUCTION

It is well known that small amplitude ion acoustic waves in plasmas can be described by Korteweg-deVries equation. However, the response of the plasma to disturbances is drastically modified by the presence of negative ions. In a plasma with electrons, one species of positive ions and one species of negative ions, ion acoustic waves of small amplitude and weak nonlinearity can be described, in terms of nondimensional quantities, by the equation[1,2]

$$\frac{\partial \phi}{\partial \tau} + \frac{1}{2}\left(3\,\frac{n_{\alpha 0}}{V^4} - 3\,\frac{n_{\beta 0}}{Q^2 V^4} - 1 \right)\phi\,\frac{\partial \phi}{\partial \xi} + \frac{1}{2}\,\frac{\partial^3 \phi}{\partial \xi^3} = 0 \qquad (1)$$

where ϕ denotes the wave potential, normalized by kT/e, k being the Boltzmann constant, and T the electron temperature. $Q = m_\beta / m_\alpha$ is the ratio of the negative ion mass to the positive ion mass. The unperturbed densities, $n_{\alpha 0}$ and $n_{\beta 0}$, of positive and negative ions are normalized by the electron density, so that the quasi-neutrality condition is $n_{\alpha 0} = 1 + n_{\beta 0}$. The time τ is normalized by the ion plasma period ω_{pi}^{-1} and the coordinate ξ normalized by the Debye length λ_D, in the frame moving with the sound velocity $V = (n_{\alpha 0} + n_{\beta 0} / Q)^{1/2}$.

There is a critical density of the negative ions at which the coefficient of the nonlinear term of the K-dV equation (1) vanishes. Therefore, at the critical density, it is necessary to consider nonlinear terms of higher orders to get, for example, the modified K-dV equation derived by Watanabe[2].

In the present work the modified K-dV equation derived by Watanabe is generalized to include cylindrical and spherical geometries, and similarity analysis is applied in order to find non-stationary solutions.

2. THE MODIFIED KORTEWEG-deVRIES EQUATION

Watanabe[2], considering a plasma with the negative ions at the critical density and by assuming that the ions are cold, has derived the modified K-dV equation

$$\frac{\partial \phi}{\partial \tau} + \alpha \phi^2 \frac{\partial \phi}{\partial \xi} + \frac{1}{2} \frac{\phi^3 \phi}{\phi \xi^3} = 0 , \qquad (2)$$

where

$$\alpha = \frac{1}{4} (15 \frac{n_{\alpha 0}}{V^6} + 15 \frac{n_{\beta 0}}{Q^3 V^6} - 1).$$

In the derivation of equation (2) Watanabe used the stretched variables $\xi = \varepsilon^{1/2} (x - Vt)$ and $\tau = \varepsilon^{3/2} Vt$, where ε is a small parameter , x is the normalized cartesian coordinate, t is the normalized time, and V is the normalized sound velocity $V = (n_{\alpha 0} + n_{\beta 0}/Q)^{1/2}$.

The equation (2) has been deduced for plane geometry, considering only one cartesian coordinate, and can be generalized to include cylindrical and spherical geometries. Maciel and Sudano[3] has derived a K-dV equation which holds for the three geometries. A similar derivation to that one presented by Maciel and Sudano yields, for the present case,

$$\frac{\partial \phi}{\partial \tau} + \frac{\nu}{2} \frac{\phi}{\tau} + \alpha \phi^2 \frac{\partial \phi}{\partial \xi} + \frac{1}{2} \frac{\partial^3 \phi}{\partial \xi^3} = 0 , \qquad (3)$$

where ν = 0, 1 and 2, respectively, for plane, cylindrical and spherical geometries.The second term represents the geometrical effect.
By writing $\phi_1 = \tau^{\nu/2}$, equation (3) becomes

$$\frac{\partial \phi_1}{\partial \tau} + \alpha \tau^{-\nu} \phi_1^2 \frac{\partial \phi_1}{\partial \xi} + \frac{1}{2} \frac{\partial^3 \phi_1}{\partial \xi^3} = 0 . \qquad (4)$$

Following the similarity method, we search for solutions of equation (4) that are invariants under a one-parameter group of transformation defined by

$$\tau = R^a \tilde{\tau} , \quad \xi = R^b \tilde{\tau} \quad \text{and} \quad \phi_1 = R^c \tilde{\phi}_1 , \qquad (5)$$

where R, a, b and c are constants. The equation (4) is invariant under this group if $b/a = 1/3$ and $c/a = \nu/\alpha - 1/3$, and the group invariants are

$$\eta = \frac{\xi}{\tau^{1/3}} \quad \text{and} \quad f(\eta) = \frac{\phi_1(\xi,\tau)}{\tau^{\nu/2 - 1/3}} \tag{6}$$

The equations (4) and (6) yield

$$(\nu - \frac{1}{3})f(\eta) - \frac{1}{3}\eta\frac{df}{d\eta} + \alpha f^2(\eta)\frac{df}{d\eta} + \frac{1}{2}\frac{d^3 f}{d\eta^3} = 0 \tag{7}$$

Let us consider the case $\nu = 0$ (plane geometry). In this case equation (7) reduces to

$$\frac{d^3 g}{d\zeta^3} - g^2\frac{dg}{d\zeta} - g(\zeta) = 0 , \tag{8}$$

where $g = 3^{1/3}2^{1/6}$ and $\zeta = (2/3)^{1/3}\eta$. (9)

Assuming that $g^2/\zeta \to 0$ when $\zeta \to \pm\infty$, the nonlinear term can be neglected for large values of $|\zeta|$ and the equation (8) reduces to the linear equation

$$\frac{d^3 g_L}{d\zeta^3} - \zeta\frac{dg_L}{d\zeta} - g_L = 0 , \tag{10}$$

which describes the asymptotic behaviour of the ion acoustic wave.

Integrating equation (10) and assuming that when $\zeta \to \pm\infty$,

$(\frac{d^2 g_L}{d\zeta^2} - \zeta g_L) \to 0$, we obtain

$$\frac{d^2 g_L}{d\zeta^2} - \zeta g_L(\zeta) = 0 , \tag{11}$$

which has a solution of the form

$$g_L(\zeta) = C\,Ai(\zeta), \tag{12}$$

where C is a constant and $Ai(\zeta)$ is the Airy function.

The asymptotic solution (12) can be used to determine the initial conditions for a numerical integration of the nonlinear equation (8). A numerical integration has been carried out where $\zeta = 2$ has been chosen as the initial point for the integration, and $C = 1$ in the asymptotic form (12). The results shows that the nonlinear wave has roughly the same behaviour as the asymptotic solution but with smaller oscilation amplitude.

For the cylindrical and spherical geometries, similar derivations to that one carried out for the plane geometry yield linearized equations whose solutions diverge as $\zeta \longrightarrow \pm\infty$. However it is possible that part of those solutions are physically meaningfull because similarity analysis sometimes gives solutions which are not valid everywhere. This question requires further analysis.

3. CONCLUSION

Similarity analysis was applied to modified K-dV equations which describe small amplitude ion acoustic waves in a plasma with negative ions at the critical density. In the case of the plane geometry, it was shown that the asymptotic solution satisfies the Airy equation. Furthermore, through numerical integration, it was shown that the nonlinear equation has solutions which resembles an Airy function but with smaller amplitude of oscillation. In the case of cylindrical and spherical geometries, the present method of analysis gives linearized equations which have divergent solutions so that their physical meaning requires further discussion.

REFERENCES

1. S. Watanabe, *J. Phys. Soc. Japan* **53** (1984), 950-956.

2. K. I. Singh and G. C. Das, *IEEE. Trans. on Plasma Science* **17** (1989), 863-869.

3. H. S. Maciel and J. P. Sudano (1986), *Int. Sympos. on Physics of Ionized Gases SPIG 86*, Sibenik, Yugoslavia, Sept.1-5, pp 523-527.

10-52

RELAXATION AND SELF-ORGANIZATION OF A NONNEUTRAL PLASMA

H. Ramachandran, G.J. Morales, and V.K. Decyk

Physics Department
University of California, Los Angeles
Los Angeles, CA 90024-1547 USA

I. Overview

The properties of nonneutral systems have been elucidated in several elegant experiments[1,2]. As plasmas, these systems have the virtue of being confinable for long times, since conservation laws place strong bounds on particle loss. Detailed experiments have explored the quasistatic evolution of a well-confined configuration near equilibrium. The transient, non-equilibrium phase during which the plasma achieves its steady-state profile is difficult to probe experimentally. However, because of the short-time scales involved this is a regime well suited to particle simulation. This paper discusses the results of a particle-simulation code of a nonneutral plasma that is confined in a slab-equivalent of a Penning trap. The early collisionless relaxation is examined, and a time-dependent steady state is observed to result. In this state, the system achieves the shape of a football, composed of a fluid-like core and a kinetic halo. When this quasi-equilibrium is externally cooled, it is found to develop spatial rings reminiscent of liquid crystals. This crystalline structure is robust and 'melts' when it is heated.

II. Geometry

This study uses a bounded, 2-1/2 D magnetized particle-simulation code[3]. The magnetic field lies along z, and the plasma is spatially localized along x. The y coordinate is ignorable. The charges are confined radially by the magnetic field, and axial confinement is achieved by an external vacuum potential

$$\phi_E(x, z) \simeq \phi_o [z^2 - x^2] \quad .$$

Fig. 1 shows the initial configuration. A rectangular region of cold plasma is placed in the confining external field. The dimensions are chosen such that the self-repulsion is too weak to balance the axial compression of the electric field. The cyclotron frequency is initially eight times the plasma frequency.

III. Collisionless Relaxation

As expected, the system in Fig. 1 initially contracts and thereafter undergoes compression oscillations. A single global mode appears, with a characteristic frequency, although the system is very nonlinear and

strongly nonuniform. This oscillation frequency is about two to three times the plasma frequency, and still several times below the cyclotron frequency. After several oscillations, the system undergoes a spatial decoupling, and the edge particles (in radius) start interacting resonantly with the global mode. The edge particles are rapidly accelerated to large energies, and the system arrives at a time-dependent steady state, as seen in Fig. 2. Note that the core region relaxes to a 'football' shape, even in the absence of collisions. The state shown in Fig. 2 persists for a long time, and external damping is required to achieve a stationary equilibrium in a reasonable time-scale.

IV. Cooling and Crystallization

The time-dependent steady state previously described is subjected to external cooling. Isotropic cooling is observed to yield expansion across the magnetic field in addition to cooling. When external damping is applied only in the x and z directions, the plasma is observed to cool without expansion. Fig. 4a shows that the 'halo' region disappears and the edge particles lose energy. The core region shows the first signs of organized structure; an outer spatial ring of particles separates out from the rest of the plasma. Further cooling causes more rings to form as seen in Fig. 4b.

Due to the strong magnetic field, charges are confined to the field lines on which they were initially placed. Thus, the final configuration contains the same line-integrated density profile as it started with. However, varying the density profile does not affect the collisionless relaxation process or the final 'football' shape significantly.

When the external damping is removed the cooled system experiences a slight rise in temperature. This heating is accompanied by a weak acceleration of the edge particles, suggesting that the edge 'halo' is a universal feature in a time dependent system that attempts to match to stationary external constraints.

The self-organizing state is quite robust. When the external electric field is suddenly increased in strength by 10%, the temperature of the particles rises only slightly and the crystalline structure remains unaffected. Most of the energy goes into a global compression mode. Heating the plasma progressively destroys the organization of the particles, the outer ring being the last one to 'melt'.

Acknowledgment:

This work is supported by the Office of Naval Research.

References

1. C.F. Driscoll, J.H. Malmberg, and K.S. Fine, Phys. Rev. Lett., 13, 1290 (1988).

2. D.J. Heinzen, J.J. Bolinger, F.L. Moore, Wayne M. Itano, and D.J. Wineland, Phys. Rev. Lett., 66, 2080 (1991).

3. V.K. Decyk, G.J. Morales, and J.M. Dawson, Phys. Fluids, 23, 826 (1980).

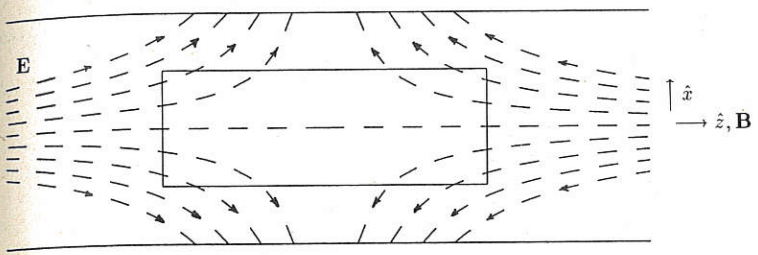

Figure 1. Initial configuration of the slab Penning trap. The solid rectangle represents a nonneutral plasma, while the dashed lines represent the externally imposed electric field that produces axial confinement. Radial confinement is achieved by a magnetic field.

Figure 2. $t = 30/\omega_p$: Time dependent steady state achieved through collisionless processes. Most of the plasma behaves as a core fluid undergoing oscillations in the external field. The low density edge plasma becomes a 'halo' having a hot ring distribution that encloses (in phase space) the core particles.

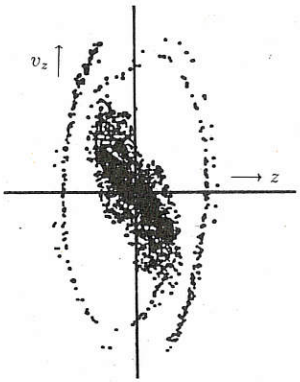

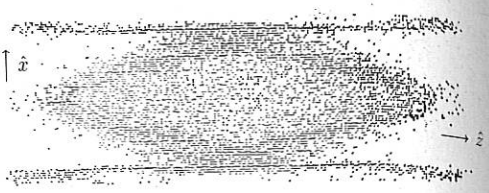

Figure 3. $t = 30/\omega_p$: Configuration space. The core region achieves the 'football' shape that is typical of the cold equilibrium. The edge 'halo' region is seen to be spatially extended in z. Its function is to match the time-dependent fields generated by the oscillating core plasma to the external time-independent confining field.

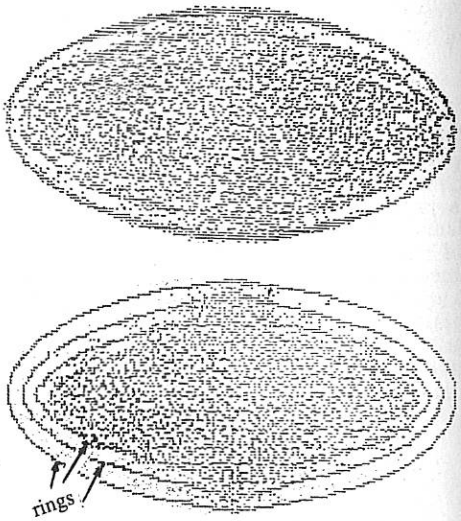

Figure 4. Cooling and crystallization: As the hot system in Fig. 3 is cooled by friction, the edge region is quickly lost and the plasma comes to a stationary equilibrium. Further cooling causes radial structure to appear, reminiscent of crystal formation. Initially an outer ring forms, but as cooling is continued, a sequence of rings appear towards the center.

LOW-DIMENSIONAL ATTRACTORS ARISING FROM THE INTERACTION OF DRIFT WAVES WITH LOW FREQUENCY INSTABILITIES

T. Klinger and A. Piel
Institut für Experimentalphysik,
Universität Kiel, Germany

1. Introduction

Nonlinear interaction of plasma waves has been the topic of many theoretical and experimental works. However, the theory of nonlinear dynamics of dissipative systems has shed new light on several plasma wave phenomena. Theroretical investigations [1,2,3] predict low-dimensional phase space attractors for interacting drift-waves and in the interaction of drift-waves with ion-sound-waves, respectively. Experimental evidence for such attractors has been given in a magnetized double-plasma device [4], where, under certain conditions, interaction between ion-sound-like waves and ion drift-waves is observed.

The present contribution gives a classification of these ion-sound-like waves and characterizes the interaction process. The phase space attractors are investigated using improved numerical methods.

2. Experiment

The KIWI-experiment is a magnetized triple plasma device which consists of two independent plasma chambers ('magnetic box', 92 cm dia. $\times$ 90 cm) and a central tube section (30 cm dia. $\times$ 200 cm) immersed in a set of 14 water-cooled magnetic field coils. A dense, quiet, and homogenous plasma ($N_e \leq 10^{11}\mathrm{cm}^{-3}, T_e = 2\mathrm{eV}$) diffuses from the magnetic boxes into the magnetized tube section. The plasma chambers and the tube section are separated by mesh grids with a transparency of about 50%, which can be biased for controlled injection of electrons or ions. The double-plasma mode is achieved by activating one plasma chamber and using a grid at the far end of the tube section as a plasma-loss surface. By positively biasing the grid between the plasma chamber and the tube section, a supra-thermal electron beam is injected into the plasma background. Langmuir-probes are used for density, temperature and potential diagnostics. Both radially and axially movable probes are available. Quantitative plasma potential measurements with emissive probes are performed in the usual manner [5]. Dynamical measurements are performed by recording time series of probe signal fluctuations, i.e., temporal changes of ion saturation current and floating potential. Power spectra of potential and density fluctuations are calculated from these high-resolution time series.

3. Experimental Results

An axial electron drift $\propto I_d$ is well known to destabilize drift waves [6]. For this reason, the axial drift voltage U_d along the magnetic field has been chosen as control parameter for the dynamical state of the plasma. In the case of additional electron rich injection into the background plasma, we observe as critical phenomenon anomalous resitivity (AR) in the $U_d(I_d)$-characteristic, the occurence of a low-frequency ion-sound-like instability and after the onset of AR a broad fluctuation power spectrum. In Figure 1, the transition to AR is shown. The dashed line is a sketch of the discharge-like resistivity characteristic for weak or no electron injection. From two selected corresponding power spectra, the transition from single-mode to turbulent spectra is clearly observable. From measured density profiles, the anomalous radial transport due to drift-wave turbulence can be seen as mechanism for this type of AR.

In order to understand this transition, a frequency-wavenumber spectral analysis [7] and the calculation of high-ordered spectra [8] has been carried out. We find a strong low-

frequency instability ($f < 3$kHz) coexistent with drift-waves. These two instabilities are clearly distinguishable by their fluctuation profile, parameter dependence and propagation properties. In case of a stable plasma, measurements of the stationary potential profile $\Phi_p(z)$ have shown the existence of a stationary weak double layer (DL) with a normalized potential jump $e\Phi_0/k_BT_e \approx 1$. This DL extends from the grid towards the tube section over about 300mm. For the unstable case, however, a sawtooth-shaped strong oscillation of the plasma with small wavenumbers $k_\parallel = \mathrm{O}(0.001\mathrm{cm}^{-1})$ is found. It propagates with a phase velocity of (2-3) times the ion-sound velocity C_s. Hence, the observed low frequency oscillation can be interpreted as 'potential relaxation instability' (PRI) of the unstable DL. This phenomenon has often been described in the context of DLs and should not be confused with ion-sound waves[9]. In addition, for $T_i/T_e = 1/10$, as in the KIWI-device, Landau-damping suppresses the global propagation of ion-sound waves.

Besides the fundamental frequencies f_D and f_P (drift-wave and PRI), the discrete power spectra show combination frequencies $f_D \pm f_P$ due to their interaction (Figure 1). For more complicated situations, bispectral analysis has been applied to distinguish between self-excited modes and waves arising from nonlinear interaction. Figure 2 shows a typical bicoherency spectrum: Nonlinear coupling between the PRI, the drift wave and its higher harmonics up to order three is clearly indicated by peaks at frequency resonance points $f_1 \pm f_2 = f_{1,2}$. The wavenumber analysis of the data, however, shows that the analogous wavenumber resonance-condition $k_1 \pm k_2 = k_{1,2}$ is not fulfilled. Therefore, the coupling process cannot be considered as resonant three-wave interaction. It rather appears to be a nonresonant, parametric modulation of the drift-wave by low-frequency electron-pressure and density oscillations.

Using Taken's theorem[10], the phase space of a dynamical system can be reconstructed from a single observed observable. We have calculated the dimensionality of phase space attractors for several different control parameter values U_d, where we have used the correlation-integral algorithm[11] with $N = 15000$ vectors to ensure a small statistical error. The resulting uncertainty is estimated with roughly $\Delta D_2 = 0.2$. The final result gives the correlation dimension D_2 as a function of the drift voltage U_d as displayed in Figure 3. For comparison, the earlier results[4] are shown in the same figure. The onset of AR is used as reference point for direct comparison. First, we find an excellent agreement between the D_2-values up to the onset of AR. Even the dip just before the onset of AR is reproduced. After the onset of AR, the dimensionality increases rapidly in both cases. In conclusion, the attractor in the coupling of PRI and drift-waves approaches values lower than $D_2 = 5$ and seems to be independent from experimental boundary conditions.

To characterize the transition process more clearly, slightly different discharge condition have been chosen. A transition from monochromatic spectra with a single drift-mode to complicated broadband spectra is found, again accompanied with AR. Figure 4 shows the corresponding dimensionalities D_2. In addition, we have calculated the largest Lyapunov-exponent λ from our experimental time series[12]. The monochromatic state appears as one-dimensional with a Lyapunov-exponent close to zero, as expected. With increased drift voltage, the PRI is excited and again, the described interaction process has a low-dimensional attractor ($3 \leq D_2 \leq 5$) with positive Lyapunov-exponents λ. After the onset of AR, both D_2 and λ diverge. For characteristic values of U_d, a three-dimensional reconstruction of the attractors is also displayed in Figure 4.

4. Conclusion

The KIWI-experiments have shown that previously observed low-dimensional attractors in the interaction of drift-waves and ion-sound-like waves are reproducable in the very details and seem to be independent from the experimental arrangement. The ion-sound-like wave is identified as potential-relaxation instability. Its interaction process with drift-waves is a nonresonant parametric modulation and not a three-wave decay scheme.

5. Acknowledgements

We thank Prof. Alan Wolf for the allowance to use his programs for the determination of Lyapunov-exponents. This work has been supported by the Deutsche Forschungsgemeinschaft under contract Pi185/2-1.

6. References

[1] M. Persson and H. Nordman, *Phys. Rev. Lett.* **67**, 3396 (1991)
[2] J.-M. Wersinger, J. M. Finn and E. Ott, *Phys. Fluids* **23**, 1142 (1980)
[3] D. Biskamp and H. Kaifen, *Phys. Fluids* **28**, 2172 (1985)
[4] G. Ströhlein and A. Piel, *Phys. Fluids B* **1**, 6 (1989)
[5] J. S. Levine and F. W. Crawford, *J. Plasma Phys.* **23**, 359 (1980)
[6] M. Yamada and H. W. Hendel, *Phys. Fluids* **21**, 1555 (1978)
[7] J. M. Beall, Y. C. Kim and E. J. Powers, *J. Appl. Phys* **53**, 3933 (1982)
[8] Y. C. Kim, J. M. Beall, E. J. Powers and R. W. Miksad, *Phys. Fluids* **23**, 258 (1980)
[9] S. Iizuka, P. Michelsen, J. Juul Rasmussen, R. Schrittwieser, R. Hatakeyama, K. Saeki and N. Sato, *Phys. Rev. Lett.* **48**, 145 (1982)
[10] F. Takens, *Lecture Notes in Mathematics Vol. 1125* Springer, Berlin (1985)
[11] P. Grassberger and I. Procaccia, *Phys. Rev. A* **28**, 2591 (1983)
[12] A. Wolf, J. B. Swift, H. L. Swinney, J. A. Vastano *Physica D* **16**, 285 (1985)

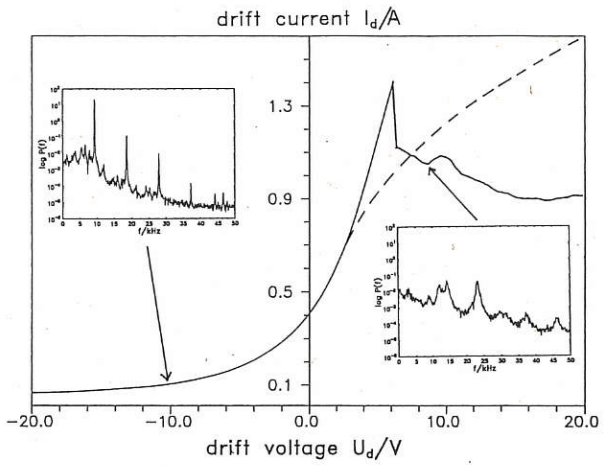

Figure 1: Transition to AR with corresponding power spectra.

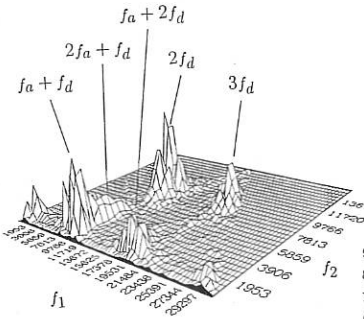

Figure 2: A typical bicoherency spectrum.

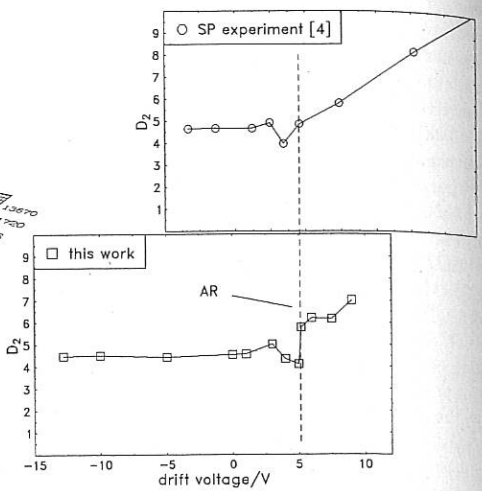

Figure 3: Correlation dimension D_2 versus U_d in comparison with [4].

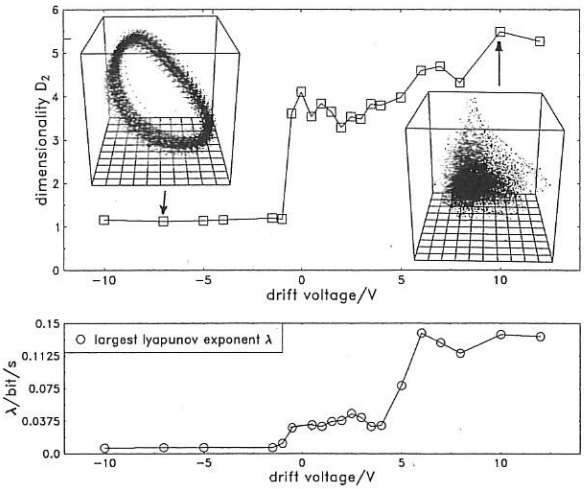

Figure 4: Correlation dimension D_2 and largest Lyapunov-exponent versus U_d.

Ion–Holes Associated with Rarefactive Ion Acoustic Pulse

A.K. Singh & Y.C. Saxena
Institute for Plasma Research
Gandhinagar, 382 424, India

The KdV equation for ion acoustic waves admits soliton-type of solutions. A compressive perturbation is known to evolve into a soliton due to the balance between the nonlinear steepening and dispersive effects [1–5]. The balance between non–linearity and dispersion cannot be achieved for rarefactive perturbations and these perturbations do not evolve into solitons. The present paper reports the observations on launching and evolution of large amplitude rarefactive ion acoustic waves in a linear unmagnetised plasma. Observations on the ion velocity distribution associated with these large amplitude waves are also presented. Particle trapping and modification of distribution function in the presence of rarefactive pulse is observed. There are also indications of phase space vortex formation in the wave train observed at the trailing end of the pulse.

The experiments were carried out in a linear, unmagnetised, uniform, plasma 50 cms dia and 120 cm in length. The chamber was pumped to a base pressure of 10^{-5} cms and operated at neutral argon pressure of 10^{-4} torr. The average plasma density obtained is $5 \times 10^8 cm^{-3}$, $T_e \sim 4.0$ eV, $T_i \sim 0.2$ eV and $C_s \sim 3.0 \times 10^5$cm/sec. Waves were launched using a square pulse of rise time $\sim \omega_{pi}^{-1} \sim 1\mu sec$, applied to a circular grid of dia 20.0 cms, with a repetetion rate of 1 kHz.

In the experiment rarefactive pulses of different amplitudes were launched. The pulses of initial amplitude $\delta n/n \sim 1.2\%$ started out as symmetric pulse of width $\sim 5.0\lambda_D$ close to the launcher. The pulse broadened due to dispersion and damped as it moved away from the launcher. The velocity of these pulses were found to be closer to 2.94×10^5cm/sec. This is slightly smaller than the acoustic speeds. The pulses with amplitude 6% also behaved in a similar fashion. But the pulses of $\delta n/n \sim 7.0\%$ and more showed some additional features. These pulses also started out as symmetric pulses very close to the launcher and were dispersed and damped as they moved away from the launcher. The leading edge of the pulse becomes sharper than the trailing edge. At a distance about 25–30 λ_D the pulses start becoming asymmetric i.e. have shoulders of unequal amplitude. Beyond this the pulse splitted into two separated by a local maxima. Fig. (1) shows the traces of density variation for a wave with initial amplitude 9%. In this case the split is observed very close to the launcher itself. The pulses after splitting moved at different speeds, one moving at a speed slightly lower than the acoustic speed. A further propagation beyond 55–60 λ_D lead to a further split into three pulses. Higher initial amplitude pulses split into even more pulses. For initial $\delta n/n \sim 9.0\%$ one of the trough was found to be moving with a speed $\sim 0.9C_s$ and the other at $\sim 1.2C_s$.

The splitting of the initial pulses into more than one pulses cannot be understood on the basis of fluid theory. These are phenomenon occuring at large amplitude of refractive pulses, having a negative potential structure, giving rise to the possibility of trapping of ions moving with speeds closer to the C_s. This would lead to wave particle interaction, modifying the particle distribution function, in the phase space. In order to investigate this phenonmenon, the ion energy distribution was measured at various positions in the pulse, as shown in top trace in the in fig (2), using a boxcar integrator and a three grid

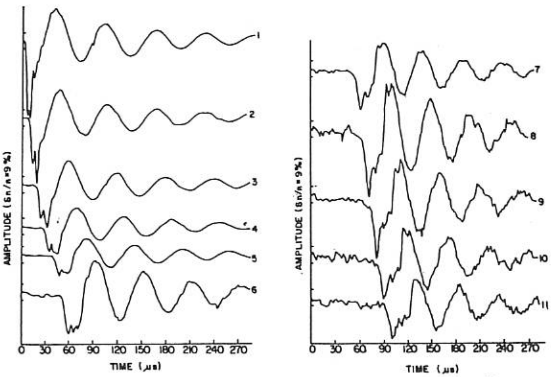

Figure 1: The density signals showing the wave propagetion for initial amplitude $\delta n/n \sim 9\%$.

retarding potential energy analyser, with a resolution better than 0.1 eV. The output of the RPA was averaged using the boxcar integrator and digitized. The collector current I(ϕ) as a function of the applied bias on the selector grid can be written as

$$I(\phi) = \int_{\phi_1}^{\infty} Aevf(x,v,t)dv$$

apart from a geometrical transparency factor. The dI/dV would be a measure of f(x,v,t). The was calculated digitally and is shown in fig. (2). Different curves have been taken at different time delays, as marked in the top trace in fig (2). The trace 1 to 6 in fig. (2) show a strong modification of the energy distribution of ions near an energy of 0.8 eV from the center of the distribution. These modifications are similar to those obtained in the numerical calculation of Sakanaka [8], where the trapping was observed in a beam interaction.

In fig. (1), the first pulse is the main pulse of the rarefactive wave. This pulse is a negative potential structure and its trailing edge resembles to a shock like structure. It was found that alongwith this symmetric pulse a low frequency ($\sim$ 30 kHz $\ll f_{pi}$) appears in the trailling edge. These oscillations appear as a wave train in the trailing edge moving with speed slightly slower than C_s. Once formed these structures travel in the system to the end of the device, without any appreciable change in the width. These oscillations do not agree to the usual Airy function type of response as reported by Ikezi et al. (1973). The Airy response was seen at a frequency ($\sim \omega_{pi}^{-1}$). This is 300 kHz for the parameter of our experiment. Also Ikezi et al. (1973) had demonstrated the period of Airy type of oscillations increase with propogation distances. No change in the time period was seen in the present experiment.

In an experiment by Saxena et al. [6], a rarefactive pulse was found to fission into several pulses. In this experiment the fissioning occured at a distance of about 65–70 λ_D whereas in the present experiment the fissioning occured very close to the launcher $\sim 25\lambda_D$ and for higher amplitude pulses this occured even further closer to the launcher. The rise time of the pulses were slow in the experiment of Sxaena et al. [6].

The measurement of energy distribution of ions showed strong modification near the phase velocity of waves. This indicates the formation of phase space holes due to trapping

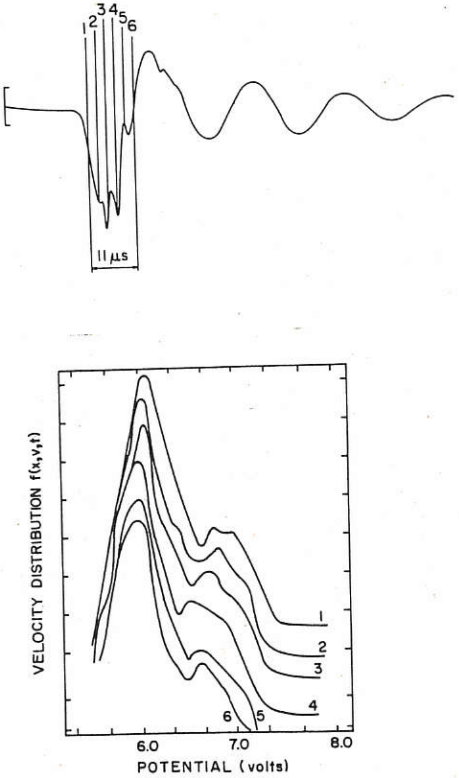

Figure 2: The top trace shows the time delays at which energy distributions were measured in the pulse. The traces in the bottom show the modified distributions of ions.

of ion in the potential of the wave. These measurements are similar to those of Pécseli et al. [9] in a double plasma device obtained for a shock wave formed by two beam interaction. The oscillations in the trailing edge and its propogation also indicate the trapping of particle in the phase space. The launched perturbation is at the time scale $\sim \omega_{pi}^{-1}$. Initial discontinuity in the density during the impulse leads to the formation of a sharply peaked electric field. The electric field would accelerate ions from this region and create a local depletion of ions. This situation is similar to one in numerical calculation by Hasegawa and Sato [11] for two beam instability. In their case the electric field generated by the initial discontinuity in density evolved into a shock followed by a hole in the ion phase space. These holes appeared as regions of density depletions in front of the shock very similar to the oscillations in trailing edge in our case. In the above mentioned numerical calculation, stable holes with width $\sim 100\lambda_D$ were observed. Widths observed in present experiments are $\sim 200\lambda_D$. Hasegawa and Sato [11] showed that a negative potential structure in the presence of a current in the plasma evolved into a double layer, which is known to be a BGK mode (Bernstein et al. [7]). The formation of double layer is facilitated by reflection of electrons from the wave potential. This impedes the current and leaves behind an ion rich region. In the absence of this current the region remains depleted of ions and a hole in the phase space is formed. The measurement of f(v) in the main pulse shows the modification of the ion distribution and provides a strong evidence for the formation of a hole in ion phase space. This hole is asymmetric hole with shoulders of unequal amplitude. A stable hole with width $\sim 200\lambda_D$ is also observed in the trailing edge of the perturbations. The behavior of these holes are similar to those obtained in the calculations of Sakanaka [8]. In his case also Airy function type of oscillations were not observed. This agrees quite well with our measurements. However there is no sustained beam in our experiment.

In conclusion rarefactive ion acoustic waves investigated in the linear unmagnetised plasma have shown several interesting characteristics of excitation and propagation. The waves with amplitude $\sim 1.2\%$ and more show several features which donot agree with the KdV equation. The rarefactive perturbations excited by a fast step ($\omega \sim \omega_{pi}$, are found to evolve into holes in ion phase space. Both asymmetric and symmetric holes, have been observed in the presence of these large amplitude rarefactive ion acoustic waves.

References

1. H. Ikezi, R. Taylor and D. Baker, Phys. Rev. Lett. **25** (1975) 11.
2. Lonngren K. E., Khazei M., Gabl E. F. and Bulson J. M., Plasma Physics,**24** (1982)
3. Ikezi H., "Solitons in Action", Lonngren K. E. and Scott A. eds., (1978) p153, Academic Press, New York.
4. Tran M. Q., Physica Scripta **20**, (1979) 317.
5. Lonngren K. E., Plasma Physics **25**, (1983) 943.
6. Y. C. Saxena, S. K. Mattoo, A. N. Sekar and V. Chandna, Phys. Lett. **84 A**, (1981) 71.
7. Bernstein I. B., Green J. M. and Kruskal M. D., Phys Rev. **108** (1957) 546.
8. Sakanaka,P. H., Phys. Fluids **15** (1972) 1323.
9. Pécseli H. L., Trulsen J. and Armstrong R. J., Physica Scripta **29** (1984) 241.
10. Ikezi H., Kiwamoto Y., and Lonngren K.E., Plasma Phys. **15** (1973) 1141.
11. Hasegawa A., and Sato T., (1982), Phys. Fluids,**25**, 832.

Cascading Bifurcations to Chaos in a Current-Carrying Ion Sheath

Mitsuo Kono, and Akio Komori†

Research Institute for Applied Mechanics,
Kyushu University, Kasuga, Fukuoka 816, Japan

†Interdisciplinary Graduate School of
Engineering Sciences,
Kyushu University, Kasuga, Fukuoka 816, Japan

Recently, cascading bifurcations followed by the onset of chaos were observed in a current-carrying plasma sheath when an external periodic oscillation was applied to a fine-meshed grid which divided the plasma produced by dc discharge. In this experimental set-up, the potential at the grid is negatively biased to the extent that electrons cannot penetrate up to the grid and, therefore, the resultant sheath is an ion sheath which is detatched from the plasma by an ordinary sheath. The ion sheath on both sides of the grid forms a potential well in which the ions oscillate to induce a primary motion responding to the external oscillation.

The structure of the ion sheath can be studied based on an ion fluid:

$$\frac{\partial n}{\partial t} + \frac{\partial}{\partial x} nv = 0, \tag{1}$$

$$\frac{\partial v}{\partial t} + v\frac{\partial}{\partial x} v = \frac{e}{M} E, \tag{2}$$

$$\frac{\partial E}{\partial x} = 4\pi e n. \tag{3}$$

For the stationary sheath, the flux is constant:

$$nv = I_0. \tag{4}$$

From eqs. (2) and (3), we have

$$\frac{d}{dx}\left\{\frac{I_0^2}{n} - \frac{E^2}{8\pi M}\right\} = 0, \tag{5}$$

which gives

$$n = \frac{n_0}{1 + (A/2)(E^2/E_0^2 - 1)}, \tag{6}$$

where $A = (\omega_{pi} E_0 / 4\pi e n_0 v_0)^2$. Substituting eq. (6) into the Poisson equation (3), we have an implicit expression for E with respect to x as

$$x - x_0 = \frac{eE_0}{M\omega_{pi}^2}\left\{(1 - A/2)(E/E_0 - 1) + (A/6)(E^3/E_0^3 - 1)\right\}. \tag{7}$$

The electric potential is expressed in terms of E as

$$\phi - \phi_0 = -\frac{1}{2}\frac{eE_0^2}{M\omega_{pi}^2}(E^2/E_0^2 - 1)\{1 + (A/4)(E^2/E_0^2 - 1)\}. \tag{8}$$

For a large electric field we have, from eqs. (7) and (8),

$$E/E_0 \simeq \left(\frac{6}{A}\frac{x - x_0}{\frac{eE_0}{M\omega_{pi}^2}}\right)^{1/3}, \tag{9}$$

$$\phi - \phi_0 \simeq -\frac{1}{2}\frac{eE_0^2}{M\omega_{pi}^2}\frac{A}{4}(\frac{E}{E_0})^4, \tag{10}$$

which are combined to give an explicit expression of the Child-Langmuir law of space-charge limited current in a plane diode:

$$\frac{\phi_0 - \phi}{\frac{eE_0^2}{M\omega_{pi}^2}} \simeq \frac{6}{8}^{4/3}\left(\frac{x - x_0}{\frac{eE_0}{M\omega_{pi}^2}}\right)^{4/3}\left(\frac{4\pi e n_0 v_0}{\omega_{pi} E_0}\right)^{2/3}. \tag{11}$$

It is worthwhile to note that for small values of current ($4\pi e n_0 v_0 < \sqrt{2}\omega_{pi} E_0$) density becomes singular, as is seen from eq.(6), and the electric field and the potential are both multivalued. This reflects the fact that the Child-Langmuir ion sheath is detached from the main part of the plasma by the sheath to which warm electrons penetrate to some extent.

Now we consider the ion dynamics in the above ion sheath, which is described by the following equations of motion:

$$\frac{dx}{dt} = v, \tag{12}$$

$$\frac{dv}{dt} = \frac{e}{M}(E_0 - E). \tag{13}$$

Differentiating eq.(3) with respect to t, and invoking an introduction of a damping term which ensures a well-defined attractor and E to be replaced by its asymptotic value $E \simeq -\frac{\nu}{\omega_p^2} J (J = 4\pi e n_0 v)$, we obtain

$$\frac{d^2J}{dt^2} + \frac{J}{1 + A[\nu J + \nu^2 J^2/2]} + \nu \frac{dJ}{dt} + \Omega E_{ext} \cos(\Omega t) = 0, \tag{14}$$

where $\omega_p t$, ν/ω_p and Ω/ω_p are replaced by t, ν and Ω, respectively. Equation (14) reduces to a form of Duffing's equation by a simple transformation when A is small and the second term can be expanded with respect to A, indicating that eq.(14) exhibits rich varieties of dynamical behavior. Equation (14) is solved numerically by changing E_{ext} with A, ν and Ω fixed or changing Ω with A, ν and E_{ext} fixed. In both cases we observe the cascading bifurcations to chaos. Figure 1 shows trajectories in $(J\ ,\ \dot{J})$ space and the Fourier spectrum of $J(t)$ for various values of E_{ext} with $A = 1.6$, $\nu = 0.25$ and $\Omega = 0.615$. In this case the period-doubling bifurcations are followed by the onset of chaos as E_{ext} increases. Further increase in E_{ext} leads to period-tripling bifurcations to chaos. Then the system reverts back to period doubling bifurcations.

A similar series of bifurcations is obtained in the case when the frequency of the external oscillation is changed with the fixed amplitude $E_{ext} = 3.0$ for $A = 1.6$ and $\nu = 0.25$.

The above scenario of bifurcations to chaos is also applicable in those cases with different values of A and ν. Which appears first, period-doubling or period-tripling, depends on the value of the parameters A and ν. For example, when A and ν are chosen as 1.0 and 0.1, respectively, with $E_{ext} = 5.2$ fixed, period-tripling appears first, and then period doubling follows as the frequency increases as is shown in Fig.2.

The bifurcation sequences revealed above agree well with the experimental results by Komori et al. Although we have not examined the mathematical structure of the chaos obtained under eq.(14), we may say that the underlying physics of the observed chaos can be explained by our theory.

Fig. 1

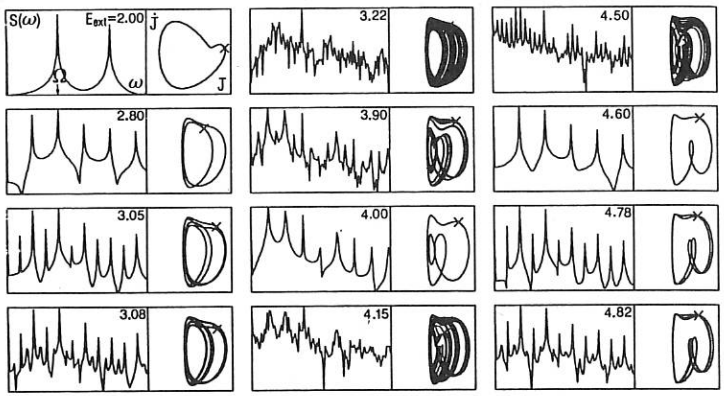

Fig. 2

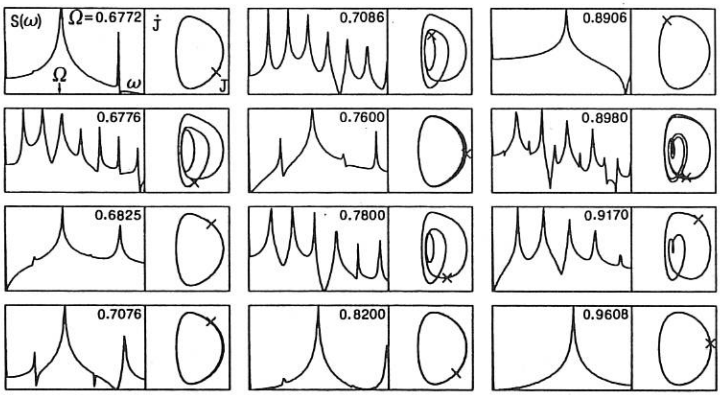

10-56

EXPERIMENTAL MEASUREMENTS OF CASCADING BIFURCATIONS TO CHAOS IN AN ION SHEATH

A. Komori, M. Kono*, T. Norimine, M. Tanaka and Y. Kawai
Interdisciplinary Graduate School of Engineering Sciences,
Kyushu University, Kasuga, Fukuoka 816, Japan
*Research Institute for Applied Mechanics,
Kyushu University, Kasuga, Fukuoka 816, Japan

Abstract Cascading bifurcations to chaos are investigated experimentally and theoretically in a current-carrying stable ion sheath. A dc plasma current is required to produce an electron-depleted thick sheath on a grid, which obeys the Child-Langmuir law of space-charge-limited current in a diode. Bifurcation cascade and chaotic behavior are exhibited when an external periodic oscillation is applied to the grid, and is in good agreement for the first time with a theory, which describes ion dynamics in a nonlinear potential well, formed as an ion sheath on the both sides of the grid. A fractal dimension predicted by the theory is verified by the experiment.

1. Introduction

It is of current interest to investigate nonlinear physical systems which exhibit chaotic behavior. Universal characteristics of chaos have been observed in experiments conducted on a variety of nonlinear media as well as in numerical simulations. Recently, several experiments have been reported on chaotic behavior in plasma systems /1, 2/. Two routes to chaos, period doubling and intermittent chaos, are demonstrated in these experiments, and fine structures such as periodic windows are also observed. However, to our knowledge, the experimental observations of chaotic behavior in plasmas are not clearly understood and are still open to studies of their underlying physics.

The present paper gives an experimental study of cascading bifurcations to chaos in a current-carrying stable plasma, and compares it with a theory which describes our nonlinear system.

2. Experimental apparatus

The experiment is performed in a large, unmagnetized plasma device 70 cm in diameter and 120 cm in length, equipped with multidipole magnets for surface plasma confinement, as shown in Fig. 1 /2, 3/. An argon plasma produced by a dc discharge between filaments and the chamber wall is divided by a fine-meshed grid made of 0.05 mm diam stainless-steel wires spaced 0.5 mm apart. Typical parameters of the plasma designated T are $n_0 = (0.9 - 7) \times 10^8$ cm^{-3}, $T_e = 0.3 - 0.7$ eV and $T_i \simeq 0.1$ eV, where n_0 is the plasma density, and controlled by changing the heater currents. At first, the density of the plasma D, n_{0D}, is chosen to be less than n_0 by about one order of

magnitude, so that the plasma space potential ϕ_{0D} of the plasma D is higher than the plasma space potential ϕ_0 of the plasma T by a few volt. The symbol $\Delta\phi$ denotes the potential difference between ϕ_{0D} and ϕ_0 ($\Delta\phi = \phi_{0D} - \phi_0$). To drive a dc plasma current, a dc voltage V_0 is applied between the grid and a 12 cm diam target, that is, the grid and target are negatively and positively biased, respectively, as shown in Fig. 1. Plane Langmuir probes 6 mm in diameter are used to measure the plasma parameters and their fluctuations. The plasma space potentials are measured with emissive probes, and the ion temperature in the two plasmas is obtained with Faraday cups. The gas pressure p is usually kept at $\sim 2 \times 10^{-4}$ Torr, and is sometimes varied in the range of $(1-4) \times 10^{-4}$ Torr. The time-averaged value I_0 and fluctuating component I of the plasma current are observed from the voltage drop across the resistor R_1.

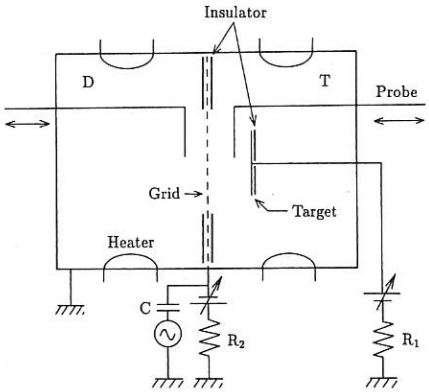

Fig. 1: Schematic of experimental apparatus. $R_1 = R_2 = 50\ \Omega$ and $C = 3.3\ \mu$F.

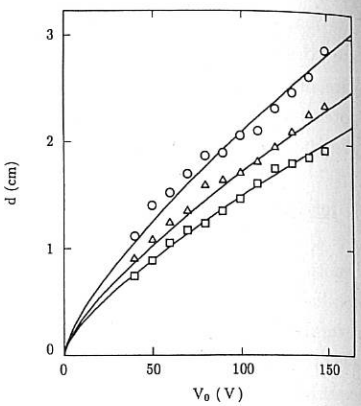

Fig. 2: Dependence of d on V_0.

3. Experimental results and discussion

Figure 2 shows the V_0 dependence of the sheath thickness d of the sheath S_{GT} on the grid, facing the plasma T. Circles, triangles, and squares are obtained at $I_0 = 1$, 1.5 and 2 mA, respectively, and solid lines represent the curves proportional to $V_0^{3/4}$. There is good agreement between the solid lines and measured d's. Thus, the potential profile in the sheath S_{GT} is confirmed to be described by the Child-Langmuir law of space-charge-limited current in a plane diode: $I_0 = (4\sqrt{2}\epsilon_0 A/9d^2)(e/m_i)^{1/2}V_0^{3/2}$, where A is the area of the grid and m_i is the ion mass. The sheath thickness d obtained experimentally is found to agree with the thickness given by this equation within a factor of 3. This factor is associated with the reflection of ions from the plasma D to the plasma T by $\Delta\phi$ /3/.

If an extremely electron-depleted sheath S_{GT} is formed on the grid, an coherent instability, associated with an ion transit in the sheath, appears for wide parameter

regimes, as shown in the top traces of Figs. 3(a) and 3(b) /3/. An important point is that there is a threshold $\Delta\phi$ ($= \phi_{0D} - \phi_0$) to excite the instability /3/, and therefore, we can stabilize the plasma by decreasing $\Delta\phi$, that is, by increasing n_{0D}. Figure 3(a) indicates that $\Delta\phi$ becomes small with an increase in n_{0D}. In this figure, n_{0D} is varied from 7×10^7 cm^{-3} to 5×10^8 cm^{-3}, while n_0 is kept at $\sim 7 \times 10^8$ cm^{-3}. Apparently, the decrease in $\Delta\phi$ leads to the stabilization of the instability, as shown in Fig. 3(b). The ion sheath S_{GT} is found to be affected little by the change of n_{0D}, so that there is the extremely electron-depleted ion sheath on the grid, as before, whose potential profile is described by the Child-Langmuir law. When an external periodic oscillation whose amplitude is denoted by V_{ext} is applied to the grid under such a condition, a sinusoidal perturbation at the driving frequency f_1 can be induced in the plasma current. Nonlinear behavior is observed by gradually increasing f_1 from 100 kHz and keeping V_{ext} at $\sim$4.7 V. The first subharmonic appears at $f_1 = 139$ kHz, and a very clear period-doubling sequence is obtained, as shown in Figs. 4(a)-4(c). Further period doublings are hardly measured, possibly because the rapid convergence rate of the doubling sequence makes it very difficult to observe them. Increasing f_1 further produces chaotic behavior. This state is characterized by broadband noise in the frequency spectrum, as shown in Fig.

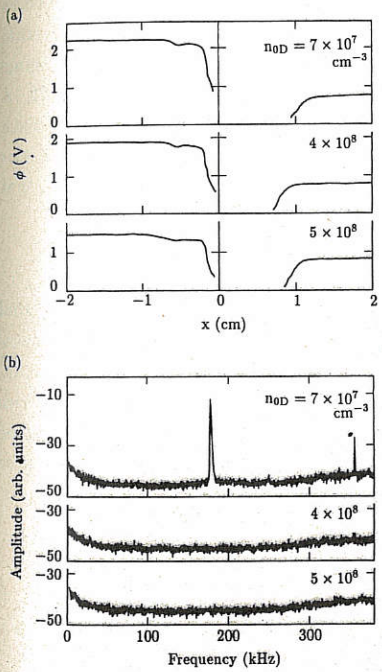

Fig. 3: Effects of n_{0D} on (a) the potential ϕ around the grid and (b) on the instability.

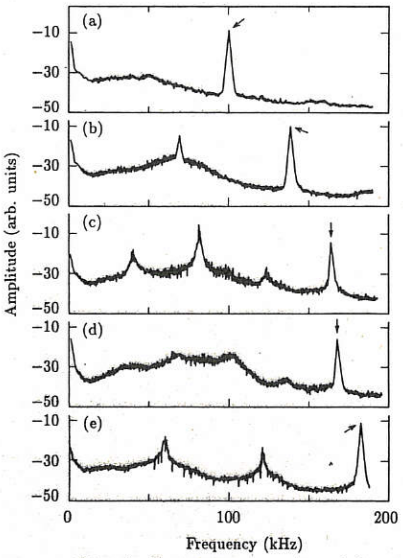

Fig. 4: Frequency spectra of I.

4(d) /2/. The correlation dimension ν is obtained to be 1.54±0.22 in this chaotic regime, suggesting that the number of degrees of freedom is small in our system. Further increases in f_1 cause period tripling [Fig. 4(e)]. Thus, it is clearly demonstrated that the bifurcation sequence leading to chaos in our system is the same as Feigenbaum's period-doubling route to chaos.

Nonlinear behavior of the oscillations is also realized by increasing n_0 with f_1 and V_{ext} fixed or increasing V_{ext} with f_1 and n_0 fixed. Although a set of cascading bifurcations to chaos is obtained when p is changed in the range of $1 \times 10^{-4} \lesssim p \lesssim 4 \times 10^{-4}$ Torr, whether p itself is relevant to the nonlinear behavior is not clear since n_0 is varied with the change of p. These observations are confirmed to be reproducible in our experiments. However, they are very sensitive to the parameters such as n_0, V_{ext}, and so forth. For example, which appears first, period doubling or period tripling, depends on these parameters. Furthermore, a mixture of period doubling and period tripling bifurcations is sometimes observed. Thus, there are many scenarios of nonlinear behavior of the oscillations, depending on the parameters.

A theory of cascading bifurcations to chaos in a current-carrying ion sheath has been developed by Kono *et al.* /4/. They have derived the differential equation with three dimension, which governs ion dynamics in an ion sheath potential well formed on the both sides of the grid. Bifurcations to chaos of I are obtained when an external oscillating term is added to the equation. The correlation dimension in the chaotic regime is found to be 1.55 ± 0.2 which agrees with the experimental results $\nu = 1.54 \pm 0.22$. A rich variety of nonlinear behavior is also observed, depending on the parameters. Such a good agreement between experiment and theory indicates that the nonlinear behavior in our system is surely caused by the ion dynamics in an anharmonic potential well, that is, in the Child-Langmuir sheath.

4. Conclusions

A set of cascading bifurcations and a chaotic state in the presence of an external periodic oscillation are experimentally demonstrated in a stable plasma, and a physical model explaining these experimental results is introduced briefly. The most important point of this study is that the nonlinearity of a thick ion sheath on a grid causes a rich variety of behavior in our system. The thick ion sheath on the grid is formed by driving a dc plasma current, and described by the Child-Langmuir law of space-charge-limited current in a plane diode.

References

/1/ P. Y. Cheung, S. Donovan and A. Y. Wong, Phys. Rev. Lett. **61**, 1360(1988).
/2/ N. Ohno, M. Tanaka, A. Komori and Y. Kawai, J. Phys. Soc. Jpn. **58**, 28(1989).
/3/ N. Ohno, A. Komori, M. Tanaka and Y. Kawai, Phys. Fluids **B3**, 228(1991).
/4/ M. Kono, H. Nakashima and A. Komori, J. Phys. Soc. Jpn. **61**, 407(1992).

NONLINEAR EVOLUTION AND LOCALIZED STRUCTURE OF UNSTABLE WAVES IN AN ELECTRON-BEAM PLASMA

K. YAMAGIWA, T. MIENO and M. TANAKA*
Department of Physics, Faculty of Science, Shizuoka University, Shizuoka 422, Japan.
*Department of High Energy Engineering Science, Interdisciplinary Graduate School of Engineering Sciences, Kyushu University, Kasuga, Fukuoka 816, Japan.

Since the pioneer work on nonlinear phenomena of Langmuir waves done by Zakharov[1], considerable progress has been made in this area[2]. There have been growing interests[3)-7)] in nonlinear evolution of high frequency modes in an unstable plasma. The dispersion properties of unstable waves there are quite different from those in a stable plasma. We[7] have experimentally investigated nonlinear wave phenomena of unstable electron beam waves and briefly reported the formation of a localized structure. In this paper, we will present experimental results on one dimensional nonlinear evolution of initial disturbance and generation of a soliton-like excitation, and discussed these with the theory developed by Yajima and Tanaka[5].

A target plasma is produced by a dc discharge in a so called multi-dipole device. The working pressure of Ar gas for the discharge is adjusted at about 1×10^{-5} Torr to reduce collisional loss of beam electrons with neutral particles. We used a pulsed electron beam with duration $7\mu s$, and injected it into a target plasma along an external magnetic field (=80G), because a dc beam injection strongly changes the initial plasma parameters. Figure 1 shows the experimental setup. The beam current passing through the plasma is monitored by a collector located at the opposite side of the beam gun. Density fluctuations $\tilde{n}_e$ are picked up with plane

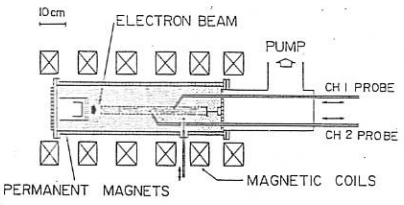

Fig.1 Experimental setup.

probes (Mo-disks of 3mm in diameter), and captured by a fast digitizing oscilloscope (HP54111D), whose bandwidth is up to 250MHz in the single shot mode and 500MHz in the repetitive mode. Typical conditions are as follows; plasma density $n_e \simeq 3\times10^8 cm^{-3}$, beam density $n_b \simeq 10^{-3} n_e$, beam velocity $v_b/v_t \simeq$ 5~6 (normalized by the themal velocity v_t, beam energy= 40~60eV), and wavelength $\lambda \simeq 2cm$ (< beam diameter 4.5cm).

When an electron beam is injected into the plasma, the plasma becomes unstable in a frequency range lower than the plasma frequency and intense noises with $\tilde{n}_e/n_e \leqq 0.1$ are observed along the beam path ($z>20cm$). The noises are thought to be electron beam instabilities[7,8]. In order to observe evolution of unstable beam waves we repetitively inject a pulsed electron beam and then a small rf signal as an initial disturbance is applied to the control grid of the beam gun. The spatial development of rf-induced unstable waves is measured by interferometry method with a boxcar integrator.

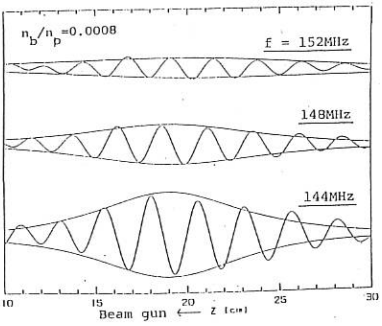

Fig.2 Spatial evolution of rf-induced perturbations, where n_b/n_e=0.0008 and v_b/v_t =5.0. The envelopes are curves described by eq.(2).

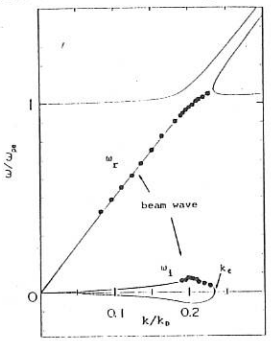

Fig.3 Dispersion relation of unstable modes in the initial stage of propagation (closed circles) and the calculation from eq.(1).

Examples are shown in Fig. 2. In the initial stage of propagation ($z \leqq 14cm$), the excited waves are linearly unstable, that is, exponentially grow along the beam path, but are stabilized in the nonlinear stage and attenuated, producing a symmetric envelope. Dispersion data extracted from the linear phase are plotted with closed circles in Fig. 3. The temporal growth rate ω_i is given by a product $|k_i v_g|$, where k_i is the

linear growth rate of unstable beam waves and v_g the group velocity. Solid curves indicate the dispersion relation for an electron-beam plasma system[8]:

$$1 = \omega_{pe}^2[\ 1/(\omega^2-k^2v_t^2) + (n_b/n_e)/(\omega-kv_b)^2\ ] \qquad (1)$$

The equation has a pair of complex conjugate roots, $\omega_r \pm j\omega_i$, for a fixed wave number k less than the critical value $k_c \simeq (\omega_{pe}/v_b)$. One of these roots, $\omega_r + j\omega_i$ corresponds to unstable waves. Experimental data agree very well with this unstable mode. Another root, $\omega_r - j\omega_i$, is responsible for the attenuation region ($z \simeq 20 \sim 30$cm in Fig. 2).

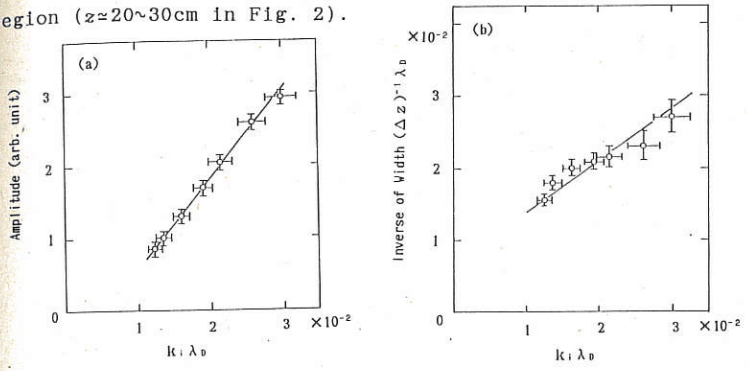

Fig.4 (a)The wave amplitude vs the linear growth rate k_i (b)the inverse of spatial widths vs the linear growth rate k_i.

As the wave frequency increases from 144MHz to 152MHz (critical frequency≃154MHz), the growth rate k_i decreases and the amplitude becomes small. On the other hand, the width of the wave envelope Δz becomes broad. Figures 4(a) and 4(b) show the amplitude vs k_i and $(\Delta z)^{-1}$ vs k_i, respectively. We found that the envelope $A(z)$ is empirically described by

$$A(z) \propto k_i \mathrm{sech}[k_i(z-z_0)] \qquad (2)$$

where z is the distance from the beam gun, z_0 the position of the maximun amplitude. Equation (2) shows the localized structure of unstable beam waves is characterized by the

initial growth rate λ_1. Figure 5 shows that how a wave grows and propagates, when a wave packet with half width of 100ns is generated by applying a small perturbation, where the digitizing oscilloscope is used in an average mode to improve the signal-to-noise ratio. The average drift velocity $v_g=2.6\times10^8$cm/sec agrees with the group velocity obtained from the data in Fig. 3. The amplitude of the wave packet spatially changes according to the localized structure given by eq.(2). It is also interested that the wave packet separates into fast and slow parts, and appears to produce a new packet in the down stream region.

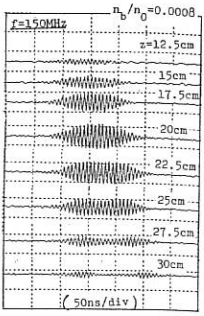

Fig.5 Spatial evolution of rf-induced wave packets.

Yajima and Tanaka[5] investigated nonlinear evolution of unstable electron beam waves with a synergetic approach, and derived a coupled nonlinear Schrödinger equation with an additional term of beam correction. They showed that localized modes, to be called soliton-like excitations, can exist in an electron-beam plasma. Yajima and Wadati[6] also showed solitons arise as the competition between instability and nonlinearity. The present observations are consistent with their results.

References

1) V. E. Zakharov, Sov. Phys. JETP **35** (1972) 908.
2) M. V. Goldman, Rev. Mod. Phys. **56** (1984) 709.
3) A. Y. Wong and P. Y. Cheung, Phys. Rev. Lett. **52** (1984) 1222.:P. Y. Cheung and A. Y. Wong, Phys. Fluids **28** (1985) 1538.
4) T. Intrator, C. Chan, N. Hershkowitz and D. Diebold, Phys. Rev. Lett. **53** (1984) 1233.
5) N. Yajima and M. Tanaka, Prog. Theor. Phys. Suppl. No.94 (1988) 138.
6) T. Yajima and M. Wadati, J. Phys. Soc. Jpn. **59** (1990) 3237.
7) K. Yamagiwa, K. Tokuda and T. Mieno, Proc. Int. Conf. Plasma Phys., (held at New Delhi, Nov. 22-28, 1989) 1021.
8) R. J. Briggs, "*Electron-Stream Interaction with Plasmas*", Research Monograph No.**29**(1964) M.I.T. Press.

Observation of two wave induced chaos in a magnetized plasma

A.Fasoli, P.J.Paris, M.Q.Tran, and F.Skiff+

Centre de Recherches en Physique des Plasmas, Association Euratom-Confédération Suisse, Ecole Polytechnique Fédérale de Lausanne, CH-1007 Lausanne, Switzerland

Introduction

The problem of wave induced stochasticity in plasmas is being studied extensively because of its general interest in chaotic dynamics and of its possible direct consequences in space and laboratory plasmas, such as anomalous transport and non-linear heating and particle acceleration [1].

Several theoretical investigations have been performed in the recent past, based mainly on hamiltonian single particle models, which predict the transition to stochasticity in terms of the wave amplitude and spectrum [2]. The majority of these theories are non self-consistent, that is, do not take into account possible mutual interactions between wave and particles. Self-consistency characterizes actual experiments, in which non-linear wave-wave interactions, in the case of several modes in the plasma, are also naturally present.

It has been shown theoretically and experimentally [3,4], that in a magnetized plasma a wave propagating at a finite angle with respect to the B-field can generate chaos in particle orbits and, consequently, fast ion heating.

The case of two (or more) waves propagating at different phase velocities is predicted to be more efficient for the heating: the threshold amplitude for the occurrence of chaos should be lower, due to a large number of resonances in phase space.

In our experiment we investigate the interaction between ions and two propagating electrostatic modes in a Q-machine plasma.

In particular, our aim is to perform and integrate observations of the collective ion response (wave characteristics), of ion kinetic features (modification of the distribution functions, time scale for heating) and of single particle orbit modifications (phase space transport).

Experimental set-up and diagnostics apparatus

The experiments are performed on the LMP barium Q-machine [5], a uniformly magnetized plasma column characterized by ion and electron temperatures of the order of 0.2 eV and densities in the range of 10^8-10^{10} cm^{-3}. The maximum axial B-field is 0.3 T ($f_{ci} \cong 30$ kHz). Sheath acceleration at the hot plate causes a supersonic ion drift $v_D \approx 10^5$ cm/s. Low degrees of spatial and temporal variations and fluctuations can be achieved in current operation (e.g. $\delta n/n < 1\%$).

Electrostatic ion waves ($f \approx f_{ci}$) are launched by a capacitive antenna consisting of 4 rings placed directly around the plasma column at variable relative distances and phase.

The diagnostic system is based on the technique of Laser Induced Fluorescence (LIF) [6], which provides a direct measurement of ion distributions with good spatial and temporal resolution (the latter allows time resolved measurements of f(v) and synchronous detection for $f^1(v)$).

LIF can be extended to an optical tagging method, based on the spin polarization of ground state ions [7]: sets of test-ions can thus be created and followed in their evolution in order to infer the nature of particle orbits. A schematic of the LMP machine, including the electrostatic antenna and the geometry for the LIF laser beam injection and detection systems, is shown in fig.1.

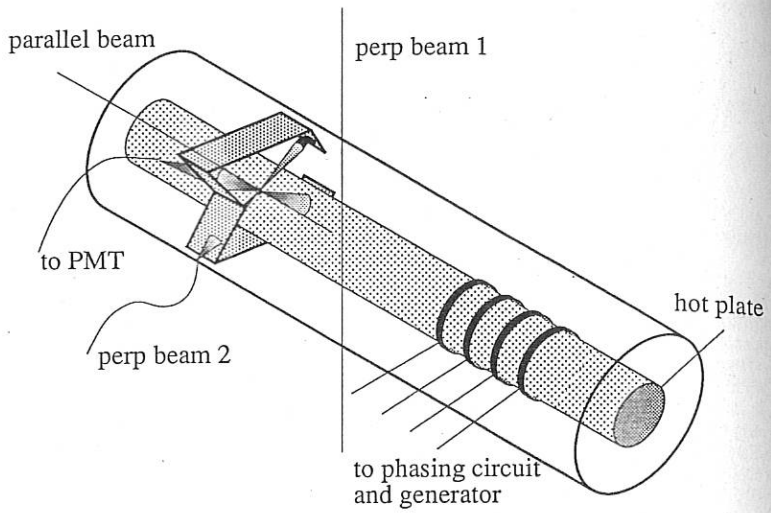

Fig.1: LMP experimental arrangement

Results and discussion

The wave spectrum excited by the 4 ring antenna in the plasma at one frequency f ($f_{ci}<f<2f_{ci}$) is composed in the parallel plane by two modes with two different phase velocities, and in the perpendicular plane by the two branches (forward and backward) of the ESICW dispersion relation [8]. In fig.2 we see the $k_{||}$ spectrum at 25 kHz ($f\approx1.1f_{ci}$), as directly evinced from the observed form of the first order perturbed distribution function. Two distinct peaks are clearly visible, corresponding to the two phase velocities $v_{\phi}1$, $v_{\phi}2$.($\Delta v_{\phi}\approx5\ 10^4$ cm/s).

The difference Δv_{ϕ} is such that on the parallel ion phase space one can consider, to a first approximation, only primary resonances and neglect the multiple island structure introduced by the non zero perpendicular wavenumber (natural cyclotron resonances should appear, spaced by $2\pi f_{ci}$; it is indeed their interaction which generates chaos in the one wave case).

The hamiltonian models predict therefore a transition to a stochastic regime when the wave amplitude is such that the two resonances start to overlap. A stochasticity parameter can be introduced: $K = 2\ (A_1^{1/2} + A_2^{1/2})$, where $A_i=e\phi_i/m(\Delta v_{\phi})^2$ is the amplitude of the mode i (i=1,2). K=1 is the threshold for the transition, in the frame of the single particle theory; in macroscopic terms, K>1 should imply a fast ion heating.

In fig.3 we plot the parallel and perpendicular ion temperatures as functions of the excitation amplitude. We notice that a threshold value exists, above which a significant heating occurs. A calibration of the wave amplitude through the ion dielectric response [9] allows us to compare the observed threshold to the theoretical prediction for the experimental wave parameters. K=1 corresponds to the shaded region on the amplitude axis of the graph. We see that, inside the error bar, mainly due to the wave amplitude calibration procedure, experiment and single particle theory agree.

By pulsing the wave excitation generator, and observing the time resolved ion distribution from the time t=0 (when the RF is started) onwards, an accurate estimation of the heating time can be achieved. More specifically, by plotting the increase in the ion temperature (or mean square ion velocity) vs. the time, if the dependence is linear, a direct estimation of the velocity space diffusion coefficient can be obtained. This is shown in fig. 4, for the case of 25 kHz and just above threshold. The resulting v-space diffusion coefficient is more than one order of magnitude larger than the collisional coefficient.

The mechanism responsible for the heating, therefore, is independent of collisional processes and can be attributed to a transition to chaos in particle trajectories. An additional proof of this mechanism comes from the tag measurements, which evidentiate an exponential separation in time of initially close ion orbits, both in velocity space and in real space.

At frequencies for which only one mode in parallel can be excited in the plasma, no heating is observed, up to amplitudes where secular perturbations of the antenna and intrinsic non-linearities (e.g. harmonic generation) become effective. The case of two waves is then experimentally demonstrated to be more favorable in the achievement of chaos and stochastic heating.

By further increasing the amplitude of the wave(s) well above threshold, another regime is observed: heating no longer takes place, and no more than one mode seems to be excited in the plasma. On the other hand, in the pulsed regime, by following time evolution further on after the heating is reached, temperature is observed to decrease and eventually to return to its unperturbed value (or even lower).

The two results can be interpreted as a manifestation of the feed-back action of the particles on the waves. In fact, the ion orbits undergo a transition in their topology, from regular to chaotic: the plasma oscillating fields, which are issued from collective motions of the charged particles and therefore are derived explicitly from integration of the particle trajectories, are necessarily modified. In particular, experimental observations close to the threshold for the transition to the chaotic regime seem to indicate that of the two modes only one survives. The conditions for the occurrence of chaos are then no longer satisfied, and the plasma tends to relax to its unperturbed equilibrium.

Conclusions

Stochasticity in ion dynamics originated by the interaction between particles and two electrostatic propagating plasma waves has been observed in a magnetized plasma. Optical measurements at different scales, from the single particle to the macroscopic, allowed a determination of the wave features, the kinetic ion response and the plasma heating mechanism.

Chaos appears to be limited by self-consistent effects. More results on these effects, as well as the modification of ion transport in the presence of the two waves will be discussed at the presentation.

This work was partially supported by the *Fonds National pour la Recherche Scientifique*.

+Laboratory for Plasma Research, Univ. of Maryland-College Park, USA.

References

[1]See for instance "Intrinsic Stochasticity in Plasmas", edited by G.Laval and D.Grésillon, Editions de Physique, Orsay 1979.
[2]D.F.Escande, *Phys. Rep.* **121**, 166 (1985).
[3]G.R.Smith and A.N.Kaufman, *Phys. Rev. Lett.* **34**, 1613 (1975).
[4]F.Skiff, F.Anderegg and M.Q.Tran, *Phys. Rev. Lett.* **58**, 1433 (1987).
[5]P.J.Paris and N.Rynn, *Rev. Sci. Instrum.* **61**, 1096 (1990).
[6]R.A.Stern, D.N.Hill and N.Rynn, *Phys. Rev. Lett.* **37**, 833 (1981).
[7]F.Skiff et al., *Phys. Lett. A*, **137**, 57 (1989).
[8]T.N.Good et al., *17th EPS Conf. on Controlled Fusion and Plasma Heating*, Amsterdam 1990, part IV, p.1811.

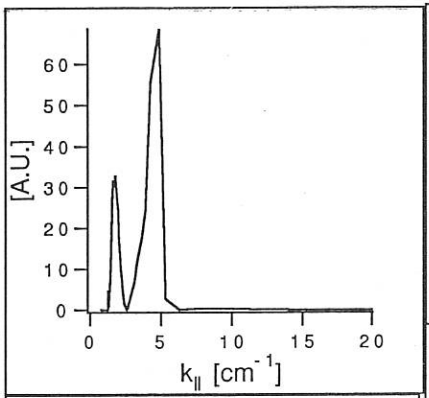

Fig.2: $k_{\parallel}$ spectrum of the wave electric field at f=25 kHZ, deduced from $f^1(v_{\parallel})$ via a 1-D Vlasov model

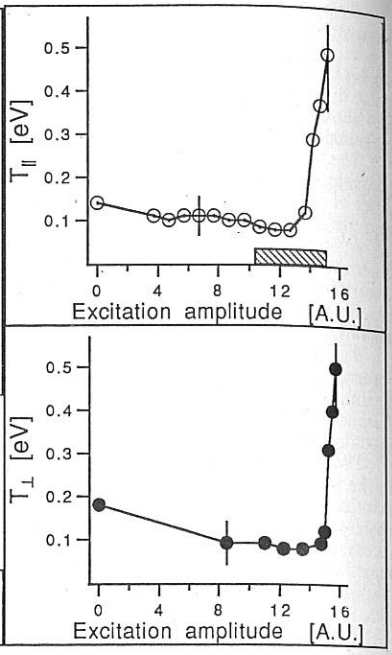

Fig.3: Parallel (top) and perpendicular (bottom) ion temperatures vs. the wave amplitude. The shaded region corresponds to K≅1.

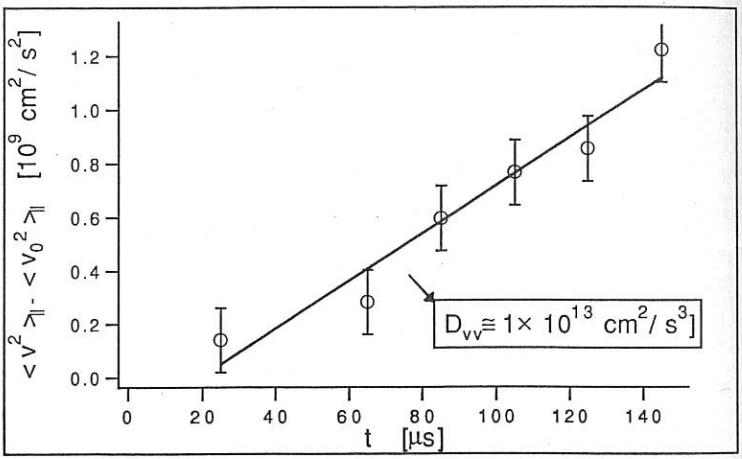

Fig.4: Temporal evolution of the increase of the mean square parallel ion velocity; the RF burst starts at t=0. f=25 kHz; exc. ampl.=15 A.U..

Observations of Intermittent Structures in association with Low Frequency turbulence in Toroidal Magnetized Plasma

A.K. Singh & Y.C. Saxena
Institute for Plasma Research
Gandhinagar, India

A plasma embedded in purely toroidal field is unstable due to free energy sources available in the form of density gradients, curvature of the magnetic field, inhomogeneity in the magnetic field, etc. The effective gravity antiparallel to density gradients favors R–T type of instabilities in these regions. The density gradients itself can provide energy for drift type of oscillations in the plasma. In the nonlinear limits these instabilities are known to give rise to vortex structures in the plasma flow (Shukla, 1984, 1989 for a review on this topic). In the present paper we report the study of resulting structures from a turbulent state. A study of plasma turbulence under above mentioned conditions has been made. The general behavior of plasma turbulence in the device have been reported earlier by Bora (1989) and Prasad et al. (1992). The turbulence was interpreted to be due to R–T and drift waves, and a modification of these due to velocity shear.

The experiment was carried out in a toroidal device called BETA (inset in figure (1))(PPP–report (1984)), major Radius 45.0 cm, minor radius 15.0 cm, having a plasma column of diameter 18.0 cm, terminated by a limiter in the form of a poloidal annular ring. The plasma is produced by electron impact ionization of Argon gas at a fill pressure of 10^{-4} Torr, base pressure 10^{-6} Torr. The present experiments were performed at 1 toroidal magnetic field of 1 kGauss, plasma density $n_e \sim 10^{11}\text{cm}^{-3}$ and $T_e \sim 5.0$ eV.

Figure (1) shows the radial profiles of plasma density and potential. Both density and potential peak near the center and fall as we go radially outward or inward. The typical density variation scale length $(1/ndn/dx)^{-1} \sim 6$ cm. The curvature on the magnetic field provides an effective $g \sim C_s^2/R$. This g and ∇n are antiparallel in the radially outer locations, making this region unstable to R-T instability. Owing to these density gradients and the potential gradients the plasma density and potential fluctuate and the plasma is in a turbulent state. This turbulence has been reported earlier by Prasad et al. (1992). The oscillation on plasma density and potential are of frequencies $\omega \leq \omega_{ci}$.

In the present paper we report the study of intermittent structures in the plasma stream lines of flow. The evidence of presence of such structures comes from the probability distribution functions of the fluctuation of potential and density. The PDF calculated at r = +8.0 cm reveal that the distribution is non-Gaussian. The value of skewness parameter is non-zero. Curtosis also deviates from a Gaussian value. For negative potentials PDF falls slowly and then exists a sharp cutoff for the fluctuation beyond $e\tilde{\phi}/KT_e \sim 60\%$. The deviation from non Gaussian PDF is more in the central region of plasma. The plasma close to limiter ring has PDF very close to the Gaussian statistics. Figure (2) shows the calculated PDF at different r & z in the poloidal cross-section. The non-Gaussian PDF is a signature of coherent states in the turbulence as discussed by (She, 1990, Kraichnan, 1990)). The statistics of small scale fluctuations in turbulence differ from Gaussian by having large probabilities for events with higher amplitudes. This contributes to the higher order moments of the PDF e.g. Skewness and curtosis (She, 1990). Under such situations secondary mechanism of energy cascade from larger wavelengths to shorter

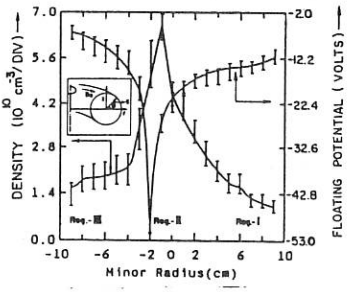

Figure 1: The radial profiles of plasma density and potential

wavelengths have been suggested by Kuznetsov et al. (1991). The bursty nature of distribution are suggestive of coherent structures in the system. Kraichnan (1990), Benzi & Biferale et al. (1991) also suggest that the higher order moments are related to strong intermittent burst in the energy transfer to small scale.

In order to study the coherent structure we measured the plasma floating potential on a grid of 15x12 using a set of movable Langmuir probes. A fixed probe at r = +8.0 cm was used as a reference probe. The auto correlations at each point was calculated. The cross correlation between reference probes and the movable probes were also calculated using FFT based techniques. On the basis of the correlation times at different positions it was found that the fluctuations have different behavior in the regions of the plasma radially. Typical correlation time varied between 150 μs to 250 μs. The contours of equal cross correlations $< \tilde{\phi}(t)\tilde{\phi}(t+\tau) >$ plotted in a plasma perpendicular to the magnetic field reveals the formation of a closed eddy in the inner central region of plasma between r = -5.0 to r = 5.0 cms. There were no closed structures found in the radial outer location in the plasma. The cross correlation are insensitive to the sign of actual potential and hence can not represent the stream lines of flows. A more detailed information about these closed structures can be obtained by the techniques of conditional averaging. This technique is widely used in fluid dynamics (Blackwelder, 1977; Adrian, 1975) for the study of two dimensional structures. This technique has also been used by Huld et al. (1988, 1990, 1991), Pécseli and Trulsen (1989) in the investigation of plasma eddies resulting from flute type of instabilities.

A time resolved contour plots of these conditionally averaged potential are obtained. Figure (3) shows the contours obtained with a condition $\phi_1 = -1.5\phi_{rms}$. Different frames are taken at a time interval of 25 μsec. The contours at time t=0.0 secs, show the presence of a large ($\sim 6.0cm$ radially $\sim L_n$) closed structure in the central region of plasma. These structures have negative polarity. There is also seen a positive structure in the inner side of the plasma cross section vertically upward. As time progresses the negative structures in the central region start shrinking in size and positive structures appear. At further delays the entire central region is occupied by large positive structure. The negative structure appear in the top left corner. This takes about $100\mu sec$. At further delays the bigger structure elongate in a direction perpendicular to the density gradient and break into smaller structures. These contours have been plotted for several conditions as

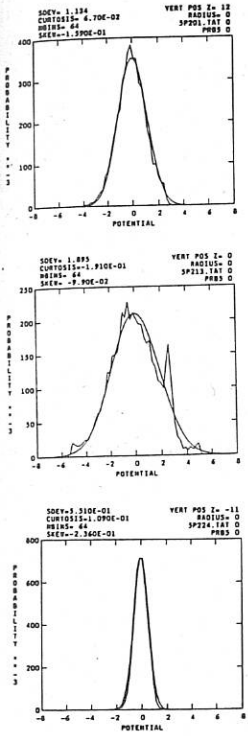

Figure 2: Calculated Prrobability distributions of ϕ. Also shown is a Gaussian with the calculated standard deviation.

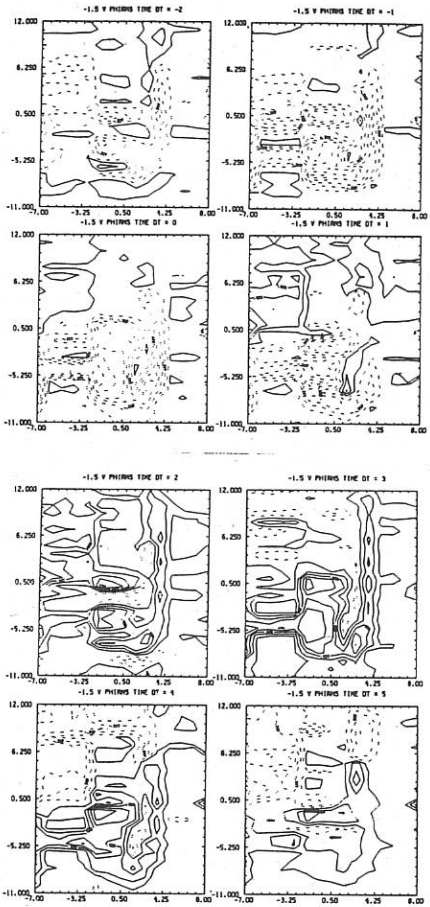

Figure 3: Contours of conditionally averaged potentials with a condition $\phi = -1.5$ volts ϕ_{rms}. See text for details.

mentioned earlier, the basic observation remains the same.

In conclusion we have studied two dimensional features of low frequency turbulence in a toroidal magnetized plasma. The fluctuations associated with the turbulence exhibit non Gaussian statistics in certain region of plasma. Short lived coherent structures have been observed in presence of turbulence, using the technique of conditional analysis on the potential signal. This analysis shows that there exists large structure in the inner and central region of plasma. Initially we see an structure having radial dimension as large as the density scale length. This at a later time develops into elongated closed eddy with the elongation in a direction perpendicular to the density gradient. At still later times the structure breaks into smaller structures. These smaller eddies are found to merge with the bigger ones of similar sign, at still longer times to form again a bigger structure. It is also observed that initially the central region was filled with negative polarity structures which disappears from this region at further time delays. These structures reappear again in a different inner top region of the cross section. The centeral region gets filled up with positive structures. This gives further signature of intermittency associated with non Gaussian statistics.

References

Adrian R.J., (1979), Phys. Fluids, **22**, 2065.

Benzi R., Biferale L., Paladin G. Vulpiani A. and Vergassola M., (1991), Phys. Rev. Lett., **67**, 2299.

Berezin Yu.A.and Karpman V.I., (1967), Soviet Physics, JETP, **24**, 1049.

Blackwelder R., (1977), Phys. Fluids, **20 S**, 232.

Beta–Modern Basic Plasma device, (1984), Int.Rep No. PPP/TR-11,PPP,PRL.

Bora D., (1989), Phys. Letts. A, **139**, 308.

Huld T., Iizuka S., Pécseli H.L. and Rasmussen J.J., (1988), Plasma Phys. & Controlled Fusion, **30**, 1297.

Huld T., Nielsen A.H., Pécseli H.L. and Jull Rasmussen J., (1990), Phys. Rev. Lett., **64**, 3023.

Huld T., Nielsen A.H., Pécseli H.L. and Jull Rasmussen J., (1991), Phys. Fluids, **B3**, 1609.

Pécseli H.L.and Trulsen J., (1989), Phys. Fluids, **B 1**, 1616.

Prasad G., Saxena Y.C. and Bora D., (1992), to appear in Geophys. Lett..

She Z., Jackson E. and Orszag S.A., (1990), Nature, **344**, 226.

Shukla P.K., Yu M.Y., Rahman H.U. and Spaschek K.H., (1984), Phys. Rep., **104**, 227.

Shukla P.K.Conf. on Plasma Physics Proc 1989 Intr., (1989), ed. by A. Sen and P.K. Kaw, 297.

Simpson J.A., (1961), Rev. Sci. Instr., **32**, 1283.

LOWER-HYBRID TURBULENCE EXCITED BY ELECTRON DIAMAGNETIC DRIFTS

Reiner Stenzel

Department of Physics, University of California

Los Angeles, CA 90024-1547, USA

A variety of instabilities can be excited by cross-field drifts in magnetized plasmas. The present work describes a sound-like cross-field instability near the lower-hybrid frequency ($f \lesssim f_{LH} \approx 100\,kHz$) in a large plasma column (1m diam. x 2.5m length) immersed in a weak magnetic field ($B_0 \approx 15G$) /1/. The magnetized electrons perform a diamagnetic drift $\underline{v}_d = \nabla p \times \underline{B}_0/neB_0^2$ relative to the essentially stationary, unmagnetized ions ($\nu_{in} > \omega_{ci}$). When the relative drift exceeds the sound speed, $v_d > c_s = (kT_e/m_i)^{1/2}$, unstable waves grow across $\underline{B}_0$ /2/. The experimental investigation includes the ω-$\underline{k}$ spectrum, saturation mechanisms, finite β effects, particle acceleration and transport.

Figure 1 summarizes the experimental arrangement. A pulsed dc discharge is created with parameters as indicated. Plasma and wave properties are diagnosed with Langmuir probes, directional velocity analyzer, electric and magnetic field probes. The latter are useful in this high-beta plasma [$\beta = nkT_e / (B_0^2/2\mu_0) \approx 0.5$] because the density fluctuations of the predominantly electrostatic instability are coupled to magnetic fluctuations. The net electron drift is obtained from $\nabla \times \underline{B}/\mu_0 = ne\underline{v}_d$. The measurement technique includes conditional averaging /3/ using digital oscilloscopes. Here, a reference probe provides a conditional trigger while a movable probe signal is ensemble-averaged to obtain coherence in time and space.

The strongest fluctuations are observed off-axis where the density gradients are largest. Fig.2a shows the typical density fluctuations vs. time during the discharge pulse while Fig.2b displays its frequency spectrum.

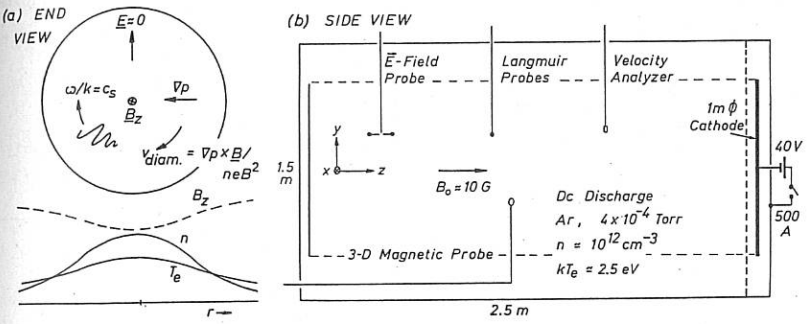

Fig.1 Schematic of the experimental set-up and plasma properties leading to the observed instability.

/1/ R.L. Stenzel, Phys. Rev. Lett. 65, 3001 (1990); Phys. Fluids B3, 2568 (1991).

/2/ B.B. Kadomtsev, Plasma Turbulence (Academic Press, London, 1965) p.94.

/3/ H. Johnsen, H.L. Pécseli and J. Trulsen, Phys. Fluids 30, 2239 (1987).

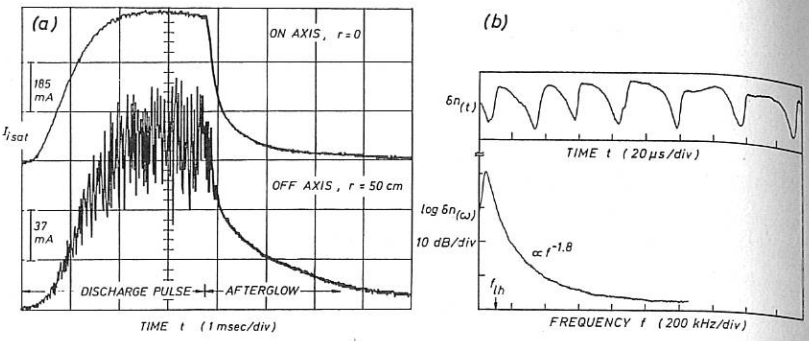

Fig.2 (a) Time-dependence of the density during a discharge pulse. Large amplitude fluctuations exist off axis where the pressure gradient maximizes.

(b) Frequency spectrum of the fluctuations showing a peak near the lower hybrid frequency, $f_{LH} \approx 120$ kHz, and high frequency tail due to wave steepening of $\delta n_{(t)}$ shown on upper trace.

The peak in the spectrum is below the lower hybrid frequency. The higher frequency components are phase-coherent and caused by wave steepening as visible in the temporal waveform of the density fluctuations.

By moving a probe axially, radially and azimuthally it is found that the fluctuations consist of waves growing and propagating initially in the azimuthal direction along the electron diamagnetic drift ($k_z, k_r \ll k_\theta$). The phase velocity matches the sound speed ($c_s \approx 2.5 \times 10^5$ cm/s $\approx v_d/5$). The plasma column exhibits no radial electric fields ($\underline{E} \times \underline{B}_0 \approx 0$) but a small radial electron temperature gradient ($\partial T_e / \partial r < 0$). Due to the

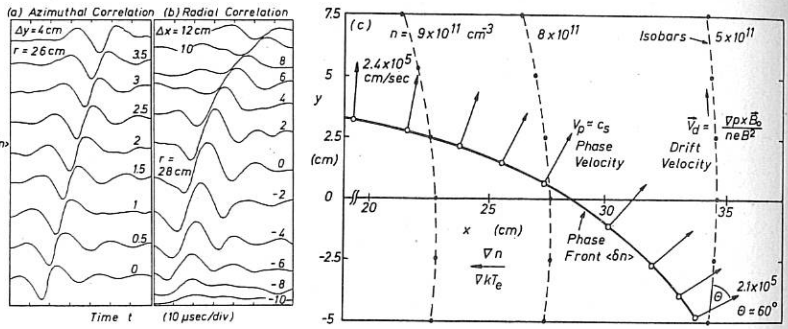

Fig.3 Conditionally averaged density fluctuations and typical wave front. (a) $<\delta n_{(t)}>$ at different azimuthal positions showing a constant velocity component. (b) $<\delta n_{(t)}>$ at different radial positions showing a decreasing radial velocity component. (c) Transverse r - θ plane with a curved phase front constructed from the measured velocity components $v_{ph} = \omega/k = (v_x^{-2} + v_y^{-2})^{-1/2}$. The curvature is due to wave refraction by temperature gradients, $v_{ph} \approx C_s \approx (kT_e/m_i)^{1/2}$.

temperature dependence of the sound speed the growing waves begin to refract radially outward /4/. Typical conditional averages of density fluctuations in azimuthal and radial direction are shown in Fig.3a,b from which the curved phase front of Fig.3c has been constructed. Due to the large size of the plasma column (average circumference 2m), the waves refract radially outward and decay rather than forming azimuthal eigenmodes as, e.g., drift waves do in small columns. As the waves refract from the azimuthal into the radial direction they stabilize since the drift no longer exceeds the azimuthal phase velocity component ($v_d < c_s/\cos\theta$). Thus, refraction provides a saturation mechanism for the instability.

A second saturation process is nonlinear wave steepening which is observed here for wave propagation across $\underline{B}_0$ while earlier studies of sound wave steepening were done for B=0 /5/. Fig.4 shows a typical waveform of a large amplitude density fluctuation ($\delta n/n \gtrsim 25\%$). The steepened wave front has a temporal and spatial scale of ~ 2% of the wave period and wavelength, respectively. The shock thickness ($\Delta s \approx 1.2$ mm) is between the Debye length ($\lambda_D \approx 0.02$ mm) and the electron Larmor radius ($r_{ce} \approx 4$ mm). The latter condition implies that finite Larmor radius effects modify the otherwise adiabatic electron dynamics. The spikey shock electric field can accelerate the electrons directly across $\underline{B}_0$ which leads to wave damping and saturation.

In addition to density fluctuations the perturbations in other physical parameters have been measured. It is found that wave density and potential are positively correlated although the Boltzmann relation is not quantitatively satisfied ($\delta n/n > e\delta\phi/kT_e$), possibly due to resistivity along $\underline{B}_0$. Axial magnetic field fluctuations are observed to be anti-correlated with density perturbations. However, the theoretical relation predicted by

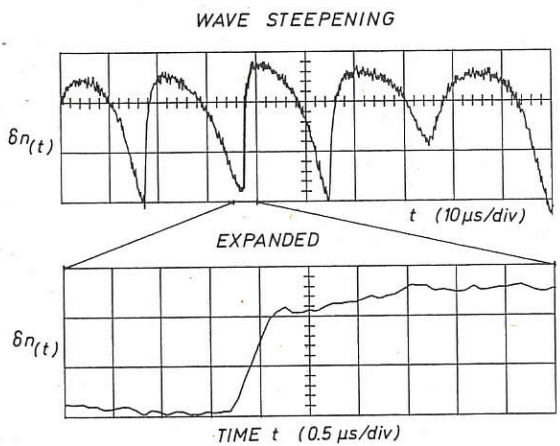

Fig.4 Wave steepening of large amplitude sound wave propagating across $\underline{B}_0$. Expanded view indicates rise time $t_r \approx 0.5\mu s \ll$ wave period $t_p \approx 20\mu s$. The corresponding shock thickness, $\Delta s = c_s t_r \approx 1.2$ mm is smaller than the electron Larmor radius, $r_{ce} \approx 4$ mm.

/4/ Y. Nishida and A. Hirose, Plasma Phys. 19, 447 (1977).

/5/ R.J. Taylor, D.R. Baker and H. Ikezi, Phys. Rev. Lett. 24, 206 (1970).

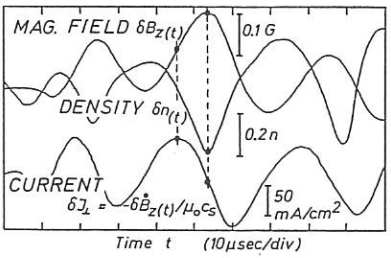

Fig.5 Comparison of density and magnetic fluctuations showing that δn and δB_z are anti-correlated. The time derivative of the magnetic fluctuations is proportional to the radial current density $\delta \underline{J}_r = \nabla \times \delta \underline{B}_z/\mu_0 \approx -\delta \dot{B}_z/(\mu_0 v_\phi)$. The current is caused by electron diamagnetic drifts opposed by Hall drifts $\delta \underline{E}_\phi \times \underline{B}_0 / B_0^2$.

pressure balance is quantitatively not fulfilled, $|\delta B_z/B_z| < (\delta n/n)\beta/2(1-\beta)$. The reason is that electron diamagnetic drifts set up by the wave $\delta \underline{v}_d = kT_e \nabla \delta n \times \underline{B}_0/neB_0^2$ are partly canceled by electron $\delta \underline{E} \times \underline{B}_0/B_0^2$ drifts. If the Boltzmann relation were satisfied $\delta \underline{E} = (kT_e/e) \nabla \delta n/n$ both drifts would exactly cancel ($\delta B_z = 0$). From $\nabla \times \delta \underline{B} = \mu \delta \underline{J}$ the net perturbed current density $\delta \underline{J} = ne\, \delta \underline{v}_d$ has been quantitatively obtained ($\delta J_{max} \approx 100$ mA/cm²). The radial electron drift in the wave ($\delta v_d \approx 8 \times 10^5$ cm/s) is as large as the azimuthal electron drift due to the background pressure gradient. Thus, the wave causes significant radial electron transport.

It is often assumed that large amplitude lower hybrid waves cause parallel electron acceleration and heating. Using a Langmuir probe the rapidly swept ($\Delta t \approx 3$ μs) current-voltage characteristics have been traced out at a wave maximum ($\delta\phi_{max}$) and minimum ($\delta\phi_{min}$). The temperature is found to be constant to within ~ 5%. Since the electron pressure gradient provides the free energy for driving the instability, ion heating rather than electron heating might be expected. Similar time-resolved ion velocity analyzer traces show small bulk ion heating ($\Delta T_i/T_i \approx 25\%$). Although the wave potential energy exceeds the ion kinetic energy ($e\delta\phi \approx 0.6$ eV > $kT_i \approx 0.4$ eV) the short interaction time between waves and particles ($v_{ph} > v_{thi}$) prevents significant ion acceleration. However, a bulk ion drift ($v_d/c_s \approx 5\%$) in the direction of wave propagation has been observed. Steepened ion acoustic waves can cause a bulk ion flow /6/.

In summary, the basic properties of a pressure-gradient driven instability in a weakly magnetized plasma column have been investigated. Although the instability grows to large amplitudes ($\delta n/n \gtrsim 50\%$) it results in little particle acceleration and heating. Numerous situations in laboratory and space plasmas exist where this instability may occur.

/6/ F.F. Chen, Introduction to Plasma Physics, (Plenum Press, New York, 1974) p.254.

EXPERIMENTAL STUDIES OF ANOMALOUS POTENTIAL DROPS DUE TO ION DENSITY INHOMOGENEITIES

I. Axnäs, M. Bohm, and S. Torvén

Royal Institute of Technology, Alfvén Laboratory, Department of Plasma Physics
S-10044 Stockholm, Sweden

Double layers form in laboratory plasmas as the response to an applied or induced voltage drop, but the significant mechanisms in different processes for double layer formation are still unclear. In a plasma maintained by local ionization of the background gas due to electron impacts, a double layer forms from an electrode sheath when a sufficiently large electron current is drawn to an electrode. The significant mechanism for the formation of the double layer is in this case the generation of positive ions in the electrode sheath /1/. Ionization phenomena also limit the voltage drop over steady double layers to relatively small values which are related to the ionization potential of the background gas /2/. In contrast to this, double layers with very large voltage drops have been observed in the "collisionless" plasmas that can be produced in Q-machines and differentially pumped triple plasma machines /3,4/.

In this paper we report experiments showing the dynamic plasma potential response when a step voltage drop is applied along the plasma column in a differentially pumped triple plasma machine. The time resolution in the potential measurements is 0.5 μs which is close to the electron transit time along the plasma column. Potential changes caused by essentially the electron motion can therefore be detected. Similar investigations have been made in the axially homogeneous plasma column of a Q-machine, operated "double-ended" in the "electron rich" regime /5/. In this case, most of the potential drop first concentrates in a narrow region at the low potential end of the plasma column. On the time scale of the ion motion this potential drop begins to propagate into the plasma as a double layer. Here we shall show that a quite different plasma potential response may be obtained when the initial ion density is inhomogeneous and has an "ion density cavity", that is, a local minimum with a width of many Debye lengths. For a sufficiently low minimum density, the potential drop becomes distributed over the cavity during the first few electron transit times, and the profile steepens slowly to a double layer on the time scale of the ion motion. Similar results have alsc been obtained in numerical simulations /6,7/ and been predicted by a theoretical model /7/. An ion density cavity may also strongly modify the non-linear evolution of plasma waves /8/.

The differentially pumped triple plasma device (Fig. 1) has a central chamber with a plasma column which is maintained by a source on each side. There plasmas are produced by discharges between filaments and the source chamber walls . The plasma column is radially confined by an axial magnetic field (5 to 50 mT). The neutral atom (argon) density in the central chamber is kept much lower than in the sources where a certain minimum neutral atom density is required to get quiescent discharges. Circular apertures, which connect the

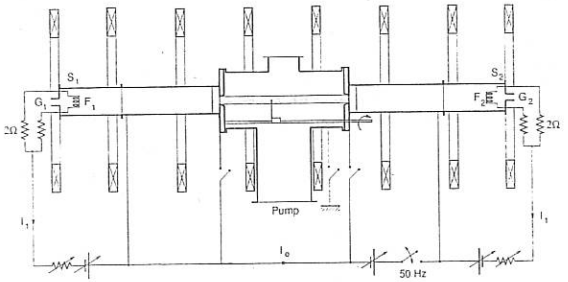

Fig 1. Differentially pumped triple plasma machine used in the experiments. A plasma column is maintained in the central chamber by the two sources S_1 and S_2. The plasma there is produced by separate discharges between the arrays of filaments F_1 and F_2 and the source chamber walls.

sources and the central chamber, define the radius of the plasma column (3 cm). Potential drops exist at the apertures. They reflect some of the source electrons back to the source and accelerate source ions into the central chamber, similar to the "electron rich" boundary conditions at the plates in the Q-machine experiment. At the apertures, the density drops from the value N_S in the sources to the value N_1 in the plasma column. For identical source parameters, a density minimum, N_1-ΔN, can be produced halfway along the plasma column which then forms a symmetric cavity with a width comparable to the length of the column (Fig. 2). Asymmetric cavities can also be produced by having different source densities. The cavity is due to radial ion losses, and the depth of the cavity can be varied ($0.1 < \Delta N/N_1 < 0.7$) by varying the magnetic field and the potential of the end plates of the central chamber. N_1 is close to 10^{15} m^{-3} and $k_B T_e$ typically 10 eV. A step voltage (rise time 20 ns) was applied periodically between the plasma sources, and plasma potentials were sampled with emissive probes. The good time resolution was obtained by reducing the distributed probe capacitance to ground, and it was checked by direct measurements of rise and fall times. Fig. 3 shows the plasma potential response for an asymmetric ion density cavity with a minimum at z≈20 cm,

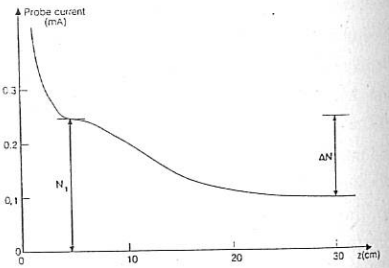

Fig 2. Initial axial density profile at the symmetry axis. Probe currents at plasma potential give a measure of the ion densities. The machine was operated symmetrically and only the variation between 3 and 30 cm is shown (length of plasma column 60 cm). The relative cavity depth, $\Delta N/N_1$, can be varied ($0.1 < \Delta N/N_1 < 0.7$). Close to the low potential aperture (z=0), the density increases sharply to the density N_S in the source.

$\Delta N/N_1 \approx 0.7$ and $N_s/N_1 \approx 10$. Here N_s and N_1 are the densities on the low potential side. The corresponding values on the high potential side were slightly higher. Radial potential profiles are given at t=1μs and t=100 μs for different axial positions. At t=1 μs (about two electron transit times) the profile varies linearly over most of the length of the plasma column, and the

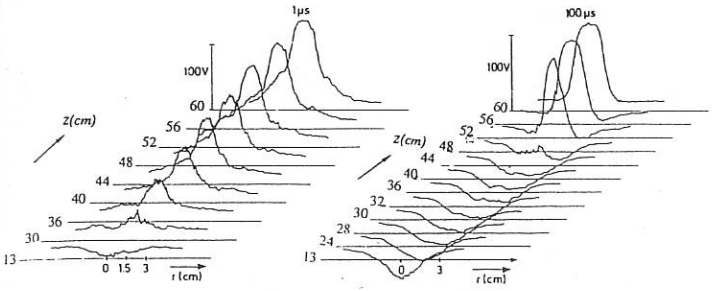

Fig. 3. Plasma potential response to a step voltage drop of 160V. An asymmetric density cavity is present initially. Radial potential profiles are shown for different axial positions at 1 μs (left) and 100 μs. z denotes the distance from the aperture on the low potential side.

electron emission from the low potential source is also limited by a potential minimum, situated at about z=7 cm (not shown in the diagrams). During the subsequent ion motion, the axial profile steepens, and a double layer has formed between z=48 cm and and z=52 cm after about 100 μs. Similar profiles were obtained for applied potential drops up to 400 V. Fig. 4 (left) shows potential profiles along the symmetry axis when again $\Delta N/N_1 \approx 0.7$ and

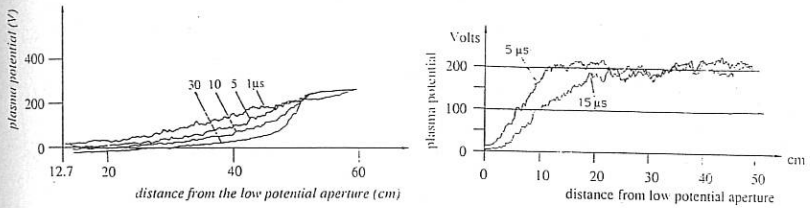

Fig 4. Potential profiles along the symmetry axis showing the response to an applied step voltage for different initial ion density distributions. (left) A density cavity is present initially as in the case shown in Fig. 3 ($\Delta N/N_1 \approx 0.7$, $N_s/N_1 \approx 10$). The potential drop is first (t=1μs) supported by an almost linearly varying potential along the magnetic field. (right) The initial density profile kept as flat as possible ($\Delta N/N_1 < 0.1$) and the source density is lower ($N_s/N_1 \approx 3$). Now most of the applied potential drop is first supported by a narrow region near the low potential aperture, and the potential along the plasma column is approximately constant. Then the potential drop propagates into the plasma on the time scale of the ion motion.

$N_s/N_1 \approx 10$. Fig. 4 (right) shows profiles when the initial profile was kept as flat as possible ($\Delta N/N_1 < 0.1$) and N_s/N_1 was reduced to 3. Now a quite different response is obtained. The potential is approximately constant along the plasma column during the first few microseconds, and most of the applied potential drop is concentrated to a narrow region close to the low potential source. Then this drop begins to propagate into the plasma as a double layer. This is the same type of response as observed in the Q-machine experiment.

We have shown that there are two different types of responses to a step voltage drop depending on the initial ion density distribution. These do not only differ during the first microsecond, but the subsequent evolutions on the time scale of the ion motion are also different. The ion density cavity can support very large potential drops for several electron transit times. In contrast to a double layer, where the Debye length is the spatial scaling constant, the cavity potential drop is extended over the cavity width. The cavity potential drop evolves slowly into a double layer on the time scale of the ion motion.

The results obtained are consistent with an analytical model and a particle-in-cell simulation /7/. Also these demonstrate the existence of two different states, similar to those observed experimentally. The natural ion to electron mass ratio is used in the simulation which covers about three electron transit times corresponding to about 1 μs in the experiment. Cavity potential drops are obtained when the applied voltage drop falls below a critical voltage drop which depends on only $N_0/(N_1-\Delta N)$. Here N_0 is the density of the injected electrons at the boundaries, and $N_0 > N_1$ in electron rich injection. For larger voltage drops applied, the potential drop instead concentrates in a "cathode sheath".

Ion density cavities may form due to nonlinear ion waves or due to the ponderomotive force from high frequency wave packets. Further investigations are required to decide whether such cavities may modify the voltage supporting capability of the plasma and introduce a new type of anomalous resistivity.

References

/1/ Torvén S. and Andersson D., 1979, J. Phys. D: Appl. Phys. 21, 286; Fujita H., Matsuo K. and Yagura S., 1984, Plasma Phys. Contr. Fusion, 26, 1039

/2/ Iizuka S., Michelsen P., Rasmussen J. Juul, Schrittwieser R., Hatakeyama R., Saeki K. and Sato N., 1981, Proc. XVth Int. Conf. on Phenomena in Ionized Gases (Minsk), Contr. Papers, p. 1020

/3/ Sato N., Hatakeyama R., Iizuka S., Mieno T., Saeki K., Rasmussen J. Juul and Michelsen P., 1981, Phys. Rev. Lett. 46, 1330

/4/ Torvén S., 1982, J. Phys. D: Appl. Phys. 15, 1943

/5/ Iizuka S., Michelsen P., Rasmussen J. Juul, Schrittwieser R., Hatakeyama R., Saeki K. and Sato N., 1985, J. Phys. Soc. Japan, 54, 2516

/6/ Rowland H.L. and Palmadesso P.J., 1987, J. Geophys. Res., 92, 299

/7/ Bohm M. and Torvén S., 1991, Phys. Rev. Lett., 66, 604; Bohm M. and Torvén S., IEEE Trans. Plasma Science, in the press

/8/ Infeld E., Rowlands G. and Torvén S., 1989, Phys. Rev. Lett. 62, 2269

ION RESONANCE CONES AND INTRINSIC DIFFRACTION

Th. PIERRE and G. BONHOMME
Laoratoire PMI, URA 835 du CNRS,Université de NANCY I
BP 239 F-54506 Vandoeuvre Cedex FRANCE

Introduction:

The radiation of a point source antenna immersed in a hot magnetized plasma has been studied during the past twenty years and is often related to the resonance cone phenomenon (see the C.M.A. diagramm). Namely, the strong anisotropy of the medium for the propagation of the electrostatic waves is the reason for the existence of a narrow angular radiation of the antenna. In the low frequency range below the ion cyclotron frequency, the ion resonance cones have been first introduced by H.H. Kuehl /1/: the reason for the existence of this phenomenon is the specific shape of the dispersion surface exhibiting a region of low damped wave-vectors with a mean group velocity dependent on the frequency value.

This phenomenon has seldom been observed experimentally /2/ in not very suitable plasma conditions, very close to the antenna and in a very limited plasma column. We are presenting here a numerical bidimensional study of the radiated potential near the point source antenna below the ion cyclotron frequency and the corresponding experimental records. The results are interpreted in terms of intrinsic diffraction in relation with a model previously introduced in the case of the electron modes.

Calculation of the radiated potential:

The dispersion relation of the electrostatic modes in the hot magnetized plasma expresses as:

$$\varepsilon(\Omega, K_\perp, K_{//}) \equiv 1 + \frac{\Omega_p^2}{\Omega_e^2}\frac{1}{K^2}\left[1 + \sum_{-\infty}^{+\infty} I_n(\lambda_e)e^{-\lambda_e}.\zeta_{oe}Z(\zeta_{ne})\right] + \frac{T_e}{T_i}\frac{\Omega_p^2}{\Omega_c^2}\frac{1}{K^2}\left[1 + \sum_{-\infty}^{+\infty} I_n(\lambda_i)e^{-\lambda_i}.\zeta_{oi}Z(\zeta_{ni})\right]$$

where $\Omega = \omega/\omega_{ci}$ $K = k\,C_s/\omega_{ci}$, $\lambda_e = K_\perp^2 m/M$, $\lambda_i = K_\perp^2\, T_i/T_e$ and

$$\zeta_{ne}=(\Omega+ nM/m)/K_z\sqrt{2\ M/m} \quad , \quad \zeta_{ni}=(\Omega+ nM/m)/K_z\sqrt{2\ M/m}$$

The corresponding dispersion branches are related to the pure ion Berstein mode when the wave vector is exactly perpendicular to the B field, to the neutralized ion Berstein mode when the wave vector departs from the perpendicular direction and to the ion cyclotron mode, i.e. the ion acoustic mode. The radiated potential is calculated following Kuehl's method /1/:

$$\Phi(\mathbf{r}) = \frac{i}{8\pi\varepsilon_0} \sum_{m=1}^{\infty} \int_{-\infty}^{+\infty} dk_{//} \frac{H_0^{(1)}(k_\perp r_\perp) \exp(ik_{//}\tau_{//})}{D'_m(k_{//})}$$

where $D'(k_z)= \dfrac{\partial D}{\partial k_\perp^2}$ and H_0^1 is the Hankel function

Numerical results:

Keeping onlu the least damped root of the dispersion equation, the domain of integration is truncated once the damping coefficient becomes large and there is no longer a significant contribution to the integral.

The typical results obtained with Helium and $\omega_{pi}/\omega_{ci}=5.$, $\omega/\omega_{ci}=0.7$ and $T_e/T_i= 20$ are diplayed on figure 1. It is in fact necessary to choose a low mass gas in order to obtain large values of the normalized distance to the antenna due to a small ion gyroradius. The map shows the potential calculated in front of the point source antenna up to a distance 50 cm in both radial and axial directions. The resonance cone is easily seen along the dashed line and moreover an axial potential modulation is observed in the axial direction. By varying the plasma parameters, this modulation has been shown to be very dependent on the ion temperature: the modulation length is continously decreasing with increasing the T_e/T_i ratio.

This phenomenon has been related to the particular shape of the dispersion surface. Figure 2 displays the dispersion curve $k_\perp(k_z)$ for $\omega/\omega_{ci}=0.3$, 0.5, 0.7 . The main point is that the damping (dashed line) is increasing very rapidly at some particular value of K_z. This behaviour is similar to the case of the electron modes, where this sharp-cut of the non-damped wave vectors has led to the intrinsic diffraction model /3/: in this model the radiated potential is shown to be modulated in

the same way as the optical intensity behind a screen with sharp edges. We show that this model can be applied to the ion waves radiated by a point source antenna below the cyclotron frequency, due to the existence of this rapid increase at some particular K_z value.

Moreover, the sensitivity of the modulation length to the ion temperature can lead to the possible use of this phenomenon for the measurement of the T_e/T_i ratio in a magnetized plasma.

Experimental results and discussion:

The theoretical results have been compared to the records obtained in a magnetized double plasma device, in a helium plasma with a B-field lower than 0.12 Tesla /4/. The diameter of the plasma column is 26 cm. The plasma is created by electric discharge in each end chamber. The emitting antenna is fed by a signal generator at the level +40 dBm. The potential radiated around the point source antenna is recorded by a HF probe located on a X-Y table. The signal is recorded by a spectrum analyzer and the results are stored on a PC for further processing.

Fig. 3 displays the map of the potential obtained at the frequency 100 KHz with $f/f_{ci}= 0.7$, $n_e= 10^{10}$ cm^{-3} and $T_e=3$ eV . A potential modulation along the direction of the B-field is easily seen, although the cone structure is not evident here. The value of the modulation length has been found consistent with the expected temperature ratio Te/Ti =60.

These preliminary results show that the measurement of the temperature ratio by using this axial modulation of the potential radiated by a point source antenna below the ion cyclotron frequency is easier than the estimation of this ratio by recording the angle and width of the ion resonance cone. In fact, only an axial displacement of the probe is needed. Moreover, only a rather simple experimental set-up and standard equipment is necessary.

REFERENCES:

/1/ H. H. Kuehl, Phys. Fluids **17**, 1636 (1974)

/2/ T. Ohnuma et al., Phys. Rev. Lett. **37**, 206 (1976)

/3/ H. de Feraudy and B. Lembège, Phys. Fluids **28**,2755 (1985)

/4/ Th. Pierre, F. Braun and G. Leclert, Rev. Sci. Instum. **58**,6 (1987)

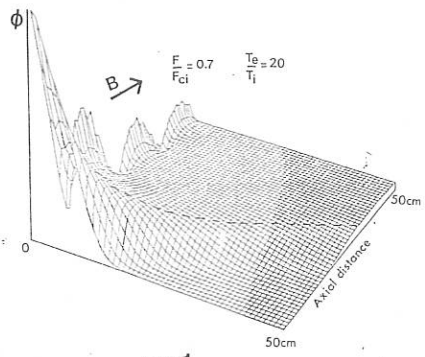

FIG 1

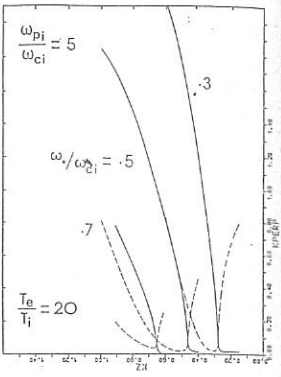

FIG. 2

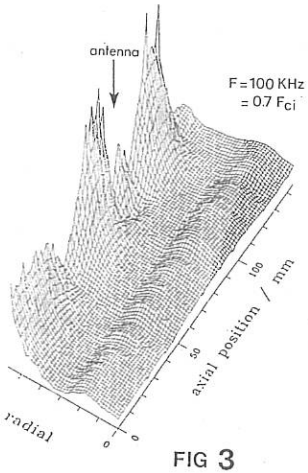

FIG 3

REFLECTION OF A DIVERGENT RESONANCE CONE NEAR THE PLASMA LAYER IN A MAGNETIZED INHOMOGENEOUS PLASMA

I. Boucher, T. Pierre and G. Leclert

Lab. Physique des Milieux Ionisés, URA CNRS 835, Université Nancy 1, BP 239, F-54506 VANDOEUVRE CEDEX FRANCE

I - INTRODUCTION

The potential radiated by a small antenna in a magnetized plasma exhibits very anisotropic features for two frequency ranges related to the lower and higher hybrid frequencies, ω_{lh} and ω_{uh}. For the lower ($\omega_{lh} < \omega < \min(\omega_p, \omega_c)$) and upper ($\max(\omega_p, \omega_c) < \omega < \omega_{uh}$) branches, the energy flows along resonance cones, having their summit on the antenna and their axis in the magnetic field direction.

The theoretical description of electrostatic resonance cones for a warm infinite homogeneous plasma has been given first by Kuehl/1/. Temperature effects produce a secondary structure of cones of smaller amplitude.

The basic properties of resonance cones have been verified in several experiments/2,3/, namely the cone angle as a function of the frequency, plasma density and magnetic field, and the structure associated to temperature effects. However, whereas the potential amplitude has been accurately measured, there are very few phase measurements. On the other hand, due to the finite size of a real experiment, the resonance cone emitted by a point-source can undergo a reflection at the surface where the frequency equals the local plasma frequency. Only one paper/4/ deals with this problem.

We report in this paper experimental results on both amplitude and phase of the potential. We find that, for a broad range of parameters, the phase variation across a single resonance cone is 2π, due to bounded plasma effects. We also study the reflection of a resonance cone at the cut-off plasma layer and give an estimate of the phase jump at the reflection.

II - EXPERIMENTAL SET-UP

Experiments have been done in a multipolar plasma device operating in a magnetic field/5/. The maximum magnetic field strength is 800 gauss. The magnetized plasma column is 1.4 m long and 26 cm in diameter. The plasma density goes up to 10^{11} cm^{-3} and the electron temperature is 3 eV.

Figure 1 gives the overall view of the experimental set-up. The emitting point-source antenna is located at the center of the plasma column. A HF detection antenna is movable along two perpendicular directions by means of step-motors. The detected signal is sent to a spectrum analyser, that records the potential amplitude, and to a digital oscilloscope, triggered by a reference signal, from which the phase evolution can be reconstructed. The data are stored and processed by a personal computer.

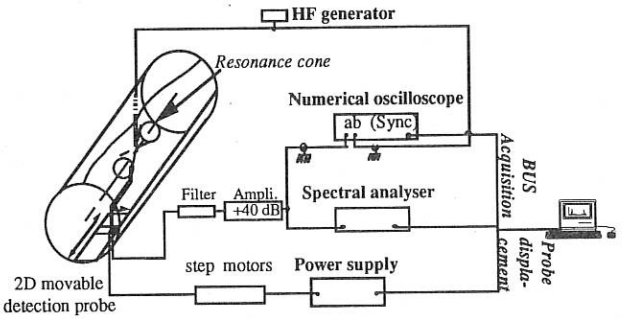

Figure 1 : Experimental set-up

III - EXPERIMENTAL RESULTS

Divergent resonance cone

We present here results for a homogeneous plasma with the following parameters: wave frequency f= 340 MHz, electron plasma frequency f_{pe}=1.5 GHz and electron gyrofrequency f_{ce}=675 MHz. Figure 2 shows 3D maps for the

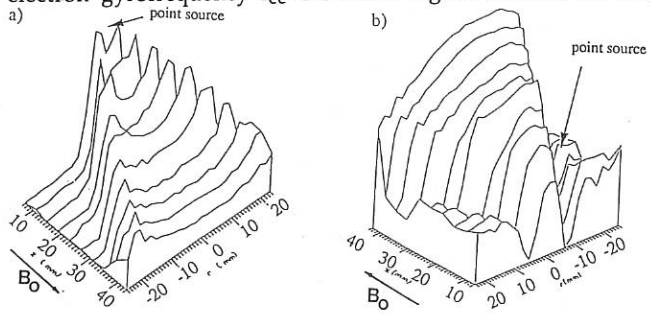

Figure 2 : Spatial amplitude and phase variation of the potential

potential evolution. The usual evolution of the amplitude is shown on Figure 2a, where the principal peak of the resonance cone as well as the secondary

thermal structure can be seen. Figure 2b displays for the first time a similar map for the phase evolution. There is a phase jump across the main peak, followed by a plateau in the inside region. Further analysis shows that equipotential curves are also equiphase curves, in agreement with the fact that the phase velocity is perpendicular to the group velocity.

The phase jump across the resonance cone is better shown on Figure 3, that displays the radial dependence of the potential. The asymptotic value of the phase is 2π. This value is found whenever the plasma density is high enough (so that there are no electromagnetic corrections) if the perturbations due to adjacent cones are negligible, so that the cone can be considered as "isolated". As a numerical computation does not predict this behavior, the phase value of 2π is probably due to bounded plasma effects: the phase variation can be perturbed by the boundaries much more easily than the amplitude.

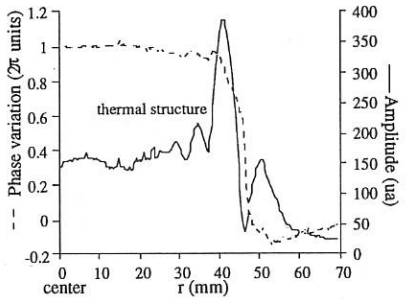

Figure 3 : radial dependence of the potential

Reflection at the plasma layer

We next study the resonance cone propagation in a linear density profile. The parameters are now: f = 697 MHz, f_{peo} = 1.2 MHz and f_{ce} = 1.1 GHz. Figure 4a displays the evolution of the amplitude of the incident and reflected resonance cones versus the axial distance z for several radial distances r. The

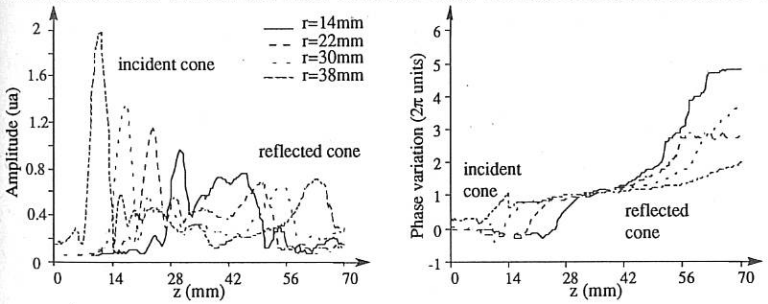

Figure 4: Amplitude and phase evolution of the potential near the cut-off plasma layer

incident cone and its thermal structure are much better defined than the reflected cone. This comes from the fact that the resonance cone is made of a broadband spectrum of wavenumbers that is stongly perturbed by the reflection process. Figure 4b shows the related phase evolution. The phase jumps associated to the incident and reflected cones are clearly seen. The total phase variation across the incident cone is again 2π. A small periodic phase variation related to the thermal peaks occurs, in good agreement with numerical calculations. To determine the phase shift produced by the reflection process itself, the phase difference between the incident and reflected peaks has been measured for various radial distances and is displayed on Figure 5.

This difference varies almost linearly with the radius r. There is obviously a phase shift introduced by the reflection; due to inhomogeneity effects and the uncertainty on the plasma layer position, only an upper bound of the order of π can be set. Theoretical arguments predict a value of $\pi/2$.

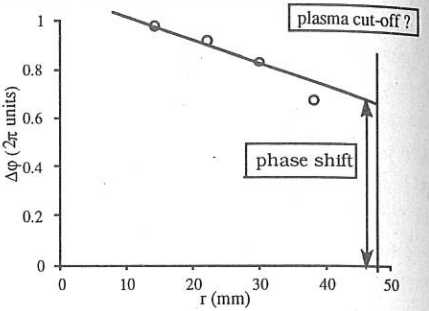

Figure 5: Phase variation between incident and reflected cones.

IV - CONCLUSIONS

The amplitude and phase of the potential radiated by a point-source antenna in a magnetized plasma have been measured simultaneously for various plasma conditions. Accurate phase measurements have been performed on the resonance cone diverging from the antenna as well as on the resonance cone reflected at the plasma layer. Phase variations associated to the thermal structure have been measured. The phase shift due to the reflexion process has been observed.

REFERENCES

/1/ KUEHL H.H., Phys. Fluids 5, p1094 (1962)
/2/ FISHER R.K. et GOULD R.W., Phys. Rev. Lett. 22, p1093 (1969)
/3/ FISHER R.K. et GOULD R.W., Phys. Fluids 14, p857 (1971)
/4/ OHNUMA T. et LEMBEGE B., Phys. Fluids 21 (12), p2339 (1978)
/5/ PIERRE T., LECLERT G. et BRAUN F., Rev. Sci. Instrum. 58, (1986)

PRODUCTION OF A HIGH DENSITY PLASMA BY HELICON WAVES

A. Komori, M. Sugimoto, M. Kono*, M. Tanaka and Y. Kawai
Interdisciplinary Graduate School of Engineering Sciences,
Kyushu University, Kasuga, Fukuoka 816, Japan
*Research Institute for Applied Mechanics,
Kyushu University, Kasuga, Fukuoka 816, Japan

Abstract A highly-ionized plasma with central density $\sim 3 \times 10^{13}$ cm^{-3} is produced by radio-frequency excitation of helicon waves, and Landau damping is experimentally demonstrated to cause efficient transfer of wave energy to electrons that subsequently suffer inelastic collisions. Nonthermal beamlike electron tails, which are considered to be closely related to the plasma production, are also observed when a small-diameter stainless-steel tube is used as a vacuum chamber.

1. Introduction

Recently, Boswell has presented a new plasma source which uses inductively coupled radio frequency power to generate a high-density plasma at low pressure, and has shown that wave properties are consistent with those expected of helicon waves /1/. In a theoretical analysis, Chen has suggested that the rate of energy absorption by wave damping may be due to Landau damping of the helicon wave which has an electric field component parallel to the magnetic field /2/.

In the present paper detailed measurements are performed of the helicon wave and the efficient plasma production. Spatial variations of damping waves are measured by interferometry to obtain damping rates and wavelengths in the plasma along the magnetic field. The damping rate of the helicon wave is consequently confirmed to have the characteristics of Landau damping although the collisional damping is not negligible in our experiments. The nonthermal beamlike electron tail is also studied to clarify its effect on the plasma production.

2. Experimental apparatus

A schematic of the experimental apparatus is shown in Fig. 1 /3/. The argon plasma produced with a helical antenna is confined in a uniform magnetic field $\mathbf{B}_0$ of up to 3 kG. The antenna is located outside the plasma, that is, on the Pyrex tube with an inner radius a of 2.5 cm and a length of 50 cm, which is connected to the end of the stainless-steel vacuum chamber of 120 cm in length and 16 cm in diameter or that of 170 cm in length and 46 cm in diameter. The stainless-steel vacuum chamber is electrically grounded.

The antenna consists of two copper ribbons of 2.5 cm in width, which are wound

around the Pyrex tube and have half of a winding, in order to excite an $m = 1$ mode, as shown in Fig. 1(b). The length of the antenna is chosen to be 25 cm. The rf power at 7 MHz, P_{rf}, is supplied from an oscillator-amplifier system and is varied up to 2 kW. To minimize damage to the rf circuit, the rf supply is pulsed at 83.3 Hz with a 16.7% duty cycle.

Measurements of n_e and T_e are performed with a Langmuir probe calibrated against a microwave interferometer. The plasma density n_e is measured at $t = 1.5$ msec after the oscillator is turned on at $t = 0$ msec with a boxcar integrator with a gate width of 0.1 msec, while T_e is obtained in the afterglow plasma because T_e of 4-6 eV at $t = 1.5$ msec is considered to be affected by the rf wave. The electron temperature T_e thus obtained is found to be always 3-4 eV, and to depend little on such parameters as B_0, P_{rf} and neutral pressure p. The wavelength of the helicon wave, $2\pi/k$, is measured by interferometry with magnetic probes, which are located inside the stainless-steel vacuum chamber, and are movable along the z axis. The magnetic probes consist of single layer solenoidal coils of 4 mm in diameter and 6 mm in length with 50 windings.

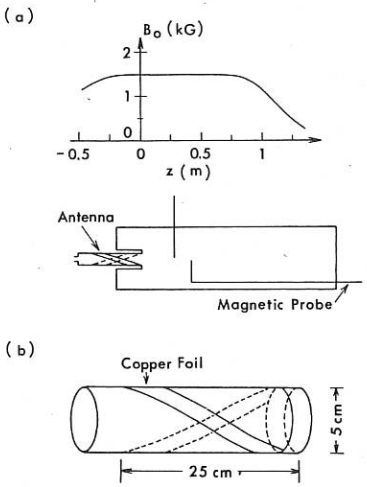

Fig. 1: Schematic of experimental apparatus.

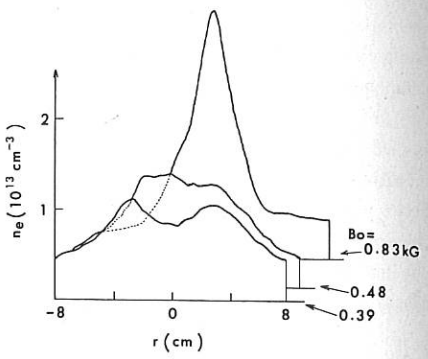

Fig. 2: Dependence of radial n_e profile on B_0.

3. Experimental results

The radial n_e profile is studied by changing B_0 at $P_{rf} = 1.4$ kW, and the result is shown in Fig. 2. When B_0 is smaller than ~0.45 kG, the n_e profile around $r = 0$ cm has a concave shape and the distance between two ridges is almost equal to the inner diameter of the Pyrex tube. By increasing B_0, the n_e profile is varied drastically

and becomes peaked at $r = 0$ cm. This dependence of the radial n_e profile on B_0 was explained by taking account of the confinement of the plasma /2, 3/. Basically, the heating and ionization will be localized near the walls, and so is the energy deposition. This causes the concave n_e profile with the ridges at the inner-wall position of the Pyrex tube. By increasing B_0, the energy confinement, which is determined by the end plate sheaths and the intensity of $\mathbf{B}_0$, was considered to be better on the axis, leading to the appearance of a dense core.

When the small-diameter stainless-steel tube is used as a vacuum chamber, nonthermal beamlike electron tails /4/ are observed at the same time that the radial n_e profile is peaked, as shown in Fig. 3. Figure 4 shows that the beam is restricted radially, is the most dense, and there is no tail for $r \gtrsim 1.5$ cm, indicating that the beam position agrees well with the peak position of the radial n_e profile. The electron energy distribution function shows that there is a bump in the range of 50-70 eV, where the cross section for the electron-impact ionization is very large. Therefore, in addition to the improved confinement of the plasma, the electron tails are considered to produce the peaked radial n_e profile, although the mechanism responsible for the nonthermal distribution tail is not yet known. If the large-diameter vacuum chamber is used, the nonthermal beam-like electron tail is not observed at a distance of ~50 cm from the antenna and the half-width of the radial n_e profile is found to be much larger than that obtained in the small-diameter vacuum chamber. The reason why the electron tail disappears is not clear at this stage, but considered to be that since there is a large amount of neutral argon atoms between the dense core and the chamber wall, compared with those in the small-diameter chamber, the electron tail is exhausted for ionizing neutral atoms which are fed radially.

The plasma density n_e is found to be proportional to p in the region of $p \lesssim 1 \times 10^{-3}$ Torr, and to saturate in the high-p region when $B_0 = 1$ kG and $P_{rf} = 1.5$ kW. The

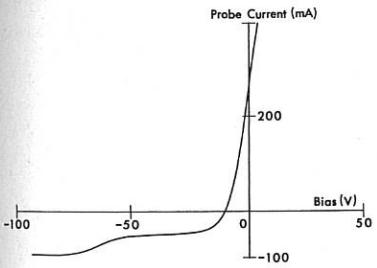

Fig. 3: Probe characteristics when beamlike electron tails are observed.

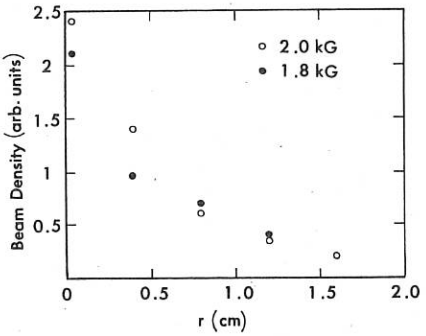

Fig. 4: Radial density profile of beamlike electron tail.

maximum n_e is $\sim 3 \times 10^{13}$ cm^{-3}. Since the density n_0 of neutral atoms at $p = 1 \times 10^{-3}$ Torr is $\sim 2.6 \times 10^{13}$ cm^{-3} at the room temperature of 300 K, it is confirmed that neutral atoms are highly or completely ionized in the range of $p \lesssim 1 \times 10^{-3}$ Torr. In the high-p region, it is considered that there is not enough rf power for all neutral atoms to be ionized.

The phase and amplitude of the helicon wave as a function of axial position z are obtained by interferometry with the magnetic probe. The wavelength is not determined by the antenna length, and is varied automatically to provide the best coupling or to satisfy the dispersion relation which is given by $\omega/k = 3.83 B_0/ae\mu_0 n_e$. Indeed, there is relatively good agreement between the experimentally and theoretically obtained dispersion relations. An important point is that $\zeta (= \omega/kv_{th}$, where v_{th} is the electron thermal velocity) approaches $\sqrt{2}$ as n_e is increased with B_0 fixed, in other words, n_e has a maximum at $\zeta \sim \sqrt{2}$ where the Landau damping rate maximizes. The variation of B_0 makes it possible to change n_e with keeping ζ at $\sim\sqrt{2}$, as known from the dispersion relation. Thus, the n_e dependence of damping rate $\mathrm{Im}(k)/\mathrm{Re}(k)$ is obtained with $\zeta \sim \sqrt{2}$. There is a tendency for $\mathrm{Im}(k)/\mathrm{Re}(k)$ to decrease with an increase in n_e. This is characteristic of Landau damping, and can not be explained by the collisional damping. However, Landau damping is smaller than the collisional damping in the range of $n_e \gtrsim 7.2 \times 10^{12}$ cm^{-3}, so that Landau damping and the collisional damping occur at the same time in our n_e range. If the Landau damping rate plus the collisional damping rate is used as a theoretical damping rate, good agreement is found between the experimentally and theoretically obtained damping rates.

4. Conclusions

Experiments reported here demonstrate the excitation of a helicon wave in a cylindrical magnetoplasma and the production of a highly-ionized plasma. It is shown that the density has a maximum at $\zeta \sim \sqrt{2}$ where the Landau damping rate maximizes, and that both Landau damping and collisional damping occur at the same time in our density range. Nonthermal beamlike electron tails observed in the small-diameter vacuum chamber are considered to play an important role in producing a peaked radial density profile.

References

/1/ R. W. Boswell, Plasma Phys. Controlled Fusion **26**, 1147(1984).

/2/ F. F. Chen, in *Proceedings of the Second International Conference on Plasma Physics*, Kiev, U. S. S. R., 1987, edited by A. G. Sitenko (Naukova Dumka, Kiev, 1987), Vol. 4, p. 321.

/3/ A. Komori, T. Shoji, K. Miyamoto, J. Kawai and Y. Kawai, Phys. Fluids B **3**, 893(1991).

/4/ Peiyuan Zhu and R. W. Boswell, Phys. Fluids B **3**, 869(1991).

DEVELOPMENT OF SPIRAL STRUCTURES ON A ROTATING PLASMA COLUMN WITH LARGE ION-GYRORADIUS

T. Ikehata and H. Mase
Department of Electric and Electronic Engineering, Ibaraki University
Hitachi, Ibaraki 316, Japan

Surface structuring of an expanding plasma in a magnetic field has been vitally investigated in space/1/ and laboratory/2,3/ experiments as well as in analytical/4/ and numerical/5/ calculations, as one of self-organizing processes in continuous media. In the AMPTE magnetotail barium release experiment/1/, the photoionized barium plasma generated a diamagnetic cavity by exclusion of the ambient geomagnetic field and later developed a large-scale coherent structure on the surface. In another laboratory experiment/2/, an aluminum target was irradiated by laser in a strong magnetic field (1.0 Tesla). The expanding plasma gave rise to a robust Rayleigh-Taylor-like instability where the plasma bulk was blocked by the magnetic field but the flute tips continued free-streaming at sub-Alfvenic speeds, often accompanying field-aligned striations. These observations have common features such as; (1) an effective gravity directed outward; (2) unmagnetized plasma ions; (3) the rapid instability growth.

The present paper reports an investigation on the temporal evolution of a Rayleigh-Taylor-like instability which has occurred in a rotating plasma with a large ion gyroradius $\rho_i \geq a$ and a large rotation frequency $\omega \geq \Omega_i$ during propagation along a uniform magnetic field, where a is the plasma core radius and Ω_i is the ion gyrofrequency. In particular, the development of a coherent pattern of "multiple spiral filament" has been observed clearly on the plasma boundary with use of the end-on framing photography and the witness plate diagnostics.

The arrangement of the experiment is shown in Fig. 1. A rotating plasma of Cu/Zn mixture is

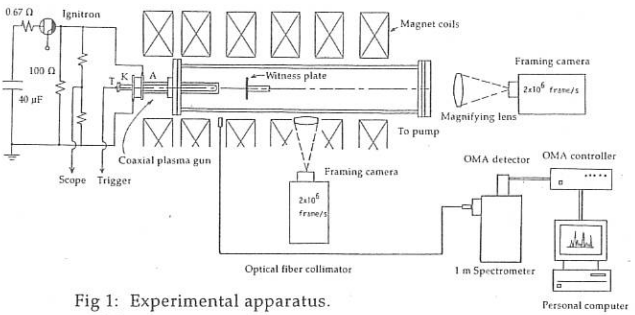

Fig 1: Experimental apparatus. and diagnostics

ejected from a coaxial plasma gun and propagates in a Pyrex vacuum chamber (10 cm in diam.×60 cm long) where a uniform magnetic field B_z of up to 3.2 kG is applied. Vacuum is better than 4×10^{-4} Pa before experiment. The plasma is produced from brass (Cu 60%/Zn 40%) of the inner cathode of the gun through intense cross-field vacuum discharge while it is energized by a 40μF capacitor bank. The current waveform is approximated to a half sine with a peak of 13 kA and a quarter period of 8 μs when a charging voltage V_c=9 kV and B_z=2.5 kG. Axial and azimuthal velocities, v_z and v_ϕ result from Lorentz forces $F_z=J_rB_\phi$ and $F_\phi=J_rB_z$ (order of 10^3 N/m^3) due to the radial current density J_r, where B_ϕ is the azimuthal magnetic field produced by J_r.

Two diagnostic methods were used to monitor plasma behaviors : A fast framing camera (2×10^6 frames/s) investigated the temporal evolution in the plasma profile from both the end and side of the plasma gun. A witness plate (black Polaroid type 47 film) recorded a time-integrated plasma profile when it was exposed to the plasma flow between z=1 and z=15 cm and the plasma flow was energetic enough to blow off the film coating. Other diagnostics are: a fiber-optic emission spectroscopy coupled to an intensified OMA system to measure the ion species, T_i and v_ϕ ; an ion time-of-flight detector to measure v_z; electrostatic probes to measure T_e and the plasma potential.

Typical plasma parameters for I=13 kA and B_z=2.5 kG are given in Table I. From the spectroscopic analysis, it was found that the plasma consists mainly of Cu and Zn although it contains smaller amounts of H, C and O. Although mass difference between Cu and Zn is negligible (~3 %), they are predicted to have singly and doubly charged ions from T_e=9 eV. This means that the plasma includes two groups of ions having a factor of two different ρ_i and Ω_i. We suppose that singly-charged ions with greater ρ_i/a and ω/Ω_i will be predominant for the instability growth.

A rotation frequency ω was evaluated mainly from end-on framing photographs which indicated a constant angular rotation of irregularities on the plasma boundary for each frame time. A radial profile in ω was determined from space-resolved, spectroscopic doppler shift of CIII464.7 nm and confirmed the rigid rotation of the plasma core. It is noted from Table I that the plasma has sub-Alfvenic and supersonic speeds; $v_\phi(r=2\text{ cm})=v_z=2\times10^4$ m/s $\approx v_A>>c_s$ and that $\omega/\Omega_i\geq1$, $\rho_i/a\geq1$ and $M_iv_\phi^2/2T_i>>1$ apply. Since a conventional MHD model is restricted to the low frequency plasma response assuming $\omega/\Omega_i<<1$ and $\rho_i/a<<1$, it can not be applied to strongly nonlinear, nonequilibrium plasmas here.

Table I: Typical plasma parameters for I=13 kA and B_z=2.5 kG

Rotation frequency ω	1.1×10^6 rad/s	Ion gyrofrequency Ω_i	0.8×10^6 rad/s
Axial velocity v_z	2.2×10^4 m/s	Alfven velocity v_A	2.2×10^4 m/s
Ion density n_i	~10^{15} cm^{-3}	Ion acoustic velocity c_s	0.4×10^4 m/s
Ion temperature T_i	10 eV	Ion gyroradius ρ_i	2-3 cm
Electron temperature T_e	9 eV	Plasma core radius a	≈2 cm

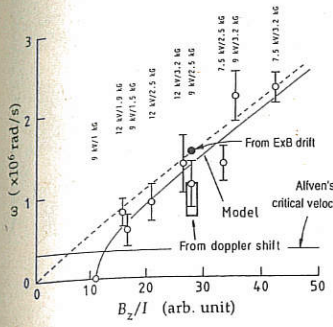

Fig 2: Rotation frequency ω as a function of B_z/I.

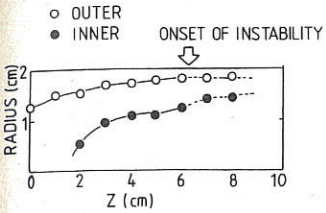

Fig 4: Change in the plasma profile during propagation along B_z.

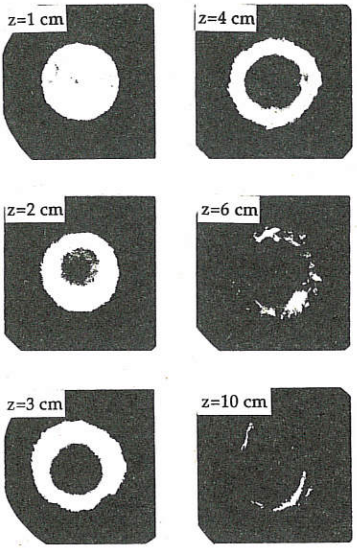

Fig 3: Damage patterns recorded on witness plates after exposure to the plasma flow. Each is obtained by a single shot.

Figure 2 shows ω as a function of a variable B_z/I. The frequency ω increases linearly with B_z/I at large B_z/I. This relation has been explained from a simplified model/6/. The reason for ω=0. at $B_z/I \leq 10$ may be that the plasma diamagnetism cancels B_z and as a result, the driving force $F_\phi = J_r B_z$. Results of witness plate measurements are shown in Fig. 3. Each corresponds to a single exposure at I=18 kA and B_z=2.5 kG. Immediately after the ejection from the gun barrel, plasma particles are transported outward due to the strong centrifugal force; the outer boundary expands to a radius of ≈2 cm from its initial value of 1.15 cm and at the same time, a cavity is formed inside; the expansion appears to reach equilibrium at a downstream distance of z=4-6 cm; the plasma finally has an annular profile with an outer diameter of ≈4 cm and an inner diameter of ≈2.5 cm (Fig. 4). We also recognize that high-order density modulations (like spikes or bubbles) appear on the annular column at z=5-6 cm and often lead to the elliptical deformation of the whole column further downstream.

Figure 5 shows end-on framing photographs taken for (a) B_z/I=17 (13 kA/1.5 kG) and (b) B_z/I=43 (11 kA/3.2 kG), where ω is (a)0.6×10⁶ rad/s and (b)2.2×10⁶ rad/s and the plasma density is of the order

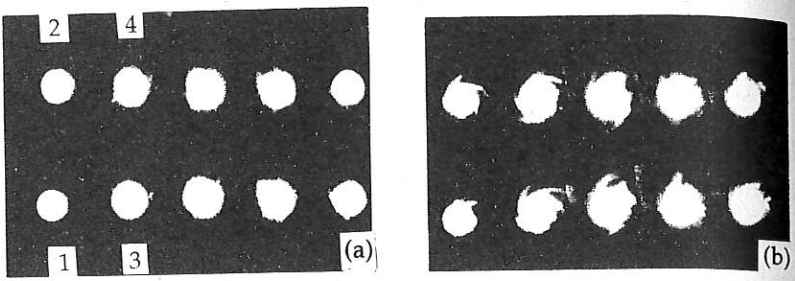

Fig 5: End-on framing photographs taken for (a) B_z/I=17(13 kA/2.5 kG) and (b) B_z/I=43(11 kA/3.2 kG). The number shows the sequence of frames.

of 10^{15} cm^{-3}. From the scaling relation $n_i \propto I^2/6/$, the plasma density for (b) is estimated to be 70% of (a). At the beginning, 8-10 pieces of thin filaments appear to grow radially in a time quite shorter than the rotation period (Fig. 5(a)). The number of filament decreases with time through the nonlinear interaction which includes coalescence or merging of filaments, to final 2-3 pieces of broader spirals. This scenario is more evident in Fig. 5 (b) where ω is increased by a factor of 3.7 and the centrifugal force by a factor of 13; strong spiral filaments are clearly observed; the interaction among filaments appears to be rather turbulent; in the later stage, a low density halo is formed around the plasma core since plasma particles are transported outward through filaments; A sheared rotation should occur between the halo and plasma core; this drives a secondary instability (probably K-H instability) generating fairly symmetrical, 2 or 3 pieces of spiral arms. This transition from short to long wavelengths of instability waves has been observed also in the laser plasma experiment/3/ and in the nonlinear plasma simulation/5/. It may be regarded as the inverse cascade process in the nonlinear evolution of instability.

In summary, the growth of the Rayleigh-Taylor like instability and the subsequent structuring have been investigated for rotating plasmas with large ion-gyroradius with the framing photography. The development of spiral filaments and their shift to longer wavelengths (lower modes) through the mode coupling have been identified as typical nonlinear phenomena. A future investigation with controlled ω and n_i will be essential to make detailed comparisons with theories and to understand the physical picture of instability.

/1/ P.A.Bernhardt, R.A.Roussel-Dupre, M.B.Pongratz, G.Haerendel, A.Valenzuela, D.A.Gurnett, R.R.Anderson, J.Geophys.Res. **92**,5777(1987).
/2/ B.H.Ripin, E.A.McLean, C.K.Manka, C.Pawley, J.A.Stamper, T.A.Peyser, A.N.Mostovych, J.Grun, A.B.Hassam, J.D.Huba, Phys.Rev.Lett. **59**,2299(1987).
/3/ G. Dimonte, L.G.Wiley, Phys.Rev.Lett. **67**,1755(1991).
/4/ J.D.Huba, A.B.Hassam, D.Winske, Phys.Fluids B **2**,1676(1990).
/5/ J.D.Huba, J.G,Lyon, A.B.Hassam, Phys.Rev.Lett. **59**,2971(1987).
/6/ T.Ikehata, T.Tanabe, H.Mase, 14th Int.Symp.Discharges and Electrical Insulation in Vacuum (Santa Fe,1990) p.218.

WAVES DRIVEN BY STRONG TRANSVERSE POTENTIAL STRUCTURES*

M. E. Koepke, M. J. Alport, T. E. Sheridan, W. E. Amatucci, and J. J. Carroll III
Department of Physics, West Virginia University
Morgantown, West Virginia 26506 USA

The mode characteristics of waves being driven by magnetic-field-aligned current and waves driven by strong transverse potential structures are compared. Experiments are performed in a Q-machine /1/ plasma column (3-cm radius and 90-cm length) with the following parameters: $n \approx 10^8$ cm^{-3}, B = 1.5 kG, $m_i/m_e = 7.15 \times 10^4$, $T_i \approx T_e \approx 0.2$ eV. Experiments are aimed at producing strong shear in azimuthal electron velocity inside a narrow (diameter $\approx$ 10 ion gyroradii) channel of axial electron current. The presence of a velocity shear layer is predicted /2/ to affect the electrostatic ion-cyclotron waves that can be excited by current drawn to the biased electrode. In this paper, measured mode characteristics of the ion-cyclotron fluctuations as modified by adjustable velocity shear are presented.

Ganguli, Lee, and Palmadesso /2/ developed a kinetic theory to investigate the electrostatic oscillations in a magnetized plasma containing a transverse, d.c. electric field. In the fluid limit and for perpendicular propagation, they recover the well known Kelvin-Helmholtz instability which explicitly depends on the gradient of the shear, i.e., the second derivative of the transverse flow. It is characterized by long wavelength ($k_\perp L_s < 1$; L_s is the characteristic length associated with the velocity shear) and low frequency ($f \ll f_{ci}$). In the short-wavelength limit, the general nonlocal dispersion condition yields a new branch of oscillation which is sustained by the inhomogeneity in the energy density of the waves. The inhomogeneous energy-density driven (IEDD) instability is generally a short-wavelength ($k_\perp L_s > 1$) fluctuation with a broadband frequency spectrum. Depending on ambient parameters, the frequency of this instability may fall around the ion gyrofrequency and can be mistaken for the current-driven electrostatic ion cyclotron (CDEIC) instability /3/, especially when magnetic-field-aligned current is also present /4/.

Unlike the CDEIC instability, which grows by inverse Landau damping onto the electrons that are resonant with the longitudinal component of the wave phase velocity, the IEDD instability requires only that the Doppler shift in frequency due to the $\vec{E} \times \vec{B}/B^2$ rotation velocity $\vec{v}_E$ makes $(\omega - k_\theta v_E) < 0$, a nonresonant effect. The nonlinear spectra of the two instabilities are very distinct as demonstrated by Nishikawa et al. /5/ While the spectrum of the CDEIC instability is coherent around a single frequency, the spectrum of the IEDD instability is spiky and broadband. In the general case where a combination of both transverse, d.c. electric field and magnetic-field-aligned current are present, the growth rate is larger than a linear combination of the two sources of free energy would indicate. The interaction of this new branch of oscillation with magnetic-field-aligned current is being used to explain the short-wavelength broadband turbulence observed in the ionosphere, magnetosphere, and the jump-region of the bow shock, and it is upon this interaction that the investigation reported here is focused.

The radial structure of the electric potential in the plasma is controlled using a disk electrode placed on the cylindrical axis of the plasma, 60 cm from the plasma-source end. The disk /6/ is made of two coplanar, concentric circular

segments that are heated to prevent surface contamination. The applied voltages on the outer annular segment and on the inner button segment are independently controlled with precision power supplies. The potential structure in the plasma is inferred from the voltage of an electrically floating Langmuir probe. Fig. 1 shows two examples from a specific sequence of radial potential profiles. The reference case of this sequence for which all end electrodes are electrically floating is included.

The features of the profiles that are relevant to plasma stability are located on magnetic field lines that map to the 2-cm-diameter segmented disk electrode. A positive potential within this region, with respect to the reference profile, induces a magnetic-field-aligned electron current. Between regions of different potential, an electric field transverse to the magnetic field exists. Potential structures representing the cases of (a) large field-aligned current and (b) large transverse, localized electric field are shown in Fig. 1. This categorization identifies one of these two aspects as that having the predominant effect on plasma stability.

For the case of large magnetic-field-aligned current (FAC), waves are observed within the region $r \leq 1$ cm (the current channel region) that are identified /6/ with the current-driven electrostatic ion cyclotron (CDEIC) instability /3/. The mode frequency of these waves is slightly larger than the ion cyclotron frequency for potassium, $f \approx 1.1\, f_{ci}$. The spectral feature associated with the mode is narrow (2-3 kHz) as shown by the thick trace at the top in Fig. 2a.

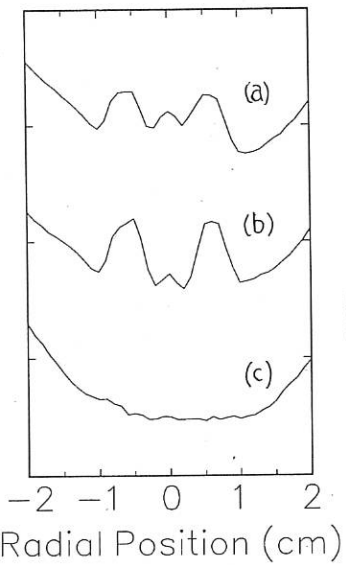

Fig. 1: Measured floating potential across the diameter of plasma column, 2 cm in front of segmented disk electrode. Profiles are displaced vertically for clarity. Annulus and button voltages are a) 5.5 V and 5.5 V, b) 10.5 V and 0.5 V, c) floating and floating, respectively. Hashmarks on vertical axis are 0.5 V increments.

For the case of large transverse, localized electric field (TLE), waves are observed that are distinctly different from the FAC-driven waves. Although the TLE-driven mode frequency is in the neighborhood of the FAC-driven mode frequency, the spectral feature associated with the TLE-driven mode is broader (~10 kHz) and spikier, as shown by the thick trace near the bottom in Fig. 2a.

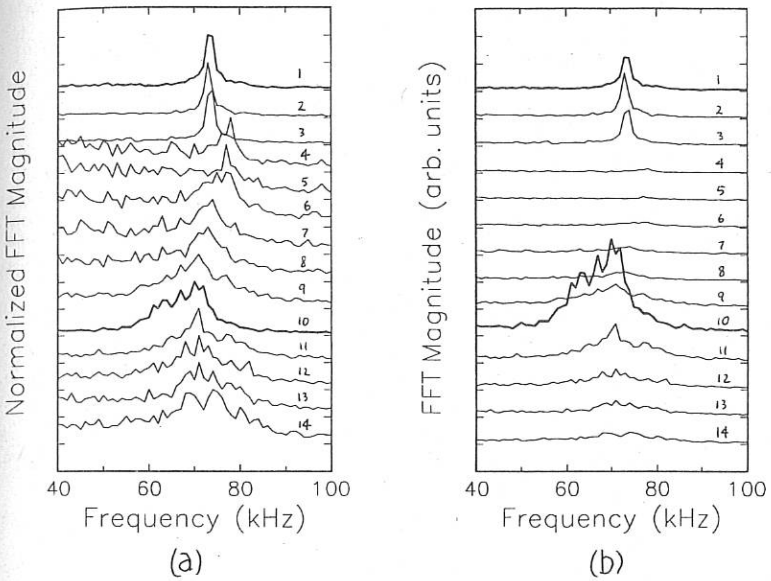

Fig. 2: Sequence of spectra from fluctuations in current collected by annulus segment of disk electrode. Spectra are displaced vertically for clarity. Thick-line traces are referred to in the text. Annulus voltage is 9.5 V and (V_a - V_b) is identified by a number next to each trace. a) Spectra are normalized to the same maximum amplitude, b) spectra are left unnormalized.

Two additional features that distinguish the two modes can be recognized in the normalized spectra in Fig. 2a (normalizing emphasizes mode frequency) and in the unnormalized spectra in Fig. 2b (not normalizing emphasizes relative mode amplitude). First, a shift in TLE-driven mode frequency is evident in traces (4) through (10) in Fig. 2a, for which the applied voltage difference between the two circular segments of the disk electrode changes in one-volt increments from 4 V to 10 V. Second, a sensitive dependence of the TLE-driven mode amplitude on the transverse electric field strength is apparent in traces (4) through (10) in Fig. 2b. The TLE-driven mode power can be significantly larger than the FAC-driven mode power. Since the channel-averaged field-aligned current decreases as the bias on either segment is decreased, Fig. 2 implies that this mode is observed for cases in which the field-aligned current is subcritical for exciting CDEIC waves. This is consistent with a report /6/ of a reduced critical electron drift velocity in the presence of this transverse, localized, d.c. electric field.

One further distinction between the two modes is that the FAC-driven waves are detected from the fluctuations in the current collected by both the annulus and button segments, however the TLE-driven waves are detected only on the annulus. This difference suggests that the TLE-driven waves are present at radii where the transverse electric field is large and are absent at radii where the transverse electric field is small.

The observed dependence of the TLE-driven mode characteristics (spectral shape, mode frequency, mode amplitude, and radial mode structure) on the transverse localized electric field conclusively eliminates the current-driven electrostatic ion cyclotron instability as the mechanism responsible for this mode. On the basis of the results presented here the inhomogeneous energy-density driven instability /4/ is believed to be responsible. Van Niekerk et al. /7/ recently reported on azimuthally propagating TLE-driven waves, which they attribute to the same instability, with a frequency 15% higher than CDEIC waves. A complete characterization of this TLE-driven mode is presently underway.

*Research supported by the Office of Naval Research and the National Science Foundation.

/1/ R. W. Motley, *Q Machines* (Academic Press, New York, 1975).
/2/ G. Ganguli, Y. C. Lee, and P. J. Palmadesso, Phys. Fluids 31, 823 (1988).
/3/ J. J. Rasmussen and R. W. Schrittwieser, IEEE Trans. Plasma Sci. 19, 457 (1991).
/4/ G. Ganguli, Y. C. Lee, P. J. Palmadesso, and S. L. Ossakow, in *Physics of Space Plasmas* , T. Chang, G. B. Crew, and J. R. Jasperse, eds. (Scientific Publishers, Inc., Cambridge, MA, 1989) p. 231.
/5/ K.-I. Nishikawa, G. Ganguli, Y. C. Lee, and P. J. Palmadesso, Phys. Fluids 31, 1568 (1988): J. Geophys. Res. 95, 1029 (1990).
/6/ M. E. Koepke and W. E. Amatucci, IEEE Trans. Plasma Sci. (October 1992, in press).
/7/ E. G. van Niekerk, P. H. Krumm, and M. J. Alport, Plasma Phys. Contr. Fusion 33, 375 (1991).

Experimental Dynamics of 2-D Vorticity Rings.

A.J. Peurrung and J. Fajans
Physics Department
University of California, Berkeley
Berkeley, California 94720 USA.

A direct analogy exists between the dynamics of a 2-D inviscid, incompressible fluid, and a magnetized pure electron plasma, with the fluid vorticity corresponding to the plasma density. Thus the U.C. Berkeley electron trap is a powerful tool for controlling and measuring the "vorticity" of an evolving fluid system. Here we study the evolution of a hollow ring of vorticity. Through the Kelvin-Helmholtz instability of fluid mechanics, and the equivalent diocotron instability[1] of electron beam theory, a symmetric ring develops into individual vortices.[2-5] A sufficently asymmetric ring, however, undergoes a "winding" instability, resulting in a spiral shape. We show various images detailing the stages of the dynamics for various initial ring parameters.

Figure 1 contains a simplified side view of our experimental geometry.[6] A magnetic field along the axis of the trap insures radial confinement of the plasma. Axial confinement is obtained by applying negative voltages to the two end cylinders. $\mathbf{E} \times \mathbf{B}$ drifts due to the applied magnetic field and the plasma's own electric field govern the plasma dynamics. These drifts are slow compared to the end to end electron bounce motion; therefore the behavior is largely two-dimensional.

Grounding the right end cylinder forces the plasma to stream out along the magnetic field lines, producing a visible image on the phosphor screen. Imaging destroys the plasma; however, time sequenced images can be produced because the plasmas are very reproducible. To obtain the asymmetric annular plasmas used in this experiment, we first form a quiescent electron plasma (length=4 cm, temperature=2.0 eV, density=1.0×10^8 cm^{-3}) and then move it a known distance off center using feedback from a wall probe. Finally, we eject the central plasma core by briefly reducing the voltage on one end cylinder.

Figure 2 shows the time history of a typical symmetric hollow plasma. First, well developed vortices form and then the vortices merge until only one central vortex remains. The initial number of vortices (the mode number) is inversely proportional to the ratio of the thickness of the ring to the ring radius. In Fig 3 we show the results for a large number of ring thicknesses. In Fig. 4 we plot the calculated[1] and measured mode number vs. this ratio. The results are in good agreement with theory for small mode numbers but are not in agreement for large mode numbers. We have also measured the instability growth rate and find that it is also far from the theoretically predicted rate for thin rings.[4,5] We suspect that these descrepancies are due to finite length effects.

For some asymmetric rings the dynamics are entirely different. As shown in Fig. 5, asymmetric rings develop into spirals. In this case the dynamics

can be divided into an "active" and a "passive" phase. In the active phase, superposition leads to a model of a section of the asymmetric ring as two vortices of opposite sign. Such a vortex pair will travel in the direction perpendicular to the line connecting the pair centers—in this case towards the device center. After the density clump gets to the center, the interaction is largely passive, with the remaining plasma spiraling around the center because of the sheared velocity fields. The number of spiral turns increases linearly with time. As shown in Fig. 6, the plasma at radius r advances in angle roughly as $d\theta/dt \propto t/r$. This regular dependence implies that a mean field approximation can be used to estimate the velocity shear. The winding process ends when the plasma smears. Kelvin-Helmholtz instabilities are surpressed by adverse shear.

This work was supported by the Office of Naval Research and by the National Science Foundation.

[1]R. H. Levy, *Phys. Fluids* **8**, 1288 (1965).

[2]C. A. Kapetanakos, D. A. Hammer, and C. D. Striffler, *Phys. Rev. Lett.* **30**, 1303 (1973).

[3]Y. Carmel and J. A. Nation, *Phys. Rev. Lett.* **31**, 286 (1973).

[4]G. Rosenthal, G. Dimonte, and A. Y. Wong, *Phys. Fluids* **30**, 3257 (1987).

[5]C. F. Driscoll, J. H. Malmberg, and K. S. Fine, *Phys. Rev. Lett.* **60**, 1290 (1988).

[6]J. H. Malmberg, C. F. Driscoll, B. Beck, D. L. Eggleston, J. Fajans, K. Fine, X. P. Huang, and A. W. Hyatt, , in C.W. Roberson and C.F. Driscoll, editors, *Nonneutral Plasma Physics*, volume AIP 175 p. 28, New York (1988), Amer. Inst. of Physics.

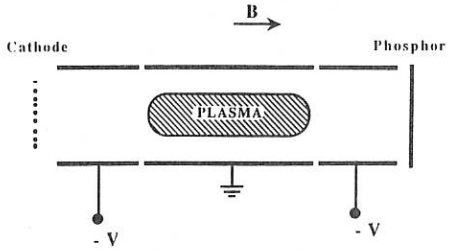

Fig. 1 Experimental schematic.

Fig. 2 Hollow plasma time sequence.

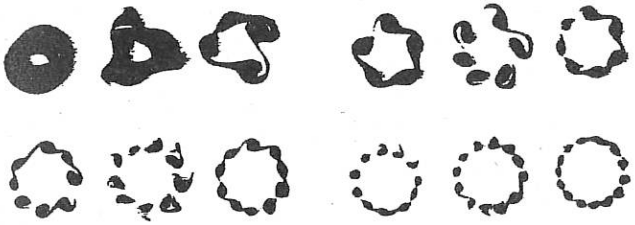

Fig. 3 Instability for varying initial ring thicknesses.

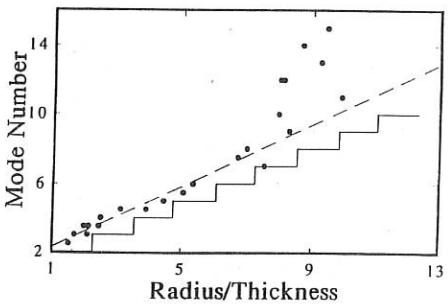

Fig. 4 Measured (dots) and calculated mode numbers.

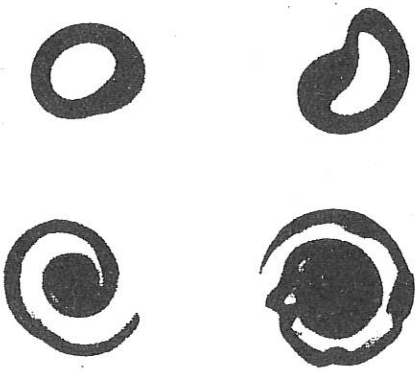

Fig. 5 Asymmetric dynamics.

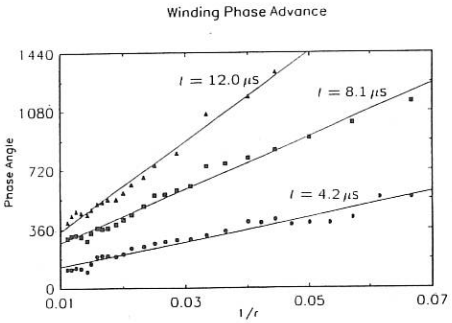

Fig. 6

III-1903

Dynamics of Non-Stationary Dipole Vortices in the Hasegawa-Mima Equation.

Jan S. Hesthaven, Jens-Peter Lynov and Jonas Nycander[1]
Association EURATOM-Risø National Laboratory,
Optics and Fluid Dynamics Dept., P.O.Box 49, DK-4000 Roskilde.

Abstract: The dynamics of tilted dipole vortices in the Hasegawa-Mima equation is studied. A recent theory is compared with numerical simulations and found to describe the short time behaviour of dipole vortices well. In the long time limit the dipoles are found to either disintegrate or relax toward a steady dipole vortex counter propagating relative to the linear drift waves. This relaxation is a consequence of nonviscous enstrophy loss by the dipole vortex.

The Hasegawa-Mima equation can be derived for nonlinear drift waves in a low-β plasma with a density gradient. In non-dimensional variables the equation is

$$\frac{D}{Dt}\Gamma = 0 \quad , \quad \Gamma = \nabla^2\phi - \phi + \beta y \quad , \qquad (1)$$
$$\frac{D}{Dt} = \frac{\partial}{\partial t} + [\phi, \ ] \quad ,$$

where Γ is the potential vorticity which is conserved for each fluid element, ϕ represents the electrostatic fluctuations, [,] the Jacobian and β is proportional to the density gradient directed along -y. The maximum phase velocity of the linear drift waves, propagating in the electron diamagnetic drift direction, is $-\beta$. It is well known that Eq.(1) conserves mass, energy and enstrophy.

Eq.(1) has a dipole vortex solution /1/, which is exact and stationary if co- or counter-propagating relative to the linear waves. It is known that if a counter-propagating dipole vortex is initially rotated slightly, it will execute regular oscillations around the steady state magnetic flux surface /2/, i.e. the positive x-axis (cf. Fig.2). This behaviour may be understood as a consequence of the Lagrancian conservation of potential vorticity. Recently Nycander and Isichenko /3/ derived an approximate equation of motion for the velocity $\vec{U}$ of dipoles propagating in arbitrary directions

$$\frac{d\vec{U}}{dt} = \vec{U} \times \hat{z} y \beta U \frac{S}{P_d} \quad , \quad \vec{P}_d = \int (\phi - \nabla^2\phi)\vec{r}\, dx dy \qquad (2)$$

where $S = \pi a^2$ is the area of the dipole inside the separatrix, y is the y-coordinate of the centre of the dipole vortex and $P_d = |\vec{P}_d|$ is the magnitude of the dipole moment, with $\vec{r} = 0$ in the centre of the dipole vortex. Equation (2) is obtained by noting that the radius of curvature of the trajectory is equal to the ratio between the dipole moment and the monopole moment of the dipole vortex, and also that the monopole moment varies linearly with the y-coordinate of the vortex. The latter is a consequence of the conservation of potential vorticity inside the separatrix. It is assumed that the internal structure of the dipole remains unchanged, implying that S and P_d are constant, and that the radius of curvature of the trajectory is much larger than the diameter of the dipole. This is justified if $\beta/U \ll 1$. The theory doesn't take into account loss of enstrophy.

[1]Permanent address : Dept. of Technology, Uppsala University, Box 534, S-751 21 Uppsala, Sweden

Equation (2) may be integrated, and the oscillation frequency, ω, obtained

$$\omega = U\frac{\pi}{2}\left(\frac{\beta S}{P_d}\right)^{1/2}\frac{1}{K(k)} \ , \tag{3}$$

where K is a complete elliptic integral of the first kind with the argument $k = |\sin(\alpha/2)|$, α is the maximum angle between the trajectory and the x-axis. $\alpha = 0$ for an exact dipole vortex counter-propagating relative to the linear waves.

The maximum displacement, y_t, along the density gradient is found to be

$$y_t = \pm\left(\frac{P_d}{\beta S}\right)^{1/2} 2\sin(\alpha/2) \ , \tag{4}$$

and the displacement , L_w, along a magnetic flux surface during one full oscillation, here referred to as the oscillation length, is

$$L_w = 4\left(\frac{P_d}{\beta S}\right)^{1/2}[2E(k,\pi/2) - K(k)] \ , \tag{5}$$

where E is an elliptic integral of the second kind.

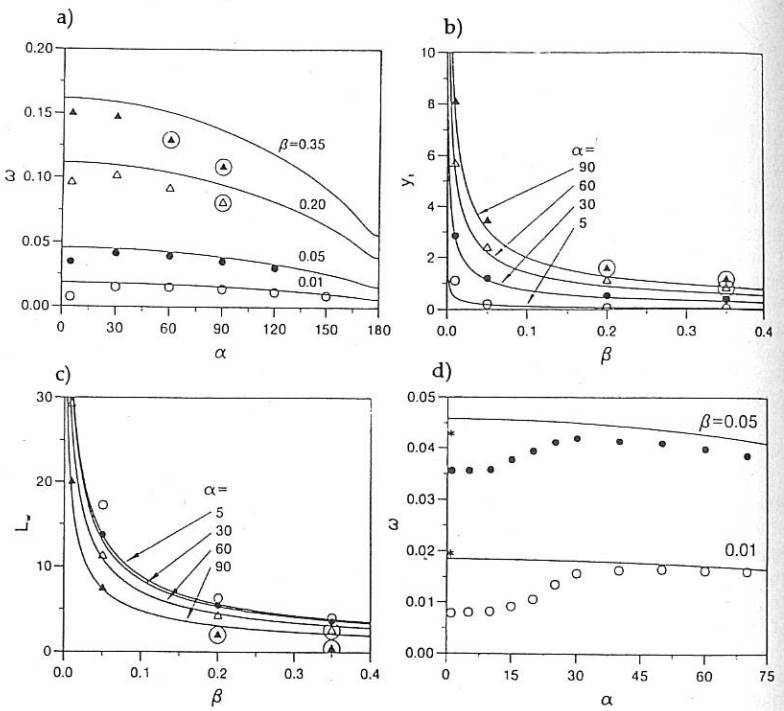

Fig.1 a) Oscillation frequency. b) Displacement along the density gradient. c) Displacement along magnetic flux surface. d) Blow up of 1a.

These expressions have been evaluated by numerical simulations. The numerical scheme is based on a pseudospectral approximation in a periodic domain and a 3rd order Adam-Bashforth predictor-corrector as time integration method. Zero-padding is used as de-aliasing. All simulations are done with a resolution of 128^2 modes. As initial conditions we used the exact solution /1/ tilted at an angle α with propagation velocity $U = 0.1$ and size of separatrix $a = 1.0$. Unless otherwise stated $\beta = 0.05$. A special 'cutting'-technique has been applied to avoid effects caused by the periodicity of the domain /4/.

To test Eqs.(3)-(5), the dipole behaviour was simulated for different values of β and α. The three characteristic parameters ω, y_t, L_w were determined at the first maximum of the oscillation, and the estimated parameters were then found by extrapolation. The reason for using only a quarter of a period is that the amplitude of the oscillations changes significantly already during one or a few periods because of processes not included in the theory.

In Fig. 1a, the simulated oscillation frequency is compared with Eq.(3). We observe good agreement between theory and simulations for $\beta/U \leq 1$ except for $\alpha \leq 30°$. The maximum displacement along the density gradient is plotted and compared with the value from Eq.(4) in Fig.1b, and comparison between simulations and the oscillation length from Eq.(5) is shown in Fig. 1c. In the limit $\beta/U \ll 1$, the figures show good correspondence between simulations and theory even for a very large initial angle. However, there is some unexpected deviation for small angles. In order to investigate this, a detailed study of this region has been performed. The result is shown in Fig. 1d. One may speculate that the deviation is caused by some internal transient process. It has been observed, that the internal reorganizing process has a stronger effect when α is small, causing the functional dependency inside the separatrix to become weakly non-linear after a quarter of an oscillation. This idea is supported by the fact that calculating the oscillation frequency of the dipole after several oscillations yields increased agreement with the theory as marked in Fig.1d with '$\star$'.

In the region $\beta/U > 1$, the qualitative dependence of the oscillation frequency, ω, as a function of the angle is correct, but the exact value is seen to be too low. This may be explained by energy loss causing the dipole vortex to decrease its propagation velocity. The good agreement for y_t and L_w supports this assumption.

Some of the dipoles disintegrate shortly after a quarter of a period, as marked by large circles in Fig.1. The large deviation for $\beta/U \gg 1$ and large initial propagation angle are most likely connected to the processes causing the disintegration.

As has been shown, the above theory seems to agree well within the given limits. However, the nonviscous loss of energy and enstrophy by the vortex to the surrounding plasma have a strong impact on the long time behaviour of the dipole, implying that the theory is only valid for the first few oscillations. After these the dipole vortex has changed significantly, and the theory fails to describe the trajectory of the oscillating dipole based on the initial conditions.

Simulations have been done with parameter scans in β and α in order to investigate the long time evolution of counter-propagating dipoles launched at the angle α. Figure 2a shows trajectories for dipoles at different initial angles. The most interesting feature is that the trajectory of the dipole after a sufficiently long time seems independent of the initial conditions, except for a phase shift.

For a large initial angle the trajectory is approximately sinusoidal, as one might expect. However, for a smaller launch angles the initial part of the trajectory is rather irregular, indicating that the dipole in this phase is affected by the internal reorganization process.

Simulations of dipoles with a very large initial launch angle are also shown in Fig. 2b. We observe that if the angle is too large, the dipole soon disintegrates. Thus there seems to be only two possible outcomes of a dipole vortex initially propagating at some angle. Either the dipole ends up as a steady counter-propagating dipole or it disintegrates.

The relaxation of the trajectories seen in Fig.2a can be explained as follows. If the vortex looses enstrophy, the amplitude $\phi - \nabla^2\phi$ must decrease in magnitude. For α being positive this implies, due to conservation of potential vorticity, that the cyclonic part must move a little down the gradient and the anticyclonic part a little up the gradient. This induces a clockwise torque around the centre of the dipole vortex and as a result we observe that the propagation angle decreases. Similar arguments may be adopted to explain why the co-propagating dipoles swing around and finally become a counter-propagating dipole vortex. The enstrophy loss also causes the two dipole halves to be pulled slightly apart implying a small decrease in the propagation velocity. This corresponds well with the speculations used in Fig. 1 to explain the deviation between the Nycander-Isichenko theory and the simulations for $\beta/U \gg 1$.

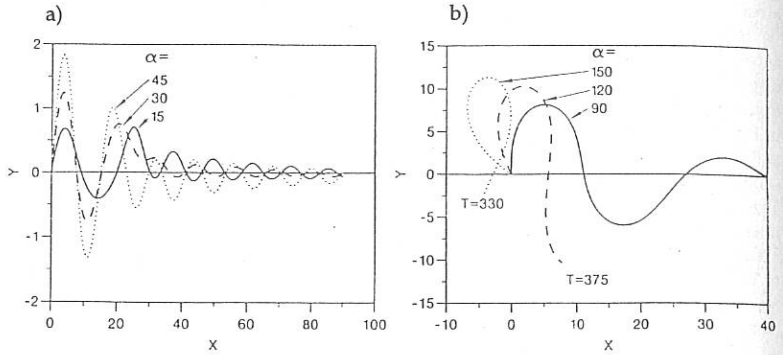

Fig.2 a) Long time behaviour for small launch angles.
b) Long time behaviour for large launch angles.

Concluding Remarks

It has been shown that the theory of Nycander and Isichenko /3/ describes the short time behaviour of the oscillating dipole vortex quite well. However, since the dynamics of the non-stationary dipole is strongly altered by loss of energy and enstrophy, the theory fails to describe the long time dynamics of the dipole vortex. It has also been shown, that in part of the parameter space the short time vortex behaviour is strongly affected by initial transient effects, caused by an internal reorganizing process.

In the long time limit dipoles launched at some finite angle are found to either end up as steady dipoles counter-propagating the linear drift waves or disintegrate shortly after the initial period. Thus, the steady counter-propagating dipole vortex may be considered as an attracting solution. Our explanation of this is that the counter-propagation state is the minimum enstrophy state of the dipole vortex. The long time behaviour can be interpreted as a relaxation toward this state, caused by enstrophy loss. However, no definite quantitative confirmation of this has been obtained.

References

/1/ V.D. Larichev and G.M. Reznik, Dokl. Akad. Nauk. SSSR **231**, 1077(1976)
/2/ M. Makino, T. Kamimura and T. Taniuti, J. Phys. Soc. of Japan **50**, 980(1981)
/3/ J.Nycander and M.B. Isichenko, Phys. Fluids B **2**, 2042(1990)
/4/ J.S. Hesthaven, J.P. Lynov and J. Nycander, (Accepted by Phys. Fluids A)

Localized vortices in η_i - modes

J. Nycander[1], J.P. Lynov, and J. Juul Rasmussen
Association EURATOM-Risø National Laboratory,
Optics and Fluid Dynamics Dept., Risø, DK-4000 Roskilde, Denmark

For a wide variety of nonlinear wave equations necessary conditions for the existence of localized, stationary structures can be found by applying a simple procedure, involving two steps /1/: First the linear dispersion relation is obtained and the regions of the phase velocity of linear waves found. Secondly, assuming that localized solutions exist, their velocities are determined by using integral relations. The obtained velocity takes the form of a "center of mass velocity". If this velocity falls outside the regions of phase velocities for linear waves then nonlinear localized vortices may exist. Otherwise, the structure will couple to the linear waves and gradually disperse. Applying this method we have shown that monopole vortex solutions exist for drift waves driven by the ion temperature gradient in a magnetized plasma, the so-called η_i-modes. Numerical solutions show that such vortices are steadily propagating and stable and they generally emerge from localized initial conditions. Our study is motivated by recent high resolution simulations of η_i-turbulence /2,3/, where it was observed that coherent vortices developed spontaneously. These had a dominating influence on the evolution of the turbulence, and the associated anomalous transport was found to be significantly reduced as compared with the predictions from quasilinear theory /2/.

The analysis is based on a simplified two-dimensional model of η_i-modes /3,4/:

$$\partial_t(1-\nabla^2)\phi - [\phi,\nabla^2\phi] + (1-2\varepsilon_n+\alpha\nabla^2)\partial_y\phi - 2\varepsilon_n\partial_y p = 0 \tag{1}$$

$$\partial_t p + [\phi, p] + \alpha\partial_y\phi = 0, \tag{2}$$

where $\varepsilon_n = L_n/R$, $\alpha = (1+\eta_i)/\tau$, $\eta_i = L_n/L_T$, $\tau = T_e/T_i$, $L_n^{-1} = \partial_x n_0/n_0$, n_0 is the background density, $L_T^{-1} = \partial_x T_i/T_i$, T_e and T_i are electron and ion temperatures, respectively, while R accounts for the curvature of the magnetic field. The time is normalized with c_s/L_n and the spatial coordinates are normalized with $\rho_s(=c_s/\Omega_i)$, where $c_s = (T_e/M_i)^{\frac{1}{2}}$, and Ω_i is the ion cyclotron frequency. The electrostatic potential, ϕ, and the ion pressure perturbation, p, are normalized with $(T_e/e)(\rho_s/L_n)$ and $p_{e0}(\rho_s/L_n)$, respectively. Here p_{e0} is the zero-order electron pressure. Finally, $[f,g]\,(=f_xg_y - f_yg_x)$ denotes the Poisson bracket. In Eqs. 1-2 we have omitted the effects of magnetic shear and thus the parallel dynamics. Curvature effects are retained and the instability is reproduced by the equations for a certain critical value of η_i.

The regions of linear wave propagation are found by deriving the dispersion relation in the local approximation. Linearizing and Fourier transforming Eqs. 1-2 we obtain

$$\omega^2(1+k^2) - \omega k_y(1-2\varepsilon_n-\alpha k^2) + 2k_y^2\alpha\varepsilon_n = 0. \tag{3}$$

By examining Eq. 3 we find that the condition for instability, i.e. $\mathrm{Im}\omega > 0$, is $\alpha > 0$. To obtain the localization condition we solve the dispersion relation for k^2 in terms of $u \equiv \omega/k_y$:

$$k^2 = -\frac{u^2-(1-2\varepsilon_n)u+2\varepsilon_n\alpha}{u(u+\alpha)}. \tag{4}$$

The condition for the existence of propagating linear waves is $k^2 > 0$, provided the phase velocity u is real. For $\alpha < 0$ linear wave propagation is possible in a restricted regime of

[1]Permanent address: Dept. Technology, Uppsala University, S-75121 Uppsala, Sweden

u-values /4,5/, and localized vortex solutions may be possible both for positive and negative u-values. It has been shown that dipole vortices exist in these regions /4,6/. To see if monopole vortices are also possible we derive the center of mass velocity V for any localized solution. This is done by multiplying Eq. 1 with y and integrating over the (x, y)–space:

$$V \equiv \frac{d}{dt}\frac{\langle y\phi\rangle}{\langle\phi\rangle} = 1 - 2\varepsilon_n - 2\varepsilon_n\frac{\langle p\rangle}{\langle\phi\rangle} \tag{5}$$

where we have introduced the notation $\langle f\rangle \equiv \int_{-\infty}^{\infty}\int_{-\infty}^{\infty} f\,dx\,dy$. Thus the velocity of localized coherent structures depends on the ratio $\langle p\rangle/\langle\phi\rangle$. It should be stressed that the local ratio between p and ϕ can only be considered a free parameter inside the separatrix, separating trapped fluid from free fluid. Outside the separatrix this ratio will be determined by the incoming fluid and the upstream boundary condition at infinity, which gives $p/\phi = \alpha/V$. Clearly V can take any value by properly choosing p and ϕ, thus localized solutions exist. Explicit monopole solutions can be constructed /5/ by a perturbation analysis /1/.

We have investigated the stability of the monopole solutions numerically. The set of equations (1-2) is solved in a two dimensional domain with periodic boundary conditions. We have employed a fully de-aliased spectral method /7/. To facilitate the numerical solutions we equipped Eqs. 1–2 with dissipative terms: $-D_1\nabla^4\phi$ accounting for cross–field dissipation in Eq. 1 and $D_2\nabla^2 p$ accounting for thermal conduction in Eq. 2. The initial value for ϕ is obtained by solving the modified Poisson equation $(1-\nabla^2)\phi = S$, where the source function is a Gaussian $S = S_0\exp[-(x^2+y^2)/r_0^2]$. This ensures that the zeroth–order solution is stable in the isotropic case. The initial value for p is equal to $Q_0\phi$. We have performed runs with $\varepsilon_n = 0.25$ and $r_0 = 1$ and various values of α and the initial amplitude ratio Q_0.

Figure 1 shows a typical example of a steadily propagating, stable monopole vortex for the case where the velocity is outside the region of linear waves and $\alpha < 0$. After an initial transient period with internal rearrangements to set up the proper solution, the vortex is seen to propagate with a constant speed in the y-direction somewhat below V_0, where $V_0 \equiv 1 - 2\varepsilon_n - 2\varepsilon_n Q_0$. (See also Fig. 2). The vortex is very slowly decaying due to the dissipative terms introduced. In all cases we found that the speed of the vortex is below $|V_0|$. (As was discussed in connection with Eq. 5 Q_0 can only determine the ratio p/ϕ inside the separatrix, while this ratio outside the separatrix will be determined self–consistently by the outer fluid. Thus, V_0 cannot be expected to give the final velocity exactly. The discrepancy is inversely proportional to the amplitude of the vortex). From Fig. 2 it is observed that although the vortex propagates mainly in the y-direction, i.e. perpendicularly to the gradients there is also a weak propagation along the gradient. In the present case the propagation occurs up the density-gradient, but due to the symmetry of Eqs. 1-2 vortices with opposite signs of p and ϕ will propagate down the gradient. It is thus evident that the vortices will transport trapped fluid much more effectively perpendicularly to the gradients (along the magnetic flux surfaces) than along the gradients (across the magnetic flux surfaces), and the presence of long-lived vortices in the turbulence may actually reduce the cross field transport. Results like those shown in Figs. 1 indicate that the monopole vortex is an attractor, at least for circularly symmetric initial conditions. Evolutions similar to Fig. 1 were also observed for moderately positive α–values when $|V_0|$ was sufficiently large. In the strongly unstable regimes the flow was dominated by the linear instability of the wake field.

For values of V_0 resulting in velocities inside the region of linear wave propagation a propagating monopole vortex was still observed to form from the initial conditions. This structure was found to radiate linear waves and gradually disperse as shown in Fig. 3. Nevertheless it was sufficiently long-lived to propagate (with a velocity below V_0) several

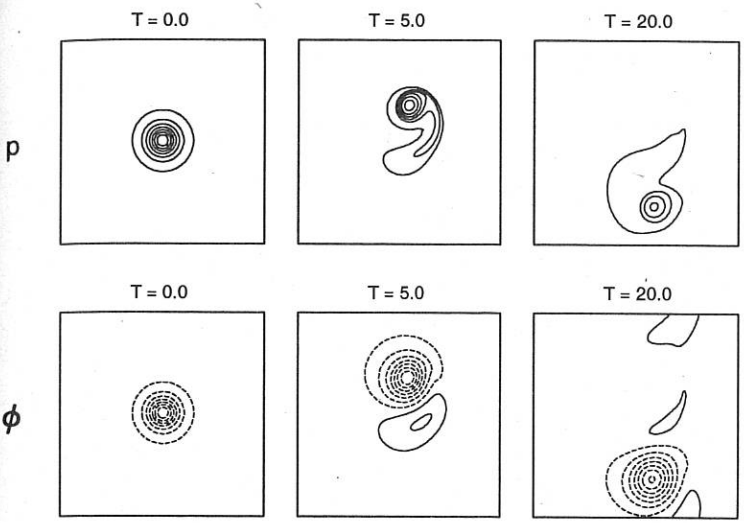

Figure 1: The evolution of a localized monopole vortex. Both the spatial structure of p and ϕ are shown. Positive values are shown with full lines, negative ones with dashed lines. Parameters are $Q_0 = -1.67$, $\alpha = -0.2$, $\varepsilon_n = 0.25$, $D_1 = 0.01$, $D_2 = 0.02$ and $V_0 = 1.3$. The calculation was performed spectrally with a resolution of 128×128.

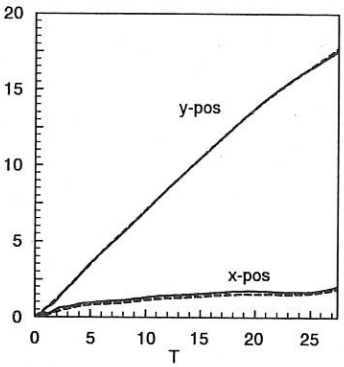

Figure 2: The x- and y-position of the maximum of p (full line) and the minimum of ϕ (dashed line).

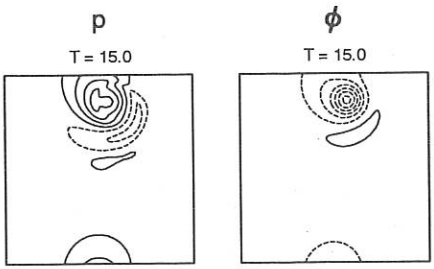

Figure 3: Evolution of a radiating monopole vortex for $Q_0 = -0.2$, i.e. $V_0 = 0.6$ and the other parameters are as in Fig. 1.

times its own width along the y-direction before it completely dispersed. Also for this case we observed a slight propagation in the x-direction.

The evolution of the single vortices as observed in the numerical studies is seen to be well described by the phenomenological theory outlined in the introduction /1/. We have also investigated the interaction among two vortices /5/. Due to the large freedom in choosing the velocity of the vortives an interaction may be realized in a number of different ways. For the head–on collision we found that after a strong interaction two vortices propagating away from each other emerge. In addition some fragments appear that may finally form a new small vortex. This interaction is markedly different from what is observed for the vortex interaction in one field models as for instance the Hasegawa–Mima model for drift waves /8/. There vortices of different sign will pair to form a dipole vortex and like–signed vortices will coalesce to form a larger vortex /8/.

In conclusion, we have revealed the existence of monopolar vortical structures in η_i–modes. In the stable regime these vortices are steadily propagating and stable and may even be attractors for a class of initial conditions. Thus we imagine that they will appear in the saturated stage of the η_i–mode driven turbulence. They may then have strong influence on the dynamics of the turbulence and on the associated transport in particular, as indicated in numerical simulations /2/.

References

/1/ J. Nycander and V.P. Pavlenko, Phys. Fluids B **3**, 1386 (1991).

/2/ M. Ottaviani, F. Romanelli, R. Benzi, M. Briscolini, P. Santangello, and S. Succi, Phys. Fluids B **2**, 67 (1990).

/3/ B.-G. Hong and W. Horton, Phys. Fluids B **2**, 978 (1990).

/4/ B.-G. Hong F. Romanelli, and M. Ottaviani, Phys. Fluids B **3**, 615 (1991).

/5/ J. Nycander, J.P. Lynov and J. Juul Rasmussen. To be published.

/6/ P.K. Shukla and J. Weiland, Phys. Lett. A **136**, 59 (1989).

/7/ E.A. Coutsias, F.R. Hansen, T. Huld, G. Knorr and J.P. Lynov, Phys. Scripta **40**, 270 (1989).

/8/ W. Horton, Phys. Fluids B **1**, 524 (1989).

BREAKING OF WAVES INTO WAVE PACKETS OBSERVED IN A BEAM-PLASMA SYSTEM

Tadao Honzawa and Sanjay Singh
Department of Electric and Electronic Engineering,
Utsunomiya University, Utsunomiya 321, Japan

Breaking of slow ion-beam modes into wave packets in an ion-beam-plasma system is experimentally studied. When pump waves of the mode with a frequency around 200 kHz have amplitudes larger than a critical one, the wave breaking into many packets is observed to start at an axial position ($x \sim 9$ cm) and the packet amplitudes to rapidly grow with increasing x. Here, resultant wave packets keep their forms for a long enough time and are reproducible. Further, the damping of packets or the creation of new packets during interaction between them is observable.

INTRODUCTION

Breaking of waves into many packets in plasmas may be caused by various kinds of causes. In particular, the modulational instability[1] is one of the most important causes among them and attracts interest of many workers in the field of plasma physics. Ikezi et al.[2], studying the possibility of the instability in ion acoustic waves, showed experimentally that the ion acoustic waves could not be modulationally unstable. However, Honzawa et al.[3] found experimentally that the *fast* ion-beam modes in a beam-plasma system were self-modulated above a threshold and this phenomenon could be explained by the modulational instability. But, in the above experiment[3] it was very difficult to have a useful information on the evolving process of individual wave packets or the interaction between packets. This is because the waveforms of resultant wave packets were always restless and irregular.

In this paper, we report experimental results on the breaking of the *slow* ion-beam modes into many packets. Here, the waveforms of packets are considerably settled and reproducible. Thus, the results obtained are expected to give a useful information on the interaction between packets.

EXPERIMENTAL METHODS AND RESULTS

Experiments were carried out using a double plasma (DP) device. In the device two argon plasmas were independently produced by dc discharges. Applying a dc voltage V_B to the 'driver' plasma chamber with respect to the grounded 'target' plasma chamber, we could inject a steady-state ion-beam into the target plasma and formed an ion-beam-plasma system there. In this case, the average energy of an injected ion-beam was usually in a range of 10-17 eV. Thus, the beam velocity v_b adopted here was estimated to be several times larger than the ion acoustic one C_s, so that the system used was regarded to be linearly stable.

In order to excite waves in such a beam-plasma system, an rf voltage V_{rf} with a frequency around 200 kHz was superimposed to the driver plasma chamber and thereby the intensity of the injected ion-beam was modulated. As a result, we could excite waves in the beam-plasma system. In such a case, generally we can have some different kinds of modes in the system. However, under our present experimental condition only the *slow* ion-beam mode was observed at large axial distances ($x \gtrsim 4$ cm). This fact was confirmed from the observed dispersion relation of excited waves and the dependence of their velocities on the beam velocity v_b, the latter of which is shown in Fig.1.

When the rf voltage V_{rf} was increased, we could observe first the rapid increase in amplitude of the excited wave and then the occurrence of the wave breaking into packets above a critical V_{rf}. Typical examples of the

wave signals, observed at a fixed position ($x \simeq 10.8$ cm) and at various values of V_{rf}, are shown in Fig.2. In each pair of traces in this figure, the upper trace corresponds to the applied rf signal, which is externally amplitude-modulated at a low frequency of about 700 Hz, and the lower to the observed wave signal. We can see from these that one or more humps are formed on the wave envelope at higher V_{rf} than a critical one and the number of humps increases with increasing V_{rf}. The result reveals that there is a threshold in V_{rf} or wave amplitude for the wave breaking to occur.

Further, the evolution of the wave envelope during propagation was also studied. Typical evolving forms of the envelopes are shown in Fig.3. Here, the frequency of the carrier wave, which is smoothed out and is not visible in Fig.3, is about 210 kHz. In this figure the top trace corresponds to the applied rf signal and the lower traces to the evolving wave envelopes observed at various x. These indicate that the observed carrier wave rapidly grows in amplitude at an early stage ($x < 9$ cm) and then breaks into many wave packets at larger x. Moreover, we can see the evolving features of individual wave packets from such pictures. Based on similar data to Fig.3, the changing wave amplitudes are plotted in Fig.4 as a function of x for three different values of V_B, which correspond to three different v_b.

REFERENCES

1. For example, V.I.Karpman, Non-Linear Waves in Dispersive Media (Pergamon Press, Oxford, 1975) p106, etc.
2. H.Ikezi, K.Schwarzenegger, A.L.Simons, Y.Ohsawa, and T.Kamimura, Phys. Fluids 21, 239 (1978).
3. T.Honzawa and Ch.Hollenstein, Phys. Fluids 24, 1806 (1981).

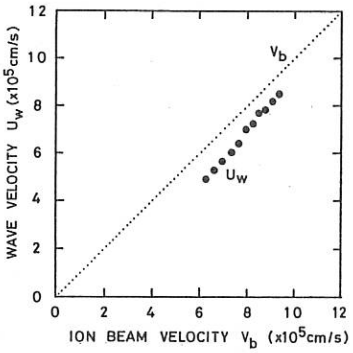

[Fig.1]

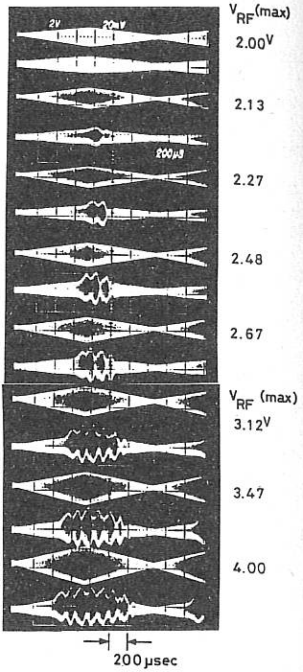

[Fig.2]

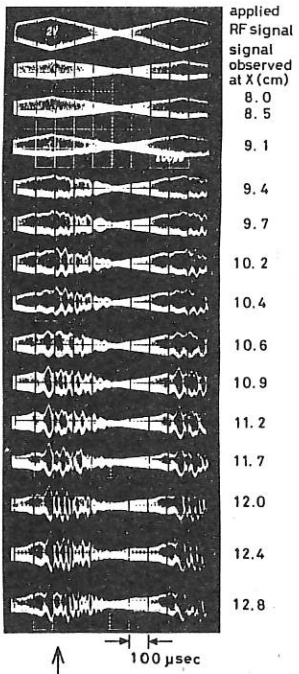

[Fig.3]

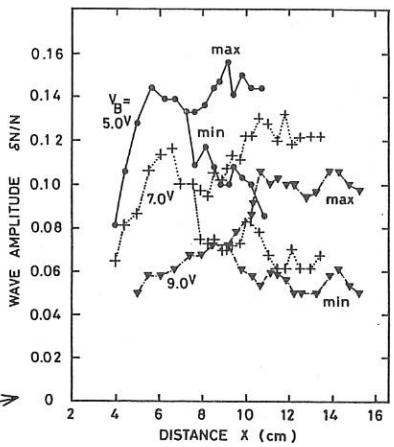

[Fig.4]

EXPERIMENTAL MEASUREMENT OF THE DEFLECTION OF AN ELECTRON BEAM DUE TO THE PONDEROMOTIVE FORCE OF A HF WAVE IN A WAVEGUIDE

Y. Hadjoudj, S. Heuraux, T. Pierre and G. Leclert

Lab. Physique des Milieux Ionisés, URA CNRS 835, Université de Nancy 1, BP 239, 54506 VANDŒUVRE CEDEX FRANCE

INTRODUCTION

A large-amplitude high-frequency wave induces on charged particles an average (low-frequency) effect due to the so-called ponderomotive force. Much theoretical work has been devoted to the determination of the ponderomotive force in a magnetic field/1/. In particular, single particle/2/ and fluid/3/ methods have been used to derive the expression of the ponderomotive force and the effects that it produces on an ensemble of particles such a plasma or a particle beam. So far, only one experiment has been done by Vaclavik et al./4/ to check the predictions of theoretical models; the perturbation of an ion beam by an azimuthal electric field was measured; the wave frequency was of the order of the ion cyclotron frequency. The conclusion was that the experimental results were in accordance with the predictions of the fluid theory. However, the electric field structure at such low frequencies is more or less well defined, and important parameters such as the Debye length were kept constant. We present in the following the results of an experiment on an electron beam. Due to the higher frequency, a rectangular waveguide can be used, thus allowing for an accurate knowledge of the wave field. Furthermore, the Debye length and other physical quantities are varied over a large range, which allows to check more carefully the theories. Our results confirm the conclusions of Vaclavik et al./4/. In particular, it is shown that the ponderomotive beam deviation exhibits a rather strong increase when the Debye length becomes smaller than the beam radius, that is when the fluid effects become significant.

THEORY

In the fluid description, in the steady state case, the non-linear

force acting on the electron beam can be written as

$$\mathbf{F}_p = -\nabla\Phi + \mathbf{B}_o \times \nabla \times \mathbf{M} \qquad (1)$$

where the ponderomotive potential $\Phi = \frac{\varepsilon_o}{4}(\delta_{jk} - \varepsilon_{jk})\, E_j^* E_k$, the RF induced magnetization $\mathbf{M} = \frac{\varepsilon_o}{4}\partial_{B_o}\varepsilon_{jk}\, E_j^* E_k$ and ε_{jk} is the dielectric tensor /1,4/. In the case of a perpendicular force induced by an azimutal electric field $E_\theta(r)$, it is easy to show from the momentum conservation equation that the electron beam experiences an azimuthal deviation with a velocity V_θ given by

$$m_e\, n_e\, V_\theta = \frac{\varepsilon_o}{4}\frac{\omega_{pe}^2}{\omega_{ce}}\frac{\omega^2 + \omega_{ce}^2}{(\omega^2 - \omega_{ce}^2)^2}\,\partial_r |E_\theta|^2. \qquad (2)$$

Since the perpendicular components of the dielectric tensor involve the quantity $(\omega^2 - \omega_{ce}^2)^{-1}$, the magnetization part of the perpendicular ponderomotive force becomes dominant in the vicinity of the cyclotron frequency. Hence the beam deviation is always in the same direction, regardless of the sign of $\omega - \omega_{ce}$.

The RF induced magnetization occurs only if collective effects come into play. In other words, the density of the electron beam must be high enough so that the Debye length is smaller than the beam diameter. From Eq.(1), it is easy to show that the RF induced magnetization current can play a dominant role only in the case of the perpendicular ponderomotive force.

EXPERIMENTAL RESULTS and DISCUSSION

The experimental set-up is reported on Figure 1. The whole system lies in a vacuum vessel (pressure 10^{-6} torr) immersed in an axial magnetic field up to 800 gauss along the z-direction (see figure 1 for the coordinates). Electron are emitted by a thin tantalum foil heated at 2300 K and accelerated by positively biased electrodes. The beam then goes through a rectangular waveguide cavity. The cavity is excited by a generator with adjustable frequency and output power. The mode in the cavity has a frequency of 1.75 GHz, with a TE_{10} polarization,

corresponding to an electric field $E_y(x)$. This reproduces the situation of the theoretical model, with F_p perpendicular to the magnetic field

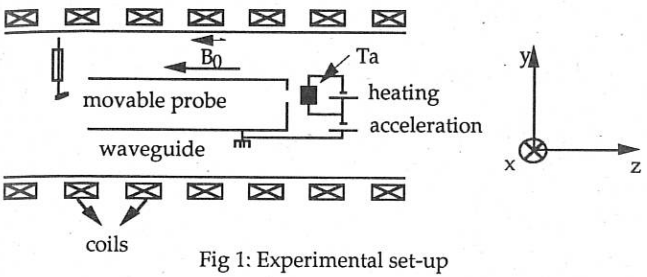

Fig 1: Experimental set-up

and the expected deflection in the y-direction (for small deflection angles, $v_y \approx v_\theta$ to second order). The electron current escaping the cavity is detected by an electrostatic probe, made of a wire, 3 cm long and .1 mm in diameter, parallel to the x-direction and movable in the y-direction. The beam has a density up to a few 10^6 cm^{-3}, its diameter is roughly 1 cm, its energy of the order of 50 eV.

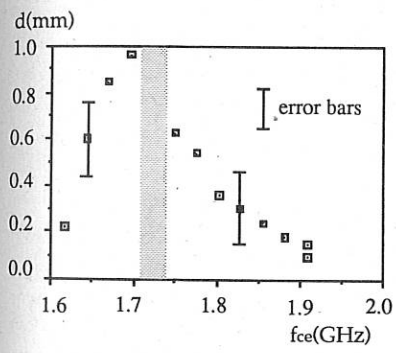

Fig 2: Beam deviation versus f_{ce}

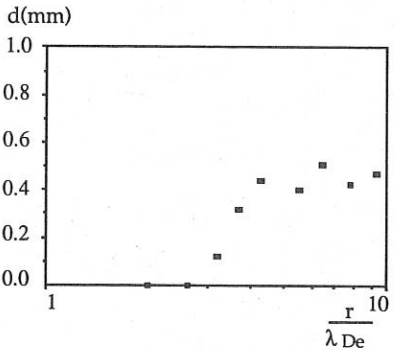

Fig 3: Beam deviation versus r/λ_{De}

Figure 2 shows the deviation amplitude of the beam as a function of the electron cyclotron frequency f_{ce}. In this figure, the width of the dotted region accounts for the magnetic field inhomogeneity in the cavity. The figure clearly shows that the deflection always occurs in the same direction, regardless of the sign of $(\omega^2-\omega_{ce}^2)^{-1}$, as predicted by the fluid theory. Figure 3 shows the influence of the Debye length λ_{De} on the deviation. The beam temperature necessary to evaluate λ_{De} is obtained by using the relationship between the beam energy E_b and its initial energy dispersion ΔE, $T_b/\Delta E = \Delta E/2E_b$ /5/. For $r/\lambda_{De} < 3$, no deflection is measured, whereas there is a fairly constant deflection for $r/\lambda_{De} > 3$. This threshold illustrates the essential role of collective effects in the beam, in agreement with the fluid theory.

In conclusion, we have directly measured the deflection of an electron beam under the action of the perpendicular ponderomotive force. The evolution of the deflection with $(\omega^2-\omega_{ce}^2)$ agrees with the results of Vaclavik et al./4/ and stresses the importance of the ponderomotive magnetization current. Furthermore, we have explicitly shown that there is a density threshold for the occurence of a significant deflection. The totality of these results confirms the existence of fluid effects in the action of the perpendicular ponderomotive force.

REFERENCES

/1/ G.W. Kentwell, D.A. Jones, Phys. Reports **145**, 320 (1988).

/2/ J. Cary, Phys. Fluids **27**, 2193 (1984).

/3/ G. Statham, D. Ter Haar, PLasma Phys. **25**, 681 (1983).

/4/ J. Vaclavik, M.L. Sawley, F. Anderegg, Phys. Fluids **29**, 2034 (1986), M.L. Sawley, J. Vaclavik, Comm. Plasma Phys. Cont. Fusion **10**,19 (1986).

/5/ N. Sato, H. Sugai, K. Hatakeyama, Phys. Rev. Lett. **34**, 931 (1975).

GENERATION OF ION CYCLOTRON WAVE IN AN ION BEAM BY A PERIODIC MAGNETIC FIELD

T. Mieno*, R. Hatakeyama and N. Sato
Department of Electronic Engineering, Tohoku University, Sendai 980, Japan
*Department of Physics, Shizuoka University, Shizuoka 422, Japan

Basic investigation of charged particle beams in a periodic structure is important for the study of stability of plasmas and excitation of electro-magnetic waves such as in the Ubitron and the free electron lasers /1-3/. In previous experiments, an ion beam injected axially along a multiple magnetic mirror field was observed to cause the spatial cyclotron resonance at a resonance condition /4/. This paper presents an observation of strong excitation of electrostatic ion cyclotron waves near this resonance condition in the multiple mirror field. It is considered that the waves are not destabilized by a linear interaction between spiral ion beams and plasma /5, 6/, but are caused by the explosive instability /7/ due to a periodic magnetic field.

When an ion beam with parallel velocity, $\mathbf{V}=V_b\mathbf{z}$ is injected along a straight magnetic field, $\mathbf{B}=B_0\mathbf{z}$, the dispersion relation of electrostatic waves in the fluid theory is shown in Fig.1, where the parameters are selected from the experimental condition ($T_e=T_i=0.009\psi_b$, T_e, electron temperature, T_i, ion temperature, ψ_b, injection beam energy, $n_b=0.2n_i$, n_b, beam density, n_i, ion density, $k_\perp=\pi/r_b$, $k_\perp$, wave number in perpendicular direction, r_b, beam radius). In addition, a new branch ($\omega=0$, $k_{//}=2\pi/L_c$) can be introduced when the magnetic field is modulated with a period length, L_c, which is regarded as a stationary wave with zero frequency. Since there are negative-energy waves and positive-energy waves in the dispersion relation, the explosive instability is expected to occur. In Fig.1, the ion cyclotron mode, m_1 ($\omega=\omega_1$, $k_{//}=k_1$) and the slow beam mode, m_2 ($\omega=\omega_2$, $k_{//}=k_2$) and the periodic structure of the magnetic field, m_3 ($\omega=0$, $k_{//}=2\pi/L_c$) can be coupled, resulting in a simultaneous growing of the former two waves. The coupling conditions are

$$\omega_1=\omega_2\approx\omega_{ci}, \qquad (1)$$

and

$$k_1\approx 0,\ k_2\approx 2\pi/L_c\,, \qquad (2)$$

where the perpendicular wave numbers for

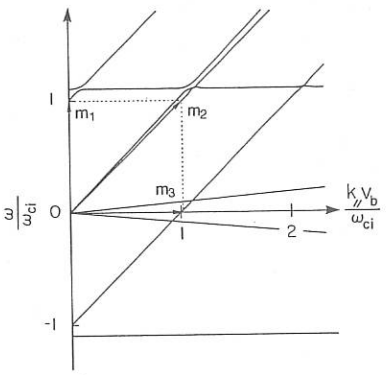

Fig.1: Dispersion relation for ion beam-plasma system. The electrostatic ion cyclotron mode, m_1 ($\omega\approx\omega_{ci}$, $k_{//}\approx 0$) and slow beam mode, m_2 ($\omega\approx\omega_{ci}$, $k_{//}\approx 2\pi/L_c$) and the periodic magnetic field, m_3 ($\omega=0$, $k_{//}=2\pi/L_c$) satisfy the coupling condition indicated by three allows.

the ion cyclotron mode and the slow beam mode are assumed to be the same.

The experiment is carried out at Tohoku university using a Double-Plasma (DP) type Q-machine /8/ as shown schematically in Fig.2(a). Two plasmas produced by the contact ionization of potassium atoms at hot plates of 35mm in diameter, are confined by a uniform magnetic field, B_0=0.1-0.4Tesla. Since plasmas are separated by a grid biased negatively, cylindrical ion beams are continuously injected into the target plasma along the magnetic field when a positive bias voltage is applied to the hot plate of the driver plasma (HP_D) as shown in Fig.2(b). The column of the target plasma is about 3m long. The target plasma has density $n=10^7$-$10^9 cm^{-3}$, $T_e=T_i$=0.2eV. The beam density, $n_b \leq 10^7 cm^{-3}$, the beam energy, ψ_b=5-100eV, the beam radius, r_b=1.1cm and the total beam current, $I_b \leq 100\mu A$. The background pressure is about 1.3×10^{-4} Pa and collisionless condition is satisfied. A periodic magnetic structure (multiple mirror field) is produced by setting iron rings with same intervals as shown in Fig. 2(c). Usually, the number of the period, N=6, the period length, L_c=10cm, the mirror ratio, R_m=1.3 at B_0=0.27Tesla. By changing the shape of iron rings, the parameters of the periodic magnetic field can be changed. The ion beam current and fluctuation of ion current are measured by a grid of Faraday-cup analyzer with 3mm in diameter and a small asterlike probe.

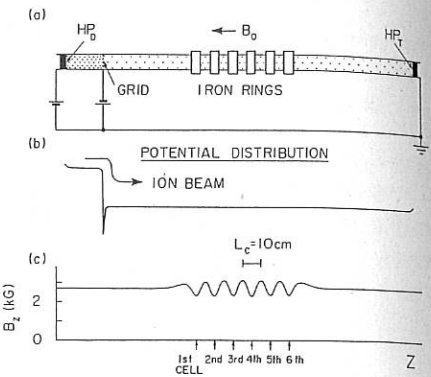

Fig.2: (a) schematic of experimental setup, (b) potential distribution along the axis and (c) measured magnetic field, B_Z along the axis at r=0.

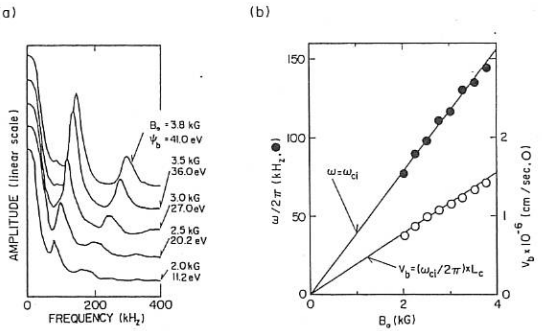

Fig.3: (a) fluctuation spectrum of ion saturation current measured 20cm downstream from the last mirror point. The beam energy is selected to maximize the amplitude. (b) the peak frequency and injection beam velocities in (a) as a function of the magnetic field.

Figure 3(a) shows the frequency spectrum of ion saturation current measured by an asterlike probe at 20cm downstream from the last mirror point of the multiple mirror field. For each magnetic field, the injection beam energy is selected to maximize the instability. Figure 3(b) gives the injection beam energy to maximize the instability and its peak frequency as a function of the magnetic field. The frequency of the instability is almost same as the ion cyclotron frequency, and the optimum condition of the instability generation is $V_b \approx \omega_{ci} L_c/2\pi$, which satisfy the coupling conditions. These results are in good agreement with the theoretical prediction.

The growth of the instability along the beam flow through the periodic magnetic field is measured by a movable analyzer. Figure 4 shows the axial variation of ion current, $\bar{j}_b$, its fluctuation amplitude, $\tilde{j}_b$ and the ratio $\tilde{j}_b/\bar{j}_b$ at the axis, where the injection beam energy, ψ_b=23eV, B_0=0.13Testla, and the frequency, f=116kHz ($=1.08\omega_{ci}/2\pi$) The ion beam current density is modulated in the periodic field by the magnetic focusing effect of the spatial cyclotron resonance /4/. On the other hand, the fluctuation with the ion cyclotron frequency is excited in the periodic magnetic field, growing along the magnetic field with strong amplitude modulation.

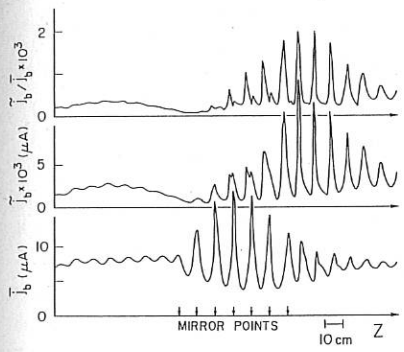

Fig.4: Axial variation of ion saturation current $\bar{j}_b$ at the axis, fluctuation amplitude of ion current, $\tilde{j}_b$ with frequency, f=116kHz, and the proportion of the fluctuation, $\tilde{j}_b/\bar{j}_b$ (initial beam energy, ψ_b =23eV and B_0= 0.27Tesla).

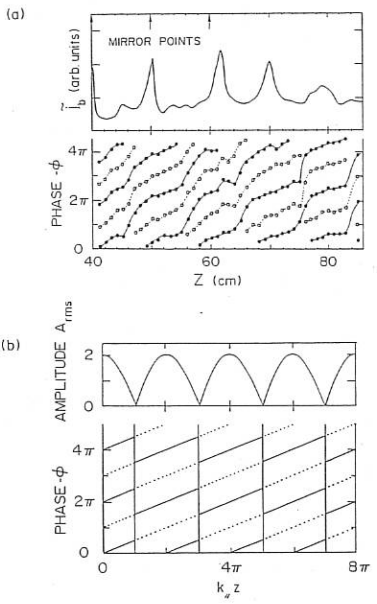

Fig.5: (a) axial variation of the fluctuation amplitude of the saturation current and corresponding phase variation along the axs at a fixed time at t=1.0cm. Closed circles and the open circles correspond to the phase variation of the top and bottom of the wave form, respectively. (b) amplitude and phase variation of a model wave, F=cos(ωt)+ cos ($\omega t - k_{//} z$). Solid lines and broken lines correspond to the top and bottom of the wave form, respectively.

The wave gradually damps after the exit of the periodic field. From this measurement, it is confirmed that the electrostatic wave with the ion cyclotron frequency is excited by the periodic structure of the magnetic field at the coupling condition. The measurement of radial profile of the fluctuation amplitude proves the wave observed not to be an ion cyclotron drift wave. According to the measurement of the amplitude of the wave vs. the injection beam energy, the condition of the maximum growth of the wave is different from the condition that the ion gyration energy becomes maximum. This result comes to a conclusion that the instability is not linearly excited by an ion beam of high perpendicular energy. On the other hand, the strong modulation of the wave amplitude observed, which is independent of the modulation of the beam current density, suggests that two waves with same frequency and different wave numbers are simultaneously excited. To get further characteristics, the axial variation of the wave phase at a fixed time is measured by using a boxcar integrator, as shown in Fig.5(a). The closed circles and open circles correspond to the top and the bottom of the excited wave form (180° different) at a fixed time. The phase change is not linear and has a periodic pattern. In order to explain the measured result, the spatial variation of amplitude and phase at a fixed time is calculated for superposed two-waves, $F=\cos(\omega t)+\cos(\omega t-k_{//}z)$, as presented in Fig.5(b). The amplitude has strong spatial modulation and the phase has a periodic jump, both of which are in good agreement with the experimental result shown in Fig.5(a). Thus, it is considered that the two waves are simultaneously excited and grow in the periodic magnetic field. The frequency of the two waves is about ion cyclotron frequency and the wave numbers in the axial direction are about 0 and $2\pi/L_c$. Our experimental results consist with the theoretical prediction of the explosive instability by the periodic magnetic field.

In conclusion, the electrostatic ion cyclotron wave and the slow beam mode are simultaneously excited at the coupling condition in an ion beam passing through the periodic magnetic field. We believe that this is the first observation of the electrostatic explosive instability induced by the periodic magnetic field. This mechanism of the coupling is same as that of the excitation of the Raman type free electron laser and various kinds of periodic structures in a coordinate system moving with the beam will give rise to this kind of instability.

References

/1/ N. Sato, *Proc. Int. Conf. on Plasma Physics, Nagoya, Japan 1980* (Fusion Research Association of Japan, Nagoya, 1980), Vol.2, p.138.

/2/ R. M. Phillips, IRE Trans. on Electron Devices **ED-7** (1960)231.

/3/ T. Kwan and J. M. Dawson and A. T. Lin, Phys. of Fluids **22** (1977)581.

/4/ T. Mieno, R. Hatakeyama and N. Sato, J. Phys. Soc. Jpn., **56** (1987)4347.

/5/ S. Seiler, M. Yamada and H. Ikezi, Phys. Rev. Lett. **37** (1976)700.

/6/ H. Bohmer, Phys. Fluids **19** (1976)1371.

/7/ A. T. Lin, P. K. Kaw and J. M. Dawson, Phys. Rev. **A8** (1973)2618.

/8/ N. Sato, H. Sugai and R. Hatakeyama, Phys Rev. Lett. **34** (1975)931.

NON-LINEAR ION ACCELERATION IN ELECTROSTATIC WAVE FIELDS

M.J. Alava and J.A. Heikkinen

Helsinki University of Technology, Department of Technical Physics,
SF-02150 Espoo, Finland

1. Introduction

The interaction of plasma ions with large amplitude electrostatic (ES) waves propagating perpendicularly to the background magnetic field shows a variety of amplitude dependent features which are important in the physics of plasma heating and ion acceleration in rf-fields. This is a result of the interesting properties of the single particle ion dynamics in the wave field. At a high enough field strength, stochastic ion heating takes place with the exact mechanism depending on the ω/Ω ratio. These processes have been invoked as possible ways of absorbing wave power in lower hybrid and ion Bernstein wave (IBW) heating of hot fusion plasmas [1,2]. Experimentally, stochastic heating has recently been observed in a single mode ES wave [3] and found to be a probable candidate for fast heating of cold ions, caused by drift waves [4]. In addition to these stochastic mechanisms, even at lower field strengths the ions are susceptible to strong acceleration on a slow time scale, which may indicate hot ion generation in modulated fields.

2. On Ions in Electrostatic Wave Fields

In rf-heating of fusion plasmas in the ion cyclotron range of frequencies some or all of the power is coupled to electrostatic modes. The latter prevails in the case of IBW-heating, while in the fast wave heating case parasitic coupling may lead to a fraction of the total power being in the ES branch [5]. The launched power propagates through a low density and temperature edge plasma in the vicinity of the antenna. In tokamaks, if we assume a typical edge density of 10^{18} m^{-3}, a temperature of 50 eV and a parasitic coupling of a few per cent of the total fast wave power flux of 1 MW/m^2, the corresponding ES wave field strength is of the order of 1000 V/cm. This estimate can be derived from a 1-D definition for the kinetic energy flux $\vec{S} = \sigma E_x^* dE_x/dx$ [6], where σ is the thermal correction to the dielectric tensor element ϵ_{xx} second order in Larmor radius and E_x is the ES wave field in the radial, or perpendicular to the magnetic field, direction.

Given high enough field strengths, the dynamics of ions with kinetic energies typical of such edge plasmas can be analyzed numerically by integrating the single particle equation of motion

$$m_i \frac{d}{dt}\vec{v} = Z_i e(\vec{E}(\vec{r}) + \vec{v} \times \vec{B}(\vec{r})). \qquad (1)$$

Here $\vec{v}$ is the ion velocity, m_i is its mass, $Z_i e$ is the charge and $\vec{E}$ and $\vec{B}$ are the ES

wave electric field and the background magnetic field, respectively. We formulate the problem by taking the magnetic field to lie in the z–direction and to be constant in space and restricting the electric field to the x–direction. The neglect of a possible parallel electric field component is of no real concern as far as $k_z \ll k_\perp$ holds for the parallel and perpendicular wavevector components. This condition is usually valid in the case of ES waves arising due to parasitic coupling in FW experiments and in most IBW experiments, as well.

Most studies on the wave–particle dynamics have assumed a single mode interacting with the ions. We allow in the following the field to consist of several modes with different wavenumbers $k_\perp$, and the electric field is thus written as $E = \sum E_i \cos(k_{\perp,i}x - \omega t + \theta_i)$, where for the relative phases $\theta_i = 0$ is used for mode–locked cases while random ones are chosen for θ_i in the case of fully dephased modes. ω is the angular frequency, common for all the modes. For simplicity, equal amplitudes $E_i = E$ are taken in the following.

3. Results

We concentrate in the following on the development of the ion kinetic energy as a function of time. The parameters of the calculations have been chosen to be appropriate for ES modes in the IBW heating or created through parasitic coupling in fast wave heating. In such experiments, the creation of fast ions at the plasma boundary is of great interest because of the sputtering of the wall structures. Accordingly, we take $\omega/\Omega = O(1)$, $B = 2.34$ T and study the behaviour of D^+ ions. The initial ion kinetic energy is 50 eV.

Fig. 1 shows a case, in which a single deuteron is accelerated in an electrostatic field with $|E| = 1000$ V/cm and $\omega/\Omega = 1.88$. The ion orbit has been integrated numerically using an accurate adaptive ODE solver. Adiabatic oscillations of the particle energy characteristic of a trapped particle with a conservative Hamiltonian [7] are clearly seen in the Figure. The present field level is well below the stochastic limit, above which irreversible heating takes place. Nevertheless, the maximum ion energy is much larger in this example than the initial one.

To study the dependence of the ion energy on the electric field we consider an ensemble of 100 ions distributed randomly at $t = 0$ in wave phase and direction of initial velocity. By increasing the field strength we see in Fig. 2 how after reaching a threshold in $|E|$ the original behaviour of oscillations around the original kinetic energy changes to those with a long period depicted in Fig. 1. With still higher fields, the maximum ion energy approaches the value of about 5 keV corresponding to the separatrix condition $J_{n=2}(k_\perp v_\perp/\Omega) = 0$ [2]. Because of averaging, the mean energy of the ensemble approaches a steady–state value depending on $|E|$. Unlike the field strength, the ω to Ω ratio has only a qualitative effect, as can be concluded on the basis of Fig. 3, where similar calculations are shown for a few values of this ratio. These demonstrate a dependence of the threshold seen in Fig. 2 on the ω to Ω ratio, while at higher field levels the picture of long term oscillations holds still. The change in the ion dynamics due to a multimode spectrum is unexpectedly large, as we show in Fig. 4. The modes have been taken to be such that $k_{\perp,i}$ is distributed equally around $k_\perp = 800$ with the spread Δk

being 10. The amplitudes of the modes are normalized so that the total energy in the spectrum remains approximately the same in every case, i.e. that contained in a single 1000 V/cm, $k_\perp = 800$ mode. The mode phases have been chosen at random and the particle kinetic energies have been distributed according to a Maxwellian with $T = 50$ eV. The distribution of the original wave energy contained in a single mode to several of equal strength does not affect the general picture of long term energy oscillations, although the dynamics is more rapid. On the other hand, the structure of the phase space becomes in the multimode cases such that the accessible range of kinetic energy to the ions becomes wider.

4. Discussion

In this paper we have considered the case of electrostatic wave interacting with low energy ions in a magnetized plasma. The numerical examples shown demonstrate that an ion population with a low enough temperature is rapidly accelerated to high energies assuming an undepleted electrostatic wave. From the point of view of heating of fusion plasmas, such acceleration is of interest as a localized source of hot ions. As the ions move with a velocity v_z along the magnetic field lines the field amplitude varies strongly along their paths. The characteristic length of the localized field in front of the antenna has a measure of the antenna width w, which gives an autocorrelation time $t_c = w/v_z$ for the wave–particle interaction. If t_c is at least of the order of the characteristic period of the slow adiabatic oscillations in the field, ions with high perpendicular energy can escape the field structure. This may result in plasma heating or sputtering of limiter and walls structures connected by the field lines. For $w = 20$ cm and $v_z = 10^5$ m/s, we have $t_c = 2 \times 10^6$ s, which is of the same order as the oscillation periods in Figs. 1 to 4. This suggests a heating mechansim in front of present ICRF antennas and can be related to the observed problems in IBW heating experiments. One question not answered by our numerical calculations is how a large amplitude ES wave propagates in low density, cold plasmas. For this purpose, a self-consistent particle simulation is needed.

References

1. Karney, C.F.F and Bers, A., Phys. Rev. Lett. **39**, (1977) 550.
2. Abe, H., Momota, H., Itatani, R. and Fukuyama, A, Phys. Fluids **23**, (1980) 2417, Abe, H. et al., Phys. Rev. Lett. **53**, (1984) 1153.
3. Skiff, F., Andregg, F. and Tran, M.Q., Phys. Rev. Lett. **58**, (1987) 1430.
4. Cheyney, J.M., Bellan, P.M. and Stern, R.A., Phys. Fluids **B3**, (1991) 3363.
5. Alava, M.J. and Heikkinen, J.A., to appear in Plasma Phys. Contr. Fusion.
6. Stix, T., *The Theory of Plasma Waves,* (Mc Graw–Hill, 1962).
7. Timofeev, A., Nucl. Fusion **14**, (1974) 165.

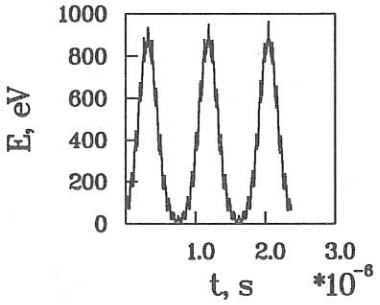

Figure 1a. The behaviour of a single deuteron kinetic energy as a function of time with $|E| = 1000$ V/cm, $\omega/\Omega = 1.88$ and $k_\perp = 800$ 1/m.

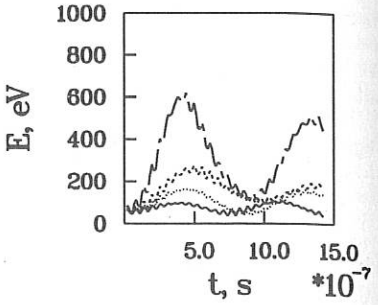

Figure 2. The average energy of 100 deuterons as a function of time. $T_0 = 50$ eV, other parameters as in Fig. 1. Solid line: 600 V/cm, dotted line: 700 V/cm, dashed: 800 V/cm, chaindashed: 1000 V/cm.

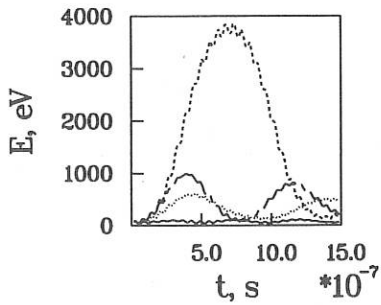

Figure 3. The energy time histories for a single mode case with $|E| = 1000$ V/cm for some values of the ω/Ω ratio. Solid line: 1.8, dotted line: 1.88, dashed: 1.98, chaindashed: 2.1.

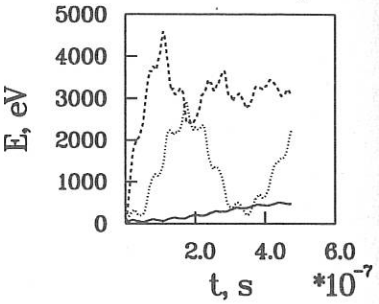

Figure 4. The energy of a Maxwellian ion population vs. time. Initial energy 50 eV, 1 mode case: solid curve, 11 modes: dotted and 51: dashed.

Electron Acceleration by $v_p \times$B Mechanism in Vacuum

Noboru Yugami and Yasushi Nishida
Department of Electrical and Electronic Engineering,
Utsunomiya University

Abstract

A new type electron linear accelerator, based on $v_p \times$B acceleration mechanism observed originally in plasma, has been demonstrated in vacuum. In this scheme a static magnetic field is applied vertically to the wave propagating direction and the particles are accelerated along the wave front at constant phase with respect to the wave. The linac consists of electron gun, magnetron for a RF source, slow wave structure and a pair of coil for an applied magnetic field. Energy gain of 12.8 keV is observed at an initial energy of 66 keV when an external magnetic field of 2.5 G is applied. The energy gain is 30 % higher than that of a conventional linac. The output energy increment is proportional to the square of the applied magnetic field B. The comparisons between the experimental and theoretical values are given.

Recent interests of charged particle accelerators are focused on generating a much higher acceleration gradient. In the last decade some of new acceleration schemes using a longitudinal electric field of the wave, including a plasma wake field accelerator (PWFA), a plasma beat wave accelerator (PBWA) and a $v_p \times$B scheme (or a surfatron), have been proposed.[1]-[8] Some of the experimental results based on the above mentioned scheme have been reported to give the higher acceleration gradient. The new schemes using plasmas can be expected to generate much higher electric field, but it is also easy to predict some difficulties of controlling plasma parameters. The $v_p \times$B acceleration phenomena have been observed in the experiments of microwave-plasma interaction.[10][11] In this scheme a static magnetic field is applied vertically to the wave propagating direction and the particles are accelerated along the wave front at constant phase with respect to the wave, and the acceleration continues until the trapping condition breaks.

In the $v_p \times$B system a charged particle is trapped in an electromagnetic wave (TM wave) with a phase velocity v_p propagating in the z direction immersed in a static magnetic field B in the x direction (Fig. 1). The Lorentz force $F_y = qv_z B_o$ accelerates the particle in the y direction, and the resulting velocity v_y produces the Lorentz force in the -z direction. If the wave electric field satisfies the following condition, the charged particle is trapped in the electric field in phase space,

$$E_m > \gamma_p B_o v_y, \tag{1}$$

where E_m, γ_p, v_y are the maximum electric field of the wave, the relativistic factor defined by $\gamma_p = (1 - v_p^2/c^2)^{-0.5}$ and the velocity component in the y direction, respectively. The particle is continuously accelerated until the condition breaks.

Energy gain in steady state for a unit length is the same as that originally obtained on the surfatron,

$$\frac{d\gamma}{dy} = \gamma_p \frac{\gamma_p c v_p}{c^2}, \tag{2}$$

$$\frac{d\gamma}{dz} = \gamma_p \frac{\omega_c^2 z}{c^2} \left(1 + \frac{\omega_c^2 z^2}{c^2}\right)^{1/2} \tag{3}$$

where $\gamma = [1 - (v/c)^2]^{-1/2}$ and ω_c is the electron cyclotron frequency.

Figure 2 is a schematic diagram showing an electron beam gun, a slow wave structure and an energy analyzer. The injected electron is initially accelerated by a high voltage power supply, with maximum energy and current of 100 keV and 1 mA, respectively. A hair-pin type cathode is made of a tungsten filament which is originally made for an electron microscope. The accelerated electrons through the accelerator are detected by an electron energy analyzer.

The pulsed electromagnetic wave is generated by a magnetron which is triggered by the external timer with a typical pulse width of 5 μs in repetition at 10 Hz. We used two different power sources, one has a maximum power of 2.5 kW and the other has 10 kW, the emitted frequencies of them were measured by comparing with the standard oscillator to give 2.465 GHz and 2.459 GHz, respectively. Although both of the original specifications are 2.45GHz, the frequencies were upper-shifted due to too much of the applied cathode voltages so as to obtain higher output power. The generated microwave is converted into TM wave through the slow wave structure, and is absorbed by a non-reflection dummy load.

The slow wave structure consists of parallel fin electrodes with 48 cm long in the wave propagation direction. Its propagation mode of the microwave is designed to be $2\pi/3$ mode and the phase velocity is $0.464c$ (corresponding energy of 66 keV) at the RF frequency of 2.45 GHz. The cross section of the structure is rectangular. In general the circular type acceleration cavity is popularly used for the linear accelerator to generate the maximum longitudinal electric field at the center of the cavity. In the $v_p \times$B scheme, however, the electron orbit is parabolically bent by the external magnetic field, in other words, the electron is accelerated in two dimensional. Although the maximum electric field strength is weaker in the present case, we can choose the structure with no obstacles in the y direction. This is convenient to demonstrate the $v_p \times$B acceleration principal. When it works in a relativistic regime, the particle orbit is strightly linear and the circular type slow wave structure could be employed so as to obtain a strongest field.

An example of experimental results with rf power of 2.5 kW is shown in Fig. 3. The horizontal and vertical axes indicate the incident electron energy E and the energy increment $\Delta\varepsilon$, respectively. Symbols □, △, ○ and stand, respectively, for the value of the external magnetic field of 0, 2 and 3 Gauss. When Bo = 0 G, the accelerator operates as the conventional linac. Therefore one can easily compare the $v_p \times$B accelerator with the conventional one in a same machine. The slow wave structure strongly resonates with the microwave around Eo = 48 and 57 keV. Data show that the energy increment of the $v_p \times$B scheme is larger than that of the conventional one at every incident electron energy. When the incident beam energy is 48 keV, for example, the observed electron energy is 56.0 keV ($\Delta\varepsilon$ = 8.0 keV) with a static magnetic field of 3 G, while in the conventional accelerator the energy reaches 52.0 keV corresponding $\Delta\varepsilon$= 4.0 keV. The expected energy increment is calculated from Eqs.(2) and (3) for the case of Bo = 3 G at Eo= 48 and 56 keV. The results are shown by the solid circles in Fig. 3. The disagreement between the experiment and the calculated value is explained as follow; The Eqs.(2) and (3) are valid only for the

steady state of the acceleration only. In the experiment, however, the electrons are not in the steady state but oscillate around the equilibrium point in the phase space because the acceleration time is not sufficient to reach the steady state. Sufficient acceleration with condition ($\omega t \gg 1$; in the present machine $t > 20$ nsec is required) is assumed in Eq. (2).

Figure 4 shows the energy increment as a function of the static magnetic field intensity. Up to 2 G, the energy increment $\Delta\varepsilon$ is proportional to B^2, i.e., $\Delta\varepsilon - \Delta\varepsilon$ (Bo = 0 G) $\propto B^2$, while over 2 G, $\Delta\varepsilon$ decreases sharply. This dependence can easily be explained by the Lorentz force acceleration in the y direction. After the value of B exceeds 2 G, the electron cannot be trapped by the wave potential anymore. These results mean that the trapping condition is no longer maintained. The underlying physics producing a critical magnetic field B = 2 G is explained using Eqs. (2) and (3).

A new electron linear accelerator based on the $v_p \times B$ acceleration scheme has been demonstrated to work successfully in a vacuum system. The experimental results show that proposed scheme accelerates the electron more effectively than the conventional linear accelerator. The measured data are in good agreement with the theoretical results containing weak relativistic effects.

References

1) T. Tajima and J. M. Dawson, Phys. Rev. Lett. **43**, 267-270 (1979).
2) P.Chen, J. M. Dawson R. W. Huff and T. Katsouleas, Phys. Rev. Lett. **54**, 693-696 (1985).
3) R. Sugihara and Y. Mizuno, J. Phys. Soc. Jpn. **47**, 1290-1295 (1979).
4) Y. Nishida, M. Yoshizumi and R. Sugihara, in Proceedings of the Thirteenth Annual Anomalous Absorption Conference, Banff, Alberta, Canada, 5-10 June 1983, (unpublished) p.F7; Phys. Lett. **105A**, 300-302 (1984); Y. Nishida, M. Yosizumi and R. Sugihara, Phys. Fulids **28**, 1574-1576 (1985).
5) C. Joshi and T. Katsouleas, in Laser Acceleration of Particles, edited by C. Joshi and T. Katsouleas, AIP Conf. Proc. No. 130 (AIP, New York,1985).
6) T. Katsouleas and J. M. Dawson Phys. Rev. Lett. **51**, 392-395 (1983).
7) Y. Nishida, N. Yugami, H. Onihashi, T. Taura and K. Otsuka, Phys. Rev. Lett. **66**, 1854-1857 (1991), and references therein.
8) A.Loeb and L. Friedland, Phys. Rev. A **33**, 1828-1835 (1986).
9) Y. Nishida, in Laser Interaction and Related Plasma Phenomena, edited by H. Hora and G. Miley (Plenum, New York, 1986), Vol. 7, pp. 811-825.
10) Y. Nishida, in Proceedings of the Nineteenth International Conference on Phenomena in Ionized Gases, Invited Papers, (July 10-14 1989, Belgrades, Yugoslavia) edited by Vida J. Zigman, pp. 186-194; A Variety of Plasma, Proceedings of the 1989 International Conference on Plasma Physics, edited by A. Sen and P. K. Kaw. Indian Academy of Sciences, pp. 39-55.

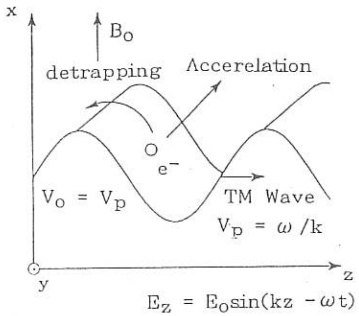

Figure 1.

Schematic diadram of $v_p \times$ B acceleration scheme

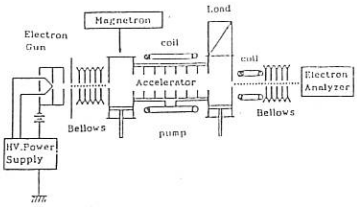

Figure 2.

Experimental setup

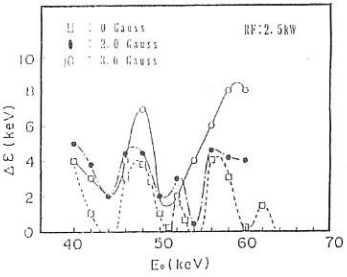

Figure 3.

Energy increment $\Delta\varepsilon$ vs incident energy

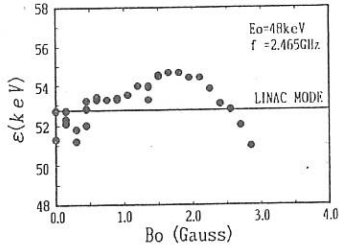

Figure 4.

Energy increment $\Delta\varepsilon$ vs the static magnetic field

Plasma Wave Wakefield Excited by Short Pulse Microwave

Y.Nishida, S.Kusaka, and N.Yugami
Department of Electrical and Electronic Engineering
Utsunomiya University
Utsunomiya, Tochigi 321, Japan

Abstract

The plasma wakefield can be excited by using short, high-power microwave pulse for demonstrating a laser wakefield accelerator principle (LWFA). Although the conditions of the experiments are different from those of the LWFA, the plasma wave is excited, non-resonantly by a short microwave pulse. Close to the resonant density for the resonance absorption of the electromagnetic wave, new nonlinear phenomena, tentatively interpreted as the electron wave soliton, have been observed. The excitation of the plasma wave is due to the ponderomotive force ($\mathrm{gradE^2}$) of the short microwave pulse.

Several electron acceleration schemes using plasma have been proposed.[1-3] They have an advantage of getting high field gradient for electron acceleration. Specifically, the $V_p \times$ B acceleration scheme has high acceleration rate with better efficiency compared with other schemes. This, however, needs strong wave fields for achieving its best qualities. Laser wakefield accelerator (LWFA) is one of the plasma-based acceleration schemes, and employs a short, high-power, single frequency laser pulse.[4] The LWFA has some advantages. For example, it can get long acceleration distance, or it is not necessary to adjust the plasma density very precisely to designed certain value. LWFA can work as an accelerator as it stands. Moreover, it could be used for a driver wave for the $V_p \times$ B accelerator, which could achieve much higher energy than the original LWFA scheme.

In this paper, first experimental results by a short microwave pulse, and some explanations for the excitation mechanism of the plasma wave are presented. This is essentially the same method of the LWFA.

The ponderomotive force produced by the microwave acting on the plasma is given by

$$\vec{F}_{pond} = e\vec{\nabla}\phi_L(r,z,t) \tag{1}$$

where, $\phi_L = -m_o c^2 a_L^2/(2|e|)$ is ponderomotive potential and $a_L = |e|A_L/(m_o c^2)$ is the normalized amplitude of vector potential radiation field. This field moves with the wave group velocity. The radial ponderomotive force expels electrons radially outward, while the front (back) of the laser pulse exerts a forward (backward) force on the electron. As the plasma electrons move around the microwave pulse, the plasma waves can be generated.

Experiments are performed in a cylindrical stainless steel chamber with multi-dipole magnets on the outside of the wall, as shown in Fig.1. To demonstrate the excitation of the wakefield, a uniform plasma density and no reflection of the microwave are required. For this purpose, the other end of the chamber from the antenna is covered with acrylic resin plate, through which the wave comes out of the chamber. The argon plasma is produced by pulse discharge (discharge duration of 3 msec and 10 Hz repetition). Typical plasma

parameters are a maximum plasma density $n_o = 2 \times 10^{11} cm^{-3}$, an electron temperature $T = 2-3$ eV, which are obtained by Langmuir probe method. The p-polarized microwave with a frequency 2.86 GHz (corresponding critical plasma-density is $n_c = 1 \times 10^{11} cm^{-3}$, a maximum power of 10 kW and typical pulse width 200 nsec is irradiated through a high gain horn antenna installed with metal plate lens in front of it. The field strength in the plasma are measured by a crystal detector or a spectrum analyzer, through a tiny plate probe ($1mm \times 1mm$) or a cylindrical probe ($0.1mm$ *dia.* $\times 1mm$).

Typical waveforms are shown in Fig.2, where bottom trace is the signal of the incident microwave, and top one is the plasma density fluctuation detected through probe which is biased to V = – 20 V at $Z = 37.6$ *cm* from the antenna edge. This position is roughly 5 *mm* down the resonance absorption layer. The scale of the horizontal axis is 200 ns/div. There are several peaks in the plasma wave. When the pulse width of the incident microwave becomes larger, these peaks go out. This instability has a threshold. They seem to be wakefield, because it is nonlinearly excited after the incident microwave power shut off.

Figure 3 shows the spectrum observed close to the resonance absorption layer with and without plasma. We can see lower frequency wave which corresponds to Fig.2. Figures. 4(a) and (b) show spectra of the plasma wave observed around 1 GHz at $Z = 14$ *cm* and 15 *cm* respectively. As clearly seen, the plasma wave can also be excited with frequencies of about 0.99 and 1.02 GHz. When the detecting point moves up to higher density layer ($Z = 15$ *cm*), both frequencies become higher. If a plasma frequency is 1 GHz, the corresponding plasma density is $1.2 \times 10^{10} cm^{-3}$. This value is in reasonable agreement with $n_o = 1.3 \times 10^{10} cm^{-3}$ which is measured by Langmuir probe method. The propagation velocities (Z -direction) of the nonlinear waves are also measured to show the velocity of $v = 2 - 3 \times 10^7 cm/s$. The larger peak has higher velocity. Since the electron thermal velocity is estimated to be $v_{th} = 1 \times 10^8 cm/s$, the velocity of this nonlinear wave is slighty slower than v_{th}. The present pulses propagate out of the resonance layer and also from the layer with highest intensity of the electric field. When a resonance layer exists within a chamber, a familiar Airy function type standing wave structure has been observed. In this case, the plasma waves can be excited, typically, at two layers, one at the resonance layer and the other at the first, highest peak position near the cut-off layer as an example is shown in Fig.5. Here, the wave can be observed through the interferometer method with the reference frequency of $f_o = 2.86$ GHz, so that other frequencies can not be detected. The waves are excited at both sides, where the ponderomotive force, which is proportional to grad E^2 , is maximum.

To explain above experimental results, the original theory for LWFA should be modified. The following conditions are required; the electron temperature T_e is non-zero, and the group velocity of the driving wave is zero, because the short pulse, electromagnetic wave forms a standing wave structure not to propagate. Still there exist areas of high gradient of E^2 . Therefore, even if the microwave pulse does not pass through the plasma, the ponderomotive force due to high gradient of E^2 can exist. Therefore, it is possible to consider that the ponderomotive force acts on electrons, and the plasma wave can be excited. Under these assumptions, the excited plasma wave is expected to propagate with the velocity less than thermal velocity v_{th}. As mentioned above, the observed propagation velocity is slightly slower than the thermal velocity in reasonable agreement with the

theoretical prediction. Near the resonance layer, we have several possibilities for exciting solitons, 1) envelope soliton of electron plasma wave, 2) ion acoustic soliton, and 3) decay instability for exciting ion acoustic wave. The decay instability has finite growth time of several microseconds such as already shown in the previous works,[5] with longer pulse duration, and we could neglect this phenomenon at present. The ion plasma frequency is estimated as 10–12 MHz, and 2nd possibility could survive. The first possibility is also expected because the caviton formation time is also order of ion plasma wave time scale. Anyhow, multiple "soliton" such as observed in the present experiments with short pulse duration have never been observed so far, and we need more theoretical works for interpretation.

In conclusion, the plasma wave (wakefield) was non-resonantly excited by short microwave pulse. The method of excitation was slightly different from that of the original LWFA theory. However, the key mechanism of the excitation can be explained by the theory with slight modification. New "soliton" phenomena have been observed near resonance absorption layer.

A present work is supported in part by a Grant-in-Aid from a Ministry of Education, Science and Culture, Japan.

References

1. Y.Nishida,T.Okazaki, N.Yugami, and T.Nagasawa, Phys. Rev. Lett. **66**, 2328 (1991), and references therein.
2. H.Nakanishi et al, Phys. Rev. Lett. **66**, 1870 (1991).
3. Y.Nishida, N.Yugami, H.Onihashi, T.Taura, and K.Otsuka, Phys. Rev. Lett. **66**, 1854 (1991).
4. P.Sprangle, E.Esarey, A.Ting, and G.Joyce, Appl. Phys. Lett. **53**, 2146-2148 (1988).
5. Y.Nishida, Ann Lee, N.C.Luhmann, Jr., and M.Rhodes, Plasma Physics and Cont. Fusion, **32**, 391 (1990), and references therein.

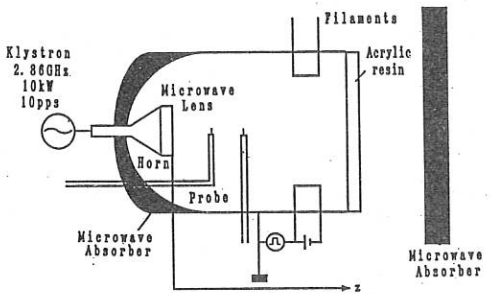

Fig.1. Schematics of experimental apparatus.

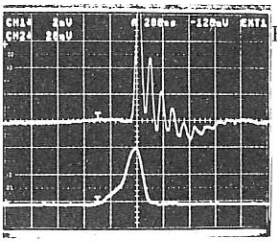

Fig.2. Typical wave forms observed near resonance layer.

(a) Electron density perturbations

(b) incident microwave pulse

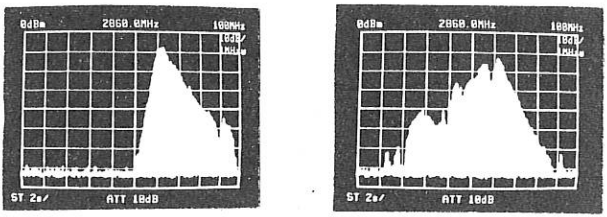

Fig.3. Typical example of the spectrum observed with and witout plasma near the reso nance layer.

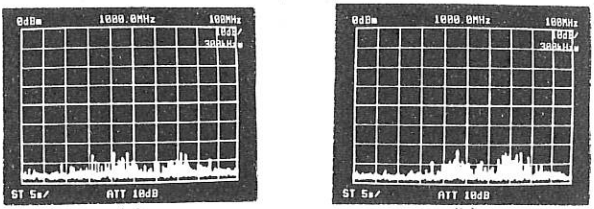

(a) (b)

Fig.4. Example of the spectrum observed in the underdense layer at (a) $Z = 14\ cm$ and (b) $Z = 15\ cm$.

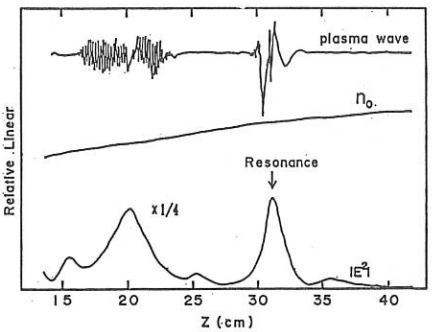

Fig.5. Typical example of the electric field E^2 and the plasma wave pattern.

Direct Measurement of Velocity Space Transport in a Fully Ionized Plasma

N. Rynn, J. Bowles, and R. McWilliams; University of California, Irvine

We report the direct measurement of velocity space transport coefficients in the direction of the confining magnetic field, which may be interpreted as the Fokker-Planck coefficients. The measurements were made using the techniques of laser induced fluorescence [LIF][1] and optical tagging[2], which allows ions to be followed in real and in phase space. In a plasma with nearly thermal fluctuations only, the results agree well with test-particle calculations made by N. Rostoker[3]. In the presence of larger amplitude drift waves, however, there is a pronounced enhancement of the diffusion coefficient at a velocity less than thermal speed. The measurements reported here are unique in that they deal with the bulk of the velocity distribution, where most particles reside, allowing direct comparison with theoretical calculations such as the Fokker-Planck coefficients. A schematic of the experiment, which was performed in the U.C.Irvine Q-Machine[4], is shown in Fig.1.

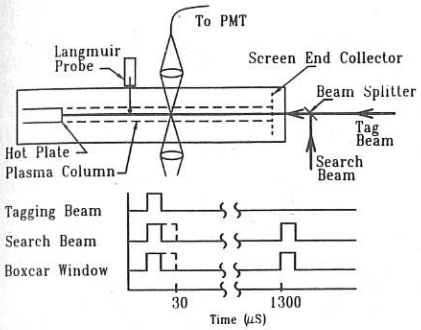

FIG. 1. Schematic of the experimental arrangement and timing sequences. The solid line in the inset indicates sequence I, the dashed lines sequence II.

The barium plasma column length was 1.3m and its diameter was 5 cm. Two laser beams were used: one, the tagging beam, pumped the ground state transition at 4934Å and filled a metastable state, and the other, at 5854Å, de-excited the metastable transition and thus identified the tagged particles. The two beams were superimposed and directed axially through the collector end of the plasma column. The usual solid cold end plate was replaced by a fine mesh grid that allowed the laser beams to pass through with minimal attenuation. The photon emission from the tagged particles was picked up by lens systems which directed the the optical signal to photomultipliers [PMT], one for each laser beam. The output of the lasers were pulsed by means of acousto-optical modulators . The pulsing sequences are shown in the figure. The pulses were 10msec. long with a basic repetition rate of 769Hz [1.3msec period].

Selecting a laser wavelength, or frequency, corresponds to selecting a plasma ion velocity. Sweeping the laser frequency amounts to scanning the plasma ion velocity, which allows the determination of the ion velocity distribution, from which the ion temperature and other information can be determined. To take the measurements the laser output was pulsed as described above except that the pump, or tagging laser was pulsed at half the repetition rate of the search laser. This allowed alternate pulses of the search laser to be used to subtract out background light. The first measurement was

made using the sequence labelled "I" in the Fig.1, which indicates that except for alternate pulses both the tagging beam, which was set at a particular frequency, or velocity, and the search beam were on simultaneously. The frequency of the search beam was then swept. Since the sweep rate was so much slower than the pulsing rate, the velocity distributions obtained were, essentially, continuous distributions of the tagged particles averaged over 10msec intervals. Ten microseconds is long enough for significant diffusion in velocity space to have taken place, but much shorter than the time required for the tagged particles to equilibrate with the background. Hence this is, essentially, a diffusion problem in which a source consisting of a single [d-function] velocity continuously feeds a diffusing population. The search beam picks up what has happened to the particles that were tagged at that particular velocity over the interval of 10msec. Thus as the laser scans over its frequency range, the result from the search beam is a distribution that shows how many particles that were originally at a specific velocity have diffused to other velocities over an interval of up to 10msec.

In principal this should yield enough information to enable the calculation of a velocity-space diffusion coefficient. However, it turns out to be simpler and easier to understand if we use this as an initial distribution, since it includes all the vagaries of pumping the metastable states etc., and then comparing it to a distribution taken at a later time with the tagging beam turned off. This was done with the pulsing sequence labelled "II" in Fig.1. Here the tagging beam is turned on for 10msec. and at the end of the pulse, as it is turned off, the search beam is turned on for 10msec. Now the problem presented is that of an initial tagged distribution that is the result of a d-function stimulus after diffusion during a time that we take to be 10msec. The moments of each distribution were calculated for many conditions and then compared with the calculation of the Fokker-Planck coefficients as explained below.

The initial distribution of tagged particles can be represented to a good approximation, by

$$f_T\,(v,t=0) = \frac{n_T}{\sqrt{2\pi\sigma_T^2}}\,\exp\frac{(v-v_T)^2}{2\sigma_T^2} \qquad (1)$$

where T refers to the tagged particle, σ_T is the standard deviation of the initial tagged particle distribution. The time evolution of eq.(1) is given by

$$\frac{\partial f_T(v)}{\partial t} + \nabla_v \cdot \vec{\Gamma} = 0 \qquad (2)$$

The experimental results can be compared with the three-dimensional theory for ion-ion collisions in a fully ionized plasma given by the Fokker-Planck equation

$$\frac{\partial f}{\partial t}\Big|_{coll} = \frac{\partial}{\partial v}\cdot\left\langle\frac{\delta v}{\delta t}\right\rangle f(v,t) + \frac{1}{2}\sum_{i,j}\frac{\partial^2}{\partial v_i \partial v_j}\left[\left\langle\frac{\delta v_i \delta v_j}{\delta t}\right\rangle f(v,t,)\right]. \qquad (3)$$

The first and second terms are interpreted as the convection and diffusion terms respectively. When $\langle \frac{\delta v}{\delta t} \rangle$ and $\langle \frac{\delta v_i \delta v_j}{\delta t} \rangle$ are known the future of the distribution is known to second order in dv.

Calculation of the Fokker-Planck coefficients for this case was done by N. Rostoker[3]. The term for parallel convection is given by

$$\langle \frac{\delta v_z}{\delta t} \rangle = C_z = \frac{2\pi e^4 n \ln\Lambda}{m_i^2} \frac{1}{v_{th}^2} \frac{\partial}{\partial x} \frac{\mathrm{erf}(x)}{x} \qquad (7)$$

The diffusion of test ions in a quiet plasma along the magnetic field is given by

$$\langle \frac{\delta v_z \delta v_z}{\delta t} \rangle = D_{v_z v_z} = \frac{-8\pi n e^4 \ln\Lambda}{m_i^2} \frac{1}{4\sqrt{2}\, x} \frac{\partial}{\partial x} \frac{\mathrm{erf}(x)}{x} \qquad (8)$$

where v_{th} represents both parallel and perpendicular contributions to the thermal energy, $x = v/(\sqrt{2}\, v_{th})$, and z represents the coordinate axis aligned with the magnetic field The results are shown in Figs. 2-3, all shown in plasma reference frame coordinates. The measurements were taken near the axis of the plasma column so as to avoid complications arising from drift waves and other phenomena associated with the steep density gradients at the edges. The techniques for determining ion density and temperature are described in ref. [1]. The data for the velocity space diffusion coefficient, $D_{v_z v_z}$, as a function of plasma density in a "quiet" plasma for a typical value of v_z show good agreement with a linear variation with density. Additional measurements of the diffusion coefficient taken with different values of v_z yielded similar results, indicating good agreement indicating classical diffusion theory.

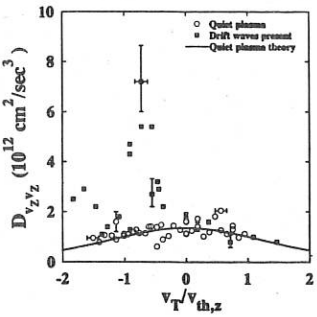

FIG. 2 Plot of the longitudinal velocity diffusion coefficient as a function of the normalized tagged-ion velocity for a quiet plasma (open circles) and one in which drift waves are present (solid squares). The solid line is the theory for quiet conditions from Eq. (3).

Fig. 2 shows a comparison of the variation of $D_{v_z v_z}$ versus the tagged velocity, v_T, normalized to the thermal velocity, $v_{th,z}$. The open circles were taken in the quiet plasma condition and show good agreement with Rostoker's theory. The solid squares show data taken when the plasma density profile was altered to have a sufficiently large gradient to destabilize drift waves with $dn/n \approx 6.0\%$. The dramatic departure from theory is quite apparent, the data indicating a peak in the axial diffusion

coefficient at a velocity about -0.7 $v_{th,z}$. At velocities higher than [plasma frame] zero, agreement with classical predictions seems to be restored. Figure 3 shows a comparison of the convective coefficient, C_{vz}, with the normalized velocity $v/v_{th,z}$. Within experimental error the mean value agrees with theory in the quiet case. However, the errors bars are too large to draw firm conclusions about agreement with classical theory insofar as the variation with velocity is concerned. When fluctuations are present, the scatter of points does not allow any further conclusions to be drawn. The relatively large error bars are due to the fact that the convective coefficient, being linear in v, is very susceptible to the relative drift of the tagging and search lasers, while the diffusion coefficient, being dependent on the square of the velocity, is not as sensitive.

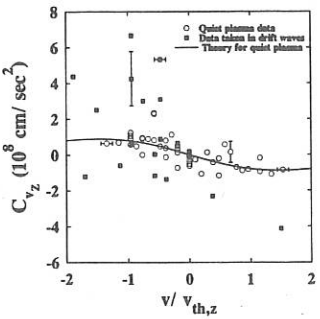

FIG. 3 Plot of the longitudinal velocity convection coefficient as a function of the normalized tagged ion velocity for a quiet plasma (open circles) and one in which drift waves are present (solid squares). The solid line is the theory for a quiet plasma, Eq. (2).

What conclusions can be drawn? First, when the plasma is near equilibrium, measurements agree well with classical predictions. Second, when fluctuations significantly greater than thermal are present, classical collisional theory is insufficient to predict results. Something very definite happens when fluctuations are present. We are actively pursuing an explanation at this writing. The dependence of the perpendicular diffusion coefficient on the magnitude of density fluctuations has already been discussed by one of the authors[6].

The authors wish to thank N. Rostoker who supplied us with the theory and calculations, and C. Oberman and A. Ron, discussions with whom gave us invaluable insights. The research reported in this letter was supported by the National Science Foundation, Grant No. PHY-9024667.

1D.N. Hill, S. Fornaca and M. Wickham, *Rev Sci. Instrum.* **54**, 309 (1983).
2R.A.Stern, D.N.Hill and N.Rynn, *Phys. Lett.* **93A** [3] 127 [1983].
3N. Rostoker, *Nuc. Fus.* **1**, 101, [1961]
4N.Rynn, *Rev. Sci. Instrum.* **35**, 40, (1964).

PHASE CONJUGATION VIA BRILLOUIN ENHANCED FOUR-WAVE MIXING IN A PLASMA

C.W. Domier, N.C. Luhmann, Jr. and W.A. Peebles

Department of Electrical Engineering, University of California, Los Angeles
Los Angeles, California 90024-1594, U.S.A.

INTRODUCTION:

Detailed studies of phase conjugation via Brillouin enhanced four-wave mixing (BEFWM) of high power microwaves in a large, well diagnosed unmagnetized hydrogen plasma have been performed. Both the transient and steady state behaviour are shown to agree well with the predictions of two-fluid plasma theory for low power, low density operation. Strong suppression of the BEFWM interaction is observed at an electron density $n_e = n_c/4$, indicative of the two plasmon decay instability. High power, high density operation is seen to deviate strongly from simple theoretical predictions; evidence of the onset of ponderomotive whole-beam self-focusing is given.

BEFWM THEORY:

BEFWM, in its simplest form, can be modeled as a pair of simultaneous three-wave mixing processes. In the first process, a strong pump wave $\underline{E}_2$ of frequency ω_o mixes with a weak signal wave $\underline{E}_s$ of frequency $\omega_s = \omega_o + \omega$ to generate a density "grating" in the plasma. In the second process, another strong pump wave $\underline{E}_1$ of frequency ω_o (antiparallel to the first) scatters off this grating to generate a phase conjugate wave $\underline{E}_c$ of frequency $\omega_c = \omega_o - \omega$. As the pump intensities are increased, however, this simple model breaks down as the grating formed by $\underline{E}_1$ and $\underline{E}_c$ begins to interfere (either constructively or destructively) with the primary grating formed by $\underline{E}_2$ and $\underline{E}_s$.

As per Williams *et al.*[1], simple two-fluid theory suffices to calculate the low frequency plasma response to the beating of two transverse electromagnetic waves. In the limit of small m/M, the quasineutral steady-state density response is found to be

$$\frac{\tilde{n}}{n_0} = \frac{(m/2M)k^2 \underline{v}_1 \cdot \underline{v}_2}{(\omega - \underline{k}\cdot\underline{U}_i)(\omega - \underline{k}\cdot\underline{U}_i - i\nu_i) - k^2 c_s^2} \tag{1}$$

where $c_s \equiv [(\gamma_e T_e + \gamma_i T_i)/M]^{1/2}$ is the ion acoustic speed, $\underline{U}_i$ is the ion drift velocity, ν_i is the ion damping rate, and $\underline{v}_j = e\underline{E}_j/m\omega_j$ is the first order response to the external field $\underline{E}_j$. The density response reaches a maximum when $(\omega - \underline{k}\cdot\underline{U}_i)^2 = k^2 c_s^2$, at which

$$\frac{\tilde{n}_{res}}{n_0} = i\frac{m}{2M}\frac{kc_s}{\nu_i}\frac{\underline{v}_1 \cdot \underline{v}_2}{c_s^2} = i\beta(\underline{E}_1 \cdot \underline{E}_2) \text{ , where } \beta = \frac{m}{2M}\frac{kc_s}{\nu_i}\left(\frac{e}{m\omega_o c_s}\right)^2 \tag{2}$$

The quasineutral pulse (step) temporal density response, at resonance, is found to be

$$\frac{\tilde{n}_{res}}{n_0} \cong \beta(\underline{E}_1 \cdot \underline{E}_2)(1 - e^{-\nu_i t/2})\sin(\omega_{res} t) \tag{3}$$

Returning to BEFWM, we consider the case where all four waves are polarized parallel to each other (but perpendicular to the interaction plane), and where grating $\tilde{n}_1$, formed by $\underline{E}_s$ and $\underline{E}_2$, is resonant. Note that this implies that grating $\tilde{n}_2$, formed by $\underline{E}_c$ and $\underline{E}_1$, is also resonant. The density gratings $\tilde{n}_1$ and $\tilde{n}_2$ at resonance are:

$$\begin{aligned} \frac{\tilde{n}_1}{n_0} &= \beta E_2 E_s \sin(kr - \omega t) \\ \frac{\tilde{n}_2}{n_0} &= \beta E_1 E_c \sin[(k + \Delta k)r - \omega t] \end{aligned} \tag{4}$$

where Δk is the wavenumber mismatch between the waves. Making the usual slowly-varying approximation for the fields (expressed in terms of their rms values) we obtain:

$$\begin{aligned} \frac{\partial E_1}{\partial r} &= \frac{g}{2} E_c [E_2 E_s \exp(-i\Delta k r) + E_1 E_c] \\ \frac{\partial E_2}{\partial r} &= \frac{g}{2} E_s [E_2 E_s + E_1 E_c \exp(+i\Delta k r)] \\ \frac{\partial E_s}{\partial r} &= \frac{g}{2} E_2 [E_2 E_s + E_1 E_c \exp(+i\Delta k r)] \\ \frac{\partial E_c}{\partial r} &= \frac{g}{2} E_1 [E_2 E_s \exp(-i\Delta k r) + E_1 E_c] \end{aligned} \tag{5}$$

with boundary conditions of $E_1(L) = E_{10}$, $E_2(0) = E_{20}$, $E_s(L) = E_{s0}$, and $E_c(0) = 0$. This set of coupled equations is expressed here in the form utilized by Scott[2] to explain BEFWM in general, nonlinear media except that the *SBS gain coefficient* g is now

$$g = \frac{\beta \omega_{p0}^2}{k_o c^2} = \frac{1}{4\pi} \frac{n_0}{n_c} \frac{k c_s}{\nu_i} \frac{r_e \lambda_o}{M c_s^2} \tag{6}$$

Equation (5) can be solved analytically assuming undepleted pump beams. Under low gain conditions and a short interaction length limit ($\Delta kL \ll 1$), the steady state response is simply $E_c = \frac{1}{2} g E_1 E_2 E_{s0} L$. The time response of the conjugate wave to the abrupt turn-on of the pump and/or signal waves in this case is identical to that of the primary grating formed by E_s and E_2, yielding

$$E_c(t) = \tfrac{1}{2} g E_1 E_2 E_{s0} L \left[1 - e^{-\nu_i t/2}\right] \tag{7}$$

EXPERIMENTAL RESULTS:

The experimental studies are performed in a cylindrical chamber[3] in which unmagnetized, low density H_3^+ plasmas are formed. Within the chamber are two large microwave horns which launch antiparallel 3.24 GHz pump waves, and a smaller horn which transmits (collects) the signal (conjugate) wave. Due to the $\approx 38°$ tilt angle between the pump and signal waves, both a large-k (formed by E_1 and E_s) and a small-k (formed by E_2 and E_s) grating are created in the plasma. The conjugate wave thus results from the scattering of E_2 off the large-k grating, and of E_1 off the small-k grating.

Figure 1 displays the large-k ion wave (grating) amplitude, obtained by a 38 GHz scattering system aligned at a 19° tilt angle, and the conjugate wave amplitude as a function of the difference frequency Δf between the signal and pump waves. The solid lines represent least squares fits using Eq. (1), summed over 28° -48° for the scattering data and 32° -76° for the conjugate wave data to account for the range of angles contained within the signal beam. The jump in the fitted responses at $\Delta f = 0$ arises from the nonstationary nature of the gratings, as ion waves observed at one location (and tilt angle) were actually formed at another location (and tilt angle) within the plasma.

The scattering data, taken at time $t = 25\ \mu$sec after the onset of E_1 and E_s, are found to be consistent with $c_s = 1.0\times10^6$ cm/sec and $\nu_i = 220$ kHz. The conjugate data, taken at $t = 14\ \mu$sec under similar conditions, are consistent with $c_s = 1.1\times10^6$ cm/sec and $\nu_i = 290$ kHz. Provided in Fig. 2 are sample time-histories of the scattering and conjugate wave signals, taken from the same data sets as Fig. 1. The data demonstrates excellent agreement with Eqs. (3) and (7), as represented by the solid lines in Fig. 2.

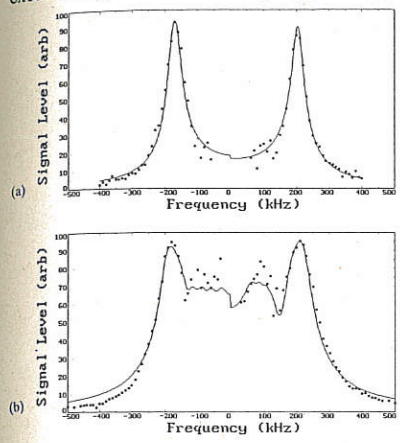

Figure 1 BEFWM resonances observed from (a) scattering, and (b) conjugate wave data in a H_2^+ plasma of density 0.18 n_c.

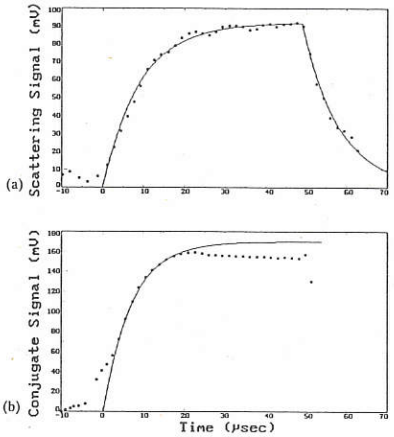

Figure 2 Typical (a) scattering, and (b) conjugate signal waveforms at resonance. Solid lines in (a) and (b) represent the damped response expected for $\nu_i = 220$ kHz and 290 kHz respectively.

Figures 3 and 4 present the scattering signal and conjugate wave power dependence on input pump wave power, at two different times into the high power microwave pulse. The signals show the expected linear dependence with pump power up to a power level of ≈ 5 kW. Figure 5 presents the conjugate wave density dependence with $P_1 = 10$ kW, $P_2 = 7.5$ kW and $P_s = 1.2$ kW. The conjugate wave amplitude is seen to deviate from linearity near $0.25\,n_c$, disrupted possibly by the large amplitude ion fluctuations often observed in the presence of the $2\omega_{pe}$ instability[4], and again at higher densities. The nonlinear effects, exhibited at high pump powers and high plasma densities, are consistent with the onset of ponderomotive whole-beam self-focusing. Although the power levels used here are low, they are sufficient to disrupt the BEFWM interaction by dephasing the wavefronts of the electromagnetic waves as plasma is pushed out of the BEFWM interaction region.

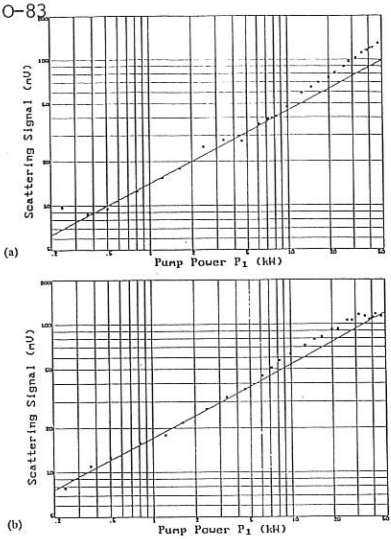

Figure 3 Scattering signal amplitude as a function of pump power P_1 for a 37° tilt angle, at time (a) t = 20 μsec, and (b) t = 45 μsec, in a hydrogen plasma of density 0.18 n_c. The data are taken with P_s = 1150 W and Δf = −170 kHz.

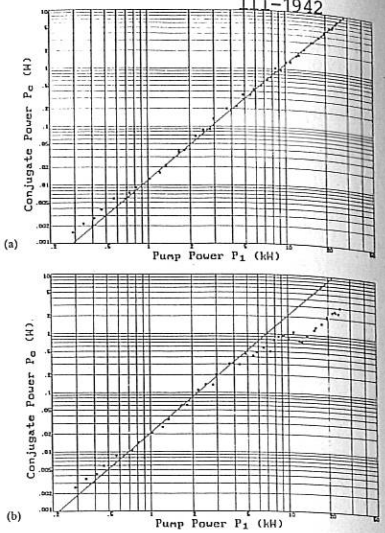

Figure 4 Conjugate power P_c as a function of pump power P_1 for a 37° tilt angle, at time (a) t = 20 μsec, and (b) t = 50 μsec, in a hydrogen plasma of density 0.20 n_c, with P_s = 1020 W, P_2/P_1 = 0.75, and a difference frequency Δf = −190 kHz.

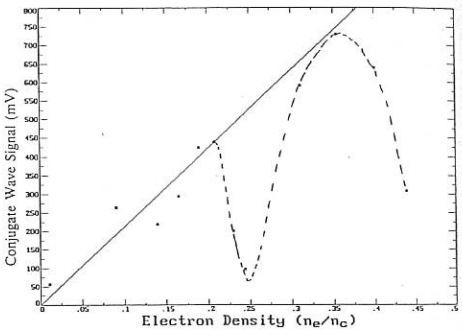

Figure 5 Conjugate wave signal, at resonance, as a function of plasma density with moderate pump wave intensities.

ACKNOWLEDGEMENTS:

This work was supported by the LLNL Laser Fusion Program. The authors acknowledge useful conversations with Dr. E. Williams and Prof. M. Goldman.

REFERENCES:

[1] E. Williams, D. Lininger, and M. Goldman, *Phys. Fluids B* **1**, 1561 (1989).
[2] A.M. Scott and K.D. Ridley, *IEEE J. Quantum Elect.* **25**, 438 (1988).
[3] C.J. Pawley, H.E. Huey, and N.C. Luhmann, Jr., *Phys. Rev. Lett.* **49**, 877 (1982).
[4] A.B. Langdon, B.F. Lasinski and W.L. Kruer, *Phys. Rev. Lett.* **43**, 133 (1979).

High Frequency Modes of a Plasma Column Loaded in a Sheath helix

A.Ganguli, P. Appala Naidu and G.Umesh,
Centre for Energy Studies, Indian Institute of Technology,
New Delhi 110016, India.

This paper investigates the high frequency ($w \geq w_{p_e}, w_{c_e}$), slow wave modes ($V_{phase} < c$) of a magnetized plasma column loaded inside a sheath helix. The system geometry is shown in Fig.1. All relevant quantities are illustrated in the figure. Consider small amplitude waves (varying as $\exp[-i(wt-kz+m\phi)]$; m: an integer) propagating in the system. This problem has been treated in [1], where the general dispersion relation (DR), was derived in connection with the Alfven wave modes of the system.

The high frequency slow wave solutions of the DR derived in [1], are presented here for the m=o, ± 1 modes ($w > w_{p_e}$). The values of the different parameters are chosen as: helix radius (r_h) = 7.35 cm and 3.5 cm; helix pitch (p) = 2.5 cm and 0.5 cm; argon plasma density (n_o) = $10^{11}/cm^3$, wave frequency ($w/2\pi$) = 2.45 GH_z, axial magnetic field (B_o) in the range $0.85 \leq w_{c_e}/w \leq 1.35$. (The wave frequency has been chosen equal to the frequency of the microwave source in our heating experiments.)

Numerical computations show that the DR yields slow wave roots for: (1) γ_1 - real, γ_2 - imaginary (Type I root); (ii) γ_1 and γ_2 both imaginary (Type II root). Here γ_1, γ_2 are the two perpendicular wave numbers inside the plasma region (see [1]).

Dispersion curves (plots of V_{phase} versus w/w_{c_e}) for the m=0, ±1 modes, for the parameters given above, are presented in Fig.2. All the waves are slow waves. For large diameter helices, the Type I and Type II roots have separate branches with the Type I roots going to resonance at $w=w_{c_e}$ and the Type II roots propagating upto low values of magnetic field. For smaller r_h some of the Type I roots may transform into Type II roots for $w \leq w_{c_e}$ (as seen for the m=0 mode for r_h = 3.5 cm). No dependence on the plasma radius is shown in these plots, since the dispersion curves are found to be highly insensitive to the plasma column radius.

The radial variations of the field amplitudes are shown in Figs. 3a-3c. The key feature revealed is that the Type I waves are all body waves. The Type II waves are surface waves at low B_o ($w/w_{c_e} \approx 1.17$) and transform into body waves at

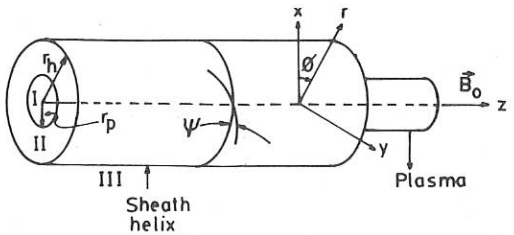

Fig 1 Plasma column of radius rp situated coaxially inside a sheath helix of radius rh in free space. ψ (=Cot^{-1} $2\pi r_h/p$, p: helix pitch) is the pitch angle. The different regions are also specified.

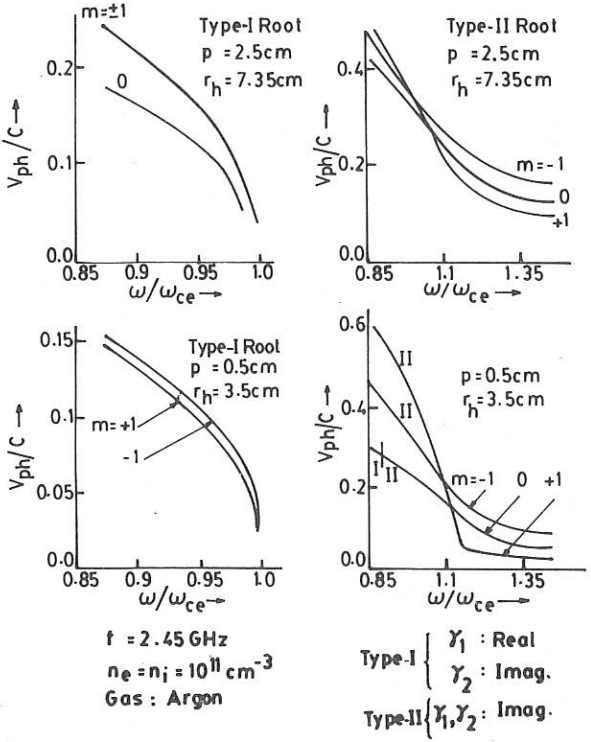

Fig.2. Dispersion curves (V_{phase} versus ω/ω_{ce}) for the m=0,±1 modes of a plasma column loaded inside a sheath helix. The plots are independent of rp. The vertical line on the m=0 mode curve for rh=3.5 cm shows the transition from Type I to Type II root.

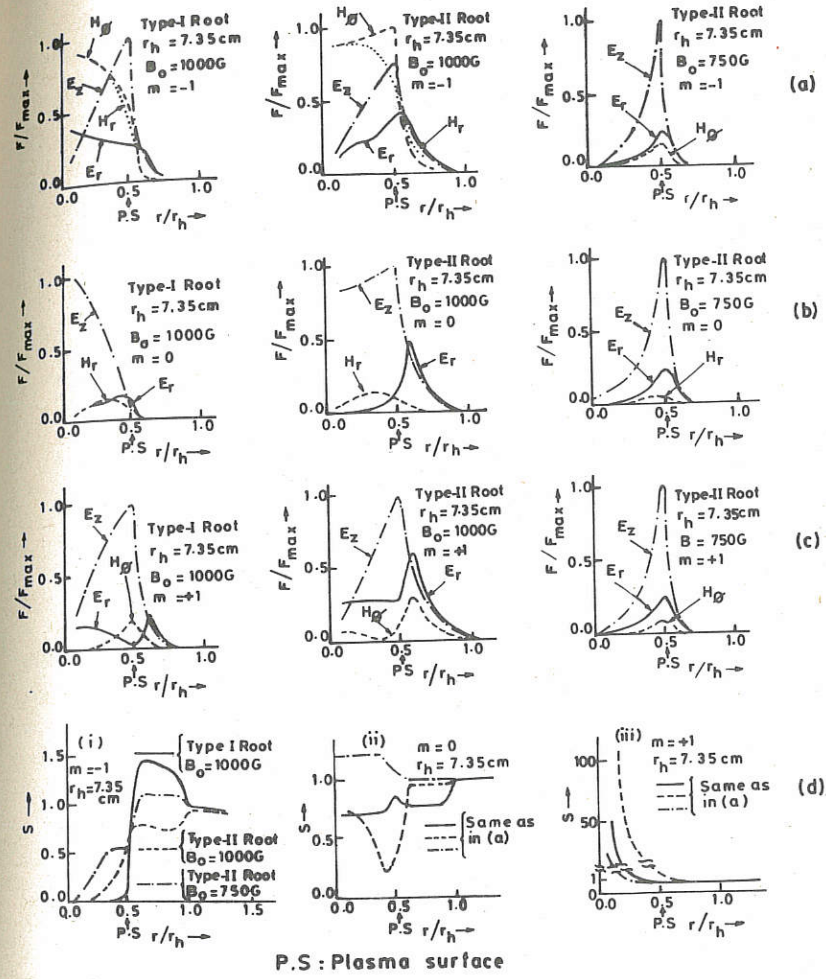

Fig.3.(a)-(c): Radial variation of the normalized e.m field components for the m=0,±1 modes and Type I, II roots for different values of B_o.
(d): Radial variation of the index of polarization s.
All parameters are the same as given in Fig.2.

higher values of B_0 ($w/w_{ce} \approx 0.88$). Ez is the largest fieldcomponent for all the modes; the other significant components are: For the Type I, m = -1 mode, H_θ, H_r and E_r are seen to be the important components; E_r and H_r are seen to be significant for m = 0 while E_r and H_θ are important for m = +1. For the Type II root at low magnetic fields (B_0 ≈ 750G), E_z and H_θ are the significant components for m = ±1 while E_r and H_r are the important components for m = 0. For the Type II root at high magnetic fields (B_0 ≈ 1000G), E_θ and H_r are the significant components for m = ± 1 while E_r and H_θ are important for m = 0.

The presence of surface waves at low magnetic fields (Type II root) may be exploited for plasma heating in a mirror machine, by coupling to these waves from an external antenna situated at the mirror mid-plane. As the waves propagate to higher B regions, they transform to body waves and the energy in the wave is transported into the plasma interior. At the resonance region ($w \approx w_{ce}$), it is expected that mode conversion to a suitable mode will lead to significant plasma heating.

Fig.3d shows the radial profiles of the index of polarization s (= $|E_L| / |E_R|$; E_L(E_R) : left (right) hand components) of the wave fields in the plasma, in the x-y plane for the Type I, Type II roots at values of B_0 corresponding to those used for the field profiles in Figs.3a-3c. It is seen that the m = -1 modes are RHP (or close to it), inside the plasma and are linearly polarized (LP) at the plasma edge and beyond it. The m=0 modes are approximately LP throughout, although the Type II root at B = 1000 G shows a tendency towards RHP. (This feature is enhanced for small diameter helices.) The m=1 mode is LHP on axis and changes to RHP either inside the plasma, or just outside it. These features of the waves will be of importance in coupling to them from outside the helix region along its axis.

References

1. A.Ganguli et.al., IEEE Trans. Plasma Sc., PS-19, 433 (1991).

2. A Ganguli and R.Baskaran, Plasma Phys. Centre Ins. 29, 729 (1987)

III-1947

ESTIMATION OF ELECTRON TEMPERATURE AND DENSITY BY DECONVOLVING THE ABSORPRTION PART OF THE PLASMA DISPERSION FUNCTION

H. Jiménez-Domínguez, A. Cabral-Prieto, L. Meléndez-Lugo, R. López-Callejas, S. Colunga-Sánchez, R. Valencia-Alvarado, S. Cruz-Jiménez*, E. Gaytán-Gallardo and E. CHávez-Alarcón.

Instituto Nacional de Investigaciones Nucleares.
Apartado Postal No. 18-1027, Col. Escandón.
México 11801, D.F., México.
* Universidad Autónoma Metropolitana, Iztapalapa.
Departamento de Física.
Av. Michoacán y Purísima, Col. Vicentina.
México 09340, D.F., México.

INTRODUCTION

The analysis of the propagation of plasma waves , could be a useful way to estimate plasma parameters such as electron temperature T_e and density n_e. The plasma dispersion function, $Z(\zeta)$, which arises in the study of linearized plasma wave propagation in Maxwellian, non-relativistic plasmas with or without a magnetic field, contains inherently two types of information which can be described as follows: 1) in the absence of non-linear phenomena, the frequency spectrum of the wave contains a Lorentzian component which provides information about the damping of the wave in the plasma. This damping depends, in general, on T_e and n_e; 2) the frequency spectrum of the wave also contains a Gaussian component which gives information about the thermal motion of the plasma electrons. Those two components are convolved with each other. The information contained in the function $Z(\zeta)$, related to the electron temperature and density of the plasma, can be extracted if one is able to find the parameters that characterize this function. In this work it is suggested that those parameters can be found by

deconvolving the absorption part of $Z(\zeta)$.

PRELIMINARY CONSIDERATIONS

In many spectroscopies, Lorentzian spectral lines determined by the lifetime of the quantum excited states are affected by external perturbations, such as instrumental instabilities and thermal motions. If those perturbations have a random origin, then the absorption line is the convolution of the Lorentzian profile with a Gaussian distribution that represents the perturbing effects. This convolution is proportional to the Voigt profile /1/:

$$H(a,\upsilon) = \frac{a}{\pi} \int_{-\infty}^{\infty} \frac{e^{-y^2} dy}{(\upsilon - y)^2 + a^2} , \qquad (1)$$

where $\upsilon = [2(\omega - \omega_o)\sqrt{ln\ 2}/\Gamma_G]$ is the dimensionless frequency variable, Γ_G being the FWHM of the Gaussian distribution in frequency units, and $a = [\Gamma_L\sqrt{ln\ 2}/\Gamma_G]$ is Posener's parameter /2/ that measures the relative contributions of the Gaussian distribution and the Lorentzian function to the Voigt profile; Γ_L is the FWHM of the Lorentzian.

On the other hand, it has been shown /3/ that the Voigt profile (1) can be written in terms of the imaginary or absorption part of the plasma dispersion function:

$$H(\upsilon,a) = \frac{1}{\sqrt{\pi}} Im\ Z(\zeta) , \qquad (2)$$

where $\zeta = \upsilon + ia$. As seen from the definitions of the variable υ and the parameter a, the function $Z(\zeta)$ inherently contains both a Lorentzian contribution representing the line shape of a spectral line of central frequency ω_o, and the perturbing Gaussian contribution that represents the thermal motions in the emitting sample and/or instrumental instabilities. Deconvolution of expression (2) yields the Lorentzian and Gaussian contributions through the values of Γ_L and Γ_G /3/. For those cases in which the Gaussian contribution is small *i. e.* $a>>1$, deconvolution is performed

by using an approximation method /4/.

APPLICATION TO THE DETERMINATION OF T_e and n_e IN A PLASMA

In this section, a way to determine T_e and n_e by deconvolving the frequency spectrum of a wave of frequency ω_o that probes a thermal plasma, is suggested. The wave amplitude should be small enough to avoid non-linear phenomena. In this application the Lorentzian contribution to (1) and (2) represents the line shape of a linearized wave of central frequency ω_o that propagates in the plasma, and the Gaussian contribution represents the Maxwellian velocity distribution of the plasma electrons. Therefore the above preliminary considerations, suggest a method to estimate electron temperature T_e and density n_e of the plasma, based on the deconvolution of expression (2) to find the values of Γ_L and Γ_G. As will be seen below, these parameters can be expressed in terms of T_e and n_e.

The complex variable z in the argument of the plasma dispersion function for wave propagation can be written as:

$$z = \frac{(\omega - \omega_o) + i\alpha}{k\, v_{th}} \quad , \tag{3}$$

where ω_o is the frequency of the wave and ω is introduced to allow for a frequency dispersion; α is the damping constant of the wave in the medium, $v_{th} = (2k_B T_e/m_e)^{1/2}$ is the electron thermal velocity and k is the wave number. It is easy to see that v_{th} can be written as: $v_{th} = \Gamma'_G / 2\sqrt{ln\ 2}$, where Γ'_G is the FWHM of the Gaussian in velocity units. Therefore (3) is rewritten as:

$$z = \frac{2(\omega - \omega_o)\sqrt{ln\ 2}}{\Gamma_G} + i\,\frac{\Gamma_L\sqrt{ln\ 2}}{\Gamma_G} \quad , \tag{4}$$

where $\Gamma_L = 2\alpha$, and $\Gamma_G = k\,\Gamma'_G$ now has frequency units.

According to the definitions of w and a, the variable (3)

can then be written as $\zeta = v + ia$, *i. e.* the argument of $Z(\zeta)$, has been explicitly written in terms of the Lorentzian and Gaussian contributions to the detected line profile of the probing wave.

Reported deconvolution methods /3,4/, can be applied to the transmitted frequency spectrum of the signal of central frequency ω_o, to obtain the values of Γ_L and Γ_G. To complete the analysis and finally obtain the values of T_e and n_e, what remains to be done is to provide expressions for Γ_L and Γ_G in terms of these parameters. An expression for Γ_G was given above in terms of the wave number k of the probing signal and of the electron temperature. To provide an expression for Γ_L in terms of T_e and n_e, let it be assumed that the amplitude of the wave, decays in such a way that Γ_L is the Landau damping:

$$\Gamma_L = 2\alpha = 2\omega_p\sqrt{(\pi/8)}\ (k_D/k)^3 exp(-3/2 - k_D^2/2k^2)\ ,\quad k<<k_D\ , \tag{5}$$

where ω_p and k_D are plasma frequency and Debye wave number respectively; these are given in terms of T_e and n_e. As indicated in (5), this method is only valid if the wave number of the probing waves, to be used in the experiment, are in the interval $k<<k_D$. Experiments to test this proposal are planned to be performed at the Laboratorio de Física de Plasmas, ININ, México.

/1/ W. Voigt and S. B. Bayer, Acad. Wiss. 603-20 (1912).
/2/ D. W. Posener, Austr. J. Phys. 12, 184 (1959).
/3/ A. Cabral-Prieto, H. Jiménez-Domínguez, L. González-Tovany, S. Galindo, H. Flores-LLamas and M. Torres-Valderrama, J. Magn. Reson, 89, 568 (1990).
/4/ H. Jiménez-Domínguez and A. Cabral-Prieto, J. Magn. Reson. 93, 178 (1991).

Kinetic Description of Modulated Electromagnetic Wave in Relativistic Plasma

Maria L. Ekiel-Jeżewska
Institute for Theoretical Physics and Institute of Fundamental Technological Research[1]
Polish Academy of Sciences, Warsaw, Poland and Lawrence Berkeley Laboratory, University of California, U.S.A.

Tor Flå
Mathematics/Statistics Division, University of Tromsö, N-9000 Tromsö, Norway [1] and
Lawrence Berkeley Laboratory, University of California,U.S.A.

Allan N. Kaufman
Physics Department & Lawrence Berkeley Laboratory, University of California, Berkeley, U.S.A.

Abstract

Evolution of a modulated electromagnetic plane wave in a collisionless, neutral, unmagnetized plasma is investigated. Particles are assumed to move with relativistic speeds, corresponding to hot or fast moving plasmas, with macroscopic velocities slowly varying in space-time.

A kinetic description of the system on the slow scale is constructed from a Hamilton variational principle connected with the oscillation center transformation. Expansion in a small parameter corresponding to weak dispersion and weak nonlinearity is carried out. In the highest order a generalization of the nonlinear Schrödinger equation is obtained. Modulational instability due to particles resonating with the group velocity is analyzed.

The modulational instability results are compared with Kates and Kaup results [1] for the electromagnetic waves in a relativistic, multispecies fluid plasma.

Introduction

Recent interest in relativistic plasmas was our motivation to generalize Dewar's description of an electrostatic wave in nonrelativistic plasma [2] on a covariant analysis of a full electromagnetic wave and relativistic kinematics of plasma particles.

Canonical formulation of relativistic plasma theory [3] was a basis for construction of a systematic procedure eliminating fast oscillations.

The assumptions

A separation of space-time scales takes place. Four-vector of the electromagnetic field potential A_0 as well as particle space-time positions x_0 and four-momenta π_0 can be devided into slowly varying parts (x, π, $\mathcal{A}$) and rapidly oscillating ones:

$$x_0 = x + \xi(x, \pi) \quad (1)$$

$$\pi_0 = \pi + D\xi \quad (2)$$

$$A_0 = \mathcal{A} + A \quad (3)$$

[1] Permanent address

where (x,π) are slowly varying phase space coordinates of a fictitious oscillation center (to be found), D is the derivative along the oscillation center trajectory.

The wave is nearly monochromatic, with weak dispersion and weak nonlinearity:

$$A = [\epsilon A_{11}(\epsilon x, \epsilon^2 x) + \epsilon^2 A_{12}(\epsilon x) + \epsilon^3 A_{13}(\epsilon x)]e^{i\theta} + \epsilon^2 A_2(\epsilon x)e^{2i\theta} + c.c. \quad (4)$$

$$\theta = k \cdot x, \qquad k = const(x) \quad (5)$$

The self-consistent field $\mathcal{A}$ scales as: $\mathcal{A} = \epsilon^2 \mathcal{A}(\epsilon x)$.

The goal is to determine evolution of the system on the slow scale, averaging out fast oscillations.

Action principle for single particles and fields

The Hamilton action principle is formulated in 8 dimensional phase space of canonical coordinates (r,p) [3]:

$$\delta S = 0, \qquad S[\gamma] = \sum_{particles} \int_{\gamma} [p \cdot dr - h(r,p)d\tau] + \int d^4x \, \ell^f \quad (6)$$

where τ is a parameter along a particle trajectory γ and ℓ^f is the free field Lagrangian density.

The 8 dim Hamiltonian h has a form

$$h(r,p) = \frac{1}{2m}[(p - \frac{e}{c}A_0)^2 + m^2c^2] \quad (7)$$

The variational principle has to include constraints, namely, the confinement of a particle motion to the mass shell:

$$h(r,p) = 0 \quad (8)$$

and the Lorentz gauge for the components of A_0.

Oscillation center transformation

The oscillation center (OC) transformation T [4]:

$$T : (x_0, \pi_0) \longrightarrow (x, \pi) \quad (9)$$

is a Lie transform, consisting of subsequent infinitesimal canonical transformations. They are determined by the requirement that the transformed OC Hamiltonian H

$$T^{*-1} : \sum_{n=0}^{4} \epsilon^n h_n = h \longrightarrow H = \sum_{n=0}^{4} \epsilon^n H_n \quad (10)$$

is practically not oscillating (contribution from oscillations is of order ϵ^5). The form invariance of Hamilton equations under OC transformation gives the required result: transformed phase space coordinates of particles (x, π) do not oscillate on the fast scale. These new coordinates

determine the 'averaged' particle positions in phase space, corresponding to positions of fictitious oscillation centers.

Electromagnetic fields are not transformed in this approach.

Action principle for oscillation centers and fields

The interaction part of the averaged action is obtained through the OC transformation and it preserves the same form as in Eq.(6) , due to the properties of the canonical transformations. The field Lagrangian density $\mathcal{L}_f$ is picked up to be a space-time average, taken over the slow scale, of the well-known free field action l_f from Eq.(6):

$$\delta S = 0, \quad S[\gamma] = \sum_{OC} \int_{\gamma} [P \cdot dR - H(R,P)d\tau] + \int d^4x \mathcal{L}^f \tag{11}$$

where γ is the OC trajectory. Variations are taken with respect to OC trajectories and field amplitudes $A_{1i}, A_2, \mathcal{A}$, i=1,2,3.

Statistical approach

The single oscillation centers approach is equivalent to the description in terms of one oscillation center Klimontovich distribution function f(R,P).

The Klimontovich approach leads to the replacement

$$\sum_{OC} \int_{\gamma} d\tau \xi(R,P) \longrightarrow \sum_{species} \int d^4R \int d^4P f(R,P)\xi(R,P) \tag{12}$$

The Hamilton equations are replaced by the Ignatiev equation:

$$\{f, H\} = 0 \tag{13}$$

with the 8 dimensional phase space Poisson brackets.

The next step is to generalize f to be a smooth Vlasov OC distribution function. In this way (13) becomes the Vlasov equation.

Consistently, f is expanded as $f = f_0 + \epsilon^2 \delta f$, where $f_0 = f_0(P)$ is the 'OC global equilibrium' distribution function.

This leads to the linearized Vlasov equation:

$$\frac{P}{m} \cdot \frac{\partial \delta f(R,P)}{\partial R} - \frac{\partial f_0}{\partial P} \cdot \frac{\partial H_2(R,P)}{\partial R} = 0 \tag{14}$$

which can be formally solved for δf in terms of the field amplitude A_{11}.

Evolution equations

We finally get a system of equations for the quantities $A_{11a}(X_1, X_2), a = 1, 2, 3$.

The notation is:

$$A_{11a} = e_a \cdot A_{11}, \quad e_a \cdot k = 0, \quad |e_a| = 1,$$
$$X_1 = \epsilon x, \quad X_2 = \epsilon^2 x, \quad \epsilon \partial_\mu A_{11a} = \frac{\partial}{\partial X_1} A_{11a}, \quad \epsilon^2 \mathcal{D}_\mu A_{11a} = \frac{\partial}{\partial X_2} A_{11a} \tag{15}$$

The equations are:

Dispersion relation: $D_a A_{11a} = 0$
Propagation with a group velocity: $V_a^\mu \partial_\mu A_{11a} = 0$
The highest order equation:

$$iV_a^\mu \mathcal{D}_\mu A_{11a} + \sum_b H_{ab}^{\mu\nu} \partial_\mu \partial_\nu A_{11b} + \delta D_a[\delta f] A_{11a} + w_a A_{11a} \sum_b |A_{11b}|^2 + v_a A_{11a}^* \sum_b A_{11b}^2 = 0 \tag{16}$$

Explicit expressions for the coefficients are given in [5].

Modulational instability

The detailed analysis of Eq.(16) is given in [5]. It leads to the conclusion that particles resonating with the group velocity cause a generic modulational instability. This result is new in comparison with modulational stability obtained by Kates and Kaup [1] in their relativistic fluid plasma model.

The longitudinal and transverse waves are treated separately.

For the longitudinal polarization to get a modulational dispersion relation the standard Fourier analysis of A_{11} into coupled modes (the large carrier wave and two small sidebands) is carried out: $A_{11a} = A_{11a}^0 + A_{a+} exp(iK \cdot X_1) + A_{a-} exp(-iK \cdot X_1)$

For the transverse polarization the four-vector k is showed to be timelike. Thus δD in Eq.(16) is real. Therefore the fields $A_{11a} = |A_{11a}| exp(i\theta_a)$ and the Eq.(16) can be simply linearized around a constant solution (of linear or circular polarization), and next Fourier transformed to give the modulational dispersion relation.

Acknowledgements

This research was partially supported by the U.S. Department of Energy under contract # DE-AC03-75SF00098, Polish Government KBN grant # 2 0201 91 01-702/2/91, the U.S. Government Fulbright grant # 12586 and NAVF & Norwegian Academy of Science and Literature.

References

[1] R.E. Kates, D.J. Kaup, J. Plasma Phys., **42**, (1989), 507.
[2] R.L. Dewar, J. Plasma Phys., **7**, (1972), 267.
[3] A.N. Kaufman, D.D. Holm, Phys. Lett. **105A**, (1984), 277.
[4] J.R. Cary, A.N. Kaufman, Phys. Fluids, **24**, (1981), 1238.
[5] M.L. Ekiel-Jeżewska, T. Flå, A.N. Kaufman, in preparation.

111-1955

Topic 11:

Partially Ionized Plasmas

EXPERIMENTAL EVIDENCE OF SELF-ORGANIZATION AND CHAOS IN SOME PLASMA DEVICES

M. Sandulovicіu, D. Alexandroaei, S. J. Talasman, B. Ianopol
Department of Plasma Physics, "Al.I.Cuza" University
RO-6600 Iasi, Romania

The presence of well-localized globular luminous space charge structures (GLSs) and their ability to act as energy sources for ordered and disordered phenomenon were already discussed /1,2 /. Here we comparatively present experimental results which were obtained on three different plasma devices in which GLSs appear. The results suggest that the GLSs (generated through a self-organization process) exist in all plasma devices where self-sustained time dependent phenomena could be observed.

First the old problem of the dc glow discharge property to generate periodical variations of the dc current /1/ is resumed. We want to show, that in reality the solution of this problem is possible only involving a self-organization phenomenon while kinetic energy of the accelerated electrons is transformed in energy stored

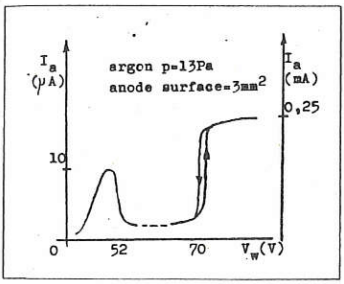

Fig.1 Static I-V characteristic including the negative branch (forming phase of the planar DL) and the suddenly increase accompanying the transition to an unstable globular DL

in the electric field localized in the SCS via quantum processes. Because the GLS becomes movable and disrupt when the potential drop V_{DL} across SSC riches the ionization potential V_i of the gas, the cumulated energy is released and could sustain time dependent phenomena in the electrical circuit including the GLS. Thus the periodical modulation of the glow

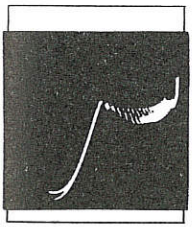

Fig. 2 Dynamical I-V characteristic which evidences the transition from a stable planar to an unstable globular DL

discharge current known as anode instabilities observed under conditions when its positive parts are contracted in a GLS in reality is produced by oscillations taking place in a proper oscillatory circuit /1,2

/, in which the GLS act as a negative resistance (NR). The forming phase of the GLS can not be evidenced in the I-V characteristic of a dc discharge produced in a glass tube because these simultaneously appears in its final (unstable) state, with the discharge ignition. However, using a metal tube whose potential is changed with respect to the anode one obtains the results shown in fig.1. The negative branch corresponds to the phase during which in front of the anode a planar one and then a stable GLS (Fig.2) is formed. The direct transition from a stable to an unstable GLS, which takes place when $V_{DL} = V_i$ /1,3/ is evidenced in the dynamic I-V characteristic presented in fig. 2 When $V_{DL} = V_i$ the GLS disrupts after it has expanded and is periodically reformed /1,3,4/. Because during the unstable state of the spherical GLS free charges are produced, the dc suddenly increases (fig.1). The parameters of the observed oscillation are mainly determinated by the reactive and ohmic circuit elements of the proper oscillating circuit /2/. In fig.3 we present the equivalent circuit which explains the oscillatory behaviour of a dc glow discharge

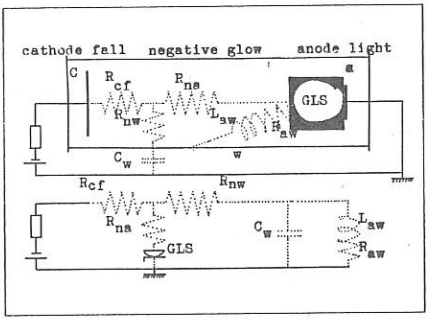

Fig. 3 Schematical device and equivalent circuit R_{cf}, R_{na}, R_{nw} equivalent ohmic resistances of the cathode fall, negative glow and of the gaseous conductor with respect to the metal wall, C_w stray capacitance of the tube wall with respect to the surroundings: L_{aw} and R_{aw} inductance and resistance between the anode and the wall.

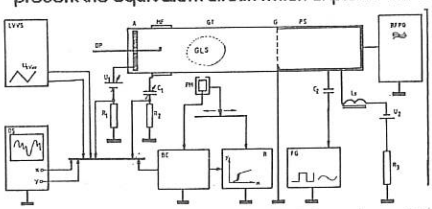

Fig. 4 Scheme of the second experimental set-up (RFPG - radiofrequency power generator, MF-metal. foil, DP - double probe, LVVS - linear variable voltage supply, BC - boxcar, PM - photomultiplier)

In certain conditions the structure of the GLS becomes complex (multiple GLSs), a fact which is accompanied in the discharge current profile by a route to chaos.

Another self-organization phenomenon has been observed in a low pressure plasma column produced by a plasma source PS (radio-frequency glow discharge). The so obtained plasma diffuses through a grounded grid G into a glass tube GT, forming a plasma column (Fig.4). When a current collecting positive biased planar electrode A is placed at the end of the column, a quasi-stationary GLS appears at a certain distance from it. The space-time in-

vestigation of this structure, reveals a space-time ordered phenomenon for both the axial electric field and the light emitted from this structure which proves that the GLS behaves in a pulsating state (Fig.5).

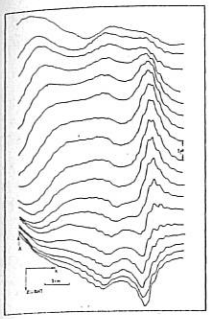

Fig.5 Space-time resolved axial distribution of the light

This phenomenon was accompanied by oscillations of both the main current collected by the anode and the capacitive wall current. For certain voltages (60 V) and pressure (10^{-3} Torr), it was possible to obtain even two spherical structures. In this case a period doubling phenomenon could be observed in the current variations. The static current-voltage characteristics show three hysteresis regions (Fig.6), each of them referring to different states of the GLS.

The results prove that the GLS is sourrounded by a double layer (DL) which is responsible for its space-time evolution. This evolution is essentially based on quantum processes such like excitation and ionization.

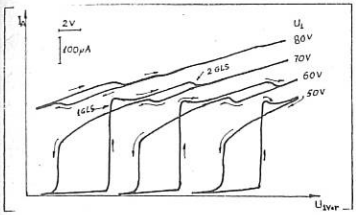

Fig. 6 Current-voltage characteristics for different U_1 voltages

New experimental results about the connections between the chaotic behavior of a plasma device and the self-organization

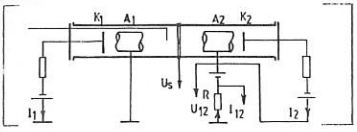

Fig. 7 Scheme of the experimental set-up (K_1, K_2 plate cathodes, A_1 A_2 ring anodes, 50 cm apart

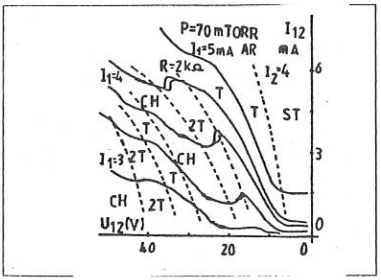

Fig.8 Averaged I_{12}-U_{12} current-voltage characteristics for different I_1 values of the K_1A_1discharge

phenomena (DL structure) were obtained using the experimental device presented in fig.7. A single DL or a multiple one, in stable or unstable state, is formed at the contact region between the two negative glow plasmas, when

between them a dc voltage is imposed /3/.

In the I-V characteristic shown in fig.8 different behaviours of the device are pointed out (ST-stable state; T, 2T, CH single period, double period and chaotic oscillations respectivelly). The I(t) - I(t+τ) phase plots for the ordered and disordered current variations toghether with the corresponding amplitude frequency characteristics are presented in Fig.9.

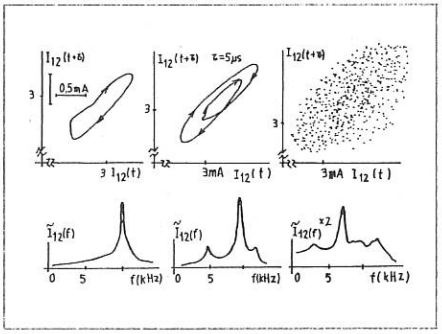

Fig.9 Trajectories in the $I_{12}(t)$-$I_{12}(t+\tau)$ phase plane and the corresponding frequency spectra of I_{12} for different values of the I_{12} mean current (I_1=I_2=4 mA, P=0.07 Torr, Ar gas)

The local temporal variations in the chaotic state of the device representing the potential of four capacitive probes placed in four different places in A_1A_2 region, are presented in (Fig.10). The contact region between the two unstable DLs seems to be the localization of the "source" for such a chaotic behaviour. The period-doubling phenomenon is observed when the second DL appears after the first one and has a correlated dynamics with it /5/.

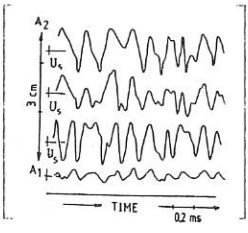

Fig.10 Simultaneous time-dependences of the signals from four capacitive probes equidistantly placed in the A_1A_2 forming-DL region (I_{12}=3.5 mA, I_1=I_2=4 mA, P=0.07 Torr).

The chaotic behaviour appears when the formation and disruption processes of the two DLs are not correlated and are controlled by aleatory processes. The portions of negative resistance on the I-V characteristics prove this.

/1/. M.Sanduloviciu (1987) Int.Conf.Plasma Phys. Kiev, Proc. Inv.Papers, 293

/2/. M.Sanduloviciu, G.Popa, An.St. Univ. Iasi (1988) XXXIV 83

/3/. D.Alexandroaei, M.Sanduloviciu (1987) Phys.Lett. A122, 173

/4/. Bin Song, N.D'Angelo, R.Merlino, J.Phys.D Appl.Phys. (1991) 24 1789

/5/. D.Alexandroaei, I.Grosu, M.Sanduloviciu, (1991)Proc. of XX ICPIG Pisa, Italy, Contr.Pap Vol.176

TOMOGRAPHIC TIME-RESOLVED RECONSTRUCTION OF THE THREE DIMENSITONAL ELECTRON VELOCITY DISTRIBUTION IN A PARTIALLY IONIZED RF PLASMA

K. Matsumoto, N. Iwama and S. Ishii

Department of Electronics & Informatics, Toyama Prefectural University, Imizu-gun, Toyama 939-03, Japan

With a rotating plane probe immersed in a rf plasma, time variations of the electron velocity distribution in three-dimensional velocity space have been studied. The angular rotation of a plane probe at a spatial point in a plasma may provide sufficient information for numerically reconstructing the three-dimensional shapes of the functions by computerized tomography.

The knowledge of the velocity distribution functions of electron in gas discharges is important for fundamental understanding of plasma processes which are applied to make new materials and to fabricate microelectric devices in industry. Electrostatic probes(Langmuir probe) and electrostatic energy analyzers(Faraday cup) are widely used as valuable diagnostic tools for studying the properties of electrons and ions in plasma. Due to the lack of angular resolution, however, it is difficult to directly measure the velocity distributions of charged particles as functions of all three velocity-space coordinates. To overcome this difficulty, a technique of computerized tomography(CT) has been proposed by Lehner /1/ and Iwama *et al.* /2/. The angular rotation of a usual type of analyzer at a spatial point in plasma may provide sufficient information for recovering the three-dimensional shapes of the functions with numerical processing.

The electron current of a plane probe with bias voltage V is expressed in terms of the projected (one dimensional) electron velocity distribution function $f_{1D}(u;\boldsymbol{n})$ in a spatial direction of $\boldsymbol{n}$, as

$$I_e(V) = Se \int_{\sqrt{(2eV)/m_e}}^{\infty} u f_{1D}(u;\boldsymbol{n})\, du, \qquad (1)$$

where $\boldsymbol{n}$ is the unit normal to the probe surface, S the probe area, e the electron charge and m_e the electron mass. Taking the first derivative with respect to V, we have

$$f_{1D}(u;\boldsymbol{n}) = -\frac{m_e}{Se^2}\frac{dI_e(V)}{dV}. \qquad (2)$$

Here the function $f_{1D}(u;\boldsymbol{n})$ is defined as the Radon transform of the three dimensional velocity distribution function $f_{3D}(\boldsymbol{v})$:

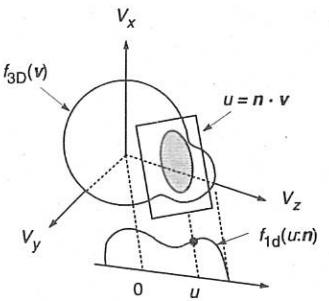

Fig.1 Planar projection $f_{1D}(u;\boldsymbol{n})$: the integration of $f_{3D}(\boldsymbol{v})$ over a $\boldsymbol{n}$-plane which is designated by $u = \boldsymbol{n} \cdot \boldsymbol{v}$.

$$f_{1D}(u;\boldsymbol{n}) = \int f_{3D}(\boldsymbol{v})\,\delta(u-\boldsymbol{n}\cdot\boldsymbol{v})\,d\boldsymbol{v} \qquad (3)$$

with the Dirac delta function δ( ) and schematically shown in Fig. 1. If $f_{1D}(u;\boldsymbol{n})$ is obtained as a function of velocity u in each of the directions of normals $\boldsymbol{n}=\boldsymbol{n}_j$ (j=1,2,...J), then the numerical recovering of $f_{3D}(\boldsymbol{v})$ as a function $\boldsymbol{v}$ is analogously a problem of CT /3,4/ in order to reconstruct the three-dimensional object from its planar projections.

The experimental apparatus is shown schematically in Fig. 2. Two parallel plate electrodes (stain-less steel, 12*cm* diameter, 4*cm* spacing) covered with Pyrex glass except for the discharge area are positioned in the center of the chamber (stain-less steel, 16*cm* inner diameter, 50*cm* length). A plane single probe (molybdenum, 3*mm* diameter) which is rotational in the azimuthal direction is inserted at the mid center of discharge region, as shown in Fig. 3. The chamber is always pumped out by using a 200 *liters/s* diffusion pump. Argon gas is used whose flow rate is arranged so as to hold pressure at 0.4 *Torr*. Low frequency pulsed rf power whose frequency is 30*kHz*, repetition frequency 1*kHz* and duty ratio 1/1 is applied to the electrodes. An unbalance-balance transformer is used in order to reduce the potential difference between the probe and the plasma; plasma space potential is fluctuating with the doubled frequency and its magnitude is nearly equal to anode potential. Therefore, the rectified rf voltage applied to electrodes is superposed on the dc bias voltage of probe. To achieve a time-resolved probe diagnostics a sampling converter is employed; the phase to sample data is manually set, whose gate pulse is synchronous with a reference signal of the rf generator. Probe characteristics are digitized by using a 12 bits A/D convertor and then recorded on a personal computer. The first derivative with respect to dc bias voltage is obtained numerically by utilizing smoothing technique of B-spline function.

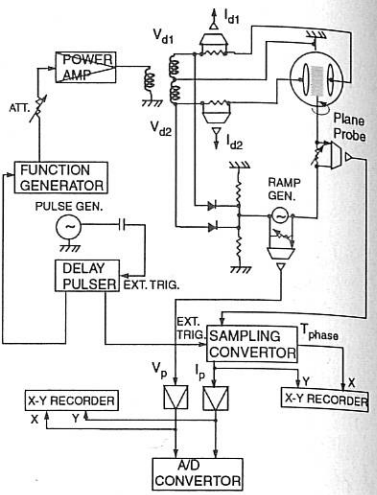

Fig. 2 Schematic diagram of the experimental setup; rectified rf potential, which varies in almost the same way as plasma space potential, is superposed on the conventional dc bias so that time resolved probe characteristic may be measured.

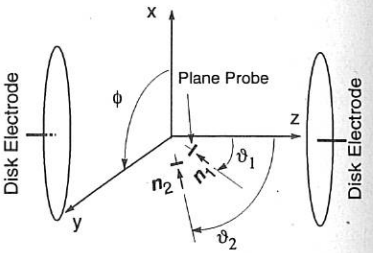

Fig. 3 Coordinate system in real space; plane disk probe is azimuthally rotational about its axis.

Waveforms of the discharge potential and current of each rf electrode, and the probe current at different dc bias voltage are shown in Fig. 4(a), (b) and (c), respectively. The potential of each electrode is symmetrically alternating. The discharge voltage is equal to the potential difference between these electrodes. The phase difference between each discharge current and applied rf potential is almost zero. This indicates that the discharge characteristic is similar to the dc discharge one in which loading impedance is purely resistive. The probe current with dc bias -10*V* is corresponding to the ion saturation current and that with +10*V* corresponding to the electron retarding current. It is found that the superposed rf potential on probe dc bias forces the probe potential to follow well the time-varying local plasma space potential. The experimental data analyzed below are obtained at the phase $t=t_1$, t_2 and t_3.

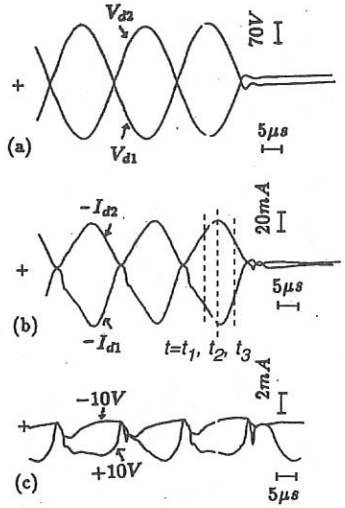

Fig. 4 Discharge characteristics and time varying probe current; waveforms of (a) potential and (b) current of each rf electrode, and (c) probe current at dc bias -10V and 10V, 0.4Torr(Ar), 30kHz.

As illustrated in Fig. 3, the probe was rotated, over the range of $0 \le \theta \le 2\pi$ in the ϕ=0 plane. For each of the 12θ-values of $\theta_j = (j-1)\,2\pi/12$ (j=1,2...12), probe characteristics were measured and numerically differentiated with respected to dc probe bias voltage. Since ion current was estimated to be very small and ion temperature to be very low, differentiated characteristics were approximately regarded as one-dimensional electron velocity distribution functions projected to θ direction in the three dimensional velocity space. Combining a pair of the differentiated curves for $\theta = \theta_j$ and $\theta = \theta_{6+j}$ at the plasma potential, we get a $f_{1D}(u; n_j)$ curve in one polar direction of $\theta = \theta_j$ (j=1,...,6). Consequently, we obtained 6 series of projection data over the range of $0 \le \theta \le \pi$.

Reconstructed electron velocity distributions by the ART (Algebraic Reconstruction Technique) are shown in Fig. 5, and Fig. 6(a), (b) and (c). Contour plot at the phase $t=t_1$ during discharge current increases is drawn in Fig. 5, where outward islands are

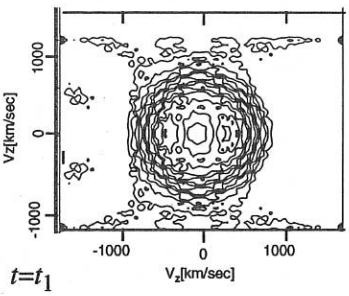

Fig. 5 Contour plot of three-dimensional reconstruction of the electron velocity distribution function by ART method. Sampling phase is $t=t_1$ when discharge current is growing with time, as shown in Fig.4(b).

meaningless, reconstruction errors due to lack of projection data. It is found that the electron velocity distribution is not isotropic, extended toward the inverse direction of the rf electric field. This distortion appears clearly only at the phase during the rf discharge current increases.

The flow of electron beams move towards the electrode with positive potential is interpreted as that of primary electrons to cause ionization. Here, the dip on the top is considered to indicate that the plane probe can not collect the whole electron current near the plasma space potential.

Time-resolved three dimensional drawings by wire frame are shown in Fig. 6(a), (b) and (c), where sampling phases are $t=t_1$ during discharge current increases, $t=t_2$ at the maximum current and $t=t_3$ during current decreases, respectively. It is found that the electron velocity distribution function changes at the twice frequency of the applied rf; in a half period, the distribution starts from a non-isotropic function and after reaching to an isotropic one relaxes into a low-temperature isotropic profile.

The authors would like to thank Mr. T. Takeda for his assistance in experiments and Mr. H. Iwasaki and Mr. M. Teranishi for their help in data-processing. We also would like to thank Mrs. M. Fukuda and M. Mori for their technical assistance. The authors wishes to thank Professor M. Sato for his continuous support.

/1/ T. Lehner, Raport de Lab. PMI d'Ecole Polytechnique **PMI** 1186 (1982).

/2/ N. Iwama, T. Lehner, H. Noziri and M. Okado, Japan J. Appl. Phys. **27**, 1732 (1988).

/3/ J. H. Williamson and M. E. Clarke, J.Plasma Phys. **6**, 211 (1971).

/4/ S. R. Deans, *The Radon Transform and Some of Its Applications* (John Wiley & Sons, New York, 1983).

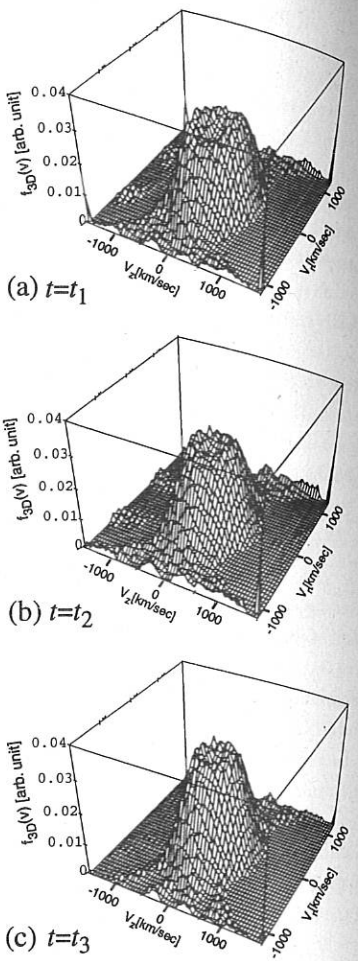

Fig. 6 Reconstruction of three dimensional electron velocity distribution function, by CT on the basis of ART method. The profiles are plotted in the two-dimensional velocity space with coordinates $v_z = |v|\cos\theta$ *and* $v_r = |v|\sin\theta$. *(a)* $t=t_1$ *during discharge current increases, (b)* $t=t_2$ *at the maximum and (c)* $t=t_3$ *during decreases.*

LARGE AMPLITUDE STRIATIONS IN AN RF DISCHARGE

Teruyuki Sato, Tatsuo Shoji, Youichi Sakawa
and Mitsuyoshi Hori

Plasma Science Center, Nagoya University
Nagoya 464-01, Japan

1. Introduction

R. T. Schneider and P. H. Handel have observed pairs of luminous disks separated by a dark-gap and emission of fast neutrons in a low-power radio-frequency (RF) discharge in deuterium at a pressure range of $0.1 - 1$ Torr /1/. The disks exist only in pairs. This structure has been interpreted as a plasma caviton, induced by a resonance between applied RF field and the ion oscillation /1, 2/. It is interesting to investigate such a plasma structure from the view point of particle trapping and acceleration.

In this paper, we present experimental data on paired luminous rings (not disks) observed in an RF discharge.

2. Experimental Setup

Figure 1 shows the experimental setup. An RF voltage of $V_{RF} = \pm 0.5 - \pm 1.7$ kV is applied to electrodes (100 mm in width) surrounding a 100 mm diameter of pyrex glass tube containing hydrogen gas. The RF voltage is pulse-modulated with a variable pulse length τ (typically $\tau \simeq 150$ μs) and a repetition frequency. The RF frequency range is f = 0.8 – 5 MHz. In our experiments, the parameters are quite similar to Ref. 1 expect for the higher pressure (p = 1 – 50 Torr) and the smaller electrode separation (d = 20 – 100 mm).

3. Results and Discussions

When the pressure is increased, a pair of luminous rings (each of them is like Saturn's ring) separated by a narrow dark-gap is produced at the middle of two electrodes (see Fig.1), at a critical value of pressure p_1. The dimensions of the rings observed by a scanning diode-array camera (SDAC) are as follows: the width of each ring is $\sim$ 1 mm, the outer diameter is $\sim$ 80 mm, the inner diameter is $\sim$ 50 mm, and the dark-gap width of paired rings is $\sim$ 2 mm. By increasing the pressure up to the next critical value p_2, two pairs of rings are adruptly produced. Photographs of 1, 2 and 3 paired rings at p = p_1, p_2 and p_3, respectively, are shown in Fig. 2. The rings are axially symmetric with respect to the midplane of two electrodes and produced only in pairs. Figure 3 shows the pressure dependence of the ring position which is observed by the SDAC. In the figure, the appearance of n pairs of rings at critical pressures p_n ($n = 1, 2, .., 9$) are shown.

Figure 4 shows a time evolution of the axial light intensity profiles when the pulse length of the RF voltage τ is changed from 10 to 55 μs at p = p_5, the pressure at which 5 pairs of rings exist at $\tau > 55$ μs. No rings are observed at $\tau < 40$ μs [Fig. 4(a)]. By

increasing τ, two paired rings appear near the both electrods at $\tau = 40$ μs [Fig. 4(b)]. At $\tau = 45$ μs, another two paired rings appear inside the first two ring pairs [Fig. 4(c)]. Finally, the fifth pair appears at the midplane at $\tau = 55$ μs [Fig. 4(d)]. With further increase in τ, the number of pairs remains at 5, i.e., the structure is in the stationary state.

It is found from Fig. 3 that the distance from the electrode-edge (x = $\pm$ 15 mm) to the outmost ring, L, and the distance between neighboring pairs, l, are inversely proportional to the pressure p. The measured values of L are very close to the calculated RF excursion length of electrons, $X_e = eE_{RF}/m_e\nu_{en}\omega \propto V_{RF}/\mathrm{p}$, where E_{RF} is the RF electric field strength and V_{RF} is the RF voltage applied to the electrodes. The measured values of l are at the same order as the ionization mean-free-path of electrons, $\lambda_{ionize} = 1/n_n\sigma_{ionize} \propto 1/\mathrm{p}$, where n_n is the neutral gas density and σ_{ionize} is the ionization cross-section. These results show that the RF excursion length and the ionization mean-free-path might be important parameters in understanding the mechanism of the luminous ring formation.

When there are no rings, the probe characteristics give the plasma density $n \simeq 10^9 - 10^{10}$ cm^{-3}, the plasma electron temperature $T_e \simeq 6$ eV and the floating potential $V_f \simeq -20$ V. Once the rings appear the floating potential becomes more negative. Axial profiles of V_f with and without rings are shown in Fig. 5. The V_f profile with a ring pair ($\tau = 500$ μs) shows a negative dip at the position of the dark-gap between paired rings. Assuming that the V_f shown in Fig. 5 indicates the time-averaged plasma potential, the calculated space charge density ($n_i - n_e$) at the dark-gap, where the potential profile has a negative dip, and at the rings, where the potential has a positive peak, are at the order of -10^8 cm^{-3} (electron rich) and 10^8 cm^{-3} (ion rich), respectively.

In our experiment no neutrons were observed. This may be caused by the difference in the pressure regions and the electrode separation from Ref. 1.

References

/1/ R. T. Schneider and P. H. Handel, Fusion Technology 7, 316 (1985).
/2/ P. H. Handel and R. T. Schneider, Fusion Technology 7, 320 (1985).

Figure Captions

Fig. 1: The experimental setup.
Fig. 2: Photographs of 1, 2 and 3 pairs of rings.
Fig. 3: The pressure dependence of the axial ring position (electrode separation d = 30 mm, f = 1.5 MHz, $V_{RF} = \pm 1.0$ kV, $\tau = 150$ μs).
Fig. 4: The time evolution of the axial light intensity profiles (d = 30 mm, f = 1.5 MHz, $V_{RF} = \pm 1.0$ kV, p = p_5 = 7.5 Torr).
Fig. 5: Axial profiles of the floating potential with ($\tau = 500$ μs) and without ($\tau = 30$ μs) rings (d = 30 mm, f = 1.5 MHz, $V_{RF} = \pm 1.0$ kV, p = p_1 = 6.15 Torr).

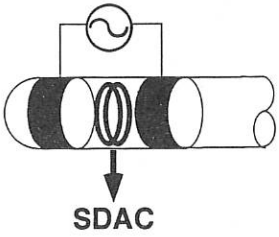

Fig.1

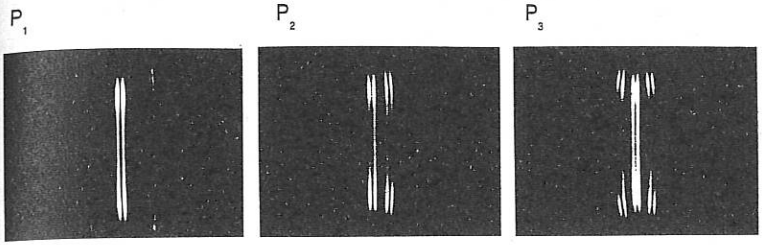

Fig.2

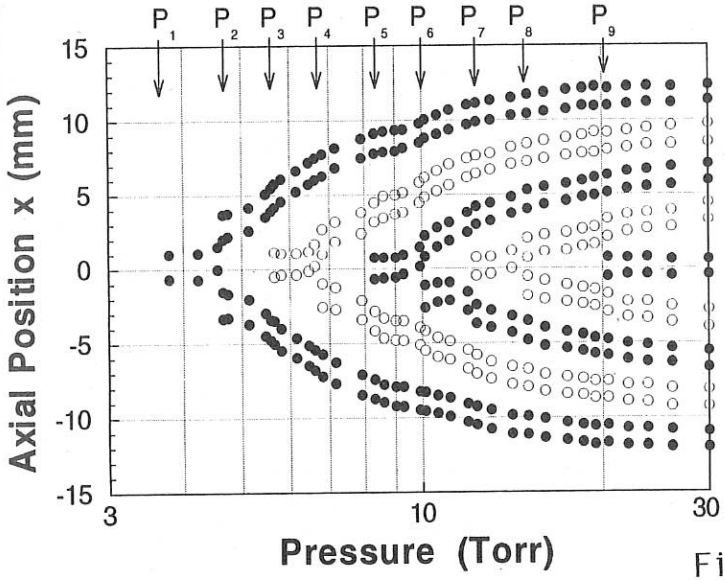

Fig.3

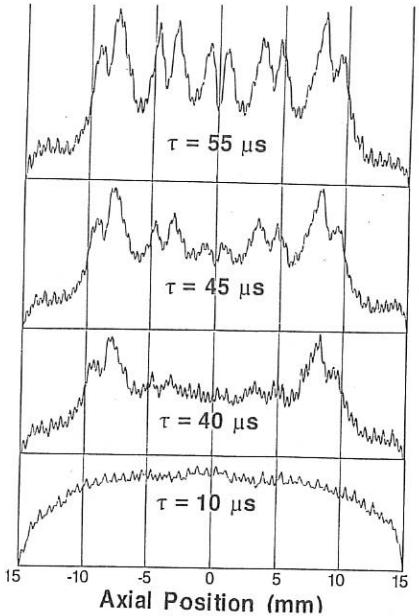
τ = 55 μs
τ = 45 μs
τ = 40 μs
τ = 10 μs
15
-10
-5
0
5
10
15
Axial Position (mm)

Fig.4

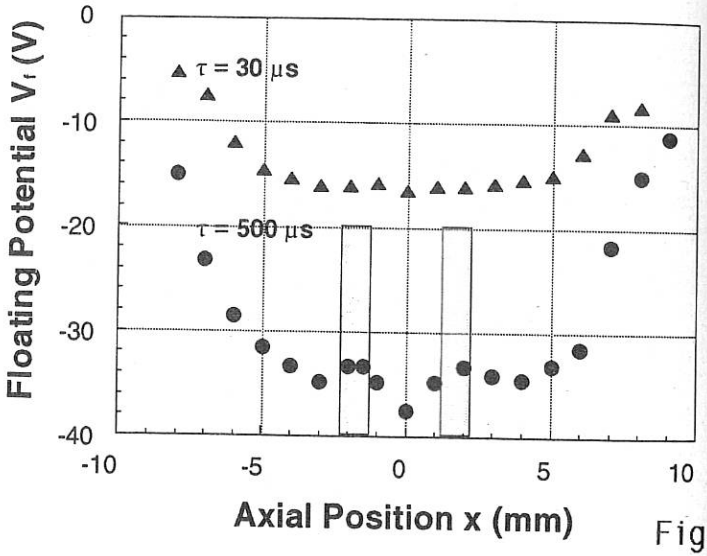
Floating Potential V_f (V)
0
-10
-20
-30
-40
τ = 30 μs
τ = 500 μs
-10
-5
0
5
10
Axial Position x (mm)

Fig.5

IONIZATION FRONT STRUCTURE IN THE LATERAL SPREADING OF A D.C. DISCHARGE ALONG CYLINDRICAL COAXIAL ELECTRODES

C.Gavrilescu and G.Popa
Department of Physics, "Al.I.Cuza" University
Iasi 6600, Romania

The lateral spreading of the breakdown ionization front (IF) in glow discharge, along cylindrical coaxial electrodes, was primarily studied by Steenbeck /1/ and later by Emeleus and von Engel /2,3/. An edged field model was taken into account to explain axial spread by axial drift of ions in the stray edge fields. Mather et al. /4/ extend such experiments to large currents and voltages, where the (IF) is comparable in axial extension with the main current sheet. Such structure might explain the rundown plasma stage by $j \times B$ force in so called snow-plough model. However, despite of large difference between the current intensities, in the above experiments performed in similar geometries of the electrodes and the same range of the gas pressure, the (IF) propagates along the axial structure with comparable velocity (10^4 m/s). That's why many reports pointed out that a better spatial and temporal resolution would be necessary to clarify the mechanism of lateral spreading.

Accordingly to this purpose Popa et al. /5/ started a set of experiments which have been lead to acquire an improvement on temporal and spatial resolution of the (IF) speed-up and on the accuracy of velocity measurements. The technique used to plot these results was the one proposed by Stirand /6/ for ionization waves studies.

Following the same line, in this paper, experimental results are presented, which have been obtained by electrical and optical means, in order to study the space-time structure of the (IF), to get detailed information about acceleration mechanism.

For this purpose, a segmented cathode was used (40 segments of 10 mm length each) and the axial distribution of

the discharge current with the above spatial resolution was registered by a box car technique, at different time intervals after the discharge ignition at one end of the structure.

Axial distribution of the light intensity was also measured by a similar technique, during axial spreading, for different gas pressures (0.1 - 2 mbar), discharge voltages (300 - 400 V) and external resistances (10^2 - 10^4 Ω).

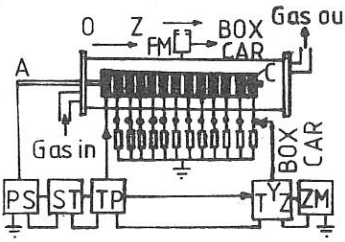

Fig.1. Experimental set-up.

The experimental set-up is shown in fig.1 : it consists of two cylindrical coaxial stainless steel electrodes (segmented cathode C - 10 mm inner diameter and anode A - 4 mm external diameter, both of 400 mm length) placed in a glass tube of 300 mm diameter. A normal d.c. discharge is ignited by means of a trigger pulse (TP) at one end of the structure and spreads lateral along the two cylinders with a speed of about 10^4 m/s. The repetition time of the discharge ignition was around 10 ms. Light emission from the discharge in visible range of spectrum had been observed through a narrow slit (1 mm broad) using a photomultiplier (FM) which had been moved along whole length of the cathode /5/. The current flowing through each one O-ring cathode had been measured independently and accordingly to the axial distance from the discharge ignition place, fig.1.

The measurements performed using a box car technique show a close connection between the spatial structure of the (IF), the spatial distribution of the total discharge current and the external working conditions. Two pattern of the (IF) evolution have been established, with the upper limitation of the total discharge current as a specification. A spatial structure of both, current flowing in the (IF) and light intensity have been observed.

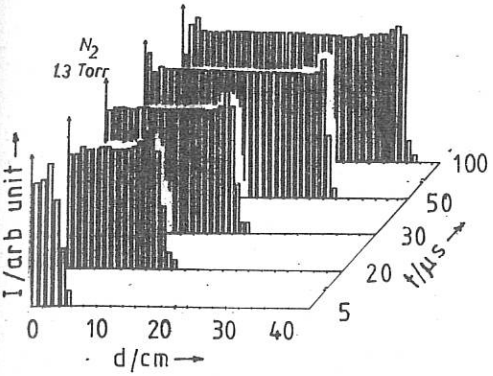

Fig.2

Figure 2 shows a space-time diagram of the current, flowing through each O-ring cathode at different time, over whole discharge (40 cm run out). Total discharge current was limited by an external resistor (U = 380 V, I less than 0.5 A). This current increases linearly with axial spreading of the discharge (see Fig.3, curve I) a fact that shows that the current of each ring remains constant during lateral spreading of the discharge.

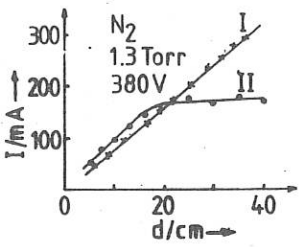

Fig.3

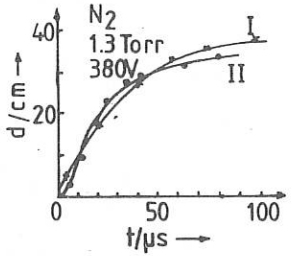

Fig.4

For this behaviour of the discharge the space-time dependence of the (IF) spreading is indicated in Fig.4, curve I. The spread velocity is a monotonically decreasing function on the axial distance from the discharge ignition point. The (IF) exhibits a distinct spatial structure that remains compact during the axial spreading and could be a double layer. Figure 5 shows electrical (bottom trace) and optical (upper trace) signals, registered by the above mentioned technique at 15 cm from the discharge ignition point. Their shape shows an identical time evolution with a

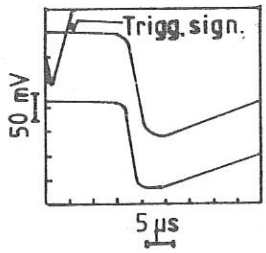

Fig.5

peak in the (IF) region. This peak increases considerably when total discharge current increases, in comparison with radial current flowing and light emission behind the (IF). Whenever total current was limited both, by an external resistor and the power supply (see Fig.3, curve II), spatial structure of the (IF) was considerably extended (see, Fig.6). Time dependence of the (IF) spreading in this case is also changed (see Fig.4, curve II). Both spatial structure of the (IF) and the range values where axial velocity of the (IF) lies (10^4 m/s) in lateral spreading of glow discharge with coaxial electrodes (discharge current less than 1 A), suggest that for such like experiments but at very large discharge currents (e.g. plasma focus, plasma guns) another mechanism than j x B, in plasma spreading between coaxial electrodes, should be also involved.

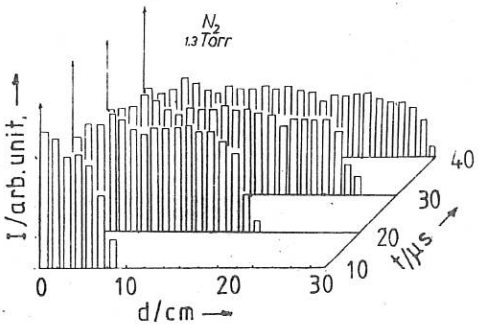

Fig.6

REFERENCES

1. M.Steenbeck, Arch. Electrotech. 26 (1932) 306
2. K.G.Emeleus and A.von Engel, J.Phys.D : Appl.Phys. 12 (1979) 555
3. K.G. Emeleus and A.von Engel , Phys.Lett., 76A (1980) 243
4. J.W.Mather and A.H.Williams, Phys.Fluids 9 (1966) 2080
5. G.Popa, D.Ruscanu and C.Birsan, Proc.XVII I.C.P.I.G, Budapest (1985) 620

Plasma heating in low pressure RF discharges

M.A.Skorik, N.St.J.Braithwaite*, and J.E.Allen

Dept. of Engineering Science, University of Oxford, Parks Road, Oxford, OX1 3PJ, UK.
* Material Discipline, The Open University, Milton Keynes, MK7 6AA, UK.

Introduction

In the present paper we consider the interaction of electrons with an oscillating sheath as a possible mechanism for plasma heating in low pressure radiofrequency discharges. The heating rate is found to be considerable and exceeds the rate of the energy loss due to electrons escaping across the sheath and recombining on the electrode surface.

Sheath model

We are interested in the range of discharge parameters where the field frequency ω_{RF} is much greater then the ion plasma frequency ω_{pi} and much less then the electron plasma frequency ω_{pe}. The following assumptions are made about the particle behaviour in the one - dimensional RF sheath:

1. The electrons have a Maxwellian velocity distribution characterized by a temperature T_e and they follow the instantaneous electric field;
2. The ions respond only to the time-average electric field and their motion within the sheath is collisionless. It is assumed that as in the DC sheath model ions enter the sheath with the Bohm speed $u_B = \sqrt{kT_e/M}$, where M is the ion mass.
3. We neglect ionization in the sheath, bulk recombination and secondary emission from the electrode.

In the calculation of the sheath potential we follow the work of Stekolnikov et al [1]. The potential waveform in the sheath is assumed to have the following form:

$$\Phi(x,t) = \bar{\Phi}(x) + \tilde{\Phi}(x)\sin\omega t \qquad (1)$$

The dimensionless variables $\eta = -e\Phi/kT_e$ and $\xi = x/\lambda_D$ are used for the potential and the distance. Taking into account the equations of the flux and energy conservation for ions, and also Poisson's equation for the potential, we obtain (for details see reference [1]) the following system of coupled differential equations for the nondimensional time-average and oscillating parts of the sheath potential:

$$\begin{aligned} \frac{d^2\bar{\eta}}{d\xi^2} &= (1+2\bar{\eta})^{-1/2} - \exp(-\bar{\eta})I_0(-\tilde{\eta}) \\ \frac{d^2\tilde{\eta}}{d\xi^2} &= -2\exp(-\bar{\eta})I_1(-\tilde{\eta}) \end{aligned} \qquad (2)$$

where $I_0(x)$ and $I_1(x)$ are the modified zero and first order Bessel functions respectively.

The numerical solution of the system (2) is obtained starting from the analytical solution in the limit $\eta \ll 1$. The boundary values at the electrode surface have been chosen to satisfy the condition of zero net current. The results for $\tilde{\eta} = -50.0$ are presented in Fig. 1.

Electron motion in the sheath

The electron motion in the time-dependent sheath potential is investigated by means of the numerical solution of the electron motion equation:

$$m_e \frac{d^2 s}{dt^2} = -e \frac{\partial \Phi(x,t)}{\partial x}\Big|_{x=s} \tag{3}$$

in the following potential:

$$\Phi(x,t) = \bar{\Phi}(x) + \tilde{\Phi}(x)\sin(\omega t + \theta) \tag{4}$$

This equation has been solved for different values of the initial phase angle θ and the initial electron energy $\varepsilon = E/kT_e$ (it is used in the dimensionless form). E is the component of the electron kinetic energy which is associated with motion perpendicular to the sheath edge.

The computations show that the result of the electron interaction with the RF-sheath depends significantly upon the initial phase θ. Fig. 2 shows the trajectories of two electrons with the same initial energy $\varepsilon = 1$ which penetrate the sheath with different phases ($\theta = 1.50\pi$ and $\theta = 0.45\pi$ respectively). It can be easily seen that the time of the e-sheath interaction and the depth of penetration in the sheath are very different for these two electrons. It is also clear from the slopes of the trajectories that the first electron on leaving the sheath has almost the same energy as it had before the interaction, while the second one gains significant energy. Fig. 3 shows the ratio of the electron energy on leaving the sheath to that on entering (curve 1) and the e-sheath interaction time (curve 2), as a function of the phase θ for electrons with initial energy $\varepsilon = 1.0$. The energy of an electron can rise rapidly if it penetrates the RF-sheath at the moment when the retarding potential is very low. Such an electron spends a large time inside the sheath and penetrates deeply into it. (curve 2 in Fig. 2; peak on the curve 2 in Fig. 3). The energy of those electrons that face a large retarding potential on entry changes very little, and the time of the e-sheath interaction is short.

Finally, we have calculated the heating and cooling fluxes to estimate the energy balance in an RF-sheath. The expression for the heat flux can be written as follows:

$$f_h = n_e \frac{(kT_e)^{3/2}}{(2\pi m_e)^{1/2}} \int_0^\infty \Delta\varepsilon \left(1 - \frac{N_w(\varepsilon)}{N(\varepsilon)}\right) \exp(-\varepsilon)\, d\varepsilon \tag{5}$$

where $\Delta\varepsilon$ is the average over all θ of the increase in the nondimensional energy of the

electrons on returning to the plasma; n_e is the electron concentration at the sheath-plasma boundary; N_W/N is an average over the phase angle of the ratio of the number of the electrons that recombine on the wall to the total number of the electrons with energy ε which enter the sheath.

Some electrons have enough energy to reach the electrode surface and recombine on it. The expression for the heat loss (cooling) flux due to these electrons has the following form:

$$f_c = n_e \frac{(kT_e)^{3/2}}{(2\pi m_e)^{1/2}} \int_0^\infty \frac{N_W(\varepsilon)}{N(\varepsilon)} (\varepsilon + 1)\exp(-\varepsilon)\, d\varepsilon \qquad (6)$$

Fig. 4 represents the expressions under the integral signs for the heating (curve 1) and cooling (curve 2) fluxes. It can be seen that the total heating flux is significantly larger than the cooling flux in this parameter range. The input of energy to the ions is a different matter; it also occurs via the sheath [5].

Discussion

The results obtained differ from those in [2] where the energy gained in the e-sheath interaction is a small fraction of that lost by those electrons which escape across the sheath. The reason for this discrepancy is that the sheath in [2] is assumed to be weakly modulated like a sheath at a large grounded electrode, while the heating obtained here is associated with a strongly modulated sheath such as that at a driven electrode. The final conclusion that e-sheath interaction is an important electron heating mechanism agrees with the results obtained by other authors [3,4]. However, an estimate of the heating flux due to the secondary emission from the electrode surface shows that this mechanism can also be significant.

Acknowledgement

One of us (MAS) is grateful for an ICI Scholarship which made this research possible.

References

/1/ A.F.Stekolnikov, N.St.J.Braithwaite and J.E.Allen, Proc. of the Eighth Int. Conf. on Gas Discharges and Their Applications, Venice, 391 (1988).

/2/ M.Uehara, N.St.J.Braithwaite & J.E.Allen, X-th ESCAMPIG Europhysics Conference Abstracts, 14E 468 (1990)

/3/ V.A.Godyak, Soviet Radio Frequency Discharge Research, Delphic Associates, Inc., (1986)

/4/ T.J.Sommerer, W.N.G.Hitchon, and J.E.Lawler, Phys. Rev. Lett., **63**, 2361 (1989)

/5/ J.E.Allen, Proc. Eighteenth Int. Conf. on Phenomena in Ionized Gases, **4**, 808 (1987)

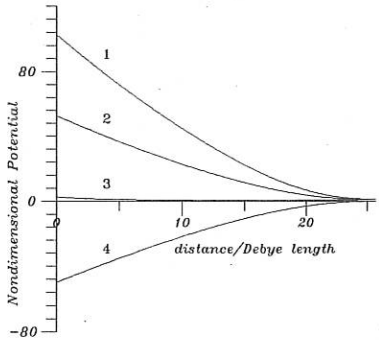

Fig. 1. The sheath potential profile
1, $\eta(\omega t=3\pi/2)$; 2, $\bar{\eta}$;
3, $\eta(\omega t=\pi/2)$; 4, $\bar{\eta}$.

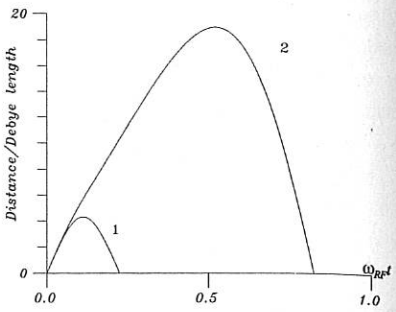

Fig. 2. The trajectories of two electrons with energy $\varepsilon=1$ entering the sheath with the phases $\theta=1.50\pi$ and $\theta=0.45\pi$ respectively. $\omega_{pe}/\omega_{RF}=42$.

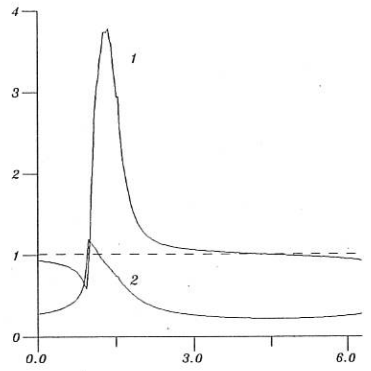

Fig. 3. The ratio of the electron energy on leaving the sheath to that on entering (curve 1) and the e-sheath interaction time (curve 2, in units of $\omega_{RF}t$) as a function of the phase angle θ. The initial electron energy $\varepsilon=1.0$.

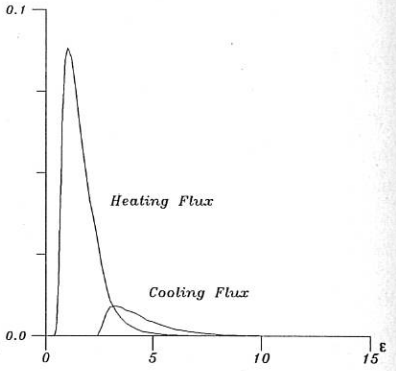

Fig. 4. The nondimensional differential fluxes with respect to the nondimensional energy ε. Areas under the curves represent the total nondimensional heating and cooling fluxes respectively.

ION ENERGY DISTRIBUTION IN AN RF ARGON PLASMA

B. M. Annaratone, M. A. Skorik, A. A. Goruppa* and J. E. Allen

Department of Engineering Science, University of Oxford, Parks Road, Oxford OX1 3PJ, UK.

* Materials Discipline, Open University., Foxcombe Hall, Boars Hill, Oxford OX1 5HR, UK.

1. Introduction

The energy of ions bombarding grounded surfaces in RF reactors is a critical parameter in many plasma processing applications. Previous experiments which have been reported in the literature on the structure of the ion energy distribution function (IEDF) at the surface of an electrode have dealt with a strongly RF modulated sheath with a large bias. In that case the large DC bias has allowed a relatively easy resolution of the multi-peak IEDF structure associated with the RF modulation of the sheath and the charge exchange collisions. The same effect (however, not so strong) is also present at the relatively large grounded electrode with a weak sheath, but is more difficult to resolve because of the smaller ion energies. In this paper we present measurements of the IEDF obtained with a retarding field ion energy analyzer mounted on the grounded electrode of an industrial etcher operating at 13.56 MHz frequency. The chamber has been filled with Argon at a pressure varying from 0.3 to 6 Pa. The experimental results are compared to the theoretical predictions based on the numerical solution of the Boltzmann Kinetic Equation for ions in the electric field of a time-varying sheath.

2. Experiment

The experiment has been carried out in an industrial etcher (Nordiko). The vacuum chamber is a cylindrical vessel made of a stainless steel (Fig. 1). The discharge is generated between two electrodes 19 cm. diameter spaced 7 cm apart. The powered electrode (lower) has a cup-like shape which is formed by inserting a copper cylinder of the same diameter as the electrodes and 5 cm height. The RF-voltage (13.56 MHz) is supplied to the electrode through a matching unit.

The grounded electrode (upper) is electrically connected to the chamber. The retarding field ion energy analyzer [5] is mounted in the surface of this electrode. A driven Langmuir probe [6] has access to the interelectrode gap through an orifice in the copper cylinder 3 cm above the powered electrode. It provides information about the plasma parameters (electron temperature, density and plasma potential).

3. Numerical model

To compare the experimental results with theoretical predictions we have calculated the ion transport through the RF-modulated sheath. The one-dimensional sheath model is similar to that developed in [1] and is subject to the following assumptions:

1. The field frequency is much larger than the ion plasma frequency and much less than the electron plasma frequency. So the ions respond only to the time-average electric field and their motion within the sheath is collisionless. Ions enter the sheath with the Bohm speed $u_b=\sqrt{kT_e/M}$.
2. The electrons have a Maxwellian velocity distribution and they follow the instantaneous electric field.
3. We neglect ionization in the sheath, bulk recombination and secondary emission from the electrode. These assumptions are applied only to the calculation of the sheath waveform, not to the consideration of the ion transport.

The sheath potential profile is obtained by a numerical solution of the system of the conservation equations for ions and Poisson's equation (for details see [1]) and has the following form:

$$\Phi(x,t)=\bar{\Phi}(x)+\tilde{\Phi}(x)\cos\omega t, \tag{1}$$

the $\bar{\Phi}(x)$ and $\tilde{\Phi}(x)$ profiles are presented in fig. 2 (the nondimensional units $\eta=-\frac{e\Phi}{\kappa T_e}$ and $\xi=\frac{x}{\lambda_D}$ are employed).

The ion transport through the RF-sheath with the potential waveform given by (1) has been calculated from a numerical solution of the Boltzmann Kinetic Equation:

$$\frac{\partial f}{\partial t}+v\frac{\partial f}{\partial x}-\frac{eE}{m_e}\frac{\partial f}{\partial v}=I_{coll}(f), \tag{2}$$

where $f=f(x,v,t)$ is the ion distribution function in phase space. The collision integral $I_{coll}(f)$ takes into account elastic and charge-transfer collisions; the cross-section data were taken from [2] and [3]. In the case of the lower pressure $(P\leq 1Pa)$ the scattering is weak, the ion mean free path is much larger than the sheath thickness, so it was assumed that ions undergo not more then one charge-transfer collision on their transit through the sheath. The solution of the weak scattering - transport equation is quite straightforward. When the pressure is higher and the ion mean free path is comparable to the sheath thickness a convective scheme [4] has been used to solve the Boltzmann Kinetic Equation. A major problem in the application of the convective scheme to the simulation of the low-pressure discharge is an artificial scattering. Not very important at the higher pressures, it can introduce a significant error when being used in the pressure range 2-10 Pa, so a special technique has been developed to suppress this effect and make it less than the elastic scattering. The calculations were performed on the 300 by 400 mesh with a nonuniform step along the v-axis. The ion velocity distribution on the sheath-plasma boundary is taken to be that calculated by Ingram and Braithwaite [5] (instead of the assumption that ions enter the sheath with the Bohm speed, which has been made for the sheath potential calculation, see above).

4. Discussion

The ion energy distribution functions, measured and calculated for different pressures, are presented

in Fig.s 3 - 5. It can be seen that there is a reasonable agreement between the experimental and theoretical results, however some difference exists, especially at the higher pressures. The reason for this discrepancy is probably that the ion energy distribution function at the electrode surface is a sensitive function of the sheath potential profile, so a little variation in a sheath thickness (perhaps due to an error in the plasma density or the electron temperature measurements) can cause a significant shift of the peaks in the tail of the ion distribution function (Fig. 5). Furthur work is required to find the reason why the experimental results show that ions undergo more scattering than that predicted by the numerical model (Fig. 5).

Acknowledgment

One of us (MAS) is grateful to ICI, the University of Oxford and the British Council for a Scholarship which made this research possible. The authors would like to thank Dr. N.St.J.Braithwaite for useful discussions.

References

[1] A.F.Stekolnikov, N.St.J.Braithwaite and J.E.Allen, Ninth Int. Conf. on Gas Discharges and their Applications, 391 (1988)

[2] R.S.Robinson, J. Vac. Sci. Technol., **16**, 185 (1979)

[3] J.W.Sheldon, Phys. Rev. Lett., **8**, 64 (1962)

[4] W.N.G.Hitchon, D.J.Koch, and J.B.Adams, J. Comput. Phys., **2**, 79 (1989)

[5] S.G.Ingram and N.St.J.Braithwaite, J. Phys. D, **21**, 1496 (1988)

[6] N.St.J.Braithwaite, N.M.P.Benjamin, J.E.Allen, J.Phys. E: Sci. Instrum., **20**, 1046 (1987)

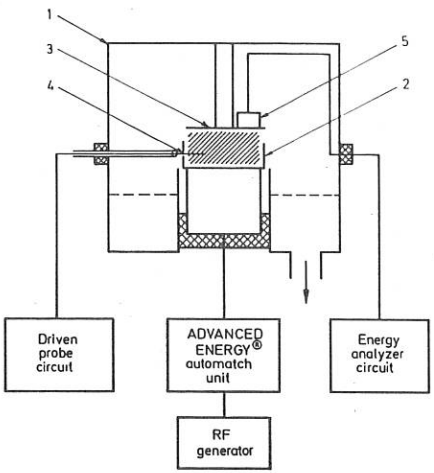

Fig. 1. Schematic diagram of the experimental device.

1 - Vacuum chamber
2 - Powered electrode
3 - Grounded electrode
4 - Driven Langmuir probe
5 - Retarding field ion energy analyzer

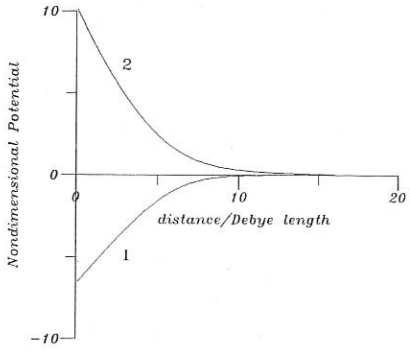

Fig. 2. A typical sheath potential waveform 1, $\bar{\eta}$; 2, $\bar{\eta}$.

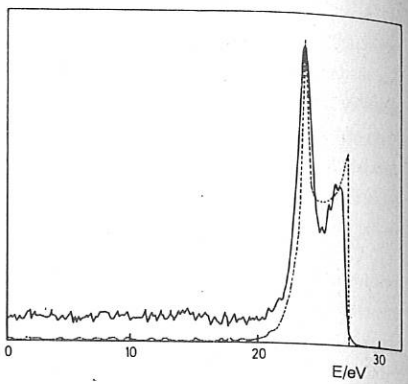

Fig. 3. Ion energy distribution function (arb. units). Pressure = 0.3 Pa, $n_e=8.4\cdot10^{15}m^{-3}$ $T_e=2.64$ eV. The solid line represents the experiment; the dashed one - simulation. The curves shown represents f(v) versus E.

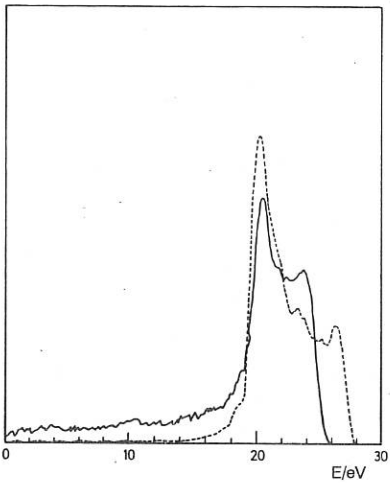

Fig. 4. Ion energy distribution function arb. units), Pressure = 1 Pa, electron density $n_e=4.1\cdot10^{16}m^{-3}$; $T_e=2.5$ eV. The solid line represents the experimental results; the dashed one - simulation. The curves shown represent f(v) versus E.

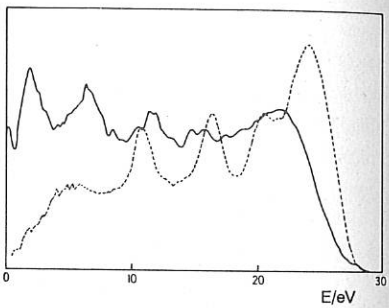

Fig. 5. Ion energy distribution function (arb. units), Pressure = 6 Pa, electron density $n_e=1.8\cdot10^{15}m^{-3}$; $T_e=2.8$ eV. The solid line represents the experimental results; the dashed one - simulation. The curves shown represent f(v) versus E.

OBSERVATION OF COHERENT DRIFT STRUCTURES IN THE TURBULENCE OF A DC DISCHARGE

U. Kauschke and H. Schlüter
Institut für Experimentalphysik II, Ruhr-Universität Bochum
D-4630 Bochum, Postfach 102148, GERMANY

The experiment is performed in a magnetized neon hot-cathode dc discharge /1,2/. Small Langmuir probes give central values of $k_B T_e \approx (4\text{-}7)\text{eV}$, $n_e \approx (7\text{-}10)\cdot 10^{16}\text{m}^{-3}$. For the floating potential one has to take care of a frequency-dependent voltage division through cable capacities and sheath resistances /3/. The plasma potential is calculated from floating potential and temperature /4/. Radial electric fields are of the order of the ambipolar fields /1/. Digital signal analysis with paired probes is performed on a PC as described in literature /5,6/. Drift waves ($0 < |k_z| \ll k$) are expected at (1) and flute-type modes ($k_z = 0$) at (2) and (3) /7/:

$$(1)\quad \omega = -k_\varphi \frac{\kappa_n k_B T_e (1-k^2 r_i^2)}{eB(1+k^2 r_s^2)} - k_\varphi \frac{E_r}{B},\quad r_i^2 = \frac{k_B T_i M_i}{e^2 B^2},\quad r_s^2 = \frac{k_B T_e M_i}{e^2 B^2},\quad v^* = \frac{-k_B T_e}{eB}\kappa_n$$

$$(2)\quad \omega_1 \approx -k_\varphi \frac{E_r}{B}\quad ,\quad (3)\quad \omega_2 \approx k_\varphi \frac{k_B T_i \kappa_n}{eB} - k_\varphi \frac{E_r}{B},\quad \kappa_n = \frac{1}{n_e}\cdot\frac{\partial n_e}{\partial r} < 0,\ \kappa_T = \frac{1}{T_e}\frac{\partial T_e}{\partial r}$$

In the regime B<40mT oscillations appear (5kHz<f<15kHz, short wavelenghts $k_\varphi r_s \approx m r_s / r > 1$) close to (1). Harmonics are of a non-resonant forced type /2/. The phase velocity - less than the electron diamagnetic speed- is equal for all harmonics /2,8/. With increasing B modes of short- and long-wavelengths establish a transition to turbulence /1,2/.

At B=48mT we observe waves propagating into the electron diamagnetic direction at frequencies of drift waves (1), potential (dashed lines) and density (solid lines) spectra being in agreement (Fig 1a). The m=1 mode is found at $k_\varphi r_s < 1$, higher mode numbers appear at $k_\varphi r_s \geq 1$. We observe $k_z \approx 6m^{-1}$.

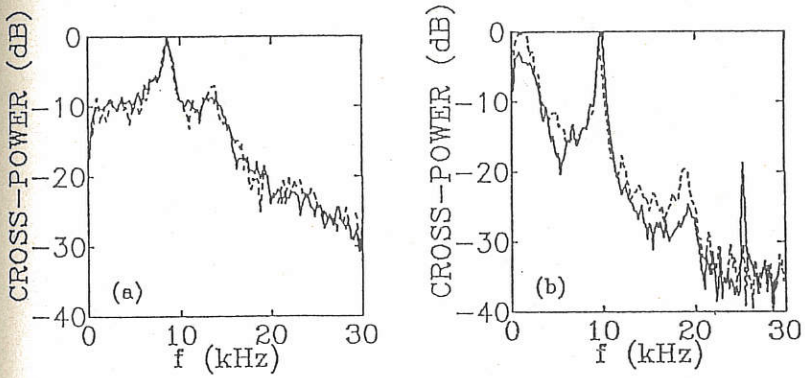

Fig 1 Cross-power (a) B=48mT, (b) B=68mT (density: solid lines, potential: dashed lines)

A dominant mode is observed at $u/v^* \approx 0.3$ with (1) predicting $u/v^* \approx 0.5$. The reduction of $u = \omega/k_\varphi$ through nonlinearities was shown in former studies /2,8/. Fig 2a gives $k = k_\varphi(\omega)$ for B=48mT. In contrast to (1) waves at 10kHz<f<20kHz propagate with constant u, $u/v^* \approx 0.12$, indicating a phase-locked behaviour /9/.

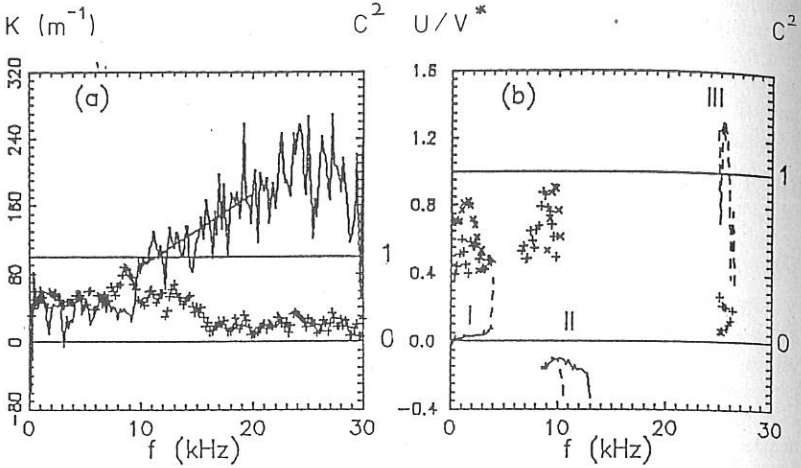

Fig 2 Dispersion characteristics and coherency c:
(a) B=48mT, $k = k_\varphi(\omega)$; (b) B=68mT, $u = \omega/k_\varphi$, 0<c<100%, I: flute modes, II: slow soliton-type, III: fast soliton-type, solid lines: u from density, dashed lines: u from potential

With B increased to 68mT (Fig 1b), the level of density fluctuation $\delta n/n$ decreases by ~ 50%, indicating a reduction of instability. Low frequency modes (<6kHz) are found propagating into the electron diamagnetic direction as given by (2), (3) with differences in density and potential expected /10/ and observed. Phase velocities u are given for density and potential, (Fig 2b, coherency of density (+) and of potential (x)). Amplitudes in the regime of linear drift waves (15kHz<f<22kHz) are reduced. The new features compared to previous results /2/ are coherent contributions with anomalous dispersive behaviour. A 9.6kHz-peak belongs to waves propagating into the ion diamagnetic direction with $(3 < |m| < 4)$ and u<0 ($u/v^* \approx -0.1 \pm 30\%$), Fig 3b). Waves at 25kHz ($m \approx 1$) propagate into the electron diamagnetic direction u>v*, $u/v^* \approx 1.3$. Wave number spectra of density and potential do not agree (Fig 3a). With signals passed through a band pass filter (6kHz - 31kHz), the spectra agree perfectly (Fig 3b). Most of the disagreement in Fig 3a is produced by the low frequency components, which obviously are not drift-, but flute-type waves.

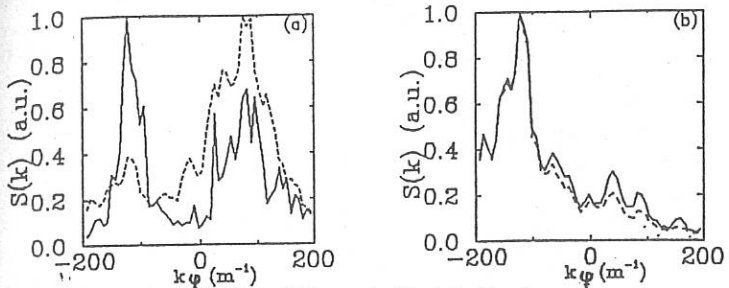

Fig 3 S(k), B=68mT (density: solid lines, potential: dashed lines)

Results of bicoherence analysis are different for both situations (Fig4). For B=(48-54)mT wave-wave-coupling processes occur between drift waves and between drift waves and flute-type modes, $b^2 \approx (0.1\text{-}0.4)$ (Fig 4a,b). At B=68mT no significant coupling occurs (Fig 4c). The frequency doubling peak ($b^2 \approx 0.15$) only accounts for a non-sinusoidal shape of the 9.6kHz-wave.

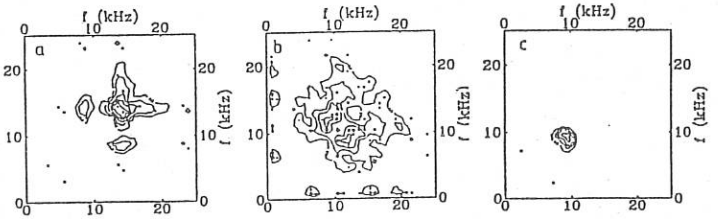

(a) B=48mT, b^2<0.4 (b) B=54mT, b^2<0.3 (c) B=68mT, b^2<0.3

Fig 4 Square of bicoherence: b^2, density fluctuations. Contour lines are drawn for b^2 = 0.1 - 0.4, step 0.05.

Detailed analysis of soliton includes the rotation of the ion-fluid v_0 due to T_i and E_r /8,12/. We consider hot Boltzmann-distributed electrons, ions in warm cross-field approximation, treat waves moving in slab geometry perpendicular to $\vec{B}$ and $(\kappa_n, \kappa_T)\vec{x}$ /8,12/. The limit of no periodicity gives the soliton solution ($\xi = y - v_0 t$, $\tau = t$, $\Phi = e\phi/k_B T_e \approx \delta n/n_0$):

$$(4)\quad \Phi = -\frac{3}{2}\cdot\frac{\Lambda}{S}\cdot sech^2\left(\frac{1}{2}\sqrt{-\Lambda}(\xi - u\tau)\right),\ \Lambda = -\frac{1}{r_s^2}\left(1+\frac{v^*}{u}\left(1+\frac{T_i}{T_e}\right)\right),\ S \approx e\frac{\omega_{ci}}{2k_B T_e u}\kappa_T$$

Two types of solitons appear, fast ($u > v_0 + v^*$) and slow ($u < v_0$) ones. Taking $\vec{E}$ and T_i into account we find the 9.6kHz-peak corresponding to $u = -490m/s < v_0 \approx +140m/s \pm 80\%$ and the 25kHz-peak to $u > v_0 + v^* \approx 4000m/s$: We obtain coherent waves in the regimes $(u-v_0)/v^* \approx -0.14 \pm 80\%$ and $(u-v_0)/v^* \approx 1.3$ (Fig 2b). In a gas of solitons it depends on the average energy density $\langle E_s \rangle \sim |\kappa_T/\kappa_n|$ whether fast or slow solitons dominate /11/. We have $\langle E_s \rangle >> 18$ and should expect ion diamagnetic, slow solitons most pronounced, in agreement with observations. Maximum activity is expected at $u/v^* \approx -0.096$, which has to be compared with the observed

$u/v^* \approx -0.1 \pm 30\%$, or including v_0: $(u-v_0)/v^* \approx -0.14 \pm 80\%$ close to theory /11/, which, however, only holds for non-interacting solitons in the "KDV-limit" $(k_\varphi r_s)^2 \ll 1$. The 9.6kHz-waves are observed at $(k_\varphi r_s)^2 \approx 2-3$. The KDV-limit is fulfilled for fast contributions (25kHz), $(k_\varphi r_s)^2 \approx 0.13$.

Waves above ω_{ci} show a phase-locked behaviour as in Fig. 2a and weak broadband coupling, too (Fig 5).

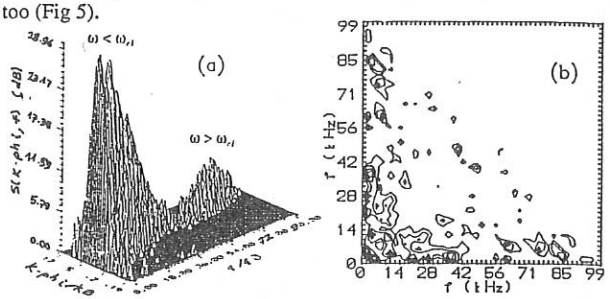

Fig. 5 $\omega < \omega_{ci}$ and $\omega > \omega_{ci}$: (a) Spectral power density $S(k/k_0, f/f_0)$, k_0=22m-1, f_0=800Hz; Contour-lines of $0.02<b^2<0.16$ step 0.02.

In conclusion, we observe spectral contributions at velocities expected for solitons, complementary to periodic waves. The ion diamagnetic propagation cannot be explained by a reversed $\vec{E} \times \vec{B}$ –rotation of the column, since the $\vec{E} \times \vec{B}$ –rotation is positive and cannot explain shifts to negative velocities. Some azimuthal modes (m=1-4) remain at positive u. If the whole plasma rotates into the ion diamagnetic direction so that a (3<m<4, f=9.6kHz)-drift-mode occurs at negative u, the other (m=3-4, f<9.6kHz)-drift modes should be reversed, too. This is not observed. The very low frequency flute-type modes f<6kHz occur at positive u, indicating positive $\vec{E} \times \vec{B}$ –rotation of the column, too. The low-frequency turbulence in a magnetized DC discharge consists of four type of waves: Broad-band drift-, flute-type and waves above ω_{ci} are found with finite coupling and coherent waves (u close to soliton-type) without coupling. Flute-type modes produce a disagreement in spectra of density and potential.

/1/ U. Kauschke, G. Oelerich-Hill, A. Piel, Phys. Fluids B 2, 38 (1990)
/2/ U. Kauschke, H. Schlüter Plasma Phys. Contr. Fus. 32, 1149 (1990)
/3/ J. R. Roth, W. M. Krawczonek Rev. Scient. Instr. 42, 589 (1971)
/4/ F. F. Chen "Modern Uses of Langmuir Probes" IPPJ-Report No. 750, Nagoya, Japan (April 25 1985)
/5/ J. M. Beall, Y. C. Kim, E. J. Powers J. Appl. Phys. 53, 3933 (1982)
/6/ Y. C. Kim, E. J. Powers IEEE Trans. Plasma Science PS-7, 120 (1979)
/7/ W. Horton in Handbook of Plasma Physics, eds.: M. N. Rosenbluth, R. Z. Sagdeev R. Z., Vol. 2, eds.: A. A. Galeev, R. N. Sudan, North Holland, Amsterdam (1984)
/8/ U. Kauschke, H. Schlüter Plasma Phys. Contr. Fus 33, 1309 (1991)
/9/ B. D. Scott, H. Biglari, P. W. Terry, P. H. Diamond Phys. Fluids B 3, 51 (1991)
/10/ P. K. Shukla, M. Y. Yu, H. U. Rahman, K. H. Spatschek Phys. Rep. 105 (1984)
/11/ J. D. Meiss, and W. Horton Phys. Fluids 25, 1838 (1982)
/12/ U. Kauschke, submitted to Plasma Phys. Contr. Fus., SFB-Report 92-A4-20 (1992)

EFFECTS OF MAGNETIC FIELD ON A MAGNETRON DISCHARGE

H.Mase, T.Tanabe, T.Ikehata and N.Y.Sato
Department of Electrical and Electronic Engineering,
Ibaraki University, Hitachi 316, Japan

Magnetron discharge is one of the crossed-field discharges in which the efficient ionization occurs in relatively low pressure range and it is widely used as the sputtering devices for thin film formation. In the commercial devices, the magnetic field is applied by permanent magnets and then the field pattern is distorted strongly. This fact seems it difficult to clear the discharge mechanism in such devices. Description of the magnetron operation is still incomplete, although there are a number of studies /1,2/.

In this paper, we describe the effect of magnetic field on the enhanced ionization in a planar magnetron device. We also discuss the mechanism for sustaining discharge and the field pattern required for the magnetron operation.

Experiments are carried out by using a planar magnetron device whose electrode separation and the magnetic field strength can be varied (see Fig.1). The ring-shaped glowing plasma is produced in the region restricted by the magnetic field. The gases used are He and H_2 in the pressure range from 2 to 0.15 Torr. The variation of the discharge voltage with the magnetic field B is measured under the conditions of fixed discharge current I_d and various electrode separation d_{AK}.

The typical results are demonstrated in Fig.2. As the magnetic field is increasing, the discharge voltage V_d rapidly falls at a critical value B_c of the field and the low impedance discharge mode (magnetron discharge mode) occurs at the magnetic field beyond B_c. This effect is distinguished in lower pressure range. The critical field B_c strongly depends on the electrode separation and is slightly affected by the

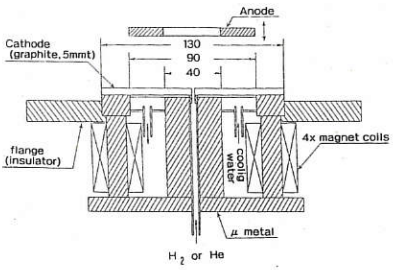

Fig 1: Illustration of planar magnetron device.

Max-Planck-Institut für Plasmaphysik
8046 Garching bei München

discharge current, the species and the pressure of gases. The relationship between B_c and d_{AK} is shown in Fig.3. Curves in Fig.3 indicate that B_c varies inversely with d_{AK} and then the product $B_c \cdot d_{AK}$ is constant. In the large electrode separation ($d_{AK} > d^*$), however, B_c is independent of d_{AK} and B_c takes a minimum value B^*. It seems to be caused by the nonuniformity of the magnetic field.

In general, the cathode fall V_c for a fixed current is expressed as the following formula obtained from the plasma balance equations /3/,

$$V_c = C(V_i/\gamma)F(n_{et}),$$

where C is the factor ($\gtrsim 1$) associated with the plasma particle loss and energy loss, V_i and γ are the ionization potential and the coefficient of γ process. $F(n_{et})$ means a factor ($\gtrsim 1$) for the primary electrons trapped between electrodes (total primary electron flux)/(trapped primary electron flux) /*/. If the potential drop across the plasma is small, V_c is nearly equal to V_d.

In the low pressure diode discharge without the magnetic field, $F(n_{et})$ is much larger than unity. In the magnetron discharge the primary electrons are sufficiently trapped by the magnetic field and then $F(n_{et}) \simeq 1$. The critical field B_c is the lower limit of the field which satisfies the condition of sufficient trapping of primary electrons. If the magnetic field is uniform and the discharge is dense glow mode (cathode sheath thickness $d_c \ll$ electron cyclotron radius r_{ce}), the condition is given by $r_{ce}=(mv/eB) \lesssim d_{AK}$,

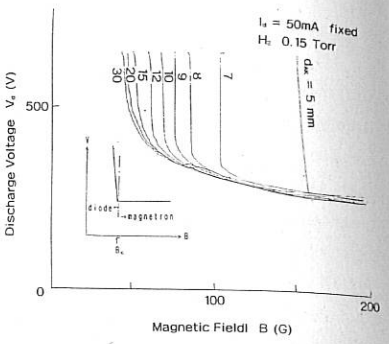

Fig 2: Variation of discharge voltage with magnetic field strength. Magnetron discharge occurs when $B > B_c$. B is measured on the cathode at the center of magnet gap.

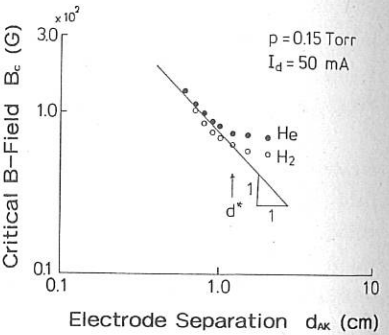

Fig 3: Relationship between the critical B-field and the electrode separation.

where v is electron velocity corresponding to V_c. We easily obtain the relationship, $B_c \cdot d_{AK}$=const., from $r_{ce}=d_{AK}$. In this situation the primary electrons drift by reflection on the cathode sheath edge as shown in Fig.4. The drift motion is different from the ExB drift /4,5/, which occurs at lower density discharge ($d_c > r_{ce}$). The effect of the nonuniform field is discussed as follows.

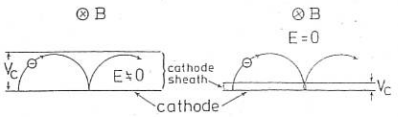

Fig 4: Electron drift due to ExB and reflection on sheath edge.

For simplicity, we consider the magnetic field due to a dipole array of gap length 2a and the orbital motion of primary electron (accelerated up to eV_c and start from z=b) on the mid plane, where the field is given by $B(z)=B_0/(1+z^2/a^2)$. From computer calculation we obtain the trajectory of electron motion. The distance, $Z_T=(z_T-b)/r_{ce0}$, from the cathode sheath edge to the turning point changes with the effective magnetic field, $A=a/r_{ce0}$, as shown in Fig.5, where $r_{ce0}=mv/eB_0$. When A is large (A>1), Z_T does not change with A very much and is found to be $Z_T \simeq 1$. In the case of $A \lesssim 1$, however, the turning point moves far away even if A slightly decreases. The electrons are trapped when Z_T is smaller than d_{AK}/r_{ce0}. The magnetron operation will be obtained when the following conditions are satisfied /6/.

$$Z_T \simeq 1 \lesssim d_{AK}/r_{ce0} \quad \text{for } d_{AK}<a, \qquad (1)$$

or

$$A=a/r_{ce0} \gtrsim 1 \quad \text{for } d_{AK}>a. \qquad (2)$$

They are corresponding to $B_c \cdot d_{AK}$=const. for $d_{AK}<d^*$ and $B_c=B^*$ for $d_{AK}>d^*$, where d^* is related to a. The calculated values are in good agreement with the experimental results. In this model the electron drift is due to the reflection on the cathode sheath and/or grad-B. Further confinement of the primary electrons does not discuss but the electrons seem to be confined by the

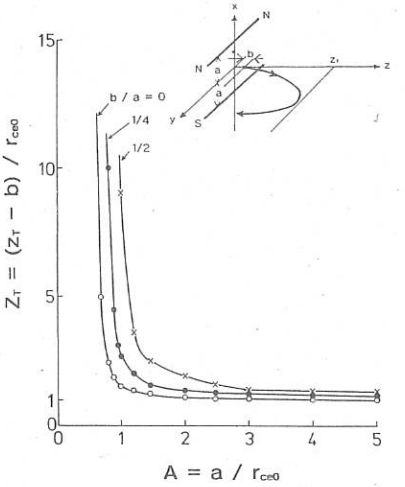

Fig 5: Variation of turning point with the aspect of magnetic filed. Electron (initial velocity $v=(2eV_c/m)^{1/2}$) starts at z=b, and $r_{ce0}=mv/eB(z=0)$.

magnetic mirror. The ring-shaped glowing plasma is produced by the bombertment of the trapped energetic electrons.

Equations (1) and (2) or Fig.5 are useful to design the field pattern and the electrode arrangement in magnetron devices. Equation (2) is same as the result obtained from a computer simulation by Goree *et al.* /7/.

Low impedance characteristics in the magnetron discharges is caused by efficient ionization due to the primary electrons which are accelerated by the cathode fall and trapped magnetically between the electrodes. The trapped electrons drift resulting in the reflection on the cathode sheath and/or grad-B and bounce between the mirror points.

/1/ Lan Gu,M.A.Lieberman, J.Vac.Sci.Technol. A6, 2960(1989)

/2/ S.M.Rossnagel,H.R.Kaufman, J.Vac.Sci.Technol. A6, 223(1989)

/3/ H.Mase,T.Tanabe,T.Ikehata, Proc.18th.ICPIG.(Swansea,1987) IV, p746

/4/ G.Francis, The glow discharge at low pressure in Handbuch der Physik ed. by S.Flugge Bd.XXII(Springer-Verlag,1956), p167

/5/ B.Chapman, Glow discharge processes (John-Wiley,1980), p262

/6/ H.Mase,T.Tanabe,T.Ikehata, Proc.7th.Sympo.Plasma Processing(Tokyo,1990), p349

/7/ J.Goree,T.E.Sheridan, Appl.Phys.Lett. 59, 1052(1991)

/*/ In the simplest case, $F(n_{et})$ is given by the formula, $F(n_{et})=(1-\exp[-(B_c d_{AK}/B\lambda_e)\sin^{-1}(B/B_c)])^{-1}$ for $B \leq B_c$, where λ_e is m.f.p. of the primary electrons.

THE LANGMUIR PROBE STUDY OF THE ELECTRON ENERGY DISTRIBUTION FUNCTION IN THE FLOWING AFTERGLOW PLASMA

J.Glosík, I.Čermák, M.Šícha, M.Tichý, P.Zakouřil

Department of Electronics and Vacuum Physics, Faculty of Mathematics and Physics, Charles University, V Holešovičkách 2, 180 00 Praha 8, Czechoslovakia

The Flowing Afterglow Langmuir Probe (FALP, [1,2]) apparatus, with microwave discharge (2.5 GHz, 25 - 75 W) as a plasma source, was used to study evolution of the Electron Energy Distribution Function (EEDF) in the low pressure (50 to 85 Pa) argon flowing afterglow plasma. The polyatomic molecular reactants such as n-hexane and benzene were added to the argon carrier gas in order to study their influence on the EEDF and its relaxation. Some aspects of the determination of the plasma parameters from the Langmuir probe measurements are discussed.

Introduction

The flowing afterglow technique was developed by Ferguson and co-workers [3] and it has been used extensively to study ion-molecule reactions. The FALP version was used to study recombination, attachment and plasma relaxation processes [2,4,5,6]. In most of the measurements He was used as a carrier gas and as a common feature fast thermalization was observed. The situation is different when Ar is used as a carrier gas; Ar has higher atomic mass and the cross-section for the electron atom collisions has pronounced minimum just in the energy range 0.1 - 1 eV (Ramsauer effect)[7]. As a consequence an energy transfer between electrons and Ar atoms is two orders of magnitude less efficient as it is in the case of He atoms, so for the investigation of the processes influencing the EEDF Ar is more suitable as a carrier gas [8].

Experimental

The experimental data have been accumulated using the flowing afterglow apparatus of the FALP type (for details see [9]). The flow tube is 1 m long with inner diameter 0.06 m. The velocity of the argon carrier gas was 50 ms^{-1}, corresponding decay times (t) are up to 20ms. Plasma parameters have been measured on the axis of the flow tube by means of an axially movable cylindrical Langmuir probe (platinum, length 4 mm, diameter 40 μm).

The probe current (I_P), as a function of probe potential (V_P), was measured. The EEDF (F(U)) was determined on the basis of its relation to the second derivative of the electron part (I_E) of the probe current [9]:

$$F(U) = Const * V^{1/2} * (d^2 I_E / dV^2)$$

where $I_E = I_P - I_+$, $V = V_P - V_{PLASMA}$ and U is the electron energy in eV corresponding to V. The second derivative of I_E (I_E'') was calculated from the probe current and correction to the second derivative of the ion current was taken into account, for details see [10]. The plasma potential was taken as a probe potential at which the second derivative is changing its sign (inflection point; $I_E' \neq 0$ and $I_E'' = 0$).

Typical examples of the measured probe characteristics and the calculated second derivatives of the electron current for the different reactant gases are plotted in Fig.1a,b,c (absolute value $|I_p|$ and $|I_E''|$ versus V in semi-logarithmic plot).
Fig.1.:

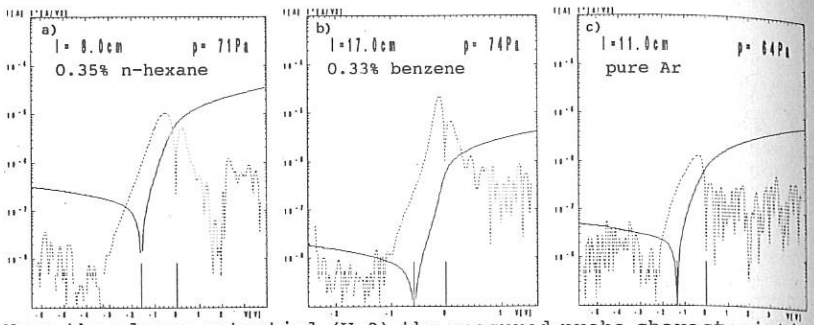

Near the plasma potential (V=0) the measured probe characteristic is influenced by processes on the surface of the probe and by fluctuations of the plasma potential; as a consequence the calculated second derivative is inaccurate for V up to ~$2kT_E/e$ and an extrapolation has to be used. In the presence of molecular reactant gases the determination of the plasma potential can be influenced by the plasma enhanced deposition on the probe surface. To avoid this problem the high negative voltage has been applied to the probe in order to clean the probe surface by ion bombardment. The high voltage was applied after each change of the probe voltage prior to the measurements of the probe current.

If the EEDF is Maxwellian the semi-logarithmic plot of d^2I_E/dV^2 versus V is linear with a slope given by the electron temperature T_E (see Fig.1a). When the "body" of the EEDF is near to Maxwellian there is a linear part of semi-logarithmic plot of d^2I_E/dV^2 versus V (see Fig.1b) and "effective" (approximative) electron temperature can be estimated. Semi-logarithmic plots of I_E'' versus V in pure Ar do not have in general a linear part (see Fig.1c) and the effective temperature cannot be estimated. The direct calculation of a mean energy of electrons from measured EEDF is inaccurate due to the mentioned inaccuracy of the obtained I_E'' in the low energy region.

The shape of the EEDF has to be considered when determining the plasma density. The probe theories usually suppose the Maxwellian EEDF, so they should be used with care. Presented electron concentrations are calculated, when possible, from the probe current at plasma potential and temperature or effective temperature is used.

Evolution of the EEDF in flowing afterglow

The evolution of the EEDF has been studied along the flowtube in pure Ar and in Ar with small admixture of polyatomic molecular reactant gas (benzene and n-hexane) introduced downstream of the microwave discharge. N-hexane and benzene have been used because of the effect of polymerization and effective

deposition in a plasma [12]. The preliminary analysis for benzene shows that the rate of the deposition, refractive index and electric conductivity of the deposited films depends on the position in the flow tube.

For the evaluation of deviation of the measured EEDF from the Maxwellian one ($F_m(U)$) corresponding to the same temperature it is useful to plot the ratio $F(U)/F_m(U)$ as a function of U/kT_E. In Fig.2a,b I_E'' and the ratio $F(U)/F_m(U)$ are plotted for different positions along the flow tube in pure Ar (distance from the reactant entry port is given in cm, 5 cm corresponds to 1 ms in time scale). It is evident that the EEDF is not Maxwellian and the deviation is increasing with increasing decay time; plasma is not thermalized even after 8 ms. The electron gas is heated mainly on the expenses of the energy of the metastable argon atoms and by the dissociative recombination of Ar_2^+ ions. The Druyvesteyn distribution is a good approximation for the measured EEDF in pure argon. This is typical of Ar flowing afterglow [6, 13]. For purpose of Fig.2b the *effective temperature* as a rough approximation has been estimated from the I_E'' Vs V semi-log plot.

Fig.2. pure Ar, P=85Pa 0.35% n-hexane, P=71Pa 0.33% benzene, P=74Pa

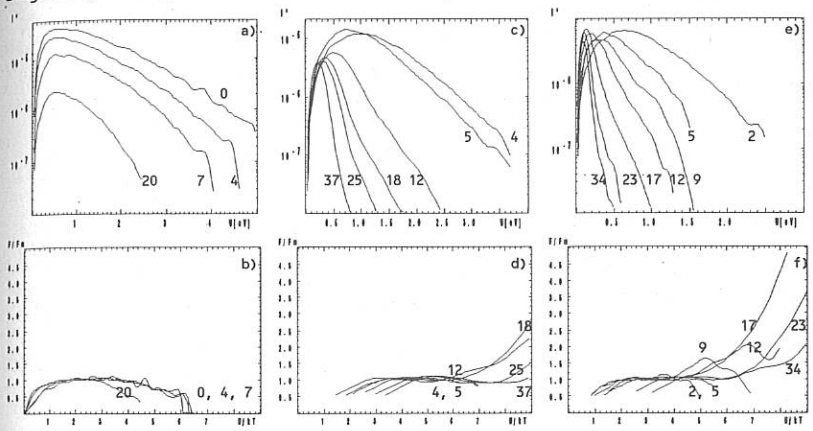

In Fig.2c,d the same dependences as in Fig.2a,b are ploted the only difference being the admixture: 0.35% of n-hexane in the flow tube. The corresponding evolutions of T_E, N_E and EEDF along the flow tube are plotted in Fig.3. As it can be seen, in presence of n-hexane, the plasma is thermalized rapidly and as a consequence the diffusion losses are smaller and the concentration changes slowly. Immediately after the entry port the Ar^+ ions are converted to molecular ions and then they are removed by dissociative recombination. The estimated recombination rate coefficient is $4.7*10^{-7} cm^3 s^{-1}$.

The same dependences for admixture of 0.33% of benzene in Ar are plotted in Fig.2e,f. The deviation from the Maxwellian distribution due to the production of the energetic electrons in the Penning ionization of benzene in energy range 1.0 - 1.5 eV is evident. It is also seen from Fig.2f that this group vanishes with increasing afterglow time.

Fig.3. 0.35% n-hexane, Ar pressure 71 Pa

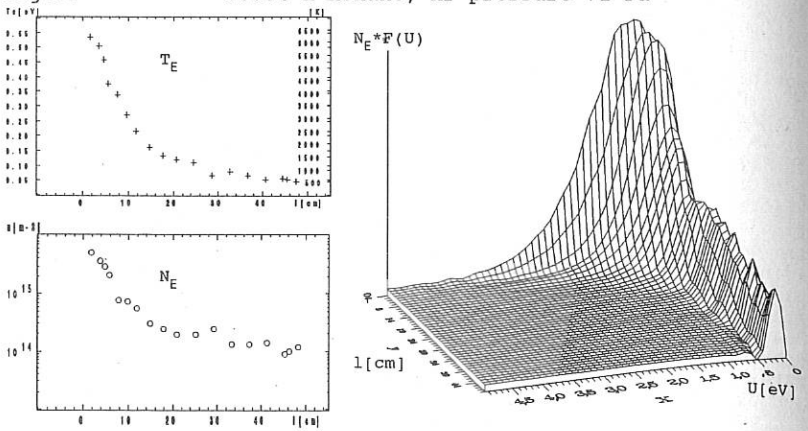

Conclusion

The evolution of the EEDF in the flowing afterglow has been studied. It was possible to show how the EEDF, electron density and effective temperature in an Ar afterglow are influenced by the addition of benzene and n-hexane.

References

[1] D.Smith, N.G.Adams, A.G.Dean and M.J.Church, J.Phys. D:Appl. Phys., **8**,141 (1975)

[2] J.Pavlík,J.Glosík,I.Havlas, Acta Phys.Slovaca,**33**,131,(1983)

[3] E.E. Ferguson, *Ion Molecule Reactions* (Ed.J.L.Franklin), Plenum Press, New York (1972)

[4] E.Alge, N.G.Adams and D.Smith, J. Phys. B: At. Mol. Phys., **16**, 1433, (1983)

[5] D.Smith and N.G.Adams,*Physics of Ion-Ion and Electron-Ion collisions* (Ed.F.Brouillard), Plenum Press, New York (1983)

[6] J.Pavlík,J.Glosík,M.Šícha,M.Tichý,P.Potoček, Contrib.Plasma Phys. **30**, 437 (1990)

[7] H.S.W.Massey, E.H.S.Burhop, *Electronic and ionic impact phenomena*,Vol.1., Clarendon press, Oxford (1969)

[8] P.Španěl, J.Glosík, EPCLP 91, Kühtai, Innsbruck, Austria, April 8-12,pp.252,(1991)

[9] J.Glosík,J.Pavlík,M.Šícha,M.Tichý, Czech.J.Phys., B **37**, 188 (1987)

[10] J.D. Swift, M.J.R. Schwar, *Electrical Probes for Plasma Diagnostic*, Iliffe Books Ltd., London (1970)

[11] M.Šícha,Zu Cham Sun,J.Glosík,M.Tichý, Contrib.Plasma Phys. **30**, 185 (1990)

[12] H.Yasuda,*Plasma polymerization*,Academic Press,Inc.,(1985)

III-1993

COMPUTER SIMULATION OF RF DISCHARGES AND COMPARISON WITH LABORATORY RESULTS

V. Vahedi, M. Surendra, G. DiPeso,
P. Mirrashidi, and C. K. Birdsall
University of California, Berkeley
Berkeley, CA 94720

RF glow discharges and other processing plasmas are used extensively in the microelectronics industry. Self-consistent fluid equations have been used recently to study the structural features of RF and DC glows[1-2]. However, since these discharges are inherently complex and the particle distributions are non-Maxwellian, there has been a considerable effort in developing self-consistent kinetic models without making any assumptions on the distribution functions[3-6].

In order to use particle-in-cell simulation codes for modeling collisional plasmas and self-sustained discharges it is necessary to include interactions between charged and neutral particles. Monte Carlo methods have been used extensively in swarm simulations[7-9]. In many Monte Carlo schemes, the time (or distance) between collisions for each particle is calculated from a random number. This allows for efficient algorithms, especially when the null collision method is used[10]. This technique is however, not compatible with PIC simulations, since all particle trajectories are integrated simultaneously in time. Hence, the collision probability for the ith charged particle is calculated from

$$P_i = 1 - \exp(-\nu \Delta t)$$

where $\nu = n\sigma_T(E_i)v_i$, σ_T is the total collision cross section, E_i is the kinetic energy of the particles and n is the neutral density. A collision takes place if a uniformly distributed random number on the interval [0, 1] is less than P_i. The null collision method can be incorporated into the collision model by picking a constant collision frequency ν' such that,

$$\nu' \geq (n\sigma_T v)_{\max}$$

which greatly reduces the computational cost, by not evaluating $\sigma_T(E_i)$ for each particle. The fraction of the total number of particles (chosen at random) in the simulation that experience collisions is given by

$$P = 1 - \exp(-\nu' \Delta t)$$

The collisions are assumed to take place at the current positions of the particles. It should be noted that the choice of Δt will affect the accuracy of the collision model. For instance, $v_i \Delta t$ should not be much larger than simulation length scales of interest (e.g. grid spacing, λ_{D_e}) and $\Delta s_i \sigma_T(E_i) n$ should be about 0.1 or less[12], which means that less than 10% of the charged particles

collide in one time step. Once a collision occurs, the type of collision, the energy of the ejected electron (for an ionizing collision) and the direction(s) are determined with new random numbers. These quantities are related back to the system coordinate axes. The procedure for electron-neutral collisions is describe in detail by Boeuf and Marode[7], and by Thompson *et al* (1988) for ion-neutral collisions. Expressions for differential cross sections that are analytically integrable are useful, as then the computational cost of determining scattering angles and energy redistribution in ionizing collisions is minimized[3, 7, 11, 12].

A Monte Carlo collision handler as described above, including the null collision method, has been developed as an addition to the PIC scheme as shown in Fig. 1. The full three dimensional character of a collision is modeled with three velocity components. The neutrals are assumed to be uniformly distributed between the boundaries with a constant density and a Maxwellian profile. The model is still valid if the neutral density is a weak function of position and time (small variations across the mean free path and collision times). This scheme can also be extended to model Coulomb collisions between charged particles.

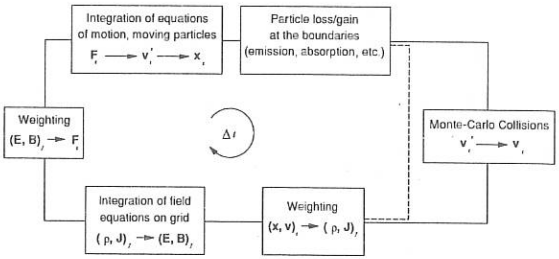

FIG. 1. The flow chart for an explicit bounded PIC scheme with the addition of the collision handler, called PIC-MCC[3].

RF discharge modeling displays many physical time scales, e.g. $\omega_\pi < \omega_{RF} \ll \omega_{pe}$. With a PIC model including an electrostatic response, the highest frequency that must be resolved by the explicit numerical methods used to solve the particle and field equations is ω_{pe}. If $\omega_{pe}\Delta t > 2$, numerical instabilities can occur for explicit methods[13]. To observe most of the physics of interest, one needs to resolve the RF timescale only, and therefore much computing time is wasted resolving the electron plasma oscillation time scale.

Implicit particle simulation[14] has been developed to relax the numerical stability constraint. Implicit particle movers advance the postion of the *i*th super particle by the equation

$$x_i^{n+1} = \alpha' E^{n+1}(x_i^{n+1}) + \bar{x}_i^{n+1}$$

where $\bar{x}$ is the portion of the position advanced, dependent on quantities known at present and previous time levels, $\alpha' = \beta \Delta t^2 q/m$, and β depends on the particular implicit scheme. Linearizing the locations x_i^{n+1} about the locations $\bar{x}_i^{n+1}$ in the superparticle-to-grid weighting equations gives the numerically implicit Poisson equation

$$\partial_x[1 + \alpha\tilde{\rho}^{n+1}]\partial_x\phi^{n+1} = -\tilde{\rho}^{n+1}/\varepsilon_0$$

where $\alpha = \alpha'/\varepsilon_0$.

Simple boundary conditions for the RF discharge are a zero potential at the left wall and an RF source voltage at the right wall. The electric field, at the left wall is then derived by taking a Gaussian pill box about the wall,

$$[(1 - \alpha\tilde{\rho})E]_{j=1/2} = \sigma_0/\varepsilon_0 + \tilde{\rho}_0 \Delta x/2\varepsilon_0$$

A similar proceedure is used for the right wall. The equations may be generalized to included more complicated boundary conditions including external circuit elements.

Many accuracy constraints still remain. One important constraint is that the fastest particle species should resolve spatial gradients in the field, i.e., $v_{max}\Delta t/s < 1$ where s is the gradient length. Another important constraint is that all particles should sample the field on the grid in a continuous manner over a single time step. This gives $v_{max}\Delta t/\Delta x < 1$. A problem with implicit methods is excessive numerical cooling which is due to poor sampling of fast particles in simulations with large time steps. Resolving fast particles is particularly important in RF discharges because it is the fast electrons which maintain the discharge through ionization collisions with the neutrals. A possible way out of this problem is to do multi-scale[15] simulations. That is, the few fast electrons that maintain the discharge may be pushed with a small time step while the remaining slow particles, essentially residing in the bulk plasma, may be pushed with a large implicit time step. Based on these algorithms, which have been implemented in PDP1, we have been able to speed up our bounded PIC-MCC code by factors of 5-20 times, when simulating RF Discharges with laboratory parameters.

We will present comparisons of results obtained from simulation with those published by Godyak *et. al.*[16,17]. Our simulation results show that the electrons have a two-temperature distribution in a 2 cm gap argon RF discharge as measured by Godyak *et. al.*[16]. The Figure on the next page shows an instantaneous electron velocity distribution in the system as a function of position.

ACKNOWLEDGEMENT

This work is supported in part by DOE Contract DE-FG03-90ER54079 and ONR Contract N00014-85-K-0809, and the San Diego Supercomputer Center.

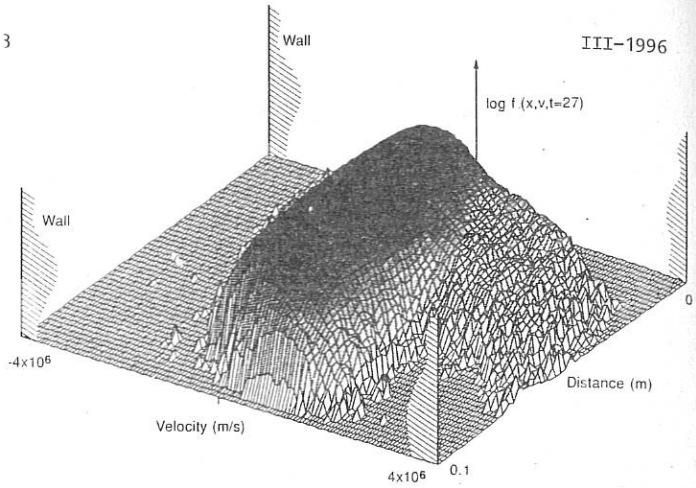

Electron Velocity Distribution in a Low-Pressure RF Discharge

REFERENCES

[1] D. B. Graves and K. F. Jensen, *IEEE Trans. Plasma Sci.* **PS-14**, 78 (1986).

[2] E. Gogolides, J. P. Nicolai, and H. H. Sawin, *J. Vac. Sci. Technol. A* **7**, 1001 (1989).

[3] Birdsall C. K., *IEEE Trans. Plasma Sci.* **19**, 65 (1991).

[4] Surendra M., and D. B. Graves, *IEEE Trans. Plasma Sci.* **19**, 144 (1991a).

[5] V. Vahedi, M. A. Lieberman, M. V. Alves, J. P. Verboncoeur, and C. K. Birdsall, *J. Appl. Phys.* **69**, 2008 (1991).

[6] Sommerer T. J., W. N. G. Hitchen, R. E. P. Harvey, and J. E. Lawler, *Phys. Rev. A* **43**, 4452 (1991).

[7] J. P. Boeuf and E. Marode, *J. Phys. D* **15**, 2169 (1982).

[8] M. J. Kushner, *J. Appl. Phys.* **58**, 4024 (1985).

[9] M. J. Kushner, *J. Appl. Phys.* **54**, 4958 (1983).

[10] S. L. Lin and J. N. Bardsley, *J. Chem. Phys.* **66**, 435 (1977).

[11] M. Surendra, D. B. Graves, and I. J. Morey, *Appl. Phys. Lett.*, **56**, 1022 (1990).

[12] M. Surendra, D. B. Graves, and G. M. Jellum, *Phys. Rev. A* **41**, 1112 (1990).

[13] C. K. Birdsall and A. B. Langdon, *Plasma Physics via Computer Simulation* (McGraw-Hill 1985, Adam Hilger 1991).

[14] A. B. Langdon, B. I. Cohen, A. Friedman, *J. Comp. Phys.* **51**, 107 (1983).

[15] A. Friedman, S. E. Parker, S. L. Ray, and C. K. Birdsall, *J. Comp. Phys.* **96**, 54 (1991).

[16] V. A. Godyak and R. B. Piejak, *Phys. Rev. Lett.*, **65**, 996 (1990).

[17] V. A. Godyak, R. B. Piejak, B. M. Alexandrovich, *IEEE Trans. Plasma Sci.* **19**, 660 (1991).

ON MODELLING OF STEADY STATES IN TOROIDAL MACHINES FOR BASIC PLASMA PHYSICS

Alf H. Øien

Department of Applied Mathematics, University of Bergen, Allégt. 55, 5007 Bergen, Norway

Introduction. Toroidal machines like ACT-I (1), BLAAMANN (2) and TORELLO (3) have a strong toroidal magnetic field, and may under steady state operation produce a plasma continously for instance between a hot filament and an anode placed diametrically opposite in the toroidal direction. Charged particles spiral in the toroidal direction, collide in between themselves and with the background gas and drift and diffuse normal to and along the magnetic field giving rise to particular density, temperature and electric potential profiles over the circular cross section. Details of measured global plasma behaviour, (2), are of interest because they reflect fundamental transport mechanisms that are important in these machines. Some typical parameters of the plasma in BLAAMANN are: Major radius, $R_0 \approx 60$cm, minor radius a≈15cm, toroidal magnetic field, $B_\phi \approx 0.1$ Tesla, electron and ion densities, $n_{e,i}=10^9\text{-}10^{10}/\text{cm}^3$, neutral particle density, $N_0 \approx 10^{12}/\text{cm}^3$, electron temperature, T_e=1-10eV, ion temperature, T_i, typically 10% of T_e. For an argon-plasma this gives the for the electron- and ion cyclotron frequencies $\Omega_e=1.8\ 10^{10}$/s and $\Omega_i=2.4\ 10^5$/s, and corresponding Larmor radii, $r_e=8\ 10^{-3}$cm and r_i=0.6 cm, for electron-ion collision frequency, $\nu_{ei}=1.4\ 10^3$/s, for electron-atom collision frequency, $\nu_{ea}=2\ 10^4$/s and for ion-atom collision frequency, $\nu_{ia}=8\ 10^2$/s. The BLAAMANN machine has been equipped with additional coils for producing small components of magnetic field in the vertical and /or major radial directions (of order 1 % of B_ϕ). In particular some effects of small magnetic field components on the plasma behaviour are discussed in this paper. Classical transport theory is assumed valid, (4), (5).

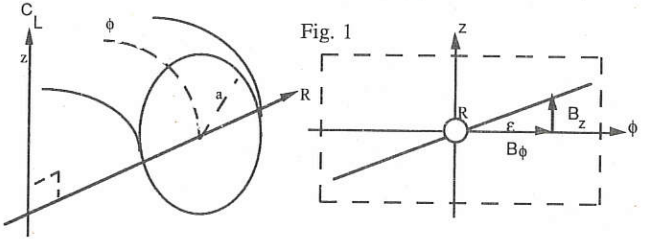

Transverse versus longitudinal B particle transport. Transverse a strong magnetic field, ions diffuse freely faster than electrons, while along the field electrons diffuse freely

faster than ions. This means that in ambipolar transport of the plasma the ions are hindered by the electrons in transverse **B** movement, while along the field the electrons are hindered by the ions. Adding small components of B in the z and/or the R-directions give rise to some pecularities: With gradients in the z and R directions, and with a small component of magnetic field in the z direction, cf. fig.1,we have typically for the free electron diffusion along (||) the field, $\Gamma_{e||}^{Free} = -D_{e||}\frac{\partial n}{\partial l_{||}} = -\frac{\kappa T_e}{m_e \nu_{ea}}\frac{\partial n}{\partial l_{||}}$, where $\frac{\partial}{\partial l_{||}} = \sin\varepsilon\frac{\partial}{\partial z} \approx \frac{B_z}{B_\phi}\frac{\partial}{\partial z}$. This diffusion has a component in the z-direction, $\Gamma_{ez}^{Free} = -\left(\frac{B_z}{B_\phi}\right)^2 \frac{\kappa T_e}{m_e \nu_{ea}}\frac{\partial n}{\partial z}$. For the ion transverse (⊥) diffusion we have typically $\Gamma_{i\perp}^{Free} = -D_{i\perp}\frac{\partial n}{\partial l_\perp} = -\frac{\nu_{ia}\kappa T_i}{2m_i\Omega_i^2}\frac{\partial n}{\partial l_\perp}$, and with $\frac{\partial}{\partial l_\perp} = \cos\varepsilon\frac{\partial}{\partial z} \approx \frac{\partial}{\partial z}$, the z component of this diffusion becomes $\Gamma_{iz}^{Free} = -\frac{\nu_{ia}\kappa T_i}{2m_i\Omega_i^2}\frac{\partial n}{\partial z}$. Between these free diffusion components in the z direction we have in the actual parameter regime the relation $\frac{\Gamma_{ez}^{Free}}{\Gamma_{iz}^{Free}} \approx \left(\frac{B_z}{B_\phi}\right)^2\left(\frac{T_e}{T_i}\right)\frac{m_i}{m_e}\frac{\Omega_i^2}{\nu_{ea}\nu_{ia}} \approx \frac{1}{4}\,10^{10}\left(\frac{B_z}{B_\phi}\right)^2$. This shows that even for a very small component of magnetic field in the z-direction the electron free diffusion component in the z direction, almost perpendicular to the magnetic field, dominates over the ion free diffusion. In turn this will influence ambipolar transport.

Particle transport equations. Equations transverse and along the magnetic field are for ions (single ionized) and electrons

$$eE_\perp + \frac{e}{c}(u_i \times B) - \frac{1}{n_i}\frac{\partial}{\partial r_\perp} n_i \kappa T_i - \mu_{ia}\nu_{ia}u_{i\perp} + m_e\nu_{ei}\frac{n_e}{n_i}(u_{e\perp} - u_{i\perp}) = 0$$

$$-eE_\perp - \frac{e}{c}(u_e \times B) - \frac{1}{n_e}\frac{\partial}{\partial r_\perp} n_e \kappa T_e - \mu_{ea}\nu_{ea}u_{e\perp} - m_e\nu_{ei}(u_{e\perp} - u_{i\perp}) = 0$$

$$eE_{||} - \frac{1}{n_i}\frac{\partial}{\partial r_{||}} n_i \kappa T_i - \mu_{ia}\nu_{ia}u_{i||} + m_e\nu_{ei}\frac{n_e}{n_i}(u_{e||} - u_{i||}) = 0$$

$$-eE_{||} - \frac{1}{n_e}\frac{\partial}{\partial r_{||}} n_e \kappa T_e - \mu_{ea}\nu_{ea}u_{e||} - m_e\nu_{ei}(u_{e||} - u_{i||}) = 0$$

The μ's are reduced masses. Accelleration terms have been neglected. Gradients are over the cross-section. Toroidal symmetry is assumed. $\mathbf{B} = \mathbf{e}_\phi B\cos\varepsilon\cos\eta + \mathbf{e}_z B\sin\varepsilon + \mathbf{e}_R B\cos\varepsilon\sin\eta$ where ε and η are small angles between **B** and its horizontal projection and between the horizontal projection and the toroidal direction, respectively.

We neglect electron-ion collisions in the following. For particle fluxes $\Gamma^{(\alpha)} = n_\alpha \mathbf{u}_\alpha$ in a cross section plane, α=(e)lectrons, (i)ons, we obtain

$$\Gamma^{(\alpha)} = -\frac{\nu_{\alpha a}}{\Omega_\alpha^2}\begin{pmatrix}(\cos\eta)^2 & 0\\ 0 & (\cos\varepsilon)^2\end{pmatrix}\cdot \boldsymbol{d}^{(\alpha)} - \frac{1}{\nu_{\alpha a}}\begin{pmatrix}(\cos\varepsilon\sin\eta)^2 & \cos\varepsilon\sin\varepsilon\sin\eta\\ \cos\varepsilon\sin\varepsilon\sin\eta & (\sin\varepsilon)^2\end{pmatrix}\cdot \boldsymbol{d}^{(\alpha)}$$
$$-\frac{1}{\Omega_\alpha}\begin{pmatrix}0 & -\cos\varepsilon\cos\eta\,\mathrm{sgn}(q_\alpha)\\ \cos\varepsilon\cos\eta\,\mathrm{sgn}(q_\alpha) & 0\end{pmatrix}\cdot \boldsymbol{d}^{(\alpha)}$$

Here $d^{(\alpha)} = \frac{1}{m_\alpha}\frac{\partial}{\partial r} n_\alpha kT_\alpha + \frac{n_\alpha q_\alpha}{m_\alpha}\frac{\partial}{\partial r}\phi$ when $E = -\frac{\partial}{\partial r}\phi$. Generally, these fluxes are substituted into the mass- and energy conservation equations for electrons and ions, which again are coupled to Poisson's equation in an electrostatic approximation.

Instead we specialize and assume quasineutrality in the main plasma volume, $n_e=n_i=n$, and ambipolar particle transport, $\Gamma^{(e)}=\Gamma^{(i)}$. The electric field is then also ambipolar. Due to lack of space it is omitted in the following. We mention a few special cases:

Case 1: $\frac{\varepsilon^2}{\nu_{ea}}$ and $\frac{\eta^2}{\nu_{ea}}$ both $<< \frac{\nu_{ea}}{\Omega_e^2}$ ($<< \frac{1}{\Omega_e} << \frac{1}{\Omega_i}$). Recall that $\frac{\nu_{ea}}{\Omega_e} \approx 10^{-6}$ in the actual parameter regime we operate. Then the effects of ε and η are negligible, and the limits $\varepsilon\to 0$, $\eta\to 0$, are appropriate. The expressions for particle flux are a special case of,

Case 2: $\eta=0$, while $\varepsilon << \frac{\nu_{ia}}{\Omega_i}$. Here $\frac{\nu_{ia}}{\Omega_i} \approx 3\cdot 10^{-3}$. The particle transport then becomes

$$\Gamma_R = -\frac{\frac{1}{m_i \nu_{ia}}}{1+\frac{\Omega_e\Omega_i\varepsilon^2}{\nu_{ea}\nu_{ia}}}\frac{\partial}{\partial R}(n\kappa\,(T_e+T_i)) - \frac{\frac{1}{m_i\,\Omega_i}}{1+\frac{\Omega_e\Omega_i\varepsilon^2}{\nu_{ea}\nu_{ia}}}\frac{\partial}{\partial z}(n\kappa\,(T_e+T_i))$$

$$\Gamma_z = -\frac{1}{m_i\nu_{ia}}\frac{\partial}{\partial z}(n\kappa\,(T_e+T_i)) + \frac{\frac{1}{m_i\Omega_i}}{1+\frac{\Omega_e\Omega_i\varepsilon^2}{\nu_{ea}\nu_{ia}}}\frac{\partial}{\partial R}(n\kappa\,(T_e+T_i))$$

The equations for Case 1 are obtained by letting $\varepsilon\to 0$.

Case 3: $\varepsilon=0$, while $\eta << \frac{\nu_{ia}}{\Omega_i}$. Then

$$\Gamma_R = -\frac{1}{m_i\nu_{ia}}\frac{\partial}{\partial R}(n\kappa\,(T_e+T_i)) - \frac{\frac{1}{m_i\,\Omega_i}}{1+\frac{\Omega_e\Omega_i\eta^2}{\nu_{ea}\nu_{ia}}}\frac{\partial}{\partial z}(n\kappa\,(T_e+T_i))$$

$$\Gamma_z = -\frac{\frac{1}{m_i\nu_{ia}}}{1+\frac{\Omega_e\Omega_i\eta^2}{\nu_{ea}\nu_{ia}}}\frac{\partial}{\partial z}(n\kappa\,(T_e+T_i)) + \frac{\frac{1}{m_i\Omega_i}}{1+\frac{\Omega_e\Omega_i\eta^2}{\nu_{ea}\nu_{ia}}}\frac{\partial}{\partial R}(n\kappa\,(T_e+T_i))$$

Case 4: $\frac{\nu_{ea}}{\Omega_e} << (\text{both } \varepsilon \text{ and } \eta) << \frac{\nu_{ia}}{\Omega_i}$. Then

$$\Gamma_R = -\frac{1}{D}\left(a_{11}+\eta^2 a_{12}\right)\frac{\partial}{\partial R}(n\kappa(T_e+T_i)) - \frac{1}{D}(a_{21}+\varepsilon\eta a_{22})\frac{\partial}{\partial z}(n\kappa(T_e+T_i))$$

$$\Gamma_z = -\frac{1}{D}\left(a_{11}+\varepsilon^2 a_{12}\right)\frac{\partial}{\partial z}(n\kappa(T_e+T_i)) + \frac{1}{D}(a_{21}-\varepsilon\eta a_{22})\frac{\partial}{\partial R}(n\kappa(T_e+T_i))$$

where $D = \frac{\nu_{ia}}{\Omega_i^2}\left(\frac{\nu_{ia}}{\Omega_i^2}+\frac{m_i}{m_e\nu_{ea}}(\varepsilon^2+\eta^2)\right)$, $a_{11} = \frac{\nu_{ia}}{m_i\Omega_i^4}$, $a_{12} = \frac{1}{m_e\nu_{ea}\Omega_i^2} = a_{22}$, $a_{21} = \left(\frac{\nu_{ia}}{\Omega_i^2}\right)^2\frac{1}{m_i\Omega_i}$.

In steady state the mass conservation equation becomes $\nabla\cdot\Gamma = \left(\frac{\partial n}{\partial t}\right)_c$ where $\left(\frac{\partial n}{\partial t}\right)_c$ is the plasma generation/plasma recombination term. When in particular electron and ion temperatures may be set constant we have typically in cases (1)–(4) for particle density the equation

$$A\frac{\partial^2 n}{\partial x^2} + 2B\frac{\partial^2 n}{\partial x\,\partial z} + C\frac{\partial^2 n}{\partial z^2} = -f(x,z)$$

We have simplified the geometry and neglected some effects using cartesian coordinates. $f(x,z) = \frac{1}{\kappa(T_e+T_i)}\left(\frac{\partial n}{\partial t}\right)_c$. In case (1) B=0, A=C=$\frac{1}{m_i\nu_{ia}}$, in case (2) B=0, A=$\frac{\frac{1}{m_i\nu_{ia}}}{1+\frac{\Omega_e\Omega_i}{\nu_{ea}\nu_{ia}}\varepsilon^2}$, C=$\frac{1}{m_i\nu_{ia}}$, in

case (3) B=0, $A=\frac{1}{m_i \nu_{ia}}$, $C=\frac{\frac{1}{m_i \nu_{ia}}}{1+\frac{\Omega_e \Omega_i \eta^2}{\nu_{ea}\nu_{ia}}}$ in case (4) $A=\frac{1}{D}(a_{11}+\eta^2 a_{12})$, $B=\frac{\varepsilon\eta a_{22}}{D}$, $C=\frac{1}{D}(a_{11}+\varepsilon^2 a_{12})$

where D, given above, also depends on ε and η.

We demonstrate in Figs.(2)-(4) some effects of ε and η on solutions of n over a quadratic cross section, $-a\le x\le a$, $0\le z\le 2a$ (a=15), in the cases (1)-(3). Shown are level curves of $n-n_0$, where n_0 is the same constant, unspecified density on the boundary ('outside' a boundary sheath). The same plasma production term $\left(\frac{\partial n}{\partial t}\right)_c$, proportional to $\delta(x+\frac{a}{2})\left(\sin\frac{\pi z}{2a}-\frac{1}{3}\sin\frac{\pi z}{a}\right)$, has been used,

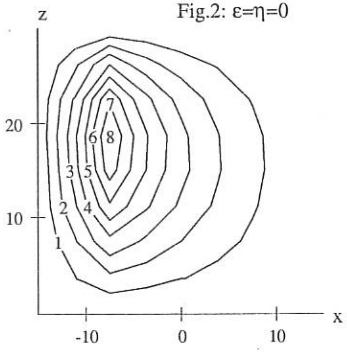

Fig.2: ε=η=0

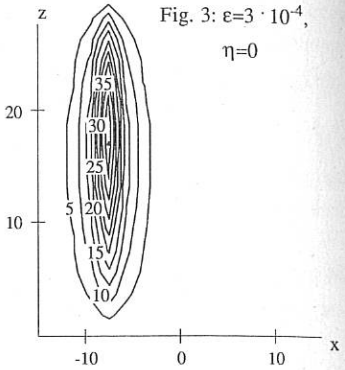

Fig. 3: $\varepsilon=3\cdot10^{-4}$, η=0

and the same numbering indicates the relative density distributions.

References. (1) Wong K.L., Ono M., Wurden G.A., Rev.Sci. Instrum. 53(4) (1982).

(2) Grønvoll E., Rypdal K., Trulsen J., Physics Reports, Inst., Math. and Phys. Sci. Univ. of Tromsø (1991).

(3) Fasoli A., Fontanesi M., Galassi A., Longari C., Sindoni E., Il Nuovo Cimento 10 D,N.12 (1988).

(4) Øien, A.H., J. Plasma Physics, 38(2), (1987).

(5) Øien, A.H., XX I.C.P.I.G., Contr. Papers, 2-422 (1991).

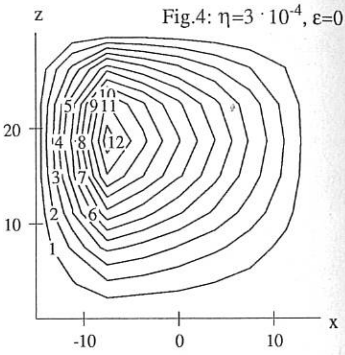

Fig.4: $\eta=3\cdot10^{-4}$, ε=0

A ONE–DIMENSIONAL Q–MACHINE MODEL TAKING INTO ACCOUNT CHARGE–EXCHANGE COLLISIONS

H. Maier and S. Kuhn

Plasma and Energy Physics Group, Institute for Theoretical Physics,
University of Innsbruck, Austria

1. Introduction and model. The Q–machine[1,2] is a nontrivial bounded plasma system which is excellently suited not only for fundamental plasma physics investigations but also for the development and testing of new theoretical methods for modeling such systems. However, although Q–machines have now been around for over thirty years, it appears that there exist no *comprehensive* theoretical models taking into account their considerable geometrical and physical complexity with a reasonable degree of self–consistency. In the present context we are concerned with the *low–density, single–emitter* Q–machine, for which the most widely used model is probably the (one–dimensional) "collisionless plane–diode model",[3,4] which has originally been developed for thermionic diodes.[5-7] Although the validity of this model is restricted to certain "axial" phenomena, we consider it a suitable starting point for extensions of various kinds. While a generalization to two–dimensional geometry (with still collisionless plasma) is is being reported elsewhere,[8] the present work represents a first extension to collisional plasma (with still one–dimensional geometry).

The model geometry is shown in Fig. 1. Both ions and electrons leave the emitter ("hot plate", located at $x = 0$ and assigned potential $V = 0$) with half Maxwellian distribution functions corresponding to the emitter temperature T. All particles reaching either the emitter or the collector ("cold plate", located at $x = L$ and biased against the hot plate with potential V_c) are absorbed. Since this work represents but a first step toward the self–consistent kinetic modeling of collisional bounded plasma systems, the ions are assumed to undergo symmetric charge–exchange collisions with the neutral background gas,[9,10] whereas the electrons are still treated as collisionless. Moreover, we restrict ourselves to dc states with monotonically decreasing potential distributions, so as to avoid the occurrence of trapped particles.

In Sec. 3, our iterative analytic–numerical method for calculating self–consistent dc states of the above configuration is briefly outlined, and some typical numerical results on the effect of charge–exchange collisions are presented in Sec. 3. Full details are given in Ref. 11.

2. Outline of the method. Starting from a suitable first guess $V_0(x)$ for the potential distribution $V(x)$ (with V_0 best taken from one–dimensional theory[3]), the velocity

distribution functions must be found by solving the Vlasov equation for the electrons,

$$\left[\mathbf{v}\cdot\frac{\partial}{\partial \mathbf{x}} + \frac{q_e}{m_e}\left[\mathbf{E}(\mathbf{x})+\mathbf{v}\times\mathbf{B}\right]\cdot\frac{\partial}{\partial \mathbf{v}}\right] f_e(\mathbf{x},\mathbf{v}) \equiv \frac{d_e}{dt} f_e(\mathbf{x},\mathbf{v}) = 0 \tag{1}$$

and an the appropriate linearized Boltzmann equation for the ions,[10] ,

$$\left[\mathbf{v}\cdot\frac{\partial}{\partial \mathbf{x}} + \frac{q_i}{m_i}\left[\mathbf{E}(\mathbf{x})+\mathbf{v}\times\mathbf{B}\right]\cdot\frac{\partial}{\partial \mathbf{v}}\right] f_i(\mathbf{x},\mathbf{v}) \equiv \frac{d_i}{dt} f_i(\mathbf{x},\mathbf{v}) = \mathscr{C}_i(\mathbf{x},\mathbf{v}) \tag{2}$$

as described below. For the ion–neutral collision term $\mathscr{C}_i$ we use the linearized form

$$\mathscr{C}_i(\mathbf{x},\mathbf{v};f_i) \equiv P(\mathbf{x},\mathbf{v};f_i) - \nu(\mathbf{x},\mathbf{v})f_i(\mathbf{x},\mathbf{v}) , \tag{3}$$

where

$$P(\mathbf{x},\mathbf{v};f_i) \equiv \int d^3V \int d^2\Omega\ f_i(\mathbf{x},\mathbf{v}')F(\mathbf{x},\mathbf{V}')v_{rel}\sigma_d \tag{4}$$

is the gain term and $-\nu f_i$ is the loss term, with

$$\nu(\mathbf{x},\mathbf{v}) \equiv \int d^3V\ F(\mathbf{x},\mathbf{V})v_{rel}\sigma_d \tag{5}$$

the ion collision frequency. For the differential and total cross–cross sections we choose the well–known analytic approximations.[9,10]

$$\sigma_d(v_{rel},\theta) = \frac{\sigma_{tot}}{2\pi}\,\delta(1+\cos\theta) , \tag{6a}$$

$$\sigma_{tot}(v_{rel}) = [a - b\,\log(v_{rel})]^2 . \tag{6b}$$

The distribution functions $f_e(\mathbf{x},\mathbf{v})$ and $f_i(\mathbf{x},\mathbf{v})$ are determined via integration of Eqs. (1) and (2), respectively, with d_a/dt denoting the Lagrangian time derivative along the species–a trajectory (a = e,i) in the given dc potential. For the one–dimensional situation considered here, the trajectory integral of Eq. (1) is simply

$$f_e(x,\mathbf{v}) = f_e(0,v_0) = A_e\exp[-m_e v_0^2/2kT]\ U(v) \tag{7}$$

with $m_e v_0^2/2 = m_e(v_x^2+v_n^2)/2 - eV(x)$ the electron's energy at the emitter and U(v) the unit step function. Analogous formal integration of Eq. (2) would lead to an integral equation for f_i, but in practice we solve that equation by direct numerical integration on a discrete spatial grid:

$$f_{i,k+1} = \frac{f_{i,k}\left[1-\frac{1}{4}\Delta t_k(v_k+v_{k+1})\right] + \frac{1}{2}\Delta t_k(P_k+P_{k+1})}{1 + \frac{1}{4}\Delta t_k(v_k+v_{k+1})} , \tag{8}$$

where the subscript k indicates quantities at the k^{th} gridpoint and Δt_k is the ion's time of flight between gridpoints k and k+1. In so doing, two types of ion trajectories must be distinguished, namely (i) those originating at the emitter with positive v_x–values (for which the initial condition is the half Maxwellian emission distribution), and (ii) those originating at the collector at negative v_x–values (for which the initial f_i equals zero).

With the velocity distributions at a given position x thus determined, we calculate

the electron and ion number densities and, from them, the space–charge density according to

$$\rho(x) = e[n_e(x) - n_i(x)] = e\left[\int d^3v\, f_i(x,v) - \int d^3v\, f_e(x,v)\right] \quad (9)$$

where the velocity–space integration is performed analytically for the electrons and numerically for the ions. With this charge–density distribution, Poisson's equation,

$$\nabla^2 V(x) = -\rho(x)/\epsilon_0 \quad (10)$$

is solved approximately by means of a well–known relaxation scheme,[12] the result being an improved potential distribution $V_1(x)$.

This improved potential distribution is now used for calculating new distribution functions, new particle densities, a new space–charge distribution and, from it, a new potential distribution $V_2(x)$, et., until a sufficiently accurate and self–consistent "final" potential distribution $V(x)$ is obtained.

3. Results and discussion. In Figs. 2(a–d) we show some representative macroscopic quantities for a Q–machine (or thermionic diode) with length $L = 5$ mm at two different background (K) densities n_b ("low": $10^{18}m^{-3}$, marked by "1", and "intermediate": $10^{19}m^{-3}$, marked by "2"). The other parameters characterizing the system are: $V_c = -2V$, $T = 2100K$, $T_b = 500K$, electron emission density $n^+_{e0} = 1.5\times10^{16}m^{-3}$, and neutralization parameter $\alpha \equiv n^+_{i0}/n^+_{e0} = 0.01$.This system is "short" in the sense that there is no significant quasineutral plasma region between the emitter and collector sheaths. (It has been found that "long" systems are prone to numerical instability, and proper treatment of these will require further development of the method presented here.)

While Figs. 2(a) and 2(c) show the potential and space–charge distributions, Figs. 2(b) and 2(d) show their differences against the collisionless case. According to these results, charge–exchange collisions have the following basic effects on the system: They tend to lower the ion average velocity and, hence, to raise the ion density. Hence, the region of positive space charge is widened, and the "plasma point" (defined by exact space–charge neutrality, marked by a small open circle) is shifted to the left. These tendencies become stronger with increasing background density.

Acknowledgment. This work is being supported by the Austrian Science Foundation under contract No. P8405–PHY.

References

[1]R.W. Motley (Princeton U., NJ, USA), *Q Machines* (Academic Press, 1975).
[2]N. Rynn and N.D. D'Angelo, Rev. Sci. Instr. **31**, 1326 (1960).
[3]S. Kuhn, Plasma Phys. **23**, 881 (1981).
[4]S. Kuhn, *1987 Int. Conf. on Plasma Phys.*, Kiev, Invited Papers **2**, 954 (1987).
[5]P.L. Auer, J. Appl. Phys. **31**, 2096 (1960).
[6]M.I. Kaganov, R.Ya. Kucherov, and L.E. Rikenglaz, Sov. Phys. Tech. Phys. **6**, 420 (1961).

[7]W. Ott, Z. Naturf. **22A**, 1057 (1967).
[8]H. Pedit and S. Kuhn, this conference.
[9]S. Kuhn, Phys. Rev. A **22**, 2460 (1980).
[10]H. Fahr and K.G. Müller, Z. Physik **200**, 343 (1967).
[11]H. Maier, Diploma thesis, Institute for Theoretical Physics, University of Innsbruck, Austria (1992).
[12]S. Koonin, *Physik auf dem Computer*, Oldenbourg Verlag (1987).

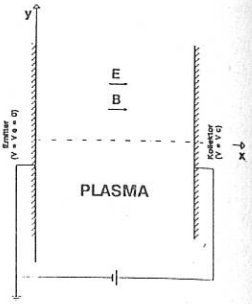

Fig. 1

Fig. 2

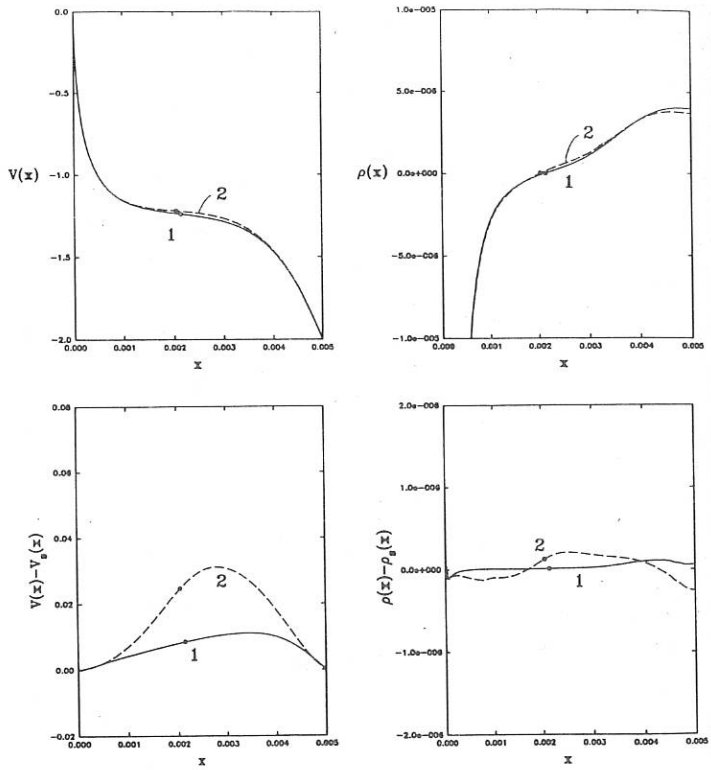

DETERMINATION OF COMPOSITION AND PHYSICAL PROPERTIES OF PARTIALLY IONIZED PLASMAS IN THE FUNCTION OF TEMPERATURE

B. Zaporowski
Technical University of Poznań, 60-965 Poznań, P.O.Box 1, Poland

1. INTRODUCTION

The investigations of various kinds of partially ionized plasma were conducted for the pressure of 0,1 MPa and in the range of temperature of 298.15 K to 24000 K. The physical properties of various kinds of partially ionized plasma depend mainly of their composition and temperature. The composition of particular kinds of partially ionized plasmas varies also in the function of temperature. Simultaneous going on of physical and chemical processes in plasma is the reason of difficulties in the calculations of plasma's physical properties. The use of the laws of macroscopic thermodynamics for to calculations of physical properties of partially ionized plasma is impossible. There are enough exact methods for measuring of physical properties of partially ionized plasma. For these reasons the theoretical method using the base of statistic physics was used to calculate the composition and physical properties of various kinds of partially ionized plasma.

2. PRINCIPLE OF THE METHOD

The composition of partially ionized plasma, in the state of local thermodynamic equilibrium (LTE), in the elaborated method, is determined by solving a corresponding system of nonlinear algebraic equations. The number of the equations in this system is equal to the number of assumed components of plasma. For the assumed n components of plasma, that is made up of k elements, the system of equations is composed of n equations:

- n-(k+1) equations of equilibrium constants of dissociation, ionization and formation of negative ions reactions in plasma,
- k-1 equations of the balance of elements,
- 1 equation of the balance of partial pressures of particular components of plasma,
- 1 equation of the balance of electric charges.

The equilibrium constants of chemical reactions in plasma were defined by the relation

$$K_p = \left(\prod_{1}^{l} (Q_{B_i}/N)^{b_i} \right) / \left(\prod_{1}^{j} (Q_{A_i}/N)^{a_i} \right) \exp\left(-\frac{\Delta e}{kT}\right) \qquad (1)$$

where

- Q_{A_i}, Q_{B_i} - temperature functions of the sums of states of the plasma components A_i, B_i,
- a_i, b_i - number of molecules, atoms, ions or electrons taking part in the given chemical reaction,
- N - Avogadro's constant,
- k - Boltzmann's constant.
- Δe - energy of activation of the chemical reaction at the temperature 0 K,
- T - temperature of the plasma.

The relations, describing the temperature functions of the sums of

states of particular components of the plasma, are given below:

- Atoms, one-atom ions and electrons

$$Q_{i(T)} = N\left(\frac{2\pi M_i}{h^2 N}\right)^{\frac{3}{2}} k^{\frac{5}{2}} T^{\frac{5}{2}} \sum_{j=0}^{j=j(i)} q_{ij} \exp\left(-\frac{\varepsilon_{ij}}{kT}\right) \qquad (2)$$

- Linear polyatomic molecules and ions

$$Q_{i(T)} = N\left(\frac{2\pi M_i}{h^2 N}\right)^{\frac{3}{2}} k^{\frac{5}{2}} T^{\frac{5}{2}} \prod_{j=1}^{j=j(m)} \frac{1}{\left(1 - \exp\left(-\frac{\nu_{ij}}{kT}\right)\right)} \frac{1}{\sigma_i} \frac{kT}{B_i} \qquad (3)$$

- Nonlinear polyatomic molecules and ions

$$Q_{i(T)} = N\left(\frac{2\pi M_i}{h^2 N}\right)^{\frac{3}{2}} k^{\frac{5}{2}} T^{\frac{5}{2}} \prod_{j=1}^{j=j(m)} \frac{1}{\left(1 - \exp\left(-\frac{\nu_{ij}}{kT}\right)\right)} \cdot \frac{1}{\sigma_i} \frac{\pi (kT)^3}{A_i B_i C_i} \qquad (4)$$

where

M_i - mass of the "i" component of gas,

h - Planck's constant,

ε_{ij} - "j" electronic energy level of the "i" gas component,

q_{ij} - statistic weight of the "j" electronic energy level,

ν_{ij} - frequency (energy) of fundamental vibration of i-th molecule or ion,

A_i, B_i, C_i - constants connected with the moments of molecule or ion inertia,

σ_i - coefficient of molecule or ion symmetry,

m - number of atoms in molecule or ion.

	Molecules or ions				
	Linear		Nonlinear		
m	2	3	3	4	5
j(m)	1	4	3	6	9

On the basis of determined composition of plasma physical properties of plasma were defined. The relations, describing the physical properties of plasma components, in the function of temperature, were determined by their sums of states.

The total enthalpy of plasma is the sum of its physical enthalpy and chemical energy and was calculated according to the relation

$$h = \frac{1}{\sum_{i=1}^{i=n} M_i p_i} \sum_{i=1}^{i=n} p_i [\Delta H_{i(T_o, T_p)} + \Delta H'_{i(T_o)}] \quad (5)$$

where

M_i - mass of 1 kmol of "i" plasma component,

p_i - partial pressure of "i" plasma component,

n - number of plasma component,

$\Delta H_{i(T_o, T_p)}$ - physical molar enthalpy increment of "i" plasma component between the reference temperature (T_o) and the plasma temperature (T_p) determined in Section 3,

$\Delta H'_{i(T_o)}$ - chemical energy of "i" plasma component in the reference temperature (T_o=298.15 K).

The increment of the physical enthalpy of the particular components of plasma ($\Delta H_{i(T_o, T_p)}$) have been determined from relation

$$\Delta H_{i(T_o, T_p)} = R[T^2 [\frac{d\ln Q_i}{dT}] - T_o^2 [\frac{d\ln Q_i}{dT}]_{T=T_o}] \quad (6)$$

where

Q_i - sum of states of the "i" plasma component (relations 2,3 and 4)

The mean specific heat of plasma in the function of temperature, can not be determined as an averaged function of the temperature functions of specific heats of the particular components of plasma. It is due to simultaneous proceeding of physical and chemical processes in plasma. Elaborated method takes into account variation of composition and chemical enthalpy of plasma in the function of temperature. Taking all this into account mean specific heat should be determined with the help of following formula

$$c_{pm} = \frac{1}{\sum_{i=1}^{i=n} M_i p_i} \sum_{i=1}^{i=n} p_i c_{pi} + \frac{1}{2\Delta T} \left[\frac{1}{\sum_{i=1}^{i=n} M_i p_i} \sum_{i=1}^{i=n} (p_{i1} - p_{i2}) \Delta H_{i(T_o)} \right] \quad (7)$$

where

M_i - mass of 1 mole of the "i" component of plasma,

n - number of plasma components,

p_i - partial pressure of "i" component of plasma in temperature T,

p_{i1} - partial pressure of "i" component of plasma in temperature T+ΔT; in the calculations assumed ΔT = 3 K,

p_{i2} - partial pressure of "i" component of plasma in temperature T-ΔT,

c_{pi} - molar specific heat of "i" component of plasma in temperature T as a function of sum of states,

$\Delta H_{i(T_o)}$ - molar chemical enthalpy of "i" component of plasma in the reference temperature T_o.

The mean molar mass, isentropic exponent, density and gas constant for various kinds of partially ionized plasmas were calculated with the help of relations valid for gaseous mixture.

Concentrations of electrons in plasma was calculated with the help of equation

$$n_e = \frac{p_e}{kT} \tag{8}$$

where p_e - partial pressure of electrons in plasma (calculated).

The formula for electrical conductivity of partially ionized plasma was presented in [1]. The other electrical properties of partially ionized plasma were calculated with the help of electron concentration in plasma (n_e) and collision cross-sections for electrons.

3. CALCULATIONS

Calculations were carried out with the help of computer programme elaborated on the basis of the mathematical model of physical and chemical proceeding in plasma. Some results of calculations are shown of the function of temperature in figure 1 and figure 2.

4. REFERENCES

[1] Bincer H.: Electron Concentration and Electrical Conductivity of Seeded Coal Combustion Plasmas. Proceedings of Symposium on Magnetohydrodynamic Electrical Power Generation, Paris, 1964, Vol. I, pp. 14-26.

[2] Zaporowski B.: Mathematical Models of the Processes of Energy Conversion in MHD Generator. Proceedings of the 29th Symposium on Engineering Aspects of Magnetohydrodynamics. New Orleans, USA, 1991, pp. 201-210.

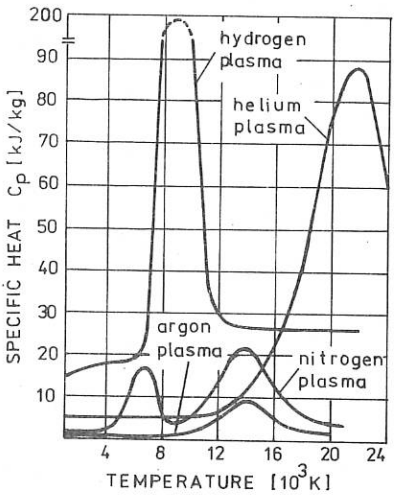

Figure 1. Dependence of specific heat of argon plasma, helium plasma hydrogen plasma and nitrogen plasma on temperature

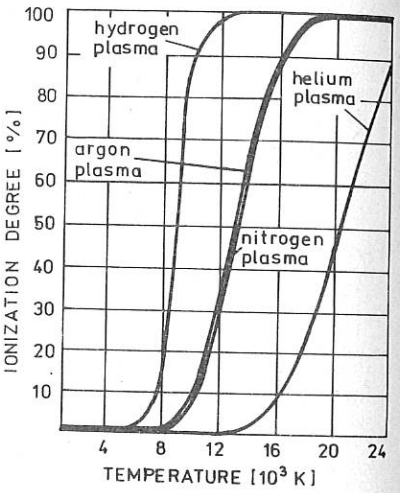

Figure 2. Dependence of degree of ionization of argon plasma, helium plasma, hydrogen plasma and nitrogen plasma on temperature

THERMODYNAMIC FUNCTIONS FOR PARTIALLY IONIZED PLASMAS IN THE MEAN SPHERICAL APPROXIMATION

Torsten Kahlbaum* and Hartmut Schneidenbach+

*WIP-Arbeitsgruppe Niedertemperaturplasmaphysik
Hausvogteiplatz 5-7, O-1086 Berlin, Germany

+Institut für Niedertemperaturplasmaphysik
Robert-Blum-Straße 8-10, O-2200 Greifswald, Germany

Abstract

We present a free energy model for partially ionized plasmas of heavier elements, which is essentially based on the mean spherical approximation (MSA) and the reduced-volume hypothesis, and discuss its limiting behavior and numerical examples for xenon.

Free energy model

Our total Helmholtz free energy density of the plasma,

$$\frac{F}{V} \equiv f = f_B + f^*_{FD} + f_{MSA} + f_{hs} + f^*_{xc} + f_{ie} \,, \qquad (1)$$

consists of the usual Boltzmann part for atoms and ions, of the Fermi-Dirac part for free electrons in the reduced volume /1/, and of several interaction contributions which are explained in the following. MSA labels the excess contribution of the interaction among the heavy particles /2/, relative to the contribution of uncharged hard spheres /3/. By using the averaged value $\langle \mathcal{F}(z) \rangle = n^{-1} \sum_0^Z n_z \mathcal{F}(z)$, $n = \sum_0^Z n_z$, we may write in compact form

$$\beta f_{MSA} = \frac{K_i^3}{3\pi} - l\left(K_i n \left\langle \frac{z^2}{1 + K_i d_z} \right\rangle + \frac{R^2}{W}\right) \,, \quad l = \frac{\beta e^2}{4\pi\varepsilon_0} \,,$$
$$R = n\left\langle \frac{z d_z}{1 + K_i d_z} \right\rangle \,, \quad W = \frac{2}{\pi} + \frac{1}{3} n \left\langle \frac{2 - K_i d_z}{1 + K_i d_z} d_z^3 \right\rangle \,. \qquad (2)$$

The inverse screening length K_i of the heavy particles has to be obtained as the iterative solution of the nonlinear equation

$$K_i^2 = \pi l \, n \left\langle \left(\frac{z - \frac{R}{W} d_z^2}{1 + K_i d_z} \right)^2 \right\rangle \,. \qquad (3)$$

The exchange-correlation contribution of free electrons in the reduced volume is an analytic formula, derived from a Padé-type fit to numerical results for the internal energy in the Singwi-Tosi-Land-Sjölander scheme /4/ and then scaled according to

$$f^*_{xc}(n_e, \eta) = f_{xc}(n_e^*) \,, \quad n_e^* = \frac{n_e}{1-\eta} \,, \quad \eta = \frac{\pi}{6} n \langle d_z^3 \rangle \,. \qquad (4)$$

Finally we constructed the excess contribution of the interaction between heavy particles and electrons in the same manner as it was done for point-like charges in the Debye limit /5/,

$$\beta f_{ie} = \frac{2}{3\pi}\left(K_i^3 + K_e^3 - K^3\right) . \tag{5}$$

The inverse Thomas-Fermi screening length K_e /6/ of free electrons is determined by the Fermi-Dirac part of their chemical potential, where I_ν is the Fermi integral and $\Lambda_e = h(2\pi m_e/\beta)^{-1/2}$,

$$K_e^2 = \pi l \left(2/\Lambda_e^3\right) I_{-1/2}\left(\beta\mu^*_{FD,e}\right) , \qquad I_{1/2}\left(\beta\mu^*_{FD,e}\right) = \frac{1}{2} n_e^* \Lambda_e^3 , \tag{6}$$

and the sum of both screening contributions, Eqs. (3) and (6), defines the inverse total screening length K according to

$$K^2 = K_i^2 + K_e^2 . \tag{7}$$

Limiting behavior of the Coulomb contributions

In the case of a dilute plasma, $\eta \to 0$, with classical electrons, K_i, K_e, and K approach one half of the corresponding inverse Debye screening lengths, and for the Coulomb contributions to the free energy in Eq. (1) we recover the Debye values so that

$$\beta\left(f_{MSA} + f^*_{xc} + f_{ie}\right) \longrightarrow - \frac{\varkappa^3}{12\pi} , \qquad \varkappa^2 = 4\pi l \left(n\langle z^2\rangle + n_e\right) . \tag{8}$$

Deviations from this behavior at higher densities are caused by the finite size of the heavy particles and by degeneration and coupling effects of the free electrons. As an example, we give the MSA excess contribution up to the lowest-order correction,

$$\begin{aligned} K_i &\longrightarrow \frac{1}{2}\varkappa_i - \pi l\, n\langle z^2 d_z\rangle , \qquad \varkappa_i^2 = 4\pi l\, n\langle z^2\rangle , \\ \beta f_{MSA} &\longrightarrow - \frac{\varkappa_i^3}{12\pi} + \frac{\varkappa_i^2 l}{4} n\langle z^2 d_z\rangle . \end{aligned} \tag{9}$$

In the opposite case of a dense plasma, $\eta \to 1$, with degenerate electrons, the atoms and ions cannot contribute to the screening any longer, $K_i \longrightarrow 0$, and hence $K \longrightarrow K_e$ and $f_{ie} \longrightarrow 0$. Further,

$$\begin{aligned} K_e &\longrightarrow \frac{1}{a_0(\pi\alpha r_s^*)^{1/2}} , \qquad r_s^* = \left(\frac{3}{4\pi n_e^* a_0^3}\right)^{1/3} , \qquad \alpha = \left(\frac{4}{9\pi}\right)^{1/3} , \\ \beta f_{MSA} &\longrightarrow - \frac{\varkappa_i^2}{4\pi d} \quad \text{for } d_z \approx d \text{ and } \langle z\rangle^2 \approx \langle z^2\rangle . \end{aligned} \tag{10}$$

Note that the neutral atoms, though generally present in the MSA, do not appear in neither of the limits, Eqs. (9) and (10).

Application to partially ionized xenon plasma

Motivated by the permanent interest in the equilibrium properties of heavy noble gas plasmas /7/, we applied the free energy model as outlined in Eqs. (1)-(7) to fluid xenon up to 50,000 K over a broad density range in the region of partial ionization. The hard-sphere diameters of the heavy particles were estimated by the simple scaling relation $d_z \approx 23\ a_0/\sqrt{I_z/eV}$ /8/, where I_z is the unperturbed ionization energy, for lack of more reliable values especially for the higher charged ions.

The limiting behavior of the inverse screening lengths (Fig. 1) and the relevance of the various contributions to the chemical potentials (Fig. 2) of the atoms and ions, $\mu_z = \partial f/\partial n_z$, and of the free electrons, $\mu_e = \partial f/\partial n_e$, are conveniently studied by assuming an arbitrarily fixed plasma composition, for which we chose two-fold charged ions with the density $n = n_2 = \frac{1}{2} n_e$. The spatial extension of the ions leads to a substantial decrease of their inverse screening length compared to the Debye value, cf. Eq. (9). In the dense fluid range K_i exhibits a maximum and the inverse screening length of the free electrons reaches the Thomas-Fermi value, Eq. (10). The behavior at still higher densities cannot be adequately described due to the limitation of the MSA to the fluid hard-sphere system. The vanishing of K_i and, consequently, of the ion-electron interaction contributions to the free energy, f_{ie}, and to the chemical potentials, $\partial f_{ie}/\partial n_z$ and $\partial f_{ie}/\partial n_e$, only occurs very close to the unphysical limit $\eta^z = 1$ and, therefore, has no significance. Moreover, the simple construction of Eq. (5) actually gives the Debye value, Eq. (8), but does not provide an appropriate treatment of the ion-electron interaction up to $\eta \approx 0.5$. Above a certain density it starts to yield qualitatively wrong results what is indicated by the change of sign in $\partial f_{ie}/\partial n_z$; see curve ie in Fig. 2.

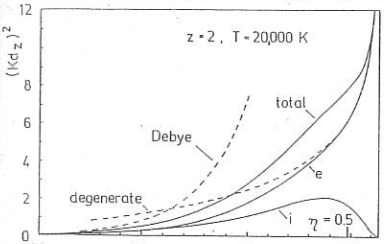

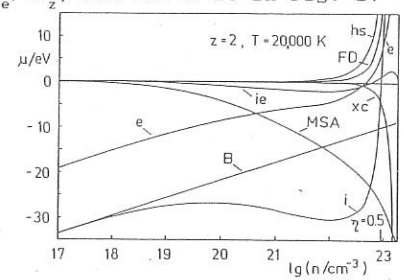

Fig. 1 (left): The inverse screening lengths and some of their limits. i - ionic contribution from Eq. (3); e - free-electron contribution, Eq. (6), and its **degenerate** limit, see Eq. (10); inverse **total** screening length, Eq. (7), and its **Debye** limit.
Fig. 2 (right): The chemical potentials of the ions (i) and of the free electrons (e) and the ionic contributions $\partial f_B/\partial n_z$, $\partial f_{MSA}/\partial n_z$, $\partial f_{hs}/\partial n_z$, $\partial f_{ie}/\partial n_z$, $\partial f^*_{FD}/\partial n_z$, and $\partial f^*_{xc}/\partial n_z$.
Both figures are calculated for a fixed plasma composition (see text) at one temperature versus ion density. The bar at $\eta = 0.5$ should roughly mark the upper bound to the fluid range of hard spheres, where the mean spherical approximation is applicable.

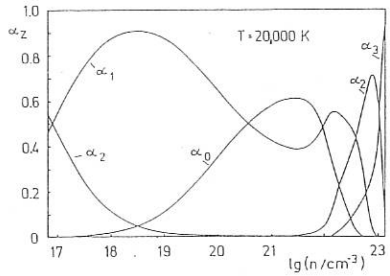

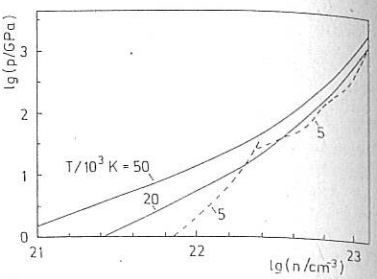

Fig. 3 (left): The detailed plasma composition at one temperature in terms of the relative abundances $\alpha_z = n_z/n$ of atoms and ions, z = 0,1,2,3,..., versus total heavy-particle density n.
Fig. 4 (right): Thermal equation of state: Pressure isotherms versus total heavy-particle density for three temperatures.

Then we determined the ionization equilibrium (Fig. 3) and the thermal equation of state (Fig. 4) /7/. As in /9/, the pressure isotherms do not show unstable branches above ≈ 8,800 K so that recent estimates /10/ of the critical temperature of the plasma phase transition /11/ seem to be far too high. However, this finding is strongly influenced by the ion-electron interaction, for a former choice of f_{ie} /5/ shifts our T_c towards 14,200 K. This illustrates the need for further improvements of the model before a new phase diagram for fluid xenon can be calculated.

Acknowledgements. We are very grateful to Professor W. Ebeling and Dr. A. Förster (both Humboldt University, Berlin) for suggesting the application of the MSA to non-ideal plasmas and for several useful discussions during the preparation of this paper.

References

/1/ T. Kahlbaum, A. Förster, *Fluid Phase Equilibria*, to appear (1992).
/2/ L. Blum, J.S. Høye, *J. Phys. Chem.* **81**, 1311 (1977).
/3/ G.A. Mansoori, N.F. Carnahan, K.E. Starling, T.W. Leland, Jr., *J. Chem. Phys.* **54**, 1523 (1971).
/4/ S. Tanaka, S. Mitake, S. Ichimaru, *Phys. Rev. A* **32**, 1896 (1985).
/5/ W. Ebeling, *Contrib. Plasma Phys.* **30**, 553 (1990).
/6/ F. Perrot, M.W.C. Dharma-wardana, *Phys. Rev. A* **30**, 2619 (1984).
/7/ T. Kahlbaum, A. Förster, *Laser Part. Beams* **8**, 753 (1990).
/8/ W. Ebeling, A. Förster, V.E. Fortov, V.K. Gryaznov, A.Ya. Polishchuk, *Thermophysical Properties of Hot Dense Plasmas* (Teubner, Stuttgart, Leipzig, 1991), p. 99.
/9/ A. Förster, W. Ebeling, in: *Physics of Nonideal Plasmas*, W. Ebeling, A. Förster, R. Radtke, eds. (Teubner, Stuttgart, Leipzig, 1992), to appear.
/10/ W. Ebeling, A. Förster, *High Press. Res.* **4**, 484 (1990).
/11/ A. Förster, T. Kahlbaum, W. Ebeling, *High Press. Res.* **7**, 375 (1991).

DIELECTRIC CONSTANT OF WEAKLY-IONIZED MAGNETIZED PLASMAS

Zh. Kiss'ovski, A. Pironkova and A. Shivarova
Faculty of Phisics, Sofia University,
BG-1126 Sofia, Bulgaria

Independently of the very large activity in the field of the low-frequency instabilities and turbulent state of magnetized plasmas /1,2/ and the current direction to investigating nonlinear phenomena in weakly-ionized plasmas /3,4/, the complicate situation in the experiments in the gas-discharge plasmas submits many questions concerning the identification of the observed instabilities. One of the reasons for these complications is the anomalous behaviour of the ambipolar electric field in the range $\Omega_i \simeq \nu_i$, $\rho_i \simeq R$ where the so-called low-frequency drift-wave instability associated with the finiteness of the ion gyroradius ρ_i /5-7/ esists. (Here Ω_i is the ion gyrofrequency, ν_i is the ion-neutral collision frequency and R is the plasma column radius.) The impossibility for explaning our recent experimental results /8/ in terms of the dispersion relation of the low-frequency drift wave instability /6/ has stimulated a discussion on the dielectric function of weakly-ionized inhomogeneuous strongly-collisional plasma in crossed magnetic and electric fields. The result we present here for the plasma dielectric function rectifies that given in /6/ and appears as a next stage which generalizes the previous derivations of the permittivity tensor presented in /9/.

In the equilibrium state we have in mind a d.c. gas discharge plasma imposed in a steady-state magnetic field $\vec{H}_o=(0,\ 0,\ H_o)$ with density inhomogeneity in transverse direction $n(x)$ and steady-state electric fields $\vec{E}_o=(E_{ox},\ 0,\ E_{oz})$, i.e. an ambipolar field and a field sustaining the discharge. For describing the plasma behaviour we start from the Boltzman equation for the particle distribution function f_α ($\alpha = e,\ i$) with a collision integral

which accounts for the collisions of the charged particles with the neutrals in BGK-approximation /9/:

$$St\ (f) = -\nu_\alpha (f - n\ \Phi_{\alpha o}) \qquad (1)$$

where $\phi_{\alpha o} = (m_\alpha / 2\pi T_\alpha)^{3/2} \exp(- m_\alpha v_\alpha^2 / 2T_\alpha)$.

The effect of the collisions (ν_α) is taken into account not only in the equilibrium state (as it is done in /9/) but in the equilibrium state, as well. The ambipolar field (E_{ox}) leads to a E x B -drift ($u = -cE_{ox}/H_o$) and the influence of the E_{oz}-field can be taken into account in the final result for the electron contribution through a Doppler shift $k_z U_e$ of the frequency ($U_e = -eE_{oz}/m_e\nu_e$). The equation describing the distribution function $f_{o\alpha}$ in the equilibrium state is:

$$v_x \frac{\partial f_{o\alpha}}{\partial x} + \Omega_\alpha (v_y - u) \frac{\partial f_{o\alpha}}{\partial v_x} - \Omega_\alpha v_x \frac{\partial f_{o\alpha}}{\partial v_y} = -\nu_\alpha f_{o\alpha}(v) + \nu_\alpha n_o \Phi_{\alpha o}(v) \qquad (2)$$

and it is solved after consecutive transformations to frames: $v_x = v_{xc} \equiv v_\perp \cos\varphi$, $v_y - u = v_{yc} \equiv v_\perp \sin\varphi$, $v_z = v_z$. The set of the characteristic equations of eq. (2) give the integral:

$$\Omega_\alpha x + v_{yc} = \text{const.} \qquad (3)$$

and the following result for $f_{\alpha o}$:

$$f_{o\alpha} = n_o(x) f_{oo\alpha} [1 + a v_{yc} - b v_{xc}] \qquad (4)$$

where $f_{oo\alpha} = (m_\alpha / 2\pi T_\alpha)^{3/2} \exp[- m_\alpha (v_{\perp\alpha}^2 + v_z^2) / 2T_\alpha]$,

$$a = \frac{\Omega_\alpha \varkappa}{\Omega_\alpha^2 + \nu_\alpha^2} \left[1 - \frac{m_\alpha u \nu_\alpha^2}{\varkappa T_\alpha \Omega_\alpha}\right], \qquad b = \frac{\nu_\alpha \varkappa}{\Omega_\alpha^2 + \nu_\alpha^2} \left[1 + \frac{m_\alpha u\, \Omega_\alpha}{\varkappa T_\alpha}\right],$$

$\Omega_\alpha = e_\alpha H_o / m_\alpha c$ and $\varkappa = (1/n_o)(dn_o/dx)$. The last two terms in expression (4) describe the contributions of the plasma inhomogeneity, of the collisions and of the particle drift in the ambipolar electric field. The characteristic equations of the first order approximation of the Boltzman equation:

$$\frac{\partial f_{i\alpha}}{\partial t} + (\vec{v} \cdot \vec{\nabla}) f_{i\alpha} + \frac{e_\alpha \vec{E}_i}{m_\alpha} \cdot \frac{\partial f_{o\alpha}}{\partial \vec{v}} + \frac{e_\alpha \vec{E}_o}{m_\alpha} \cdot \frac{\partial f_{i\alpha}}{\partial \vec{v}}$$

$$+\frac{e_\alpha}{m_\alpha c}[\vec{v}\,\vec{H}]\cdot\frac{\partial f_{1\alpha}}{\partial \vec{v}} = -\nu_\alpha(f_1 - n_1\phi_o) \qquad (5)$$

used for describing quasi-static pertubations $\vec{E}_1 = -\vec{\nabla}\varphi_1$ of the type $f_1 \alpha f_1(x)\exp[-i\omega t + ik_y y + ik_z z)$ lead to the integral (3) and to:

$$\frac{df_{1\alpha}}{d\varphi} + \frac{i}{\Omega_\alpha}[\omega + i\nu_\alpha - k_y(v_{yc} + u) - k_z v_z]f_{1\alpha}$$

$$= -\frac{1}{\Omega_\alpha} f_{oo}\left\{\nu_\alpha n_1 \exp[-\frac{m_\alpha}{2T_\alpha}(u^2 + 2uv_{yc})]\right. \qquad (6)$$

$$-i\frac{e_\alpha}{m_\alpha} n_o(x)\varphi_1[k_y\frac{m_\alpha}{T_\alpha}v_{yc}(1 + av_{yc} - bv_{xc}) - k_y a$$

$$\left.+k_z\frac{m_\alpha}{T_\alpha}v_z\,(1 + av_{yc} - bv_{xc})]\right\}.$$

Leughly calculations performed according to the method of integration over φ /9/ gives a solution of eq. (6) of the form:

$$\frac{n_{1\alpha}}{n_o} B_\alpha = -\frac{e\varphi_1}{T_\alpha}(A_\alpha + C_\alpha) \qquad (7)$$

which results into the following expression for the longitudinal plasma permittivity:

$$\varepsilon = 1 + \sum_\alpha \frac{\omega_{p\alpha}^2}{k^2 v_{T\alpha}^2}\frac{A_\alpha + C_\alpha}{B_\alpha} \qquad (8)$$

where $v_{T\alpha} = (T_\alpha/m_\alpha)^{1/2}$, $\omega_{p\alpha} = (4\pi e^2 n_o/m_\alpha)^{1/2}$ and

$$A_\alpha = 1 - (\omega' - k_y a v_{T\alpha}^2)\sum_{n=-\infty}^{\infty}\frac{A_n(z_\alpha)}{\omega' - n\Omega_\alpha} J_+(\beta_{n\alpha})$$

$$B_\alpha = 1 - i\nu_\alpha\sum_{n=-\infty}^{\infty}\frac{A_n(z_\alpha(1-\beta_i^2)^{1/2})}{\omega' - n\Omega_\alpha} J_+(\beta_{n\alpha})\left(\frac{1 - \beta_i}{1 + \beta_i}\right)^{n/2}$$

$$C_\alpha = -i\frac{b\Omega_\alpha}{k_y}\left\{(\omega' - i\nu_\alpha)\sum_{n=-\infty}^{\infty} z_\alpha\frac{A_n'(z_\alpha)}{\omega' - n\Omega_\alpha} J_+(\beta_{n\alpha})\right.$$

$$+ \left[i \frac{\nu_\alpha \omega'}{\Omega_\alpha^2} \left(1 - \frac{\varkappa}{\nu_\alpha b}\right) - 1\right] \Omega_\alpha \sum_{n=-\infty}^{\infty} \frac{n A_n(z_\alpha)}{\omega' - n\Omega_\alpha} J_+(\beta_{n\alpha}) \Bigg\}$$

with $\omega' = \omega + i\nu_\alpha - k_y u$, $\beta_i = u\Omega_\alpha / k_y v_{T\alpha}^2$, $z_\alpha = k_y^2 \rho_\alpha^2$,

$\beta_{n\alpha} = (\omega' - n\Omega_\alpha) / |k_z| v_{T\alpha}$, $A_n(z_\alpha) = \exp(-z_\alpha)\, I_n(z_\alpha)$,

$$J_+(x) = x \exp(-x^2/2) \int_{i\infty}^{\infty} \exp(\tau^2/2) d\tau .$$

In the results (7) and (8), B_α accounts for the effect of the collisions when the collision integral is included only in the equation for $f_{i\alpha}$ whereas A_α with the first term in a (expression (5)) accounts for the net effect of the inhomogeneity. The contribution to A_α given by the second term in a together with C_α are the new terms (in comparison with /9/) which are due to the combined effect of the collisions, of the ambipolar field and the inhomogeneity on the distribution function in the stationary state. These terms differ from those obtained in /6/ where a relation which should correlate to (7) is obtained by using the method of integration over the trajectories. The calculations we have made by using the same method confirm the our result (7).

This work was supported by projects n° 123 and F 27.

/1/ A.B. Michailovskii, in: Fundamentals of Plasma Physics, ed. A.A. Galeev and R. Sudan (Energoatomizdat,Moscow), v.1, p.502 (1983), in Russian

/2/ V.Horton, in: Fundamentals of Plasma Physics, ed. A.A. Galeev and R. Sudan (Energoatomizdat, Moskow), v.2, p.362 (1984), in Russian

/3/ U. Kauschke , H. Schlüter, Plasma Physics and Contr. Fusion 32, 1149 (1990); 33, 1309 (1991)

/4/ A.V. Chechkin, Izv.VUZ-Radiophys. 33, 35 (1990)

/5/ A.V. Timofeev, B.N. Shvilkin, Usp. Fiz. Nauk 118, 273 (1976)

/6/ S.V. Pytvinckii, A.V. Timofeev, Zh. Tekh. Fiz., 44, 2085 (1974).

/7/ M.I. Belavin, A.V. Timofeev,B.N. Shvilkin, Fizika Plasmy 6, 705 (1980)

/8/ Zh. Kiss'ovski, A. Shivarova, T. Stoychev, E. Tatarova, Contr. Papers XIX th ICPIG (Belgrade) ed. J.M. Jabat (Fac. Phys., Univ. Belgrade) v.4, p.790 (1989)

/9/ A.F.Aleksandrov, L.S. Bondankevich, A.A. Rukhadze, Fundamentals of Plasma Electrodynamics (Vysshay shkola, Moscow) (1988), in Russian.

ION BERNSTEIN WAVES IN A TOROIDAL STEADY-STATE DEVICE

D.Batani, M.Fontanesi, A.Galassi, C.Riccardi and E.Sindoni
Dipartimento di Fisica, Via Celoria 16, 20133 Milano, Italy

INTRODUCTION

In recent years the Ion Bernstein Waves Heating (IBWH) has been subject of great interest, as it allows a direct heating of the bulk ions of tokamak plasmas.
IBWs can be indirectly excited via Electron Plasma Waves (EPW) mode transformation or directly launched into the plasma. In this paper we present some experimental results on IBW propagation in a steady-state magnetized plasma. The aim of the experiment is the study of the basic phenomena involved in the IBW propagation characteristics. Moreover the dispersion relation of IBWs is strongly dependent on the ion temperature T_i and hence it offers the possibility of an indirect diagnostic of this plasma parameter. This method was already used in a previous work /1/ where the dispersion relation of Neutralized Ion Bernstein Waves (NIBWs) was experimentally reconstructed. The use of IBWs should confirm the validity of this diagnostic method.

EQUIPMENT SET-UP

The experiment was performed on the Thorello device, which has the following main characteristics: major radius R = 40 cm, minor radius r = 9 cm, on-axis magnetic toroidal field B = 2.3 kG /2/.
The steady-state magnetized plasma was produced in hydrogen neutral gas by means of hot-filament electron emission and voltage-induced acceleration. The electron density and temperature were measured with electrostatic Langmuir probes.

/1/ S.Alba, G.Carbone, M.Fontanesi, A.Galassi, C.Riccardi and E.Sindoni Plasma Physics and Controlled Fusion, vol.34, N.1, 1987.

/2/ G.Agosti, L.Ferrucci, M.Fontanesi, A.Galassi, E.Sindoni, Il Nuovo Cimento D, vol.9, N.2, 1992.

Typical parameters of the plasma are as follows: density $n_e = (10^8 - 10^{10})$ cm^3, electron temperature $T_e \approx 1eV$, ion temperature $T_i \approx 0.3$ eV, neutral gas pressure $P=(10^{-5} - 10^{-4})$ mbar. The capability of operating in different discharge regimes makes the weakly ionized plasma of Thorello particularly suitable to study plasma-waves interaction phenomena. In particular Ion Bernstein Waves are analyzed at the second harmonic of the ion cyclotron frequency, typically f=(3-6) MHz.

The e.s. waves are excited by means of a launching system located at the plasma edge, in the low field side. The antenna consists of four thin metallic blades lying in a vertical plane, along the direction of B and fed with a relative phase of 90°. In this configuration the antenna system excites waves with $k_{||} \leq 0.1$ cm^{-1}; the wavevector component perpendicular to B, $k_{\perp}$ was measured by means of an interferometric system.

The signal propagating in the plasma is detected by means of a double r.f. probe moving radially in the plasma; it is compared to the input signal with a mixer. The interferometric trace, proportional to the wave electric field, obtained by filtering the mixer output, in order to suppress time-dependent terms, is sent to the Y-channel of a digital oscilloscope.

EXPERIMENTAL RESULTS

The experimental results were compared with the numerically solved full electrostatic dispersion relation in the range of the ion cyclotron frequency /3/.

The IBW are indirectly excited via EPW mode transformation in the range of the second ion cyclotron harmonic frequencies $f \approx 2 f_i = 6$ MHz. The EPW is coupled to the plasma edge by means of a slow-wave antenna, with a good efficiency $\leq$ 50% at low power level ($\leq$ 1 W). The EPW to IBW transformation process is located in the resonant region where the injection frequency is equal to the Lower Hybrid frequency ($\omega = \omega_{lh} \approx \omega_{pi}$).

The experimental interferogram shown in Fig. 1 , gives the dependence of the wave electric field versus the probe distance from

/3/ Petrillo V., Maroli C., Fasoli A., Galassi A. and Longari C., Il Nuovo Cimento 11D, 1337 (1988).

the antenna system, obtained in Hydrogen plasma at the frequency f = 1.85 f_i, (f_i ion cyclotron frequency). The wave signal has been detected with an r.f. probe located at a toroidal angle of 100° with respect to the antenna system.
The lower hybrid resonance region is very close to the antenna surface and the conversion process is located at few millimeters from the antenna; therefore the only IBW appears in the interferometric trace.
By varying the transmitted frequency and measuring at a fixed radial position the wavelength, the dispersion relation can then be experimentally reconstructed .
In Fig. 2 the experimental values of the $k_\perp$ real component, obtained in the range of the frequencies between 1.8 f_i and 2.0 f_i, at 3 cm from the antenna, have been compared with the theoretical dispersion relation.
The 10% experimental systematic error at lower and higher frequencies is due to the plasma disomogeneities along a wavelength distance.
The strong dependence of the backward branch wavelength with respect to the ion temperature makes possible to obtain an estimate of the local ion temperature. In the case of figure 2, the estimated ion temperature is 0.3 eV.

CONCLUSIONS

The propagation of IBW has been experimentally investigated in hydrogen plasmas produced in a steady-state toroidal device Thorello. It results that a slow-wave antenna efficiently launches the EPW, which propagates along the magnetic field and then is converted in IBW. The experimental reconstruction of the dispersion relation has been obtained by means of an interferometric system. Comparing the experimental relation dispersion with the theoretical one, it has been possible to perform an indirect diagnostic of the ion temperature.

ACNOWLEDGMENTS

We would like to thank Prof.G.Lampis, dr.A.Cardinali and dr.S.Alba, for the very helpful discussions and Mr.G.Braga for the technical assistance.

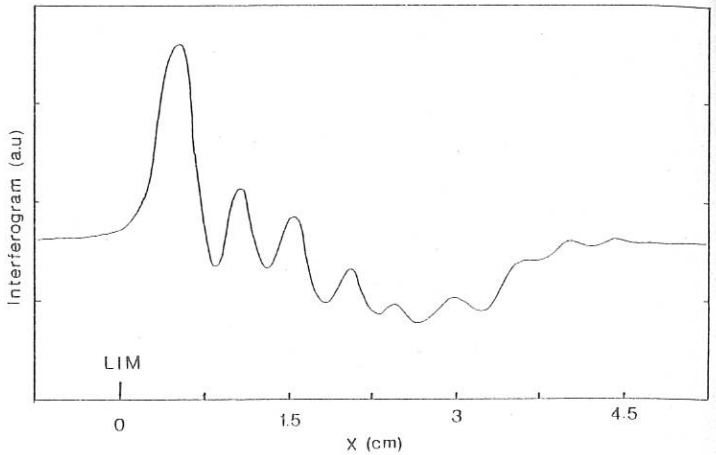

Fig. 1. - Plot of experimental interferogram in a. u., versus the plasma radius, obtained in H_2 plasma for $n_e = 10^{10}$ cm^{-3}, $T_e \approx 1$eV, $T_i \approx 0.3$ eV, neutral gas pressure P= 6×10^{-5} mbar, f = 5.5 MHz; the limiter is located at the origin x=0.

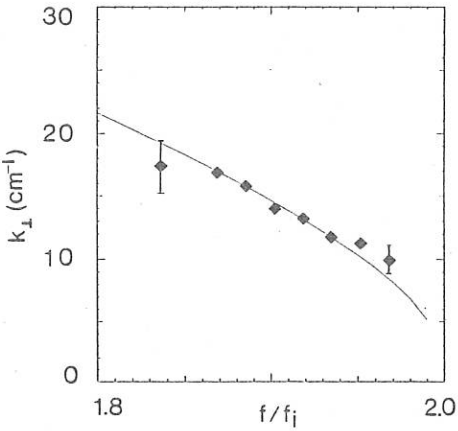

Fig. 2. - Fitting of experimental data by theoretical dispersion relation in H plasma with $n_e = 10^{10}$ cm^{-3}, $T_e \approx 1$eV, $T_i \approx 0.3$ eV, neutral gas pressure P= 6×10^{-5} mbar, f = 5.5 MHz.

Study of Low Frequency Flute Type Oscillations and their nonlinear Interaction in Toroidal Plasma

G. Prasad, D. Bora, Y. C. Saxena and G. C. Sethia
Institute for Plasma Research, Gandhinagar 382 424, INDIA

Magnetically confined low–β plasma is subjected to basically two types of low–frequency ($\omega \ll \Omega_i$, where ω is the observed frequency of the wave and Ω_i is the ion gyrofrequency) flute ($\mathbf{k}\cdot\mathbf{B} = 0$) instabilities viz., Kelvin – Helmholtz instability driven by velocity shear and curvature induced Rayleigh – Taylor instability (R–T). A number of experimental investigations pertaining to such instabilities have been carried out in different magnetic field geometries (Sugai et al.,1977; Komori et al.,1978; Bora 1989 and references therein). In all the above experiments the study of instability is confined to identification of the self excited modes and comparision with theoretical dispersion relations. In this paper we report a detailed study of the curvature induced R–T instability in a plasma confined by a pure toroidal magnetic field with its evolution from a coherent state to a turbulent state. The expriments have been carried out in toroidal device BETA and diagnostics and data acquistion system is described in detail by Prasad et al.(1992). The data is analysed using standard FFT technique as outlined by Smith et al., (1974) in order to obtain information of the cross power, mode number and coherence spectrum of the fluctuations.

The plasma density and floating potential profiles at 200 gauss of toroidal magnetic field is shown in figure 1. The density and potential profiles exhibit sharp gradients between radial locations from 0 to $\pm$ 3 cm and the rest of the regions have weak gradients. The density gradient scale length ($L_n = [1/n\partial n/\partial r]^{-1}$) as calculated from figure 1

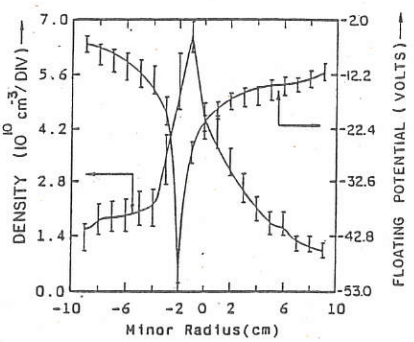

Figure 1: Radial profiles of the Density and Potential in BETA

between radial locations 0 to $\pm$ 3 cm is $\approx$ 6 cm and between radial locations $\pm$3 to $\pm$9 $\approx$ 10 cm. The electric field between radial locations 0 to $\pm$ 3 cm is $\approx$ 6.3 V/cm and between radial locations $\pm$3 to $\pm$9 cm is $\approx$ 0.6 V/cm. The electron temperature varies from 13 to 18 eV between radial locations 0 to $\pm$ 3 cm and has a value between 5 to 9 eV at other radial locations. Plasma has magnetised electrons ($\nu_{en}/\Omega_e \ll 1$) and ions ($\nu_{in}/\Omega_i \ll 1$).

The instability results presented here are obtained from measurements made in the regions away from the sharp density and electric field gradient locations. The measured value of $\tilde{n}_{rms}/n_o$ at 200 gauss of toroidal magnetic field varies from 10 to 50%. The fluctuations have $\tilde{n}/n_o \simeq e\tilde{\phi}/T_e$ at all radial locations. The curvature of the applied

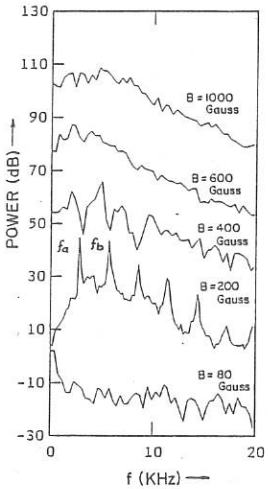

Figure 2: Cross Power spectra for density fluctuations at different magnetic fields. The vertical scale for each trace is shifted fo clarity.

magnetic field represents by effective gravity $g = C_s^2/R$ where C_s is the ion-sound speed and R is the major radius. The plasma in bad curvature region is subjected to R – T instability. In our experiment electric field varies nonuniformly with the radial locations (E(r) as shown in figure 1). This gives rise to a velocity shear $\perp$ to B, creating a possibility of exciting velocity shear instability. Due to curvature effects in curved magnetic fields, velocity shear instability tends to localise in the bad curvature region (Sugai et al.,1977). However, Guzdar et al.(1984) investigated the influence of velocity shear on R–T instability and arrived at a conclusion that the presence of velocity shear increases the growth rate of long wavelength portion of the R–T instability and reduces the growth rate of short wavelength portion of the R–T instability.

At low toroidal magnetic fields ($\leq$ 200 gauss) the fluctuations observed in floating potential and density are coherent. Cross power spectra of the oscillations picked up in bad curvature region of the plasma for various magnetic fields are shown in figure 2. The spectrum at 200 Gauss exhibits oscillations at frequency 2.8 $\pm$ 0.3 kHz together with peaks at integer multiples of this frequency with mode number m = 1, 2, 3, 4. The frequencies of these modes are less than Ω_i. The phase spectrum of these fluctuations indicates that the waves travel in azimuthal direction with a phase velocity $\simeq 2.4 \times 10^5$ cm/sec. The coherence spectrum ($\gamma_{12}(f)$) of fluctuations picked by two probes one of which was located in the good curvature region and other in the bad curvature region at a radial location 8 cm on the equatorial plane exhibits $\gamma_{12} \approx 0.9$ for the frequencies where the cross power peaks. This indicates that the same fluctuations are observed in both the regions. The phase difference between the density and floating potential fluctuations as measured by two probes seperated by 5 mm exhibits a phase difference of 165^o up to frequency 15 kHz which suggest that the observed modes are of flute type. The

measurement of radial and parallel wave numbers indicate that $\lambda_{\|} \gg \lambda_r$. The localisation condition $k_r L_n \approx 1$ is marginally satisfied .

In this geometry we may have basically two types of flute instabilities viz., velocity shear instability, due to $V_E(r) = E(r)/B$ where r is minor radius, and curvature induced instabilities. In a curved magnetic field the instabilities excited due to velocity shear and due to curvature of the magnetic field are coupled and modify one another. The velocity shear instability (Suagai et al.,1977) due to the curvature effects is localised in bad curvature region, which is also the favourable region for excitation of curvature induced Rayleigh–Taylor instability. The velocity shear scale length in our experiment is smaller than the azimuthal wave length, the radius of plasma and is nearly equal to the density scale length. The empirical value of the observed frequency for velocity shear instability for mode number m, as given by Perkins et al., (1971), is ≈ 0.2 to 0.5 times the maximum value of ω_E. Here $f_E = mE/(2\pi Br)$. In our experiment for m = 1, r = 8 cm, and $E/B \approx 3 \times 10^6$ cm/sec, $f_E \approx 13$ kHz to 32 kHz which is very large compared with the observed frequency. The real part of the frequency calculated using the dispersion relation given by Sugai et al. (1977) for velocity shear instability gives f$\approx$ 50 kHz for m=1 mode, which is again very large compared with the observed frequency. The real part of the frequency for R–T instability (Komari et al. 1979) has dominant contribution from $k_\theta E/B$. In our experiment it is ≈ 4.7 kHz. Guzdar et al. (1984) have discussed in detail the effect of velocity shear on the R–T instability. They suggest that pure R–T instability favours the excitation of $k_\perp L_n > 1$ modes while pure Kelvin–Helmholtz instability driven by velocity shear favours the excitation of $k_\perp L_n < 1$ modes. For generalized Rayleigh–Taylor instability, in which both these instabilities coexist, the velocity shear preferentially excites the long wave length modes of R–T instability. All these arguments indicate that the observed peak at 3 kHz with m = 1, may be due to the curvature induced R–T instability favoured by the presence of velocity shear. The observation of similar fluctuations in the good curvature region in our experiment cannot be explained by linear theories. The reason may be that the large $\vec{E} \times \vec{B}$ motion of the plasma might carry these flucutuations, from the bad curature region where they are generated, to the good curvature region. It is seen from figure 2 that the coherent fluctuations gradually disappear as the magnetic field is increased and the spectrum becomes turbulent beyond 600 Gauss.

The coherent modes observed at low magnetic field of 200 Gauss, besides being harmonics of the fundamental frwuency at 3 kHz, also satisfy the resonance conditions on ω and k viz. $\omega_3 = \omega_2 + \omega_1$ and $k_3 = k_2 + k_1$. Bispectral analysis (Kim and Powers, 1979) is used to identify the spontaneously excited modes and nonlinearly coupled modes in self excited oscillations. Bicoherence is a measure of degree of phase coherence between the waves which is defined as follows:

$$b^2(\omega_1, \omega_2) = \frac{| B(\omega_1, \omega_2) |}{P(\omega_1) P(\omega_2) P(\omega_1 + \omega_2)} \quad (1)$$

where $P(\omega)$ is autopower spectrum. If $b^2 = 0$ the three spectral components are completely independent and randomly phase mixed. The power at ω_3 then has source other than the coupling between ω_1 and ω_2. $b^2 = 1$ will indicate a high degree of phase coherence, in which case the wave at ω_3 will be produced by efficient coupling between the waves at ω_1 and ω_2. The variance on bicoherence is estimated by

$$var(b) = \frac{(1 - b^2(\omega, \omega_2))}{M} \quad (2)$$

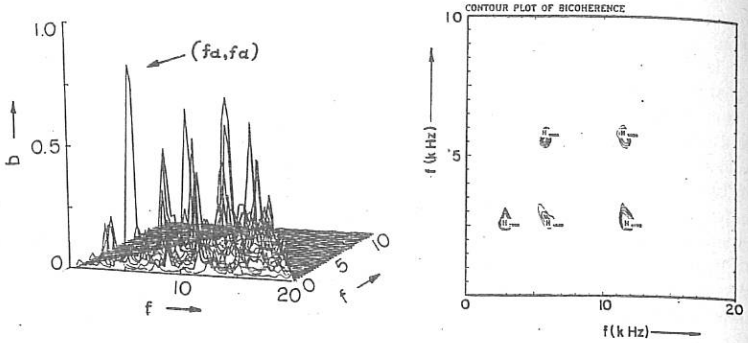

Figure 3: (a) Bispectrum of density fluctuations at 200 Gauss field. (b) Countour plot of the bicohrence spectrum of figure 3(a).

The strength of the coupling for the interaction is estimated by coupling coefficient which is defined as follows

$$A_{1,2} = \frac{B^*(\omega_1, \omega_2)}{P(\omega_1)P(\omega_2)} \tag{3}$$

The bicoherence spectrum for the case of fluctuations at 200 Gauss is shown in figure 3a and the contour plot of the same is shown in figure 3b. The bispectrum has one prominent peak at (f_a, f_a) with bicohrence of $\sim$0.8 indicating that f_b is first harmonic of f_a. The bicoherence spectrum has a small preak with bichorence of 0.45 indicating that half the power is contributed by the nonlinear interaction of waves at $(f_a, 2f_a)$. There are strong peaks at interaction frequencies $(f_a, 3f_a)$ and $(f_a, 4f_a)$ with a bichorence of 0.7 which cannot be analysed by using bispectral analysis.

To summarise, an experimental investigation of flute type electrostatic fluctuations in toroidal low-β plasma is reported. The transition from coherent state to turbulent state as a function of toroidal magnetic field strength is described. The fluctuations are coherent at low toroidal magnetic field values ($\leq$ 200 gauss). The coherent mode with mode number m = 1 and $f \approx 3$ kHz is identified as due to curvature induced R–T instability favoured by velocity shear. When the toroidal field is increased the fluctuations become turbulent.

References

Bora, D., *Phy.lett A.* **137(7)**, 308 (1989).
Chen F. F, *Phys. Fluids* **8**, 912 (1965).
Guzdar, P. N., P. Satyanarayana, J.D. Hubba & S.L. Ossakow, *Geophys. Res. lett.* **9**, 547 (1982).
Komori, A., N. Sato & Y. Hatta, *Phys. Rev. lett.* **15**, 381 (1978) .
Kim Y. C & Powers E. J *IEEE. Trans. Plasma. Sci.* PS-7, 120 (1979).
Perkins, F. W., & D.L. Jassbay, *Phys. Fluids* **14**, 102 (1971).
Prasad, G., D. Bora & Y.C. Saxena, *Geophys. Res. Lett.*, **19**, 241, (1992).
Sugai, H., A. Komari, T. Sawafuzi, N. Sato & Y. Hatta, *Phys. Fluids* **20**, 90 (1977).
Smith D. E., E. J. Powers & G. C. Caldwell *IEEE. Trans. Plasma. Sci.* **PS-2**, 260 (1974).

BEHAVIOUR OF CHARGED PARTICLE MOTION ALONG AN INHOMOGENEOUS MAGNETIC FIELD AND A RETARDING ELECTRIC FIELD - EVIDENCE FOR THE EXISTENCE OF DISCRETE ENERGY STATES

R.K.Varma and A.M.Punithavelu

Physical Research Laboratory, Ahmedabad-380009, India

We report here rather astonishing observations in the motion of charged particles (electrons) in an (in general) inhomogeneous magnetic field in the presence of a retarding electrostatic potential. The motivation for this study is a theoretical prediction[2] made for this system, based on a formalism developed by Varma[1]. The comparison of the experimental results with theory is presented in the later part of the paper.

To study the above motion electrons from an electron gun are injected from one end of an SS vacuum chamber (3m long and 27cm dia) permeated by an axial magnetic field, with a small pitch angle ($<5^{o}$) to it. At the other end of the chamber is a Faraday cup detector which can be moved along the axis of the chamber so as to vary its distance from the gun. The Faraday cup itself consists of a grounded collector plate with a grid, at 10mm in front of it which can be raised to any desired potential. The electron gun, capable of producing a beam in the energy range zero and 3KeV, gives an electron beam which gets focussed to a fine spot ($\approx$ 2mm dia) in the presence of a magnetic field, at points along the magnetic field at distances, $L \cong 2\pi n \upsilon_{\parallel}/\Omega$, away from the gun ($\upsilon_{\parallel}$ = parallel velocity component and Ω = eB/mc, the gyrofrequency). The magnetic field in the chamber is produced by a set of 35 current carrying coils equally spaced at a distance of 8.5cm. The system is shown as a scale drawing in Fig 1.

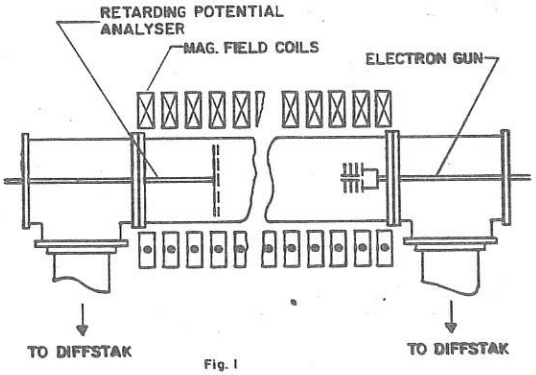

Fig. 1

The experiment is carried out by first fixing a certain distance L (= 30cm), between the gun and the detector and choosing an electron energy $\mathcal{E}$ (= 600eV), and a spatially averaged magnetic field $\bar{B}$ (= 170gauss). The detector grid is then raised to a negative potential $\Phi_m > (\mathcal{E}/e)$. All the beam electrons are thus stopped by the retarding potential and the plate current is then recorded as the grid voltage is allowed to drop from $-\Phi_m$ to zero. The record of the plate current as a function of the applied negative grid potential actually obtained in the experiment is shown in Fig 2a. The plot is clearly far from monotonic and indeed exhibits a number of maxima and minima whose separation decreases monotonically with the retarding potential Φ. Moreover, the envelope of the oscillations also exhibits a modulation with the potential.

However, before we discuss the various conventional possibilities that may conceivably lead to these effects we shall first see whether the allowed, observed energy peaks in Fig 2a can be fitted into the relation(1) given below which is supposed to describe these peaks according to the theory[1,2]

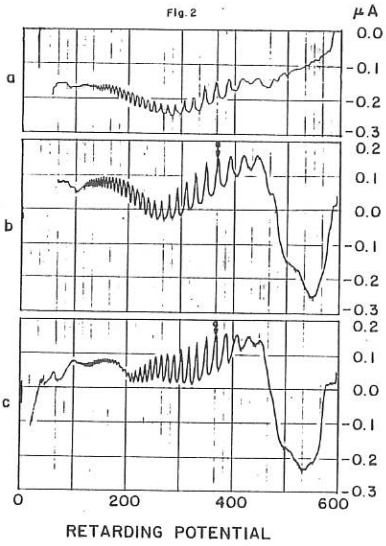

$$E_j = \frac{1}{2} m \left(\frac{3\Omega L}{2\pi}\right)^2 \Big/ (j + 1/4 - \phi/2\pi)^2; \quad (1)$$

where E_j is the energy corresponding to an integer j labelling the peak, (j is an analogue of a quantum number), L is the distance between the electron gun and the detector, and ϕ is an undeterminned phase.

We choose for simplicity every third peak starting from a peak labelled as 'a' in the figure. The energies E_j corresponding to these peaks and the values of $(j + 1/4 - \phi/2\pi)$ as calculated from (1) and the j (integer) values so identified are given in the following Table.

peaks	Energy E_j (eV)		$j + 1/4 - \phi/2\pi$		j	
	plot 2b	plot 2c	plot 2b	plot 2c	plot 2b	plot 2c
a	367	368	36+0.0	45-0.7	36	45
b	308	317	39+0.2	48-0.2	39	48
c	262	278	42+0.6	51+0.0	42	51
d	227	245	45+0.7	54+0.4	45	54
e	198	217	48+0.9	57+0.8	48	57

It is found that within the accuracy of the determination of the average magnetic field, the integers j do differ from each other by three in surprising conformity with the choices made. Lest it should be regarded as accidental, we have found such integer identifications for energy peaks with other values of the magnetic field and length L. Of course, the j values for a particular neighbourhood of an energy value would be smaller or larger depending on the smaller or the larger value of (ΩL). The important point, however, is that they do differ by unity for consecutive peaks; this is particularly significant when large j values (~ 35-50)are identified. It is, of course clear that the lower values of j would correspond to higher energies, for a given value of Ω and L, so that a higher energy beam is required to explore lower 'quantum numbers'. This has also been verified to be the case.

Since the observed behaviour is so unexpected à la the standard paradigm, it is desirable to try to rule out various conventional possibilities as its explanation. The first of these is the question whether the periodic structure of the grid may be playing a role. This was ruled out, both by measuring the grid current (besides the plate current) as well as by removing the grid and applying the bias to the plate itself as we measure the plate current. The observed effect persists in the latter case, while the grid current also (Fig 2b) shows a behaviour in phase with the plate current. Thus grid could not be playing any role in causing this effect. The grid current profile obtained for a different value of magnetic field B (= 210 gauss) is shown in Fig 2c.

Another possibility is to argue that the dips in the transmitted current may be caused by the scattering of the beam electrons by electrostatic fluctuations generated by some beam instability. However with the beam current as low as ~ 0.1μA, and a vacuum of ~ 5.10^{-7} torr, the beam number density n ~ 10^4-10^5 cm^{-3}, falls far too short for the beam instability condition to be satisfied.

It should finally be mentioned that perhaps, the most striking feature of the observed result, as indeed of the relation (1), is the dependence of the allowed energy peaks on the length L of the box - the distance between the gun and the detector. Such a dependence signifies a wave-like nonlocality which is contained in the formalism of Ref 1, and hence the relation (1), but which is difficult to understand in terms of the standard initial value paradigm of classical mechanics.

In summary it is important to highlight again the following facts that we have demonstrated:

(i) That the discrete allowed states of motion do exist in the domain of parameters where one would use classical mechanical equation of motion to determine the motion.

(ii) That the energies of these allowed states are well represented by the relation (1) which in fact, formed the basis of the prediction. This relation is obviously non quantal, as there is no Planck quantum $\hbar$ in it.

(iii) That the allowed states E_j , form a hydrogen-like sequence for which 'quantum numbers' j and the phases ϕ can be identified as shown in the Table.

(iv) That the allowed energy values E_j and the associated quantum numbers j depend in a continuous manner on the length L of the 'box'. This is a manifestation of wave-like nonlocality which is not known to be a characteristic of the standard initial value paradigm of classical mechanics.

Finally, astonishing as it may sound, it is clear that because of the above mentioned characteristics of the observed effect, nonlocality in particular, the solution of the classical mechanical Lorentz equation of motion with appropriate initial conditions would not be able to reproduce the observed behaviour.

References:

1. Varma R.K. 1985 Phys. Rev. A31. 3951.

2. Varma R.K. 1991, A variety of Plasmas, proc. Intl. Conf. Plasma Phys. Delhi, p.235.

UNSTABLE BEHAVIOUR OF GLOBULAR ANODE STRUCTURES

L.Biborosch, M.Toma and M.Sandulovicіu
Faculty of Physics, "Al.I.Cuza" University
R-6600 Iasi, Romania

It was shown that using a small and narrow transverse magnetic field applied near the hollow cathode of a d.c. glow discharge in He, different states of nearly globular luminous space charge structures (GLSs) formed in front of the anode can be obtained /1/. Depending on the intensity ($B_\perp$) and axial position ($d_{B_\perp}$) of this magnetic field from the cathode (see also fig.1), the spatial dimensions and the transition from a regular to the chaotic behaviour of the GLSs can be determined. The experimental device shown in fig.1 was used with regard to the influence of secondary electron emission at the discharge tube wall on the GLS stability /2/. Therefore, a small hollow anode A_1 was connected through the variable resistor R_v with a stainless steel mesh grid A_2, which covers the inner surface of the glass tube wall and acts as a second anode /3/.

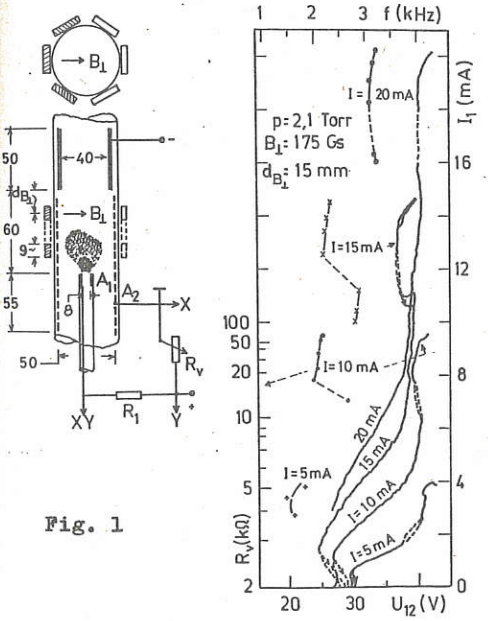

Fig. 1

Thus, without changing the discharge current I, the current-voltage I_1-U_{12} characteristic of the circuit between the small anode and the large one, can be plotted as in fig.1.

It is seen that, almost independent on the discharge current I, the I_1-U_{12} characteristics are showing two different branches with negative slopes (indicated by the

dotted segments). The first one is started at very small currents I_1 through the small anode and potential differences to the large one of about $U_{12} = 30$ V, when a small but stable GLS is also pelling off from the small anode cavity. For an increase of the variable resistance with approx. 50 % from its initial value of $R_v = 2$ kΩ, this first negative slope disappears at currents of $I_1 = 2$ mA and potential differences of at least $U_{12} \geq 24$ V. By the further increase of the resistance R_v to about ~ 10 kΩ, the spatial dimensions of a general unstable GLS are gradually increased up to the conditions when the second negative slope on the same I_1-U_{12} characteristic is set in. These slopes are obtained for currents I_1 which are approx. 75% of the discharge current I and potential differences which are not exceeding $U_{12} \leq 40$ V. During of the run through this second negative slope, the spatial dimensions and structure of the GLSs are suddenly changed together with their temporal behaviour. Finally, the maximum I_1- U_{12} values are obtained for $R_v \geq 100$ kΩ when the large anode returns to its usual floating potential. Obviously, the value of the negative resistances, which correspond to these two negative slopes, are also differing by an order of magnitude.

In the same figure the values of the fundamental frequency for the current and potential fluctuations in the anode circuit are indicated by dots. Those amplitudes can attain up to 20 % of their d.c. values, but the fundamental frequencies remain nearly constant over the I_1 - U_{12} domain situated above the second negative slope.

Therefore, to obtain a better insight into the correlation between the features of the I_1 - U_{12} characteristics and the unstable behaviour of the GLSs, we have analyzed the frequency spectra of these current and potential fluctuations for different He pressures and transverse magnetic fields. Thus, for an increasing He pressure (fig.2) and magnetic field intensity near the cathode (fig.3) or the GLS (fig.4), the chaotic behaviour of the unstable GLSs and also the second negative slope on the I_1 - U_{12} characteristics become more evidently. This is true under the conditions corresponding to

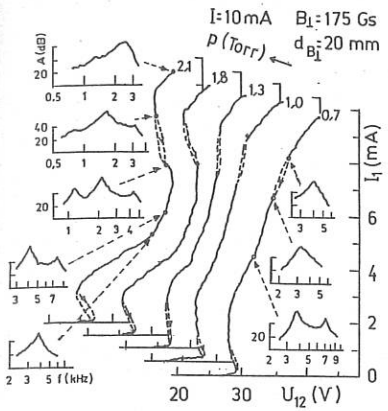

Fig. 2

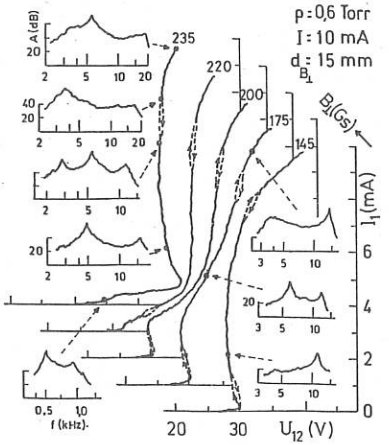

Fig. 3

the I_1-U_{12} values situated above the second negative slope and also to the floating anode A_2. The unstable GLSs with a rather regular behaviour are obtained for lower gas pressures and magnetic field intensities, usually for I_1 - U_{12} values which are situated below the second negative slope.

As is also seen in the figs.2, 3 and 4, for these last conditions the initial negative slope is gradually changing into a positive one in spite of the regular instability of the GLSs. This can be due to the decrease of the negative resistance value below those of the $R_\sim$ ones with decreasing He pressures or/and magnetic field intensities. It must be noted that under our experimental conditions the regular behaviour of the unstable GLSs is rather an exception. Only by using the proposed anode circuit we can enlarge the He pressures and magnetic field domain where this regular behaviour of GLSs can be obtained. As a limit situation, at very small currents $I_1 \leq 1$ mA typical relaxation oscillations with a very low frequency (~ 1 kHz) are found for higher magnetic fields nearly independently of the He pressure (the

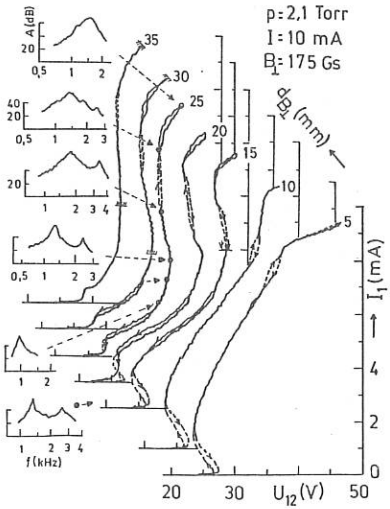

Fig. 4

frequency spectra from the left in the bottom of fig.3 and 4). These are rather similarly with the unstable anode spots studied in /4/.

In conclusion, the presented data prove that: i) the deviation of the fast electrons originating from the cathode by the help of a transverse magnetic field allows us to control the GLSs appearance and ii) the currents collected by an usual anode and a very large one placed at the discharge tube wall are able to control the reciprocal dynamics of the double layers (DL) which are involved in the GLSs instability in order to be correlated.

In this manner it was possible to determine the transition from an ordered to a disordered (chaotic) behaviour of this d.c. glow discharge at higher pressures and to emphasize that the same processes which are implied in the generation and disruption of the GLSs stand also at the origin of the spatio-temporal structures (oscillations, noise and chaos) which are observed as a rule in several plasma devices.

/1/ L.Biborosch and M.Sanduloviciu, XXth ICPIG, Pisa 1991, Contr.Pap., vol.2, p.460

/2/ M.Sanduloviciu, Z.Physik, 225, 248 (1969); Z. amgew. Phys., 26, 319 (1969)

/3/ R.Arndt, Beitr.Plasmaphys., 16, 145 (1976)

/4/ Bin Song, N.D'Angelo and R.L.Merlino, J.Phys.D : Appl.Phys., 24, 1789 (1991)

ON THE ELECTRODYNAMIC EXPLANATION OF THE RETROGRADE MOTION OF THE ELECTRIC ARC

J.S.Hong and J.E.Allen
Department of Engineering Science, University of Oxford,
Parks Rd, Oxford, OX1 3PJ, UK

1 Introduction

The retrograde motion of the cathode spot in a transverse magnetic field is one of the more intriguing phenomena of the electric arc. Although the phenomenon has been known for nearly ninety years since its discovery by Stark [1] and has stimulated numerous investigations which result in many models giving explanation from different points of view, there is still no theory that can account both qualitatively and quantitatively for all the observations.

Most of the explanations of the retrograde motion involve the study of cathode processes to give the preferential formation of new cathode spots along the retrograde direction [2]. One line of explanation, which is rather different from the others, is based on electrodynamics [3,4]. In this approach the retrograde motion is treated as an electrodynamic event.

The present paper develops the theory suggested by Robson and von Engel [3,4]. A more complete model is proposed and studied in detail by means of electromagnetic field theory. The results obtained not only show that the retrograde motion can be explained by the electrodynamics, but also confirm that the average current density on the cathode spot must be around the order of $10^{12} A/m^2$. Recent studies of spot current density have shown values of this order [6].

2 The Model

The physical model to be investigated is shown in Fig.1, which is based on the following facts (i) that the radius of the cathode spot, which is no greater than $10^{-3} cm$ [6,7,8] , is much smaller than the dimensions of the cathode; (ii) that the distance from the anode to the cathode is much larger than the radius of the cathode spot and (iii) that the arc column is deflected in the Lorentzian direction [3,9,11,20].

According to Robson and von Engel [3,4] that the magnetic field acting upon the cathode spot is the sum of the applied field B_a and a self-field $-\mu_o I/R$, where I is the arc current and R an effective radius of curvature of the arc column where it joins the spot (see Fig.1). The direction of motion is then determined by the direction of the field B, given by

$$B = B_a - \mu_o I/R \tag{1}$$

Retrograde motion occurs if the self-field exceeds the applied field.

Smith [11] has criticised this model on the grounds that the self-field is unable to exceed the applied field according to his calculations. However, Guile and Seeker [14] pointed out that the magnetic field values deduced by Smith are open to doubt inasmuch as the current density in a discharge varies considerably over the cross section so that the calculation of the forces is somewhat complicated and the fields cannot be determined in the simple way employed by Smith.

We believe as Robson and von Engel, that the retrograde motion can be understood in terms of electrodynamics, but we do not agree with their criterion for occurence of the retrograde motion because the cathode spot in reality is not just a point and over it the fields change from point to point, so do the forces. Therefore the retrograde motion cannot be judged by the field given by Eqn.(1).

Following the above arguments, we suggest that the direction of motion is determined by

$$F_R + F_L = \iint_{spot} \mathbf{f}(\mathbf{r}) \cdot \mathbf{a}_\perp \, dS \tag{2}$$

where $\mathbf{f}(\mathbf{r})$ is the electrodynamic force density; $\mathbf{a}_\perp$ is the unit vector parallel to the spot surface but perpendicar to the applied magnetic field; F_R and F_L represent the resultant forces per unit length exerted on the spot in the retrograde and the Lorentzian directions respectively. If $|F_R| > |F_L|$, retrograde motion occurs.

3 Theory

The model used here is a steady-state one employing Ohm's law, $\mathbf{J}(\mathbf{r}) = \sigma\mathbf{E}(\mathbf{r})$, so that

$$\nabla^2 V(\mathbf{r}) = 0 \ \textit{where} \ \mathbf{E}(\mathbf{r}) = -\nabla V(\mathbf{r}) \tag{3}$$

The magnetic induction is given by

$$\mathbf{B}(\mathbf{r}) = \nabla \times \mathbf{A}(\mathbf{r}) \ \textit{where} \ \mathbf{A}(\mathbf{r}) = \frac{\mu_o}{4\pi} \int_{v'} \frac{\mathbf{J}(\mathbf{r}')}{|\mathbf{r} - \mathbf{r}'|} \, dv' \tag{4}$$

where $\mathbf{r}'$ is the source position vector. Hence the magnetic force per unit volume can be calculated

$$\mathbf{f}(\mathbf{r}) = \mathbf{J}(\mathbf{r}) \times (\mathbf{B}(\mathbf{r}) + \mathbf{B}_a) \tag{5}$$

where $\mathbf{B}_a$ is the known constant magnetic induction applied. Eqn. (3) is the familar Laplace's equation. It is obvious that if the scalar potential is known the other field quantities of interest can be determined.

The solution of Laplace's equation can be found in terms of the integration equation

$$V(\mathbf{r}) = \frac{1}{c} \iint_{\Gamma} \left(G(\mathbf{r}, \mathbf{r}') \frac{\partial V}{\partial n} - V \frac{\partial G(\mathbf{r}, \mathbf{r}')}{\partial n} \right) d\Gamma \tag{6}$$

where $c = 1$ if $\mathbf{r}$ is inside the homogenous region Ω enclosed by the boundary Γ and $G(\mathbf{r}, \mathbf{r}')$ is the Green function. The boundary element method (BEM) is employed to solve Eqn. (6) for various shapes of the arc column. The details of the solution will be the subject of another paper and will not be discussed further here.

4 Results and Discussion

For our investigation, the plasma column is bent step by step as Fig.2 shown. The field components in which we are interested are computed and ploted in Fig.3, where the normalized current density is given by j_z/j_a with $j_a = I_o/\pi r_o^2$, the average current density of the cathode spot; the normalized magnetic induction is defined by $B_x/\mu_o\sqrt{I_o j_a}$ and the normalized force density results from the multiplication of the normalized current density and the normalized magnetic induction. It should be noted that the applied magnetic field is not involved in Fig.3.

One can see from Fig.3 that the numerical results for arc 1 (refer to Fig.2) are in good agreement with the analytical one denoted by the dotted lines. As the plasma column becomes more bent, the numerical results for the bent arcs change smoothly in the direction indicated by the arrows. It turns out that as the plasma column is bent in the Lorentzian direction due to the applied magnetic field, the current density over the cathode spot is no longer uniform and becomes stronger on the Lorentzian side while weaker on the retrograde side. The similar tendency for changing the distributions of the self magnetic induction and the force density due to the self-field is obtained. These distributions for a typical bent arc can be clearer seen in Fig.4.

It is obvious that in the absence of the applied magnetic field, the cathode spot of the bent arc would always move in the retrograde direction. However, it should be kept in mind that the bending of the plasma column is attributed to the applied field which is in favour of the motion in the Lorentzian direction. According to our model, therefore, there exist the two opposite motion tendencies within the cathode spot region and the spot will move as a whole in the direction in which the force is dominant.

To demonstrate our model, we chose a set of experimental data from different sources and inserted them into our theory. Because of the limitation on space only one set of results is tabulated in Table 1. One can first see that the retrograde motion can indeed be predicted by our model if the average current density j_a is of the order of $10^8/cm^2$, which is in agreement with the values suggested by recent studies of spot current density [6,8,15]. A number of the reported features of the retrograde motion can be explained by our model as below.

- *The retrograde motion is temperature dependent. With increasing cathode temperature, the retrograde velocity decreases [18]; and the retrograde motion can be reversed if the temperature is sufficiently high [13].* As the cathode temperature is increased, the spot current density is observed to decrease [18]. In our model the ratio of $|F_R/F_L|$ decreases with decreasing spot current

j_a (A/cm^2)	arc (Fig.2)	$\lvert F_L\rvert/r_e^2$ (N/m^3)	$\lvert F_R\rvert/r_e^2$ (N/m^3)	$\lvert\frac{F_R}{F_L}\rvert$	motion predicted
10^6	2	7.99×10^{-8}	0.00	0.00	Lorentzian
	3	7.37×10^{-8}	7.89×10^{-8}	1.07×10^{-3}	Lorentzian
	4	6.60×10^{-8}	6.96×10^{-7}	0.01	Lorentzian
10^7	2	8.71×10^{10}	3.70×10^{10}	0.42	Lorentzian
	3	7.66×10^{10}	4.64×10^{10}	0.61	Lorentzian
	4	6.31×10^{10}	7.18×10^{10}	1.13	retrograde
10^8	2	1.64×10^{12}	2.08×10^{12}	1.27	retrograde
	3	1.40×10^{12}	2.47×10^{12}	1.76	retrograde
	4	1.10×10^{12}	3.52×10^{12}	3.20	retrograde

Table 1. $I_0 = 50\,A$, $B_a = 0.3\,Tesla$, copper cathode, motion observed: retrograde, ref. [9]

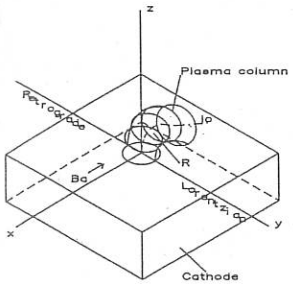

Fig.1 Physical model of an arc

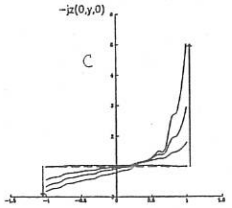

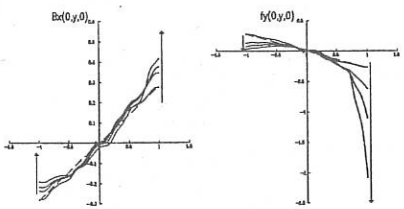

Fig.3 Fields of arcs

— — — : analytical ——— : numerical

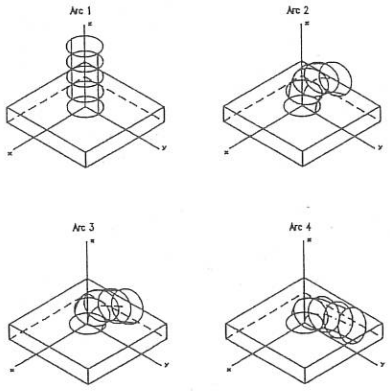

Fig.2 Deformation of arcs

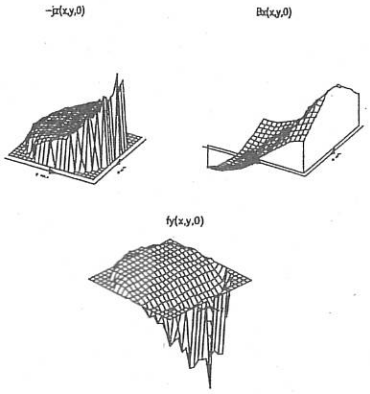

Fig.4 Field distributions

density; thus the retrograde velocity decreases with increasing cathode temperature. If the cathode is heated to a sufficiently high temperature, which can vary with the cathode material, the spot current density can be so low that $|F_R/F_L| < 1$ and the motion is reversed.

- *Lower background gas pressures favour the retrograde motion and the motion can be reversed if the gas pressure rises above a critical value.* The bending of the arc also depends on the background gas pressure. The lower the pressure, the more bent is the arc column. As a result, the ratio of $|F_R/F_L|$ increases and so does the retrograde velocity. On the contrary, if the pressure is increased, the arc column becomes straight and the ratio of $|F_R/F_L|$ decreases and can be smaller than one above a certain pressure so that the direction of motion changes to the Lorentzian direction.

- *The retrograde velocity is generally found to increase with an increase in the magnitude of the applied magnetic field. However, reversal of the motion occurs with a very strong field.* The model proposed clearly shows that the two simultaneous effects of the applied magnetic field, namely (a) bending the arc column in the Lorentzian direction; (b) enhancing the force component F_L. Because the first effect is in favour of the retrograde motion and is opposite to the second one, the resultant effect of increasing the applied magnetic field will depend on the dominant one of the two effects. As the applied magnetic field is increased from a lower level, the arc column is expected to be bent at first rapidly and then less so due to a limit of the bending. Hence, the first effect is dominant and the retrograde velocity increases before this limit is reached. Then, the second effect becomes dominant and the motion will be reversed when $|F_L| > |F_R|$.

- *The critical pressure increases with an increase of the applied magnetic field.* As previously stated an increase in the applied magnetic field will cause the arc column to bent before reaching a limit. On the other hand, an increase in the background gas pressure makes the arc column straighter. At a reversal position of the arc column, the effects of the increase in the two quantities can cancell each other out which directly leads to the observed result.

- *In vacuum or low pressure the retrograde velocity was found to increase with an increase in arc current [16,17,19].* According to the proposed model it can be shown that the ratio of $|F_R/F_L|$ increases with an increase in arc current, so does the retrograde velocity.

- *The retrograde motion depends on the material and surface condition of the cathode [14,22].* The connection of the present model to this feature is twofold. First, the cathode current density is found to be material-sensitive, so is the force predicted by the model. Secondly, the spot is a plasma source of dense metal vapour evaporated from the cathode material so that the plasma mass density of the spot will also affect the spot motion.

References

[1] Stark J, *Phys.Zeit. 4 (1903) 440*

[2] Drouet MG, *IEEE Trans. PS-13 (1985) 235*

[3] Robson AE and von Engel A, *Phys. Rev. 93 (1954) 653*

[4] Robson AE and von Engel A, *Phys. Rev. 104 (1956) 15*

[5] Robson AE, *J. Phys.D: Appl. Phys.11 (1978) 1917*

[6] Juttner B, *IEEE Trans. PS-15 (1987) 474*

[7] Daalder JE, *IEEE Trans. PAS-93 (1974) 1747*

[8] Daalder JE, *Ph.D. Thesis, Eindhoven University of Technology (1978)*

[9] Roman WC, *Proc. 6th Int. Conf. Ion. Gases, 2 (1963) 287*

[10] Carter RP and Murphree DL, *J.Appl. Phys. 44 (1973) 5190*

[11] Smith CG, *J.Appl. Phys. 28 (1957) 1328*

[12] Smith CG, *Phys. Rev. 63 (1943) 217*

[13] Smith CG, *Phys. Rev. 73 (1948) 543*

[14] Guile AE and Secker RE, *J.Appl Phys. 29 (1958) 1662*

[15] Smeets P, *Ph.D. Thesis, Eindhoven University of Technology (1987)*

[16] Gallagher CJ, *J.Appl.Phys. 21 (1950) 768*

[17] Fang DY, *J.Phys.D: Appl.Phys. 15 (1982) 833*

[18] Fang DY, *IEEE Trans. PS-11 (1983) 110*

[19] Swift PD, McKenzie DR and Falconer IS, *J.Appl.Phys. 66 (1989) 505*

[20] Carter RP and Murphree DL, *J.Appl.Phys. 44 (1973) 5190*

[21] Yamamura J, *J.Appl.Phys. 21 (1950) 193*

[22] Hermoch V, *IEEE Trans. PS-1 (1973) 62*

NONEQUILIBRIUM TRANSPORT PHENOMENA OF A PLASMA IN NONUNIFORM ELECTRIC FIELD

G.Cicconi, V.G.Molinari* and M.Sumini*
Dipartimento di Ingegneria Elettrica, Universita' di Genova (Italy)
* Laboratorio di Ingegneria Nucleare, Universita' di Bologna (Italy)

It is well known that the charged particles of a weakly ionized plasma in their random thermal motion from one region of the gas to another tend to transport with them the properties of the region from they come. In particular if these macroscopic properties are nonuniform, the particles become themselves out of equilibrium with properties where they arrive. In this context we analyze, in cylindrical coordinates, these transport phenomena in the presence of nonuniforn static electric field generated between a cylindrical conductor, considered as point form, and a planar conducting wall (this field is known as corona or also marconian dipole field). A strong steep temperature gradient is considered present between the hot charged conductor and the cold wall.

The analysis method applied here is based on the integral form of the Boltzmann equation of the test particles, especially electrons, linearized and with the effects of the boundaries taken into full account. This formulation may be considered valid for any arbitrary ratio of the scale length to the mean free path /1/. It is known that this integral Boltzmann equation may be reduced to an inhomogeneous system of differential equations by choosing a proper degenerate (elementary) scattering kernel /1/. The associate homogeneous system may give a dispersion determinantal equation for diffusion waves along with the stability and resonance conditions for the wave propagation.

In particular as a first approach, a BGK model is presented, analyzed and harmonic eigenmodes calculated. An experimental test based on the measurements of the electron density and current distributions in a low density and temperature plasma is here proposed.

We consider the linearized integral Boltzmann equation with a scattering kernel of elementary type as follows

$$K(\underline{v}' \to \underline{v}) = \sum_{1}^{N} \Phi_1(\underline{v}')\, \Psi_1(\underline{v})$$

where $\Phi_1(\underline{v}')$ and $\Psi_1(\underline{v})$ are two proper sets of functions convergent in

v-space and with the moment of the distribution function

$$\xi_i(\underline{x},t) = (\Phi_i,f) = \int_{\mathbb{R}_3} \Phi_i(\underline{v}')\, f(\underline{v}')\, d^3v'.$$

Then we may write the Boltzmann equation for test particles of mass m_t in the following integral form

$$f = h + K_1 \sum_{1}^{N} \Psi_i \xi_i - K_2 \sum_{1}^{N} \left((\underline{F}/m_t) \frac{\partial \Psi_i}{\partial \underline{v}} \xi_i + \Psi_i \frac{d\xi_i}{dt} \right), \tag{1}$$

where

$$h = f(\underline{x}(L),\underline{v}(L),t-L)\, \exp\left[-\int_0^L \nu d\tau\right] + \int_0^L \underline{Q}(\underline{x}(\tau),\underline{v}(\tau),t-\tau)\, \exp\left[-\int_0^L \nu d\tau'\right] d\tau ,$$

$\underline{Q}$ and $\underline{F}$ are the external source term and force respectively,

$$\frac{d}{dt} = \frac{\partial}{\partial t} + \underline{v} \frac{\partial}{\partial \underline{x}},$$

ν is the collision frequency generally considered velocity dependent, L is the boundary phase of the temporal solution to the characteristic equation

$$\frac{1}{2} \frac{\underline{F}}{m_e} t^2 - \underline{v}t + \underline{x} = 0 \tag{2}$$

where $(\underline{x},\underline{v})$ is a point of the phase space,

$$K_1 = \int_0^L \exp\left[-\int_0^\tau \nu d\tau'\right] d\tau, \quad K_2 = \int_0^L \tau \exp\left[-\int_0^\tau \nu d\tau'\right] d\tau,$$

are two collisional moments dependent on the phase $(\underline{x},\underline{v},L)$. By operating a scalar product in v-space, eq. (1) may be reduced to a linear system of differential equations, as follows

$$\sum_{1}^{N} (\Phi_j, K_2 \Psi_i \frac{d}{dt}) \xi_i + \sum_{i}^{N} \frac{\underline{F}}{m_t} (\Phi_j, K_2 \frac{\partial}{\partial \underline{v}} \Psi_i) \xi_i - \sum_{1}^{N} (\Phi_j, K_1 \Psi_i) \xi_i + \xi_j = (\Phi_j, h) \tag{3}$$

$$j = 1,2,\ldots,N.$$

The BGK solution for electron dynamics. In this case, we assume the collision frequency ν = const, N = 1 in (3), $\Psi_1(v) = \nu(\Gamma/\pi)^{3/2} \exp[-\Gamma v^2(\tau)]$ where $\Gamma = m_e/(2T_e)$ and $\Phi_1 = 1$. The external force in cylindrical coordinates has the following polar components

$$F_r(r,\vartheta) = \frac{q^2 l^2}{r^3} \cos\vartheta, \quad F_\vartheta(r,\vartheta) = \frac{q^2 l^2}{r^3} \sin\vartheta$$

of an electric dipole where, as shown in Fig.1A, q=-Ze is the electric charge located in (1/2,0) of the cylindrical conductor (point form) generating the electric field with respect to the line $G(0,\pm\pi/2)$ which

is supposed to zero potential. The point charge q and the line G represent, in the (r,ϑ) plane, respectively the section of a line and a plane both perpendicular to the (r,ϑ) meridian plane and parallel to the z-axis (Fig. 1B). For a steady state equilibrium $(\partial/\partial t=0)$ the linear system (3) is reduced to the following linear differential equation,

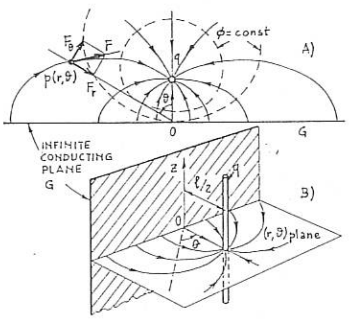

Fig. 1

$$(1,K_2 v_r \Psi_1)\frac{\partial \xi}{\partial r} + (1,K_2 v_r \Psi_1)\frac{\partial \xi}{r\partial \vartheta} - (1,K_1\Psi_1)\xi + \frac{F_r}{m_e}(1,K_2\frac{\partial \Psi_1}{\partial v_r}) + \frac{F_\vartheta}{m_e}(1,K_2\frac{\partial \Psi_1}{\partial v_\vartheta}) + \xi =$$

(4)

$$= (1,h), \qquad \xi = (1,f) = n_e$$

that may be given in the synthetic form

$$A_1\frac{\partial \xi}{\partial r} + A_2\frac{\partial \xi}{r\partial \vartheta} - A_3\xi = C$$

By taking $\xi(r,\vartheta) = \xi_1(r)\,\xi_2(\vartheta)$, the solutions to this equation are the following,

$$\xi_1 = \exp\left[-\int_0^r \mathcal{P}dr'\right]\left\{\int_0^r\left(\exp\left[-\int_0^{r'}\mathcal{P}'d\rho\right]\right)Q\,dr' + C_0\right\}$$

$$\xi_2 = \xi_2(0)\,\exp\left[-m^2\,\frac{r\vartheta}{A_2}\right]$$

where m^2 is the separation constant, dependent from boundaries, $\mathcal{P}(r,\vartheta) = (A_2 + m^2)/A_1$, $Q(r,\vartheta) = (C\xi_2)/A_1$. The solution may be easily expressed in terms of series of hyperbolic Bessel functions by taking

$$\exp\left[\pm\int_0^r \mathcal{P}dr'\right] = \sum_m\sum_n (\pm i)^m(\pm)^n I_n(p_2 r^{-2})I_m(p_3 r^{-2})\,\exp(\pm p_1 r + i(m+n)\vartheta)$$

where

$$p_1 = \frac{(1,K_1\Psi_1)-1}{(1,K_2 v_r\Psi_1)}\,,\quad p_2 = \frac{F_r(1,K_2\partial\Psi_1/\partial v_r)}{2m_e(1,K_2 v_r\Psi_1)}\,,\quad p_3 = \frac{F_\vartheta(1,K_2\partial\Psi_1/\partial v_\vartheta)}{2m_e(1,K_2 v_r\Psi_1)}\,.$$

The source term h(x,v) is composed by two sources of electrons:

1) the charged conductor of density n_1 and at temperature T_1,

2) the surface G at temperature T_2 and density n_2. It is written as,

$$h(\underline{x},\underline{v}) = n_1\left(\frac{\Gamma_1}{\pi}\right)^{3/2} g_1 \exp\left(-\Gamma_1 v^2(\underline{x})\right) - \nu(\tau_1) + n_2\left(\frac{\Gamma_2}{\pi}\right)^{3/2} g_2\,\exp\left(-\Gamma_2 v^2(\underline{x})\right) - \nu(\tau_2)$$

The weights $g_1(\tau_1,\tau_2,L)$ and $g_2(\tau_1,\tau_2,L)$ are calculated considering the

boundary conditions on the temporal solutions of the characteristic equation (2) where L that may be τ_1 or τ_2, is the phase t of the point $(\underline{x},\underline{v},t)$ respectively from the boundary sources 1) or 2) and L=t from a point inside the medium $(\underline{x},\underline{v},t)$ /1/.

The BGK eigenmodes are determined by solving the determinantal equation of the associate homogeneous equation to (4), considered as time-dependent equation with a solution

$$\xi = \xi_0 + \xi_1 \exp[i(\underline{k}\,\underline{x} - \omega t)], \quad \xi_1 \ll \xi_0 ,$$

where $\underline{k}\,\underline{x}=kr\cos\vartheta$. In particular the condition for the Cherenkov resonance is considered. The determinantal equation to solve is the following

$$i\left[(1,K_2 v_r \Psi_1)k\cos\vartheta - (1,K_2 v_\vartheta \Psi_1)k\sin\vartheta - \omega(1,K_2\Psi_1)\right] + (1,K_1\Psi_1) -$$

$$- \frac{F_r}{m_e}(1,K_2\partial\Psi_1/\partial v_r) - \frac{F_\vartheta}{m_e}(1,K_2\partial\Psi_1/\partial v_\vartheta) = 1$$

which, in this approximation, is linear and of the type

$$\omega = F(\vartheta)\,k + A_0 ,$$

in general complex, which, in principle, implies also backward modes.

In order to verify the approximation of this simple BGK model we consider an experiment in which the diffusion plasma is generated by a DC discharge between an hot filament (cathode) and a planar conductor (anode) where it is possible to measure the electron density and the electron current density distribution and, as well as, the electron temperature. For this test we write the linearized BGK Boltzmann equation (1) in the suitable form

$$f = h + \left[K_1 n - K_2 v\cos\vartheta\left(\frac{nF}{T_e} - |\nabla n|\right)\right]\nu\,(\Gamma_e/\pi)^{3/2}\exp(-\Gamma_e v^2).$$

In particular, in the case of plasma at low temperature and density with a low degree of ionization by detecting, experimentally via Langmuir probe, the first and second derivatives of the Langmuir I/V characteristic it is possible to derive the experimental electron distribution function.

References.

1) V.G.Molinari and L.Rondoni. Proc. of 15th Int. Symp. on Rarefied Gas Dynamics. Vol. II, Teubner, Stuttgart, 384 (1986).

2) W.G. Vincenti. Introduction to Physical Gas Dynamics. John Wiley, New York, 1965.

3) D.H.Menzel. Fundamental Formulas of Physics. Vol.1. Dover Publ. Inc. New York. 1960.

EXPERIMENTAL STUDY OF THE AXIAL STRUCTURE OF AN ARGON PLASMA COLUMN SUSTAINED BY AN ELECTROMAGNETIC WAVE IN THE PRESENCE OF AN EXTERNAL MAGNETIC FIELD

P. Staikov, D. Grozev, I. Zhelyazkov and E. Benova*

Faculty of Physics, Sofia University, BG-1126 Sofia, Bulgaria

* Department of Physics, Institute for Foreign Students, BG-1111 Sofia, Bulgaria

A typical feature of the plasma columns sustained by travelling azimuthally-symmetric electromagnetic waves is their axial inhomogeneity. An imposed magnetic field decreases the axial gradient /1,2/. The goal of this study is to measure the axial density profiles at different discharge conditions and compare them with the theory.

The experimental equipment used is shown in Fig. 1. It consists of a

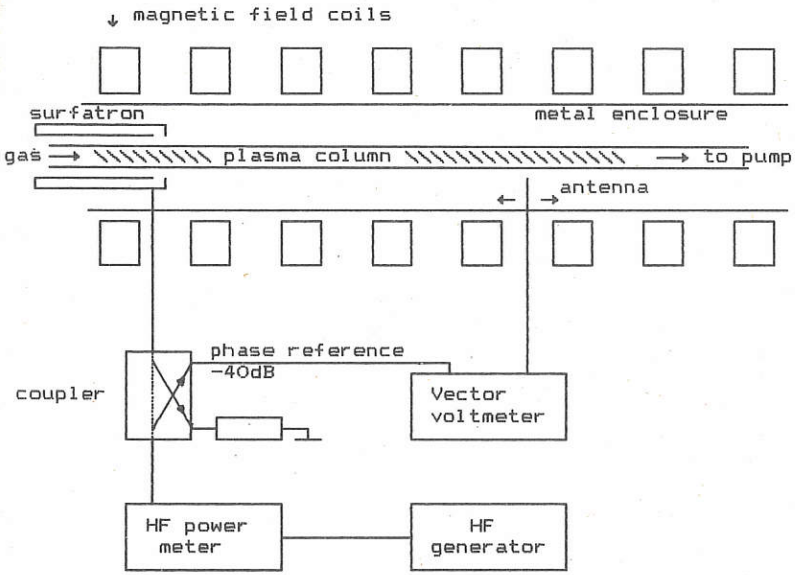

Fig. 1. Scheme of the experimental setup

glass tube of radius R, thickness d and permittivity ε surrounded by a metal enclosure, a HF generator of frequency $\omega/2\pi$ = 510 MHz, a HF power meter, a wave launcher of type "surfatron", eight Helmholtz coils creating the external axially homogeneous magnetic field, a coupler giving the reference signal for the vector milivoltmeter and a movable along the z-axis antenna.

The relevant experimental procedure is as follows: The vector milivoltmeter measures the phase difference φ between the reference signal and the signal from the movable antenna as a function of the axial coordinate z. Next, the wave number k(z) is obtained as $k = d\varphi/dz$. Then the phase diagram gives the plasma density n as a function of k. It is convenient for easier comparing with the theory to introduce the following dimensionless quantities: axial coordinate $\zeta = \nu z/\omega R$ (ν being the collision frequency for momentum transfer), wave number $x = kR$ and electron number density $N = n/n_c$, where n_c is the cut-off plasma density, $n_c = m\omega^2/4\pi e^2$. Since the derivative $d\varphi/dz$ has been used, small fluctuations in the raw experimental data give great deviations of N. That is why the $\varphi(z)$ curves must be fitted with smooth ones.

The experiment has been carried out in argon in two tubes with radii of 0.82 cm and 2.05 cm (identified by the numerical parameter $\sigma \equiv \omega R/c$ = 0.088 and 0.219 respectively), at pressures of 20, 50, and 100 mTorr and magnetic field inductions of 146 G and 218 G corresponding to ω_c/ω = 0.8 (weak magnetic field) and ω_c/ω = 1.2 (strong magnetic field) /2/. The wave power ranges from 10 to 70 W. In order to be able to compare the experimental data with the theory we have to set the power level in such a way that the end of the plasma column does not reach the end of the tube. Otherwise the propagation of reflected waves is quite possible. It is worth noting also that in contrast to the case of an isotropic ionized medium (when the column ends relatively sharply), the end of a magnetized wave produced plasma column tapers off, resembling the tip of a well sharpened pencil. With further increasing of the magnetic field the plasma column shrinks and reduces to a thin plasma wire along the tube axis and the theoretical models /1,2/ are not applicable. Also the lower the pressure, the smaller the contraction magnetic field.

By using this method the plasma density can be measured at arbitrary number of points. In our opinion 15 to 20 points are enough. Figures 2 to 5 show the experimental data compared with the corresponding theoretical

profiles. These profiles are derived from an improved numerical code of /2/ taking into account the presence of the dielectric tube and the metal enclosure.

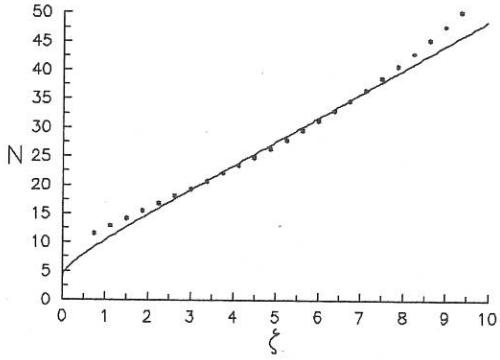

Fig. 2. Theoretical axial plasma density profile and experimental points for Ω=0.8, σ=0.088 and pressure p=50 mTorr

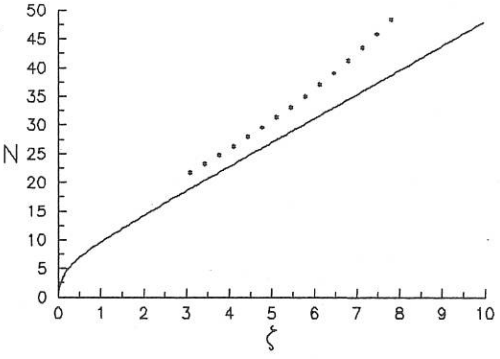

Fig. 3. Theoretical axial plasma density profile and experimental points for Ω=1.2, σ=0.088 and pressure p=100 mTorr

The experimental error can reach 30 % mainly because for large N the phase diagrams are very steep and a small deviation of the measured wavenumber cause large deviation of the obtained plasma density. We think that the agreement between theory and experiment is acceptable.

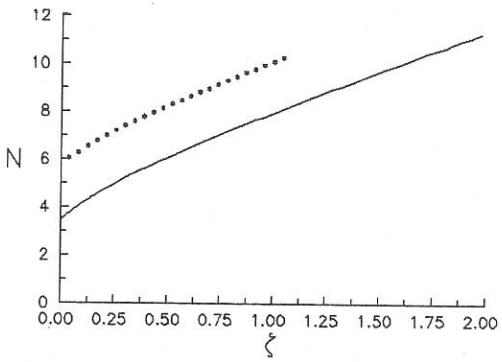

Fig. 4. Theoretical axial plasma density profile and experimental points for Ω=0.8, σ=0.219 and pressure p=20 mTorr

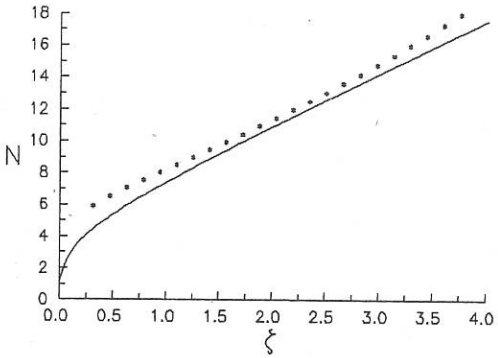

Fig. 5. Theoretical axial plasma density profile and experimental points for Ω=1.2, σ=0.219 and pressure p=100 mTorr

Acknowledgements: This work was supported by the Ministry of Education and Science under Grant F-42/91.

References

/1/ S. Pasquiers, C. Boisse-Laporte, A. Granier, E. Bloyet, P. Leprince, J. Marec, J. Appl. Phys. 65, 1465 (1989)
/2/ E. Benova, I. Zhelyazkov, P. Staikov, F. Cap, Phys. Rev. A 44, 2625 (1991)

III-2045

Electromagnetic Surface Waves for Large-Area RF Plasma Productions between Large-Area Planar Electrodes

Shigehiko NONAKA
Toyota Technological Institute,
2-12-1 Hisakata, Tempaku, Nagoya 468, Japan

Recently, large-area plasma production has been tested by means of a 13.56 MHz radio-frequency (RF) discharge between a pair of large-area planar electrodes, approximately 0.5 m x 1.4 m, as one of the semiconductor technologies for fabrication of large-area amorphous silicon solar cells in the "Sunshine Project" of the Agency of Industrial Science and Technology in Japan/1/. We also confirmed long plasma production between a pair of long electrodes/2/.

In this paper, normal electromagnetic (EM) waves propagating in a region between a planar waveguide with one plasma and two dielectric layers are analyzed in order to study the feasibility of large-area plasma productions by EM wave-discharges between a pair of large-area RF electrodes larger than the half-wavelength of RF wave. In conclusion, plasmas higher than an electron plasma frequency will be produced by an odd TMoo surface mode.

$ 1. Normal Mode Analysis

In this analysis, as shown by an one-dimensional waveguide model in cartesian coordinates (x,y,z) in Fig. 3 (b), the plasma layer ($-a \leqq x \leqq a$) is separated from the metal electrodes by dielectric layers with thickness d (= b-a) and dielectric constant Kg so as to support surface waves. The EM waves are assumed to propagate in the z-direction in the form of $\exp j(\omega t - \beta z)$, and the wave fields are uniform in the y-direction ($d/dy = 0$), where ω and β are wave frequency and wave number, respectively. The metals ($b \leqq |x|$) and the plasma ($-a \leqq x \leqq a$) are assumed cold, lossless and uniform, as expressed by equivalent dielectric constants Km and Kp, respectively: $Km = 1 - (\omega m/\omega)^2$ and $Kp = 1 - (\omega p/\omega)^2$, where $\omega m = \sqrt{Nme^2/\varepsilon_0 m}$ $\omega p = \sqrt{Npe^2/\varepsilon_0 m}$, Nm and Np are electron density numbers in metal and in plasma, respectively, and the other notations are standard.

We employed standard procedures to solve Maxwell's equations. The results are summarized as follows; (I) the EM wave usually separates into two independent TM and TE waves/3/. (2) Each of the TE and TM waves splits into

two modes, even and odd modes. (3) Each even or odd mode splits further into three modes: (I) surface wave mode, (II) EM mode in dielectrics and (III) EM mode in plasma. All the fields are represented by either a hyperbolic or sinusoidal function in each layer, as shown in Fig. 1 for an odd TM surface mode.

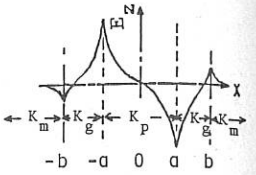

Fig. 1 : Profile of electric field Ez for an odd TMoo mode.

Boundary conditions for wave fields at two surfaces $x = \pm a$ and $\pm b$ gives dispersion equations, for examples, for odd TMln modes as follows:

$$Dm \cdot Dp = \{(Kp/Up)-(Kg/Ug)\tanh(Upa)\}\{(Km/Um)-(Kg/Ug)\}\exp(-2Ugd) \quad , (1)$$

where $Dm = (Km/Um) + (Kg/Ug)$, $Dp = (Kp/Up) + (Kg/Ug)\tanh(Upa)$,

$Um^2 = \beta^2-\beta m^2 \equiv \beta^2-ko^2Km$, $Up^2 = \beta^2-\beta p^2 \equiv \beta^2-ko^2Kp$,

$Ug^2 = \beta^2-\beta g^2 \equiv \beta^2-ko^2Kg$, $k_o^2 = \omega^2\varepsilon_o\mu_o$,

Um,p,g are wave numbers in the x-direction, in the metal, in the plasma and in the dielectric, respectively. Subscripts l and n denote mode numbers in plasma and in dielectric regions, respectively.

Thus, we have ten normal modes in total because the TE wave has no surface wave solutions. However, the most efficient mode for plasma production is an odd TMoo surface mode/4/, so that we omit here all the other normal modes.

$ 2. Dispersion Characteristics

Equation (1) contains two dispersion relations for surface waves propagating along the plasma and metal surfaces $x = \pm a$ and $\pm b$. Thus, eq. (1) expresses the coupled dispersion equation of the two odd surface waves. When the plasma thickness 2a becomes zero, dispersion relation for an odd metal surface wave (MSo) along $x = \pm b$ is derived from eq. (1) as follows:

$$(Km/Um) + (Kg/Ug)\coth(Ugb) = 0 \qquad \text{(for odd MSo)} \quad , (2)$$

Whereas, when the metals are perfect conductors, another dispersion relation for an odd plasma surface mode (PSo) along $x = \pm a$ is derived from eq. (1) as:

$$(Kp/Up)\coth(Upa) + (Kg/Ug)\coth(Uga) = 0 \qquad \text{(for odd PSo)} \quad . (3)$$

Dispersion characteristics for MSo and PSo modes are obtained qualitatively from graphical inspections of eqs. (2) and (3), as shown in Figs. 2 and 3, respectively, where λ and λg are wavelengths corresponding to β and βg. The results are summarized as follows: (I) both surface waves have slow phase velocities $(\lambda g/\lambda)^2 \geqq 1$, and (II) the density Nm and Np go to infinity when $(\lambda g/\lambda)^2$ approaches 1, and (III) go to 1 + Kg when $(\lambda g/\lambda)^2$ approaches infinity.

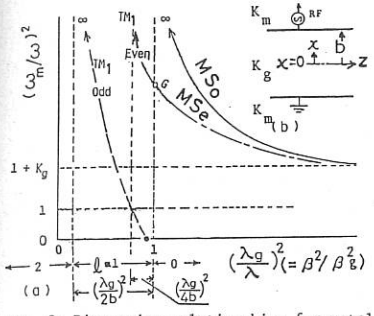

Fig. 2: Dispersion relationships for metal surface (MS) modes (a), and sideview of one dimensional model of the waveguide (b).
MSo: odd mode. MSe: even mode.

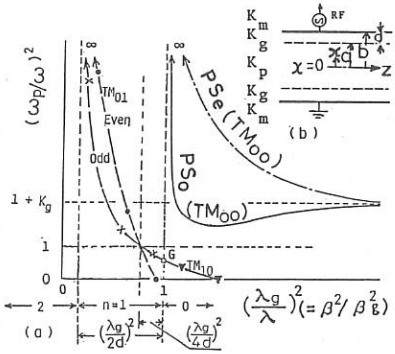

Fig. 3: Dispersion relationships for plasma surface (PS) modes (a), and sideview of one dimensional model of the waveguide (b).
PSo: odd mode. PSe: even mode.

Next, we take into account lossy plasmas in dielectric constant Kp: $Kp = 1 - (\omega p/\omega)^2/(1+\eta^2) - j\eta(\omega p/\omega)^2/(1+\eta^2)$, where $\eta = \nu c/\omega$ and νc is an electron-gas collision frequency for momentum transfer. The dispersion curves in Fig. 3 are modified to some extent, depending on the value η, to shift toward the upper side of $(\omega p/\omega)^2$ and/or to shift toward the larger side of $(\lambda g/\lambda)^2$, as is known from eq. (3). Furthermore, when the PSo mode is coupled with the MSo mode as in eq. (1), the dispersion curve in Fig. 3 will also go down somewhat to the bottom side, but the value $(\omega p/\omega)^2$ is more than 1.

$ 3. Theory for Plasma Productions and Discussions

For this purpose, we begin with the case when a ready-made DC plasma is set up for the plasma layer. RF voltage $V\exp(j\omega t)$ is then applied to the metal electrodes at an arbitrary point defined as z = 0, using a coaxial cable as is the standard procedure.

First, in order to simplify the theory, eq. (1) is rewritten, using a

quasistatic approximation ($\beta \rightarrow$large), as follows:

$$\{Kp + Kg\tanh(\beta a)\}\{Km + Kg\} = \{Kp - Kg\tanh(\beta a)\}\{Km - Kg\}\exp(-2\beta d) \quad , (4)$$

whereas, the profile of the wave potential is the same as Ez in Fig. 1. Thus, one can define an RF wave voltage V between metals; that is, V = 0 for even TMoo mode, and V $\neq$ 0 for odd TMoo mode. Therefore, this odd mode is directly coupled with an applied RF voltage V at z = 0. Then, this odd TMoo mode can propagate inducing the RF voltage in the form of $V = V\exp j(\omega t - \beta z)$. These results also shows that the odd MSo mode will play a role of modifying the odd PSo mode and exciting it at the position far away from the z = 0. When we take into account finite dimension of electrodes, standing wave resonances will occur within the electrode area.

Next, we change the focus of our interest to RF plasma production. Even in such circumstances, all the concepts and results are basically the same as in the above case of DC, as long as we use coaxial cables. Thus, the most efficient mode for plasma productions is identified an odd TMoo surface mode.

The present theory suggests the feasibility of large-area or long plasma productions that may be required for mass production of large-area silicon solar cells at the ground level/1/ or in a space factory in the near future. The remaining problems in terms of these purposes are now being prepared for publications.

$ 4. Conclusions

When we use coaxial cables for the generation of large-area plasma between a pair of large-area planar electrodes larger than the half-wavelength of the TEM wave $\lambda g/2$, (I) the RF plasmas are produced by an odd metal and plasma surface mode TMoo with the wavelength range $\lambda < \lambda g$, and (II) then the produced plasma density is higher than the critical value of an electron plasma oscillation ($\omega p^2 \geqq \omega^2$).

References

1) H. Sakai and Y. Ichikawa:J. Inst:Electr. Eng. D-108-2,p.123(1988).
2) S. Nonaka: Jpn. J. Appl. Phys. 29,p.571(1990).
3) J. A. Stratton: Electromagnetic Theory (McGraw-Hill, New York,1941).
4) S. Nonaka: (in press).

11-49

CO_2-TE LASER PRODUCED CADMIUM PLASMA IN VACUUM EXPERIMENT AND KINETICS

I. Apostol, B. Bahrim, C. Bahrim, C. Vasilescu
Institute of Atomic Physics, Laser Department
P. O. Box MG-6, RO-76900, Bucharest-Magurele, Romania

The rapidly transient character of the plasmas generated under the action of pulsed, high-intensity laser radiation may lead especially through relaxation processes to important deviations from the thermodynamic equilibrium distributions and sometimes to population inversions and lasing action.

Related to the investigation of lasing action in the visible region, our results on laser emission at λ = 5378 Å recombination line in CO_2-TE laser produced cadmium plasma in vacuum, were previously reported /1/.

A detailed further study of the visible emission spectrum and the related parameters of the laser produced cadmium plasma are now presented. For the plasma production we have used a CO_2-TE laser with a typical pulse shape (a peak of 200 nsec. and a tail of 2 μsec.).

The analysis of the emission spectrum has put into evidence lines belonging to Cd I and Cd II species, but the presence of the recombination lines of Cd II ions indicates also the existence of Cd III ions in plasma, in its early evolution stages at least. These lines were not directly detected because Cd III ions have not emission lines in the visible region.

The plasma electron temperature was obtained using the ratio of the relative line intensities of subsequent ionisation stages, /2/ taking into account that for times between 0.2 and 1 μsec. in its evolution, plasma can be considered in local thermodynamic equilibrium.

The electron density was not directly measured. This is the reason why the electron temperature calculations were considered for two electron densities: $10^{17}cm^{-3}$ and $10^{18}cm^{-3}$.

For a moment situated at 0.2 μsec. after the plasma ignition, the corresponding temperature values are 1.4 eV and 1.7 eV; after 0.7 μsec. the temperature decreases slowly to 1.3 eV and respectively 1.5 eV. The determined temperatures are averaged over the plasma length at the considered times.

The theoretical values for temperature, were calculated using a hydrodynamic model /3/. The parameter α from this treatment takes into account the two limitting cases for the ion temperature: $\alpha = 1$ for an ionic temperature equated to zero and $\alpha = (z+1)/z$ for an equal temperature of the ions and electrons (z is the plasma charge). In the case of $\alpha = 1$, the results give a value of 37.72 eV for the maximum electrons temperature and a corresponding electron density value of $6.37\ 10^{18} cm^{-3}$. The calculated values for temperature as a function of the distance from the target surface, which correspond to different moments in plasma evolution, are greater than the spectral estimated temperatures for a region situated near the target, becaming lower for greater distances. The corresponding values for temperature and density at 5 mm in front of the target are 1.30 eV and respectively $4\ 10^{16} cm^{-3}$.

Taking into account that the interaction time of the laser pulse is about 2 μsec., we have considered useful to do some considerations about the absorption coefficient (K) in plasma /4/. With the same hydrodynamic model we obtained a value of $K = 17\ cm^{-1}$ in the period of plasma formation, after which the value decreases rapidly at $K = 0.064\ cm^{-1}$ at 5 mm from the target surface, indicating that the tail of the laser pulse is weakly absorbed in the expanded plasma.

The number of heavy particles in plasma produced by laser ablation, considering that the process is most powerful under the action of the laser peak, is $4\ 10^{15}$ particles for a value of $2\ 10^{8}\ W\ cm^{-2}$ for the laser intensity. This indicates an ionisation coefficient for the maximum calculated electron density of 28 %, considering that the number of ions is equal to the number of electrons. In the real case (a medium charge

in the plasma of about z = 2), the number of ions represent approximately 14 % .

In order to analyse kinetics of the laser-produced plasma, the collisional excitation and - using the detailed equilibrium principle - de-excitation rate coefficients were calculated at different temperatures, taking into account two lines: λ = 5378 A laser recombination line and another line, which has not a recombination character, λ = 4415 A line. The calculated values of the rate coefficients put into evidence that they are much greater for λ = 5378 A line, than for λ = 4415 A line.

The results were obtained using Bates-Damgaard approximation /5/ (for the first line) and Van Regemorter semiempirical formula /5/ (for the second line), the temperatures involved in the calculations being of interest for the "hot" period of the plasma evolution. The values are presented in table I.

Table I

λ (A)	T = 4 eV	T = 8 eV
	$K_{ex}(cm^3s^{-1})$; $K_{dex}(cm^3s^{-1})$	$K_{ex}(cm^3s^{-1})$; $K_{dex}(cm^3s^{-1})$
4415.63	9.88(-9)	1.10(-8)
	2.99(-8)	2.34(-8)
5378.13	2.64(-5)	2.38(-5)
	5.58(-5)	4.90(-5)

We mention that the transitions analysis was made in the case of a single electron involved in the transition.

References:

/1/ I. Apostol, D. Craciun, M. Ristici, D. Apostol, A. Hening, M. Stoica, Proc. Third Int. Conf. on T. Q. E., SPIE vol. 1033, 2, 1988

/2/ H. R. Griem, *Plasma Spectroscopy*, (Mc Graw-Hill), 1964

/3/ H. Puell, Z. Naturforsch 25 a, 1807, 1970

/4/ J. Dawson, C. Oberman, Phys. Fluids 5, 517, 1962

/5/ I. I. Sobelman, L. Vainshtein, E. Yukov, *Excitation of Atoms and Broadening of Spectral Lines*, (Springer-Verlag, Berlin, New York) vol.7, 1981

Topic 12:

Elementary Processes in Plasmas

MEASURED AND CALCULATED CHARGE DENSITY IN Ce and Cu VAPOR PRODUCED BY AN ELECTRON GUN

L. Blumenfeld, C. Gonella and M. Morin
SPEA, CE SACLAY, 91191 GIF SUR YVETTE CEDEX, France

Abstract

A measure of electron density by Langmuir probe is reported and compared with a calculation taking into account electron-atom collisions.

1. Introduction

The charge rates of cerium and copper vapor, created by an electron gun, were measured. A Langmuir probe measured the charge density n_e and a quartz crystal measured the flux of atoms. The atomic density n_{at} is deduced, by the knowledge of the atomic velocity along the vertical axis /1/.

To interprete this experimental charge rate $\tau_i = n_e/n_{at}$, we solve the rate equations for each class of electrons present in the vapor, taking into account electron impact ionisation, excitation, deexcitation processes and radiative decay.

2. Experimental Set-Up

Evaporation was produced using a commercial electron gun of 11 kV and power P varying between 500 W and 5 kW (see fig(1)). The beam, deflected by 270°, heated a metal contained in a water cooled copper crucible, which can move along the vertical axis. The vapor, generated at the source (S), is collimated in A. The Langmuir probe is located 50mm above (S) for Ce and 80mm for Cu, out of the electron beam. The flux of atoms is mesured with a quartz crystal above A.

3. Electronic population

A proportion of the incident electrons is backscattered (see fig. 2). Their energy is slightly smaller than the beam energy. The backscattering coefficient is 0.28 for Cu and 0.40 for Ce /2/. Energetic electrons create "vapor electrons" in the vapor, along the beam direction. According to /3/ and /4/, we estimate that the energy distribution of the "vapor electrons" is initially

maxwellian, with a temperature T_i equal to 22eV and 42eV for Ce and Cu.

In addition, secondary processes between beam and metal produce secondary electrons with a mean energy of a few eV. Due to the high temperature T_S of the source (≈2500K), thermoionic electrons can be present at the point of beam impact.

4.Model

We describe the states of copper by 7 levels /5/, and the states of cerium by 9 levels (2 states and 7 pseudo-states).

We solve the stationary rate equation for ion density versus the altitude h above the source:

$$v \cdot dn_i/dh = \text{Loss} + \text{Gain} \qquad (a)$$

where v is the mean velocity of the atoms

n_i is the population of the state i

and Loss and Gain terms are the contributions of radiative decay, excitation, desexcitation and ionisation by electron impact.

For the ionization cross section, we use the Drawin semi-empirical formula /6/, which reproduce well the cross section data of /7/ and /8/, if we adjust the parameter n_D (see Fig 3).

We first solve equation (a) for energetic electrons. The reduction of their energy (≈11keV) by collision with the vapor atoms is negligible. These electrons create 60% and 38% of multicharged A^{n+} ions for Ce and Cu respectively.

Then, to calculate the contribution of "vapor electrons", we solve equations (a) and (b):

$$d(n_e \cdot 5/2T_e) / dh = L + G \qquad \text{(see /9/)} \qquad (b)$$

where L and G energy loss and gain terms due to the same sort of collisional processes than in equation (a).
The h variation temperature T_e shows a decrease from T_i to less then 1eV in few micrometers.

Secondary electrons contribution is negligible, since they are very cold. The thermoionic charge density

calculated by the Saha equation is too high (0.08%) to yield a good agreement with the Ce experimental rate. We don't take it into account.

5. Results and conclusion

In order to perform a more realistic calculation of charge rate versus power, it would be necessary to know the evolution of the surface S (impact of the beam on the source with power). We estimate the radius R_S of S at approximatively 0.3cm.

We checked two simple situations, following the model described in part 4: one where P/S is constant, and one where S is constant.

Fig. 4 shows the experimental (see part 2) and calculated charge rate. In the case of Ce, the agreement between experiment and calculation is good enough if S=cte, except for lowest beam power. For Cu, the calculation reproduce experiment, but the fluctuations of the rates are too small to see a difference between the two calculations.

With this very simple model, we reproduce the order of magnitude of charge density in terms of gun power for different elements, wherefore we conclude that the main processes are taken into account with right order of magnitude of rate coefficients.

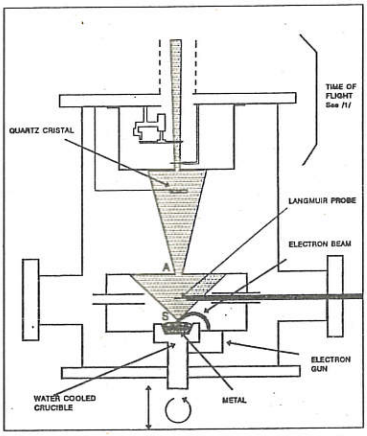

Fig 1: Experimental Set Up

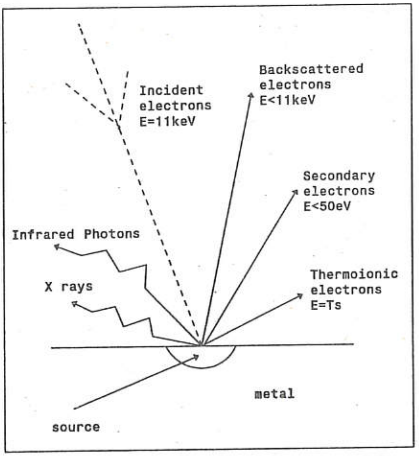

Fig 2: Electronic Populations (See/10/)

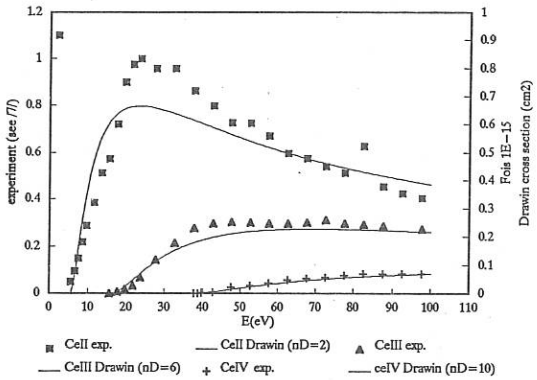

Fig 3: Ionization Cross Section of Cerium

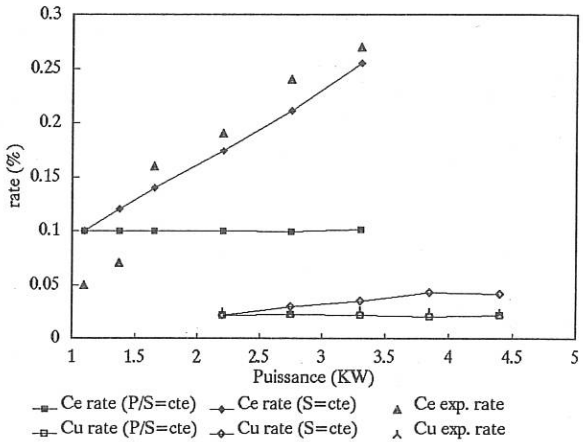

Fig 4: Charge Rates

/1/J.L. Flèche, C. Gonella, L. Blumenfeld, M. Morin, M. A. Gaveau, submitted to R. G. D. Conference (1992)
/2/M. Dapor, Phys. Lett A, Vol 151, n°1,2 p.84(1990)
/3/Y. K. Kim, Elect. Impact Ionization, Märk and Dünn(1985)
/4/J. M. Dolique, M. Khodja, A. Piquemal P24-2, ICPP84
/5/M.J. Kushner and B.E. Warner,J.App.Phys. 54,2970(1983)
/6/H. W. Drawin, Z. Physic 164,513(1961)
/7/J. J. Poupeau, private communication(1992)
/8/C.F. Barnett, At. Data for Cont. Fusion, ORNL 5207(1977)
/9/R.W.Schunk,Rev. of Geo. and Sp. Ph.,V15 n°4, p.429(1977)
/10/S. Schiller,U. Heisig, S. Panzer,El. Beam Tech.(1982)

Stokes Parameters for Compton Scattering in a Strong Magnetic Field

CHIH-KANG CHOU and HUI-HWA CHEN

Institute of Physics and Astronomy, National Central University
Chung-Li, Taiwan 32054, Republic of China.

1. Introduction

The role played by superstrong magnetic fields in astrophysical plasmas has attracted considerable attention. It is generally believed that enormously strong magnetic fields seem to be characteristic of collapsed stars. Exterior fields of $10^{12}G$ or even greater are required by models which try to relate pulsar observations to rotating neutron stars /1/. On the other hand, the observation of polarized light and X-rays from white dwarfs suggests that such stars also possess huge surface magnetic fields in excess of $10^{8}G$ /2/. Moreover, the discovery of X-ray cyclotron emission from Her X-1 by Trumper et al. /3/ provides further direct evidence for strong magnetic fields of $10^{12}G$. More recently, the detection of effects due to electron cyclotron resonance, in the spectrum of mass-accreting X-ray pulsars from Ginga satellite provides further direct and accurate measurements for the surface magnetic fields of strength $(1 \sim 4) \times 10^{12}G$ /4/. Such huge magnetic fields can greatly affect the motion of electrons in the outer parts of the star by tending to confine their motion perpendicular to the magnetic field. The interaction of photons with electrons will be greatly altered whenever the magnetic field is sufficiently strong to restrict the electron motion to orbits parallel to the field. Thus, the magnetic field may possibly greatly reduce the opacity in such stars so that they may cool much more rapidly than is indicated by those calculations which ignore it.

In recent years, several theoretical investigations have been focused to study the dynamics of resonant and nonresonant scattering of photons by electrons in a plasma permeated by a superstrong magnetic field /5,6,7/. The most distinguishing features is the fact that the superstrong magnetic field greatly affects the Compton scattering process, resulting in resonances in the scattering cross-section /8,9,10/. The important consequences of these cyclotron resonances are the increase in the photon mean free path in the scattering regions, and greatly increased electron energy-loss rates /11/, strongly affecting the angular distribution, and polarization properties of the scattered photons /12/. More recently, analytical expression for the Compton scattering cross-section in an intense magnetic field has been presented by several authors /9, 13/. In particular, Lieu derived simpler and more usable expressions for the tolal cross-section which reduce to the magnetic Thomson cross-section in the low frequency and weak field limit (i.e., $\hbar\omega \ll mc^2, B \ll B_q$ where m is the mass of the electron and

$B_q \equiv m^2c^3/e\hbar = 4.414 \times 10^{13}G$). This limiting cross-section obtained by Lieu is essentially the same as the one previously given by Canuto et al. who derived it in the low density and weak field limit ($\omega \gg \omega_p, \omega \gg \omega_c$ where ω_p and ω_c denote respectively the plasma frequency and cyclotron frequency of the electrons). The indices of refraction for photons propagating in such huge magnetic fields was determined by Adler /14/ who showed that except for propagation along the external field direction, the vacuum polarized by an external constant magnetic field is birefringent. In 1979, Iacopini and Zavattini /15/ proposed to measure this birefringence in the laboratory by a precision determination of the induced ellipticity on a laser beam down to 10^{-11}. More recently, Ni et al. /16/ even proposed schemes to detect the change of index of refraction in ultra-high sensitive interferometers.

Despite the possible significant laboratory and astrophysical applications of the scattering of photons by electrons in a strongly magnetized electron gas in connection with precision measurement in the laboratory, X-ray or γ -ray source and neutron star cooling, it appears that magnetic Compton scattering has not been treated thoroughly. In this paper we present a detailed analysis of the Stokes's parameters for Compton scattering in a superstrong magnetic field by the method of relativistic quantum field theory. The Stokes's parameters for the scattered photons are computed explicitly in terms of the state of polarization of the incident wave, the electron-cyclotron frequency, the angle of incidence and the angle of scattering. Various appropriate limits will be considered. Specific application to high energy astrophysics such as neutron star cooling and models for compact γ -ray source will be briefly discussed.

2. Results and Discussion

We consider the scattering of a photon by an electron located at the origin of a Cartesian coordinate system, in a uniform magnetic field $\vec{B} = B\hat{z}$ where $\hat{z}$ denotes the unit vector and B represents the constant field strength. The propagation vector $\vec{k}$ of the incident photon makes an angle θ with the static magnetic field. We shall only be concerned with the zero-order approximation, which consists of the two graphs (Figure 1). We note that the effects of the magnetic field on the photon via vacuum polarization is at least of first order and can be ignored. For applications to compact stellar objects (such as in the vicinity of neutron stars) the radiation energy density is much less than the magnetic energy density for field strength of 10^{12} Gauss /17/. Using the standard prescription of relativistic quantum field theory, the formal expression for the S-matrix for magnetic Compton scattering may be written in natural units ($\hbar = c = 1$) as

$$S_{fi} = \frac{1}{2}ie^2 \int \psi_f(x') \not{A}(k', x') i S_F(x' - x) \not{A}(k, x) \psi_i(x) \bar{d}^4x \bar{d}^4x' + (\text{ cross term })$$

where $\bar{d}^4x = d^4x/(2\pi)$, f denotes final, i initial, and $\vec{x} = (x, y, z, t)$ and $\vec{x}' = (x', y', z', t')$ are 4-vectors. $\not{A} = \gamma^\mu A_\mu$ where γ are Dirac matrices and $A_\mu(\vec{k}, \vec{x}) =$

$\epsilon_\mu e^{-i\vec{k}\cdot\vec{x}}$ for absorbed photon, $A_\mu(\vec{k}',\vec{x}') = \epsilon_\mu' e^{+i\vec{k}'\cdot\vec{x}'}$ for emitted photon; $\epsilon_\mu = e_\mu/\sqrt{V\omega}$, e_μ are polarization vectors of the photons and $k_\mu = (\vec{k},\omega)$, etc.

Using the standard method of quantum electrodynamics and the density matrix $\rho_{ij} \equiv \epsilon_i \cdot \epsilon_j^* = \rho_{ji}{}^*$, the Stokes's polarization parameters may be defined as $S_n \equiv (S_0, S_1, S_2, S_3)$ for the incident photon where $S_0 = \rho_{11} + \rho_{22}, S_1 = \rho_{11} - \rho_{22}, S_2 = \rho_{12} + \rho_{21}, S_3 = i(\rho_{12} - \rho_{21})$. Expressions for the scattered photons may be similarly defined as $S_n' \equiv (S_0', S_1', S_2', S_3')$ etc. The first Stokes's parameter S_0' represents the scattered radiation intensity and is proportional to the differential scattering cross section as follows $\frac{d\sigma}{d\Omega'} = \frac{S_0'}{S_0}R^2$ where R is the distance between the scattering region and the point of observation and S_0 refers to the incident photon. The other Stokes's parameters S_1', S_2' and S_3' describe the state of polarization for the scattered photon. Without giving the details of the straightforward but rather tedious calculation we now write the Stokes's parameters S_n' after scattering in terms of the state of polarization of the incident photon ω, the electron-cyclotron frequency ω_c, the angle of incidence (θ, φ) and the angle of scattering (θ', φ').

$$S_n' = \frac{e^4 S_0}{R^2} \frac{2m + \omega - \omega'}{2m} \frac{\omega'}{m + \omega(1 - cos\theta cos\theta') - \omega' sin^2\theta'} M_n.$$

The matrix $M_n (n = 0,1,2,3)$ is a very complicated expression and will not be given here /18/.

In the nonrelativistic limit ($\omega \ll m, \omega_c \ll m$), our results for the tolal cross section reduce to the well known form for magnetic Thomson scattering , namely

$$\sigma = \sigma_T \{ sin^2\theta + \frac{1 + cos^2\theta}{2} [(\frac{\omega}{\omega + \omega_c})^2 + (\frac{\omega}{\omega - \omega_c})^2] \}$$

where σ_T is the canonical Thomson cross section /7,9/. The total cross section derived from S_0' in this case may be cast in the form $\sigma(B) = (\frac{\omega}{\omega_c})^2 \sigma(0)$ where $\sigma(B)$ and $\sigma(0)$ respectively denote the Thomson cross section with and without the presence of the magnetic field, ω_c represents the classical gyrofrequency for the electrons and ω is the frequency of the incident wave. It is clear that the criterion for the magnetic field to substantially affect the Stokes's parameters is that the photon frequency be less than the electron-cyclotron frequency. for instance, the Thomson cross section is significantly reduced and the photon mean free path is greatly enhanced for photons with $\omega \ll \omega_c$. On the other hand, in the absence of the external magnetic field, the differential cross section (derived from S_0') becomes the famous Klein-Nishina formula. To conclude our discussion we note that although the nonrelativistic cross section shows only one resonance at $\omega = \omega_c$, the relativistic cross section exhibits a series of resonances as shown in Figure 2. Specific applications to high energy astrophysics in connection with neutron star cooling and models for γ-ray source are currently in progress and will be published elsewhere.

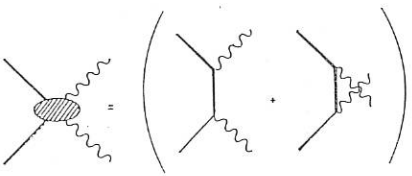

Figure 1. Lowest order Feynman diagrams for Compton Scattering in strong magnetic fields. Double lines represent electrons in Landau states.

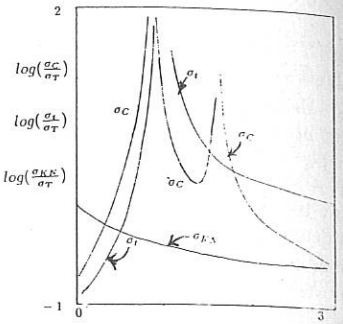

Figure 2. Total cross sections in unit of $log(\frac{\sigma}{\sigma_T})$ v.s. frequency ω in unit of ω_c for a magnetic field strength $B_0 = 4 \times 10^{12}$ Gauss and $\theta' = \frac{\pi}{3}$, where σ_t and σ_C are the cross-sections for magnetic Thomson and Compton scattering, σ_{KN} is the Klein-Nishina cross-section.

References

/1/ J. E. Gunn and J. P. Ostriker, Nature, 221, 454 (1969).
/2/ J. C. Kemp, J. B. Smedlund, J. D. Landstreet and J. R. P. Angel, J. Appl. Phys. Letters 161, L77 (1978).
/3/ J. Trumper, W. Pietsch, C. Reppin, W. Voges, R. Staubert and E. Kendziorra, Ap. J. Lett. 219, L125 (1978).
/4/ K. Makishima et al. Astrophys. J. (Letters),365, L59 (1990).
/5/ J. K. Daugherty and A. K. Harding, Ap. J. 309, 362 (1986).
/6/ C. K. Chou and H. H. Chen, Astrophys. and Space Sci. 174, 217 (1990).
/7/ D. Q. Lamb, J. L. Wang and I. Wasserman, Astrophys. J. 363, 670 (1990).
/8/ V. Canuto, J. Lodenquai and M. Ruderman, Phys. Rev. D3, 2303 (1971).
/9/ H. Herold, Phys. Rev. D19, 2868 (1979).
/10/ C. K. Chou, Astrophys. and Sp. Sci. 121, 333 (1986).
/11/ X. Y. Xia, G. J. Qiao, X. J. Wu and Y. Q. Hou, Astr. Ap., 152, 93 (1985).
/12/ C. K. Chou and H. H. Chen, Stokes Parmenters for Thomson Scattering in Magnetized Plasma, the IAU Symposium 142 (Basic Plasma Processes on the Sun) held in Bangalore, India (1989).
/13/ R. Lieu, Astrophys. and Sp. Sci., 73, 481 (1980).
/14/ S. L. Adler, Ann. Phys. (USA) 87, 599 (1971).
/15/ E. Iacopini and E. Zavattini, Phys. Lett. 85B, 151 (1979).
/16/ W. T. Ni, K. Tsubono, N. Mio, K. Narihara, S. C. Chen, S. K. King and S. S. Pan, Mod. Phys. Lett. A (1991).
/17/ Yu. N. Gnedin and R. A. Sunyaev, Astron. and Astrophys. 25, 233 (1973).
/18/ H. H. Chen and C. K. Chou (to be published)

CTMC STUDY OF COLLISIONS OF CARBON IONS WITH H AND HE, RELEVANT TO MAGNETICALLY CONFINED FUSION PLASMAS

K. Katsonis, G. Maynard
Laboratoire de Physique des Gaz et des Plasmas, UA 073,
Bât. 212, Université Paris XII, 91405 Orsay CEDEX, France

At the beginning of the last decennium it was well understood that the balance of the impurity content of a magnetically confined plasma is dominated by interaction between plasma particles and the material walls /1/. Accordingly, a systematic effort was oriented towards the study of the plasma-surface interaction and of the relevant atomic processes of ion-atom collisions. Atomic processes involving hydrogen, helium, carbon, oxygen and metallic impurities were of first priority in this domain. Systematic evaluation and compilation of cross sections relevant to fusion was already initiated by C.F. Barnett, founder of the ORNL Controlled Fusion Atomic Data Centre /2/. The status of the atomic data base for reactions occurring mostly in the plasma core or concerning mainly the plasma heating by energetic ion beams has been reviewed elsewhere /3/. Studies of H and He collisions involving metallic impurities /4,5/ or oxygen /6/ have been recently made available. The status of such data was recently reviewed in /7/ and /8/. Here we concentrate to our calculations in progress of collision cross sections for the carbon ions colliding with hydrogen and helium.

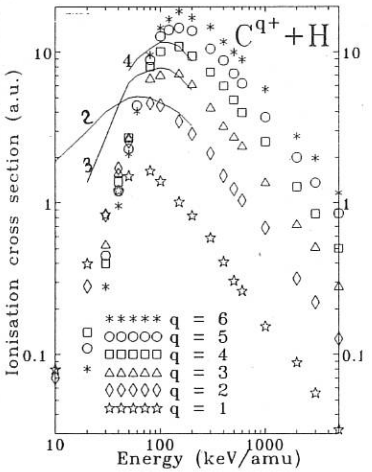

Figure 1 Our CTMC results. Plain curves: Experimental data from /10,1-1/

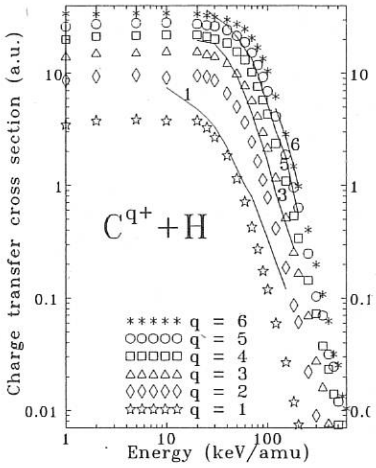

Figure 2 Same as Figure 1

The CTMC method was used for calculating total ionisation and one electron capture cross sections for H - C^{q+} collisions in the energy region of 10 to 5000 and of 1 to 1000 keV/u correspondingly.
Three different potentials for the ions have been lately used with this method: An empirical

potential which has been used previously for studying hydrogen collisions with medium- and high-Z plasma impurity ions as in /4/, a modified version of it incorporating a detailed Thomas-Fermi radius and a Coulomb potential. As expected, in comparison with existing experimental and theoretical data, the results show that among them, only the Coulomb potential is giving acceptable cross section values; it is to be noted that this is the case for all low-Z ions colliding with hydrogen. This, together with previous high-Z results, allows for a better understanding of the model potential influence on the CTMC calculations for all the species of relevance to fusion research. For light atom - ion collisions, specific model-potentials taking into account their atomic structure were also developed /9/; use of these potentials is in principle giving the possibility to improve the CTMC results, although the computation time increases drastically. Especially for H - C^{q+} collisions, preliminary calculations are not showing a substantial improvement of the results.

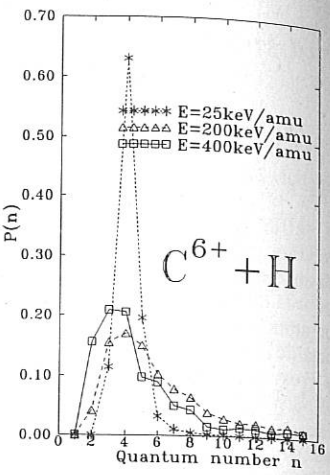

Figure 3 Probability for partial recombination on each principal quantum level n

A glimpse of the obtained results is given in Figs. 1 and 2.
For clarity reasons only our results obtained with Coulomb potentials are given, together with a set of pertinent experimental results /10,11/. Although the obtained results are quite satisfactory, mainly in the restricted validity area of the CTMC method, it appears that an extension of the method has to be devised in order to obtain confident results in the entire energy region from 10 eV/u to 5 MeV/u which are potentially of interest to magnetic fusion research.

n-resolved partial cross sections for one electron capture into the various ions levels have also been computed. As an example, we are presenting in Fig. 3 the results for H - C^{6+} collisions.

In CTMC calculations for collisions with helium atoms more assumptions than in the hydrogen case are necessary. First the independent electron model has been used: each of the two helium electrons moves independently of the other in an effective potential $V_{ef}(r)$ which has still to be determined. Next a statistical average of the correlated electrons is needed for processes involving two electrons : double charge transfer, double ionisation and transfer ionisation. In our group at Orsay, we have made a systematic study of the various parameters entering CTMC calculations namely the influence of the effective potential and the different approximations to take correlations into account. Some of our results are presented here.

Looking the well known Binary Encounter Approximation we can see that in the case of a bare incident projectile all the different cross sections depend only on the ionisation energy and on the velocity distribution of the target electron. For helium atom ionisation energy is 0.9a.u. and the mean kinetic energy is 1.43a.u.. When using hydrogenic approximation for V_{ef} with an effective charge $Z_{ef} = 1.69$ ($1.69^2/2 = 1.43$) one can either have the good ionisation energy or the good kinetic energy. Our calculations show that the

two approximations give quite different results for projectile charges larger to three and then one needs a more appropriate potential. From the analytical effective potentials proposed /9/,/12/ we used either the potential of /1/ or the one given by the simpler formula:

$$V_{ef}(r) = -(1.+0.255/(0.255+r)/r.$$

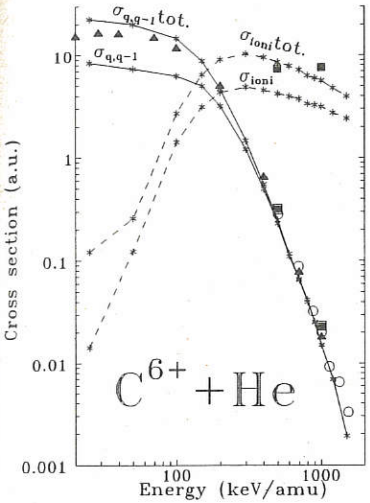

Figure 4 Our CTMC results compared with : ▲ /13/, ■ /15/ and o /14/

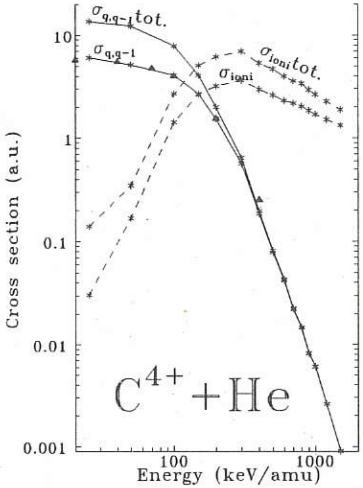

Figure 5 same as Figure 4

Using the last one, we have calculated the total charge transfer cross section $\sigma_{q,q-1}$ for the reactions $C^{q+} + He \rightarrow C^{(q-1)+} + He^{+}$, and the ionisation cross section σ_i for the reactions $C^{q+} + He \rightarrow C^{q+} + He^{+} + e^{-}$, q=6,4 which are shown on Figure 4 and 5 together with some published results/13/,/14/,/15/.

The influence of the statistical correlation can be quantified using the values of σtot reported in Figures 4 and 5. As an example the ionisation cross section σ_i is calculated summing on the impact parameter twice the probability that one electron is ionised and one electron is excited, whereas $\sigma_i$tot is calculated summing only twice the probability that one electron is ionised. The results show that the correlation greatly reduces the one electron cross section except for the total charge transfer cross section at high energy.

Comparisons with experiment show that cross section for the two electrons reaction is too large. For example the ratio of the cross section for transfer ionisation to the cross section for single charge transfer is nearly ten times the experimental results given in /15/. This is not due to the CTMC calculation but mainly to the independent electron approximation. The same results were obtained in /12/ using a quantal calculation. One solution proposed in /2/ is to use different effective potential for the double electrons reaction and the best way is to suppose a two steps mechanism : The projectile interacts first with one electron and then with the second one which is bound to a hydrogenic potential with a charge $Z_{ef} = 2$. The results for C^{6+} where the influence of correlation is the most important, reported in Figure 6, are satisfactory; it remains now to compare the two steps approximation with a full dynamic two electrons CTMC code. Work in this direction is under way in our group.

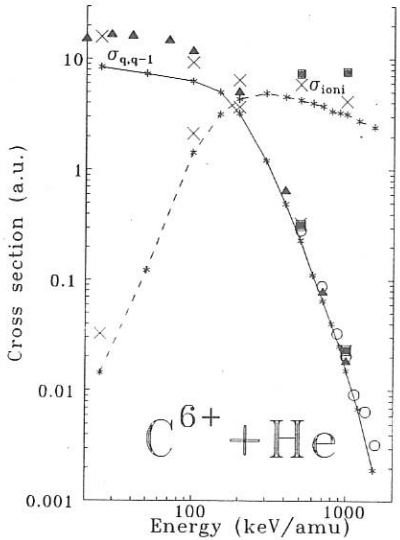

Figure 6 Same as Figure 4;X are the two steps CTMC results

/1/ H.W. Drawin, K. Katsonis, Edts, "Atomic and Molecular Data for Fusion", Phys. Scr. **23**, No 2 (1981).
/2/ C.F. Barnett et al., Oak Ridge National Laboratory, "Atomic Data for Fusion series", "Red Book" e.g. ORNL-6086, **1** (1990) or /13/
/3/ R.K. Janev, K. Katsonis, Nucl. Fusion **27**, 1493 (1987).
/4/ K. Katsonis, G. Maynard and R.K. Janev, Phys. Scr. **T37**, 80 (1991).
/5/ G. Maynard, R.K. Katsonis and R.K. Janev, Nucl. Fusion, in press.
/6/ C.C. Havener, F.W. Meyer and R.A. Phaneuf, XVII ICPEAC, Brisbane, 381 (1991).
/7/ W. Fritsch, H.B. Gilbody, R.E. Olson, H. Cederquist, R.K. Janev, K. Katsonis and G. Yudin, Phys. Scr. T37 11 (1991).
/8/ R.A. Phaneuf, "Assessment of Ion-Atom Collision Data for Magnetic Fusion Plasma Edge Modelling", in "IAEA Co-ordinated Research Programme Meeting" Report INDC(NDS) - Vienna (1990).
/9/ G. Peach, S.L. Willis and M.R.C. McDowell, J. Phys. B **18** 3921 (1985).
/10/ T.V. Goffe, M.B. Shah and H.B. Gilbody, J. Phys. B **12** 3763 (1979)
/11/ M.B. Shah and H.B. Gilbody, J. Phys. B **14** 2831 (1981)
/12/R. Shingal and C.D. Lin, J. Phys. **B 24** 251 (1991)
/13/R.A. Phaneuf, R.K. Janev and M.S. Pindzola *"Atomic Data for Fusion"* ORNL-6090/v5 (1987)
/14/T.R. Dillingham, J.R. Macdonald and P. Richard, Phys. Rev. **A 24** 1237 (1981)
/15/J.L. Shinpaugh, J.M. Sanders, J.M. Hall, D.H. Lee, H. Schmidt-Böcking, T.N. Tipping, T.J.M. Zouros and P. Richard, Phys. Rev. **A 45** 2922 (1992)

Investigation on the metastable fragmentation of mixed argon-oxygen and argon-krypton cluster ions: The observation of two new fragmentation decay channels - evidence for the existence of metastable excited dimer ions ArO^{+*} and $ArKr^{+*}$

M. Foltin, P. Lukáč[#] and T.D. Märk

Institut für Ionenphysik, Leopold Franzens Universität, Technikerstrasse 25, A-6020 Innsbruck, Austria

Introduction

Recently we have discovered a new metastable fragmentation reaction channel of Ar_n^+ and Ne_n^+ cluster ions, initiated by the radiative decay and subsequent dissociation of an $Ar_2^*(^3\Sigma_u^+)$ or $Ne_2^*(^3\Sigma_u^+)$ excimer, respectively, embedded within the cluster [1,2]. This observation provided clear evidence for a possible coexistence of an ionized "chromophore" (e.g. Ar_2^+ or Ne_2^+) and a localized long-living electronically excited state ($Ar_2^*(^3\Sigma_u^+)$ or $Ne_2^*(^3\Sigma_u^+)$) inside the cluster. The interesting question which still remains open is the type of bonding (or the type of interaction) between the ionized chromophore and the excited state.

In order to explain the red spectral shift between a new observed emission continuum attributed to the emission of an Rg_2^* excimer embedded within the Rg_n^+ cluster *ion* and the well known "main" continuum observed in free excimers and excimers embedded in neutral clusters, Bondarenko and coworkers [3] have recently developed a simple model based on the polarization interaction between the Rg_2^+ ionic chromophore and the Rg_2^* excimer. Using this model, our preliminary molecular dynamics (MD) simulations on Ar_n^{+*} cluster ions [4] have shown good agreement with the experimantal values of the number p of evaporated monomers for cluster sizes n>20, i.e for the case when the first icosahedral shell of the parent ion Ar_n^{+*} is filled completely and the second shell is filled at least partially. For smaller cluster sizes (n<20), however, agreement between the MD simulations and the experiment is poor, i.e. the number of evaporated monomers predicted by the MD simulation is too small. This disagreement indicates that it is important to examine the possibility of stronger (covalent) bonding between the Ar_2^* excimer and the ionic chromophore of the cluster ion, allowing the formation of an Ar_4^{+*} complex in the centre of the cluster ion, surrounded by the first shell of neutral Ar atoms, which might be boiled off when the complex dissociates. It is important to note that the ion core of the $Ar_2^*(^3\Sigma_u^+)$ excimer is equivalent to the Ar_2^+ $(^2\Sigma_u^+)$ ion, i.e. the resonant electron exchange between the Ar_2^* excimer and the Ar_2^+ ionic chromophore in the cluster ion: $Ar_2^* + Ar_2^+ \rightarrow Ar_2^+ + Ar_2^*$ might promote formation of such a complex.

To give more insight into this phenomenon, we have studied in this work the metastable fragmentation in systems where the ionic chromophore of the cluster ion is different from the ion core of the excimer and where the above mentioned resonant electron exchange would be impossible.

[#] Dept. of Plasmaphysik, Faculty of Mathematics and Physics, Comenius University, CS-842 15 Bratislava, CSFR

The metastable fragmentation of the stoichiometric and the nonstoichiometric argon-oxygen cluster ions

Electron impact ionization of $Ar_m(O_2)_r$ clusters leads to production of both the stoichiometric $Ar_n(O_2)_q^+$ and the nonstoichiometric $Ar_n(O_2)_{q-1}O^+$ cluster ions. Whereas all of those ions decay via the usual single monomer evaporation, only Ar_nO^+ cluster ions are showing evaporation of more than one monomer in the metastable time regime. Fig. 1 shows the dependence of the metastable fraction (which is the ratio between the fragment ion current and the parent ion current measured at an electron energy of 70 eV) on the number of evaporated monomers p for Ar_8O^+ and $Ar_{10}O^+$ cluster ions decaying in the first field-free region of our mass spectrometer via the decay reaction

$$Ar_nO^+ \rightarrow Ar_{n-p}O^+ + p.Ar \quad (p>1). \qquad (1)$$

For comparison, the same dependence is shown in Fig. 2 for the metastable fragmentation of Ar_9^+ and Ar_{11}^+ cluster ions, decaying by excimer-induced fragmentation. In both cases the average number of evaporated monomers from the parent ions of comparable size is similar, indicating that the excess energy which has to be released from intramolecular to intermolecular modes prior to the fragmentation is also similar (appr. 1 eV, see e.g. [1]).

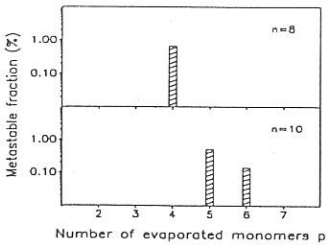

Fig.1. $Ar_nO^+ \rightarrow Ar_{n-p}O^+ + p.Ar$

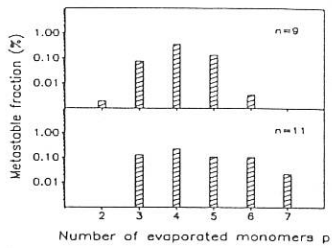

Fig.2. $Ar_n^+ \rightarrow Ar_{n-p}^+ + p.Ar$

In the case of pure Ar cluster ions the strongest evidence pointing to Ar_2^* as the origin of the metastable fragmentation was provided by the electron energy dependence of the fragment ion current, which is starting to appear at a threshold electron energy shifted by approx. 12 eV to higher energies with respect to the appearance energy of the Ar_n^+ parent ions. Since there exists no metastable excited state of the Ar^+ ion at these energies, it was concluded that a *neutral* excited state ($Ar^*(^{1,3}P)$) is formed within the cluster, giving rise to production of the $Ar_2^*(^3\Sigma_u^+)$ excimer [1,2]. In this work the electron energy dependence was measured for both the parent and the fragment ion currents of the metastable decay reaction channel $Ar_{10}O^+ \rightarrow Ar_5O^+ + 5.Ar$ (see Fig.3). For comparision, the electron energy dependence of the excimer-induced fragmentation $Ar_{10}^+ \rightarrow Ar_5^+ + 5.Ar$ is also shown (Fig. 4).

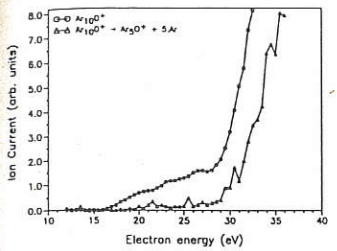

Fig.3. Dependence of the ion current on the electron energy for the parent (o) and the fragment (Δ) cluster ions for the metastable decay reaction $Ar_{10}O^+ \rightarrow Ar_5O^+ + 5.Ar$

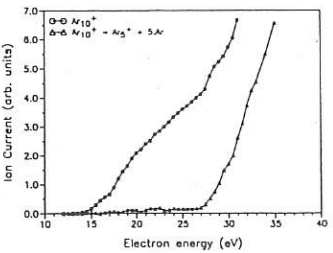

Fig.4. Dependence of the ion current on the electron energy for the parent (o) and the fragment (Δ) cluster ions for the metastable decay reaction $Ar_{10}^+ \rightarrow Ar_5^+ + 5.Ar$

Interestingly, the appearance energy (AP) of the metastable fragmentation $Ar_{10}O^+ \rightarrow Ar_5O^+ + 5.Ar$ (appr. 28 eV, see Fig. 3) is very similar to the AP of the excimer-induced fragmentation $Ar_{10}^+ \rightarrow Ar_5^+ + 5.Ar$ (which is appr. 27 eV, see Fig. 4). Since the AP of the ground state O^+ is around 19 eV, one would expect that an excimer-induced fragmentation in the $Ar_{10}O^+$ cluster ion should start at around 30 to 31 eV, but this value could be lowered somewhat due to the solvation (see the parent ion signal of $Ar_{10}O^+$, which starts to appear at 17 eV instead of 19 eV, Fig. 3). However, in contrast to the pure argon, there exist *ionic* metastable excited states $O^{+*}(^2D)$ and $O^{+*}(^2P)$ which are populated by the dissociative ionization of O_2 molecules just in the energy region of 22 to 30 eV. The fact that these states are populated with a high probability also in $Ar_{10}O^+$ cluster ions is proved by the electron energy dependence of the parent ion current.

This leads to the conclusion that the metastable fragmentation (1) is *not* an excimer-induced decay, but (as follows from the electron energy dependence, Fig. 3) the metastable *ions* $O^{+*}(^2D)$ and $O^{+*}(^2P)$ are involved in the fragmentation. The fact that this fragmentation is not observed for $Ar_n(O_2)_qO^+$ (q>0) cluster ions can be explained by the quenching of the metastable O^{+*} ions in the fast charge-transfer reaction $O^{+*} + O_2 \rightarrow O_2^+ + O$, which is observable in the gas phase with a reaction rate of more than 5.10^{-10} $cm^3.s^{-1}$. It is known that the radiative lifetime of the $O^{+*}(^2D)$ and $O^{+*}(^2P)$ ions is several seconds.

In the gas phase under thermal conditions these ions can react with argon by the charge-transfer reaction $O^{+*} + Ar \rightarrow O + Ar^+$. The fact that during the metastable fragmentation (1) the oxygen atom (or atomic ion) remains within the cluster indicates that (in contrast to the Ar_2^* excimer-induced decay) the fragmentation is initiated by a *bound-bound* transition, followed (most presumably) by quenching of the vibrational excitation of the lower electronic state populated in this very transition. Thus we propose that a metastable dimer ArO^{+*} (corresponding to $O^{+*}(^2D,^2P)$ ion bound with the neighbouring Ar atom) is formed after the ionization within the cluster, which decays (radiatively or via curve-crossing) in the metastable μs time regime to a vibrationally excited lower bound state Ar^+O or ArO^+, which is then vibrationally quenched.

The metastable fragmentation of argon-krypton cluster ions

We found that in case of mixed $Ar_nKr_q^+$ cluster ions (n<41, q<4) the rare gas excimer-induced metastable fragmentation channel is completely quenched. Since there is a spectral overlap between the Ar_2^* emission and the Kr absorption, this effect can be explained by a fast energy transfer from the Ar_2^* excimer to the Kr impurity, proceeding either via the Förster-Dexter long-range electronic energy transfer mechanism (known in solids) or by direct energy transfer during bimolecular collision of Kr and Ar_2^* inside the cluster. Surprisingly, when only one Kr atom is present in an argon cluster ion, a new metastable fragmentation channel is appearing, very much different from the excimer-induced fragmentation (both in the appearance energy, the time dependence and the number of evaporated monomers) and not observed up to now.

The number of evaporated monomers p in this new decay channel increases from p=2-3 for n=11 to p=4-6 for n=40. For n<11 this fragmentation channel cannot be resolved from the usual single-monomer evaporation. For n>24 the number of evaporated monomers is reaching an assymptotic value of p_{max}=4-6. When comparing this value with the number of monomers evaporated during the photofragmentation of argon cluster ions , it is possible to estimate the energy needed for this evaporation to be approx. 0.45 to 0.55 eV.

The electron energy dependence of the fragment ion current for this metastable decay reaction of Ar_nKr^+ cluster ions follows the electron energy dependence of the parent ion current and the difference in appearance energies is smaller than 1 eV. It was found that this metastable decay reaction is much slower than both the excimer-induced fragmentation of pure Ar_n^+ cluster ions and the new metastable fragmentation (1) of Ar_nO^+ cluster ions.

This new metastable fragmentation channel is quenched when two Kr atoms are present in the cluster. This fact and the appearance energy indicate that a metastable state of the $ArKr^+$ chromophore (e.g. a $Ar(^1S_0)+Kr^+(^2P_{1/2})$ or $Ar^+(^2P_{1/2,3/2})+Kr(^1S_0)$ bound state) is responsible for this fragmentation. When more than one Kr atoms are present inside the cluster, this state is apparently quenched by a $ArKr^+ + Kr \rightarrow Ar + Kr_2^+$ switching reaction.

Acknowledgement

This work was partially supported by the Österreichischer Fonds zur Förderung der Wissenschaftlichen Forschung and by the Bundesministerium für Wissenschaft und Forschung, Wien. It is a pleasure to thank Dr. Gerhard Walder (Univ. Innsbruck) for assistance during the argon-krypton measurements and Dr. Y. Ji (Academica Sinica, Hefei) for assistance during the argon-oxygen measurements. We also wish to thank Prof. U. Landman (Georgia Tech., Atlanta) for providing us with a basic program package for the molecular dynamics simulations.

References

1. M. Foltin, G. Walder, A.W. Castleman, Jr., and T.D. Märk, J. Chem. Phys. **94** (1991) 810
2. M. Foltin and T.D. Märk, Chem. Phys. Lett. **180** (1991) 317
3. E.A. Bondarenko, E.T. Verkhovtseva, Yu.S. Doronin and A.M. Ratner, Chem. Phys. Lett. **182** (1991) 637
4. M. Foltin, M. Kolibiar, U. Landman and T.D. Märk, unpublished results

ION ATTACHMENT TO VAN DER WAALS CLUSTERS: REACTIONS OF NO^+ WITH Ar_m

M. Lezius, P. Scheier and T.D. Märk

Institut für Ionenphysik, Leopold Franzens Universität, Technikerstr. 25, A 6020 Innsbruck, Austria

1. Introduction

Besides electron impact ionization /1/ as the major tool in producing cluster ions from expanded cluster jets, photon ionization /2/, Penning and associative ionization /2,3/ and electron attachment /4/ have been used to prepare in many ways and to study in detail atomic and molecular cluster ions /5/. In the present communication we present for the first time (see also Ref. /6/) an alternative ionization method based on the interaction of ions with neutral van der Waals clusters, i.e. the attachment of NO^+ ions to Ar_m clusters.

2. Experimental technique

The supersonic expansion type cluster source, the electron impact ion source and the double focussing sector field mass spectrometer analyzer used in the present studies have been described in detail previously /1 /. The present use of this apparatus differs from this earlier configuration in that a second reagant port has been added to the ion source and the operating conditions of the ion source have been changed. In operation, a neutral argon cluster beam is produced by expanding pure Ar gas at a constant temperature (typically - 160°C) and a constant pressure (typically 1.5 bar) through a 20 μm nozzle into vacuum. The ensuing supersonic beam proceeds through a skimmer into a differentially pumped Nier type ion source. In this ion source stagnant NO gas (introduced into the ion source via a supplementary gas port) is ionized by an electron beam (directed at right angles to the cluster beam) of variable energy thereby producing thermal NO^+ ions. Primary NO^+ ions and NO^+ ions reacted with Ar_m clusters (yielding associates of

the form $Ar_n.NO^+$) are then (i) extracted at right angles from this ion reactor, (ii) accelerated by an acceleration voltage U (up to 3 keV), (iii) analyzed in a 48.5° magnetic sector field (with a radius of 60 cm) followed by a 90° electric sector field (with a radius of 21 cm), and (iv) detected after postacceleration with a Faraday cup or an electron multiplier. This two sector configuration has several uses. Its combined action permits mass analysis with high resolution and sensitivity, whereas separate use allows quantitative studies on metastable decay reactions.

Because the reacting NO^+ ions are produced by electron impact ionization at the very position where the Ar_m clusters are to react with the NO^+ ions, it would appear impossible to distinguish $Ar_n.NO^+$ ions produced by NO^+ ion attachment to Ar_m clusters from other growth processes, such as a possible two step process where the Ar_m cluster are first ionized by the electron beam and the Ar_m^+ cluster ions formed are then reacting with the stagnant NO gas. Using however, electrons with energies below the appearance energies of argon and argon cluster ions (i.e. 15.8 eV and 14.6 eV, respectively /1 /), it is possible to only ionize NO molecules. Varying the electron energy and the NO gas pressure, we are able to demonstrate that these experimental conditions actually do allow the NO^+ attachment reactivity to be readily isolated from other processes.

3. Results and Discussion

Fig. 1a shows a mass spectrum of an argon cluster beam obtained by NO^+ attachment. The resulting mixed cluster ions $(Ar_{n-1}.NO)^+$ show strong peaks at cluster sizes 13,19,23, 26, 29, 49 and 55 (where for instance cluster size 13 corresponds to 12 Ar plus one NO constituent). It is interesting to compare these results with those found for direct electron impact ionization of neutral Ar_m or $Ar_m.NO$ clusters produced by jet expansion. Whereas the mass spectrum for the mixed clusters $Ar_m.NO$ is rather similar to the one shown in Fig. 1a, the mass spectrum for pure Ar_m clusters (see Fig. 1b) is

significantly different in general shape and in the sequence of maxima (i.e. strong peaks at 14, 16, 19, 21 and 27).

From previous investigations on the electron impact ionization of vdW clusters /1,5/ it can be concluded that the different shape (i.e. shift of the maximum of the distribution and the center of gravity of the distribution to lower n in case of electron ionization) is due to stronger fragmentation during the ionization events. That is, NO^+ attachment is a softer ionization technique preserving more of the neutral distribution than electron impact ionization. Similar effects have been observed when comparing electron impact ionization with electron attachment spectra /4/.

This point also leads to an interpretation of the difference in the structure of the well defined anomalies (magic numbers). Very likely, in case of electron impact ionization, in addition to structure in the spectrum arising from the initial neutral cluster distribution, additional anomalies may be introduced by a size dependent ionization and fragmentation cross section, by size dependent energy deposition and disposal, and by variation in the stability of the resulting charged clusters.

4. Acknowledgements

Work partially supported by the Österreichischer Fonds zur Förderung der Wissenschaftlichen Forschung and the Österreichische Nationalbank, Wien.

5. References

/1/ T.D. Märk, Int. J. Mass Spectrom. Ion Proc., 79 (1987) 1
/2/ C.Y. Ng, Vacuum Ultraviolet Photoionisation and Photodissociation of Molecules and Clusters, World Scientific, Singapure (1991)
/3/ H.P. Birkhofer, H. Haberland, M. Winterer and D.R. Worsnop, Ber. Bunsenges. Phys. Chem., 88 (1984) 207
/4/ T.D. Märk, Int. J. Mass Spectrom. Ion Proc., 107 (1991) 143
/5/ T.D. Märk and O. Echt, Chapter 5.6 in Clusters of Atoms and Molecules (H. Haberland, Ed.) Springer, Heidelberg (1992) in print
/6/ M. Lezius, P. Scheier and T.D. Märk, Verhandlungen Deutsch. Phys. Ges., 5 (1992) 1230

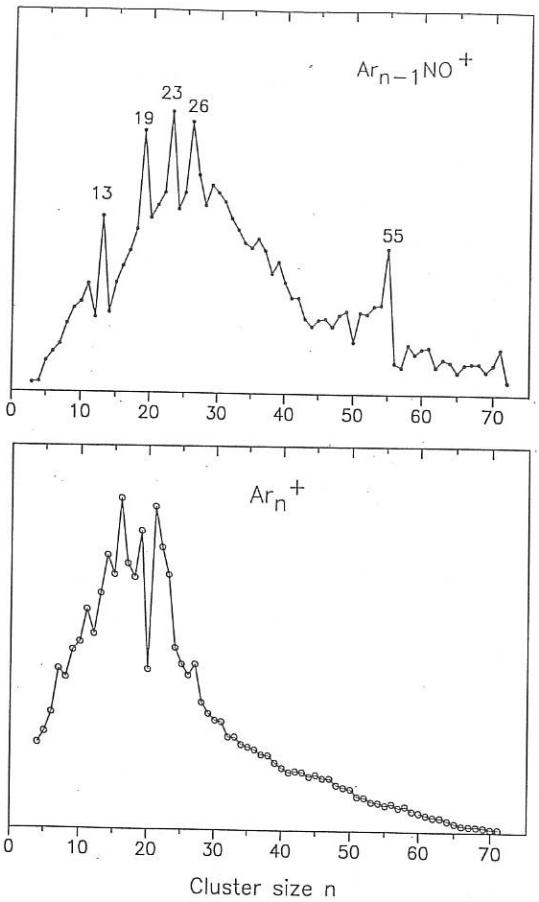

Fig. 1. Mass spectra of an argon cluster beam produced by nozzle expansion.
Upper part: NO^+ attachment ionization
Lower part: Electron impact ionization (electron energy 17 eV)

On the Interaction of Low Energy Electrons with vdW-Clusters : Electron Attachment Reactions and Auto-Scavenging

T.Rauth, M.Lezius, M.Foltin, V.Grill, T.D.Märk

Institut für Ionenphysik, Leopold Franzens Universität Technikerstraße 25, A-6020 Innsbruck, Austria

1. Introduction :

Besides investigations on electron impact ionization, studies on electron attachment reactions and on electron scavenging helps to elucidate elementary processes occurring in various plasmas. In this respect it is not only interesting to study interactions with atoms or molecules, but also with clusters due to their unique properties and the possibility to study ions not being easily accessed otherwise, e.g. CO_2^- or SF_7^-.

We are presenting here relative electron attachment cross sections, called electron attachment spectra (EAS), of (i) the non-stoichiometric cluster anions $(CO_2)_n \cdot O^-$, $(CO_2)_n \cdot O_2^-$, $(SF_6)_n \cdot SF_5^-$, $(SF_6)_n \cdot SF_4^-$, $(SF_6)_n \cdot SF_3^-$, and the superhalogenic $(SF_6)_n \cdot SF_7^-$ formed by direct and indirect electron attachment processes and of (ii) mixed rare gas/molecule cluster anions, i.e. $Xe \cdot SF_6^-$, $Ar \cdot O_4^-$, and $Ar \cdot O_3^-$, giving clear evidence on sequential inelastic scattering processes of the incoming electron within these clusters (auto-scavenging).

The interaction of low energy electrons (with energies below the ionization potential) with neutral clusters produces negatively charged cluster ions according to the following three schemes :

(1) direct attachment processes (assoziative and dissoziative) [1]

(2) indirect mechanisms (ion molecule and charge transfer reactions within clusters, quenching of dissoziative attachment channels)

(3) scavenging processes (within clusters we term them "auto-scavenging")

2. CO_2 cluster anions :

The interaction of near thermal electrons with clusters gives rise to the well known zero-resonance in almost all systems [2]. It is therefore possible to produce the CO_2 anion and higher homologues via the interaction of thermal electrons with a CO_2 cluster beam despite the fact that CO_2 has a negative electron affinity of EA ≅ -0.6 eV.

Rising the energy of the electrons interacting with the CO_2 cluster beam we are also able to detect non-stoichiometric compounds $(CO_2)_n \cdot O^-$ and, for the first time, $(CO_2)_n \cdot O_2^-$. Both complexes are formed above an electron energy of 8 eV by direct dissoziative electron attachment (1). The $(CO_2)_n \cdot O_2^-$ compounds can also be produced via a second, indirect process (2) : i.e., by an ion molecule reaction of a primary O^- ion with a neighbouring CO_2 molecule within the cluster in the following steps :

$$(CO_2)_{n+2} + e^- \quad \text{-->} \quad (CO_2)_{n-p'+1}\cdot O^- + CO^* + p'\cdot CO_2$$
$$\text{I-->} \quad (CO_2)_{n-p'-p}\cdot O_2^- + CO + p\cdot CO_2$$

The second step of the reaction has an exothermicity of about 1.35 eV. The resulting O_2^- molecule will probably be stabilized into a CO_4^- molecule in a reaction, which is found to be very fast in the gas phase [3]. Fig.1 shows the EAS (a) of $(CO_2)_n\cdot O^-$ (n = 2, 10) peaking at appr. 4, 9, and 12 eV and (b) of $(CO_2)_{10}\cdot O_2^-$ peaking at about 13 eV and of $(CO_2)_5^-$ peaking at appr. 3, 9, and 12 eV (for more details see [4]).

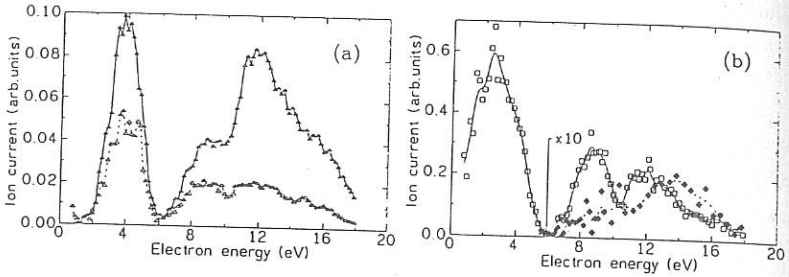

Fig.1: (a) EAS of $(CO_2)_2\cdot O^-$ (Δ) and $(CO_2)_{10}\cdot O^-$ (▲)
(b) EAS of $(CO_2)_5^-$ (□) and $(CO_2)_{10}\cdot O_2^-$ (◆)

3. SF_6 cluster anions :

In the case of SF_6 cluster anions the situation is totally different. Besides the well known zero-resonance of SF_6 clusters there are no other resonant structures in the EAS and it was well accepted, that non-stoichiometric SF_6 cluster anions do not exist in the mass spectrum of SF_6 clusters. The formation of e.g. $(SF_6)_n\cdot SF_5^-$ via direct dissoziative electron attachment was reported to be effectively quenched within the cluster [5]. Expanding our electron energy scale up to 20 eV we have for the first time been able to detect anions of the structure $(SF_6)_n\cdot SF_5^-$ (5.5 and 10 eV), $(SF_6)_n\cdot SF_4^-$ (6 and 13 eV), $(SF_6)_n\cdot SF_3^-$ (14.5 eV), and of the superhalogenic structure $(SF_6)_n\cdot SF_7^-$ (6 and 13 eV) - in brackets are given the peak positions of the resonances shown in the EAS of Fig.2 . Comparing the positions of the observed resonance maxima of the cluster beam with those of the various fragments of gas phase molecules [6] it is clear, that the non-stoichiometric SF_6 cluster anions cannot be produced via direct (1) but must be generated via indirect processes (2).

Considering the energetics of reactions between primary fragments with a neighbouring cluster constituent we have to conclude, that this kind of indirect anion production is

endothermic in almost all cases. Nevertheless the position of the resonance peaks in the EAS of the various complexes gives clear hints as to the energetics of possible primary fragment ions. Taking into account this information we propose that non-stoichiometric SF_6 cluster ions are produced via a two step mechanism, where a primary fragment ion reacts with one of its neutral counterparts caged inside the cluster (and not with a neighbouring molecule).

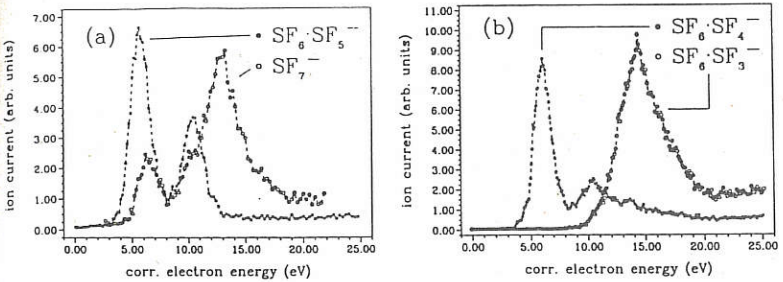

Fig.2 : (a) EAS of $SF_6 \cdot SF_5^-$ and SF_7^- ; (b) EAS of $SF_6 \cdot SF_4^-$ and $SF_6 \cdot SF_3^-$

One example is the production of $(SF_6)_n \cdot SF_4^-$ at about 12 eV :

$SF_6 + e^- \quad \text{-->} \quad SF_2^- + F_2 + F_2$ ..... in the isolated molecule

i.e. within the cluster complex

$$(SF_6)_n + e^- \quad \text{-->} \quad (SF_6)_{n-p'-1} \cdot [SF_2^- + F_2] + F_2 + p' \cdot SF_6$$
$$\text{|-->} \quad (SF_6)_{n-p'-p-1} \cdot SF_4^- + p \cdot SF_6$$

It is interesting to note that we have some experimental evidence, these caging reactions give rise to more excess energy in the energy region below 8 eV than in the region above 8 eV (see [7]).

4. Autoscavenging :

SF_6 is widely used in high voltage devices and in plasma etching processes due to its unique scavenging property . We tried successfully to use this specific property to monitor excited states of the neutral Xe atom in mass spectrometric investigations studying the EAS of mixed Xe/SF_6 cluster anions shown in Fig. 3(a) [8]. The first maximum corresponds to the zero-resonance of SF_6 (the only one in the EAS of neat SF_6 cluster anions); the second resonance rises at about 8.5 eV and shows two maxima appr. 1 eV apart. We attribute the second structure to the first metastable (8.315 and 9.447 eV) and the first radiative (8.44,

9.57, and 10.03 eV) states of the Xe atom [9], respectively. These states are populated via an inelastically scattered electron exciting the Xe atom, loosing all of its energy, and attaching to the SF_6 molecule (3).

Is this third class of anion production mechanisms also observable in other systems, not known as scavenger-gas ? Yes, it is. Producing mixed Ar/O_2 cluster anions the EAS shows two additional structures compared to neat O_2 cluster anions. In Fig. 3(b) the EAS of $Ar{\cdot}O_4^-$ is compared with that of $O_4^-/(O_2)_n$. The resonant structure at 11.5 eV may be ascribed to excitation of the first excited states of the neutral Ar atom within the mixed cluster prior to zero energy attachment to an O_2 compound. For more details see Ref. 10.

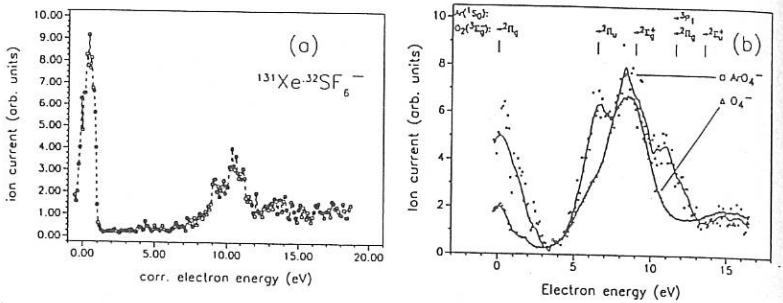

Fig.3 : (a) EAS of $^{131}Xe{\cdot}^{32}SF_6^-$; (b) EAS of $Ar{\cdot}O_4^-$ and $O_4^-/(O_2)_n$

This work was partially supported by the Österreichischer Fonds zur Förderung der wiss. Forschung and by the Österreichische Nationalbank, Wien.

[1] L.G.Christophorou, D.L.McCorkle, A.A.Christodoules, in "Electron-Molecuke Inerteractions and their Applications" (L.G.Christophorou, ed.), Vol.1, Academic Press, Orlando, 1984, p. 477

[2] T.D.Märk, Int.J. Mss Spectrom.Ion Proc. 107 (1991) 143

[3] Y.Kokaku, Y. Hatano, J.Chem.Phys. 77 (1979) 12

[4] M.Lezius, T.Rauth, V.Grill, G.Walder, T.D.Märk, Proc. SASP'92 (D.Bassi, M.Scotoni, P.Tosi, eds.), Pampeago, Trentino, Italy, 1992, p. 3.3

[5] A.Stamatovic, P.Scheier, T.D.Märk, J.Chem.Phys. 88 (1988) 6884

[6] L.E.Kline, D.K.Davies, C.L.Chen, P.J.Chantry, J.Appl.Phys. 50 (1979) 6789

[7] T.Rauth, O.Echt, T.D.Märk, to be published; T.Rauth, Thesis, Innsbruck, 1992

[8] T.Rauth, M.Foltin, T.D.Märk, J.Phys.Chem. 96 (1992) 1528

[9] A.A.Radzig, B.M.Smirnov, Reference Data on Atoms, Molecules, and Ions, Springer, Berlin, 1985

[10] M.Foltin, V.Grill, T.D.Märk, Proc. SASP'92 (D.Bassi, M.Scotoni, P.Tosi, eds.), Pampeago, Trentino, Italy, 1992, p. 3.33

Particle Exchange Reactions at Low Kinetic Energies

C. Praxmarer, W. Freysinger, A. Hansel and W. Lindinger

Institut für Ionenphysik, Universität Innsbruck, Technikerstr. 25, A 6020 Innsbruck, Austria

A Selected Ion Flow Drift Tube (SIFDT)[1] was used to investigate particle exchange reactions of N_4^+, Ar_2^+, Kr_2^+ and ArN_2^+ dimer or dimer like ions colliding with various neutrals at mean center of mass energies, KE_{cm}, ranging from 0.05 to about 2 eV. The KE_{cm} is changed by variation of E/N (E is the axial electric field strength and N the buffer gas density) and is calculated in the usual way[2] using the relation

$$KE_{cm} = \frac{M}{m+M} \left(KE_{ion} - 3/2\ k_b T\right) + 3/2\ k_b T,$$

where KE_{ion} is the mean kinetic lab energy of the reactant ions according to Wannier[3],

$$KE_{ion} = 3/2\ k_b T + 1/2\ m v_d^2 + 1/2\ M v_d^2.$$

Here, v_d is the drift velocity of the reactant ions, T is the buffer gas temperature, k_b is the Boltzmann constant and m,M and M_{ion} are the masses of the buffer gas, the reactant gas and the ions, respectively. As helium was used as a buffer gas, the relative kinetic energy between the ions and neutral reactants (all having much larger masses than the buffer gas atoms) is always larger at elevated E/N than the relative energy between the ions and the buffer gas atoms. The latter one determines the internal excitation of the ions[4], therefore any changes observed (as dependent on E/N) in the rate coefficients or product channels are mainly due to the variation in KE_{cm} and do not primarily reflect an influence of the internal energy (vibrational excitation) of the ions. The present results indicate, that particle exchange (switching) is competing with charge transfer, but is usually not dominant, when the recombination energy RE(I) of the dimer ions is larger or at least close to the ionization potential IP(R) of the neutral reactant. Switching is the only possible reaction mechanism if charge transfer is endothermic. The overall rate coefficients

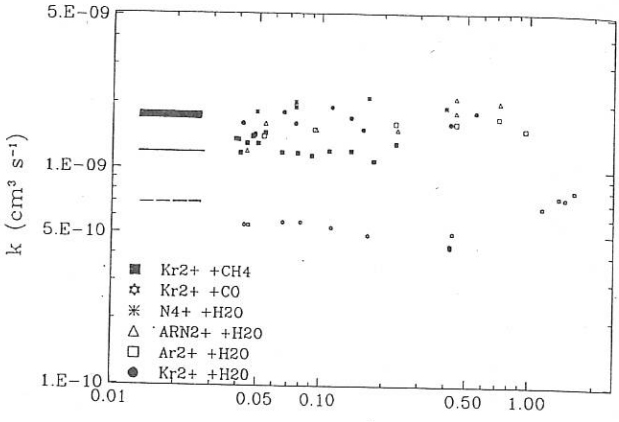

Fig.1:
Rate coefficients of the overal reactions indicated in the Figure as dependent on KE_{cm}. (▬▬) indicates the collisional limiting values for the reactions of N_4^+, N_2Ar^+, Ar_2^+ and Kr_2^+ with H_2O, and for Kr_2^+ with CO (— — —) and CH_4 (——) respectively.

observed are close to the collisional or Langevin limit[5] in most cases and independent of KE_{cm} (see Fig.1), whereas the product channels resulting in particle exchange decline at elevated KE_{cm} (see e.g. Fig. 2). As Fig. 2 shows, there is a qualitative correlation between the bond strengths of the product ions and the KE_{cm} values, where a significant decline of the fraction of the switching channel occurs.

Several reactions of N_2Ar^+ ions show additionally interesting details. The main

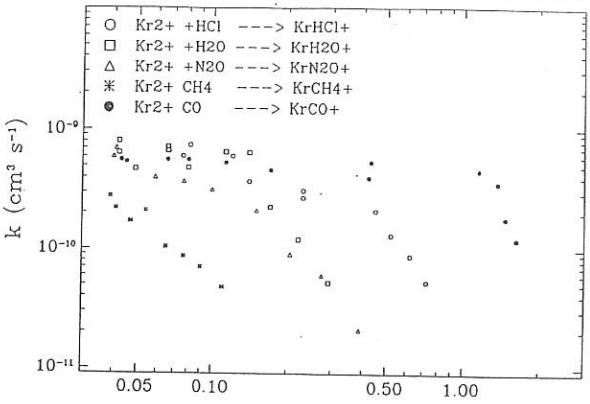

Fig.2:
Rate coefficients for the switching channels only of the reactions indicated in the figure.

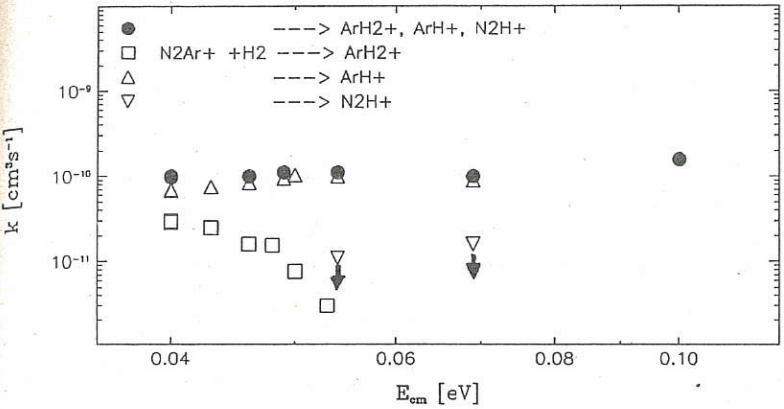

Fig.3:
Energy dependencies for the reactions of N_2Ar^+ with H_2.

products in the reaction with H_2 are ArH^+ and ArH_2^+ (Fig.3), while hardly any N_2H^+ (or $N_2H_2^+$) is observed. This infers, that the charge in the N_2Ar^+ ion is connected with the Ar-atom rather than with the N_2 molecule, despite of the slightly larger ionization potential of Ar as compared to the one of N_2. Probably the internuclear distance R in the N_2, bound within the N_2Ar^+ ion is slightly shifted with respect to R_o of the isolated neutral N_2, so that the position of the charge on the Ar-atom is energetically favoured. This is also supported by recent calculations of K. Hiraoka et.al[6]. Additional support for that arises from data on the reaction of N_2Ar+ with Kr, where ArKr+ is the only switching product observed.

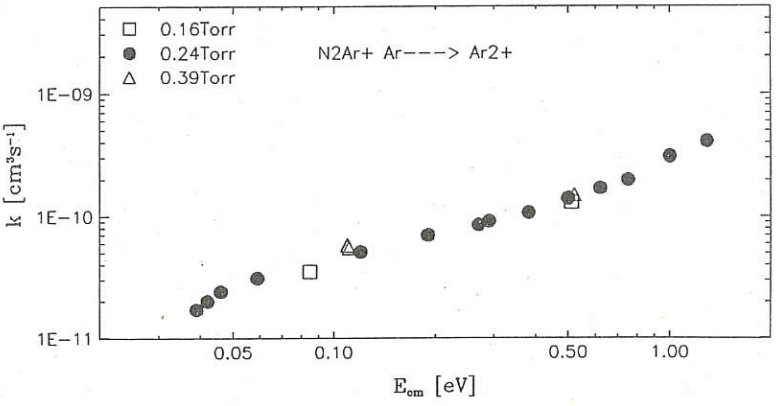

Fig.4:
Energy dependencies for the reactions of N_2Ar^+ with Ar.

No charge transfer product H_2^+ was observed as the recombination energy of N_2Ar+ (RE= 14.5eV) is smaller than the ionisation potential of H_2 (IP= 15.43eV). At elevated KE_{cm} the loosely bound ArH_2+ ion becomes unstable and presumably a successive proton transfer $H_2^+ + Ar \rightarrow ArH^+ + H$ occurs before the H_2^+ could leave the $(Ar \ldots H_2^+)$ collision complex.

In the case of N_2Ar^+ colliding with Ar an increase of the overall rate coefficient from $k = 2x10^{-11}$ cm^3sec^{-1} at KE_{cm} = 0.04 eV to $k \sim 5 \times 10^{-10} cm^3sec^{-1}$ at 1.2 eV is observed (Fig.4). At low energies obviously an exchange of Ar-Ar is favoured due to the better mass-match as compared to the Ar-N_2 exchange. The Ar-Ar exchange however cannot be seen as long as no isotopically labelled Ar is used, thus the observed rate coefficient reflects only the ion-mass changing Ar-N_2 exchange channel, resulting in the product Ar_2^+. Also an increase of k is observed in the analogous reaction of N_2Ar^+ with N_2, where only the exchange Ar-N_2 results in a product ion of different mass (N_4^+) but not the N_2-N_2 exchange, which again due to the better mass-match is favoured at low collision-energies.

This work was supported by the Fonds zur Förderung der Wissenschaftlichen Forschung.

References

1. M. Kriegel, R. Richter, W. Lindinger, L. Barbier, and E.E. Ferguson,J. Chem. Phys.,88 (1988) 213

2. M. Mc Farland, D.L. Albritton, F.C. Fehsenfeld, E.E. Ferguson and A.L. Schmeltekopf, J. Chem. Phys. 59, 6620, (1973)

3. G.H. Wannier, Bell Syst. Tech. J., 32 (1953) 170

4. L. Viehland, and D.W. Fahey, J. Chem. Phys., 78 (1983) 435

5. T. Su, and M.T.Bowers, Int. J. Mass Spectrom. Ion Phys., 12 (1973) 347

6. K. Hiraoka, T. Mori, and S. Yamato, Chem. Phys. Lett., 189 (1992) 7

Collisional Induced Dissociation of Kr_2^+, $(CO)_2^+$, N_4^+ and N_2Ar^+

C. Praxmarer, J. Glosik§, D. Smith, W. Freysinger and W. Lindinger

Institut für Ionenphysik, Leopold Franzens Universität,
Technikerstr. 25, A 6020 Innsbruck, Austria

§Department of Electronics and Vacuumphysics, Mathematics and Physics Faculty,
Charles University, V. Holesovickach 2, Prague, CSFR

INTRODUCTION

Static drift tubes and flow drift tubes have been used for many years to study ion - molecule reactions in the energy regime from thermal to a few electron volts [1]. Thus the rate coefficient, k, and product ions have been determined for many ion - molecule reactions, and it has been the usual procedure to present the data as plots of k versus E_r (the reactant ion/reactant neutral center-of-mass energy) and to describe the variation of k with E_r as due to the variation of kinetic energy of the reactants. When the reactant ions are atomic this is clearly a sensible procedure, since no significant internal (electronic) excitation of the ions can occur in collisions with the buffer (or reactant) gas atoms at the ion energies involved. Obviously this is not the case when molecular ions are involved, because of the high probability that rotational/vibrational excitation will occur, and which can immediately influence the reactivity of the ion. Several drift tube studies of this phenomena have been reported and it is with this that this paper is largely concerned. Clearly in this case the relevant energy to consider is the reactant ion/carrier gas atom center-of-mass energy which here we designate as E_c. Both internal excitation and de-excitation will occur in collisions of the ion with the carrier gas, and under steady state conditions (i.e. excitation rate = de-excitation rate) then the internal energy state distribution of the ion will be characterised by E_c. This has been demonstrated by Lindinger and his colleagues for the vibrational excitation of N_2^+ and O_2^+ in helium carrier gas in a selected ion flow drift tube (SIFDT) experiment, who have also shown how vibrational excitation (and kinetic excitation) influences the course of ion/molecule reactions in SIFDT experiments in He and Ar carrier gases (these studies have been summarised by Lindinger [2]). The data are in agreement with theoretical calculations of Viehland et al. [3] predicting that molecular ions drifting in an atomic buffer gas will reach an effective internal temperature, T_{eff}, given by

$$3/2k_bT_{eff} = [1+ (M_b/M_i)\xi]^{-1} \times (3/2k_bT + 1/2M_bv_d^2) \times (1+\beta),$$

where k_b is Boltzmann's constant, M_b and M_i are the masses of the buffer gas atom and the ion, ξ is a dimensionless ratio of collision integrals that characterizes the fractional energy loss due to inelastic collisions, T is the Temperature of the buffer gas, v_d is the drift velocity and β is a minor correction term.

On the addition of a reactant gas to the drift tube (which almost invariably has a larger atomic (molecular) mass than the carrier gas which usually is helium) then reactant ions which are already vibrationally excited (according to E_c) collide with the reactant gas, the relevant collisional energy then being E_r. The total energy brought into the reaction is then in some way determined by both E_c and E_r and not by E_r alone. In order to gain further understanding of the relative influence of E_c and E_r we have chosen to study perhaps the simplest of reactive systems involving molecular ions which is the collisional induced dissociation (CID) of

some molecular ions, specifically Kr_2^+, N_4^+, $(CO)_2^+$, and N_2Ar^+ dimer and dimer-like ions, firstly in pure helium carrier gas to properly appraise the dependence of the dissociation rates on E_c, alone and then secondly by adding chemically inert 'heavy' gases (i.e. variously Ne, Ar and N_2) to investigate how the combination of E_c and E_r influences the dissociation rates of these ions.

EXPERIMENTAL

The experiments were carried out using the Innsbruck SIFDT [4]. The experimental approach used to the study of the collisional dissociation has been described previously by Smith et al [5]. The mobilities of Kr_2^+ and $(CO)_2^+$ were determined in our laboratory using the SIFDT; the mobilities of N_4^+ and N_2Ar^+ were taken from [6].

In order to determine k values for the dissociation of these ions in collisions with other gases, conventional SIFDT experiments were carried out in which the length of the drift field is fixed and the flow of the "reactant gas" is varied. Thus k is obtained as a function of E_r (remembering that E_c also varies with ε/N). It is important to note that no variations of k were observed with helium pressure over the limited range over which meaningful measurements could be made (i.e. 0.13 to 0.23 torr).

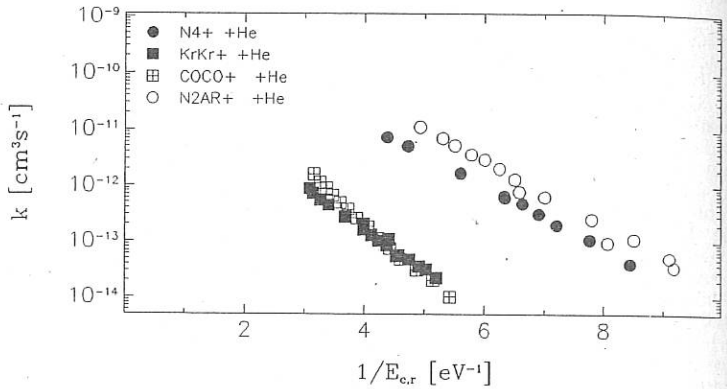

Fig.1: Arrhenius-type plots for the rate coefficients for the dissociation of Kr_2^+, $(CO)_2^+$, N_4^+ and N_2Ar^+ drifting in pure Helium.

RESULTS and DISCUSSION

Typical data are presented in Fig.1 as plots of k versus E_c^{-1}. The good linearity of these plots indicates that k is related to E_c according to an expression of the form $k = A*\exp(-3E_a/2E_c)$. This is of the form of the well-known Arrhenius equation ($k = A*\exp(-E_a/kT)$) in which E_a is equated to an "activation energy" for the reaction (in this case the reaction is dissociation. Note: The 2/3 is introduced since E_c can be equated to 3/2kT). The constant A can be related (with caution !) to the collisional rate coefficient, k_L, for the reactant ion/He atom collisions. Thus, values of E_a and A have been obtained for the reactions studied and they are given in Table 1 together with the experimentally-determined dissociation energies of the ions, D,and the calculated k_L values. The similarity of the E_a and D values is striking and indicates that, at least, for these ions the nonthermal drift tube experiment

approximates to a thermal system. It also indicates that the Viehland expression mentioned above describes quite well the internal excitation of the ions and that the factor including ξ represents only a minor correction.

Table 1 Ion	E_a(eV)	D(eV)	A($*10^9 cm^3 s^{-1}$)	k_L($*10^9 cm^3 s^{-1}$)
Kr_2^+	1.1	1.1- 1.5[a]	0.2	0.54
$(CO)_2^+$	1.0- 1.3	0.97- 1.21[b]	1.0	0.55
N_4^+	0.9	0.9- 1.05[c]	2.0	0.55
N_2Ar^+	0.9	0.94- 1.09[d]	5.0	0.55

[a] see ref. [7], [b] see ref. [8], [c] see ref. [9], [d] see ref. [6]

The derived values of A are within a factor of four of the k_L values. Intuitively, it is expected that the A value should relate to the efficiency of the reaction, (i.e. the probability that dissociation will occur above the threshold energy for dissociation). Thus for efficient reactions A should approximate to k_L as is observed. However, it is difficult to see why A should exceed k_L. Clearly, much more work is required before a complete understanding of this is obtained. Fig.2 shows additional data on the dissociation of N_2Ar^+ due to collisions with Ne and N_2.

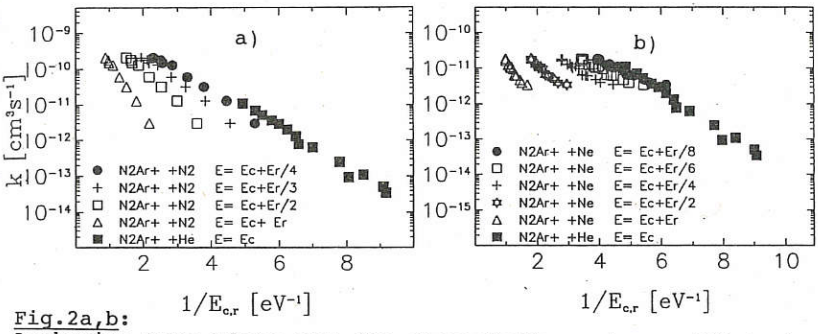

Fig.2a,b: Arrhenius-type plots for the dissociation rate coefficients of N_2Ar^+ drifting in pure Helium and similar plots for the dissociation of this ion in collisions with a) N_2 and b) Ne, added in small amounts to the helium buffer gas. The numbers in the figures correspond to different f- factors.

On the addition of 'reactant gas'to the SIFDT, the drifting ions, with internal energy characterised by E_c established by multiple collisions with the helium buffer gas, undergo collisions with the reactant gas atoms or molecules, the center-of-mass energy being E_r. Such collisions are relatively infrequent, the collision frequency obviously depending on the amount of reactant gas introduced into the helium. In effect, these are single collisions, the total energy in the collision being $E_c + E_r$. This results in an increase of the internal energy of the ion and hence an increase in the probability of and the rate coefficient for dissociation. Obviously in these 'single' collisions the internal energy state distribution cannot be equalibrated to E_r (as it is

to E_c), and thus to use E_r alone in an Arrhenius-type plot with the expectation of deriving E_a values for dissociation is unsound. As can be seen in Fig.2, the plots involving E_r alone result both in in a large displacement along the E^{-1} axis (and hence to high E) from the equilibrium plots involving E_c alone and non-linear plots from which 'E_a' values cannot be obtained. Clearly E_r alone is not the appopriate energy to characterise the dissociation rate; the following is a more appropriate (albeit crude) description of the interaction.

Immediately following the collision with the impurity gas (i.e. Ne, Ar or N_2), a fraction of E_r is converted into internal energy of the ion. Assume that all the E_r is converted to vibrational energy of the ion (i.e. rotational and translational excitation are relatively unimportant). However, at the E_r involved it is unlikely that all the modes of vibration of the polyatomic ions are accessible. Now assume that f modes are accessible and the E_r is shared equally amongst them in some quasi-equilibrium fashion. Then a more appropriate characteristic energy in the interaction is $(E_c + E_r/f)$. Thus Arrhenius-type plots involving $(E_c + E_r/f)^{-1}$ for various f are included in Fig.2. As one might expect, a higher fraction of the kinetic energy is converted into "dissociating energy" for N_2 than for Ne. In the combination of N_2Ar^+-N_2 more modes for energy storage are accessible than the in N_2Ar^+-Ne-complex.

The above represents only a first attempt to explain the respective importance of E_c and E_r in drift tube studies. The phenomenon of collisional dissociation offers the opportunity to gain some understanding on this, but these considerations must be applied also to the study of ion-molecule reactions, for the study of which SIFDT experiments are widely used.

Aknowledgement

This work was supported by the Fonds zur Förderung der Wissenschaftlichen Forschung.

References

[1] W. Lindinger and D. Smith in "Reactions of Small Transcient Species" (eds. A. Fontijn, and M. A. A. Clyne), Academic Press Inc. (London),(1983)

[2] W. Lindinger, Int. J. Mass Spectr. Ion Proc., 80, 115 (1987)

[3] L. Viehland, and D.W. Fahey, J. Chem. Phys., 78, 435 (1983)

[4] W. Dobler, Ph.D. Thesis, University of Innsbruck (1982)

[5] S. C. Smith, M. J. McEwan, K. Giles, D. Smith, and N. G. Adams, Int. J. Mass Spectr. Ion Proc., 96, 77 (1990)

[6] M. Tichy, N. D. Twiddy, D. P. Wareing, N. G. Adams, and D. Smith, Int. J. Mass. Spectr. Ion Proc., 81, 235 (1987)

[7] K. Giles, N. G. Adams, and D. Smith, J. Chem. Phys., 90, 6213 (1989)

[8] C. Y. Ng, Advanc. Chem. Phys., 52, 263 (1983)

[9] K. Stephan, T. D. Märk, J. H. Futrell, and H. Helm, J. Chem. Phys., 80, 3185 (1984)

Theoretical studies of the vibrational relaxation of $N_2^+(v=1)$ in collisions with He using the semiclassical method

V.A. Zenevich*), W. Freysinger and W. Lindinger,
Institut für Ionenphysik der Universität Innsbruck, Technikerstraße 25, A - 6020 Innsbruck, Austria
*) Chemical Physics Laboratory, Heat and Mass Transfer Institute, Byelorussian Academy of Sciences, 220072 Minsk, BYELARUS

Introduction

Rigorous theoretical studies of vibrational relaxation of diatomic ions in collisions with neutrals are, in contrast to to their neutral-neutral analogues, relatively scarce. At the same time the vibrationally inelastic scattering processes in ion-neutral collision systems are of great interest for dynamical investigations in connection with their pronounced long-range electrostatic interaction potential (see for details, see Ref. 1). A number of recent experimental studies in this field (for a review see /1-3/) form a sound experimental background to begin with systematic theoretical investigations.

In this contribution we present the theoretical studies of vibrational relaxation of $N_2^+(v=1)$ in collision with He atoms, a process which was investigated experimentally in our laboratory /4/ using the *SIFDT*-technique in the mean kinetic centre-of-mass energy (KE_{cm}) range from thermal of 0.8 eV. The semiclassical (SC) method /5/, which has proven to give adequate descriptions of vibrationally inelastic processes for a number of neutral and charged collision systems, was used to perform dynamical calculations.

Modelling the *ab initio* potential energy surface

The analytic potential energy surfaces (PES) used in the framework of the SC model were obtained as fits to recent 2D quantum-chemical data /6/. The missing vibrational coordinate dependence in the *ab initio* data /6/ was modelled using the following dumb-bell-like expressions:

$$V_A = -\frac{P}{R^4} + Ae^{-BR} + \sum_{i=1}^{2} D_i\left[e^{-2\beta_i\left(R_i - R_i^*\right)} - 2e^{\beta_i\left(R_i - R_i^*\right)}\right] \qquad (1)$$

$$V_B = \sum_{i=1}^{2}\left[C_i e^{-\alpha_i R_i} - a_i R_i^{-1}\right] \qquad (2)$$

$$V_C = -\frac{P}{R^4} + \sum_{i=1}^{2} \hat{C}_i e^{-\hat{\alpha}_i R_i} \qquad (3)$$

where R is the distance between the He atom and the centre-of-mass of the N_2^+ ion, R_i are the distances between the He atom and the i-th atom of the N_2^+ ion. The values of parameters in all three forms (1) - (3) were obtained using a non-linear constrained minimization algorithm /7/. The following minimization function (weighted rms-fitting) was adopted:

$$G = \left[\frac{1}{N}\sum_{i=1}^{N}\omega_i\left(V_i - E_i\right)^2\right]^{1/2} \qquad (4)$$

where N is the number of *ab initio* points (N= 39), E_i - *ab initio* energies, V_i - values of the analytic PES, ω_i weighting coefficients. Different weighting conditions, more or less emphasizing the *ab initio* points in the vicinity of the potential well, were analyzed.

Results and discussion

The sets of potential parameters for A- and B- type of the interaction potential and different weighting conditions are given in Tables 1 and 2, respectively. The dynamical results obtained using the abovementioned analytic PES are shown in Fig. 1. Similar results are obtained for a PES of the C-type (eq. (3)). It is to see that the dynamical results satisfactorily reproduce the experimental data /4/ in the high and intermediate energy/temperature range. A somewhat poorer agreement is achieved in the near-thermal range (300-500 K). Two reasons can be given to explain the observed difference.

First, though our analytic PES are the fits to the 2D *ab initio* data, the vibrational coordinate dependence - a feature of crucial importance in the vibrational energy exchange processes - is a model construction in the present study. It is not possible to exclude that for this particular ion-neutral interaction potential the dumb-bell-like fitting forms used are not capable to predict the vibrational coordinate dependence accurately. A more detailed discussion of this subject is given in /8/.

Secondly, in spite of the large basis set and the powerful MCSCF-CI method used, the quantum-chemical data /6/ probably, as it is sometimes the case for other systems, to some extent underestimate the dispersion contribution and, accordingly, the potential well depth. But just this feature of the interaction potential strongly influences the low-temperature reaction attributes, as it was discussed earlier /9/.

Thus, it seems that the observed difference between experimental and theoretical results in the near-thermal range is mainly caused by probably not quite adequate vibrational coordinate dependence in the dumb-bell potential representation, though also some influence of the possible underestimation of the potential well depth in the ab initio data /6/ can not be exluded.

From the experimental point of view, more complex reaction mechanisms like clustering processes can eventually take place to some extent in the near-thermal range and thus influence the experimental results. These processes certainly can not be taken into account in terms of the direct, adiabatic binary collision reaction mechanism, assumed in the present theoretical investigation.

Figure 1

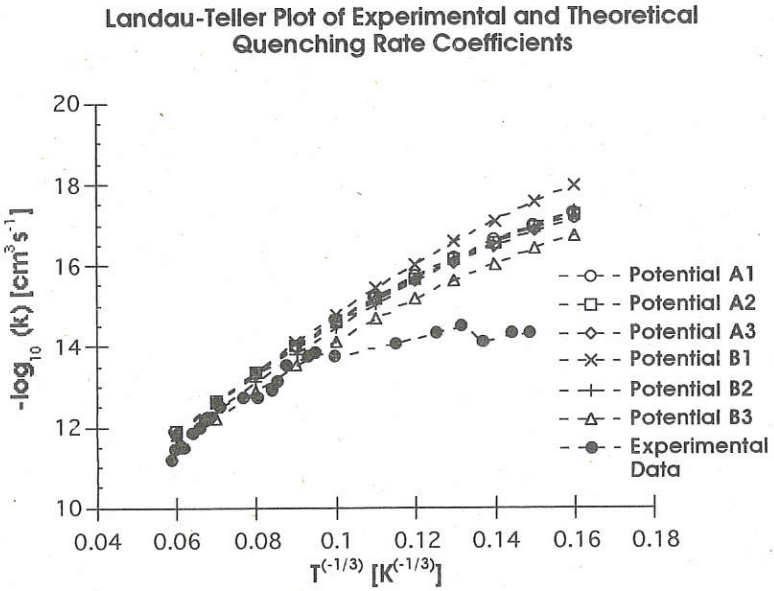

Thus, to explore more completely the dynamics of vibrational relaxation in collisions between N_2^+ and He, additional theoretical and experimental work is needed. Such investigations are under way.

Table 1: Potential parameter sets for different weighting conditions for the A-type potential eq.(1).

Parameter	**A_1**	**A_2**	**A_3**
P [eVÅ^4]	1.494	1.494	1.494
A [eV]	89.80	815.7	159.9
B [Å^{-1}]	2.985	4.277	3.292
D_i [eV]	0.00715	0.00233	0.00559
β_i [Å^{-1}]	1.732	1.703	1.765
R_i^* [Å]	2.921	3.242	2.955

Table 2: Potential parameter sets for different weighting conditions for B-type potential eq. (2).

Parameter	B_1	B_2	B_3
a_i [eVÅ^4]	0.7468	0.7468	0.7468
C_i [eV]	181.9	256.7	389.2
α_i [Å^{-1}]	3.397	3.646	3.921

Acknowledgements

This work was done in the frame of a bilateral agreement between the Institut für Ionenphysik der Universität Innsbruck and the Heat and Mass Transfer Institute of the Byelorussian Academy of Sciences. V.A.Z. thanks the Bundesministerium für Wissenschaft und Forschung for financial support. It is a pleasure to thank Prof. G.D. Billing for useful discussions. The work was partly supported by the Fonds zur Förderung der wissenschaftlichen Forschung.

References

1. E. E. Ferguson, Comments At. Mol. Phys. **24**, 327 (1990)
2. W. Lindinger, Int. J. Mass Spectrom. Ion Proc. **80**, 115 (1987), and refs. cited therein.
3. E. E. Ferguson, Adv. At. Mol. Phys. **25**, 61 (1988)
4. M. Kriegel, R. Richter, W. Lindinger, L. Barbier, E. E. Ferguson, J. Chem. Phys. **88**, 213 (1988), **91**, 4426 (E) (1989)
5. G.D. Billing, Comput. Phys. Rep. **1**, 237 (1987)
6. S. Miller, J. Tennyson, B. Follmeg, P. Rosmus, H.-J. Werner, J. Chem. Phys. **89**, 2178 (1988)
7. G.D. Billing and A. Hunding, Chem. Phys. Lett., **44**, 189 (1976)
8. V.A. Zenevich, W. Freysinger and W. Lindinger (submitted to publication)
9. V. A. Zenevich, W. Freysinger, S. K. Pogrebnya, W. Lindinger, I. K. Dmitrieva, P. I. Porshnev, P. Tosi, J. Chem. Phys. **94**, 7972 (1991)

Ionization and Recombination Processes in Dense Nonideal Plasmas

T. Bornath, M. Schlanges, D. Kremp and M. Bonitz

Universität Rostock, Fachbereich Physik
Universitätsplatz 3, O-2500 Rostock, Germany

In this paper, we consider the nonequilibrium properties of nonideal plasmas which are of interest from the theoretical point of view as well as from that of experimental investigations e.g. in shock wave or laser compression. Especially we are interested in the influence of nonideality effects on the ionization kinetics and on diffusion. The behaviour and the properties of a nonideal plasma are determined by the Coulomb interaction and degeneracy. The Coulomb interaction is important in the "corner of correlation" which is enclosed in the density–temperature–plane by the parameter lines

$$n_e l^3 = 1 \qquad r_s = 1$$

Here $l = e^2/(k_B T)$ is the Landau length and $r_s = d/a_B$ is the Brueckner parameter. In this area, many-particle effects are important, such as dynamical screening of the Coulomb interaction, dynamical self energy, Pauli blocking, formation of bound states and pressure ionization (Mott-effect) [1].

Reaction–diffusion processes are described phenomenologically by coupled reaction–diffusion equations:

$$\frac{\partial n_a}{\partial t} + \nabla j_a = W_a(n_1, ..., n_f), \qquad a = 1, 2, ...f \tag{1}$$

with $j_a = - D_a \nabla n_a$ being the diffusion current and $W_a(n_1, ..., n_f)$ the source function describing the ionization kinetics. An essential problem is the foundation of such reaction-diffusion equations from the fundamental equations of non-equilibrium statistical mechanics.

In order to describe the nonequilibrium properties of nonideal plasmas we have to start from generalized kinetic equations. Then, reaction-diffusion equations can be derived with generalized expressions for the reaction rate and diffusion coefficients which become density-dependent in a complicated nonlinear way due to the nonideality. Therefore, nonlinear macroscopic phenomena like ionization fronts, phase separation etc. can be expected.

Kinetic equations for nonideal reactive systems in which many–body effects must be taken into account were derived in [7] using the method of nonequlibrium real-time Green's functions with the following result for the Wigner distribution function f_a of the free quasiparticles of species a

$$\left\{ \frac{\partial}{\partial t} + \frac{\partial E_a}{\partial p}\frac{\partial}{\partial r} - \frac{\partial E_a}{\partial r}\frac{\partial}{\partial p} \right\} f_a(prt) = \sum_b I_{ab}(p, r, t) + \sum_{bc} I_{abc}(p, r, t) \tag{2}$$

The single-particle energies on the l.h.s. are given by the dispersion relation

$$E_a(prt) = \frac{p^2}{2m_a} + Re\Sigma_a^R(p\omega rt)|_{\hbar\omega = E_a(prt)} \tag{3}$$

where $\Sigma_a^R(p\omega rt)$ is the retarded selfenergy function.

On the r.h.s. of the kinetic equation (2) the collisions between quasiparticles are taken into account. The integrals I_{abc} contain all the possible three-body scattering processes with free and bound particles. Especially, break-up and formation reactions are taken into account. The dynamics of the scattering processes enter the collision integrals via two- and three-particle

T-matrices. Additionally to the kinetic equation (2), a similar equation for the distribution functions F_j of the bound particles can be derived [2].

In the following we consider a plasma consisting of electrons, one-fold charged ions and atoms in the state $|j>$, where j denotes the set of internal quantum numbers. The number densities are n_e, n_i and n_j, respectively.
There are different many–particle effects which have to be taken into account:

1.It is well-known that the properties of strongly coupled plasmas are essentially determined by the screening of the long–ranged Coulomb interaction, i.e. the Coulomb potential has to be replaced by a screened one.

2.The quasiparticle approximation leads to momentum dependent energy shifts to work with is rather difficult. Instead, we used the "rigid shift" approximation [3] in which the energy shift is replaced by a momentum-independent shift reproducing the correct normalization (the correct density n_a). It can be shown that the thermally averaged shift is related to the chemical potential by

$$\mu_a = \mu_a^{id} + \Delta_a \tag{4}$$

3. The two–particle bound states have to be determined from an effective wave equation which was determined on the basis of Green's function techniques [1].

$$\left(\varepsilon_a(p_a) + \varepsilon_b(p_b) + \Delta_{12}^{eff}(p_a p_b z) - z\right) \Psi(p_a p_b)$$
$$- \quad (1 - f_a(p_a) - f_b(p_b)) \int V^{eff}(p_a p_b q z) \Psi(p_a + q, p_b - q) d^3q = 0 \tag{5}$$

In comparison to the Schrödinger equation of an isolated pair of particles there are some differences arising from the self energy corrections Δ^{eff}, Pauli–blocking and the effective potential. Dynamical self energy and effective potential are not independent: thus there is a compensation between self energy and Pauli–blocking effects for bound states whereas the continuum edge is determined by the self energies only . This results in a lowering of the ionization energy with increasing plasma density. The cross over of the continuum edge and the ground state energy defines the so–called Mott density. Above this density, bound states do not exist.

Equations governing the evolution of the number densities in space and time can be obtained by integrating the kinetic equations with respect to the corresponding momentum. The result is an equation similar to (1). The explicit form of the source function W_a follows from the r.h.s. of the kinetic equations, especially from the reaction terms in the three-particle collision integrals. If in the equation for the electron density the source function is written in the form

$$W_e = \sum_{c=e,i} \sum_j (\alpha_c^j n_c n_j - \beta_c^j n_c n_e n_i) \tag{6}$$

defining the coefficients of impact ionization and three body recombination of the atomic level j, these rate coefficients are given in terms of scattering quantities (T-matrices) and distribution functions [5]. The calculation of the rate coefficients is considerably simplificated if we take into account that there are different time scales during the approach to thermodynamic equilibrium. In the following we will assume that with respect to the translational degrees of freedom local equilibrium has been reached already. Thus the distribution functions are Maxwellian.

In this approximation, the following simple relation between the rate coefficients holds

$$\beta_j = \alpha_j \Lambda_e^3 exp(I_j^{eff}/k_B T), \qquad I_j^{eff} = |E_j| - (\Delta_e + \Delta_i - \Delta_j) \tag{7}$$

The ionization coefficient for electron impact can be written in the form

$$\alpha_j = \frac{8\pi m_e}{(2\pi m_e k_B T)^{3/2}} \int_{I_j^{eff}}^{\infty} d\varepsilon\ \varepsilon\ \sigma_j^{ion}(\varepsilon)\ e^{-\beta\varepsilon} \quad ; \quad \varepsilon = \frac{p^2}{2m_e} \tag{8}$$

Here σ_j^{ion} is the impact ionization cross section from the atomic state $|j>$ which in statically screened first Born approximation reads

$$\sigma_j^{ion} = \frac{8\pi\hbar^2}{p_e^2 a_B^2} \int_0^{(p_e^2 - 2m_e I^{eff})^{1/2}} d\bar{p}\bar{p}^2 d\Omega_{\bar{p}} \int_{q_{min}}^{q_{max}} qdq \left[V_{ee}^{eff}(q)\right]^2 \left| \int d^3r \Psi_j^*(\mathbf{r}) \Psi_{\mathbf{p}}^+(\mathbf{r}) e^{\frac{i}{\hbar}\mathbf{q}\cdot\mathbf{r}} \right|^2 \tag{9}$$

The two-particle wave functions $\Psi_j(\mathbf{r})$ for the atomic bound states and $\Psi_{\bar{p}}^+(\mathbf{r})$ for the scattering states were determined from the effective wave equation (5) in static approximation .
Results for the ionization coefficient from the ground state and the respective recombination coefficient are given in Figs. 1 and 2 [2]. The most important feature is the strong nonlinear density dependence of the ionization coefficient which is mainly caused by the lowering of the ionization energy. The results are compared with the simple formula $\alpha = \alpha^{id} exp[(\Delta_1 - \Delta_e - \Delta_p)/k_B T]$ (dashed lines) given in [5].

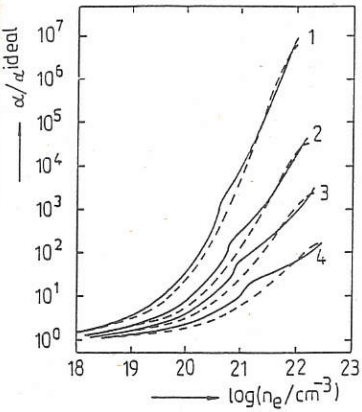

Fig.1: Ionization coefficient versus free electron density ($T = 10.000K$ (1), 15.000 K (2), 20.000 K (3) and 30.000 K (4)).

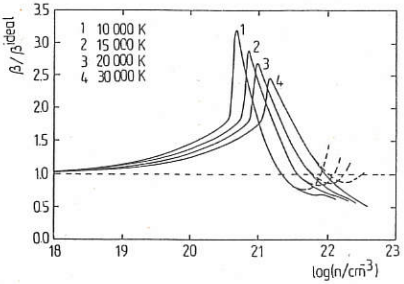

Fig.2: Recombination coefficient versus free electron density. Curves are shown for the cases where degeneracy was taken into account (solid lines) and where not (dashed).

An expression for the diffusion current density can be obtained from the equation of motion for the mean velocity [8, 6]. Results shall be given here for the case of the ambipolar diffusion stage with $n_e(r,t) = n_i(r,t)$ and $j_e^D(r,t) = j_i^D(r,t)$ Then, the system of reaction-diffusion equations reduces to only one equation. The electron diffusion current density can be written as

$$\mathrm{j}_e^D = -D_{AMB}\nabla n_e = -D_{AMB}^0 \frac{n_e}{k_B T}\left(\frac{\partial}{\partial n_e} + \frac{\partial}{\partial n_i}\right)(\mu_e + \mu_i)\nabla n_e \tag{10}$$

where D^0_{AMB} is the usual ambipolar diffusion coefficient. Results for the nonideal ambipolar diffusion coefficient are given for hydrogen (Fig.3).The classical result $D_{AMB} = 2\mathcal{D}_{pH}$ occurs only for electron densities below $10^{15} cm^{-3}$. For higher densities the many-body effects cause a minimum and below T=17000K even negative values of D_{AMB} being a direct consequence of the "Van-der-Waals-loop" in the plasma chemical potential (for which Padé–approximations were used including the Hartree–Fock and Montroll–Ward contributions [4]) and indicating mechanical instability and a phase transition. Obviously, the diffusion of particles in a region of high electron density will differ from that at low concentration.

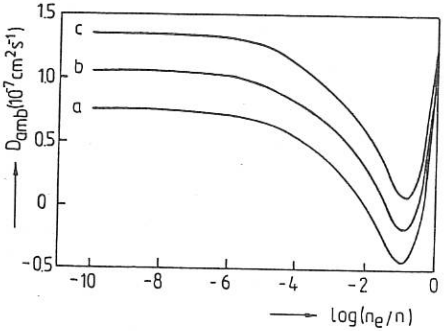

Fig.3: Ambipolar diffusion coefficient for hydrogen versus the degree of ionization for the temperatures T = 10.000 K (a), 14.000 K (b) und 18.000 K (c). The total density is $n = 5 \cdot 10^{23} cm^{-3}$.

Due to the nonideality, the source function in the reaction-diffusion equation depends on the density in a complicated nonlinear way. A numerical analysis of the r.d.e shows the possibility of ionization fronts, nonequilibrium phase separation and droplet growth in such a dense nonideal plasma.

References

[1] W.-D. Kraeft, D. Kremp, W. Ebeling, and G. Röpke. *Quantum Statistics of Charged Particle Systems.* Plenum, London, New York, 1986.

[2] M. Schlanges and T. Bornath. Phys.Rev.A (submitted).

[3] R. Zimmermann. *Many-Particle Theory of Highly Excited Semiconductors.* Teubner, Leipzig, 1987.

[4] W. Ebeling and W. Richert. *phys.stat.sol.(b)*, **128**:467, 1985.

[5] M. Schlanges, T. Bornath, and D. Kremp. *Phys.Rev.A*, **38**:2174, 1988.

[6] D. Kremp, M. Schlanges, M. Bonitz, and T. Bornath. Phys.Fluids B (submitted).

[7] D. Kremp, M. Schlanges, and T. Bornath. In J. Popielawski, editor, *The Dynamics of Systems with Chemical Reactions*, page 3, Singapore, 1989. World-Scientific.

[8] M. Schlanges, T. Bornath, M. Bonitz, and D. Kremp. In J. Popielawski, editor, *Far–From–Equilibrium Dynamics of Chemical Systems*, page 192, Singapore, 1991. World-Scientific.

Experimental and theoretical determination of electron impact ionization cross sections of atoms and molecules

V.Grill, D.Margreiter, G.Walder, P.Scheier, C.Winkler, M.Kurdel, H.U.Poll, H.Deutsch, K.Stephan and T.D.Märk

Institut für Ionenphysik, Leopold Franzens Universität, A-6020 Innsbruck, Austria

INTRODUCTION

The data of total and partial electron impact ionization cross sections of molecules are of great interest in different fields of applied physics, like plasma etching or mass spectrometry. But the experimental determination of these cross sections is rather difficult, especially for polyatomic molecules, as their fragment ions suffer discrimination during extraction from the ion source and fligth through the mass spectrometer. This discrimination is due to the excessive kinetic energy of the ions, and therefore the discrimination effects are biggest for high-energetic fragment ions. In the following a method will be presented, which enables to correct the measured partial cross sections by taking into account these effects.
Moreover, to be able to predict absolute cross sections for atoms and molecules theoretically, we have developed a semiclassical formula.

EXPERIMENTAL SETUP

A detailed description of the apparatus, the experimental procedure and the method of detecting ions with high translational kinetic energies has been given previously /1/. Briefly the experimental set-up used consists of a conventional three-electrode type electron impact ion source, and a high-

resolution double focussing (reversed geometry) sector field mass spectrometer. The properties of the ion source and the mass spectrometer have been studied in detail previously and essential improvements in the performance could be achieved /2/. With the help of these improved operating conditions, like penetrating field extraction or the ion-beam deflection method /1/, it was possible to measure with high accuracy absolute partial ionization cross sections for atomic or molecular parent ions. But it was found that smaller fragment ions of polyatomic molecules, which have larger excess kinetic energies, are not extracted from the ion source with the same efficiency as the larger fragment ions. In order to account for this discrimination an additional correction procedure has been developed in our laboratory.

CORRECTION PROCEDURE

This correction procedure is based on a study of the discrimination in our ion source and mass spectrometer by means of computer simulations of the electric field distribution and the corresponding ion trajectories. With the help of these simulations we were able to determine a discrimination factor D as a function of the kinetic energies of the ions. This relationship allows to correct fragment ion currents to the same extraction efficiency as the parent ion.

In order to apply this correction procedure the respective kinetic energies of the fragment ions under study must be known. A simple method to determine these properties using the same experimental set-up has been described previously /3/. According to this work and references therein the kinetic energies can be determined from the relation

$$E_{kin} = 10^{-3} \cdot U_z(HWFM)^2,$$

where $U_z(HWFM)$ is the half width at full maximum of the measured ion beam profile in z-direction (direction of the entrance slit of the mass spec-

trometer). The agreement of the kinetic energies calculated with previously reported values /4/ was satisfactory.

We have applied and tested this correction method to several gases, like CF_4, SF_6, C_3H_8, C_2H_6, H_2, N_2 and C_2H_5OH, and have found good agreement with cross section data of other groups. For example the absolute cross section for propane as shown in the following figure in comparison with the data of Kurepa et al. /5/ and those of Schram et al. /6/ has been obtained with the described correction method.

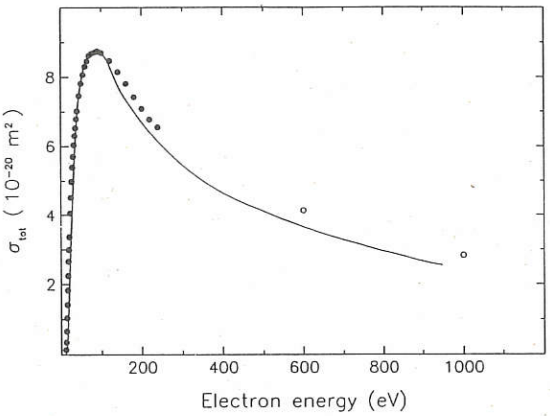

FIG.1 Total ionisation cross section for propane: our results (solid line) in comparison with the absolute data of Kurepa et al. /5/ (o) and Schram et al. /6/ (o).

THEORETICAL WORK

For the prediction of absolute electron ionization cross section functions we have developed /1/ a semiclassical formula. This formula consists of an

energy dependent part (classical binary encounter approximation) and an additional factor equal to the weighted sum of the squared electron radii (Born-Bethe approximation).

$$\sigma=\sum_{n,l} g_{nl}\cdot\pi\cdot r_{nl}^{2}\cdot\xi_{nl}\cdot u^{-1}\cdot\left[\frac{u-1}{u+1}\right]^{1.5}\cdot\left\{1+\frac{2}{3}\cdot\left(1-\frac{1}{2\cdot u}\right)\cdot\ln\left(2.7+(u-1)^{0.5}\right)\right\}$$

with g_{nl} = weigthing factors (see also Bethe /7/, who calculated these *Ionisierungsfaktoren* as a function of the quantum numbers n and l by using hydrogen wave functions). Here these factors were determined via a fitting procedure;

r_{nl}^{2} = mean square radius of the nl shell;

ξ_{nl} = number of electrons in the nl subshell;

E = energy of the incident electron;

E_{in} = ionization energy in the n-th subshell;

$u = \frac{E}{E_{in}}$

REFERENCES

1. D.Margreiter, G.Walder, H.Deutsch, H.U.Poll, C. Winkler, K. Stephan and T.D.Märk; Int.J.Mass Spectrom.Ion Proc.,100 (1990) 143 and 157;
2. K.Stephan, H.Helm and T.D.Märk, J.Chem.Phys., 73 (1980) 3763
3. H.U.Poll, C. Winkler, V.Grill, D.Margreiter and T.D.Märk, Int.J.Mass Spectrom. Ion Proc., 112 (1992) 1-17
4. R.Fuchs and R.Taubert, Z.Naturforschg. 19a (1964) 494
5. N.Djuric, I. Cadez and M.Kurepa, Int.J.Mass Spectrom. Ion Proc., 108 (1991) R1
6. B.L.Schram, M.J.Van der Wiel, F.J. de Heer and H.R.Moustafa, J.Chem. Phys. 44 (1966) 49
7. H.Bethe, Ann. Physik 5 (1930) 325

MICROWAVE DETERMINATION OF THE COEFFICIENT OF DISSOCIATIVE RECOMBINATION OF MOLECULAR IONS OF ARGON

T.Okada* and M.Sugawara**
* Department of Electronic Technology, Gunma Polytechnic College
918 Yamana, Takasaki 370-12, Japan
** Department of Electrical and Electronic Engineering,
Faculty of Engineering, Gunma University, Kiryu 376, Japan

1. Introduction

In several experiments of determining the coefficient of dissociative recombination α, there have been wide-spreading values ranging from 3×10^{-7} to 1.1×10^{-6} cm^3s^{-1}. These discrepancies may be due to the ignorance of microwave power dissipation throughout the glass discharge tube immerged in the microwave cavity. Therefore, this study is to take into account the power dissipation in addition to the other loss and the form factor and to calibrate the cavity.

Using a calibrated cavity taken into consideration electric field loss from the end holes and the presence of a glass discharge tube, we have determined the value of α of molecular ion of argon at 300 K by means of the computer fitting of the rate equation of electrons to the measured decay of electron density.

2. Calibration of the cavity technique

The electron density on the axis $n_e(0)$ is deduced from the equation given by reference/1/ as

$$n_e(0) = \frac{C}{K_d} \cdot \frac{\int_{Plasma} E^2 dv}{\int_{Plasma} g(r) E^2 dv} \cdot f \cdot \Delta f, \qquad (1)$$

where $K_d = \int_{Plasma} E^2 dv / (2 \int_{cavity} E^2 dv)$; $C = (4\pi^2 m \varepsilon_0)/e^2$; f, f_0 are the resonant frequencies of the cavity with and without the plasma; $\Delta f = f - f_0$; e, m, n are electron charge, mass and density, respectively; E is the electric field strength; $g(r)$ is radial distribution of electrons; ε_0 is the permittivity of free space. In order to determine absolute electron density, K_d, E^2 and $g(r)$ have to be measured.

A TM_{010}- mode cavity was used. The resonant frequency of the cavity with the empty discharge tube is 2.7253 GHz. When the inside of the discharge tube is filled with a uniform dielectric rod, frequency shift is given by/2/

$$\Delta f_d / f = -(\varepsilon_r - 1) K_d, \qquad (2)$$

where ε_r is the relative permittivity of the rod. We have measured the frequency shifts Δf_d by immersing rods of different ε_r ranging from 1.029 to 2.9. The value of $\Delta f_d/f$ is plotted against $-(\varepsilon_r - 1)$ in Fig.1. From the slope of the line K_d=0.140 is determined.

A small probing dielectric ball(ε_r= 4.5, 2.0) with radius a=1 mm was used and moved in radial and axial direction inside the empty discharge tube. Since the frequency shift Δf_E by the presence of the ball is proportional to E^2/3/ we have determined the spatial distribution of E^2 at f_0=2.7253 GHz by measuring the change of Δf_E. The result is shown in Fig.2.

The profile of $g(r)$ was measured with a movable Langmuir probe in dc argon discharges. Substituting values of K_d, E^2 and $g(r)$ into equation (1), we have calculated $n_e(0)$. Values of $n_e(0)$ obtained above were compared with data obtained by Langmuir probe technique.

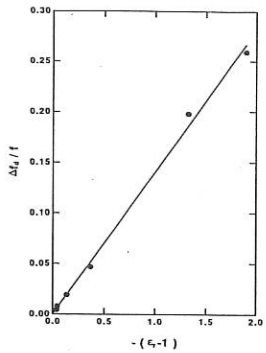

Fig.1: $\Delta f_d/f$ against $-(\varepsilon_r - 1)$

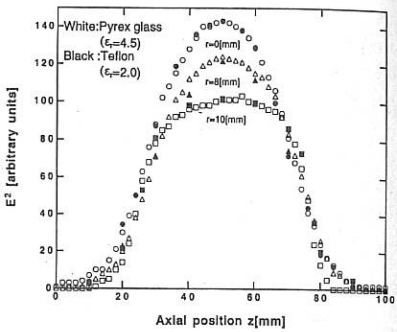

Fig.2: Spatial distribution of E^2 inside the discharge tube

3. Determination of the coefficient of dissociative recombination of molecular ions of argon

Taking into consideration the ionization as the result of collisions between two metastable atoms, we have

$$\partial M/\partial t = D_m \nabla^2 M - (\sigma \langle v \rangle n_g + \gamma n_g^2) M - \beta M^2, \quad (3)$$

$$\partial n_1/\partial t = D_{a1} \nabla^2 n_1 - k n_g^2 n_1 + \beta M^2, \quad (4)$$

$$\partial n_2/\partial t = D_{a2} \nabla^2 n_2 + k n_g^2 n_2 - \alpha n_e n_2. \quad (5)$$

Here, no distinction is made between 6^3P_2 and 6^3P_0 metastable atoms; M, n_1, n_2, n_g and n_e denote the densities of metastable atoms, atomic ions, molecular ions, ground-state atoms of argon and electrons which are functions of space and time; D_m, D_{a1} and D_{a2} are the diffusion

coefficient of the metastable atoms and the ambipolar diffusion coefficients of atomic ions and molecular ions, respectively; σ and γ are the de-excitation cross section of two-body and the de-excitation coefficient of three-body of metastable atoms; $\langle v \rangle$ is the mean relative speed of the colliding atoms; k is the rate coefficient of conversion of atomic ions into molecular ions; β is the rate coefficient of ionizing collisions between two metastable atoms.

Assuming quasi-neutrality, we put electrons as $n_e = n_1 + n_2$. Since the electron temperature dependence of α was introduced to be proportional to $T_e^{-0.5}$/4/, we put $\alpha(T_e) = \alpha_0 (T_e/300)^{-0.5}$, where T_e and α_0 denote electron temperature and the value of α at 300 K, respectively.

Experiments were carried out in a Pyrex glass discharge tube with 3.1 cm in inner diameter and 56 cm in electrode separation. The discharge current was conducted in dc pulse operation of time interval of 9 ms, duration of 1 ms and peak current of 0.35 A. The operating pressure was 5 Torr. The discharge tube was baked out at 200 ℃ for several days before the experiments were carried out. The ultimate vacuum attained was 2×10^{-7} Torr. The purity of 99.999 % of argon gas was used. Electron temperature decay was measured with a time-resolving 2.8 GHz radiometer with the time resolution of 5 μs/5/. Probing microwave power into the cavity was adjusted below several μW.

The frequency shifts at moments of the afterglow period were measured. The radial distributions of electrons were also measured with an asymmetric double probe. By substituting these data into equation (1) $n_e(0)_E$ was obtained. On the other hand, by solving equations (3),(4) and (5) we have calculated $n_e(0)_T$. Coefficients and initial values used are listed in Table 1.

Table 1:Parameters and initial values.

Items	Parameters		References	
Ar^+	$D_{a1} n_g = 2.34 \times 10^{18}$	$cm^{-1}s^{-1}$	/5/	(a)
	$k = 2.26 \times 10^{-31}$	$cm^6 s^{-1}$	/5/	(a)
Ar_2^+	$D_{a2} n_g = 2.28 \times 10^{18}$	$cm^{-1}s^{-1}$	/8/	(a)
Metastable	$D_m n_g = 1.77 \times 10^{18}$	$cm^{-1}s^{-1}$	/9/	(a)
Atoms	$\sigma = 10 \times 10^{-20}$	cm^2	/9/	(a)
	$\gamma = 1.14 \times 10^{-32}$	$cm^6 s^{-1}$	/9/	(a)
	$n_e(0,0) = 3.42 \times 10^{11}$	cm^{-3}	present	(b)
Initial	$n_1(0,0) = 2.8 \times 10^{11}$	cm^{-3}	present	(b)
Values	$n_2(0,0) = 6.2 \times 10^{10}$	cm^{-3}	present	(b)
	$M(0.0) = 1.56 \times 10^{12}$	cm^{-3}	present	(c)

(a):room temperature, (b):measurement,
(c): calculated followed the same manner as reference/10/

The values of α_0 and β were determined so that $n_e(0)_T$ fitted well $n_e(0)_E$. We have consequently determined $\alpha_0=(8.2\pm0.5)\times10^{-7}$ cm^3s^{-1} and $\beta=(1.5\pm0.1)\times10^{-9}$ cm^3s^{-1}. The calculated values of temporal behaviors of electrons, atomic and molecular ions and metastable atoms of argon are shown in figure 3. The present value of α_0 is compared well with previous values of $(8.5\pm0.8)\times10^{-7}$ cm^3s^{-1}/6/ and $(9.1\pm0.9)\times10^{-7}$ cm^3s^{-1}/7/ at 300 K. No comparison of the value of β is made because other data are not available as far as we know.

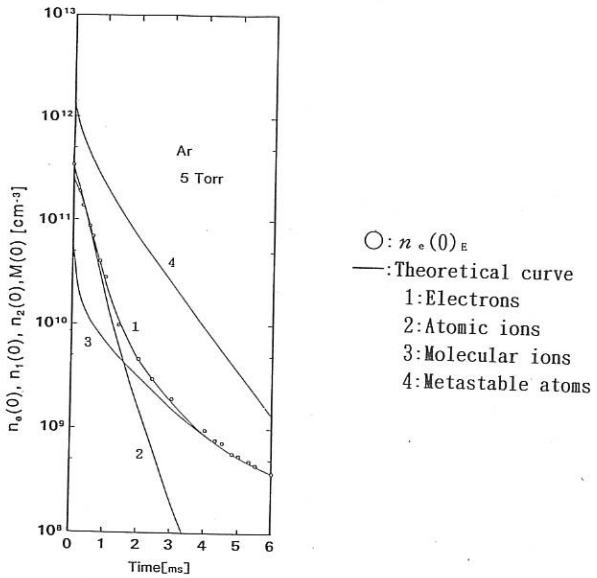

Fig.3:Temporal behaviors of electrons, atomic and molecular ions and metastable atoms of argon.

/1/ L.Frommhold and M.A.Biondi, Ann.Phys.48 407(1968)
/2/ H.F.Wellenstein,L.Frommhold and W.W.Robertson,J.Appl.Phys.43 3719 (1972)
/3/ A.Pipišková and P.Lukáč,J.Phys.D: Appl.Phys.3 1381(1970)
/4/ T.F.O'Malley,Phys.Rev.185 101(1969)
/5/ M.Sugawara,T.Okada and Y.Kobayashi,J.Phys.D:Appl.Phys.19 1213(1986)
/6/ F.J.Mehr and M.A.Biondi,Phys.Rev.176 322(1968)
/7/ Y.J.Shiu and M.A.Biiondi,Phys.Rev.A 17 868(1978)
/8/ D.G.Armour,J.Phys.B:Atom.Molec.Phys.7 1213(1974)
/9/ E.Ellis and N.D.Twiddy,J.Phys.B:Atom.Molec.Phys.2 1366(1969)
/10/ Y.Ichikawa and S.Teii,J.Phys.D:Appl,Phys.13 2031(1980)

On the Laser Cooling of Ions in Oscillating Traps

L. G. Reyna
IBM Research Division, T.J. Watson Research Center
Yorktown Heights, New York 10598

J .R. Sobehart
División Fusión Nuclear, Gerencia de Desarrollo,
Comisión Nacional de Energía Atómica
Av. Libertador 8250, 1429 Buenos Aires, Argentina

Abstract:

The probability distribution of a two-level ion trapped in an oscillating potential well is calculated. The ion absorbs photons from an incident laser beam and relaxes back to the ground state by either induced or spontaneous emissions. The present calculations reproduce the quantum results for heavy particles in static traps, and the classical results for radio-frequency confining wells.

1. Introduction

The development of techniques to confine clusters of a small number of ions [1], and even individual ions [2], has largely improved the understanding of the interaction of atoms and light. Ion clusters may now be confined combining static and oscillating potential wells, or traps, and cooled to milidegree Kelvin temperatures with a light resonance technique termed laser cooling [3][4].

The cooling is produced by a laser beam with a frequency slightly lower than the resonance frequency of an atomic transition of the ion. When the ion moves towards the laser beam, the frequency of the laser is Doppler shifted towards resonance with a resulting increase in the photon absorption rate. The opposite effect takes place when the ion moves away from the laser beam. When the ion absorbs a photon, it goes into an excited state with a change of momentum $\hbar q$. The transition back to the ground state can happen either through induced emission, in which case the ion looses the momentum gained during the photon absorption, or through spontaneous emission. During an spontaneous emission, the ion emits a photon of total momentum $\hbar q$ but in a randomly distributed direction, thus the combination of an absorption followed by an spontaneous emission results in a total momentum loss [4].

The ion confinement and cooling in oscillating traps is characterized by parametric instabilities resulting from the time dependence of the trapping potential: ions can only be confined if the voltage of the trap is restricted to stable regions [5].

2. Ions driven by laser beams

In this work we present a one dimensional model for the confinement of ions in a Paul trap. We describe the dynamics of the trapped ion in terms of a system of stochastic differential equations accounting for the main features of the laser cooling process. We analyze the laser cooling of ions in static potential traps and in radio-frequency traps.

The absorption and emission times of photons are assumed to be randomly distributed according to Poisson statistics. For simplicity here we assume that the absorption is immediately followed by an spontaneous emission, resulting in a maximum ion velocity change $k = 2\hbar q/m$, where q is the wavenumber of the laser and m the ion mass. The Doppler shift effect responsible for the cooling results in a velocity dependent rate for

the distribution of the absorption/emission events:

$$\tilde{\gamma}(u) = \frac{\gamma r(u)}{2r(u)+\gamma}, \quad \text{where} \quad r(u) = \frac{\gamma}{4}\frac{\chi^2}{(\Delta - qu)^2 + \gamma^2/4}. \tag{1}$$

Here $u = dx/dt$ is the ion velocity and γ is the spontaneous emission rate, which sets up the linewidth of the spectral line. Other parameters: Δ, the detunning between the laser frequency and the atomic transition frequency, and χ, the coupling constant between the light beam and the ion [3][4]. Note that in this model quantum effects are only taken into account in the discrete nature of the applied radiation field.

The confining potential is assumed harmonic: $\Phi(x,t) = m(a - 2b\cos(2\omega t))\omega^2 x^2/2$, where a and b are independent parameters describing the potential. The equation of motions result in

$$\frac{d^2x}{dt^2} + \omega^2(a - 2b\cos(2\omega t))x = k\sum_{t_n}\delta(t - t_n)R_n, \tag{2}$$

where the noise is applied at times t_n distributed according to Poisson statistics with rate given by Eqn.(1). R_n is a random number uniformly distributed in the interval $[0,1]$. This is the one dimensional projection of the resulting change in velocity of the fully three dimensional laser cooling process. Discussions on the limitations of this simplification as well as results for the static trap may found in [4].

The interaction between the light beam and the ion is characterized by two very different time-scales: the lifetime of the excited state and the time scale of the cooling process. The lifetime of the excited state is determined by the spontaneous emission frequency γ while the cooling is given by the rate of change in the spontaneous emission: $k\, d\gamma(u)/du$. The time scale of the ion cooling, induced by the laser beam, is very slow compared to γ^{-1}. We restrict the present analysis to the limiting situation $\omega a^{1/2},\ \omega b^{1/2} \ll \gamma$, termed the heavy particle limit because the ion velocity changes slowly during the absorption-emission processes [3][4].

An equation for the probability density $P(x,u,t)$ may be found by studying the changes in velocity and position over a small time interval Δt. If X and V are the position and velocity after the time interval Δt: we have that

$$\begin{aligned}
&\langle X - x\rangle = u\Delta t, \quad \langle U - u\rangle = \left(-\omega^2(a - 2b\cos(2\omega t))x + \frac{k\tilde{\gamma}(u)}{2}\right)\Delta t \\
&\langle (X-x)^2\rangle = \mathcal{O}(\Delta t^2), \quad \langle (X-x)(U-u)\rangle = \mathcal{O}(\Delta t^2), \\
&\langle (U-u)^n\rangle = \frac{\tilde{\gamma}(u)k^n}{n+1}\Delta t, \quad n \geq 2,
\end{aligned} \tag{3}$$

to the leading order in Δt. Here $< Q >$ is the expected values of any of the considered quantities. Thus,

$$\frac{\partial P}{\partial t} + u\frac{\partial P}{\partial x} - \omega^2(a - 2b\cos(2\omega t))x\frac{\partial P}{\partial u} = \sum_{n=1}^{\infty}\frac{(-k)^n}{(n+1)!}\frac{\partial^n}{\partial u^n}(\tilde{\gamma}(u)P). \tag{4}$$

Expanding this equation to order $\mathcal{O}(k^3)$ yields the Fokker-Planck equation derived in [4].

Since the change in momentum is small compared to a typical momentum of the ion, the probability distribution should be peaked around the deterministic limit, i.e. $k = 0$. Thus, we introduce the following singular expansion based on the smallness of the driving noise amplitude:

$$P(x,u,t,\tau) \sim \mathrm{e}^{\phi(x,u,t,\tau)/k}(z_0(x,u,t,\tau) + \mathcal{O}(k)), \quad \tau = kt, \tag{5}$$

which combined with Eqn.(3) results in

$$\begin{aligned}
&\frac{dx}{dt} = u, \quad \frac{du}{dt} = -\omega^2(a - 2b\cos(2\omega t))x \\
&\frac{d\phi}{dt} = 0, \quad \frac{dz_0}{dt} = -\left(\gamma(u)\frac{\mathrm{e}^{-\phi_u} + \phi_u - 1}{\phi_u^2} + \frac{\partial\phi}{\partial\tau}\right)z_0.
\end{aligned} \tag{6}$$

Thus

$$x = A\ M_A(t) + B\ M_B(t), \quad u = A\frac{dM_A}{dt}(t) + B\frac{dM_B}{dt}(t) \tag{7}$$

where the functions $M_A(t)$ and $M_B(t)$ are two independent solutions of the Mathieu oscillator Eqn.(6) given by

$$\begin{aligned} M_A &= \frac{1}{2}(M^+ + M^-)\,; \qquad M_A(0) = 1, \quad \frac{dM_A}{dt}(0) = 0 \\ M_B &= \frac{1}{2i}(M^+ - M^-)\,; \qquad M_B(0) = 0, \quad \frac{dM_B}{dt}(0) = \mu + 2\omega \sum_{k=-\infty}^{\infty} c_{2k} \\ M^+ &= e^{i\mu t} \sum_{k=-\infty}^{\infty} c_{2k}\ e^{2i\omega kt}\,, \quad M^- = e^{-i\mu t} \sum_{k=-\infty}^{\infty} c_{2k}\ e^{-2i\omega kt}. \end{aligned} \tag{8}$$

The coefficients c_{2k} satisfy a three point recursion formula and μ is called the Floquet exponent [6]. The secular frequency of the ion in the trap corresponds to the Floquet exponent μ.

Solution to Eqn. (6) for z_0 must be bounded if the ion is assumed to be confined, thus

$$\lim_{T\to\infty} \frac{1}{T} \int_0^T \left\{ \tilde{\gamma}(u) \frac{e^{-\phi_u} + \phi_u - 1}{\phi_u} + \frac{\partial \phi}{\partial \tau} \right\} d\tau = 0, \tag{9a}$$

where

$$\phi_u = \frac{1}{W}\left(M_A(t)\frac{\partial \phi}{\partial B} - M_B(t)\frac{\partial \phi}{\partial A} \right) \quad \text{and} \quad W = M_A(t)\frac{dM_B}{dt}(t) - \frac{dM_A}{dt}(t)M_B(t) = \frac{dM_B}{dt}(0). \tag{9b}$$

After the dynamical initial stage, the ion velocity becomes smaller than the resonant value Δ/q and photon absorption is largely reduced. At this stage we may assume the approximation

$$\tilde{\gamma}(u) = \tilde{\gamma}_0(1 - \tilde{\beta}u + \ldots) \quad \text{where} \quad \tilde{\gamma}_0 = \frac{\chi^2\gamma}{2\chi^2 + 4\Delta^2 + \gamma^2} \quad \text{and} \quad \tilde{\beta} = -\frac{8\Delta q}{2\chi^2 + 4\Delta^2 + \gamma^2}, \tag{10}$$

which reduces Eqns. (9) to

$$\frac{\partial \phi}{\partial \tau} = \frac{\tilde{\gamma}_0}{12} \left\{ 3\tilde{\beta}\left(A\frac{\partial \phi}{\partial A} + B\frac{\partial \phi}{\partial A} \right) + \frac{2\|M\|}{W^2} \left[\left(\frac{\partial \phi}{\partial A} \right)^2 + \left(\frac{\partial \phi}{\partial B} \right)^2 \right] \right\}. \tag{11}$$

Here $\|M\| = \overline{M_A^2} = \overline{M_B^2} = \dfrac{\omega}{2\pi}\displaystyle\int_0^{\pi/\omega} |M^+|^2 dt$, , $\overline{M_A M_B} = 0$, and $\overline{M} = \lim_{T\to\infty} 1/T \displaystyle\int_0^T M(t)dt$.

The shift of the ion in the trap, z_0, can be found from Eqns. (6) and (11)

$$\log(z_0) = \frac{\tilde{\gamma}_0}{2W} \int_0^t \left(M_B(s)\ \frac{\partial \phi}{\partial A} - M_A(s)\ \frac{\partial \phi}{\partial B} \right) ds. \tag{12}$$

Assuming an initial distribution $\phi(A, B, \tau) = -(A^2 + B^2)/\psi$ and an initial uncertainty ψ_0, a particular solution to Eqn. (11) is

$$\psi(\tau) = \left(\psi_0 - \frac{4\|M\|}{3\tilde{\beta}W^2} \right) e^{-\tilde{\gamma}_0\tilde{\beta}\tau/2} + \frac{4\|M\|}{3\tilde{\beta}W^2}, \tag{13}$$

leading to a cooling time scale $t_c = 2/\tilde{\gamma}_0\tilde{\beta}k$, and final variances of the probability distribution $\langle (A - < A >)^2 \rangle$ $= \langle (B - < B >)^2 \rangle = 4k\|M\|/3\tilde{\beta}W^2$.

The variances of the probability distribution of the dynamical variables x and u can be obtained using the change of variables (7) and the result provided in Eqn. (13), which yields

$$\overline{\langle (x- < x >)^2 \rangle} = \frac{4k\|M\|^2}{3\tilde{\beta}W^2} \quad \text{and} \quad \overline{\langle (u- < u >)^2 \rangle} = \frac{2k\|M\|}{3\tilde{\beta}W^2} \left\| \frac{dM}{dt} \right\| \tag{14}$$

where

$$\left\| \frac{dM}{dt} \right\| = \overline{\left(\frac{dM_A}{dt} \right)^2} = \overline{\left(\frac{dM_B}{dt} \right)^2} = \frac{\omega}{2\pi} \int_0^{\pi/\omega} \left| \frac{dM^+}{dt} \right|^2 dt. \tag{15}$$

4. Discussion

The above Eqn.(14), agrees with the quantum calculations derived by Javanainen and Stenholm for heavy atoms confined in static harmonic traps ($a = 1, b = 0$) [3][4]. The lowest energy that can be achieved using laser cooling technique is of order $\hbar\gamma$, and is basically limited by the spontaneous emission line width, which is the energy uncertainty of the emitted radiation [3][4]. The final energy is independent of the photon momentum provided $\hbar^2 q^2/m \ll \hbar\gamma$.

Our analysis indicates the existence of stable and unstable ion confinement resulting from the relation between the potential parameters a and b [7]. A general discussion about Mathieu oscillator instabilities can be found elsewhere [6][7]. The current results are in agreement with those previously derived by Blatt et al. in terms of continued fractions expansions if we assume the limit of negligible small damping in their results [5].

We stress that pseudopotential models [4], usually assumed to describe ion traps, fail to predict the correct laser cooling dynamics close to a parametric instability of the radio-frequency trap.

References

[1] W. Neuhauser, M. Hohenstatt, and P. E. Toschek, *Visual Observation and Optical Cooling of Electrodynamically Contained Ions*, Appl. Phys. **17**, pp. 123-129 (1978).

[2] J. D. Sankey and A. A. Madej, *The production of Ions for single Ion Traps*, Appl. Phys. B **49**, pp. 69-72 (1989).

[3] J. Javanaiven, and S. Stenholm, *Laser Cooling of Trapped Particles I*, Appl. Phys. **21**, pp. 283-291 (1980).

[4] S. Stenholm, *The semiclassical Theory of Laser Cooling*, Rev. Mod. Phys. **58**, pp. 699-739 (1986).

[5] R. Blatt, P. Zoller, G. Holzmuller, I. Siemers, *Brownian Motion of Parametric Oscillator: A Model for Ion Confinement in Radio Frequency Traps*, Z. Phys. D **4**, 121-126 (1986).

[6] M. Abramowitz, I. Stegun, *in Handbook of Mathematical Functions*, Dover, N.Y (1970), pp. 772-731.

[7] L.G. Reyna, J.R. Sobëhart, *On the Dynamics of Two-Level Ions in Potential Wells*, in preparation (1992).

Topic 13:

Plasma Applications

ONE-DIMENSIONAL MODELING FOR MAGNETO-MICROWAVE PLASMA USING THE MONTE CARLO METHOD

Masato Ikegawa, Yutaka Kakehi, and Junichi Kobayashi*
Mech. Eng. Res. Lab., Hitachi Ltd., 502 Kandatsumachi Tsuchiura-shi, Ibaraki 300 JAPAN
* R&D Promotion Office, Hitachi Ltd., 1-5-1 Marunouchi, Chiyodaku, Tokyo 100 JAPAN

1. Introduction

Integrated circuit (IC) chips are advancing towards high integration and small features, and the most recent development is VLSI (very large scale integration). VLSI devices have at least 10^5 components per chip and their minimum device dimensions are scaled down to submicron dimensions. Magneto-microwave plasma, or ECR (electron cyclotron resonance) plasma, is often used in etching processes for VLSI fabrication /1//2/. This is because this plasma reactor has several advantages compared with conventional RF plasma reactors, such as anisotropic etching (due to a low working gas pressure) and less contamination (due to the absence of electrodes). However, our understanding of the magneto-microwave plasma production mechanism used for the etching process is far from complete. A self-consistent plasma simulator has to be built to analyze the plasma distribution in the reactor. Fewer simulations have been reported for the magneto-microwave plasma process than for RF or DC plasma processes. Such simulators have recently been reported /3//4//5/. However, these do not seem to be sufficient for modeling the ECR phenomenon.

We have developed a one-dimensional plasma simulator which combines a particle plasma model and a microwave damping model based on a "cold plasma" approximation. This paper demonstrates this model and some approximate results obtained from it. In particular, the effects of gas pressure on the plasma distribution in the direction of microwave propagation are described.

2. Modeling

In this simulator, the microwave and the plasma are solved in different ways. The plasma is simulated using the Monte Carlo particle model, while the microwave is simulated using a dispersion equation based on a wave equation and a fluid (cold) plasma model. Figure 2.1 shows a schematic view of these two models combined. A discharge occurs in the space between two infinite parallel plates (solid walls). The x, y axes are set on the left wall. The z axis is set perpendicular to the wall. The magnetic field is formed in the $-z$ direction. The intensity of this field increases linearly in the z direction and has a strength of 0.0875 T (875 Gauss), corresponding to the ECR condition, at the mid-point between the two walls. The microwave (transverse electromagnetic wave, 2.45 GHz) propagates in the same direction as the magnetic field (from the higher magnetic field). The discharge space is divided into many cells for the Monte Carlo particle plasma method.

2.1 Plasma analysis

Several particle plasma models have been reported to date /6//7//8//9/. Our particle plasma simulator was derived from a rarefied gas flow simulator that had been developed using the DSMC method /10/. The weakly ionized plasma used in the semiconductor manufacturing processes consists of an overwhelmingly large amount of neutral species and a very small amount (about 0.01%) of charged species. Consequently, in the simulation, only the motion of charged particles (ions and electrons) is calculated in the group of neutral molecules having a Maxwellian velocity distribution. The plasma is calculated in this particle simulation with Poisson's equation :

$$\nabla \cdot \boldsymbol{E} = \rho / \varepsilon_0 \qquad (2\text{-}1)$$

where $\boldsymbol{E}$ is the electric field intensity, ρ is the charge density and ε_0 is the dielectric permittivity of free space.

Figure 2.2 shows the calculation sequence for our simulator in time step Δt. The flight paths and collisions of molecules, charge density ρ, electric field intensity of charged particles E_z, and the microwave electric field intensity E_x, E_y are calculated in order during this timestep. The timestep is 1.02×10^{-11} s in this paper. The equation of motion is integrated using the leapfrog scheme with the frequency correction factor /9/. The collisions are calculated using a simplified time-counter method that has been modified from Bird's method /11/ as a multi-test particle method. Elastic collisions and ionization collisions are calculated for electrons. Hence, one electron and one ion is produced if ionization occurs during the electron-neutral molecule collisions. Only elastic collisions are considered for ions. A model gas like argon is used in this simulation. The collision frequencies for electron (0.67 Pa) are given by $\nu_{en}=1.8\times10^8$ (s^{-1}) (elastic), $\nu_i=\nu_{i0}\cdot\exp[-(\varepsilon-E_i)/100]$ (s^{-1}) (ionization), $\nu_{i0}=1.1\times10^7$ (s^{-1}), ($\nu_i=0$ if $\varepsilon<E_i$), where ε (eV) is the electron energy, E_i(=15.8 eV) is the ionization potential. The collision frequency for ion (0.67 Pa) is given by $\nu_{in}=1.6\times10^5$ (s^{-1}) (elastic).

Charged particles bombarding the solid walls are assumed to be absorbed by the walls. Secondary emmisive electrons, with probability $\gamma_e=0.046$, are produced by the ion bombardment on the walls.

The Poisson's equation is integrated using the following equation /8/:

$$E_z=-\frac{1}{\varepsilon_0}\int_z^H \rho(z)\,dz+\frac{1}{\varepsilon_0 H}\int_0^H z\rho(z)\,dz \tag{2-2}$$

where H is the distance between the two parallel walls.

2.2 Microwave analysis

The microwave propagating in the $-z$ direction is assumed to be given by the following plane wave equation:

$$E=E_0\cdot\exp\{\gamma z+j\omega t)=E_0\cdot\exp\{\alpha z\}\exp\{j(\kappa z+\omega t)\},\ \gamma\equiv\alpha+j\kappa \tag{2-3}$$

where E is the electric field intensity, $\omega(=2\pi f)$ is the angular frequency (f=2.45 GHz), γ is the propagation constant, α is the attenuation constant, and κ is the wave number.

The microwave dispersion equation with the "cold plasma" model, including electron and neutral molecule collisions, is given by the following equation /12/.

$$\gamma=jK,\ K=\kappa_0\left\{1-j\frac{\sigma_1^*}{\omega\varepsilon_0}\left(1\pm\frac{j\sigma_2^*}{\sigma_1^*}\right)\right\}^{0.5},\ \kappa_0\equiv\omega(\varepsilon_0\mu_0)^{0.5} \tag{2-4}$$

$$\sigma_0\equiv n_e e^2/m_e,\ \sigma_1^*\equiv\sigma_0^*\sigma_1,\ \sigma_2^*\equiv\sigma_0^*\sigma_2,\ \sigma_3^*\equiv\sigma_0^*\sigma_3,\ \sigma_0^*\equiv\sigma_0/(\sigma_1^2+\sigma_2^2),$$

$$\sigma_1\equiv j\omega+\nu_{en},\ \sigma_2\equiv\omega_c,\ \sigma_3\equiv(\sigma_1^2+\sigma_2^2)/\sigma_1$$

where σ_1^*, σ_2^*, and σ_3^* are components of the conductivity tensor σ, $\omega_c(\equiv eB_{ex}/m_e)$ is the electron cyclotron frequency, n_e is the electron density, e is the charge of electron, m_e is the mass of electron and μ_0 is the permeability of free space. The + sign represents a left-hand circularly polarized wave (L wave) and the - sign represents a right-hand circularly polarized wave (R wave). Thus, the propagation constant γ in each cell is calculated using the electron density distribution n_e obtained by plasma particle simulation. If wave reflection is disregarded,

the R wave is given by

$$E_x = E_0 \cdot \exp(\alpha z)\cos(\kappa z + \omega t) \quad (2\text{-}5)$$

$$E_y = -E_0 \cdot \exp(\alpha z)\sin(\kappa z + \omega t). \quad (2\text{-}6)$$

The whole curve in the discharge space can be obtained for the microwave electric field by connecting the amplitudes and the phases at the cell boundaries from the right wall. The wave numbers at arbitrary positions in the cell are obtained by a Cubic spline function. Numerical parameters for the following calculations are shown in Table 1.

3. Results and discussion

3.1 Characteristics of microwave damping with constant plasma density

First, the characteristics of microwave damping with constant plasma density has to be clarified. Figure 3.1 shows the numerical results for the electric field amplitude damping of an R wave in the z direction using the dispersion relation Eq. (2-4). The damping of the L wave at the left wall was very small (about 1 % of the input electric field amplitude at the right wall). Therefore, the L wave is not considered in the following simulations because it seems that it is not important for plasma production. Figure 3.1a shows the R wave damping curves at different gas pressures in the plasma with a density of 1×10^{17} m^{-3}. The R wave at the lower gas pressure is dampened near the ECR point due to resonance damping, while that at the higher gas pressure is dampened earlier due to the effect of collision damping. Figure 3.1b shows the R wave damping curves with different plasma densities at a gas pressure of 0.67 Pa. The R wave with the higher plasma density is dampened more sharply than that with the lower one.

3.2 Interaction of plasma and microwave

Figure 3.2 shows the simulation results when combining a particle model and a microwave damping model for the plasma density and the microwave damping distribution, where the gas pressure was changed to 0.13, 0.67, 9.3 Pa. As the plasma density is not constant, the microwave damping curve of the simulation differs from the results (Fig. 3.1b) obtained when density remained constant. The plasma density distribution shows very different curves for each pressure. The maximum moves towards the right side (upstream of the microwave) from the ECR point as the gas pressure increases. The plasma distribution for lower gas pressures becomes symmetrical about the center line. This is due to the higher diffusion coefficient and the sharper absorption of microwaves near the ECR point which is set as the center line.

References

/1/ K. Suzuki et al., Jpn. J. Appl. Phys.16, No.11, p1979(1977).
/2/ Y. Kakehi et al., Proc. 8th Symp. Plasma Processing, The Electrochem. Soc., p393(1990).
/3/ Y. Weng and M.J.Kushner, 43rd Gas. Electronics Conf. Abs., Illinois, p123(1990).
/4/ M.A. Hussein and G.A. Emmert, J. Vac. Sci. Technol. A8(3), p2913(1990).
/5/ Y. Yasaka et al., Proc. of 8th Symp. on Plasma Processing, Nagoya, JSAP, p49(1991).
/6/ R.W. Boswel and I.J. Morey, Appl. Phys. Lett. 52(1), p21(1988).
/7/ C.K. Birdsall and A.B. Langdon, Plasma Physics via Computer Simulation, McGraw-Hill Book Company(1985).
/8/ A. Yokozawa et al, Papers of Technical Meeting on Electrical Discharges, ED-88-42, IEEE Japan, p1(1988).
/9/ R.W. Hockney and J.W. Eastwood, Computer Simulation Using Particles, Adam Hilger,Bristol and New York (1988).
/10/ M. Ikegawa and J. Kobayashi, JSME Inter. J. Ser. II 33, No.3, p463(1990).
/11/ G.A. Bird, Molecular Dynamics, Clarendon Press (1976).
/12/ A.B. Cambel, Plasma Physics and Magnetofluidmechanics, McGraw-Hill(1963).

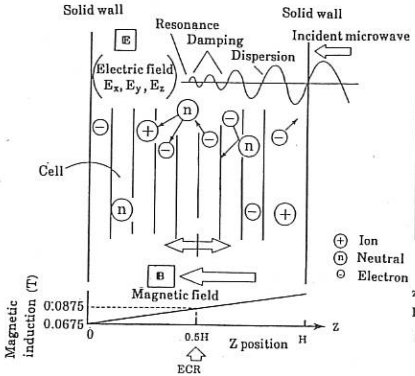

Fig. 2.1 Schematic view of calculation model

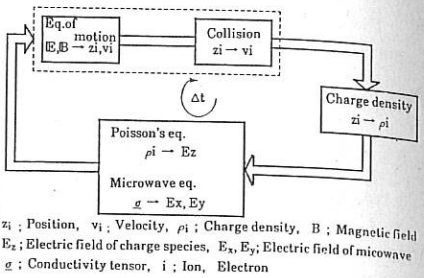

z_i ; Position, v_i ; Velocity, ρ_i ; Charge density, B ; Magnetic field
E_z ; Electric field of charge species, E_x, E_y; Electric field of micowave
g ; Conductivity tensor, i ; Ion, Electron

Fig. 2.2 Calculation sequence of the simulator in timestep Δt

Table 1 Numerical parameters

Wall distance	$H=8$ cm
Microwave ;	
Input electric field amplitude	$E_I=900$ V/m
Frequency	$f=2.45$ GHz
Cell number	$N_c=100$
Simulated particle number ;	
Electron	40000
Ion	40000
Timestep	$\Delta t=1.02\times10^{-11}$ s

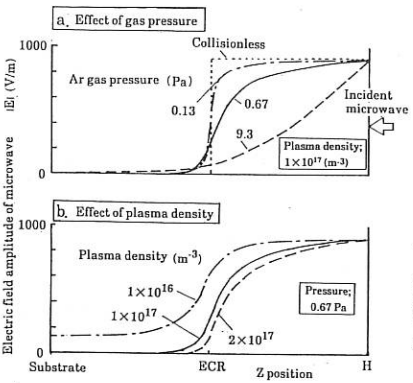

Fig. 3.1 Characteristics of microwave damping with the constant plasma density distribution

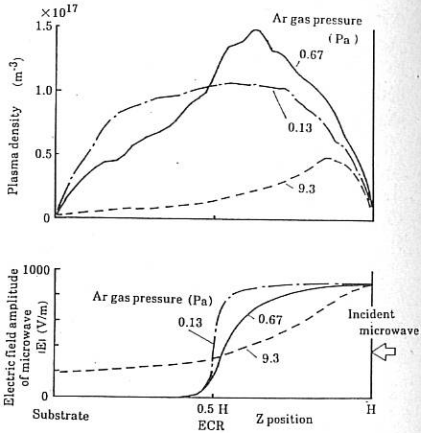

Fig. 3.2 The simulation results with the different gas pressures

ECR PLASMA SOURCE IN ICR ISOTOPE SEPARATION DEVICE.

C. Meis, A. Compant La Fontaine, P. Louvet and R.L. Meyer*.
Centre d'Etudes Nucléaires de Saclay - 91191 Gif-sur-Yvette.
* Université de Nancy I, 54506 Vandoeuvre Les Nancy. France.

Abstract.

We have used a ray tracing method in order to describe the propagation and absorption of the ordinary and the extraordinary modes, of an electromagnetic wave, from an emission point outside the plasma, till the electron cyclotron zone, for several angles of incidence. The plasma is confined in a flaring magnetic field. The electronic temperature is 1-5 eV and the density 10^{11} - 10^{12} cm^{-3}. Temperature effects and electron - neutral collisions have been taken into account in the dielectric tensor.

Introduction.

In recent years, plasma heating by Electron Cyclotron Resonance (ECRH) has found a wide field of applications. The plasma source of ERIC, a device for stable isotopes separation by ion cyclotron resonance [1], is also based on this principle. The ERIC apparatus consists of the microwave ECRH plasma source, the ion cyclotron resonance excitation zone and finally the isotope collector (Fig.1).

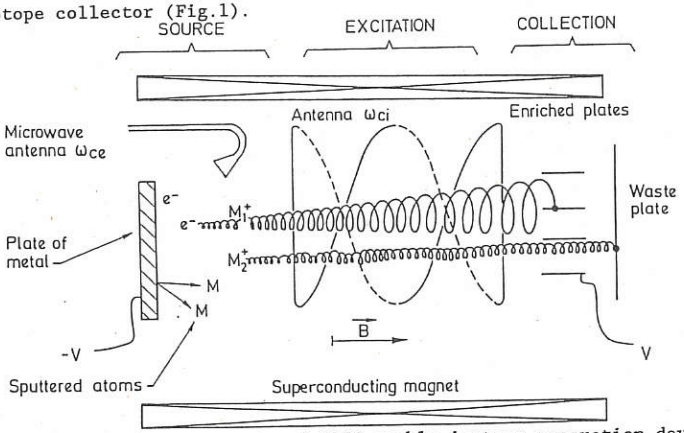

Fig. 1. Scheme of the components of ERIC stable isotope separation device.

The source region has a cylindrical shape of a 30 cm diameter and about 60 cm length, situated in the flaring magnetic field zone. Plasma ignition takes place by ECRH in Argon (or Krypton) atmosphere at 10^{-4} Torr using cw 1.5 kW klystrons at 10, 18 or 29 GHz. A horn type microwave antenna couples the electromagnetic wave to the plasma. The rare gas ions initialize sputtering on a metal plate biased to -2 kV and containing the isotopes to be separated. The plasma is thus composed of metal and gas atoms, electrons,

metal and gas ions. Using experimental values of the electronic density and temperature spatial distributions, we study here the absorption of different rays penetrating the plasma at various angles with respect to the magnetic field direction.

Ray tracing calculation.

The cold dispersion relation for the extraordinary and ordinary modes of an electromagnetic wave with frequency $\omega/2\pi$ and wave vector $\vec{k}$ propagating in a plasma with electronic density n_e and refractive index $\vec{N}$, confined in a magnetic field $\vec{B}$, writes [2]:

$$D = N_\perp^2 + N_{/\!/}^2 - 1 + X \pm \frac{XY\left(\sqrt{(1-N_{/\!/}^2)^2Y^2 + 4N_{/\!/}^2(1-X)} \pm Y\left(1+N_{/\!/}^2\right)\right)}{2(1-X-Y^2)} = 0 \qquad (1)$$

where: $X=\left(\frac{\omega_p}{\omega}\right)^2$ with $\omega_p=\sqrt{\frac{e^2 n_e}{\epsilon_0 m_e}}$ the plasma frequency and $Y=\left(\frac{\omega_c}{\omega}\right)$ with $\omega_c=\frac{|e|B}{m_e}$ the electron cyclotron frequency. Also, $|\vec{N}|^2 = N_\perp^2 + N_{/\!/}^2 = \frac{|\vec{k}|^2 c^2}{\omega^2}$ and $N_{/\!/} = \frac{\vec{B}}{|\vec{B}|}\cdot\vec{N}$

Using (1), the ray trajectories are determined by [3,4]:

$$\frac{d\vec{r}}{dt} = \vec{v_g} = -\frac{\partial D/\partial \vec{k}}{\partial D/\partial \omega} \quad \text{and} \quad \frac{d\vec{k}}{dt} = \frac{\partial D/\partial \vec{r}}{\partial D/\partial \omega} \qquad (2)$$

In our case, the components of the flaring magnetic field can be expressed analytically in cylindrical coordinates (r,θ,z) as follows:

$$B_r = \frac{2zrr_0^2}{\mathbb{Z}\left(r_0+(z^2/\mathbb{Z})\right)^3} B_0, \qquad B_\theta = 0,$$

$$B_z = \frac{r_0^2}{\left(r_0+(z^2/\mathbb{Z})\right)^2} B_0 \qquad (3)$$

$\vec{z}$ being the axis of the magnetic coil and B_0 the homogeneous zone magnetic field whose maximum intensity is 3 Tesla. $\mathbb{Z}$ = 340 cm, r_0 = 15 cm, r and z in centimeters. The radial profile of the electronic density and temperature has been determined experimentally using Langmuir probes:

$$\mathbb{G}(r) \simeq \left(1-\left(\frac{r}{a}\right)^2\right)^{3/2}\mathbb{G}(0) \qquad (4)$$

where $\mathbb{G} = T_e$ or n_e, a = 7.8 cm and r in cm. A ray trajectories exemple at 10°, 20° and 25° degrees emission angles with respect to the magnetic field direction, for $\omega/2\pi$ = 29 GHz $T_e(0)$ = 5 eV, $n_e(0) = 5\cdot10^{11}\,cm^{-3}$ and

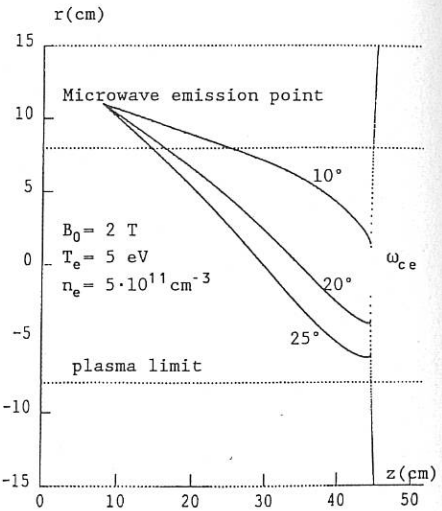

Fig.2 Ray trajectories at 10°, 20° and 25° degrees emission angles.

$B_0 = 2$ T is shown in Fig. 2. The ordinary mode absorption is extremely low. The relationship between the wave polarization and the extraordinary mode has been discussed elsewhere [5]. At a given point s of the trajectory, the power absorption is given by:

$$P(s) = P_0 \exp\left(-2 \int_0^s \mathrm{Imag}(k_\perp) ds'\right) \tag{5}$$

The quantity $\mathrm{Imag}(k_\perp)$ is determined by resolving the worm dispersion relation expressed in terms of the dielectric tensor components ϵ_{ij} assuming a maxwellien electron distribution function [2,6]:

$$N_\perp^4\left(\epsilon_{11}(1 - \chi_{33}) + \chi_{13}(2N_{/\!/} + \chi_{13}) + N_{/\!/}^2\chi_{33}\right) - N_{/\!/}^2 \times \left(\epsilon_{12}^2(1-\chi_{33}) + (\epsilon_{11} - N_{/\!/}^2)X\left((\epsilon_{11} - N_{/\!/}^2)(1-\chi_{33}) + \epsilon_{33}^0 + \chi_{13}^2 + (N_{/\!/}+\chi_{13})^2\right) - 2i\epsilon_{12}\chi_{13}(N_{/\!/}+\chi_{13})\right) + \epsilon_{33}^0\left((\epsilon_{11} - N_{/\!/}^2)^2 + \epsilon_{12}^2\right) = 0 \tag{6}$$

with $\epsilon_{13} = N_\perp \chi_{13}$ and $\epsilon_{33} = \epsilon_{33}^0 + N_\perp^2 \chi_{33}$, where [6]:

$$\epsilon_{33}^0 = 1\text{-}X, \quad \epsilon_{11} = 1 + \frac{1}{2} X\zeta_0 (Z(\zeta_1) + Z(\zeta_{-1})), \quad \epsilon_{12} = -i \frac{X\zeta_0}{2} (Z(\zeta_1) - Z(\zeta_{-1})) \text{ and}$$

$$\chi_{13} = \frac{X}{2Y} \left(\frac{v_e}{c}\right) \zeta_0 (1 + \zeta_1 Z(\zeta_1)), \qquad \chi_{33} = \frac{X}{2Y^2} \left(\frac{v_e}{c}\right)^2 \zeta_0 \zeta_1 (1 + \zeta_1 Z(\zeta_1)) \tag{7}$$

$v_e = \sqrt{\dfrac{2T_e(r)}{m_e}}$ being the electron mean velocity and $Z(\zeta_p)$ the Fried and Conte function: $Z(\zeta_p) = \exp\left(-\zeta_p^2\right)\left(-2 \int_0^{\zeta_p} e^{t^2} dt + i\sqrt{\pi}\right)$ with $p = 0, \pm 1$ (8)

In fact, the electrons move within a neutral gas of density $n_n = 10^{12}$ to 10^{13} cm^{-3}. In order to study the influence of electron - neutral elastic collisions we have used in (8) ζ functions with imaginary arguments [7]:

$$\zeta_p = \frac{c}{N_{/\!/} v_e} \left(1 - pY + \frac{i\nu_{e-n}}{\omega}\right) \tag{9}$$

Of course, $\nu_{e-n} = \sigma_{e-n}^{el} n_n v_e$ is the electron - neutral elastic collision frequency and $\sigma_{e-n}^{el} \approx 10^{-15} cm^2$ [8] the corresponding cross section. In fact, in our experimental conditions ν_{e-n} is typically of the order $10^5 s^{-1}$. The neutral gas influence upon the power absorption of the extraordinary mode along the ray trajectory abscissa until the electron cyclotron zone (ω_{ce}) is presented in Fig.3.

An increase of the thickness of the absorption region is observed. As a conclusion, we can calculate the microwave power absorption distribution near the electron cyclotron

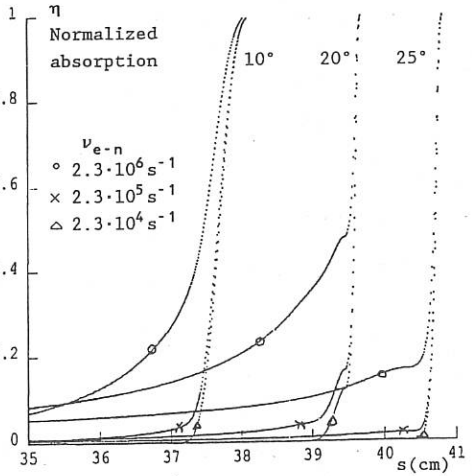

Fig. 3. Influence of the electron - neutral elastic collisions on the ray absorption.

zone in a flaring magnetic field at low electronic temperatures. The electron - neutral elastic collisions have no significant influence except a slight increase of the thickness of the absorption zone.

References

[1] P. Louvet
"Isotope Separation by Ionic Cyclotron Resonance"
Workshop on Separation Phenomena in Liquids and Gases
Darmstadt (1987) CEA Conf.9292.

[2] I. Fidone, G. Granata, G. Ramponi and R.L. Meyer.
Phys. Fluids 21, 645 (1978).

[3] G. Bekefi
"Radiation Processes in Plasmas"
John Wiley and Sons, New York (1966).

[4] V. Krivenski, I. Fidone, G. Giruzzi, R.L. Meyer and E. Mazzucato
Nuclear Fusion 25, 127 (1985).

[5] C. Meis, A. Compant La Fontaine, P. Louvet and R.L. Meyer.
"Electron cyclotron resonance plasma heating in a flaring magnetic field"
AIP Conference proceedings - "Radiofreqency Power In Plasmas".
Charleston SC, 1991. p.356.

[6] I. Fidone, G. Granata and R.L. Meyer
Phys. Fluids 25, 2249 (1982).

[7] D.G. Swanson
"Plasma waves"
Academic Press, 1989.

[8] David L. Book.
Naval Research Laboratory - Plasma Formulary.
Whashington DC 20370-5000. NRL Publication 0084-4040, Revised 1987.

CURRENT AND GEOMETRY DEPENDENCE OF MASS AND ENERGY FLUXES IN CAPILLARY, ABLATIVE CRITICAL FLOWS

S. Cuperman[1], D. Zoler[1], J. Ashkenazy[2], M. Caner[2] and Z. Kaplan[2]
[1]School of Physics and Astronomy Tel Aviv University, Tel Aviv, ISRAEL
[2]Soreq Nuclear Research Center, Yavne 70600

There is growing interest in high pressure discharges in ablative capillaries which are also essential components of Electrothermal Launchers.[1-5] In these devices, the out flow of the plasma through the hollow electrode is balanced by the ablation of the tube walls that are made of low atomic weight material, such as polyethylene. This ablation is caused by energy losses (especially radiative ones) from the plasma to the wall and can yield steady state operation conditions.

In this work we investigate theoretically the current and geometry dependence of the mass and energy fluxes in the capillary ablative discharges described above. For this, we solve numerically radius-averaged one-dimensional steady state continuity, momentum and energy equations for a cylindrical ablative capillary discharge plasma. The following main features of the work should be mentioned:

1. The spatial (z) dependence of the ionization degree of the plasma, $\bar{Z}$, as well as of the correction factor to the Spitzer conductivity, β, are taken into account by using for $\bar{Z}(z)$ and $\beta(z)$ best fits to numerical results obtained in a separate, parametric ionization study providing, $\bar{Z}(\tilde{\rho},\tilde{T})$ and $\beta(\tilde{\rho},\tilde{T})$ ($\tilde{\rho}$ and $\tilde{T}$ are the normalized mass density and temperature, respectively).
2. A non-ideal equation of state is used to calculate the thermodynamical quantities entering the problem. Thus, from the SESAME-Los Alamos library[5] one extracts discrete numerical values and subsequently, by best fit techniques one obtains continuous functions for the pressure and internal energy required by the integration method of the equations.
3. Self-consistent boundary conditions are obtained and used for the solution. This is of major importance since we are faced with a closed physical system whose parameters (current, radius, length) are kept fixed during the experiment; the axial profiles of the plasma characteristics (mass density, temperature, pressure and flow velocity), including their values at the ends of the capillary are determined in a self consistent manner by the physical processes involved.

BASIC EQUATIONS.

The radius-averaged steady state fluid equations for a viscous conductive and radiative one-dimensional flow in a cylindrical capillary can be written.[1,2]

$$\rho \frac{dV_z}{dz} + V_z \frac{d\rho}{dz} = \dot{\rho}_a , \tag{1}$$

$$\rho V_z \frac{dV_z}{dz} + \frac{dP}{dz} = \frac{4}{3} \frac{d}{dz}\left[\eta \frac{dV_z}{dz}\right], \tag{2}$$

$$P \frac{dV_z}{dz} + \rho V_z \frac{d\epsilon}{dz} = \frac{4}{3}\eta\left(\frac{dV_z}{dz}\right)^2 + \frac{d}{dz}[(K_{rad,z} + K_{cond,z}) \frac{dT}{dz}] + L_J . \tag{3}$$

In eqs. (1)-(3), ρ, V_z, T, P and ϵ are the mass density, axial velocity, temperature, pressure and the internal energy respectively; η, $K_{rad,z}$ and $K_{cond,z}$ are respectively, the viscosity, radiative heat conduction and thermal heat conduction coefficients; $\dot{\rho}_a$ and L_J represent, respectively, the ablation and Joule heating terms.[1-3]

For convenience, we here use the normalizations:

$$y = z/\ell_0 , \tilde{\rho} = \rho/\rho_0 , V = V_z/V_0,$$
$$\tilde{T} = T/T_0 , \tilde{P} = P/P_0 , \tilde{\epsilon} = \epsilon/\epsilon_0. \tag{4}$$

For length, mass density and temperature we chose the following reference values

$$\ell_0 = 24\text{cm}, \rho_0 = 1.36\times10^{-3}\ \text{g/cm}^3 , T_0 = 4\text{eV} . \tag{5}$$

For pressure and internal energy we use as reference the corresponding expressions holding for ideal gases, namely

$$P_0 = k\left(1 + \bar{Z}_1\right) T_0\rho_0/\bar{m}; \ \epsilon_0 = k\left(1 + \bar{Z}_1\right)T_0/\bar{m}(\gamma - 1). \tag{6}$$

Here, γ is the adiabatic coefficient, $\bar{m}$-the average-mass, k-Boltzmann's constant and $\bar{Z}_1$ - the average ion charge in the uniform plasma case. For the polyethylene considered here, we take $\bar{m} = 5m_p$ (m_p being the proton mass) and $\bar{Z}_1 = 1$.

For the flow velocity we take as reference value the sound speed, namely

$$V_0 = \left[\gamma k\left(1+ \bar{Z}_1\right)T_0/\bar{m}\right]^{1/2} = 1.47\times 10^6\text{cms}^{-1} . \tag{7}$$

To eqs. (1)-(7) we add the (normalized) expressions for the mass flux, F_m, energy density, E and energy flux, F_E, namely

$$F_m = \tilde{\rho}V, F_E = F_m E$$
$$E = \tilde{P}/\gamma\tilde{\rho} + \tilde{\epsilon}/\gamma(\gamma-1) + 0.5\ V^2 . \tag{8}$$

SOLUTION METHOD AND RESULTS

A. For a fixed set of physical parameters (namely current I and capillary radius, a) one solves eqs. (1)-(3) for <u>different sets</u> of arbitrarily chosen boundary conditions $\tilde{\rho}(y=0)$ and $\tilde{T}(y=0)$; in

all cases, one uses the obvious condition V(y= 0). For each set of b.c. one finds specific axial profiles $\tilde{\rho}$, $\tilde{T}$, V and $\tilde{P}$ as well as a corresponding critical (optimal) axial distance, y_{opt}, at which the flow velocity reaches the local sound velocity. The analysis of these results reveals the following important features (see Fig.1): 1. The critical flow characteristics $\tilde{\rho}_{min}(y_{opt})$, $\tilde{T}_{min}(y_{opt})$, $V_{max}(y=0)$ and $\tilde{P}_{min}(y_{opt})$ as well as $\tilde{P}_{max,y=0}(y_{opt})$ are almost linear functions of y_{opt}; 2. To a particular y_{opt} -value always correspond the same values $\tilde{\rho}(y_{opt})$.....$\tilde{P}_{max,y=0}(y_{opt})$ independent of the pair of boundary values $\tilde{\rho}(y=0)$ and $\tilde{T}(y=0)$.

B. From the results given in Fig.1. (which are based on arbitrary b.c. at y= 0) it is now possible to obtain consistent boundary conditions.

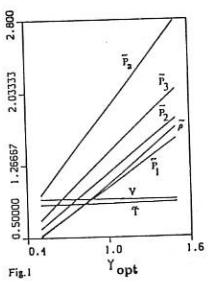

Fig.1

Thus, consider a capillary length l_i ($l_i/l_0 \equiv y_i$); from the results given in Fig.1, obtain the maximum pressure corresponding to $y_{opt}= y_i$, namely $P_{max,y=0}(y_{opt}= y_i)$. Now, solution of eqs.(1)-(3) at y= 0 together with the best fit values for $\bar{Z}$, $\tilde{\beta}$, $\tilde{P}$ and $\tilde{\epsilon}$ indicated above, as well as the $\tilde{P}_{max,y=0}$-value indicated by Fig.1 determine the values of $\tilde{\rho}$ and $\tilde{T}$ at y= 0; these, together with the natural condition V(y= 0)= 0 represent the consistent boundary conditions for the intepration of the eqs.(1)-(3).

Using this method we carried out a systematic investigation of the effect which various parameters - such as, electrical current, I, capillary radius, a, and capillary length, l, have on the plasma characteristics, namely energy flux, F_E and mass flux, F_m. The results are presented in Fig. 2 and table 1.

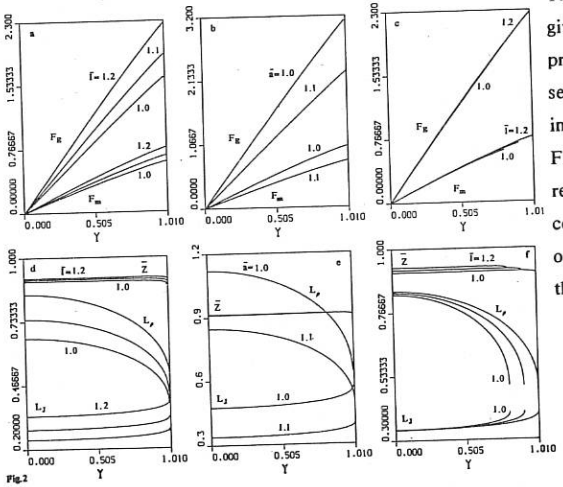

Fig.2

Thus, Figs. 2a, 2b and 2c give, respectively, the axial profiles $F_E(y)$ and $F_m(y)$ for several values of I, a and l (as indicated on the curves); Figs. 2d, 2e and 2f give, respectively, the corresponding axial profiles of the Joule heating term, L_J, the ionization degree, $\bar{Z}$, and

the ablation contribution, L_ρ. Thus, within the parameter range considered here, the critical (exit mass and energy fluxes F_m and F_E) increase almost linearily with the increase of the current (I) and capillary length (l); they decrease with increasing capillary radius (a). This is so because increasing I means increasing the energy supply to the discharge, which affects F_m as well as the ablation rate; as a result, F_E, is enhanced. Next, since the total ablated mass depends on the capillary length, also the l-dependence is simply understood. Finally, the decrease (for constant current) of F_m and F_E with increasing radius is a result of the decrease of the energy supplied to the unit volume of plasma and its consequences.

Table1. Dependence of the exit values of F_m, F_E and $\bar{Z}$ on I.

$\left(\bar{I}= I/I_0,\ I_0= 9000A;\ a= 0.2cm,\ l= 24cm\right)$

$\bar{I}$	$\bar{F}_m= F_m(I)/F_m(I_0)$	$\bar{F}_E= F_E(I)/F_E(I_0)$	$\bar{Z}= \bar{Z}(\bar{I})$
1.000	1.000	1	0.886
1.111	1.122	1.200	1.012× 0.886
1.255	1.287	1.416	1.023× 0.886

REFERENCES

/1/ D.A. Tidman, Y.C. Thio, S.A. Goldstein, D.S. Spicer, GT-Devices Report 86-7 (1986)

/2/ A. Loeb, Z. Kaplan, IEEE Trans. Magnetics 25, 342 (1989)

/3/ S. Cuperman and D. Zoler, Tel Aviv University Report, TAUP 1869-91 (1991)

/4/ D. Zoler and S. Cuperman, Tel Aviv University Report, TAUP 1915-91 (1991)

/5/ Equation-of-State Listing, SESAME Tables, Los Alamos Science Liason Company, 253 Ria Bravo, Los Alamos, NM 87544

Fig 1: Dependence of mass density velocity, temperature and pressure values at $y= y_{opt}$ as well as of the pressure at $y= 0$ on y_{opt} (where chocking occurs), as obtained by solving eqs. (1)-(3) for a large number of pairs of $\tilde{\rho}$ and $\tilde{T}$-values used as boundary conditions at $y= 0$. In all cases, $V(y= 0)= 0$; $\tilde{P}_1$, $\tilde{P}_2$ and $\tilde{P}_3$ correspond to $\bar{I}= I/I_0 = 1.000$, 1.111 and 1.255 , $I_0= 9000A$, $a= 0.2cm$; $\tilde{P}_a - a= 0.18cm$.

Fig 2: Results of integration of eqs. (1)-(3), upon consistent boundary conditions at $y= 0$, the $\tilde{\rho}$ and $\tilde{T}$ values obtained by the method described above.

New Method of Ion Extraction from Plasma by Using Radio-frequency Electric Field

T. Matsui, K. Tuchida, R. Nishio, K. Suzuki and T. Shoji*
Energy Research Laboratory, Hitachi, Ltd.,1168 Moriyama, Hitachi, Ibaraki 316 Japan
*Plasma Science Center, Nagoya University, Nagoya 464-01 Japan

1. Introduction

Ion extraction from plasmas has become of considerable importance for such applications as plasma processing, an ion source or atomic vapor laser isotope separation (AVLIS). A conventional ion extraction is carried out with an electrostatic field. Ion flux, extracted by the electrostatic field, however, is limited to the space charge limited current at the ion sheath according to the Child-Langmuir law, because the electric field cannot penetrate the plasma due to its shielding effect[1]. Although the ion flux increases with the applied voltage, the voltage is limited by an electric discharge or breakdown[2,3].

A new ion extraction method has been developed with the use of a radio-frequency (RF) electric field. In it, the frequencies of the RF field are chosen to excite eigen modes of the plasma in a low magnetic field. The RF field in the plasma makes ions drift to the electrodes. This paper presents the principle of the method and the results of its experimental proof.

2. Principle

Figure 1 shows a simple model for a plasma and RF electrodes system. A uniform slab plasma is sandwiched by a pair of parallel plate electrodes and the magnetic field B is applied perpendicular to the electrodes. The impedance of the electrodes is written by

$$Z=i\left(\frac{1}{\omega C_v}+\frac{1}{\omega C_p}\right), \tag{1}$$

where,

$$C_v\equiv\frac{\varepsilon_0 S}{d-p},\quad C_p\equiv\frac{\varepsilon_0\varepsilon_p S}{p},$$

and ε_0, ε_p, S, d and p are the dielectric permittivity of vacuum, the plasma permittivity, the electrode area, the distance between the electrodes, and the plasma thickness, respectively[4]. If the resistance of the plasma is negligible, a series resonance appears in the circuit where Z = 0. The RF field in the plasma is expected to become a maximum at the resonance. When the resistance is taken into account, the Q value of the resonance becomes low and the RF field in the plasma becomes small. The plasma permittivity which satisfies the resonance condition is obtained by Eq. 1 as

$$\varepsilon_p = -\frac{p}{d-p} \quad . \tag{2}$$

Here we analyze a low magnetic field case, where Larmor radii ρ_i, ρ_e and d satisfy $\rho_i \gg d$, $\rho_e \ll d$. The frequency dependence of ε_p under these conditions was calculated by using a dielectric permittivity for electrostatic waves for an infinite uniform plasma[4, 5]. An example of ε_p in the frequency range of $\omega_{ci} \ll \omega \ll \omega_{ce}$ is shown in Fig. 2. Parameters used are listed in the figure caption. Resonances, where $\mathrm{Re}(\varepsilon_p)$ satisfies Eq. 2, exist at 2.6 MHz and 12.0 MHz. At these resonant frequencies, the large electric field is expected to be excited in the plasma. Then, ions are oscillated and they drift away to the electrodes with the drift velocity depending on the initial phase between ions and the RF field.

3. Experimental Setup

To prove the existence of the predicted resonances, a preliminary ion extraction experiment has been carried out by using Xe plasma in low B field (5×10^{-3} T). An experimental apparatus is shown schematically in Fig. 3. The Xe plasma is generated by the RF electric discharge. The RF frequency and the power for the plasma generation are 13.56 MHz and about 700 W, respectively. The Xe gas pressure in the plasma generation region is 10^{-2} Torr. The plasma is transferred along the B field to the extraction test region. The electron density and electron temperature there are 5×10^{15} m^{-3} and 7.5 eV, respectively, as measured by a double probe method. The test region is constructed by the parallel plate electrode (length: 300 mm or 150 mm, gap

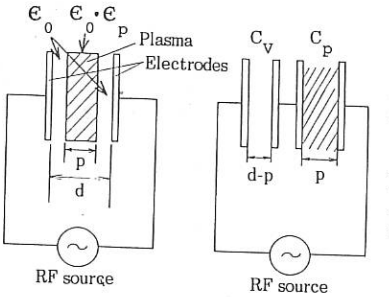

a) The RF system b) The equivalent circuit

Fig. 1 The RF electrodes and oscillator system and the system equivalent circuit.

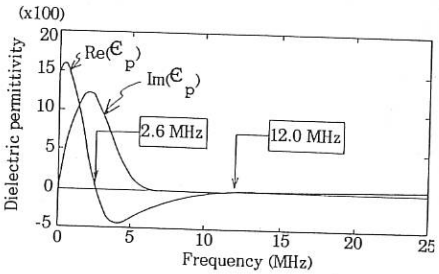

Fig. 2 Frequency dependence of ε_p. $Ne=5\times10^{15}$ m^{-3}; Te=7.5 eV; Ti=0.5 eV; $B=5\times10^{-3}$ T; d=42 mm; p=37.5 mm.

distance: 42 mm) and the RF circuits. The RF field frequency is swept in the range from 1 MHz to 30 MHz. The RF voltage and the RF current at the electrode are measured by the voltage and current probe. The electric field strength perpendicular to the B field is obtained by measuring the difference of floating potential at two points in the plasma using a differential FET probe. The ion flux is measured by a Faraday cup with two grids, which is set behind the electrode.

4. Results and Discussion

The frequency dependencies of the electric field strength in the plasma and the ion flux are measured when the RF power is constant (about 1 W). The results (electrode length: 300 mm) are shown in Fig. 4. The electron density and temperature are almost constant in Fig. 4. The electric field strength in Fig. 4 is the ratio of the measured electric field strength to the RF voltage applied on the electrodes. It is shown that the electric field strength has a sharp peak at 4.2 MHz and a broad peak at 12 MHz, and the ion flux also has two peaks near these frequencies. The calculated resonant frequencies are 2.6 MHz and 12 MHz for this experimental condition and these are well agree with the experimental values.

When the electrode length is 150 mm (half of that in Fig. 4), the experimental resonant frequencies are found to be 5 MHz and 15 MHz. On the other hand, the calculated values are 5 MHz and 24 MHz. Although there is the quantitative discrepancy between the experiment and the calculation for the higher resonant frequencies, the tendency for the resonant frequency to increase with decreasing electrode length is the same for both.

The RF voltage dependencies of the electric field strength and the ion flux at the resonant frequency are studied (Fig. 5). The electric field strength is observed to be proportional to the RF voltage. The ion flux is also proportional to the RF voltage beyond about 8 V. The results indicate that the ion extraction efficiency increases with the RF voltage.

4. Conclusion

A new method to extract ions from the plasma, by using the RF field, has been developed and tested experimentally. It is shown in the experiments that the electric field in the plasma becomes resonantly large at the frequencies, which are predicted by the calculation, and the resonant ion flux to the electrodes is observed around the resonant frequencies.

Reference

1) F. F. Chen, "Introduction to Plasma Physics", (Plenum, New York, 1974), Sec. 8.2.
2) K. Yamada, T. Tetsuka and Y. Deguchi, J. Appl. Phys., 67, 6734 (1990)
3) K. Yamada, T. Tetsuka and Y. Deguchi, J. Appl. Phys., 69, 6962 (1991)
4) T. Shoji, J. Phys. Soc. Jpn., 49, 327 (1980)
5) S. Ichimaru, "Basic Principles of Plasma Physics", (W. A. Benjamin, Inc., Massachusetts, 1973), Secs. 4 and 5.

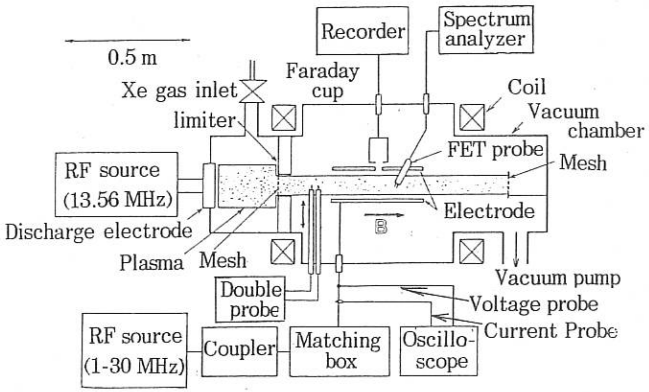

Fig. 3 Schematic diagram of experimental apparatus.

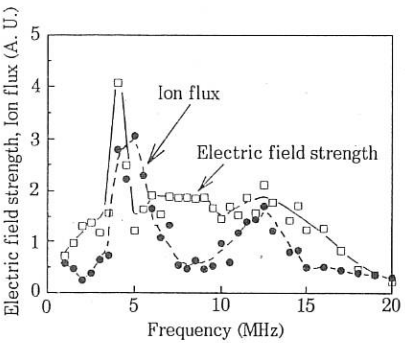

Fig. 4 The frequency dependences of the electric field strength and the ion flux. The electrode length is 300 mm.

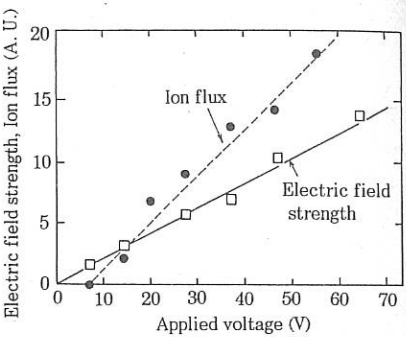

Fig. 5 The RF voltage dependences of the electric field strength and the ion flux at the resonant frequency. The frequency is 4.2 MHz and the electrode length is 300 mm.

DENSITY AND TEMPERATURE MEASUREMENTS BY LASER ABSORPTION DIAGNOSTIC ON A MAGNETIZED PLASMA

A. COMPANT LA FONTAINE, P. LE GOURRIEREC and P. LOUVET
DPE/SPEA, CEA-CEN Saclay - 91191 Gif/Yvette
Cedex - FRANCE

The ion cyclotron resonance process (ICR) designed to separate isotopes has been studied at Saclay on the ERIC device which has been described elsewere /1-3/. In order to achieve the separation in a cylindrical plasma column confined by an homogeneous magnetic field ($\vec{B}$) of about 1 Tesla, an external helicoïdal antenna generates an electromagnetic field with a frequency matched to the ion cyclotron frequency of a selected isotope which is progressively heated (up to a few hundred eV). On the contrary the other non-resonant isotopes are only slightly heated (up to a few eV, i.e. a few times their initial temperature). The separation itself is done geometrically at the end of the plasma column : the resonant species with a greater Larmor radius are collected on parallel blades (with respect to $\vec{B}$), while the other non-resonant species are collected on an end plate.

The separation factor α is very sensitive to the plasma source parameters as the transverse ionic temperature that must be minimized /1/. So, in order to optimise α, a laser absorption diagnostic has been developed and tested on the ERIC device with a barium plasma. The barium atoms produced by a Joule oven are ionized by the electrons heated by microwaves at their cyclotron frequency, namely 10 GHz.

Theory :

The intensity of a parallel beam transmitted at the frequency ν through an homogeneous absorption cell of length l can be written according the well known relation /4/ :

$$I_\nu = I_o \, e^{-k_\nu l} \qquad (1)$$

where k_ν is the absorption coefficient and I_o the incident intensity. Following the Einstein theory of radiation, ones gets :

$$k_\nu = 2\sqrt{\pi \ln 2}.\frac{e^2}{m_e c \Delta\nu_D}.N_1 \; f_{12} \exp\left(2\sqrt{\ln 2}.\frac{\nu - \nu_o}{\Delta\nu_D}\right)^2 \qquad (2)$$

where $\Delta\nu_D = 2\nu_o \left(2\ln 2 \; T_i / m_i c^2\right)^{1/2}$ is the Doppler width, T_i beeing the temperature of the ions with mass m_i, ν_o the frequency at the center of the line, f_{12} the absorption oscillator strength of the transition $2 \longrightarrow 1$ from the level with density N_2 to the level with density N_1, providing that : $N_2 \ll N_1$.

When a magnetic field is present, the degeneracy of the levels is revealed by a Zeeman structure on the absorption profile (fig.1). The density of the lower level can be written as follows :

$$N_1 = \frac{4\ \Pi^{3/2}}{\sqrt{\ln 2}} \cdot \frac{g_1}{g_2} \cdot \frac{\Delta\nu_D}{A_{21}\ \lambda_o^2\ 1\ \gamma_i} \cdot \ln \frac{I_o}{I_{\nu_{i_o}}} \qquad (3)$$

where γ_i is the ratio of the intensity of a component i of the multiplet relative to its total intensity /5/, $I_{\nu_{i_o}}$ is the intensity at the center of the component i, g_1 and g_2 are the degeneracy of the lower and upper levels respectively and A_{21} the transition probability between these levels.

Experimental set-up

The different parts of the laser absorption diagnostic are represented on the fig.2. We use a 3800 SPECTRA-PHYSICS dye laser (Rh 6G) pumped by a 164 SPECTRA-PHYSICS A_r^+ laser (4 Watts). The laser is monomode and frequency stabilized, its line-width is 1-2 MHz, the band-width is about 54 nm, the frequency sweeping for each record is about 30 GHz and the output power is laying between 30 and 200 mW. The control in wavelength is made by a 0.6 m JOBIN-YVON spectrometer, within 90 GHz with an iode lamp. The detection is done with photodiodes. The parasite emission due to the laser and to the plasma is suppressed by using a synchronous detector analyser ATNE ADS2.

Note that this diagnostic currently used in non-magnetized plasmas /6/ is utilized here for the first time to our knowledge in a plasma confined by a strong magnetic field.

Experimental results

The laser beam is directed transversally to the magnetic field so that both the Π and σ components of the Zeeman structure appear. The selected line is Ba II 6141.72 Å$(2d\ ^2D_{5/2} - 6p\ ^2P^o_{3/2})$ and its lower metastable level has an energy equal to 5675 cm^{-1}. Its experimental record of the Π components of the Zeeman structure is represented on the fig.3, while the theoretical structure is shown on the fig.4.

For this case, the density of the metastable level at 5675 cm^{-1} is found to be equal to $1.2 \pm 0.6 \times 10^{11}$ cm^{-3}, while the transverse ionic temperature is $T_i = 0.38 \pm 0.01$ eV.

As it is found that the optimum operating condition for the isotopic separation corresponds to the higher temperature of the Joule oven, 750°C (T_i minimal and N_i maximal), a separation experiment of ^{132}Ba has been performed with these conditions /3/. The effect of the radio-frequency (RF) heating (at the ion cyclotron frequency) on the ionic temperatures at the collector side is represented on the fig.5.

The rather high separation factor $\alpha = 8.5$ for ^{132}Ba, justifies the efficiency of the absorption diagnostic used here to optimize the ICR process.

REFERENCES

/1/ P.LOUVET. Proc. of the 2nd workshop on separation phenomena in liquids and gases, Versailles, CEA-Saclay Ed.(1989) p 5.

/2/ A. COMPANT LA FONTAINE, C. GIL and P. LOUVET. C.R. Acad. Sci. Paris, t.308, Série II (1989) p 821.

/3/ A. COMPANT LA FONTAINE and P. LOUVET. Ibid /1/ p 139.

/4/ A.C.G. MITCHELL and M.W. ZEMANSKY. "Resonance radiation and excited atoms", Cambridge University press (1971) p 92.

/5/ I.I. SOBEMAN. "Atomic data and radiative transitions", New York Springer-Verlag (1979) p 1989.

/6/ J.M. GAGNE, B. MONGEAU, B. LEBLANC, J.P. SAINT-DIZIER, P. PIANAROSA et L. BERTRAND. Appl. Opt. Vol.17, N°16 (1978) p 2507.

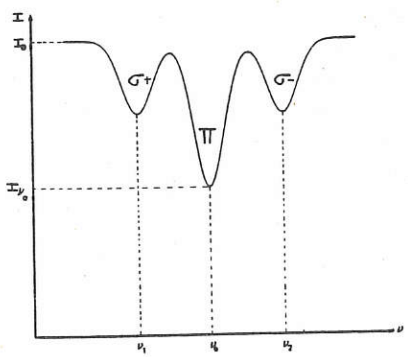

Fig.1 : Absorption profile of a Zeeman triplet

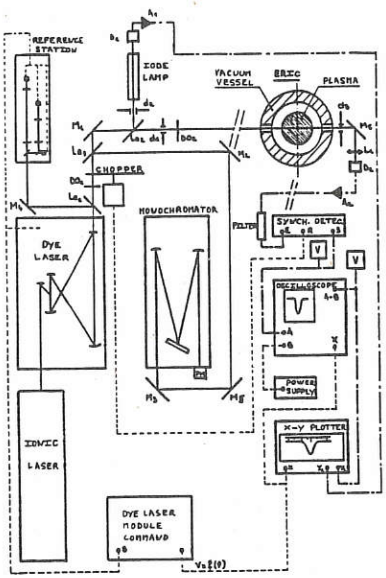

Fig.2 : Experimental set up for laser absorption diagnostic

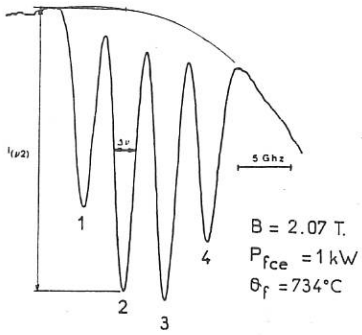

Fig.3 : Π components of a Zeeman pattern of Ba II 6141 Å on ERIC

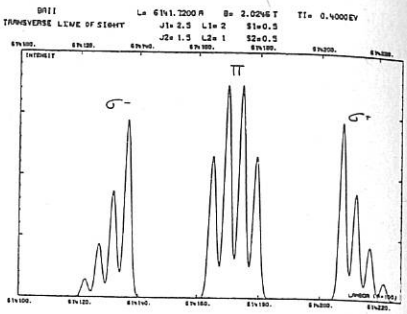

Fig.4 : Theoretical Zeeman pattern of Ba II 6141 Å

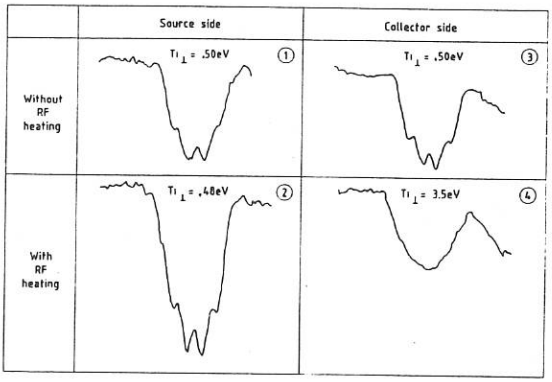

Fig.5 : Laser absorption measurements of the line Ba II 6141.72 Å

THE PLASMACHEMICAL REACTIONS IN NEGATIVE CORONA DISCHARGES

J.D. Skalný, P. Lukáč and R. Gábriš
Department of Plasma Physics, Comenius University
Mlynská dolina F-2, 842 15 Bratislava, Czecho-Slovakia

1. INRODUCTION

The sulfur hexafluoride SF_6, either pure or mixed with other gases, is widely used as an insulator gas in high voltage equipment or as a reactive gas for dry etching of materials used for VLSI integrated technologies. The SF_6 gas is known to be chemically inert gas under the normal conditions. However, in gas discharges the decomposition of SF_6 was observed /1/. If pure oxygen or oxygen containing compounds are added into the SF_6 the decomposition of gaseous SF_6 by negative corona discharge leads to formation of oxyfluorides, predominantly to thionyl tetrafluoride SOF_4 /1/. The concentration of neutral by-products formed by corona discharge has a back effect on the properties of discharge /2/. The oxyfluorides have a similar influence like ozone produced by negative corona in oxygen containing gas mixtures /3/. All these species cause the formation of new ions different from the primary ions. Because the processes of O_3 and SOF_4 generation are initiated by atomic oxygen, the activities of mentioned species will be dependent on the amount of oxygen in the mixture. The purpose of this work is to study the generation of ozone by negative corona discharge in mixtures of oxygen with sulfur hexafluoride.

2. EXPERIMENTAL

The mixture of oxygen with SF_6 flew down the cylindrical discharge tube at constant flow rate 1 $cm.s^{-1}$ what corresponds to the retention time 100 sec. The tube contains a central wire electrode and is divided to five insulated parts allowing the parallel measurements of currents in each individual part of discharge tube. The mixture of gases leaving the discharge tube passed through the cell of UV spectrometer. From measured transparency of gas mixture the concentration of ozone in the mixture was estimated. The temperature and the pressure of gas mixture were equal to ambient values.

3. EXPERIMENTAL RESULTS AND DISSCUSION

The dependence of ozone concentration in the mixture of gases leaving the discharge tube on the mean energy η consumed by discharge is shown in fig. 1. The mean energy η is defined like a ratio of discharge power P = U.I [W] and the flow rate Q $[cm^3.s^{-1}]$. The decrease of ozone concentration at constant value of η which is evidently caused by the increase of SF_6 concentration can be explained in the following way.

In the pure oxygen an electron-impact dissociation

$$e + O_2 \longrightarrow O + O + e \quad (1)$$

is a very effective source of oxygen atoms needed for generation of ozone. If molecules of sulfur hexafluoride are added into the oxygen, they can be also dissociated very effectively by electron impact

$$e + SF_6 \longrightarrow F + SF_5 + e \quad (2)$$

The intermediate by-products O and SF_5 can react between themselves or with the other components of mixture

$$O + O_2 + M \longrightarrow O_3 + M \quad (3)$$

$$O + SF_5 \longrightarrow F + SOF_4 \quad (4)$$

The electrons which are generated in the ionization region in the vicinity of thin wire electrode undergo also the collisions in which they are attached both with oxygen and sulfur hexafluoride molecules. Because the detachment of electrons from negative ions is very slow process in investigated gas mixtures, thus this can be neglected. The removal of free electrons from a gas under electrical stress by formation of negative ions can be formaly expressed by equation

$$e + X \longrightarrow X^- + \text{energy} \quad (5)$$

The equation includes all attachment processes of electrons i.e. dissociative and three-body attachment. Because the electron-impact dissociation processes (1) and (2) belong to the reactions having rather high energy thresholds, the main part of collisions resulting to dissociation of O_2 and SF_6 molecules is realized in the region of high electric field near the wire electrode. Thus in the equation (5) predominantly the dissociative attachment of electrons is active.

The system of equations characterizing the main processes in

the ionizing region of negative corona discharge in mixture of oxygen with sulfur hexafluoride, was used for estimation of the relationship between the production of ozone and production of oxyfluoride SOF_4. The gas mixture O_2 + SF_6 was considered at normal pressure 101.3 kPa and normal temperature 273.15 K. The reaction of electrons with oxygen and sulfur hexafluoride and consequent reactions of of by-products were simulated by solving of system of differential equations

$$\frac{d[O]}{dt} = 2k_1[e][O_2] - k_3[O][O_2] - k_4[O][SF_5] \quad (I)$$

$$\frac{d[O_2]}{dt} = -k_1[e][O_2] - k_3[O][O_2] \quad (II)$$

$$\frac{d[O_3]}{dt} = k_3[O][O_2] \quad (III)$$

$$\frac{d[SOF_4]}{dt} = k_4[O][SF_5] \quad (IV)$$

$$\frac{d[SF_5]}{dt} = k_2[e][SF_6] - k_4[O][SF_5] \quad (V)$$

$$\frac{d[SF_6]}{dt} = -(k_2 + k_5)[e][SF_6] \quad (VI)$$

$$\frac{d[SF_5^-]}{dt} = k_5[e][SF_6] \quad (VII)$$

$$\frac{d[e]}{dt} = -k_5[e][SF_6^-] \quad (VIII)$$

The system was solved for following parameters:
k_1 = 6.2E(-9), k_2 = 3.1E(-8), k_3 = 2.8E(-14), k_4= 2.0E(-12), k_5 = 3.1E(-10). The unit for all rate constants is $cm^3.s^{-1}$. The initial value of electron density [e] = 1.0 E(14) cm^{-3} is convenient value in ionization region of negative corona discharge. The dependence of calculated equilibrium values $[SOF_4]/[O_3]$ on the initial concentration of SF_6 in the mixture is shown in fig. 2. From this the negligible effect of reaction (4) on the ozone formation is evidently clear if the concentration of SF_6 is below 1%.

4. RERERENCES

/1/ R.J.Van Brunt, J.T.Herron, IEEE Trans. on Electr. Ins. **25**, 75 (1990)
/2/ I.Sauers, Proc. Gas Discharges IX, Venezia (Italy 1988), p. 589
/3/ M.Černák, J.Skalný, Š.Veis, D.Dindošová, Acta Phys. Slov. **25**, 97 (1979)

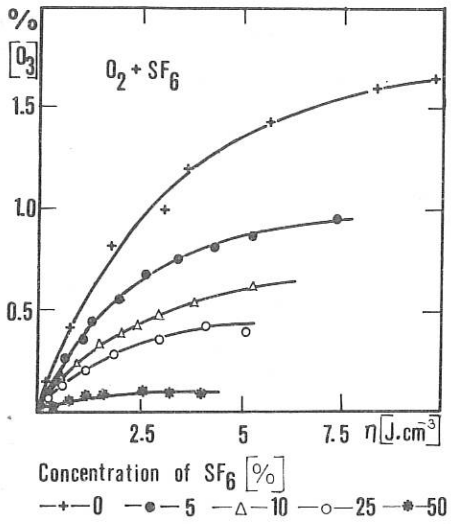
%
[O3]
O2 + SF6
1.5
1.0
0.5
2.5
5
7.5
η[J.cm-3]
Concentration of SF6 [%]
—+— 0 —●— 5 —△— 10 —○— 25 —✱— 50

Fig.1

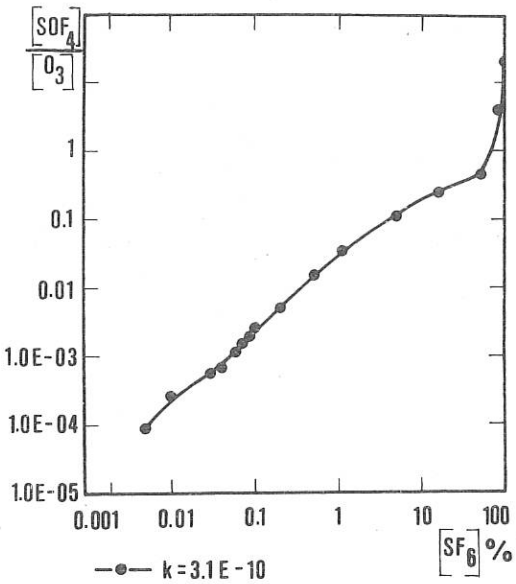
[SOF4]
[O3]
1
0.1
0.01
1.0E-03
1.0E-04
1.0E-05
0.001
0.01
0.1
1
10
100
[SF6] %
—●— k = 3.1 E - 10

Fig. 2

Plasma parameter profiles and fluctuation properties of an ECR process plasma source for Si etching at LN_2 temperatures.

S.K. Kim, C.W. Park, S. Cho, E.H. Choi, J.K. Kwak*, J.K. Park*, C. Rhee,
Plasma Laboratory, Korea Research Inst. of Standards and Science (KRISS)
Daedok Science Town, Daejon, Korea.
** Dept. of Nuclear Engineering, Seoul National University, Seoul, Korea*

Recently ECR plasma is being utilized for various types of process devices in the ULSI semiconductor development and production lines such as 16 and 64 mega D-RAM's due to its high ionization effeiciency and resultant low pressure operation capability with higher plasma density and lower space potential compared to RF discharges. However, problems like unstable microwave coupling to the plasma, inhomogeneity and fluctuations in the plasma properties at the position of the sample remain as obstacles to overcome for semiconductor fabrication and other applications.

We designed and constructed an ECR plasma source operating at 2.45 GHz with emphasis on plasma diagnostics and parameter control to investigate these problems. Initially operational diagnostics include Langmuir probes and gridded ion energy analyzers, and measurements of basic plasma parameters such as plasma density and plasma potential in argon plasma have been performed. Additional diagnostics being prepared are: 70GHz microwave interferometer/scattering system for plasma density and fluctuation measurement nd a laser induced fluorescence (LIF) measurement system. The LIF measurement is to monitor behaviours of radicals and products such as SiF_2 from SF_6/Ar etching of polysilicon, and to investigate possibilities of end-point detection from the measurement results. There are reports of observations [1] of SiF_2 and similar radicals in CF_4/O2 plasma, but no reports from SF6 or SF_6/Ar plasma as far as we know. Probe beam utilizes 220 nm UV radiation from BBO second harmonic generator which is pumped by 440 nm radiation from Coumarine 450 pulsed dye laser (50 nsec, 100mJ, 1A linewidth tuned with a birefringent tuner). Fluorescence emission is observed with 1m monochromator and detected by a PM tube and a 1024 element gated photodiode array conncected to an OMA. In addition a CARS spectrometer will join the measurement from flame/combustion research group at KRISS.

The machine has three coils for the magnetic field, two of which produce ECR field of 875 gauss. Current in each coil can be adjusted independently to change the resonance layer. The third coil is located in the downstream area at the position of the substrate holder, to change the magnetic field line shape and to investigate its effect on plasma and the etching process (Figure 1). Substrate mount for maximum 8" diameter wafer has been designed, constructed and tested for vacuum and cooling performances. With all the diagnostics and the holder installed, the base pressure is 4 x 10-8 mbarr (with LN_2 circulating). Mounting surface was measured with Pt resistance thermometer to be cooled down to -100°C in 30 minutes, and to -180°C in 90 minutes. Space potential in the vicinity of the wafer can be adjusted by producing an RF plasma layer from 13.56

MHz, 1 kW RF generator connected to the mount. Test etching of "line-and-space" patterned polysilicon wafer at liquid nitrogen temperature (-100~-140 °C) in the SF_6 plasma is planned during May-June, and the initial result will be presented during the conference. In addition, as a supporting experiment, a double plasma[2] source is being equipped with a magnetron to investigate ECR plasma production scheme with surface field[3]. This DP machine will soon be expanded to a magnetized triple plasma source where microwave-plasma interaction and other wave-plasma interactions will be investigated.

Some of the measured profiles of the ECR plasma and their dependence on external parameters such as pressure and magnetic field shape at the substrate holder position are shown in figure 2. $T_e(r)$ profiles is very irregular, due to noisy probe signal. However, at all positions and field shapes, Te decreases with increasing pressure. Space potential data from ion analyzer is cleaner, and the profile becomes flatter when the 3rd magnet is turned on to make the field line parallel at the substrate holder position. Like T_e, V_p decreases with increasing gas pressure, but when parallel field line is produced by the 3rd magnet, the decrease is much weaker. Ion temperature show much less dependence on pressure, with sudden increase around pressure value of $\sim 4 \times 10^{-3}$ mbarr, the reason of which is not understood yet but being investigated in relation to density fluctuation properties described in the next paragraph.

Fluctuations in plasma density was measured from electron saturation current of Langmuir probe and ion analyzer collector current. Fluctuation signals were compared with microwave reflected power level behaviour from crystal detector which consistently showed coherent fluctuation of 2 - 10 kHz when the magnetic field by the 3rd coil is weak and the field line is somewhat diverging. During normal operation conditions ($P_{Argon} = 4 \times 10^{-4}$ mbarr, 200W microwave in, $I_3 = 50$ Amperes to make B parallel and normal to the substrate holder), ion analyzer located on axis (r = 0 cm) and facing up along the field line showed periodic sawtooth-like modulation in the fluctuation (figure 3). This modulation becomes irregular in poeriod and weaker in amplitude as the analyzer is pulled out. At the plasma boundary (r ~ 14 cm), modulation disappears and looks similar to random fluctuation of crystal signal. When facing down along the field line ion current shows no modulation at all radial position. However, the analyzer I-V characteristics (i.e. ion distribution) does not reveal any gross difference between the two directions. Furthermore, the fluctuation level increases suddenly as the gas pressure crosses $3 \sim 4 \times 10^{-3}$ mbarr from below, and dependence on analyzer direction and location is more complicated than lower gas pressure case. To further investigate properties of this fluctuation such as relation to possible ion drift and to microwave coupling to the plasma, a correlation measurement with two ion analyzer is being performed, and a 70GHz heterodyne collective scattering system is being assembled and tested on bench.

REFERENCES

[1] Y. Matsumi et al., *J. Appl. Phys.* 60 (1986), p.4102.
[2] R.J. Taylor et al., *Rev. Sc. Inst.* 42 (1972), p.1615.
[3] T. Namura et al., *Rev. Sc. Inst.* 62 (1992), p.21.

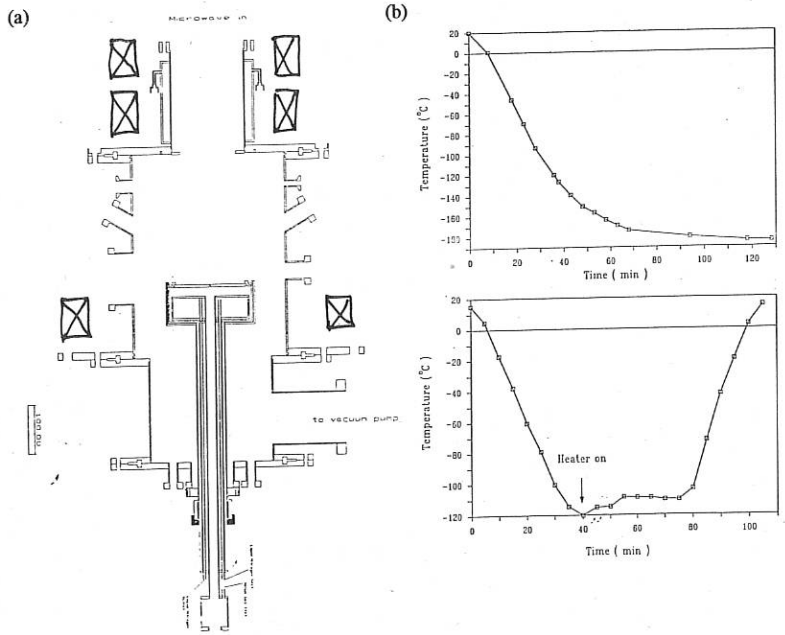

Figure 1. (a) Schematic diagram of the ECR plasma source. (b)Cooling and reheating of the holder surface.

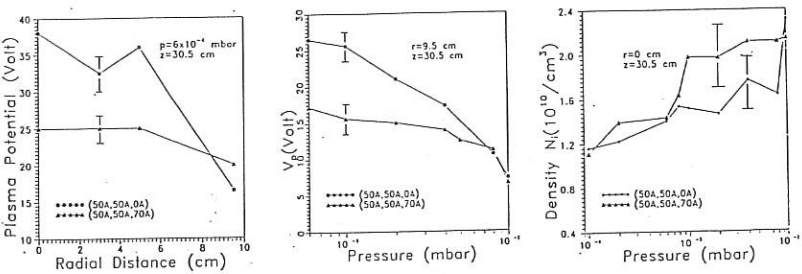

(a) (b) (c)

Figure 2. (a) Radial profile and (b) pressure dependence of the plasma potential, (c) pressure dependence of central density.

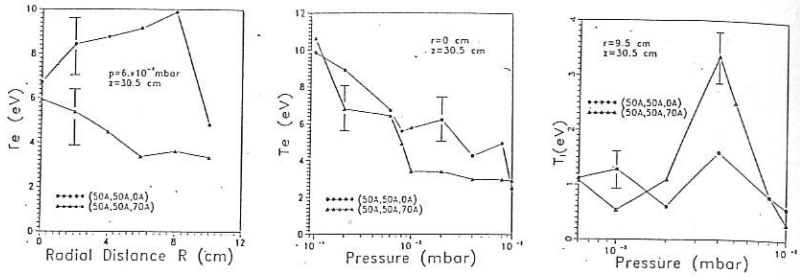

(d) (e) (f)

Figure 2 (cont). (d) radial profile and (e) pressure dependence of electron temperature; (f) pressure dependence of ion temperature.

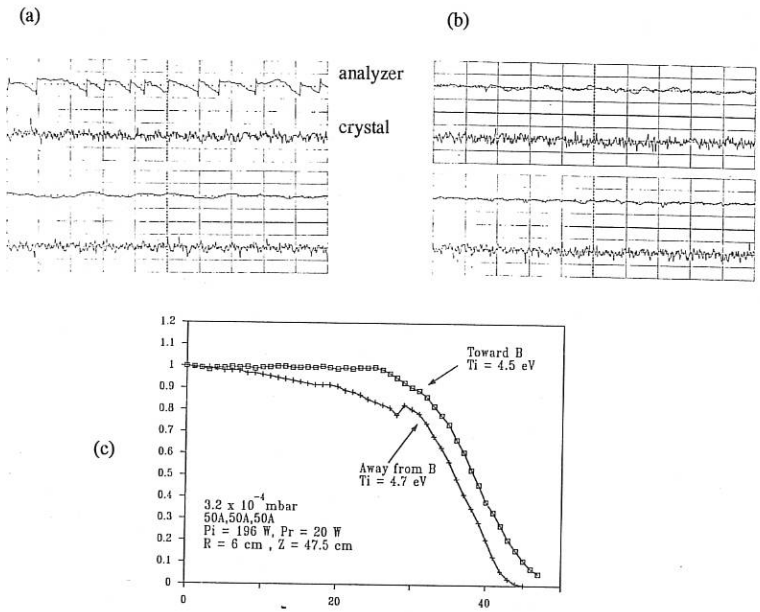

Figure 3. (a,b) Ion analyzer collector current fluctuation signal compared to reflected microwave power fluctuation. (a) analyzer at r = 0 cm facing toward and away from the field line, (b) at r = 12 cm. (c) I-V curves at r = 6 cm.

MAGNET PLASMA DYNAMIC ACCELERATOR WITH ULTRA HIGH FREQUENCY RESONATOR

Kubarev J.V., Tashaev J.N., Safronov V.P., Kholin N.N.
Moscow Instrument-Making Institute
20 Stromynka str., Moscow, 107076, Russia

With the purpose of service time increasing and plasma flow admixture decreasing, an experimental model accelerator with ultra high frequency (UHF) discharge is created. In given installation (Fig.1) in distinction from Magnet Plasma Dynamic (MPD) accelerator [1,2], thermionic emitter cathode is absent, the discharge appearing at UHF power feeding into the cavity resonator from the magnetron, running at quasi pulse mode. The resonator is placed in axisymmetric magnetic field and has coaxial anode in the form of convergen-divergent nozzle for plasma streaming into outer space.

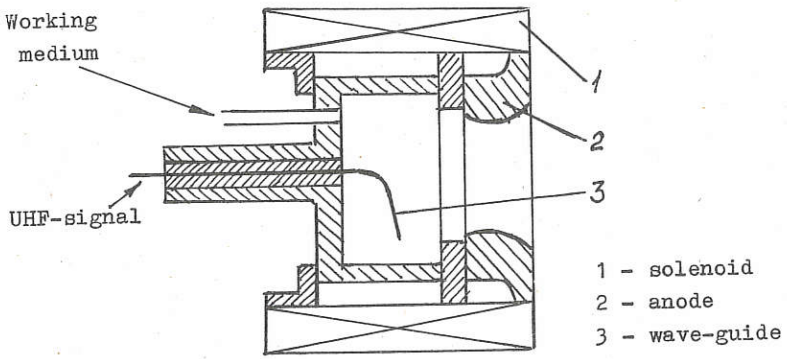

Fig.1

Anode hole diameter is chosen in the absence output condition of UHF radiation into outer space, that is, the anode is a piece of an unlimited wave-guide [3].

To define the cutoff root mean square (RMS) of high frequency electric force (HFEF) and magnetron power of UHF ge-

nerator necessary for plasma creation, the electron movement, in crossed E and B fields at its collisions with atoms and molecules, is examined. In the region of "throat" of the magnetic nozzle, where a discharge arises, a magnetic field created by solenoid is homogeneous and is directed along the symmetry axis of the accelerator, and HFEF also being homogeneous, is directed on the radius. The electron movement in the plane, perpendicular to the magnetic field, may be divided into cyclotron rotation and drift movement representing rotation on elliptical orbit with the frequency of high frequency field.

While evaluating the magnetic movement due to electron rotation on elliptical orbit, its initial movement conditions were chosen in such a way to that cyclotron rotation be absent. The electron movement equation solving, in the supposition of electric field harmonic dependence upon time $\vec{E}=\vec{E}\cos(wt+\varphi)$ enabled to find electron coordinates as time functions

$$X=\frac{qE}{m}\left(I+\frac{\nu_m^2}{w^2}\right)^{1/2}\frac{I}{\Omega^2}\cos(wt+\varphi-\gamma_1-\gamma_2) \qquad (1)$$

$$Y=\frac{qE}{m}\frac{w_L}{w}\frac{1}{\Omega^2}\cos\left(wt+\varphi-\gamma_1+\frac{\pi}{2}\right)$$

where $\vec{E}$ is directed along X axis, $\vec{B}$ along Z-axis, q, m - charge and mass of the electron, w_L - electron cyclotron frequency, ν_m - electron elasticity collision frequency, w - frequency high frequency field,

$$\gamma_1=\operatorname{arctg}\left[2w\cdot\nu_m/(w_L^2+\nu_m^2-w^2)\right],$$

$$\gamma_2=\operatorname{arctg}(\nu_m/w),\ \Omega=\left[(w_L^2+\nu_m^2-w^2)^2+4w^2\cdot\nu_m^2\right]^{1/4}$$

Expressions (1) present a written parametric form of ellipse equation, the axes of which are turned relative to coordinate axes to the angle

$$\alpha=0.5\operatorname{arctg}\left[2\cdot\nu_m\cdot w_L/(w_L^2-w^2-\nu_m^2)\right]$$

Magnetic current moment, carried by revolving electron on elliptical orbit, is directed against solenoid magnetic

field and equals

$$\vec{f} = \frac{-q^4 E^2}{2m^3 \Omega^4} \vec{B}$$

Similar consideration of ion movement along with given data, results in the conclusion that in described system, high frequency electric field, perpendicular to the magnetic one, increases plasma diamagnetizm, which in high frequency field absence is due to just a cyclotron revolution of charged particles.

Average high frequency field work in a period, done in time unit above the electron against friction force, defines average speed of increasing heat electron energy.

$$\overline{\frac{d\varepsilon}{dt}} = \frac{q^2 E^2_{aver.} \cdot \nu_m}{m} \frac{w^2 + \frac{2}{m} + w^2}{\Omega^4}$$

where ε - heat electron energy, $E_{aver.} = E/\sqrt{2}$ - RMS of HFEF.

The electron will take the energy needed for exciting working medium atom I^*, during $\tau_i = I^* / \frac{d\varepsilon}{dt}$ if, certainly, it does not leave discharge region during this time due to diffusion. Break down possibility is defined by $\tau_i = R^2/D_\perp$ condition, from which threshold RMS of HFEF is found

$$E_{aver.} = \left[I^* \cdot \Omega^4 \cdot D_\perp \cdot m \left(q^2 R^2 \cdot \nu_m \cdot (W_L^2 + \nu_m^2 + W^2) \right)^{-1} \right]^{1/2}$$

Here $D_\perp$ - electron diffusion coefficient across the magnetic field, in the investigated installation $W_L \simeq 2\ 10^{10} c^{-1}$, $\nu_m \simeq 10^8 c^{-1}$, $W = 2\ 10^{10}\ c^{-1}$, $R \simeq 3$cm - the radius of critical section of discharged chamber and the working medium -argon.

The power of the energy necessary for discharge combustion is defined by the extracting speed of Joule heat

$$P = \overline{\frac{d\varepsilon}{dt}} \cdot n_e V_k \sim 50\ Vt,$$

where V_k - discharge chamber volume, n_e - electron concentration, the peak value of which ($n_e^{peak} \sim 10^{17}\ m^{-3}$) is calculated using electromagnet wave reflex condition from ionized gas region, where $n_e \geqslant \varepsilon_o \cdot mw^2 / q^2$.

In experiments use was made of 500 VT magnetron, opera-

ting in quasi momentum regime, which created electrical field in the resonator of $3 \cdot 10^4$ v/m. intensity.

Local parameters of plasma flow n_e, T_e, directed ion speed V_i and plasma potential φ were defined by directed probes [2], which were placed on the axis of source directly behind the anode nozzle and at a distance of 20 cm from it. The effective operation of the described installation was watched both at constant positive voltage absence on the anode and at potential difference availability between the anode and the cathode. Average electron concentration behind the nozzle cut, in both cases, roughly was $\sim 10^{17} m^{-3}$ and decreased to $10^{16} m^{-3}$ at 20cm distance. The directed jet speed was $V_i \simeq (5 - 10)\ 10^3$ m/s.

Note, that the measured value of plasma jet directed speed is in agreement with the speed, obtained from the examination evaluation of elementary diamagnetic acceleration in divergent magnetic field. In the region of "throat" of the magnetic nozzle, where the magnetic field intensity is a maximum, the plasma with cyclotron resonance heating is being created. At plasma jet movement in the direction of magnetic field decreasing, the energy transformation of crossed movement of charged particles takes place into the directed movement energy along the axis of the system. The strength of high frequency pressure, arising while electromagnetic wave reflection from the plasma occupied region, does not greatly contribute into the jet acceleration due to negligible value of electric field intensity.

At positive voltage feeding on the anode, plasma jet intensity increasing was registrated due to the jet speed increase.

References

1. Авторское свидетельство №166974 СССР. Источник газоразрядной плазмы. Ю.В.Кубарев. Заявлено 04.02.1963, №818030/26-25. Опубл. Бюл. Изобретений, 1964, №24.

2. Kubarev J.V., Kotelnikov V.A., Shirokov M.F. Investigation of Non-Isothermal Plasma Flows by Electric Probes. VII Inter.Conf.on Phen.in Ion.Gases.Contr.papers,Vienna, 1967,p.477.

3. Лебедев И.В."Техника и приборы СВЧ",М.,ВШ,1970,43с.

ION IRRADITION STUDIES FROM DENSE PLASMA FOCUS FOR CHANGE OF PHASE OF THIN FILM OF CdS

Ratna Sagar, M.P. Srivastava and R.S. Rawat
Department of Physics and Astrophysics, University of Delhi
Delhi - 110 007, INDIA

There has been a growing interest in the structural transformations in non-metallic solids induced by energetic ions. Structural transformations take the form of amorphization, crystallization and stoichiometric changes. Naguib and Kelly/1/ have reported the criteria for bombardment-induced structural changes in such solids. Tell and Gibson/2/ studied the Bi and Xe implanted CdS and observed that the chemical properties are obscured by the radiation damage effects. Their measurements were restricted to optical effects. Therefore, an extensive investigation was undertaken on Bi-ion implanted CdS. Eldridge et al./3/ found gross structural changes on the surface with the help of Reflection Electron Diffraction (RED). However, their studies were not sensitive enough to indicate the type and extent of radiation damage in CdS specimen. Subsequently, Govind and Fraikor/4/ studied radiation damage of Bi-ion implanted CdS single crystal qualitatively with the help of transmission electron microscopy. They observed black spots and interpreted them to be interstitial clusters. However, they did not observe amorphization of CdS crystals. The study of CdS thin film is of interest because of its applications as solar cells/5/ piezo electric transducers/6/ and photo activated light valves.

Due to above mentioned applications, we have investigated in the present paper, the change of phase of Argon-ion implanted amorphous and crystalline thin films of CdS having thickness $\simeq$ .6μm. The film is as-grown by vaccum evaporation technique and irradiated by the energetic Argon-ions of Dense Plasma Focus (DPF). The energetic ions from DPF have already been used by Rawat et al./7/ for the crystallization of amorphous thin film of Lead Zirconate Titanate. The thin films of CdS have been analysed before and after irradiation with the help of X-ray diffractometer (Rigaku Rotaflex), UV-visible spectrophotometer (Shimadzu-260), and Scanning electron microscope (Shimadzu - JSM 840).

Mather type DPF device of 3.3 kJ energy as shown in fig.1 is used to produce plasma of very high densities ($\simeq 10^{25} - 10^{26}$ m^{-3}) and having

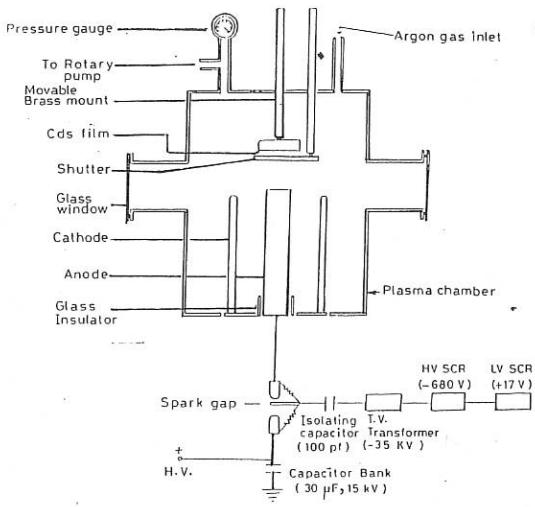

Fig.1 Schematic of the Experimental Set-up

temperature in the range of 1-2 Kev. DPF is a source of X-rays, energetic ions/8/andelectrons/9/. The sub-systems of DPF are shown in fig.1. The sample is being placed on a mount which moves vertically along the axis of the chamber from the tip of the anode. In this way, the energetic ions can be bombarded on the sample at different distances from the anode. At first, the amorphous film of CdS is analysed by X-ray diffractometer and then irradiated by Ar-ions present in DPF. The irradiated film is again analysed with the help of X-ray diffractometer. The parent sample and the irradiated sample are also studied with the help of UV-visible spectrophotometer and Scanning electron microscope. In the similar manner, the crystalline thin film of CdS is irradiated and studied.

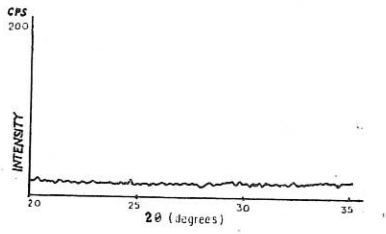

Fig.2 X-ray diffraction spectrum of as-grown amorphous film of CdS

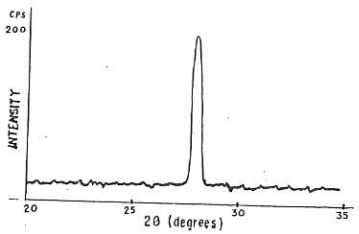

Fig.3 X-ray diffraction spectrum of as-grown amorphous film of CdS after irradiation.

X-ray diffraction spectrum for initially amorphous and crystalline CdS films as well as irradiated by energetic ions of DPF are shown in fig.2 - fig.5. Fig.2 shows the pattern for amorphous CdS film. When this film is irradiated by Ar-ions, a peak is recorded in the X-ray diffraction pattern as shown in fig.3. This peak indicates the change in phase of the CdS film. On the other hand, for the as - grown crystalline CdS film the spectrum is as shown in fig.4.

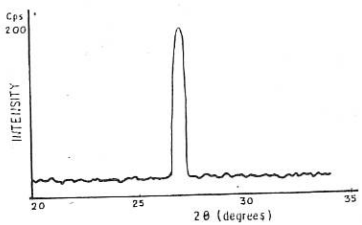

Fig.4 X-ray diffraction spectrum of as-grown crystalline film of CdS.

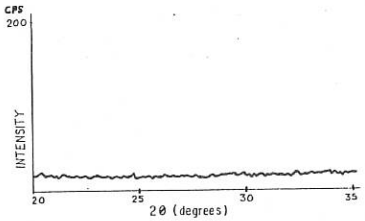

Fig.5 X-ray diffraction spectrum of as-grown crystalline film of CdS after irradiation.

This film is then irradiated by Ar-ions of DPF and the X-ray diffraction pattern of such a film is shown in fig.5. This figure exhibits the amorphization of the CdS film.

These results lead us to conclude that Ar-ion bombardment is responsible for the change of phase of CdS films. Structural changes have also been observed in the scanning electron micrographs, taken for the irradiated thin films of CdS. The transmission and absorption characteristics are also found to change due to irradiation.

Acknowledgements

We wish to thank Prof. P.C.Mathur and Dr. P.K. Sisodia for making CdS film available to us. R.S. is grateful to University Grants Commission, India for the award of Senior Research Fellowship and R.S.R. is grateful to Council of Scientific and Industrial Research, India for the award of Senior Research Fellowship which enabled them to complete this investigation.

/1/ H.M.Naguib, Roger Kelly, Radiation Effects **25**, 1 (1975).

/2/ B. Tell and W.M. Gibson, J. Appl. Phys. **40**, 5320 (1969).

/3/ G. Eldridge, P.K. Govind, D.A. Nieman, and F. Chernow, Proc. Europ. Conf. on Ion Implantation (P. Peregrinus, Stevenage, U.K. 1970) p. 143.

/4/ P.K. Govind, and F.J. Fraikor, J. Appl. Phys. **42**, 2476 (1971).

/5/ F.A. Shirland, Adv. Energy Convers. **6**, 201 (1966).

/6/ J. Deklerk and E.F. Kelly, Rev. Sci. Instrum. **36**, 506 (1965).

/7/ R.S. Rawat, M.P. Srivastava, S. Tandon, A. Mansingh, Communicated for publication.

/8/ R.L. Gullickson, and H.L. Sahlin, J. Appl. Phys. **49**, 1099 (1978).

/9/ K. Schmitt, H. Krompholz, F. Ruhl, and G. Herziger, Phys. Lett. A. **95**, 239 (1975).

Influence of Metastable Atoms on the Characteristics of Surface Wave Produced Plasmas

U.Kortshagen and H.Schlüter

Institut für Experimentalphysik II, Ruhr–Universität Bochum,
D–4630 Bochum, Postfach 102148, GERMANY

Plasmas generated by surface waves ($\omega/2\pi$ = 60 MHz–2.45 GHz) in many cases exhibit a rather homogeneous structure of electric rf field strength /1/, simplifying modelling. Dominance of the axial component of the electric field $|E_z|$ and its radial homogeneity are assured when the "thin cylinder approximation" is fulfilled, whereas axial constancy of $|E_z|$ is achieved when dominant diffusion losses ($\approx n_e D_{eff}/\Lambda_{eff}^2$) are balanced by ionization purely from the ground state ($n_e \nu_{igr}(|E_z|)$); the continuity equation enforces $|E_z|$ as well as (non–Maxwellian /1/) electron energy distribution functions ("temperature") to be constant axially in spite of axially decreasing n_e ("diffusion regime").

However, ionization via excited states ($n_e \nu_{im}$) complicates and slightly modifies this regime, since the population density of excited states N_m is generally itself dependent on the electron density n_e: Balancing processes such as collisional excitation from the ground state, depopulation by superelastic collisions (and by ionization), all linear in n_e, compete with radiative depopulation not dependent on n_e (corona situation). The importance of radiative losses may be reduced – and simultaneously that of step–ionization increased – by optical thickness (effectively lengthening the lifetime of excited states) and in particular by metastability; in the latter case the lifetime, however, is limited by diffusion of metastables. Thus N_m should generally be assumed to depend on n_e, though tending to saturation at large n_e. Now the continuity equation reads:

$$\frac{n_e D_{eff}}{\Lambda_{eff}^2} = n_e \nu_{igr}(|E_z|) + n_e \nu_{im}(|E_z|, n_e) \qquad (1)$$

With axial decreasing n_e according to (1) inevitably $|E_z|$ has to increase slightly and the electron energy distribution function has to change.

This can be supported by numerically solving simultaneously the electron and ion continuity and momentum equations with the Boltzmann equation (including electron–electron and electron–ion collisions /2/), coupled with a collisonal–radiative model describing processes of excited states; the solutions have to satisfy Bohm's boundary criterion. In this treatment radial variations are accounted for in more detail. Self–consistent numerical results are presented for a simple He model including all states of main quantum number n=2 and their interactions and two n=4 states.

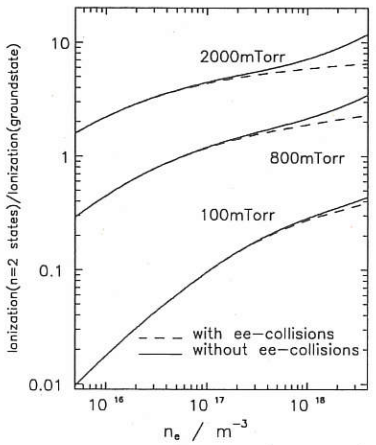

Fig.1 Self–consistent $\nu_{im}(|E_z|,n_e)/\nu_{igr}(|E_z|)$ versus n_e, including Penning effects (He).

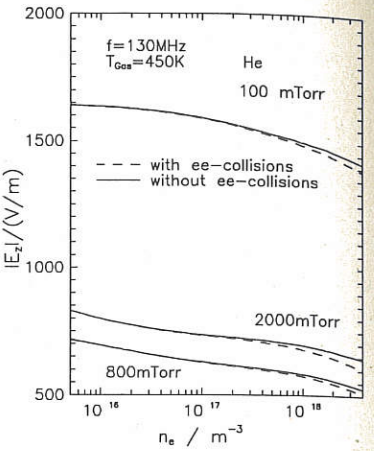

Fig.2 Self–consistent $|E_z|$ versus n_e.

As to be expected the total ionization frequency $\nu_{igr} + \nu_{im}$ tends to stay reasonably constant with (axially decreasing) n_e, whereas $\nu_{im}\left(|E_z|, n_e\right)/\nu_{igr}\left(|E_z|\right)$ in Fig.1 changes substantially. Penning effects are included which mitigate the changes up to a factor of 2. In Fig.2 the predicted change of the self–consistent $|E_z|$ is depicted. A variation of, for instance, 10 % when n_e (averaged over the discharge cross section) changes a factor 10 axially, is of modest size and may seem almost inperceptible, but it suffices to regulate the large variation of inelastic processes. Therefore the point is not so much the quantitative deviation from $|E_z| = \text{const}$, rather than the resultant consequences for ionization and excitation rates and spectroscopic observations, influenced by n_e directly and indirectly through varying $|E_z|$.

To transform dependencies on n_e into those on the axial coordinate z, Maxwell's equations have to be involved which ensure a self–consistent power flow. Only a minor adjustment due to metastables is necessary as compared to the regime $|E_z| = \text{const}$. This can easily be seen from the simple relation /3/:

$$\frac{dn_e}{dz} = -\frac{1}{2+\frac{1}{s}} \frac{\omega\nu}{a} \frac{\epsilon_0 m_0}{e^2} \frac{1}{\overline{f}} \tag{2}$$

The usual notations are used, with ν the elastic collision frequency and a the plasma radius; $\overline{f}$ is a slowly varying function essentially due to the cylindrical geometry , in thin cylinder approximation ≈ 0.16 in the range $\omega/\omega_p \approx 0.1 - 0.3$ and $\nu/\omega < 1$, slightly smaller in the presence of glass tubes and decreasing for smaller ω/ω_p. s stems from

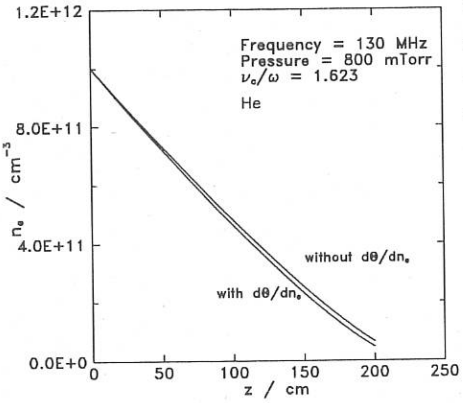

Fig.3 $n_e(z)$ integrated from (3) (He).

the relation: $n_e \propto |E_z|^{2s}$. Here s is negative and $|s|$ about 10, e.g., when the above mentioned large n_e-drop is accompanied by a minor increase of $|E_z|$. Thus basically a steepening of the slope of $n_e(z)$ can be concluded, but the factor -0.5 almost imperceptibly changes to -0.53, for instance. This can also be ascertained by integrating an alternative expression /4,5/:

$$\frac{dn_e}{dz} = -\frac{2n_e\alpha}{1 - \frac{n_e}{\alpha}\frac{d\alpha}{dn_e} + \frac{n_e}{\Theta}\frac{d\Theta}{dn_e}} \quad (3)$$

α is the absorption coefficient of the dispersion relation /6/, Θ the energy absorbed per electron (from self-consistent $|E_z|$ and distribution functions). Since $d\Theta/dn_e$ gives small negative contributions again basically a steepening as well as an usually immeasurable effect on $n_e(z)$ can be concluded. This is demonstrated in Fig.3 by an example. When electron–elctron collisions are included the effect is almost imperceptibly increased. The – virtually unchanged – and almost linear profiles predicted by (2) and (3) and Fig.3 are consistent with observed ones to be reported elsewhere.

The effect of metastables and step–processes really shows up in excitation rates and observed line intensities, for instance in the intensity ratio of the He singulet 504.7 nm line to the triplet 471.3 nm line, often referred to as a measure of temperature. The results of Fig.4 give witness to the influence of axially varying n_e, directly entering the collisonal–radiative model as well as causing changes in $|E_z(n_e)|$ and thus a changing distribution function ("temperature"). In this sense the results testify – only to a smaller extent – to an axially changing "electron temperature", caused originally also by changing n_e. It should also be emphasized that the trends such as in Fig.4 can be understood properly only if the correct self–consistent non–Maxwellian distribution functions (with "depressed" tail in the energy range of inelastic processes) are used /7/. The remaining differences between calculations and observations can easily be accounted for by uncertainties of cross–sections. Moreover the collisional–radiative model used is incomplete. Also errors in the n_e–determination give rise to small horizontal displacements, and the interferrometrically determined T_{gas} carries

some inaccuracies. Analysis of all these effects leaves essentially untouched the trends showing up in calculations as well as in observations.

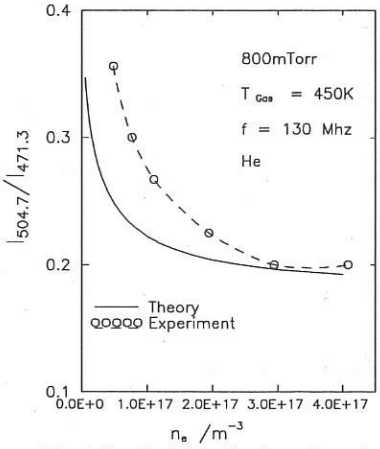

Fig.4 Singulet/triplet line intensity ratio.

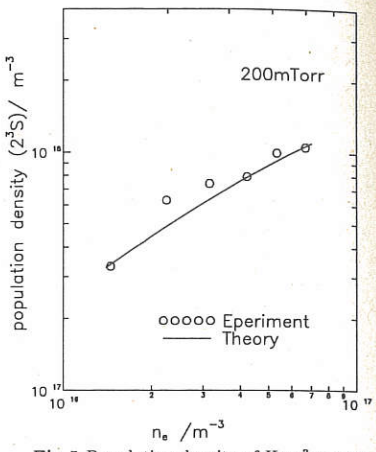

Fig.5 Population density of He 2^3S state.

Finally as an obvious check on the model used, in Fig.5 calculated and observed (via absorption measurements) population densities of the 2^3S state for 200 mTorr are compared, yielding agreement actually better than to be expected. It should be noted that the n_e–dependence for higher pressures is weaker, but then the contributions of the resonance states (2^3P in particular) to ν_{im} become more noticeable.

In summary it may be concluded that the influence of metastables leads to interesting, but seemingly small modifications in the characteristics of the diffusion regime, i.e. small changes of the constancy of $|E_z|$ with only imperceptible steeping of $n_e(z)$. The resultant influence on inelastic collision rates, however, may be large and has to be taken into account in order to properly understand spectroscopic data. In doing so the use of non–Maxwellian distribution functions is essential.

/1/ U.Kortshagen, H.Schlüter, A.Shivarova, J.Phys.D:Appl.Phys. 24, 1571 (1991)
/2/ U.Kortshagen, H.Schlüter, J.Phys.D:Appl.Phys., 25, 664 (1992)
/3/ A.Shivarova, in: Spatial Dispersion in Solids and Plasmas, P.Halevi ed., North Holland, Amsterdam, in press (1992)
/4/ C.M.Ferreira, J.Phys.D:Appl.Phys. 16, 1673 (1983)
/5/ A.Granier, C.Boisse-Laporte, P.Leprince, J.Marec, P.Nghiem, J.Phys.D:Appl.Phys. 20, 204 (1987)
/6/ M.Zethoff, thesis Univ.Bochum, 1991
/7/ J.Berndt, thesis Univ.Bochum, 1992

Use of Cold Plasmas in Film Deposition and Structuring

J. Edlinger*, H.K. Pulker*, E. Rille**, G.W. Vogl
*Balzers AG, FL-9496 Balzers, Liechtenstein, **Leica AG, CH-9435 Heerbrugg, Switzerland
Institut für Experimentalphysik Universität Innsbruck, A-6020 Innsbruck, Austria

1. INTRODUCTION

In general chemical compounds decompose during evaporation and sputtering. The highly volatile reactive components oxygen and nitrogen, disappear rapidly within the pumping system and compound films formed on the substrates are therefore often non-stoichiometric. Direct evaporation as well as direct sputtering of Al_2O_3 results in oxygen deficient films [1] and the same occurs with TiO_2 and other compounds. To overcome this difficulty, Auwärter [2] and Brinsmaid [3] suggested that the deposition should be carried out in the presence of oxygen or generally, depending on the compound processed, of other reactive gases. In the meanwhile reactive deposition has developed into a powerful technology.

In recent developments considerable attention has been paid to techniques to improve all optical and mechanical film properties besides stoichiometry and residual absorption.

These techniques avoid high substrate temperatures and supply the required energy to achieve proper optical, chemical and mechanical film characteristics by the use of high energy of coating material atoms and working or reactive gas atoms. The increase of the average particle-energy in the growing film by energetic ion processes appears to be beneficial. Ion-assisted reactive evaporation is therefore a very effective technology, along with reactive sputtering variants and reactive ion plating.

Sputter etching is often included in sputtering systems and used mainly to clean substrate surfaces (prior to film growth) to promote adhesion and to structure substrate-surface or films..

2. REACTIVE AND ACTIVATED REACTIVE EVAPORATION

The properties of thin films deposited on various substrates by conventional evaporation are generally found to be different from those of the corresponding bulk materials.

Oxygen loose, which usually occurs during evaporation of many oxides may cause optical absorption in the films. The effect could be appreciably corrected in the reactive deposition process [2] by adding oxygen to the residual gas. For all that, however, oxide coatings produced in this way are often still partially non-stoichiometric and slightly absorbing.

Heating the substrates to about 300 °C during reactive evaporation improved a number of film properties including stoichiometry, purity, density, refractive index and adhesion. Therefore substrate heating became the standard procedure in this process although it favours generally undesirable coarser film micrcstructure and surface roughness.

Reactive evaporations performed under standard conditions, but with additional activation and partial ionisation of the reactive gas, further improved film quality [4]. Better stoichiometry and rather low absorption values have been obtained when films were prepared by activated reactive evaporation (ARE) [5]. These coating experiments with Ions and excited molecules clearly showed that chemical reactivity is enhanced in the presence of a

gas-discharge plasma. To activate oxygen for ARE cold glow discharge ion sources with a hollow cathode inside a quartz tube are used [5].

3. ION ASSISTED DEPOSITION

Most properties of evaporated films are highly determined by the lack of mobility of the condensing atoms and molecules due to their low thermal energies of about 0.1 eV. Controlled bombardment of a growing film by argon or/and oxygen ions with energies up to several hundred electron volts has been shown to improve density and stoichiometry[6,7]. Adding energy to the film growth process appears to improve also adhesion [8] and to modify stress [9]. Ion beam techniques can be applied, however, also before and after film deposition. Substrates can be ion beam cleaned with inert or reactive gas ions, depending upon substrate materials involved, and freshly deposited films can be bombarded by ions for further improvement of their properties.

Hot-cathode Kaufman-type [10] ion guns are used usually in ion beam assisted deposition processes (IBAD), but also other installations have been applied. It is impossible to discuss and compare here all the variants of this technique. Considerable efforts have been directed to the analysis of plasma conditions and their correlation with deposited film properties. The mechanism responsible for densification seems to be momentum transfer as was shown recently by molecular-dynamics calculation [11].

4. GAS DISCHARGE AND ION BEAM SPUTTERING

During sputtering atoms or molecules are ejected from a target by momentum transfer processes caused by noble gas ions, e.g. Ar^+ bombardment. The coating material atoms with energies between 1 and 40 eV pass through the gas phase, loose energy by collisions and condense on substrates which, in case of gas discharge sputtering, are arranged opposite the target at a small distance.

Ions stem from a dc or rf gas discharge or from special ion guns. In the first case the typical working gas pressure is in the 10^{-2} to 10^{-3} mbar range whereas in ion beam sputtering lower background pressures and therefore larger target to substrate distances can be applied. With all variants [12] of sputter processes reactive gas procedures can be performed, but conventional gas discharge sputtering is a rather slow process. The deposition rate is increased by magnetrons, in which in addition to the electric field a magnetic field encreases the number of ionising collisions by keeping the electrons in trajectories close above the target surface. These procedures are used for film deposition on large flat substrates, e.g. architectural glass and plastic foils [13,14].

In ion beam sputtering (IBS) the target erosion is caused by a mono-energetic argon ion beam. This beam is usually produced by a Kaufman-type ion gun but also high frequency ion sources should be considered [15]. In dual ion beam sputtering a second ion gun is used, whose beam aims directly towards the growing film similar to ion assisted deposition [16]. With the IBS techniques dense, well adherent and stoichiometric films of low optical absorption can be obtained. In all variants care must be taken to avoid unwanted sputtering of plant installations by high energetic neutral atoms which causes film contamination.

5. STRUCTURING BY SPUTTER-ETCHING AND REACTIVE ION-ETCHING

Although it is not common, sputter etching can be used to etch patterns into thin films (or into the substrates themselves) first covered by a pattern-defining mask. The patterning mask may be either mechanical or an developed photoresist mask as used in

exhibits a monotonical increase. On the other hand for 2.7 Pa O_2 where the plasma density is lower, it is notified that $\delta\Delta$ exhibits a peak at discharge time of 100 s (P).

The results of Fig.3 and Fig. 4 show that oxygen pressure change leads to the plasma density change and affects the time evolution of relative phase shift. $\delta\Delta$ is a function of a refractive index and a film thickness /6/. On the ignition of the plasma, the film thickness starts to increase and at the same time the refractive index decreases rapidly. The time evolution of $\delta\Delta$ can be determined by a competition between the refractive index and the film thickness. Very rapid decrease in the refractive index accompanying film growth leads to the peak in the $\delta\Delta$ versus discharge time /5/. For the plasma oxidation at 2.0 Pa O_2 the peak was not observed (Fig. 3). This is because the growth rate of the silicon oxide is high because of high plasma density at this pressure (a weak shoulder seen at around 50 s (S in Fig. 4) may be related to the rapid decrease of the refractive index for the higher plasma density).

In conclusion, the change rate of $\delta\Delta$ was observed by ISDP RE immediately after starting the RF discharge as being strongly dependent on O_2^+ density. In the thin oxide film region, the oxidant species of O_2^+ and/or O atoms were suggested to readily react on silicon surface, and the time evolution of $\delta\Delta$ was sensitive to the plasma density.

REFERENCES

/1/ S. Kimura, E. Murakami, K. Miyake, T. Warabisato, H. Sunami, and T. Tokuyama, J. Electrochem. Soc. **132**, 1460 (1985).

/2/ Y. Z. Hu, J. Joseph, and E. A. Irene, Appl. Phys. Lett. **59**, 1353 (1991).

/3/ H. Kuroki, H. Shinno, K. G. Nakamura, M. Kitajima, and T. Kawabe, J. Appl. Phys. **71**(1992); Proc. Mater. Chemistry '92, March 12-13, 1992, Tsukuba, Japan (Mitsubishi Research Institute, Tokyo, 1992), p407.

/4/ F. Chen, *Introduction to Plasma Physics* (Plenum Press, New York, 1974).

/5/ M. Kitajima, H. Kuroki, H. Shinno, and K. G. Nakamura, to appear in Sol. St. Commun.

/6/ C. E. Leberknight, and B. Lustman, J. Opt. Soc. Amer. **29**, 59 (1939).

/7/ S. Bashkin and J. O. Stoner, Jr., *Atomic Energy Levels and Grotrian Diagrams Vol. I. Hydrogen I-Phosphorous XV* (North-Holland, Amsterdam, 1975).

/8/ P. H. Krupenie, J. Phys. Chem. Ref. Data **1**, 423 (1972).

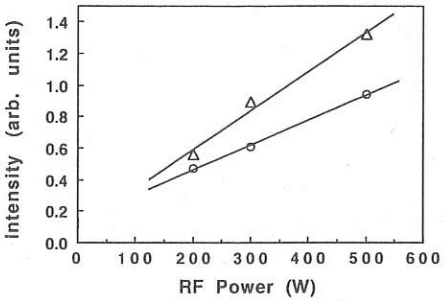

Fig. 3. RF power dependence of emission intensities of O_2^+ ions at an O_2 gas pressure of 2.0 Pa (Δ), and 2.7 Pa (o). Solid lines show least squares curve fitting. Error is within symbol size.

on the plasma density. To observe chemical species in oxygen plasma, the OES measurements were performed. Very sharp lines of O atoms were observed at 436.8 nm ($^3P \rightarrow {}^3S^0$), 532.9 nm ($^5D^0 \rightarrow {}^5P$), 615.8 nm ($^5D^0 \rightarrow {}^5P$), and 777.5 nm ($^5P \rightarrow {}^5S^0$) /3,7/. Somewhat broader lines from molecular oxygen ions (O_2^+) at 525.1, 559.7, 597.3, and 635.1 nm were also observed. All lines are assigned to the $b^4\Sigma_g^- \rightarrow a^4\Pi_u$ transition /3,8/. Figure 3 shows that the sum of the O_2^+ ions emission spectrum intensity increases quite linearly as RF power increases. The O atoms emission intensity also increased with respect to the RF power. Furthermore, plasma potential (V_p) was larger by 13-16 eV than floating potential (V_f), therefore suggesting that negative ions generated in the plasma does not dominate plasma oxidation directly. The present results indicate that positive ions and/or O atoms predominate in the plasma oxidation immediately after starting the plasma discharge. Further investigation on the sheath area is needed for understanding more detailed reaction mechanism.

Figure 4 shows δΔ versus discharge time at RF power of 300 W at an O_2 pressure of 2.7 Pa and 2.0 Pa. The change in δΔ at 2.0 Pa O_2 is larger than that at 2.7 Pa O_2. For 2.0 Pa O_2, δΔ

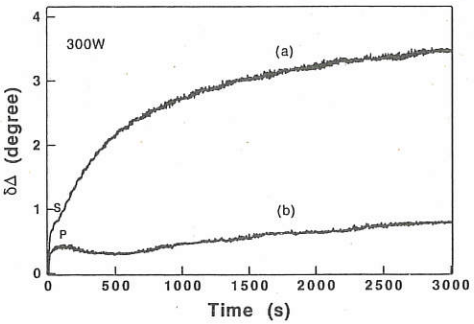

Fig. 4. Relative phase shift change δΔ versus time at RF power of 300 W at an oxygen gas pressure of a) 2.0 Pa and b) 2.7 Pa.

3. RESULTS AND DISCUSSION

Change in Ψ was very small. Figure 1 shows the relative change in Δ , $\delta\Delta=\Delta_0-\Delta$ (Δ_0 is a value of Δ at starting the discharge), monitored by ISDP RE as a function of discharge time at RF power of 200 W, 300 W, and 500 W at an O_2 pressure of 2.0 Pa. $\delta\Delta$ exhibits an increase with a high speed for a short time and a slow speed for a long time.

The change rate of $\delta\Delta$ ($\delta\Delta' \equiv \partial\delta\Delta/\partial t$) immediately after starting the RF discharge was determined as 1.1×10^{-1}, 1.7×10^{-1}, and 2.0×10^{-1} degree/s for respective RF powers of 200, 300, and 500 W. In contrast, there was not such a strong correlation between $\delta\Delta'$ and RF power 1.0×10^{4} s after starting the discharge. The main process in this stage may be the drift motion of oxygen ions across the oxide film /1/.

With the exception of the plasma density, which increased with respect to RF power increase, the plasma parameters are independent of RF power. Figure 2 shows the relation of $\delta\Delta'$ immediately after starting the RF discharge and the plasma density. $\delta\Delta'$ linearly increases as the plasma density increases between 6.4×10^{7} and 2.2×10^{8} cm^{-3}. This shows the initial oxidation rate strongly depends

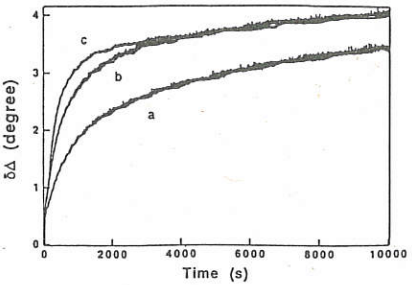

Fig. 1. Time dependence of relative change in Δ measured by *in-situ* during process rapid ellipso-metry at an O_2 gas pressure of 2.0 Pa and RF power of a) 200 W, b) 300 W, and c) 500 W, respectively. The film thickness was estimated to be about 1.4 nm after a plasma oxidation for 16000 s at 2.0 Pa O_2 and 300 W RF power /5/.

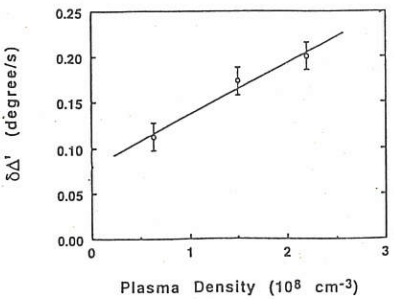

Fig. 2. Change rate ($\delta\Delta'$) immediately after starting the RF discharge versus plasma density obtained by the Langmuir probe method at an O_2 gas pressure of 2.0 Pa. Solid line shows least squares curve fitting.

EXPERIMENTAL STUDY OF PLASMA EFFECT ON OXIDATION OF SOLID SURFACE

M. Kitajima[1], H. Kuroki[1,2], H. Shinno[1], and T. Kawabe[2]

[1]National Research Institute for Metals, Tsukuba-shi, Ibaraki, Japan
[2]University of Tsukuba, Tsukuba-shi, Ibaraki, Japan

1. INTRODUCTION

Characterization of plasma is one of the most important issues for understanding mechanism of plasma-surface interaction and also the plasma processing for semiconductor. The plasma oxidation is a current technique being used for growing insulator films on semiconductor surfaces at lower temperatures than when using thermal oxidation/1-3/. However, there is no conclusive interpretation for the oxidation mechanism, and little research has been performed on effects of plasma on the oxidation rate. This paper reports detailed experimental study on the oxidation of silicon surface in thin film region in an oxygen plasma. We measured parameters and chemical species of the plasma using a Langmuir probe (LP) and optical emission spectroscopy (OES), and compared the results with those of in situ during process (ISDP) rapid ellipsometry (RE) to investigate effect of plasma on oxidation reaction kinetics on solid surface.

2. EXPERIMENTAL

Samples used were p-Si(100) with resistivity of $1x10^{-4}$~$3x10^{-4}$ Ωm. It was immersed in an HF solution for 5 min, rinsed with water, and annealed at 873 K in vacuum of about 10^{-7} Pa. The plasma oxidation of silicon was performed in a UHV chamber of 0.15 m in a diameter and 1.5 m in a length. An oxygen plasma was generated by RF discharge at 13.56 MHz, with its power of 100 to 600 W. The electrically isolated substrate was set up 1 m apart from the RF coil. Oxygen pressure ranged 1 to 3 Pa.

Electron temperature, plasma density, and other plasma parameters were measured by the LP method. The probe was placed ≈ 2 cm from the substrate, which is over 100 times greater than the Debye length (≈ 0.1 cm) /4/. The growth of silicon oxide films was monitored by ISDP RE (1s resolution). Ellipsometric parameters (Δ) and (Ψ) were measured *in situ* by a photo elastic modulator dual lock-in method ellipsometer (JASCO PME-30p) using He-Ne laser (632.8 nm), having a 0.1 s minimum resolution and interval /3/.

with many applications.

It is impossible to discuss and compare all the ion and plasma techniques currently used for optical film deposition. In this paper all reactive PVD techniques were mentioned but plasma assisted CVD, plasma polymerisation and plasma etching and the non-reactive energetic PVD techniques have been omitted intentionally. Because of their importance it should be mentioned here that some fluorides, particularly AlF_3 , CeF_3 and LaF_3, have also been successfully deposited by ion assisted deposition and low-voltage ion plating. Many rare earth metal fluorides as those of Sm, Gd, Tb, Ho, Er and Y have been successfully processed by IBAD [21]. Deposition of MgF_2 is more critical because of slight impact dissociation. Only few results are available on plated sulphide films. ZnS-films on Ge substrates deposited by dc ion plating [22,23] improved considerably humidity resistance and adhesion compared to films obtained by conventional evaporation, but Clearly further work is required on this topic.

REFERENCES

[1] D. Hoffman, D. Leibowitz, J.Vac.Sci.Technol., 8 (1971) 107
[2] M. Auwärter, Balzers AG, Austrian Pat. No. 192 650 (1952) USA Pat. No. 2.920.002 (1960), FRG Pat. No. 1.104.283 (1968), and in many other countries
[3] D.S. Brinsmaid et al., Kodak, USA Pat. No. 2.784.115 (1957), Application made on May 4, 1953
[4] H.K. Pulker, Coatings on Glass, Chapter 6, p 262, Elsevier, Amsterdam 1984, 1985 and 1987
[5] J. Ebert, Proc. SPIE, Vol. 325 (1982) 29
[6] P.J. Martin, H.A. Macleod, R.P. Netterfield, C.G. Pacey, w.G. Sainty, Appl. Optics, 22 (1983) 178
[7] T.H. Allen, Proc. Internat. Ion Engineering Congress, ISIAT 83 and IPAT 83, Kyoto, Japan, Vol. 2 (1983) 1305,
[8] E.H. Hirsch, I.K. Varga, Thin Solid Films 52 (1978) 445
[9] W.C. Herrmann, J.R. McNeil, Proc. SPIE, Vol. 325 (1982) 101
[10] H.R. Kaufman, J.J. Cuomo, J.M.E. Harper, J.Vac.Sci.Technol., 21 (1982) 725,
[11] K.H. Müller, J.Vac.Sci.Technol., A4 (1986) 461 and Physical Rev. B, Vol. 35, No. 15 (1987-II) 7906
[12] J.L. Vossen, W. Kern, Thin Film Processes, Academic Press, NY, 1978,
[13] J.A. Thornton, V.L. Hedgcoth, J.Vac.Sci.Technol., 13 (1976) 117,
[14] M.I. Ridge, R.P. Howson, I.Ten Have, Proc. SPIE, Vol. 401 (1983) 301
[15] J.L. Vossen, W. Kern (Ed) Academic Press, NY 1978,
[16] S. Scaglione, G. Emiliani, Proc. IPAT 85, Munich, 1985 p. 399,
[17] D.M. Mattox, E'ectro Chem. Techn., Vol. 2 (1964) 295
[18] H.K. Pulker, W. Haag, E. Moll, Balzers AG, Swiss Pat. applied, 00928/85-05 (1.3.1985), USA Pat. No. 4.619.748 (1986), and other countries
[19] H.K. Pulker, W. Haag, M. Buehler, E. Moll, Proc. IPAT 85, Munich, 1985, p. 299,
[20] J. Edlinger, M. Buehler. H.K. Pulker, Proc. Internat. Svmpos. on Trends and New Applications in Thin Films, Strasbourg (F), March 1987, Vol. II, p. 735,
[21] M.J. Messerly, J.D. Targove, Proc. SPIE, Vol. 652 (1986) 222,
[22] E. Henderson, Proc. IPAT 77, Edinburgh, 1977, p. 122, CEP Consultants Ltd., Edinburgh, 1977
[23] I.M. Reid, H.A. Macleod, E. Henderson, M.J. Carter, Proc. IPAT 79, London, 1979, p. 114, CEP Consultants Ltd., Edinburgh, 1979

Reactive PVD coating Technologies

nnology	Gases Vapors Ions	Ion current density (substrate)	Film properties	Known since:
ctive Evaporation	O_2-neutral coating material atoms		Columnar microstructure, close to stoichiometry	Auwärter 1952
vated Reactive Evaporation E)	O_2-Ions and activated states coating material atoms	0.3 µA/cm² < 100 eV	Reduction in opt. losses, improved stoichiometry	Heitmann 1971 Bunshah 1972 Ebert (1982)
Assisted Deposition D)	Ar- and O_2-ions coating material atoms	300 µA/cm² 50–500 eV	Densification by Ion bombardment, good adhesion	McNeil 1982 Macleod 1983
ctive Gasdischarge Sputtering S)	Energetic actvated neutral atoms	Power density on target 2–15 W/cm²	Dense microstructure, good stoichiometry and adhesion	Coleman 1974 Pawlewicz 1978
ctive Ion Beam Sputtering BS)	Energetic atoms and ions	Target: ~ 4 mA/cm² Substr.: 0.5–1 mA/cm² Beam energy: 500–2000 V		Wei 1979
Plating	Coating material- and Ar-ions		Very dense microstructure, improved adhesion	Berghaus 1937 Mattox 1964
ctive Low-Voltage Ion Plating VIP)	Coating material-Ar-, O_2- and N_2-ions	1 mA/cm² 5–25 eV	Very dense microstructure, smooth surface, improved stoichiometry and adhesion	Pulker 1985 Moll

7. DISCUSSION AND CONCLUSION

The possibilities to improve film performance in conventional reactive and even in activated reactive evaporation is rather limited. However, the process is effective, special with recently developed ion processes with higher particle energies as ion assisted deposition, sputtering, ion beam sputtering and reactive low voltage ion plating. Many of the property modifications observed using concurrent ion bombardment during film deposition are a combination of physical and structural changes as well as chemical changes in the film.

Important features of coatings made by these techniques are: dense homogeneous micro structure resulting in relatively high refractive indices, low optical losses, insensitivity to changes in humidity, high hardness and abrasion resistance and stability at high temperatures.

Bombardment of growing films with noble or reactive gas ions in ion assisted deposition and generation of coating material atoms with high energies in ion beam sputtering are powerful tools for basic parameter investigations in ion process developments and optimisation studies. The techniques are very effective for the deposition of low-loss dielectric films on small to medium size substrates.

Up scaling of directed ion beam processes for production purposes is difficult and requires for IBAD and IBS large size ion guns and highly efficient pumping systems. In film production the deposition time is important. Particularly with ion beam sputtering the low deposition rate of 15-20 minutes for a quarter wave thick film (visible range) is extremely time consuming in multilayer depositions. The new low-voltage reactive ion plating technology is an optimised and fast process for high volume production and it seems that RLVIP becomes an extremely useful production technique for high quality optical coatings

semiconductor and integrated device fabrication.

Then sputter etching proceeds to bombard the substrate surface removing both substrate and the resist mask (there is no preferential etching of the substrate compared to the mask as in chemical etching for sputtering is a physical process). Therefore the resist must be thick enough to last long enough till the substrate is etched to the desired depth.

The key advantage of Sputter etching compared to chemical etching is that there is extremely little undercutting and the exact pattern of the resist mask can be maintained in the substrate. This is vital for very high resolution Very Large Scale Integration circuitry with patterns of under 3μ dimensions. Etch rates are also well controlled and there are no chemical residues. Unfortunately the sputter etching process is slow compared to chemical etching and the polymeric photoresist materials are burned by high energy sputter etching.

The answer to occurring problems is the reactive ion etching (RIE) which is a form of the rather new plasma etching. In RIE gas is introduced into the system which produces chemically reactive etching species in the plasma. Combined with the sputter etching process this provides higher etch rates, but still relatively vertical etching walls. Plasma etching and RIE are actively pursued for fine line lithography .

6. REACTIVE ION PLATING

In the ion plating process [17] evaporation is performed in the presence of an argon gas discharge. In collisions and electron impact reactions ions of coating material are formed and accelerated in the electric field of biased substrates, so that condensation and film formation take place under the influence of ion bombardment . The bombardment involves ions of the working gas, of the f film material vapour or of a mixture of both. In addition, neutral atoms of vapour and gas with a higher average energy are important for the deposition process too. This complex action is typical for ion plating. A large number of process variants is possible and different components can be combined to more complex triode and tetrode ion plating systems. It is furthermore remarkable that also high-speed sputtering cathodes are used as vapour sources in special ion plating arrangements. Bias sputtering and some types of plasma CVD also fulfil the definition of ion plating. In conventional ion plating the degree of ionisation is low and the accelerating voltage must be rather high, in general between 3 and 5 keV, to supply the necessary energy for the formation of well adherent and dense films. The small number of ions is also disadvantageous for a reactive gas process. To overcome this problems a new form of reactive ion plating has been developed [18].

The new reactive low voltage ion plating process (RLVIP) [19] can be used for the deposition of single and multilayer dielectric coatings on unheated substrates. Evaporations are made by two special 270°-type electron beam evaporators. The starting materials form electrically conducting melts. Very effective ionisation and activation of the evaporating coating material atoms and the admitted reactive gas molecules occur by a low-voltage high-current argon plasma beam (hot cathode type) directed to the crucibles (anode). The substrate holder is electrically insulated. In contact with the formed plasma cloud the substrates receive a relatively high negative self-biasing potential of 15 - 20 V with respect to the plasma, which acts as accelerating voltage for positive ions. The total pressure in the plant is in the low 10^{-3} mbar range. The film deposition is started and stopped by opening or closing the shutters in front of the electron beam evaporators. Deposition rate is controlled by an oscillating quartz crystal monitor [20], and the film thickness is determined by a quartz crystal monitor or by optical thickness monitoring. The RLVIP-system can be tooled for both reactive ion plating and conventional reactive evaporation allowing alternating processes without requiring any changes in the plant.

LANGEVIN-EQUATION FOR CHARGED PARTICLES IN MICROTURBULENT PLASMA

C.-V. Meister
Max-Planck-Institut für extraterrestrische Physik - Außenstelle Berlin

Microinstabilities seem to be rather important for momentum and energy transport in nearly collision-free plasmas. They play a role in anomalous particle diffusion, heating or acceleration. Driving forces of microinstabilities are usually strong currents and drifts, but also magnetic stresses and plasma anisotropy. Microinstabilities generate turbulent field fluctuations interacting in turn with the plasma particles, so that the free energy causing the instability will be reduced.

A special problem is the relation of microturbulence to magnetic reconnection, the restructuring of magnetic field lines, which can be connected with a transformation of large amounts of magnetic energy into kinetic and thermal energy [1]. Here one question is, whether reconnection may be caused by microturbulence even before the magnetic field is compressed strong enough, so that electrons move chaotically. Although the most favoured for reconnection electrostatic instabilities seem to generate too narrow diffusion regions or are saturated in the actual reconnection region with its high plasma-β, the idea of remote scattering [2] and the observation of magnetic noise bursts in the rather high-β region of the Earth's magnetotail [3] give some hints, that microturbulence seems to contribute to reconnection in some cases.

The motion of the plasma particles (of type a) in a microturbulent system can be described by the Langevin-equation, which is found adding in the equation of motion of the particles the time-dependent force of the waves

$$\frac{d\vec{r}}{dt} = \vec{v}, \quad m_a \frac{d\vec{v}}{dt} = q_a \left(\vec{E}_o(\vec{r}) + [\vec{v} \times \vec{B}_o(\vec{r})] \right) + \vec{F}_a(\vec{x}, t), \quad \{\vec{x}\} = \{\vec{r}, \vec{v}\} \tag{1}$$

($\vec{E}_o(\vec{r})$ - external electric field, $\vec{H}_o(\vec{r}) = \vec{B}_o(\vec{r})/\mu_o$ - external magnetic field). This wave-force

$$\vec{F}_a(\vec{x}, t) = \langle \vec{F}_a(\vec{x}) \rangle + \delta \vec{F}_a(\vec{x}, t) \tag{2}$$

is as usual divided in the ensemble average $\langle \vec{F}_a(\vec{x}) \rangle$ and a stochastic force $\delta \vec{F}_a(\vec{x}, t)$ with vanishing mean value $\langle \delta \vec{F}_a(\vec{x}, t) \rangle = 0$.

Assuming Gaussian stochastic processes with a stochastic-force distribution

$$f_{\delta \vec{F}_a}(\delta \vec{F}_a) = exp \left\{ -(\delta \vec{F}_a)^2 / 2\sigma^2 \right\} / \sqrt{2\pi}\sigma \tag{3}$$

all correlation functions of the stochastic force of odd order are zero, correlation functions of even order can be expressed by functions of order $n = 2$,

$$\langle \delta F_{ai}(\vec{x}, t_1) \delta F_{aj}(\vec{x}, t_2) \rangle = 2\delta_{ij} \delta(t_1 - t_2) D^a_{ij}(\vec{x}). \tag{4}$$

Components of the stochastic force in different directions and at different instants of time are uncorrelated. Usually the mean force $\langle F_{ai} \rangle$ is expressed by a friction term $-\gamma_a(\vec{x})v_i$. But here, according to an idea of [4], a second yet unknown term is added,

$$\langle F_{ai}(\vec{x}) \rangle = -\gamma_a(\vec{x})v_i + \frac{\partial R^a_{ii}(\vec{x})}{\partial v_i}. \tag{5}$$

Instead of solving the Langevin-equation (1) for given initial conditions $\vec{v}_o = \vec{v}(t_o)$, $\vec{r}_o = \vec{r}(t_o)$ and to determine the probabilities of all its solutions it is also possible to find an equation of motion for the one-particle distribution function $f_a(\vec{x}, t)$. Thus, now $\partial R^a_{ii}(\vec{x})/\partial v_i$ will be found regarding consistency between the Langevin-equation (1) and the Fokker-Planck-form of a corresponding kinetic equation.

Suggesting that some inverse effective wave-particle collision frequencies $1/\nu_{eff}$ are much smaller than the dissipation time of the plasma process t_d, $1/\nu_{eff} \ll t_d$, this process can be considered as Markovian during time intervalls $1/\nu_{eff} < \Delta t < t_d \sim 1/\gamma_w$ (γ_w- growth rate of the wave generated by the instability). That means, the distribution function at time t, $f_a(\vec{x}, t)$, can be found knowing the distribution $f_a(\vec{x^*}, t^*)$ and the transition probability $p(\vec{x}, t \mid \vec{x^*}, t^*)$ from the state $\vec{x^*}$ at t^* to $\vec{x}$ at $t = t^* + \Delta t$, $\Delta t \to 0$. Than the Master-equation yields,

$$\frac{\partial}{\partial t} f_a(\vec{x}, t) = \int [w(\vec{x}, t \mid \vec{x^*}, t) f_a(\vec{x^*}, t) - w(\vec{x^*}, t \mid \vec{x}, t) f_a(\vec{x}, t)] d\vec{x^*}. \tag{6}$$

$$w(\vec{x}, t \mid \vec{x^*}, t) = w(\vec{x^*}, t \mid \vec{x}, t) = \lim_{\Delta t \to 0} \frac{1}{\Delta t} p(\vec{x}, t^* + \Delta t \mid \vec{x^*}, t^*) \tag{7}$$

is the transition rate. For Gaussian processes [5] with

$$p(\vec{x}, t \mid \vec{x^*}, t^*) = (2\pi \mathrm{const}_1 \Delta t)^{-1/2} exp\left(-(\vec{x} - \vec{x^*} - \mathrm{const}_2 \Delta t)^2 / 2\mathrm{const}_1 \Delta t\right) \tag{8}$$

only the first two moments of the transition rate

$$\alpha_1^{(i)}(\vec{x}, t) = \int (x_i^* - x_i) w(\vec{x}, t \mid \vec{x^*}, t) d\vec{x^*}, \tag{9}$$

$$\alpha_2^{(i,j)}(\vec{x}, t) = \int (x_i^* - x_i)(x_j^* - x_j) w(\vec{x}, t \mid \vec{x^*}, t) d\vec{x^*}$$

are non-vanishing. Expanding in (6) $f_a(\vec{x}, t)$ at $\vec{x}$ in a Taylor-series (Kramers-Moyal-series) one obtains

$$\frac{\partial}{\partial t} f_a(\vec{x}, t) = -\sum_i \frac{\partial}{\partial x_i} [\alpha_1^{(i)}(\vec{x}, t) f_a(\vec{x}, t)] + \frac{1}{2} \sum_{i,j} \frac{\partial^2}{\partial x_i \partial x_j} [\alpha_2^{(i,j)}(\vec{x}, t) f_a(\vec{x}, t)] \tag{10}$$

$$= -\vec{v} \frac{\partial}{\partial \vec{r}} f_a(\vec{x}, t) - \frac{q_a}{m_a} \left(\vec{E}_o(\vec{r}) + [\vec{v} \times \vec{B}_o(\vec{r})]\right) \frac{\partial}{\partial \vec{v}} f_a(\vec{x}, t) + \frac{1}{m_a} \frac{\partial}{\partial \vec{v}} (\gamma_a(\vec{x}) \vec{v} f_a(\vec{x}, t))$$

$$+\frac{1}{m_a^2}\sum_i \frac{\partial}{\partial v_i} D^a_{ii}(\vec{x}) \frac{\partial}{\partial v_i} f_a(\vec{x},t) + \sum_i \frac{\partial}{\partial v_i} f_a(\vec{x},t) \frac{\partial}{\partial v_i}\left(\frac{D^a_{ii}(\vec{x})}{m_a^2} - \frac{R^a_{ii}(\vec{x})}{m_a}\right).$$

From (10) it is clear that $D^a_{ii}(\vec{x})$ should be equal to $m_a R^a_{ii}(\vec{x})$ to develop from (1) a kinetic equation in usual form. In [4] it was found $m_a R^a_{ii}(\vec{x}) = D^a_{ii}(\vec{x})/2$ obtaining the Fokker-Planck-equation by Stratonovich-method. But there the mean stochastic force was $\langle \partial D^a_{ii}(\vec{x})/\partial v_i \rangle/2$.

If one generalizes the kinetic equation for microturbulent isotropic plasma in polarization approximation [6] to anisotropic plasmas with electromagnetic wave fields $\delta\vec{E}$, $\delta\vec{B}$ (taking into account also the influence of the magnetic field $\delta\vec{B}$ of the waves on the density fluctuations) and compares the result with (10), the friction coefficient

$$\gamma_a v_\beta = \frac{q_a^2}{2\pi^2}\int \omega^3 \delta(\omega - \vec{k}\vec{v})\Big(\frac{v_\alpha Im\varepsilon_{\alpha\beta}}{\mid \omega^2\varepsilon_{\alpha\beta} - c^2k^2\delta_{\alpha\beta} + c^2k_\alpha k_\beta \mid^2}(1 - \frac{k_r v_r + k_s v_s}{\omega}) \quad (11)$$

$$+\frac{v_s^2 k_\beta Im\varepsilon_{\alpha s}}{\omega \mid \omega^2\varepsilon_{\alpha s} - c^2k^2\delta_{\alpha s} + c^2k_\alpha k_s \mid^2} + \frac{v_r^2 k_\beta Im\varepsilon_{\alpha r}}{\omega \mid \omega^2\varepsilon_{\alpha r} - c^2k^2\delta_{\alpha r} + c^2k_\alpha k_r \mid^2}\Big) d\omega d\vec{k}$$

can be expressed by the tensor of the dielectric function $\varepsilon_{\alpha\beta}(\omega,\vec{k})$, and the velocity-diffusion tensor ($r \neq s, \alpha \neq r \neq \beta, \{\alpha;\beta\} = \{x;y;z\}$)

$$D^a_{\alpha\beta} = \frac{q_a^2}{16\pi^3}\int \delta(\omega - \vec{k}\vec{v})\left(\delta F^*_\alpha \delta F^*_\beta\right)_{\omega\vec{k}} d\omega d\vec{k} = \begin{pmatrix} D^a_{xx} & D^a_{xy} & D^a_{xz} \\ D^a_{xy} & D^a_{yy} & D^a_{yz} \\ D^a_{xz} & D^a_{yz} & D^a_{zz} \end{pmatrix} \quad (12)$$

$$\delta F^*_\alpha = \delta E_\alpha\left(1 - \frac{k_r v_r + k_s v_s}{\omega}\right) + \delta E_s \frac{v_s k_\alpha}{\omega} + \delta E_r \frac{v_r k_\alpha}{\omega}$$

by the space-time spectral density of the energy of the waves ($\{\gamma;\delta\} = \{x;y;z\}$)

$$\left(\delta E_\alpha \delta E_\beta\right)_{\omega\vec{k}} = \frac{16\pi^2\omega^2 \sum_a q_a^2 n_a^o 2\pi \int v_\gamma v_\delta \delta(\omega - \vec{k}\vec{v}) f_a(\vec{x},t)}{(\omega^2\varepsilon_{\gamma\alpha} - c^2k^2\delta_{\gamma\alpha} + c^2k_\gamma k_\alpha)(\omega^2\varepsilon^*_{\delta\beta} - c^2k^2\delta_{\delta\beta} + c^2k_\delta k_\beta)} d\vec{p}. \quad (13)$$

As a consequence of the fact that stochastic forces in different directions are uncorrelated (eq.(4)) in (10) only diagonal components of the diffusion tensor appear. But according to (12-13) the velocity-diffusion tensor in polarization approximation $D^a_{\alpha\beta}$ is also a symmetric tensor in the case of inhomogeneous plasma. Thus it is always possible to find a corresponding diagonal tensor

$$D^a_{diagonal} = \begin{pmatrix} b_{11} & b_{12} & b_{13} \\ b_{21} & b_{22} & b_{23} \\ b_{31} & b_{32} & b_{33} \end{pmatrix} D^a \begin{pmatrix} b_{11} & b_{21} & b_{31} \\ b_{12} & b_{22} & b_{32} \\ b_{13} & b_{23} & b_{33} \end{pmatrix}, \quad (14)$$

$$\vec{b}_1 = \vec{x}_1/\mid \vec{x}_1 \mid, \quad \vec{b}_2 = (\vec{x}_2 - (\vec{x}_2\vec{b}_1)\vec{b}_1)/\mid \vec{x}_2 - (\vec{x}_2\vec{b}_1)\vec{b}_1 \mid,$$

$$\vec{b}_3 = (\vec{x}_3 - (\vec{x}_3\vec{b}_1)\vec{b}_1 - (\vec{x}_3\vec{b}_2)\vec{b}_2)/\mid \vec{x}_3 - (\vec{x}_3\vec{b}_1)\vec{b}_1 - (\vec{x}_3\vec{b}_2)\vec{b}_2 \mid .$$

$\vec{x}_l\{l = 1; 2; 3\}$ is the eigenvector of the matrix of the diffusion tensor D^a_{ij} belonging to the zero d_l of the characteristic polynomial of D^a_{ij}. The coordinates of $\vec{x}_l\{x_{l1}, x_{l2}, x_{l3}\}$ are the non-trivial solutions of the homogeneous, linear system of equations

$$\begin{aligned}(D^a_{xx} - d_l)x_{l1} + D^a_{xy}x_{l2} + D^a_{xz}x_{l3} = 0,\\ D^a_{xy}x_{l1} + (D^a_{yy} - d_l)x_{l2} + D^a_{yz}x_{l3} = 0,\\ D^a_{xz}x_{l1} + D^a_{yz}x_{l2} + (D^a_{zz} - d_l)x_{l3} = 0,\end{aligned} \tag{15}$$

$$d_1 = u + v - \frac{r}{3},\ d_2 = \varepsilon_1 u + \varepsilon_2 v - \frac{r}{3},\ d_3 = \varepsilon_2 u + \varepsilon_1 v - \frac{r}{3}, \tag{16}$$

$$\varepsilon_{1,2} = -\frac{1}{2} \pm i\frac{\sqrt{3}}{2},\ u = \left(-\frac{q}{2} + \sqrt{H}\right)^{1/3},\ v = \left(-\frac{q}{2} - \sqrt{H}\right)^{1/3},$$

$$H = \frac{p^3}{27} + \frac{q^2}{4},\ p = s - \frac{r^2}{3},\ q = \frac{2r^3}{27} - \frac{rs}{3} + w,$$

$$r = -D^a_{xx} - D^a_{yy} - D^a_{zz},\ s = D^a_{xx}D^a_{yy} + D^a_{xx}D^a_{zz} + D^a_{yy}D^a_{zz} - D^{a2}_{xy} - D^{a2}_{xz} - D^{a2}_{yz},$$

$$w = D^a_{xx}D^{a2}_{yz} + D^a_{yy}D^{a2}_{xz} + D^a_{zz}D^{a2}_{xy} - D^a_{xx}D^a_{yy}D^a_{zz} - 2D^a_{xy}D^a_{xz}D^a_{yz}.$$

In the simple case of the ion-sound instability $D^a_{xx} = D^a_{xy} = D^a_{yy}$, $D^a_{xz} = D^a_{yz}$, so that

$$D^a_{diagonal} = \begin{pmatrix} 2D^a_{xx} + Y & 0 \\ 0 & D^a_{zz} - Y \end{pmatrix}, \tag{17}$$

$$Y = 2D^{a2}_{xz}(2g - 2D^a_{xx} - D^a_{zz})/((g - D^a_{zz})^2 + 2D^{a2}_{xz}),$$

$$g = D^a_{xx} + \frac{D^a_{zz}}{2} + \sqrt{D^{a2}_{xx} + D^{a2}_{zz}/4 - D^a_{xx}D^a_{zz} + 2D^{a2}_{xz}}.$$

Now the Gaussian-distributed stochastic force $\delta F_{ai}(\vec{x}, t)$ can be estimated by its intensity $\sigma = (2D^a_{diagonal,ii})^{1/2}$.

[1] V.M. Vasyliunas, Relation between global and local aspects of reconnection, Proc. Potsdam Int. Workshop on Reconnection in Space Plasma, ESA SP-285, Vol.II, 11-14 (1988)
[2] K. Schindler, Magnetic reconnection, Proc. Tbilisi 10th European School on Plasma Physics, Ed. N.L. Tsintsadze, World Scientific, Singapore, 136-156 (1991)
[3] D.A.Gurnett, L.A.Frank, R.P.Lepping, Plasma waves in the distant magnetotail, J. Geophys. Res. **81**, 6059-6071 (1976)
[4] Yu.L. Klimontovich, Turbulent Motion and Structure of Chaos. A New Approach to the Statistical Theory of Open Systems, Nauka, Moscow 1990
[5] G. Röpke, Statistische Mechanik für das Nichtgleichgewicht, Deutscher Verlag der Wissenschaften, Berlin 1987
[6] Yu.L. Klimontovich, Statistical Physics, Nauka, Moscow 1982

AUTHOR INDEX

Aceto S. I-525,I-529
Adams J.M. I-67,I-251
Afanasyev V.I. I-151,II-1031
Agarici G. II-885
Agren O. II-1369
Airoldi A. II-973
Akiyama H. I-403
Akiyama R. I-517
Al-Karkhy A. I-639
Al-Mashhadany E.M. I-691
Alava M.J. III-1923
Alejaldre C. I-565
Aleksandrov V.O. I-111
Alexandroaei D. III-1957
Alexandrov V.O. II-997
Ali-Arshad S. I-227,I-335,I-339
Alladio F. I-23,I-545,II-1525
Allen J.E. III-1973,III-1977,III-2033
Alper B. I-331,I-335,I-339,II-1051
Alport M.J. III-1895
Amatucci W.E. III-1895
Anabitarte E. II-1183
Anderson D. I-391
Anderson D.V. I-557
Annaratone B.M. III-1977
Antani S.N. II-1009
Antoni V. I-631
Antsiferov P. I-683
Aoyama K. III-1765
Apostol I. III-2049
Appala N.P. III-1943
Appel L.C. I-31
Apruzzese G. I-463
Aragon F. I-299
Arakawa M. II-1337
Aramaki E.A. I-675
Araujo M.S.T. I-419
Arhipenko V.I. II-1203
Arimoto H. I-513,I-517
Asakura N. II-949
Ascasibar E. I-565,II-933
Ashida H. II-1405
Ashkenazy J. III-2117
Assis A.S. II-1549
Assis A.S. I-679,III-1619,III-1667,III-1785
Atanasiu C.V. I-367
Aumayr F. II-1163
Austin M.E. I-115
Avakian M. I-479
Axnäs I. II-1175,III-1875
Azevedo C.A. I-679,III-1619
Azizov E.A. I-47
Baang S. II-1071
Baba T. I-489
Baboolal S. III-1819
Bachin I.V. II-1345
Bachmann P. II-747
Badalec J. I-219
Baelmans T. II-747
Bagatin M. I-631
Bagdasarov A. I-371
Bagryansky P.A. II-1123
Bahrim B. III-2049
Bahrim C. III-2049
Baity F.W. II-893
Baker K.B. III-1591
Bakos J.S. I-303
Balbin R. II-783,II-791
Baldzuhn J. II-1119
Balet B. I-3,I-19,I-59,I-63,I-263,II-881
Barabaschi P. I-167
Baranowski J. II-1211
Barnsley R. I-291
Barrett P.J. III-1803
Bartiromo R. II-957,II-961,II-1127
Bartlett D.V. I-119,I-147,I-163,
I-255,I-407,II-973
Basiuk V. I-175
Basu B. II-1373,II-1509
Batani D. II-1207,III-2017
Batchelor D.B. II-913
Batistoni P. I-545
Baumgärtel K. III-1571
Baylor L.R. I-255,I-521,I-525
Bazdenkov S.V. II-1453
Beaumont B. II-885
Becker G. II-1457
Becoulet A. I-175,II-885,II-905
Behrisch R. II-843
Beidler C.D. I-533,I-569,I-581
Belik V.P. II-1039
Bell J.D. I-525,I-529
Bell M.G. I-39
Bell R. I-39,II-949
Belli M. II-1207
Belmont G. II-1297
Belyakov V.A. I-471
Bender S.E. I-471
Bengtson R.D. I-91
Benova E. II-1517,III-2041
Berbece D. II-1561
Berge G. II-1401
Berger By G. II-885
Bergsåker H. I-607
Berk H. II-1469
Bernabei S. II-949,II-957
Berni L.A. I-675
Bertolini E. I-167
Berton F. I-23
Bertrand P. II-807,II-1005,III-1737,III-1741
Besedin N.T. I-569
Besshou S. I-489,II-1131
Bharuthram R. II-1445
Bhatnagar V.P. I-327,II-897,II-901
Bibet P. I-159,II-885
Biborosch L. III-2029
Bickley A. I-379
Bigelow T.S. I-521,I-525
Bilbao L. II-1253
Bingham R. II-1271,III-1627
Birdsall C.K. III-1993
Bizarro J.P. I-27,II-885
Blazquez J.F.M. II-1237
Blumenfeld L. III-2055
Boedo J. I-155
Boerner E.D. II-1275
Bohm M. III-1875
Boileau A. I-215
Bollanti S. II-1207
Bond D.S. I-251
Bondarenko E.A. II-1261
Bondeson A. I-343,I-399
Bonhomme G. III-1737,III-1879
Bonitz M. III-2091
Bonoli P.T. II-965
Boozer A.H. II-863,III-1713
Bora D. III-1575,III-1583,III-2021
Borba D. I-439

Borisov N.D. III-1587
Bornath Th. III-2091
Bornatici M. II-1493
Borrass K. II-735
Bortolotti A. I-695,II-1253
Bosch H.-S. II-747
Bosia G. II-897
Bosia P. II-901
Boucher C. I-215
Boucher D. I-59
Boucher I. III-1883
Bowles J. III-1935
Braams B. II-747
Bracco G. I-23,I-127,I-295
Braithwaite N.St.J. III-1973
Brambilla M. II-925
Branas B. I-99,II-1075
Brasilio Z.A. II-803
Bravanec R.V. I-115
Bravo E. III-1607
Bretz N. I-203
Breun R. II-839
Brouchous D. II-839
Brower D.L. I-115,I-363
Browning P.K. I-639
Brusati M. I-3,I-119,I-307,II-897,II-973,II-977
Bruschi A. I-23
Bryant D.A. III-1627
Brzosko J.S. I-695
Brzozowski B.P. I-595
Brzozowski J. I-291,I-611
Büchl K. I-459,II-743
Büchse R. I-375,I-379
Bud'ko A. I-635,I-671,II-1261
Budnikov V.N. II-997,II-1203
Budny R.V. I-39,I-43,I-203
Buffa A. I-619
Bulanin V.V. I-111
Bulanov S.V. I-541,II-1305,II-1317,II-1429
Buneman O. III-1579
Buratti P. I-23,I-127,I-463
Bures M. I-3,I-19,I-255,I-307,II-881,II-897
Bürger G. I-303
Burgos C. I-299,II-1135
Burrell K.H. I-11,I-179,I-183,I-243,I-275
Bush C.E. I-203
Bustamante E.G. II-1183
Buzhinskij O.I. I-47
Cabral J.A.C. II-1111
Cabral-Prieto A. III-1947
Cabrit B. II-1083,III-1591
Caldas I.L. I-419,II-803
Calderon M.A.G. II-1183
Callen J.D. II-1413
Calvin M. I-211
Campbell D.J. I-227,I-239,I-375,
II-735,II-881,II-897
Caner M. III-2117
Capes H. I-107
Capitain J.J. II-885
Carlson A. II-783,II-787
Carlstrom T.N. I-235
Carolan P.G. I-411
Carrasco J. I-175,II-885
Carreras B.A. I-521,I-525,I-565,I-569,II-1417
Carroll III J.J. III-1895
Carter M.D. II-913
Castejon F. II-933,II-1135
Castiglioni S. II-1087
Castro R.M. II-803
Catto P.J. I-91
Cercek M. II-1171,III-1761
Cereceda C. II-1513
Cermak I. III-1989
Cha S.S. I-451
Chakraborty B. II-1257
Challis C.D. I-15,I-311,I-335,I-379
Chance M.S. I-435,II-949
Chang C.S. I-315
Chang T. II-1509
Chankin A.V. II-779
Chao J.K. III-1615
Chatelier M. I-159
Chavez-Alarcon E. I-483,III-1947
Chekroud D. III-1729
Chen F.F. III-1701,III-1789
Chen H.H. III-2059
Chen J.Y. I-363
Chen X.P. I-107
Cherkhani R. III-1737
Chernobaj A.P. I-47
Cherubini A. II-901
Chevlaier G. III-1701
Chittenden J.P. I-655
Chiu C.Y. III-1615
Chiu S.C. II-893
Chiueh T.H. III-1615
Cho S. III-2133
Chodura R. II-871
Choi E.H. III-2133
Chou A.E. II-1071
Chou C.K. III-2059
Christensen M. I-279
Christiansen J.P. I-15
Chu M.S. I-243,I-435
Chu R. III-1811
Chu T.K. II-949
Chudin N.V. I-367
Cicconi G. II-1187,III-2037
Ciubotariu-Jassy C.I. III-1681
Claaßen H.A. II-771
Clement S. I-307,II-723,II-727,II-735,II-823
Clupek M. I-713
Coffey I.H. I-291
Cohen D. II-1017
Cohen R.H. II-1275
Colborn J.A. II-965
Colchin R.J. I-525
Colton A. I-227
Colunga-Sanchez S. I-483,III-1947
Compant La Fontaine A. III-2113,III-2125
Conceicao P. II-977
Condé H. II-1047
Condrea I. I-295,II-1127
Connor J.W. II-1393
Connor K.A. I-529
Conrads H. II-775
Conroy S. I-67,I-167,I-251
Cook D. II-937
Cooper W.A. I-557,I-589
Coppi B. I-139
Coppins M. I-663
Cordey J.G. I-15,I-191-59,I-63,I-263
Core W.G.F. II-1035
Correa-Restrepo D. II-1329,III-1753
Correia C. II-1063
Corti S. I-151,II-1031
Costa S. I-619
Costley A.E. I-163,I-199,I-407
Cottrell G.A. I-327,II-881,II-897
Coulon J.P. I-107
Couture P. I-215
Cowley S.C. II-1393
Cox M. II-897,II-1341
Cripwell P. I-199,I-227,I-407,I-439
Crisanti F. I-463
Cross R.C. II-815
Cruz-Jimenez S. III-1947
Cunningham G. I-639
Cuperman S. III-2117

Cupido L. II-1063
D'haeseleer W.D. I-533,II-755
da Costa O. I-327
da Cruz Jr. D.F. I-267
da Silva R.P. II-803,II-973
Darrow D.S. I-203,I-431
Das A.C. II-1257,III-1611
Dawson J.M. II-1271,III-1627
De Angelis R. I-279,I-295
de Blank H.J. I-247,I-339
de Esch B. I-167
de Esch H.P.L. I-339
de Gentile B. I-27
De Haas J.C.M. I-83,I-87
De Kock L. I-227,II-723
De la Luna E. II-1075
De Luca F. I-23,I-75
De Nicola S. II-1313
De Villiers J.A.M. I-387,I-415,II-795
DeBlank H.J. I-335
DeBoo J.C. I-11
DeChiara P. I-695
Decker D.T. II-1509
Decoste R. I-215
Decyk V.K. III-1839
DeEsch H. II-897
DeGrassie J.S. II-893
Deksnis E. I-167
DeMichelis C. II-847
Dempers C.A. III-1773
Dendy R.O. I-327
Deng C.B. I-347
Deng H.C. I-223
Deng Z.C. I-223
Deutsch C. II-1245
Deutsch H. III-2095
Devynck P. I-107,II-1079
Di Lazzaro P. II-1207
Diamond P.H. II-1417
Dias J.M. II-1111
Diaz-Pinto A. III-1607
Diebold D. II-839
Dietz J. I-167
Dimits A.M. II-1275
Ding W.X. III-1765
DiPeso G. III-1993
Dippel K.H. I-403
Dmitriev V.I. I-47
Dodel G. I-191
Domier C.W. II-1071
Domier D.W. III-1939
Dominguez N. I-525,I-561,I-565,I-569
Donaldson N. I-647
Dong J.F. I-223,I-395
Donné A.J.H. II-1091,II-1143
Donoso G. III-1795
Dory R.A. I-521
Doyle E.J. I-179,I-243
Drachev V.P. II-1123
Drake J.F. I-351
Drake J.R. I-595,I-599
Drawin H.W. I-159
Dubois M.A. I-103,II-1409
Duck R. I-31,I-399
Dudnikova G.I. III-1639
Dumitrascu N. II-1561
Duncan P.J. III-1729
Dunlap J.L. I-525,II-949
Duong H. I-435
Durst R. I-203
Dwivedi C.B. III-1611
Dyabilin K.S. I-493
Dyachenko V.V. II-997
Dyakov V.E. II-933,II-941
Dyer G.R. I-521,I-525
Eberhagen A. II-1107
Edery D. II-855,II-1421
Edlinger J. III-2149
Edwards A.W. I-255,I-327,I-331,I-339,I-355, I-375,I-379,II-897,II-1051
Ehrenberg J. I-307
Ekiel-Jezewska M. III-1951
Elevant T. II-881
Elfimov A.G. I-319
Elliott J.A. III-1725
Emmoth B. I-607
Endler M. II-783,II-787
Engelhardt W. II-743
England A.C. I-521,I-525,II-949
Erba M. I-623
Erckmann V. I-497
Erdweg M. II-827
Erents S.K. II-723
Eriksson L.-G. I-343,II-881,II-897, II-1469,II-1485
Esipov L.A. II-997
Estrada T. I-99,II-1075
Euringer H. II-775
Fahrbach H.U. II-961
Fajans J. III-1811,III-1899
Fang S. I-615
Farynski A. I-717
Fasoli A. III-1863
Fedele R. II-1293
Fedorov O.V. I-471
Feix G. III-1643
Feix M. III-1741
Feneberg W. II-1477,II-1481
Fernandes C. II-1063
Ferron J.R. I-55
Fiedler S. II-1163
Fiedorowicz H. I-717
Fielding S.J. I-31
Fijalkow E. III-1741
Finken K.H. I-155,I-403
Finkenthal D. I-275
Fischer B. II-1095
Fishman H. II-949
Fitzpatrick R. I-411,I-423
Flå T. II-937,II-1309,III-1951
Fletcher J.D. I-387,I-415,II-795
Flora F. II-1207
Foltin M. III-2067,III-2075
Fonck R. I-203,II-839
Fontanesi M. III-2017
Foote J.H. II-1191
Foster C.A. I-159
Fowler T.K. I-711
Franz D. I-683
Fredrickson E.D. I-39,I-203,I-351,I-431
Freidberg J.P. II-1401
Freysinger W. III-2079,III-2083,III-2087
Friaca A.C.S. III-1647
Friedland L. II-1017
Frieling J. II-1035
Frigione D. I-463
Froissard P. I-119,II-973,II-977
Fröjdh M. II-1441
Fu B.Z. I-395
Fuchs C. I-403,II-835
Fujiwara M. I-513
Fukuda T. I-87,I-199
Fussmann G. II-831,II-835
Gabris R. III-2129
Gadeberg M. I-255
Galassi A. III-2017
Galkowski A. II-1537
Gandy R. I-115
Gangadhara R.T. III-1671
Ganguli A. III-1943

Garbet X. I-107,II-1079,II-1433
Garcia D. III-1607
Garcia L. I-565,II-1417
Garcia-Cortes I. II-791
Gasparino U. I-493,I-497,I-505,I-581,II-1001
Gavrilescu C. III-1969
Gaytan-Gallardo E. I-483,III-1947
Gee S.J. I-639
Gentle K.W. I-115
Georgieva M. II-1353
Géraud A. I-159
Gernhardt J. I-455,I-459
Gervais F. I-107,II-1079
Gettelfinger G. II-949
Ghanashev I. II-1517
Ghanem E.-S. I-131
Ghendrih Ph. II-851
Ghizzo A. II-807,II-1005,III-1737,III-1741
Ghorannevisse M. I-479
Giammanco F. II-1241
Giannella R. I-279,I-283,I-287
Giannone L. I-497,II-783,II-787
Gibson K.J. I-31
Gil C. I-107
Gill R.D. I-331,I-355,I-375,II-1051
Gimblett C. I-335
Giruzzi G. II-905,II-1103
Gladuschak V.I. II-1219
Glagolev V.M. I-703
Glosik J. III-1989,III-2083
Glowienka J.C. I-529
Goedbloed J.P. I-247
Gohil P. I-183,I-243,I-275
Golant V.E. I-471
Goldfinger R.C. II-913
Golubyatnikov G.Yu. III-1831
Gondhalekar A. I-151,I-239,II-1031
Gonella C. III-2055
Gong D.F. I-395
Gonhhalekar A. I-147
Goniche M. II-885
Goree J. II-1365
Gorini G. I-75,II-1047
Gormezano C. I-15,I-119,II-897,II-973
Goruppa A.A. III-1977
Gottardi N. I-255,I-279,II-723,II-727
Goulding R.H. II-893
Gowers C. I-15
Graffmann E. II-771
Green B. I-167
Greene J.M. I-435
Greenfield C.M. I-11
Greenough N. II-949
Greenwald R.A. III-1591
Gregory B. I-215
Grek B. I-39
Grekov D.L. I-569
Grésillon D. II-1079,II-1083,III-1591
Gribok V.A. II-929
Grigull P. II-1167
Grill V. III-2075,III-2095
Grisham L. I-43
Groebner R.J. I-179,I-183,I-187,I-275
Grosman A. II-847,II-851
Grozev D. III-2041
Gruber O. I-451,I-455,I-459,II-743
Gruber R. I-557,I-589
Gryaznevich M. I-399
Gudowska I. I-607
Günther K. II-875
Guo D.Q. I-347
Guo G.C. I-223,I-395
Guo S.C. II-1437
Gusakov E.Z. II-1203
Gusev V.K. II-1219
Gyergyek T. II-1171,III-1761
Hadjoudj Y. III-1915
Hahnheuser R. I-647
Haines M.G. I-655
Hakr J. I-667
Hall D.S. III-1627
Hamilton R.L. II-1349
Han J. I-335
Hanada K. I-79
Hanatani K. I-489,II-1131
Hansel A. III-2079
Hansen B.M.S. II-1397
Hanson G.R. I-525
Hanssen A. II-1279
Hanuise C. III-1591
Harbour P.J. II-723
Harmeyer E. I-581
Harris G. I-107
Harris J.H. I-525,II-949
Hartfuß H.J. I-497,II-1001,II-1099
Harvey R.W. II-893
Hasegawa A. I-711
Hastie R.J. II-1393
Hatakeyama R. III-1705,III-1709, III-1765,III-1919
Hatcher R. II-949
Hazeltine R. I-211
Hegna C.C. II-1413
Heidbrink W.W. I-435
Heijnen S.H. II-1059
Heikkinen J.A. II-1021,III-1923
Hellberg M.A. I-387,II-1397,II-1477,III-1819
Hellblom G. I-595
Heller M.V.A.P. II-803
Hender T.C. I-335,I-339,I-399,I-411,I-423
Hennequin P. I-107,II-1079,II-1409
Hensler E. II-1389
Herrmann H. II-949
Hershkowitz N. II-839,II-909
Hess W. II-847
Hesthaven J.S. III-1903
Heuraux S. III-1915
Hidalgo C. II-783,II-791
Higashijma S. II-1131
Hill D.N. I-243,II-751
Hill K.W. I-39
Hillis D.L. I-275
Hirano Y. II-917
Hirayama S. I-699
Hirshman S.P. I-589
Hoang G.T. I-27,I-103,II-885,II-945
Hoenen F. I-155
Hoffman D.J. II-893
Hofmann F. I-343,I-467
Hofmann J.V. II-1155
Hogan J.T. I-275
Hogeweij G.M.D. I-71,I-75
Holzhauer E. I-191
Honda C. II-1159
Honda R.Y. I-675
Hong J.S. III-2033
Honzawa T. II-1337,III-1603,III-1911
Hörhager M. III-1685
Hori M. III-1965
Hörling P. I-611
Horton L.D. I-307,II-1035
Hoshino K. II-1191
Hosokawa M. I-513,I-517
Howarth P.J.A. I-251
Huang K.Q. I-223
Huang R. I-347
Huart M. I-167
Hübner G. II-1541
Hübner K. II-1485
Hugenholtz C.A.J. II-1059

Hugill J. I-31
Hugon M. I-3,I-119
Huguet M. I-167
Humbert P. II-1249
Hutchinson D.P. I-521
Hutter T. I-27,I-107
Huysmans G.T.A. I-247
Hyatt A.W. I-187
Ianopol B. III-1957
Ida K. I-513,I-517
Ide S. II-953,II-969,II-985
Idei H. I-513,I-517
Ignacz P.N. I-303
Ignat D. II-949
Iguchi H. I-513,I-517
Iima M. I-489
Ijiri Y. I-489
Ikeda Y. II-953,II-969,II-985
Ikegawa M. III-2109
Ikehata T. III-1891,III-1985
Imai T. II-953,II-969,II-985
Ingesson L.C. II-1143
Inoue M. III-1651
Inovenkov I.N. II-1305,II-1317
Intrator T. II-839
Irie M. I-643
Irzak M.A. II-1025
Ishii H. II-917
Ishii S. III-1961
Isler R.C. I-521,I-525,I-529,II-949
Its E.R. II-997
Iwama N. III-1961
Jacchia A. I-23,I-75
Jäckel H.J. II-723,II-823
Jackson G.L. I-11
Jacquinot J. I-167,I-311,I-327,I-335,
II-881,II-897,II-901
Jadoul M. I-359
Jaeger E.F. II-913
Jaenicke R. I-549
Jafelice L.C. III-1647
Jäger H. II-1151
Jakovenko V.P. I-47
Jakubka K. I-219
Jakubowski L. II-1215
James R.A. II-893
Janeschitz G. II-723,II-727
Janicki C. I-215
Jardin S. II-949
Jarmen A. II-1441
Jarvis N. II-881
Jarvis O.N. I-67,I-167,I-251
Jaspers R. I-155
Jasperse J.R. II-1373,II-1509
Jassby D.L. I-39,I-43
Jelic N. II-1171,III-1761
Jenichen F. II-835
Jensen V.O. II-1545
Jernigan T.C. I-521,I-525
Ji H. I-521
Jiang Y. I-363
Jiang Y.X. I-223
Jiang Z.X. I-603
Jimenez J.A. I-561
Jimenez-Dominguez H. I-483,III-1947
Jobes F. I-39
Joffrin E. II-855,II-945,II-1421
Johnson D.W. I-39
Johnson J.L. I-577
Johnson L.C. I-39
Jones I.R. I-647
Jones S.E. I-163,I-407,II-949
Jones T. I-255,II-881
Jones T.C.C. I-19
Jones T.T.C. I-3,I-263,I-307
Jong R.A. II-751
Jülich A. I-455
Junker J. I-509
Junker W. II-743
Kahlbaum T. III-2009
Kaita R. II-949
Kajiwara T. II-1159
Kakehi Y. III-2109
Kakoulidis E. II-767
Kallenbach A. I-231,I-459,II-835
Källne E. I-611
Källne J. II-1047
Kalvin S. I-303
Kamp L.P.J. III-1745
Kanaev A.I. I-47
Kaneko O. I-517
Kantor M.Yu. II-1219
Kaplan Z. III-2117
Kardaun O.J.W.F. I-7,I-35
Kardon B. I-303
Karlson E.T. I-635,I-671
Karlsson P. I-595
Karpman V.I. II-1283
Karttunen S.J. II-1005
Katsonis K. II-1245,III-2063
Katsouleas T. II-1301
Kaufmann A.N. II-937,III-1951
Kaufmann M. II-743,II-747
Kauschke U. III-1981
KavinA.A. I-471
Kaw P.K. II-1301
Kawabe T. I-699,III-2155
Kawachi T. II-981
Kawaguchi N. III-1651
Kawai Y. III-1733,III-1807,III-1855,III-1887
Kawashima H. II-893
Kaye S. II-949
Kennel C.F. II-1349
Kerner W. I-247,I-335,I-439
Kesner J. I-407,II-949
Khan M. II-1257
Kholin N.N. III-2137
Khristova D. II-1353
Khudoleev A.V. I-151,I-167,II-1031
Kick M. I-505,I-509
Kilic H. I-695,II-1253
Kim J. I-183
Kim S.K. III-2133
Kinsey J. I-131
Kirsanov V.I. II-1305,II-1317
Kishino T. I-79
Kisigami Y. I-79
Kislov D.A. I-207,I-371
Kiss`ovski Zh. III-2013
Kißlinger J. I-501,I-549,I-585,I-569,I-581
Kitajima M. III-2155
Kiyama H. II-799
Kiyama S. II-799,III-1781
Klepper C.C. I-275
Kletecka P. I-219
Kleva R.G. I-351
Klinger T. III-1677,III-1843
Knorr G. II-807,III-1721
Kobayashi J. III-2109
Kobayashi S. I-489
Kocsis G. I-303
Koepke M.E. III-1895
Kogoshi S. I-403
Kohmoto T. I-517
Kolesnichenko Y.I. I-391
Komori A. III-1733,III-1807,III-1851,
III-1855,III-1887
Kondo K. I-489,II-1131
Kondoh T. II-953,II-969,II-985
Kondoh Y. II-917

König R. I-167,I-263,I-339,I-379, II-881,II-1035
Konings J.A. I-71
Kono M. III-1851,III-1855,III-1887
Köppendörfer W. I-451
Korchinsky G.M. II-1377
Korn J. III-1717
Korneev D.O. I-111
Korolev A. III-1599
Korotkov A.A. II-1031,II-1039,II-1043
Kortshagen U. III-2145
Koslovski H.R. I-383,I-403
Kostsov Y.A. I-471
Kovan I.A. I-47
Kovrizhnykh L.M. I-525
Koyama K. II-1225
Kozochkin S.M. II-1229
Krafft C. II-1297
Kramer G.J. I-15,I-227,I-259,I-335,I-339
Krämer M. II-1095
Krämer-Flecken A. I-95,I-383
Krasilnikov A.V. I-47
Krasnikov Yu.I. II-1123
Krause A. I-451
Kravarik J. I-667
Kremp D. III-2091
Krieger K. II-831
Krishan V. III-1671
Krlin L. II-1013
Kroegler H. I-463
Krumm P. III-1773
Kryska L. I-219
Kuang G. I-359
Kubarev Y.V. III-2137
Kubes P. I-667
Kubo H. III-1631
Kubo S. I-513,I-517
Kugel H. II-949
Kuhn S. II-1549,III-1685,III-1777, III-1785,III-2001
Kühner G. I-501,I-581
Kukharkin N.N. II-1453
Kulhanek P. I-667
Kupfer K. II-885,II-905
Kupschus P. I-255
Kurasawa T. II-1405
Kurdel M. III-2095
Kuroki H. III-2155
Kus A. I-7,I-35
Kusaka S. III-1931
Kusano K. III-1631
Kuus H. II-885
Kuvshinov B.N. I-703
Kuyanov A.Yu. II-1521
Kwak J.K. III-2133
Kyriakakis G. II-767
La Haye R.J. I-179,I-187
Lachambre J.-L. I-215
Lackner K. I-455,I-459
Lafrance D. I-215
Laing E.W. II-1505
Lakhina G.S. III-1623
Lalousis P. II-1525
Lao L.L. I-11,I-55,I-243,I-435
Larenz R.W. II-1381
Larsson J. III-1749
Lashkul S.I. II-997
Last J. I-167
Laurent L. I-27,II-1433
Lauro-Taroni L. I-279,I-283,I-287
Laviron C. I-107,II-1079
Lawande S.V. II-1257
Lawson K.D. I-3,I-19,I-291,I-307
Lazaros A. I-549
Lazzaro E. I-443
Le Clair G. I-215
Le Gourrierec P. III-2125
LeBlanc B. II-949
Leboeuf J.N. I-525
Leclert G. III-1883,III-1915
Lecoustey P. II-855,II-945,II-1421
Lee D.K. I-525
Lehnert B. II-1529
Lengyel L.L. I-323
Lesourd M. II-727,II-823
Letardi T. II-1207
Leubner C. III-1667
Leuterer F. II-957,II-961
Levinton F. II-949
Levitsky A.N. I-471
Leys C. II-1147
Lezius M. III-2071,III-2075
Li G.X. I-347
Li H.Z. I-223
Li J. I-31,I-615
Li K.H. I-223
Li L.H I-347
Li Q. I-615
Li W.L. I-115
Liang W.X. I-395
Liberman M.A. I-635,I-671,II-1261,III-1599
Lieder G. I-459
Likin K.M. I-525
Lim C.S. II-1501
Lin H. I-363
Lindinger W. III-2079,III-2083,III-2087
Lingertat J. II-727,II-823
Linhart J.G. II-1253,II-1265
Liniers M. II-791
Lisak M. I-391
Litaudon X. I-27,II-885
Liu W.D. II-1103
Liu-Hinz C. I-215
Loarte A. II-723
Lohr J.L.T.C. II-893
Lok J. I-267
Lomas P.J. I-3,I-19,I-147,I-255,I-307, II-881,II-897
Longinov A.V. II-921,II-929,II-933,II-941
Lontano M. II-1087
Lopes Cardozo N.J. I-71,I-75,I-123,I-155
Lopez-Callejas R. I-483,III-1947
Lopez-Fraguas A. I-565,I-577
Loughlin M.J. I-167,I-251
Loureiro C. II-1063
Louvet P. III-2113,III-2125
Lovisetto L. I-463
Lowry C.J. I-239,II-723,II-727
Lozneanu E. III-1769
Luckhardt S.C. I-407,II-949
Luhmann Jr. N.C. I-363,I-179,II-1071,III-1939
Lukac P. III-2067,III-2129
Lukinov V.A. II-921,II-929
Luo C. I-615
Lyadina E. I-371
Lynch V.E. I-569,II-1417
Lynov J.-P. II-811,II-1283,III-1903,III-1907
Lyon J.F. I-525
Ma C.H. I-521,I-525
Maafa N. II-1083
Maas A.C. I-151,I-167,II-1031
Maaßberg H. I-493,I-497,I-505,I-509, I-549,I-569,I-581
Mace R.L. III-1819
Machida M. I-675
Maciel H.S. III-1835
MacLatchy C. I-215
Maeda H. II-1191
Maeda M. I-517,II-1159
Maehara T. I-79

Maekawa T. I-79,II-981
Maggi C.F. II-823
Magula P. I-219
Magyar G. I-283
Maier H. III-2001
Majeski R. II-839
Makino K. I-79
Malaquias A. II-1111
Maluyta D.D. II-1229
Mancuso A. I-545
Mandl W. II-1035
Manhood S.J. I-31
Manickam J. I-43,I-351,II-949
Mank G. I-155
Mansfield D.K. I-39
Manso M.E. I-231,II-1063
Mantica P. I-23,I-75
Marcus F.B. I-67,I-251,I-263,I-339,I-379, II-881,II-897
Margreiter D. III-2095
Märk T.D. III-2067,III-2071,III-2075,III-2095
Martin F. I-215
Martin G. I-175
Martin P. I-623,II-1361,III-1795
Martin R. I-639
Martin T.J. II-1393
Martin-Solis R. I-147
Martinell J.J. II-1461
Martines E. I-631
Mase H. III-1891,III-1985
Mast K.F. II-835
Matias J. I-231
Matsui T. III-2121
Matsukawa M. I-447
Matsumoto K. II-989,III-1961
Matsumoto Y. II-1225
Matsuoka K. I-513,I-517
Matsuoka M. I-171
Matsushima I. II-1225
Matsuura H. I-489
Matsuura O.T. III-1619
Matthews G.F. II-823
Matthieussent G. II-1297
Mattioli M. I-279,I-283,II-847
Mauel M.E. I-711
Mayberry M.J. II-893
Mayer H.-M. II-835
Maynard G. II-1245,III-2063
Mazur S. I-595,I-599
Mazzitelli G. I-295,I-463,II-1127
Mazzucato E. I-203,II-1055
McCarthy P.J. I-451,I-455,I-459
McCormick K. II-763,II-767,II-1163
McCracken G.M. II-779
McCune D.C. I-39,I-43
McGuire K.M. I-43,I-203,I-351
McKee G. II-839
McLoud W.S. II-1397
McNeill D.H. I-295,II-1127
McWilliams R. III-1935
Medley S.S. I-203
Medvedev S.Yu. I-319
Meigs A. I-211
Meis C. III-2113
Meister C.-V. III-2159
Melendez-Lugo L. I-483,III-1947
Melnick I.M. I-291
Merazzi S. I-557,I-589
Merkel P. I-585
Mertens V. I-451,II-743
Meyer R.L. III-2113
Mezzetti F. I-695
Michaud D. I-215
Michelsen P. II-1067,II-1283
Micozzi P. II-1525
Mieno T. III-1859,III-1919
Miklaszewski R. I-717
Mikoshiba H. III-1651
Miljak D.G. II-815
Minami T. I-79
Minardi E. II-1465
Minyaev O.A. I-471
Mioduszewski P.K. I-275
Mirnov S.V. I-47
Mirrashidi P. III-1993
Miura S. I-171
Miyakuni S. III-1709
Miyamoto T. I-659
Mizuno K. II-1191
Mizuno N. I-699
Mizuuchi T. I-489,II-1131
Mjølhus E. II-1279,II-1349
Mlynar J. I-219
Mohamed-Benkadda M.S. II-855
Mohanty S.R. II-1195
Moiseev S.S. I-707
Molinari V. III-2037
Monakhov I.A. I-47
Monier-Garbet P. II-847
Monterde P. II-1183
Monticello D.A. I-351,I-577
Moradshahi M. I-479
Morales G.J. I-135,III-1839
Moreau D. I-27,I-159,I-175,II-885, II-905,II-945
Moreira A. II-1063
Morera J.P. II-1421
Morgan P.D. I-3,I-119,I-255,I-307,II-1485
Morimoto S. I-521
Morin M. III-2055
Morita S. I-513,I-517
Moroz P.E. II-909
Morris A.W. I-31,I-411,I-423
Morsi H. I-3,I-255
Morsi H.W. I-19
Moser F. II-1497
Motojima O. I-521
Mroczkowski M. I-717
Muir D. I-59
Murakami M. I-521,I-525,I-529
Muraoka K. I-517,II-1159
Murawski K. III-1635
Murmann H.D. II-961
Mynick H.E. I-431
Myra J.R. I-91
Nagao K. III-1733
Nagasaki K. I-489,II-1131
Nagasawa T. III-1815
Nagashima K. I-83,I-87
Nagayama Y. I-351
Naito O. II-953
Naitou O. II-985
Nakach R. II-1409
Nakamura M. I-79,II-981
Nakamura Y. I-489,I-557
Nakasuga M. I-489,II-1131
Nambu M. III-1693
Nappi C. II-1313
Nardi V. I-695,II-1253
Naujoks D. II-843
Naumova N.M. II-1305,II-1317
Navarro A.P. II-933
Nave M.F.F. I-227,I-247,I-327,I-335, I-339,I-439
Nazikian R. I-203,I-431,II-1055
Neger T. II-1151
Neill G.F. I-227
Nejoh Y. III-1655,III-1799
Nemoto M. II-953,II-985
Nenovski P. III-1635

Neubert T. . . . III-1579
Neudatchin S.V. . . . I-59
Neuhauser J. . . . II-743,II-747,II-767
Neves J. . . . II-1063
Neyatani Y. . . . I-171,I-447
Nguyen F. . . . II-851
Niedermeyer H. . . . II-783,II-787
Nielsen A.H. . . . II-811
Nielsen P. . . . I-3,I-19,I-255,I-307
Nilson D.G. . . . II-1191
Ninomiya H. . . . I-447
Nishida Y. . . . III-1815,III-1927,III-1931
Nishikawa K.-I. . . . III-1579
Nishimura K. . . . I-513,I-517
Nishio R. . . . III-2121
Nishitani T. . . . I-171
Noda N. . . . I-403,I-513,I-517
Nonaka S. . . . III-2045
Nordlund P. . . . I-595,I-599
Norimine T. . . . III-1855
Nothnagel G. . . . I-415,II-795
Notte J. . . . III-1811
Novik K.M. . . . II-997
Nührenberg J. . . . I-553
Nunes F. . . . II-1063
Nycander J. . . . III-1903,III-1907
O'Brien D.P. . . . I-63,I-311,I-335,I-339
O'Brien M.R. . . . I-147,I-423,II-897,II-1341
O'Rourke J. . . . I-15,I-255,I-259,I-311, I-335,I-339,I-379
Obiki T. . . . I-489,II-1131
Ochando M.A. . . . I-99,II-791
Ochirov B.D. . . . II-1229
Oda T. . . . II-1191
Oda Y. . . . II-859
Odajima K. . . . II-1191
Ogawa T. . . . II-1191
Ohasa K. . . . II-1191
Ohkubo K. . . . II-989
Ohno N. . . . II-1115,III-1807
Øien A.H. . . . III-1997
Okabayashi M. . . . II-949
Okada H. . . . I-489,II-1131
Okada T. . . . II-1159,III-2099
Okamura S. . . . I-513,I-517
Ongena J. . . . II-1147
Ono M. . . . II-949
Oomens A.A.M. . . . I-71,I-267
Orishich A.M. . . . III-1689
Orsitto F. . . . I-295
Ortolani S. . . . I-623
Osborne T.H. . . . I-11,I-235
Osborne T.O. . . . I-243
Owadano Y. . . . II-1225
Oyevaar Th. . . . II-1091
Ozaki T. . . . I-517
Paccagnella R. . . . I-627
Pacher G.W. . . . I-475,II-755
Pacher H.D. . . . I-475,II-755
Pacios L. . . . I-299
Pakter R. . . . III-1697
Palladino L. . . . II-1207
Panaccione L. . . . I-295
Pantis G. . . . I-143
Parail V.V. . . . I-207
Pardo C. . . . I-99,I-299
Paris P.J. . . . II-1187,III-1863
Park C.W. . . . III-2133
Park H.K. . . . I-39
Park J.K. . . . III-2133
Park W. . . . I-351
Parker R.D. . . . I-427
Parlange F. . . . II-885,II-945
Parys P. . . . I-717
Pasini D. . . . I-279,I-283,I-331
Patel A. . . . I-291
Patel T.K. . . . I-291
Pättikangas T.J.H. . . . II-1005,II-1021
Paul S. . . . I-203,II-949
Pavlenko V. . . . II-1441
Pavlichenko O.S. . . . I-569,II-933
Pavlov I.P. . . . II-1025
Pavlov S.S. . . . II-921,II-933
Payan J. . . . I-107,II-1079
Peacock N.J. . . . I-291
Pech P. . . . II-1167
Pecquet A.L. . . . I-107,II-855,II-1421
Pécseli H.L. . . . II-811,II-1067
Pedit H. . . . III-1777
Pedrosa M.A. . . . II-791
Peebles W.A. . . . I-363,I-179,II-1071,III-1939
Pegoraro F. . . . I-139,II-1425,II-1429
Pégourié B. . . . I-103,I-159
Penningsfeld F.-P. . . . I-537
Pereira J. . . . II-1063
Pereverzev G.V. . . . II-961,II-1489
Persson H. . . . II-1369
Pestryakova G.A. . . . I-319
Peters M. . . . I-75
Petrov A.A. . . . I-47
Petrov M.P. . . . I-151,I-167,II-1031
Petrov V.G. . . . I-47
Petrov Y.V. . . . II-1219
Petrzilka V. . . . I-271
Petty C.C. . . . II-893
Peurrung A.J. . . . III-1899
Peysson Y. . . . I-27,I-159,II-885
Pfau R. . . . I-683
Pfirsch D. . . . II-1329,III-1753
Philipona R. . . . I-179
Philipps V. . . . II-827
Phillips P.E. . . . I-115
Pichal J. . . . I-667
Pickalov V.V. . . . II-1143
Piel A. . . . II-1199,III-1677,III-1843
Pierre T. . . . III-1879,III-1883,III-1915
Pietrzyk Z.A. . . . II-763
Piffl V. . . . I-713
Piliya A.D. . . . II-1203
Pinsker R.I. . . . II-893
Pironkova A. . . . III-2013
Pisarczyk T. . . . I-717
Plapp B.B. . . . III-1659
Platonov Yu.Ya. . . . II-1039
Pöckl M. . . . II-1163
Podda S. . . . I-463
Poll H.U. . . . III-2095
Ponomarenko A.G. . . . III-1689
Popa G. . . . II-1179,II-1561,III-1757,III-1969
Popel S.I. . . . II-993
Popov G.H. . . . III-1803
Porcelli F. . . . I-439,II-897,II-901,II-1469
Porkolab M. . . . II-893,II-965
Porte L. . . . I-119,I-163,I-407
Porter G.D. . . . II-751
Portnov D.V. . . . I-47
Poschenrieder W. . . . II-1167
Potempski S. . . . II-1537
Poutchy L. . . . II-847
Powell C. . . . I-695
Prasad G. . . . III-1575,III-1583,III-2021
Prater R. . . . II-893
Praxedes A. . . . II-1111
Praxmarer C. . . . III-2079,III-2083
Preische S. . . . II-949
Probert P. . . . II-839
Proshin M.A. . . . I-703
Prudsky V.V. . . . II-1345
Pryadko J.M. . . . II-1321
Puerta J. . . . II-1513

Pulker H.K. III-2149
Punithavelu A.M. III-2025
Punjabi A. II-863
Putvinskii S. I-167
Qin Y.W. I-223
Quallis A.L. I-525
Quéméneur A. I-107,II-1079
Radford G. II-727
Ramachandran H. I-135,III-1839
Ramos G. II-1461
Ramos J.J. I-407
Ramponi G. II-973
Ramsay D. II-1505
Ramsey A.T. I-39,I-203
Ran L.B. I-223
Rao N.N. III-1643
Rasmussen D.A. I-521,I-525
Rasmussen J.J. II-811,II-1283,III-1907
Rau F. I-569,I-581
Raus J. I-713
Rauth T. III-2075
Rawat R.S. II-1195,III-2141
Razdobarin G.T. II-1219
Razumova K.A. I-207,I-371
Reale A. II-1207
Rebut P.-H. II-731
Reiman A.H. I-577
Reiter D. II-739,II-747
Rem J. II-1425
Renberg P.U. II-1047
Renner H. I-493,I-501,I-505
Rensink M.E. II-751
Retterer J.M. II-1509
Rettig C.L. I-11,I-179
Rewoldt G. II-1437
Rey G. II-885
Reyna L.G. III-2103
Rhee C. III-2133
Rhodes T.L. I-179,II-1071
Riccardi C. III-2017
Rice W.K.M. III-1819
Richards B. I-115
Righi E. II-881
Rille E. III-2149
Rimini F. I-119,II-897,II-973
Ringler H. I-493,I-501,I-505,I-581
Rizzato F.B. III-1697
Roach C.M. II-1139
Roberts D.E. I-387,I-415,II-795,II-1397
Robinson D.C. I-31,I-399
Rodriguez L. II-933
Rodriguez-Yunta A. I-99
Roe G. I-639
Rognlien T.D. II-751
Rohde V. II-1199
Röhr H. II-743
Romanelli F. I-463,II-1437
Romannikov A.N. I-47
Rommers J.H. I-267
Roney P. II-949
Rosatelli C. II-1187
Ross D.W. I-115
Ross G.G. I-215
Rossi A. I-623
Roth J. II-831,II-1167
Roubin J.-P. I-175,II-1433
Rousculp C. III-1827,III-1831
Rowan W.L. I-115,I-211
Rubenchik A.M. II-1229
Rudyj A. II-783,II-787
Ruiz J. II-1513
Rupasov A. I-683
Rusbridge M.G. I-639,III-1725,III-1729
Rusbüldt D. I-155,II-775
Ruscanu D. II-1179
Rynn N. III-1935
Ryter F. I-7,I-195,II-889
Sabbagh S.A. I-43
Sabot R. I-103,II-1409
Sadler G. I-3,I-67,I-167,I-251,I-255,
I-263,I-439,II-881,II-1485
Sadowski M. I-691,II-1211,II-1215
Safronov V.P. III-2137
Sagar R. III-2141
Sagara A. I-513,I-517
Saha S.K. I-107,II-1079
Saibene G. II-723,II-727
Saito K. II-917
Sakakibara S. I-517
Sakamoto K. I-489
Sakamoto M. I-403
Sakanaka P.H. I-675,I-679,II-1233,III-1619
Sakasai A. I-87
Sakawa Y. III-1965
Sakharov A.S. II-1305,II-1317,II-1429
Sakharov I.E. II-997
Sakharov N.V. I-471
Sakurai S. II-859,II-1115
Salas A. I-577
Salashchenko N.N. II-1039
Salat A. I-573
Salmon N.A. II-1107
Salomaa R.R.E. II-1005
Salvetti A. II-1241
Samain A. II-851,II-855,II-1421,II-1433
Samm U. II-759
San Jose M.A.G. II-1183
Sanchez J. II-1075
Sandeman J. III-1725
Sandulovíciu M. III-1769,III-1957,III-2029
Sano F. I-489,II-1131
Santiago M.A.M. I-675,III-1785
Santos J. II-1063
Sanuki H. I-513,I-517
Saoutic B. I-175,II-885,II-905
Sardei F. I-505,I-509,I-549
Sarksyan K.A. I-525
Sartori R. I-3,I-307
Sasao M. I-67
Sato K.N. I-403,II-1191
Sato M. I-489,I-521,II-953
Sato N. III-1705,III-1709,III-1765,III-1919
Sato N.Y. III-1705,III-1709,III-1985
Sato T. III-1631,III-1965
Sattler S. II-1099
Sauer K. III-1571
Sauthoff N. II-949
Savrukhin P. I-371
Sawada K. II-981
Sawahata M. II-985
Saxena Y.C. III-1575,III-1583,III-1847,
III-1867,III-2021
Sayal V.K. III-1823
Sborchia C. I-167
Scafati A. II-1207
Schamel H. II-1385,III-1717
Scheffel J. I-663
Scheier P. III-2071,III-2095
Schep T.J. II-1425
Schiavi A. I-619
Schina G. II-1207
Schissel D.P. I-11,I-235
Schivell J. I-203
Schlanges M. III-2091
Schlüter H. III-1981,III-2145
Schlüter M. II-1449
Schmid M. I-327
Schmidt G.L. I-59,I-255,I-307
Schmidt H. I-683
Schneidenbach H. III-2009

Schneider R.S. II-747,III-1697
Schneider W. I-459
Schoch P.M. I-115
Schoon N. II-1147
Schram D.C. II-1143
Schrittwieser R. III-1757,III-1773
Schüller F.C. I-71,I-123,I-155,II-1091
Schulz D. I-683
Schumacher U. II-835
Schupfer N. III-1785
Schwab C. I-549
Schweinzer J. II-763,II-1163
Schwelberger J.G. I-529
Schwenn U. I-557
Scott B.D. II-1449
Scott S.D. I-39,I-43,I-203
Scoville J.T. I-187
Segre S.E. I-127,I-295
Seidel U. I-451,I-455
Seki M. II-953,II-969,II-985
Seki S. II-949
Selenin V.L. II-1203
Semenov I.B. I-47
Semenov V.V. II-1219
Sen A. II-1301
Senju T. I-489
Senties J.M. II-1183
Seraydarian R.P. I-183,I-275
Sergeyev A.A. I-111
Serichol N. III-1607
Serra F. I-231,II-1063
Sesnic S. II-949
Sethia G.C. III-2021
Shah H.A. II-1317
Shakhovets K.G. I-471
Shapiro V.D. II-1271
Sharapov V.M. I-47
Sharma R.P. II-1325
Sharma S.K. III-1567,III-1595
Sharma S.R. III-1823
Shasharina S.G. I-541
Shatalin S.V. II-997
Shats M.G. I-525
Shcherbinin O.N. II-997,II-1025
Sheridan T.E. III-1895
Sherwell D. II-795,II-1397
Shevchenko V. II-1271
Shi M.L. I-395
Shigueoka H. I-679,III-1619
Shiina S. II-917
Shimada T. II-917
Shinno H. III-2155
Shirai H. I-83
Shirokikh A.V. II-1229
Shishkin A.A. I-569
Shivarova A. II-1353,III-2013
Shmaenok L.A. II-1039
Shmykov V. II-1557
Shoji T. III-1965,III-2121
Shoucri M. II-807,II-1005,III-1721,III-1741
Shoyama H. III-1733
Shukla P.K. II-1293,II-1445,III-1587, III-1611,III-1643
Sibley A. I-327
Sicha M. III-1989
Silva A. I-231,II-1063
Simonchik L.V. II-1203
Simonetto A. I-443
Simonini R. I-259
Sindoni E. III-2017
Sing D.C. I-115
Singer C. I-131
Singh A.K. III-1847,III-1867
Singh D.P. II-1241
Singh S. II-1337,III-1603,III-1911
Sinman A. I-651
Sinman S. I-651
Sipilö S.K. II-1021
Sips A.C.C. I-259
Sitenko A.G. II-1287
Skalny J.D. III-2129
Skiff F. III-1863
Skladnik-Sadowska E. II-1211
Skorik M.A. III-1973,III-1977
Skovoroda A.A. II-1521
Sluijter F.W. III-1745
Smeulders P. I-251,I-327,I-331, I-335,I-339,I-439
Smith D. III-2083
Smith G.R. II-1275
Smith R. I-163
Smith R.J. I-407
Snipes J.A. I-39
Snytnikov V.N. III-1689
Sobehart J. III-2103
Solano E. I-211
Söldner F.X. II-957,II-961,II-1063
Soltwisch H. I-403
Sørensen J. II-839
Sosenko P.P. II-1287
Sotnikov S.M. I-47
Spangler S.R. III-1659
Spathis P.N. I-323
Squire J.P. II-965
Srivastava M.K. II-1257
Srivastava M.P. II-1195,III-2141
St.-Onge M. I-215
Stäbler A. II-743
Staikov P. III-2041
Staines G.W. I-647
Stallings D.C. II-913
Stamate E. II-1179
Stamp M.F. I-119,I-307,I-311,I-335, I-339,II-727,II-819
Stankiewicz R. II-1469,II-1537
Stanojevic M. II-1171,III-1761
Stansfield B. I-215
Start D.F.H. I-3,I-19,I-255,I-327, II-881,II-897,II-901
Stenflo L. II-1533,III-1587
Stenzel R.L. III-1827,III-1831,III-1871
Stepanov A.Yu. II-997
Stepanov K.N. II-933
Stephan K. III-2095
Steuer K.-H. II-743,II-961
Stevens J. II-949
Stöckel J. I-219
Stork D. I-167,I-311,I-339,I-379,II-897
Stotler D. I-43
Strait E.J. I-435
Stratton B.C. I-203
Stratton B.E. I-39
Strel'tsov A.P. II-1229
Stroth U. I-7,I-35,I-195I-509,
Stubberfield P.M. I-15,I-63,I-255,I-263,I-311
Su J.J. II-1271,III-1627
Subbotin A.A. I-367
Suchy K. II-1501
Sudarshan A. III-1567,III-1595
Sudo S. I-489,II-1131
Suemitu H. II-981
Suganuma K. II-985
Sugawara M. III-2099
Sugimoto H. II-1405
Sugimoto M. III-1887
Sumini M. III-2037
Summers D.D.R. I-3,I-307,I-335,II-723, II-727,II-779,II-823
Summers H.P. II-823,II-1035
Sun S.Q. I-223

Sunka P. I-713
Surendra M. III-1993
Sutcliffe M. III-1725
Suyazov N.V. I-707
Suzuki K. III-2121
Sykes A. I-31,I-399
Synakowski E.J. I-39,I-203
Szczurek M. I-717
Szigeti J. I-303
Szydlowski A. I-691
Tabares F.L. I-99
Tägle J.A. II-723
Taglieri G. II-1207
Takahashi C. I-513,I-517
Takahashi H. II-949
Takahashi S. II-985
Takamura S. II-859,II-1115,III-1807
Takasa A. II-985
Takeiri Y. I-517
Takenaga H. I-517,II-1159
Takeuchi H. I-171,II-953,II-969,II-985
Takita Y. I-513,I-517
Takiyama K. II-1191
Takizuka T. I-51
Talasman S.J. III-1957
Talvard M. II-855,II-1103,II-1421
Tamano T. III-1631
Tamaoki M. III-1733
Tammen H.F. II-1091
Tanabe T. III-1985
Tanaka M. II-1357,III-1733,III-1855, III-1859,III-1887
Tanaka S. I-79,II-981
Tanaka T. II-839
Tang W.M. II-1437
Tanga A. I-3,I-19,I-255,I-443,II-881,II-897
Tani K. I-171
Tanizuka N. III-1651
Tanzi C. II-973
Tarditi A. II-1187
Taroni A. I-3,I-15,I-19,II-727,II-901
Tartari U. II-1087
Tashaev Y.N. III-2137
Tataronis J.A. II-909,II-1009
Tavares-Azevedo M. I-675
Taylor G. I-39,I-203,I-351
Taylor T.S. I-11,I-55,I-243,I-435
Telesca G. II-771,II-1147
Tennfors E. I-607
Terreault B. I-215
Terumichi Y. I-79,II-981
Teubel A. I-537
Theimer G. II-783,II-787
Thomas C.E. I-525
Thomas P.R. I-239,II-727,II-819
Thomsen K. I-19
Thomsen K. I-3,I-63
Throumoulopoulos G.N. I-143
Tibone F. I-15,I-19,I-311,I-335,I-339
Tichy M. III-1989
Tielemans A.J.H. I-267
Timm R. III-1677
Timofeev A.V. I-703,II-1521
Tobita K. I-171
Todoroki J. I-513
Toi K. I-513
Tokar M.Z. I-95,II-739,II-759
Tolstyakov S.Yu. II-1219
Toma M. III-2029
Tomie T. II-1225
Tonon G. I-27,II-885,II-945
Torres-Silva H. II-1233
Torvén S. II-1175,III-1875
Toshi K. I-489
Towner H.H. I-39
Tracy E. II-937
Tran M.Q. III-1863
Tribaldos V. II-1001
Truc A. I-107,II-1079
Tsintsadze L.N. II-1485
Tsois N. II-767
Tsui K.-H. I-675
Tsytovich V.N. II-993,II-1271,II-1321,II-1333
Tubbing B.J.D. I-15,I-167,I-311,I-335, I-339,II-897
Tuchida K. III-2121
Tudisco O. I-23,I-463
Tugarinov S.N. I-47
Turnbull A.D. I-243,I-435
Turner M.F. I-31
Tuszewski M. I-431
Tutter M. I-497,II-1001
Uberoi C. III-1663
Uchino K. I-517,II-1159
Uckan T. I-525,I-529
Ueda M. I-513,I-517
Uehara K. II-1473
Uehara M. III-1835
Umesh G. III-1943
Urrutia J.M. III-1827,III-1831
Ushigusa K. I-447,II-953,II-969,II-985
Vahedi V. III-1993
Valanju P.M. I-115,I-211
Valencia-Alvarado R. I-483,III-1947
Valeo E. II-949
Vallet J.C. II-847,II-855,II-945,II-1421
Valovic M. I-31
Van Belle P. I-67,I-167,I-251,II-881
Van Blokland A.A.E. II-1091
Van Bruggen-Kerkhof M.J. III-1745
Van de Pol M.J. II-1059
Van Dijk G. I-267
Van Gelder J.F.M. I-267
Van Houtte D. I-27,II-885,II-945
Van Lammeren A.C.A.P. I-123
Van Milligen B.Ph. I-123
Van Oost G. II-771,II-1147
Van Toledo W. II-1111
Van Vurren G.W. I-387,I-415
Vannucci A. I-419
Varandas C.A.F. II-977,II-1111
Varela P. I-231,II-1063
Varias A. I-561,I-565
Varma R.K. III-2025
Vaselli M. II-1241
Vasilescu C. III-2049
Vasiliev V.I. I-471
Vega J. I-99,I-299
Veres G. I-303
Verga A.D. II-1325
Verheest F. III-1623
Verma A. II-863
Verreck M. I-123
Vietzke E. II-827
Vila J. II-1183
Villain J.P. III-1591
Villard L. I-343
Villasenor J. II-965
Vladimirov S.V. II-993,II-1333
Vlases G. II-723,II-727,II-735
Vogl G. III-2149
Voitsekhovich I.A. I-207
Volkov V. I-371
Vollmer O. I-7
Von Goeler S. II-949
Von Hellermann M.G. I-63,I-263,I-439, II-881,II-1035,II-1485
Voss K. II-949
Vshivkov V.A. III-1639
Wade M.R. I-275

Wagner F. I-7,I-195,I-231
Wahlberg C. I-603
Waidmann G. I-95,I-359
Wakatani M. I-489,I-557,II-1131
Walder G. III-2095
Walsh M.J. I-31
Walters P.E. II-795
Wang E.Y. I-223
Wang J. I-695
Wang Z.H. I-215,I-223
Ward D.J. I-3,I-19,I-255,I-343,I-467
Warrick C.D. II-897
Watkins M.L. II-731
Watkins N. I-251
Weiland J. II-1441
Weinlich M. II-787
Welander A. I-595
Weller A. I-549
Werthmann H. II-925
Wesson J. II-897
West W.P. I-275
White R.B. I-431
Wieland R.M. I-43,I-203
Wilgen J.B. I-521,I-525
Wing W.R. I-521
Winkler C. III-2095
Winter H. II-1163
Winter J. I-11
Wising F. I-391
Wittenberg R.W. II-1477
Wobig H. I-569,I-581,II-867
Wolf G.H. I-95
Wolf U. II-1385
Wolfe S. II-953
Wolff H. II-1167
Wolle B. II-1035,II-1485
Wong K.-L. I-431
Wootton A.J. I-91,I-115
Woskov P.P. I-407
Woyke W. I-451,I-455
Wunderlich R. I-459
Wurtele J.S. III-1811
Wyller J. II-1309
Xie J.K. I-347
Xu S. I-647
Xu Y. I-615
Yadav L.L. III-1823
Yaguchi K. I-489
Yakimenko I.P. I-707,II-1377
Yakovenko Yu.V. I-391
Yamada H. I-513,I-517,I-521
Yamada I. I-513,I-517
Yamagiwa K. III-1859
Yamaguchi H. I-699
Yamamoto T. II-985
Yang H.R. I-223
Yang J.W. I-223,I-395
Yang Q.W. I-223
Yang S.K. I-223
Yang X.Z. I-363
Yao L.H. I-223
Yao Q. III-1713
Yi P. I-615
Yu C.X. I-363
Yu M.Y. II-1533
Yuan C.J. I-223
Yugami N. III-1927,III-1931
Zacek F. I-219
Zagorodny A.G. II-1377
Zaitsev F.S. II-1341
Zakharov A.P. I-47
Zakharov L.E. I-367
Zakharov Yu.P. III-1689
Zakouril P. III-1989
Zambreanu V. I-687
Zanza V. I-127,I-295
Zaporowski B. III-2005
Zarnstorff M.C. I-39,I-43
Zastrow K.-D. I-595,I-611
Zebrowski J. I-691,II-1215
Zehrfeld H.P. I-459
Zelazny R. II-1537
Zenevich V.A. III-2087
Zerbini M. I-127,I-463
Zhang G.Y. I-395
Zhang P. I-615
Zhang S. I-615
Zhang S.X. I-223
Zhao S.J. I-363
Zhelyazkov I. II-1517,III-1635,III-2041
Zheng L.-J. I-553
Zheng Y.Z. I-223
Zhong Y.Z. I-395
Zhuravlev V. II-1075
Zhykharsky A. II-1553,II-1557
Zielinski J.J. I-525,I-529
Zilker F. II-1063
Zohm H. I-231,I-235,I-243,II-743
Zoita V. I-687
Zoler D. III-2117
Zoletnik S. I-303
Zolfaghari A. I-163,I-335,I-339,I-407
Zolotukhin A.V. I-569
Zöpfel S. I-509
Zuo H.N. I-223
Zurro B. I-99,I-299,II-1135
Zushi H. I-489,II-1131
Zvonkov A.V. II-1521
Zweben S.J. I-43,I-203,I-431
Zwingmann P.W. I-311,I-335,I-339